International E-Conference on
Recent Advances in Material Science
and Nanotechnology
Date : 7 th to 9 th Feb 2021

IJSRST

SHETKARI SHIKSHAN SANTHA'S.
ARTS, COMMERCE&SCIENCE COLLEGE
MAREGAON. DIST.-YAVATMAL. 445303   (ESTD-1991)

**NAAC
ACCREDITED
WITH B+ GRADE
(CGPA 2.51)
ISO 9001: 2015
CERTIFIED**

Organised by
Department of Physics, Arts, Commerce and Science College,
Maregaon, Maharashtra, India
In Association with
Department of Physics, P.N. College, Pusad, Maharashtra, India

INTERNATIONAL JOURNAL OF SCIENTIFIC

RESEARCH IN

SCIENCE & TECHNOLOGY

**TECHNO SCIENCE
ACADEMY**
THE INTERNATIONAL OPEN ACCESS PUBLISHER

INTERNATIONAL E-CONFERENCE
ON
RECENT ADVANCES IN MATERIAL SCIENCE AND NANOTECHNOLOGY

(RAMAN-2021)

7th - 9th February 2021

MESSAGE

I am extremely happy to know that the Department of Physics is organizing an International e-Conference in association with Department of Physics, Phulsing Naik Mahavidyalaya, Pusad on Advances in Material Science and Nanotechnology (RAMAN-2021) on February 7-9, 2021 and bringing out e-proceeding on the occasion. I hope that the conference will be meaningful, purposive, relevant and credible worth remembrance and will be the best platform for dealing with all issues related to the field.

The format of the conference will provide immense opportunities for interaction among the participants and the resource persons and detailed discussion in the conference will motivate the young, budding scientists, research scholars and students.

I convey my best wishes to the organizers and all those who are associated with this conference.

I wish the conference a grand success.

Mr. Jivanpatil Kapse
President
Shetkari Shikshan Sanstha, Maregaon

MESSAGE

I am immensely delighted to know that the Department of Physics is organizing an International e-Conference in association with Department of Physics on Recent Advances in Material Science and Nanotechnology (RAMAN-2021) during February 7-9, 2021 and bringing out e-proceeding to commemorate the occasion.

This conference will provide a unique platform to all the participants to widen their knowledge domains and to explore and exchange new ideas, techniques and models in the area of material Science. It will motivate young scholars and researchers in a meaningful way. It is indeed a fulfilling and enriching experience to organize an event of this scale on e-platform where great minds will come together. The conference will offer opportunity for in depth talks and discussions which will go a long way to help create an academic ambience in the Department and the college.

Further, this conference will also bring together the renowned experts from the core field and other allied areas to a common platform to deliberate on such an important theme and forge linkages and bonds for mutual research benefits.

I congratulate the Department of Physics for organizing RAMAN-2021 and wish them all success in this scientific endeavor.

Dr. A. N. Gharde
Chairman, RAMAN-2021
Principal
Arts, Commerce & Science College, Maregaon

MESSAGE

I am extremely delighted to welcome you to International **e-Conference on Recent Advances in Material Science (RAMAN-2021)** being organized by the Department of Physics, Arts, Commerce & Science College, Maregaon in association with Department of Physics, Phulsing Naik Mahavidyalaya, Pusad during February 7-9, 2021.

This conference will provide an opportunity on a vibrant and dynamic e-platform to all participants to exchange information and new advancements of the concerning fields among scientists, engineers, industrialists, researchers and academicians. The conference is focus mainly on Material Science and potential applications of Nanotechnology in everyday life for the betterment of human society. I hope this conference will provide a unique opportunity for teachers, educators, experts and scholars of higher education from all over the world to convene and share novel ideas on the field and trends in higher education development.

Further, the conference is organized with an aim, to exchange new thoughts and share the latest knowledge in field of material science and Nanotechnology by the eminent experts and to motivate budding Scientist and young researchers. I trust all the participants and delegates would be with some value addition to their current knowledge after attending the conference.

It has been my personal endeavor in a very small way by organizing this conference to highlight the importance of the field. The Proceedings brought out include a number of original research papers received from various regions of the world. It is heartening to note that conference has excellent response. We have received more than 115 full length papers of high standard in addition to keynote address, 4 plenary talk and 9 invited talks by the experts. More than 160 papers will be displayed for interactive oral presentation.

I wish the RAMAN-2021 will be an enjoyable, memorable and productive for the participants. I believe all delegates will benefit substantially from the conference through the presentations of expert speakers and exchanges of ideas with one another.

I am grateful to all the renowned speakers and delegates for their participation that makes this conference possible. I thank the management and all who have contributed in their own way to make this conference a success.

Looking forward for you all to come enhance your experience and to make this conference a success!

Dr. N. R. Pawar
Convener, RAMAN-2021

Dr. Mahavir Singh

Chief Scientist, CSIR-National Physical Laboratory, Dr. K. S. Krishnan Road, New Delhi

Welcome Message

International E-Conference on Recent Advances in Material Science and Nanotechnology, February 7-9, 2021 | Maregaon, Maharashtra, India

It is with great pleasure that I extend a warm welcome to all the participants of RAMAN 2021 International E-Conference on Advances in Material Science and Nanotechnology to be held in the beautiful city of Maregaon, Maharashtra, February 7-9, 2021. Just to underline how Materials and Nanotechnology represent a very promising role to develop novel economic and environmentally friendly industrial processes. Thus, the adjective sustainable appears more appropriate for novel industrial processes, for which both economic and environmental aspects must be considered if we want to remove relevant drawbacks of some current processes, preserving the added value and having real application perspectives. To achieve this goal, a multidisciplinary approach is necessary to be able to revise critically the existing literature and develop new ideas and collaborations focused to open new scientific courses.

The quest for knowledge has been from the beginning of time but knowledge only becomes valuable when it is disseminated and applied to benefit humankind. It is hoped that Raman 2021 will be a platform to gather and disseminate the latest knowledge in recent advancements in emerging areas of diversified research fields covered during this conference. Academicians, Scientist, Researchers will be able to share and discuss new findings and applications of engineering and science. I hope that participants enjoy the conference and have a memorable experience at Maregaon. It is envisaged that the intellectual discourse will result in future collaborations between universities, research institutions, and industry both locally and internationally. From this point of view, Raman 2021 represents an exciting opportunity to meet different competencies and establish contacts focused to develop new research collaborations, Thus, welcome and enjoy the Meeting!

DR. F. C. RAGHUWANSHI

Dean, Faculty of Science & Technology

SGB Amravati University

MESSAGE

I am pleased that Department of Physics, Arts, Commerce and Science College, Maregaon in Association with Department of Physics, Phulsing Naik Mahavidylaya, Pusad is organizing an International e-Conference on "Recent Advances in Material Science and Nanotechnology (RAMAN-2021) on February 7-9, 2021.

The conference will provide a unique platform for students, academician and researchers in the field of Material Science and Nanotechnology to interact and update themselves with the recent advancements. Novel research is being carried out in this field worldwide and I am sure it will revolutionize the areas of material science.

The conference will also provide immense opportunities for interaction among the participants and the resource person and learning experience for students and academician and enable them to move forward in the field of material science and nanotechnology.

RAMAN-2021's goal is to bring together scientists, researchers and academician from all over the world to present and exchange their knowledge, thoughts and novel ideas relating to the materials. It promotes top level research and to globalize the quality research in general, thus making discussions, presentations more internationally competitive and focusing attention on the recent outstanding achievements in the field of Material Science and Nanotechnology, and future trends and needs.

On behalf of the Conference, it is my pleasure to invite all of the great scientists, academicians, young researchers, Business delegates and students from all over the world to attend the International e-Conference RAMAN-2021 on February 7-9, 2021

I wish the Conference a grand success.

No./ PNM

Date 05.02.2021

Message

It gives me immense pleasure to know that **Shetkari Shikshan Santha's Arts, Commerce And Science College, Maregaon** is organizing the 'International E – Conference On Recent Advances In Material Science And Nano-Technology' in association with the **Department Of Physics, Phulsing Naik Mahavidyalaya, Pusad**. It is a matter of appreciation that the college in a rural and tribal region is endeavoring to provide an international platform to publish the research work of science community in this pandemic situation of Covid 19.

In this background the deliberation of the conference will definitely bring out recent advances in material science and nano-technology.

I congratulate all the members of the society, the principal and all faculty members who are associated with the most excellent academic activity. I extend my warm greetings to the delegates and the orgenisers and wish the conference and souvenir a grand success.

(Prof. Dr. A B Patil)

Offg. Principal

Phulsing Naik Mahavidyalaya.

Pusad

RASHTRASANT TUKADOJI MAHARAJ NAGPUR UNIVERSITY, NAGPUR
POST GRADUATE TEACHING DEPARTMENT OF PHYSICS
MJF University Campus, Amravati Road, NAGPUR 440033

O.P.Chimankar   Ph.No.(0712) 2041093,2042086 Professor & Head

_____
_
**(Established by government of Central Provinces Education Department by Notification No.513 Dated the
1st of August 1923 & Presently a State University governed by Maharashtra Public Universities Act, 2016
(Mah. Act No. VI of 2017)**

Date: 06/ 01 /2021

Message

`   I am happy to know that Department of Physics, Arts, Commerce & Science College, Maregaon in association with P. N. College, Pusad are organizing 3 days International E-Conference on Recent Advances in Materials Science and Nanotechnology (RAMAN-2021) on 7-9 February 2021. I am also pleased to know that the organisers are bringing out a souvenir & publication of research papers from well reputed journal on this occasion and invited the applications for Outstanding Academic Excellence award from young researchers. This would motivate the researcher of young minds.

I hope that the deliberations by the learned & eminent speakers are bound to bring well meaning thoughtful preposition which will be of long term relevance to the society. The modern invention in the advanced field of science & multidisciplinary nature of applications will be discussed in the conference. I sure that the sessions will add to the knowledge of the participants & also give them modern view to look at the field & it would be applicable to betterment of society.

I extend my best wishes for successful International E-Conference.

Vidya Prasarak Mandal's

Registered Under B.P.T. Act 1950, No. F/27 Yavatmal Society Registration No. 122 of 1955-56

AMOLAKCHAND MAHAVIDYALAYA

Godhani Road, Umarsara, Yavatmal- 445001

DEPARTMENT OF PHYSICS

Dr. Ajay B. Lad	**Contact Details**
Professor & Head, PG Dept of Physics	**E-mail:drajay_lad@rediffmail.com**
Chairman, BoS(Physics) SGBAU	**drajaylad71@gmail.com**
President, IAPT, Maharashtra(RC-08)	**(M) +919822460072, +917843048326**

<u>Message</u>

I am glad to know that Department of Physics, Arts, Commerce and Science College, Maregaon (Road) organizing the International Conference on 'Recent Advances in Material Science and Nanotechnology (RAMAN-2021)' during February 7-9, 2021.

Today the problem of Society based research is the major concern for the India as well as for the world. Researchers in the field of Materials Science can open the gateway of innovation and theymay help to solve these problems.Such types kind of conferences regarding these current issues are appreciable. I hope RAMAN-2021 will discuss the various related issues and bring out the fruitful discussions, conclusions and innovative suggestions.

I am also certain that RAMAN-2021 is going to form new multicultural and interdisciplinary scientific bonding's amongst the Indian andworld community which make them as whole.

My heartily congratulation to the organizers of RAMAN-2021 and my best wishes to them.

As a Chairman of BoS Physics, SGB Amravati University I welcome all the delegates and I wish them all the success of RAMAN-2021.

With Best Regards

(Dr. Ajay Lad)

DEPARTMENT OF PHYSICS

SANT GADGE BABA AMRAVATI UNIVERSITY, UNIVERSITY CAMPUS, NEAR TAPOVAN AMRAVATI-444602 (MS), INDIA

NAAC A Grade with CGPA 3.07 3rd Cycle w. e. f. 20-January 2016

Dr. S. K. Omanwar
UGC-BSR-Fellow
Sr. Professor
(HAG Scale)

Website: www.sgbau.ac.in   Phone : 0721-26662279, 49 Extn. 269
Fax: 0721-2662135, 2660949   Res : 0721-2676100 Cell: 094228 56844
E-mail: omanwar@sgbau.ac.in, omanwar@rediffmail.com

MESSAGE

At the outset I congratulate the organizing team led by Dr. N. R. Pawar for the unique and ever charming event RAMAN-21. I reminded Sir C V Raman the first Nobel Laurette of our land. Here, the RAMAN-21 stands for **Advances in Material Science and Nanotechnology-2021.** I strongly feel that in the changing global economic scenario, there is a need of organizing such a conference on the emerging issue like **'Recent (RAMAN-2021)'.**

I am confident that this event will deliberate over the challenges, opportunities and new gateways for innovation and invention in the field of research and development under the umbrella of materials Science and Nanotechnology. The development of recent advanced materials with desired characteristics has been playing a critical role in the growth of material science and Nanotechnology. India is currently developing highly talented human resource to meet future challenges in the area of Material science and Nanotechnology. The aim of RAMAN-2021 is to promote and encourage research activities in our country in the field of Material Science and Nantechnology.

I am confident that the participants and experts will take into consideration the various aspects of global as well as local challenges, and come forward with enduring, fruitful result so that the expectations of the organizers get fulfilled with regard to making this event as a vibrating and dynamics platform for the Scientist, academia and researchers. I convey my gracious wishes to the organizing team, participants and delegates of the conference for a grand success.

Last but not least, I appreciate the efforts of the team led by Dr. N. R. Pawar to schedule this event since "Good Planning is half done". Congratulations.

Regards,

S. K. Omanwar

Residance Address   104-B, saibhakti Appartments, Samartha Colony, Amravati-444606 (M.S.), India
Phone : 0721-2676100 Cell: 094228 56844 E-mail: omanwar@rediffmail.com

X

प्रो० देवराज सिंह
निदेशक
प्रो०राजेन्द्र सिंह (रज्जू भइया) भौतिकीय विज्ञान
अध्ययन एवम् शोध संस्थान
Prof. Devraj Singh
Director
Prof. Rajendra Singh (RajjuBhaiya) Institute
of Physical Sciences for Study and Research

वीर बहादुर सिंह पूर्वाञ्चल विश्वविद्यालय,
जौनपुर- 222003 (उ. प्र.)
Veer Bahadur Singh Purvanchal University,
Jaunpur 222003 (U.P.)
E-Mail.:devraj2001@gmail.com
Mob.: +91-9810549461

MESSAGE

It gives me immense pleasure to know that Dr. N. R. Pawar is organising International e-Conference on Recent Advances in Material Science and Technology (RAMAN-2021) at Art, Science and Commerce College, Maregaon, Yavatmal, M.S. during 7th to 9th February, 2021.

The topic of e-conference is of much importance and relevance today as new materials have developed for the technological development. There is need to develop an atmosphere among budding researchers, scientists and technocrats. I do hope that deliberations of the e-Conference would be able to present a definite action plan in this context.

I am sure that this conference brings together the knowledge and novel research with diverse experiences and orientations. I wish to inform that the young researchers and academia to explore new ideas and links that will Wisden our research collaborations.

The conference will also provide an opportunity to the scientific community to deliberate at the international level over a wide range of topic.

My sincere and best wishes for the success of the e- Conference.

Devraj Singh
Director & Professor
Prof. Rajendra Singh (Rajju Bhaiya)
Institute of Physical Sciences for Study
and Research
Veer Bahadur Singh Purvanchal
University
Jaunpur-222003, India

Patron

Mr. Jivanpatil Kapse

Chairman, Shetkari Shikshan Sanstha, Maregaon

Co-Patrons

Mr. Adv. Sudhir J. Damle

Secretary, Shetkari Shikshan Sanstha, Maregaon

Co-Convener

Prof. Dr. P. D. Bageshwar, M. M. College, Darwha Dr. D. R. Bijwe, G. S. Tompe College, Chandur Bazar Dr. Amit Bansod, Dr. Ambedkar College, Nagpur

Prof. R. P. Gadpayale, ACS College, Maregaon

Organizing Secretory

Dr. A. N. Gharde

Principal

ACS College, Maregaon

Prof. P. T. Hamjade

HOD, Physics

P. N. College, Pusad

Dr. N. R. Pawar

HOD, Physics

ACS College, Maregaon

International Advisory Committee

- ✓ Dr. Nico F. Declercq, France
- ✓ Dr. Lehlohonolo F. Koao, South Africa Dr. Abdul Hakeem Deshmukh, China Dr. Y. K. Mishra, Germany
- ✓ Dr. Shivakant Shukla, Madrid Spain Dr. Bogumil B. J. Linde, Poland
- ✓ Dr. V. V. Petrov, Russia Dr. Andrei Dukhin, USA Dr. Priev Abba, Israel
- ✓ Dr. Luis Elvira, Madrid Spain Dr. Christ Glorieux, Belgium Dr. Zheng Fan, NTU, Singapore
- ✓ Dr. Lingcai Zhou, Vienna, Austria
- ✓ Dr. F. C. Raghuwanshi, Dean Faculty of Science & Technology, SGB Amravati University
- ✓ Prof. R. R. Yadav, Former VC, Purvanchal University Prof. V. A. Tabhane, Pune University
- ✓ Dr. Mahavir Singh, CSIR-NPL, New Delhi

- ✓ Prof. S. K. Omanwar, SGB Amravati University Prof. O.P. Chimankar, RTM Nagpur University Prof. S. J. Dhoble, RTM Nagpur University
- ✓ Dr. S. R. Aswale, Principal and Former Finance & Accounts Officer, SGB Amravati University
- ✓ Dr. Rita Paikaray, Ravenshaw University, Cuttack Prof. Devraj Singh, Purvanchal University, Jaunpur Dr. Yudhishter Kumar Yadav, CSIR-NPL, New Delhi Dr. P. K. Yadawa, Purvanchal University, Jaunpur Dr. Kishor Rewatkar, Dr. Ambedkar College, Nagpur Dr. (Mrs.) N. S. Dhoble, Sewadal Mahila Mv., Nagpur Prof. A. B. Lad, Chairman BoS Physics, SGBU, Amravati Dr. V. B. Pawade, LIT, RTM Nagpur University
- ✓ Dr. Ganesh Nath, V. V. S. University, Burla

National Advisory Committee

- ✓ Dr. S. R. Vadrabade, Gawande College, Umarkhed Dr. G. G. Muley, SGB Amravati University
- ✓ Dr. S. A. Waghuley, SGB Amravati University Prof. N. L. Jadhao, Bhartiya Mv. Amravati
- ✓ Dr. Umakant Thakare, Gilani College, Ghatanji Prof. G. T. Lamdhade, Vidyabharti Mv., Amravati
- ✓ Dr. Giridhar Mishra, Purvanchal University, Jaunpur Dr. K. Sakthipandi, Sethu Institute of Tech., Madurai Dr. K. K. Pandey, Sharda University, Noida
- ✓ Dr. A. U. Bajpeyee, ACS College, Amravati Dr. V. D. Kapse, ASC College, Chikhaldara Dr. G. R. Dhokane, ASC College, Chikhaldara Dr. V. S. Kalyamwar, Bharatiya Mv. Amravati Dr. R. R. Risodkar, R. A. College, Washim
- ✓ Dr. C. S. Ulhe, Yashwant Chavhan Mv. Mangrulpir Dr. J. N. Ramteke, SMM College, Nagpur
- ✓ Dr. Deoram V. Nandanwar, SMM College, Nagpur Prof. D. S. Chavhan, Amolakchand Mv., Yavatmal Dr. V.K. Jadhao, B. P. Science College, Digras Prof. K. K. Hurde, M. M. College, Darwha
- ✓ Dr. Pravin Chandak, B. P. Science College, Digras Dr. Kartik Shinde, N.S. College, Bhadrawati
- ✓ Prof. R. A. Patil, S.S.S.K.R. Innani College, Karanja Dr. G. A. Aghalte, L.T. College, Wani
- ✓ Dr. S. S. Aswale, L. T. College, Wani Dr. V. R. Bhat, L.T. College, Wani
- ✓ Dr. P. S. Deole, G. S. Tompe College, Chandur Bazar Dr. D. R. Bijwe, G. S. Tompe College, Chandur Bazar Dr. A, A, Mistry, Anand Niketan College, Waora
- ✓ Dr. S. A. Shah, Anand Niketan College, Waora
- ✓ Dr. Nilesh Ugemuge, Anand Niketan College, Warora Dr. S. S. Kawar, Shri. R. G. Rathod College, Murtijapur Dr. R. P. Sonekar, G. S. Science College, Khamgaon Dr. S. P. Hargunami, G. S. Science College, Khamgaon Dr. R. V. Barde, GVISH, Amravati
- ✓ Prof. Zakir Khan, GVISH, Amravati Dr. N. N. Padole, SSCET, Bhadrawati
- ✓ Dr. G. M. Jamankar, Vidyaniketan College, Chandrapur Prof. K. D. Jagtap, Indira Gandhi College, Ralegaon
- ✓ Dr. Nikhilesh S. Bajaj, Toshniwal College, Sengaon

- ✓ Dr. S. S. Mankar, Shivramji Moghe Mv., Pandharkawada Dr. D. L. Arakh Gawande College, Umarhked
- ✓ DR. P. D. Shirbhate, Gawande College, Umarkhed Dr. K. R. Nemade, Indira Mahavidyalaya, Kalamb Dr. Y. S. Sakhare, Late P. G. College, Shirpur Jain
- ✓ Dr. R. D. Chavhan, Registrar, Agriculture College, Nagpur Dr. R. B. Mankar, Smt. Radhabai Sarda College, Anjangaon Dr. V. R. Panse, Prof. N. G. Science College, Sakharkherda Dr. A. N. Yerpude, N. H. College, Bramhapuri
- ✓ Dr. S. S. Arsad, Mahatma Fule, Mahavidyalaya, Warud Prof. Bhaskar V. Tupte, Arts & Science College, Kurkheda Dr. P. M. Wankhede, R. Bharti Science College, Arni
- ✓ Dr. D. P. Deshmukh, R. Bharti Science College, Arni

Organizing Committee

- ✓ Prof. M.B. Thikare, ACS College, Maregaon Prof. S. K. Khade, ACS College, Maregaon Dr. A. B. Yawale, ACS College, Maregaon
- ✓ Prof. D. A. Gundawar, ACS College, Maregaon Prof. G. L. Sodnar, ACS College, Maregaon Dr. R. R. Chaware, ACS College, Maregaon
- ✓ Dr. V. N. Chavhan, ACS College, Maregaon Dr. N.R. Sharma, ACS College, Maregaon Dr. S. R. Kelode, ACS College, Maregaon Dr. M. K. Tanurkar, ACS College, Maregaon
- ✓ Dr. V. C. Ghodkhande, ACS College, Maregaon Dr. M. H. Pardeshi, ACS College, Maregaon Prof. B.R. Deshmukh, ACS College, Maregaon Prof. S. S. Kamble, ACS College, Maregaon
- ✓ Dr. P.P. Kulkarni, ACS College, Maregaon Dr. S.B. Gaikwad, ACS College, Maregaon Prof. N.S. Kadam, ACS College, Maregaon Prof. V.S. Bhagat, ACS College, Maregaon Mr. M. D. Zade, ACS College, Maregaon Dr. M. M. Kamble, ACS College, Maregaon Dr. N. B. Raut, ACS College, Maregaon
- ✓ Prof. S. T. Bhandakkar, ACS College, Maregaon Dr. A. D. Adsare, ACS College, Maregaon
- ✓ Prof. M. P. Shende, ACS College, Maregaon

Technical Committee

- ✓ Dr. Gulshan Kuthe, L. T. College, Wani Dr. B. D. Watode, P. N. College, Pusad
- ✓ Prof. A. P. Jenekar, ACS College, Maregaon Prof. S. G. Atram, ACS College, Maregaon Dr. S. G. Chirde, ACS College, Maregaon Dr. P. R. Makade, ACS College, Maregaon Mrs. Mrunal Pawar, SVPCET, Nagpur

Our Guests, Resource Persons and Eminent Experts

INAUGURATOR
Dr. F. C. Raghuwanshi
Dean, Faculty of Science & Technology, SGB Amravati, University

Dr. Mahavir Singh
Chief Scientist
CSIR-NPL, New Delhi

Dr. S. K. Omanwar
Former Prof. & Head Dept of Physics
SGB Amravati, University

Dr. O. P. Chimankar
Professor & Head Dept of Physics
RTM Nagpur, University

Dr. Pramod B. Lanjewar
HOD, Mechanical Engineering
SVPCET, Nagpur

Dr. S. J. Dhoble
Professor, Dept of Physics
RTM Nagpur, University

Dr. Nico F. Declercq
Georgia Institute of Technology, France

Dr. Lehlohonolo F. Koao
University of the Free State
South Africa

Dr. Abdul Hakeem Deshmukh
Guangdong University of
Technology, Guangzhou, China

Dr. S. R. Aswale
Former Finance & Accounts
Officer, SGB Amravati, University

Dr. Kishor Rewatkar
Professor & Head, Dept of Physics
Dr. Ambedkar College, Nagpur

Dr. A. B. Lad
Professor, Dept of Physics
Amolakchand Mv. Yavatmal
Chairman BOS, Phy SGBU, Amravati

Dr. Devraj Singh
Director & Professor
Purvanchal University
Jaupur

Dr. G. G. Muley
Associate Professor & Head
Dept of Physics
SGB Amravati, University

Dr. S.. A. Waghuley
Associate Professor
Dept of Physics
SGB Amravati, University

Dr. N. S. Dhoble
Professor
Dept of Chemistry
Sevadal Mahila Mv. Nagpur

Dr. U. P. Manik
Professor & Head
Dept of Physics
S. P. College, Chandrapur

Dr. S. S. Aswale
Associate Professor & Head
Dept of Chemistry
L. T. College, Wani

Dr. A. U. Bajpeyee
HOD, Physics
ACS College, Amravati

Dr. V. D. Kapse
HOD, Physics
ASC College, Chikhaldarai

Dr. V. B. Pawade
Dept of Applied Physics
LIT, RTM Nagpur, University

Dr. K. K. Pandey
Dept of Physics, SBSR
Sharda University, Noida

Dr. Nikhilesh S. Bajaj
Dept of Physics Toshniwal
College, Sonegaon

Dr. N. N. Padole
HOD, Physics
SSCET, Bhadrawati

Co-convener

Prof. P. D. Bageshwar
M. M. College, Darwha

Dr. D. R. Bijwe
G. S. Tompe College, Chandur Bazar

Dr. Amit Bansod
Dr. Ambedkar College, Nagpur

Prof. R. P. Gadpayale
ACS College, Maregaon

Prof. Rupesh Wandhare
ACS College, Maregaon

CHAIRMAN
Dr. A. N. Gharde
Principal,
ACS College, Maregaon

CO-CHAIRMAN
Prof. Dr. A. B. Patil
Principal
P. N. College, Pusad

Organizing Secretrary
Prof. P. T. Hamjade
HOD, Physics
P. N. College, Pusad

Convener
Dr. N. R. Pawar
HOD, Physics
ACS College, Maregaon

XV

About College

Arts, Commerce and Science College, Maregaon is a premier college of excellence, engaged in knowledge building for inclusive social development and molding globally competent and socially sensitive professionals towards social transformation and enlighten students of rural and tribal area and to contribute their services for universal development by promoting education. The college had a meteoric rise and developed into an excellent institution for education. The college impart knowledge in various disciplines to meet global challenges of the 21st century. Giving appropriate emphasis on curricular and co- curricular activities, college attempts to develop rounded personalities through teaching, learning and evaluation and committed to empowering students to think independently. The college outreaches to the widest range of students from backward as well as tribal area. College is situated in an eco-friendly environment which makes students happy and energetic. Upholding the noble traditions lay down by the founders, the institution surges ahead towards excellence.

Conference Structure

Conference will have key note lectures, Plenary talk, Invited talk and Oral Presentation Hardcopy of the certificate will be posted on the institutional registered address of the participants

Background

Recent Advances in Material Science and Nanotechnology has born fruit in bringing together young and dynamic researchers, academicians and industrialists to explore, their knowledge and novel ideas to improve the concepts in this vital multidisciplinary areas of research for economic growth and sustainable development of the society. 'RAMAN-2021' is timely need to produce many need-based products in different industrial sectors. The conference aims to provide open discussion forum through e-platform and bringing together academicians, young scientists, researchers and technologists to meet the global demand of novel materials and challenges in the field of Material Science and Nanotechnology.

Outstanding Academic Excellence Award

Applications are invited for 'Outstanding Academic Excellence Award' along with the following documents

Photocopy of PhD degree obtained Teaching and research experience Publication details (Papers, Books, etc) Awards at National/International level Talk delivered/Chaired session in National/International conferences PhD awarded under supervision

Conference Topics

The focus of the conference will be on Recent Advances in Material Science and Nanotechnology and related issues like:

- ✓ Nanomaterials and Applications Nanoscience & Nanotechnology Material Science
- ✓ Ultrasonics and Acoustics Luminescent materials Thin film and polymers
- ✓ Semiconductor materials and devices Ceramic Advanced smart materials Chemical materials and its characterization Bio-materials and Biosensor
- ✓ Cosmetic materials
- ✓ Ultrasonic transducers materials
- ✓ Non-destructive Testing and evaluation Laser and X-rays
- ✓ Mathematical Physics Green chemistry

CONTENT

Synthesis and Spectroscopic Characterization of Silicon Carbide (SiC) nanoparticles

Ankit Chavhan[1], D. S. Chavhan[1], N. R. Pawar[2]

[1]Department of Physics, Amolakchand Mahavidyalaya, Yavatmal, Maharashtra, India

[2]Department of Physics, Arts, Commerce and Science College, Maregaon, Maharashtra, India

ABSTRACT

Silicon carbide (SiC) nanoparticles have been synthesized via sol-gel method. The size, morphologies and bonding states of synthesized SiC nanoparticles were investigated by X-ray diffraction (XRD), scanning electron microscopy (SEM) and Fourier transform infrared spectroscopy (FTIR). The results show that the synthesized SiC nanoparticles are high-quality crystals with high aspect ratios. The thermodynamics analysis of SiC nanoparticles in organic base fluids were studied with purpose of applications in various fields. X-ray diffraction (XRD) results indicated the major phases of SiC. Scanning electron microscopy (SEM) images shows that SiC particles mainly composed of crystalline nanoparticles. FTIR provides valuable and practical information about the chemical bond states of the materials. FTIR spectra of the SiC nanoparticles have revealed strong absorption bands with a very small variation [1-5].

Keywords : SiC nanoparticles; Sol-gel technique; XRD; SEM.

I. INTRODUCTION

In nanoparticle synthesis it is very important to control not only the particle size but also the particle shape and morphology as well. In the present investigation, the synthesis of SiC Nanoparticles via solgel method is discussed, which is an easy, simple, cost effective and convenient route for preparing nanoparticles. Silicon carbide is a well-known ceramic type nanoparticle which shows diverse scope due to its exclusive properties like high strength, hardness, chemical, thermal stability, high melting point, oxidation resistance, etc. Therefore, they used in high temperature electronic devices, abrasion and cutting applications [6,8].

II. Synthesis of SiC nanoparticles:

During the synthesis of SiC nanoparticles, the mixture of SiO_2:Mg in the molar ratio 1:2 were heated in the furnace at 650°C for 6 hours. For an acid etching of the obtained product for 5 hour a mixture of HF 10% wt and HNO_3 4 M were used. Then the mixture is formed washed with distilled water and dried at room temperature. The final product is SiC in powder form [9-11].

III. Spectroscopic Characterization of SiC Nanoparticles:

X-Ray Diffraction (XRD) was obtained with a diffractometer 'PAN analytical,' Model: Xpert PRO, equipped with Cu Kα_1 radiation. Scanning Electron Microscopy (SEM) research was made using a field

emission JSM-7401F Scanning Electron Microscope. Infrared spectrum of absorption or emission of nanoparticles was obtained by Fourier Transform Infrared (FTIR) spectrophotometer Nicolet.

a X-Ray Diffraction (XRD)

Many techniques are used to identify the various properties of nanomaterials. Some of the most important techniques are: XRD is a non-destructive versatile technique used to analyze the structure of crystalline materials and to identify the crystalline phases present in a material. It provides detail information about the chemical composition and crystallographic structure of natural and manufactured materials. In a crystalline solid, the constituent particles are arranged in regular periodic manner. An interaction of a particular crystalline solid with X-ray helps in investigation of its actual structure. Crystal is found to act as diffraction grating for X-ray and this indicates that the constituent particles in the crystal are arranged in planes at close distance in repeating patterns. The 2θ a value corresponding to peak in the X- ray diffraction is an important tool to understand the properties of characterizes materials. In nanomaterials number of atoms is very small. Nanoparticles cannot be considered as an infinite arrangement of atoms. In case of amorphous nanoparticles broad diffraction peaks are expected to occur similar to amorphous bulk solid materials. However, in case of nanoparticles atoms do not have ordered lattices, some changes in diffraction are to be expected as compared to single crystal. Nanoparticles do not have grain boundaries. It has been found that diffraction peaks in nanocrystalline particles are broadened compared to a single or polycrystalline solid of same materials. From XRD pattern, Debye Scherrer gives an equation to determine nanoparticles size as,

$$D = \frac{0.9\lambda}{\beta Cos\theta} \ \text{----------------------------------- (1)}$$

In above equation β is the broadening caused by nanoparticles size, θ is the Bragg's angle and λ is the wavelength of X-ray beam. Figure 1 shows the XRD pattern of Silicon carbide (SiC) nanoparticles reporting some silicon and carbon phases centered at $2\theta = 35^0$. The XRD measurement carried out by using "PAN analytical" X-ray diffractometer keeping the parameter constant at start position [°2Th.]: 10.0154 End Position [°2Th.]: 89.9834, Step Size [°2Th.]: 0.0170, Scan Step Time [s]: 5.7150, Scan Type: Continuous, Measurement Temperature [°C]: 25.00 Anode Material: Cu, K-Alpha1 [Å]: 1.54060. It is seen that the materials are well crystalline in nature and well agreed with standard JCPDS file number 029-1129 file. The estimate size of SiC nanoparticles using Debye Scherrer formula is found about 30 nm.
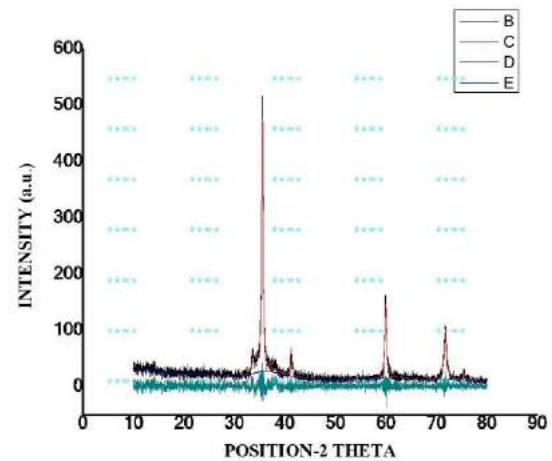
(a) XRD pattern of Silicon carbide
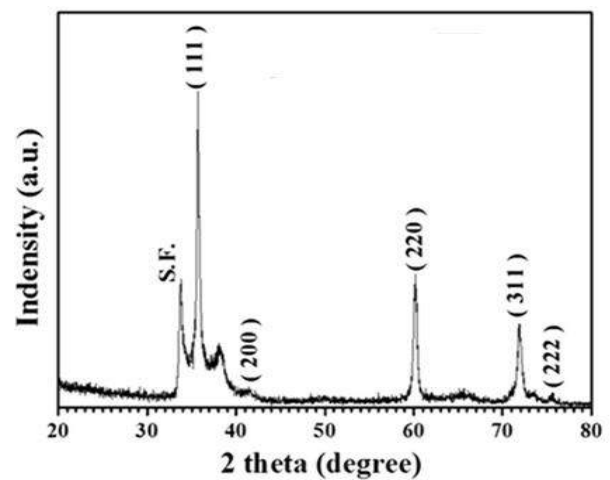
(b) XRD pattern of silicon carbide nanoparticles JCPDS file No 029-1129

Figure 1. X- ray diffraction pattern of Silicon carbide (SiC) nanoparticles

b Fourier Transform Infrared Spectroscopy (FTIR)

An infrared spectrum of absorption or emission of nanoparticles is obtained by FTIR technique. This technique collects simultaneously high spectral resolution data over a wide spectral range. FTIR analysis indicated the vibrations of Silicon-oxygen (Si–O) groups. FTIR spectroscopy shows the degradation phases and absorption in different regions which indicates structural relationship between them. From figure 3 it is seen that the inorganic groups is gradually decomposed at 1078.95 cm^{-1} and 804.72 cm^{-1}. Also the Si-OH absorption peak observed at 2887.74 cm^{-1} due to the symmetrical stretching vibrations of the N–O group, which might have come from the nitrate of the starting material. The spectrum shows a peak at 1078.95 cm^{-1}, which is due to the Si-C vibrations in the spinel block alumina structure.
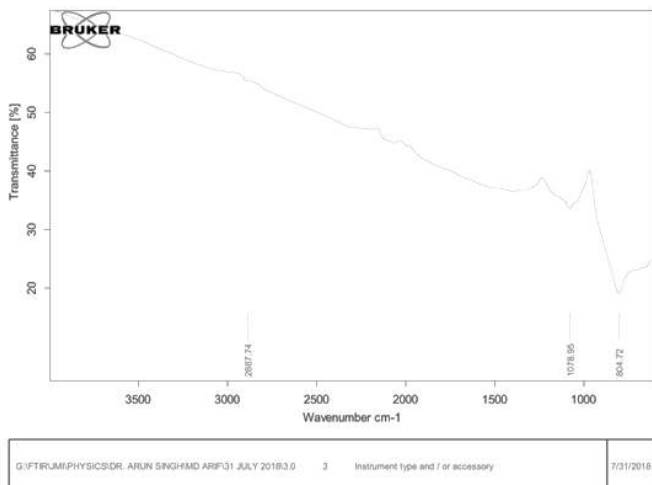
Figure 2. FTIR of Silicon carbide (SiC) nanoparticle

c Scanning Electron Microscopy (SEM):

The electrons in the samples interact with atoms and generate various signals that contain information about surface topography and composition of the sample. The images of a sample are produced by SEM technique by scanning the surface with a focused beam of electrons. SEM study is carried out to observe the overall surface morphology and crystallite sizes of the prepared nanomaterials. This material has been synthesis by sol-gel method. From the SEM images are observed under 10 μm resolutions which shows the foam like surface morphology as shown in figure 4. In the depicted images of SiC nanomaterials, it can be clearly seen that the micrograph crystallite sizes may vary from a 10 μm to few microns range if we magnify further. The crystallites look like having a sharp surface edge as well as crystalline grains and the particles foam-like morphology can be formed from highly agglomerated crystallites. Also, it is confirmed that the crystallite sizes are nearly equal for all sample.
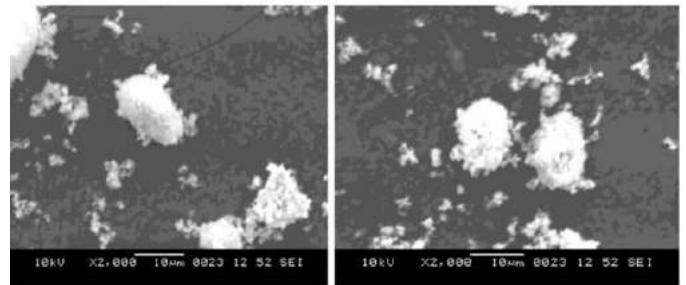
Figure 4. SEM images of SiC nanoparticles

IV. CONCLUSION

1. Nanoparticles of SiC were synthesized via sol technique.
2. The estimate size of SiC nanoparticles using Debye Scherrer formula is found about 30 nm.
3. Characterization of SiC nanoparticles via XRD and SEM showed that nanocrystalline SiC is formed.
4. FTIR spectra of the SiC nanoparticles have revealed strong absorption bands with a very small variation.

V. REFERENCES

[1]. H.K. Seong, H.J. Choi, S.K. Lee, J.I. Lee and D.J. Choi, Applied Physics Letters, 85, 1256, 2004.
[2]. Z.L. Wang, Z.R. Dai, Z.G. Bai, R.P. Gao, J.L. Gole, Applied Physics Letters, 77, 3349–3351, 2000.
[3]. Z.W. Pan, Z.R. Dai, Z.L. Wang, Science, 291, 1947–1949, 2001

[4]. L. Hyun-Lee, K. Jong-Kyu, L. Sang-Nam, K. Yong-Heack. Consisten heat transfer analysis for performance evaluation of multichannel solar absorbers. Solar Energy, 2012. 1576-1585.

[5]. G. Amaral-Labat, C. Zollfrank, A. Ortona, S. Pusterla, A. Pizzi, V. Fierro, A. Celzard. Structure and oxidation resistance of micro-cellular Si-SiC foams derived from natural resins. Ceramics International. 2013. 39: 1941-1851.

[6]. W. Guo, H. Xiao, W. Xie, J. Hu, Q. Li, P. Gao. A new design for preparation of high performance recrystallized silicon carbide. Ceramics International. 2012. 38: 2475-2481.

[7]. T. Menigault, G. Flamant, B. Rivoire. Advanced high-temperature two-slab selective volumetric receiver. Solar Energy Materials. 1991. 24: 192-203.

[8]. F. Bai. One dimensional thermal analysis of silicon carbide ceramic foam used solar air receiver. International Journal of Thermal Sciences. 2010. 49: 2400-2404.

[9]. Q. Li, N. Guérin de Tourville, I. Yadroitsev, X. Yuan and G. Flamant, 2013. Micro-Channel pressurized- air receiver based on compact heat exchanger concept, Solar Energy. 91: 186-195.

[10]. L. Hyun-Lee, K. Jong-Kyu, L. Sang-Nam, K and Yong-Heack, 2012. Consisten heat transfer analysis for performance evaluation of multichannel solar absorbers. Solar Energy. 1576- 1585.

[11]. G. Amaral-Labat, C. Zollfrank, A. Ortona, S. Pusterla, A. Pizzi, V. Fierro and A. Celzard, 2013. Structure and oxidation resistance of micro-cellular Si-SiC foams derived from natural resins. Ceramics International, 39: 1941-1851.

Stability and Zeta Potential measurement of Nanofluids of Ag Nanoparticles

[1]D. S. Chavhan, [1]Ankit Chavhan, [2]N. N. Padole, [3]N. R. Pawar

[1]Department of Physics, Amolakch and Mahavidyalaya Yavatmal, Maharashtra, India
[2]Department of Physics, Shri Sai College of Engineering and Technology, Bhadrawati, Maharashtra, India
[3]Department of Physics, Arts, Commerce and Science College, Maregaon, Maharashtra, India

ABSTRACT

The silver nanoparticle was synthesized via thermal decomposition method at 700℃. Reducing agent NH_2CONH_2 is added to the mixture of $AgNO_3$ in order to form the silver nanoparticle. In the present work we have prepared the silver nanoparticle in powder form from silver nitrate of AR grade by thermal decomposition method. As silver is monovalent therefore 3gm $AgNO_3$ is taken in crucible then it is grinding and mixed at atomic level with 0.8834 gm of urea used as a fuel. Then combustion was taking place in furnace at 700℃. Then sample was again grinding in crucible. Attempt has been made to characterize the nanoparticle by XRD. Nanofluids of Ag Nanoparticles were prepared by two step method in methanol base fluid and study its stability by measuring thermal conductivity and Zeta potential and predicts the surface of nanoparticle and nanoparticle surfactant interactions [1-4].

Keywords : Ag Nanoparticle, XRD, Thermal Conductivity, Zeta Potential.

I. INTRODUCTION

Nanofluids are solid-liquid composite materials consisting of solid nanoparticles with size typically of 1-100 nm suspended in liquid. Nanofluids have attracted great interest recently because of reports of greatly enhanced thermal properties. Surface area of the nanomaterial is increased with reduced in their size. At the nanoscale dimensions, the material properties change significantly from their bulk matter. When matter is reduced in size, it changes its characteristics, caused by the change of mechanical, electronic, physical, chemical, optical, magnetic and biological properties. The stability of nanofluids provides useful information regarding the interaction at the atomic level in the suspension.

II. Synthesis of Ag Nanoparticles

The silver nanoparticle was synthesized by thermal decomposition method at 700℃. Reducing agent NH_2CONH_2 is added to the mixture of $AgNO_3$ in order to form the silver nanoparticle. XRD pattern of silver nanoparticle is taken and it is compared with standard JCPDS data of silver, it is hold good. All the chemical reagent are AR grade. Most metal nitrates thermally decompose to the respective oxides, but silver oxide decomposes at a lower temperature than silver nitrate, so the decomposition of silver nitrate yields elemental silver instead. The structure of prepared silver nanoparticle has been investigated by X-ray diffraction (XRD) analysis. Typical XRD pattern of sample, prepared by the present chemical method are shown in

the Figure1. The XRD study indicates the formation of silver nanoparticles.
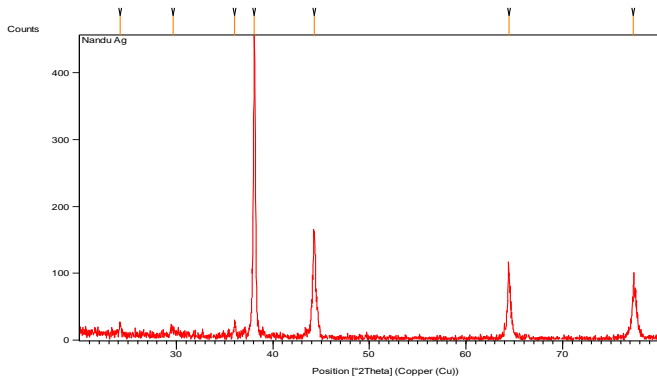
Figure 1. XRD pattern of Ag nanoparticles.

From this study, average particle size has been estimated by using Debye-Scherrer formula

$$D = \frac{0.9\lambda}{WCos\theta} \qquad \text{.....................(1)}$$

Where 'λ' is the wavelength of X-ray (0.1541nm), 'W' is FWHM (full width at half maximum), 'θ' is the diffraction angle and 'D' is particle diameter (size). The average particle size is calculated to be around 30 nm.

III. Zeta Potential measurements

Zeta potential of the prepared Ag nanofluids was measured by using Zeta potential analyser. It is the potential difference across phase boundaries between solids and liquids. It is observed that zeta potential for molar concentration 0.4 have higher values indicating more stability of Ag nanofluids indicating in figure 2. Moreever it has less values for other molar concentration indicating less stability. From the graph the values of zeta potential has been greater than 30 either positive or negative exhibit the more stability of the nanofluids.
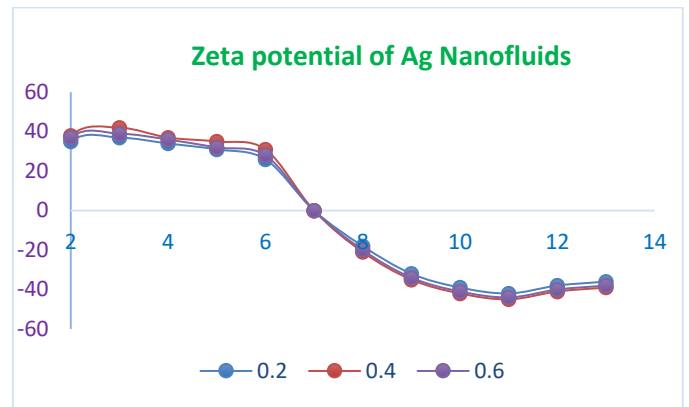
Figure 2. Zeta potential of Ag nanofluids in methanol

IV. Thermal conductivity

Figure 3 shows the variation of thermal conductivity with molar concentration of Ag Nanoparticles of nanofluids in methanol. The results clearly show that the effective thermal conductivity of nanofluid increases with temperature. It has substantially higher value for molar concentration 0.6 indicating more stability of nanofluids because of high specific surface area and therefore more heat transfer surface between nanoparticles and fluids. The thermal conductivity enhancements are highly dependent on specific surface area of nanoparticle, with an optimal surface area for the highest thermal conductivity. The strong relationship between Brownian motion and temperature of nanoparticles are also responsible for increase in thermal conductivity [24-34].
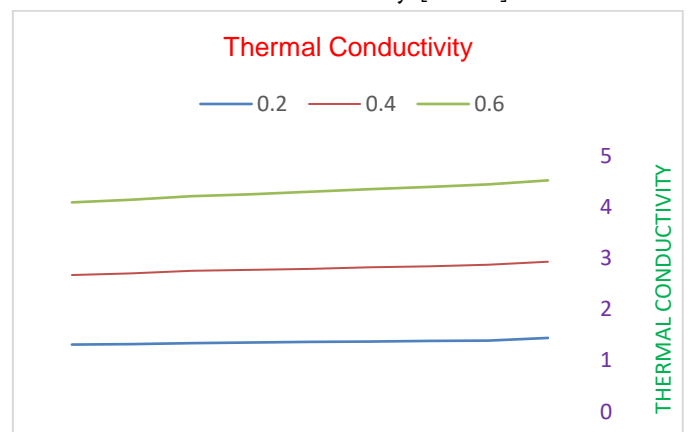
Figure 3. shows the variation of thermal conductivity with molar concentration at 20^0C, 25^0C & 30^0C

V. CONCLUSION

1. The observed higher values of zeta potential indicate the stability of nanofluids.

2. Besides thermal conductivity effect, future research should consider other properties, especially viscosity and wettability, and examine systematically their influence on flow and heat transfer. An in depth understanding of the interactions between particles, stabilizers, the suspending liquid and the heating surface will be important for applications.

3. Enhancement in thermal conductivity of Ag nanofluids is due to the stability of Ag nanoparticles in dispersion medium.

VI. REFERENCES

[1]. W. Guo, H. Xiao, W. Xie, J. Hu, Q. Li and P. Gao, 2012. A new design for preparation of high-performance recrystallized silicon carbide. Ceramics International, 38: 2475-2481.

[2]. Mishra G., Verma S.K., Singh D., Yadawa P.K. and Yadav R.R., Synthesis and ultrasonic characterization Cu/PVP nanoparticles-polymer suspensions, J. Acoustics, 1 (2011) 9-14.

[3]. Yu W. and Xie H., A review of nanofluids: preparation, stability mechanisms and applications, J. Nanomaterials, 2012 (2011) 1-17.

[4]. Eastman J.A., Choi S.U.S., Li S., Yu W. and Thompson L., Anomalously increased effective thermal conductivities of ethylene glycol-based nanofluids containing copper nanoparticles, J. Appl. Phys. Lett., 78 (2001) 718-723.

[5]. Lee S., Choi S.U.S., Li S. and Eastman J.A., Measuring thermal conductivity of fluids containing oxide nanoparticles, J. Heat Transfer, 121 (1999) 280-289.

[6]. Kulkarni D.P., Das D.K. and Chukwu G.A., Temperature dependent rheological property of copper oxide nanoparticles suspensions, J. Nanosci. Nanotechnol, 6 (2006) 1150-1154.

[7]. Zhengping Qiao., Yi Xie., Yingjie Zhu. and Yitan Qian., Synthesis of PbS/polyacrylonitrile nanocomposites at room temperature by Y-radiation, J. Mater. Chem, 9 (1999) 1001-1002.

[8]. Eastman J.A., Choi S.U.S., Li S., Yu W. and Thompson L., Anomalously increased effective thermal conductivities of ethylene glycol-based nanofluids containing copper nanoparticles, J. Appl. Phys. Lett., 78 (2001) 718-723.

[9]. Lee S., Choi S.U.S., Li S. and Eastman J.A., Measuring thermal conductivity of fluids containing oxide nanoparticles, J. Heat Transfer, 121 (1999) 280-289.

[10]. Liu M.S., Lin M.C.C., Huang I.T. and Wang C.C., Enhancement of thermal conductivity with CuO for nanofluids, Chem. Eng. Technol., 29 (2006) 72-77.

[11]. Wen D. and Ding Y., Effective thermal conductivity of aqueous suspensions of carbon nanotubes (carbon nanotube nanofluids), J. Thermophys. Heat Transfer, 18 (2004) 481-485.

Luminescence Characteristic of LiMgBO3 Phosphor

G. A. Aghalte[1], N. R. Pawar[2]
[1]Department of Physics, Lokmanya Tilak Mahavidyalaya, Wani, Maharashtra, India
[2]Department of Physics, Arts, Commerce and Science College, Maregaon, Maharashtra, India

ABSTRACT

The present paper reports the combustion synthesis of $LiMgBO_3$ phosphor with Dy and Mn dopants. During the combustion synthesis we have used Dy and Mn activators so as to explore the possible compound for TL glow curve analysis and their application for TL dosimetry. The combustion synthesis method, though tricky but it is very simple and time saving method. This work deals with detail procedure for synthesis of $LiMgBO_3$ phosphor with Dy and Mn dopants. We have also studied their TL glow curve analysis and luminescent characteristics for TL dosimetry. Preparation of Lithium Borate host materials is tricky work. The synthesis is not straightforward. We became successful in synthesizing few mixed borate compounds by combustion synthesis method. Thermoluminescence studies were carried out on all the possible combinations of $LiMBO_3$:Re (M = Mg, Ca, Sr, Ba & Re = Ce, Eu, Dy, Mn). The TL sensitivity of $LiSrBO_3$:Dy is comparable with the $CaSO_4$:Dy. We have successfully achieved the 71% TL sensitivity in this phosphor however it has high Z_{eff} value because of Strontium. Whereas the TL peak temperature was found to be 178°C, lower than that of $CaSO_4$: Dy.

Keywords: LiMgBO, combustion method, TL intensity, TL

I. INTRODUCTION

Borate compounds are known for their wide band gap, strong nonlinear optical properties, chemical and environmental stabilities and mechanical robustness. They are the best hosts for various activators. From the literature it is found that Borate compounds find several interesting applications. In borate compounds boron atom is coordinated by oxygen atoms to form a variety of atomic groups that affect the physical properties in general and optical properties in particular. In the past decades, much research interest has been focused on the synthesis and characterization of inorganic borates for exploring nonlinear optical materials [1-5]. Several borate compounds find important application as TLD phosphors. However, they have not observed promising TL sensitivity in the phosphor so as to propose the same for TLD applications. Recently, a series of attempts have been made to investigate new borate materials as useful optical crystals in view of the demand for the nonlinear optical crystals in the deep UV band [6-9]. The demand for such material is increasing consistently because of the development of optical communications and the semiconductor large-scale integrated circuit. Synthesis of luminescent materials

specifically for borates by combustion method is found to be very useful and economically viable technique. Since this method provides uniform and narrow distribution of the particle size of the product, we have attempted combustion method for the synthesis of $LiMgBO_3$ [10-15].

Synthesis of $LiMgBO_3$ phosphors:

The stoichiometric amounts of high purity starting materials (Lithium Carbonate) Li_2CO_3, (Magneshium Nitrate) $Mg(NO_3)_2 \cdot 6H_2O$, (Boric Acid) H_3BO_3, (Urea) $CO(NH_2)_2$ and (Ammonium Nitrate) NH_4NO_3 were mixed thoroughly in agate mortar for about 30 minutes, so that the paste was formed. A stock solution of Dy_2O_3 and $MnCl_2 \cdot 4H_2O$ in stoichiometric amount was then mixed separately in paste. Above paste was put in the pre-heated furnace (550℃) after warming it for 5 minutes. (we have used the Laboratory made Muffle Furnace). The self-heat generating redox reaction was completed within 5 minutes and the fine powder of $LiMgBO_3$:Dy and $LiMgBO_3$:Mn was obtained. The obtained raw powders were sintered for 1.5 hour at 700⁰C and quenched to room temperature on aluminum plate. The balanced chemical reactions for $LiMgBO_3$:Dy and $LiMgBO_3$:Mn phosphors are reported as below :

$0.5Li_2CO_3 + Mg(NO_3)_2 \cdot 6H_2O + H_3BO_3 + 5(NH_2)_2CO + 4NH_4NO_3 + 0.0005Dy_2O_3$ (1000ppm) $+ 2.5O_2 \rightarrow$

$LiMgBO_3$:Dy $+ (5.5CO_2 + 4NH_3 + 4NO_2 + 19.5H_2O + 6N_2)\uparrow$

$0.5Li_2CO_3 + Mg(NO_3)_2 \cdot 6H_2O + H_3BO_3 + 5(NH_2)_2CO + 4NH_4NO_3 + 0.001 MnCl_2 \cdot 4H_2O$ (1000ppm) $+ 2.5O_2 \rightarrow$

$LiMgBO_3$:Mn $+ (5.5CO_2 + 4NH_3 + 4NO_2 + 19.5H_2O + 6N_2)\uparrow$
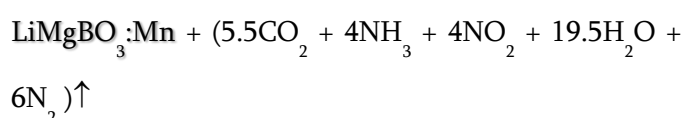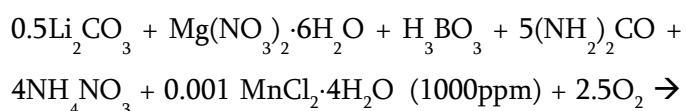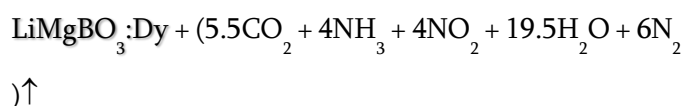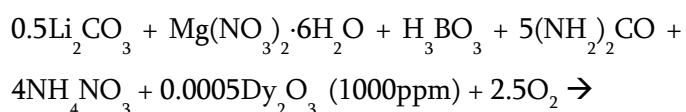
XRD of Synthesized Phosphor:

Figure 1 shows the XRD pattern of $LiMgBO_3$ Phosphor synthesized by combustion synthesis, it is exactly match with the standard available data.
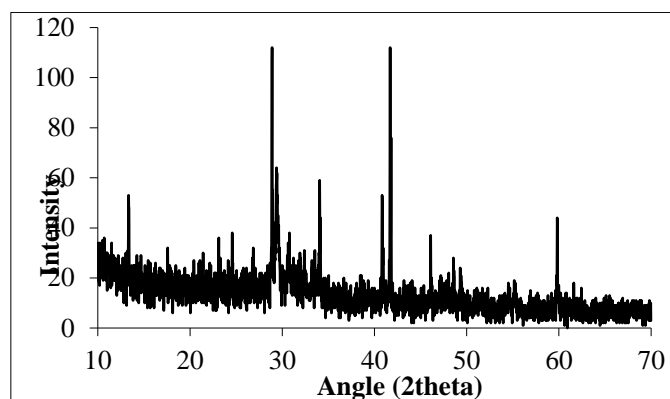
TL Study of $LiMgBO_3$ Phosphor:

Figure 2 shows the typical glow curves for $LiMgBO_3$ doped with various impurities exposed to γ ray (exposure of 5 Joule/Kg). Curve (a), (b), (c), (d) & (e) are for Dy, Cu, Ce, Eu, & Mn respectively. The intensity for the activator Dy was found to be more than 10 times than the other activators. Therefore the glow curve of $LiMgBO_3$:Dy (curve a) is divided by 10 to fit in the scale. The main peak in this host for all activators is found around 165C. It is close to the TL peak of most of the TLD phosphors currently used. Since the peak is single and simple (symmetric) and further moderate value of its full width at half maximum, it could be used for the dosimetry studies provided. It satisfies the other requirements. In short, the activator Dy is found to be suitable dopant in $LiMgBO_3$ host [16-23].
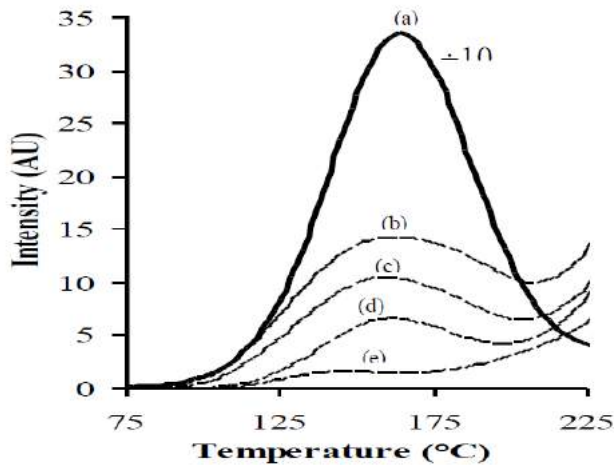
Fig.2 Typical glow curves for LiMgBO3 doped with various impurities exposed to 5 Joule/kg.

(a) Dy, (b) Cu, (c) Ce, (d) Eu (e) Mn. Curves (a) is divided by 10 to fit the ordinate scale.

II. CONCLUSION

1. The combustion synthesis is successfully employed for the preparation of the new potential phosphors namely $LiMgBO_3$ doped with the activators Cu, Ce, Eu, Dy & Mn.

2. The XRD profile of the phosphor is found to show good agreement with the literature.

3. This agreement has proved the combustion method is very useful for the synthesis of $LiMgBO_3$

4. Dy is most suitable dopant in $LiMgBO_3$ host out of all activators with regard to Thermoluminescence behavior.

5. $LiMgBO_3$:Dy seems to be promising TLD materials because of their low Z values, provided it is improved further for TL sensitivity.

6. $LiMgBO_3$:Dy is having 5% of the TL sensitivity as compared to $CaSO_4$:Dy (RchenTech, TT88) whereas it is about 22 % in case of $LiCaBO_3$:Dy when exposed to γ rays.

7. There is scope for improvement in the TL sensitivity of these materials.

8. These phosphors also found to respond β radiations equally as well.

9. The reusability is also been tested and it is found that even after 10 cycles of use, there is no much reduction (<15%) in the TL sensitivity.

III. REFERENCES

[1]. D. W. Hughes and J. R. M. Barr, J. Phys. D, Appl. Phys. 25 (1992) 563

[2]. M. A. Dubinskii, V. V. Semashko, A. K. Naumov, R. Y. Abdulsabirov and S. L. Korableva, Laser Phys. 3,(1993)216

[3]. V.B.Bhatkar ,S.K.Omanwar and S.V. Moharil, Phys.Stat.Sol.(A)191, No.1 (2002) 272

[4]. D. S. Thakare, S. K. Omanwar, P. L. Muthal, S. M. Dhopte, V. K. Kondawar, S. V. Moharil, Physica Status Solidi (A), Volume 201,Issue 3 (2004) 574

[5]. C. D. Marshall, S. A. Payne, J. A. Spaeth, W. F. Krupke, G. J. Quarles, V. Castillo and B. H. T. Chai, J. Opt. Soc. Am. B 11 (1994) 2054

[6]. M. A. Dubinskii, V. V. Semashko, A. K. Naumov, R. Y. Abdulsabirov and S. L. Korableva, J. Mod. Opt. 40,(1993) 1

[7]. T. Tsuboi, V. Petrov, F. Noack and K. Shimamura, J. Alloys Compd. 323 (2001) 688

[8]. E. Sarantopolou, Z. Kollia and A. C. Cefalas, Microelectron. Eng. 53 (2000) 105

[9]. Z. Liu, T. Kozeki, Y. Suzuki and N. Sarukura, Opt. Lett. 26 (2001) 301

[10].B. H. T. Chai, J. L. Lefaucheur, M. Stalder and M. Bass, Opt. Lett. 17 (1992) 1584

[11].H. Sato, H. Machida, K. Shimamura, A. Bensalah, T. Satonaga, T. Fukuda, E. Mihokova, M. Dusek, M. Nikl and A. Vedda, J. Appl. Phys. 91 (2002) 5666

[12]. H. Sato, K. Shimamura, A. Bensalah, N. Solovieva, A. Beitlerova, A. Vedda, M. Martini, H. Machida, T. Fukuda and M. Nikl, Jpn. J. Appl. Phys. 41 (2002) 2028

[13]. N. Shiran, A. Gektin, S. Neicheva, V. Voronova, V. Kornienko, K. Shimamura and N. Ichinose, Radiat. Meas. 38 (2004) 459

[14]. A. Bensalah, M. Nikl, E. Mihokova, N. Solovieva, A. Vedda, H. Sato, T. Fukuda and G. Boulon, Radiat. Meas. 38 (2004) 545

[15]. J. B. Amaral, D. F. Plant, M. E. G. Valerio and R. A. Jackson, J. Phys.: Condens. Matter 15 (2003) 2523

[16]. D. Kulesza, J. Cybinska, L. Seijo, Z. Barandiara and E. Zych, J. Phys. Chem. C 119, 27649 (2015).

[17]. Synthesis and TL characteristics of MgB4O7:Mn by Tb phosphor P.D. Sahare, Manveer Singh, Pratik Kumar, Journal of Luminescence 160 (2015) 158–164.

[18]. E. Zych, D. Kulesza, J. Zeler, J. Cybinska, K. Fiaczyk, and A. Wiatrowskac, ECS J. Solid State Sci. Technol. 5, R3078 (2016)

[19]. Mirjana Prokic, Lithium borate solid TL detectors, Radiation Measurements 33 (2001) 393–396

[20]. Schulman J.H., Kirk R.D., West E.J., Use of lithium borate for thermoluminescence dosimetry. Proceedings of the International Conference on Luminescence Dosimetry, Stanford University, CONF-650637,(1967)113–118

[21]. Hyunsoo Park and Jacques Barbier, Journal of Solid State Chemistry 154, 598-602 (2000)

[22]. Kashinath C. Patil , S.T. Aruna, Tanu Mimani, Current Opinion in Solid State and Materials Science 6 (2002) 507–512

[23]. L. Wu, X.L. Chen, Q.Y. Tu, M. He, Y. Zhang, Y.P. Xu, J. Alloys Compds. 358 (2003) 23

Dielectric Relaxation Study of 2-Pentenenitrile and 1, 2 Dichloroethane at 450c Temperature Using TDR

Ishwar G. Shere*

Department of Electronics, Shri. Havagiswami Mahavidyalaya, Udgir, Maharashtra, India

ABSTRACT

The dielectric relaxation study of 2-pentenenitrile with 1, 2 dichloroethane mixture has been carried out at temperature 45^0C. The dielectric relaxation study of solute-solvent mixture at microwave frequencies gives information about the formation of monomers and multimers as well as interaction between the molecules of the mixture. The dielectric parameters viz. static dielectric constant (ε_0) and relaxation time (τ) have been obtained by the least squares fit method. The static dielectric constant increases and relaxation time decreases with increase in concentration of 2-pentenenitrile in 1, 2-dichloroethane in the system. The time domain reflectometry (TDR) has been used for the study of dielectric relaxation spectra of 2-pentenenitrile (PN) and 1,2 dichloroethane (DCE) binary mixtures. The frequency range has been used as 10 MHz to 20 GHz. The relaxation in this system can be described by a single relaxation time using the Debye model. The Excess parameters such as excess permittivity (ε^E) and excess inverse relaxation time $(1/\tau)^E$ of the mixtures have been determined. In the mixtures excess permittivity (ε^E) found positive and the excess inverse relaxation time $(1/\tau)^E$ found negative.. The investigation shows that the effective dipoles of the system increases. It also shows that due to the hindering field between the constituent molecules the dipole rotates slowly.

Keywords: TDR, Nitrile, Chlorine, Excess permittivity, Excess inverse relaxation time.

I. INTRODUCTION

The dielectric relaxation parameters of binary mixture give information about solute-solvent interaction. Time Domain Reflectometer (TDR) is used to obtain the dielectric parameters of the system [1-3]. It also provides the information about the charge distribution in a molecular system. The liquid PN is of C≡N group and DCE of chlorine group. It is interesting to see the interaction of nitrile group with chlorine-group. The frequency dependent complex permittivity measurements using TDR is more powerful technique because a single measurement covers a wide frequency range in a very short time. Several workers have studied the temperature dependent dielectric relaxation parameters.

II. MATERIAL AND APPARATUS

A spectrograde 2-pentenenitrile(PN) (Fluka cheme Gmbh-9471 Buchs, Steinheim, Switzerland) and AR grade 1, 2 dichloroethane(DCE) (E-Merck) were used without further purification The solutions were prepared at 11 different volume percentages of PN in DCE from 0 % to 100 % just before the measurements. Using these volume percents the mole fraction is calculated as

$x_1 = (v_1\rho_1/m_1) /[(v_1\rho_1/m_1) + (v_2\rho_2/m_2)]$

Where m_i, v_i, and ρ_i represent the molecular weight, volume percent and density of the ith (i=1, 2) liquids, respectively. The density and molecular weight of the liquids are as follows:

2-pentenenitrile(PN)- density:$0.821 gmcm^{-3}$; mol.wt.-81.12

1, 2 Dichloroethane(DCE)-density:$1.256 gmcm^{-3}$;mol.wt.-98.96

The complex permittivity spectra were studied using the time domain reflectometry [4-5] method. The Hewlett Packard HP 54750 sampling oscilloscope with HP 54754A TDR plug in module has been used. A fast rising step voltage pulse of about 39 ps rise time generated by a pulse generator was propagated through a coaxial line system of characteristic impedance 50 Ohm. Transmission line system under test was placed at the end of coaxial line in the standard military applications (SMA) coaxial connector with 3.5 mm outer diameter and 1.35 mm effective pin length. All measurements were carried out under open load conditions. The change in the pulse after reflection from the sample placed in the cell was monitored by the sampling oscilloscope. In the experiment, time window of 5 ns was used. The reflected pulse without sample $R_l(t)$ and with sample $R_x(t)$ were digitized in 1024 points in the memory of the oscilloscope and transferred to a PC through 1.44 MB floppy diskette drive.

III. DATA ANALYSIS

The time dependent data were processed to obtain complex reflection coefficient spectra $\rho^*(\omega)$ over the frequency range from 10 MHz to 20 GHz using Fourier transformation [6, 7] as

$$\rho^*(\omega)=(c/j\omega d)[p(\omega)/q(\omega)] \tag{1}$$

Where $p(\omega)$ and $q(\omega)$ are Fourier transforms of $[R_1(t)-R_x(t)])$ and $[R_1(t)+R_x(t)]$ respectively, c is the velocity of light, ω is angular frequency, d is the effective pin length and j= $\sqrt{-1}$.

The complex permittivity spectra $\varepsilon^*(\omega)$ were obtained from reflection coefficient spectra $\rho^*(\omega)$ by applying bilinear calibration method [5].

The experimental values of ε^* are fitted with the Debye equation [8]

$$\varepsilon^*(\omega) \;\; = \;\; \varepsilon_\infty + \frac{\varepsilon_0 - \varepsilon_\infty}{1 + j\omega\tau} \tag{2}$$

with ε_0, ε_∞ and τ as fitting parameters. A nonlinear least-squares fit method [9] was used to determine the values of dielectric parameters. In Eq.(2), ε_0 is the static dielectric constant, ε_∞ is the limiting high-frequency dielectric constant and τ is the relaxation time.

IV. RESULTS AND DISCUSSION

The static dielectric constant (ε_0) and relaxation time (τ) obtained by fitting experimental data with the Debye equation are listed in Table 1.The values of static dielectric constant (ε_0) increases and relaxation time (τ) values decrease at 10% then increase for 20% and then it shows decreasing trend with the increase of concentration of PN into DCE.

The information related to liquids 1 and 2 interaction may be obtained by excess properties [10] related to the permittivity and relaxation times in the mixture. The excess permittivity ε^E is defined as

$$\varepsilon^E = (\varepsilon_0 - \varepsilon_\infty)_m - [(\varepsilon_0 - \varepsilon_\infty)_1 \; x_1 + (\varepsilon_0 - \varepsilon_\infty)_2 \; x_2] \tag{3}$$

Where x- mole fraction and suffices m, 1, 2 represents mixture, liquid 1 (PN) and liquid 2 (DCE) respectively. The excess permittivity may provide qualitative information about multimers formation in the mixture.

Similarly, the excess inverse relaxation time is defined as

$$(1/\tau)^E = (1/\tau)_m - [(1/\tau)_1 x_1 + (1/\tau)_2 x_2] \tag{4}$$

Where $(1/\tau)^E$ is excess inverse relaxation time which represents the average broadening of dielectric spectra.

The inverse relaxation time analogy is taken from spectral line broadening (which is inverse of the relaxation time) in the resonant spectroscopy [11].

The experimental values of both the excess parameters were fitted to the Redlich-Kister equation [12, 13]

$$A^E = (x_1 x_2) \sum_n B_n (x_1 - x_2)^n$$

Where A is either ε^E or $(1/\tau)^E$. By using these B_n values, A^E values were calculated.

Figure 1, shows behavior of excess permittivity and excess inverse relaxation time for the system as a function of volume concentration of PN in DCE at 45^0C temperature.

Table1: Static dielectric constant (ε_0) and relaxation time (τ) for 45^0C temperature.

Vol. percentage of PN in DCE	ε_0	τ (ps)
0	10.88	11.46
10	13.11	11.2
20	15.69	11.67
30	18.24	11.37
40	20.83	11.04
50	23.43	10.33
60	25.87	9.36
70	28.98	8.84
80	31.99	6.78
90	35.19	5.2
100	37.48	3.52

In the system of PN-DCE, from the excess permittivity (ε^E) curve we can see that the excess permittivity (ε^E) values are positive for all concentrations. The positive peak is obtained at 0.1618

Figure 1. (a) The excess permittivity (ε^E) versus volume fraction of PN in DCE **(b)** The excess inverse relaxation time $(1/\tau)^E$ versus volume fraction of PN in DCE.

concentrations. From positive peak the values are gradually decreases. The positive values indicate that; there is formation of monomeric structures which leads to increase in total number of dipoles in the system. It also shows parallel alignment of the dipoles.

The excess inverse relaxation time $(1/\tau)^E$ values are negatives for all concentrations. The negative peak is obtained at 0.1618 concentrations. From the peak point to pure PN the values are decreases continuously. The negative values of $(1/\tau)^E$ indicates that; the effective dipoles in the system creates hindering field. It also represents that; the effective dipole rotation becomes slowly.

V. CONCLUSION

The dielectric parameters such as dielectric constant (ε_0) and relaxation time (τ) values of 2-pentenenitrile (PN)

and 1, 2 dichloroethane (DCE) mixture are obtained by analyzing dielectric relaxation spectra. The excess permittivity and excess inverse relaxation time values are also reported at 45^0C temperature for 11 different concentrations in the frequency range of 10 MHz to 20 GHz. This data provides information regarding solute-solvent interaction. From the present study we can conclude that; the total number of dipoles in the system increases and shows the parallel alignment of the dipoles in the system. We also conclude that; the dipoles produces opposing field to each other in the mixture and the dipoles in the system rotates slowly.

VI. REFERENCES

[1]. Helambe SN, Lokhande MP, Kumbharkhane AC and Mehrotra SC. Pramana-J. Phy. 1995; 45(1): 19

[2]. Pawar VP and Mehrotra SC. J. Mol. Liq. 2002; 95: 63.

[3]. Helambe SN, Chaudhary AS and Mehrotra SC. J. Mol. Liq. 2000; 84: 235

[4]. Puranik SM, Kumbharkhane AC and Mehrotra SC. J. Mol. Liq. 1994; 59:173.

[5]. Cole RH, Berbarian JG, Mashimo S, Chryssikos G, Burns A and Tombari E. J. Appl. Phys. 1989; 66: 793.

[6]. Shannon CE. Proc. IRE. 1949; 37:10.

[7]. Samulan HA. Proc. IRE. 1951; 39:175.

[8]. Debye P. Polar molecules, Chemical Catalog, New York. 1929.

[9]. Bevington PR. Data reduction and error analysis for the physical sciences, Mc-Graw Hill, New York. 1969.

[10]. Tabellout M, Lanceleur P, Emery JR, Hayward D and Pethrick RA. J. Chem. Soc. Faraday Trans. 1990, 86: 1493.

[11]. Mehrotra SC and Boggs J E. J. Chem. Phys. 1975; 66: 306.

[12]. Aralaguppi MI, Aminabhavi TM, Balundgi RH and Joshi SS. J. Phy. Chem. 1991; 95: 5299.

[13]. Al-Azzawl SF, Awwad AM, Al-Dujaili AM and Al-Noori MK. J. Chem. Engg. Data. 1990; 35: 463.

A Discussion of Acoustical Parameters in Binary Mixtures at different Temperatures: An Ultrasonic Study

Padmavathi P[1*], Irudaya Sahaya Lancy A[1], Krishna Kumar Pandey[2], Mathana Gopal A[1], Moses Ezhil Raj A[3], Poongodi J[4]

[1,3]PG & Research Deptt. of Physics, Scott Christian College, Nagercoil, Tamil Nadu, India

(Affiliated to Manonmaniam Sundaranar University, Tirunelveli, Tamil Nadu, India)

[2]Department of Physics, School of Basic Sciences and Research, Sharda University, Greater Noida, India

[4]Department of Physics, Kamaraj College, Thoothukudi, Tamil Nadu, India

(Affiliated to Manonmaniam Sundaranar University, Tirunelveli, Tamil Nadu, India)

ABSTRACT

In this analysis, the ultrasonic velocity, density and viscosity of DMSO were measured at different temperatures of 308K, 313K, 318K, 323K, 328K and 333K with butanol. Acoustical parameters such asacoustic impedance (Z), adiabatic compressibility (β_a), Intermolecular freelength (L_f), relaxation time (τ), internal pressure (π_i) have been determined from these. The variety of derived parameters was used to analyze the form and scope of interactions between the binary molecules.

Keywords : Ultrasonic velocity, DMSO, Alcohol, Acoustical parameters, free length, adiabatic compressibility

I. INTRODUCTION

In understanding the nature of the molecular interaction between them, thermodynamic and acoustical research on binary/ternary liquid mixtures play a vital role [1,2]. Ultrasonic studies are commonly used in the food industry, the pharmaceutical sector and the automotive industry [3-5]. Ultrasonic techniques have clarified the essence of the bonding, the frequency of the interactions, the properties and the composition of the binary and ternary liquid mixtures.

Butanol is used to raise octane and oxygenate as a solvent, ethanol denaturant, paint remover component and gasoline. To minimize pain and accelerate the healing of wounds, burns, and muscle and skeletal injuries, DMSO is used topically. To treat painful conditions such as headache, inflammation, osteoarthritis, rheumatoid arthritis and extreme facial pain called tic douloureux, DMSO is often used topically. The present study records the acoustical parameters of the DMSO binary system with butanol at different temperatures.

II. Materials and Methods

AR graded samples of DMSO and butanol were purchased from chempure pvt. Ltd. and used without purification. Ultrasonic interferometer (Model F-81, Mittal Enterprises) is used to measure ultrasonic velocity at 2MHz frequency. The temperature can be varied and maintained constant by

an electronically digital operated variable temperature bath. Density of pure and binary liquid mixtures is determined by using 5ml specific gravity bottle by relative measurement method. Viscosity is measured by Oswald viscometer with water sample as reference. The measurement of velocities, densities and viscosities for all liquid mixtures has been studied at 303K, 308K, 313K,318K, 323K and 328K.

From these measured data, various acoustical parameters are computed using the standard relations:

Adiabatic compressibility $(\beta_a) = \frac{1}{U^2 \rho}$ ------(1)

Acoustic impedance (Z) = Uρ ------(2)

Relaxation time (τ) = 4/3 β_a η ------(3)

Free length$(L_f) = K_T \, \beta_a{}^{1/2}$ ------(4)

Internal pressure $(\pi_i) = bRT \left(\frac{K\eta}{V}\right)^{1/2} (\rho^{2/3}/M_{eff}{}^{7/6})$

------(5)

DMSO+ Butanol at 308K

Mole fraction		U ms^{-1}	ρ 10^{-3} Nsm^{-2}	η 10^{-3} Nsm^{-2}	β_a 10^{-10} ms^2kg^{-1}	z 10^6 $kgm^{-2}s^{-1}$	L_f 10^{-10} m	τ 10^{-13} s	π_i 10^8 Nm^{-2}
X_1	X_2								
1.000	0.000	1455.6	1072.6	1.152	4.400	1.561	0.478	0.676	6.114
0.814	0.186	1380.4	1020.2	1.543	5.144	1.408	0.517	1.059	7.108
0.622	0.378	1290.6	946.6	1.540	6.342	1.222	0.574	1.302	7.068
0.385	0.615	1206.0	874.2	1.697	7.865	1.054	0.639	1.779	7.385
0.192	0.808	1142.4	816.4	2.110	9.386	0.933	0.698	2.642	8.182
0.000	1.000	1090.0	759.8	1.906	11.078	0.828	0.758	2.816	7.679

DMSO+ Butanol at 313K

Mole fraction		U ms^{-1}	ρ 10^{-3} Nsm^{-2}	η 10^{-3} Nsm^{-2}	β_a 10^{-10} ms^2kg^{-1}	z 10^6 $kgm^{-2}s^{-1}$	L_f 10^{-10} m	τ 10^{-13} s	π_i 10^8 Nm^{-2}
X_1	X_2								
1.000	0.000	1431.6	1072.4	1.110	4.549	1.535	0.491	0.673	6.149
0.814	0.186	1349.2	1020	1.447	5.386	1.376	0.534	1.039	7.073
0.622	0.378	1262.8	946.4	1.447	6.626	1.195	0.592	1.279	7.039
0.385	0.615	1170.8	874.2	1.575	8.345	1.024	0.665	1.753	7.338
0.192	0.808	1123.2	816.2	1.939	9.712	0.917	0.717	2.512	8.038
0.000	1.000	1049.2	758.6	1.598	11.975	0.796	0.796	2.553	7.278

DMSO+ Butanol at 318K

Mole fraction		U ms^{-1}	ρ 10^{-3} Nsm^{-2}	η 10^{-3} Nsm^{-2}	β_a 10^{-10} ms^2kg^{-1}	z 10^6 $kgm^{-2}s^{-1}$	L_f 10^{-10} m	τ 10^{-13} s	π_i 10^8 Nm^{-2}
X_1	X_2								
1.000	0.000	1422.8	1072.2	1.061	4.607	1.526	0.498	0.651	6.127
0.814	0.186	1332.8	1019.8	1.418	5.520	1.359	0.545	1.044	7.157
0.622	0.378	1254.0	946.2	1.401	6.721	1.187	0.602	1.255	7.059
0.385	0.615	1148.4	874.0	1.512	8.676	1.004	0.684	1.749	7.375
0.192	0.808	1114.4	816.0	1.857	9.868	0.909	0.729	2.444	8.021
0.000	1.000	1030.0	757.2	1.484	12.448	0.780	0.819	2.468	7.182

DMSO+Butanol at 323K

Mole fraction		U ms^{-1}	ρ 10^{-3} Nsm^{-2}	η 10^{-3} Nsm^{-2}	β_a 10^{-10} ms^2kg^{-1}	z 10^6 $kgm^{-2}s^{-1}$	L_f 10^{-10} m	τ 10^{-13} s	π_i 10^8 Nm^{-2}
X_1	X_2								
1.000	0.000	1406.0	1072.0	1.040	4.718	1.507	0.509	0.654	6.195
0.814	0.186	1317.8	1019.8	1.363	5.647	1.344	0.557	1.026	7.168
0.622	0.378	1238.8	946.0	1.360	6.888	1.172	0.615	1.249	7.106
0.385	0.615	1143.6	874.0	1.477	8.749	1.000	0.693	1.723	7.419
0.192	0.808	1092	815.8	1.758	1.0279	0.891	0.751	2.410	8.007
0.000	1.000	1017.6	755.2	1.324	12.787	0.768	0.838	2.258	6.921

DMSO+ Butanol at 328K

Mole fraction		U ms^{-1}	ρ 10^{-3} Nsm^{-2}	η 10^{-3} Nsm^{-2}	β_a 10^{-10} ms^2kg^{-1}	z 10^6 $kgm^{-2}s^{-1}$	L_f 10^{-10} m	τ 10^{-13} s	π_i 10^8 Nm^{-2}
X_1	X_2								
1.000	0.000	1385.6	1071.8	1.022	4.859	1.485	0.521	0.662	6.283
0.814	0.186	1305.2	1019.8	1.343	5.756	1.331	0.566	1.031	7.260
0.622	0.378	1226.4	946.0	1.317	7.028	1.160	0.627	1.234	7.137
0.385	0.615	1127.2	873.8	1.418	9.007	0.985	0.709	1.704	7.435
0.192	0.808	1074.6	815.6	1.672	10.626	0.877	0.771	2.367	7.991
0.000	1.000	990.0	754.2	1.197	13.528	0.747	0.870	2.159	6.768

DMSO+ Butanol at 333K

Mole fraction		U ms^{-1}	ρ 10^{-3} Nsm^{-2}	η 10^{-3} Nsm^{-2}	β_a 10^{-10} ms^2kg^{-1}	z 10^6 $kgm^{-2}s^{-1}$	L_f 10^{-10} m	τ 10^{-13} s	π_i 10^8 Nm^{-2}
X_1	X_2								
1.000	0.000	1374.4	1071.6	0.992	4.940	1.473	0.530	0.653	6.309
0.814	0.186	1285.6	1019.8	1.310	5.933	1.311	0.581	1.037	7.335
0.622	0.378	1213.2	946	1.286	7.182	1.148	0.639	1.231	7.199
0.385	0.615	1108.0	873.8	1.334	9.322	0.968	0.729	1.659	7.385
0.192	0.808	1060.0	815.4	1.568	10.915	0.864	0.789	2.283	7.910
0.000	1.000	974.8	751.8	1.058	13.998	0.733	0.893	1.975	6.496

III. RESULTS AND DISCUSSION

The table clearly shows that the ultrasonic velocity decreases at temperatures of 303K, 308K, 313K, 318K, 323K and 328K with the rising concentration of butanol and DMSO. The decline in cohesive forces due to poor molecular interactions was followed by a linear decrease in density and ultrasonic velocity with increased solute concentration. Ultrasonic speed in the solutions relies on the length of the intermolecular free path. Figure 1 shows that with changes in concentration, adiabatic compressibility increases. The rise in adiabatic compressibility in these binary mixtures indicates that less hydrogen bonding is produced, indicating a weak intermolecular interaction between solvent and solute. It is also known that the interactions are lower at a higher temperature than at a lower temperature [6].

The velocity decreases as the temperature increases, suggesting more spacing between the molecules. Compared to the ultrasonic velocity in the mixtures.The adiabatic compressibility and Intermolecular free length indicate an inverse behavior. Intermolecular free length, which relies on the adiabatic compressibility and shows a behavior close to that of compressibility. The change in free length also implies that due to which structural rearrangement is also impacted, there is a major interaction between solvent and solute molecule [7].

With the rise in the mole fraction, the relaxation time increases because of the structural relaxation mechanism [8] and in a situation in which the molecules are rearranged due to the cooperative process. A measure of inter-molecular attraction between the components is the internal pressure in a binary mixtures. When the concentration of butanol increases, the internal pressure increases, implying heavy intermolecular bonding of hydrogen due to the polarity of butanol [9].

IV. CONCLUSION

In conclusion, the molecular interaction of DMSO binary mixtures with butanol across the entire composition range has been studied at atmospheric pressure and at temperatures of 303K, 308K, 313K, 318K, 323K and 328K. Acoustical parameters such as acoustic impedance (Z), adiabatic compressibility (β_a), Intermolecular free length

(L_f), relaxation time (τ), internal pressure (π_i) have been determined and the results are interpreted and the observed results will definitely help the researchers for their further research work.

V. REFERENCES

[1]. A. Ali, A. K. Nain, V. K Sharma and S. Ahmad, Study of molecular interaction in ternary mixtures through ultrasonic speed, Physics and chemistry of liquids, vol:24, issue:4, pages 375-383 2004.

[2]. R Kumar, S Jayakumar and V Kannappan, Study of molecular interactions in binary liquid mixtures, Indian Journal of Pure & Applied Physics, Vol. 46, pp. 169-175 2008.

[3]. Srilatha Manukonda, G. Pavan Kumar, Ch. Praveen Babu, Molecular Interactions in Binary Organic Liquid Mixtures Containing Ethyl Oleate and Ethanol at 2MHz Frequency, International Letters of Chemistry Physics and Astronomy, vol: 1, pp. 17-25 2015.

[4]. Kirandeep Kaur and Kailash C. Juglan, Studies of molecular interaction in the binary mixture of chloroform and methanol by using ultrasonic technique, Der Pharma Chemica, vol:7, issue:2, pp. 160-167 2015.

[5]. G. Nath, A. Tripathy and R. Paikaray,Study of Acoustic parameters in binary mixture at variable frequency, International journal of thermophysics, vol:34, pp. 2160-2172 2013.

[6]. R. K. Kolhe and B. B. Bhosale, Study of excess acoustical parameters of DMSO in 2-propanol as binary liquid mixtures at various temperature, International journal of scientific and research publications, Vol 7, Issue 8 2017.

[7]. PB Morey, Study of molecular interaction in ternary liquid mixtures by ultrasonic velocity measurement, Vidyabharathi International interdisciplinary research journal, vol: 2 , issue: 1,pp. 7-13 2013.

[8]. Kinsler L. E. & Rray A. R., Fundamental of Acoustic, Wiley eastern, New Delhi, 1989.

[9]. N. E. Hammami, M. Bouanz and A. Toumi, Acoustical and thermodynamical study of binary mixture cyclohexane – methanol using ultrasonic interferometer at different temperatures, Indian journal of pure and applied Physics, vol 56, pp 461-467 2018.

Ultrasonic Characterization of different Polymers and Organic Liquids : A Review

Krishna Kumar Pandey[1*], Sandeep Verma[1] , Vikas Lahariya[2]

[1]Department of Physics, School of Basic Sciences and Research, Sharda University, Greater Noida, India
[2]Amity School of Applied Sciences, Amity University Haryana, Gurgaon, Haryana, India
*Corresponding and the sole author: Dr. Krishna Kumar Pandey
E-mail Id: krishnakumar.pandey2@sharda.ac.in

ABSTRACT

A review on ultrasonic characterization of different polymers and organic liquids gives a perception into the physico-chemical and thermal properties of base liquid. In this present review we have reviewed some research papers for understanding the same. Several acoustical parameters like Adiabatic compressibility (β), acoustic impedance (Z), relaxation time (t), ultrasonic attenuation (α / f^2), free path length (L_f) have been evaluated. From the experimental values of ultrasonic velocity (v), densities (d) and viscosity of base liquids and the investigation about ultrasonic techniques gives an information and idea to understand the molecular responses and intermolecular arrangement of liquids and polymers. The ultrasonic interferometer is used for measuring the ultrasonic velocity while Ostwald viscometer and Pyknometer (specific gravity bottle) are used to determine the viscosity and density respectively.

Keywords: Ultrasonic velocity, Adiabatic compressibility, Acoustic impedance, Relaxation time, Ultrasonic attenuation

I. INTRODUCTION

This review paper consists the ultrasonic technique as an alternate to characterize polymers and organic liquids over other standard techniques. The current review presents ultrasonic technique as more systematic, malleable and appropriate perspective for characterization and fulfills the requirements of industries. Sound velocity measurements are always been attracted due to their various applications, particularly for the chemical industry. Understanding of the sound velocity and its variants are exceptionally useful in characterizing liquids such as electrolytes and organic solutions (Semwal H. K. et al 2015).

In modern years the quantification of ultrasonic velocity has been appropriately worked in consideration of the nature of molecular interconnection in pure liquid and liquids mixture. Ultrasonic parameters submit precious information regarding the behavior of the molecules in liquid system, because intermolecular and intermolecular association, dipolar interaction, complex formation and related structure change and affects the compressibility of the system (Bhatt S. C. et al 2010).

The intermolecular force is a function of the concentration of liquid and temperature but variation in the temperature shows more effect than concentration. At the low concentration there may be less numbers of hydrogen bond and at high concentration there may be more numbers of hydrogen bond (Hariharakrishnan V. et al 2015).

This paper consists the study about molecular behavior in single organic liquid, binary and ternary mixtures of some organic liquids and in polymers. "The investigations regarding The molecular interaction in some organic ternary liquid mixtures as explained (Geetha P. et al 2010).

II. Physico-Chemical Properties

Ultrasound develops physical and chemical changes in a liquid medium and produced destruction of cavitations bubbles. Ultrasound is propagated through a series of rarefaction and compression waves induced in the molecules of the medium through which it passes (Puri S. et al 2013).

Polyvinydene floride (PVDF) has a semicrystalline and a simple chemical structure. PVDF has ferroelectric and piezo, pyro quality. These qualities have vast use in device applications like as sonar instruments, solar cells, ultrasound transducers, nonvolatic memory, sensors, actuators. The literature in PVDF helps us to realize the "effect of concentration and nature of solvents on molecular interconnection in polymer solution" (Kulkarni S. S. et al 2016). The polymer Polyvinyl acetate (PVA) is used in adhesives (Bhatt S. C. et al 2010).

Dimethylformamide (DMF) is a polar molecule which has dipole moment as equal as nitrobenjene. When DMF relate with nitrobenzene then dipoar-dipole interaction is obtained and volume of the mixture going to decrease due to small size of N, N-DMF and linear aliphatic configuration. Nitrobenzene is comparatively complex molecule. It is non-ideal due to its polarity arising out of C-N and N-O bonds. Cyclohexane be a part of alicyclic hydrocarbon and it attracts towards an electrophile or nucleophile at normal temperature. Cyclohexane does not make strong interaction with other components of mixture because of its non-polar poperty (Praharaj M. K.et at 2013). Organic ternary liquids consists the aromatic hydrocarbon group that is highly polar (Geetha P. et al 2010). With the help of measurement of ultrasonic velocity, density and viscosity and using the formulae physico-chemical behavior of liquids can be identified (Semwal H. K. et al 2015).

Table 1. Details of Various Reviewed Parameters

S.No.	Name of liquid studied	Conc. %	Fixed freq.	T (K)	Density Kg/m^3	Viscosity NSm^{-2}	Ultrasonic velocity m/s	A.comp. (ß) X 10^{-10} (N^{-1}m^2)	Impadaence Kg m^{-2}/s	Free path length X 10^{-11}	References
1	PVDF in Acetone	0.2	1 MHz	…………	784.1	0.3672	1166.5	…………	………..	…….	Kulkarni S. S. et al 2015

2	Aqueous solution of Digitaline + double distilled water	0.6	2 MHz	303K	1.043	0.01064	1543	4.0291	…………	1.27	Hariharakrishnan V. et al 2015
3	Isopropyl alcohol% + Benzene %+ cyclohexane %	10 20 70	1 MHz	273K	0.703	--------	1468	--------	1.032	------	**Semwal H. K. et al 2015**
4	N-N dimethylformamide Cyclohexane Nitrobenzene	0.09 0.4 0.49	2MHz	318K	856.69	0.6459	1170.2	8.3355	1.012	5.864	Praharaj M. K. al 2013
5	Polyvinyl acetate	0.5	1 MHz	35^0 C	1023	0.00102	1020.6	9.381	10.44	------	Bhatt S. C. et al 2010

Applications and future prospective

The details of various reviewed parameters are as shown in the above table. As observed in the reviewed research papers (as per the details shown in the table) it has been seen that:

For different regions 308.15K, 313.5K and 318.5K in the case of different binary liquids Cyclohexane, benzene, Methylebenzene, 1,2-dimethyl benzene, 1,4-dimethyle benzene and 1,4-dichlorobutane, 1,3,5-trimethylebenzene, the value of intermolecular free path length (L_f) in binary liquid decrease by increasing the mole fraction of 1,4-dichlorobutane in binary mixture at all three temperatures 308.15 K, 313.5 K and 318.5 K.

The value of Acoustic impedance (Z) increase for all the binary mixtures with 1,4-dichlorobutane at the three temperatures 308.15 K, 313.5 K and 318.5 K.

Ultrasonic velocity increase by increasing the concentration of nanofluiud because of weak intermolecular force and due to surface effect and hydrogen bonding between particle and water molecules. Density and ultrasonic velocity increase by increasing the concentration because cohesive forces increase due to strong intermolecular attraction.

Intermolecular free path length (Distance between the surfaces of the adjoining molecules) deceases by increasing the velocity. Acoustical impedance (a specific property of the liquid) by increasing the concentration of liquid acoustical impedance also increase, it show strong attraction force between molecules.

At a particular frequency ultrasonic velocity in ternary liquid change with composition (not linear) but at a fix composition ultrasonic velocity increases

by increasing in the frequency in liquid mixture (Isopropyl Alcohol, Benzene and Cyclohexane).

Isentropic compressibility of ternary liquid mixture decreases by increasing the frequency and it changes with composition also.Acoustical impedance of ternary liquid slightly increases by increasing the frequency.

While ultrasonic velocity decreases by increasing the frequency for liquid mixture of N-N-Dimethyleformamide, nitrobenzene, and cyclohexane.

Due to weak interaction between unlike molecules acoustical impedance decreases by increasing frequency in N-N-Dimethyleformamide, nitrobenzene, and cyclohexane liquid mixture. Viscosity of the liquid (polyvinyl acetate) slightly decreases by increasing the temperature at fix concentration while it increases by increasing by concentration of liquid.

Ultrasonic velocity going decreases by increasing the temperature at a particular concentration while velocity increases by increasing the concentration of liquid (polyvinyl acetate).

Therefore from the above observed results from different Research papers as shown in the table as a whole, it can be stated that these findings of various research papers as reviewed will definitely help a lot to different researchers of this area.

III. CONCLUSION

For understanding the nature and strength of intermolecular force in the liquid ultrasonic technique is a important tool. Now a day's ultrasonic is a developing field for research, which has been used in the polymer as well as organic liquids for investigation and conversion. The values of acoustical parameter for polymers, single organic, liquid binary organic liquid, and ternary organic liquids has been successfully understood by reviewing the various research paper of the same area.

IV. REFERENCES

[1]. Yao Y. et al (2020) "Power ultrasound and its applications: A state-of-the-art review" elsivier pp.1-20.

[2]. Kulkarni S. S., Khadke U. V., (2016) "Effect of Solvent on the Ultrasonic Velocity and Acoustic Parameters of Polyvinylidene Fluoride Solution", Indian Journal of Material Science, vol.10, pp.1-6.

[3]. Hariharakrishnan V. Ramasamy R., Sekar S. (2015) "Intermolecular Interaction through Ultrasonic Studies", Indian journal of Applied Research, vol.5, no., pp.255-258.

[4]. Semwal H. K. Bhatt S. C. (2015) "Some Acoustical Parameters of Ternary Liquid Mixture (Isopropyl Alcohol, Benzene and Cyclohexane)", International Journal of Science and Research (IJSR), vol.5, pp. 585-588.

[5]. Praharaj M. K., Satapathy A., Mishra P., Mishra S. (2013) "Ultasonic studies of ternary liquid mixture of N-N-Dimethyleformamide, nitrobenzene, and cyclohexane at different frequencies at 318K" Journal of Theoretical and Applied Physics, pp.1-6.

[6]. Puri S. Chopra H. (2013) "Applications of Ultrasound in Organic Synthesis-A Green Approach" Bentham Science Publishers, vol.17, no.16, pp 1790-1828.

[7]. Geetha P., Ramesh P., Raju K., Varghese H. T., Panicekr Y. (2010) "Ultrasonic Studies on binary and ternary mixture of some organic liquids", Material Science Research India vol.7, pp. 255-260.

[8]. Bhatt S. C. Singh P. K. (2010) "Investigation of Acoustical parameters of polyvinyl acetate" Applied Physics Research, vol.2, no.1, pp.35-45.

Excess Parameter Study of Aqueous Benzene at Various Temperatures

L. V. Thakre

Department of Physics, Dayanand Science College, Latur, Maharashtra, India

ABSTRACT

The present paper reports the study of excess parameters of aqueous benzene namely excess adiabatic compressibility (βa^E), excess relaxation time (τ^E) and excess molar volume (V_m^E) at various temperatures and at frequency 5 MHz, In order to study the nature of interactions between the components of binary liquid mixtures. Excess parameters play a vital role in assessing the compactness due to molecular arrangement and the extent of molecular interaction in the liquid mixtures through charge transfer, dipole-dipole and dipole-induced dipole interaction. Non–ideal liquid mixtures show considerable deviation from linearity in their physical behavior with respect to concentrations which interpreted the presence of strong or weak interactions. The thermo acoustic parameters were calculated from the velocity, density and the viscosity measurements. By taking measurements over entire range of concentrations and temperatures, we obtained information about the aggregation of constituents in aqueous benzene.

Keywords : α-Al_2O_3, Ethanol, Free Length, Nanosuspension

I. INTRODUCTION

From the observed spectra, weak molecular interactions cannot be resolved. These weak molecular interactions can be resolved by ultrasonic nondestructive technique. The thermoacoustic measurement provides useful information regarding physical and chemical behavior of pure liquids and liquid mixtures. It is therefore important to obtain the fundamental information such as molecular association, dissociation, internal structure making or breaking, miscibility or compatibility, semi-miscibility or semi compatibility etc. Excess parameters study of binary liquid mixtures plays very important role in understanding molecular interaction in pure, binary and ternary liquid mixtures for possible applications in biomedical industries, chemical, pharmaceutical industries and technology. Liquid mixtures consisting of ions, polar and non-polar components are of immense importance in industries, such as in pharmaceutical, petrochemical and dye.

II. RESULT AND DISCUSSION

Figure 1 shows the variation of excess values of relaxation time (τ^E), adiabatic compressibility βa^E and molar volume V_m^E of aqueous benzene. It is seen that; excess values are positive over the entire range of concentration and at temperature 293 K. The positive excess values of relaxation time indicate the strong molecular interaction between the unlike component molecules of liquid mixture. The nonlinear variation may be due to solvent-solute or ion-dipole interactions. When temperature is increased positive excess values of relaxation time τ^E slightly decreases with same trend of variation.

Excess values of adiabatic compressibility βa^E and excess molar volume V_m^E are negative. The negative deviation of excess values is an indication of existence of strong interaction between the component molecules and molecular association between the unlike molecules.
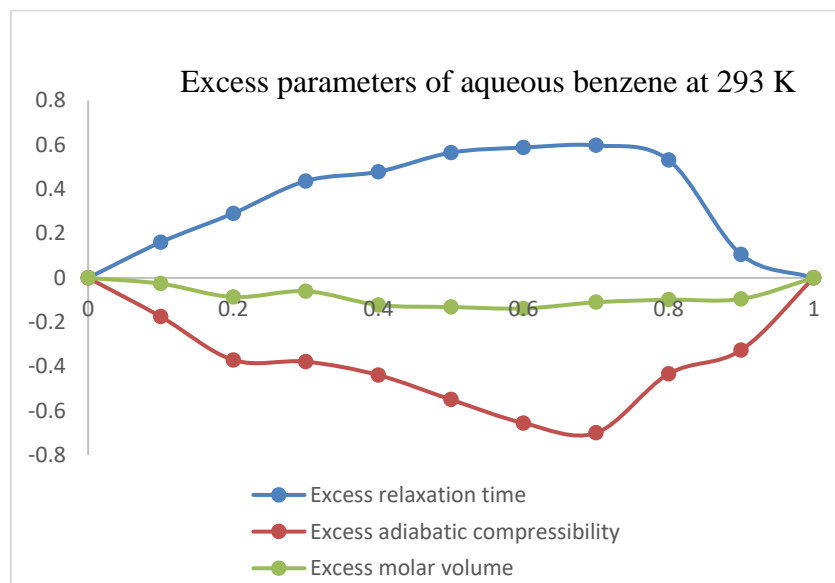
Figure 1 Variation of excess values of relaxation time (τ^E), adiabatic compressibility βa^E and molar volume V_m^E of aqueous benzene at 293 K

Figure 2 shows the variation of excess values of relaxation time τ^E of aqueous benzene. It is seen that; excess values are positive over the entire range of concentration and at temperature 298 K. The positive excess values of relaxation time indicate the strong molecular interaction between the unlike component molecules of liquid mixture. The nonlinear variation may be due to solvent-solute or ion-dipole interactions. When temperature is increased positive excess values of relaxation time τ^E slightly decreases with same trend of variation. Excess values of adiabatic compressibility βa^E and excess molar volume V_m^E are negative. The negative deviation of excess values is an indication of existence of strong interaction between the component molecules and molecular dissociation between the unlike molecules, it also shows that maximum structural changes take place in peak region of the mixture. It further suggests that the negative excess values of βa^E are due to the closely packed molecules which account for the existence of strong molecular interaction with increase in temperature, for entire range of

concentration, there are decreasing negative excess values of βa^E and L_f^E, indicates molecular association, which leads to less closer packing in binary liquid mixture.
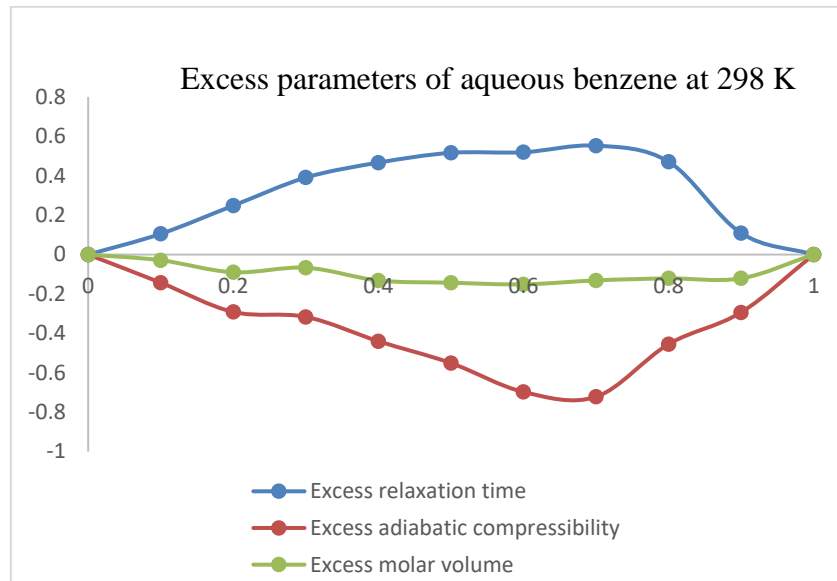
Figure 2 Variation of excess values of relaxation time (τ^E), adiabatic compressibility βa^E and molar volume V_m^E of aqueous benzene at 298 K

Figure 3 shows the variation of excess values of relaxation time (τ^E), adiabatic compressibility βa^E and molar volume V_m^E of aqueous benzene. It is seen that; excess values are positive over the entire range of concentration and at temperature 303 K. The positive excess values of relaxation time indicate the strong molecular interaction between the unlike component molecules of liquid mixture. The nonlinear variation may be due to solvent-solute or ion-dipole interactions. When temperature is increased positive excess values of relaxation time τ^E slightly decreases with same trend of variation. With increase in temperature, negative excess values of βa^E and V_m^E again decreases keeping same variation trend negative excess values and trend which are applicable in Broad classification.
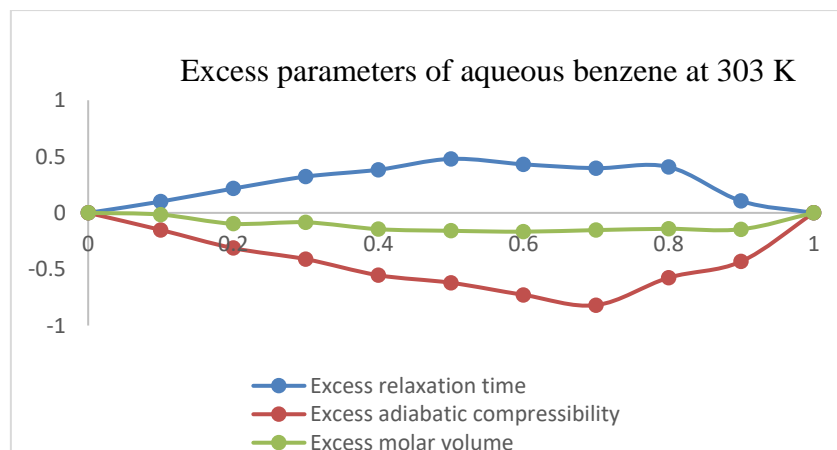
Figure 3 Variation of excess values of relaxation time (τ^E), adiabatic compressibility βa^E and molar volume V_m^E of aqueous benzene at 298 K

III. CONCLUSIONS

In broad classification $\%\beta a^E$ and $\%V_m^E$ indicating strong interactions between the component molecules.

Broad classification on the basis of negative $\% \beta a^E$ values the relative strength of heteromolecular AB interaction

IV. REFERENCES

[1]. Syal V K, Chauhan S and Uma Kumari, Ind. P. Pure Appl. And appl. Physics, 43, 844-848, (2005).

[2]. Jing-Rim, Meyung – Ha Y, J. of Korean Physical Society, 4(1), 171-174, (2002).

[3]. Bitak J K et al., International J. of Physics and Mathematical sciences, 3(1), 113-119, (2013).

[4]. Prahraj M K et al., Arch. Phy. Res. 3(3), 192-200 (2012).

[5]. Palaniappan L. and Velusamy V., Ultrasonic study of human cerebrospinal fluid, Indian J Pure Appl Phys., 42, 591-594, (2004).

[6]. Saravana Kumar K. and Kubendran T.R., Density and Viscosities for the Binary Mixtures of 1, 4-Dioxane and Benzene or Chlorobenzene at 303.15, 308.15, 313.15 K and a Pressure of 0.1MPa, Research Journal of Chemical Sciences, 2(4), 50-56, (2012).

[7]. Anbarasu S. and Devarajan Prem Anand, Uniaxial Growth and Characterization studies of [(para methoxy phenyl) imino] benzene NLO crystal by Sankaranarayanan- Ramasamy Method, Res. J. Recent Sci., 1(10), 37-44 (2012).

[8]. Sharma C.K. and Kanwar S.S., Synthesis of methyl cinnamate using immobilized lipase from B. licheniformis MTCC-10498, Res. J. Recent Sci., 1(3), 68-71 (2012).

[9]. Nithiyanantham S. and Palaniappan L., Metals Materials and Processes, 20(3), 203 (2008).

[10]. Nithya R., Mullainathan S., Nithiyanantham S. and Rajasekaran R., Synthesis of some new pyrazolylfuropyrimidinethiones and triazolofuropyrimidinethiones, E Journal of Chemistry, 6(1), 138 (2009).

[11]. B. Samuel Ebinezer, L. Palaniappan, Effect of Field Strength in the Velocity Anisotropy of Ferrofluids, J Phy Sci., 18(1), 11-21 (2007).

[12]. Velusamy V., Nithiyanantham S., Palaniappan L., Ultrasonic study of adsorption in disaccharide (maltose) metabolism, Main Group Chemistry, 6(1), 53-61, (2007).

Structural, Morphological and Supercapacitive Performance of Electrodeposited PPy/Co$_3$O$_4$ Thin Film

P. M. Kharade[1]*, J. V. Thombare[2], S. S. Dhasade[2], P. B. Abhange[3], R.S.Gaikwad[4], S. D. Patil[5], D. J. Salunkhe[6]

[1]Department of Physics, Shankarrao Mohite Patil Mahavidyalaya, Akluj, Dist-Solapur, Maharashtra, India

[2]Department of Physics, Vidnyan Mahavidyalaya, Sangola, Dist-Solapur, Maharashtra, India

[3]Department of Physics, G.M. Vedak College of Science, Tala, Raigad, Maharashtra, India [4]Department of Chemistry, Vidnyan Mahavidyalaya, Sangola, Dist-Solapur, Maharashtra, India

[5]Department of Physics, Pratapsingh Mohite Mahavidyalaya, Karmala, Dist-Solapur, Maharashtra, India

[6]Nanocomposite Research Laboratory, K.B.P. Mahavidyalaya, Pandharpur, Dist-Solapur, Maharashtra, India

*Corresponding Authors E-mail:pravink150@gmail.com@gmail.com

ABSTRACT

The PPy/Co$_3$O$_4$ thin film was deposited by electrodeposition method for supercapacitor application. The structural, surface morphological and supercapacitive study of PPy/Co$_3$O$_4$ thin film was carried out with the help of X-ray diffraction (XRD) and Scanning Electron Microscopy (SEM) study. The structural study of PPy/Co$_3$O$_4$ thin film show cubic crystal structure. The supercapacitive study of electrodeposited PPy/Co$_3$O$_4$ thin film was carried out with the help of cyclic voltammetry (CV), charging-discharging (CD) and electrochemical impedance Spectroscopy (EIS) study. The PPy/Co$_3$O$_4$ thin film gives maximum specific capacitance of 435 F.g^{-1} at 5 mV.s^{-1} in 0.5M Na$_2$SO$_4$ aqueous electrolyte solution. The PPy/Co$_3$O$_4$ thin film shows coulombic efficiency of 98% while specific energy and specific power was observed to be 80.4 Wh. kg^{-1} and 20.4 kW kg^{-1} respectively. From EIS study, PPy/Co$_3$O$_4$ thin film has values of R$_s$ and R$_{CT}$ to be 0.62 Ω and 2.22 Ω respectively at 1V.

Keywords: Supercapacitor, Electrodeposition, PPy/Co$_3$O$_4$, XRD, SEM, EIS.

I. INTRODUCTION

Supercapacitor is an electrochemical device having better energy density and power density as compared to conventional capacitor and ordinary batteries. The most of the researchers are trying to develop a new materials which having a good capacity of both delivering energy density and power density in a particular application. Generally, supercapacitors are broadly classified as Pseudocapacitors and electric double layer capacitors (EDLC). The classification is purely based on the types of mechanism of charge storage inside the electrode materials [1].

The Pseudocapacitors are the class of supercapacitors, shown by metal oxide and conducting polymers while the EDLC class of supercapacitors are shown by carbon based materials

[2]. The most studied and better metal oxide for supercapacitive study is ruthenium oxide, but unfortunately ruthenium oxide has some drawbacks such as toxic in nature and too much cost as compare to others. Hence, other metal oxide can replaced for ruthenium oxides such as manganese oxide [3-4], cobalt oxide [5], nickel oxides [6] etc. Amongst of all oxides, cobalt oxide has some features such as availability of source of materials, less toxic than ruthenium oxide, better cycling stability etc. In spite of this, it has less conducting. Conductivity of cobalt oxide electrodes can be improved with the help of some dopant or any other methods such as annealing, making hetero structure with conducting polymer. So by keeping this view in mind we have developed a PPy/Co_3O_4 layered heterostructures by electrochemical deposition method.

In the present study, efforts have been taken to prepare a PPy/Co_3O_4 hetero structure based thin film. The electrochemically prepared PPy/Co_3O_4 thin film have been characterized for structural and morphological study by means X-ray diffraction (XRD) study and Scanning electron microscopy (SEM) study, respectively. The supercapacitive study was carried out in 0.5 M Na_2SO_4 electrolyte solution with the help of cyclic voltammetry, charging-discharge study and electrochemical impedance spectroscopy study.

II. EXPERIMENTAL

2.1. Synthesis of PPy/Co_3O_4 thin film:

The PPy/Co_3O_4 thin film was synthesized following procedure reported earlier literature [7]. Before deposition, the SS substrates was polished with emery polish paper rough to finish and rinsed with double distilled water and acetone. Firstly for deposition of PPy thin film, the bath contains aqueous 0.12 M pyrrole solution was mixed with aqueous 0.12 M H_2SO_4 solution and PPy thin films were deposited on stainless steel (SS) substrates using electrodeposition method at constant current

density of 5 mA cm^{-2} for 10 minutes. The PPy thin film deposited on SS substrate was used for further deposition of layered PPy/Co_3O_4 thin film. The cobalt was deposited on PPy at constant current density of 5 mA for 10 minutes and anodically oxidized in 0.5 M KOH solution. The deposited layered PPy/Co_3O_4 thin film was used for further characterization.

2.2. Characterization Techniques:

The structural study of PPy/Co_3O_4 thin film was carried out with the help of XRD using Bruker axes D8 Advance Model with cu radiation (K_α of $\lambda = 1.54$ A$^\circ$) within 2θ range between 20° to 80°. The surface morphology of PPy/Co_3O_4 thin film was carried out by using SEM (Model: JSM-6160). The supercapacitive performance of PPy/Co_3O_4 thin film was studied by using CV, CD and EIS techniques by using electrochemical workstation (CHI 660 A). The electrochemical cell consists of three electrode systems. PPy/Co_3O_4 thin film was used as a working electrode, graphite was used as a counter electrode and saturated calomel electrode (SCE) was used as a reference electrode. All measurements were carried out in 0.5 M Na_2SO_4 electrolyte solution.

III. RESULTS AND DISCUSSION

3.1. XRD Study:

XRD is an imperative tool to analyze the crystal structure of the prepared film. Fig. 1 show XRD spectra of PPy/Co_3O_4 thin film in 2θ range between 20° to 80°. The XRD spectra of PPy/Co_3O_4 thin film shows all peaks corresponds to Co_3O_4 thin film. The peak indexed in XRD spectra was well matched with JCPDS data (Card No 42‑1467) having cubic crystal structure [5]. The most intense peak was found to be (220). The Co_3O_4 thin film deposited on PPy layer was found to be polycrystalline in nature also the peak broadening indicates the formation of nanostructure. The most intense peak (220) indicating the overall growth of Co_3O_4 material is along the direction perpendicular to the (220) plane

(i.e. along [220] direction). The peak marked with SS in XRD spectra is stainless steel substrate only and no additional peak was observed in the XRD of PPy/Co_3O_4 thin film. The low intensity peak in XRD spectra reveals the nanostructured formation of layered PPy/Co_3O_4 thin film.

3.1.2. SEM study:

Fig. 2 (A-B) shows SEM micrographs of PPy/Co_3O_4 thin films at two different magnifications. The SEM micrographs indicating that the substrate was well covered with thin layered structure of polypyrrole followed by Co_3O_4. At higher magnification in Fig. 2(B), it is observed that the nano-grains like structure of Co_3O_4 is formed on polypyrrole layer. Also, it shows some voids within the layered structure of Co_3O_4. Such morphology provides more active sites for electrochemical reactions. The electrochemical reactions may be due to both polypyrrole and Co_3O_4 thin films. Polypyrrole improves conductivity of thin film Co_3O_4 enhances supercapacitive performance because of availability of more reactive sites.

3.2. Supercapacitive Study:
3.2.1. Cyclic Voltammetry (CV) Study:

CV techniques is an important tool to measure the specific capacitance of the electrode material. Fig. 3(A) shows the CV curves of PPy/Co_3O_4 thin film at scan rate of 5 and 10 mV/s within potential limit between -1.00 to +1.00 V vs SCE, respectively. The nature of CV curve nearly rectangular in shape. Also as scan rate increases, area under curve increases and cathodic and anodic peak shift towards more positive and negative direction indicating the ideal pseudocapacitive behaviour of PPy/Co_3O_4 thin film. The specific capacitance of the PPy/Co_3O_4 thin film was evaluated using following formulae,

$$\text{Specific capacitance } (C_s) = \frac{C}{W} \quad \text{-------------- (1)}$$

Where, C is capacitance in farad and W is the mass of the active electrode material.

The calculated value of specific capacitance of PPy/Co_3O_4 thin film was found to be 435 F.g^{-1}. The high value of specific capacitance of PPy/Co_3O_4 thin film is may be due to porous and nanostructured surface behaviour of PPy/Co_3O_4 thin film, which is confirmed from XRD and SEM study. This increase in specific capacitance is attributed to synergistic effect of PPy and Co_3O_4 thin film. It is believed that nanostructured electrode material provide high surface area of electron intercalation and de-intercalation into from electrode/electrolyte interface to store more charge. It improves the capacitive character [8].

3.2.2. Charging-discharging study:

Fig. 3 (B) shows charge-discharge curves of PPy/Co_3O_4 thin film at current density of 5 mA/cm^2. The exponential increment in potential was observed in charging curve reveals charge storage capability of PPy/Co_3O_4 thin film. The potential drop at the starting of discharge curve is due to internal resistance of the electrode. The discharge curve also shows that slow decrement in potential indicate good capacitive behaviour of PPy/Co_3O_4 thin film. The supercapacitive parameters such as, coulombic efficiency, specific energy and specific power of PPy/Co_3O_4 thin film were calculated by following formulae:

$$\text{Coulombic Efficiency } (\eta) = \frac{T_d}{T_c} \times 100 \quad \text{----------- (2)}$$

$$\text{Specific power } (P) = \frac{V \times I}{W} \quad \text{--------------- (3)}$$

$$\text{Specific energy } (E) = \frac{V \times I \times T_d}{W} \quad \text{------------- (4)}$$

Where, T_d and T_c is discharge and charge time in sec, V is voltage in volts, I is current in A, W is the mass of the electrode in gm.

The coulombic efficiency of PPy/Co_3O_4 thin film was found to be 98%. The values of specific energy and specific power of PPy/Co_3O_4 thin film were observed to be 80.4 Wh. kg^{-1} and 20.4 kW kg^{-1} respectively.

3.2.3. EIS Study:

Fig.4 shows EIS study in terms of Nyquist plot of PPy/Co_3O_4 thin film within frequency range of 10 Hz to 1MHz at different potential such as 1V, 1.2V and 1.4V, respectively. The Nyquist plot PPy/Co_3O_4 thin film shows semicircle in high frequency region and straight line in low frequency region [9]. The intercept of the semicircle on Z' axis gives value of solution resistance (R_s) and diameter of semicircle gives value of charge transfer resistance (R_{CT}). The value R_s and R_{CT} calculated from Nyquist plot were found to be 0.62 Ω and 2.22 Ω, respectively for 1V; that of 0.74 Ω and 2.89 Ω, respectively for 1.2V; and that of 0.90 and 3.15 Ω, respectively for 1.4 potential of PPy/Co_3O_4 thin film. It was observed that as applied potential increases values of R_s and R_{CT} increases. The applied potential of 1V for PPy/Co_3O_4 thin film shows small values of R_s and R_{CT} than other potentials indicating superior rate capability of electrode due to porous and nanostructured PPy/Co_3O_4 thin film [4].

IV. CONCLUSION

Nanostructured layered heterostructures of PPy/Co_3O_4 thin film was successfully synthesized by electrochemical deposition method. Their structural and surface morphological behaviour were studied by using XRD and SEM techniques. The SEM study of PPy/Co_3O_4 thin film reveals that porous and nano-grains morphology which is favourable for electrochemical capacitor application it provide high surface area, easy transfer of electron for calation and decalation process. The layered PPy/Co_3O_4 thin film show better values of specific capacitance, specific energy and specific power due to synergistic effect of PPy and Co_3O_4 thin film. Thus, electrochemically deposited layered PPy/Co_3O_4 thin film is good electrode material for supercapacitor.

VI. REFERENCES

[1]. P. Simon, Y. Gogotsi, Materials for electrochemical capacitors, Nat. Mater. 7(2008) 845-854.

[2]. D. Wei, M.R. Scherer, C. Bower, P. Andrew, T. Ryhanen, U. Steiner, A Nanostructured Electrochromic Supercapacitor, Nano Lett. 12 (2012)1857-1862.

[3]. Z. Yu, B. Duong, D. Abbott, J. Thomas, Highly ordered MnO2 nanopillars for enhanced supercapacitor performance, Adv. Mater. 25(2013)3302-3306.

[4]. P.M. Kharade, S.B. Kulkarni, D.J. Salunkhe, Nanoflakes like hydrophilic Mn2O3 thin film as a supercapacitor electrode, Chinese J. Phy. 55 (2017)1684-1689.

[5]. P.M. Kharade, J.V. Thombare, A.R. Babar, R.N. Bulakhe, S.B. Kulkarni, D.J. Salunkhe, Electrodeposited nanoflakes like hydrophilic Co3O4 as a supercapacitor electrode, J Phys Chem Solids. 120 (2018)207–210.

[6]. L. Gu, Y. Wang, R. Lu, L. Guan, X, Peng, J. Sha, Anodic electrodeposition of a porous nickel oxide-hydroxide film on passivated nickel foam for supercapacitors, J. Mater. Chem. A. 2 (2014) 7161-1764. 7161-1764.

[7]. P. M. Kharade, S. M. Mane, S. B. Kulkarni, P. B. Joshi, D. J. Salunkhe, Ground nut seed like hydrophilic polypyrrole based thin film as a supercapacitor electrode, J. Mater. Sci. 27 (2016)3499–3505.

[8]. P. M. Kharade, J. V. Thombare, S. L. Kadam, S. B. Kulkarni, D. J. Salunkhe, Layered PPy/Cr2O3 as a supercapacitor electrode with improved electrochemical performance, J Mater Sci: Mater Electron (2017) 28:17908–17916.

[9]. J. Zhao, B. Tang, J. Cao, J. Feng, P. Liu, J. Zhao, Effect of hydrothermal temperature on the structure and electrochemical performance of manganese compound/ordered mesoporous carbon composites for supercapacitors, Mater. Manuf. Process. 27(2012)119-124.
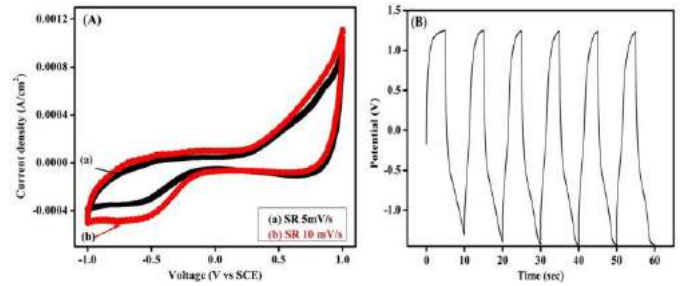
Figure 3 (A) CV study of PPy/Co₃O₄ thin film at scan rate of 5 and 10mV/s and **(B)** Charging-discharging study of PPy/Co₃O₄ thin film.

Figures:
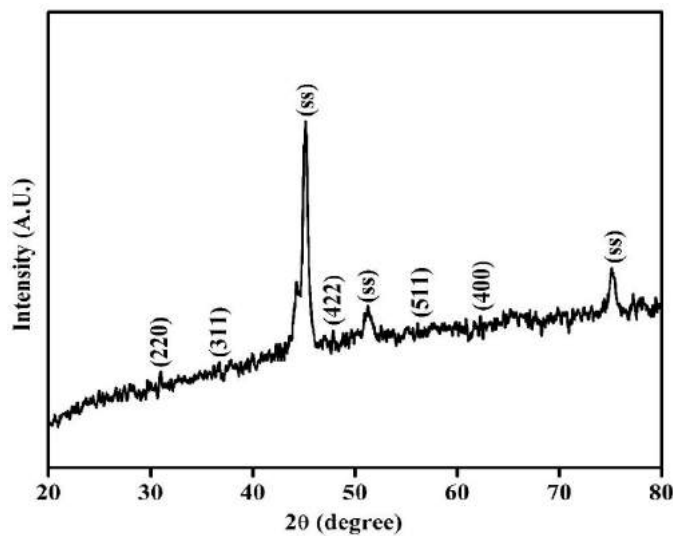
Figure 1. XRD spectra of PPy/Co₃O₄ thin film.
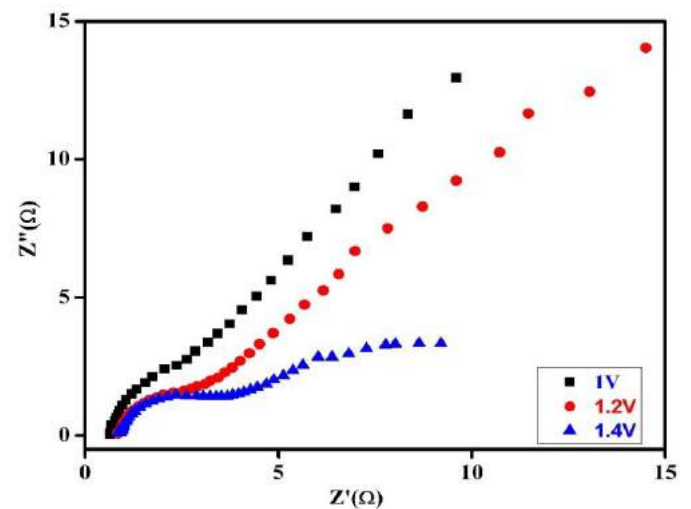
Figure 4. EIS study of PPy/Co₃O₄ thin film**.**
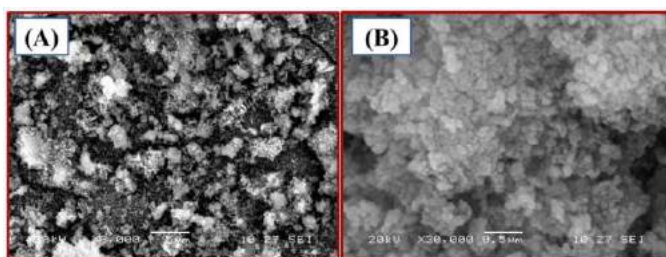
Figure 2. SEM images of PPy/Co₃O₄ thin film at **(A)** 3000kX and **(B)** 30000kX magnifications respectively

Stability of α-Alumina Nanofluids in Organic Base Fluid

Mrunal Pawar[1], R. D. Chavhan[2], O. P. Chimankar[2] & N. R. Pawar[3]

[1]St.Vincent Pallotti College of Engineering and Technology, Nagpur, Maharashtra, India

[2]Department of Physics, RTM Nagpur University, Nagpur, Maharashtra, India [3]Department of Physics, Arts, Commerce and Science College, Maregaon, Maharashtra, India

* Corresponding author: mrunalpawarsept2000@gmail.com

Highlights

- The thermoacoustic parameters of nanofluids are highly dependent on specific surface area to volume ratio of the nanoparticles in nanofluids.
- α- Alumina nanoparticles were synthesized via sol-gel method.

ABSTRACT

Nanoparticles of alpha alumina (α-Al_2O_3) was prepared via sol-gel method [4-7] from Aluminum isopropoxide [Al $(OC_3H_7)_3$] and aluminum nitrate. Starting solution was prepared by adding aluminum isopropoxide [Al $(OC_3H_7)_3$] gradually in 0.2 M aluminum nitrate and solution continuously stirred for 48 hours. Later, Sodium dodecylbenzen sulfonate (SDBS) was added and stirred for one hour. Now this solution was heated up to 60℃ and stirred constantly for evaporation process. Now the paste so obtained was heated at 90℃ for 8 hours, we get nanoparticles of alpha alumina (α-Al_2O_3) in powder form. The prepared sample was characterized by X- ray diffraction (XRD), Scanning electron microscopy (SEM), thermal conductivity and Zeta potential. Average particle size has been estimated by using Debye-Scherrer formula [8-9]. It was found to be in the range of 20-30 nm. Nanofluids of α-Al_2O_3 in methanol base fluid were prepared by two step method.

Keywords : α-Al_2O_3 Nanofluids; XRD; SEM; Zeta potential; Thermal conductivity

I. INTRODUCTION

α-Al_2O_3 is one of the most widely used oxide ceramic material. It is used in a variety of plastics, rubber, ceramics, and refractory products. As the α-phase ultrafine Al_2O_3 is a high-performance material of far infrared emission, it is used in fiber fabric products and high-pressure sodium lamp as far-infrared emission and thermal insulation materials. In addition, α-phase nano-Al_2O_3 with high resistivity and good insulation property, it is widely used as the main components for YGA laser crystal and integrated circuit substrates. Recently, advances in manufacturing technology have permitted the production of particles in the 10 nm to 100 nm range.

In the present investigation the synthesis of α-Al_2O_3 nanoparticles by sol-gel method is discussed. Thermal conductivity related to the surface of nanoparticle and

nanoparticles surfactant interactions. α-Al$_2$O$_3$ nanoparticles with surface areas 30 nm have been prepared, their thermal conductivities and characterization have been investigated.

II. Preparation of Samples

Nanoparticles of alpha alumina (α-Al$_2$O$_3$) was prepared by sol-gel method [4-9] from Aluminum isopropoxide [Al (OC$_3$H$_7$)$_3$] and aluminum nitrate. Starting solution was prepared by adding aluminum isopropoxide [Al (OC$_3$H$_7$)$_3$] gradually in aluminum nitrate and solution continuously stirred for 48 hours. Later, Sodium dodecylbenzen sulfonate (SDBS) were added and stirred for one hour. The obtained solution was heated up to 60°C and stirred constantly for evaporation process. Now the paste so obtained was heated at 90°C for 8 hours, we get nanoparticles of alpha alumina (α-Al$_2$O$_3$) in powder form [8-13].

III. Results and Discussion

Spectroscopic Characterization:

The prepared sample was characterized for their phase purity and crystallinity by X-ray powder diffraction (XRD), FTIR and SEM. Formation of the compound confirmed by XRD pattern matched with the standard data available in JCPDS file. Average particle size of α-Al$_2$O$_3$ nanoparticles has been estimated by using Debye-Scherrer formula.

$$D = \frac{0.9\lambda}{W Cos\theta} \qquad \text{.. (1)}$$

Where 'λ' is the wavelength of X-ray (0.15460 nm), 'W' is FWHM (full width at half maximum), 'θ' is the diffraction angle and 'D' is particle diameter (size). The estimate size of α-Al$_2$O$_3$ nano particles is found to be 30 nm. Nanofluids of α-Al$_2$O$_3$ nanoparticles were prepared by two step method in methanol base fluid.
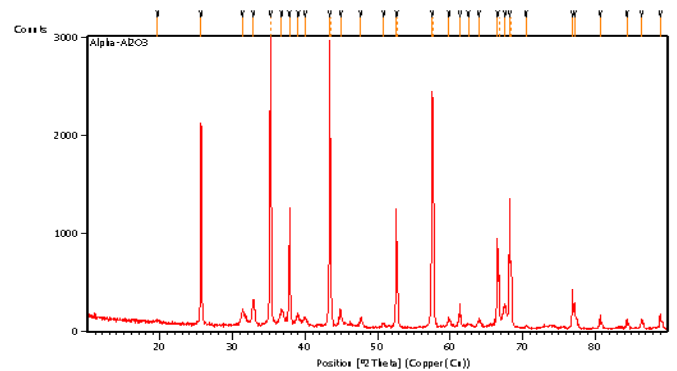
Fig.1 XRD pattern of α-Al$_2$O$_3$ nanoparticles

Fig.1 shows the XRD pattern of α-Al$_2$O$_3$ nanoparticles. The XRD measurement carried out by using "PAN analytical" X-ray diffractometer keeping the parameter constant at Start Position [°2Th.]: 10.0154 End Position [°2Th.]: 89.9834, Step Size [°2Th.]: 0.0170, Scan Step Time [s]: 5.7150, Scan Type: Continuous, Measurement Temperature [°C]: 25.00 Anode Material: Cu, K-Alpha1 [Å]: 1.54060. It is seen that the materials are well crystalline in nature and well agreed with standard JCPDS file no. 71-1127.

SEM

SEM study is carried out to observe the overall surface morphology and crystallite sizes of the prepared materials. This material has been synthesis by sol-gel method. From the SEM images are observed under 10 micrometer resolutions which show the foam like surface morphology as shown in fig.2. In the depicted images of α-Al$_2$O$_3$ materials, it can be clearly seen that the micrograph crystallite sizes may vary from a 10 μm to few microns range if we magnify further. The crystallite looks like having a sharp surface edge as well as crystalline grains and the particles foam like morphology，can be formed from highly agglomerated crystallites. Also, it is confirmed that the crystallite sizes are nearly equal for all sample [14-15].

Fig.2 SEM images of α-Al₂O₃ nanoparticles
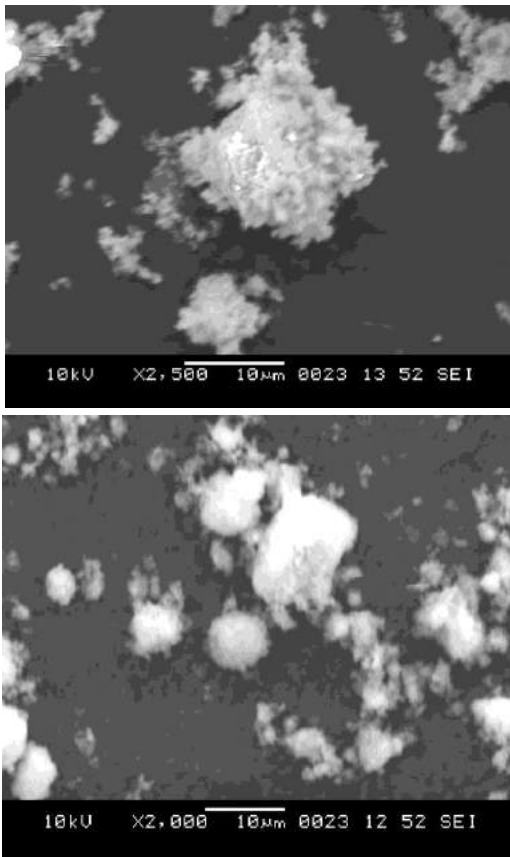
Fig.3 Zeta potential of the prepared α-Al₂O₃ nanofluids

Zeta potential:

Zeta potential of the prepared α-Al₂O₃ nanofluids was measured by using Zeta potential analyser. It is the potential difference across phase boundaries between solids and liquids. It is observed that zeta potential for molar concentration 0.6 have higher values indicating more stability of α-Al₂O₃ nanofluids indicating in figure 3. Moreever it has less values for other molar concentration indicating less stability. From the graph the values of zeta potential has been greater than 30 either positive or negative exhibit the more stability of the nanofluids.
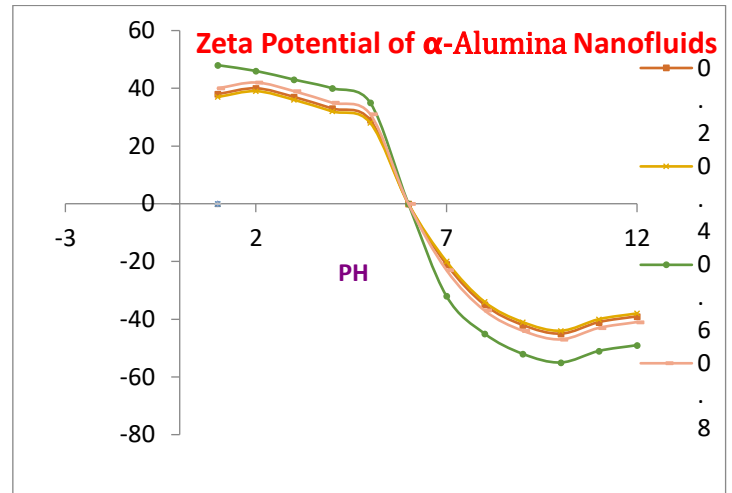
Thermal conductivity:

Fig.4 shows the variation of thermal conductivity with molar concentration of α-Al₂O₃ nanoparticles in methanol base nanofluids. The results clearly show that the effective thermal conductivity of α-Al₂O₃ increases with temperature. It has substantially higher value at molar concentration 0.6 of α-Al₂O₃ in methanol base nanofluids. The thermal conductivity enhancements are highly dependent on specific surface area of nanoparticle, with an optimal surface area for the highest thermal conductivity. The results of Kumar *et al.* and Koo and Kleinstreuer show the strong relationship between Brownian motion and temperature of nanoparticles. Furthermore, the effect of temperature on thermal conductivity is not very well understood and documented.
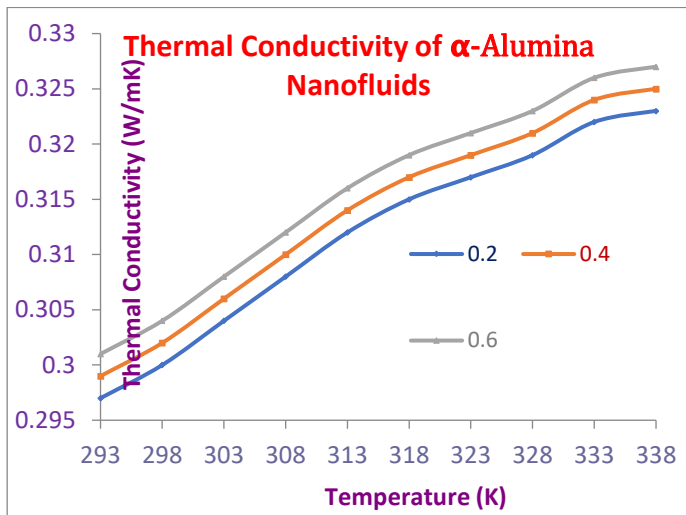
Fig. 4 Thermal conductivity of α-Al₂O₃ nanofluids at 20⁰C, 25⁰C and 30⁰C.

IV. CONCLUSION

1. The structural, optical and thermal properties of the α-Al₂O₃ nanofluids are characterized by XRD, SEM and thermal conductivity.
2. The observed higher values of zeta potential indicate the stability of the α-Al₂O₃ nanofluids.
3. Characterization of α-Al₂O₃ nanoparticles via XRD and SEM shows its nanocrystalline formed.
4. Enhancement in thermal conductivity of α-Al₂O₃ nanofluids is due to the stability of α-Al₂O₃ nanoparticles in dispersion medium.

V. REFERENCES

[1]. M. S. Liu, M.C.C. Lin, I. T. Huang, C.C. Wang, Chem. Eng. Technol., 29 (2006) 72-77.

[2]. Yi Jiang, Ruiyuan Tian, Haiqiang Liu, Jain Kun Chen, Xinghau Tan, Lina Zhang, Guangyao Liu, Hanfu Wang, Nano Research, 8 (2015) 1-12.

[3]. Yu W. and Xie H., A review of nanofluids: preparation, stability mechanisms and applications, J. Nanomaterials, 2012 (2011) 1-17.

[4]. Lee S., Choi S.U.S., Li S. and Eastman J.A., Measuring thermal conductivity of fluids Containing oxide nanoparticles, J. Heat Transfer, 121 (1999) 280-289.

[5]. Kulkarni D.P., Das D.K. and Chukwu G.A., Temperature dependent rheological property of copper oxide nanoparticles suspensions, J. Nanosci. Nanotechnol, 6 (2006) 1150-1154.

[6]. D.H. KUMAR, H.E. PATEL, V.R.R. KUMAR, T. SUNDARARAJAN, T. PRADEEP and S.K. DAS, 2004. Model for heat conduction of nanofluids, Physical Review Letters, 94(14), 1-3.

[7]. S. RAJAGOPALAN, S. J. SHARMA and V.Y. NANOTKAR, 2005. Ultrasonic Characterization of Silver Nanoparticles, Journal of Metastable and Nanocrystalline Materials, 23, 271-274.

[8]. Z. GAN, G. NING, Y. LIN and Y. CONG, 2007. Morphological control of mesoporous alumina nanostructures via template-free solvothermal synthesis. Mater Lett. 61(31), 3758- 3761.

[9]. X. ZHAN, M. HONKANEN and E. LEVA, 2008. Transition alumina nanoparticles and nanorods from boehmite nanoflakes. J Crystal Growth. 310(30), 3674-3679.

[10]. Y.K. PARK, E.H. TADD, M. ZUBRIS and R. TANNENBAUM, 2005. Size controlled synthesis of alumina nanoparticles from aluminum alkoxides, Materials Reasearch Bulletin, 40(9), 1512.

[11]. D.G. WANG, F. GUO, J.F. CHEN, H. LIU and Z. ZHAG, 2006. Preparation of nano aluminium trihydroxide by high gravity reactive precipitation, Chemical Engineering Journal, 121(2-3), 109-114.

[12]. R. AGHABABAZADEH, A.R. MIRHABIBI, J. POURASAD, A. BROWN, A. BRYDSON and N. AMERI MAHABAD, 2007. Economical synthesis of Nanocrystalline alumina using an environmentally low-cost binder, Journal of Surface Science. 601(13), 2864-2867.

[13]. P. CHRISTIAN and M. BROMFIELD, 2010. Preparation of small silver, gold and copper nanoparticles which disperse in both polar and

non-polar solvents, J. Mater. Chem. 20, 1135-1139.

[14]. R. ROGOJAN, E. ANDRONESCU, C. GHITULICA and B. STEFAN, 2011. Synthesis and characterization of alumina nano-powder by sol-gel method. UPB Sci Bull Ser B. 73(2, 27), 67-76.

[15]. V. Bhalla, R. Kumar, S. Tripathi and D. Sing, 2013. Mechanical and thermal properties of Praseodymium nanoparticles: an ultrasonic study, Int. J. Mod. Phys. B, 27, 1350116.

Advantages and Applications of Nanotechnology in Energy Sector

Suyog Surendra Mankar

H.O.D. Department of Physics, Shivramji Moghe Arts, Commerce and Science college, Pandharkawada dist.

Yavatmal Maharashtra, India

ABSTRACT

Nanotechnology in energy sector is an interesting topic for research. Use of Nanotechnology in energy sector has the capability of improving life all over the world. Nanotechnology plays very interesting and important role in energy sector at different stages such as production, storage and transmission. Use of Nanotechnology in conventional and non conventional energy sources is the fascinating topic for research and development of new technologies. Nanotechnology innovations could impact different fields such as energy conservation, development in available energy sources and energy usage. This paper highlights the advantages, applications of nanotechnology in Energy sector, different nanomaterials used in energy sector and recent development of nanotechnology in Energy sector.

Keywords : Nanotechnology, nanomaterials, energy sector, conventional and non conventional energy sources.

I. INTRODUCTION

Nanotechnology is a field of research and innovation in building things , generally materials and devices at nanoscale to take advantage of enhance properties of the material that are not present in their bulk form. Properties of nanomaterials are much differs than bulk materials. The main factors behind this are Increase in surface to volume ratio and Quantum size effect. Nanotechnology has numerous applications in everyday life in all fields. Nanotechnology shows major impact on many industries such as electronics, computers, medical, transportations, defense, agriculture, textile, sports etc. Nanotechnology provides multiple approaches to energy sector. Nanomaterials and nanotechnology play a very important role in the development in traditional energy sources and of new energy in future. Energy production faces many problems. Fossil fuels are limited and new focus is on renewable energy sources. Nanotechnology is being used in different forms in several applications to improve the efficiency of energy generation or to develop new methods to generate energy in various forms including renewable and non renewable energies. Nanotechnology is a promising solution to many problems in energy generation, energy storage and energy transfer. This paper gives a general advantages and applications of nanotechnology for sustainable energy generation, storage and transportation.

Nanotechnology in energy Generation

Nanotechnology has shown promising development in the area of solar energy. Nanotechnology can be incorporated in solar energy technology for many applications which are more eco friendly, inexpensive

and efficient. Nanomaterials incorporated in solar panel to convert solar energy to electricity , heat and steam more efficiently. Solar panels with nano materials could be cheaper to manufacture and they are easier to install. Nanomaterial coatings and nano paints being used for collection of solar energy with high efficiency. Sunlight concentrated on nano materials can produce steam with high energy efficiency. Solar steam device can be used in water purification and disinfecting instruments. In solar energy generation nanotechnology shows wide range of applications including thin films ,coating, tailored electronic structure etc.Nanotechnology is improving the efficiency of fuel production from row petroleum product through better catalysis. The use of nanoparticals in enhanced oil recovery is one of the important applications with reduction in cost of production. The amount of electricity generation by wind mills can be increases by using windmill blades made with the help of carbon nanotubes that are longer, stronger and light weighted. Other applications in wind energy includes nanopartical bearings, stronger turbine, self cleaning coating etc. Nanotechnology is very useful in the generation of geothermal energy by reducing operating mechanism at lower temperature. The most exciting use of nanotechnology in hydrogen energy is the hydrogen storage. In hydrogen transports, use of carbon nanotubes would have increased strength , conductivity and stability at high temperature. The controlled introduction of nanoparticals in organic waste treatment can increase the production of biogas. Fuel cell technology being advanced by nanotechnology. Nanotechnology is being used to reduce the cost of catalysts used in fuel cells. Various nanoscience based technologies can be used to convert waste heat and excess pressure into usable electric power. Flexible piezoelectric nanowires woven into clothing can generate useable energy for charging electronic devices. Nano enabled paints are self cleaning and are used to generate electricity to power our houses.

Nanotechnology in Transmission of Energy

Electricity is produced at limited places and then distributed every where it is needed with the help of power lines. ' Energy transmission is the movement of energy which could be electrical or petroleum from generating site to the respective stations for use.' In traditional ways for the purpose of transmission of electrical energy cables are used and pipes are used for transmission of petroleum products. In long distance transmission energy loss occurs due to resistance of wires but wires containing carbon nano tubes / quantum wires transfer electricity with significantly reduce resistance and thus transmission losses. Conducting materials with nanomaterial coating found to be more efficient with less power loss. Electrical conductivity of quantum wire is much greater than traditional wires. Many researches are going on to find the superconducting materials made up of nanomaterials for loss less current conduction. Quantum wires are light weighted and stronger than traditional wires. Nanosensors are useful in managing smart grids. Nanomaterials play a key role in wireless power transmission systems development. Efficient heat in and out flow system based on use of nanomaterials found to be more efficient. Nanomaterial coated surfaces shows numerous advantages than non coated surfaces. Nanotechnology is also very useful in transmission of petroleum products and gases. Nano material coated pipelines shows better performance than traditional pipelines in terms of wear and tear, insulation, corrosion and erosion. Nanosensors are used in gas and liquid transmission for detecting breakages and leaks. Nanocoating on metallic surfaces can help in attaining low friction and improving oxidation protection. Thus it is observed that different nanomaterials such as nanodots, nanotubes, buckyballs etc are very useful and efficient for energy transmission.

Nanotechnology in Energy storage

Nanotechnology is being favored for energy storage because of efficiency, taking up more energy and holding it longer time. Nanotechnology provides suitable material for electrodes for proper battery operation. Nanomaterials based electrodes able to tolerate high currents offering a promising solution for high energy and high power. Nanotechnology is very useful for supercapacitors mechanism. Nanomaterials are used to increase performance of batteries that can recharge significantly faster and long lasting than conventional batteries. Nanotechnology can improve capacity and safety of battery. Nanomaterials are used to make light weight fuel tank which can store more amount of hydrogen. Nanomaterials helps to manufacture high capacity batteries for portable electronic devices. Nanomaterials helps to increase the life span battery. Nanotechnology helps to store thermal energy more conveniently.

II. CONCLUSION

Nanotechnology could provide a efficiency boost needed to energy sector. Nanotechnology is a sustainable solution to many problems and drawbacks in three main parts of energy sector that are energy generation, storage and transmission. Nanotechnology increase the efficiency, performance and life span of material with reduction in maintenance cost. Nanotechnology provides a way for future research and development in energy sector.

III. REFERENCES

[1]. Nano-Material's and its Potential Applications in the Field of Renewable Energy - Ramesh Kumar Sahu, Rajesh Kumar Ojha   International Journal of Engineering Research & Technology (IJERT) ISSN: 2278-0181 ISNCESR-2015 Conference Proceedings

[2]. Opportunities and challenges of nanotechnology in the green economy- Ivo Iavicoli1*, Veruscka Leso1, Walter Ricciardi1, Laura L Hodson2 and Mark D Hoover3 Iavicoli et al. Environmental Health 2014, 13:78

[3]. Lossless and Efficient Transmission of Electrical Energy using Nanotechnology - G K Naveen Kumar1 , Akanksha Thakur2 , Renu Yadav3 International Journal of Engineering Research & Technology (IJERT) IJERT ISSN: 2278-0181 IJERTV3IS110154 Vol. 3 Issue 11, November-2014

[4]. Applications of Nanotechnology in Renewable Energy Sources Exploitation - Steevan Sequeira Manipal Technologies Limited

[5]. Energy storage: The future enabled by nanomaterials- Ekaterina Pomerantseva*, Francesco Bonaccorso*, Xinliang Feng*, Yi Cui*, Yury Gogotsi*

Website

[6]. https://www.npep.co.za/
[7]. https://www.technologieland-hessen.de/
[8]. https://www.nano.gov/
[9]. https://www.understandingnano.com/
[10]. https://www.phys.sinica.edu.tw/
[11]. https://www.nanowerk.com/
[12]. https://digital.library.unt.edu/

Synthesis and Characterization of Dy³⁺ Activated Ca₂Al₂SiO₇ Nanophosphors for Environment Friendly Lighting

R.L. Kohale[1*], Rajdip Utane[2] and S. J. Dhoble[3]

[1]Department of Physics, Sant Gadge Maharaj Mahavidyalaya, Hingna, Dist-Nagpur, Maharashtra, India

[2]Department of Chemistry, Sant Gadge Maharaj Mahavidyalaya, Hingna,Dist-Nagpur, Maharashtra, India

[3]Department of Physics, R.T.M. Nagpur University, Nagpur, Maharashtra, India

*Corresponding author email: riteshkohale@gmail.com

ABSTRACT

In the present study Dy³⁺ activated Ca₂Al₂SiO₇ phosphors were synthesized by combustion synthesis. Formation of crystalline phases were identified by X ray diffraction (XRD) pattern and their photoluminescence (PL) properties were investigated using excitation and emission spectra under ultraviolet (UV) ray excitation ranging from 200 to 400 nm. When Ca₂Al₂SiO₇:Dy³⁺ phosphor was excited at 350 nm, the emission spectrum showed intense bands at 480 nm (blue) and 575 nm (yellow) emission due to Dy³⁺ ions. The external morphology of Ca₂Al₂SiO₇ phosphor has been studied by SEM.The results obtained showed that phosphors have the promising applications for solid state lighting and near-UV white light-emitting diodes (LEDs).

Keywords: Photoluminescence, Light-Emitting Diodes, Lamp Phosphor, Silicate

I. INTRODUCTION

Rare earth-doped inorganic phosphors are widely used in variety of applications such as for the lamp industry, X-ray imaging, scintillators and for color display. Recently there has been a growing focus on research in the area of light-emitting diodes (LEDs) due to their many merits such as being environmental friendly, highly efficient and having a longer lifetime [1,2]. After a decade of intense research, phosphor-converted light-emitting diodes (pc-LEDs) have attracted worldwide attention owing to their high luminescence efficiency and variety wide range of applications, such as in flashlights, display backlighting, traffic signals, and especially for solid-state lighting. The huge potential market in home lighting encourages the rapid development of pc-LEDs because of their advantages over the existing incandescent and fluorescent lamps in power efficiency, reliability, long lifetime, low energy consumption, and environmentally friendly characteristics [3]

Zhang reported the tunable bluish green to yellowish green Ca₂ (1–x) Sr₂xAl₂SiO₇:Eu²⁺ phosphors. Wu reported the Dy³⁺ and Tb³⁺ and co-doped Ca₂Al₂SiO₇ phosphor and deliberated photoluminescence properties [4]. Li also reported the luminescent properties Sr₂Al₂SiO₇:Ce³⁺, Eu²⁺ phosphors and discussed the possible application for near UV-excited white light-emitting diodes (*w*- LEDs) [5].

Silicate-based phosphors have increased enormous informative and commercial benefits since their rigid crystal structure, ample crystalline phase, multi-color emission and extraordinary luminous proficiency, and appropriate physical and chemical structures [6].Therefore, it is necessary to continue the development of new PL materials with suitable silicate hosts and activators to expand the color range, and at the same time to contribute to a better understanding of the PL mechanism. Here in this work we have prepared many silicate-based phosphors doped with RE ions (RE=) as the significant constituents used in different optical application arenas.

The single doped $Ca_2Al_2SiO_7:Dy^{3+}$ powders were synthesized by conventional combustion synthesis have reported in this work. And their detailed luminescence properties have been discussed and investigated systematically.

Zhang reported the tunable bluish green to yellowish green $Ca_{2(1-x)}Sr_2xAl_2SiO_7:Eu^{2+}$ phosphors. Wu reported the Tb^{3+} and Dy^{3+} doped $Ca_2Al_2SiO_7$ phosphor and deliberated photoluminescence properties [7]. Li also reported the luminescent properties $Sr_2Al_2SiO_7:Ce^{3+}$, Eu^{2+} phosphors and discussed the possible application for near UV-excited white light-emitting diodes (w- LEDs) [8].

The host $Ca_2Al_2SiO_7$ belongs to the family of melilite compounds whose luminescence properties have been widely studied in various fields of solid state lighting Here in this work we have prepared many silicate-based phosphors doped with RE ions (RE=Dy^{3+}) as the significant constituents used in different optical application arenas.

II. EXPERIMENTAL DETAILS

The series of rare earth-doped Gehlenite ($Ca_2Al_2SiO_7$) phosphor reported in this paper were synthesized using the combustion method. This is a simple, cheap technology for aluminosilicate based materials, as other techniques require long reaction times and high temperatures to achieve the desired phase purity. For the synthesis of the $Ca_2Al_2SiO_7:Dy^{3+}$ phosphor, we selected $Ca(NO3)3.4H2O$ (99.9%), $Al(NO_3)_3.9H_2O$ (99.9%), SiO_2 (99.9%), NH_2CONH_2, $La(NO_3)_3.6H_2O$, Dy_2O_3.All materials were taken in stoichiometric ratio, Details experimental details of the combustion methods and its advantages have been discussed previously by Pawde et al.[9]

III. RESULT AND DISCUSSION

3.1 X-ray diffraction pattern and structural behavior of $Ca_2Al_2SiO_7$ phosphor

The phase purities of $Ca_2Al_2SiO_7$ phosphor was checked by powder X-ray diffraction (XRD) using a PAN-analytical diffractometer with $CuK\alpha$ radiation (1.5405 Å) operating voltage at 40 kV, 30 mA and scan step time at 10.3377s.The XRD pattern of the resulted material is shown in figure 1 It is found that the obtained diffraction peaks of the phosphor prepared at 550 ^{0}C are in well match with the standard JCPDS standard file no. 89-1489.
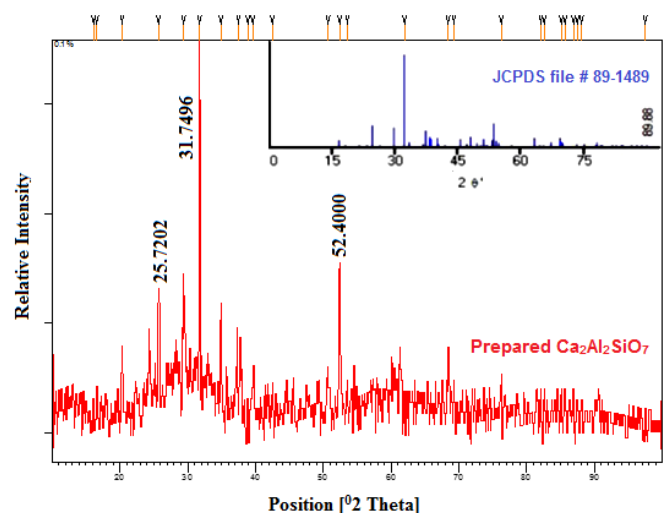
Figure 1 : The XRD pattern of the $Ca_2Al_2SiO_7$ phosphor

Peak List : Table 3.1 Peak least of XRD data

Pos. [°2Th.]	Height [cts]	FWHM [°2Th.]	d-spacing [Å]	Rel. Int. [%]
16.1014	1.73	0.2856	5.50021	5.43
16.6125	2.91	0.2448	5.33212	9.16
20.3157	5.88	0.3264	4.36776	18.52
25.7202	**11.24**	**0.2448**	**3.46090**	**35.37**
29.4436	8.86	0.4080	3.03117	27.89
31.7496	**31.77**	**0.2856**	**2.81608**	**100.00**
34.8964	9.20	0.2448	2.56901	28.94
37.5069	3.99	0.9792	2.39598	12.57
38.8160	2.13	0.2448	2.31813	6.70
39.6139	4.91	0.4896	2.27326	15.46
42.5244	3.10	0.2856	2.12416	9.75
50.7274	3.41	0.4896	1.79824	10.72
52.4000	**14.05**	**0.2856**	**1.74471**	**44.22**
53.5433	2.93	0.2856	1.71012	9.23
61.9871	1.53	0.2448	1.49590	4.81
68.4339	4.79	0.4896	1.36984	15.06
69.2768	2.70	0.2448	1.35522	8.51
76.2084	3.41	0.2856	1.24827	10.72
82.0617	3.30	0.3264	1.17340	10.40
82.5825	2.65	0.2448	1.16732	8.33
85.0512	2.69	0.2448	1.13963	8.45
85.6288	3.29	0.4488	1.13342	10.35
86.8495	3.47	0.2856	1.12060	10.94
87.4429	2.25	0.4080	1.11451	7.08
88.0730	2.34	0.2448	1.10816	7.36
97.5293	1.89	0.3264	1.02432	5.93

The XRD pattern of aforesaid sample did not indicate presence of the constituents like $Ca(NO_3)$, $Al(NO_3)$ or $NH_4H_2PO_4$ and other likely phases which are direct confirmation for the formation of desired compound. The reported crystal structure of $Ca_2Al_2SiO_7$ phosphor has been distinguished in *P421m* space group with tetragonal crystalline phases [10]. The crystallographic planes with unit cell parameters a = 7.694 (1) A°, c = 5.077 (1) A°, and atomic no Z=2. From figure 1 it is concluded that the peaks at 25.7202 (35.37 %), 31.7496(100.00 %), 52.4000 (44.22 %) are well matched with peaks in standard JCPDS file No. 89-1489 which confirms the formation of $Ca_2Al_2SiO_7$ phosphor. Figure 2 indicated the representative crystal structure of $Ca_2Al_2SiO_7$ [11].
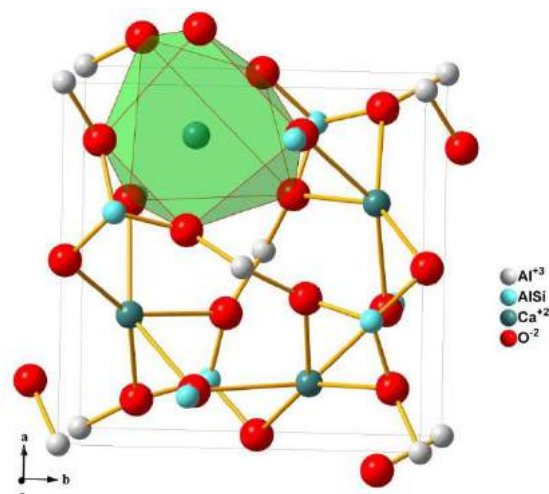
Figure 2 : representative crystal structure of $Ca_2Al_2SiO_7$

3.2 SEM (Scanning Electron Microscope) characterization of $Ca_2Al_2SiO_7$ phosphor

Figure 3.3 shows micrograph of the $Ca_2Al_2SiO_7$ phosphor powder. It is detected that the phosphor powder is composed of asymmetrical particles of a few μm in size, which are essentially made from accumulation of considerably smaller particles of a submicron size. The particles retain foamy morphology made from highly agglomerated crystallites. When the phosphor was synthesized by combustion synthesis the particles growth took place quickly forming bigger size particles. The particles shape has fixed boundary and the average particle size is increased to about 1-5 μm. $Ca_2Al_2SiO_7$ phosphors clearly show that the grains are asymmetrical shaped with an average crystallite size in sub-micrometer range of 1 -5 μm seen in SEM images. Additionally high magnification study indicated that grains are tetragonal shaped which is in good agreement with obtained XRD data. From Figure 3 it is concluded that particles are unselective in appearance, composing of different sizes as observed in submicron range 416 nm, 610 nm, 760 nm, 870 nm and 891 nm which are measured under 1 μm resolution.
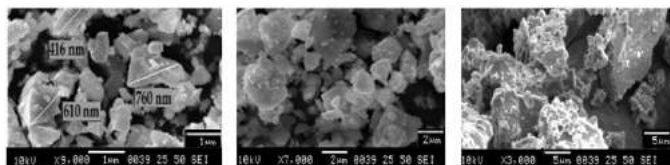
Figure 3 : SEM micrograph of the $Ca_2Al_2SiO_7$ phosphor

3.3 Photoluminescence properties of Dy^{3+} activated $Ca_2Al_2SiO_7$ phosphor

The excitation spectra of $Ca_2Al_2SiO_7$:Dy^{3+} phosphor monitored at around 575nm is shown in figure 4. The excitation spectrum monitored at yellow emission from Dy^{3+} ions indicates several bands in wavelength region of 300 - 400 nm, which are due to excitation of f–f shell transitions of Dy^{3+} [12]. The several peaks at 350 nm, 365 nm and 390 nm, correspond to the transitions from the ground state $^6H_{15/2}$ to the excited states; $^4P_{7/2}$; $^4P_{3/2}$

and $^4F_{7/2}$ respectively [13, 14].The maximum PL intensity of the excitation wavelength is located at 350 nm which is a characteristics of solid state lighting and suitable NUV excited LEDs, consequently it was chosen for the PL investigation in the present study.
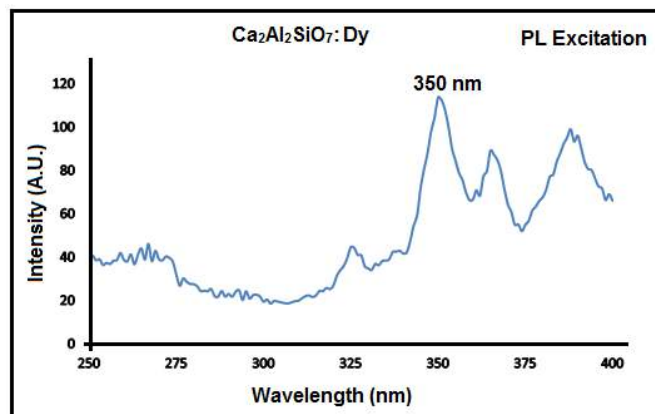
Figure 4 : Excitation spectrum of $a_2Al_2SiO_7$:Dy^{3+} phosphor

The emission spectra were measured between 400–700 nm. Two emission bands peaked at 480 nm and 575 nm are observed as shown in figure 5. The blue emission at 480 nm is related to $^4F_{9/2} \rightarrow ^6H_{15/2}$ magnetic dipole transition, the yellow emission at 575 nm is ascribed to $^4F_{9/2} \rightarrow ^6H_{13/2}$ electric dipole transition [15].These yellow and the blue emission transitions are the predominant transitions. The $^4F_{9/2} \rightarrow ^6H_{13/2}$ transition is hypersensitive (ΔL-2; ΔJ-2), and it can be influenced by its microscopic environment so their intensity strongly depends on the host. The influence of divergent crystal field surrounding has been observed on the luminescent intensity.
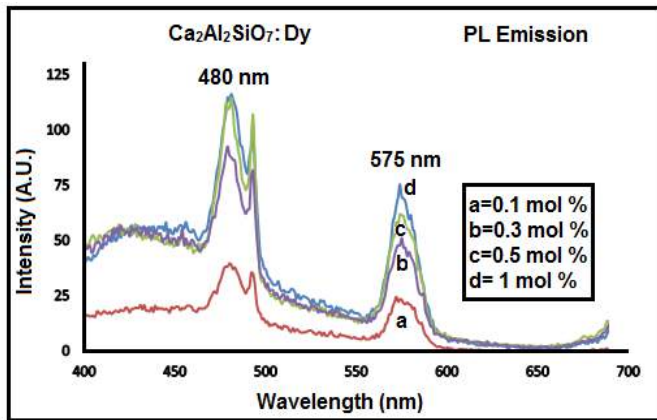
Figure 5 : Emission spectrum of Ca₂Al₂SiO₇:Dy³⁺ phosphor

Incorporation of activator ions can influence photoluminescence characteristics of a phosphor; evidently the addition of Dy ion into Ca₂Al₂SiO₇ host increased the crystallinity which affects the particle size as well complexity of host material. The electronic transitions of Dy³⁺ involve only redistribution of electrons within the inner 4f sub-shell. The Photoluminescence study of Ca₂Al₂SiO₇:Dy³⁺ reveals that fluorescence intensity ratio increases gradually. Usually, a low doping gives weak luminescence, but excess doping can cause quenching of luminescence. A series of Ca₂Al₂SiO₇:Dy³⁺ phosphor with various Dy³⁺ concentrations (x=0.1, 0.3, 0.5 and 1mol %) were prepared and the effect of doped Dy³⁺concentration on the emission intensity was investigated. With increasing concentration of Dy³⁺ ions the photoluminescence intensity increased gradually up to 1 mol.% Dy³⁺ ion which was maximum among all the concentrations. Nevertheless the position of emission bands is not manipulated by the variation in incorporation of Dy³⁺ ions. Energy level transitions of Dy³⁺ ions is shown in figure 6 below.
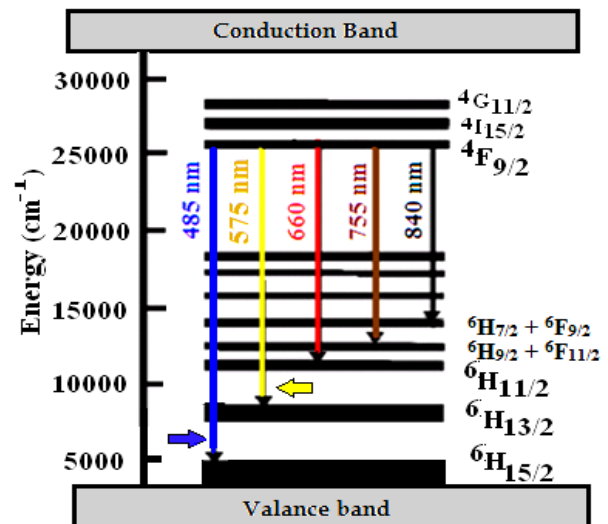
Figure 6 : Energy level transitions of Dy³⁺ ions.

IV. CONCLUSION

In the present study, calcium aluminum silicate (Ca₂Al₂SiO₇) based phosphate phosphors activated with rare earth ions Dy³⁺ prepared by combustion synthesis and confirmed by XRD are reported. An average crystallite size is found out to be in sub-micrometer range of 200-800 nm from SEM study. The PL spectroscopic characterizations of the prepared phosphors were performed using excitation and emission spectra. Photoluminescence spectra of rare earth activated Ca₂Al₂SiO₇ silicate based phosphor shows emission at 400-700 nm when excited between 200-400 nm. The obtained results suggests that this phosphor might be useful for the blue and orange light. The most efficient concentration of RE³⁺ for the maximum emission intensity is 1 mol%. The entire results suggests that the prepared phosphors could be the potential phosphors for possible applications in the field of solid state lighting and Light emitting diodes (LED).

V. REFERENCES

[1]. K. Van den Eeckhout, P.F. Smet, D. Poelman, Materials 3 (2010) 2536-2566.

[2]. K. Van den Eeckhout, D. Poelman, P. Smet, Materials 6 (2013) 2789-2818.

[3]. Y. Li, M. Gecevicius, J. Qiu, Chem. Soc. Rev. 45 (2016) 2090–2136.

[4]. H. Y. Wu, Y. H. Hu, G. F. Ju, L. Chen, X. J. Wang and Z. F. Yang, J. Lumin.,2011, 131, 2441-2445.G.

[5]. R.L. Kohale, S.J. Dhoble , Luminescence 28(2013), 656, DOI 10.1002/bio.2411

[6]. V. Castaing, A.D. Sontakke, A.J. Fernández-Carrión, N. Touati, L. Binet, M. Allix, D. Gourier, B. Viana, Eur. J. Inorg. Chem. (2017) 5114-5120.

[7]. H. Li, M. M. Li, L. L. Li, H. Yu, H. F. Zou, L. C. Zou, S. C. Gan and X. C. Xu,Mater. Lett., 2011, 65, 3418-3420.

[8]. R.L. Kohale, S.J. Dhoble, J. Lumin. 138 (2013) 153.

[9]. V. B. Pawade, H. C. Swart, S. J. Dhoble, Renew. Sustain. Energy Rev, 2015, 52, 596.

[10]. M. Li, L. Wang, W.Ran, Q. Liu, C. Ren, H. Jiang and J. Shi, New J. Chem.,2016, DOI: 10.1039/C6NJ01755J.

[11]. B. Yan, C. Wang, J. Alloys Compd. 462 (2008) 147.

[12]. P. L. Li, Z. P. Yang, Z. J. Wang, Q. L. Guo, Mater. Lett. 62 (2008) 1455.

[13]. C. H. Yang, Y. X. Pan, Q. Y. Zhang, Chin. Rare Metal Mater. Eng. 37 (2008)568.

[14]. B. Yan, X. Q. Zhang, H. S. Lai, Chin. J. Lumin. 28 (2007) 531.

[15]. R.T Wegh, et al. Phys. Rev. B 56, 13841 (1997).

Microwave Assisted Synthesis and Antimicrobial Activity of Some New Thiopyrimidine Derivatives

S. S. Ubarhande[1], P. P. Chaudhari[1], P. R. Padole*[2]

[1]G. S. Tompe Arts, Commerce and Science College, Chandur Bazar Dist. - Amravati , Maharashtra, India

*[2]Shri Shivaji Science College, Amravati , Maharashtra, India

ABSTRACT

4-(4-chlorophenylamino)-6-(4-substitutedphenyl)-5,6-dihydropyrimidin-2-thiones(3a-d) were synthesized by condensation of (E)-N-(4-chlorophenyl) 3-(4-substitutedphenyl) acryl amide (2a-d) with thiourea in the presence of catalytic amount of 40% KOH respectively. The antimicrobial evolutions have been performed for their antibacterial activity and antifungal activities.

Keywords: - Microwave Synthesis, Thiopyrimidine Antimicrobial.

I. INTRODUCTION

In the last decade much interest has been focused on the study of oxopyrimidine and thiopyrimidine derivatives. Several publications have been pointed out the values of Oxopyrimidines and thiopyrimidines[1-2]. They have potential bioactive agents Due to their wide spectrum of pharmacological activities like anti-inflammatory[3], amimicrobial[4],calcium chanel blockes[5], antihypertensive[6], analgesic[7],antitumor[8], antiviral[9],antibacterial[10],anti HIV[11]. Looking to versatile activities exhibited and in continuation to our work on the biological active heterocyclics.

In our last publication we were reported the synthesis of thiopyrimidine derivatives (3a-e). in continuation to that we are reported here the biological study of some newly synthesized thiopyrimidine derivatives (3a-e).

All the synthesized compounds were screened for their antimicrobial activity against various microbs under condition, the standard antibiotics were used for comparison purpose like amoxicillin, benzyl penicillin ciprofloxacin and erythromycin against bacterial strain against *Aspergillus niger.* All the newly synthesized compound have been screened for in *vitro* antimicrobial activity.

II. EXPERIMENTAL

The melting points of all synthesized compound were recorded using hot paraffin bath and are uncorrected. ^{1}H NMR spectra (CDCl₃) were recorded on Bruker Advance II 400 NMR spectrophotometer using TMS as internal standard. IR spectra were recorded on Perkin-Elmer-1800 FTIR spectrophotometer in the frequency range 4000-450 cm^{-1} in Nujol mull and as KBr pellets. Mass spectra were recorded on a LC-MS Q-Tof Micro, Mass analyzer (Shimadzu). Chemicals used were of AR grade. The purity of the compound was checked on silica gel-G plates by TLC.

The melting points of all synthesized compound were recorded using hot paraffin bath and are uncorrected. ^{1}H NMR spectra (CDCl₃) were recorded on Bruker

Advance II 400 NMR spectrophotometer using TMS as internal standard. IR spectra were recorded on Perkin-Elmer-1800 FTIR spectrophotometer in the frequency range 4000-450 cm^{-1} in Nujol mull and as KBr pellets. Mass spectra were recorded on a LC-MS Q-Tof Micro, Mass analyzer (Shimadzu). Chemicals used were of AR grade. The purity of the compound was checked on silica gel-G plates by TLC.

Synthesis of 4-(4-chlorophenylamino)-6-(4-hydroxyphenyl)-5,6-dihydropyrimidine-2-thione(3a-d).

A mixture of (E)-N-(4-chlorophenyl) 3-(4-hydroxyphenyl)acryl amide **(2 a-d)** (0.01 mol) and thiourea (0.01 mol) was moist with ethanol containing KOH (1 mL) and refluxed for 60sec. in microwave oven. The excess solvent was distilled off and the residue was neutralized with dilute HCl. The separated solid was filtered out and crystallized from ethanol to afford compound **(3a-d)**.

Spectral data of compound (IVa): IR (KBr, cm^{-1}): 3550 (O-H), 1670 (C=S), 1580 (C=N), 3290 (N-H), 3100 Ar (C-H), 1450(C-N), 1360 (C-Cl), 680-750 (monosubstituted benzene ring); ^{1}H NMR (EtOH): δ 1.3 (s, 1H, OH), 2.45 (s, 2H, CH), 4.35 (s, 1H NH), 7.78 (d, 2H, Ar-H), 7.68 (d, 2H, Ar-H), 7.90 (d, 2H, Ar-H), 7.58 (d, 2H, Ar-H).Mass :- m/e 330.81.

Synthesis of 4-(4-chlorophenylamino)-6-(4-chlorophenyl)-5,6-dihydropyrimidine -2-thione.

A mixture of (E)-N-(4-chlorophenyl)-3-(4-chlorophenyl)acryl amide (0.01 mol) and thiourea (0.01 mol) was moist with alcoholic KOH (1 mL)and the refluxed for 1min in microwave oven. The excess solvent was distilled off and the residue was neutralized with dilute with HCl. The separated solid was filtered out and crystallized from ethanol to afford compound.

Spectral data of compound (Va): IR (KBr, cm^{-1}): 3300 (N-H), 3050 (Ar C-H), 1690(C=S), 1510 (Ar C=C), 1560 (C=N), 1335 (C-N), 810 (p-disubstituted benzene ring), 780(C-Cl); ^{1}H NMR (CDCl$_3$): δ 4.4 (s,1H, NH), 7.89 (d,2H,Ar -H), 7.90 (d,2H,Ar -H), 7.95 (d,2H,Ar-H),7.67 (d,2H,Ar-H),2.25 (s,2H,Allylic-H).Mass:- m/e -350.0.

All other compounds (2a,2c-d) were prepared in similar manner by the reaction of 4-chloroacetanlide with aromatic aldehyde (1a, 1c-d) respectively.

REACTION SCHEME

Where R= H,-OH, -Cl, -OCH$_3$
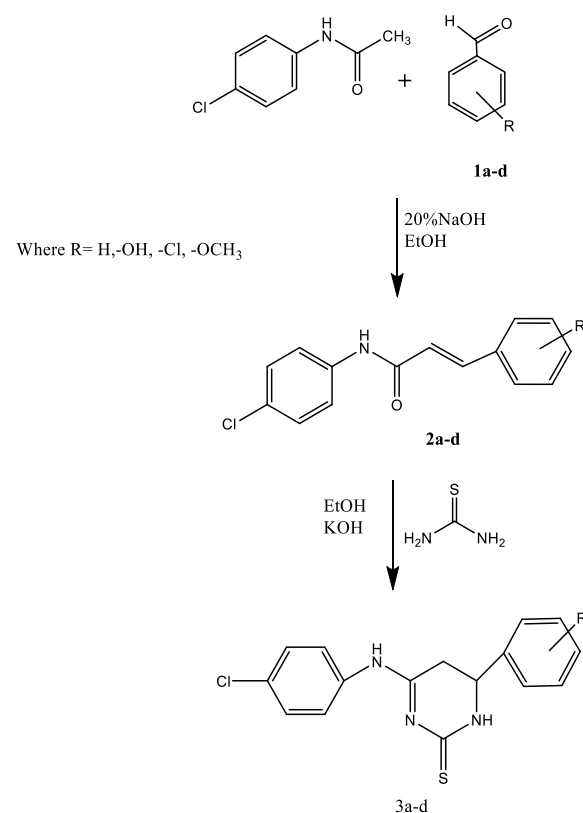
III. RESULTS AND DISCUSSION

In present work we argue the antimicrobial and antifungal activity of 4-(4-chlorophenylamino)-6-(4-substitutedphenyl)-5,6-dihydropyrimidin-2-thione (3a-d) by the condensation of (E)-N-(4-chlorophenyl) 3-(4-substitutedphenyl) acryl amide (2a-d) with thiourea in the presence of catalytic amount of 40% KOH respectively. The starting material (E)-N-(4-chlorophenyl) 3-(4-substitutedphenyl) acryl amide

(2a-d) were prepared by condensation of 4-chloroacetanilide with different aromatic aldehyde (1a-d). All these synthesized compounds were screened for their antimicrobial activity using the cup-plate agar diffusion method[12] by measuring the zone of inhibition in mm. All the compound were screened for their in vitro antimicrobial activity against different bacteria strain *Bacillus megaterium, Staphylococcus aureus, Pasteurella aerogenes and fungi Aspergillus niger at 40 μg/ml concentration. Standard drug like* amoxicillin, benzyl penicillin, ciprofloxacin and erythromycin were used for the comparison purpose. (**Table no. 1**)

Table 1. Antimicrobil screeing result of compound 3a-d					
Zone of inhibition (mm)					
			Antimicrobial activity		Antifungal activity
Compound	**R**	***B. megaterium***	***S. aureus***	***P. aerogenes***	***A. niger***
3a	-H	12	14	16	25
3b	-OH	19	11	22	17
3c	-Cl	10	16	11	17
3d	-OCH$_3$	18	21	20	21
Amoxicillin		25	23	8	19
Benzyl penicillin		15	22	21	18
Ciprofloxacin		22	21	19	17
Erythromycin		18	23	24	21

IV. AKNOLEGEMENT

V. REFERENCES

[1]. P.T. Chovatia, J.D. Akbari. P.K. Kachhadia, P.D. Zalavadia and H.S. Joshi, J. Serb. Chem. Soc., 2007,71, 713.

[2]. K.H. Popat, D.H. Purohit, P.T. Chovatia and H.S. Joshi, J. Indian Chem. Soc., 2005,82,940.

[3]. S.S.Bahekar and D.B. Shinde, Acta Pharm., 2003, 80,709.

[4]. A.M. El-Agrody, F.M. Ali, F.A.Eid, Mohammed A.A.El-Nassag,G.El-Sherbeny and A.H. Besair, Phosporus Sulfur and Silicon,2006 ,181,839.

[5]. L. Gaurneri, A.Patrizia, I. Marina, P.Elena, T. Carlo, L.Amedeo and T. Rodolfo, Arzneimittel Forschung , 1996,46,15;Biol,Abstr1998,101,32842.

[6]. P.Pathak, R. Kaur and B. Kaur, Arkivoc, 2006,(xvi),160.

[7]. V.Alagarsamy, D. Shankar and V. Raja Solomon, Arkivoc,2006,(xvi),149.

[8]. Y. L. Huang.c>F. Lin, Y.J. Lee.W.W. Li and T.C. Chao. Bio.Org.Med.Chem.,2003,11,145.

[9]. S. Shigeta S.Mori, F. Watanabe and M. Saneyoshi, Antivir.Chem.Chemther., 2002,13,67.

[10].S. Nag, R. Pathak, M. Kumar, P.K. Shukla and S. Batra, Bioorganic & Medicinal Chemistry, 2006,16,3824.

[11].G.F.Sun, Y. Y. Kuag, F. E. Chen, De Clercq and C. Pannecouque, Arch. Pharm.(Weinheim),2005,338,457.

[12].A.L. Barry, " The Antimcrobial Susceptibility Test, Principal and Practics" eds. IIIus Lea and Febiger Philadephia PA, USA, 1976,180; Biol. Abstr.,1976,64, 25183.

Synthesis and Photoluminescence of Lithium Aluminium Borate Phosphors LiAlB$_2$O$_5$:Eu^{3+}

S. R. Khandekar[1], R. S. Palaspagar[2#]

[1]Department of Physics, Indira Mahavidyalaya, Kalamb, Maharashtra, India

[2]Department of Physics, Shivramji Moghe College, Kelapur (Pandharkawada) , Maharashtra, India

Corresponding author E-mail: palaspagarritesh@gmail.com

ABSTRACT

The Lithium mixed Borates are good host materials for luminescent ions. The powder sample of the Eu^{3+} doped Lithium Alumino-Borate Phosphor LiAlB$_2$O$_5$:Eu^{3+} has been prepared by solution Combustion method. The phase and structure of the as prepared material was confirmed by powder XRD technique. The photoluminescence properties of LiAlB$_2$O$_5$:Eu^{3+} have been investigated. The phosphor LiAlB$_2$O$_5$:Eu^{3+} exhibits strong absorption over a wide UV range from 300 – 500 nm. It can be seen clearly that the charge transfer transition from the O^{2-} to Eu^{3+} excitation line at 254 nm wavelengths is very stronger than the intraconfiguration 4f^6 excitation lines (394 nm, 382 nm). The phosphor LiAlB$_2$O$_5$:Eu^{3+} shows intense red emission 614 nm corresponds to 5D0→7F2 when excited by 254 nm radiation. The red emission could be excited by NUV radiation of 390 nm. The phosphor LiAlB$_2$O$_5$:Eu^{3+} could be a potential red emitting component in lamps and display applications and also in solid state lighting.

Keywords : Borate, Red Phosphor, Combustion synthesis, Photoluminescence.

I. INTRODUCTION

In the past few years aluminum borates have attracted much research interest because of their potential applications as nonlinear optical materials [i-ii], low thermal expansive ceramics [iii], and luminescence hosts [iv-v]. The excellent nonlinear optical property of alkali borate crystals mainly comes from their anionic groups [vi]. According to the previous work [vii], the larger the distortions in oxygen polyhedra or any other anionic groups of a structure and the more inhomogeneous the electron density distribution on the bonds in these groups, the higher the values of the second-order microscopic susceptibility. The charge distribution on the conjugated n orbital of [B3O7]**5-** is

asymmetry, so this kind of anionic group has a great second order microscopic susceptibility. In order to enhance the second-order microscopic susceptibility, we hope to replace tetra-coordinate B of [B3O7]**5-** groups with other atoms. Al seems a good candidate since it is often tetrahedrally coordinated in compounds and has an outer electronic structure similar to B. Therefore, a new compound LiAlB2O5 is expected to exist if the tetra-coordinated B can be replaced by Al. The diffraction pattern of LiAlB2O5 is reported by He et al. [viii].

II. MATERIAL AND METHOD

The powder samples of LiAl(1-x)B2O5:xEu3+ (x = 0.005, 0.01, 0.03, 0.05, and 0.07) were prepared by a

solution combustion technique which is described earlier [ix-xii]. The stoichiometric amounts of high purity starting materials, Li(NO3)2 (A.R.), Al(NO3)3.9H2O (A.R.), Eu2O3, (high purity 99.9%), H3BO3 (A.R.), CO(NH2)2 (A.R.) have been used for phosphor preparation. The stoichiometric amounts of the ingredients were thoroughly mixed in an agate mortar, adding little amount of de-ionized water to obtain an aqueous homogeneous solution. The aqueous solution was then transferred into a china basin and slowly heated at lower temperature of 70°C in order to remove the excess water. The solution was then introduced into a preheated muffle furnace maintained at 550°C. The solution boils foams and ignites to burn with flame; a voluminous, foamy powder was obtained. The entire combustion process was over in about 5 min. Following the combustion, the resulting fine powders were annealed in a carbon reducing atmosphere at temperature 850°C for 90 min. and suddenly cooled to room temperature. The prepared materials were characterized by powder XRD and FE-SEM. Powder X-ray diffraction measurements were taken on Rigaku Miniflex II X-ray Diffractometer and compared with the ICDD files. Surface morphology of the calcined particles was observed by scanning electron microscopy (FE-SEM). PL & PLE measurements at room temperature were performed on Hitachi F-7000 spectroflurometer with spectral resolution of 2.5 nm.

III.   RESULTS AND DISCUSSION

3.1 X-ray Diffraction Pattern

The XRD pattern of the host lattice of LiAlB2O5 shown in **Fig. 1** found to be in good agreement with the standard ICDD file No. 01-070-5423. The compound LiAlB2O5 can be characterized as networks formed by [B2AlO7]**5-** rings and the structural units connect with each other. Every [B2AlO7]**5-** ring connects with four adjacent rings via bridging-oxygen atoms. Al has been introduced successfully into benzene-ring-like [B3O7]**5-** groups, but the properties of the Al atom are much different from those of B. The bond length of Al-

O is more than 1.7 Å while that of B-O is less than 1.5 Å, so the distribution of electron density on the [B2AlO7]**5-** ring will be more inhomogeneous.
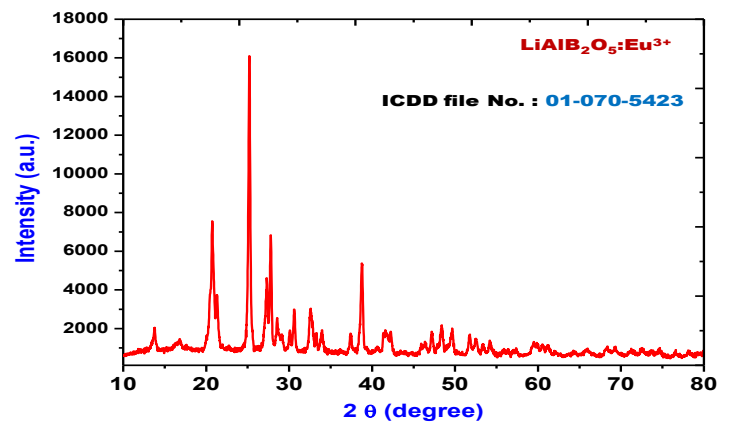
FIG. 1   XRD PATTERN OF LIAL(0.95)B2O5:0.05EU3+ PHOSPHOR.

3.2 FE-SEM micrographs of phosphor powders

FE-SEM Image of LiAl(1-x)B2O5:Eu3+ is shown in **Fig.** . FE-SEM study was carried out to investigate the surface morphology of the phosphor. The first time investigation on the morphology of LiAl(1-x)B2O5 phosphor was reported in this work as morphology of the phosphor is not reported till date which has spherical like structure. The particles possess foamy like morphology formed from highly agglomerated crystallites.
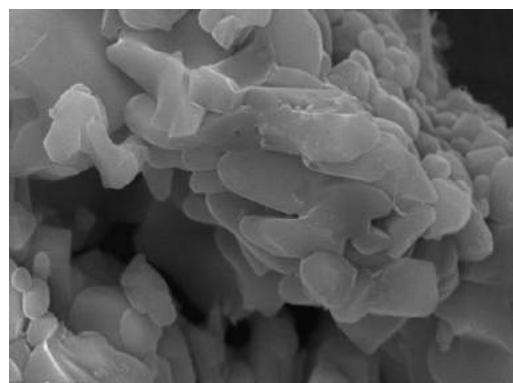
FIG. 2 FE-SEM MICROGRAPH OF LIAL(0.95)B2O5:0.05EU3+ PHOSPHOR.

3.3 Photoluminescence analysis of LiAl2B2O5:Eu3+

The excitation and emission spectra of LiAl(1-x)B2O5:xEu3+ (LABO:Eu) (x=0.005, 0.01, 0.03, 0.05, and 0.07) phosphors at λem = 614 nm is shown in **Fig.** . The excitation spectrum of LABO:Eu contains an intense broad band in the wavelength range 200–300 nm with a maximum at 254 nm and a group of peaks in the longer wavelength region. The former is due to the charge transfer band (CTB) of Eu3+ → O2– and the latter f-f transitions within Eu3+ 4f6 configuration. The excitation spectra consist of sharp f–f transition lines in the wavelength range 300 nm to 500 nm, including 7F0→5H3 (319 nm), 7F0→5D4 (362 nm), 7F0→5L7 (382 nm), 7F0→5L6 (394 nm, stronger), and 7F0→5D3 (415 nm). It can be seen clearly that the charge transfer transition from the O2- to Eu3+excitation line at 254 nm wavelengths is very stronger than the intraconfiguration 4f6 excitation lines (394 nm, 382 nm). The emission spectra of LABO:Eu under 254 nm excitation with different Eu contents shows several emission lines peaking at 579, 592, 614, and 655 nm. The most intense emission peak is observed at 614 nm due to 5D0→7F2 electric dipole transition, and the other emission peaks are ascribed to 5D0→7F1 and 5D0→7F4 magnetic dipole transition of Eu3+, respectively. The result indicates that most of the Eu3+ is located at sites without inversion symmetry. **Fig.** shows the effect of Eu-doped concentration on the emission (at 614 nm) intensity of LABO:Eu phosphors for 254 nm excitation. It indicates that the emission intensity increases with increasing Eu3+ concentration from x=0.005 to x=0.05. The most intense peak is observed at a concentration of x=0.05, and then the intensity decreases, this is due to the facts that the substitution of Eu3+ for Al3+ increases and that the CTB wavelength increases with the concentration increasing of Eu3+ ions. The most prominent emission peak is observed at 614 nm which can be assigned to 5D0→7F2 transition.
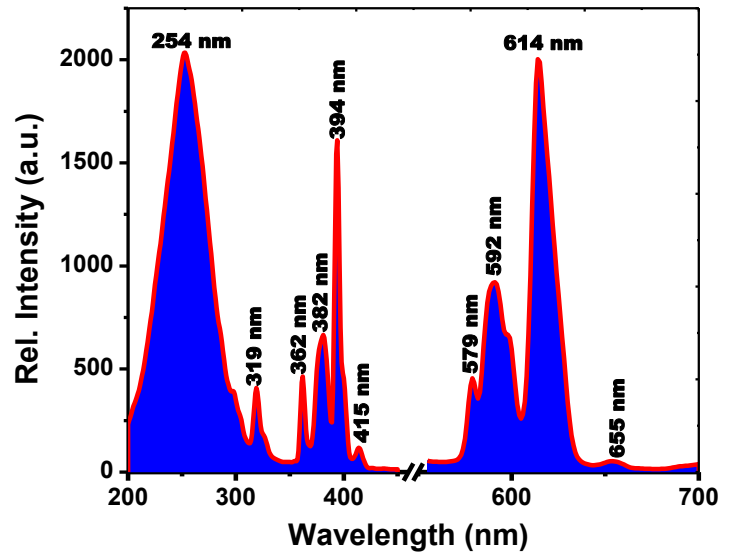
Fig. 3 The excitation and emission spectra of LiAl(0.95)B2O5:0.05Eu3+ phosphors. (λex= 254 nm, and λem= 614 nm).
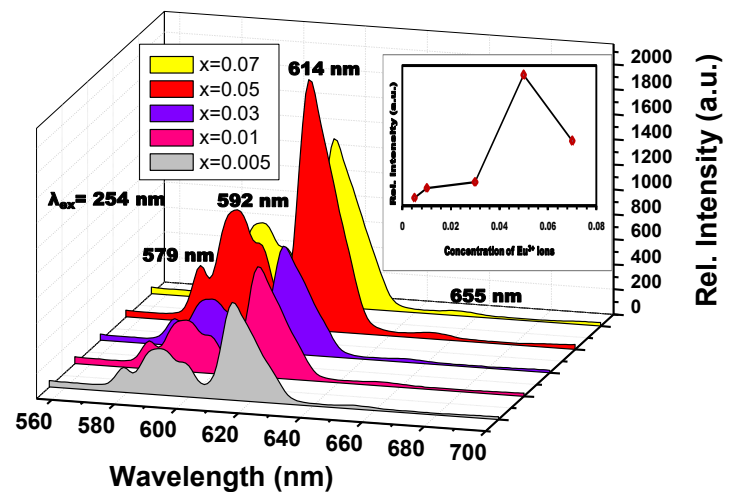
Fig. 4 The emission spectra of LiAl(1-x)B2O5:xEu3+, with x equal to 0.005, 0.01, 0.03, 0.05, and 0.07, respectively.

The CIE chromaticity coordinates for LiAl(0.95)B2O5:0.05Eu3+ were calculated from the PL spectra under 254 nm excitation and marked with a white star in the CIE 1931 chromaticity diagram in **Fig.** . The chromaticity coordinates (x, y) of this phosphor are calculated to be (0.67, 0.32), respectively, which indicates that the emission color of the LiAl(0.95)B2O5:0.05Eu3+ phosphors is located in the reddish-orange region.
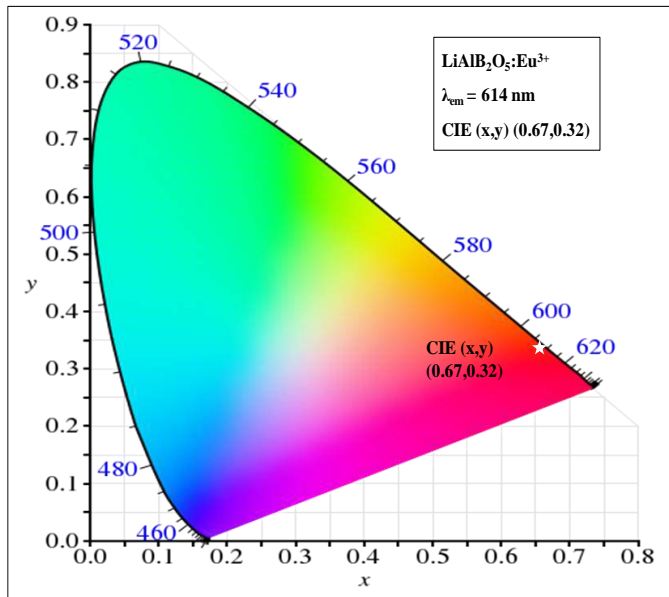
Fig. 5 Chromaticity coordinates of LiAl(0.95)B2O5:0.05Eu3+ phosphor in the CIE 1931chromaticity diagram.

IV. CONCLUSION

The phosphor LiAlB2O5:Eu3+ can be synthesized by a simple, time saving and cost effective solution combustion technique. The excitation spectra show that the intraconfiguration 4f6 excitation lines are weaker than the charge transfer transition from O2- to Eu3+. The PL spectra show the strongest emission at 614 nm corresponding to the electric dipole 5D0→7F2 transition of Eu3+ in LiAlB2O5 due to the non-centrosymmetric nature of the Eu3+ site, which results in pure red color emission. The phosphor possesses excellent red emitting property which can be attractive to a wide range of potential applications.

V. ACKNOWLEDGEMENT

REFERENCES

N. Ye, W. R. Zeng, B. C. Wu, X. Y. Huang, C. T. Chen, Z. Kristallogr., New Cryst. Struct., 213 (1998) 452.

[ii] N. Ye, W. R. Zeng, J. Jiang, B. C. Wu, C. T. Chen, B. H. Feng, X. L. Zhang, J. Opt. Soc. Am. B, 17 (2000) 764.

[iii] J. F. MacDowell, J. Am. Ceram. Soc., 73 (1990) 2287.

[iv] F. Lucas, S. Jaulmes, M. Quarton, T. Le Mercier, F. Guillen, C. Fouassier, J. Solid State Chem., 150 (2000) 404.

[v] H. You, G. Hong, Mater. Res. Bull., 32 (1997) 78.

[vi] W. D. Cheng, J. X. Lu, Chin. Sci. Bull., 42 (1997) 606.

[vii] S. F. Radaev, B. A. Maximov, V. I. Simonov, B. V. Andreev, V. A. D'yakov, Acta Crystallogr. B, 48 (1992) 154.

[viii]   M. He, X. L. Chen,1 Y. C. Lan, H. Li, and Y. P. Xu, J. Solid State Chem., 156 (2001) 181.

[ix]   R. S. Palaspagar, R. P. Sonekar, S. K. Omanwar, AIP Conf.Proc. 1536 (2013) 895-897.

[x]   A.B. Gawande, R.P. Sonekar, S.K. Omanwar, J. Lumin. 149 (2014) 200-203.

[xi]   R. S. Palaspagar, R. P. Sonekar, S. K. Omanwar, IOSR J. App. Phy. Special issue (2014) 11-14.

[xii]   R. J. Xie, N. Hirosaki, Sci. Technol. Adv. Mater., 8 (2007) 588.

Sample Holder for the Measurement of AC conductivity of Solid Electrolyte

*Thakare N R[1], Gandhi P R [2], Nande AV[3], Patil S A [4]

[1,4]Department of Physics, P.R.Pote College of Engineering and Management Amravati, Maharashtra, India

[2]Department of Physics Ramdeobaba college of Engineering College Nagpur, Maharashtra, India

[3]Department of Physics Gurunanak College of Science, Ballarpur Dist Chandrapur, Maharashtra, India

*Corresponding author: nilesh_thakarey@rediffmail.com

ABSTRACT

The development alternative energy source is a race among the researchers from last five decades. Even today the scientist and labs are trying to find the competitive materials which will have high reliability in energy source like Solid state battery. The materials used in solid state battery called as solid electrolytes. The high ionic conductivity is the dior and prior need of this solid electrolyte. The measurement of ionic conductivity is always a challenging for the researcher, where a good sample holder satisfying the requirement of the AC conductivity measurement is the need. The effect of pressure, frequency and temperature are the common parameters of measured to understand the properties of the solid electrolyte .In the present paper the design of sample holder and various properties related to sample holder are discussed.

Keywords : AC Conductivity, Alternative Energy Source, Solid Electrolytes

I. INTRODUCTION

The sample holder (known also as flat specimen holder) is used for holding flat, circular or square/rectangular samples. It enables contacting the sample from the front and from the back The large electrical contact with copper foil surface (not being in contact with an electrolyte) ensures optimal current collection by minimizing electrical resistance and unifying current distribution. The sample holder elements are constructed with materials that are inert to the electrochemical system. It well fits aqueous and organic solvent electrolyte requirements. The construction is well sealed which prevents the electrolyte to leak inside. It can be used wherever it is necessary to make an electrode using a thin layer of an active material deposited on a flat substrate. The effect of pressure, frequency and temperature are the common parameters of measured to understand the properties of the solid electrolyte [1-4]. In the present paper the design of sample holder and various properties related to sample holder are discussed.

II. Sample holder Assembly

Sample holder is mainly design to measure AC conductivity of the solid electrolyte materials synthesized in the laboratory. The prepared samples are either in the form of pellets or

quenched one, used directly. The materials used for prepared sample holders are ceramic 12 holes pipe, alumina pipe, spring, Teflon pipe, silver electrodes, antimagnetic steel rod etc. The dimensions of the parts used for the sample holder given in the following table1.

1	**Ceramic ring**	Diameter	4.9 cm
		Thickness	1.6cm
2	**Ceramic Holder**	Length	7.7 cm
		Diameter	5.1 cm
3	**Syndhanium plate**	Length	14.5 cm
		Breath	13.4 cm
		Thickness	0.9 cm
		Diagonal	19.4 cm
4	**Silver electrode**	Diameter	1.5 cm
		Length of Ag wire	40 cm

Table 1. Dimensions of Sample Holder

The assembling stages of are shown in the figure 1 given below.

Fig1. Sample Holder

III. Parameter of the Sample holder considered and measurements carried out before using it for measurement

3.1 Contact of electrodes and its Ohmic behavior:

The pair of silver electrodes used for the measurement of electrical conductivity. The method of measurement used is two probes method where the sample is connected to a voltage source either AC or DC and the corresponding current through it is measured. Using the electronic gadgets the V-I measurement is converted into suitable parameters like R-X, C-tanδ, ε'-ε" etc. The measurement of above parameters is possible using impedance analyzer like HP4192A, Agilent 4292A in the frequency range varying from Hz to MHz While doing such measurement the most important parameter to be taken care is the Ohmic contacts. The Ohmic contacts are always confirmed by taking the V-I characteristics of the sample holder. The DC and AC (at frequency 10KHz and 100KHz) V-I measurement carried out for the sample holder over the voltage range varying from 1mV to 2 Volt found to be linear and passing through the origin as shown in the figure 2(A,B). This ensures the Ohmic contact between sample and electrodes.
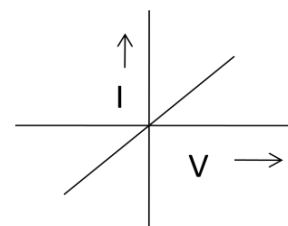
Fig 2A (DC)
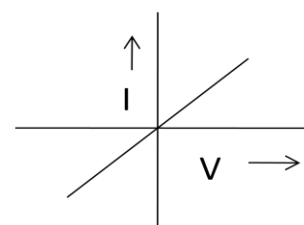
Fig 2B (AC)

Fig 2: V-I characteristics of the sample holder

When the V-I characteristics is not a straight line (as shown above) then contact is not Ohmic. To ensure the Ohmic contact different conducting paints are used depending upon the composition of the sample. Using different conducting paints for various sample compositions is given in the following table 2[5].

Table 2 : The use of conducting paint for different solid electrolytes

Type of Electrolyte	Nature of Solid electrolyte	
	Crystal line	Amorphous
Silver (Ag) Based	Silver (Ag) / Graphite (Gr)	Silver (Ag) / Graphite (Gr)
Lithium (Li) Based	Silver(Ag) /Aluminum (Al) / Graphite (Gr)	Silver(Ag) /Aluminum (Al) / Graphite (Gr)
Sodium (Na) Based	Silver(Ag) /Aluminum (Al) / Graphite (Gr)	Silver(Ag) /Aluminum (Al) / Graphite (Gr)
Potassium (K) Based	Silver(Ag) /Aluminum (Al) / Graphite (Gr)	Silver(Ag) /Aluminum (Al) / Graphite (Gr)
OH⁻ Based	Graphite(Gr)	Graphite(Gr)
Protonic Conductor	Aluminum (Al) /Graphite (Gr)	Aluminum (Al) /Graphite (Gr)

The testing the sample holder for Ohmic contact is needed for the reason of usage of blocking electrodes [5]. The blocking electrodes (silver electrodes) mean which do not have the common ions as that of the solid electrolyte used for the measurement of the conductivity. The best contacts can be established only after making the contact of non-blocking electrodes.

The use of non-blocking electrodes is not possible every time, like lithium based solid electrolytes require lithium as electrodes. Handling the lithium has many constraints as it needs spec pure inert atmosphere and sample holder of different design for holding the sample,

3.1 Impedance and capacitance measurement of sample holder with sample and without Sample.

The Impedance measurement of glassy solid electrolyte is carried out using Agilent4292A impedance analyzer over the frequency range of 20Hz to 2MHz. The Impedance plot for the same is shown in figure 3.
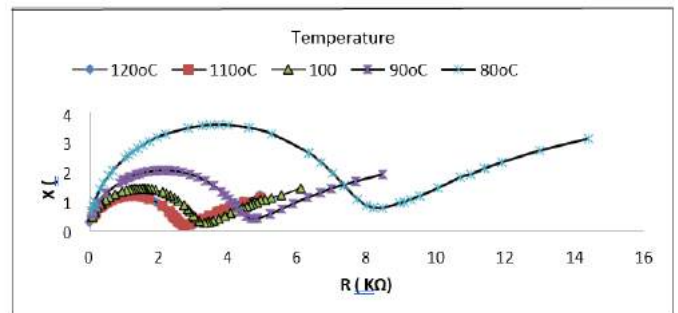
Fig 3 : Complex impedance lot of amorphous potassium doped lithium Borate Solid electrolyte at different temperature.

The impedance plot reveals the characteristics of sample and electrode-sample contact. The amorphous solid electrolyte does not contribute to grain boundary therefore one can get only the contribution of sample electrode-sample contact. Many researchers has developed the conductivity modelsRef for amorphous solid electrolyte and given the possible equivalent circuit for it.

The AC equivalent circuit [6] for solid electrolyte (amorphous) is shown in the figure 4.
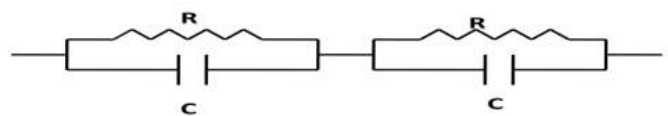
Fig 4 : R-C Equivalent Circuit

The equivalent circuit comprises the effect of solid electrolyte sample, contact between sample and electrodes during the impedance measurement.

What is important in this is the net contribution of electrodes to impedance and it should reflect uniformity in its value over temperature range of measurement. This can be understood in the following manner.

The semicircular part of the impedance plot in figure 3 is for sample under measurement; the increase in the value of reactance at the peak maxima and at the onset of the impedance plot with decrease in temperature has been extensively studied and explained by many authors Ref. This is the reactance of the sample arising due capacitive effect as seen from equivalent circuit. The linear nature of the impedance plot is due to the sample-electrode contact impedance. Moreover the linearity in the graph remains unchanged with temperature this reflects the uniform contribution of impedance arising due to sample –electrode contact.

This linear nature is then further analyzed to understand the net contribution of resistance and capacitance of sample holder electrodes to the contact. The equivalent circuit shown above is the parallel combination of R and C, the resultant reactance of the circuit is given by equation

$$Requ = \frac{R \; Xc}{R \; + \; Xc}$$

The Requ decreases with increase in frequency as shown in figure 5. The range of the Requ varies from 2.758KΩ to 0.4389KΩ over the frequency. When the contribution of the Xc is isolated from it, it is seen that it decreases with frequency as shown in figure 6. This behavior goes well with that observed for parallel plate capacitor with air as dielectric.
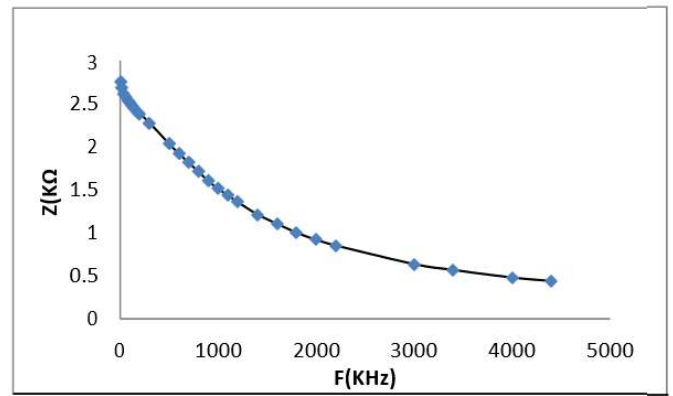
Fig : 5

The R and X, C and tanδ are measured as a function of frequency and temperature without sample (keeping the separation of electrodes same as that of sample thickness) has carried out. The variation in R-X with frequency and temperature is not reflected in the measurement. Therefore it has been cleared that the contribution of electrodes alone to the impedance is negligible. Whereas the C – tanδ measurements as a function of frequency shows similar nature as that is observed for air. This reflects that the electrodes contribution towards R-X and C can be ignored during the AC measurements of the sample. Therefore the net effects of the electrodes of the sample holder do not contribute to the conductivity measurement of the solid electrolyte sample under study.
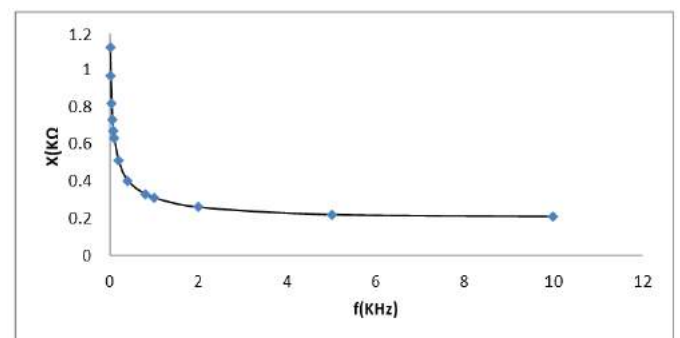
Fig 6

IV. REFERENCES

[1]. A.F.Orliukas, A.Kezionis, E.Kazakevicius, Solid State Ionics 176(2005) 2037-2043.

[2]. A.S. Nowick, B.S.Lim, A.V.Vaysleyb, Journal of Crystalline Solid 172-174(1994) 1243- 1251

[3]. A.W.Imre, S.Voss, F.Berkemeier, H.Mehrer, I.Konidakis, M.D.Ingram, Solid State Ionics 169 (2004) 963-969

[4]. K.Funke, R.D.Banhatti, Solid State Ionics 169 (2004) 1-8

[5]. Xin Guo, Wilfried Sigle, Jurgen Fleig, Joachim Maier, Solid State Ionics 154-155 (2002) 555-561

[6]. Jozef R.Dyges Solid State Ionics 176 (2005) 2065-2078.

Structural and Thermogravimetric Analysis of Piezoelectric KNbO3

A. R. Khobragade[1], A. R. Bansod[2], O. P. Chimankar[3]

[1]R. D. Science of College Aheri, Maharashtra, India
[2]Dr. Ambedkar College Deekshabhoomi, Nagpur, India
[3]Department of Physics, Rashatrasant Tukadoji Maharaj Nagpur University, Nagpur, India

ABSTRACT

Piezoelectric ceramic $KNbO_3$ powder was prepared by hydrothermal reaction using Nb_2O_5 in K_2CO_3 solution. A single phase of $KNbO_3$ was obtained when the molar ratio of K_2CO_3/Nb_2O_5 was above 1.2. It shows the orthorhombic structure at room temperature from XRD analysis. The morphology of the prepared ceramic is done using SEM analysis. Two dips in DTA at 70°C and 1080°C indicate the absorption of energy. At temperature up to 100°C the crystal shows endothermic behavior, while above 100°C, the behavior is exothermic up to 1000°C. After 1000°C the crystal shows the endothermic behavior again with a valley at near 1080°C.

Keywords : Piezoelectric, Ceramic, XRD, $KNbO_3$, Endothermic.

I. INTRODUCTION

Lead-based piezoelectric ceramics (PZT) have good piezoelectric properties and therefore frequently used in many applications[1-2]. however since they contain large concentration of PbO, unfavourable to environment, search for lead-free or low lead materials has been initiated. As far as PZT are concerned, considerable attention has been paid to (K, Na)NbO_3(KNN)-based ceramics because of their excellent piezoelectric properties, high Curie temperature [3-4], and environmental friendliness [5-7]. KNN with perovskite structure is known for its better nonlinear optical and electro-optic properties.

Although recent researches reported many KNN-based lead-free ceramics with improved piezoelectric properties, it still has a long way to run for lead-free

piezoelectric materials to substitute commercial PZT. Similar to the more extensively studied isomorphous analog, $BaTiO_3$, There are two phase transition temperatures above room temperature for $KNbO_3$: structural phase transformations on cooling from high temperature with the crystallographic symmetry being reduced from cubic - tetragonal -orthorhombic - rhombohedral. The mechanisms for the phase transformations (i.e., their displacive or order-disorder character) are still under discussion. Unlike tetragonal $BaTiO_3$, $KNbO_3$ is orthorhombic at room temperature. In PZT perovskite structure, the acceptor (hard) dopants such as K^+, Rb^+, Na^+ (occupy A-site, i.e., Pb-site) and Sc^{3+}, Mg^{2+}, Fe^{3+}, Fe^{2+}, Co^{2+}, Co^{3+}, Mn^{2+}, Mn^{3+}, Ni^{2+}, Ga^{3+}, In^{3+}, Al^{3+}, Cr^{3+} (occupy B-site, i.e. Ti-site) in the perovskite structure[8-10]. The properties of hard doping are

lower dielectric constant, lower dielectric loss, higher coercive field, low k_p and high Q_m where different acceptor doping ions affect different properties. The effect of dopant Al^{3+} on the crystals growth mechanism and the crystal textures is studied in this work.

II. EXPERIMENTATION

2.1. Synthesis

KNbO$_3$ ceramics were prepared by modified conventional ceramic fabrication process. The growing large size single crystals are somewhat difficult. The present method is used to grow the large size single crystals of KNbO$_3$. The K$_2$CO$_3$ and Nb$_2$O$_5$ were taken in the molar ratio of 1.2:1. The dopant Al$_2$O$_3$ was added to the mixture of K$_2$CO$_3$ and Nb$_2$O$_5$. This mixture was mixed thoroughly by grounding them together in the mortar for a sufficiently long time (4 to 5 hrs) and packed in a 50 ml flat bottom platinum crucible covered with a platinum lid. The crucible was heated till 900°C at the rate of 50°C/h. After a temperature of 900°C, the rate of heating was reduced to 20°C/h, till a temperature of 1100°C was reached. The crucible was maintained at this temperature for a period of 24 h. After soaking for 24 h, the homogeneous mixture was then cooled to 840°C at the rate of 14 to 17°C /h to allow for crystallization. The material was reheated to 1000°C, maintained at this temperature for 18 h and slowly cooled to room temperature at the rate of 20°C /h for the complete crystal growth. The crystal blocks separated from flux were found at the top by a thick crystalline layer projecting from the walls of the crucible. A thin layer of small crystals was also found near the thick layer. Crystal plates could also obtain on the bed of flux. The crystal plates found on the bed of the flux are mostly white. Some crystal plates are colourless. The size of the colourless plates range from 2 mm to 50 mm on edge length. The thickness is about 0.4mm. The crystals plates usually show quite simple twinning and are very good for dielectric as well as domain studies. The white crystal plates are larger in area and smaller in thickness (of the order of 0.1mm.), very fragile and highly twinned. The large size single crystals is of greenish colour and transparent. Also the crystal could be easily doped with Al$_2$O$_3$. The crystals doped with Al$_2$O$_3$ produced some interesting effects on the domain structures which will be discussed later in a different paper. The aluminum doped single crystals of KNbO$_3$ were characterized using X-ray diffractometer. The thermal properties using DTA and DSC were also carried out to observe phase transitions.

2.2 Characterization

The structural properties of KNbO$_3$ were identified by X-ray powder diffraction (XRD) with a X'Pert PRO advanced diffractometer using Cu (K$_\alpha$) radiation (λ=1.5406 Å). The morphology of selected synthesized KNbO$_3$ films was examined using scanning electron microscopy (SEM, model S-4500, Hitachi, Japan) at 5-kV accelerating voltage. The thermal properties using DTA and DSC were carried out to observe phase transitions.

III. RESULT AND DISCUSSION

3.1 structural characterization

The XRD studies of the sample were carried out to determine the lattice parameters. The XRD pattern of KNbO$_3$ is shown in the Fig. 1 and the data is shown in table 1. From the XRD studies the lattice parameters of doped KNbO$_3$ single crystals are found as a=5.6632 Å, b=3.9745 Å, c=5.7218 Å. This is like an orthorhombic structure at room temperature.
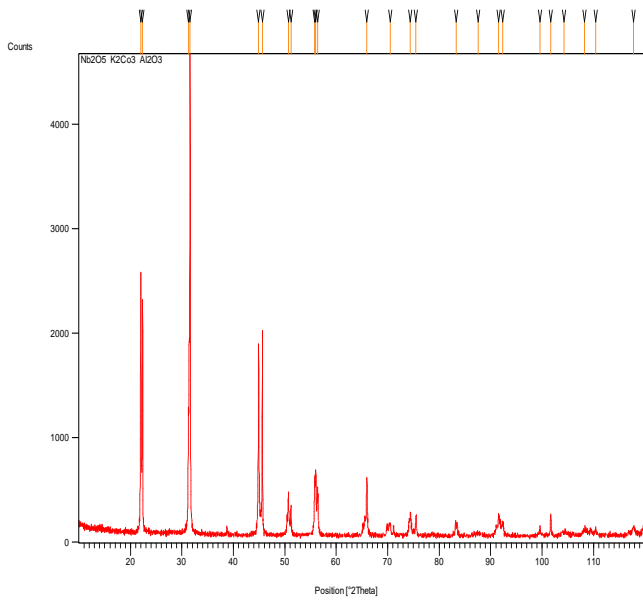
Fig. 1. The XRD Spectra of KNbO₃ sample.

Table: 1: X-ray diffraction data of KNbO₃

Sr. No.	2θ	d_{obs}	d_{cal}	hkl	I/I0 (%)
1	22.3448	3.97549	3.9745	010	47.66
2	31.5705	2.83164	2.8316	200	100
3	44.8906	2.01754	2.01252	202	38.67
4	45.6177	1.98706	1.9872	020	41.86
5	50.6702	1.80014	1.8075	103	8.40
6	51.2021	1.78268	1.79546	212	6.05
7	55.8036	1.64609	1.64535	113	11.12
8	56.3745	1.63076	1.63413	311	8.79
9	65.9354	1.41556	1.4158	400	12
10	70.4516	1.33547	1.33110	321	2.33
11	74.4055	1.27399	1.27120	313	4.59
12	75.4907	1.25834	1.234646	322	4
13	83.3304	1.15873	1.14436	005	2.34
14	91.5603	1.07483	1.07357	413	3.91
15	92.3886	1.06735	1.0609907	205	2.63
16	99.5828	1.00864	1.006261	404	1.37
17	101.6695	0.99351	0.9936	040	4.16
18	108.2186	0.95083	0.950211	315	1.16
19	110.4443	0.93782	0.935948	225	1.09
20	117.7966	0.89962	0.8935	422	1.59

3.2 Morphological Charecherization

The SEM of the different samples was carried out to determine the grain size and it is found in the range of 1.2 to 2.5μm.
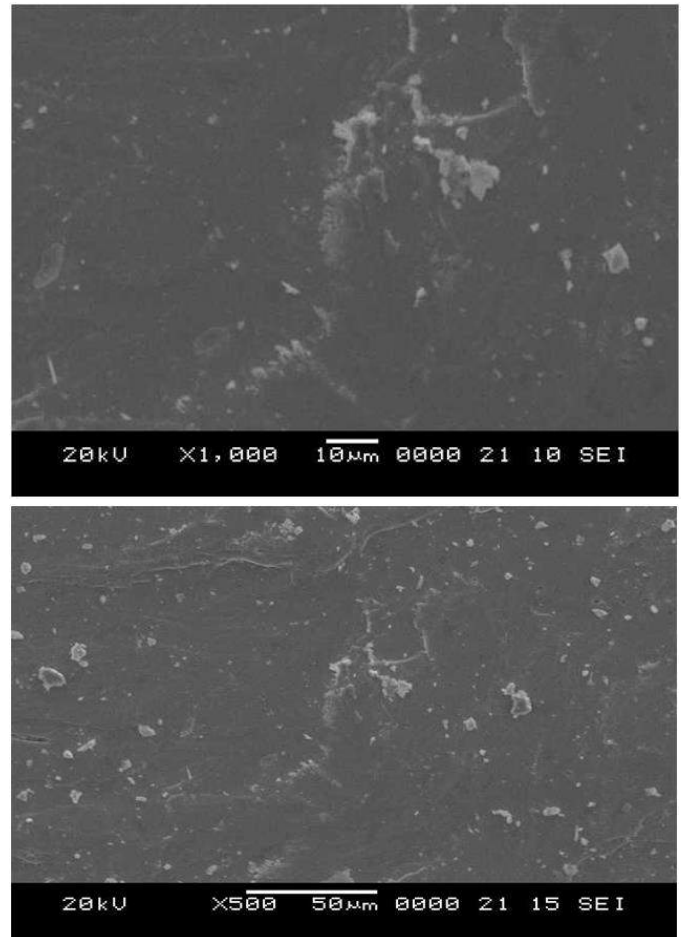
Fig. 2 SEM micrographs of KNbO₃ ceramics

3.3 Thermogravimetric charecterization

The thermal studies were carried out using TGA, DTA. The DTA curves in fig. 3 and fig. 4 shows two dips or valleys at temperatures of 70⁰C and 1080⁰C. These valleys indicate the absorption of energy. The reason for this is not clear here. But, at temperature up to 100⁰C the crystal shows endothermic behavior, while above 100⁰C, the behavior is exothermic up to 1000⁰C.

After 1000^{0}C the crystal shows the endothermic behavior again with a valley at near 1080^{0}C.
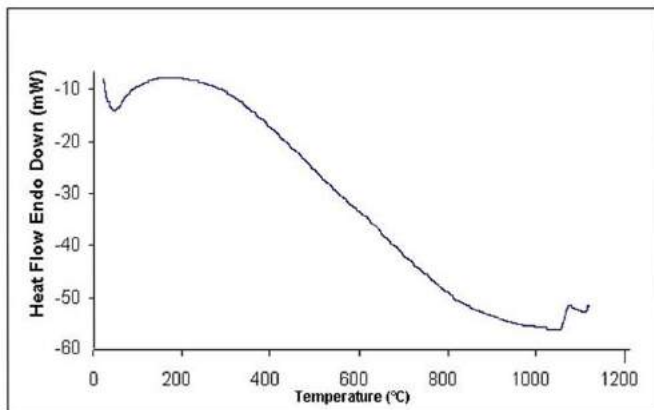
Fig.3: TGA - DTA curve for heat flow (mW) Vs temperature.
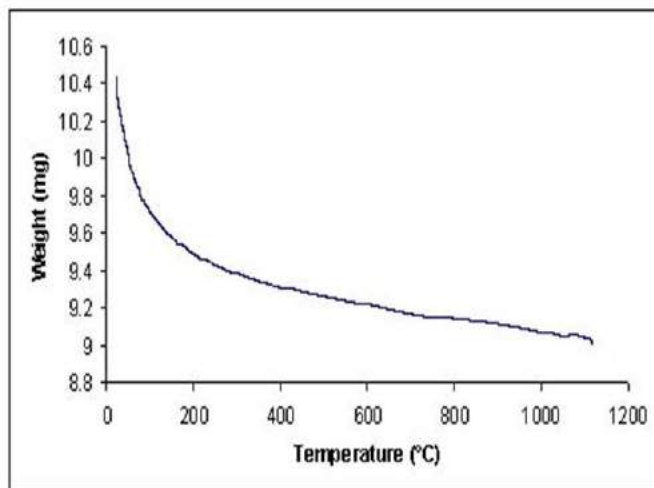
Fig.4: TGA - DTA curve for weight (mg) Vs temperature.

IV. CONCLUSION

A single phase of $KNbO_3$ with Al dopant was successfully synthesised by hydrothermal method. . From the XRD studies the lattice parameters of orthorhombic structure $KNbO_3$ single crystals are calculated as a=5.6632 Å, b=3.9745 Å, c=5.7218 Å. The crystals of average 1.2 to 2.5 μm size of $KNbO_3$ ceramics are measured from SEM. Two dips in DTA at

70°C and 1080°C indicated the absorption of energy. At temperature up to 100°C the crystal shows endothermic behavior, while above 100°C, the behavior is exothermic up to 1000°C. After 1000°C the crystal shows the endothermic behavior again with a valley at near 1080°C.

V. REFERENCES

[1]. K. Ramam and M. Lopez, Dielectric, ferroelectric and piezoelectric studies of neodymium-modified PLZNT ce- ramic for sensor nd actuator applications, J. Alloys Compd., 466 (12) (2008) 398.

[2]. T.M. Kamel and G. de With, Poling of hard ferroelectric PZT ceramics, J. Eur. Ceram. Soc., 28 (9) (2008) 9, 1827.

[3]. Z.G. Xia and Q. Li, Phase transformation in (0.90 – x)Pb(Mg1/3Nb2/3)O3-xPbTiO3-0.1PbZrO3 piesoelec- tric ceramic: X-ray diffraction and Raman investigation, Solid State Commun., 142 (6) (2007) 323.

[4]. P. Marˊechal, L. Haumesser, L.P. Tran-Huu-Hue, J. Holc, D. Kuˇsˇcer, M. Lethiecq, and G. Feuillard, Modeling of a high frequency ultrasonic transducer using periodic struc- tures, Ultrasonics, 48 (2) (2008) 141.

[5]. Y.T. Chen, C.I. Sheu, S.C. Lin, and S.Y. Cheng, Effects of microwave heating on dielectric and piezoelectric properties of PZT ceramic tapes, Ceram. Int., 34 (3) (2008) 621.

[6]. Y.Y. Wang, J.G. Wu, D.Q. Xiao, J.G. Zhu, P. Yu, L. Wu, and X. Li, Piezoelectric properties of (Li, Ag) modified (Na0.50K0.50)NbO3 lead-free ceramics with high Curie temperature, J. Alloys Compd., 459 (12) (2008) 414.

[7]. J.G. Wu, D.Q. Xiao, Y.Y. Wang, W.J. Wu, B. Zhang, J. Li, and J.G. Zhu, CaTiO3-modified (K0.5Na0.5)0.94Li0.06](Nb0.94Sb0.06)O3 lead-free piezoelectric ceramics with improved

temperature stability, Scripta Mater., 59 (7) (2008) 750.

[8]. K. Wang and J.F. Li, Analysis of crystallographic evolution in (Na,K)NbO3-based lead-free piezoceramics by X-ray diffraction, Appl. Phys. Lett., 91 (26) (2007) 262902.

[9]. P. Zhao, B.P. Zhang, and J.F. Li, Enhanced dielectric and piezoelectric properties in LiTaO3-doped lead-free (K,Na)NbO3 ceramics by optimizing sintering temperature, Scripta Mater., 58 (6) (2008) 429.

[10]. E. Ringgaard and T. Wurlitzer, Lead-free piezoceramics based on alkali niobates, J. Eur. Ceram. Soc., 25 (12)(2005) 2701.

Synthesis and Photoluminescence study of Gd3+ doped YP3O9 phosphor prepared by Citric sol-gel method

A. A. Sharma[1], A. O Chauhan*[2], C. B. Palan[3], S. K. Omanwar[1]

[1]Department of Physics, Sant Gadge Baba Amravati University, Amravati (MH), India

[2]Vidya Bharati Mahavidyalaya, Amravati (MH), India

[3]Bapumiya Sirajoddin Arts, Commers & Science College Pimpalgaon Kale, Tq. Jalgaon Jamod, Dist. Buldana, India

ABSTRACT

Gd^{3+} doped YP_3O_9 phosphor was synthesized by Citric sol-gel method. The phosphor was characterized by X-ray diffraction (XRD), Photoluminescence (PL). The Phase purityand crystallinity of phosphor is confirmed by X- ray diffraction (XRD)analysis while surface morphology studied by scanning electron microscopy (SEM).The photoluminescence properties of the $Y_{0.99}P_3O_{9:0.01}Gd^{3+}$ sample was investigated by excitation and emission spectra. The PL excitation spectra of $Y_{0.99}P_3O_{9:0.01}Gd^{3+}$ phosphor exhibitsbroad spectra having high intense peak at 275 nm. Under UV excitation (275 nm), $Y_{0.99}P_3O_{9:0.01}Gd^{3+}$ shows emission peak at 312 nm. The obtained results show that the prepared phosphor is suitable for Phototherapyapplication.

Keyword : XRD, Photoluminescence, SEM, UV excitation

I. INTRODUCTION

The use of ultraviolet radiation for treatment of variousskin diseases is well recognized for long time by the meanof phototherapy. It was an effective treatment for many skindisorders, such as Psoriasis [1], Vitiligo [2], Ofujisdisease[3], ErythropoeticProtoporphyria [4], Pityriasisrosea [5],Uremicpruitus [6] Lichen SclerosusetAtrophicus [7], Morphea [8], Scleroderma [9], Cutaneous T-cell lymphoma,Lupus Erythematosus [10].In that method we use artificial ultraviolet radiation ranging from 220 nm to 400nm delivered by fluorescent lamps to cure skin diseases.

According to thebiological and optical properties UV radiation was dividedinto three categories i.e. UV-C from 220 to 280 nm; UV-Bfrom 280 to 320 nm and UV-A from 320 to 400 nm. UV-Ais further divided into two categories UVA1 (340–400 nm)and UV-A2 (320–340 nm).

The inorganic compounds with general formula $Ln(PO_3)_3$ (Ln = La to Lu and Y) belong to the broader class of phosphate materials which have been extensively investigated because of a suitable absorption in the VUV region, a wide band gap together with a high chemical stability and the relative simplicity of powder synthesis [11-15].

These materials are potential good phosphors, scintillators and detectors for ionizing radiation. Serra and Giesbrecht were the first to describe three rare-earth salts of general formula $TP_3O_9.3H_2O$ with [T = La, Ce and Nd] [16]. Later on, Birke and Kempe described chemical preparations and thermal behavior for $PrP_3O_9.4H_2O$, $LaP_3O_9.4H_2O$ and $ErP_3O_9.4H_2O$ [17-19].Jouini*et. al.,* studied the scintillator properties of $Pr(PO_3)_3$ phosphor [20]. The first investigation of Nd^{3+} luminescence in $La(PO_3)_3$ was reported by Jouini and co-authors in the framework of laser materials research [21]. The luminescence properties of Eu^{3+} and Tb^{3+} in $La(PO_3)_3$ and $Y(PO_3)_3$ as potential phosphors under VUV excitation have been discussed [22, 23]. Much attention has been paid to the energy migration and transfer processes in Ln-based phosphate compounds [24-26].

Practically, the rare-earth polyphosphates $Ln(PO_3)_3$ can adopt two different crystal structures, depending on the ionic radius of the RE ions. The polyphosphates with large RE^{3+} ions (La-Eu) have an orthorhombic structure with C2221 space group, while those with small RE^{3+} ions (Gd-Lu, Y) have a monoclinic structure with P21/c space group [27, 28].X. Zhang *et al.,* reported Eu^{3+} doped $Y(PO_3)_3$ phosphor successfully prepared by a conventional solid-state reaction and it shows intense orange-red emission under near-UV excitation. The result also reflects that the phase transformation from monoclinic to orthorhombic when Y^{3+} is totally replaced by Eu^{3+} [29].

In the present work, phosphor YP_3O_9 doped with Gd^{3+} was synthesized via a Citric sol-gel method. The synthesized material was characterized using the powder X-Ray Diffraction. The optical properties of Gd^{3+} in YP_3O_9 was studiedin detail using a fluorescence spectrometer.

II. EXPERIMENTAL

The powder sample $YP_3O_9:Gd^{3+}$ was synthesized for the first time by the Citric acid sol-gel method.The Stoichiometric amounts of high purity precursors Yttrium Oxide (Y_2O_3)(99.99%AR), Ammonia dihydrogen orthophosphate $(NH_4H_2PO_4)$, Citric acid, Gadolium Oxide (99.90%, AR), Ethylene glycol and Acetic acid weretaken for the preparation of phosphor.

The starting chemicals Y_2O_3 (99.99%,AR) and Gd_2O_3 (99.99%,AR) was taken in a china clay basin. A small quantity of double distilled water was added and paste was formed. 10 ml ofHNO_3 was added drop by drop and mixture was heated slowly under observation to 80°C till the paste dissolved completely. The solution was further heated till the excess of acid was boiled off. Afterword small amount of double distilled water was again added and slowly evaporated to dryness. After that solution of citric acid as well as $NH_4H_2PO_4$ were added drop by drop. Mix it well and place it on hot plate at 70ºC with continuous stirring for 15 min till the precursors dissolved completely leading to a colorless solution. During stirring add 0.5ml of ethylene glycol & 2-3 drops of acetic acid.

On further heating to 100°C, bubbles were evolved from the bottom of the china clay basin; solution turned pale yellow at 170°C, turned red & start boiling.The solution was then allowed to cool. Pale yellow gel was formed on cooling. The dry gel was then slowly heated which burnt slowly into dull red flame with the evolution of thin sized and light weighted carbon flakes at 230°C. The residue was pyrolysis at ~ 400°C into black charcoal / resin which burnt at ~ 700°C and lastly the powder was sintered at 950°C for 1 hr to obtained final crystalline powder of YP_3O_9: Gd^{3+}. The Flow chart of synthesis method is shown in **Fig.1.**
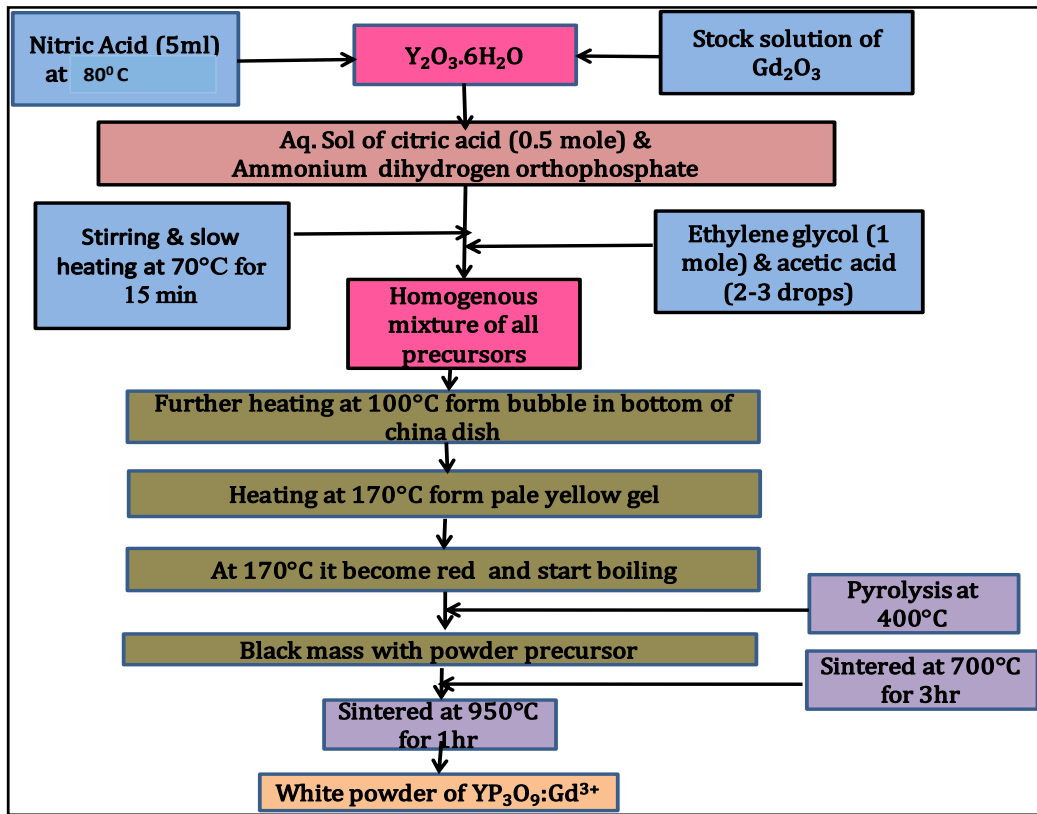
Fig.1. Flow chart citric sol-gel method

III. RESULT AND DISCUSSION

1.1. XRD Analysis

The phase purity and crystal structureof YP_3O_9phosphor was confirmed byX-ray diffraction patterns of (as shown in **Fig.2.**). The X-raypattern of sample indicated a pure phase of the standardYP_3O_9 and all the peaks were in good agreement withthe **(ICDD File 00-042-0501)**.There were no additional peaks found in X-raypattern.

Also, the XRD shows thatthe formed material was completely crystalline and was insingle phase with Monoclinic structure having lattice parameter with values a= 14.1520, b= 20.1490, c= 10.0610 also α = 90.00, β= 127.900, γ=90.00 with volume = 2263.788 & Z = 1.
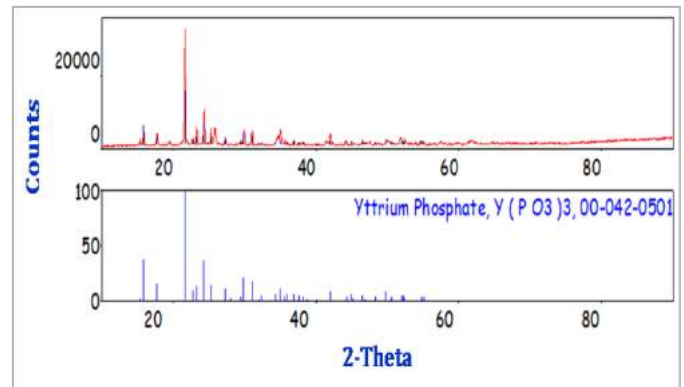
Fig.2. X-ray diffraction of YP_3O_9 phosphor

1.2. Surface Morphology

It is well known that the morphology is one of the aspects that required for the more efficient luminescence of phosphor materials. **Fig.3.** represented the SEM image of the host $Y_{0.99}P_3O_{9:0.01}Gd^{3+}$. The phosphor was synthesized by citric sol-gel method by following step by step sintering temperature. The phosphor morphology shows irregular grain with an average size of about 2μm.
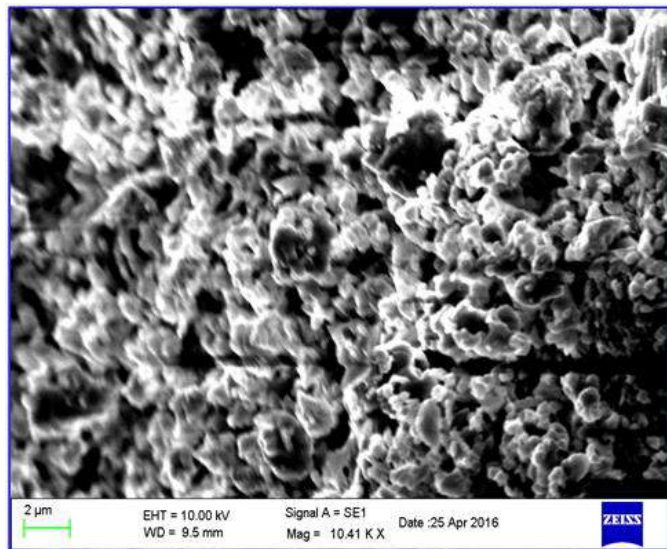
Fig.3. SEM image of $Y_{0.99}P_3O_9{:}_{0.01}Gd^{3+}$ phosphor

1.3. Photoluminescence Analysis

Fig.4. shows the combined emission & excitation spectra of $Y_{0.99}P_3O_9{:}_{0.01}Gd^{3+}$ phosphor synthesized by Citric sol gel method. The phosphor shows excitation spectra at 275nm having corresponding transition $^8S_{7/2} \rightarrow ^6G_J$. Under the excitation of 275nm the phosphor exhibits emission at 312 nm having corresponding transitions $^6P_{7/2} \rightarrow ^8S_{7/2}$. The emission spectra consist of a weak line at 306 nm followed by a strong one at 312 nm, which correspond to the $^6P_{5/2} \rightarrow ^8S$.
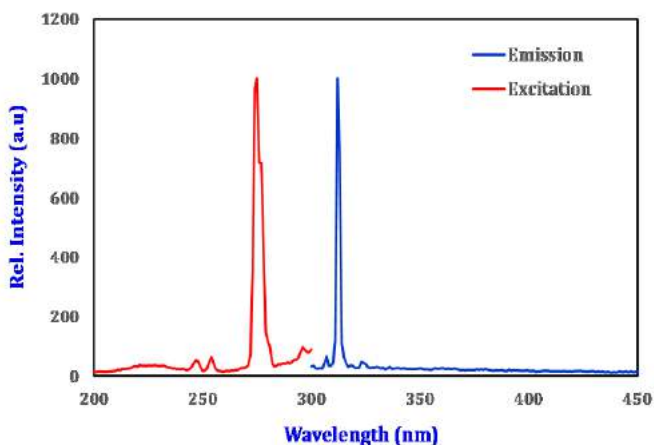
Fig.4. Combined Excitation and Emission spectra of $Y_{0.99}P_3O_9{:}_{0.01}Gd^{3+}$

IV. CONCLUSION

The $Y_{0.99}P_3O_9{:}_{0.01}Gd^{3+}$ powder phosphor was successfullysynthesized via the Citric Sol-gel method and theirphase purity was confirmed by X-ray diffraction analyses.The SEM images show agglomeration particle because ofhigh sintering temperature. The photoluminescence spectraillustrate that under the excitation of 275 nm phosphor emits sharp and intense emission in Narrowband UVB region (i.e. 312 nm). The obtained result shows that the prepared phosphor i.e. $Y_{0.99}P_3O_9{:}_{0.01}Gd^{3+}$ could be potential candidate for Phototherapy Application.

V. ACKNOWLEDGEMENTS

VI. REFERENCES

[1]. H. Honigsmann, W. Brenuer, W. Rauschmeier, Photochemotherapy for cutaneous T cell lymphoma. A follow-up study. Am.Acad. Dermatol. 10, 238 (1984)

[2]. L. Scherschun, J.J. Kim, W.H. Lim, Narrow band ultraviolet Bis a useful and well tolerated treatment for vitiligo. J. Am. Acad.Dermatol. 44, 999 (2001)

[3]. T. Ota, Y. Hata, A. Tanikawa, M. Amagai, M. Tanaka, T. Nishikawa, Eosinophilic pustularfolliculitis (Ofuji's disease): indomethacin as a first choice of treatment. Clin. Exp. Dermatol.26(2), 179 (2001)

[4]. L.J. Warren, S. George, Erythropoietic protoporphyria treatedwith narrow-band (TL-01) UVB phototherapy. J. Dermatol. 39,179 (1998)

[5]. V. Leenutaphng, S. Jiamton. UVB phototherapy for pityriasis rosea: a bilateral comparison study. J. Am. Acad. Dermatol.33(6), 996 (1995)

[6]. J.D. Blachley, D.M. Blankenship, A. Menter, T.F. Parker, J.P.Knochelam, Uremic pruritus: skin divalent ion content andresponse to ultraviolet phototherapy. Am. J. Kidney Dis. 5(5),237 (1985)

[7]. A. Kreuler, T. Jansen, M. Stucker, M. Herde, K. Hoffmann, P.Altmeyer, G. Vonkobyletzki,Low-dose ultraviolet-A1 phototherapy for lichen sclerosus et atrophicus. Clin. Exp. Dermatol. 26,30 (2001)

[8]. J.L.M. Hawk, Sunbeds. Radiat. Prot. Dosim. 91, 143 (2000)

[9]. A. Morita, K. Kobayashi, I. Isomura, T. Tsuji, J. Krutmann, Ultraviolet A1 (340–400 nm) phototherapy for Scleroderma in systemicsclerosis. J. Am. Acad. Dermatol. 43, 670 (2000)

[10]. T.P. Millard, J.L.M. Hawk, Ultraviolet therapy in lupus. Lupus 10,185 (2001)

[11]. S. Hachani, B. Moine, A. El-akrmi, M. Ferid, J. Lumin. 130 (2010) 1774.

[12]. Yu. Wang, D. Wang, J. Sol. State Chem. 180 (2007) 3450.

[13]. L.N. Zorina, Zh.A. Ezhova, I.V. Tananaev, N.P. Soshchin, V.P. Orlovskii, A.V. Lavrov, Izv. AN USSR Inorg. Mater. 20 (1984) 2014.

[14]. RiadhTernanea, Mokhtar Ferid, Ge´rardPanczer, Malika Trabelsi-Ayadi, Georges Boulon, Opt. Mater. 27 (2005) 1832.

[15]. S. Briche, D. Zambon, D. Boyer, G. Chadeyron, R. Mahiou, Opt. Mater. 28 (2006) 615.

[16]. O.A. Serra and E. Giesbrecht, J. Inorg. Nucl. Chem., 30 (1968) 793.

[17]. P. Birke and G. Kempe, Z Chem., 13 (1973) 151.

[18]. P. Birke and G. Kempe, Z Chem., 13 (1973) 65.

[19]. P. Birke and G. Kempe, Z Chem., 13 (1973) 110.

[20]. A. Jouini, J.C. Gâcon, M. Ferid, M. Trabelsi-Ayadi, Opt. Mater. 24 (2003) 175.

[21]. A. Jouini, J.C. Gâcona, A. Brenier, M. Ferid, M. Trabelsi-Ayadi, J. Lumin. 99 (2002) 365.

[22]. D. Wang, Y. Wang, Y. Shi, J. Lumin. 131 (2011) 1154.

[23]. R. Ternanea, M. Ferid, G. Panczer, M. Trabelsi-Ayadi, G. Boulon, Opt. Mater. 27 (2005) 1832.

[24]. H. S.Kiliaan, F P van Herwijnen, G Blasse, J. Solid State Chem. 74 (1988) 39.

[25]. M.Buijs, G.Blasse, J. Lumin. 39 (1988) 323.

[26]. S. Hachani, B. Moine, A. El-akrmi, M.Ferid, J. Lumin. 130 (2010) 1774.

[27]. H.Y.P. Hong, The crystal structure of ytterbium metaphosphate, YbP3O9, Acta Cryst. B30 (1974) 1857e1861.

[28]. J. Matuszewski, J. Kropiwnicka, T. Znamierowska, The crystal structure of lanthanum metaphosphate LaP3O9, J. Solid State Chem. 75 (1988) 285e290.

[29]. Xinguo Zhang, Peican Chen, Zizhou Wang, Liya Zhou, Fangxiang Zhou, Solid State Sciences 58 (2016) 80-85

Effect of Methanolic Extract of Achyranthes Aspera Linn on the Larvae of Silkworm, Bombyx Mori L.

A. N. Khade, C. J. Hiware, S. N. Khade

Department of Zoology, Dr. Babasaheb Ambedkar Marathwada University, Aurangabad (M.S.), India

ABSTRACT

Some medicinal plants are widely used in the field of agriculture to protect the crops from the insect pests. In the present study the Achyranthes aspera is used to find out the larvicidal and antifeedants activity on the larvae of silkworm, Bombyx mori. The silkworm B. mori L.is used in the study as an experimental model as an insect larvae.

The crude methanolic extract of Achyranthes aspera Linn. Seeds, foliar spray was used in different concentration on the leaves of mulberry and fed to fifth instar larvae of Bombyx mori. The growth rate, feed consumption index, approximate digestibility, Efficiency of Conversion of Ingestion (E.C.I.), Efficiency of Conversion of Digestion (E.C.D.) of food and the Mortality rate of the larvae are recorded.

The result of plant extract reveals that, there is marked decrease in the Growth rate, E. C. I. and E.C.D. as compare to control group. The feed Consumption rate of the larvae was increased in 25% and 75% concentration; whereas E.C.D. decreased value was observed in 75%. During the overall study period, in experimental group showed less mortality, whereas 30% mortality was observed in 75%concentration. The details are explained in the text.

Keywords : Achyranthes Aspera, Bombyx Mori, Methanolic Extracts, Growth Rate, Mortality, Digestibility

I. INTRODUCTION

India is an agriculture dominated country, over 1012.4 million people are dependent on the agricultural activity (Krishna et al. 2000). To increase the agricultural productivity and the quality of the crops, various chemical insecticides are used in the agricultural field. However the chemically prepared drugs can act quickly and effectively but they have several side effects which can alter the ecosystem. Many chemical pesticides have the potential to cause some serious diseases to the human, like Parkinson`s disease, Alzheimer's, disease, headache, fatigue and depression (David, 2008).

From prehistoric times several medicinal plants have been used in the traditional medicinal practices and agricultural field. The Plants synthesizes several chemical compounds for different functions including defense against insect, fungi, diseases and herbivorous mammals. Some medicinal plants are widely used in the field of agriculture to protect the crop from the insect pests, because of their rich and diverse occurrence of phytochemicals, which has insect repellent or deterrent properties (Vishnubhai, 2011); these phytochemicals do not have any primary functions in the plants, like growth, reproduction or photosynthesis in the plants.

Achyranthes aspera is a species of Amaranthaceae family of plant, it is a weed plant and distributed throughout the India. This plant contains various medicinal properties andin traditional systems of medicine it is used to treat various diseases like, malaria, Hyperlipidemia, estrogenic, leprosy, spasm, cardio tonic, bacterial, and antiviral infectionas well as it is used to treat asthma, tussive and snakebite, hydrophobia, urinary calculi, rabies, influenza, otorrhoea, piles, bronchitis, diarrhea, abdominal pain(Bhosale et al. 2012). In the phytochemical screening of the seeds of Achyranthes aspera L.it has been reported that it contains alkaloids, flavonoids, saponins, glycosides, terpenoids, proteins, amino acids and steroids (Somagari et al. 2014). It is also found that the seeds of A. aspera having higher insecticidal and growth inhibition activities, due to the presence of secondary plant compounds (Jeyasankar et al. 2014).

II. METHODS AND MATERIAL

Rearing of Bombyx mori L.

The eggs of Bombyx moriwere procured from the district Sericulture office, Aurangabad, during August 2018 brought in the laboratory after the hatching, first instar to fourth instars larvaewere reared on fresh Mulberry leaves, fifth instars larvae were taken for experimental study, and they were grouped into five batches. The Rearing was carried out and incubated as per Hiware (2001).

Collection of plant material

Seeds of Achyranthes aspera were collected from fields located at Patoda, Taluka,District Aurangabad. After shade dried the seeds are ground to make fine powder by the electric grinder, and stored into the air tight polythene bags.

Preparation and treatment of crude plant extract

The 40 gram powder of the seeds of Achyranthes aspera was extracted with 400 ml methanol by the Soxhlet extraction apparatus (Lolge et al, 2016). After the completion of extraction the final extract was kept

open to evaporate the solvent and remaining as stock solution was kept in refrigerator until use. Three different concentrations was prepared for larval treatment, 15 ml of crude extract was dissolve in 100 ml of distilled water, out of that 25%, 50% and 75% concentrated samplewere prepared by adding required amount of distilled water and sprayed separately by asprayeron mulberry leaf which were air dried and given as food to larvae. The weight of larvae, weight of excreta, weight of provided leaves and the weight of unconsumed leaves were recorded daily for nine days.

Calculations of nutritional indices of Bombyx mori L. have been done according to the equations used by Waldbauer (1968) on the basis of fresh body weight, dry weight of food consumed and dry weight of faeces per larva. Consumption index (C.I.), Growth rate (G.R.), approximate digestibility (A.D.), efficiency of conversion of ingested food (E.C.D) were calculated as follows:

$$(C.I.) = \frac{\text{Weight of eaten food}}{\text{Mean weight of larvae during feeding period} \times \text{Duration of feeding period (day)}}$$

$$(G.R.) = \frac{\text{Gained weight of larvae during feeding period}}{\text{Mean weight of larvae during feeding period} \times \text{Duration of feeding period (day)}}$$

$$\text{Mean weight of insect during feeding period} = \frac{\text{initial weight of insect} + \text{Final weight of insect}}{2}$$

$$(A.D.) = \frac{\text{Weight of ingested food} - \text{weight of faeces}}{\text{Weight of ingested food}} \times 100$$

$$(E.C.I) = \frac{\text{Gained weight of insect}}{\text{Weight of ingested food}} \times 100$$

$$(E.C.D.) = \frac{\text{Gained weight of insect}}{\text{Weight of ingested food} - \text{weight of faeces}} \times 100$$

III. RESULTS AND DISCUSSION

The crude methanolic extract of Achyranthes aspera sprayed in different concentration on the leaves of mulberry plantwas used and fed to fifth instars larvae

of Silkworm Bombyx moriL. In the present study, the growth rate, consumption index, approximate digestibility, Efficiency of digested food, and the Efficiency of conversion of ingested food and the mortality of the larvae have recorded. The results of the nutritional indices of fifth, larval instars of Bombyx mori L. has shown in Table 1. Nutritional indices of the fifth instars larvae of B. mori were significantly different in different concentration of the plant extracts. Growth rate shows how much nutrients increased in the body of insect per day per gram of body weight. The growth rate can alter the speed of development of insect, which depends onavailability of food and also on abiotic factors like temperature and humidity (Jasjinder, 2013). Growth rate of the larvae was noticeably decreased in the all group of larvae reared on treated leaves of mulberry with extract of Achyranthes aspera. Lowest value of growth rate was observed in 25% (0.090) followed by 50% (0.114) concentration of plant extract.

Consumption index shows the rate at which nutrients enter into the digestive system of the insect. In the present study the consumption index is almost same or there are not considerable changes in the consumption index of larvae those fed on 25% and 75% concentration of plant extract containing food, as compare to the larvae of control group. The larvae fed on 5% methanol (control II) sprayed food had the highest CI (*0.867*) value. However, the lowest CI (0.638) value was observed on 50% concentration of the plant extract.

Efficiency of conversion of ingested food is the general index which measure insect's ability to utilize the ingested food for its growth and development. The larvae reared on 50% concentration of plant extract showed the highest value of ECD (26.5) and ECI (*17.8*) compared with the other group of larvae. However, the lowest value (14.6) of ECD was on 75% concentration of plant extract.

Table no. I : Nutritional indices of Fifth instar larvae of Bombyx mori L. on the different concentration of Achyranthes asperaseed extracts.

Treatment groups		G.R.	C.I.	A.D.%	E.C.I.%	E.C.D.%	Mortality (In %)
Control		0.124	0.803	69.4	15.5	22.4	00
Control (M)		0.117	0.867	69.8	13.5	19.4	00
A. aspera	25%	0.090	0.846	71.3	11.4	16.1	10
	50%	0.114	0.638	67.3	17.8	26.5	10
	75%	0.119	0.818	70.5	14.5	14.6	30

G. R. = Growth Rate, C. I. = Consumption Index, A. D. = Approximate Digestibility, E. C. I. = Efficiency of Conversion of Ingested Food, E. C. D. = Efficiency of Conversion of Digested Food.

The lowest CI value observed in the 50% concentration of plant extract, but it had the highest values of ECI and ECD (Table 1) and it also had lower growth rate than control group, indicating that larvae feeding on this concentration could not grow faster than the normal larvae of silkworm but they were more effective in converting ingested and digested food to biomass. The growth of insect is depending on the efficiency of conversion of food material to the body matter, result is indicating that the larvae fed with 25% and 75% was less effective to convert ingested and digested food into the body matter. Jadhav et al(2016) reported that the efficiency of conversion of ingested food (ECI) and efficiency of conversion of digested food (ECD) of all the medicinal plant extract were superior over the control group due to the presence of some medicinal growth stimulants.

In the present study the decreased ECI and ECD value of seed extract of *Achyranthes aspera* was observed than the control group.

Insecticidal activity of plant extract

The effect of crude seeds extract of *Achyranthes aspera*has been studied on the 5th instars larvae of silkworm *Bombyx mori L.* with different concentrations. The mortality of larvae was calculated after the treatment of plant extract and the result showed in the table no. 1 revealed that the larvae fed with 75% concentration had the higher mortality and both of the control group there was no mortality observed.In the previous study, the supplementation with phytoecdysone containing extract of *Achyranthes aspera,*showed moderate mortality in the silkworm *Bombyx mori*observed in the triple treatment of 70% concentration of the plant extract (Pandey and Upadhyay, 2013). The significant mortality and antifeedants activity also observed by the treatment of leaves extract of *Achyranthes aspera* on the cauliflower borer, *Hellulaundalis* and *Spodoptera litura (*Girija and Valarmathy, 2008). It was previously demonstrated that, the dietary supplementation with the 20-hydroxyecdysone hormone,degenerate or disrupt the midgut of the larvae of *Bombyx mori L.*due to which the premature death of the larvae was observed*(*Tanaka and Yukuhiro, 1999). Thus, the seed extract of the *Achyranthes aspera*may have some toxic components which affect the physiology of the insect. In the present study the affected larvae shown slow growth, stunted body and the consumption of mulberry leaves was also reduced.

Figure: dead larvae by the different concentrations of seeds extract of Achyranthes aspera.

FIGURE 1: 75% CONC.   FIGURE 2: 50% CONC.   FIGURE 3: 25% CONC.

IV. CONCLUSION

Thus, it is concluded that the seed extract of *Achyranthes aspera* has the highly insect deterrent and have insecticidal activity. The seed extract of *Achyranthes aspera*can be used as a natural insecticide (larvicide) in 75% concentration with the detailed study on the particular larval pests occurring on different crops, and have the future scope to use at farmer level.

V. ACKNOWLEDGEMENT

VI. REFERENCES

[1]. Alagarmalai Jeyasankar1, Selvaraj Premalatha2, KuppusamyElumalai., Antifeedant and insecticidal activities of selected plant extracts against Epilachna beetle, Henosepilachnavigintioctopunctata (Coleoptera: Coccinellidae). Advances in Entomology. Vol.2, No.1, 14-19 (2014).

[2]. Dinesh Reddy Somagari, KarisettyBasappa, Srikanth Rolla, PothugantiJithender, Rajshekar B. Phytochemical investigation of seeds of Achyranthes aspera Linn., Journal of Pharmacognosy and Phytochemistry 2014; 3 (1): 190-193

[3]. Hiware C. J. (2001). Agro-Cottage Industry Sericulture. Daya Publishing House, Delhi, India 57-93.

[4]. Jadhav D. V., K. Sathyanarayana, Hugar I.I. and Singh K. K., (2016). Effect Of Medicinal Plant Extract Of Asparagus Racemosus And Asteracantha Longifolia Nees As Food Supplement Of Silkworm Bombyx Mori L For Improved Cocoon Traits, Journal of Global Biosciences, Vol. 5(4), 3986-3993.

[5]. Jasjinder, K., (2013).Development of Tobacco Caterpillar, Spodoptera Litura (Fabricius) (Lepidoptera: Noctuidae) On Different Cultivars of Cabbage. Thesis, Submitted to the Punjab Agricultural University, page no. 32

[6]. Pandey, P.and Upadhyay, V.B. (2013)Impact of Phytoecdysteroid treatment on the larval performance of multivoltine mulberry silkworm Bombyx mori Linn. Malays. Appl. Biol. (2013) 42(1P)H: Y51T–O6E

[7]. Prajapati H. Vishnubhai , 2011, Investigation on some medicinal and aromatic plants for their biological activities on Spodoptera litura Fabricius Under laboratory condition. Thesis, submitted to the Anand Agricultural University, page no. 1.

[8]. S. Girija and N. Valarmathy, (2008). Antifeedant effect of Achyranthes aspera Linn onCauliflower Borer (Hellulaundalis), Fruit and Leaf Borer of Cauliflower (Spodoptera litura) and Brinjal Fruit Borer(Leucinodesarbonalis), Biosciences, Biotechnology Research Asia, Vol. 5(2), 663-672.

[9]. Shital Chandrashekhar Lolge, Sunita PanditZanke, DiptiRamrao Patil and Sureshchandra Popat Zambare "In vitro Antimicrobial Activity and Phytochemical Screening of Local Plants" Journal of Pharmacy and Pharmacology 4 (2016) 151-154.

[10]. Stephen David.Pesticides, more than pests, a problem for Indian farmers , https://www.indiatoday.in/latest-headlines/story/pesticides-more-than-pests-a-problem-for-indian-farmers-31225-2008-10-08

[11]. Uma A. Bhosale, Radha Yegnanarayan, PrachiPophale, and Rahul Somani.Effect of aqueous extracts of Achyranthes aspera Linn. on experimental animal model for inflammation. AncSci Life. 2012 Apr-Jun; 31(4): 202–206.

[12]. Vijesh V. Krishna, N. G. Byju, S. Tamizheniyan (2000). Integrated Pest Management In Indian Agriculture: A Developing Economy Perspective, https://ipmworld.umn.edu/krishna-indian-ag,

[13]. Yoshiaki Tanaka and Fumiko Yukuhiro, (1999).Ecdysone Has an Effect on the Regeneration of MidgutEpithelial Cells That Is Distinct from20-Hydroxyecdysone in the Silkworm Bombyx moriGeneral and Comparative Endocrinology 116,382–395.

Investigation of Thermo-Acoustic Properties of Water-1-Propanolbinary Mixture at Different Temperatures

Wakulkar A. P.[1], Lanjewar M. R.[2], Shah S. A.[3]

[1]Asst. Professor, Dept. of Chemistry, A.N. College, Warora (M.S.) INDIA
[2]Professor, Dept. of Chemistry, RTM Nagpur University, Nagpur(M.S.) INDIA
[3]Asso. Professor, Dept. of Chemistry, A.N. College, Warora (M.S.) INDIA

ABSTRACT

Ultrasonic velocity, density and viscosity have been measured using Anton Paar DSA 5000 M in the binary mixtures of 1-Propanol with water at various mole fractions from 0.1 to 0.9 with temperature ranging from 288K to 318K. Various derived parameters like adiabatic compressibility, acoustic impedance, free length and relaxation time have been calculated using standard formulae. Non covalent interaction taking place in the liquid mixture has been discussed on the basis of the values obtained from experimental parameters and derived parameters.

Keywords : Binary Liquid Mixtures, Ultrasonic Velocity, Density, Viscosity, Adiabatic Compressibility, Acoustic Impedance, Relaxation Time, Free Length, Intermolecular Interactions.

I. INTRODUCTION

The knowledge of the structure and molecular interactions of liquid mixtures is very important from fundamental and engineering point of view. Fundamental thermodynamic and thermo-acoustic properties are essential sources of information necessary for a better understanding of the non-ideal behavior of complex systems because of physical and chemical effects, which are caused by molecular interactions, intermolecular forces, *etc.*, of unlike molecules. From a practical point of view, these properties are necessary for the development of thermodynamic models required in adequate and optimized processes of the chemical, petrochemical, pharmaceutical, food processing, drugs industries, paint industries, fluid mechanicsetc.[1,2]. In the recent years much important has been given to the behavior of mixed components rather than the single component because of their widespread range of applications. Thermodynamic properties derived from the measurement of ultrasonic velocities, densities and viscosities for binary mixtures are useful in understanding the nature and type of intermolecular interactions present between the constituent molecules. In chemical process industries, materials are normally handled in fluid form and as a consequence, the physical, chemical and transport properties of fluids, assume importance. Thus, data on some of the properties associated with the liquids and liquid mixtures like ultrasonic velocity, viscosity and density invention extensive application in solution theory models and molecular dynamics[3,4].

Properties of liquid–liquid mixtures are thermodynamically very important as part of studies

of the thermodynamic, acoustic and transport aspects. The compositional dependence of thermodynamic properties has proved to be very useful tool in understanding the nature and extent of pattern of molecular aggregation resulting from intermolecular interaction between components. Molecular interaction in liquid mixtures has been extensively studied using ultrasonic technique by many workers. The thermodynamic and acoustic properties are very essential for understanding the physicochemical behavior of the binary adult-component liquid mixtures[5].Ultrasonic velocity of sound waves in a medium is fundamentally related to the binding forces between the molecules. Ultrasonic velocities of the liquid mixtures consisting of polar and non-polar components are of considerable importance in understanding intermolecular interaction between components molecules and find application in several industrial and technological processes. Ultrasonic velocity measurements have been employed extensively to detect and assess weak and strong molecular interactions in binary mixtures[6,7]. Acoustical and thermo dynamical study of liquid mixtures provide enough knowledge about the association of molecular packing, molecular motion and strength of intermolecular interactions. Thermodynamic and acoustical properties such as adiabatic compressibility, intermolecular free length, internal pressure, acoustic impedance, relaxation time, molar volume, classical absorption and surface tension are calculated from measured ultrasonic velocity, density and viscosity for binary mixtures and they are very much helpful to interpret nature and type of intermolecular interactions between the component molecules[,8,9,10].

Using the measured values of sound velocity (u) and density (r), the thermodynamic parameters such as isentropic compressibility (KS) and intermolecular free length (Fl) can be computed. The intermolecular free length (Lf) is an important physical property of

liquid mixtures which mainly affects the sound velocity[11,12].

Binary liquid mixtures due to their unusual behavior have attracted considerable attention. In chemical process industries, the materials are normally handled in liquid form and as a consequence, the physical chemical, and transport properties of fluids assume importance. Thus, data on some of the properties associated with the liquids and liquid mixtures like density, viscosity and ultrasonic velocity, to find extensive application in solution theory and molecular dynamics. Such results are necessary for interpretation of data obtained from thermo chemical, electrochemical, biochemical and kinetic studies[13, 14,.]

II. METHODS AND MATERIAL

The chemical1-propanol used in present work was procured from LobaChemie Pvt. Ltd., Palghar (INDIA) with assay of 99.5% and distilled water used was three times distilled (tripple distilled). 1-propanol was of AR (HPLC) grade and used without further purification. The instrument used for measurements of density, viscosity and ultrasonic velocity was Anton Paar DSA 5000 M having range, up to 3g/cc with 0.000007 g/cc accuracy for density, 1000 to 2000 m/s with 0.01 m/s accuracy for ultrasonic velocity, 0.2 to 30,000 mm^2/s range for viscosity with 0.1% accuracy and temperature range from 0^{0}C to 100^{0}C with repeatability of 0.001^{0}C.

Literature survey showed that measurements have been previously reported for the 1-propanol-Water binary mixture at limited range of temperature. The objective of the present investigation was to find out the density (ρ), viscosity (η) and ultrasonic velocity (U) for the binary system constituted by these components at 288K, 293K, 298K, 303K, 308K, 313K and 318K over the concentration range of 0.1 to 0.9 mole fraction. The experimental values were used to calculate adiabatic compressibility (βa), acoustic impedance (Z), relaxation time (τ) and free length (Lf)

over the entire mole fraction range for the binary mixtures. The results are discussed in terms of the molecular interactions.

III. THEORY AND CALCULATIONS

The various acoustical parameters computed from experimental parameters using the following relations,

Adiabatic compressibility(βa)	$\beta a = 1/(U^2 \rho)$
Acoustic Impedance (Z)	$Z = \rho U$
Relaxation Time (Sec) (τ)	$\tau = (4/3)\eta \beta a$
Free Length (Lf)	$Lf = K^* \sqrt{\beta a}$,

Where K is the temperature independent Jacobson's constant

The evaluation of theoretical values of ultrasonic velocity, viscosity and density in binary mixture those obtained experimentally in the binary mixture is expected to interpret the nature of interaction between components of the mixture. Such theoretical study is useful in the wide-ranging theoretical modeling for the liquid mixtures[3].

IV. RESULTS AND DISCUSSION

1. Density is defined as mass per unit volume. In our present system, density decreases with increase in concentration of 1-propanol. It indicates water has greater density than 1-propanol. Initially water has higher concentration and having compact structure than 1-propanol due to strong hydrogen bonding compared to 1-propanol. At higher concentration of 1-propanol, concentration of water diminishes and 1-propanol shows the predominance in the solution. It has smaller dipole moment compared to water and also has long carbon chain. Hence density decreases with increase in composition of 1-propanol.

As the temperature increases the translational, rotational and vibrational energy of components in the given mixture increases. Due to increase in energy the compactness of the solution decreases and more volume occupied by same number of molecules in the given mixture. Hence, density of the system decreases with increase in temperature. Above system shows same variation with temperature[15,16].
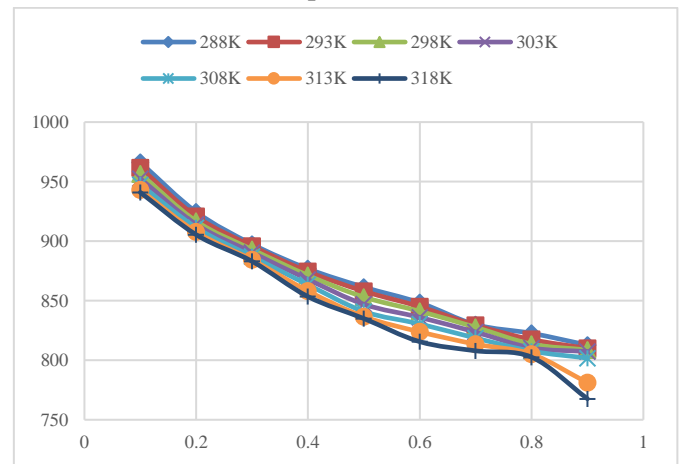
Fig. 1- Concentration Vs Density

2. Viscosity depends on compact structure of the medium. If there is a strong interaction of Van der Waal forcesand hydrogen bonding, system has greater viscosity and vice versa. In our present system, viscosity increases with increase in concentration of 1-propanol up to 0.4 mol fraction then viscosity slightly decreases up to end. Even though water forms strong hydrogen bonding but its viscosity is lesser than 1-propanol. It may be due to the size of 1-propanol. Greater the size of molecule, greater will be its polarizability. Higher the polarizability, higher will be the Van der Waal forces of attraction. It will contribute to increase in viscosity. 1-propanol also forms hydrogen bonding hence viscosity of 1-propanol is higher as compared to water. Higher viscosity up to concentration of 0.4 mol fraction may be due to hydrogen bond formation by 1-propanol with water is stronger than 1-propanol with itself.

As the temperature increases the translational, rotational and vibrational energy of components in the given mixture increases resulting in weakening of Van der Waal forces and hydrogen bonding. Hence, viscosity of the system decreases with increase in temperature. Above system shows same variation with temperature[17,18].
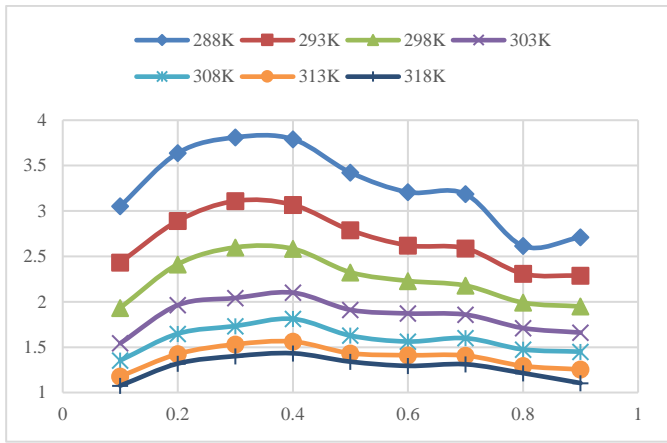
Fig. 2- Concentration Vs Viscosity

3. Ultrasonic velocity depends on stiffness of the medium. Stiffness of the medium not only depends on strong interaction of Van der Waal forces and hydrogen bonding but also on the compact structure of medium. As the stiffness of the system increases, ultrasonic velocity also increases. In our present system, ultrasonic velocity decreases with increase in concentration of 1-propanol.1-propanol has the capacity to form hydrogen bonding as well as Van der Waal forces but due to its bigger size, it will not form compact structure as like in water. Hence ultrasonic velocity decreases with increase in concentration of 1-propanol.
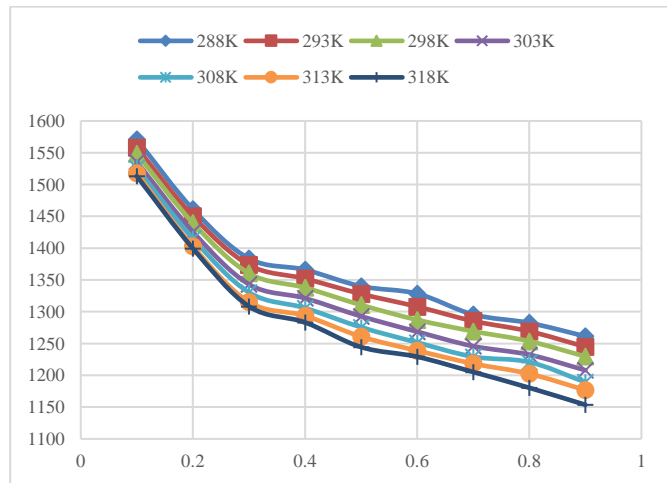
Fig. 3- Concentration Vs Ultrasonic Velocity

As the temperature increases the translational, rotational and vibrational energy of components in the given mixture increases resulting in weakening of Van der Waal forces and hydrogen bonding leading to reduce the stiffness of the medium. Hence, ultrasonic

velocity of the system decreases with increase in temperature[19-21].

4. Adiabatic compressibility of gases is higher than liquids and liquids has greater compressibility than solids. Compressibility is directly proportional to the compactness of the medium.

In our present system, adiabatic compressibility increases with increase in concentration of 1-propanol. 1-propanol has the capacity to form hydrogen bonding as well as Van der Waal forces but due to its bigger size, it will not form compact structure as like in water. Hence Adiabatic compressibility increases with increase in concentration of 1-propanol.
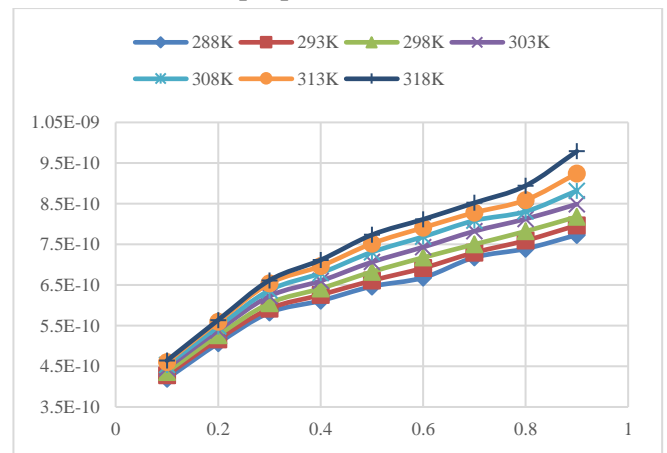
Fig. 4 - Concentration Vs Adiabatic Compressibility

As the temperature increases the kinetic energy of components in the given mixture increases which leads to weakening of Van der Waal forces and hydrogen bonding and reduces the compactness of the structure of the medium. Hence, adiabatic compressibility of the system increases with increase in temperature[22-24].

5. Acoustic impedance depends on density and ultrasonic velocity of the medium. Density depends on molecular arrangement per unit volume and sound velocity depends on stiffness of the medium. As the concentration of 1-propanol increases, acoustic impedance decreases indicating decrease in stiffness of the medium.

As the temperature increases the kinetic energy of components in the given mixture increases which

leads to decrease in Van der Waal forces and hydrogen bonding and reduces the compactness of the structure of the medium. Hence, acoustic impedance of the system decreases with increase in temperature[25,26].
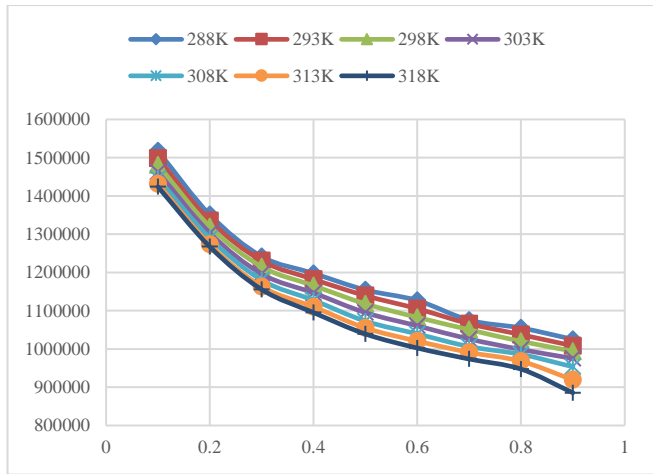
Fig. 5 - Concentration Vs Acoustic Impedance

6. Relaxation time depends mostly on viscosity of the medium. In our present system, viscosity increases with increase in concentration of 1-propanol. Hence relaxation time increases in accordance with concentration of 1-propanol.

The agitation in the system increases with increase in temperature resulting in the decrease in viscosity of the medium and hence the relaxation time[27,28].
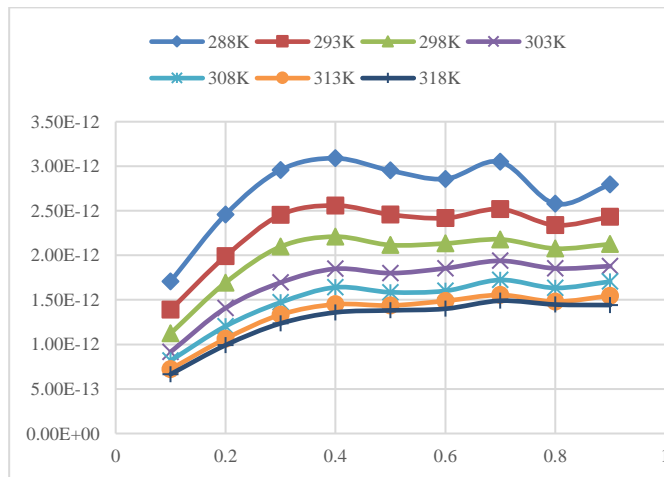
Fig. 6- Concentration Vs Relaxation Time

7. Free length depends on adiabatic compressibility and is directly proportional to its square root. So, in our present system free length is following the same

order with increase in temperature and concentration of 1-propanol as the adiabatic compressibility does, indicating lack of compact structure in the system at higher concentrations and at high temperatures[29].
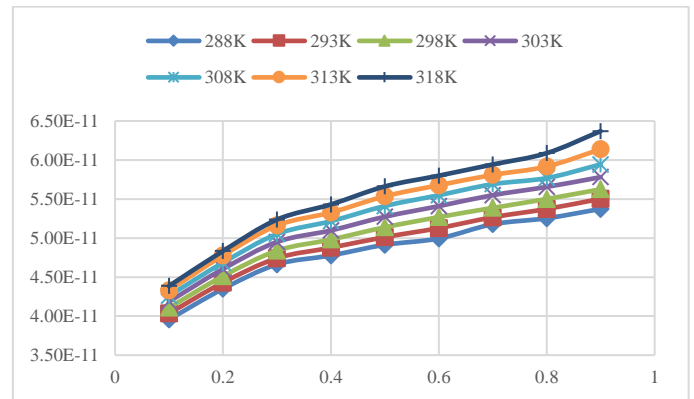
Fig. 7- Concentration Vs Free Length

V. CONCLUSION

It has been observed that the inter molecular interactions depends not only on Van-der-Waal forces and hydrogen bonding but also on the size of the molecules.

VI. REFERENCES

[1]. Bojan DDjordjević et al, JSerbChemSoc74 (5) 477–491 (2009)

[2]. SRDandwate and SBDeshmukh, IJUP, Vol4, Issue 4, 196-201

[3]. NSiddharthan and SJayakumar, IntJChemSci.: 14(4), 2016, 2981-2996

[4]. G.Siva Reddy et alInternational Journal of Chemical and Petroleum Sciences, 2014, 3(2), 32-44

[5]. Dheeraj Kumar et al, IJRPC 2014, 4(4), 825-828

[6]. J.Thennarasu and GMeenakshi, Rasayan JChem, Vol.4, No.4 (2011), 904-909

[7]. SBahadur Alisha et al, Indian Journal of Advances in Chemical Science 5(3) (2017) 142-147

[8]. SAnuradha et al, JPure ApplUltrason27 (2005) pp49-54

[9]. D.Ubagaramary, Dr.P.Neeraja, IRJES, Volume 1, Issue 4(December 2012), PP.54-77

[10]. KRathina et al, IJEAT, Volume-8 Issue-6S, August 2019, PP 151-159

[11]. RNatarajan and PRamesh, JPure Appl& IndPhysVol.1 (4), 252-258 (2011)

[12]. Apurba M Ghosh* and J N Ramteke, Der ChemicaSinica, 2017, 8(2):291-297

[13]. Vijaya Lakshmi et al, IJCR, Vol.6, issue 5, PP 6814-6820, May 2014

[14]. AMary Girija et al, IJSRST, - Volume 3, Issue 11, November-December-2017, PP 89-96

[15]. C.DGeorge, P.MThomas and C.DJoseph, Physical and Theoretical Chemistry, SChand and CompLtdNew Delhi, 1986.

[16]. SNithiyanantham and LPalaniappan, ArabJChem., 5(2012)25-30

[17]. C.N.R, Rao, University General Chemistryan Introduction to Chemical Science, , Macmillan pubIndia LtdChennai,1973.

[18]. DVJahagirdar, BRArbad, S.RMirgane, M.KLande and A.G.Shankarwar, JMolLiq., 75(1998)33-43.

[19]. N.PRao, Ronaldand EVerrall, CanJChem65(1987)810.

[20]. MSRaman and GAmirthaganesan, Indian JPhys78(2004) 1329

[21]. M..J Povey, Ultrasonic Techniques for Fluid Characterisation, London .Academic Press,1997

[22]. SRavichandran and KRamanathan, Polymer-Plastics Technology and Engineering, 47 (2008)169-173.

[23]. KGekko and H.Noguchi, JPhysChem., 83(1979)2706-27

[24]. MSRaman, MKesavan, KSenthilkumar and VPonnuswamy, JMolLiq., 202 (2015)115-124

[25]. NMehra, HSanjnami, Indian JPure ApplPhys., 38 (2000) 760.

[26]. RPalani and SBalkrishnan, ArchPhysRes., 1(2010)111-118.

[27]. MSRaman et al, JMolLiq.,151(2010) 97-106.

[28]. V.K.Syal., AChauhan and SChauhan, JPure ApplUltrandson., 27(2005)61-69.

[29]. BJacobson, ActaChemica Scandinavia, 6(1952)1485

Determination of Secondary Forces in Polar Organic Binary Mixture by Refractivity Method

Avinash M. Nannaware, Sandip M. Parkhi, Shaukat A. Shah

Department of Chemistry, Anand Niketan College Warora, Maharashtra, India

ABSTRACT

Densities and Refractive indices have been experimentally determined for the binary mixture of Methanol – Water at room temperature over the entire range of mole fraction. The experimental values of densities and refractive index are utilize to calculate excess refractive indices, molar refractions, excess molar refractions, excess molar volume and calculated molar refractions. Outcome obtained indicate that the refractive method is more useful as compare to the volumetric method. From the result it is found that strong association is observed in studied system.

Keywords: Mole Fraction, Density, Refractive Index, Excess Refractive Indices, Molar Refractions, Excess Molar Volume.

I. INTRODUCTION

Refractive index is also called as index of refraction, measure of bending of ray of light when passing from one medium to another transparent medium. Measurement of refractive index is a significant part of thermodynamics studies of liquid-liquid mixtures, used to explain intermolecular interactions present amongst the mixing components [1].It is also essential for the determination of composition of binary liquid mixture[2]. Complex formation in liquid mixtures has been widely studied using refractivity method .The behavior of solvent medium in presence of other species affect the structural properties of solution

In our present research work, we select polar molecule as methanol and water these molecule are very useful in a different field of a chemical science. In our present study densities and refractive index of binary liquid-liquid mixture of methanol-water

system at room temperature [at 293 K] over the entire range of mole fraction have been determined. Along with densities and refractive index, excess refractive indices [Δn_D], molar refraction, excess molar volume [V^E], calculated molar refraction and excess molar refraction [R_M^E] have been calculated. The behavior of this parameter is used to investigate intermolecular interaction present amongst the component of the mixture.

II. METHODS AND MATERIAL

Methanol used was of A.R.grade. The water used for the preparation of binary mixture was distilled. The binary methanol-water systems were prepared by mole fraction method. The weighing was done by using electronic balance with precision of ± 0.1 mg. Refractive indices were measured by using Abbes refractometer with constant temperature thermostat

with the precision of ±0.001. Densities were measured by using specific density bottles at constant temperature.

III. RESULTS AND DISCUSSION

The density [ρ] and refractive index [η] data of methanol-water system over the entire range of mole fractions measured at 293 K from these experimental data excess refractive indices [Δn_D], molar refraction, excess molar volume [V^E], calculated molar refraction and excess molar refraction [R_M^E] have been calculated.

The values of excess refractive indices [Δn_D], excess molar volume [V^E] and excess molar refraction [R^E_M] for binary mixture of methanol-water system were calculated from density and refractive index data and molar mass using following equation.

$$\Delta n = n_D - (x_1 n_{D1} + x_2 n_{D2}) \quad \ldots\ldots\ldots\ldots(1)$$

Where, x_1 and x_2 are the mole fractions.

n_D, n_{D1} and n_{D2} are the refractive index of mixture, methanol and water respectively.

Excess molar volume is the difference between value of molar volume of real mixture and the value of molar volume exist in an ideal solution under same condition.

$$V^E = \frac{x_1 M_1 + x_2 M_2}{\rho} - \frac{x_1 M_1}{\rho 1} - \frac{x_2 M_2}{\rho 2} \ldots\ldots\ldots\ldots\ldots (2)$$

Where, x_1 and x_2 are the mole fractions.

M_1 and M_2 are the molar masses.

ρ, ρ_1 and ρ_2 are the densities of mixture, methanol and water respectively.

$$R_M^E = R_M - [x_1 R_{M1} + x_2 R_{M2}] \ldots\ldots\ldots\ldots\ldots (3)$$

Where, R_M, R_{M1} and R_{M2} are the molar refraction of binary mixture, pure methanol and water respectively.

Table no.1 - For pure liquids.

Compounds	Molar mass	Density (ρ) [g/cm³]	Refractive index [n]	Molar refraction (R_M) [cm³/mol]	Calculated molar refraction [cm³/mol]
Methanol	32.04	0.7931	1.319	7.9908	8.36
Water	18.02	0.9982	1.324	3.6209	3.37

Table no.2 – For Methanol–Water system.

X_1 [Methanol]	X_2 [Water]	Density (ρ) [g/cm³]	Refractive index [n]	Excess Refractive index	Molar refraction (R_M) [cm³/mol]	Excess Molar volume (V^E) [cm³/mol]	R_M Calculated [cm³/mol]	Excess Molar refraction (R_M^E) [cm³/mol]
0.1	0.9	0.9808	1.327	0.0035	4.0060	-0.4844	4.193	-0.05189
0.2	0.8	0.9463	1.330	0.0070	4.4892	-0.5155	4.656	-0.00568
0.3	0.7	0.9239	1.332	0.0095	4.9364	-0.6992	5.119	0.00453
0.4	0.6	0.9016	1.333	0.0110	5.3907	-0.7839	5.582	0.02184
0.5	0.5	0.8853	1.332	0.0105	5.8016	-0.9523	6.045	-0.00425
0.6	0.4	0.8588	1.329	0.0080	6.2602	-0.6821	6.508	0.01736
0.7	0.3	0.8412	1.328	0.0075	6.5813	-0.6061	6.971	-0.09853
0.8	0.2	0.8236	1.326	0.0060	7.1635	-0.4313	7.434	0.04668
0.9	0.1	0.8099	1.322	0.0025	7.5470	-0.3344	7.897	-0.00681

From the above observation it is found that the value of excess molar volume are negative for given system which indicate that resultant volume of binary mixture decreases due to some secondary forces in polar organic binary mixture i.e. intermolecular forces of interaction. This is again confirmed from the fact that experimental values are smaller than ideal value of Methanol-Water system. This information suggest that molecules of given components are closely associated than pure liquid.

The value of excess refractive index for polar-polar [methanol-water] system over entire range of mole fraction is positive which indicate that molecular association is weak in given solution. The value of experimental molar refraction and calculated molar refraction suggested that molar refraction is an additive and constructive property. The value of excess molar volume and excess refractive index for binary mixture suggest that refractivity method is more useful over volumetric method.

IV. CONCLUSION

From above discussion, It is concluded that in methanol-water system [i.e polar-polar binary mixture] shows molecular association but intermolecular forces of interaction are weak.

V. REFERENCES

[1]. D.S.Wankhede, Acta Chim.Slov., 59, 258-263 (2012).

[2]. Rita Mehara, Proc. Indian Acad. Sci. (Chem.Sci.), vol. 115, No.2,pp 147-154 April (2003).

[3]. B.Gonzalez, A.Dominguez, Jose Tojo, R.Cores, J.Chem. Eng. Data 49, 1225 (2004).

[4]. U.B.Kadam, A.P.Hiray, A.B.Sawant, M.Hassan, J.Chem. Eng. Data 51, 60 (2006).

[5]. Piyush Thakur, Sandhya Patre and Rama pande. International journal of bioscience, biochemistry, and bioinformetics.Vol.1 No.4 November 2011.

[6]. P.W.Atkins, Physical Chemistry, Oxford University press, Oxford Mebourne Tokyo 6th edition 654 (1998).

Drug Design and Medicinal Chemistry of Thiourea Derivatives : A Review

Balasaheb Deshmukh

Arts, Commerce and Science College, Maregaon Dist. Yavatmal, Maharashtra, India

ABSTRACT

The literature concerning thiourea and its derivatives is voluminous. These compounds have found their way into almost every branch of chemistry. In the academic field thioureas are of great value in the characterization of organic compounds and great medicinal applications as well as non-medicinal activities in industry, analytical chemistry and metallurgy. This review is a sight of methods of synthesis and applications of thioureas in the field of medicine and agriculture. thioureas have a number of medicinal applications and a number of thioureas are in clinical use. Medicinal applications of thioureas are increasing with the passage of time. In the field of agriculture, Thiourea has been investigated for its multiple desirable properties as a fertilizer especially under the condition of environmental stress and are used as insect growth regulator, anti-fungal agents and herbicides.

I. INTRODUCTION

Thiourea, also called thiocarbamide, an organic compound that resembles urea (*q.v.*) but contains sulfur instead of oxygen; *i.e.,* the molecular formula is CS(NH2)2, while that of urea is CO(NH2)2. It plays an important role in the construction of heterocycles.These have structural resemblance to ureas, except that the oxygen atom of ureas is replaced by a sulfur atom; the chemical properties of urea and thiourea are quite different from each other.
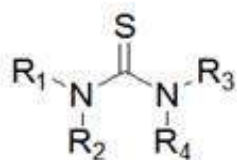
Thioureas

1
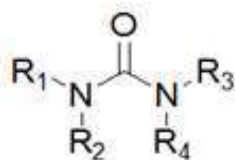
Ureas

2

The Thiourea system is numbered as shown below:
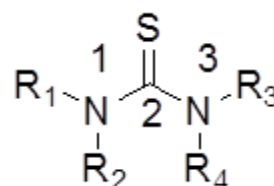
Compounds produced from urea, isourea, or their derivatives by substituting sulfur by oxygen are named by adding a prefix thio before urea. S-Substituted thioureas are referred to as pseudothioureas rather than isothioureas.

Thiourea subsidiaries have different natural properties, for example, antibacterial, anticancer, antimicrobial, antifungal, antimalarial and antituberculosis that make them broadly utilized in many field particularly pharmaceutical enterprises. This is on the grounds that oxygen, nitrogen and sulfur contributor iotas in thiourea subordinates give

different restricting conceivable outcomes. Other than that, the protonation of sulfur particle that can happen in acidic arrangement causes thiourea subsidiaries to be known as fascinating natural inhibitors with regards to consumption action. Some of the thioures are,

1-(3-cyanophenyl)thiourea	1-(2-bromophenyl)-3-o-tolylthiourea	2-benzylisothiourea
3	4	5
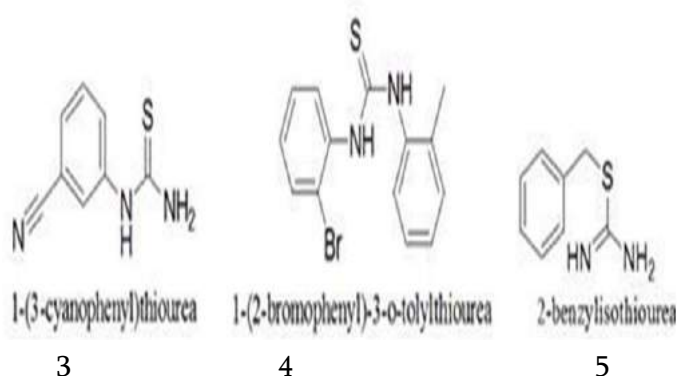
II. GENERAL METHODS OF SYNTHESIS

There are several common synthesis for derivatives of thiourea. Many variations have been applied to each of these when circumstances demanded it. As might be expected, certain advantages and disadvantages arise from the use of any one of these methods of Synthesis.

a)   Thioureas from Carbon disulphide
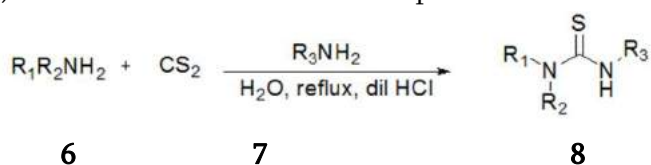
Where R1=R2= H, alkyl or aryl.

The reaction shown in the above equation is the common way of describing the overall reaction of primary amines **6** ($R_1 = R_2 = H$) with carbon disulfide **7** to give 1,3-disubstituted thioureas **8**. It does not, however, tell the whole story. Many theories concerning the mechanism of this reaction have been published and the conclusions are somewhat conflicting. Reaction intermediate in this case is amino dithiol derivative instead of isothiocyanate.

b)   Thioureas from Isothiocynates

Alkyl Isothiocynates**9** on reaction with primary and secondary amines**10** yield thiourea derivatives**11**.

9   **10**   **11**
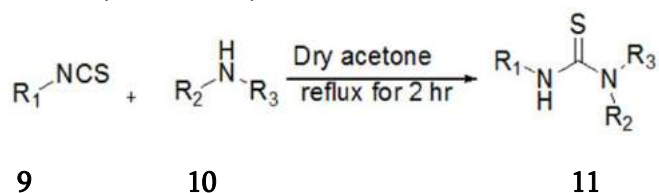
Where R1 = alkyl, aryl or benzoyl. R2 = alkyl or phenyl and R3 = alkyl, phenyl or H.

This is the most common method of preparing unsymmetrical thioureas. The addition of the amine to the isothiocyanate is usually carried out in the presence of a solvent such as alcohol. Frequently the reaction is exothermic, and cooling may be necessary to keep it from getting out of hand. In some cases it is necessary to heat, the mixture, and then a higher alcoholor preferably an inert solvent such as benzene or toluene may be used. Since similarly substituted thioureas melt at nearly the same temperature and isomorphism may make mixed melting points unreliable, elemental analysis or an infrared spectrum is often essential in the identification of the reaction product.

c)   Thioureas from Thiophosgene

Primary amines react with thiophosgene to give either an isothiocyanate **12** or a 1,3-disubstituted thiourea depending upon the ratio of the reactants. Secondary amines give only symmetrical thioureas

$CSCl_2 + RNH_2 \longrightarrow RNCS + 2HCl$

12
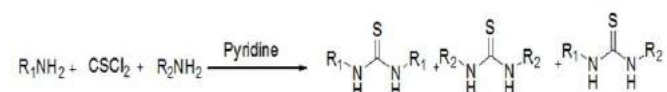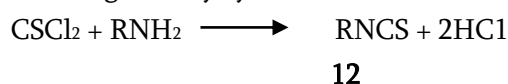
Preparation of thioureas by this method is best carried out by refluxing one mole of thiophosgene with two moles of the amine in an aqueous, chloroform-aqueous or acetone-aqueous medium. When thiophosgene no longer appears in the reflux condenser, a mole of potassium carbonate is added and the heating continued for several hours. The product

is then isolated and purified in a manner appropriate to the particular compound.

d)   From Thioureas

Symmetrical thioureas are precursor of unsymmetrical thioureas. This method is used to prepare disubstituted and trisubstituted thiourea derivatives. **13** (Symmetrical thioureas) on reaction with **14**(amine) yield **15**(Thiourea derivative).
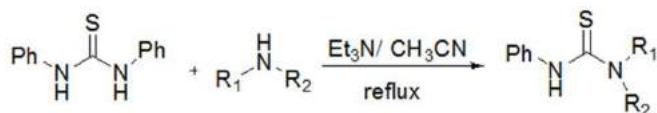
13   **14**   **15**
Where R1=R2 = alkyl, aryl or R2 = H

III. APPLICATION OF THIOUREA DERIVATIVES

Thioureas have a variety of applications in different fields of life. Some of these are discussed below.

3.1 Application in Agriculture

Thioureas have versatile application in field of agriculture. These are used as to control the growth of insects, effect plant growth and seed germination, as fungicide and herbicide.

a)   Insect Growth Regulator

IGRs are chemicals that are used to control the population of insects by inhibiting their life cycle. Hormonal IGRs and chitin synthesis inhibitors are types of IGRs. The brown planthooper Nilaparvata lugens stal is an insect of rice crop. This insect destroys the crop by sucking cell sap and transmitting viral diseases.

16
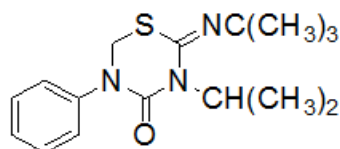
16 (thiourera derivative) control the growth of insects by destroying nymph at a conc. less than 1 ppm. This is environment friendly because don't destroy beneficial insects.

Thiocarbamido- DDT is more effective than DDT against bed bugs, although its action is of shorter duration

Simple compounds such as phenyl-, allyl-, and tolyl-thiourea are useful in destroying larvae and adults of various strains of Drosophila melanogaster. 1-Allyl-3-(4-chloro-2-methylphenyl) thiourea has been claimed to be effective in controlling the Japanese beetle or the mexican jumping bean beetle.

b)   Antifungal Activity

The chemicals or biological organisms that are used to kill fungus and fungal spores are called fungicide. Fungicides are very important in agriculture because fungus cause serious damage to crop. Thiourea derivatives **17**, **18** and **19** are active fungicides. **17** and its p-chloro and p- nitro derivatives are most active ones.
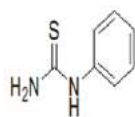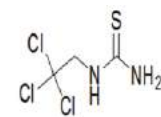
phenyl thiourea   trichloroethyl thiourea   pyridyl thiourea
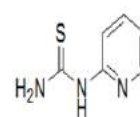
17   **18**   **19**

c)   Herbicidal Activity

20 and **21** show herbicidal activity against cucumber seedlings and former also showed activity against wheat seedlings. **22** is effective against root and stalk of Amaranthus retroflexus L.
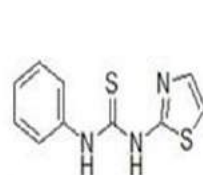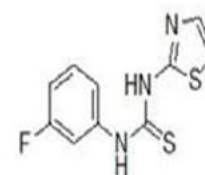
1-phenyl-3-(2-thiazolyl)thiourea   1-(3-fluorophenyl)-3-(2-thiazolyl)thiourea

20   **21**
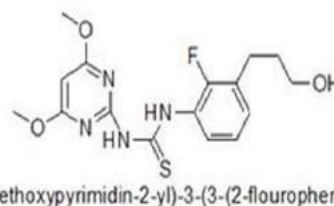
1-(4, 6-dimethoxypyrimidin-2-yl)-3-(3-(2-flourophenyl)propanol) thiourea

22

3.2 Medicinal Applications of Thiourea Derivatives

Applications of thiourea derivatives in field of medicine can't be neglected. These are being used in all aspects of medicine.

a)   Antibacterial activity of thiourea derivatives

Various types of thioureas have been reported to have antibacterial activity. An aromatic or heterocyclic amine with an alkyl side chain when incorporated into a thiourea shows specific action for the bacteria which cause abortion in cattle. Some 1-aroyl-3-aryl thioureas **23** have activity against Staphylococcus aureus, Bacillus subtilis and E-Coli.
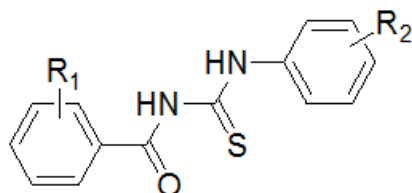
23

Thiocarbamido derivatives of diaryl sulfones and sulfides, both mono and bis, have shown marked antibacterial properties.

b)   For treatment of co-infections

Patients that are carrier of H. I. V have greater risk of T. B and other infections. So there was a need to develop a single class of drug that can be used for the treatment of both diseases simultaneously. In this regard thiourea derivatives act as a promising class. Due this development patient avoid from

pill burden as well overlapping toxicity developed by treatment of H. I. V and T. B.
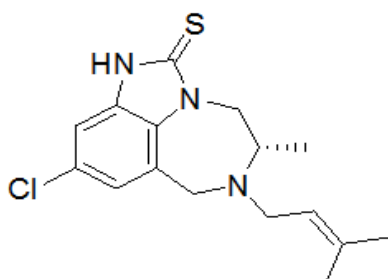
24
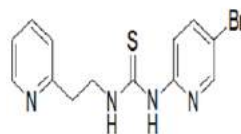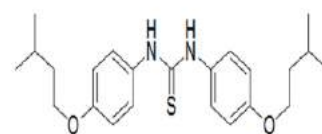
25   **26**

Tetrahydroimidazobenzodiazepinthiones (TIBO) derivative **24** (9-chloro TIBO), **25** (Trovirdine) and are used for H. I. V treatment. **26** (ISOXYL) is used for treatment of T. B.

c)   Thiourea derivatives as anti-inflammatory

Iminothiazolines on reaction with phenyl isothiocyanate yield thioureas 73 having anti-inflammatory activity.
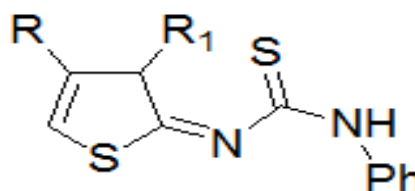
27

d)   Thiourea derivatives as anti-thyroid drugs

Goiter is caused by Hyperthyroidism is cured by anti-thyroid drugs. Following thiourea derivatives are used for treatment of hyperthyroidism. Thiourea has approximately one-tenth the activity of thiouracil. Replacement of one, two, or three of its hydrogen atoms by methyl groups has no appreciable effect on the activity.**28,29** and **30** are shows anti-thyroid activity.
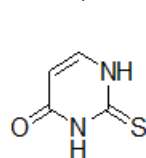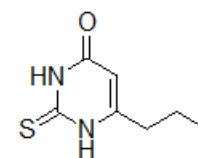
2-thiouracil   6-n-propylthiouracil   6-methylthiouracil
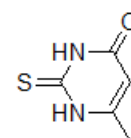
28   **29**   **30**

e)   Thiourea derivatives as anti-cancer drug

Cancer is an alarming ailment; different types of cancers can be treated effectively, if diagnosed at start. The following are the methods applied for the treatment of cancer; organ transplantation, surgery, palliative care, biotherapy, chemotherapy and

radiation therapy. But commonly used are chemotherapy and radiation therapy. Mostly these are used in combination. Nature of disease decides the type of treatment. Every treatment has its own risks and benefits. Generally, chemotherapy is the most common method. Many thioureas are being used as anti-cancer therapeutics and a lot of are in clinical trial. Because of genotoxicity and cytotoxicity to normal cells caused by anti-cancer drugs medical science is in search of novel and safer anti- cancer agents. These side effects limit both their use and efficiency. Thioureas, ureas and benzothiazoles are the most active anti-cancer drugs. Ureas and thioureas in combination with benzothiazoles produce DNA topoisomerase or HIV reverse transcriptase inhibitors.

31

32
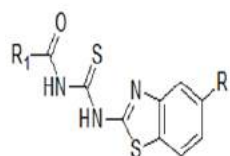
used for lung Cancer
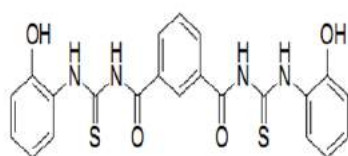
used for pancreatic and Brain tumor Cancer cells
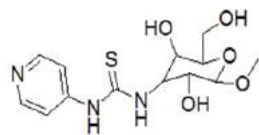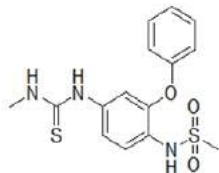
IV. CONCLUSION

Thioureas are versatile chemicals with outstanding biological applications. These are used in agriculture, analytical industry, metallurgy, industry and in the field of medicine. Most prominent biological applications of Thioureas is for treatment of co-infection, as antioxidant, as ant allergens, as anti bacterial agents, as anti-inflammatory, as anti-thyroid drugs, as anti-epileptic drugs, as anti-hypertensive, as rodenticide, as anti-cancer drug, as DNA binder and as Urease Inhibitors. Complexes of thioureas are used as precursors and antibacterial agents. Thioureas act as precursor of gaunidines and hetrocyclic ring systems.

V. REFERENCES

[1]. Abdullah, B. H.; Salh, Y. M.; Oriental Journal of Chemistry. 2010, 26, 763.

[2]. Ajibade, P. A.; Zulu, N. H.; International journal of molecular sciences. 2011, 12, 7186-98.

[3]. Arcangelo, V. P.; Peterson, A. M. Pharmacotherapeutics for advanced practice: a practical approach: Lippincott Williams & Wilkins; 2006.

[4]. Azeem, S.; Journal of Drug Design and Medicinal Chemistry. 2016, 2(1):10

[5]. Binzet, G.; Kavak, G.; Külcü, N.; Özbey, S.; Flörke, U.; Arslan, H.; Journal of Chemistry. 2013.

[6]. Brown, B.; Harris, R.; Pesticide Science. 1973, 4, 215-25.

[7]. Cragg, G. M.; Kingston, D. G. I.; Newman, D. J. Anticancer agents from natural products: CRC Press; 2011.

[8]. De Souza, M. V. N.; Bispo, M. d. L. F.; Gonçalves, R. S. B.; Kaiser, C. R.

[9]. Dorothy, C. S.; Thioureas: Chemical Reviews.1955, 55.1, 181-228.

[10]. Eastman, A.; Cancer cells (Cold Spring Harbor, NY: 1989). 1990, 2, 275.

[11]. Esteller, M.; Garcia-Foncillas, J.; Andion, E.; Goodman, S. N.; Hidalgo, O. F.; Vanaclocha, V.; Baylin, S. B.; Herman, J. G.; New England Journal of Medicine. 2000, 343, 1350-4.

[12]. Halim, N. I. M.; Kassim, K.; Fadzil, A. H.; Yamin, B. M.: IPCBEE; 2011.

[13]. Hargrave, K. D.; Hess, F. K.; Oliver, J. T.; Journal of medicinal chemistry. 1983, 26, 1158-63.

[14]. Heinelt, U.; Schultheis, D.; Jäger, S.; Lindenmaier, M.; Pollex, A.; Beckmann, H. S.; Tetrahedron. 2004, 60, 9883-8.

[15]. Huang, Y.-B.; Yi, W.-B.; Cai, C. Thiourea based fluorous organocatalyst. Fluorous Chemistry: Springer; 2012. p. 191-212.

[16]. Hussain, S.; Badshah, A.; Lal, B.; Hussain, R. A.; Ali, S.; Tahir, M. N.; Altaf, A. A.; Journal of Coordination Chemistry. 67, 2148-59.

[17]. Kim, K. S.; Qian, L.; Tetrahedron letters. 1993, 34, 7677-80.

[18]. Lowe, S. W.; Ruley, H. E.; Jacks, T.; Housman, D. E.; Cell. 1993, 74, 957.

[19]. Maddani, M. R.; Prabhu, K. R.; The Journal of Organic Chemistry. 2010, 75, 2327-32.

[20]. Sharma, S. V.; Haber, D. A.; Settleman, J.; Nature Reviews Cancer. 2010, 10, 241-53.

[21]. Sondhi, S.; Sharma, V. K.; Singhal, N.; Verma, R.; Shukla, R.; Raghubir, R.; Dubey, M.; Phosphorus, Sulfur, and Silicon and the Related Elements. 2000, 156, 21-33.

[22]. Trotti, A.; Colevas, A. D.; Setser, A.; Rusch, V.; Jaques, D.; Budach, V.; Langer, C.; Murphy, B.; Cumberlin, R.; Coleman, C. N., editors. Seminars in radiation oncology; 2003: Elsevier.

[23]. Tunaz, H.; Uygun, N.; Turkish Journal of Agriculture and Forestry. 2004, 28, 377-87.

[24]. Vanneman, M.; Dranoff, G.; Nature reviews cancer. 2012, 12, 237-51.

[25]. Venkatesh, P.; Pandeya, S.; International Journal of ChemTech Research. 2009, 1, 733-41.

[26]. Wu, J.; Shi, Q.; Chen, Z.; He, M.; Jin, L.; Hu, D.; Molecules. 2012, 17, 5139-50.

[27]. Yarbro, C. H.; Frogge, M. H.; Goodman, M. Cancer symptom management: Jones & Bartlett Learning; 2004.

[28]. Yonova, P.; Guleva, E.; Bulgarian Journal of Plant Physiology. 1997, 23, 72-9.

Acoustical Properties of Binary Mixture at 298k and at 2 MHz Frequency

G. R. Bedare, A. B. Dhote

N. S. Science and Arts College, Bhadrawati, Dist- Chandrapur, Maharashtra, India

ABSTRACT

Measurements of ultrasonic velocity, density and viscosity have been carried out in Acetonitrile in 1,4 Dioxane at different concentrations at 298 K temperature and 2 MHz frequency. Ultrasonic studies may throw more light on the molecular interaction to know the behavior of solute and solvent molecules in liquid mixtures and solutions. Acoustical parameters as adiabatic compressibility (β_a), intermolecular free length (L_f) and free length (τ)for Acetonitrile in 1,4 Dioxane were calculated from ultrasonic velocity and effect of concentration on molecular interaction was predicted.

Keywords: Acetonitrile, Concentration, 1,4 Dioxane, Molecular, Ultrasonic

I. INTRODUCTION

study of ultrasonic waves in pure liquids and liquid mixtures is useful to predict the nature of intermolecular interactions exist in these liquids and liquid mixtures. Liquid mixtures consisting of polar and non-polar components are of immense importance. When two or more liquids are mixed, there occur some changes in physical and thermodynamic properties because of free volume change, change in energy and change in molecular orientations. Thermodynamic and acoustical parameters like adiabatic compressibility (βa), intermolecular free length (L_f) and relaxation time (τ) are of considerable interest in understanding the inter-molecular interactions in binary liquid mixtures. Ultrasonic studies have been found to be useful in describing the theory of liquid state of matter. The density (ρ), ultrasonic velocity (U) and viscosity (η) can be used to study the physicochemical behavior and molecular interactions in pure liquids, liquid mixtures and solutions [1-6].

The various acoustic parameters such as ultrasonic velocity, density, viscosity, adiabatic compressibility, free length and free volume are useful in understanding molecular structure and molecular interactions in the medium. Thermodynamics studies of binary liquid mixtures have attracted much attention of scientists. These physico-chemical analyses are used to handle the mixtures of hydrocarbons, alcohols, aldehydes, ketones etc. The measurement of ultrasonic speed enables us to the accurate measurement of some useful acoustic and thermodynamic parameters and their excess values [7-9]. These excess values of ultrasonic velocity, adiabatic compressibility, molar volume and viscosity in binary liquid mixture are useful in predicting the solute-solvent interactions. The variation in ultrasonic velocity gives information about the bonding between

molecules and formation of complexes at various concentration and temperature through molecular interactions. Acetonitrile is used to make perfumes,pharmaceuticals, rubber products, pesticides, acrylic nail removers and batteries. It is also used to extract fatty acids from animal and vegetable oils. [10-11].

II. METHODS AND MATERIAL

The ultrasonic velocity (U) in liquid mixtures have been measured using an ultrasonic interferometer (Mittal type, Model F-81) working at 2 MHz frequency and at temperature 298K. The accuracy of sound velocity was ± 0.1 ms^{-1}. An electronically digital operated constant temperature water bath has been used to circulate water through the double walled measuring cell made up of steel containing the experimental solution at the desire temperature. The density of pure liquids and liquid mixtures was determined using pycknometer by relative measurement method with an accuracy of ± 0.1Kgm^{-3}. All the precautions were taken to minimize the possible experimental error.

Adiabatic compressibility (β_a), Intermolecular free length (L$_f$) and free length (τ)have been calculated from the measured data using the following standard expressions:

$$\beta_a = (U^2\rho)^{-1} \qquad \text{.... (1)}$$

$$L_f = K_T\beta a^{1/2} \qquad \text{.... (2)}$$

$$\tau = 4/3\ \eta\ \beta a \qquad \text{… (3)}$$

Where, K_T is the temperature dependent constant, η be the viscosity.

III. RESULTS AND DISCUSSION

Table-I shows that, Ultrasonic velocity and density decreases with concentration in Acetonitrileat temperature 298K. The viscosity decreases in the system, suggesting thereby less association between solute and solvent molecules. Decrease of velocity with increase in molefraction suggest weak solute solvent interaction existing in the solution.

From the Table-I, the adiabatic compressibility and free length increases with increase of mole fraction of the Acetonitrile. This may lead to the presence of weak molecular interaction between the molecules of the liquid mixture. The adiabatic compressibility and free length are the deciding factors of the ultrasonic velocity in liquid systems. Increase in intermolecular free length in the system leads to deviation in compressibility.

The free length increases with increasing mole fraction of the solute in this system. The increase in free length show that the strength of interaction decreases gradually with the increase in Acetonitrile concentration. It represents that there is weak molecular interaction between the Acetonitrile and 1,4 Dioxane. [12-14].
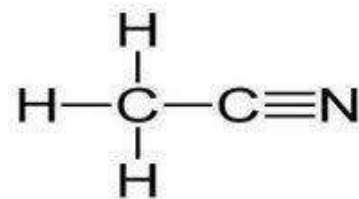
Table 1: Measured values of Ultrasonicvelocity (U), density (ρ) and viscosity (η) and calculated values of Adiabatic compressibility (β$_a$), free length (L$_f$) and free length (τ) of Acetonitrile + 1,4 Dioxaneat 298K and 2 MHz Frequency.

Mole fraction	U (m/s)	ρ (kg/m³)	$\eta * 10^{-3}$ (CP)	$\beta_a * 10^{-10}$ (Pa⁻¹)	$L_f * 10^{-10}$ (m)	$\tau * 10^{-12}$ (s)
0	1350.00	1030.00	0.5	5.33	0.475	0.3551
0.1	1338.10	1003.14	0.484	5.57	0.486	0.3592
0.2	1328.66	982.10	0.471	5.77	0.494	0.3622
0.3	1319.33	956.00	0.457	6.01	0.505	0.3661
0.4	1313.00	825.16	0.445	7.03	0.546	0.4170
0.5	1307.67	891.10	0.431	6.56	0.527	0.3771
0.6	1302.00	866.23	0.421	6.81	0.537	0.3822
0.7	1299.00	843.00	0.407	7.03	0.546	0.3814
0.8	1295.10	828.36	0.395	7.20	0.552	0.3855
0.9	1289.66	815.96	0.382	7.37	0.559	0.3895
1.0	1284.00	803.00	0.371	7.55	0.565	0.3947

IV. CONCLUSION

The ultrasonic velocity, density, viscosity and other related parameters were calculated. The existence of molecular interaction in solute-solvent is favored in the system, confirmed from the U, ρ, η, βa, L$_f$ and τ data. The variation in ultrasonic velocity (U), density (ρ) and viscosity (η) and other related thermodynamic parameters such as βa, L$_f$ and τ at various concentrations and at 298K temperature in the Acetonitrile in 1,4 Dioxaneshows the variation - linear. Weak intermolecular interactions are confirmed in the systems investigated.This provides useful information about solute solvent interactions in the mixture as existing in the liquid system.

V. REFERENCES

[1]. V Kannappam and Chidambara Vinayagam S, Indian J. Pure & Applied Physics, 44,2006, 670-676.

[2]. B Voleisiene and A.Voleisis, Ultragarsas (Ultrasound),63(4),2008, 7-9.

[3]. C. Senthamilselvi, S.Ravichandran, K. Rathin A and C.Thenmozhi, Proc Indian NatnSciAcad 79, 2013, 445-449

[4]. C. V. Suryanarayana, J AcoustSoc Ind.,13,1983, 11.

[5]. A.Fletcher, J Phys Chem., 73,1969, 2217.

[6]. M. E. Obbs and WW Bates, J Am Chem Soc., 74, 1952, 746.

[7]. W. Lin W and S. J.Tsay, J Phys Chem., 74, 1970,1037.

[8]. A. N. Kannappan, N,R. Kesavasamy and V.Ponnuswamy V, ARPN J. of Engineering and Applied Sciences,3, 2008,41.

[9]. S.Acharya, R.Palikray.,G. C.Mohanty, ,Ind. J. Pure and Appl. Phys., 41, 855 –857

[10]. G. R. Bedare, B. M. Suryavanshi and V. D. Bhandakkar,International Journal of Advanced Research in Physical Science (IJARPS) Vol. 1, Issue 5, September 2014, PP 1-5.

[11]. G. R. Bedare., V. D. Bhandakkar. B. M. Suryavanshi, I. J. of Res. in Pure and App. Physics, 3(3), 2013, 20-25.

[12]. G. R. Bedare ,V. D. Bhandakkar and B. M. Suryavanshi, International J. of Applied Physics and Mathematics, 2 (3) , 2012, 197-200.

[13]. G. R. Bedare, V. D. Bhandakkar and B. M. Suryavanshi, International Journal of Research in Pure and Applied Physics2013; 3(3): 20-22.

[14]. A. B. Dhote, G. R. Bedare, International Journal of Advance Research in Science and Engineering, 6(4), 2017, 548-550.

Synthesis and Characterization Zinc Oxide Thin Films Prepared by Chemical Bath Deposition

C. V. Chanmal*[1], S. S. Bandgar[1], C. D. Mungamode[2], S. G. Pawar[1], R. N. Mulik[1]

*[1]Department of Physics, D. B. F. Dayanand College of Arts & Science, Solapur, Maharashtra, India

[2]Department of Physics, Mahatma Gandhi College, Armori, Maharashtra, India

ABSTRACT

In the present work, zinc oxide thin films were prepared by simple chemical bath deposition (CBD) method. The deposition conditions such as pH and temperature were optimized to obtain well adherent uniform thin films. The prepared zinc oxide thin films were characterized for structural and morphological studies. The structural characterization was carried out by using X-ray diffraction (XRD) and Fourier transform Infra Red (FTIR) spectroscopy. The structural characterization indicates the uniform deposition of zinc oxide thin films onto glass substrate. The X-ray diffraction pattern of chemical bath deposited zinc oxide shows all the characteristic peaks related to wurtzite phase of zinc oxide. Further, structural characterization was carried out using FTIR spectroscopy which also confirms the deposition of zinc oxide thin films. The morphology study of zinc oxide thin film was carried out using scanning electron microscopy (SEM). The SEM micrograph show granular structural morphology of zinc oxide thin films. In conclusion, zinc oxide thin films were successfully prepared by chemical bath deposition technique and the films shows uniform well adherent morphology.

Keywords : Zinc Oxide, Thin Films, Chemical Bath Deposition, Structure, Morphology

I. INTRODUCTION

Semiconductor nanoparticles have attracted significant research interest in recent years due to its novel optical, electrical and mechanicals properties. [1-2] These interesting properties of nanoparticles results from quantum confinement effects due to nano dimensions as compared with their bulk counterparts. Among various semiconductor nanoparticles, nano sized zinc oxide (ZnO) particles is studied extensively as its structure and properties can be easily tailored by choosing various synthesis methods. [3-5] Zinc oxide is a semiconductor with a wide band gap of 3.37 eV and large exciton binding energy of 60 meV. Till date,

numerous application of ZnO nanoparticles have been explored in number of different fields such as in dye sensitized solar cell, gas sensors and light emitting diodes. [6-8] Zinc oxide is one of the most important nanomaterials for integration in microsystems and biotechnology. Furthermore, the optical properties of zinc oxide make it useful in the application of transparent conducting anode in photovoltaic cells.[9] Additionally, the structure of zinc oxide has non-centrosymmetric characteristics which exhibit piezoelectric properties useful in electromechanical coupled sensors and transducers property.[10]

To explore the full potential of nanomaterials for various applications, it is highly desirable to prepare the semiconductor in the form of thin films by using simple fabrication method. Ultimately, the properties of semiconductor thin film depend upon the method of preparation. To date, various techniques have been used for the deposition of ZnO thin films namely pulsed laser deposition, magnetron sputtering, spray pyrolysis, molecular beam epitaxy. [11-17] However, the above mentioned techniques require precise control over process parameter to obtain thin films with desired properties. The ZnO thin films deposited from the above techniques were also found to have low resistivity and high transparency in the visible region which becomes hindrance to the solar cell applications. The complexity of processing method also brings the lot of variation in the obtained results. Therefore, there is a need to understand the structure property relation and develop simple fabrication method for thin films which can be used in various nanotechnology applications such as sensors and molecular electronics for next generation's high performance nano-devices. In the present work, we adopt a simple chemical bath deposition technique to deposit thin films of Zinc oxide. The chemical bath deposition is a simple, cost effective technique to fabricate the thin films of ZnO. The structure and morphology study of prepared thin films of zinc oxide were reported.

II. METHODS AND MATERIAL

Materials and synthesis method

AR grade Zinc acetate ($Zn(CH_3COO)_2.2H_2O$), Sodium Hydroxide (NaOH) and Triethylamine were used as precursor materials. The ZnO thin films were grown onto glass substrate from solutions containing zinc acetate $Zn(CH_3COO)_2.2H_2O$ (0.5 M) and one drop triethylamine of analytical reagent grade. A hot plate with a magnetic stirrer was used to heat and stir the bath solution. The pH of the final bath was raised by the addition of a small quantity of base (0.5 M NaOH) to maintain pH in the range of 10-11. The reaction mixture was maintained at a temperature of 80 °C along with continuous stirring. The glass substrates were cleaned with acetone before immersing into the reaction bath. Substrates were taken out of reaction bath after 90 minutes of reaction time and then washed with distilled water. Finally, the substrate with deposition were dried at temperature of 100 °C and annealed at 290 °C for 30 minutes in a muffle furnace to get ZnO thin film.

Characterization details

Thin films were characterized by X-ray diffraction technique (XRD) for its structural analysis. A X-ray diffractometer with Cu Kα radiation (λ = 1.54 A°) Philips PW-3710 was used for this purpose. The diffraction pattern is recorded with 2θ angle ranging from 20° to 80°. Nicolet iN5 FTIR microscope in the range of 500 cm^{-1} to 5000 cm^{-1} was recorded for IR spectrum of prepared sample. The SEM (JEOL JSM 6360) operating at 20 kV is used for surface morphology studies of the thin films.

Reaction mechanism

Zinc acetate provides Zn^{2+} ions required for formation of ZnO films and the water molecules in the double distilled water provide O^{2-} ions. The reaction mechanism during this procedure is shown in the following equation. The deposition process mainly consists of the formation of ionic species and transport of these species through the medium and condensation of these species on the substrate. The main principle of chemical bath deposition technique is controlled precipitation of compounds in the solution of its constituent.

The reaction mechanism for the deposition of ZnO by chemical bath deposition method is illustrated below,

$Zn(CH_3COO)_2 \cdot 2H_2O$ + TEA → $[Zn(TEA)]^{2+}$ + $2CH_3COO^-$

$[Zn(TEA)]^{2+}$ → Zn^{2+} + TEA

$2NaOH → 2Na^+ + 2OH^-$

$Zn^{2+} + 2OH^- → Zn(OH)_2↓$

$Zn(OH)_2 → ZnO + H_2O↑$
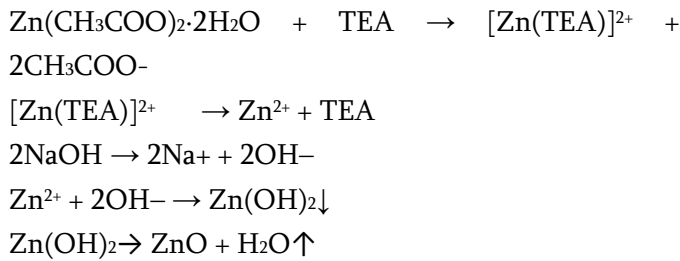
III. RESULTS AND DISCUSSION

A. XRD results

The XRD pattern of prepared ZnO thin film was studied for its structural properties. The XRD pattern shown in (Figure 1) clearly indicates the formation of hexagonal wurtzite phase of ZnO which is in good agreement with the standard JCPDS Card No. 036-1451. The peak broadening and sharp diffraction peaks in the XRD pattern indicate the presence of small nanocrystals and good crystallinity of the prepared film.
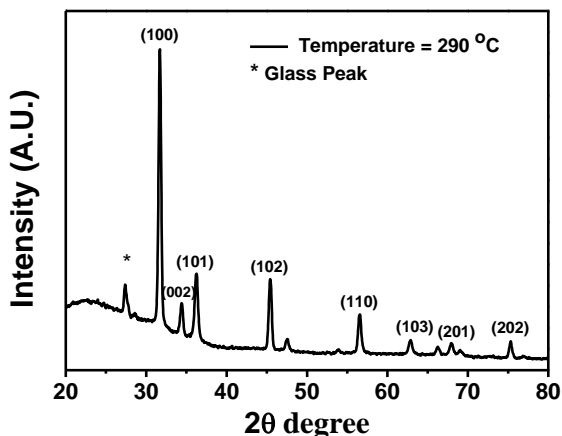
Figure 1. XRD Pattern of ZnO thin film deposited by chemical bath deposition.

The wurtzite phase crystallization of ZnO occurs when the oxygen atoms are arranged in a hexagonal close packed (HCP) type with zinc atoms occupying half the tetrahedral sites. The Zn and O atoms are tetrahedrally coordinated to each other and have its equivalent position. The zinc structure is open with all the octahedral and half the tetrahedral sites empty. [18] According to Bragg's law,

$$2d \, Sin \, θ = nλ \qquad (1)$$

Where, n is order of diffraction (usually n = 1), λ is X-ray wavelength and d is the interplanar spacing between planes of given Miller indices h, k and l. In ZnO hexagonal structure, the spacing in d is related to the lattice constants a, c and the Miller indices by the following relation[1].

$$\frac{1}{d_{hkl}^2} = \left[\frac{4}{3}\frac{h^2+hk+k^2}{a^2}\right] + \frac{l^2}{c^2} \qquad (2)$$

The lattice constant a and c are calculated for (100) and (002) plane respectively by following relation[19],

$$a = \frac{λ}{\sqrt{3} \, sinθ} \qquad (3)$$

$$c = \frac{λ}{sinθ} \qquad (4)$$

The lattice constants (a = b = 3.2256 A° and c = 5.1932 A°, c/a = 1.6099) and diffraction peaks corresponding to the planes (100), (002), (101), (102), (110), (103) are obtained from X-ray diffraction data consistent with the JCPDS data of ZnO. The interplanar spacing (d h k l) calculated from XRD is compared with JCPDS data card and corresponding (h k l) planes are summarized in Table 1. The XRD peak profile analysis is a simple and powerful method to evaluate the peak broadening with crystallite size and lattice strain due to dislocation.

In ZnO thin films, the (101) diffraction peak is much stronger than the (002) peak. This indicates that the ZnO nanocrystals have a preferential crystallographic (101) orientation. The average crystallite size was calculated from strongest XRD peak of (101) based on the Debye–Scherrer equation. [20,21]

$$D = \frac{0.89 \, λ}{β Cosθ} \qquad (5)$$

Where, β is the full width at half maximum (FWHM), λ is the wavelength of the incident X-ray (λ = 0.1540 nm), D is the grain size, and θ is the Bragg angle. The average crystallite size calculated for synthesized ZnO nanoparticles was 17.07 nm. The size of crystallite is assumed to be the size of a coherently diffracting

domain and it is not necessarily the same as particle size.

The dislocation density (delta), which represents the amount of defects in the sample is defined as the length of dislocation lines per unit volume of the crystal and is calculated using the following equation. [22]

$$\delta = \frac{1}{D^2} \qquad (6)$$

Where, D is the crystallite size. The dislocation density (d) is 3.4318×10^{-3} $(nm)^{-2}$.

Table 1. Interplanar Spacing (Dhkl) from XRD and JCPDS Data Card for corresponding (hkl) planes.

Plane (hkl)	d JCPDS(A°)	d XRD(A°)
100	2.8143	2.8193
002	2.6033	2.6039
101	2.4759	2.4745
102	1.9111	1.9944
110	1.6247	1.6200
103	1.4771	1.4753
200	1.4072	1.4021
201	1.3583	1.3794
202	1.2380	1.2591

B. FTIR results

FTIR technique is a powerful tool to understand and analyze the structure of thin films of ZnO prepared by chemical bath deposition method. The frequencies at which absorption occurs may indicate the type of functional groups present in the substance. The FTIR spectrum illustrates a series of absorption bands in the range of 500-4000 cm^{-1}. Figure 2 shows the FTIR absorbance spectra of ZnO thin films samples prepared by chemical bath deposition. The small peaks at 917 cm^{-1}, 683 cm^{-1} and 487 cm^{-1} which are attributed to the stretching mode of a ZnO bond.[23-24] The characteristic peaks at 1550 cm^{-1} and 1450 cm^{-1} are attributed to symmetric and asymmetric C=O bonds vibrations respectively.[25] The X-ray diffraction

study also indicated successful deposition of ZnO thin films on glass substrate. Thus, the structural characterization done using XRD and FTIR studies indicates stoichiometric deposition of ZnO along with formation of nanocrystallites onto glass substrate. [26]
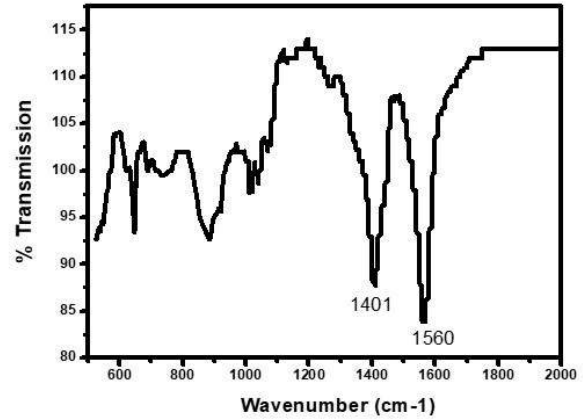
Figure 2. FTIR spectra of zinc oxide (ZnO) thin films.

C. SEM results

The scanning electron micrograph image of zinc oxide (ZnO) thin films deposited by chemical bath deposition is shown in Figure 3. The SEM image shows that zinc oxide has spherical morphology. The film consists of nanocrystalline grains with uniform distribution on the entire substrate surface with randomly oriented morphology. The zinc oxide thin film morphology shows uniform dispersion of nanoparticles with slight agglomeration. The crystallite size of ZnO nanoparticles is in the range of 20 nm. Thus, the SEM analysis of crystallite size shows a good agreement with that results obtained from XRD analysis. [27]
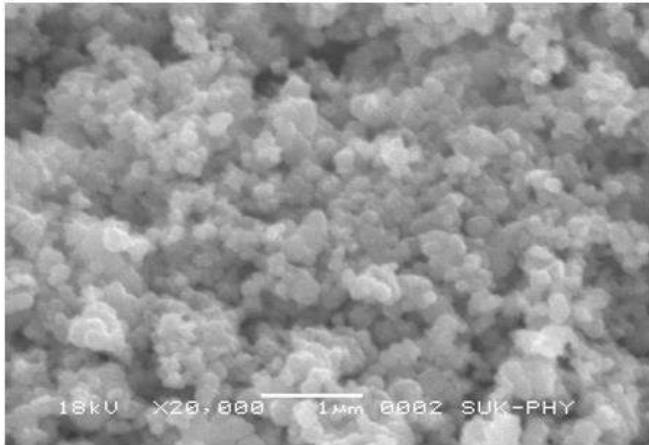
Figure 3. Scanning electron micrograph of zinc oxide (ZnO) thin films.

IV. CONCLUSION

The zinc oxide thin films were successfully prepared by simple chemical bath deposition (CBD) technique. The thin films having uniform morphology were deposited onto glass substrate. The ZnO thin films characterized by structural and morphological study shows the uniform deposition of ZnO thin films onto glass substrate. The X-ray diffraction spectra show all the characteristics peaks of zinc oxide indicating stoichiometric transformation of zinc oxide into thin film. The FTIR results also corroborate the formation of ZnO nanocrystallites onto glass substrate. The SEM image shows that spherical morphology of zinc oxide thin films with uniform dispersion. In conclusion, the zinc oxide thin films deposited by chemical bath deposition method shows excellent structural and morphological properties which can be potentially useful for applications in solar cell.

V. ACKNOWLEDGMENTS

VI. REFERENCES

[1]. J. Li, J. Z. Zhang, Coordination Chemistry Reviews 2009, 253, 3015.

[2]. Z. Cheng, N. Javed, D. M. O'Carroll, ACS Appl. Mater. Interfaces 2020, 31, 35579.

[3]. G. Gao, W. Shi, L. Xiang, J. Electrochem. Soc. 2009, 156, K155.

[4]. Ü. Özgür, Y. I. Alivov, C. Liu, A. Teke, M. A. Reshchikov, S. Doğan, V. Avrutin, S. J.Cho, H. Morko, Journal of Applied Physics 2005, 98, 041301.

[5]. M. Kahouli, A. Barhoumi, A. Bouzid, A. Al-Hajry, S. Guermazi, Superlattices and Microstructures 2015, 85, 7.

[6]. S. J. Pearton, D. P. Norton, K. Ip, Y.W. Heo, T. Steiner, Progr. Mater. Sci. 2005, 50, 293–340.

[7]. C. Klingshirn, Phys. Status Solidi b 2007, 244, 3027.

[8]. V. S. Bhati, M. H., M. Kumar, Energy Reports 2020, 6, 46.

[9]. W.N. Shafarman, L. Stolt, Handbook of Photovoltaic Science and Engineering, Wiley, Chichester 2003, 567.

[10]. J. L. Deschanvres, P. Rey, G. Delabouglise, M. Labeau, J. C. Joubert, Sensors and Actuators A 1992, 33, 43.

[11]. S. V. Prasad, S. D. Walck, J. S. Zabinski, Thin Solid Films 2000, 360, 107.

[12]. N. Noghavi, A. Rougier, C. Marcel, C. Guéry, J. B. Leriche, J. M. Tarascon, Thin Solid Films 2000, 360, 233.

[13]. T. Minami, T. Yamamoto, T. Miyata, Thin Solid Films 2000, 366, 63.

[14]. T. K. Subramanyam, B. S. Naidu, S. Uthanna, Phys. Stat. Sol.a 1999, 173, 425.

[15]. L. J. Meng, M. P. Dos Santos, Thin Solid Films 1994, 250, 26.

[16]. F. D. Paraguay, W. L. Estrada, D. R. N. Acasta, A. Andrade, M. Miki-Yoshida, Thin Solid Films 1999, 350, 192.

[17]. Y. F. Chen, D. M. Bagnall, H. J. Koh, K. T. Park, K. Hiraga, Z. Q. Zhu, T. J. Yao, J. Appl. Phys. 1998, 84, 3912.

[18]. B. D. Cullity, S. R. Stock, "Elements of X-ray diffraction", 3rd ed., Prentice Hall, New Jersey 2001.

[19]. C. Suryanarayana, M. G. Norton, "X-ray diffraction: a practical approach", Plenum Press Publishing, New York 1998.

[20]. M. Saleem, L. Fang, H. B. Ruan, F. Wu, Q. L. Huang, C. L. Xu, C. Y. Kong, Intl. J. Phy. Sci. 2012, 7, 2971.

[21]. A. Kathalingam, N. Ambika, M. R. Kim, J. Elanchezhiyan, Y. S. Chae, J. K. Rhee, Materials Science-Poland 2010, 28, 513.

[22]. K. Raja, P.S. Ramesh, D. Geetha, Spectrochimica Acta Part A: Molecular and Biomolecular Spectroscopy 2014, 120, 19.

[23]. A. Djelloul, M. S. Aida, J. Bougdira, Journal of Luminescence 2010,130, 2117.

[24]. T. Ivanova, A. Harizanova, T. Koutzarova, B. Vertruyen, Materials Letters 2010, 64, 1147.

[25]. Z. R. Khan, M. S. Khan, M. Zulfequar, M. S. Khan, Materials Sciences and Applications 2011, 2, 340.

[26]. R. Sharma, F. Alam, A. K. Sharma, V. Dutta, S. K. Dhawan, J. Mater. Chem. C 2014, 5, 8142.

[27]. M. A. Chougule, S. Sen, V. B. Patil, Ceramics International 2012, 38, 2685.

Study of Morphological and Dielectrical Properties of Zr-Co Doped Barium Hexaferrite

D.J.Roy[1*], A.R.Bansod[2], K.G.Rewatkar[2], N.S.Kokode[3]

[1]AbhaGaikwad- Patil College of Engg., Nagpur, Maharashtra, India

[2]Dr. Ambedkar College Dikshabhoomi, Nagpur, Maharashtra, India

[3]N.H.College, Bramhapuri, Chandrapur, Maharashtra, India

ABSTRACT

A sequence of hexaferrite specimen with a molecular formula $BaFe_{12-2x}Co_xZr_xO_{19}$ were synthesised using a traditional Microwave assisted Sol-gel auto-combustion process, where ferrites powder were processed by continual heat in the form of radiation through microwave. All the required nitrates were taken in stoichemetric proportion along with Urea, which provide requisite energy during the exothermic reaction in order to form ferrites materials powder. Microwave used in these method provide uniform heating leads to the ultrafast morphological transformation which results into nano-sized ferrites powder obtained. The structural and morphological properties studied by using X-ray diffractometer and Scanning Electron Microscope which reveals the prevalent hexagonal structure of space group symmetry $P6_3/mmc$. The dielectric features of the ferrites powder were studied at a frequency ranging from 100 Hz to 1 MHz at room temperature. The dielectric observation of synthesized hexaferrites reveals a drop in dielectric constants and a rise in dielectric loss with an increase in Co-Zr substitutions.

Keywords : XRD; SEM, Dielectric Properties, Ba- hexaferrites

I. INTRODUCTION

Substances possessing substantial dielectric and magnetic assets at the same time seem to be of considerable interest to contemporary science from the point of view with their ability for technical implementations to electrical equipment and structures. The sudden growth of elevated speed wireless communications involves the advancement of efficient, portable,and affordable technologies which could be utilized across a large frequency band [1-4]. Dielectric materials carry a vital character in international community of an extensive variety of implementations ranging through conventional to satellite telecommunications, which include radio, GPS and DBS Television. Microwave devices relying upon substances containing enhanced dielectric features are needed to meet the needs of existing as well as futuristic technologies. Hexaferrites are a large class one of ferrite materials attributable towards various uses throughout audio media, filters, oscilloscopes and antennas within that telecommunication sector[5, 6].A further benefit being there chemical consistency enables themselves

as environment-friendly and effective. The electrical and magnetic characteristics of barium hexaferrites ($BaFe_{12}O_{19}$) has been modified by composition variation, that results into morphological alteration of barium hexaferrites by orientation and positioning of the inclusion ions. Hexa-ferrites show the phenomena of universal ferromagnetic resonance which may be used successfully even an absence of applied magnetic field and often used in communications and military purposes [5, 7, 8]. A substantial amount of research being executed in the domain of hexaferrites within a past decade, wherein coupled replacements has been made in spite of Fe ions [9,10] or altered the methodology of formulation[11,12]. In this research module, trivalent Fe ions in barium hexaferrites are replaced by a group of divalent Cobalt (Co^{2+}) and tetravalent Zirconium (Zr^{4+}) ions in various concentrations. In addition, hexaferrites have been of concern for not only their magnetic behaviour, but also because of their dielectric polarisation found in their composition [14].

II. EXPERIMENTAL

Numbers of technique is available to synthesize ferrites materials such as co-precipitation method, glass crystallization, hydrothermal method of synthesis, solid state reaction, [6]etc. Out of which we use simple and efficient Sol-gel Induced auto-combustion method for synthesis of required hexaferrites due to its simplicity in processing, low annealing temperature, and very short reaction time. In addition the Sol-gel auto-combustion method produces ultra-fine nano materials with a substantial circulation of particle sizes, outstanding chemical uniformity and the probability of creating a unified single domain structure.

Hexaferrite powders with compounds with chemical formula $BaFe_{12-2x}(CoZr)_xO_{19}$ (with x = 0.0, 0.2, 0.4, 0.6, 1.0) were synthesized by Microwave Induce

sol-gel auto combustion technique in which microwave provides an uniform radiation in the form of heat to the specimen within the process of combustions. AR grade Nitrates such as $Ba(NO_3)_2$, $Co(NO_3)_2$, $ZrO(NO_3)_2$ and $Fe(NO_3)_3$ with urea are taken in stoichiometric proportion then dissolve into unionized double filtered distilled water at temperature of about 70^0C for 20-25 minutes. Urea supply sufficient amount of energy to start an exothermic reaction. Converted gel placed a side for an hour at room temperature. And then gel is placed within digitally controlled microwave of 2.5 GHz for 15 minutes, The gel get burnt and finally converted into ferrites powders. As obtained ferrites powder are grinded for 4 hour then housed in a muffle furnace for sintering at about 800^0C for 4 hours with gradually slow cooling at rate of 50^0C/minute along with further grinding of few hours.

XRD and SEM were utilized to analyzed the Structural and morphological properties of fabricated ferrites materials. A comprehensive study on the dielectric nature and electricalconductivity of $BaFe_{12-2x}(CoZr)_xO_{19}$has been undertaken within the frequency band from 10 kHz to 1MHz employing Wayne Kerr-WK6500B Impedance Analyzer.

III. RESULTS AND DISCUSSION

X-ray Diffraction (XRD) Analysis:

The X-ray diffractograph of BaFe(12-2x)(CoZr) xO19hexaferrites (x=0.0,0.2,0.4,0.6,and 1.0) specimens within analysis have been collected by using Philips X'pertDiffractometerutilising Cu-Kα radiation of wavelength $\lambda = 1.542$ **Å** which are shown in Fig.1, consisting reference peaks of M-type Barium nanoferrites relating to space group symmetry P63/mmc alluded fromthe standard JCPDS index. From the most intense peaks, the values of Miller indices (h k l) correlating to the inter-planer

distance d(hkl)are employing to determine the values of lattice constants 'a' and'c' according to the equation

$$\frac{1}{d_{hkl}^2} = \frac{4}{3}\left[\frac{h^2+hk+k^2}{a^2}\right] + \frac{l^2}{c^2}$$

The unit cell volume can beobtained by using formula

$$V = 0.866a^2c$$

The X- ray density Dxoftendeterminedusing the equation

$$Dx = \frac{zM}{VN_A}$$

In which z represent the number of molecules in a unit cell and equal to 2 for hexaferrites, M is themolecular weight of sample, N_A is Avogadro's number.From the **Table 1**, the values of c/a are below the value 3.98 for all synthesized materials give the confirmation of formation of BaMhexaferrites. The unit cell volume (V) continues to increase as replacement level grows, owing to the greater radii of the replaced $Zr^{4+}(0.72A°)$ and $Co^{2+}(0.70A°)$ ions than the $Fe^{3+}(0.64A°)$ showed in **Figure 2**.The value of lattice parameter 'c' rises from 23.1619 to 23.1972 A° for doping concentration x = 0.0 to x = 1.0, that suggests unit cell enhancement throughthe c-axis that is attributed to the increased gapwithin the Fe^{3+}- O^{2-} ions as well as the decreased super-exchange interactions of $Fe^{3+}\leftrightarrow Fe^{2+}$.

Table 1: Structural parameters such as lattice parameters (a, c,), c/a ratio, Unit cell volume (V), densities ($\rho_{x\text{-ray}}$, ρ_m), and porosity (P).

Conc. (x)	Lattice parameters (Å)		$\frac{c}{a}$	Volume (Å³)	Density x-ray ($\rho_{x\text{-ray}}$) (gm/cm³)	Density Mass (ρ_m) (gm/cm³)	Porosity (%)
	a	c					
0.0	5.8835	23.1619	3.93	694.32	5.32	2.607	50.99
0.2	5.8846	23.1940	3.93	694.64	5.35	2.655	50.37
0.4	5.8920	23.1943	3.93	697.30	5.36	2.701	49.60
0.6	5.8835	23.1942	3.94	695.29	5.42	2.741	49.42
1.0	5.8801	23.1972	3.94	695.30	5.49	2.826	48.52
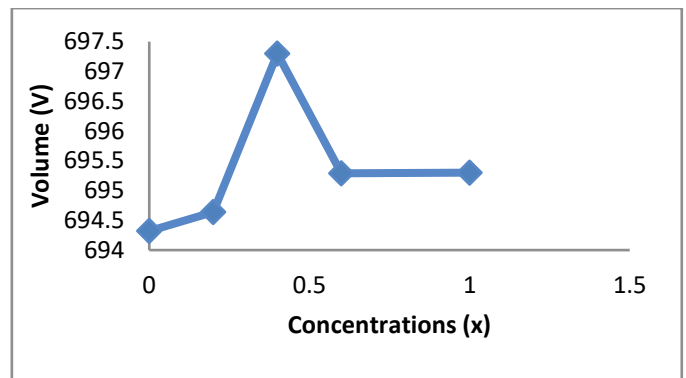
Figure 2: Unit cell volumes for different doping Concentrations (x)

Figure 1: XRD images for Ba(Co-Zr)xFe12-2xO19(x =0.0(a),0.2(b),0.4(c),0.6(d), 1(e))

Scanning Electron Microscope (SEM):

Themorphological characterization of thefabricated ferrites materialswas done by utilizing SEM (Model7600F)IIT Bombay[18]and isdepictedin **Figure 3**. The SEM micrograph demonstrates the development nanohexaferrites specimens have approximate grain sizes in between 35 and 50 nm. The photos reveal that the crystallites aren't packaged tightly during the whole sample, highlighting the porous nature of the specimens.It can be shown from the SEM images that the porosity is decreasing as the

volume of doping increases. This outcome complies with the measured porosity values in **Table 1**.
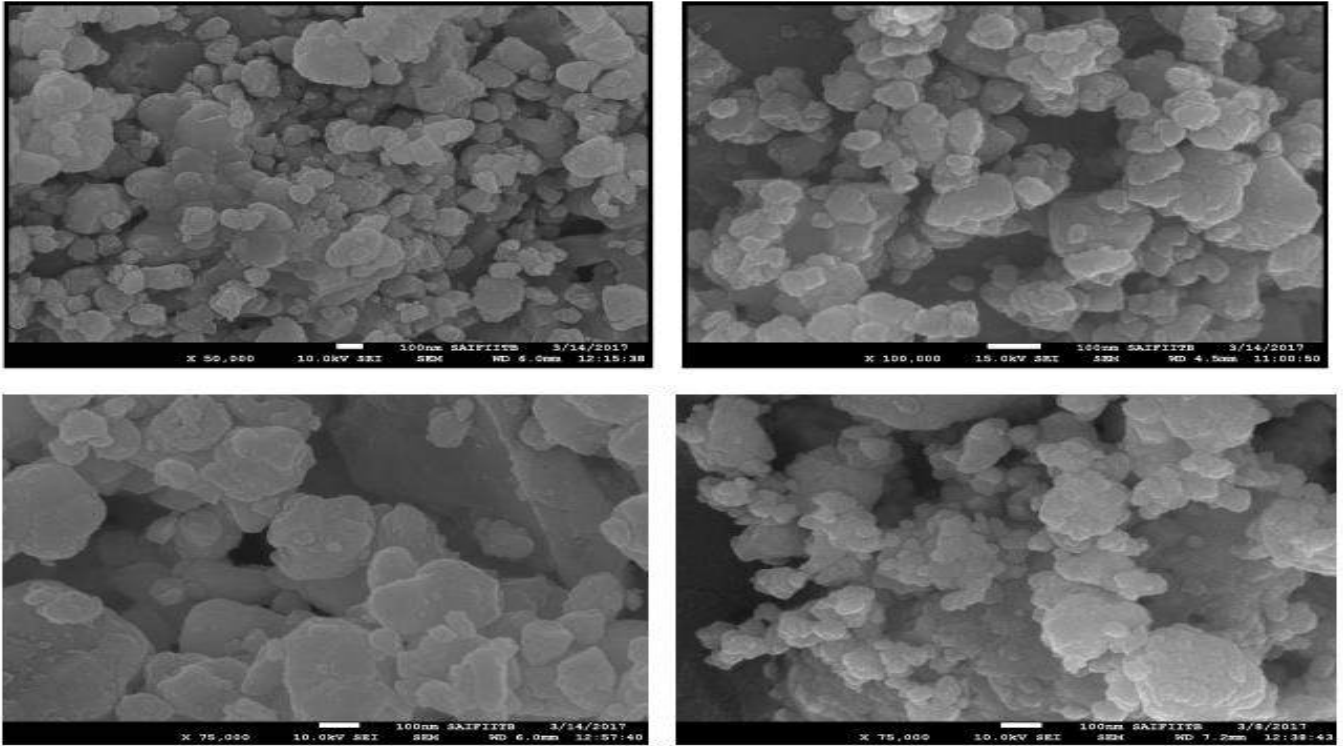
Figure 3: SEM micrograph of Ba(Co-Zr)xFe12-2xO19,(x=0, 0.4, 0.6, 1)

Electrical Conductivity:

With the help of Wanyekerr Impedance Analyzer data sheet, Electrical Conductivity have been calculated by using simple equation

$$\sigma_{ac} = \frac{Gt}{A}$$

G- represents conductance, A- represents cross sectional area, and t-represents thickness of material pellets [5].
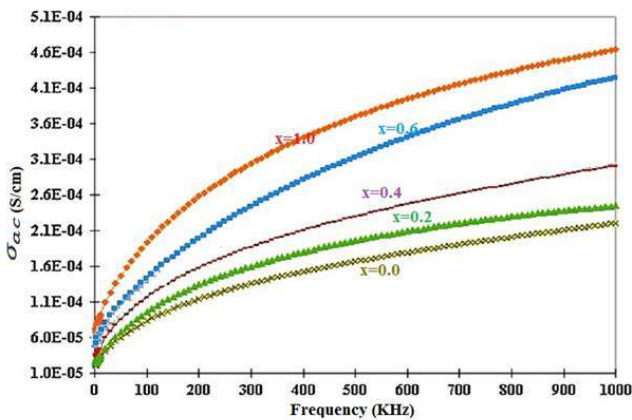
Figure 4: Ac Conductivity of Ba(CoZr)xFe12-2xO19 at different Concentrations and at frequency(KHz)

It's evident from Figure 4, that an electrical conductivity (σ_{ac})goes on increases with the frequency of an external field, which may be interpreted according toVerwey's hopping mechanism, which implies that the conductivity in the ferrites is partly attributable to the hopping of electrons amongst ions of the identical element found in more than one valence state, arbitrarily spread over crystallographically similar lattice sites.Ferrites contain structurally cubic-closed, packed oxygen lattices containing cations at the octahedral (B) and tetrahedral (A) sites. The separation between the two metal (Fe) ions at the B site is less than the difference between a metal ion at the B site and another metal ion at the A site. Thus the probability of the electron hopping between B and A sites is very lesscompare to that of B–B hopping. Andhopping among A-A sites doesn't occur as there are only Fe^{3+} ions at A sites and

any Fe^{2+} ions produced throughout manufacturing ideally settled only on B sites[19, 20].Under the impact of the applied field the charges will transfer, resulting in the electrical behaviour of the specimens. If the applied signal frequency increases, electron hopping increases, leads to an increase in AC conductivity [21, 22]. Electrical conductivity declinesby increase in the concentration of Zr^{4+}-Co^{2+} ions. The porosity of the specimen decreases with an increase in concentrations of substituent's **(Table 1)**, because of which the distance amongst the grains increases, leading to an impediment in the conduction within grains.

Dielectric Analysis:

Impedance Analyzer is utilised to study the Dielectric behavioursof specimen materialswithin a frequency ranging from 1 KHz to 1MHz.The dielectric constant(ε') ofthefabricated materialis obtained by

$$\varepsilon'= Ct/A\varepsilon_0$$

ε_0 - represents permittivity of free space = 8.85 x 10^{-12}F/m, C- represents capacitance of the specimen, t - represents thickness of the specimen pellets, and A - represents cross-sectional area of the specimen pellets [4].

The dielectric tangent loss is again measure using the equation

$$\tan\delta =\varepsilon''/ \varepsilon'$$

wheretanδ is dielectric loss.

The response of dielectric constant (ε') of formulated ferrites materialsto the frequency and doping concentrationsis presented in **Figure 5.**
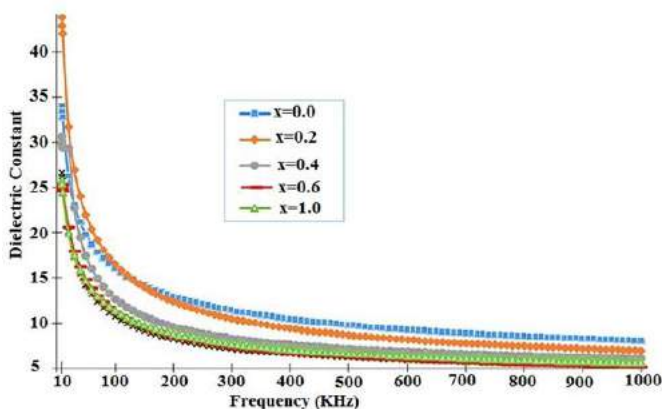
Figure 5:Frequency dependent Dielectric Constant for $Ba(CoZr)_xFe_{12-2x}O_{19}$.
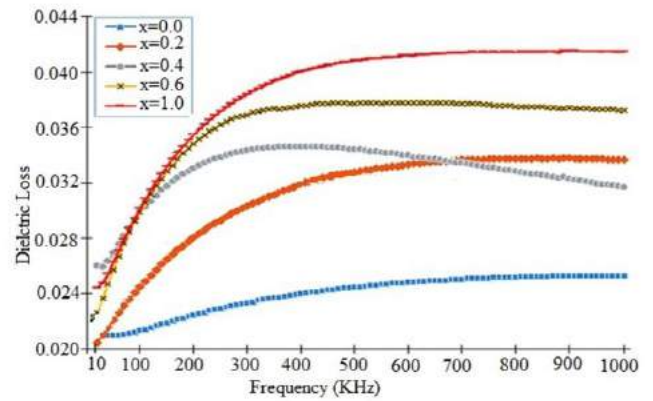
Figure 6: Variation of Dielectric losses for $Ba(CoZr)_xFe_{12-2x}O19$ with Frequency at different concentration.

Figure 5 displays the dielectric constant (ε') for all synthesised ferrites materials are frequency dependant. With increase in the frequency of an applied field, the dielectric constant (ε') reduces. At the lower frequency the dielectric constant is maximum, and that is reduces with increase in frequency owing to dielectric relaxation and dielectric dispersion, that Koop's theory can clarify. In Accordance to Koop's theory, the dielectric system is comprised of two layers, one is conducting grains and the next one is of non-conducting grain boundaries. The charged particles in the substance require a definite time to line up in the direction of applied field, and this time is preferred asrelaxation time. If the frequency of applied field is raisebeyonda defined limit, then the material ions unable to line upalongside the field direction in such a way that the polarisation unable toachieve at its saturation sothere is decrease in Dielectric Constant [23, 24].With the increased Zr-Co ions, ferric ions are decreased inB-sites. Fe^{3+} ions were essentially accountable for the polarisation of space charges as well asfor the hopping mechanism within localised state. Consequently, a rise in the content of Zr-Co ions induces a decrease in polarisation and hopping amongst theFe^{3+} and Fe^{2+} that cause lowering the value of ε' of formulated samples being examined. The higher values

of ε' obtained withdoping were favourable forimpedance matching.It is obvious from**Figure 6,** the loss tangent rise by up to 500 kHz and later it become nearly constant for all samples. The key element that governs dielectric losses is the hopping of electrons ($Fe^{3+} \leftrightarrow Fe^{2+}$)from octahedral to tetrahedral sites.Initially, the loss parameter increases because of polarisation losses and loss due to electric conductancebesidefrequency [25]. At sufficiently elevated frequency, ions areunable to hopp and thus interfacial polarisation can be reduced [26]. Thus, after 500 kHz, dielectric loss activity is almost constant (Fig. 6).The increasing dielectric losses have also been observed as a result of a raise in the doping concentration which is resulting from the increasing hopping process from octaredral (B) to tetrahedral (A)sites. In addition, the radii of Zr^{4+} and Co^{2+} ions greater as compared to Fe^{3+}, an extra intrinsic electric moment developed. These intrinsic moment rises through rise in doping concentration leading to an increasingDielectric loss[27].The improvement in dielectric loss byreplacement make this ferrites sample compressed, thereby making them ideal for absorption purposes.

IV. CONCLUSION

The Zr^{4+}- Co^{2+} substituted Ba hexaferritesof chemical formulaBaFe$_{(12-2x)}$Co$_x$Zr$_x$O$_{19}$(x= 0.0 to 1.0) have been processed by Microwave induced Sol-gel auto-combustion route.The XRD investigation of the synthesized nano-particles documented the formulation of mono phase M- type hexagonal ferrites. As the frequency increases, electrical conductivity and loss tangent increases, simultaneously the values of Di-electric constant decreases. But, as the Zr^{4+}-Co^{2+} as doping concentration raises, the value of electrical conductivity and dielectric constant decreases, simultaneously loss tangent increases. The study of suchhexagonal ferritesput forward as an effective choice for applications in microwave such as absorption and Impedance matching.

V. REFERENCES

[1]. R.D.C. Lima, M.S. Pinho, M.L. Gregori, R.C.R. Nunes, T. Ogasawara, Mater. Sci-Poland.2004,22(3), 245–252.

[2]. S.P. Gairola, V. Verma, A. Singh, L.P. Purohit, R.K. Kotnala, Solid State Commun.2010,150(3–4), 147–151.

[3]. M.R. Meshram, N.K. Agrawal, B. Sinha, P.S. Misra, J. Magn. Mater.2004,271(2–3), 207–214.

[4]. U. Ozgur, Y. Alivov, H. Morkoc, J. Mater. Sci. Mater. Electron.2009, 20(9), 789–834.

[5]. A. Singh, S.B. Narang, K. Singh, O.P. Pandey, R.K. Kotnala, J. Ceram. Process. Res.2010,11(2), 241–249.

[6]. F.J. Berry, J.F. Marco, C.B. Ponton, K.R. White, J. Mater. Sci. Mater. Electron.2001,20(5), 431–434.

[7]. S.B. Narang, A. Singh, K. Singh, J. Ceram. Process. Res.2007,8(5), 347–351.

[8]. S. Pignard, H. Vincent, E. Flavin, F. Boust, J. Magn. Magn. Mater.2003, 260, 437–446.

[9]. Y. Chen, X. Ren, J. Mater. Sci. Mater. Electron.2016, 27(1), 772–775.

[10]. 10.Y. Song, J. Zheng, M. Sun, S. Zhao, J. Mater. Sci. Mater. Electron.2016, 27(4), 4131–4138.

[11]. M.M. Rashad, I.A. Ibrahim, J. Mater. Sci. Mater. Electron.2011, 22,1796.

[12]. C.L. Yuan, J. Mater. Sci. Mater. Electron.2016, 27(5), 4908–4912.

[13]. C. Doroftei, E. Rezlescu, P.D. Popa, N. Rezlescu, J. Optoelectron. Adv. Mater.2006, 8(3), 1023–1027.

[14]. R.S. Meena, S. Bhattachrya, R. Chatterjee, J. Magn. Magn. Mater.2010, 322(14), 1923–1928.

[15]. A. Ghasemi, A. Hossienpour, A. Morisako, A. Saatchi, M. Salehi, J. Magn. Magn. Mater.2006,302(2), 429–435.

[16]. A. Ghasemi, A. Hossienpour, A. Morisako, X. Liu, A. Ashrafizadeh, Mater. Design.2008, 29(1), 112–117.

[17]. Y.J. Kim, S.S. Kim, J. Electroceram.2009, 24(4), 314–318.

[18]. C. Singh, S.B. Narang, I.S. Hudiara, K. Sudheendran, K.C.J. Raju, J. Magn. Magn. Mater.2008, 320, 1657–1665.

[19]. E. Pervaiz, I.H. Gul, J. Magn. Magn. Mater.2014, 349, 27–34.

[20]. S.M. El-Sayed, T.M. Meaz, M.A. Amer, H.A. El Shersaby, Phys. B Phys. Condens. Matter.2013, 426, 137–143.

[21]. S. Hussain, A. Maqsood, J. Alloys Compd.2008, 466(1–2), 293–298.

Thermal Behavior of Polythiophene Composite Thin Films doped with Iodine

D. P. Deshmukh

Department of Physics, Lt. R. Bharti Arts, Comm. And Smt. S. R. Bharti Sci. College Arni, Dist- Yavatmal, Maharashtra, India

ABSTRACT

Synthesis of polymer composites poly (vinyl acetate) (PVAc) and polythiopene (PTh) was done by chemical oxidative method using ferric chloride oxidant in methanol. Thin films with PTh-PVAc polymer composite were prepared for 5.5, 10.4, 14.9, 18.9 and 22.5 wt % of Iodine as a dopant. Dielectric relaxation activation energy and relaxation time is found to be maximum for 10.4 wt% of Iodine. Bulk capacitance is found to be maximum for 5.5 wt % of Iodine.

Keywords: Poly (vinyl acetate) (PVAc), Polythiophene (PTh), Iodine, dc, ac.

I. INTRODUCTION

Numbers of applications have been proposed for PThs such as field effect transistors, electroluminescent devices solar cells, photochemical resists, nonlinear optic devices, batteries, diodes and chemical sensors [1]. Roncali [2,3] surveyed electrochemical synthesis of PThs in 1992 and the electronic properties of substituted PThs in 1997.The overall review on chemical synthesis of PThs and applications as chemical sensors, organic memory devices, photo conductivity etc. is given by many researchers[4-7].

List of optimized samples along with their wt %, sample codes and thicknesses are given in table. The present paper focuses on the thermal behavior of PTh-PVAc composite films using $FeCl_3$ oxidant and Iodine as a dopant with an aim to study durability mechanism. Thermal Gravimetry / Differential Scanning Calorimetry is useful for the determination of changes in weight in relation to change in temperature [8], determination of glass transition

temperature etc. TGA/DSC for all the samples of PTh-PVAc composites doped with iodine was obtained from department of Material Engineering, VNIT, Nagpur and SAIF/CRNTS, IIT, Mumbai. In TGA/DSC temperature is maintained upto 973K. The TGA/DSC of the samples was carried out on instrument from Dupont, U.S.A. and heating rate of the sample was $10^{\circ}C/min$.

II. RESULTS AND DISCUSSION

Miscibility between any two polymers in the amorphous state is evidenced by the presence of a single Tg [9,12]. Fig shows the TG curves of Iodine doped PTh-PVAc films in the temperature range 273 to 900 K. It is observed that the thin films lost 50.42 to 55.26 % of its weight when it was heated up to 900 K. This fact indicates that 50.42 to 55.26 % of the sample consisted of polymers and softeners. The residual 20.61 to 26.55 % considered to account for metallic compounds added as sulphides and dopants [13-14].

The two step degradation is observed from the curve [20-21]. The first step occurs in the temperature range 423 to 493 K and the weight loss in this temperature range is quite high 44.58 to 47.01 %. Beyond the temperature 493 K, the weight loss curve appears to be horizontal showing that weight loss is very small which indicating that the physical properties of the polymer content remains constant. In second step degradation the weight loss is observed to be smaller than the first, it is 3.99 to 8.25 % in the temperature range 683 to 773 K for all the samples [13-14]. Weight loss in each step and total weight loss for different wt % of Iodine are tabulated in table . The two step degradation is observed from the curve[15-16]. The first step occurs in the temperature range 423 to 493 K and the weight loss in this temperature range is quite high 44.58 to 47.01 %. Beyond the temperature 493 K, the weight loss curve appears to be horizontal showing that weight loss is very small which indicating that the physical properties of the polymer content remains constant. In second step degradation the weight loss is observed to be smaller than the first, it is 3.99 to 8.25 % in the temperature range 683 to 773 K for all the samples [13-14].

Table1: Weight loss in each step and total weight loss for different Samples.

Composition Iodine (wt%) and sample code	Weight loss (%)		Total Weight loss in step I and II (%)	Residue (%)
	Step I 448 to 513 K	Step II 480 to 683 K		
5.5	46.43	3.99	50.42	24.34
10.4	47.01	8.25	55.26	26.55
14.9	44.58	7.15	51.73	20.61
18.9	47.45	12.93	60.38	18.87
22.5	27.31	8.29	35.60	28.41

Table 2: Thermodynamic Parameters from DTA Curve

Composition Iodine (wt %)	Glass Transition temperature (T_g) (K)	Crystallization exothermic peak			
		Onset Temp.(K)	Peak Temp.(K)	End Temp.(K)	Enthalpy $(\Delta H_c)(J/g)$
5.5(DV$_1$)	388	424	445	472	35.77
10.4(DV$_2$)	385	425	447	477	27.21
14.9(DV$_3$)	362	414	444	463	26.87
18.9(DV$_4$)	376	415	442	466	27.89
22.5(DV$_5$)	380	449	465	486	49.26
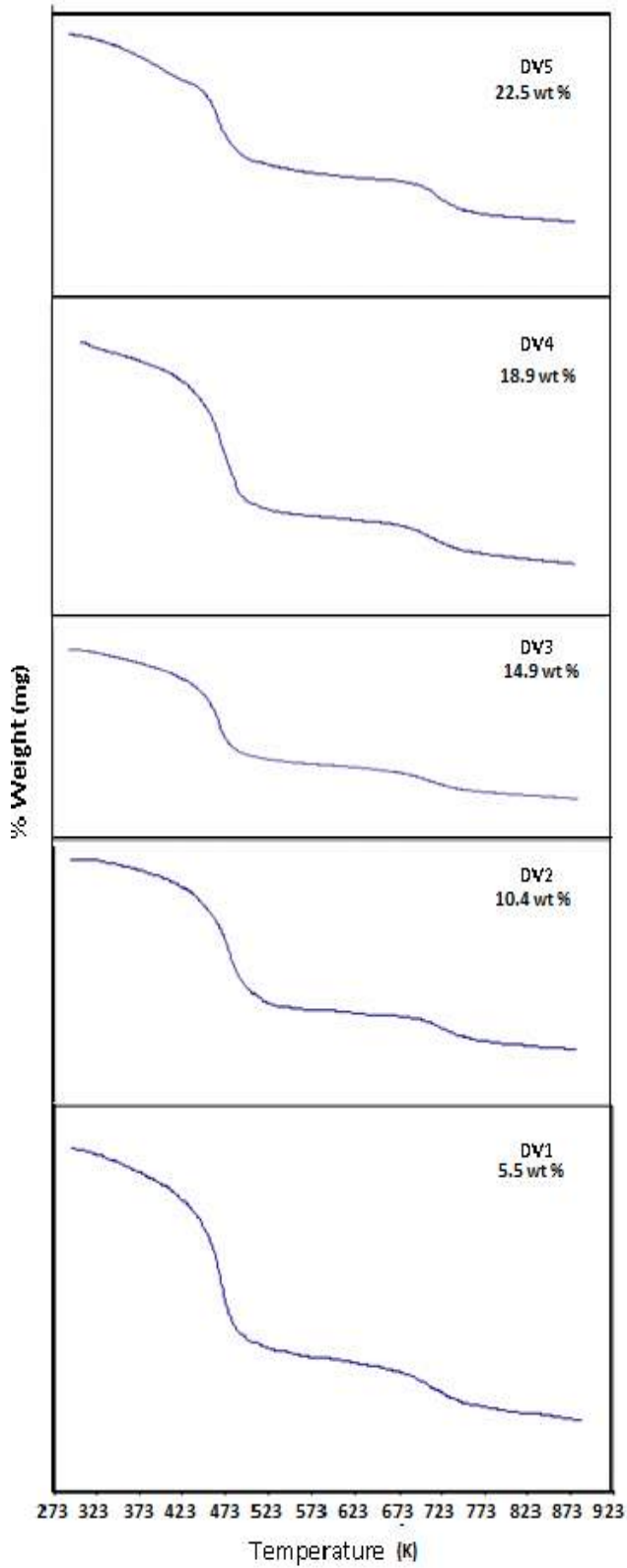
Fig.3: TG Curve for Iodine doped PTh-PVAc films
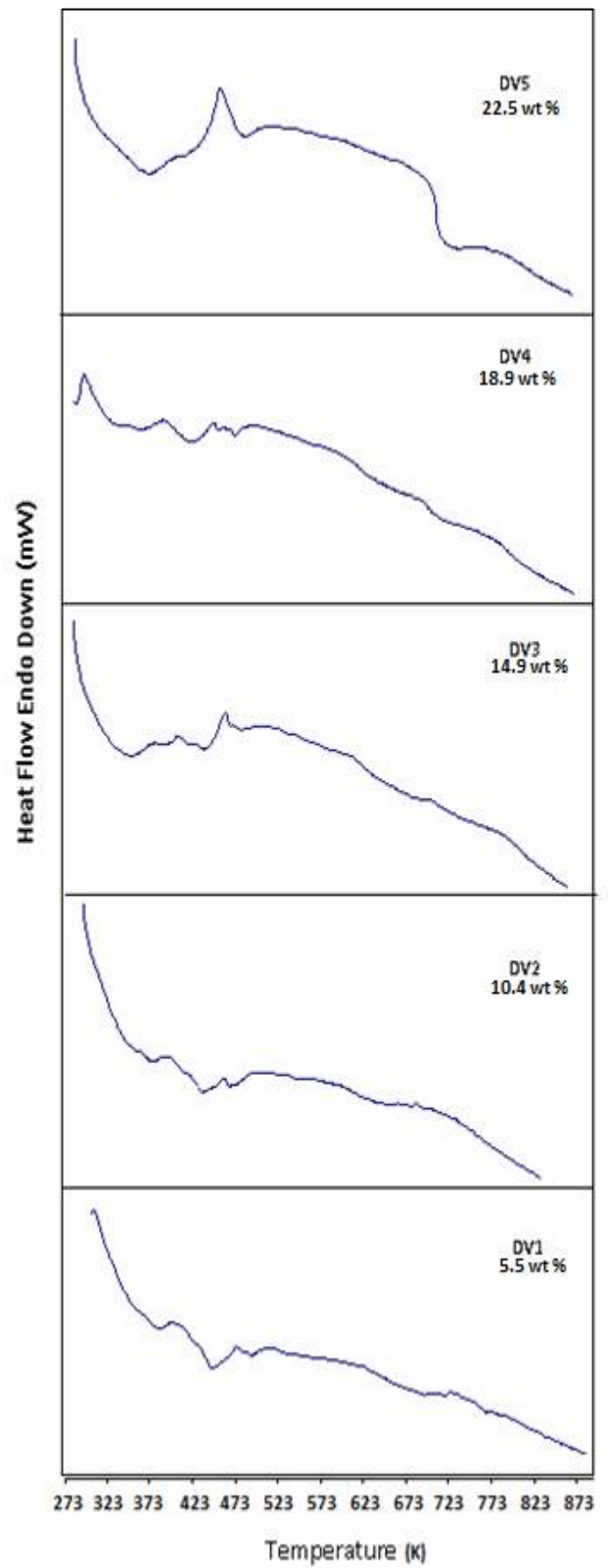
Fig.4: DTA Curve for Iodine doped PTh-PVAc films

III. CONCLUSION

It is observed that all the samples with different wt % of Iodine give the degradation in the range 75 to 81 % when heated up to 888 K. The glass transition temperature is also noted for all the samples which found in the range 362 to 388 K [20]. It is observed that the glass transition temperature decreases with increasing content of Iodine as well as Fe. This means addition of Iodine or Fe relieves the structure of polymer composites and it becomes soft. Also the enthalpy of the composites decreases with increasing content of Iodine

IV. REFERENCES

[1]. Heuer, H. W.; Wehrmann, R.; Kirchmeyer, S. Adv. Funct. Mater. 12 (2002)89–94.

[2]. Roncali, J. Chem. Rev. 92 (1992)711–738.

[3]. Roncali, J. Chem. Rev. 97 (1997)173–205.

[4]. McCullough, R. D. Adv. Mater. 10 (1998) 93–116.

[5]. Reddinger, J. L.; Reynolds, J. R. Adv. Polym. Sci. 145 (1999)57–122.

[6]. McQuade, D. T.; Pullen, A. E.; Swager, T. M. Chem. Rev. 100 (2000)2537–2574.

[7]. T.Anjos, S.J.Roberts-Bleming, A.Charlton,J. Mater. Chem., 18 (2008)475 – 483.

[8]. M.A.Golub and R.J. Gargiulo, Polymeric Lett., 10, pp.41 (1972).

[9]. H. Tang, Mater. Lett., pp.1024,59 (2005).

[10]. S Kim, J. Adhesion Sci. Technol., pp.209–219, 20(2-3), (2006).

[11]. H.P. Wong, B.C. Dave, F. Levioux, J. Harreld, B. Dunn , J. Mater. Chem., pp.1019-1027, 8 (1998).

[12]. J. Aguilar-Hernandez, J. Appl. Phys., pp.1700-1711, 34(2001).

[13]. P A Kurian, C. Vijayan, Nanoscale Res. Lett., pp. 561–568, 2(11), (2007).

[14]. Nilam Shah, Bull. Mater. Sci., pp. 477–480, 30 (5), (2007).

[15]. T. Gupta, B. Adhikari , Thermochimica Acta, pp.169–181,402 (2003).

[16]. C.A. Gracia-Fernandez, Progress in Organic Coatings, pp. 332–336, 54 (2005).

Composites : Poly Aniline–Polyvinyl Alcohol- Cuprous Chlorides Applied Different Temperature for Gas Detector

D. B. Dupare*

* Department of Chemistry, Shri Dr R. G. Rathod Arts and Science College. Murtizapur, Di. Akola, Maharashtra, India

ABSTRACT

In our present study, we have developed Polyaniline –Polyvinyl alcohol -Cuprous chloride doped thin films polymeric composites. These films were synthesized by chemical oxidative polymerization in aqueous medium. These polymeric composites were characterized by U. V. -visible, FTIR, surface morphology by Scanning electron microscope (SEM). Their electrical conductivity was measured by four probe techniques. The ohmic behaviour observed by I-V characteristics. Gas monitoring properties of the sensor was checked against hazardous gases like Ammonia. The sensor shows almost stable and repeatable response for minimum 5 ppm and maxmum 500 ppm for at varies at 25-40 degree temperate.

Keywords: Polymer, Polyanailine, Cuprous Chloride, Conducting Polymer, Ammonia Gas Sensor.

I. INTRODUCTION

Materials have been vital in the historical background of human undertakings and their study. One of the most significant group of materials in our lives today is composite material. The man made composite material, is a three-dimensional blend of at least two artificially unmissable materials, with a particular interface isolating the segments, made to acquire properties that can't be accomplished by any of the segments acting alone(1) . Nanocomposites are composites in which at any rate one of the stages shows measurements in the nanometer range. These materials have been arisen as reasonable choices to conquer impediments of miniature composites and solid (2). The polymers having poly-formed structures and have poor electrical conductivity however the oxidized polymers show apparent electrical conductivity. Among synthesis polymers Polyaniline (PANI) is novel among the directing and the most investigated, natural occurring polymer which is nothing but difficult to incorporate, having reasonable great synthetic dependability and generally read for electronic and optical applications(3). Various metal constantly oxide particles have been epitomized into the conductive polymer to structure nano-composites. Over the most recent 20 years, there has been a strong emphasis on the turn of development of the PANI-based nanocomposites. These composite of nanomaterials are required to show a few synergistic properties between the polymer and the metal nanoparticles, making them expected contender for application in a few fields, for example, catalysis, sensors, memory

devices(4). Cu nanoparticles have been applied in numerous fields since it has size impacts as well as high conductivity. Conductivity of Cu is in a similar request of magnitude as honorable metals like Au and Ag. Cu is a lot less expensive than the honorable metals; it can diminish the expense of items in useful applications. Then again, Cu nanoparticles can go about as impetus during polymerization to increment creation yield and change in the nanoparticles content may bring about various different changes like, thermal,mechanical, and electrical properties of the nanocomposites(5). These nanocomposites display the electrolytic and gas detecting properties.

The investigation deals with a study of the influence ofCuprous chloride dopant on synthesis of Polyaniline –Polyvinyl alcohol doped thin films. These synthesized films were characterized by U. V. -visible, Fourier transform Infrared spectroscopy (FTIR), surface morphology by Scanning Electron Microscopy (SEM),electrical conductivity and I-V characteristics. The gas sensing behavior for monitoring of ammonia gas vapors at repeatable response for minimum 5 ppm and maxmum 500 ppm concentrationfor at varies at 25-40 degree temperate .

II. METHODS AND MATERIAL

2. 1. Materials-

Analytical-reagent-grade aniline,Cuprous chloride and polyvinyl alcohol granular form (AR-grade) were obtained and used in the present study. Aniline monomer was purified by distillation under reduced pressure and stored in dark at 10° C. oxidising agents are used again AR grade ammonium persulfate $(NH_4)_2S_2O_8$, Each process was done with double distilled conductivity water. (qualigen fine–chem. India) were used.

2. 2. Synthesis Polyaniline–Polyvinyl alcohol-Cuprous chlorideof Composites-.

For chemical polarization of aniline, ammonium persulfate $(NH_4)_2S_2O_8$ was used as an oxidant5 mL of aniline having 1N solution was dissolved in 20 mL of Aqueous ammonium persulfate $(NH_4)_2S_2O_8$ solution with doped with 5 ml of Cuprous chloride in ethanol and stirred for 25 min was added drop wise to the solution of aniline. Cuprous chloride was varied in, 0. 5N,1N,1. 5N and 2N,3N added to the aniline solution. This reaction mixture was stirred for 3 hr with magnetic stirrer in order to disperse Cuprous chloridein the polymer solution and inserted glass plate to obtained coated uniform thin films. The obtained product was filtered and washed thoroughly with distilled water in order to remove the unreacted aniline and excess ammonium persulfate the thin film are kept to observe the uniform effect of therefore it kept in ultarsonicate to control the thickness and smoothness of thin film fornation . Thethin film samples were kept vacuum-dried for 1 hr at 60–70°c with unreacted to humid environment to remove the humidity also.

III. RESULTS AND DISCUSSION

1) UV-Visible spectra -

UV-visible spectroscopy is a very sensitive tool for the study of Cuprous chloridedoped Polyaniline – Polyvinyl alcohol thin films protonation and more precisely for the elucidations of the dopant Cuprous chlorideinto the thin films. UV-visible study selected those films, which have uniform, and good sensor response time. These sample films were dissolved in (DMSO) solvent, and then the UV-visible spectra recorded in the range 200-700 nm. The sample yields sharp peaks within 360-380nm and a broad band at 465-580nm wavelength ranges. In DMSO the sample, however exhibits broad peak around 680 nm indicating formation of emerladine base. Fig-. 1.

Fig-1. Polyaniline–Polyvinyl alcohol-Cuprous chloride –
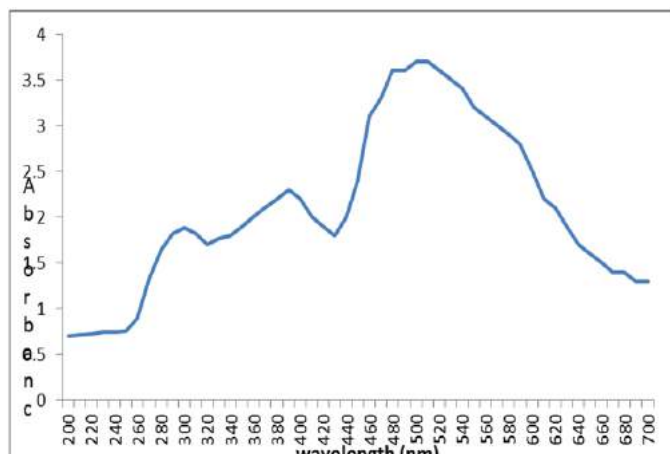
Fig 2. The FTIR spectra of Polyaniline–Polyvinyl alcohol-Cuprous chloride

2) FTIR-spectra

The FTIR- spectra of doped Cuprous chloridedoped Polyaniline –Polyvinyl alcohol thin composites thin films were recorded in the range of 4000-400 cm^{-1} usingDMSO as solvent The principal characteristics band occurrence indicates the type of functional group present in the polymer. The medium strong band observed at 3350 cm^{-1} suggests the presence of N-H stretch. The spectra shows the peak at 1620 cm^{-1}, which is due the presence of C=C group of aromatic benzonids ring. The observed medium intensity band in the region 1410-1244 cm^{-1} suggests the presence of C-N stretch). Cuprous chloride in Polyaniline – Polyvinyl alcoholmaterial (doublet) splits into triplets and shifts towards lower frequency at 1213 cm^{-1}. leading to exposure of the hidden C-N$^+$ group as (NH, $^+$NH$_2$, $^+$NH=, C=N$^+$) in Cuprous chloridedoped Polyaniline –Polyvinyl alcohol on the nature and percentage of doping which may effect the population of charge defect center (polaron and bipolaron) and ultimately the electrical conductivity. The C-O stretching vibrations in plane and out of plane, the bending vibration were observed at 1065cm^{-1} and 704 cm^{-1}.

The entire characteristics of band confirm the presence of doped conducting Cuprous chloridedoped Polyaniline –Polyvinyl alcohol thin films in Fig-2.

3) SEM study

A typical SEM image of 2NCuprous chloride dopedPolyaniline –Polyvinyl alcohol films having uniform and good stability. This film is shown in fig-3. Therefore SEM images give first hand information about a molecular level combination of the components and possibility for application as gas sensors. This thin films surface morphology study indicates that the films have porous surface and uniform in nature, which is one of the essential conditions for gas sensors.
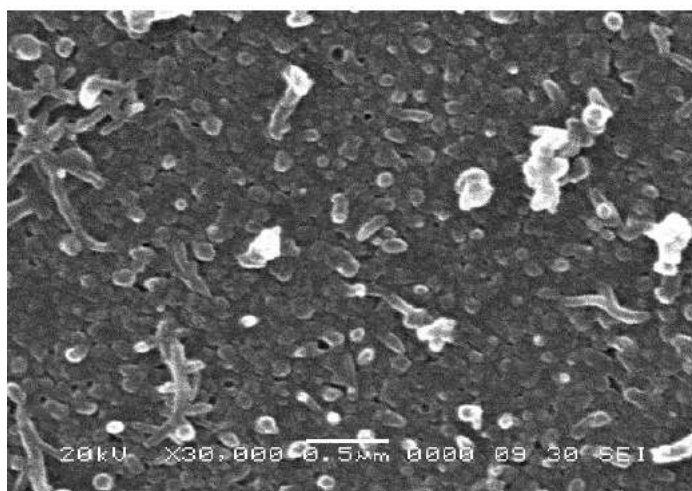
Fig -3. SEM image of 2NCuprous chloride dopedPolyaniline –Polyvinyl alcohol

3. 4) I-V characteristics-

The electrical conductivity of the synthesized Cuprous chloride having 1N,2N,3N dopedPolyaniline – Polyvinyl alcohol films studied at room temperature by four probe indigenous developed computer controlled (I-V) system. It is observed that, with the increasing concentration level, the electrical conductivity of thin films gradually increases.

The current-voltage (I-V) characteristics of synthesized films were studied to ensure an Ohmic behavior of all thin films samples but 2N,Cuprous chloride is more accurate linear relationship of I-V curve is shown in fig-4.
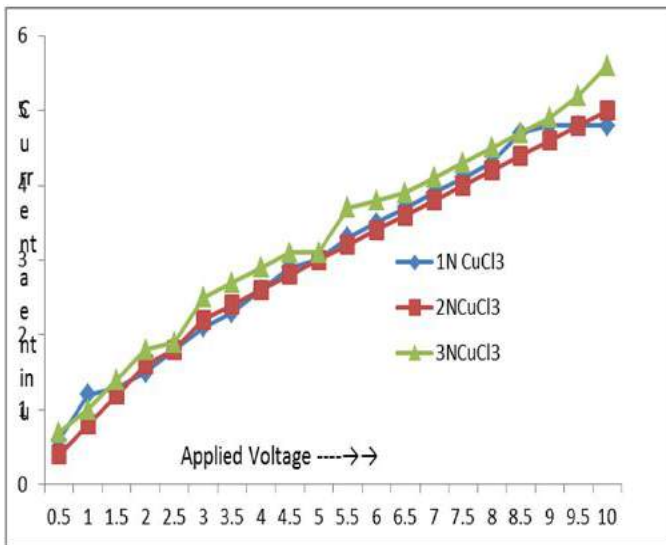
Fig-3. . I-V curve

3. 6) Ammonia Gas sensing behaviors-

The synthesized Cuprous chloride dopedPolyaniline – Polyvinyl alcohol thin films were studied for ammonia gas at different temperature by using indigenous developed computer controlled gas sensing system. Initially the films were allowed to saturate for 5minutes to expose to ammonia gas then after 7 minutes recovery time for minimum5ppm to maximum 500 ppm at 25,30,35,40,45 Degree temperature.
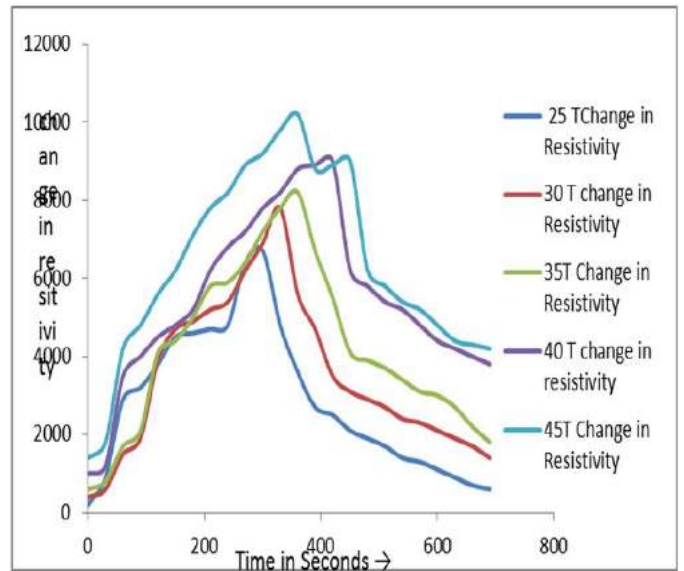
Fig-3. 6: TMA and ammonia Gas Monitoring Minimum 5ppm &Maximum-500ppm

IV. CONCLUSION

The present investigation concluded that, the synthesis of Cuprous chloride dopedPolyaniline – Polyvinyl alcoholcomposite films using chemical bath deposition method and successful fabrication of chemiresistive ammine sensors based onCuprous chloride dopedi composite films for ammine leakage detection at 25,30 and 35 degree Temperature good reposes and recovery time but whenever it increase the temperature the 2NCuprous chloride doped Composites not good response and recovery time . The I-V characterization study clear that the 2N Cuprous chloride dopedPolyaniline –Polyvinyl alcoholcomposite have liner ohmic behavior than that of 1N, 3N other synthesis films. Thus the usefulness of this study Cuprous chloride dopedPolyaniline – Polyvinyl alcoholcomposite films having good ohmic behavior as well as very nice ammonia sensor for minimum 5ppm level at indigenous developed sensor.

V. REFERENCES

[1]. Sangamesha,M. A. ,Pushpalatha K. and Shekar G. L. (2014) "Synthesis and Characterizationof Conducting Polyaniline/Copper Selenide Nanocomposites"Indian Journal of Advances in Chemical Science 2(3)223-227

[2]. Yan B. ,wu . Y. and Liang G. (2017). "Recent advance on polypurole elecrtroactuators" mdpi . com /journal /polymer ppm 1-20.

[3]. Aije Liu and Bac Luong (2012)"Preparation and Characterization of polyaniline-Copper composites by Electrical Explosion of wire"Journal of Nanoscience and Nanotechnology · Vol. 12, 6031–6035,

[4]. Dunst K. J, Cysewska K. , Kalinowski P. , Jasiński P. (2015) "Polypyrrole based gas sensor for ammonia detection" Materials Science and Engineering, pp 102-108.

[5]. Mohammad A. S and Bashir I. M(2018). "Characterization of a Novel Polypyrrole (PPy) Conductive Polymer Coated Patterned Vertical CNT (pvCNT) Dry ECG Electrode" Chemosensors, 6, 27pp1-12.

[6]. D. B. Dupare and M. D. Shirsat (2019)"polypyrrole–polyvinyl alcohol doped al2o3 composites as ammine gas sensor"International Journal of Advance and Innovative ResearchISSN 2394 - 7780 Volume 6, Issue 1 (XIX) PP-17-21.

[7]. Sayad Seema and M. V. N Ambika Prasad (2014) "Dielectric Spectroscopy of Nanostructured Polypyrrole-NiO Composites"Journal of Polymers pp-1-5.

[8]. Sarah Zayan, Ahmed Elshazly and Marwa Elkady (2020)"In Situ Polymerization of Polypyrrole @ Aluminum Fumarate Metal–Organic Framework Hybrid Nanocomposites for the Application of Wastewater Treatment"JournalPolymers, 12, 1764 pp 2-14.

[9]. Agnieszka Brzózka, Krzysztof Fic, Joanna Bogusz, Anna M. Brudzisz, Mateusz M. Marzec, Marta Gajewskaand Grzegorz D. Sulka, (2019)"Polypyrrole–Nickel Hydroxide Hybrid Nanowires as Future Materials for Energy Storage" Nanomaterials, 9, 307pp 1-15

Physico-Chemical Analysis of Soil Samples from Area near Wardha River, Maharashtra, India

Aswale S. S., Pimpalshende G. A., Raut S. D.

Lokmanya Tilak Mahavidyalaya, Wani, Maharashtra, India

ABSTRACT

An investigation was carried out for characterization of soils of areas near Wardha river. The selected area include villages of Yavatmal, Chandrapur and Wardha district. Standard analytical methods and procedures were followed for analysis of physico-chemical parameters of soils. Total 9 samples of soil from Patala, Kapasi and Pohana were analyzed for pH, Phosphate, hardness, alkalinity, chloride, sulphate, Calcium, Magnesium, and the results were compared with the limits of Indian Standards: 10500.

Keywords : Physico-Chemical, Ph, Phosphate, Potassium, Sulphate, And Cloride, Soil Analysis, Wardha River

I. INTRODUCTION

The soil forms the intermediate zone between the atmosphere and the rock cover of the earth, the lithosphere. It also forms the interface between water bodies (hydrosphere) and the lithosphere and thus forming a part of biosphere[1]. The soil may be defined as the uppermost weathered layer of the earth's crust in which are mixed organisms and products of their death and decay. It may also be defined as the part of the earth's crust in which plants are anchored[2]. The soil is a complex organization being made up of some six constituents' namely inorganic matter, organic matter, soil organisms, soil moisture, soil solution and soil air. Roughly, the soil contains 50-60% mineral matter, 25-35% water, 15-25% air and little percentage of organic matter (Chatwal et al, 2005). The soil pollution due to sewage is also very high. Several diseases are inflicted in human beings due to pathogenic forms present in the soil. It is the need of time that we have to study the physico-chemical parameters of soil to know its quality[3]. Nine representative samples were collected from various parts of the Patala, Kapasi and Pohana and its physico-chemical analysis have been performed to know its different parameters like pH, Phosphate, Potassium, Total Alkalinity, Total Hardness, Calcium, Magnesium, Sulphate, Chloride, Fluoride.

II. METHODS AND MATERIAL

Nine surface soil samples from 3 different villages besides Wardha River belonging to Yavatmal, Chandrapur and Wardha district of Maharashtra state. All the chemicals used were of GR/AR grade. Standard methods of American Public Health Association (APHA 18th edition) were used for the analysis of samples. Estimation of cations were carried out on Atomic Absorption Spectrometer (Make GBC Australia, Model GBC 932) at RSIC, Nagpur University Nagpur.

III. RESULTS AND DISCUSSION

The values of physicochemical parameters are presented in table 1: -

Table 1 - Soil quality at Kapasi (Ramtirtha) village

Village: Kapasi		Soil Samples			IS: 10500 Limits	
Sr. No.	Parameters	S1	S2	S3	Desirable	Maximum
1	pH	6.8	7.18	7.62	6.5-8.5	6.5-8.5
2	Total Alkalinity	209	374	524	200	600
3	Total Hardness	520.2	559.3	531.2	300	600
4	Potassium	11.8	13.7	18.1	----	----
5	Calcium	183.1	202.2	184.2	75	200
6	Magnesium	14.8	13.2	16.9	30	100
7	Phosphate	74.1	29.3	19.5	----	----
8	Sulphate	47.5	95.1	113.1	200	400
9	Chloride	134.1	123.7	99.5	250	1000
10	Fluoride	3.54	3.24	4.00	0.5-1.5	0.5-1.5

* **All parameters in ppm**

Table 2 - Soil quality at Pohana village

Village: Pohana		Soil Samples			IS: 10500 Limits	
Sr. No.	Parameters	S1	S2	S3	Desirable	Maximum
1	pH	7.85	7.44	7.45	6.5-8.5	6.5-8.5
2	Total Alkalinity	590	587	585	200	600
3	Total Hardness	95.1	329.3	352.6	300	600
4	Potassium	36.1	23.2	5.1		
5	Calcium	35.5	119.5	125.1	75	200
6	Magnesium	1.2	7.1	9.3	30	100
7	Phosphate	13.9	21.0	23.8		
8	Sulphate	58.1	118.1	77.2	200	400
9	Chloride	82.2	62.4	33.9	250	1000
10	Fluoride	3.22	4.10	3.1	0.5-1.5	0.5-1.5

* **All parameters in ppm**

Table 3 - Soil quality at Patala village

Village: Patala		Soil Samples			IS: 10500 Limits	
Sr. No.	Parameters	S1	S2	S3	Desirable	Maximum
1	Ph	7.25	7.45	7.50	6.5-8.5	6.5-8.5
2	Total Alkalinity	549	411	464	200	600
3	Total Hardness	391.7	413.4	372.1	300	600
4	Potassium	25.0	7.1	15.1		
5	Calcium	121.3	142.3	125.1	75	200
6	Magnesium	21.1	13.8	14.1	30	100
7	Phosphate	4.2	29.3	60.1		
8	Sulphate	172.1	142.8	113.1	200	400
9	Chloride	162.2	97.1	43.6	250	1000
10	Fluoride	4.33	5.77	5.83	0.5-1.5	0.5-1.5

* **All parameters in ppm**

Most of the farmers are using excessive chemical fertilizers and the too much dose of such fertilizers in few soils has rendered high values of P and K. The retention of K could also be due the clay minerals formed by chemical weathering of basalts which is the parent material for the soil. Such type of monitoring of soil sample is beneficial to know the concentrations of various parameters present in soil samples. Due to presence of near wardha river suchtypes of soil are superior for the cotton crop. Concentration of sulphate in agriculture soil of different observed area of wardha river less than that of desirable ranges. Due to deficiency of sulphate include yellowing of leaves & stunted growth of crop & delay in crop. From above observation we can suggested that to farmers use desirable amount of sulphate containing fertilizers in their agriculture area.

IV. CONCLUSION

It was observed that different areas of soil had influences on the physicochemical characteristics of the soils. However, application of more labile organic inputs, liming materials and suitable inorganic fertilizers would be effective for sustainable man-agreement and improving fertility status of the soils.

V. ACKNOWLEDGMENT

VI. REFERENCES

[1]. Chandak Nisha, Maiti Barnali Pathan Shabana, Desai Meena And Kamlesh Shah, Analysis of Soil Samples for its Physico-Chemical Parameters from Kadi City

[2]. Sandip Kumar Gupta, Ashok Kumar Singh, Anil Kumar Singh, Ashish Ranjan and Naveen Kumar Shukla, Physico-chemical characterization of soils of Bairia block of district Ballia, Uttar Pradesh

[3]. Wagh G. S., Chavhan D. M., and Sayyed M. R. G., Physicochemical Analysis of Soils from Eastern Part of Pune City

Structural and Electrical Properties of Nano [Ni $_{0.6}$ Zn $_{0.4}$ Fe$_2$ O$_4$] Spinel Ferrite

Dr. Ramesh N. Taikar [1], Sadanand R. Sarve [2*], Disha T. Yele [3], Dr. Deepak R. Taikar [4], Kalpana R. Nagde [5]

[1]Assistant Professor, Department of Physics, C. J. Patel College, Tirora, Gondia, Maharashtra, India

[2*]Assistant Professor, Department of Physics, Vidya Vikas College, Samadrapur, Maharashtra, India

[3] Department of Physics, C. J. Patel College, Tirora, Maharashtra, India

[4]Assistant Professor, Department of Physics, Shri. Lemdeo Patil Mahavidyalaya, Mandhal, Maharashtra, India

[5]Assistant Professor, Department of Physics, Institute of Science, Nagpur, Maharashtra, India

*Corresponding Author Email: sarve.sadanand@gmail.com

ABSTRACT

Nano Ni-Zn ferrite with composition Ni $_{0.6}$ Zn $_{0.4}$ Fe$_2$O$_4$ is prepared by using sol-gel auto-combustion method with citric acid as a fuel. The structural properties of synthesized nano-ferrite is characterized by powder X-ray diffraction (XRD) technique while the electrical properties have been studied using two probe method. The X-ray diffraction study confirms that, there is a formation of single-phase cubic spinel with most intense peak at [311] having lattice constant of 8.3585 A^0 and the average particle size is found to be 45.63 nm. In addition to this, the electrical resistivity of Ni-Zn Ferrite decreases with increase in temperature which exhibits semiconductor nature.

Keywords : Nano Ni-Zn ferrite, sol-gel technique, XRD, Electrical Resistivity.

I. INTRODUCTION

Ferrites have generated diverse technical interest due to their most interesting applications in electronic circuits as inductors, in high frequency systems, in power delivering devices, in magnetic recording media, transformer core, microwave absorber (1) (2). Among the various ferrites, nickel (Ni) substituted zinc (Zn) ferrites plays important role in technological application due to their high saturation magnetisation, low coercivity, high resistivity and low electric loss (3). The choice of cations and their distribution in tetrahedral 'A' and octahedral 'B' sites in a ferrite is interesting and useful for the characterisation (4). ZnFe$_2$O$_4$ has normal spinel structure, where Zn^{2+} ions in 'A' site and all Fe^{3+} ions are distributed in 'B' sites, whereas NiFe$_2$O$_4$ has inverse spinel structure in which Ni^{2+} ions mainly in 'B' sites and Fe^{3+} ions equally distributed in 'A' sites and 'B' sites. Thus, Ni-Zn ferrites forms a mixed spinel in which tetrahedral sites occupied by Zn^{2+} and Fe^{3+} and octahedral sites occupied by Ni^{2+} ions and Fe^{3+} in the lattice (5).

A wide verity work has been done on the structural, electrical and magnetic properties of Ni-Zn ferrite. Verma and Goel found that, the DC electrical resistivity of Ni-Zn ferrite greater than 108 Ω cm can be prepared by precursor method (6). The different experimental technique used for the preparation of Ni-Zn ferrite such as, sol-gel auto combustion (7), co-precipitation (8), ball milling (9), micro-emulsion (10), hydrothermal (11). Sol-gel auto combustion synthesis process is low cost, easy to control the particle size and efficient for homogeneous mixing of all components for the formation of nanocrystallites. In combustion synthesis process, organic compounds such as urea, glycine, citric acid and alanine have been used as a fuel to enhance the efficiency of combustion and metal nitrate acts as oxidant as well as cation sources. The fuel monohydrated citric acid presented the greatest time and temperature of combustion reaction (12) (13).

The present work deals with the synthesis of Ni $_{0.6}$ Zn $_{0.4}$ Fe$_2$O$_4$ by sol-gel auto combustion method using citric acid as fuel. The purpose of the study is to investigate structural and electrical properties of Ni-Zn Spinel ferrites for various application.

II. EXPERIMENTAL

Initially the AR grade precursor in the form of nitrates i.e. Ni(NO$_3$)$_2$.6H$_2$O, Zn(NO$_3$)$_2$.6H$_2$O and Fe(NO$_3$)$_3$.9H$_2$O are mixed in molar proportion in an aqueous solution of deionised water with constant stirring to transform into the gel. The gel was burnt in a self-propagating combustion way to form a loose powder. Then the powder is grounded in an agate mortar and annealed at 900 ^{0}C for 8 hrs in the furnace with a cooling at a rate of 75 ^{0}C/hr. In this way, the crystalline powder of Ni $_{0.6}$ Zn $_{0.4}$ Fe$_2$O$_4$ was prepared. The crystallinity of such sample was investigated by X-ray diffraction method using Phillips diffractometer (Model - PW 1051).

To carry out electrical studies, the crystalline powder is again grounded with polyvinyl alcohol which acts as a binder. Afterward, the fine powder is pressed by using a hydraulic press with a pressure of 5 tons to form a pellet. These pellets were again sintered at 1000 ^{0}C for 8 hours to reduce the porosity and increase the density. The silver paste was applied on both sides of pallet to obtain good ohmic contacts. The electrical characterization have been done by using a two-probe method in the temperature range 100 ^{0}C - 550 ^{0}C.

III. RESULTS AND DISCUSSION

The characterisations which have been carried out in the present work are discussed as follows:

X-ray Diffraction:

Fig.1 illustrate the X-ray diffraction (XRD) pattern of prepared Ni $_{0.6}$ Zn $_{0.4}$ Fe$_2$O$_4$ sample annealed at 1000 ^{0}C. The broadening of peaks is an indication for the formation of nano -crystalline nature of the present spinel ferrite. From the XRD data, it is reveal that, the most intense peak corresponds to the crystal plane [311] while, the crystallite size of 49 nm having d value 2.5202 A^0 is calculated by Debye-Scherrer equation (14).

$$D = 0.9 \lambda / \beta \cos\theta$$

where, D is a crystalline size, β is a full width half maxima, λ is a wavelength of X-ray beam of Cu - K$_\alpha$ (1.5406 A^0) and θ is the angle of diffraction. The prominent peaks in XRD data are corresponding to planes [111], [220], [311], [400], [422], [511], [440], [620], [533] which indicates the formation of cubic spinel structure. The average crystalline size found to be 45.63 nm. The lattice parameter 'a' is found to be 8.3585 A^0.
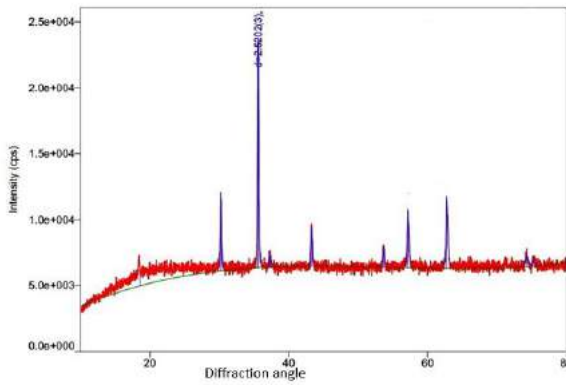
Fig. 1 : XRD Patterns of Ni $_{0.6}$ Zn $_{0.4}$ Fe$_2$O$_4$

DC Electrical Resistivity:

The DC electrical resistivity of the Ni-Zn spinel ferrite sample have been carried out in the range 100 ^{0}C - 550 ^{0}C using two probe method. The DC resistivity were calculated using the equation

$$\rho = \frac{A\,R}{t}$$

where, A is the area of the pellet, R is the resistance of the sample and t is the thickness of the pellet.
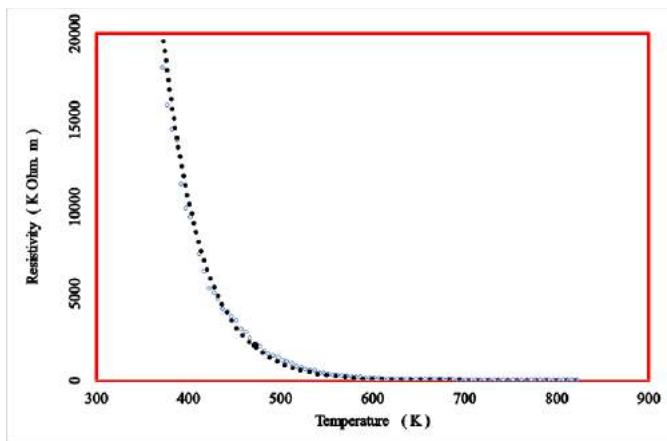
Fig. 2. Variation of Resistivity (K Ω m) with Temperature (K)

The variation DC electrical resistivity (KΩ m) with the temperature (K) is as shown in Fig.2. From this figure it can be seen that, the resistivity of the sample goes on decreasing with rapid rate of loss at initial level i.e. broadly in the range 400 K - 450 K. This rate of decrease

becomes lower down after 450 K and remains almost constant after 550 K temperature. Such decrease in electrical resistivity with temperature can be very well explained with the help of Verwey and de-Boer mechanism (15). According to them, the high sintering temperature leads to the formation Fe^{2+} ions and at the same time Ni^{2+} ion which oxidises to Ni^{3+} ion at octahedral site. The spinel ferrite consists of cations at tetrahedral sites and octahedral sites and the Fe^{2+} and Ni^{3+} ions have strong preference for octahedral sites hence, there is exchange of valence electron between Fe^{2+} and Fe^{3+} and holes between Ni^{3+} and Ni^{2+} which results into the conduction in ferrite and the magnitude of exchange depends on number of ion pair of Fe^{2+} and Fe^{3+} on octahedral sites. Such decrease of resistivity with increasing temperature also indicates the semiconductor nature of the ferrites (16).

IV. CONCLUSION

The Nanosize Ni-Zn ferrite with composition [Ni $_{0.6}$ Zn $_{0.4}$ Fe$_2$O$_4$] have been prepared by sol-gel auto-combustion method. The X-ray diffraction study confirms the formation of single-phase cubic spinel structure with most intense peak at [311] and the average particle size is found to be 45.63 nm calculated by using the Debye-Scherrer equation. Whereas, the DC resistivity is found to decrease with the increase in temperature which exhibits the semiconductor nature of the sample.

V. ACKNOWLEDGEMENT

VI. REFERENCES

[1]. Novel Applications of Ferrites Valenzuela, Raul s.l : Hindawi Publishing Corporation, 2012, Physics Research International, Vol 2012, p 9.

[2]. The Past, Present, and Future of Ferrites sugimoto, mitsuo 2, 1999, The American ceramic society, Vol 82, pp 269-280.

[3]. synthesis and chararcterizaion of pure singal phase Ni-Zn ferrite nanopowder by oxalate based precurser method Prita Pant Sarangi, SR Vadera, MK Patra, NN Ghosh 2, s.l : Elsevier, 2010, Powder Technology, Vol 203, pp 348-353.

[4]. Wijin, J Smith and H P J ferrites london, UK : Jhon Wiley & Sons, 1959.

[5]. Nanocrystalline spinel Ni0.6Zn0.4Fe2O4 : A novel material for H2S sensing VD Kapse, SA Ghosh, FC Raghuwanshi, SD Kapse 2-3, 2009, Materials Chemistry and Physics, Vol 113, pp 638-644.

[6]. High-resistivity nickel–zinc ferrites by the citrate precursor method A Verma, T C Goel, R G Mendiratta, R G Gupta 2, 1999, Journal of Magnetism and Magnetic material, Vol 192, pp 271-276.

[7]. Effect of Zn substitution on the structural and magnetic properties of nanocrystalline NiFe2O4 ferrites M.K Anupamaa, N Srinatha, Shidaling Matteppanavar, Basavaraj Angadi, Balaram Sahoo, B Rudraswammy 2018, Ceramics International, Vol 44, pp 4946-4954.

[8]. Structural and magnetic characterization of co-precipitated NixZn1-xFe2O4 ferrite nanoparticles C Srinivas, B.V Tirupanyam, S.S Meena, S.M Yusuf, C.S Babu, K.S Ramakrishna, D.M Potukuchi, D.L Sastry 2016, Journal of Magnetism and Magnetic Materials, Vol 407, pp 135-141.

[9]. Characterization of crystalline structure of ball-milled nano-Ni–Zn-ferrite by Rietveld method S Bid, S.K Pradhan 2004, Materials Chemistry and Physics, Vol 84, pp 291-301.

[10]. An overview of the Structre and Magnetism of spinel ferrite nanoparicles and Their synthesis in Microemulssion D S Mathew, R S Juang 2007, Chemical engineering journal , Vol 129, pp 51-65.

[11]. Studies on the Magnetism of Cobalt Ferrite Nanocrystals Synthesized by Hydrothermal Method Zhao, L., Zhang, H., Xing, Y., Song, S., Yu, S., Shi, W., Guo, X., Yang, J., Lei, Y and Cao, F 2008, Journal of Solid State Chemistry,, Vol 181, pp 245-252.

[12]. Combustion Synthesis: Effect of Urea on the Reaction and Characteristics of Ni-Zn Ferrite Powders Ana Cristina, F M Costa, Marico R Morelli & Ruth H G A Kiminami 2001, Journal of material synthesis and processing, Vol 9, pp 347-352.

[13]. Synthesis of Ni-Zn Ferrite Catalysts by Combustion Reaction Using Different Fuels N L Freitas, J P Coutinho, M C Silva, H L Lira, R H G A Kiminami, A C F M Costa 2010 October, Material science forum, Vols 660-661, pp 943-947.

[14]. Cullity, B D Elements of X-raydiffraction s.l : Addison-Wesley Publishing Co Inc., 1976.

[15]. Cation arrangement in a few oxides with crystal structures of the spinel type E J W Verwey, J H de Boer 6, 1936, Recueil des Travaux Chimiques des Pays-Bas, Vol 55, pp 531-540.

[16]. Temperature dependence of electrical properties of nickel-zinc processed by the citrate precursor technique A Verma, O.P Thakur, C Prakash, T.C Goel, R.G Mendiratta 1, 2005, Materials Science and Engineering: B, Vol 116, pp 1-6.

Using Fourier Transform Technique Investigate of Temporal and Spatial Coherence of Radiative Material

A. P. Pachkawade

Rajarshee Shahu Science College, Chandur Railway, Amaravati, Maharashtra, India

ABSTRACT

Fourier transform spectroscopy has progressed in research area like molecular structure examination and analyses. This type of spectroscopy is a measurement technique in which spectra are collected with respect to the measurements of the temporal coherence of radiative materials. We investigate the Coherence lengths of a light source, which is obtained by dc glow discharge of different electrolytic solution in the interface of solid and liquid with the help of Fourier Transform Spectroscopic method. The respective coherence time and fringe width (spectral width) of the 16 sources has been calculated from the measured respective coherence length.

Keywords : Radiative Materials, Dc Glow Discharge, Coherence Length, Fringe Width

I. INTRODUCTION

Study of optical coherence theory [4] and experiments is currently an area of active research. Coherence of light [1,2,3] is the property of wave-like states that enables to exhibit interference phenomenon. This parameter of light quantifies the quality of interference (known as degree of coherence). It can be stated that the coherence is a measure of the correlation between the phases of the wave measured at different points and it depends on the characteristics of its source. Coherence of light waves distinguishes two types of coherences such as 1) Temporal coherence and 2) Spatial coherence. The former relates [4] directly to the finite bandwidth of the source, the latter to its finite extent in space. The electron transitions responsible for the generation of light have duration on the order of 10-8s to 10-9s [1]. Because the emitted wave trains are finite, there will be a spread in the frequencies present, known as the natural line width. Moreover, since the atoms are in random thermal motion, the frequency spectrum will be altered by the Doppler Effect [4]. In addition, the atoms suffer collisions that interrupt the wave trains and again tend to broaden the frequency distribution. The total effect of all these mechanisms is that each spectral line has a bandwidth Dn rather than one single frequency and it is given [4] by

$$\Delta \nu = \frac{c}{\Delta Lc}$$

where Lc is the coherence length. Coherence length [7] is a very useful measure of temporal coherence because it tells us how far apart two points along the light beam can be, and remain coherent with each other. Spatial coherence is a measure of the correlation between the hases of a light wave at different point's transverse to the direction of propagation [6]. It has been

experimentally observed that the light waves produced by a laser always have high temporal and spatial coherence [1]. Review: The coherence property of the laser is an important aspect for theunderstanding of the optical Physics [5]. Using Michelson Interferometer and reversible shear interference P.D.Shukla and co-workers reported the measurement of temporal and spatial coherence of laser [5]. The spatial coherence width of the copper vapour laser (beam size ˜ 45 mm) measured approximately as 8 mm and temporal coherence of the CVL measured as 8 cm. They also reported the temporal coherence of the He-Ne laser as 15 cm using Michelson interferometer. Lasers can have very long coherence lengths [1]. LED are less monochromatic (Dl » 50 nm) than the most monochromatic lasers and tungsten filament lights are less monochromatic (Dl » 300nm) and so these sources have shorter coherence time than the most monochromatic lasers [1]. E.B.M. Steers and A.P.Thorne applied [8] high resolution Fourier transform spectroscopy to the study of glow discharge sources. They record the spectra from glow discharge source with and without supplementary microwave excitation and also recorded true line profiles. The contribution of charge exchange processes to the excitation of ionic lines was discussed in detail. J.E.Murray and co-workers investigated [9] the transition element spectra by using high resolution Fourier

transform spectrometry. In 1995 A.P.Thorne [10] published the Calibration of Line width standards and Lamp intensities using FT-UV Spectrometry. High resolution FTS studies of Glow Discharge spectra Line-profiles and Line-widths were done by E.B.M Steers and A.P.Thorne [11] and published in 1996. They described the high resolution Fourier transform instrument to study Line-width and Line-profiles for Fe and Ti using microwave boosted GD source. Anne Thorne have studied [12] high resolution Fourier transform spectrometry in the visible and ultraviolet regions and described the suitability of FTS for

upgrading databases, both for atomic emission spectroscopy and for astrophysical and atmospheric physics applications. DC glow discharges, as discussed by Winchester et al. [13] are mostly photon noise limited and it is possible to apply Fourier transform spectrometry as shown by Broekaert et al. [14]. The measurement of temporal coherence can be done by Fourier transform spectrometer i.e. Michelson Interferometer in which wave is combined with a copy of itself that is delayed by time t [1]. Method the measurement of Coherence lengths of a light source, which is obtained by dc glow discharge of different electrolytic solution in the interface of solid and liquid with the help of Fourier Transform Spectroscopic method. When dc glow discharge of an electrolytic solution is initiated, the emitted light beam is collimated by lens and made incident on the beam splitter of the Michelson Interferometer. The light beam is divided by it into two parts: partially as reflected beam and partially as transmitted beam. One arm of interferometer consists of fixed mirror M2, while other arm contains a movable mirror M1. Both the beams are recombined at the beam splitter (compensating plate) and produce an interference pattern after having been reflected once and transmitted once and then proceed to the sample area and detector. The interference condition for the two rays is determined by their path differences. When mirrors M1 and M2 are exactly made perpendicular to each other the interference pattern of the bright and dark concentric circular fringes is obtained. When the amplitudes of the two light beams are equal, the intensity of dark fringe is zero and the intensity of bright fringe is maximum consequently the clear interference pattern of concentric circles is obtained. The distinctness of the fringes depends upon the position of the mirror M1. When the path difference between the two rays is zero the well-defined fringe system is obtained. As the mirror M1 is moved a very clear interference pattern is observed while optical path difference is small, but if the path difference is

increased to a distance of several millimeters, the bright circular fringes becomes more and more indistinct and finally completely disappear. The circular fringes remain distinct for a limiting value of the optical path difference. This limiting value is the coherence length of the source of radiation. In this way the distance over which the fringes are obtained can be measured and the coherence length of source of light is measured. It was observed that when optical path difference is increased, the fringe visibility decreases.

II. RESULTS AND DISCUSSION

By the above-mentioned procedure the measurement of 28 glow discharges were carried out and used the respective sources for the measurement of Coherence lengths. Out of 28 glow discharges, only 16 sources could give the respective colour well-defined fringes showing monochromacity and coherence of the light emitted by the discharge and the remaining 12 sources could not give the fringe system. The coherence lengths of the 16 sources using the Fourier Transform Spectroscopic method were measured and listed in table. Using Fourier Transform Spectrometer i.e. Michelson interferometer the well defined interference pattern of circular fringes has been obtained. The interference pattern is very clear and well defined when the path difference between the rays is zero. The mirror M2 is continuously moved back and its effect on the visibility of fringes is observed. As the mirror M2 moves back the visibility of the fringes is influenced and a stage comes when the fringe system disappears. This reading is noted. Now the mirror is moved in opposite (forward) direction. Initially fringe system start appearing and we may get well-defined fringes. The mirror is moved still ahead so that fringe system once again disappears. This reading is noted and the coherence length of the source is found. A table shows that the coherence length lies between .1014 – 1.004 cm. Out of 16 sources the coherence length is maximum for the glow

discharge of MgSO4 electrolytic solution and minimum for NiSO4 solution. The respective coherence time and fringe width (spectral width) of the 16 sources has been calculated from the measured respective coherence length and the details are tabulated in table. The study of the observations shows that as the coherence length or coherence time is decreased, the fringe width increases. Furthermore, the product of coherence time tc and fringe width Dn is equal to unity. If the fringe width is narrowed by a filter the coherence length of the source may increase.

III. CONCLUSION

The measurement of coherence lengths of the material sources and the study of the fringe system shows that many sources can be used as monochromatic sources and the fringe system may be obtained and studied. The correlation between the coherence length and the properties of the sources may be obtained.

IV. REFERENCES

[1].   C.C.Homes, Fourier Transform Infrared Spectroscopy, Department of Physics, Brookhaven National Laboratory, June 24 2003(infrared.phy.bnl.gov/pdf/homes/FIR.PDF)

[2].   Optics (fourth edition) by Eugene Hecht, Adelphi University, pp.314

[3].   P.K.Shukla, K.K.Sarangpani, S.Talwar, G.S. Purbia, S.V.Nakhe,H.S.Vora, Centre for Advanced Technology, Indore, ETOP-2005

[4].   http:electron9.phys.utk.edu/optics421/molecules/ ms/coherence.htm

[5].   M.N.Avadhanulu, An Introduction to LASER theory and applications, 2001, S.Chand and Company Ltd. New Delhi

[6].   E.B.M. Steers and A.P.Thorne, J.Anal.At.Spectrom.8, pp.309-315, 1993

[7]. J.E.Murray, J.C.Pickering, G.Nave, R.C.M. Learner and A.Thorne, NIST special publication 850, 154-155, 1993

[8]. A.P.Thorne, Elsevier Science, pp.355-367, 1995

[9]. E.B.M. Steers and A.P.Thorne, Fresenius J.Anal.Chem. 355, pp. 868-872, 1996

[10]. Anne Thorne, Journal of Analytical Atomic Spectrometry, Vol. 13, pp. 407-411, May 1998

[11]. M.R.Winchester, J.C.Travis and M.L.Salit, Spectrochim. Acta, Part B, Vol. 48, pp. 1325, 1993

[12]. J.A.C. Broekaert, K.R.Brushwyler, C.A.Monnig and G.M.Hieftje, Spectrochim. Acta, Part B, Vol. 45, pp. 769, 1990

Table 1 . Coherence Lengths of Few Sources of Light

Sr. No	Electrolytic solution	Coherence length in cm	I.P.in eV		Coherence time in sec	Fringe width In Hz
			I	II		
1	0.5 N MgSO4.7H_2O	1.004	7.644	15.03	3.3467×10^{-11}	0.2988×10^{11}
2	0.5 N Cd(NO3)2.4H_2O	0.9884	8.99	16.904	3.2947×10^{-11}	0.3035×10^{11}
3	0.5 N NaCl	0.9108	5.138	47.29	3.0360×10^{-11}	0.3294×10^{11}
4	0.5 N	0.9058	5.138	47.29	3.0193×10	0.3312×10^{11}
5	0.5 N KNO3	0.8048	4.339	31.81	2.6827×10^{-11}	0.3728×10^{11}
6	0.5 N KOH	0.8038	4.339	31.81	2.6793×10^{-11}	0.3732×10^{11}
7	0.5 N K2SO4	0.7978	4.339	31.81	2.6593×10^{-11}	0.3760×10^{11}
8	0.5 N KCl	0.7952	4.339	31.81	2.6507×10^{-11}	0.3773×10^{11}
9	0.05 N AgNO3	0.4990	7.524	21.48	1.6633×10^{-11}	0.6012×10^{11}
10	0.25 N SeO2	0.4990	9.75	21.5	1.6633×10^{-11}	0.6012×10^{11}
11	0.5 N CuCl2.2H_2O	0.4052	7.724	20.29	1.3507×10^{-11}	0.7404×10^{11}
12	0.5 N CuSO4.5H_2O	0.4044	7.724	20.29	1.3480×10^{-11}	0.7418×10^{11}
13	0.25 N ZrOCl2.8H_2O	0.3994	6.95	14.03	1.3313×10^{-11}	0.7511×10^{11}
14	0.25 N LiNO3	0.2932	5.390	75.6193	0.9773×10^{-11}	1.0232×10^{11}
15	0.5 N BaCl2	0.2876	5.210	10.001	0.9587×10^{-11}	1.0431×10^{11}
16	0.5 N NiSO4	0.1014	7.633	18.15	0.3380×10^{-11}	2.9586×10^{11}

Selective Photo thermolysis Induced by Solid State Diode Laser for Permanent Hair Reduction

S. S. Arsad

Department of physics Shri Shivaji Science College Amravati, Maharashtra, India

ABSTRACT

We used pulsed laser emitting 20 msec pulses at 800 nm wavelength having peak power 1600 W (Frequency=2Hz) for removing the hairs from the human face. The energy density of the pulse used for removing hair is about 30 J/cm^2. The size of the laser beam utilized was about 9mm^2. About six or more sessions are essential for reducing the number of hairs. [1] In an average 650 to 950 pulses were used per patient per laser treatment session corresponding to 20.8 to 30.4 kJ energy. The number of hairs exponentially decreased as a function of sessions. (A gap of about 1-month is essential between two consecutive sessions for allowing the possible wounds to heal.) We utilize the diode laser for removing the hairs of about 300 patients. It is observed in many cases that the hair are either completely reduced or the hair become thinner. The method has very less side effect. [10]

I. INTRODUCTION

The hair of the human body plays very important role in deciding the personality and appearance. At some places presence of hair adds the beauty and at some places the presence of hair is unwanted. It may cause human face to look ugly or cruel. It is essential to remove the hairs from the human body where they add to cruelty and ugliness. Particularly the hairs for example on the chin of a female are cosmetically disfiguring the face value. Laser induced photothermolysis is one of the effective way to remove and reduce the hair from the body surface. [3,4]

In the present work we remove the hair from the different portions of face specifically over chin and upper lip of the 200 female patients. Average six sessions was required for the removal of hairs[5] and it is observed that all patients show long term hairs reduction. [2,8]

II. EXPERIMENTAL SETUP

It has been observed from several cases that the anesthesia is not required in this type of hair reduction. [6] the headpiece of the laser is covered with sapphire window chill tip. Before use the sapphire tip of laser was perfectly cleaned with alcohol. While removing hairs headpiece was kept in close contact perpendicular with the skin as the chill tip keeps the skin cold and protects it from damage and brings out the hair follicles or shafts for efficient treatment above the skin. The diode laser pulse was made incident on the hairs and the hairs were removed by evaporation. The foot switch was continuously and intermittently pressed and laser pulses were delivered. The laser pulse peak

power is of the order of 1600 W and pulse width is about 20 msec corresponding to pulse energy of each pulse was 3.2 J and average energy density or fluence of about 30 J/cm² When focused and irradiated on the target the size of the laser beam was about 9 mm ² . After the laser treatment the hairs were completely reduced. In an average 650 to 950 pulses were used per patient per laser session corresponding to 20.8 kJ to 30.4 kJ energy. The lowest fluence used was 16 J/cm² and the maximum fluence used was 36 J/cm² .

III. RESULTS AND DISCUSSION

When the laser beam is made incident on the skin, the skin of few patients shows a kind of swelling (which was purely temporary). In case of few patients after few days of laser sessions some hairs reappeared. After careful observation it is found that the hairs whose follicles are removed do not reappear but the hairs whose shaft or upper part i.e. hair entering from telogen to anagen phase is removed by laser may reappear. For removal of the remaining hairs few more sessions are essential.

We used about six sessions for all patients. It was observed that in case of all the patients almost all the hairs were reduced after six sessions. The number of reappearing hairs were measured with manual method and with digital photographs after each session and it is found that the number of hairs reduced exponentially. Depending upon the type of hairs, sex, age of patient (hirsutism in case of female patient), hair density, portion or site of body part and hair treatment session number hair reduction vary from patient to patient.
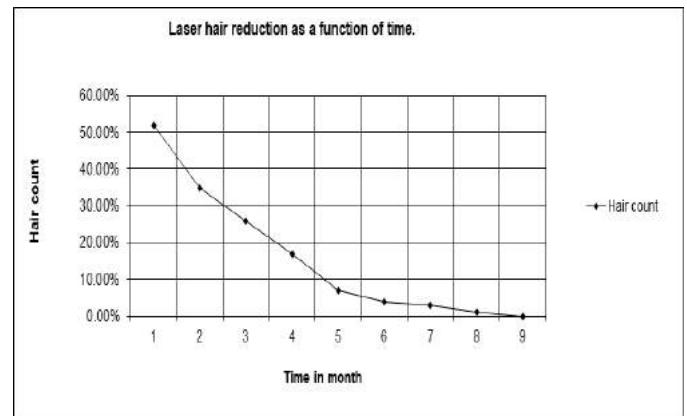
IV. CONCLUSION

The irradiation of 800 nm diode laser pulses removes the hairs and number of hairs were reduced considerably.7 After the exposures to the laser the skin of patients does not show degradation. The skin of few patients showed temporary recoverable swelling. The hair reduction using pulsed diode laser exhibits the exponential behavior. The absorption spectra of the melanin and the competing chromophores water and oxyhemoglobin shows that the ruby laser wavelength would be more effective having relatively less side effects in hairs removal.8 But the ruby laser setup is relatively costly and system is bulky also the ruby laser is not well suited for treating dark skin types due to epidermal melanin interference. If the pulse width of the diode laser is reduced further, the effectiveness of the hair removal may be improved. If the hair detector was used along with the control system the hair would be reduced in one or two sessions.9,11

V. REFERENCES

[1]. Sadick NS, Prieto VG : The use of a new diode laser for hair removal.Dermatol Surg 2003; (29) : 30-34

[2]. Adrian R Shay KP : 800 nanometer diode laser hair removal in African American patients : a clinical and hitologic study. J Cut Laser Ther 2000; (2): 183-190

[3]. Hussain M, Polnikorn N, Goldberg DJ : Laser - assisted hair removal in Asian skin: efficacy, comlications and the effect of single versus multiple treatments. Dermatol Surg 2003;(29):249-254.

[4]. Galadari I : Comparative evaluation of different hair removal lasers in skin types IV, V and VI. Int J Dermatol 2003; 42: 68-70.

[5]. Dierickx CC : Hair removal by laser and intense pulsed light sources. Semin Cut Med Surg 2000; 19(4):267-275.

[6]. Lepselter J, Elman M : Biological and clinical aspects in laser hair removal. J dermatol treatment 2004; (15):72-83.

[7]. Grossman MC, Dierickx C, Farinelli W. et. al. : Damage to hair follicles by normal mode ruby laser pulses. J Am Acad Dermatol 1996; (35) : 889-894.

[8]. Lask G, ELman M, Slatkine M. : Laser assisted hair removal by selective photothermolysis. Preliminary results. Dermatol Surg. 1997; (23) : 737-739.

[9]. B.H.Pawar, S.S. Arsad, Dr. Sandip Arsad, et.al. Selective photothermolysis induced by laser for the permanent hair reduction. NCOL 2007, Abstract, pp. 106.

[10]. B.H.Pawar, S.S. Arsad, Dr. Sandip Arsad, et.al. Selective photothermolysis induced by laser for the permanent hair reduction. Indian Journal of Dermatology venerology and leprology (under review).

[11]. B.H.Pawar, S.S. Arsad, Dr. Sandip Arsad, et.al. Study of permanent hair reductionby using diode laser. NLS-6 Indore 2006 Abstract, pp. 86.

[12]. Jae Dong Lee, Jong Kook Lee, Min Jin Maya Oh, Jae Dong Lee, Jong Kook Lee, Min Jin Maya Oh, Laser Hair Removal, Principles and Choice of Laser Treatment in Dermatology, 10.1007/978-981-15-6556-4, (161-185), (2020).

[13]. Jae Dong Lee, Jong Kook Lee, Min Jin Maya Oh, Jae Dong Lee, Jong Kook Lee, Min Jin Maya Oh, Korean Skin and Types of Lasers, Principles and Choice of Laser Treatment in Dermatology, 10.1007/978-981-15-6556-4, (95-109), (2020).

[14]. Magdalena Atta-Motte, Izabela Załęska, Diode Laser 805 Hair Removal Side Effects in Groups of Various Ethnicities – Cohort Study Results, Journal of Lasers in Medical Sciences, 10.34172/jlms.2020.23, 11, 2, (132-137), (2020).

[15]. Mohammad AlKhowailed, Shorug AlWayili, Saad Altalhab, Mohammed I. AlJasser, Abdullah Al-Hargan, Laser safety in isotretinoin use: online survey of public perception, Journal of Dermatological Treatment, 10.1080/09546634.2020.1775772, (1-4), (2020).

[16]. Laser hair removal,Omar A. Ibrahimi,Mathew M. Avram,C. William Hanke, Suzanne L. Kilmer,R. Rox Anderson:January 2011 https://onlinelibrary.wiley.com/doi/epdf/ 10.1111/ j.1529-8019.2010.01382.x

Structural and Morphological Characterization of $Ni_{1-x}Co_xO$-SDC Nano-Powder Synthesized by Glycine - Nitrate Combustion Synthesis for Its Application in IT-SOFC

B. B. Patil[1*] and A.R. Mali[2]

[1]Maharaja Jivajirao Shinde Mahavidyalaya Shrigonda, Dist. Ahmednagar, Maharashtra, India.

[2]Yashwantrao Chavan Institute of Science, Satara, Maharashtra, India.

ABSTRACT

$Ni_{1-x}Co_xO$-SDC nano-composite powder was synthesized by single step Glycine Nitrate Combustion Process (GNP). In case of GNP, glycine to nitrate ratio (g/n) plays an important role in deciding the powder characteristics. In the present study, selected (g/n) ratio is 0.97. The powder properties were studied by using X-ray Diffraction Technique (XRD), Scanning Electron Microscope (SEM) and Energy Dispersive X-ray Analysis Technique (EDAX). XRD study revealed, the formation of composite powder consisting of separate phases corresponding to cubic NiO, cubic SDC and cubic Co_2O_4. Crystallite size of the powder is found to increase with the increase in annealing temperature. Calculated crystallite size of the as synthesized powder by using XRD technique is found to be 4.7 nm and 7.5 nm for powder heated at 600 °C for 2hr. XRD studies confirmed the formation of nano-crystalline powders. SEM studies revealed the highly porous nature of the powder. No other impurity peaks were detected from the EDAX study. Thus nano-crystalline, composite, $Ni_{1-x}Co_xO$-SDC powder was synthesized successfully by using environmental friendly, inexpensive, rapid, single step glycine nitrate combustion method for its possible application to fabricate an anode for Intermediate Temperature Solid Oxide Fuel Cells (IT-SOFCs).

Keywords : $Ni_{1-x}Co_xO$-SDC, Glycine Nitrate Combustion Process, intermediate temperature solid oxide fuel cells, Nickel based anodes

I. INTRODUCTION

Solid Oxide Fuel Cell is an electrochemical device which converts the chemical energy in fuels to electrical energy directly with high system efficiency and low emissions [1]. Ni-based cermet has been considered as the most promising anode material for SOFCs fed with hydrogen due to its high catalytic activity, sufficient electrical conductivity and low cost [2].

Ni - Samaria Doped Ceria (SDC) is reported as potential candidate as anode material [3] for Intermediate Temperature Solid Oxide Fuel Cells (IT-SOFCs). It is reported as most suitable anode for SDC electrolyte - based SOFCs [4]. But Ni-based anodes have the Carbon deposition problem when used with hydrocarbon as a fuel. Also a marked drop in electrical conductivity of the anode cermet has been observed, which is associated with the growth of the Ni particle size [5]. This drop in anode performance may be due to a

reduction in both three phase boundary and electrical conductivity.

And hence there is necessity to modify the Ni –SDC anodes, to make them catalytic active, carbon resistant, and these modified anodes will help to improved cell stability, and decrease the polarization resistance [6-8]. Attempts have been made by the researchers to replace Ni by metals and alloys such as Zn [6], Co [7], Mo [8], Mo-Co [9], Fe-Co [10], to maintain the electrochemical catalytic activity and electronic conductivity of NiO-SDC anodes.

Earlier, $Ni_{1-x}Co_xO$-SDC powders have been synthesized successfully by using hydrothermal method [7], but almost negligible reports are present on single step synthesis of $Ni_{1-x}Co_xO$-SDC powder using glycine nitrate combustion process (GNP) method. In GNP glycine is used as fuel and metal nitrates are used as oxidants. These react to undergo redox reaction and forms desired product. In the present work attempts have been made to synthesize and to study the structural and morphological characteristics of $Ni_{0.25}Co_{0.75}O$-SDC Nano-Powder for its application in IT-SOFC.

II. EXPERIMENTAL

2.1 Powder Synthesis

In order to prepare nano-crystalline $Ni_{0.25}Co_{0.75}O$-SDC powder, precursor solution was prepared by dissolving stoichiometric amount of reagent grade nickel (II) nitrate $[Ni (NO_3)_3.6H_2O]$, cerium (III) nitrate $[Ce(NO_3)_3.6H_2O]$, samarium (III) nitrate $[Sm(NO_3)_3.6H_2O]$ and cobalt nitrate $Co(NO_3)_2.6H_2O$ in deionized water with Ni: $Ce_{0.8}Sm_{0.2}O_{1.9}$ as 7:3. Glycine (NH_2-CH_2-COOH) was also dissolved in deionized water separately. Glycine and metal nitrate solutions were then mixed thoroughly to form a homogeneous solution. Alfa Aesar (India) company's chemicals were used. As powder characteristics dependent on nature of the fuel and fuel to oxidant (g/n) ratio [11]. Here selected (g/n) ration is 0.97. The solution was then

heated on hot plate at 80 ºC till dark purple color gel forms. The temperature of the hot plate was then raised to 180-220 ºC. Because of this the resultant viscous gel ignited automatically and an intense and self-sustaining flame was formed, and resulted into the formation of foamy, highly porous coffee brown color powder. The conversion process lasts for about a minute. The powder was sintered at 600 ºC for 2 h to remove the residual carbon and promote the crystallization and further used for characterization.

2.2 Powder Characterization

The phase identification of synthesized $Ni_{0.25}Co_{0.75}O$-SDC powders was made with X-ray diffraction (XRD) technique using Phillips PW-1710 diffractometer The micro-structural and compositional analysis of the synthesized powders was conducted with scanning electron microscope (2ELSS EVO series, model EVO 50) equipped with an energy dispersive X-ray (EDS) analyzer (Bruker–AXS, model Quan Tax 200).

III. RESULTS AND DISCUSSION

3.1 XRD Analysis

Fig. 1 shows the comparison of the XRD plot obtained for the as synthesized $Ni_{0.25}Co_{0.75}O$-SDC powder with fuel lean 0.97 ratio and powder heat treated at 600 ºC for 2h. Powder is showing polycrystalline nature. All the peaks have been identified and indexed from the known patterns of the standard data files [12-14].
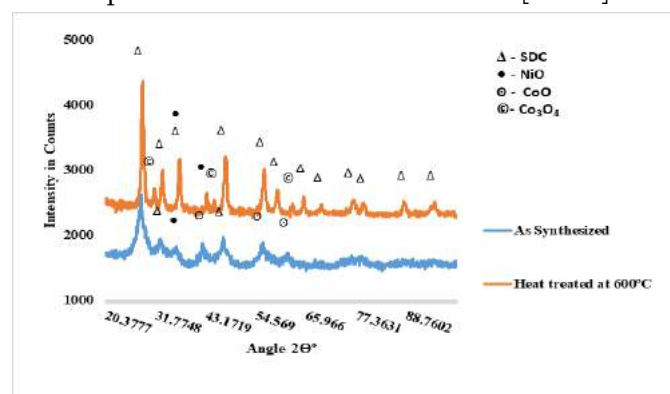
Fig. 1. XRD Patterns of as synthesized $Ni_{0.25}Co_{0.75}O$-SDC powder and powder heat treated at 600 ºC for 2h.

The XRD pattern corresponding to as synthesized powder shows separate peaks corresponding to cubic NiO phase - (111), cubic fluorite SDC phases - (111), (002), (022), (113) and cubic cobalt oxide (CoO) phases - (111), (200), (220). Calculated lattice parameters for NiO, SDC matches well with the reported values [15]. XRD plot obtained for powder heat treated at 600 ºC for 2 h, shows more crystallinity with peaks corresponding to cubic NiO as (111) and (311); cubic SDC as (111), (002), (022), (113), (222), (004), (133), (244), (115), and cubic Co_3O_4 as (440). It is seen that as synthesized powder consists of peaks corresponding to CoO but after heat treatment CoO gets converted to cubic Co_3O_4 [16]. For both the powders (111) peak corresponding to cubic (SDC) is most intense, hence it was further analyzed for getting the crystallite size by using Scherrer's formula. Calculated crystallite size of as synthesized powder and powder heat treated at 600 ºC for 2 h is mentioned in Table 1.

Table 1 Effect of calcinations temperature on the crystallite size of the $Ni_{0.25}Co_{0.75}O$-SDC powder

Calcination Temperature (ºC)	Powder Color	Crystallite size (from XRD) nm
0	Coffee brown	4.7
600	Coffee brown	7.5

From Table 1 it is concluded that, the crystallinity of the powder increases with the increase in the calcination temperature. The lattice constants (a) of Ceria and SDC are reported as 0.5411 nm and 0.5433 nm respectively [17]. Their comparison showed, increase in 'a' value. This increase in 'a' value is due to the substitution of Sm^{3+} at Ce^{3+} site. This gives rise to increase in lattice parameter.

Thus, powder synthesized by using glycine nitrate combustion synthesis is having nanometer size grains. This is due to atomic and molecular level mixing of reagents during combustion synthesis process. The large volume of the gases evolved during the combustion reaction limits the inter particle contact. Also the combustion process occurs at such a fast rate that, sufficient energy and time are not available for long path diffusion of the atoms or molecules as a result of which the initial nano-size of the powder is retained [18].

3.2 Powder Microstructure

Fig. 2 shows Scanning Electron Microscope (SEM) image of as synthesized $Ni_{0.25}Co_{0.75}O$-SDC powder. The powder is found to be highly porous, this is due to release of large amount of gases during combustion synthesis. This helps to restrict the further grain growth of the powder to maintain its nano-crystallinity [18].
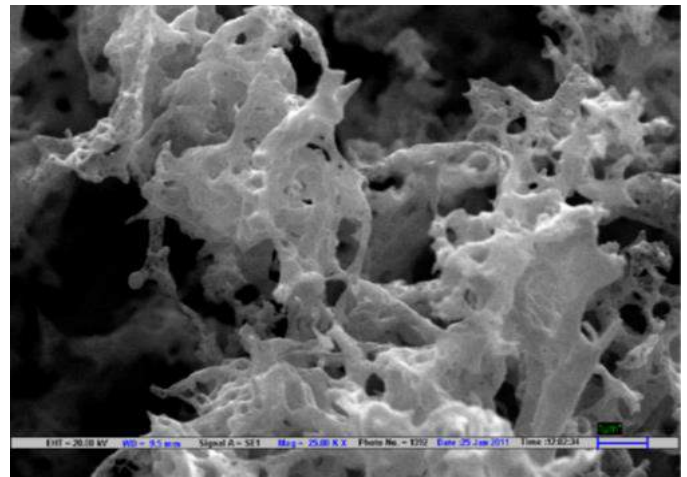
Fig. 2 SEM image of $Ni_{0.25}Co_{0.75}O$-SDC powders heat treated at 600℃ for 2 h.

3.3 EDAX Analysis

Fig. 3. shows, the Energy Dispersive X-ray Analysis (EDS) plot of the $Ni_{0.25}Co_{0.75}O$-SDC powder, heat treated at 600 ºC for 2h. From Fig. 3 it is clear that, synthesized powder shows elemental peaks corresponding to Ni, Ce, Sm, Co, O and C only. No peaks other than these were observed, showing the formation of phase pure powder. Presence of C is due to the carbon tape used during sample mounting.
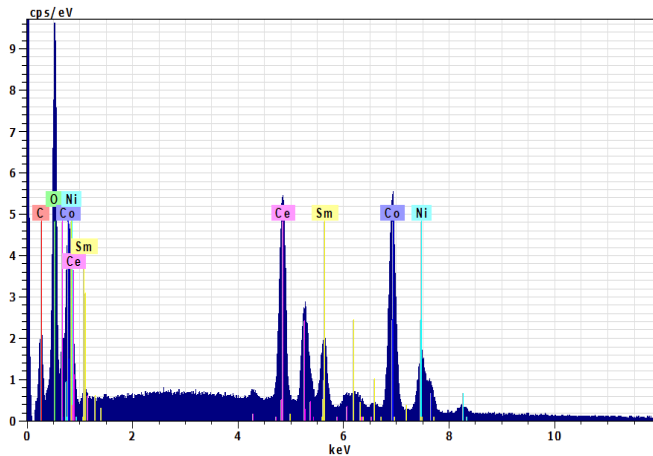
Fig.3 EDAX Plot of $Ni_{0.25}Co_{0.75}O$-SDC powders heat treated at 600ºC for 2h.

IV. CONCLUSION

Nano-crystalline, composite power of $Ni_{0.25}Co_{0.75}O$-SDC have been successfully synthesized by single step glycine nitrate combustion synthesis. We are among the few to report such type of synthesis of $Ni_{0.25}Co_{0.75}O$-SDC. Synthesized powder is highly porous, having high crystallinity, physical and chemical homogeneity and light weight. Nano-crystalline and highly porous nature of the powder will definitely help to increase the three phase boundary (TPB) area, and in turn the performance of anode. Hence $Ni_{0.25}Co_{0.75}O$-SDC nano-powder synthesized by environmental friendly, inexpensive, fast, energy efficient, single step glycine nitrate combustion method is going to be useful to fabricate efficient anodes for intermediate temperature solid oxide fuel cells (IT-SOFCs).

V. ACKNOWLEDGEMENTS

VI. REFERENCES

[1]. B.C.H. Steele, A. Heinzel, Nature 414 (2001) 245-252.

[2]. S. Alayoglu, K. An, G. Maelaet, S. Chen, F .Bernardi, L.W. Wang, A.E. Lindeman, N.Musselwhite, J. Guo, Z. Lin, M.A. Marcus, G.A. Somorjai, J. Physics Chemistry-C, 117 (2013) 26608-26616.

[3]. B.B. Patil, V. Ganesan, S.H. Pawar, J. of Alloys and Compounds, 460 (2008) 680- 687.

[4]. J. Molenda, K. Swierczek, W. Zajac, Journal of Power Sources, 173 (2007), 657-670.

[5]. D. Simwonis, F. Tietz, D. Stover, Solid State Ionics, 132 (2000) 241.

[6]. X. Zhi, T. Gan, N. Hou, L.Fan, T. Yao, J. Wang, Y. Zhao, Y. Li, Journal of Power Sources, 423 (2019) 290-296.

[7]. G. Ding, T.Gan, J.Yu, P.Li, N.Hou, L.Fan, Y. Zhao, Y.Li, Catalysis Today, 298 (2017)250-257.

[8]. P. Li, B. Yu, J. Li, X. Yao, Y. Zhao, Y. Li, Journal of Power Sources, 320 (2016) 251-256.

[9]. J. Zhao, X. Xu, W. Zhou, Z. Zhu, J. of Materials Chemistry-A,14 (2017) 6494-6503.

[10]. Z. Xie, W. Zhu, B. Zhu, C. Xia, Electrochemica. Acta, 51 (2006) 3052-3057.

[11]. R.D. Purohit, B.P. Sharma, K.T. Pillai, A. K. Tyagi, Materials Research Bulletin, 36(2001) 2711.

[12]. ICSD database Code 28792.

[13]. Data file: PDF#780431

[14]. Data file: PDF#780643

[15]. B. B. Patil, S. Basu, Energy Procedia, 54 (2014) 669-679.

[16]. Data file: PDF#781970

[17]. H. Yoshida, H. Deguchi, M. Kawano, K. Hashino, T. Inagaki, H. Ijichi, M. Horiuchi,K. Kawahara, S. Suda, Solid State Ionics, 178 (2007) 399.

[18]. B. Liu, Y. Zhang, J. of Alloys and Compounds, 453 (2008) 418-422.

Pholumineascence Properties of Some Molybdate Phosphors Containing Bismuth

B.V. Tupte[1*], D.H. Gahane[2*], M.M. Bhave[3], C.D. Mungmode[3], S.V. Moharil[4]

[1*]Department of Physics, SGM College, Kurkheda, Maharashtra, India

[2*]Department of Electronics, N.H. College, Bramhapuri, Maharashtra, India

[3]Department of Physics, N.H. College, Bramhapuri, Maharashtra, India

[3]Department of Physics, M.G. College, Armori, Maharashtra, India

[4]Department of Physics, RTM Nagpur University, Nagpur, Maharashtra, India

ABSTRACT

Eu^{3+}- doped Molybdate Phosphors Containing Bismuth are prepared by a combustion method and characterized by X-ray diffraction (XRD) patterns, photoluminescence (PL) spectroscopy. PL properties have an impact on factors along with molar ratio of Bismuth (Bi^{3+}) and Molybdate (Mo^{6+}) ions, dopants concentration are Studied. The results show that Molybdate Phosphors Containing Bismuth can act as a useful host for Eu^{3+} ions doping, and energy transferring from Bi^{3+} to Eu^{3+} achieved efficiently hence this phosphor displayed intense red color emission under ultraviolet light excitation.

Keywords : Combustion Method, Molybdates, Photoluminescence, Phosphor.

I. INTRODUCTION

Nowadays, great amply of efforts have been paid for the development of phosphors, due to the extensive applications of white light-emitting diodes (LEDs), as it was known that LEDs had the advantage of low power consumption, high efficiency, long durability, fast response and lack of toxic mercury. [1,2] Among the oxides and sulfides phosphors, molybdates could be a perfect host for rare Earth luminescent material, ascribe to their good thermal and chemical stability. Bismuth molybdate is an important inorganic material due to its perfect luminescent and structural properties, however, it other potential applications in modern fields, such as optical sensors, magnetic nano-device,

biomedical reagent, photocatalysis, organic molecules ammonia-oxidizing agent, and so on forth. [3-6]

The Bi3+ and RE3+ ions possess close ionic radii and therefore the Bi-containing compounds could be easily doped with luminescent ions like Eu3+, Yb3+, etc. It was demonstrated recently that K2Bi(PO4) (MoO4): Eu3+ is a phosphor for white light-emitting diodes. Yb3+ and Nd3+-doped K5Bi(MoO4)4 is considered as a promising material for laser in the near-IR region [7, 8].

Recently, the molybdate family has aroused great interest and been chosen as host materials for new luminescent materials which can be activated in the deep UV region (200–250 nm) based on their good stability, low costs, simple synthesis conditions and good luminescence properties. [9,10,11] However,

most of the reports focus on the luminescence properties of Eu3+ doped CaMoO4 for the applications in white LED. Here in this manuscript, we synthesized rare earth ions Eu3+ doped R5Bi(MoO4)4 (R=K, Na) phosphors, and investigated their luminescence properties in detail.

II. EXPERIMENTAL

The Eu3+ activated R5Bi1-x(MoO4): xEu3+ (R=K, Na) (where x = 0.05 mole) phosphors were prepared by the combustion synthesis. The starting AR grade materials (99.99% purity) were taken as Potassium nitrate KNO3, Sodium nitrate (NaNO3), ammonium molybdate ((NH4)6Mo7O24.4H2O), Bismuth Oxide (Bi2O3), Europium oxide (Eu2O3) & Urea (NH2CONH2) was used as fuel. In the present investigation, materials were prepared according to the chemical formula R5Bi1-x(MoO4)4: xEu3+ (R=K, Na). The mixture of reagents was grind together to obtain a homogeneous powder. Bi3+ and Eu3+ ions were introduced as a Bi(NO3)3 and Eu(NO3)3 solution by dissolving Bi2O3 and Eu2O3 into a dil. HNO3 solution. For various compositions of the metal nitrates (oxidizers), the amount of urea (fuel) was calculated maintaining total oxidizing and reducing valences of the components equal to unity, so that the heat liberated during combustion is a maximum. After stirring for about 30 min, the precursor solution was transferred to a furnace which was preheated to 750 0C. Porous products were obtained.

III. RESULTS AND DISCUSSION

Fig.1(a) and 1(b) shows excitation spectra of $R_2Bi_{0.95}(MoO_4)_4$:0.05Eu^{3+} (R = K, Na) doped with 5% Eu^{3+} monitoring the emission at 617nm ($^5D_0 \rightarrow ^7F_2$ transition). The band located between 250 and 350 nm can be attributed to the charge transfer (CT) from $[MoO_4]^{2-}$ groups to Eu^{3+}. It shows broadening and a slight red-shift with increasing Eu^{3+} content. The red shift of the CT band is caused by the decreasing size of the Eu^{3+} sites, upon substitution of Bi^{3+} by smaller Eu^{3+}, thus resulting in shorter Eu–O bonds, which eases the charge transfer. There are several sets of lines in the range of 350–600 nm which are associated with the typical intra-configurational 4f^6 transitions of Eu^{3+}.

Lines originating from $^7F_0 \rightarrow ^5L_6$ and $^7F_0 \rightarrow ^5D_2$ transitions are located at 395 and 465 nm, respectively, and are of special interest. The spectral position of these lines match well with the emission spectra of near-UV and blue LEDs, respectively, thus making the synthesized phosphors suitable for solid-state light sources. Moreover, it should be noted that the intensity ratio between $^7F_0 \rightarrow ^5L_6$ and $^7F_0 \rightarrow ^5L_J$, ^5G_J is different. We assume that the $^7F_0 \rightarrow ^5L_J$, ^5G_J transitions become more probable due to the broadening of the CT-level with increasing Eu^{3+} concentration and thus the admixing of the CT-level with those excited terms of the [Xe]4f^6 ground state configuration, which are energy wise close to the CT state.
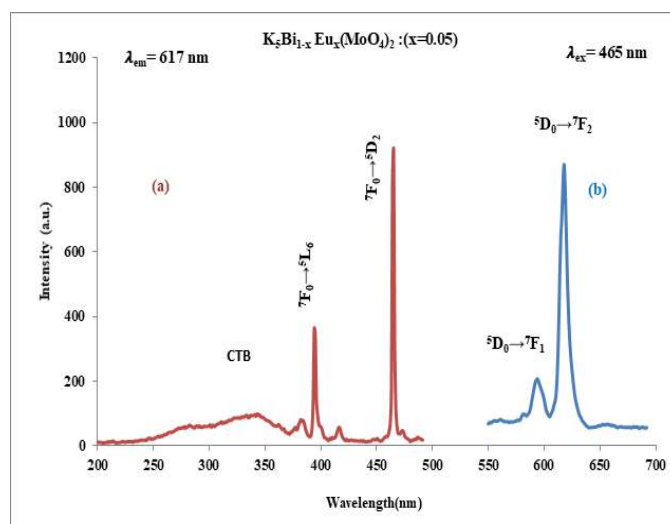
Fig. (1) Photoluminescence spectrum of Eu^{3+} activated K$_5$Bi $_{1-x}$Eu$_x$(MoO$_4$)$_4$:(x=0.05) Phosphor
(a) Excitation spectra of K$_5$Bi$_{1-x}$Eu$_x$ (MoO$_4$)$_4$:(x=0.05) for 617 nm emission
(b) Emission Spectra of K$_5$Bi$_{1-x}$Eu$_x$ (MoO$_4$)$_4$:(x=0.05) for 465 nm excitation.

The O→Eu^{3+} CT transitions can be manifested only in the case of R$_5$Bi(MoO$_4$)$_4$(R=K, Na), where the bismuth-oxygen polyhedra have BiO$_6$ structure rather than BiO$_8$ in three other crystals.
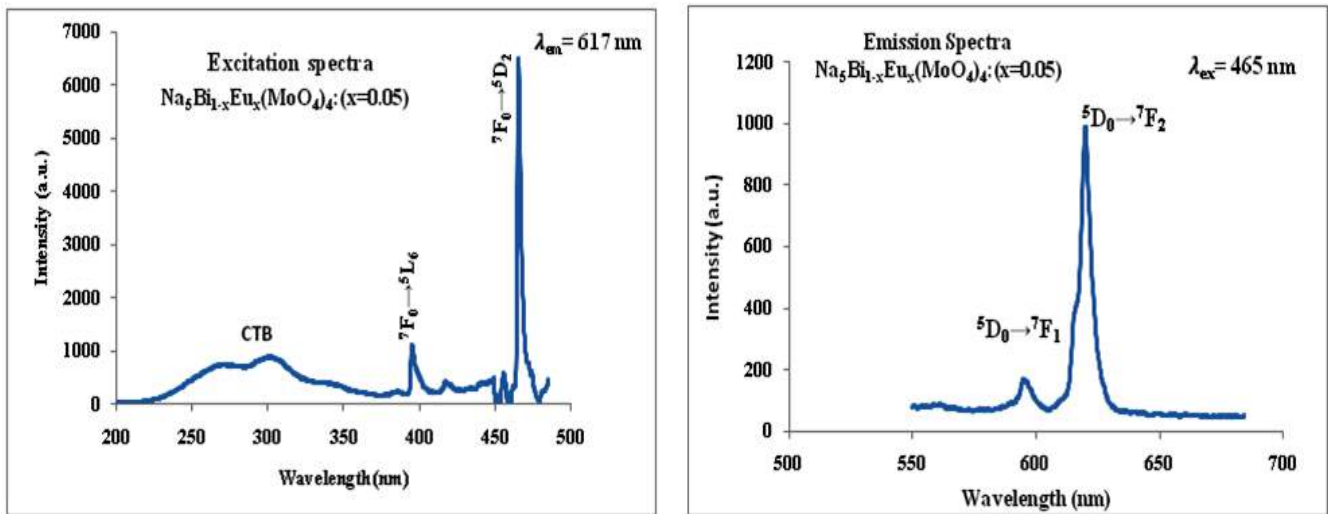
Fig. (2) Photoluminescence spectrum of Eu^{3+} activated Na$_5$Bi$_{1-x}$Eu$_x$ (MoO$_4$)$_4$:(x=0.05) Phosphor
(a) Excitation spectra of Na$_5$Bi$_{1-x}$Eu$_x$ (MoO$_4$)$_4$:(x=0.05) for 617 nm emission
(b) Emission Spectra of Na$_5$Bi$_{1-x}$Eu$_x$ (MoO$_4$)$_4$:(x=0.05) for 465 nm excitation.

The excitation band of Eu^{3+} PL in R$_5$Bi(MoO$_4$)$_4$(R=K, Na) with peak position near 300 nm can be tentatively ascribed to O→ Eu^{3+} CT transitions. The spectral position of this band corresponds to positions the CT excitation bands of the Eu^{3+} PL usually observed in the molybdate hosts. The emission spectra of R$_2$Bi$_{0.95}$(MoO$_4$)$_4$:0.05Eu^{3+} (R = K, Na) samples doped with 5% Eu^{3+} under 465 nm excitation are depicted in Fig.2(a) and 2(b). The strongest emission lines located at 617nm are ascribed to the $^5D_0$ →$^7F_2$ transition. The intensity of lines originating from $^5D_0$→$^7F_1$ (595 nm) is much weaker if compared to $^5D_0$→$^7F_2$ transition. $^5D_0$→$^7F_2$ is an electric dipole transition, [12,13] which requires a lower symmetry on the respective Eu^{3+} sites.

It is known that the emission of Bi^{3+} ions at low temperatures, originates from $^3P_0$→$^1S_0$ transitions. At higher temperatures the emission occurs mainly from the higher level $^3P_1$ and transition $^3P_1$→$^1S_0$ becomes allowed due to spin-orbit coupling of $^3P_1$ and $^1P_1$ states. Generalizing the data on the luminescence properties of Bi^{3+} ions in oxygen coordination we can note that the spectral position of the PL bands depends on number of

the oxygen ions in the nearest surrounding, the symmetry of this surrounding, and the presence of defects, first of all the oxygen vacancies in it. Dependence between these structural characteristics and Stokes shift of luminescence was found too [14]. Analysis of this dependence leads to the conclusion that the described above emission components should be attributed to the transitions in Bi^{3+} ions in polyhedral oxygen coordination - [BiO$_8$]^{13} -groups.

The bismuth ions in K$_5$Bi(MoO$_4$)$_4$ and Na$_5$Bi(MoO$_4$)$_4$ hosts have eight oxygen's in the nearest surrounding form irregular 8-vertex polyhedra BiO$_8$. However, three nonequivalent positions of Bi ions exist in K$_5$Bi(MoO$_4$)$_4$ and Na$_5$Bi(MoO$_4$)$_4$ lattice, and each of them is characterized by a specific geometric structure of BiO$_8$ polyhedron [14, 15]. At the same time, it is well known that spectral properties of Bi^{3+}-related emissions in molybdate hosts strongly depend on the configuration of the nearest oxygen surrounding [16]. Taking into account these facts, two spectral components of K$_5$Bi(MoO$_4$)$_4$ and Na$_5$Bi(MoO$_4$)$_4$ emission can be tentatively attributed to the emission

of the Bi^{3+}-related centers which originate from three nonequivalent lattice positions of the bismuth ions.
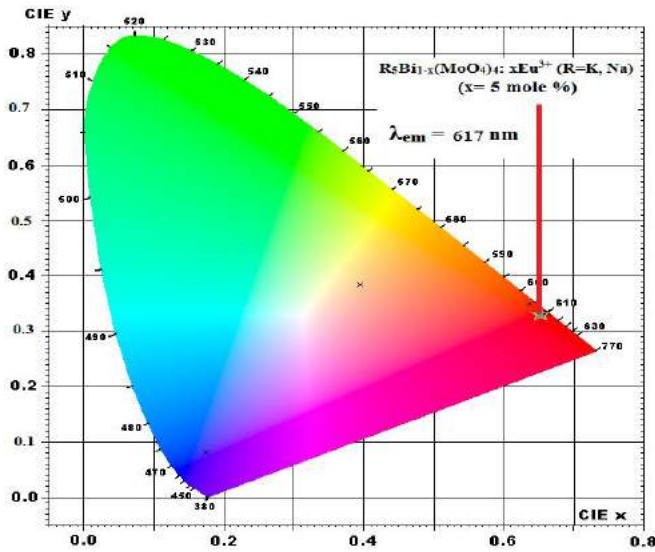
Fig. (3): CIE chromaticity diagram for
$R_2Bi_{0.95}(MoO_4)_4$:$0.05Eu^{3+}$ (R = K, Na) phosphor.

Fig. (3) shows the CIE chromaticity diagram for the emission spectra of $R_2Bi_{0.95}(MoO_4)_4$:$0.05Eu^{3+}$ (R = K, Na) phosphors. The CIE chromaticity coordinates (x, y) of the $R_2Bi_{0.95}(MoO_4)_4$:$0.05Eu^{3+}$ (R = K, Na) phosphors upon 465 nm excitation wavelength lie at x = 0.678 and y = 0.322 which are very close to the standard chromaticity coordinate values of NTSC (x = 0.670, y = 0.330).Hence, the CIE diagram illustrates that the obtained phosphor particles show red emissions when excited by a single wavelength (λex=465 nm) and thus the obtained results confirm that the combustion method prepared $R_2Bi_{0.95}(MoO_4)_4$:$0.05Eu^{3+}$ (R = K, Na) phosphors is a promising red emitting components for white LEDs.

IV. CONCLUSION

In summary, Eu^{3+} doped Molybdate containing Bi compounds $K_5Bi(MoO_4)_4$, $Na_5Bi(MoO_4)_4$ were successfully synthesized under combustion method and photoluminescence properties were studied. Upon excitation with UV light and blue light, the as-prepared products show a strong red emission at 617 nm corresponding to $^5D_0 \rightarrow {}^7F_2$ transition of Eu^{3+}. Observed intrinsic PL mainly originates from the excitation transitions in Bi-oxygen polyhedrons followed by the related backward radiation transitions. Excitation energy transfer from the host to Eu^{3+} ions was observed for all investigated Eu-doped compounds. The Eu-doped samples at nUV and UV excitation reveal narrow lines of Eu^{3+} related emission grouped around the main lines peaking at 595 nm and 617 nm which originate from intra-configurational $4f_6$ transitions in Eu^{3+} ions (radiative transitions from the excited $^5D_0$ level to ^7F_J (J = 0, 1, 2, 3, 4) manifolds of the ground state). The results indicate that the Molybdate containing Bi compounds doped with Eu^{3+} phosphor is a promising candidate as a red component.

V. REFERENCES

[1]. C. Shivakumara and R. Saraf, Opt. Mater. 42 (2015) 178.

[2]. N. Zhang, D. J. Wang, L. Li, Y. S. Meng, X. S. Zhang and N. Ming, J. Rare Earth. 24 (2006) 294.

[3]. C. S. Guo, J. Xu, S. F. Wang, L. Li, Y. Zhang and X. C. Li, Cryst. Eng. Commun. 14 (2012) 3602.

[4]. E. Vila, J. E. Iglesias, J. Galy and A. Castro, Solid State Sci. 7 (2005) 1369.

[5]. T. T. Fang and T. F. Ko, J. Am. Ceram. Soc. 86 (2003) 1453.

[6]. R. B. Licht, D. Vogt and A. T. Bell, J. Catal. 339 (2016) 228.

[7]. M.Voda, R.Balda, I.Saez de Ocariz et al., J. Alloys Compd., 275-278, 214 (1998).

[8]. H.Canibano, G.Boulon, L.Palatella et al., J. Luminescence, 102-103, 318 (2003).

[9]. S. X. Yan, J. H. Zhang, X. Zhang, S. Z. Lu, X. G. Ren, Z. G. Nie, and X. J. Wang, J. Phys. Chem. C 111, 13256 (2007).

[10]. Y. Jin, J. H. Zhang, S. Z. Lu, H. F. Zhao, X. Zhang, and X. J. Wang, J. Phys. Chem. C 112, 5860 (2008).

[11]. Y. G. Su, C. F. Du, Q. Y. Jia, L. Lv, Q. L. Liu, and X. J. Wang, J. Nanosci. Nanotechnol. 11, 9855 (2011).

[12]. G. Blasse and B. C. Grabmaier, Luminescent Materials, SpringerVerlag, Berlin, 1994.

[13]. W. M. Yen, S. Shionoya and H. Yamamoto, Phosphor Handbook, CRC Press/Taylor and Francis, Boca Raton, 2007.

[14]. G. Blasse, A. C. van der Steen, Solid State Comm., 31, 993 (1979).

[15]. Zatovsky, K. Terebilenko, M. Slobodyanik et al., J. Solid State Chem., 180, 3351 (2007).

[16]. B. Romero, S. Bruque, M. A. G. Aranda, J. E. Iglesias, Inorg. Chem;33, 1869 (1994).

[17]. C. Timmermans, G. Blasse, J. Solid State Chem., 52, 222 (1984).

Optically Stimulated Luminescence (OSL) properties of CaF$_2$: Ce phosphor for radiation dosimetry

C.B. Palan[1*], A.O. Chauhan[2], S. R. Jaiswal[3], S.K.Omanwar[4]

[*1]Department of Physics, Bapumiya Sirajoddin Patel Arts, Commerce and Science College Pimpalgaon Kale Ta. Jalgaon Jamod, Dist Buldhana, Maharashtra, India

[2]Department of Physics, Vidya Bharti Mahavidyalaya Amravati, Maharashtra, India

[3]Department of Physics Shri R.L.T. College of Science, Akola, Maharashtra, India

[4]Department of Physics, Sant Gadge Baba Amravati University, Amravati, Maharashtra, India

ABSTRACT

OSL technique is a now well-developed for its application in radiation dosimetry. Antonov Romanovskii *et al.* were firstly suggested use of OSL for personal dosimetry. However compared to thermoluminescence (TL) technique, Optically Stimulated Luminescence (OSL) is becoming more popular in radiation dosimetry. The polycrystalline CaF$_2$:Ce phosphor was successfully synthesized via Reactive Atmosphere Process (RAP). The structural properties of prepared phosphors were evaluated X-ray diffraction (XRD) technique. The XRD pattern of prepared phosphor well match with ICDD (International centers for diffraction data) file and synthesis methods were not affected on XRD pattern. The CaF$_2$:Ce^{3+} phosphor show good CW-OSL response under γ irradiation. The CW-OSL decay pattern of prepared CaF$_2$:Ce^{3+} phosphor is similar to the CW-OSL decay pattern of commercially available α-Al$_2$O$_3$:C phosphor. The photoluminescence (PL) excitation and emission spectra were observed at 305 nm and 338 nm, respectively. The effective atomic number (Z$_{eff}$) of CaF$_2$:Ce^{3+} is 16.3 and the phosphor is a candidate for radiation dosimetry.

Keywords : Reactive Atmosphere Process, Γ Irradiation, Effective Atomic Number, Caf$_2$:Ce^{3+} Phosphor.

I. INTRODUCTION

The OSL is one of the class of measurements known as stimulated phenomena. Such phenomena may be stimulated thermally (thermally stimulated phenomena or TSP) or optically (optically stimulated phenomena or OSP).

The use of OSL for radiation dosimetry was first suggested in 1955 by Antonov Romanovskii *et al.* [1]. It was later used by Braunlich *et al.* (1965) and Sanborn and Beard (1965) [2, 3]. The OSL technique had not been used widely in radiation dosimetry until 1965, because of the lack of superior OSL materials. In 1990 Akselrod *et al.* reported TL properties of α-Al$_2$O$_3$:C crystal and found that TL sensitivity of α-Al$_2$O$_3$:C crystal was 50 times than LiF:Mg,Ti phosphor. Also α-Al$_2$O$_3$:C crystal showed excellent dosimetry properties such as low fading, dose threshold (μGy), a single peak at 460 K, emission band at 420 nm [4].

The OSL technique brought attention of scientific community for personnel dosimetry after the development of α-Al$_2$O$_3$:C because of its excellent OSL

properties and introduction of the pulsed OSL (POSL) method [5, 6]. The α-Al$_2$O$_3$:C crystal was mainly grown by Czochralski method in Landauer, Inc. Kulkarni *et al.* prepared α-Al$_2$O$_3$:C phosphor in presence of graphite and this approach is an alternative method for obtaining dosimetry grade α-Al$_2$O$_3$:C [7]. However is still limited to artificially grown Al$_2$O$_3$:C phosphor and some problem in synthesis method reported by Dhabekar et al. [8].

Several efforts have been made to prepare other promising OSL materials, like Li$_2$B$_4$O$_7$:Cu-Ag [9], CaB$_4$O$_7$:Ce [10], LiMgPO$_4$:Tb-B [11], CaSO$_4$:Ce [12], Li$_3$PO$_4$:Tb^{3+} [13], LiBaPO$_4$:Tb [14], KMgPO$_4$:Tb [15], CaSiO$_3$:Ce [16], LiCaPO$_4$:Ce [17], NaCaPO$_4$:Ce [18], KCaPO$_4$:Ce [19], MgB$_4$O$_7$:Ag [20] KSrPO$_4$:Eu [21], SrB$_4$O$_7$:Eu [22], CaSO$_4$:Ce [23], SrSO$_4$:Eu [24], MCaPO$_4$:Ce [25]. In the present report we developed CaF$_2$:Ce phosphor via Reactive Atmosphere Process (RAP) for radiation dosimetry application.

II. EXPERIMENTAL

The polycrystalline CaF2:Ce3+ phosphor was successfully synthesized by using Reactive Atmosphere Process (RAP) [26]. Phase purity of the final products was checked by X-ray diffraction (XRD) using a Rigaku miniflex II diffractometer with Cu Kα (λ= 1.5405 Å) operating at 5 kV. Irradiation of samples was performed at room temperature using a calibrated γ (60Co) source at Department of chemistry of RTM University, Nagpur. The dose rate was 0.3712KGy/hr. The OSL measurements were carried out using PC CONTROLLED TL/OSL-1008 reader. The PL and PL excitation (PLE) spectra were measured on (Hitachi F-7000) fluorescence spectrophotometer with a 450W xenon lamp in the range of 200-450 nm with spectral slit width of 1 nm and PMT voltage at 700V and room temperature.

III. RESULTS AND DISCUSSION

3.1 XRD (X-ray diffraction) Pattern

In order to determine the phase purity, chemical nature of the phosphor, X-ray diffraction (XRD) analysis was carried out. Fig. 1 shows the XRD pattern of CaF$_2$:Ce^{3+} phosphor along with the standard XRD pattern (International Centre for Diffraction Data (ICDD) Card no. 00-004-0864).
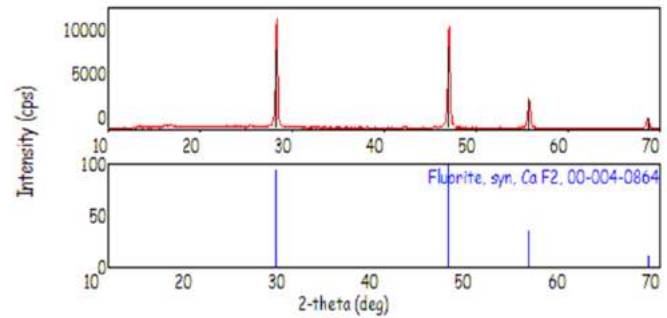
Fig. 1. XRD diffraction patterns of CaF$_2$:Ce^{3+} phosphor compared with the ICDD file with card no. 00-004-0864.

3.2 Photoluminescence (PL) Properties

The excitation and emission spectra of CaF$_2$:Ce^{3+} phosphor is shown in Fig. 2. The excitation and emission spectra were observed at 338 and 305 nm, respectively.
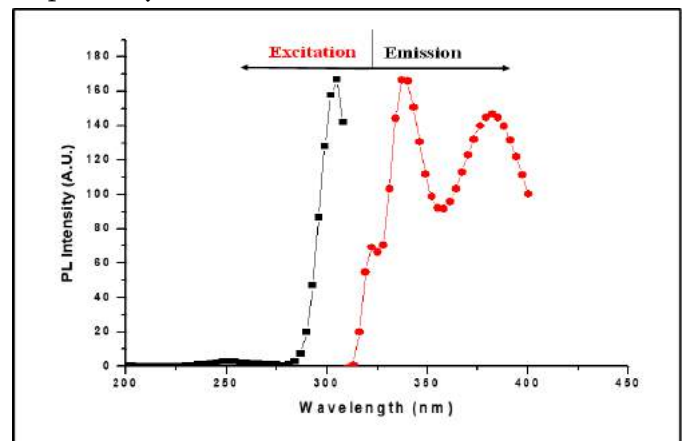
Fig. 2 Excitation and Emission spectra of CaF$_2$:Ce^{3+}phosphor

3.3 Optically stimulated luminescence (OSL)

The sample was studied for its Continuous-wave OSL (CW-OSL) response using blue LED stimulation (470 nm). The CW-OSL response of $Ca_{(1-x)}F_2:Ce^{3+}$ (X=0.01,0.02) under γ irradiation was shown in Fig 3. The CW-OSL decay pattern of prepared $CaF_2:Ce^{3+}$ phosphor is similar to the CW-OSL decay pattern of commercially available α-Al_2O_3:C phosphor.
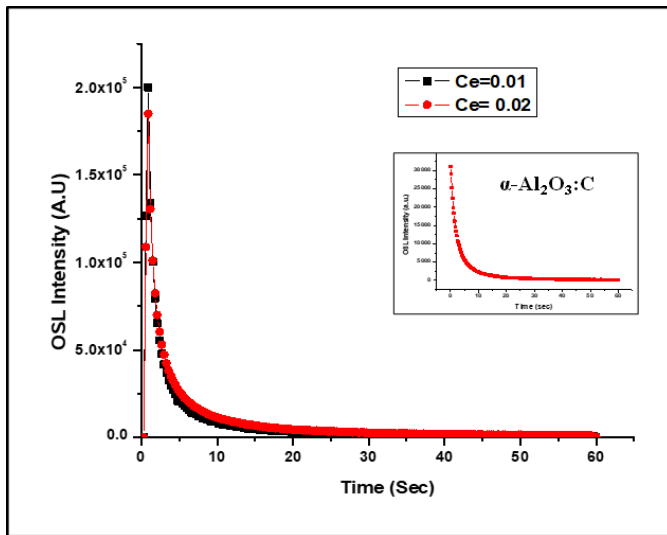
Fig. 3. CW-OSL responsed of $Ca_{(1-x)}F_2:Ce^{3+}$ phopshors under γ irradiation

IV. CONCLUSION

In this report $Ca_{(1-x)}F_2:Ce^{3+}$ (X=0.01,0.02) phosphor was synthesized via Reactive Atmosphere Process (RAP) and discussed its OSL and PL properties. The X-ray diffraction patterns well match with ICDD card number 00-004-0864. The PL excitation and emission spectra of prepared $Ca_{(1-x)}F_2:Ce^{3+}$ were observed at 305 and 338 nm, respectively. The CW-OSL measurements were carried out under the blue stimulation at λ = 470 nm and The OSL decay patterns of the $Ca_{(1-x)}F_2:Ce^{3+}$ phosphor were faster than the OSL decay patterns of the a- Al_2O_3:C (BARC) phosphor. The effective atomic number (Z_{eff}) of prepared CaF_2:Ce phosphor is 16.3 and phosphor show excellent CW-OSL response under γ irradiation. Hence, prepared $Ca_{(1-x)}F_2:Ce^{3+}$ phosphor can be applicable for radiation dosimetry.

V. REFERENCES

[1]. V. V. Antonov-Romanovskii, I. F. Keirum-Markus, M. S. Poroshina, Z. A. Trapeznikova Conference of the Academy of Sciences of the USSR on the Peaceful Uses of Atomic Eenrgy, Moscow, USAEC Report - AEC-tr-2435 (Pt.1), (1955) 239.

[2]. P. Braunlich, D. Schafer, A. Scharman Proc. First Int. Conf. Lumin. Dosim. Stanford, USAEC (1965) 57.

[3]. E. N. Sanborn, E. L. Beard Proc. First Int. Conf. Lumin. Dosim. Stanford, USAEC (1965) 183.

[4]. M. S. Akselrod, S. W. S. McKeever Radiat. Prot. Dosim. 81 (1999) 167.

[5]. M. S. Akselrod, V. S. Kortov, D. J. Kravetsky, V. I. Gotlib Radiat. Prot. Dosim. 32 (1990) 15.

[6]. S. W. S. McKeever, M. S. Akselrod, B. G. Markey Radiat. Prot. Dosim. 65 (1996) 267.

[7]. M. S. Kulkarni, D. R. Mishra, K. P. Muthe, A. Singh, M. Roy, S. K. Gupta, S. Kannan Radiat. Meas. 39 (2005) 277.

[8]. B. Dhabekar, S.N. Menon, E. Alagu Raja, A.K. Bakshi, A.K. Singh, M.P. Chougaonkar, Y.S. Mayya, Nuclear Nucl Instrum. Methods Phys. Res. B. 269, (2011) 1844

[9]. C.B. Palan, A.O. Chauhan, N.S. Sawala, N.S. Bajaj, S.K. Omanwar Optik-International Journal for Light and Electron Optics 127, (2016) 6419

[10]. C.B. Palan, K.A. Koparkar, N.S. Bajaj, A. Soni, S.K. Omanwar Journal of Materials Science: Materials in Electronics 27, (2016) 5600

[11]. N.S. Bajaj, C.B. Palan, K.A. Koparkar, M.S. Kulkarni, S.K. Omanwar Journal of Luminescence 175, (2016) 9

[12]. S.K. Omanwar, C.B. Palan Journal of Materials Science: Materials in Electronics 29, (2018) 7388

[13]. C.B. Palan, N.S. Bajaj, S.K. Omanwar Bulletin of Materials Science 39, (2016) 1619

[14]. C.B. Palan, N.S. Bajaj, A. Soni, M.S. Kulkarni, S.K. Omanwar Bulletin of Materials Science 38, (2015) 1527

[15]. C.B. Palan, N.S. Bajaj, A. Soni, S.K. Omanwar Journal of Luminescence 176, (2016) 106

[16]. C.B. Palan, K.A. Koparkar, N.S. Bajaj, S.K. Omanwar Materials Letters 175, (2016) 288

[17]. C.B. Palan, S.K. Omanwar C.B. Palan, S.K. Omanwar Journal of Luminescence 178, (2016) 340

[18]. C.B. Palan, S.K. Omanwar Research on Chemical Intermediates, 43, (2017) 4043

[19]. C.B. Palan, K.A. Koparkar, N.S. Bajaj, A. Soni, S.K. Omanwar Research on Chemical Intermediates 42, (2016) 7637

[20]. C.B. Palan, A.O. Chauhan, N.S. Sawala, N.S. Bajaj, S.K. Omanwar International Journal of Luminescence and applications 5, (2015) 408

[21]. C.B. Palan, N.S. Bajaj, S.K. Omanwar AIP Conference Proceedings 20474, (2016) 1728

[22]. C.B. Palan, N.S. Bajaj, S.K. Omanwar Materials Research Bulletin 76, (2016) 216

[23]. S.K. Omanwar, C.B. Palan Journal of Materials Science: Materials in Electronics 29 (2018) 7388.

[24]. C.B. Palan, N.S.Bajaj, S.K. Omanwar St Petersburg Polytechnical University Journal Physics and Mathematics 1, (2015) 410

[25]. C.B. Palan, S.K. Omanwar Optik 127 (2016) 7137

[26]. P. D. Belsare, C. P. Joshi, S. V. Moharil, S. K. Omanwar AIP Conf. Proc. 1675, 020015-1–020015-4; doi: 10.1063/1.4929173

Ultrasonic Investigation of Aqueous Ascorbic Acid in Koh At Temperature 308.15k

V. G. Dudhe

Department of Physics, Shri Shivaji Arts, Commerce and Science College, Rajura , Dist-Chandrapur, Maharashtra, India

ABSTRACT

For the study of molecular interaction of aqueous ascorbic acid in KOH solution using ultrasonic at temperature 308.15K, we measure three impartment parameters that are ultrasonic velocity (U), density (ρ) and viscosity (η). The measurement of ultrasonic velocity were carried out by using the ultrasonic pulse eco overlap (PEO) technique at frequency 5 MHz. The measurement of density has been carried out by using hydrostatic plunger method and viscosity by Oswald's viscometer. The temperature 308.15K have been kept constant using thermostat by circulating water. Experimental data have been used to calculate the thermo-acoustical parameters such as adiabatic compressibility (β), acoustic impedance (Z), free length (L_f), free volume (V_f) , wada's constant (β_m) and Rao's constant (R). These parameters   have been used to give the interpretations of solute- solvent interaction of aqueous ascorbic acid and KOH molecules. This study also shows the nature of molecular interaction and complex formation in the given solution. It also provides important information regarding molecular properties of a mixture of solute and solvent.

Keywords : Ultrasonic velocity, adiabatic compressibility, free volume, Wada's constant, Rao's constant and ascorbic acid.

I. INTRODUCTION

Ultrasonic method are based either on the determination of the characteristics of propagation (velocity or attenuation) or by the measurement of the reflection coefficients. In the ultrasonic based experimental devices, the measurement of the velocity and attenuation during the propagation allow to determine the physical properties of the medium.

The ultrasonic velocity, density, viscosity and other thermo acoustical parameters are very useful and helpful to study the nature of intermolecular forces in liquid mixtures and also give idea about association, dissociation and complex formation in a given mixture. [1-4]

Ascorbic acid is a colorless and water soluble vitamin. It is found in many plants and animals. Among plants, it is present in all fresh fruits and vegetables like tomatoes, melons, raw cabbage and green pepper. New potatoes contain relatively large amount of vitamin C. It is found in human milk is nearly 3 to 4 times more than cow's milk. However vitamin C is absent in fish, fats and oils [5-8]. The structure of ascorbic acid was established mainly by Haworth. The chemical formula of ascorbic acid is C6H8O6 and its molecular weight is 176.13. The structure of ascorbic acid is.
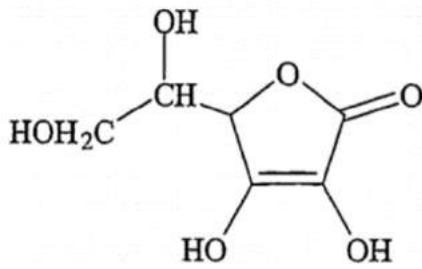
II. METHODS AND MATERIAL

The aqueous ascorbic acid solution (0.1M) was prepared using double distilled water. The solution of different concentration was prepared using 0.1M KOH solvent. The ultrasonic velocity for different concentration of aqueous ascorbic acid with KOH solutions measurement were carried out with a highly versatile and accurate 'pulse echo overlap technique (PEO) method by using automatic ultrasonic recorder (AUAR-102) and frequency counter. The frequency of the pulses was kept at 5MHz. The density and viscosity were measured using hydrostatic plunger method and Oswald's viscometer respectively. Temperature 308.15K is maintained using thermostatically controlled water circulation system with accuracy of 0.50C. The other thermo-acoustical parameters such as acoustic impedance, adiabatic compressibility, free length, free volume, Wada's constant and Rao's constant ware evaluated using ultrasonic velocity, density and viscosity. The formulae for calculation of various thermo-acoustical parameters are as fallows [9].

[1]. Ultrasonic velocity: $u = 2d / t$

   Where,   d = Separation between   transducer & reflector

   t = Traveling time period of   ultrasonic wave

[2]. Density $\rho = \left(\dfrac{W_a - W_1}{W_a - W_w}\right) \times \rho_w$

   Where, W_a = Weight of the plunger in air

   W_1 = Weight of the plunger in the experimental liquid

   W_w = Weight of the plunger in water

   ρ_w = Density of water

[3]. Viscosity $\eta = \dfrac{\rho \times t_1}{\rho_w \times t_w} \times \eta_w$

   Where, t_1 = Flow Time of experimental liquid

   t_w = Flow Time of water

   η_w = Viscosity of water

[4]. Adiabatic Compressibility: $\beta = [1 / u^2 \rho]$

[5]. Acoustic impedance : $Z = u \cdot \rho$

[6]. Intermolecular free length: $(L_f) = \dfrac{k}{u \, \rho^{\frac{1}{2}}}$

   Where, k = Jacobson's constant = $(93.875 + 0.345T) \times 10^{-8}$ (T is temperature)

[7]. Free volume : (V_f) = $M_w u / k \eta$

   Where,   k = Time independent constant = 4.28×10^9

   M_w =   molecular weight of solution

[8]. Wada's Constant : $(\beta_m) = (M_w / \rho) \times \beta^{-1/7}$

[9]. Rao's Constant $(R) = (M_w / \rho) \times u^{1/3}$

Table no. 1

Concentration	Ultrasonic Velocity (u) cm s^{-1}	Density (ρ) g cm^{-3}	Viscosity (η) Centi poise	Adiabatic compressibility ($\beta \times 10^{-11}$) cm^2 dyne^{-1}	Acoustic impedance (Zx10^5) g cm^{-2} s^{-1}
0	152136	0.9982	0.7229	4.3283	1.5186
0.02	152503	0.9988	0.7203	4.3049	1.5232
0.04	152998	0.9994	0.7336	4.2745	1.5291
0.06	152610	1.0007	0.7289	4.2907	1.5272
0.08	152512	1.0012	0.7445	4.2941	1.5269
0.10	152525	1.0028	0.7431	4.2865hy	1.5295

Table no. 2

Concentration	Free length (L$_f$ x 10^{-11}) cm	Free Volume (V$_f$ X 10^{-8}) cm^3/Mole	Wada's constant (βm) cm$^{19/7}$/dyne$^{1/7}$	Rao's constant(R) cm$^{10/3}$/s$^{1/3}$
0	1.3167	1.8017	547.7697	967.1249
0.02	1.3131	1.7924	549.1654	969.6169
0.04	1.3085	1.7795	550.6970	972.3871
0.06	1.3109	1.7893	550.9898	972.6065
0.08	1.3115	1.7942	551.9597	974.2021
0.10	1.3103	1.7909	552.5293	975.0065

III. RESULTS AND DISCUSSION

The experimental data of ultrasonic velocity, density, viscosity, adiabatic compressibility and acoustic impedance of aqueous ascorbic acid with KOH at 308.15K, are recorded in table 1, and Intermolecular free length, free volume, Wada's constant and Rao's constant are given in table 2.

The variation of ultrasonic velocity and acoustic impedance with molar concentration are shown in figure (1) and figure (5). It is observed that ultrasonic velocity and acoustic impedance have non linear variations with increase in concentration having peak at 0.04 molar concentrations. Initially an increase in velocity with increase in molar concentration suggests increase in cohesive forces due to vitamin and KOH molecules interaction [10]. Then decrease in ultrasonic velocity after 0.04 molar concentration suggests breaking up of molecular bonds when the concentration of vitamin is more in the solution. This suggests the dissociation take place in the solution. When 0.01M KOH is added to aqueous ascorbic acid it form a induced dipole interaction with aqueous vitamin C and undergo association, But after 0.04 molar concentration dissociation take place because vitamin C is type of conjugate system hence it ultimately decomposed and undergo dissociation. The adiabatic compressibility has reverse trend as shown in figure (4).

Variation of density with molar concentration is shown in figure (2), which are increases after addition of vitamin in KOH solution. Increase in density due to the fact that numbers of vitamin molecules are added to the

solution increase with increase in vitamin concentration [11].

Figure (3) gives the variation of viscosity of aqueous ascorbic acid solution with the molar concentration. Variation of viscosity is non linear with increase in molar concentration, which indicate that there is existence of strong molecular interaction in between vitamin and KOH molecules. [12].

The variation of free length and free volume with concentration as showed in figure (6) and figure (7). Free length and free volume decreases first and after 0.04 molar concentration increases. This shows that initially there is association take place with increase in molar concentration and after 0.04 molar concentration dissociation take place [13].

The variation of Wada's constant and Rao's constant with concentration is shown in figure (8) and (9). It is observed that Wada's constant and Rao's constant increase with increasing molar concentration. This indicates that there is strong molecular interaction between solute and solvent molecules due to hydrogen bonding and ion-covalent interaction.

Fig 1: Variation of Ultra. Velocity with Conc.

Fig. 2 : Variation of Density with concentration
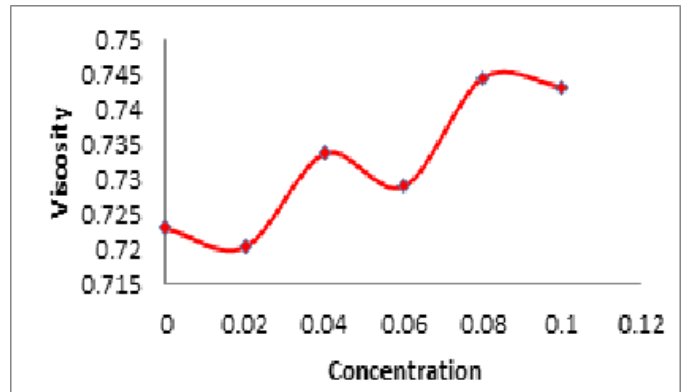
Fig 3: Variation of Viscosity with Concentration
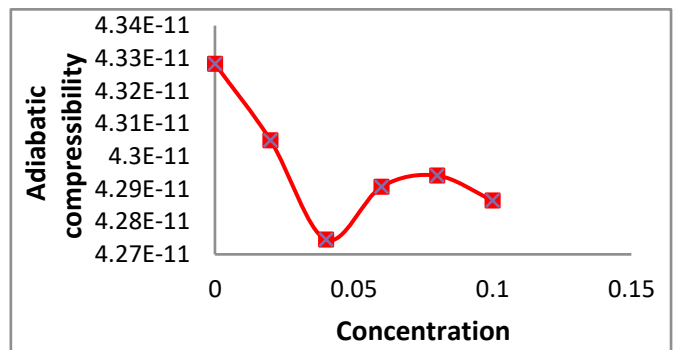
Fig 4; Variation of Adia. Compressibility with con.
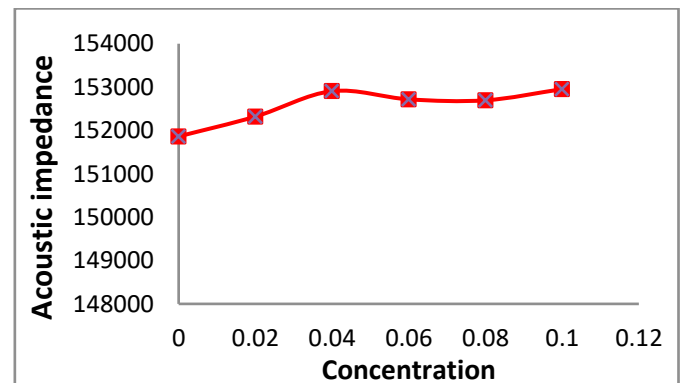
Fig 5 :Variation of Acoustic Impedance with conc.
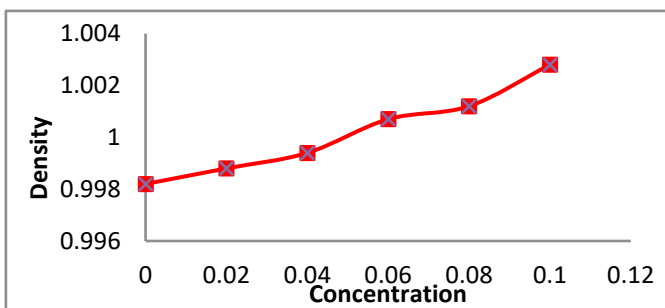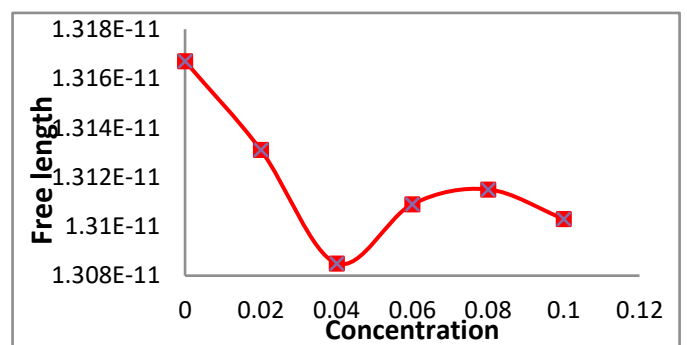
Fig6:Variation of Free length with conc.
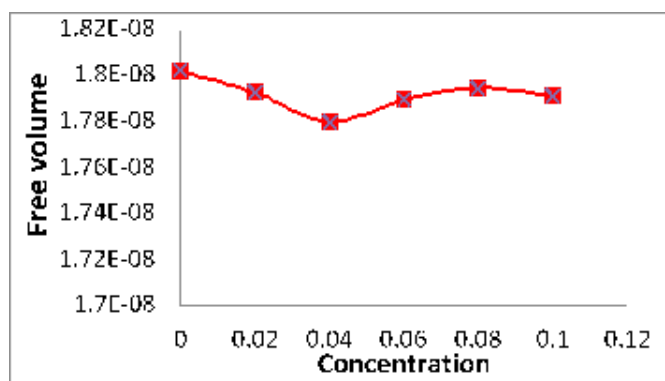
Fig 7: Variation of Free volume with Con.
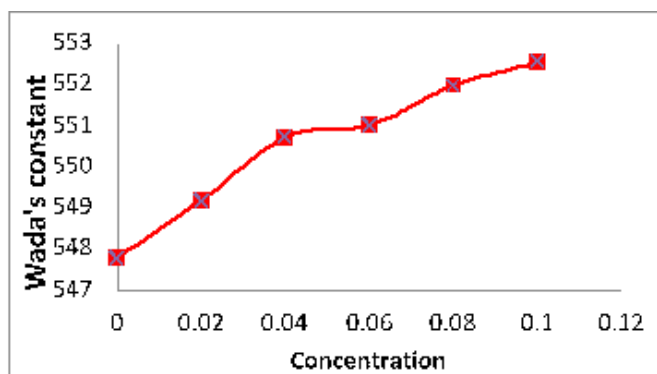
Fig. 8 : Variation of Wada's constant with con.
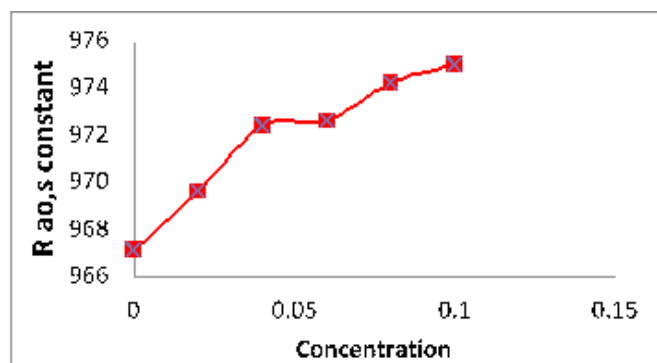
Fig 9: Variation of Rao's constant with Concentration

IV. CONCLUSION

Ultrasonic velocity, density and viscosity of different concentration of aqueous ascorbic acid with KOH are measured at 308.15K and thermo-acoustical parameters are calculated. The non linear variation in ultrasonic velocity and other acoustical parameters indicates that there is a strong molecular interaction between vitamin C and KOH molecules with complex formation take place at 0.04 molar concentrations.

V. REFERENCES

[1]. Anyranci. G, et al, J. Chem. Themodyn (2007), doi:10,1016/j 2007.04.009.

[2]. Tabhane.P.V, Chimankar.O.P., Dudhe.C.M, Tabhane.V.A, (2012), Lop Conf. series material sci & Engg. 42 012033, doi : 10.1088/1757-899A/42/012033.

[3]. Ali A.,Nain A. K ,(1996), Acoustic let. 19-53

[4]. Tabhane.P.V, Chimankar.O.P., Dudhe.C.M, Tabhane.V.A, (2012) Der Chemic Sinica, 3(4) 944-947.

[5]. Voet D. J., Voet J. G., Pratt C. W., Principle of biochemistry, (2008), 137.

[6]. Taylar T. V., Ascorbic acid supplementation in the treatment of pressure sores, 1974, 544-546.

[7]. Khalid Iqbal, Alam Khan and M. Muzaffar Ali Khan, Pakistan J. of nutrition, 3(1), (2004), 5-13.

[8]. Gaby S. K. and Singh V. N., Vitamin C, Vitamin intake and health, A scientific review, 1991.

[9]. Dudhe C.M. , Patil K.C.,(2012), Int.J. of Natural Product research, 2(4) 76-78.

[10]. Rao K., Rajulu A. V. and Naidu S. V. Journal Polym. Mater., 1989, 8,149.

[11]. Tabhane V. A., Agrawal S. and Rewatkar K.G., (2000) , J.Acous.soc. India vol. 28 no.. 1-4, 369-372.

[12]. Chimankar.O.P, Shrivas Ranjeeta, Tabhane.V.A,(2010), Archives of Applied science research. 2(6):285-289

[13]. Chimankar.O.P, Shrivas Ranjeeta, Chopade P S., Tabhane.V.A., (2011), J.Chem. Pharm Res, 3(3):579-586.

Synthesis and Photoluminescence Properties of White Emitting CaS Phosphor doped with Sn for Solid State Lighting

D. N. Game[1*], C. B. Palan[2], N. B. Ingale[3], S. K. Omanwar[4]

[1*]Modern Education Society's Cusrow Wadia Institute of Technology, Wadia Colleges Campus, Pune, Maharashtra, India

[2]B. S. Arts, Commerce and Science College, Pimpalgaon Kale, Jalgaon Jamod, Buldana, Maharashtra, India

[3] Prof. Ram Meghe Institutes of Technology and Research, Badnera, Amravati, Maharashtra, India

[4]Department of Physics, Sant Gadge Baba, Amravati University, Amravati, Maharashtra, India

ABSTRACT

We have synthesized Sn^{2+} doped CaS white emitting phosphors by carbo-thermal reduction method. In this method special requirement such as H_2S gas flow is not required as a source of sulphur and is comparatively easy method to prepare sulfides. The phase purity and surface morphology of prepared material was investigated by using X-ray diffraction (XRD) and Scanning Electron Microscope (SEM). Phosphor exhibit broad band excitation which has excellent spread over nUV as well as Blue region. Emission is in the form of characteristic broad band of Sn^{2+} covering entire regions of visible spectrum with HWFM of 60 nm. The XRD pattern of prepared phosphor well matches with ICDD (International center for diffraction data) file. Synthesized phosphor particles are of different sizes, with smooth surfaces, from less than 1 micron to few microns. CIE coordinates are (0.304, 0.361) under the excitation at 469 nm. The prominent excitation peaks located at 370 nm (nUV) and 469 nm (blue light i.e. 440–480 nm), which indicates that the phosphors are promising material for a color converter using blue LED as the primary light (pumping) source in phosphor converted white LED (pc wLED) for solid state lighting.

Keywords : Solid State Lighting, Carbo-Thermal Reduction Method, White Phosphor, Photoluminescence

I. INTRODUCTION

In the past few decades energy-efficient solid-state lighting and less power consuming white light emitting diodes (w-LEDs), which are regarded as the source of light in coming generation, used in display lighting sources and illuminating systems for domestic as well industrial applications. In present situation, white light-emitting diodes (w-LEDs), as the next generation of solid-state lighting, have attracted much attention due to their special advantages, such as high efficiency, long lifetimes, weak environmental impact, absence of mercury, short response times, applicability in final products of various sizes, and so on [1, 2]. In the case of the phosphor converted white light LEDs (pc wLED), the phosphor materials play an important role. For example, the most common and simple wLED source is combined of a blue-emitting InGaN chip and a Ce^{3+}

doped yttrium aluminium garnets (YAG:Ce³⁺) yellow phosphor [3], which is very stable and exhibits high luminescence efficiency. However, in some respects YAG:Ce³⁺ based dichromatic systems often suffer from reduced thermal stability and exhibit a poor color-rendering index (CRI) caused by the color deficiency in the red and blue-green of the phosphor. In principle, using a single white phosphor instead of phosphor blends could help to reduce some of this variability, which relies critically on the phosphor properties. In recent years, numerous efforts have been made to develop single-phase white-light-emitting phosphors for near-ultraviolet or blue excitation to solve the above challenges with certain achievements.

II. EXPERIMENTAL

2.1. Material and method

Polycrystalline samples of Sn2+ doped CaS phosphors for different dopant concentrations were prepared by two step synthesis technique of carbo-thermal reduction method starting from high purity AR grade nitrate precursors. In first step extremely fine sized snow white CaSO4:Sn2+were produced [4, 5]. In second step this sulphate in reduced by carbo-thermal reduction method at 750 0C for 3 h in reducing atmosphere produced by activated charcoal and then allowed to cool slowly to room temperature [6]. The fine sized soft powders of dull white body color CaS:Sn2+ phosphor were obtained.

2.2. Characterization

The prepared materials were characterized by powder XRD. Powder X-ray diffraction measurements were taken on Rigaku Miniflex II X-ray Diffractometer and compared with the ICDD file. The Surface morphology of the annealed particles was performed on Hitachi Field Emission Scanning Electron Microscope model S-4800. It is equipped with energy-dispersive X-ray spectroscopy (EDS) system that enables sample element analysis. The photoluminescence (PL) and PL excitation (PLE) spectra were measured on Hitachi F-7000 fluorescence spectrophotometer at room temperature. The parameters such as spectral resolution, width of the monochromatic slits (1.0 nm), photomultiplier tube (PMT) detector voltage and scan speed were kept constant throughout the analysis of samples. The color chromaticity coordinates were obtained according to Commission International de I'Eclairage (CIE).

III. RESULTS AND DISCUSSION

3.1. X-Ray Diffraction Patterns (XRD)

The XRD pattern of the as synthesized phosphors CaS:Sn2+ shows good agreement with standard ICDD Files No. 03-065-2926 of host matrix. Figure 1(a) shows that for different concentrations of Sn2+ XRD pattern remains unchanged indicating no other phase is formed and there no residue of precursor is present.
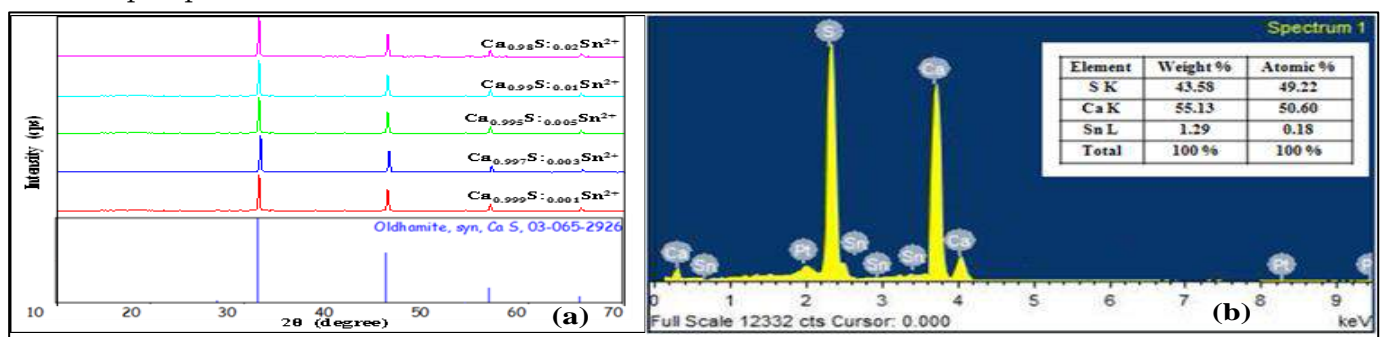
Figure 1: X-ray diffraction patterns with different Sn²⁺ concentrations (a) and EDS pattern (b) of as synthesized CaS:Sn²⁺ phosphor

3.2. EDS Patterns

The corresponding EDS spectrum as shown in Figure 1 (b) mainly composed of Ca and S atoms in appropriate proportion of elemental composition in prepared phosphors. No other impurity was detected except small amount of Sn indicating that Sn element is successfully doped in the prepared phosphors. In addition to these small peaks corresponding to Pt arises as platinum was used during sample preparation for scanning electron microscopy

3.3. Morphology study (SEM)

SEM images in Figure 4 (a) shows synthesized phosphor particles are of different sizes with smooth surfaces. Shape of particles is elongated and spherical with sizes from less than 1 micron to few microns which is a suitable size for fabrication of SSL devices [7].

3.4. Photoluminescence study

3.4.1. Energy level diagrams for Sn2+ doped alkaline earth sulfide phosphors

Schematic energy level diagrams for Sn2+ doped CaS are shown in Figure 2. An s2 ion, such as Sb3+, Pb2+, Bi3+ or Sn2+, has 1S0 ground state and sp excited states (3P0, 3P1, 3P2, 1P1) Figure 2 (a). The triplet states 3P0, 3P1, and 3P2 can be split owing to the spin–orbit interaction Figure 2 (c). The energies of these absorption peaks are usually dependent on the metal and are typically modified by the host matrix material. The 1S0→3P0 transition is forbidden and is therefore usually not observed in any optical spectra Figure 2 (b) [8].
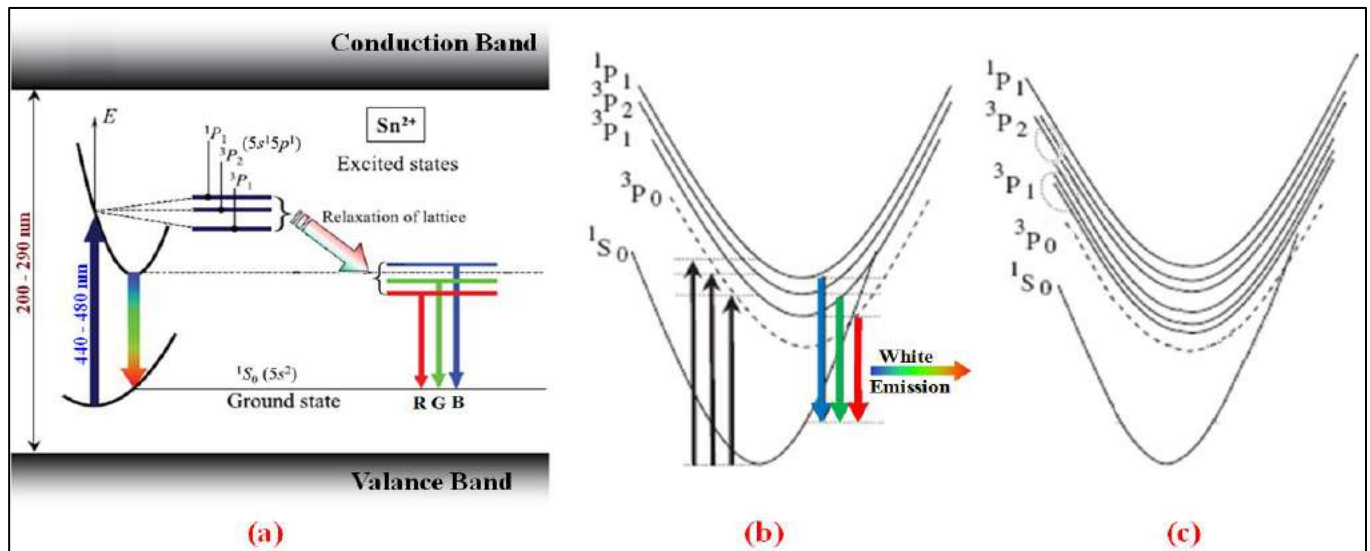
Figure 2: Schematic energy level diagrams for Sn²⁺ ions in CaS host

3.4.2. Combined Excitation and Emission spectra of CaS:Sn2+ phosphor

Combined excitation and emission spectrum of prepared phosphor is shown in Figure 3 (a). Photoluminescence properties CaS:Sn2+ can be explain in the view of Figure 2. The fundamental excitation band in CaS occurs at 200–290 nm was characterized as host excitation centered at 260 nm Figure 2 (a). Along with this band other bands due to 1S0 →3P1, 1S0 →3P2 and 1S0 →1P1 transitions of Sn2+ centers are present, in the order of increasing photon energy, with maximum intensity band centered at 469 nm [9] Figure 2 (a) and (b). The excited states in these transitions have triplet (3P1), doublet (3P2), and singlet (1P1) structures respectively Figure 2 (c).The high energy low intensity narrow excitation band due to singlet is in the range of 290 nm to 312 nm centered at 300 nm, moderate energy medium intensity band due to doublet structure has multiple peaks in the range of 312 nm to 423 nm with maximum intensity peak at 370 nm followed by low

energy high intensity band due to triplet structure again has multiple peaks from 423 nm onwards with highest intensity peak centered at 469 nm. The PL spectrum in of CaS:Sn2+ consists of moderate intensity multiple peak Blue and Green broad emission bands with high intensity single peak broad band centered at 568 nm in green-yellow region of visible spectrum

followed by very low intensity Red band located at 636 nm. These emission bands are traditionally assigned to energy levels arising from the Jahn–Teller effect on the triplet state of s2 ions in alkaline earth sulfides [9]. The experimental data in Figure 3 (a) clearly indicate that the observed luminescence in CaS is due to the Sn^{2+} center [Figure 2].
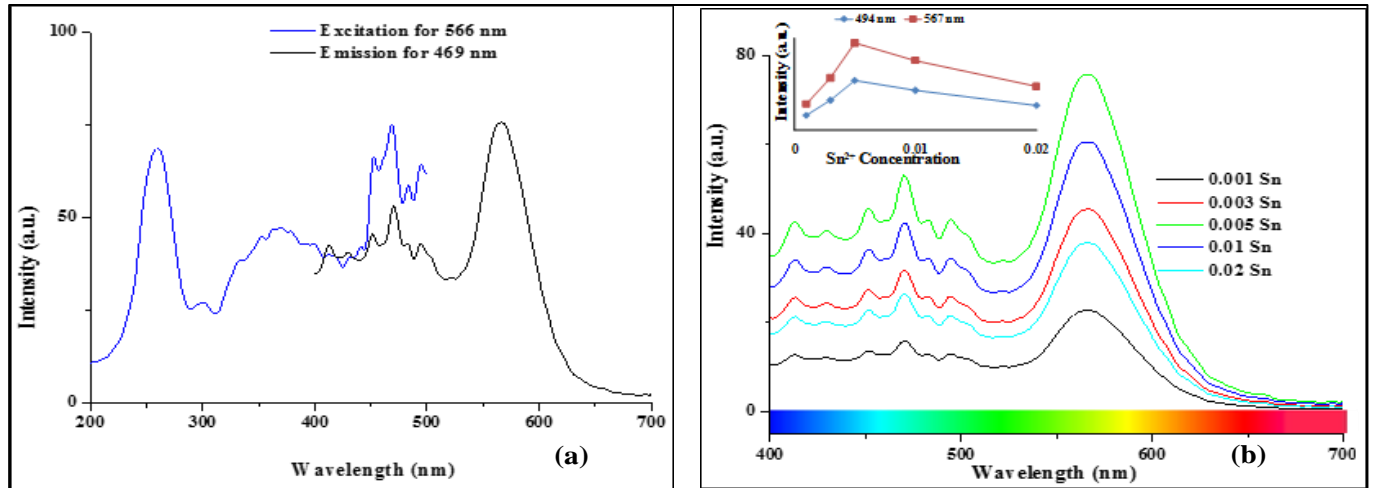
Figure 3: (a) The excitation and emission spectra and (b) effect of Sn^{2+} concentrations on emission of as synthesized CaS:Sn^{2+} phosphor, the inset shows relative luminescence intensity at 494 nm and 567 nm for different Sn^{2+}concentration

3.4.3. Effect of Sn2+ concentrations on emission intensity of CaS:Sn2+

For different concentrations of Sn2+ there is no change in shape and position of emission band except emission intensity [Figure 3 (b)]. Optimum concentration is 0.005 mole of Sn2+. The ratio (G/Y) of luminous intensities of green (494 nm) and greenish-yellow (567 nm) emission bands for different Sn2+ concentration is constant (0.57). The inset shows relative luminescence intensity at 494 nm and 567 nm as a function of Sn2+ concentrations.

3.5. Study of colour chromaticity of CaS:Sn2+

The chromaticity coordinates of CaS:Sn2+ phosphor have been calculated from its corresponding emission spectra monitored at 469 nm. They are (0.304, 0.361) falls in white region of CIE diagram. This point is in close proximity to standard white points D65 and E as shown in Figure 4 (b), corresponding to daylight and equal energy having correlated colour temperature

(CCT) 6500°K and 5400°K respectively , indicating better colour purity of the synthesized phosphor.

IV. CONCLUSION

The white emitting sulfide phosphors CaS:Sn^{2+} covering almost entire region except prominent red of visible spectrum with highest intensity emission bands centered at 567 nm and 496 nm respectively are successfully synthesized by carbo-thermal reduction method. The CIE coordinates of as prepared phosphors are (0.304, 0.361). The prominent excitation peak of phosphor is located at 469 nm (blue light i.e. 440–480 nm), which indicates that the phosphors are very suitable for a color converter using blue LED as the primary light source in pc wLED. When the phosphor will be excited using blue LED broad emission bands can be accomplished due to characteristic emissions of Sn^{2+} ion in the phosphor along with blue LED emission,

which when used as a pumping source. This will occurs because the absorption wavelength of Sn^2 ion in this phosphor will match with that of the LED blue emission. Therefore upon illumination with the LED blue light, the part of blue light is absorbed by the phosphor and rest will be emitted along with the other colour light emitted from the phosphors to realize better spectral properties. The obtained spectrum in

the present form will not result in good CRI due to lack of red component. This can be achieved either by blending these phosphors with that emits in red region or co-doping them with appropriate red emitting activator along with Sn^{2+}. Thus phosphor is promising phosphor to be used along with red emitting phosphors to obtain white light in pc wLED for solid state lighting.
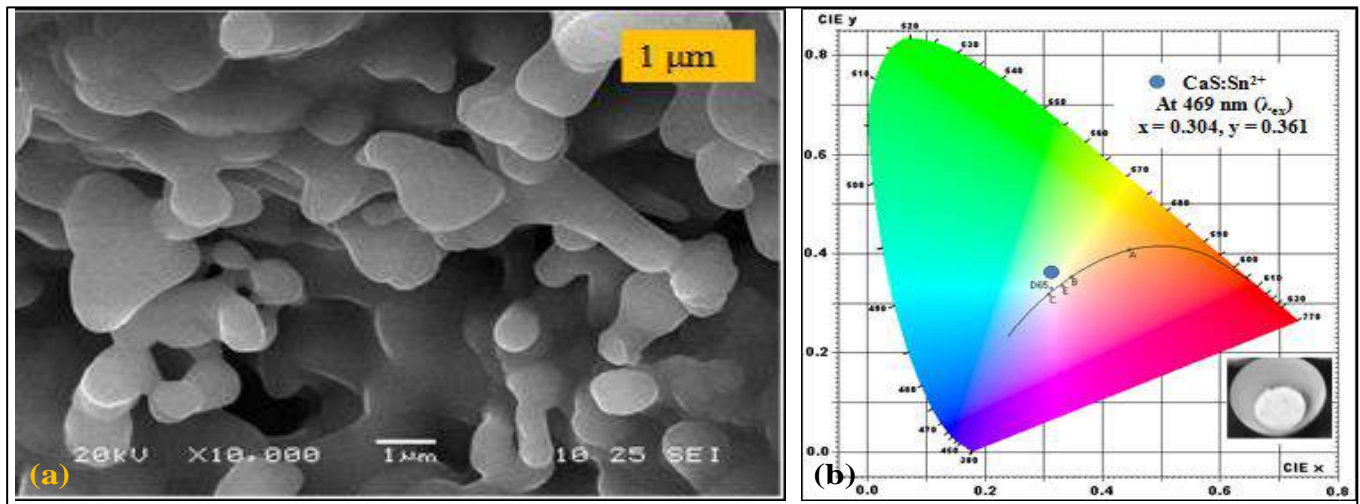
Figure 4: (a) SEM image and (b) CIE diagram of with image of as synthesized CaS:Sn^{2+} phosphor

V. ACKNOWLEDGMENTS

VI. REFERENCES

[1]. E. Radkov, R. Bompiedi, A.M. Srivastava, A.A. Setlur, C. Becker, Proc. SPIE, 5187 (2004) 171.

[2]. Z. C. Wu, J. Liu, W.-G. Hou, J. Xu and M.-L. Gong, J. Alloys Compd., 498 (2010)139.

[3]. J. S. Kim, P. E. Jeon, Y. H. Park, J. C. Choi, H. L. Park, G. C. Kim and T. W. Kim, Appl. Phys. Lett., 85 (2004) 3696.

[4]. N.B. Ingale, S.K. Omanwar, P.L. Muthal, S.M. Dhopte, V.K. Kondawar, T.K. Gundurao, S.V. Moharil, Radiat. Meas. 43, 1191(2008).

[5]. C.B. Palan, N.S. Bajaj, S.K. Omanwar, St. Petersb. Polytech.Univ. J.: Phys. Math. 1, 410 (2015).

[6]. D. N. Game, N. B. Ingale, S. K. Omanwar, Journal of Materials Science: Materials in Electronics, 28, 915–922 (2017).

[7]. B.K. Grandhea, V.R. Bandia, K. Janga, S.S. Kima, D.S. Shinb, Y.I. Leeb, J.M. Limb, T. Songc, J. Alloys Compd. 509, 7937 (2011).

[8]. M. Nagata, S. Okamoto, K. Tanaka, T. Sakai, A. Tamaki, Phys. Status Solidi (a), 206 (2009) 2613.

[9]. M. Kondo and S. Adachi, ECS J. Solid State Sci. Technol., 2 (2013) R9.

High Frequency Dielectric Properties of DMA with 1, 4-Dioxane using picosecond Time Domain Reflectometry

Shamsundar. S. Kadam

Department of Physics, N. W. College A. Balapur, Maharashtra, India

ABSTRACT

The Complex dielectric spectra $\varepsilon^*(\omega) = \varepsilon' - j\varepsilon''$ of binary mixture of N, N –dimethylaniline (DMA) with 1,4 Dioxane were obtained in the frequency range 10 MHz to 30 GHz using Time Domain Reflectometry (TDR) technique. The static dielectric constant (ε_0) and relaxation time (τ) have been obtained. On the basis of dielectric parameters intermolecular interaction are predicated.

Keywords : Time Domain Refelctometry, Complex Dielectric Spectra, Relaxation Time.

I. INTRODUCTION

The dielectric properties of a substance such as dielectric constant, dielectric loss, relaxation time have provided an insight into the structure of the molecules of the system. In liquids, the molecule has rotational freedom and its dispersion occurs at microwave frequency. Hence studying the dielectric properties at microwave frequency will reveal the dielectric relaxation of polar molecules and its variation with respect to the interaction with the neighbouring polar as well as non polar molecules. Deogaonkar & coworkers [1] found that aniline and N, N-dimethylaniline (DMA) form complexes with o-chlorophenol through hydrogen bonding at room temperature. In the present paper, the detail study of dielectric behaviour of N, N-dimethylaniline-1, 4 dioxane (DMA-DX) mixture in the frequency range of 10 MHz to 30 GHz using Time Domain Reflectometry (TDR) at temperature 25^0C. On the basis of dielectric parameters, intermolecular interaction and dynamics of molecules are discussed.

II. EXPERIMENTAL METHOD AND DATA ANALYSIS

The dielectric spectra were obtained by the time domain reflectometry (TDR) technique. The Tektronix model no. DSA8200 Digital Serial Analyzer sampling mainframe along with the sampling module 80E08 has been used for the time domain reflectometry (TDR). A repetitive fast rising voltage pulse with 18ps incident rise time was fed through coaxial line system of impedance 50 ohm. Sampling oscilloscope monitors changes in step pulse after reflection from the end of line. Reflected pulse without sample R_1 (t) and with sample R_x (t) were recorded in time window of 2ns and digitized in 2000 points.

The time dependent data were processed to obtain complex reflection coefficient spectra $\rho^*(\omega)$ over the frequency range from 10 MHz to 30 GHz as [2, 3].

$$\rho * (\omega) = \left(\frac{c}{j\omega d} \right) \left[\frac{p(\omega)}{q(\omega)} \right] \quad (1)$$

where $p(\omega) \,\&\, q(\omega)$ are Fourier transforms of [R_1 (t)-R_x (t)] and [R_1 (t) +R_x (t)] respectively, c is the speed of

light, ω is the angular frequency, d is the effective pin length and $j = \sqrt{-1}$. The complex permittivity spectra ε*(ω) was obtained from reflection coefficient ρ*(ω) by applying calibration method as described earlier [4].The dielectric permittivity ε′ and dielectric loss ε″ of DMA with1, 4 Dioxane at 25°C are shown in Figure. From dispersion plot it is observed that in DMA-DX system dielectric loss is independent of volume fraction of DX.
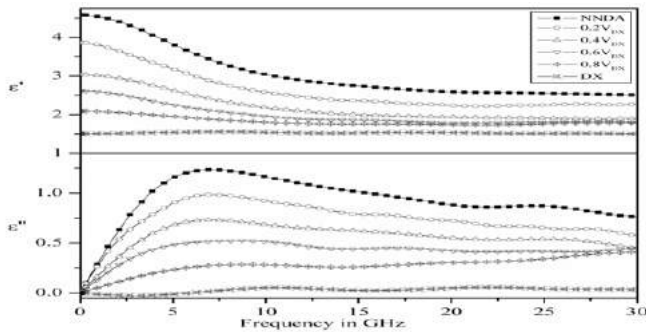
III. RESULTS AND DISCUSSION

The complex dielectric permittivity data were fitted to a Havriliak-Negami model using non linear least squares fit method in order to extract dielectric relaxation parameters with the following expression [5].

$$\varepsilon*(\omega) = \varepsilon_\infty + \frac{\varepsilon_0 - \varepsilon_\infty}{[1 + (j\omega\tau)^{1-\alpha}]^\beta} \qquad (2)$$

where ε*(ω) is complex permittivity at an angular frequencyω, ε0 is the static permittivity, ε∞ permittivity at high frequency, τ is the relaxation time, α is shape parameter representing symmetrical distribution of relaxation time and β shape parameter of an asymmetric relaxation curve. Equation (2) includes Cole-Cole (β=1), Davidson-Cole (α=0) [6], and Debye (α=0, β=1) relaxation models. The dielectric relaxation model for fitting dielectric parameters suitable for present systems is Davidson-Cole model. Therefore the complex permittivity spectra has been fitted in Davidson-Cole model with (α=0) and β (0 <β ≤ 1) as one of the fitting parameters along with ε0 &τ. The values of dielectric parameters ε0 and τ obtained from equation (2) for DMA-DX with volume fraction of DX at 250C are reported in table. The experimental

values of ε0 and τ are in good agreement reported earlier [7, 8]. It can be observed that ε0 decrease with increase in volume fraction of DX. The τ values are nearly constant upto 0.60 fraction of DX in DMA and after that decreases. The decrease in τ values indicates that number of dipoles decreases in the solution.

Vol. Frac. of DX	ε_0	τ
0.0	4.486(2)	21.01(3)
0.2	3.90(1)	21.67(24)
0.4	3.82(2)	21.48(40)
0.6	3.46(3)	21.43(59)
0.8	2.760(3)	16.42(26)
1.0	2.301(2)	7.2(20)

IV. CONCLUSION

The complex dielectric permittivity spectra of DMA with DX have been studied at 25⁰C, using time domain reflectometry technique in the frequency range 10 MHz to 30 GHz. The values of ε0 shows systematic change with increase in volume fraction of DX in the system. The τ values are nearly constant upto 0.60 fraction of DX in DMA and after that decreases. The decrease in τ values indicates that number of dipoles decreases in the solution.

V. REFERENCES

[1]. V.S.Deogaonkar, C.S.Adgaonkar, and S.N.Jajoo, Indian J.Pure and Appl.Phys. 20,617(1982).

[2]. C.E.Shanon, Proc.IRE, 37, 10(1949).

[3]. H.A.Samulan, Proc.IRE, 39, 175(1951).

[4]. A. C. Kumbharkhane, S. M. Puranik, and S. C. Mehrotra, J. Chem Soc. Faraday Trans., 87, 1569 (1991).

[5]. S.Havriliak, and S.Negami, J.Polymer Sci. C 14, 99(1966).

[6]. D.W.Davidson, and R.H.Cole, J. Chem.Phys. 18, 1484(1950).

[7]. V.A.Rana, and A.D.Vyas, J.Mol.Liquids, 102/1-3,379(2002).

[8]. CRC Handbook of Chemistry and Physics 87th ed., ed. D.R.Lide (CRCPress, 2006).

Measuring Diversity: Importance of Species Distribution by Using Mathematical Methods

Sunil N. Khade* , Priyanka B. Gaikwad

Department of Zoology Department of Mathematics P. N. College, Pusad, District Yavatmal, Maharashtra, India

ABSTRACT

The calculation done according to Shannon Wiener Diversity Index, quadrant method use for the calculation for the concentration of diversity, Wiener index showing varies according to different habitats, so calculation explore on the possibility of ecological value, The measurement of diversity of species of four sampling stations varies according to habitat such as mangrove habitat, rocky substrata, sandy shore, and muddy habitat, present data statistically analysis done given time period, so that the index is useful for practical applications.

Keywords : Diversity, Shannon Wiener Index.

I. INTRODUCTION

index of diversity' defined by Fisher are two measures of the degree of concentration or diversity achieved when the individuals of a population are classified into groups. Both are defined as statistics to be calculated from sample data and not in terms of population constants. The index of diversity has so far been used chiefly with the logarithmic distribution. It cannot be used everywhere, as it does not always give values which are independent of sample size; it cannot do so, for example, when applied to an infinite population of individuals classified into a finite number of groups [26].

The occurrence of diversity in sea grass beds, also at greater depth in the sea, they are more diverse obtained in the rocky intertidal zone along the coast, Sandy stones, inter tidal flats, mangrove areas [1]. Mangroves are one of the biologically diverse ecosystems in the world, rich in organic matter and nutrients and support

very huge biomass of flora and fauna [2]. An oysters, mussels and clams serve the nutritional needs of the coastal population they are good source of minerals, protein, and glycogen and easily digestible compared to other animal food [3]. In India, till today, 5,070 species of molluscs have been recorded of which, 3,370 are from marine [4]. The gastropods such as Sacred chank, *Trochus*, *Turbo* are exploited from the Indian marine region [5]. The present papers investigate the diversity of gastropod molluscs of mangrove, rocky coasts, sandy beach from study localities.

II. METHODS AND MATERIAL

2.1 The study area divided in four localities of Raigad district viz. [A]. Harihareshwar: (Rocky area) (Lat. 17°59.568" North and Long. 073°01.187" East). [B]. Lada: Muddy region (Lat. 18°01.686" North and Long. 073°01.752" East). [C]. Shrivardhan: Sandy beach (Lat. 18°02.556" North and Long.

073°00.598" East). [D]. Jivanabander: Rocky area (Lat. 18°03.062" North and Long. 072°59.944" East).

2.2 Live animals collected by handpicking including mangrove associated gastropod species during low tide. Five quadrates of nylon rope each 1-m² was prepared, randomly at each locality just over the bed. Twice in each season post-monsoon, winter and summer October 2015 to September 2016. Localities viz. I,II,III and IV. Soon after fishing were brought to the laboratory, the shells were brushed to clean the fouling biomass for accuracy of the measurement, then stocked in filtered seawater pumped in the laboratory from the estuaries for observation of movement, then specimens preserved in 70% alcohol for taxonomical identification of morphological characters, especially, lunal, umbo, operculum. Internal parts teeth, specimens identified by Zoological Survey of India, Kolkata.

III. RESULTS

3.1 According to quadrant method diversity noted i.e. C<IV (obtained umber of species), B<IV (obtained umber of spices), A<IV (obtained umber of spices) sites are varies from one another. At B has large swampy region with mangroves due to this reason species diversity is high. (A,B,C,D indicating name of sites)

According to Shannon Wiener Diversity Index

Name of the sites	No. of sample	pi=sample/sum	ln (pi)	pi*ln (pi)
A	21	0.31	-1.17	-0.362
B	12	0.17	-1.77	-0.300
C	03	0.04	-3.21	-0.128
D	29	0.43	-0.84	-0.361
	sum=67			Sum=-1.151

H= 1.151

$H_{max}= \ln(N) = \ln(4)=1.38$

Evenness = H/H_{max} = 1.151/1.38 =0.834

Result: Shannon diversity index (H) = 1.151

Evenness = 0.834
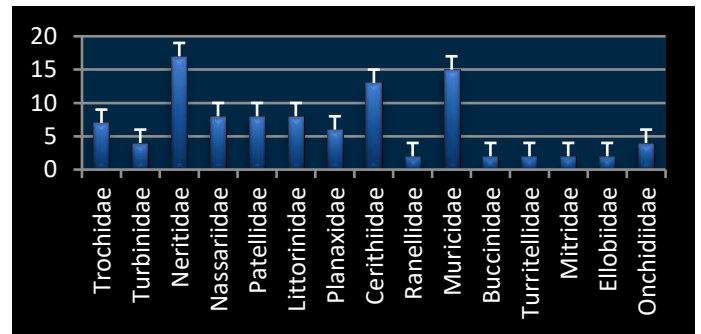
Fig. 1.Distribution of families of gastropod species from study sites.

3.2 According to "fig. 1". 4 is an indicates more diversity index showing on rocky habitats. The onchidiidae families with 02 species recorded in muddy habitats. The gastropod fourty nine spp, from fifteen families, five orders i.e. given in (Table 1). The data presented on diversity of ecological importance molluscs from muddy-mangrove, rocky as well as sandy habitats. Higher number of gastropods at site B-12, D-29, A-22, C-03 species were noted. The gastropods are playing a vital role in the homeostasis.

IV. DISCUSSION

4.1 The diversity of species from coastal sites varies significantly, the importance of ecology the relatively high temperature, high oxygen content, low wave energy and the semi-enclosed nature of the habitat. [6]. Dozens of mathematical indices have been proposed for this purpose, but these can provide contradictory results leading to misleading or incorrect conclusions about community's diversity [9]. The population density was at its peak in the month of November 2015 during post monsoon period. The mangroves support high density of every type of molluscan species especially,

Telescopium, Potamides, Natica, Nerita, and *Littorina* and *oysters.* [6].

4.2 The observation of these species populations in mangrove ecosystem is important to evaluate their condition [10].

4.3 The numerical abundance & biomass of molluscs can be equally impressive. The numerous investigation of mangroves associated molluscs in the world wide, thirty nine noted of gastropods in as Australian mangroves, [11]. Twenty three molluscs from mangroves in Hong Kong [12]. Fourty four sp., of Sematan mangrove forest of Malaysia noted [13]. A total account of Sundarban fifty six sp. of molluscs thirty one gastropods & twenty five bivalves [14]. Twelve bivalve & thirteen gastropods mangrove associated at Ratnagiri coast noted [15] thirty-nine gastropods from fifteen families from Raigad district coast noted [16]. Gastropods are typically one of the dominant, most conspicuous macrofauna in mangrove, and occupy wide range of ecological niches.

V. CONCLUSION

According to Shannon diversity index (H) = 1.151, Evenness = 0.834, number of obtained species is sum=67, and According to quadrant method diversity noted i.e. C<IV (obtained umber of species), B<IV (obtained umber of spices), A<IV (obtained umber of spices) sites of coast are varies from one another, data analysis showing at site B & D has greater commercial value & biodiversity importance, probably is influenced by their habitat & geographical condition. Site A & B probably have suitable habitat to support greater number of edible, commercial & ecological species diversity. However very little information is available on the gastropod biodiversity of mangroves. Hence, it is necessary to document the biodiversity of the group of threatened ecosystems. There in urgent need conservation & sustainable utilization of gastropod species.

VI. REFERENCES

[1]. Ramakrishna and A. Dey. Annotated checklist of Indian Marine Molluscs (Cephalopoda, Bivalve and Scaphopoda) Part-1. Rec.Zool.Surv.India, Occ. Paper no., 320:1-357. (Published by the Director, Zool.Surv.India, Kolkata).

[2]. Pawar R. Prabhakar, Molluscan Diversity in Mangrove Ecosystem of Uran (Raigad), Navi Mumbai, Maharashtra, West coast of India. Bull. Environ. Pharmacol. Life Sci. Vol. 1(6) May 2012: 55-59.

[3]. G. D. Suryavanshi, A.M.Shaikh and U.H.Mane: Impact of Zink on protein content of oyster Crassostrea cattuckensis from Ratnagiri coast, Department of zoology, Yogeshwari Mahavidyalaya, Ambajogai, Dist. Beed-431517. J. Ecotoxicol. Envriron. Monit. 22. (4), 323-328, (2012). Palani Paramount Publications- Printed in India.

[4]. Subba Rao,N. V., Mollusca in Animal Resources of India (Zoological Survey of India, Calcutta): 1991, 125-147.

[5]. Venkataraman, K. and M. Wafar, Coastal and marine biodiversity of India. Ind.J.Mar.Sci., 2005, 34 (1) : 57-75.

[6]. Thakur S., Yeragi S.G. and Yeragi S.S. Population Density and Biomass of Organisms in the Mangrove Region of Akshi Creek, Alibag Taluka,Raigad District Maharashtra. International Day for Marine Biological Diversity, Marine Biodiversity 2012.

[7]. Dious, S.R.J. and R.Kasinathan. Environmental Ecology, 1994. 12(4):845849.

[8]. Palpandi, C. Journal of Biodiversity Conservation. 2011. 3(4): 121-130.

[9]. Aisling J. Daly. Ecology Diversity: Measuring the Unmeasurable, Mathematica, 2018, 6, 119.

[10]. Dewiyanti Irma, Karina Sofuatuddin. Diversity of Gastropods and Bivalves in mangrove ecosystem rehabilitation areas in Aceh Besar and Banda Aceh districts, Indonesia. 2012. Aquaculture,

Aquarium, Conservation & Legislation International Journal of the Bioflux Society.

[11]. Camilleri,J.C. Mar.Bio, 1992, 114 (1): 139-145.

[12]. Wells F.E. Distribution of marine invertebrates in a Hong Kong mangrove, with emphasis on molluscs. 1990. In: Morton, B.S. (Ed.), Proceedings of the Second International Marine Biological Workshop: The marine Flora and Fauna of Hong Kong and Southern China, 1986, Hong Kong University Press, Hong Kong, 783-793.

[13]. Elizabeth C., Ashton, Donald J. Macintosh, J. Peter and Hogarth. J. Trop. Eco., 2003, 19: 127-142.

[14]. Anirudha Dey, Handbook on Mangrove Associate Molluscs of Sundarbans: 2006, 1-96. (Zool. Surv.India, Kolkata).

[15]. Khade S.N. and Mane U.H. Diversity of edible Bivalve and Gastropod Molluscs from Ratnagiri, Maharashtra. IJSPER, Vol. (8), July 2012. (1-4).

[16]. Khade S.N. and Mane U.H. Diversity of Bivalve and Gastropod Molluscs from selected localities of Raigad district, Maharashtra, West coast of India. World Journal of Science and Technology 2012, 2 (6):35-41.

[17]. Simpson, E. Measurement of diversity. Nature, Vol-163, 688, 1949.

Underwater-Coastal Diversity, Statistical Analysis of Species Distribution

Sunil N. Khade[1] , Priyanka B. Gaikwad[2]

[1]Department of Zoology, Phulsing Naik Mahavidyalaya, Pusad, Maharashtra, India
[2]Department of Mathematics, Phulsing Naik Mahavidyalaya, Pusad, Maharashtra, India

ABSTRACT

Diversity of bivalve and Gastropod molluscs was studied twice in each season monsoon, post monsoon, winter and summer July 2016 to June 2017. At each locality diversity of species were collected from Bhatye estuary, Shirgaon creek, Mirya, Bhawati-bander and local markets. From various locality like rocky habitat, Muddy habitat, Sandy beaches including Mangrove areas, these study localities is a wide chance of research to further explore both on the possibility of commercial value and ecosystem conservation.

Keywords: Edible Bivalve, Gastropod Molluscs, Diversity.

I. INTRODUCTION

'index of diversity' defined by Fisher are two measures of the degree of concentration or diversity achieved when the individuals of a population are classified into groups. Both are defined as statistics to be calculated from sample data and not in terms of population constants. The index of diversity has so far been used chiefly with the logarithmic distribution. It cannot be used everywhere, as it does not always give values which are independent of sample size; it cannot do so, for example, when applied to an infinite population of individuals classified into a finite number of groups [26].

Mangroves are one of the biologically diverse ecosystems in the world, rich in organic matter and nutrients and support very large biomass of flora and fauna[1]. Edible species of oysters, mussels, cockles, and gastropods are collected extensively for local consumption. The blood clam, *Anadara granosa* and other cockles can be found in large numbers in mudflats on mangrove strands, where it lies partially buried in the sediment[2]. The total number of mangrove inhabiting faunal species in Indian mangroves is 3,111, which include prawns, crabs and molluscs, fish, fish parasites, insects, reptiles, amphibian and mammals[3]. An oysters, mussels, clams serve the nutritional needs source of minerals, protein, glycogen and easily digestible compared to other animal food[4]. In India, till today, 5,070 molluscs have been recorded of which, 3,370 are from marine habitats[5]. Eight oysters, two mussels, seventeen clams, six pearl oysters, four giant clams, one window pane oyster, other gastropods fifteen cephalopods are exploited from the Indian marine region[6]. The present papers investigate the diversity of bivalve and gastropod molluscs of mangrove ecosystem in selected study area of Raigad district coast.

II. METHODS AND MATERIAL

Live animals were collected twice in each season monsoon, post monsoon, winter and summer July 2016 to June 2017. From Bhatye estuary, Shirgaon creek,

Mirya (rocky shore), and Bhagwati bander (rocky shore), Ratnagiri coast where as Kajali river meets to the sea. Soon after fishing, they were brought to the laboratory and the shells were brushed to clean the fouling biomass and mud. They were then stocked in filtered seawater pumped in the laboratory from the estuary for observation then animal preserved in 70% alcohol for taxonomical identification of external structure of typical shells, especially, lunal, umbo, and operculum. Internal parts teeth, adductor muscles, hinged scars. The shells were identified from Zoological Survey of India, Kolkata.

III. RESULTS AND DISCUSSION

The total 12 bivalves from 7 families and 13 gastropod species from 8 families of edible molluscs from four localities of Ratnagiri were recorded (Tables 1 & 2).

Class	Bhatye (1)	Shirgaon (2)	Mirya (3)	B. bander (4)
Bivalve	6	5	3	2
Gastropod	2	1	6	6

Table 1. Localities wise family distribution of Ratnagiri coast.

Study site	Bivalve	Gastropod
1	9	2
2	8	1
3	4	11
4	3	10

Table 2 Localities wise species distribution of Ratnagiri Coast.
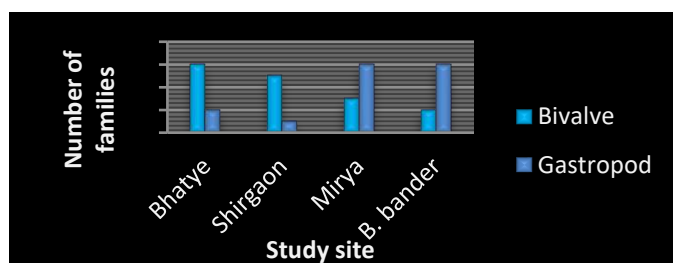
Figure no. 1 Showing edible bivalve and gastropod by localities of Ratnagiri coast.
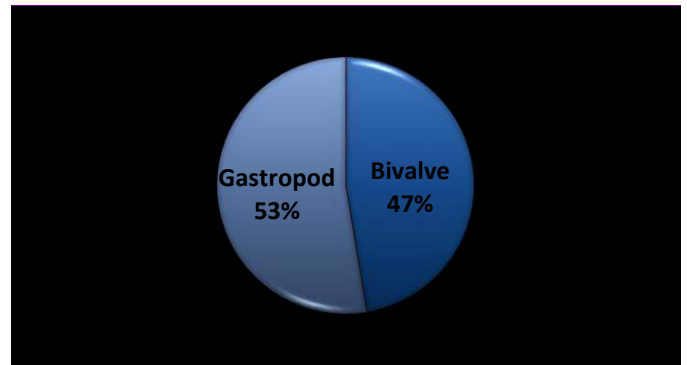
Figure no. 2 Showing edible bivalve and gastropod in percentage of Ratnagiri coast.
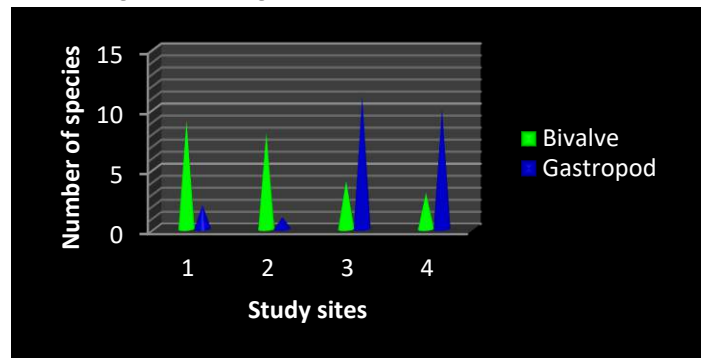
Figure no. 3 Showing localities wise edible bivalve and gastropod of Ratnagiri coast.

The 52% gastropod species and 48% bivalve species found from the selected study localities of of Ratnagiri coast. Bivalve species were found higher at Bhatye estuary while gastropods species were higher in Mirya probably due to habitat differences. The overall molluscs diversity was found higher (13 including bivalve and gastropod species) while lower at Mirya bander. Decomposed material of the plant litter from August onwards is an important component of nutrient cycling in wetlands and it harbours a large number of diverse species[7]. in the month of July, the salinity and temperature dropped down which made the condition adverse for the molluscs[10]. It is good harvesting place for variety of molluscan species[7]. Molluscs populations in mangrove ecosystem is important to evaluate their condition[11]. In Malaysia some of marine bivalve such as *Anadara granosa* is being cultured for commercialization. In Sarawak mangrove forest covered 173,792 ha of the land which is suitable for molluscan habitat[12]. The bivalves in favor of the more

active and therefore more conspicuous mangrove, with chemo-symbiotic associations have also been reported[13]. The hard substratum is available such as prop-roots and pneumatophores and oysters beds[14] .The numerical abundance and biomass of molluscs can be equally impressive[15]. The numerous investigation of mangroves associated molluscs in the world wide, 39 species of gastropods in as Australian mangrove[16]. Twenty eight species in the Chinese mangrove[17]. Twenty three molluscs species from the mangrove forest in Hong Kong[18]. Twenty nine bivalves from the mangrove root on the Atlantic coast of Colombia and Wood-boring bivalves are also common in the mangrove forest[19]. Fourty four species of Sematan mangrove forest of Malaysia[20]. In general, numerous surveys of Indian mangrove molluscs were reported by[21&22]. A total account of Sundarban 56 species of molluscs including 31 gastropods and 25 bivalves[23]. 12 bivalves and 13 gastropods mangrove associated at Ratnagiri [24]. Gastropods are typically one of the dominant and most conspicuous macrofauna in mangrove systems, and occupy wide range of ecological niches[25].

IV. CONCLUSION

The diversity of edible molluscs at four localities at Ratnagiri varies significantly. During the study period 53% gastropod species and 47% bivalve species recorded on selected localities of Ratnagiri coast (given in figure no 1.). There was a considerable difference within the study localities. High species diversity was found in a certain locality it was due to the presence of higher number of different species. The molluscs are indigenous species of Bhatye estuary have greater commercial value and biodiversity importance. The total numbers and type of edible molluscs probably is influenced by habitat and geographical condition. Shirgaon creek and Bhatye estuary probably have suitable habitat to support large number of edible molluscs diversity.

V. REFERENCES

[1]. Pawar R. Prabhakar, Molluscan Diversity in Mangrove Ecosystem of Uran (Raigad), Navi Mumbai, Maharashtra, West coast of India. Bull. Environ. Pharmacol. Life Sci. Vol. 1(6) May 2012: 55-59.

[2]. Macintosh, D.J. and E. C. Ashton. A review of mangrove biodiversity conservation and management. Final Report 10/06/2002. 2002. Centre for Tropical Ecosystems Research, University of Aarhus, Denmark.

[3]. Kathiresan, K. and S.Z. Quasim, Biodiversity in Mangrove ecosystems, 2005. Hindustan Publishers, New Delhi.

[4]. G. D. Suryavanshi, A.M.Shaikh and U.H.Mane: Impact of Zink on protein content of oyster Crassostrea cattuckensis from Ratnagiri coast, Department of zoology, Yogeshwari Mahavidyalaya, Ambajogai, Dist. Beed-431517. J. Ecotoxicol. Envriron. Monit. 22. (4), 323-328, (2012). Palani Paramount Publications- Printed in India.

[5]. Subba Rao,N. V., Mollusca in Animal Resources of India (Zoological Survey of India, Calcutta): 1991, 125-147.

[6]. Venkataraman, K. and M. Wafar, Coastal and marine biodiversity of India. Ind.J.Mar.Sci., 2005, 34 (1) : 57-75.

[7]. Thakur S., Yeragi S.G. and Yeragi S.S. Population Density and Biomass of Organisms in the Mangrove Region of Akshi Creek, Alibag Taluka,Raigad District Maharashtra. International Day for Marine Biological Diversity, Marine Biodiversity 2012.

[8]. Dious, S.R.J. and R.Kasinathan. Environmental Ecology, 1994. 12(4):845849.

[9]. Palpandi, C. Journal of Biodiversity Conservation. 2011. 3(4): 121-130.

[10]. Patole,V.M. Ecology and biodiversity Mangroves in Mochemad Estuary of Vengurla, South

Konkan, Maharashtra. Ph.D. Thesis, (2010). University of Mumbai.

[11]. Dewiyanti Irma, Karina Sofuatuddin. Diversity of Gastropods and Bivalves in mangrove ecosystem rehabilitation areas in Aceh Besar and Banda Aceh districts, Indonesia. 2012. Aquaculture, Aquarium, Conservation & Legislation International Journal of the Bioflux Society.

[12]. Paul C.P.K. Management of Mangrove Forest of Sarawak.2012. (Online). Wetland 10 pdf.

[13]. Lebata, J.H.L. and J.H.Primavera. Journal of shellfish Research, 2011. 20:1273-1278.

[14]. Suresh M., S.Arularasan and K. Ponnusamy Distribution of molluscan fauna in the artificial mangroves of Pazhayar back water canal, Southeast Coast of India. Advanced in Applied Science Research, 2012, 3 (3):1795-1798.

[15]. Sasekumar, A. J. Anim. Ecol, 1974, 43: 51-69.

[16]. Camilleri,J.C. Mar.Bio, 1992, 114 (1): 139-145.

[17]. Jiang J.X. and R.G.Li, Hydrobiologia,1995, 295:213-220.

[18]. Wells F.E. Distribution of marine invertebrates in a Hong Kong mangrove, with emphasis on molluscs. 1990. In: Morton, B.S. (Ed.), Proceedings of the Second International Marine Biological Workshop: The marine Flora and Fauna of Hong Kong and Southern China, 1986, Hong Kong University Press, Hong Kong, 783-793.

[19]. Alvarez- Leon, R. Mangrove ecosystems of Colombia. Conservation and sustainable utilization of mangrove forests in Latin America and Africa Region. ITTO/ISME Project PDI, 14/90, Yokohama, Japan. 1983, 75-113.

[20]. Elizabeth C., Ashton, Donald J. Macintosh, J. Peter and Hogarth. J. Trop. Eco., 2003, 19: 127-142.

[21]. Rambabu, A.V.S., B.V.Prasad and M.B.Rao. J.Mar.Bio.Ass.India 1987, 20, (1&2): 140-143.

[22]. Venkatesan, V.,C.Kalidas, U.Pariyappanal, Zacharia, and S. Rajagopal, 2010. AES Bioflux, 2(2): 113-119.

[23]. Anirudha Dey, Handbook on Mangrove Associate Molluscs of Sundarbans: 2006, 1-96. (Zool. Surv.India, Kolkata).

[24]. Khade S.N. and Mane U.H. Diversity of edible Bivalve and Gastropod Molluscs from Ratnagiri, Maharashtra. IJSPER, Vol. (8), July 2012. (1-4).

[25]. Cantera, J., P.M. Arnaud and B.A.Thomassin. Journal of Molluscan Studies, 49: 1983, 10-26.

[26]. Simpson, E. Measurement of diversity. Nature, Vol-163, 688, 1949

Diversity of Snake Species from Pusad Region, Maharashtra, India

Sunil N. Khade[1], Priyanka B. Gaikwad[2]

[1]Department of Zoology, Phulsing Naik Mahavidyalaya, Pusad, Maharashtra, India
[2]Department of Mathematics, Phulsing Naik Mahavidyalaya, Pusad, Maharashtra, India

ABSTRACT

The study of venomous, semi venomous and Non venomous snakes species by different habitat from the Pusad region (Vidarbha), and common species found like Common kukri, Common Wolf snake, Green keelback, Russell's viper, Worm snake, Bamboo pit viper, Common trinket, Indian rat snake, total seventeen species observed survey conduct day time and night time, from study period during July 2016 to August 2017. The study is essential for the enrichment of the individual species survival and will helps to provide information, awareness and conservation of snake species from Pusad Tahasil of Maharashtra state, India

Keywords : Snakes, Pusad Region, Common Kukri, Common Wolf Snake, Green Keelback, Russell's Viper, Worm Snake, Bamboo Pit Viper

I. INTRODUCTION

Every year, about 5.4 million snakebites occur worldwide. These cause up to 2.7 million envenoming's, almost 138,000 deaths, and 400,000 cases of squeal or disability Various [1,2] Every year, two million snakebites occur in Asia, with India presenting more than 46,000 deaths each year [1,3]. kinds of snakes are existing all over the world by various habitat. It is postulated that there are about 3000 species of terrestrial snakes in the world and they are predominant in the warm climates and lush-green regions of the tropics. About 278 species are found in India out of which 58 species are poisonous [1]. 3000 species of snakes are distributed worldwide. 500 are venomous species 52 venomous species are found in Indian subcontinent [2]. Snake bite is an acute life threatening time limiting medical emergency an occupational hazard often faced by farm laborers and farmers. It is in endemic form all over tropical countries like India. In India there are 2.5 lakhs snake bites out of which 35,000 to 50,000 deaths per year due to snake bite. There are 216 species of snakes identified in India which 52 are known to be poisonous. The dominant families of poisonous snakes in India are Elapidae which is includescommon cobra (*Naja naja*), King cobra and common krait (bungaruscaerulus), viperidae includes *Russell's viper* echiscarinatus (saw scaled or carpet viper) and pit viper and hydrophidae (Sea snakes) [4]. The present study is essential for conservation of snakes species.

II. METHODS AND MATERIAL

For the study initially requires well-trained snake rescuers on his own risk for the observation, it needs courage, self-daring, confidence, and very essential

experience and most important is the study of behavior and nature of the snake to be caught. Snake rescue records of survey was made from July 2016 to August 2017, Sampling was done as per the need, request of the local people or stress calls made by residents, for twenty four hrs. Individual species of snakes were located and try to catch by hand, sticks and through pitfall traps in association with drift fences. After catching the snakes, their characteristics, predominant features were observed then noted for taxonomical study, take the photographs and identified up to species level using keys and other publications as per [5], [6], [7], [8]. After the study the captured snakes species were released in the forest/safely area as per the guidelines of wildlife and forest department rescued

and released into the proper habitat without harm them.

III. RESULTS AND DISCUSSION

Total sixteen Species sixteen genus of snakes belong to five families were recorded in and around the human habitations of resident people of Pusad Tehsil , it is indicated in the table no I. Out of these rescued species four species were poisonous, two were semi-venomous and remaining ten was non- venomous. The unavailability of suitable habitat and prey base, snakes have to move outside which leading to such conflicts that sometimes leads to death of a snake. However, some citizen ecofriendly or some stressfully call to expert snake catcher for stressfully call to expert snake catcher for the escape and survival of the species.

Sr. No.	Family	Genus	Species	Common name	Local Name	Nature	Status
1	Elapidae	Naja	naja	Spectacled cobra	Naag	***	C
		Bungarus	caeruleus	Common krait		***	C
2	Viperidae	Daboia	russelii	Russell's viper	Ghonus	***	C
		Echis	carinatus	Indian saw-scaled viper	Furase	***	C
3	Colubridae	Boiga	trigonata	Common cat snake	Manjarya	**	C
		Ahaetulla	nasuta	Common vine snake	Harantol	**	C
		Ptyas	mucosa	Indian rat snake	Dhaman	*	C
		Coelognathus	helena	Common trinket snake	Taskar	*	C
		Macropisthodon	plumbicolor	Grass snake	-	*	U
		Amphiesma	stolatum	Striped keelback	Iral/Pand hivad	*	R
		Lycodon	aulicus	Common wolf snake	Kawadya	*	C
		Xenochrophis	piscator	Checkered keelback water snake		*	C
4	Boidae	Eryx	johnii	Earth boa/Red sand boa	Mandul	*	C
		Gongylophis	conicus	Common Sand boa		*	C
		Python	morulus	Indian rock python	Ajgar	*	R
5	Typhlopidae	Ramphotyphlops	braminus	Brahminy worm snake		*	U

Table No.I: Diversity of Snakes from Pusad Tehsil, (MS), India (Note 1: C- common, U-uncommon, R-rare.) (Note 2: Non-venomous=*, Semi-venomous=**,Venomous=***)

Among the non- venomous snakes the rare species reported here as Indian rock python, Python morulus and Striped keel back, Amphiesma stolatum belongs from Boidae and Colubridae family respectively. The anthropogenic activities, physical development, civilization and mainly the changing environmental conditions, like global warming are affecting the habitat of the animals. Therefore this important part of the ecology conflict against man. In the present investigation abundance of snake fauna rescued opined that snake produced unimaginable fear and anxiety. Right from the cases where earliest man lived, snakes would have caused first kind of poisoning [9]. Present study also observed the tress calls and down to root level at any time calls of the infrastructural development including townships etc. and as such these areas are prone to habitat loss due to which different types of snake including poisonous, semi-poisonous, non-poisonous are being noticed in the residential areas during monsoons and winter seasons. The present studies are an attempt to evaluate the information, occurrence, abundance &species richness and further assist in the knowledge, awareness and conservation of snake fauna in this region since there is acute paucity of established work and data on this subject till date. Snake bite is an acute life threatening time limiting medical emergency an occupational hazard often faced by farm laborers and farmers. It is in endemic form all over tropical countries like India. In India there are 2.5 lakhs snake bites out of which 35,000 to 50,000 deaths per year due to snake bite and this is because of less information amongst the people.

IV. CONCLUSION

The study of snakes from Pusad region including remote area, having rich diversity and it urgent need to provide correct knowledge regarding snakes especially which are venomous and nonvenomous if they pursue the knowledge, they will not panic themselves and kill the snakes, instead of they will leave them in their natural habitat, unnecessary these species use to killed by people in this way this article help to conserve snakes species for ecosystem which is essential.

V. REFERENCES

[1]. WHO Snakebite Envenoming—Key Facts 2019 Available online: https://www.who.int/news-room/factsheets/detail/snakebite-envenoming (accessed on 22 April 2020)

[2]. Bolon, I.; Durso, A.M.; Mesa, S.B.; Ray, N.; Alcoba, G.; Chappuis, F.; de Castañeda, R.R Identifying the snake: First scoping review on practices of communities and healthcare providers confronted with snakebite across the world PLoS ONE 2020, 15, e0229989 CrossRef PubMed].

[3]. Mohapatra, B.; Warrell, D.A.; Suraweera, W.; Bhatia, P.; Dhingra, N.; Jotkar, R.M.; Rodriguez, P.S.; Mishra, K.; Whitaker, R.; Jha, P.; et al Snakebite mortality in India: A nationally representative mortality survey PLoS Negl Trop Dis 2011, 5, e1018 CrossRef PubMed].

[4]. Sonali R Raut1, Shantaj M Deshbhratar1, Jyotsna A Mahaley2, Vijay K Hile3, Ankita J Thakur PS and NE Warghat, 2014 Documentation of Road Killed and Rescued Harpatofauna in and Around Amravati City, Maharashtra, Advances in Applied Science Research, 5(2):373-381.

[5]. Punde DP, 2008 Meet the Expert :Management of Snake Bite 9Report APICON , Kochi), Medicine update Volume 18, 2008

[6]. Deoras PJ, 1965.Snakes of India, National Book Trust (NBT), New Delhi.

[7]. Government of India dat: pp 107-108 of http://cbhidghs.nic.in/writereaddata/mainlinkFile/Health %20Status%Indicators.pdf) 2017

[8]. Khaire N, 2010 Snakes, Indian Herpetological Society, Pune

[9]. Daniels JC, 2002 The book of Indian Reptiles and Amphibians, Bombay Natural History Society and Oxford University Press Mumbai

[10]. Whitaker, R and A Captain, 2008 Snakes of India The Field Guide Draco Books.Chengalpattu, Tamil Nadu, xiv+479

[11]. Aengals, R, VM Sathish Kumar and MJ Palot, 2012 Updated Checklist of Indian Reptiles

[12]. Lingayat AM and PR Wankhade, 2015 Study of clinical profile complications and outcome in patients of snake bite in pediatric age group, Healthcare and Biomedical Research, 03 (03): 203-208

Comparison of Ac Conductivity of PVC-PS Blend and PANI Doped PVC-PS Blend

Dr. L. A. Sharma

Brijlal Biyani Science College , Amravati, Maharashtra, India

ABSTRACT

The polyblend of polyvinyl chloride (PVC) and polystyrene (PS), in the weight ratio 5: I were prepared by using 1.25 gm of PVC and 0.25 gm of PS. Polyaniline (PANI) has been used as dopant with 2.5 % of the total weight of the two polymers. The ac conductivity of polyaniline doped PVC-PS thin films have been investigated in the temperature range 313 K -353 K and in the frequency range 0.5 KHz - 200 KHz. Plot between log σ_{ac} and 1000/T is used to calculate activation energy.

Keywords: Polyblend, PVC, PS, PANI, ac conduction.

I. INTRODUCTION

In recent years, conducting polymer composites and blends have attracted the attention of material researchers, with increase in interest in obtaining properties that are intermediate between those of homopolymers[[1,2] Generally polyvinyl chloride (PVC) is being used for the consumer products like cables, pipes, window frames, packaging bottles, Hit cards and audio recording. It is also used in car interiors and in hospital as medical disposables. The presense of chlorine in the PVC structure is the reason of its better properties like fine resistance and durability. Dielectric properties and surface morphology of proton irradiated ferric oxalate dispersed PVC films has been studied [3]. Poly vinyl chloride (PVC) can act as a mechanical stiffener in the electrolyte due to its immiscibility with the plasticizer. A novel composite film of PANI doped with azobenzene sulfonic acid (ABSA) blended with PS was obtained by a simple and inexpensive electrospinning method [4].The ac electrical conductivity of the blend of polypyrrole doped with iron (III) chloride in PVA matrix at different temperatures has been studied [5]. In the past two decades different polymer hosts such as PMMA [6], PANI [7],PVC [8], PVdf[9] had been studied as the gel forming polymer electrolytes, this plasticized or gelled polymer electrolytes possess higher room temperature ionic conductivity could be useful for lithium and lithium ion battery application. The effect of ZrO_2 on conductivity of PVC - PMMA - $LIBF_4$ DBP polymer elecctrolytes has been investigated. [10]

II. METHODS AND MATERIAL

Experimental

The polyvinyl chloride (PVO) and polysterene (PS) of standard grade product supplied by Polychem Industries, Mumbai were used for the study The conducting polymer (polyaniline)was prepared by chemical oxidation using ferric chloride by conventional procedure. Polyaniline was used as a dopant

Sample Preparation

For the preparation of PVC-PS polyblend, the two polymers PVC (1.25g) and PS (0.25g) were taken in the ratio 5:1 by weight. 1.25 g of PVC in 15 ml tetrahydrofuran (THF) and 0.5g of PS in 10 ml of THF dissolved seperately and subsequently mixed together. For the preparation of Polyaniline doped thin films the two polymers PVC (1.25g) and PS (0.25g) were taken in the ratio 5:1 by weight. 1.25 g of PVC in 15 ml tetrahydrofuran (THF) and 0.5g of PS in 10 ml of THF dissolved seperately and subsequently mixed together. Polyaniline was taken in 25 wt % and was dissolved in 5 ml of THE to produce Polyaniline solution . After allowing them to dissolve completely. the three solutions were mixed together The solution was heated at 60° c for two hours to allow polymers to dissolve completely to yield a clear solution . A glass plate thoroughly cleaned with hot water and then with acetone was used as a substrate, To achieve perfect levelling and uniformity in the thickness of the film, a pool of mercury was used in a plastic tray in which the glass plate was freely suspended .The solution was poured on the glass plate and allowed to spread uniformly in all directions on the substrate. The whole assembly was placed in a dust free chamber maintained at a constant temperature (40°C). In this way, the film was prepared by isothermal evaporation technique [11.12]. The film was subjected to 12 hours heating at constant temperature of 50°C and for another 12 hours at room temperature to remove traces of solvent .Finally, the film was removed from the glass plate, it was cut into small pieces of suitable size which were washed with ethyl alcohol to remove the surface impurities

Thickness measurement

For measuring the thickness, micrometer screw guage [12] with least count 0.001cm (10 μ m) was used. But for greater accuracy and resolution, a compound microscope in conjunction with an acculometer which gives least count 1.3 μ m and 3.3 μ m, at the magnification of 1:10 and 1 100 respectively was used. A small section of the sample was taken mounted vertically to get a clear section of view of the thickness. The film used for the present study was of the thickness 70 μ m

Electrode coating

The electrode coating on the film of measured thickness was done by quick drying and highly conducting silver paste [12] supplied by Eltecks Corporation, Bangalore. A mask of a circular aperture of 25 cm diameter was used while coating to ensure uniformity in size of coated silver electrode

Structural characterization

The X-ray powder diffractogram of polyaniline doped PVC-PS blend have been recorded from a Phillips automated diffractometer (RS IC, Nagpur) and as shown in fig1 and fig2 .The X-ray diffractograms of all the samples were obtained for ensuring the nature of the file (amorphous or crystalline)

AC conductivity measurement

The film coated with silver electrodes was sandwiched between the electrodes of (2.5 cm diameter each) the sample holder forming Metal Insulator Metal(MIM) system was connected to precise LCR meter having temperature range of 313K-353K,and frequency range of 0.5KHz-200KHz. Using precise LCR meter, TH 281613, Tonghul values of Z and θ was measured,

III. RESULTS AND DISCUSSION

XRD Analyisis

Fig. 1 shows the diffraction pattern of polyaniline doped PVC-PS blend. of peak in X-ray spectra of polyaniline doped PVC-PS blend confirmed the amorphous nature of the polymer sample [13]
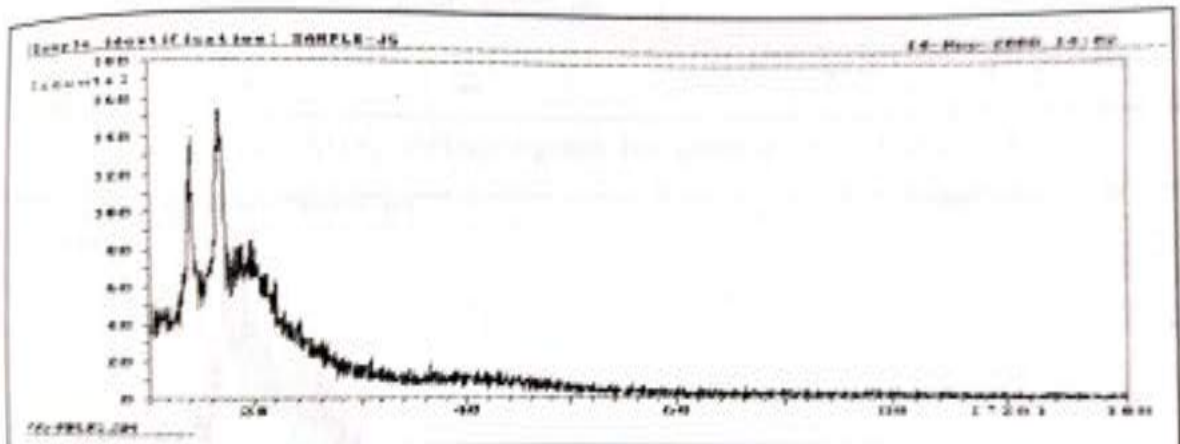
Figure 1. X-ray diffractogram of sample, PVC-PS polymer blend
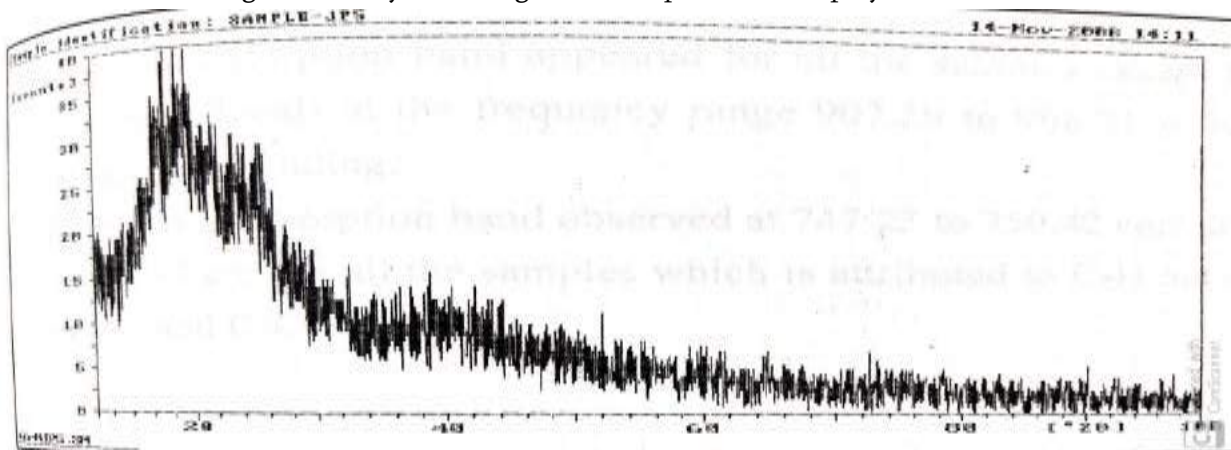
Figure 2. X-ray diffractogram of sample, polyaniline doped PVC-PS polymer blend

AC Conductivity

Fig 3 and 4 shows variations of AC conductivity σ_{ac} with different temperature at frequencies 10KHz to 200KHz .With increase in temperature conductivity increases
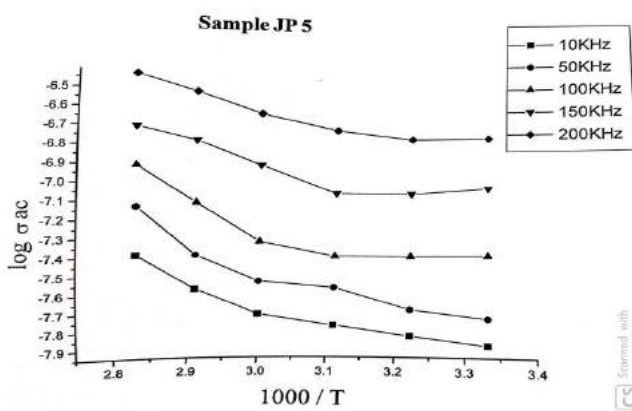
J5 pvc –ps Polymer blend
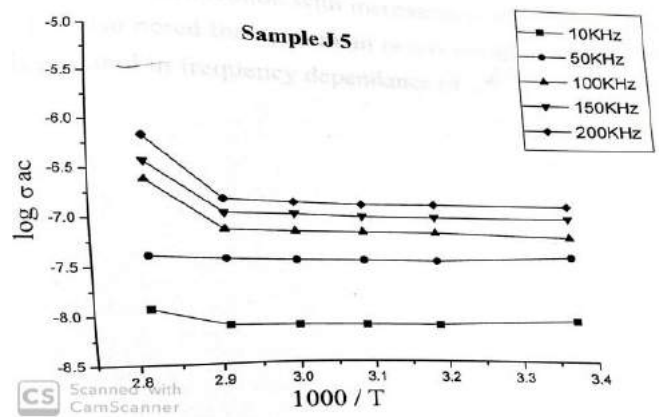
JP5 – Polyaniline doped pvc –ps Polymer blend

Table 1 Values of activation energy at two different frequencies for J5 and JP5

Sample	Activation energy in eV	
	100KHz	200KHz
J5	0.0128	0.0177
JP5	0.1539	0.0521

The values of activation energy Ea the following trends

1. Activation energy of PVC-PS polymer blend increases with increase in frequency and Activation energy of Polyanilline doped PVC- PS blend decreases with increase in frequency.
2. At constant frequency activation increases when dopant is added.

IV. CONCLUSION

At low temperature ac conductivity is frequency dependent and at high temperature ac conductivity is weakly dependent on frequency. Such dependence has been observed in disordered amorphous matrial(14,15)

V. ACKNOWLEDGEMENT

Author wish to thank Dr D.S. Dhote, Principal , Brijlal biyani science college, Amravati for encouragement

VI. REFERENCES

[1]. Bhat N. V., Qader A. P. and Bambale V. A. J. Appl. Polym. Sci., 25|1, 80 (2001).

[2]. Kim B. J. Oh S. G., Hon M. G. and Im S. S. Palym. I11,43 (2002)

[3]. Shah Sejal, Singh Dolly Qureshi Anjum, Singh N. L, Singh K P and Shrine v Indian Journal of Pure and Appl. Physics, Vol. 46, June 493-442 (2008).

[4]. Sanders E. H., Kloefkorn R, Bowlin G. L., Simpson D G and and Wnek G. E.Macromolecules,36,3803(2003)

[5]. Megelski S., Stephens J. S., Chase D B and Pabolt J. L Macromolecules, 8456, 35 (2002)

[6]. Vincent C. and Scrosati B.: Modem Batteries: An introduction to electrochemical power sources, John Wiley and Sons, Newyork (1997),

[7]. Kim K S. Kum K S., Cho H W. and Woncho B. J. Power Sources, 221, 124 (2003)

[8]. Watnabe M., Kanba M., Nagaoka, Shinohara J. J. Polym Sci. Poly, Phys., Ed 21, 939 (1983).

[9]. Sukeshini A. M., Nishimoto A. and Watanabe M Solid State Ionics, 385, 86-88 IS.(1996).

[10]. Tsuchida E., Ohno H. and Tusunemi E. Electrochem. Actd., 833, 28 (1983)

[11]. Rajendran S. and UMAT Bull Mater Sci vol 31-34,23, Nov, February (2000) [17]

[12]. Bahri R. and Sood B. R. Thin solid films, 100, 15 (1983) Mehendri P. C.. Agrawal J. P. and Jain K., Indian J. Pure and Appl. Phys. 34, 101 (1996)

[13]. Sangawar V.S. Ph.D Thesis Amaravati University, Amravati (1995)

[14]. Dhokne R. J, Sangawar V. S., Chikhalikar P. S., Thool V. S., Ubale A. Junghare A. R.: Indian J. Physics, 82-10, 1309-1318 (2008)

[15]. Debye P ; Polar Molecules, Chemical Catalog Co, Newyork (1929).

Effect of Co-Doping on Structural and Optical Properties of ZnO Thin Films

L. V. Thakre, L. H. Kathwate, V. D. Mote*

Thin Films and Materials Science Research Laboratory, Department of Physics, Dayanand Science College,
Latur- 413512, Maharashtra, India

ABSTRACT

Here, we report the effect of Co-doping on structural and optical properties of ZnO thin films prepared via simple and cost effective spray pyrolysis technique. The x-ray diffraction (XRD) confirmed the formation of the hexagonal wurtzite structure of undoped and Co-doped ZnO thin films with preferential growth along c-axis and had no phase impurity. The average crystallite size of prepared films calculated by Scherrer's formula and found to be 18.11 nm for ZnO and 14.12 nm for Co doped ZnO films. The calculated energy band gap exhibited a red shift upon doping with energy band gap reduced from 3.20 eV to 3.12 eV for the studied doping content. These studies show that the synthesized films have the potential to be used as a transparent electrode in optoelectronic devices such as solar cells.

Keywords : Thin Films, Zno, Spray Pyrolysis, X-Ray Diffraction, Uv-Vis Spectroscopy.

I. INTRODUCTION

Zinc oxide (ZnO) is perhaps the most prominent metal oxide semiconductors. It is an n-type semiconductor of hexagonal (wurtzite) structure with direct and wide band gap energy of about 3.37 eV at room temperature [1]. It is a flexible material with great electrical and optical properties, thermal and chemical stability, abundant in nature, low cost and non-harmful [2-3]. Due to this versatility ZnO is generally used in various commercial applications such as integrated optics, chemical sensors, solar cell, transition, photocatalysis, gas sensor etc. [4-6]. There are various techniques for the deposition of ZnO thin film such as pulsed laser deposition, spray pyrolysis, SILAR, chemical bath deposition, RF magnetron sputtering and electrochemical deposition method [7-11]. Considering the inexpensiveness and ease of fabrication spray pyrolysis has been adopted as widely used deposition method.

Over the last few years transition metal doped ZnO has been studied briefly by researcher due its potential application in spintronic and photonic devices. Through the literature review ZnO based semiconductor can present ferromagnetic behaviour at room temperature when doped with transition metal such as Co, Ni and Mn [12-14]. Undoped ZnO material has much intrinsic defects so, when transition metal is doped with ZnO structure it can alter the intrinsic defects levels which helps to improve magnetic properties of spintronic as well as for gas sensing application. In this work undoped and Co-doped ZnO thin films were synthesized oncorning borosilicate glass substrate by chemical spray pyrolysis method. The structural and optical properties of the obtained thin films were systematically investigated.

II. EXPERIMENTAL DETAILS

The undoped and Co-doped ZnO thin films were prepared by spray pyrolysis technique onto a glass substrate using zinc acetate dehydrate (Zn (CH$_3$CO)$_2$2H$_2$O) (99.5%, Merck India) and cobalt acetate monohydrate (Co (CH$_3$CO)$_2$2H$_2$O) (99.0%, Merck India). Before the deposition the substrate were cleaned with freshly prepared chromic acid, followed by labolene solution and double distilled water. Lastly the substrate was ultrasonically cleaned for 10 min. The precursor solution (0.1 M) was prepared by dissolving required amount of zinc acetate in double distilled water and stirred at room temperature for 30 min, to obtain a clear and homogeneous solution. Precursor solution was sprayed with the constant flow rate onto preheated corning borosilicate glass substrate held at optimized substrate temperature of 400°C by large area spray pyrolysis. Compressed air was used as carrier gas. Nozzles to substrate distance and carrier gas pressure were kept constant during the deposition. Similarly Co-doped ZnO thin film deposition was carried out by using the atomic ratio of C/Zn is 2 at %. The structural properties and crystallinity of the deposited thin films was studied by X-ray diffraction (Philips PW-3710) with Cu Kα radiation. Optical absorptionsof the films were recorded by UV-visible spectrophotometer (Shimadzu 2450).

III. RESULTS AND DISCUSSION

3.1 Structural properties

Figure 1 shows the XRD patterns of undoped and Co-doped ZnO thin films. The diffraction peaks are quite sharp and intense which shows the polycrystalline nature of the films with wurtzite crystal structure. XRD patterns are in agreement with the JCPDS card No. 36-1451. There are no other peaks in the Co doped ZnO thin film confirms the formation of single phase films and reveals that substitution of Zn ions

with Co without altering the crystal structure of ZnO. In the observed (100), (002), (102), (110) and (103) crystallographic planes, it is found that the intensity of (002) plane was predominant. In addition, the position of (002) plane shifted slightly ($\approx 0.05^o$) from $2\theta = 34.44^o$ in undoped ZnO film to higher angle as Co-doping ($2\theta = 34.44^o$) indicating that Co ions substitute Zn ions in the ZnO lattice.
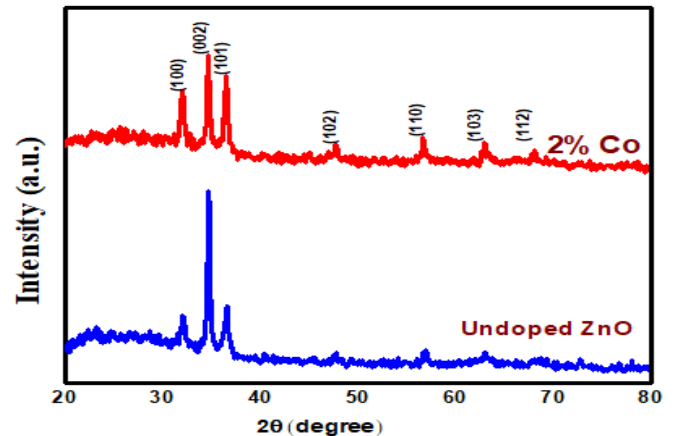
Figure 1. The XRD pattern of undoped and Co-doped ZnO thin films

The lattice parameters of 'a' and 'c' of the prepared film was calculated by using relation [15];

$$\frac{1}{d_{hkl}^2} = \frac{4(h^2+hk+k^2)}{3a^2} + \frac{l^2}{c^2} \qquad (1)$$

Where d$_{hkl}$ is the lattice planesdistance and h,k, and l are Miller indices. This was done by calculating d$_{hkl}$ using Bragg's law, where θ is Bragg's angle; λ is the X-ray wavelength which is 1.5406 Å for the CuKα line, and n is an integer representing the order. The calculated value of lattice parameter listed in table 1. The lattice parameters of undoped ZnO is found to be a = 0.324 nm and c = 0.520 nm, which is consistence with JCPDC Card No. 36-1451. In addition, the lattice parameters for Co – doped ZnO thin films are a = 0.3230 nm and c = 0.519 nm. It is observed that value of lattice parameters decrease for Co-doped ZnO film. The decrease in crystallite size and slight shift in (002) peak position of Co-doped film may be due to the lower radii of Co^{+2} ($\sim$ 0.65 Å) [16] ions than that of

Zn^{+2} ($\sim$0.74 Å) ions [17]. The average crystallite size of the undoped and Co doped ZnO thin films were calculated from the broadening of diffracting peaks of the plane using Scherrer formula [18];

$$D = \frac{0.94\lambda}{\beta \cos\theta} \qquad (2)$$

Where λ = 1.5406Å, β is the full width at half maxima and θ is Bragg's angle. The calculated value depicted in table 1. The estimated crystallite size was found to be 18.11nm and 14.12nm for undoped and Co-doped ZnO thin films. It is may be due the presence of scattered Co ions which might have create thermodynamical barriers in turn slowed down the growth process [19]. The microstrain of films was calculated using the following formula [20];

$$\varepsilon p = \frac{\beta}{4\tan\theta} \qquad (3)$$

The value microstrain for Co-doped ZnO thin film has increased compared to the undoped ZnO thin film. The increasing value of microstrain may be due to the decrease in crystallite size.

3.2 Optical Study

In order to study optical properties of prepared films, the optical absorption of the samples has been recorded in the range 200 - 800 nm using UV-visible spectroscopy as shown in figure 2(a). The spectrum shows the decrease in absorption with an increase in wavelength near band edge for Co-doped ZnO thin film. In addition, the redshift for Co-doped ZnO thin film. This implies that increase in effective band gap of the film. The band gap of the prepared film was calculated using the equation [21];

$$\alpha h\nu = A\big(h\nu - E_g\big)^2 \qquad (4)$$

Where, α-absorption coefficient, $h\nu$-incident photon energy, E_g-optical band gap energy. From the linear fit of the plot $(\alpha h\nu)^2$ versus photon energy (E) as shown in figure 2(b), we estimate the value of 3.20 eV and 3.12eV for undoped and Co-doped ZnO films respectively. The decrease in the optical band gap of ZnO films with Co-doping is related to the sp-d exchange interaction between the band electrons and

localized d electrons of Co^{2+} ions. The value of bandgap obtained agrees with the previously results [22-23].
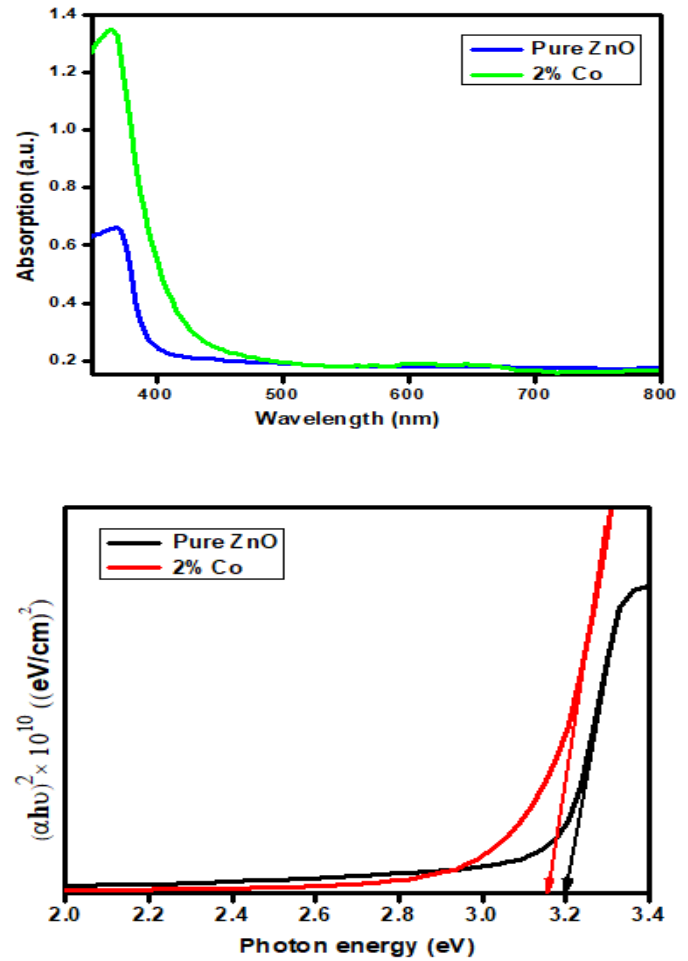
Figure 2. (a) Optical absorption spectra of undoped and Co-doped ZnO thin films. (b) The plot of $(\alpha h\nu)^2$ vs. $(h\nu)$ for undoped and Co-doped ZnO thin films.

IV. CONCLUSION

Nanostructured undoped and Co-doped ZnO thin films were successfully prepared by simple and cost effective spray pyrolysis technique at substrate temperature 400°C. The XRD analysis reveals that all prepared thin films have hexagonal wurtzite crystal structure with a (002) preferential growth. The decrease in the lattice parameter of Co-doped ZnO thin films implying Co^{+2} ions were homogenously incorporation into ZnO lattices. The average crystallite size increases with Co-doping, while the

value of microstrain decreases with Co-doping. The UV-visible spectroscopy analysis indicates the band gap energy decreased from 3.20 eV to 3.22 eV due to Co-doping. The structural and optical properties of prepared films show that films might be useful for the optoelectronic application devices.

V. REFERENCES

[1]. S. Inamdar, V. Ganbavle, K.Rajpure, SuperlatticesMicrostruct. 76 (2014), 253–263.

[2]. O. Lupan, T. Pauporte, L. Chow, B. Viana, F. Pelle′, L.K. Ono, B. RoldanCuenya, H. Heinrich, Appl. Surf. Sci. 256 (2010), 1895–1907.

[3]. M.Alex, M. Gupta, F. R. Chowdhury, M. Shen, K. Bothe, K. Shankar, Y.Tsui, D. W. Barlage, Solid-State Electron. 76 (2012), 104–108 .

[4]. D. Look, Mater. Sci. Eng. B 80 (2001), 383.

[5]. A.Djurisic, X. Chen, Y.H. Leung, A. Man Ching Ng, J. Mater. Chem. 22 (2012), 6526.

[6]. D.C. Look, J. Electron. Mater. 35 (2006), 1299.

[7]. S. Balamurali, R. Chandramohan, N. Suriyamurthy, T. Mahalingam, Journal of Materials Science: Materials in Electronics 24 (2013), 1782–7.

[8]. Deva Arun Kumar K et al. Solid State Sciences 78 (2018), 58–68.

[9]. L. Mustafaa, S. Anjuma, S. Waseema, S. Bashirb, K. Mahmoodb, M. Saleemcand E. Ahmad, Optik 161 (2018), 54–63.

[10]. S. Benramachea, A. Rahalb, B.Benhaoua, Optik 125 (2014), 663–666.

[11]. S. Kahraman, H.M. Cakmak, S. Cetinkaya, F. Bayansal, H.A. Cetinkara, H.S. Guder, J. Cryst. Growth 363 (2013), 86–92.

[12]. H. Ohno, D. Chiba, F. Matsukura, T. Omlya, Abe E, Dietl T, Ohno Y and Ohtani K, Nature 408, (2000), 944–6

[13]. Z. Wang1, R. Samaraweera, C. Reichl , W. Wegscheider andR. Mani, Scientific Reports 6 (2016), 38516.

[14]. J. Lenz and A. Edelstein, IEEE Sensors Journal 6 (2016), 631–49.

[15]. R. Wahab, G. Ansari, Y. Kim, H. Seo, G. Kim, G. Khang, et al., Mater Res Bull 42 (2007), 1640-8.

[16]. M. Nair, M. Nirmala, K. Rekha, A. Anukaliani, Mater. Lett, 65 (2011), 1797-1800.

[17]. M. Vagadia, A. Ravalia, U. Khachar, P. Solanki, R. Doshi, S. Rayaprol, Mater. Res. Bull. 46, (2011), 1933-1937.

[18]. S.Maniv, A.Zangvil, J. Appl. Phys.47 (1978), 2787–2792.

[19]. S. Wang, P. Li, H. Liu, J. Li, Y. Wei, J. Alloys Compd. 505, (2010), 362-366.

[20]. P. Suat, M. Reza, S.Ozen, V. Senay, H.Yudar, S.Korkmaz, Vacuum 141 (2017), 210-215.

[21]. J.Tauc, R.Grigorovici, A.Vancu,Phys.Stat.Sol.15 (1966), 627–637

[22]. Z.Kayani, I. Shah,B.Zulfiqar, S.Riaz, S.Naseemand A. Sabah,Zeitschrift fur Naturforschung A 73 (2017),13–21.

[23]. L. Mustafaa, S. Anjuma, S. Waseema, S. Bashirb, K. Mahmoodb, A. Saleemc, Optik 161(2018), 54–63.

Aeromycological Investigations of Intramural Environment of Hospital and Library in Nagpur City (M.S.) India

Bhonde M. C, Chaudhary R. R., Thakare M. U.

Sant Gadge Maharaj Mahavidyalaya, Hingna Dist. Nagpur, Maharashtra, India

ABSTRACT

An intramural aeromycoflora of two different sites viz. Hospital (Bhoyar Hospital) and Library (RTMNU, University Library) at Nagpur city was carried out for two consecutive years September 2007 to August 2008 by sampling air with the help of rotorod air sampler, to study the incidence of fungal spores.

Total airspora concentration 48065 spore /m^3, were observed at both the sites. Although the composition of aeromycoflora of both environments were more/less similar. 59 types of fungal spores were identified from the total catch of indoor environments from hospital 26485 spores /m^3 and 21580 spore /m^3 from Library by using rotorod sampler. The different fungal spores in both the sites are in the order of dominance are *Aspergilli* (11.44%, 12.27%), *Cladosporium* (8.53%, 10.98%) *Curvularia* (8.08%, 8.89%), *Alternaria* (5.87%, 6.32%), *Nigrospora* (2.68%, 5.25%), *Smuts* (2.05%, 1.69%) *Helminthosporium* (4.00%, 4.0%) and Other types (28.84%, 20.18%) in including pollen grains and unidentified spores respectively. Among the fungal groups, *Deuteromycotina* in Hospital and in Library contributed most at both the sites viz. Hospital (54.20%) & Library (62.92%) followed by *Ascomycotina* (8.53%, 11.49%), *Basidiomycotina* (7.30%, 4.54%) & *Zygomycotina* (1.11% ,0.85%) respectively.

The occurrence of different spore types was co-related with the meteorological parameters. Airborne fungal spores are known to cause allergy in human beings. Hence efforts were also taken to survey of allergy patients in the study area.

Key words – Aspergilli, Intramural aeromycoflora, allergy, meteorological parameters. (Note: Aspergilli was a group having the spores of similar appearance i.e. small and rounded e.g. *Aspergillus, Penicillium, Rhizopus Mucor Tricoderma* etc.)

I. INTRODUCTION

Air is a complex mixture of various gases, various living and non-living particles, water vapours, pollen grains and fungal spores. Without air no one can survive but air is very important medium through which diseases spread. The spores and pollen grains release from their source and become suspended in air. Fungal spores numerically dominant than the other components of air. Meteorological factors like temperature, humidity, and rainfall plays an important role in occurrence of airspora.

Intramural environment of hospital is responsible for transmitting pathogenic micro-organisms and hence responsible for spread the diseases. *Aspergillus* sp. are major cause of hospital infections. The microbes have been also reported in the beddings of patients. *A.*

fumigatus in air have been reported from the hospitals. Many airborne fungi are responsible for spoil library materials. Increasing humidity is favorable for the growth of moulds and mildews which cause loosening of paste and glue, weakening of fibers of paper and leather.

Plumbe (1964) stated that fungal spores are always present in the atmosphere of library. Parker & Munshi (1973) also reported the highest percentage of *Cladosporium* in the airspora of library. Investigation in India & biodeterioration of paper by the activity of the micro-organisms were known by the work of Kathapalia (1960) and Mukharjee (1973). Dominance of *Aspergillus* spp. in Library environment is also reported by Vittal & Glory (1984, 1985), Burge *et al* (1985), Chaturvedi *et. al* (1992) while Verma & Khare (1987), Tripathi (1987), Tilak & Pillai (1988) reported highest contribution of *Cladosporium* followed by *Penicillium* in library. Spore type recorded more or less similar in both the environments. The largest spore concentration of *Aspergillus* followed by *Cladosporium* were found in both environments.

II. METHODS AND MATERIAL

Sampling Sites:
The present study was carried out at two different sites Bhoyar Hospital and University Library, Nagpur for the period of 1year September 2007 to August 2008 at Nagpur City. Nagpur is situated in the central part of India in Maharashtra State. It is located between 21* 45° N to 20* 30°N & 78*15°E to 79*45° E.

Sampling Method:
The present qualitative and quantitative study was carried out to determine the fungal spores count types and their seasonal variation during the period of investigation. Investigation carried out by rotorod air sampler This air sampling device was developed by Perkins (1957) modified by Harrington (1959). It is a portable air sampler hence was used for the present work. It is a battery operated with a constant rotating

speed of 2300 r.p.m. it was placed constant height of 1 meter above the ground level for 30 minutes twice a month at fortnightly intervals. Studies carried out in OPD and general ward and in Library investigation was done in reading room and book self room. The exposed tape strips were mounted on slides by using glycerine jelly. Slide preparation and scanning was carried out by the method after Tilak and Shrinivasulu (1967). Spores counts on strip was expressed as number of spore/m^3. The calculated conversion factor for the sample was 5. Identification of fungal spores was done by comparison with reference slides and by consulting the literature after Burnett and Hunter (1972).

Meteorological Data –
The aeromycoflora is co-related with weather parameters and also with the incidence of allergy in the area. Temperature and Humidity was obtained from personal instrument and rainfall data obtained from Dr. Babasaheb Ambedkar Airport Sonegaon, Nagpur (Table no.1and 2)

III. RESULTS AND DISCUSSION

The observation and data obtained during the course of investigation at both site (Hospital & Library) using rotorod air sampler for nonculturable fungal types over a period of one year viz. September 2006 to August 2007. Both the environments i.e. Hospital and Library the major contributors are *Aspergilli* which is followed by *Cladosporium*, *Curvularia*, *Alternaria*, *Nigrospora*, *Helminthosporium*, *Drechslera*, *Diploidia*, *Ganoderma*, Smut spores *Uredospores* and *Chaetomium*. A total no of 26485 spore /m^3 of air belonging to 55 fungi were recorded from site I (Hospital). Among these 55 types, 30 belongs to Deuteromycotina, 18 to Ascomycotina, 4 to Basidiomycotina & 3 to Zygomycotina. On the other hand, Maximum no of fungal spores 21580 spores/m^3 belonging to 59 fungal types were observed from site II (Library). In library also Deuteromycotina (34) was

the most dominating group followed by 19 belonging to Ascomycotina, 3 from Basidiomycotina & 3 from Zygomycotina.

Site I – Hospital:

Total 26485 spores/ m³ airspora types were recorded during the study period. Highest incidence of fungal spores were recorded in the months of June to August. Highest peak was observed in the month of June (2845 spores /m³).

Chaetomium (235/m³) was the dominant fungal forms in the group of Ascomycotina while Basidiomycotina showed the abundance. The largest spore conc. of *Aspergilli* (11.44%) followed by *Cladosporium* (8.53%), *Curvularia* (8.08%), *Alternaria* (5.87%), *Helminthosporium* (4.22%), *Nigrospora* (2.68%), *Ganoderma* (2.94%) and *Smut spores* (2.05%). In other types Hyphal Fragments (5.64%) contributes most percentage which is followed by Algal filaments (5.56%), Insect Parts (5.09%), Trichomes (4.02%), Pollen grains (3.53%), Tracheideal elements (3.03%), Unidentified spores and this data was also reported by others (Tilak & Talib, 1980; Tilak & Saibaba 1984; Vittal & Glory 1985; Tripathi 1987; Santra & Chanda, 1981; Singh & Chatterji 1990).

Site II – Library:

The total no of biopollutants recorded during one year of investigation in library were 21580 spore /m³. The highest incidence of fungal spores was recorded in the months of June, July and August. The highest pick was observed in month of August (1920 spore /m³).

Chaetomium (1445/m3) is the most dominant among the group Ascomycotina. Basidiomycotina recorded the occurrence of *Ganoderma* (390/m³), Smut spores (365/m³) *Uredospores* (225/m³) as the dominant spores. In Deuteromycotina group the dominant fungal spores Aspergilli 2650 spore /m³, (12.27%) which is followed by *Cladosporium* 2370/m(10.98%), *Curvularia* (1920/m³) 8.89%, *Alternaria* (1365/m³) 6.32%, *Helminthosporium* (785/m³), 4% , *Diplodia* (230/m³) 1.06% , *Drechslera*

(615/m³) 2.84% . Among the other types, Insect parts (1540/m³), 7.13% contributes more which is followed by fungal fragments (755/m³) 3.49%, Algal filaments (670/m³) 3.10% , Pollen grains (440/m³) 2.03%, Trichomes (325/m³) 1.50%, Tracheideal elements (355/m³) 1.64% & unidentified spores (270/m³).

Increase in the humidity is favorable for the growth of moulds and mildews which cause loosen in of paste and glue weakening of fibers and paper and leather. Investigation in India and deterioration of paper by the activity of the microorganisms were known by the works of Kathapalia (1960), & Mukherjee (1973) has implications these spores in allergy. Concentration of Aspergilli spores was high in Hospital ward (3030 spores/m³, 11.44%) as compared to the Library (2650spores/m³,12.27%)

Table 1: No. of Biopollutants from September 2006 to August 2007 along with average monthly temperature and relative humidity in Hospital

Sr. No	Months	No. of Bipollutants	Average temp	Relative Humidity
1	Sept 2006	1870/ m³	21.0	66%
2	Oct 2006	2020/m³	22.30	64%
3	Nov 2006	1975/m³	24.8	63%
4	Dec 2006	1925/m³	24.5	58%
5	Jan 2007	2010/m³	23.2	59%
6	Feb 2007	1920/m³	24.0	62%
7	Mar 2007	1930/m³	27.5	63%
8	Apr 2007	1960/m³	28.7	60%
9	May 2007	2390/m³	29.2	47%
10	June 2007	2845/m³	24.3	61%
11	July 2007	2355/m³	21.3	63%
12	Aug 2007	2675/m³	21.0	65%

Table 2: No. of Bipollutants from September 2006 to August 2007 along with average monthly temperature and relative humidity in Library

Sr. No	Months	No of Bipollutants	Average temp	Relative Humidity
1	Sept 2006	1830/m³	20.2	64%
2	Oct 2006	1785/m³	22.3	65%
3	Nov 2006	1720/m³	24.7	61%
4	Dec 2006	1700/m³	24.5	61%
5	Jan 2007	1855/m³	26.3	58%
6	Feb 2007	1820/m³	26.5	60%
7	Mar 2007	1680/m³	29.6	59%
8	April 2007	1750/m³	31.3	64%
9	May 2007	1675/m³	28.9	47%
10	June 2007	1870/m³	25.7	61%
11	July 2007	1895/m³	27.2	60%
12	Aug 2007	1920/m3	27.0	65%
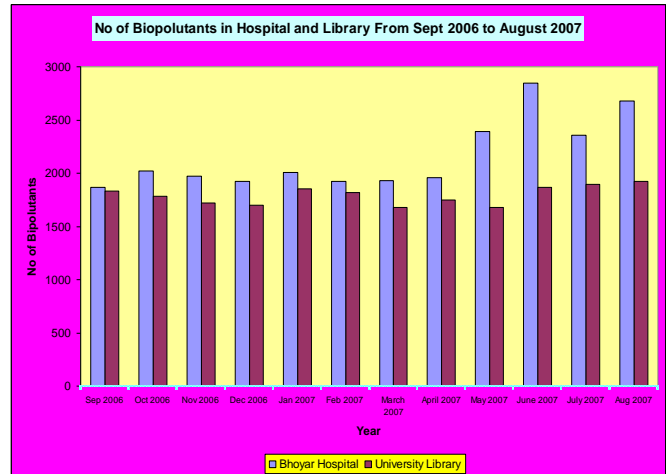
Fig: 2
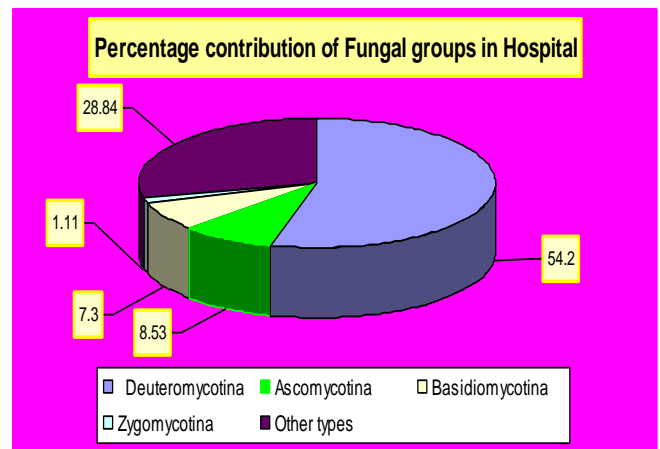
Fig: 1

Fig: 3
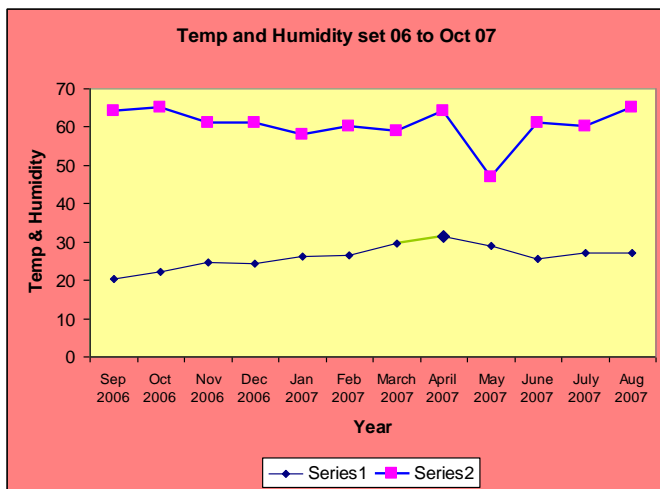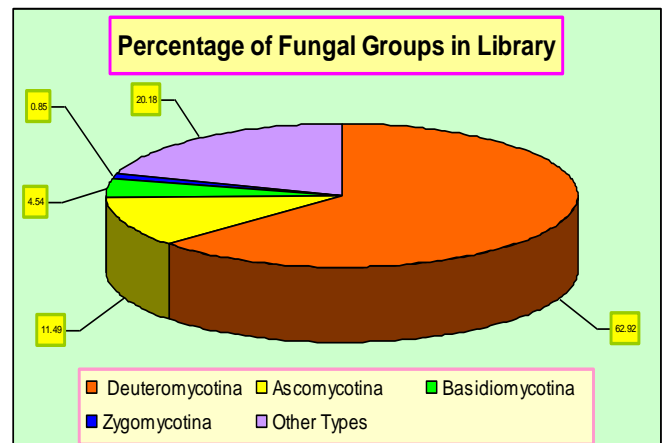
Fig: 4

IV. REFERENCES

[1]. Burnett, H.L. & Hunter B.B. (1972) Illustrated genera of Imperfect fungi. 3rd ed. Burgess Publishing Company Minneapolis, Minnesota.

[2]. Chaturvedy M., Dutta K. and Nair P.K.K. 1992 Incidence of grass pollen in Indian environment. Indian J. Aerobiology : 5 : 20-24.

[3]. Chaubal, P.D. and Kotmire, S.Y. 1985. Airborne fungal spores in hospital premises at Kolhapur. Ind. Bot. Soc. 64 : 109-112.

[4]. Kathapalia Y.P. 1960. Deterioration and conservation of paper –I deterioration IInd IndianPulp and Paper 18: 117-125

[5]. Mukherjee B.B. 1973 Preservation of Library material archives and documents. The world Press Ltd., Calcutta 1-104.

[6]. Parker, M. J. & Munshi (1973), Transmission in hospital. IV int. Symp. Aerobiol. 428-448. Oostchecks Publ. Co. Utrechti. Netherland.

[7]. Plumbe, W.J. 1964. reservation of books in tropical subtropical countries Oxford Univ. pres. London.

[8]. Santra, S.C. & Chanda, S. 1981. Indoor airborne fungal spore flora of Calcutta. West BengalProc. 1st National Conference. Environ. Bio : 45-58.

[9]. Tilak. S.T., & Pillai S.G., (1988). Fungi In Library : An Aerobiological Survey, Ind. J Aerobiology 92-94.

[10]. Singh, A. B., Chatterji, M. Singh, B.P. & Gangal, S.V. 1990. Airborne viable fungi in library : before and afteragitation of books. Indian J. Aerobiol. 3 : 32-38.

[11]. Tilak, S.T. & Pillai, S.G., (1988), Fungi in Library: An Aerobiological Survey Ind. J. Aerobiol. 1 : 92-94.

[12]. Tilak, S.T. & Saibaba, M. 1984.Aerobiological approach to book deterioration in libraries. J.Pl. Nature 1(2) : 1-10.

[13]. Tilak, S.T. & Vishwe, D.B. (1975), Microbial content of air inside Library, Bioviguanum. 1:187-190.

[14]. Tilak, S.T., Talib, S.H., & Bhasale, S.S. (1981). Inhalant allergens inside the Hospital ward. Proc. Nat. Con. Envi.Bio. 113-116.

[15]. Tripathi, R. N., (1987) Fungal Airspora inside the Central Library of Gorakhpur University, Water, Air, Soil pollution. 34 :125-134.

[16]. Verma, K.S. and Khare, K. 1987. Fungal agent which damage paper materials in Library. Atmospheric Biopollution, edited by N. Chandra Environmental Publication, Karad.

[17]. Vittal, B.P.R. & Glory, L.A. (1984), Airborne fungus Spores of a library of India. Grana 24 : 129-133

Thermo-Acoustical and Excess Parameters in Ternary Mixture of Containing Aqueous KOH in Dimethyl Sulfoxide at Different Temperatures

A. A. Mistry

Department of Physics, Anand Niketan College, Warora, Maharashtra, India

ABSTRACT

The thermo-physical parameters such as density (ρ), ultrasonic velocity (U) and viscosity (η) are determined for a ternary mixture (n=3) of aqueous potassium hydroxide (aq. KOH) and dimethyl sulfoxide (DMSO) system at 0.0% to 100% (v/v) and at different temperatures. Using the experimental data, adiabatic compressibility (β), free length (L_f) and free volume (V_f) are evaluated at different temperatures.. The excess values of adiabatic compressibility (β^E), excess free length (L^E_f) and free volume (V^E_f) have also been computed by using the experimental data. The behavior of these parameters with composition of the mixture has been discussed in terms of molecular interaction between the components of the liquids. The deviation in the excess values reveal that intermolecular interactions obtaining in the solution.

Keywords : *Ultrasonic velocity, acoustical parameters, molecular interactions, aqueous potassium hydroxide (aq. KOH) and* dimethyl sulfoxide (DMSO).

I. INTRODUCTION

The adaptable non-destructive technique like Ultrasonic interferometer is highly helpful for the characterization of various physico-chemical properties.Uitrasonic velocity jointly with density and viscosity investigations in liquid mixtures find widely applications in recognizing physico-chemical behavior[1-2].The temperatures dependence of the ultrasonic parameters provide wealth of information about the interactions between the ions,dipoles,hydrogen bonding and weak Vander Waals forces between the components of the liquid mixtures[3-5]. The studies on the physio-chemical properties of organic liquid such as: dimethyl sulfoxide in aqueous solution of potassium hydroxide provides useful information, which is used to assess the information of molecular interaction [6-7]. The ultrasonic velocity data for ternary liquid mixtures have been used by many researchers [8-10]. The deviation from ideally is expressed by many thermo-acoustic parameters ,particular by excess properties [11-12].In this paper the authors report on the ultrasonic velocity, density, and viscosity of 1N aqueous potassium hydroxide with dimethyl sulfoxide at different temperatures over the different volume ratio (v/v) of aqueous KOH in DMSO. From these experimental values, a number of thermodynamics parameters, namely adiabatic compressibility (βa), intermolecular free length (L_f), free volume (V_f), internal pressure (π_i) and Gibb's free energy (ΔG) were calculated and the results such as excess parameters are analyzed in the light of molecular interactions in the ternary liquid mixtures.

II. METHODS AND MATERIAL

A simple and direct device which is ultrasonic interferometer technique, operating frequencies ranging from 1 to 10 MHz has been utilized to calculate the ultrasonic velocity. The temperature was maintained by a constant temperature water bath using circulated water through the double walled measuring cell. The density of liquid mixtures was determined using a 10ml specific gravity bottle with an accuracy of ± 0.1 Kgm⁻³. An Ostwald's viscometer was used for the viscosity measurement of pure liquids and liquid mixtures with accuracy 0.001 NSm⁻². The time required for the flow of water (t_w) and time required for the flow of mixture (t_s) was measured with a digital stop watch having an accuracy ±1x10⁻⁶ NSm⁻². All precautions were taken to minimize the possible experimental error.

III. RESULTS AND DISCUSSION

The experimental values of density, velocity and viscosity of 1N aqueous potassium hydroxide with 1,4 dioxane over entire range concentration (v/v) at different temperature using ultrasonic interferometer are shown in **table-1.** It is observed that density decrease with increase in concentration (vol. %) of aqueous potassium hydroxide in dimethyl sulfoxide. The decrease in density indicates the decrease in solute-solvent and solvent- solvent interactions which results in a structure- breaking of the solvent. If temperature of the mixture rises, its density (ρ) decreases. The decrease in density (ρ) with rise in temperature indicates decrease in cohesive force. It is also observed that ultrasonic velocity increases with increase in concentration (vol. %) of aqueous potassium hydroxide in dimethyl sulfoxide up to 80%, indicating the increase in stiffness of the mixture and hence association in the molecules of the component liquids. As the concentration goes higher (above 80%), the ultrasonic velocity gradually decreases indicating stiffness of the mixture decrease and hence

dissociation. It is observed that viscosity slightly decreases with increase in concentration (vol. %) of potassium hydroxide in dimethyl sulfoxide. Increase in temperature of the mixture, increases disorder of the medium and hence entropy increases. As entropy increases, viscosity of the ternary mixture decreases.

From table-2, it is observed that adiabatic compressibility (β$_a$) decreases with increase in concentration (vol. %) of aqueous potassium hydroxide in dimethyl sulfoxide up to 80%, indicating strong intermolecular interaction between aqueous potassium hydroxide and dimethyl sulfoxide. As the concentration goes higher (above 80%), adiabatic compressibility (β$_a$) gradually increases indicating weak molecular interaction among dimethyl sulfoxide and aqueous potassium hydroxide. It is also observed that free length decreases with increase in concentration of aqueous potassium hydroxide in dimethyl sulfoxide up to 80%. The decrease in free length is a result of dipole-dipole and ion-dipole interaction between dimethyl sulfoxide and aqueous potassium hydroxide indicating association. As the concentration (vol. %) of aqueous potassium hydroxide in dimethyl sulfoxide goes higher (above 80%), the intermolecular free length gradually increases indicating weak interaction among solvent and solute.

The excess thermo-acoustical parameters which play a major role in understanding the nature of molecular interactions in liquid mixtures have been studied by many researchers [13-15].From table-3, it is clear that with the increase in concentration (vol. %) of aqueous potassium hydroxide in dimethyl sulfoxide the excess values of β_a^E and L_f^E decrease negatively in magnitude and approach to minimum at around 40% concentration of aqueous potassium hydroxide in dimethyl sulfoxide which suggest that maximum structural changes take place in this region of the mixture. Decreasing negative excess values of β_a^E and L_f^E with increase in temperature may be accounted

for the molecular dissociation which leads to less closer packing in aqueous potassium hydroxide in dimethyl sulfoxide and hence increase in compressibility and free length. The excess values of free volume (V_f^E) are negative as shown in table-3. The negative deviation of excess values of free volume is an indication of the existence of strong interaction between the component molecules. Negative free volume decreases with increasing concentration (vol. %) of aqueous potassium hydroxide in Dimethyl sulfoxide.

TABLE-1: - Density (ρ), Velocity (U) and Viscosity (η) of the ternary systems Aqueous KOH + dimethyl sulfoxide (DMSO) at different temperature.

Vol. % of Aq.KOH in DMSO	ρ (Kgm⁻³)			U (ms⁻¹)			η*10⁻³ (NSm⁻²)		
	298K	303K	308K	298K	303K	308K	298K	303K	308K
00	1104.91	1103.62	1102.09	1464.00	1437.28	1424.00	1.86	1.64	1.44
10	1100.32	1098.12	1095.46	1489.60	1477.60	1448.00	3.34	2.93	2.55
20	1095.52	1093.41	1090.55	1561.60	1538.40	1512.00	3.17	2.78	2.4
30	1090.74	1088.63	1085.57	1592.00	1568.00	1552.00	3.09	2.71	2.4
40	1083.45	1082.15	1080.31	1656.00	1605.60	1588.00	3.01	2.64	2.37
50	1080.21	1078.92	1077.28	1660.00	1608.00	1592.00	2.83	2.48	2.07
60	1072.51	1071.02	1069.09	1668.80	1650.40	1641.60	2.26	1.98	1.76
70	1068.25	1065.91	1065.40	1677.60	1664.00	1652.00	1.89	1.62	1.41
80	1064.19	1061.10	1058.08	1684.80	1667.20	1653.60	1.49	1.3	1.13
90	1061.52	1059.75	1057.44	1644.00	1610.40	1604.00	1.18	1.03	0.905
100	1058.04	1055.89	1055.42	1590.00	1598.00	1612.00	1.05	0.914	0.799

TABLE-2: - Adiabatic compressibility (β_a), free length (Lf) and free volume (Vf) of the ternary systems Aqueous KOH + dimethyl sulfoxide (DMSO) at different temperature.

Vol. % of Aq. KOH in DMSO	β_a *10⁻¹⁰ (m²N⁻¹)			L_f*10⁻¹⁰ (m)			V_f*10⁻⁷ (m³mol⁻¹)		
	298K	303K	308K	298K	303K	308K	298K	303K	308K
00	4.222	4.386	4.474	0.4068	0.4188	0.4251	0.5445	0.6413	0.7647
10	4.095	4.170	4.562	0.4007	0.4084	0.4293	0.2059	0.2481	0.2962
20	3.743	3.864	4.01	0.3830	0.3931	0.4025	0.2104	0.2508	0.3042
30	3.617	3.736	3.824	0.3765	0.3865	0.3930	0.1953	0.2327	0.2750
40	3.365	3.584	3.670	0.3632	0.3786	0.3850	0.1848	0.2150	0.2536
50	3.359	3.584	3.662	0.3629	0.3786	0.3846	0.1710	0.1983	0.2572
60	3.348	3.427	3.470	0.3622	0.3702	0.3744	0.1985	0.2376	0.2824
70	3.326	3.385	3.439	0.3611	0.3679	0.3727	0.2085	0.2587	0.3173
80	3.310	3.390	3.456	0.3602	0.3682	0.3736	0.2296	0.2787	0.3366
90	3.485	3.638	3.675	0.3696	0.3815	0.3853	0.2262	0.2698	0.3258
100	3.738	3.705	3.646	0.3828	0.3849	0.3838	0.1706	0.2111	0.2617

TABLE-3: - Excess values of adiabatic compressibility ($\beta_a{}^E$), intermolecular free length ($L_f{}^E$) and free volume ($V_f{}^E$), of the ternary systems Aqueous KOH + dimethyl sulfoxide (DMSO) at different temperature.

Vol. % of Aq. KOH in DMSO	$\beta_a{}^E$ $*10^{-10}$ (m²N⁻¹)			$L_f{}^E$ $*10^{-10}$ (m)			$V_f{}^E$ $*10^{-7}$ (m3/mol)		
	298K	303K	308K	298K	303K	308K	298K	303K	308K
10	-0.0786	-0.1479	0.1708	-0.0037	-0.0070	0.0083	-0.3012	-0.3501	-0.4182
20	-0.3822	-0.3858	-0.2984	-0.0190	-0.0189	-0.0143	-0.2593	-0.3044	-0.3599
30	-0.4548	-0.4457	-0.4016	-0.0231	-0.0221	-0.0197	-0.2370	-0.2795	-0.3388
40	-0.6634	-0.5296	-0.4728	-0.0340	-0.0266	-0.0235	-0.2101	-0.2542	-0.3099
50	-0.6210	-0.4615	-0.3980	-0.0319	-0.0232	-0.0198	-0.1865	-0.2279	-0.2560
60	-0.5836	-0.5504	-0.5072	-0.0302	-0.0282	-0.0259	-0.1216	-0.1455	-0.1805
70	-0.5572	-0.5243	-0.4554	-0.0289	-0.0271	-0.0234	-0.0742	-0.0814	-0.0953
80	-0.5248	-0.4512	-0.3556	-0.0274	-0.0234	-0.0184	-0.0157	-0.0184	-0.0257
90	-0.3014	-0.1351	-0.0538	-0.0156	-0.0067	-0.0026	0.01821	0.0156	0.0138

IV. CONCLUSION

- The ion-dipole interactions between K^+ of potassium hydroxide and dimethyl sulfoxide are found to be responsible for association whereas the ion-dipole interactions between K^+ of potassium hydroxide and water molecules are found to be responsible for dissociation in the liquid mixtures.

- The excess values of adiabatic compressibility ($\beta_a{}^E$), intermolecular free length ($L_f{}^E$) and free volume ($V_f{}^E$) are sensitive to nature of interaction in liquids.

V. REFERENCES

[1]. Narendra K., Srinivasu Ch., Kalpana Ch., and Narayanmurthy P. (2012) J.Therm.Anal.Calorim.107, 25.

[2]. Thirumaran S., Mathammal R. and Bharati M.(2012),ARPN Journal of Science and Technology 2,7

[3]. Chimankar O. P., Rewatkar K. G. & Tabhane V. A. (2001) , I. Journal of Physics, 75 B (2), 141-145.

[4]. Bhandakkar V. D., Chimankar O. P. & Power N. R.(2010), J. of Chemical & Pharmaceutical Research, 4, 873-877.

[5]. Saxena Indu, Pathak R.N., Vijay Kumar and Rikkam Devi (2015), International journal of applied Research 1(9), 562-569.

[6]. Mistry A.A and Ugemuge N.S.(2020),IRJSE,A7:201-205.

[7]. Tabhane V. A. (1983), Indian J. Pure & Applied Physics 23, 155.

[8]. Kannapan A. N. and Rajendran V.(1992), Indian J. Pure Appl. Phys 30, 240.

[9]. Praharaj M.(2017),Int.J.Curr.Res.Aca.Rev.,5(6),1-5

[10]. Bhandakkar V. D. et al. (2013), J. Pure appl. and Ind. Phys. 3(2), 80-86.

[11]. Shukla B. P, Jha L. K and Dubey G. P. (1992), Indian J. Pure Appl. Phys.30, 754.

[12]. Tadkalkar A. P. (2012), Archives of Physics Research, 3(4), 287-291.

[13]. Prakash O., Darbari S.,(1988),Acoust. Lett.12 (2), 35.

[14]. Jiri Polak, (1970), Canad J. Chem.48, 2457.

[15]. Narayanaswamy G.(1980), Canad J. Chem.58, 229.

Enhancement of Efficiency of Solar Plate Receiver Using Selective Coating of TiO₂ Nanofluids

Nandkishor N. Padole[1*], Omprakash P. Chimankar[2], Nilesh R.Pawar[3]

[1*]Department of Physics, Shri Sai College of Engg. & Tech. Bhadrawati, Maharashtra, India

[2]Department of Physics, RTM Nagpur University, Nagpur, Maharashtra, India

[3]Department of Physics, ACS College Maregaon, Maharashtra, India

ABSTRACT

The main objective of this paper is to minimize irradiative heat loss and to enhance absorption of incoming solar radiation as much as possible using TiO₂ nanofluids. The cavity receiver is an important part for solar energy collection. Currently efficiency of solar cell is very less around 10 percent. The performance of solar system can be improved by effective coating of TiO₂ nanoparticles at receiver end. The utilization of sunlight from UV to visible range or near IR range is an active issue in this field. The energy transfer process activates the photo catalytic reaction on the surface of TiO₂. On the other hand, plasmonic materials show size dependable surface Plasmon resonance. Due to oscillations of free electrons in the plasmonic metals, strong light absorption take place and can generate large electric field near the surface. Quantum confinement plays the role with particle size reduction thereby causing changes in energy band. Combining both effect using semiconductor nanoparticles (TiO₂) is effective to enhance the efficiency of solar plate receiver.

Keywords : Solar Energy, Tio₂ Nanoparticles, Surface Coating, Quantum Confinement

I. INTRODUCTION

Entire world's facing the problems of global warming due to release of hazardous gases in the atmosphere from fossil fuel consumption. India is the world's third largest electricity generator with total installed capacity of 3,26,832 MW out of which 1,92,162 MW is coal based. Due to increase in population makes larger energy users in the country [1]. The pollution and temperature of world enhancing continuously and world facing the problems of shortage of conventional energy sources such as fossils fuels. Therefore researcher found a renewable source of energy which is non pollutant, clean source of energy and can fulfil the world total energy consumption. Solar energy seems to be the most viable choice to meet our clean energy demand [2]. The sun continuously delivers to the earth almost 5×10^{24} J of energy per year and hits the surface of the earth. This quantity is 10,000 times higher than the actual annual energy consumption of the whole world. [3]. Solar energy has many advantages over any other renewable energy sources. But solar systems are facing the problems of low optical and thermal performance. So researcher need to design a solar collector system using various shapes of collector plate for efficient

absorption of solar radiation and to be converted into heat and electricity for useful applications. The receiver cavity is the important components for solar energy receiver. Different types of heat losses observed in case of cavity receiver of solar thermal systems. Various types of receiver are being used in the concentrated solar system such as, cylindrical cavity receiver, conical cavity receiver, spherical cavity receiver etc.

Nanotechnology Boosts Solar Cells Performance

Nanotechnology is the synthesis and applications of ideas from science and Engineering towards the understanding and production of novels materials with small scale [4]. Currently though solar cell is use for conversion of light energy into useful ones but it cannot convert all incident light into useful energy because of poor absorption. Sunlight includes electromagnetic spectrum of all wavelengths and absorption efficiency varies from wavelength to wavelength. Light of energy less than band gap energy does not excite electrons from valence band to conduction band and hence it is not useful. Light of energy greater than band gap energy excite electrons from valence band to conduction band but excess energy is given out in the form of heat. If these excited electrons aren't captured and redirected, they will spontaneously recombine with the created holes, and the energy will be lost as heat or light [5].
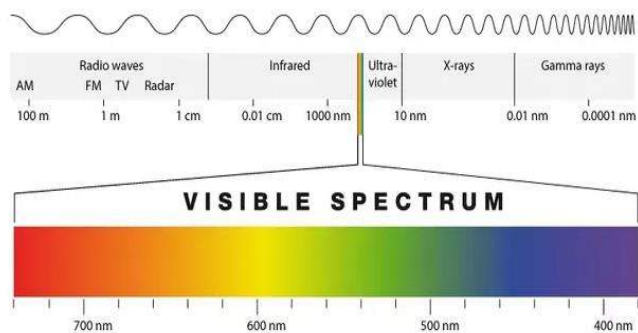
Figure 1. Electromagnetic spectrum

II. EXPERIMENTAL DETAILS/ANALYSIS

2.1 Synthesis of TiO2 nanoparticles

All chemicals used were of analytical grade. Aniline, ammonium persulphate, ammonium hydroxide from SD Fine Chemical, India. Titanium tetrechloride and sulphuric acid from Merk were used as received without further purification. Double distilled water was used throughout this work. The flow chart for the preparation of TiO2 nanoparticles as shown in figure 2.
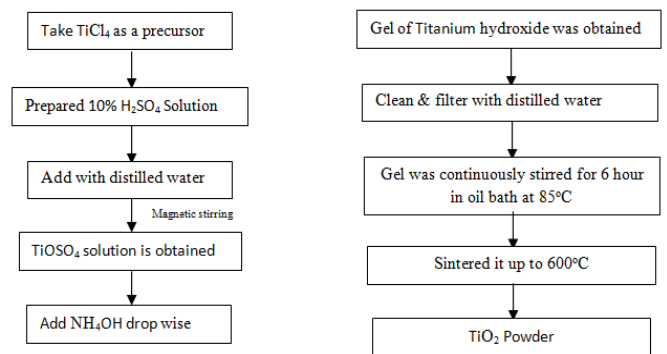
Figure2. Flow chart for synthesis of TiO2 Nanoparticles

2.2 X-ray Diffractometry (XRD) Analysis

The x-ray difractogram of the nano sized tin oxide is obtained by using a Philips Holland, PW-1710 x-ray difractometer having Cu k_α x-ray radiation of wavelength $\lambda=1.5405A^0$ and $1.5443A^0$ and a continuous scan of 2^0/ min at 35 KV and 20 mA. The crystal structure of prepared sample was characterized by X-ray diffraction (XRD). A XRD pattern of the prepared TiO2 powder is shown in figure 3. The broadness of the diffraction peaks as obtained in XRD spectrum gives the direct consequence of the reduced particle size. The diffraction peaks are observed around 25, 35.83, 48.01 and 62.07 respectively. All diffraction peaks can be perfectly indexed to the rutile structured TiO2, which match well to the reported value for TiO2 crystal (JCPDS card, No. 41-1445) and but some impurity phases was observed. It is clear to see that the width of the reflections are considerably broadened, indicating a small crystalline domain size.
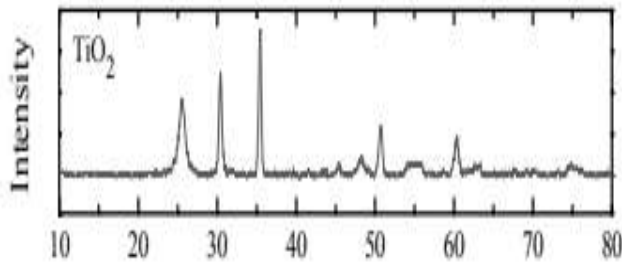
Figure 3. XRD pattern of TiO2 nanoparticles

2.3 Types of Solar Collector

There are three types of solar collectors that are described below.

A. FLAT PLATE COLLECTOR

A simple construction of flat-plate solar collector consists of a waterproof, metal or fiber glass insulated box with dark black colored absorber plate, with one or more transparent glazing. The absorber plates of solar flat collector are typically made out of metal due to its high thermal conductivity and it is painted with special selective surface coatings in order to absorb and transfer heat better than regular black paint. The glazing covers reduce the convection and radiation heat losses to the environment. The collector gains energy from the photons of sun.

B. INTEGRAL COLLECTOR STORAGE SYSTEMS

Furthermore, ICS (integral collector storage) or batch systems contain one or more black tanks or tubes in an insulated, glazed box. The water then continues on the conventional backup water heater, providing a steady source of hot water. Generally it should be installed only in the mild freeze climates because the possibility of to freeze the outdoor pipes in the cold weather.

C. EVACUATED TUBE SOLAR COLLECTORS

They feature parallel rows of transparent glass tubes. In each Evacuated tube contains a glass outer tube and metal absorber tube attached to a fin. The fin's coating absorbs solar thermal energy but inhibits radioactive heat loss. It is a very popular solar collector is in present time. This is a direct and very effective way to heat the water from the sun, but it is also expensive to set up

III. RESULTS AND DISCUSSION

3.1 Ultrasonic velocity measurement

Ultrasonic velocity measurements were carried out using multifrequency interferometer (Mittal F-83 model) techniques at the frequency of piezoelectric transducers 1MHz with accuracy ± 1m/sec. A Thermostat (Lab Slab) controls the temperature of the liquid to an accuracy of ± 0.1°C. Fig.4 shows the variations of ultrasonic velocity with increase in concentration of TiO2 nanoparticles in methanol at 300K. The variation in ultrasonic velocity initially increases, exhibit a pick at molar concentration of 0.004 and dip at 0.006 molar concentrations. Due to highly polar nature of methanol, it induces dipole moment in TiO2 nanoparticles and methanol molecule gets interact with TiO2 nanoparticles through dipole-induced dipole type of interaction. Therefore the rise in ultrasonic velocity can be concluded as the strong interaction among the components of the mixture, molecular agglomerisation and hence sound will travel faster through the more compact structure by means of longitudinal waves. Hence, there might be particle-fluid interaction which favors increase in the ultrasonic velocity values [6].

3.2 Thermal conductivity Measurement

The thermal conductivity of TiO2 nanofluids are studied at low volume concentration by non destructive techniques using obtained experimental acoustical data at 300K. Author used M. Nabeel Rashin, J. Hemalatha model [7] to determine thermal conductivity of nanofluids from obtained experimental values of ultrasonic velocities. Figure 5 shows the increase in thermal conductivity with rise in concentration of TiO2 nanoparticles in methanol.

The maximum rise in the value of thermal conductivity at 0.004 molar concentration indicates that there is more particle- fluids interaction. This result therefore reflects the influence of addition of nanoparticles in a suspension medium upon thermal conductivity at low volume concentration.
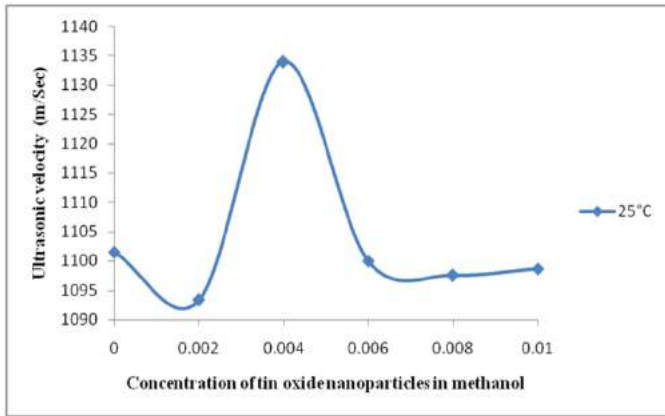
Figure 4. Variation of ultrasonic velocity with concentration of TiO2 NPs in methanol
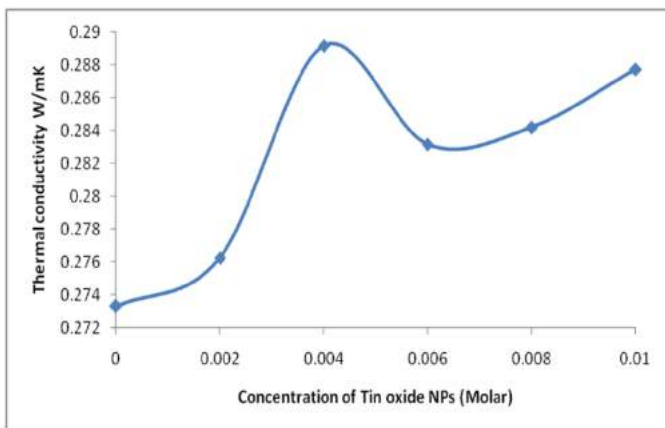
Figure 5. Variation of thermal conductivity with concentration of TiO2 NPs in methanol

3.3 Roll of surface coating of TiO2 nanoparticles
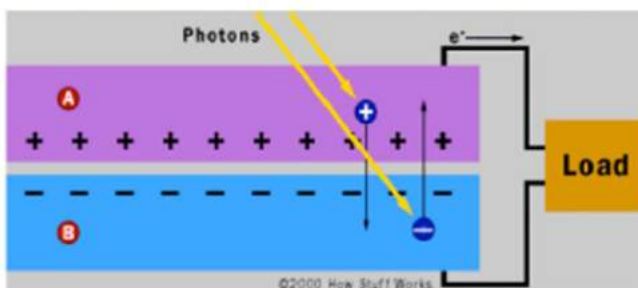
Figure 6. Solar photovoltaic cell

Figure 6 shows the solar photovoltaic cell arrangement. When a photons having energy equal to or greater than band gap energy is incident upon a Collector plate which is coated by TiO2 nanofluids at effective 0.004 molar concentration then photons gets absorbed by the materials and it activate the different processes in the materials. Energy of photons is utilized to excite an electron from valence band to the conduction band thereby creating positive holes in valence band. An atom goes from stable state to unstable state. After 10-3 sec electrons dropped to ground state either by radiative or non radiative transition or electrons in an excited state gets trapped and react with electrons donors or acceptors adsorbed on the surface of photo catalyst. These charge carriers can recombine, non-radiatively or radiatively or get trapped and react with electron donors or acceptors adsorbed on the surface of the photo catalyst. The competition between these processes determines the overall efficiency of TiO2 nanoparticles. For maximum efficiency, electrons should be adsorbed by the photo catalyst. TiO2 can absorb light into the visible light region and convert solar energy into electrical energy for solar cell applications [8]. To obtain reasonable efficiencies comparable to established solar cell technologies, the surface area is enlarged by a factor of 1000, by using nanoparticles of TiO2 with a diameter of approximately 10 -20 nm [9]. The use of TiO2 nanoparticles increases the surface area and enhances the concentration of available surface-active sites, thus leading to higher photo catalytic activity. However, an increase in the surface area increases the number of surface defects which are electron-hole recombination centers. Therefore, an optimization of the crystallinity and of the particle size is required to maximize the efficiency of solar plate [10].

IV. CONCLUSION

The concentration at which particle–fluid interaction is most effective is identified for nanofluids applications by non destructive ultrasonic techniques.

At molar concentration of 0.004, dipole-induced dipole type of interaction between particles and fluids is responsible for rise in ultrasonic velocity. The strong interaction between suspended particles and fluids is considered to be a main reason for thermal conductivity enhancement. Selective materials coating of TiO2 nanoparticles at effective concentration enhance intrinsic as well as extrinsic interaction with surrounding medium through more light absorption, charge generation in material, charge transport, charge trapping either by acceptor or donar catalyst thereby increasing the overall efficiency of solar cell.

V. REFERENCES

[1]. www.eviewglobal.com

[2]. Kehan Yu and Junhong chen, Enhancing Solar Cell Efficiencies through 1-D Nanostructures, Nanoscaleresearch letters, 4 (2008) 1

[3]. Mohammad Sayem Mozumder, Abdel-Hamid I.Mourad, Hifsa Pervez, RihamSurkatti, Recent developments inmultifunctional coatings for solar panel applications: A review, Solar Energy Materials and Solar Cells,189 (2019) 75-102

[4]. Chimankar O P, Padole N N, Pawar N R, & Dhoble S J, acoustic wave propagation in CaCO3 nanofluids, Journal ofnanofluids, 4 (2015) 1

[5]. V. K. Sethi, Mukesh Pandey and Priti Shukla, Use of Nanotechnology in Solar PV Cell, International Journal of Chemical Engineering and Applications, 2 (2011) 2

[6]. Mostafizur R. M.,Saidur R.,Abdul Aziz A. R.,Bhuiyan M. H. U. (2015), Thermophysical properties ofmethanol based Al2O3 nanofluids, International Journal of Heat and Mass Transfer 85, 414-419, doi.org/10.1016/j.ijheatmasstransfer.2015.01.075 .

[7]. M. Nabeel Rashin, J. Hemalatha, A novel ultrasonic approach to determine thermal conductivity in CuO–ethylene glycol nanofluids, Journal of Molecular Liquids 197 (2014) 257–262, DOI: 10.1016/j.molliq.2014.05.024

[8]. Tian, G.-L He, H.-B.; Shao, J.-D. Effects of microstructure of TiO2 thin films on optical band gap energy.Chin. Phys. Lett., 22 (2005)

[9]. Chen, X.; Mao, S.S. Titanium dioxide nanomaterials: Synthesis, properties, modifications and applications, Chem. Rev, (2007)

[10]. Rajendra T. Hiware, Suhas Kongre, Performance improvement techniques in solar flat plate collector: a review,IJARIIE, 2 (2016)

Thermal Characterisation of Polypyrole/Rhodamine-B Dye Composite Synthesized by Simple Chemical Method

N. S. Dixit[1], S. G. Khobragade[2], M. S. Dixit[3], P. P. Chaudhari[4]

[1,4]Department of Chemistry, G.S.Tompe Arts, Commerce & Science college, Chandur Bazar, Amravati, Maharashtra, India

[2] Department of Chemistry, Brijlal Biyani Science College, Amravati, Maharashtra, India

[3]Department of Physics, Jagadamba Mahavidyalaya, Achalpur, Maharashtra, India

ABSTRACT

In-situ chemical oxidative polymerization of pyrrole (Py) was carried out by doping it with xanthene dyes such as Rhodamine-B in the presence of oxidizing agent ammonium peroxydisulphate to synthesize polypyrrole/Rhodamine-B composites. The PPY Rhodamine-B composites were synthesized with various compositions 0.0001 M and 0.00001 M Rhodamine-B in pyrrole. Thermal characterization of synthesized composites was carried out by TGA and DTA analysis. These studies suggest that they exhibit amorphous behavior and change in surface morphology due to insertion of dopant molecules.

Key words : PPy, PPy, Rhodamine-B, APS.

I. INTRODUCTION

Until about 30 years ago all carbon based polymers were rigidly regarded as insulators. The breakthrough happened in year 1977 when somewhat accidentally Alan J. Heeger, Alan G. MacDiramid and Hideki Shirakawa discovered that plastics that are generally referred to as insulators can under certain circumstances be made to behave like metals. Today the overall insight into polymer science and technology is so deep that a chemist and material scientist can create an almost limitless range of new advanced materials with enormous number of applications. They stand with numerous applications in the textile, pharmaceutical, agricultural, electronics, and automotive industries, polymers are used today in the largest quantity of all synthetic materials [1]. The organic materials that generally possess an extended conjugation of Π-electron system along a polymer backbone chain are recognized as electroactive conducting polymers.[2] These materials with interesting electron-transport behavior to a material exhibits immense potential in technological applications such as in electrochromic devices, non-linear optical system OLEDs, photoelectrochemical devices, gas sensors, biomechanical sensors.[3]

Polypyrrole is chosen as a model conducting polymer in this research work because among conducing polymers polypyrrole is one of the extensively studied electronic materials, because it exhibits relatively high electrical conductivity, good environmental stability, low toxicity and versatility of synthesis and ease of tailoring to synthesize functionalized polypyrrole.[4] However, PPy is limited in practical use due to its very

fragile structure and insolubility. It exhibits poor processability and lacks essential mechanical properties.[5] These properties and applicability of polypyrrole can be improved by some suitable modifications of existing polymers structures. This can be achieved by judicious choice of making composites of PPy by doping it with suitable dopant material in order to prepare multifunctional molecular structures that open possibilities for almost any desired applications.[6-7]

The association of PPy with xanthene dyes such as Rhodamine-B in order to prepare its composite to study its various properties have been taken in this research paper.

II. METHODS AND MATERIAL

The oxidizing agent ammonium peroxydisulphate solution and pyrrole solution was mixed and reacted under 1:1 concentration with continuous stirring maintaining the temperature below 5°C for 5-6 hours. The precipitated polypyrrole (PPy) was filtered and dried in hot air oven and subsequently in a muffle furnace at 100 °C. for preparing PPy/0.0001 M Rhodamine composite pyrrole solution was mixed thoroughly with 0.0001 M Rhodamine B composite further mixed and reacted with oxidizing agent ammonium peroxydisulphate. Similarly PPy/0.00001M Rhodamine-B composite is also prepared by following the above procedure. The pure PPy and PPy/Rhodamine-B thin films were prepared by bath deposition technique.

The synthesized composite materials were subjected to thermal studies through TGA and DTA Analysis

III. RESULTS AND DISCUSSION

TGA/DTA Analysis of PPy/ Rhodamine-B composites

As the conducting polymers are useful in number of electronic applications, it is necessary to study its

themal properties. The effect of temperature on stability of polymer is studied by TGA/ DTA analysis.TGA gives the information regarding to weight loss in material with increasing temperature and DTA is useful to determine glass transition temperature (Tg). The TGA thermograms of PPy and PP/Rhd-B composites are given in following figures.

The thermal characteristics of PPy and PPy/Rhodamine-B composite was studied by using thermogravimetric (TGA) technique (instrument DTG-60) by heating in the range 10^0 C/min from room temperature to 550°C in air.
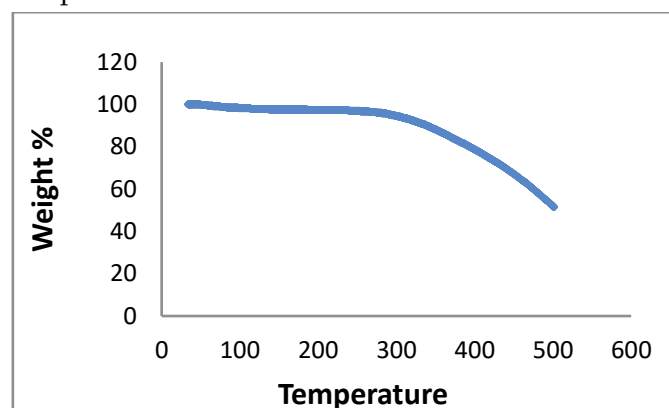
Fig (A)
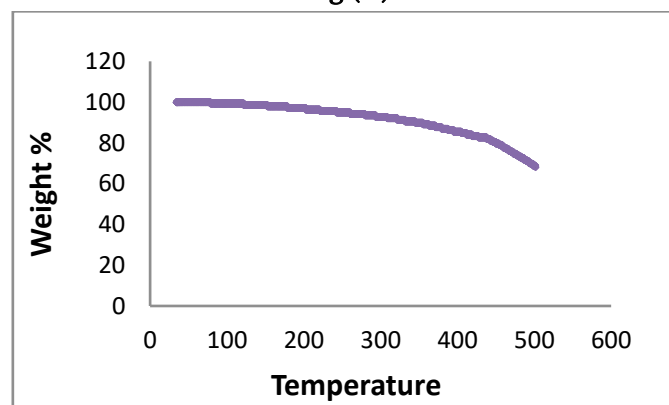
Fig (B)

Fig (A): TGA curve of PPy/0.00001M Rhd-B composite

Fig (B): TGA curve of PPy/0.0001M Rhd-B composite

All the samples of PPy and PPy/Rhodamine-B were observed to exhibit three distinct weight losses as shown in fig. The first stage of weight loss (~3%) at about 80-120°C is associated with the evaporation of solvents, moisture as well as unreacted monomers

elimination. The further heating of material at 250-400°C, a weight of about 15-20% occurs due to the loss of dopant component of the PPy. The drop in weight (~30-40 %) observed at 400-500°C is due to the degradation of the PPy itself. PPy samples are thermally stable in the temperature range of 25-400°C and beyond this range; the decomposition route becomes very rapid. The residual weight of the PPy is about 40% in the oxygen atmosphere; this indicates that PPy does not completely decompose in O_2 even at high temperature.

The weight loss in each step and total weight loss for different weight % at different temperature for different composite materials of PPy composite is given in table below

Table: Weight Loss in each step for PPy/Rhd-B composite

S. N.	Polymer Composite	Weight Loss (%)				
		Step I 50-120^{0}C	Step II 250-400^{0}C	Step III 400-500^{0}C	Total wt loss (%)	Resi due
1.	Pure PPy	0.38	12.57	47.65	60.6	39.4
2.	PPy/0.00001 Rhd-B	0.82	18.45	50.41	69.68	30.32
3.	PPy/0.0001 Rhd-B	0.48	13.01	40.29	53.78	46.22

Thermal properties and interaction between the polymers can also be noted from the DTA studies. DTA is most commonly used to determine transition temperatures such as glass transitions, melting cross-linking reactions and decomposition. However, it measures only the total heat flow and the sum of all thermal transitions in the sample.

DTA curves for PPy/Rhodamine-B composites are explained in figures 4.47 and 4.48, which give the glass transition temperature which determines the softening of the polymer. The TG curve is analogous to DTA curves as the variation in TG curve will give the simultaneous variation in DTA curve.
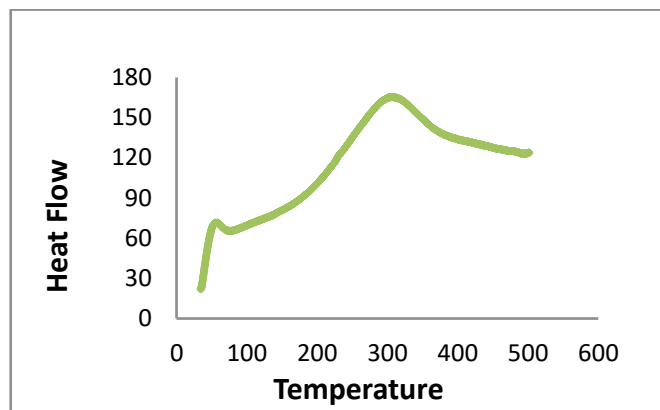
Fig (C)
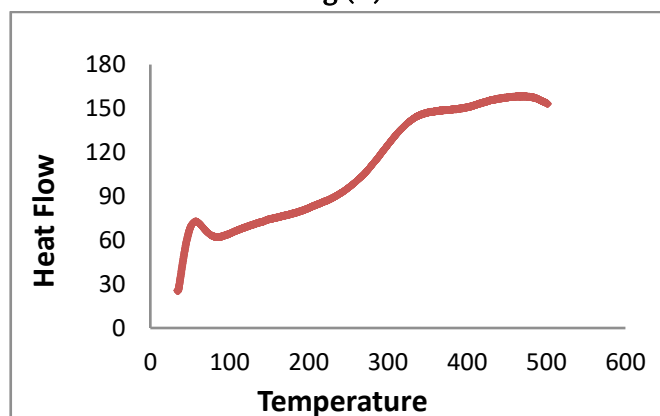
Fig (D)

Fig (C): DTA curve of PPy/0.00001M Rhd-B composite
Fig (D): DTA curve of PPy/0.0001M Rhd-B composite

The various parameters such as glass transition, onset and peak and end temperatures from DTA curves are tabulated in the table below.

It is observed that the glass transition temperature decreases with increasing content of Rhodamine-B. This means that the addition of Rhd-B relives the structure of polymer composites and it becomes soft.

The various thermodynamic parameters from DTA curve of PPy/Rhd-B composites are given in table.

Table: Thermodynamic parameters from DTA curve of PPy/Rhd-B composites

Polymer Composite	Glass transition Temp. (°C)	Crystallization Exothermic Peak		
		Onset temperature (°C)	Peak temperature (°C)	End temperature (°C)
PPy	63.49	221.42	328.21	479.23
PPy/0.00001 Rhd-B	47.39	200.44	307.22	470.6
PPy/0.0001 Rhd-B	47.19	227.96	343.57	482.64

IV. CONCLUSION

Efforts have been made to synthesize the polypyrrole/Rhodamine B composites to tailor the structural, morphological, and thermal properties of polypyrrole. Detailed morphological characterizations of the synthesized composites through XRD studies indicate the incorporation of dopant into the polymeric chain. The TGA study indicates The residual weight of the PPy dye composites is about 40% in the oxygen atmosphere; this indicates that PPy does not completely decompose in O2 even at high temperature. The various parameters such as glass transition, onset and peak and end temperatures from DTA curves is observed that the glass transition temperature decreases with increasing content of Rhodamine-B. This means that the addition of Rhd-B relives the structure of polymer composites and it becomes soft and thermally quite stable.

V. REFERENCES

[1]. Heeger A J, Reviews of Modern Physics, 73, 2001, 681-699

[2]. T A Skotheim, Ed. Handbook of conducting Polymers, vol 1& 2, Marceldekker, New York, 1986.

[3]. Baurele J.E., J Phys. Chem.Solids, , 30, 1969, 2657-2670.

[4]. Kaiser, A. B., et al., Curr. Appl. Phys., 4, 2004, 497–500.

[5]. S.N. Hoier, S.-M. Park, J. Phys. Chem., 96, 1992, 5188.

[6]. Wagner J. B, Wagner C J, J. Chem Phys., 26, 1957, 1597.

[7]. Balint R, Nigel J, Cassidy, Sarah H. Cartmella, Acta Biomateriala, 10, 2014, 2341-2353.

Determination of Phytoconstituents of Blepharis Repens (VAHL) Roth. Stem Through GC-MS

Dr. Purushottam Gangadhar Dhawale

Department of Botany, Shivramji Moghe Arts, Commerce and Science College Padharkawada (Kelapur), Maharashtra, India.

ABSTRACT

Phytochemical constituents are responsible for medicinal activity of plant species. Hence in the present study phytochemical constituents presents in the *Blepharis repens* (Vahl) Roth stem. The shade-dried stem of *Blepharis repens* were extracted with methanol, the concentrated extracts was further subjected to GC-MS. The GC-MS analyses determined the presence of 13 different phytochemical compounds in the methanol stem extract of *Blepharis repens*. The phytochemical compounds were found in the mass spectra was matched with the National Institute of Standards and Technology (NIST) library. In methanol extract of stem 13 compounds were detected. The major phytoconstituents are vitamin-E (20.77%), squalene (18.77%), stigmasterol (23.36%), β-sitosterol (21.31%). The results of the present study reveal that the stem of *B.repens* having effective potential bioactive compounds, which may be leads to the formulation of new drugs to treat various diseases.

Keywords: *Blepharis repens*, phytomedicines, phytoconstituents, GC-MS, secondary metabolites.

I. INTRODUCTION

Plants and various plant products have been used to treat or prevent illness since before recorded history. 'Virikhayurveda' and 'Rig Veda' are few of the well known documentation in traditional herbal medicine available in the form of literature written around 2000 B.C. (Sharma *et al.*, 2011). Drugs from the plants are easily available; they are less expensive, safe, and efficient and rarely have side effects (Yadav *et al.*, 2011).

According to the estimate of WHO, 80% of the population use traditional medicine as their primary health care measure and 85% of this include plant extracts, which may be in crude form or as their active ingredient (WHO, 1993). Phytochemicals are the compounds formed during the plants normal metabolic processes. Being the by-products, these chemicals are often referred to as "secondary metabolites". The major classes of these metabolites includes alkaloids, phenolic components and flavonoids, tannins, terpenoids, coumerins and glycosides (Harborne, 1973 and Okwu, 2004).

To determine the potential and promote the use of herbal medicine, it is essential to intensify the study on medicinal plants that has been used as folklore (Awadh *et al.*, 2001). Plants are used medicinally in different countries and are a source of many potent and powerful drugs (Shrivastava *et al.*, 1996). There is a continuous and an urgent need to discover new compounds with diverse chemical structures and novel mechanisms of

action for new and re-emerging infectious diseases (Rojas *et al.*, 2003). Therefore the present investigation was planned to investigate the major phytoconstituents present in *Blepharis repens* (Vahl) Roth stem.

II. METHODS AND MATERIAL

Collection of plant materials:

The plant was collected from forest localities of Yavatmal District . Identification were made with the help of standard floras (Karthikeyan and kumar, 1993, Naik, 1998).

Preparation of powder and extract of various parts of selected plants :

The collected plant material was shade dried and mechanically powdered and stored in an airtight container. Various extracts was prepared according to the methodology of Sadashivan and Manickam (2005). The shade dried plants parts were allowed to pulverization to get coarse powder. The coarse powder materials were subjected to Soxhlet extraction separately and successively with acetone and methanol extracts.

Gas Chromatography and Mass Spectroscopy (GC-MS) Profiling:

The analysis was carried out using gas chromatography – high resolution mass spectrophotometer. Dried extract were dissolved in the 5 ml of methanol solvent 0.4 µl of this solution is employed for GC – MS analysis. The GC-MS analysis was carried out using Trace GC Ultra (Thermo Scientific) with column (HP-5) of 30 meter length, 0.25 mm diameter and 0.25 film. Helium gas is used as carrier gas at constant flow rate of 1ml/ minute. Injector temperature was set at 250 ^{0}C. The oven temperature were programmed from 80^{0}C to 280 ^{0}C. 80^{0}C 1 minute hold up to 200 ^{0}C at 8 ^{0}C/ minutes, 7 minutes hold up to 280 ^{0}C at the rate of 10 ^{0}C/minutes. The sample was injected in split mode as 20:1. Identification of the compounds was done by comparing the spectral data of sample compound with the compound spectra present in spectral libraries (NIST).
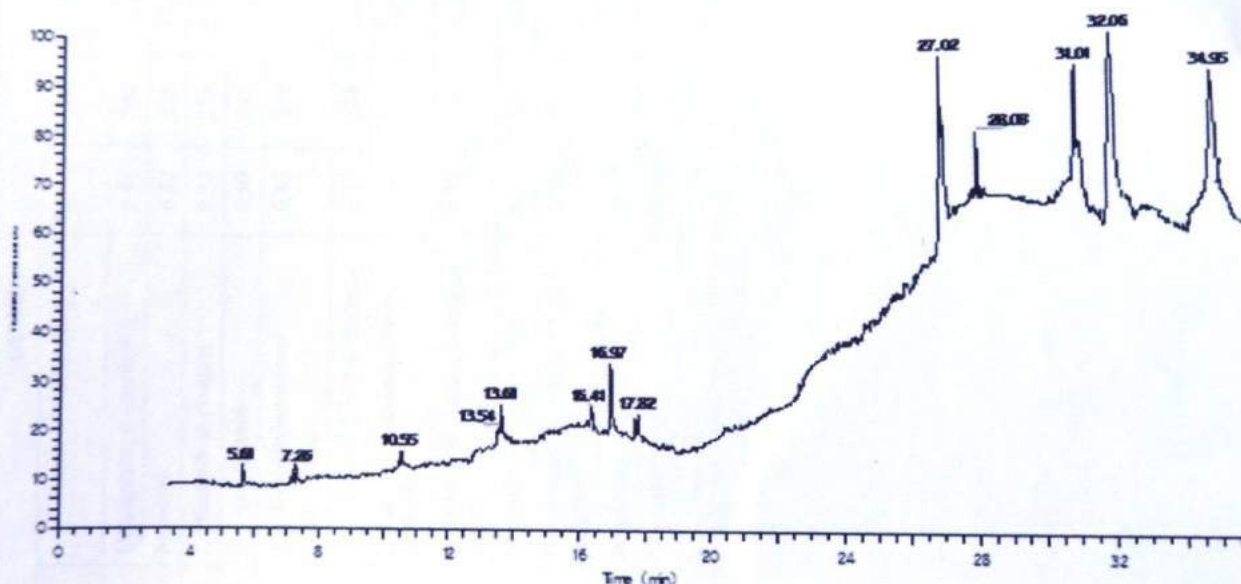
Fig 4.1: Total ion Chromatogram of Methanol extract of *Blepharis repens* Stem

Table 4.1: Phytochemical Profiling of methanol extract of *B. repens* stem by GC-MS

Sr.No.	R.T.	Name of Compound	Rel. %	MW	MF
1	5.61	Octadecane, 6 – methyl	0.41	268	$C_{19}H_{40}$
2	7.25	Menthol	0.37	156	$C_{10}H_{20}O$
3	10.55	Limonen-6-ol-pivalate	0.33	236	$C_{15}H_{24}O_2$
4	13.54	2- Hexadecanol	0.50	242	$C_{16}H_{34}O$
5	13.61	1,1- Dimethyltetradecyl Hydrosulfide	0.83	258	$C_{16}H_{34}S$
6	16.41	1-Dodecanol,3,7,11-trimethyl-	0.37	228	$C_{15}H_{32}O$
7	16.97	2- Cis - 9 - Octadecenyloxy- ethanol	1.33	312	$C_{20}H_{40}O_2$
8	17.82	Phthalic acid , butyl , tetradecyl ester	0.75	418	$C_{26}H_{42}O_4$
9	27.02	Vitami-E	20.77	430	$C_{29}H_{50}O_2$
10	28.08	Octadecane , 3 – ethyl – 5 - (2-ethylbutyl)-	10.84	366	$C_{26}H_{54}$
11	31.01	Squalene	18.77	410	$C_{30}H_{50}$
12	32.06	Stigmasterol	23.36	412	$C_{29}H_{48}O$
13	34.95	β – Sitosterol	21.31	414	$C_{29}H_{50}O$

III. RESULTS AND DISCUSSION

The phytochemical profiling of plant extract was determined by GC-MS technique. Table 4.1 represent the finding of GC-MS analysis of plant extract. In methanol extract of stem 13 compounds were detected. The major phytoconstituents are vitamin-E (20.77%), squalene (18.77%), stigmasterol (23.36%), β-sitosterol (21.31%).

IV. CONCLUSION

This is the first report of documentation of active constituents from stem of *B. repens*. The results of the present study reveal that the stem of *B.repens* having effective potential bioactive compounds, which may be leads to the formulation of new drugs to treat various diseases.

V. ACKNOWLEDGMENT

VI. REFERENCES

[1]. Awadh, A., Juelich, N.A., Kusnick, W.D. and Lindequist, U. (2001).Screening of Yemeni Medicinal Plants for Antibacterial and Cytotoxic Activities.J Ethnopharmacol :173-179.

[2]. Harboane, J. B. (1973). Phytochemical methods: A guide to modern techniques of plant analysis. Chapman And Hall Ltd.,London.

[3]. Karthikeyan, S. and Kumar, A. (1993).Flora of Yavatmal District, Maharashtra.Botanical Survey of India, Calcutta.

[4]. Naik,V. N. (1998). Flora of Marathwada.Vol.I&II,Amrut prakashan, Aurangabad.

[5]. Okwu, D.E. (2004). Phytochemicals and vitamin content of indigenous spices of SouthEastern Nigeria. J. Sustain Agric. Enviran., 6: 30-34.

[6]. Rojas, R., Bustamante, B., Bauer, J., Fernandez, I., Alban, J.L. (2003). Antimicrobial activity of Selected Peruvian Medicinal Plants.Journal of Ethnopharmacology, 88:199-204.

[7]. Sadashivan, S. and Manickam, A. (2005).Biochemical Methods. 2nd Edn., New Age International (P) Ltd., Publisher New Delhi.

[8]. Sharma, A., Joseph, L. and George, M. (2011).Phytochemical and Antimicrobial Evaluations of Leaf Extractof Lantana Camara.International Journal of Pharmaceutical & Medicinal Innovations,1(1):22-31.

[9]. Srivastava, Lambert, J. J. and Vietmeyer, N. (1996). Medicinal Plants: An Expanding Role In Development, World Bank Technical Paper, No. 320.

[10]. World Health Organisation (1993). Summary of WHO guidelines for the assessment of herbal medicines, Herbal Gram., 28:13-14.

[11]. Yadav, R. N. S. and Agarwala, M. (2011).Phytochemical analysis of some medicinal plants. Journal of Phytology., 3 (12): 10-14.

Biosensors in Medicine

Dr. Manju H. Pardeshi

Department of Zoology, Arts Commerce & Science College Maregaon, Dist. Yavatmal, Maharashtra, India

ABSTRACT

Biosensors devices have attracted the attention of many researchers across the world. They have the capability to solve a large number of analytical problems and challenges. They are future ubiquitous devices for disease diagnosis, monitoring, treatment and health management. Biosensors and their role in medical science including early stage detection of human interleukin-10 causing heart diseases, rapid detection of human papilloma virus, etc. are important aspects. In this research paper we have been highlighted applications of biosensors in medicinal field.

Keywords : Biosensors, Biosensors In Medicine, Environmental Monitoring, Genetic Enginnering.

I. INTRODUCTION

Biosensors have shown to be very helpful in our daily life and to play a relevant role in agriculture, food safety, homeland security, bioprocessing, environmental and industrial monitoring. However, biosensing in medicine is the most promising application of the field, since there is a need for new and improved devices with sensitivity, specificity, reliability and biocompatibility for the diagnosis, monitoring and treatment of several health conditions. Additionally, to the troubleshooting, real-time monitoring and management of health problems, biosensors must also be able to simultaneously detect multiple analytes or stimulus, within biological fluids, outside and inside the body (Perumal and Hashim 2014). The demand for constant monitoring of vital signs aims to solve the issue related to the conventional need of hospitalization and supervision of the patient. Therefore, several studies have been made in researching and developing skin-integrated and implantable medical devices. In these devices, the most often monitored vital signs are heart electrical signals, blood pressure, pulse rate, blood glucose level, and respiration efficacy (Lee 2015). Advances in this field have provided freer patient motion and uninterrupted diagnostic data streams for medical monitoring (Rebelo et al. 2019).

In a biomedical context, biosensors need specific requirements, such as biocompatibility (sometimes, biodegradability and/or bioresorbability), miniaturization and reliability. All this progress in biosensors field has opened new routes to improve the medical care, diagnostic systems and the patient's commodity. The aim of this review is to give a brief overview in the biosensors field and applications of biosensors in medicine.

II. BIOSENSORS IN MEDICINE

Biosensors, as a fast-growing field by virtue of their ability to drastically help a number of analytical challenges and problems, have found applications in distinct areas, like agriculture and food safety,

environmental monitoring, biotechnology, genetic engineering, pharmacology, defence, homeland security, industry, and essentially, in medicine and health care. In agricultural industry, biosensors are used for certain cases such as enzymes biosensors, to detect organophosphates and carbamates from pesticides, microbial biosensors for measurement of methane and ammonia, and bacteria-based biosensors for wastewater quality control. Regarding the food industry, biosensors are being used to measure amino acids, carbohydrates, inorganic ions, alcohols, acids, etc.(Hasanet al.,2014); Kirsch (2013); Mohanty and Koucianos 2006). Despite all the mentioned application areas, the most popular and with enormous potential is the application in medicine and biomedical diagnosis. This potential is driven by the need to solve medical and health problems including diabetes, cancer, chronic diseases such as heart disease, respiratory diseases, stroke, obesity, and so many others. Hence, measurements that are being established in health care are related to blood metabolites like glucose, lactate, and urea, and also to cancer biomarkers, folic acid, biotin, vitamin B12 and pantothenic acid. The first introduction of a biosensor in medicine was in 1962, with the development of an amperometric enzyme electrode (platinum) for a glucose sensor by Leland C. Clark and Champ Lyons. These platinum electrodes detected oxygen as a result of the change on the enzymatic activity of the enzyme glucose oxidase which was entrapped with a dialysis membrane at the electrodes, depending on the surrounding concentration of oxygen(Clark and Lyons 1962); (Mohanty and Koucianos 2006).Since then, glucose biosensors have so far been the most frequent, and many other biosensors have been developed for medicine, regarding improvements in the sensitivity, selectivity, and multiplexing capacity. Lately, there is a growing interest in the application of biosensors in tissue engineering, notably in microfluidic tissue engineering models, since they can help sense specific biological molecules within the miniaturized tissue

constructs in real-time, by means of ultrasensitive optical, electrochemical, or acoustic systems (Hasan et al. 2014); (Systems et al.2019). In medical and biomedical fields, biosensors must be very accurate, reliable, and should exhibit a high long-term stability with very little drift, and be resistant to the application of mechanical force, such as the ones generated by pulsatile blood flow (Kim 2011); (Bandodkar, Jia, and Wang2015). Furthermore, implantable or wearable medical devices also need to be small, or otherwise they can be uncomfortable and bulky for the patient, especially when employed in confined volume areas, like blood vessels, lungs or the brain. In addition, biosensors should not affect the measurement environment or patient's well-being (Poeggel 2015). Although more challenging in terms of technology advances, both implantable and wearable devices, have in common the fact that they allow the collection of vital signals information (such as heart rate, respiration rate, skin temperature) and consequently, the monitoring of patients' health over long periods of time.

III. APPLICATIONS OF BIOSENSORS IN MEDICAL FIELD

In the discipline of medical science, the applications of biosensors are growing rapidly. Glucose biosensors are widely used in clinical applications for diagnosis of diabetes mellitus, which requires precise control over blood-glucose levels (Scognamiglio, Pezzotti G. and Pezzotti I.2010). Blood-glucose biosensors usage at home accounts for 85% of the gigantic world market (Rea, Polticelli and Antonacci 2009).

Biosensors are being used pervasively in the medical field to diagnose infectious diseases. A promising biosensor technology for urinary tract infection (UTI) diagnosis along with pathogen identification and anti-microbial susceptibility is under study.

Identifying end-stage heart failure patients, prone to adverse outcomes during the early phase of left ventricular assisted device implantation, is important.

A novel biosensor, based on hafnium oxide (HfO2), has been used for early stage detection of human interleukin (IL)-10 (Lee, Zine and Baraket 2012). Interaction between recombinant human IL-10 with corresponding monoclonal antibody is studied for early cytokine detection after device implantation. Fluorescence patterns and electromechanical impedance spectroscopy characterize the interaction between the antibody–antigen and bio-recognition of the protein is achieved by fluorescence pattern. Chen et al. applied HfO2 as a greatly sensitive bio-field-effect transistor (Chen, Liu, Kaneko and McIntyre 2010). HfO2 biosensor has been functionalized for antibody deposition with detection of a human antigen by electrochemical impedance spectroscopy.

The biggest dilemma faced today is of heart failure with about one million people suffering from it. Techniques for detection of cardiovascular diseases include immunoaffinity column assay, fluorometric, and enzyme-linked immunosorbent assay (Ooi et al. 2006); Caruso, Trunfio and Milazzo 2010) ; Caruso, Verde and Cabiati 2012) ; Watson, Ledwidge and Phelan 2011); Maurer, Burri and de Marchi 2010). These are laborious, require qualified personnel and are time consuming. Biosensors established on electric measurement employ biochemical molecular recognition for desired selectivity with a particular biomarker of interest.

The various other biosensors applications include: quantitative measurement of cardiac markers in undiluted serum, microfluidic impedance assay for controlling endothelin-induced cardiac hypertrophy, immunosensor array for clinical immunophenotyping of acute leukemias, effect of oxazaborolidines on immobilized fructosyltransferase in dental diseases; histone deacylase (HDAC) inhibitor assay from resonance energy transfer, biochip for a quick and accurate detection of multiple cancer markers and neurochemical detection by diamond microneedle electrodes.

IV. CONCLUSION

Biosensors have been miniaturised extensively in the recent years. Keeping in line with such developments , microbial cells with high enzyme activities may be required. This is essential especially when microbial cells are used as substitutes to enzyme based sensors. Microorganisms, due to their low cost, long lifetime and wide range of suitable pH and temperature, have been widely employed as the biosensing element in the construction of biosensors.

V. FUTURE SCOPE

Cell and tissue-based biosensors consist of genetically engineered proteins that are infused into cells ex vivo or in vivo. They allow the researcher to sense levels of hormones, drugs, or toxins, continuously and noninvasively, using biophotonics or other physical principles. The scope in this regard could be of value in ageing research.

VI. CONFLICTS OF INTEREST

The author has none to declare.

VII. REFERENCES

[1]. Bandodkar A.J., Jia W., Wang J.(2015). Tattoo-Based Wearable Electrochemical Devices: A Review. Electroanalysis 27, 562–572. biochemical response to a measurable output biological components is also possible. [4]capturing the matching analyte from the

[2]. Caruso R., Trunfio S., Milazzo F. (2010). Early expression of pro- and anti-inflammatory cytokines in left ventricular assist device recipients with multiple organ failure syndrome. Am Soc Art Int Org J. ;56:313–318.

[3]. Caruso R., Verde A., Cabiati M. (2012). Association of pre-operative interleukin-6 levels

with interagency registry for mechanically assisted circulatory support profiles and intensive care unit stay in left ventricular assist device patients. J Heart Lung Transplant. 31(6):625–633.

[4]. Chen Y.W., Liu M., Kaneko T., McIntyre P.C. (2010). Atomic layer deposited hafnium oxide gate dielectrics for charge-based biosensors. Electrochem Solid State Lett. ;13:G29–G32

[5]. Clark L.C., Lyons C.(1962). Electrode Systems for Continuous Monitoring in Cardiovascular Surgery. Ann. N. Y. Acad. Sci. 1962, 102, 29–45. comparing cell, properties like morphology, components are unavoidable: the transducer

[6]. Hasan A., Nurunnabi M., Morshed M.,Paul A.,Polini A., Kuila T., Al Hariri M., Lee Y.K., Jaa A.A.(2014). Recent advances in application of biosensors in tissue engineering. Biomed Res. Int., 307519.In medical field, biosensor placed a including mutations in DNA or RNA, changes in

[7]. Kim D.H., Lu N., Ma R., Kim Y.S., Kim R.H., Wang S., Wu J., Won S.M., Tao H., Islam A. et al.(2011). Epidermal electronics. Science , 333, 838–843.

[8]. Kirsch J., Siltanen C., Zhou Q., Revzin A., Simonian A.(2013). Biosensor technology: Recent advances in threat agent detection and medicine. Chem. Soc. Rev., 42, 8733–8768.

[9]. Lee M., Zine N., Baraket A. (2012). A novel biosensor based on hafnium oxide: application for early stage detection of human interleukin-10. Sens Actuators B., 175:201–207.

[10]. Lee, J.(2015). Human Implantable Arrhythmia Monitoring Sensor with Wireless Power and Data TransmissionTechnique. Austin J. Biosens. Bioelectron., 1, 1008.major path in detecting diagnosed cell. Cancer

[11]. Maurer M., Burri S., de Marchi S. (2010). Plasma homocysteine and cardiovascular risk in heart failure with and without cardiorenal syndrome. Int J Cardiol. 141:32–38.

[12]. Mohanty S.P., Koucianos E(.2006). Biosensors: A tutorial review. IEEE Potentials, 25, 35–40.

[13]. Ooi K.G.J., Galatowicz G., Towler H.M.A., Lightman S.L., Calder V.L. (2006). Multiplex cytokine detection versus ELISA for aqueous humor: IL-5, IL-10, and IFN profiles in uveitis. Investig Ophthalmol Vis Sci. ;47:272–277.

[14]. Perumal V., Hashim U.(2014). Advances in biosensors: Principle, architecture and applications. J. Appl. Biomed. 12, 1–15.

[15]. Poeggal S., Duraibabu D., Kalli K., Leen G., Dooly G., Lewis E., Kelly J., Munroe M.(2015). Recent improvement of medical optical fibre presure and temperature sensors. Biosensors, 5, 432-449.proteins and protein level as well as on

[16]. Rea G., Polticelli F., Antonacci A.(2009). Structure-based design of novel Chlamydomonas reinhardtii D1-D2 photosynthetic proteins for herbicide monitoring. Protein Sci. ;18:2139–2151.

[17]. Rebelo R., Barbosa A.I.,Caballero D., Kwon I.K.,Oliveira J.M., Kundu S.C., Reis R.L.,Correlo V.M.(2019). 3D biosensors in advanced medical diagnostics of high mortality diseases. Biosens. Bioelectron., 130, 20–39.

[18]. Scognamiglio V., Pezzotti G., Pezzotti I. (2010). Biosensors for effective environmental and agrifood protection and commercialization: from research to market. Mikrochim Acta170:215–225. sensor surface. Transducer transforms the signal. The bio recognition elements solution sample. The detection of metabolic or

[19]. Systems B., Rudi S.,Kratz A., Höll G., Schuller P.,Ertl P.,Rothbauer M.(2019). Latest Trends in Biosensing for Microphysiological. Biosensors, 9, 110.

[20]. Watson C.J., Ledwidge M.T., Phelan D. (2011). Proteomic analysis of coronary sinus serum reveals leucine-rich 2-glycoprotein as a novel biomarker of ventricular dysfunction and heart failure. Circulation: Heart Fail.,4:188–197.

Analysis of Water Quality Using Physico-Chemical Parameters, Jamwadi Reservoir in Yavatmal District, MS, India

P. H. Bhagwat

Assistant Professor in Chemistry, Mungasaji Maharaj Mahavidyalaya Darwha, District Yavatmal, Maharashtra, India

ABSTRACT

Jamwadi Reservoir is a small local reservoir located in the village, Jamwadi, District Yavatmal, Maharashtra, India, is a construction above the water flow of Yavatmal apart from the surrounding areas. Physico-chemical character of the Jamwadi reservoir, pollution studies have been studied from February 2021 to March 2021. Apart from disinfectants in the reservoir, it is nutritious as well as sufficient for the growth of aquatic plants. The above study suggests that the Jamwadi reservoir tends to atrophy somewhat below the class of mesotrophic water bodies. Therefore, apart from the administration of this water body, management is also needed. At this time we will study about chloride, total hardness MIG hardness, CA hardness, alkalinity, temperature, pH parameters.

Keywords : quality, tropic status, physicochemical, chloride content, hardness.

I. INTRODUCTION

In the investigation of population expansion, the height of the water is mainly due to the lack of natural resources. Water is the most important natural resource, in addition to valuable national resources, human needs are also needed. For this purpose, proper scheduling, improvement and administration are required for its use. However, studies of environmental sciences and the environment are often seen as counter-developmental as well as contrary to normal development and human well-being, and are viewed with skepticism and are generally disturbing. - The tropical state of the body of water depends on the neighborhood and the landscape. It is essential for all kinds of life, food production, economic growth and global well-being. Due to the amazing expansion of engineering and agriculture, aquatic plants and organisms have spread more and more in recent times, and despite all these things, wherever they occur, they all face local unrest. Increasing industrial, urbanization and development work bring in the inevitable water disaster to counter population explosions. The health of the lakes and their biodiversity is linked to the physical condition. In freshwater enterprises, the importance of nutrients plays the most important role as their outline extends from esophagus to atrophication. Excessive macrophage plant life, which also monitors eutrophication of aquifers. Testing Water Excellence is the first march to drive and protect vehicles in the aquatic environment. It is also true that the purpose of any aquatic biobank network is to protect its habitat, which can adequately withstand the physicochemical deficiencies of water. Therefore, according to the present study, an attempt has been made to study the physicochemical parameters of the Jamwali reservoir in

the Yatammal district of the Indian state of Maharashtra, as well as to draw some conclusions on the structural and objective aspects of the reservoir. The meaning of its protection.

II. METHODS AND MATERIAL

Jam Wadi is a small man-made reservoir with a 1.0.07 hectare water table built on Jam Wadi . The dam is located about 10 km northwest of Jamwadi tehsil Zakhair and 20 km south of Yavatmal. This reservoir is for drinking water supply, irrigation, fishing etc. Is a multi-purpose reservoir for various works like. The three sample stations are showing the sample stations on the map of the Jamwadi reservoir. Point 01, Point 02 and Point 03 stations were selected for the analysis of physiochemical details of water in the entire reservoir. Sample processing as well as laboratory tests: All three water samples were taken between February and March 2021. At the beginning of the day, in the first week of each month, monthly samples of surface water were collected in all three samples. 9 a.m. to 9 p.m.). Iodine treats, two-stop SIM polyclinic bottles were used to collect water samples. The bottles were placed in an ice bucket and brought to the laboratory for analysis. Physical chemical properties of water including water temperature, depth, color, transparency, pH are measured by mercury thermometer, graduation string, visual, arc disc, digital pH meter, total alkalinity, total hardness, chloride, calcium and sample.

Table-1 Parameters of Jamwadi Reservoir water

PARAMETER	POINT 01	POINT 02	POINT 03
Colour	Light yellow	Light yellow	yellow
Odour	Light sweet	Light alcoholic	Light sweet
P^H	5.89	5.32	5.45
Temprature	34	35	32
Total hardness	800	785	760
Ca hardness	165.2	200.4	160.32
Mg hardness	625.5	599.68	602.32
Alkalinity	90	85	83
Chloride content	71.0	63.9	78.1
Electrical conductivity	248.30 µS/cm	109.00 µS/cm	236.40 µS/cm
Transparency	90.40cm	118.00cm	68.59cm

III. RESULTS AND DISCUSSION

Table 1 shows the average deviation of the different physiochemical properties of the reservoir water and their annual indicator range of similarity in Table 1. Reservoirs: Reservoirs in Jam Kho Valley recorded maximum water levels during the post-monsoon period, but minimum water levels were recorded during the summer season in both the years of the study. In the rainy season the water is yellowish-gray and in winter it is green and in summer it is transparent. Water transparency mainly affects factors such as biological productivity, suspended particles and water color 4. Transparency in reservoirs in Jam Kho Valley ranged from 68.59-118.00 cm during monsoon season with low cost. After rains, sand, soil and clay settlements become more transparent and reach a maximum of 118.00 cm in the reservoir. Conductivity measures the capacity of a substance or the solution of electrical action. The electrical conductivity of this reservoir is found to fluctuate between 109.00µS / cm and 248.30µS / cm and it falls in the stored range of Indian water. According to these standards, reservoir water in the Jam Kho Valley falls into the category of mesotrophic water bodies. Soil, soil, organic matter, plankton and other micro-organisms cause turbulence in natural water. Reservoir water quality: Water temperature increased during summer months and decreased during cold months. The survey looked at

changes similar to climate change. Water levels play an important role in controlling water levels.

IV. CONCLUSION

In addition to "natural" extinction, conservatives are trying to save human diversity from the threat of humanity. Major obstacles to the conservation of biodiversity for sustainable life in the future include the lack of an adequate data base, insufficient funding for research, and confusion and controversy over the choice of areas for conservation. This has made the task more and more difficult. Based on its physical-chemical properties, it can be said that the Jam Valley Reservoir is a mesotropic aquatic body, slightly inclined towards the material. The transport conditions of the reservoir guarantee proper protection and management and the best use will be made of these reservoirs, macrophages. It can be obtained from mechanical sources by mechanical extraction or by grass carp. This is because the removal of nutrients in the form of biomass is only tested for eutrophication. Reservoirs, rivers and streams should be blocked and dams should be constructed. This will prevent depletion of water in the reservoir.

V. ACKNOWLEDGMENTS

VI. REFERENCES

[1]. Hujare M.S., Seasonal variation of physico-chemical parameters in the perennial tank of Talsande, Maharashtra, Ecotoxicol Environ Monit 18(3), 233- 242(2008)

[2]. Kadam M.S Pampatwar D.V and Mali R.P., Seasonal variations in different physico-chemical characteristics in Masoli reservoir of Parbhani district, Maharashtra, J Aqua Biol 22(1), 110 112 (2007)

[3]. Kamble S.M., Kamble A.H and Narke S.Y., Study of physico-chemical parameters of Ruti dam, Tq Ashti, dist Beed, Maharashtra, J Aqua Biol., 24(2), 86-89 (2009)

[4]. Kodarkar M S., Methodology for water analysis, physicochemical, Biological and Microbiological Indian Association of Aquatic Biologists Hyderbad; Pub., 2, 50 (1992) 5 Khan M.A.G and Choudhary S.H., Physical and chemical limnology of lake Kaptai, Bangladesh, Trop Eco 35(1), 35-51 (1994)

[5]. Masood Ahmed and Krishnamurthy R., Hydrobiological studies of Wohar reservoir Aurangabad (Maharashtra state), India, J Environ Biol., 11(3), 335-343.(1990)

[6]. Pandey A.K., Siddiqi S.Z and Rama Rao, Physicochemical and biological characteristics of Husain sagar, an industrially polluted lake, Hyderabad Proc Acad Environ Biol 2(2), 161-167 (1993)

[7]. Salve V.B and Hiware C.J Study on water quality of Wanparakalpa reservoir Nagpur, Near Parli Vaijnath, District Beed Marathwada region, J Aqua Biol., 21(2), 113-117 (2008)

[8]. Swaranlatha S and A Narsingrao Ecological studies of Banjara Lake with reference to water pollution J Envi Biol., 19(2), 179-186 (1998) 10 Jayabhaye U.M., Pentewar M.S and Hiware C.J., A Study on Physico-Chemical Parameters of a Minor Reservoir, Sawana, Hingoli District, Maharashtra (2006)

Bianchi Type-VIh Cosmological Model with Quadratic EOS in f(R, T) Theory

Madhuri Purandare[1], Prachi Agrawal[2*]

[1]Department of Mathematics, MKSSSS's Cummins College of Engineering for Women, Karvenagar, Pune, Maharashtra, India

[2*]Department of Mathematics, Brijlal Biyani Science College, Amravati, Maharashtra, India

ABSTRACT

In this paper, we study the spatially homogenous and anisotropic Bianchi type-VIh cosmological model in $f(R,T)$ modified theory with variable cosmological term Λ. Solutions are found by assuming forms of the function $f(R,T)$ as $f(R,T) = f_1(R) + f_2(T)$ and with a quadratic equation of state. It is found that some of which are decelerating and others accelerating. Here, the cosmological parameter is not constant, but it is taken as variable, which can solve the cosmological constant problem.

Keywords : Cosmological Model, Equation of State, f(R,T) Theory, Bianchi Type VIh.

I. INTRODUCTION

The most successful theory in application to cosmology is the theory of General relativity (GR). Until recently, our mental picture of the universe was based more on our philosophical prejudices (or religious beliefs) than on observational data [1]. Cosmology refers to study of the origin of the universe, it's structure evolution, and future of the universe as a whole based upon the interpretations of astronomical observations at different wave-lengths through laws of physics. Relativistic cosmological models are described as the exact solutions of the EFEs that help in understanding the important features of our universe. Many generalizations of EFEs have been proposed in last few decades. Einstein's general theory of relativity (GR) is considered as one of the most beautiful structures of theoretical physics. Among several theories of gravitation, GR has been designated as the most

successful one. In fact, GR is regarded as a geometric theory of gravitation. Mathematical elegance and outstanding formal beauty using tools of Riemannian geometry are the characteristics of Einstein's theory of gravitation. It leads to gravitational action. In 1917, Einstein introduced the cosmological constant L as the universal repulsion to make the universe static in accordance with a generally accepted picture of that time.

For better understanding, researchers proposed various generalizations of general theory relativity, viz., bimetric theory, scalar tensor theory, $f(G), f(R, G), f(R), f(T)$ and $f(R, T)$ gravitational theories. From these, some theories have been studied to learn the behavior of dark energy and its aspects related to the cosmological constant problem. One of the most popular alternatives to Einstein's theory of gravitation is the $f(R, T)$ theory and was proposed by

Harko et al. (2011) [2]. He introduced an arbitrary function of the Ricci scalar R and the trace T of the energy-momentum tensor. The field equations are obtained from the Hilbert-Einstein type variational principle [3, 4]. In $f(R,T)$ theory it is assumed that the gravitational part of the action still depends on a generic function of the Ricci scalar R, but also presents a generic dependence on T [5]. This kind of dependence on T may come because of the consideration of quantum effects[6]. [7, 8] gave modifications in $f(R,T)$ theory.The $f(R,T)$ theory provides An alternative way is given in $f(R,T)$ theory, which explains the cosmic acceleration as presented by current observations. In this theory there remains no need to introduce either the existence of extra spatial dimension or a component like dark energy [9, 10]. Application of this theory will help in exploring various issues which are of current interests and may give rise to some good inferences [11].

Generally many researchers use a linear equation of state (EOS). which give a linear relation between pressure and energy density. But, recent studies shows that there is a accleratd expansion of the universe. To explain this, one can use a more general EOS's. The generalization to the linear EOS is the quadratic EOS:

$$p = p_0 + \beta\rho + \alpha\rho^2 \qquad (1.1)$$

where p_0, α and β are constants. Here, if we express pressure as a function of density $p = p(\rho)$ in a Taylor's series about $\rho = 0$, this gives equation (1.1) to second order.

In the present study, an attempt has been made to solve Binchi Type VI$_h$ cosmological model by considering the following quadratic EOS of the type

$$p = \alpha\rho^2 - \rho \qquad (1.2)$$

where $\alpha \neq 0$. Here we consider variable cosmological parameter. In this paper, Section 2, briefly explains the $f(R,T)$ theory, Section 3, gives the field equations and Section 4, discusses the solutions. Conclusion is presented in Section 5.

II. THE BASIC EQUATIONS

The $f(R,T)$ theory is a modified theory of General Relativity. The field equations of $f(R,T)$ gravity are formulated from a Hilbert-Einstein type variational principle as follows

$$S = \int \left(\frac{f(R,T)}{16\pi G} + L_m \right) \sqrt{g}\, d^4x \qquad (2.1)$$

where R is the Ricci scalar and T is the trace of the energy momentum tensor T_{ab}. Here L_m is matter Lagrangian density. The energy-momentum tensor is:

$$T_{\mu\nu} = \frac{-2}{\sqrt{g}} \frac{\delta(\sqrt{g}L_m)}{\delta g^{\mu\nu}} \qquad (2.2)$$

where, L_m is the Lagrangian density of the matter and it depends only on g_{ab}. Thus

$$T_{\mu\nu} = L_m g_{\mu\nu} - 2\frac{\partial L_m}{\partial g^{\mu\nu}} \qquad (2.3)$$

Now, varying (2.1) with respect to g_{ab}, the following field equations are obtained

$$f_R(R,T)R_{\mu\nu} - \frac{1}{2}f(R,T)g_{\mu\nu} + (g_{\mu\nu}\,\Box$$
$$-\nabla_\mu\nabla_\nu)f_R(R,T) = 8\pi - f_T(R,T)T_{\mu\nu} - f_T(R,T)\Theta_{\mu\nu}$$
$$(2.4)$$

Where

$$\Theta_{\mu\nu} = -2T_{\mu\nu} + L_m g_{\mu\nu} - 2g^{ij}\frac{\partial^2 L_m}{\partial g^{\mu\nu}\partial g^{ij}} \qquad (2.5)$$

Here $T_{\mu\nu}$ is the energy-momentum tensor associated with the Lagrangian L_m and $\Box = \nabla^\mu\nabla_\nu$ is the d' Alembert's operator, $f_T(R,T) = \frac{\partial f(R,T)}{\partial T}$, $f_R(R,T) = \frac{\partial f(R,T)}{\partial R}$. Now, by contracting (2.4) leads to

$$f_R(R,T)R + 3\,\Box\, f_R(R,T) - 2f(R,T) = 8\pi T - (T + \Theta)f_T(R,T) \qquad (2.6)$$

where, $\Theta = g^{\mu\nu}\Theta_{\mu\nu}$. Using equations (2.4) and (2.6), the gravitational equations can be derived as

$$f_R(R,T)\left(R_{\mu\nu} - \frac{1}{3}Rg_{\mu\nu}\right) + \frac{1}{6}f(R,T)g_{\mu\nu}$$
$$= \left(8\pi - f_T(R,T)\right)\left(T_{\mu\nu} - \right.$$
$$\frac{1}{3}g_{\mu\nu}\right) - f_T(R,T)\left(\Theta_{\mu\nu} - \frac{1}{3}\Theta g_{\mu\nu}\right) + \nabla_\mu\nabla_\nu f_R(R,T) \quad (2.7)$$

For perfect fluid

$$T_{\mu\nu} = (\rho + p)u_\mu u_\nu - pg_{\mu\nu} \qquad (2.8)$$

with $u^\mu = (1,0,0,0)$ being the four velocity for which $u^\mu u_\mu = 1$, $u^\mu\nabla_\nu u_\mu = 0$. From equation (2.5), we get

$$\Theta_{\mu\nu} = -2T_{\mu\nu} - pg_{\mu\nu} \qquad (2.9)$$

There is freedom of choice for $f(R,T)$, following, Harko et al. (2011) [4] to construct different kinds $f(R,T)$ modified cosmological models by specifying following three forms of $f(R,T)$ as,

$$f(R,T) = \begin{cases} R + 2f(T) \\ f_1(R) + f_2(T) \\ f_1(R) + f_2(R)f_3(T) \end{cases} \quad (2.10)$$

In this paper, we choose $f(R,T) = f_1(R) + f_2(T)$. Now, using equations (2.8) and (2.9) equation (2.4) becomes

$$f_1'(R)R_{\mu v} - \frac{1}{2}f_1(R)g_{\mu v} + (g_{\mu v} \Box - \nabla_\mu \nabla_v)f_1'(R)$$
$$= (8\pi - f_2'(T))T_{\mu v} + \left(f_2'(T)p + \frac{1}{2}f_1(T)\right)g_{\mu v} \quad (2.11)$$

III. METRIC AND FIELD EQUATIONS

We consider generalized space metric which will cover spatially homogeneous Bianchi type VI$_h$ represented by
$$ds^2 = dt^2 - A^2(t)dx^2 - B^2(t)e^{2x}dy^2 - C^2(t)e^{2hx}dz^2 \quad (3.1)$$

Where h arbitrary constants and A, B, C are metric functions of cosmic time.

In equation (2.11) we take $f_1(R) = \lambda R$ and $f_2(T) = \lambda T$ then the Einstein field equations take the form
$$G_{ij} = \left(\frac{8\pi + \lambda}{\lambda}\right)T_{ij} + \left(\frac{\rho - p + 2\Lambda}{2}\right)g_{ij} \quad (3.2)$$

where the symbols have their usual meaning.

Einstein field equations (3.2) for the metric (3.1) can be written as

$$\frac{\ddot{B}}{B} + \frac{\ddot{C}}{C} + \frac{\dot{B}\dot{C}}{BC} - \frac{h}{A^2} = \left(\frac{16\pi + 3\lambda}{2\lambda}\right)p - \frac{\rho}{2} - \Lambda \quad (3.3)$$

$$\frac{\ddot{A}}{A} + \frac{\ddot{C}}{C} + \frac{\dot{A}\dot{C}}{AC} - \frac{h^2}{A^2} = \left(\frac{16\pi + 3\lambda}{2\lambda}\right)p - \frac{\rho}{2} - \Lambda \quad (3.4)$$

$$\frac{\ddot{A}}{A} + \frac{\ddot{B}}{B} + \frac{\dot{A}\dot{B}}{AB} - \frac{1}{A^2} = \left(\frac{16\pi + 3\lambda}{2\lambda}\right)p - \frac{\rho}{2} - \Lambda \quad (3.5)$$

$$\frac{\dot{A}\dot{B}}{AB} + \frac{\dot{B}\dot{C}}{BC} + \frac{\dot{A}\dot{C}}{AC} - \frac{1 + h + h^2}{A^2} = -\left(\frac{16\pi + 3\lambda}{2\lambda}\right)\rho + \frac{p}{2} - \Lambda \quad (3.6)$$

$$(1 + h)\frac{\dot{A}}{A} - \frac{\dot{B}}{B} - h\frac{\dot{C}}{C} = 0 \quad (3.7)$$

The energy conservation equation is given by $T_{ij}; j = 0$ gives

$$\dot{\rho} + (\rho + p)\left(\frac{\dot{A}}{A} + \frac{\dot{B}}{B} + \frac{\dot{C}}{C}\right) = 0 \quad (3.8)$$

Where overhead dots denote differentiation with respect to time t.

Now, the field equations (3.3) – (3.7) form a system of four independent equations with six unknown parameters $, B, C, p, \rho, \Lambda$. Hence in order to find explicit solution of the system, two additional conditions are to be considered.

So following (Yadav and Sharma 2013;Yadav 2012;Pradhan et al.2013d)first we consider the average scale factor is an increasing function of time as given below

$$a = (t^n e^t)^{\frac{1}{k}} \quad (3.9)$$

Where $k > 0$ and n ≥ 0 are constants.

Secondly we consider quadratic barotropic equation of state (EOS) relating pressure and density given as follows.

$$p = \alpha\rho^2 - \rho \quad (3.10)$$

Where $\alpha \neq 0$

Spatial volume for the model (3.1) is written as
$$V = ABC \quad (3.11)$$

We define average scale factor a of anisotropic model as
$$a = V^{\frac{1}{3}} = (ABC)^{\frac{1}{3}} \quad (3.12)$$

Generalized mean Hubble parameter H is given by
$$H = \frac{1}{3}(H_1 + H_2 + H_3) \quad (3.13)$$

Where $H_1 = \frac{\dot{A}}{A}, H_2 = \frac{\dot{B}}{B}, H_3 = \frac{\dot{C}}{C}$ are the directional Hubble parameters in the direction of x, y, z resp.

Expansion scalar (θ) , anisotropy parameter (A_m) and shear scalar (σ) are defined as usual as follows

$$\theta = 3H$$

(3.14)

$$A_m = \frac{1}{3}\sum_{i=1}^{3}\left(\frac{H_i - H}{H}\right)^2$$

(3.15)

$$\sigma^2 = \frac{1}{2}\left[\left(\frac{\dot{A}}{A}\right)^2 + \left(\frac{\dot{B}}{B}\right)^2 + \left(\frac{\dot{C}}{C}\right)^2\right] - \frac{\theta^2}{6}$$

(3.16)

Deceleration parameter q is defined as

$$q = -\frac{a\ddot{a}}{\dot{a}^2} = -\left(\frac{\dot{H} + H^2}{H^2}\right)$$

(3.17)

Case I) $h = 1$

We consider $h = 1$ then the field eqns (3.3) – (3.7) take the form

$$\frac{\ddot{B}}{B} + \frac{\ddot{C}}{C} + \frac{\dot{B}\dot{C}}{BC} - \frac{1}{A^2} = \left(\frac{16\pi + 3\lambda}{2\lambda}\right)p - \frac{\rho}{2} - \Lambda$$

(3.18)

$$\frac{\ddot{A}}{A} + \frac{\ddot{C}}{C} + \frac{\dot{A}\dot{C}}{AC} - \frac{1}{A^2} = \left(\frac{16\pi + 3\lambda}{2\lambda}\right)p - \frac{\rho}{2} - \Lambda$$

(3.19)

$$\frac{\ddot{A}}{A} + \frac{\ddot{B}}{B} + \frac{\dot{A}\dot{B}}{AB} - \frac{1}{A^2} = \left(\frac{16\pi + 3\lambda}{2\lambda}\right)p - \frac{\rho}{2} - \Lambda$$

(3.20)

$$\frac{\dot{A}\dot{B}}{AB} + \frac{\dot{B}\dot{C}}{BC} + \frac{\dot{A}\dot{C}}{AC} - \frac{3}{A^2} = -\left(\frac{16\pi + 3\lambda}{2\lambda}\right)\rho + \frac{p}{2} - \Lambda$$

(3.21)

$$2\frac{\dot{A}}{A} - \frac{\dot{B}}{B} - \frac{\dot{C}}{C} = 0$$

(3.22)

From (3.22) we obtain

$$A^2 = BC$$

(3.23)

Solving (3.18) – (3.21) by usual technique we obtain

$$\frac{A}{B} = d_1 \exp\left(q_1 \int \frac{dt}{V}\right)$$

(3.24)

$$\frac{B}{C} = d_2 \exp\left(q_2 \int \frac{dt}{V}\right)$$

(3.25)

$$\frac{A}{C} = d_3 \exp\left(q_3 \int \frac{dt}{V}\right)$$

(3.26)

Where d_1, d_2, d_3 and q_1, q_2, q_3 are constants of integration.

From (3.23)-(3.25) and (3.11) we obtain

$$A(t) = L_1 a \, exp(Q_1 \int a^{-3} dt)$$

(3.27)

$$B(t) = L_2 a \, exp(Q_2 \int a^{-3} dt)$$

(3.28)

$$C(t) = L_3 a \, exp(Q_3 \int a^{-3} dt)$$

(3.29)

Where $L_1 L_2 L_3 = 1$ and $Q_1 + Q_2 + Q_3 = 0$

In particular

$$L_1 = \left(\frac{l_3^2}{l_2}\right)^{\frac{1}{3}}, L_2 = \left(\frac{l_2}{l_1}\right)^{\frac{1}{3}}, L_3 = \left(\frac{l_1}{l_3^2}\right)^{\frac{1}{3}}$$

And

$$Q_1 = \frac{2q_3 - q_2}{3}, Q_2 = \frac{q_2 - q_1}{3}, Q_3 = \frac{q_1 - 2q_3}{3}$$

From eqn (3.26) – (3.28) and (3.8) we obtain

$$A(t) = L_1 (t^n e^t)^{\frac{1}{k}} exp(Q_1 F(t))$$

(3.30)

$$B(t) = L_2 (t^n e^t)^{\frac{1}{k}} exp(Q_2 F(t))$$

(3.31)

$$C(t) = L_3 (t^n e^t)^{\frac{1}{k}} exp(Q_3 F(t))$$

(3.32)

Where

$$F(t) = \int (t^n e^t)^{-\frac{3}{k}} dt = \sum_{i=0}^{\infty} \frac{(-3)^{i-1} t^{i - \frac{3n}{k}}}{n^{i-2}(ni - 3k)(i-1)!}$$

(3.33)

Hence from (3.29)-(3.31) the metric takes the form

$$ds^2 = dt^2 - L_1^2 (t^n e^t)^{\frac{2}{k}} exp\big(2Q_1 F(t)\big) dx^2 -$$
$$e^{2x}[L_2^2 (t^n e^t)^{\frac{2}{k}} exp\big(2Q_2 F(t)\big) dy^2 +$$
$$L_3^2 (t^n e^t)^{\frac{2}{k}} exp\big(2Q_3 F(t)\big) dz^2] \qquad (3.34)$$

Case II) $h = -1$

In this section we have considered $h = -1$, then the set of field equations (3.3) – (3.7) reduce to

$$\frac{\ddot{B}}{B} + \frac{\ddot{C}}{C} + \frac{\dot{B}\dot{C}}{BC} + \frac{1}{A^2} = \left(\frac{16\pi + 3\lambda}{2\lambda}\right)p - \frac{\rho}{2} - \Lambda$$

(3.46)

$$\frac{\ddot{A}}{A} + \frac{\ddot{C}}{C} + \frac{\dot{A}\dot{C}}{AC} - \frac{1}{A^2} = \left(\frac{16\pi + 3\lambda}{2\lambda}\right)p - \frac{\rho}{2} - \Lambda$$

(3.47)

$$\frac{\ddot{A}}{A} + \frac{\ddot{B}}{B} + \frac{\dot{A}\dot{B}}{AB} - \frac{1}{A^2} = \left(\frac{16\pi + 3\lambda}{2\lambda}\right)p - \frac{\rho}{2} - \Lambda$$

(3.48)

$$\frac{\dot{A}\dot{B}}{AB} + \frac{\dot{B}\dot{C}}{BC} + \frac{\dot{A}\dot{C}}{AC} - \frac{1}{A^2} = -\left(\frac{16\pi+3\lambda}{2\lambda}\right)\rho + \frac{p}{2} - \Lambda$$

(3.49)

$$\frac{\dot{C}}{C} - \frac{\dot{B}}{B} = 0$$

(3.50)

From eqn (3.50) we obtain

$$B = C$$

(3.51)

Eqn (3.46) – (3.49) with the use of eqn (3.50) form the system of 3 independent equations with five unknowns $A\ B, p\ , \rho, \Lambda$. So to find explicit solutions for the system we consider two conditions given by eqn (3.9) and (3.10) .

Solving eqn. (3.46)-(3.47) in usual way we obtain

$$\frac{A}{B} = c_2 exp\ [c_1 F(t)]$$

(3.52)

$$\frac{A}{C} = c_4 exp\ [c_3 F(t)]$$

(3.53)

Where

$$F\ (t) = \int \frac{e^t}{a^3}\ dt = \int t^{-\frac{3n}{k}} e^{t\left(1-\frac{3}{k}\right)} dt$$

$$= \sum_{i=0}^{n} \frac{(k-3)^{i-1} t^{i-\frac{3n}{k}}}{k^{i-2}(ki-3n)(i-1)!}$$

And $c_1\ , c_2\ , c_3\ , c_4$ are constant of integration.

From (3.11) , (3.52) and (3.53) we obtain

$$A = c_2^{\frac{2}{3}}(t^n e^t)^{\frac{1}{k}}\ exp\left[\frac{2c_1}{3}F(t)\right]$$

(3.54)

$$B = C = c_2^{-\frac{1}{3}}(t^n e^t)^{\frac{1}{k}}\ exp\left[-\frac{c_1}{3}F(t)\right]$$

(3.55)

Now the metric (3.1) can be rewritten as

$$ds^2 = dt^2 - c_2^{\frac{4}{3}}(t^n e^t)^{\frac{2}{k}}\ exp\left[\frac{4c_1}{3}F(t)\right]dx^2 - c_2^{-\frac{2}{3}}(t^n e^t)^{\frac{2}{k}}\ exp\left[-\frac{2c_1}{3}F(t)\right](e^{2x}dy^2 + e^{-2x}dz^2)$$

(3.56)

IV. RESULTS AND DISCUSSION

For both the cases expression for energy density and pressure, Hubble parameter (H), expansion scalar (θ) and deceleration parameter (q) are obtained as

$$\rho = \left[\frac{3\alpha}{k}\log(t^n e^t)\right]^{-1}$$

(4.1)

$$p = \alpha\left[\frac{3\alpha}{k}\log(t^n e^t)\right]^{-2} - \left[\frac{3\alpha}{k}\log(t^n e^t)\right]^{-1}$$

(4.2)

$$H = \frac{1}{k}\left(\frac{n}{t} + 1\right)$$

(4.3)

$$\theta = \frac{3}{k}\left(\frac{n}{t} + 1\right)$$

(4.4)

$$q = -1 + \frac{kn}{(n+t)^2}$$

(4.5)

Other physical parameters such as cosmological parameter (Λ), mean shear scalar (σ) and an anisotropy parameter (A_m) are obtained as

For $h = 1$

$$\Lambda = -\left(\frac{16\pi+3\lambda}{2\lambda}\right)\left[\frac{3\alpha}{k}\log(t^n e^t)\right]^{-1} + \frac{1}{2}\left\{\alpha\left[\frac{3\alpha}{k}\log(t^n e^t)\right]^{-2} - \left[\frac{3\alpha}{k}\log(t^n e^t)\right]^{-1}\right\} - \frac{3}{k^2}\left(\frac{n}{t} + 1\right)^2 - Q_4 t^{-\frac{6n}{k}} e^{\left(-\frac{6t}{k}\right)} + \frac{3}{l_1^2}(t^n e^t)^{-\frac{2}{k}} exp[-Q_1 F(t)]$$

(4.6)

$$A_m = k^2 Q(t^n e^t)^{-\frac{6}{k}}\left(\frac{n}{t} + 1\right)^{-2}$$

(4.7)

where $Q = Q_1^2 + Q_2^2 + Q_3^2$

$$\sigma^2 = \frac{Q}{2}\ (t^n e^t)^{-\frac{6}{k}}$$

(4.8)

For $h = -1$

$$\Lambda = -\left(\frac{16\pi+3\lambda}{2\lambda}\right)\left[\frac{3\alpha}{k}\log(t^n e^t)\right]^{-1} + \frac{1}{2}\left\{\alpha\left[\frac{3\alpha}{k}\log(t^n e^t)\right]^{-2} - \left[\frac{3\alpha}{k}\log(t^n e^t)\right]^{-1}\right\} - \frac{3}{k^2}\left(\frac{n}{t} + 1\right)^2 - Q_4 t^{-\frac{6n}{k}} e^{\left(-\frac{6t}{k}\right)} + \frac{3}{l_1^2}(t^n e^t)^{-\frac{2}{k}} exp[-Q_1 F(t)]$$

(4.9)

$$\sigma^2 = \frac{c_1^2}{3} t^{-\frac{6n}{k}} e^{2t\left(1-\frac{3}{k}\right)}$$

(4.10)

$$A_m = \frac{2c_1{}^2}{9\left(\frac{1}{k}\left(\frac{n}{t}+1\right)\right)^2} \, t^{-\frac{6n}{k}} \, e^{2t\left(1-\frac{3}{k}\right)}$$

(4.11)

From the above result, we can note that the volume of the universe increases as there is an increase in cosmic time t. We observe that energy density (ρ) and barotropic pressure (p) of the fluid is a decreasing function of time. From above eqns we can observe that at t = 0, the spatial volume scale factor (V) vanishes. While the parameters such as scalar of expansion (θ), mean Hubble parameter (H) and shear scalar (σ) are infinite, this is big bang scenario. As t → ∞, V diverges to ∞ whereas θ, H and σ approach to zero whenever $k > 0 \; and \; n \in \mathbb{R}$

Anisotropy parameter A_m is a decreasing function of time t and tends to 0 for large values of time t in both the cases whenever $k > 0 \; and \; Q \, , n \in \mathbb{R}$. Hence, at late times, the Bianchi type VI$_h$ model is isotropic for positive values of k.

The deceleration parameter for this model is positive if t < $\sqrt{nk} - n$ which shows that the universe is in a decelerating phase and, and negative for t > $\sqrt{nk} - n$ which indicates that the universe is accelerating.

V. CONCLUSION

In this paper, we have presented new exact solutions of the Bianchi VI$_h$ cosmological model. The model a spatially homogenous and anisotropic in $f(R,T)$ gravitation theory along with variable cosmological parameter Λ. The solutions of the field equations in $f(R,T)$ are obtained by considering that $f(R,T) = f_1(R) + f_2(T)$, the quadratic equation of state. We have considered two variations of h, $h = 1$ and $h = -1$. For both the values we have obtained exact solutions of the field equations almost identical observations.

VI. REFERENCES

[1]. Cotsakis S., Papantonopoulos E.: Cosmological Crossroads: An Advanced Course in Mathematical, Physical and String Cosmology, Springer Sci. & Business Media, 2002.

[2]. Harko T., Lobo F. S., Nojiri S., Odintsov S. D.: f (R,T) Gravity, Phys. Rev. D, 84(2) (2011), 024020-1 to 024020-14.

[3]. Harko T., Lobo F. S.: Generalized dark gravity, Int. J. of Modern Phys. D, 21(11) (2012), 1242019-1 to 1242019-8, https://doi.org/10.1142/S0218-271812420199.

[4]. Sahoo P.K., Mishra B., Reddy G. C.: Axially symmetric cosmological model in f (R;T) gravity, Eur. Phys. J. Plus, 129(3) (2014), 1-8, https://doi.org/10.1140/epjp/i2014-14049-7.

[5]. Moraes P., Sahoo P.K.: The simplest non-minimal matter-geometry coupling in the f (R;T) cosmology, The Eur. Phys. J. C, 77(7) (2017), 1-8, https://doi/10.1140/epjc/s10052-017-5062-8.

[6]. Adhav K.S.: LRS Bianchi type-I cosmological model in f (R;T) theory of gravity, Astrophys. Space Sci., 339(2) (2012), 365-369, https://doi.org/10.10-07/s10509-011-09638.

[7]. Agrawal P.K., Pawar D.D.: Plane symmetric cosmological model with quark and strange quark matter in f (R;T) theory of gravity, J. Astrophys. Astr., 38(2)(2017), 1-7, https://doi.org/10.1007/s12036-016-9420-y.

[8]. Chaubey R., Shukla A.: A new class of Bianchi cosmological models in f (R;T) gravity, Astrophys. Space Sci., 343(1) (2013), 415-422, https://doi.org/10.1007/s10509-012-1204-5.

[9]. Pawar D.D., Agrawal P.K.: Dark energy cosmological model in f (R;T) theory of gravity, Prespacetime J., 6(3) (2015), 719-732.

[10]. Pawar D.D., Agrawal P.K.: Role of constant deceleration parameter in cosmological model filled with dark energy in f (R;T) theory, Bulg. J. of Phys., 43(2),(2016), 148-155.

[11]. Pawar D.D., Bhuttampalle G., Agrawal P.K.: Kaluza-klein string cosmological model in f(R;T) theory of gravity, New Astronomy, 65 (2018), 1-6, https://doi.org/10.1016/j.newast.2018.05.002.

Ultrasonic Investigations of Substituted 2-oxo-2H-Chromene-3-Carbohydrazide Derivatives in 80% (DMF+Water) Mixture at 305K

P. P. Choudhari[1], N. S. Dixit[1], P. R. Yawale [1], S. S. Ubarhande[1], M. N. Pawar[1], M. P. Wadekar[2*]

[1]G. S. Tompe Arts, Commerce and Science College, Chandur Bazar, Amravati, Maharashtra, India

[2*]Government Vidarbha Institute of Science and Humanities, Amravati, Maharashtra, India

ABSTRACT

Ultrasonic study of substituted 2-oxo-2H-chromene-3-carbohydrazide derivatives is done. In the present work, different properties such as apparent molal volume (ϕ_v), apparent molal compressibility (ϕ_k), relative association (R_A) and solvation number (S_n) have evaluated for following substituted 2-oxo-2H-chromene-3-carbohydrazide derivatives in 80% (DMF+water) mixture at 305K in different concentrations of ligands.

Keywords: - Substituted 2-oxo-2H-chromene-3-carbohydrazide derivatives, apparent molal volume (ϕ_v), apparent molal compressibility (ϕ_k), relative association (R_A) and solvation number (S_n).

I. INTRODUCTION

Ultrasonic technique is also useful to study the weak and strong molecular interactions. Studies of ultrasonic velocity and acoustic properties of binary liquid mixtures consisting of methyl benzoate are of interest because of its use as dye carrier formulations in textile processing and in purification of reagents . Acoustical properties of some substituted pyrazolines in acetone-water are observed with variation of ultrasonic velocity with concentration . Density and ultrasonic velocity for the binary mixtures of toluene with heptan-1-ol, octan-1-ol and decan-1-ol at different temperature (298.15 and 308.15K) have reported . The important acoustical parameters like apparent molal compressibility, relative association, apparent molal volume and solvation number of substituted N, N'bis(salicyliden)-arylmethanediamines in binary mixture of DMF-water have reported . The physico-chemical behavior in pure liquid components and their mixture is studied on the basis of acoustic and thermodynamic properties . The determination of ultrasonic properties of pure solvents and their solutions find wide range of applications in chemical, pharmaceutical, polymer and bio-chemical industries . Acoustic characteristics have studied for sodium salt of N-chloro-p-toluene sulphonamide in aqueous and binary aqueous media . Ultrasonic velocity and density have measured in non-aqueous solution of the ligands in DMSO solvent at 306K . Acoustical properties are studied for 1-(2'-hydroxy-5' bromophenyl)-3-(4'-chlorophenyl)-1, 3 pronandione in dioxane-water mixture and also in different percentage of dioxane . Ultrasonic study of substituted dihydroformazan at 288.15K and chlorosubstituted pyrazole have studied at different concentration and different percentages in dioxane-water mixture at 305K

There is no acoustical data for substituted 2-oxo-2H-chromene-3-carbohydrazide derivatives in literature survey. In the present work, different properties such

as apparent molal volume (□v), apparent molal compressibility (□k), relative association (RA) and solvation number (Sn) have evaluated for following substituted 2-oxo-2H-chromene-3-carbohydrazide derivatives in 80% (DMF+water) mixture at different concentrations of ligands. In the present work, following substituted coumarines have synthesized by standard method .

Ligand (LA) = N-[(E)-1-(5-bromo-2-hydroxy-phenyl)ethylideneamino]-2-oxo-chromene-3-carboxamide

Ligand (LB) = N-[(E)-1-(5-chloro-2-hydroxy-phenyl)ethylideneamino]-2-oxo-chromene-3-carboxamide

Ligand (LC) = N-[(E)-1-(3,5-dichloro-2-hydroxy-phenyl)ethylideneamino]-2-oxo-chromene-3-carboxamide

Ligand (LD) = N-[(E)-1-(2-hydroxy-5-methyl-phenyl)ethylideneamino]-2-oxo-chromene-3-carboxamide

II. METHODS AND MATERIAL

THEORY AND FORMULAE

Single frequency ultrasonic interferometer is use to measured sound speeds. The micrometer is slowly moved until the anode current meter on a high frequency generator shows a maximum. The distance thus moved by the micrometer gives the values of wavelength .

The distance traveled by micrometer screw to get one maximum in ammeter (D) is used to calculate wavelength of ultrasonic wave using following relation:

$$2D = \lambda \qquad (1)$$

Where, λ is wavelength and D is distance in mm.

From the knowledge of the wavelength, the ultrasonic velocity can be obtained by the relation:

Ultrasonic velocity (U) = λ x Frequency x 103 (2)

Using the measured data some acoustical parameters can be calculated using the standard relations.

Do and ds are density of solvent and solution respectively.

The apparent molal volume (□v) and apparent molal compressibility (□k) are given by following equations .

Apparent molal volume $(\square_v) = M/d_s + ((d_o - d_s) \times 10^3)/((m d_s d_0))$ (3)

Apparent molal compressibility $(\square_k) = (1000(\square_s d_o - \square_o d_s))/(m d_s d_o) + (\square_s M)/d_s$ (4)

Where, do and ds are the densities of the pure solvent and solution, respectively.

m is the molality and M is the molecular weight of solute.

The relative association (RA) is given by the equation:

Relative association $(R_A) = (d_s/d_o) \times (U_o/U_s)^{(1/3)}$ (5)

The solvation number (Sn) is given by the equation.

Solvation number (Sn) = $\square k /\beta 0$ x (M/ d0) (6)

EXPERIMENTAL

All the chemicals used are of analytical grade. The density measurements are made with the specific gravity bottle. All the weighings are made on one pan digital balance (petit balance AD-50B) with an accuracy of + 0.001 gm. The speed of sound is obtained by using variable path crystal interferrometer (Mittal Enterprises, Model MX-3) with accuracy of + 0.03% and frequency 1MHz. In the present work, a steel cell fitted with a quartz crystal of variable frequency is employed. The instrument is calibrated by measuring ultrasonic velocity of water at 32o C.

III. RESULTS AND DISCUSSION

In this work ultrasonic measurement of substituted 2-oxo-2H-chromene-3-carbohydrazide derivatives in 80% DMF+water solvent. The data which is from this is use to determine acoustical parameters such as relative association(RA), apparent molal volume (□v), apparent molal compressibility (□k) and solvation

number (Sn) of of substituted 2-oxo-2H-chromene-3-carbohydrazide derivatives in 80% DMF+water solvent. From table no. 1 shows that there is decrease in concentration, ultrasonic velocity also decreases for all the system this is due to the very strong dipole-induce dipole interaction between the components. Table no. 1 shows the apparent molal volume (φv) increases with decreases in concentration in all the system indicate the existence of strong ion solvent interaction. The apparent molal compressibility (φk) increases with decreases in concentration show the weak electrostatic attractive force in the vicinity of ion causing electrostatic salvation of ion. The relative association (RA) increases with decreases found that there is weak solute solvent interaction. The salvation number (SN) increases as the concentration decreases due to the solute solvent interaction in all the system.

IV. CONCLUSION

The value of intermolecular free length corresponds to the molecular shape. The increase in value of apparent molal compressibility (φk) with decrease in concentrations shows the weak electrostatic attractive force in the vicinity of ions causing electrostatic salvation of ions. Relative association (RA) is the property useful to understand the solute-solvent interaction. The solvation number (Sn) increases with decrease in concentration due to weak solute-solvent interaction in all the systems.

Table-1 Concentration (m), Apparent molal volume (φv), Apparent molal compressibility (φk), Relative association (RA) and Solvation number (Sn) at 80% (DMF+Water) solvent at 305K

Conc. (m) (mol lit^{-1})	Density (d_s) (kg m^{-3})	Ultrasonic Velocity (U_s) (m s^{-1})	Apparent molal volume (ϕ_v) (m^{3}mol^{-1})	Apparent molal compressibility (ϕ_k) x 10^{-10} (m^{2}N^{-1})	Relative association (R_A)	Solvation number (S_n)
Ligand L_A
0.01	1222.7	851.0	6.8961	4.4084	1.2155	0.6133
0.005	1219.9	842.8	13.5005	4.8974	1.2226	0.6813
0.0025	1218.1	831.6	26.8553	5.1081	1.2256	0.7106
0.00125	1215.4	827.2	53.3225	5.2073	1.2270	0.7244
0.000625	1213.6	821.5	105.391	5.5394	1.2294	0.7700
Ligand L_B
0.01	1167.6	867.6	5.1220	3.8554	1.1666	0.6049
0.005	1164.9	853.2	10.0812	4.0109	1.1688	0.6293
0.0025	1161.2	843.6	19.8978	4.2085	1.1600	0.6603
0.00125	1158.5	831.5	39.5284	4.2585	1.1718	0.6682
0.000625	1154.9	829.2	78.4884	4.3676	1.1725	0.6853
Ligand L_C
0.01	1193.8	857.8	6.0806	4.2742	1.1970	0.6130
0.005	1188.3	843.4	11.9961	4.4297	1.1971	0.6353
0.0025	1185.6	838.6	23.8614	4.6552	1.1989	0.6662

0.00125	1182.9	830.8	47.4593	4.7268	1.2014	0.6779
0.000625	1182.0	827.4	94.3881	4.8441	1.2058	0.6947
Ligand L$_D$						
0.01	1166.7	879.8	4.7957	3.6220	1.1726	0.6012
0.005	1163.1	862.4	9.4672	3.8086	1.1797	0.6322
0.0025	1158.5	853.6	18.6827	3.9370	1.1844	0.6535
0.00125	1154.9	839.4	36.8404	3.9990	1.1869	0.6639
0.000625	1152.2	833.6	72.9052	4.1314	1.1924	0.6858

Graphical representation of acoustical parameters in 80% of DMF-Water solvent

Fig-1: Plot of Ultrasonic velocity (Us) m s^{-1} Vs concentration (mol / lit) in 80% DMF solvent

Plots of Apparent molal volume (ϕ_v) of different ligand at different concentration in 80% (DMF + water) solvents

Fig. 2 : Plot of Apparent molal volume (ϕ_V) m^{3}mole^{-1} Vs concentration (mole / lit) in 80% DMF+ Water solvent
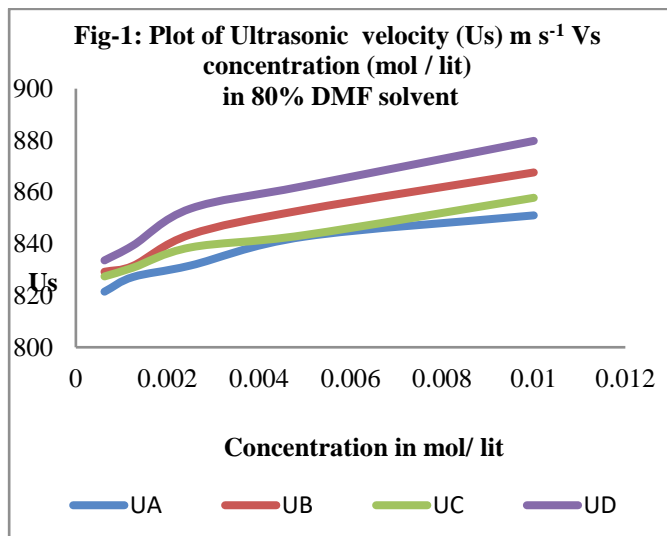
Plots of Apparent molal compressibility (ϕk) of different ligand at different concentration in 80% (DMF + water) solvents

Fig. 3: Plot of Apparent molal compressibility (ϕ_k) x 10^{-10} m^{2}N^{-1} Vs concentration (mole / lit) in 80% DMF+ Water solvent.
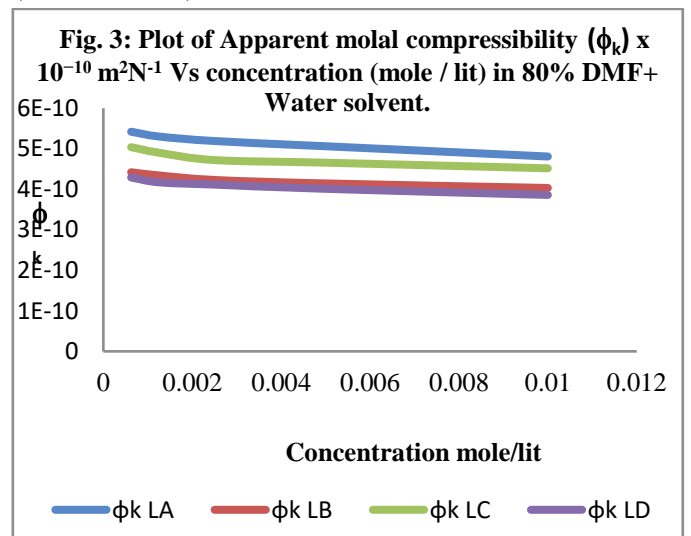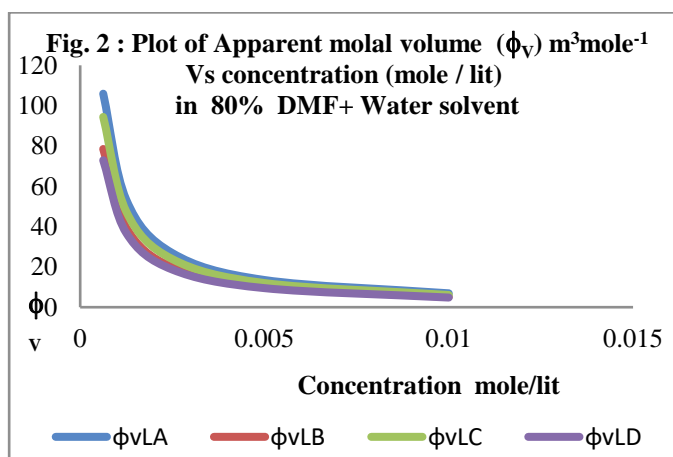
Plots of Relative association (RA) of different ligand at different concentration in 60%, 70% and 80% (DMF + water) solvents

Fig-4: Plot of Relative association (R_A) Vs concentration (mol / lit) in 80% DMF+ Water solvent
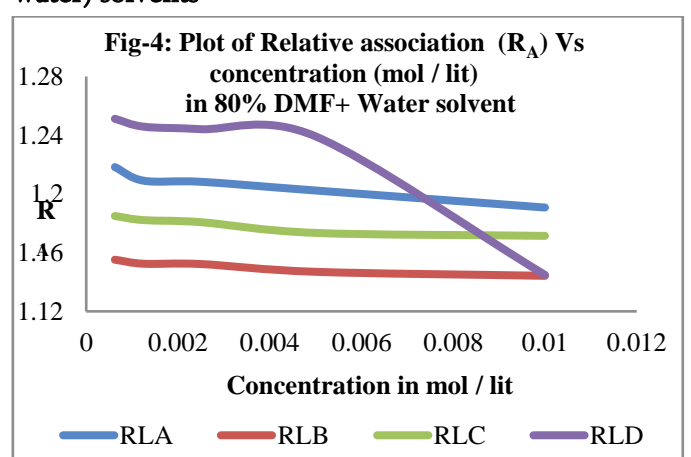
Plots of Salvation number (Sn) of different ligand at different concentration in 80% (DMF + Water) solvents

Fig. 5 : Plot of solvation number (Sn) Vs concentration (mole / lit) in 80% DMF+ Water solvent.
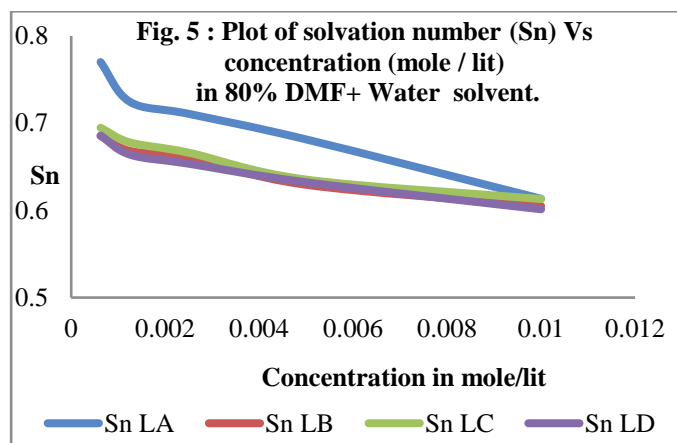
V. REFERENCES

[1]. Semeniuk B, Wachnik H W, Fluid Phase Equilib., 152, (1998), 337

[2]. Meshram Y K, Narwade M L, Acta. Ciencia Indica, 2, (2001), 67.

[3]. Nikam P S, Jagdale B S, Sawant A B, Hasan M, J. Chem. Eng. Data, 45, (2000), 559.

[4]. Chandami A S, Hedaoo D S, Wadekar M P, J. Chem. Bio. Phy. Sci. Sec. A., 6(2), (2016), 541.

[5]. Sreekanth K, Sravana D, Krishnarao D, J. Chem. Pharm. Res., 3(4), (2011), 29.

[6]. Bhuva B D, Parsania P H, J. Appl. Polym. Sci., 121, (2011), 1304.

[7]. Bhat J I, Sabatha N V, Indian J. Chem., 42(A), (2003), 520.

[8]. Wadekar M P, Arch. Appl. Sci. Res., 5(5), (2013), 11.

[9]. Thakur S D, Mahajan D T, Narwade M L, J. Indian Chem. Soc., 84 (5), (2007), 480.

[10]. Kharkale S S, Wagh M S, Agrawal P S, Paliwal L, J, Arc. Apl. Sci. Res., 3(4), (2011), 36.

[11]. Narwade M L, Arch. Appl. Sci. Res., 4(1), (2012), 254.

[12]. Ramganesh C K, Yadav D, Bodke S, Venktesh K B, Indian J. Chem. Sect. B, 49, (2010),1151.

[13]. Mehra R, Gaur A K, J. Chem. Eng. Data, 53, (2008), 863.

[14]. a) Kumar A, J. Chem. Eng. Data, 32, (1987), 109; b) Tayade R R, Chandami A S, Wadekar M P, J. Chem. Pharm. Res., 6(9), (2014), 114.

[15]. a) Mehrotra K N, Jain M, J. Chem. Eng. Data, 40, (1995), 91; b) Aswale S S, Aswale S R, Dhote A B, Int. J. Res. Chem. Environ., 2(4), (2012), 154.

[16]. Wadekar M P, Shrirao A S, Tayade R R, J. Chem. Bio. Phy. Sci. Sect A, 5(1), (2015), 19.

Determination of Adiabatic Compressibility, Intermolecular Free Length and Specific Acoustic Impedance of Substituted 2-oxo-2H-Chromene-3-Carbohydrazide Derivatives in 60% (DMF+Water) Solvent at 305K

P. P. Choudhari[1], P. R. Yawale[1], S. S. Ubarhande[1], M. P. Wadekar[2*]

[1]G. S. Tompe Arts, Commerce and Science College, Chandur Bazar, Amravati, Maharashtra, India
[2*]Government Vidarbha Institute of Science and Humanities, Amravati, Maharashtra, India

ABSTRACT

Investigation of adiabatic compressibility (βS), intermolecular free length (Lf) and specific acoustic impedance (Z) of substituted 2-oxo-2H-chromene-3-carbohydrazide derivatives in 60% (DMF+water) Solvent at 305K. The solute solvent interaction is understood from the magnitude of partial molar volume and partial molar compressibility at various concentration.

Keywords: - Substituted 2-oxo-2H-chromene-3-carbohydrazide derivatives, Apparent molal compressibility, Solvation number, Apparent molal volume and Adiabatic compressibility.

I. INTRODUCTION

In the recent years, an ultrasonic study has acquired the status of an important tool to know the structure and properties of matter. Ultrasonic investigations find extensive applications in characterizing and physico-chemical study of binary and ternary liquid mixtures. The ultrasonic velocity measurements are highly sensitive to molecular interaction. Ultrasonic investigation has wide range of application in material science, agriculture, medicine, biology, industry, oceanography and sonochemistry research due to its non-destructive nature . Ultrasonic velocity, density, adiabatic compressibility (βs), intermolecular free length (Lf) and specific acoustic impedance (Z) in binary mixture of substituted azomethine drugs are studied . Ultrasonic velocities have applications in several industrial and technological processes .

Ultrasonic studies of substituted imidazolinones in DMF-solvent at constant temperature and different concentrations have done . Acoustic study of 2-hydroxi diethylammonium lactatein in different media at 288-323.15K is done . Acoustical properties of four different drugs have investigated in methanol and water . Specific acoustic impedance (Z), intermolecular free length (Lf) and adiabatic compressibility (βS) are studied for substituted -2, 3- dihydroquinazolin-4(1H)-ones in DMF-water as solvent . Molecular interaction of amide with aliphatic amine in benzene at different temperatures is reported . Ultrasonic velocity is done for levofloxacin, hemihydrate, tacrolimus, monohydrate and lisinoprildihydrate at two different temperatures .

Literature survey indicates that no acoustical data on substituted 2-oxo-2H-chromene-3-carbohydrazide derivatives has produced. In the present work,

different properties such as adiabatic compressibility (βs), intermolecular free length (Lf), specific acoustic impedance (Z) have evaluated for following substituted 2-oxo-2H-chromene-3-carbohydrazide derivatives in 60% of (DMF+water) mixture at different concentrations of ligands. In the present work, following substituted coumarines have synthesized by standard method .

Ligand (LA) =N-[(E)-1-(5-bromo-2-hydroxy-phenyl) ethylideneamino]-2-oxo-chromene-3-carboxamide

Ligand (LB) =N-[(E)-1-(5-chloro-2-hydroxy-phenyl) ethylideneamino]-2-oxo-chromene-3-carboxamide

Ligand (LC) =N-[(E)-1-(3,5-dichloro-2-hydroxy-phenyl) ethylideneamino]-2-oxo-chromene-3-carboxamide

Ligand (LD) = N-[(E)-1-(2-hydroxy-5-methyl-phenyl) ethylideneamino]-2-oxo-chromene-3-carboxamide

II. METHODS AND MATERIAL

THEORY AND FORMULAE

Sound speeds can be measured using a single frequency ultrasonic interferometer. The ultrasonic waves of known frequency produced by a quartz crystal are reflected by a movable metallic plate kept parallel to the quartz plate. When the state of acoustic resonance is reached due to the formation of standing waves, an electrical reaction occurs on the generator driving the quartz plate and its anode current becomes maximum. The micrometer is slowly moved until the anode current meter on a high frequency generator shows a maximum. The distance thus moved by the micrometer gives the values of wavelength .

The distance traveled by micrometer screw to get one maximum in ammeter (D) is used to calculate wavelength of ultrasonic wave using following relation:

$$2D = \lambda \qquad (1)$$

Where, λ is wavelength and D is distance in mm.

From the knowledge of the wavelength, the ultrasonic velocity can be obtained by the relation:

$$\text{Ultrasonic velocity (U)} = \lambda \times \text{Frequency} \times 10^3 \qquad (2)$$

Using the measured data some acoustical parameters can be calculated using the standard relations.

The adiabatic compressibility of solvent and solution can be calculated by using equations:

$$\text{Adiabatic compressibility of solution } (\beta s) = 1/ Us^2 \times ds \qquad (3)$$

$$\text{Adiabatic compressibility of solvent } (\beta 0) = 1/ U0^2 \times d0 \qquad (4)$$

The acoustic impedance (Z) is calculated using equation:

$$\text{Acoustic impedance (Z)} = Us \times ds \qquad (5)$$

Where, Uo and Us are ultrasonic velocity in solvent and solution respectively.

Do and ds are density of solvent and solution respectively.

Where, do and ds are the densities of the pure solvent and solution, respectively.

m is the molality and M is the molecular weight of solute.

⎕o and ⎕s are the adiabatic compressibility of pure solvent and solution respectively.

According to the studies intermolecular free length (Lf) is given by:

$$\text{Intermolecular free length (Lf)} = K\sqrt{\beta s} \qquad (6)$$

The constant K is called the Jacobson's constant.

The value of Jacobson's constant can be calculated by using relation

$$K = (93.875 + 0.375 \times T) \times 10^{-8} \qquad (7)$$

Where, T is the temperature at which experiment is carried out.

EXPERIMENTAL

All the chemicals used are of analytical grade. The density measurements are made with the specific gravity bottle. All the weighings are made on one pan digital balance (petit balance AD-50B) with an accuracy of + 0.001 gm. The speed of sound is obtained by using variable path crystal interferrometer (Mittal

Enterprises, Model MX-3) with accuracy of + 0.03% and frequency 1MHz. In the present work, a steel cell fitted with a quartz crystal of variable frequency is employed. The instrument is calibrated by measuring ultrasonic velocity of water at 32o C.

III. RESULTS AND DISCUSSION

In present work the measurement of ultrasonic velocity and density at a different concentration of substituted 2-oxo-2H-chromene-3-carbohydrazide derivatives in 60% of DMF+water solvent is carried out at 305K temperature. From the table no 1 it is observed that as the concentration decreases ultrasonic velocity decreases for all the system. This is only happen due to the strong dipole-induce dipole interaction between the components. Adiabatic compressibility increases with decrease in the concentration it is observed in fig. no. 2. The decrease in adiabatic compressibility due to the more cohesion is expected in more concentration solution. The dispersion of solvent molecules around ion supporting weak ion solvent interaction due to this adiabatic compressibility increases with decreasing the concentration of solvent. Table no. 1 shows that

intermolecular free length (Lf) is more in more dilute solution. The positive deviation in sound velocity and negative deviation in compressibility is only happen because of decrease in intermolecular free length. Table no. 1 shows that the specific acoustic impedance decreases as the concentrate decreases. Fig no. 4 shows that the variation of specific acoustic impedance.

IV. CONCLUSION

The ultrasonic velocity increases in more concentrated solution due to the possibility of making hydrogen bond increase which gives the packed structure. In this system it shows ion solvent interaction it is only because of decreases in adiabatic compressibility with increase in concentration. Specific acoustic impedance increases with increases in concentration indicate that there is associative molecular interaction. Decreases in intermolecular free length (Lf) leads to positive deviation in sound velocity and negative deviation in compressibility. From this it is concluded that in this system there is significant interaction between solute and solvent molecules.

Table-1 Ultrasonic velocity, Density, Adiabatic compressibility (β_S), Intermolecular free length (L_f) and Specific acoustic impedance (Z) in 60% (DMF+Water) solvent at 305K

Conc. (m) (mol lit^{-1})	Density (d_s) (kg m^{-3})	Ultrasonic Velocity (U_s) (m s^{-1})	Adiabatic compressibility (β_S) x 10^{-9} (m^{2}N^{-1})	Intermolecular free length (L_f) x 10^{-11} (m)	Specific acoustic impedance (Z) x 10^5 (kg m^{-2}s^{-1})
Ligand L$_A$					
0.01	1230.1	842.1	1.1533	6.9886	10.3566
0.005	1221.2	832.8	1.1819	7.0918	10.1684
0.0025	1218.8	820.6	1.2184	7.2038	10.0014
0.00125	1215.9	814.2	1.2406	7.2690	9.8998
0.000625	1213.2	804.5	1.2735	7.3649	9.7601
Ligand L$_B$					
0.01	1167.8	858.6	1.1616	7.0337	10.0267

0.005	1163.3	848.2	1.1948	7.1337	9.8671
0.0025	1159.7	837.6	1.2291	7.2352	9.7136
0.00125	1157.9	821.5	1.2797	7.3827	9.5121
0.000625	1156.1	816.2	1.2985	7.4367	9.4352
Ligand L$_C$					
0.01	1193.3	847.8	1.1659	7.0467	10.1168
0.005	1188.7	838.4	1.1968	7.1395	9.9660
0.0025	1186.9	826.6	1.2331	7.2469	9.8109
0.00125	1185.1	821.8	1.2494	7.2948	9.7391
0.000625	1183.3	818.4	1.2681	7.3307	9.6841
Ligand L$_D$					
0.01	1165.1	869.8	1.1346	6.9511	10.1340
0.005	1161.5	851.4	1.1877	7.1124	9.8890
0.0025	1157.9	841.6	1.2193	7.2064	9.7448
0.00125	1154.2	827.4	1.2656	7.3418	9.5498
0.000625	1151.5	818.6	1.2960	7.4294	9.4261

Plots of Ultrasonic velocity (Us) of different ligands at different concentration in 60%(DMF + water) solvents

Fig-1: Plot of Ultrasonic velocity (Us) m s^{-1} Vs concentration (mol / lit) in 60% DMF solvent
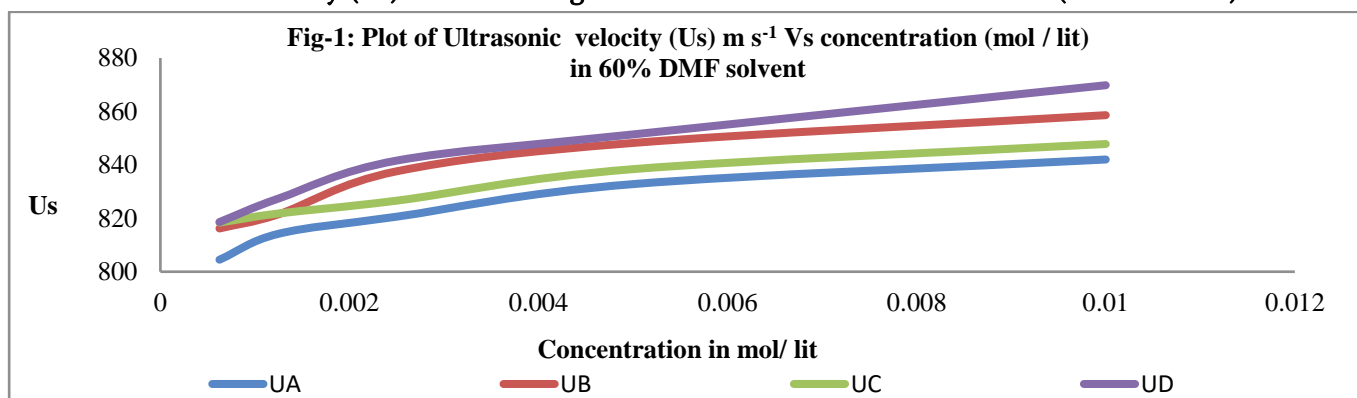
Plots of Adiabatic compressibility (βS) of different ligand at different concentration in 60%(DMF + water) solvents

Fig-2: Plot of Adiabatic compressibility (B$_s$) m s^{-1} Vs concentration (mol / lit) in 60% DMF solvent
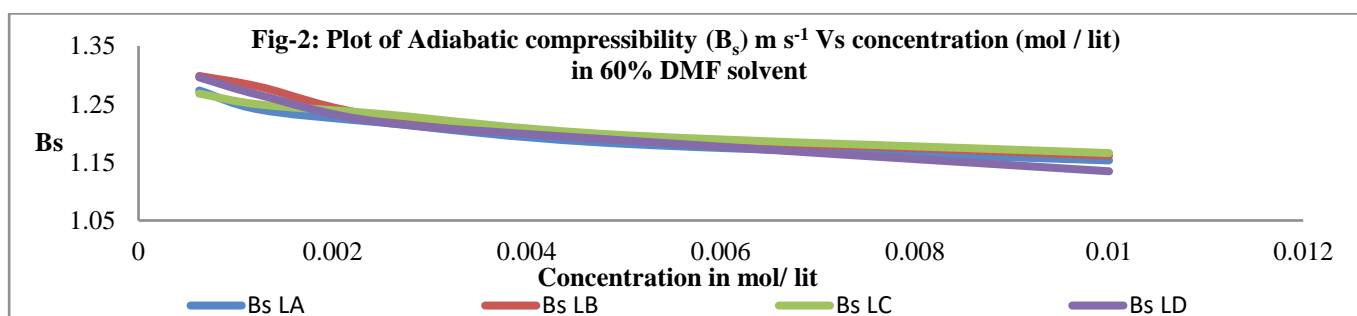
Plots of Intermolecular free length (Lf) of different ligand at different concentration in 60%(DMF + water) solvents

Fig-3: Plot of Intermolecular free length (L$_f$) x 10^{-11} m Vs concentration (mol / lit) in 60% DMF solvent
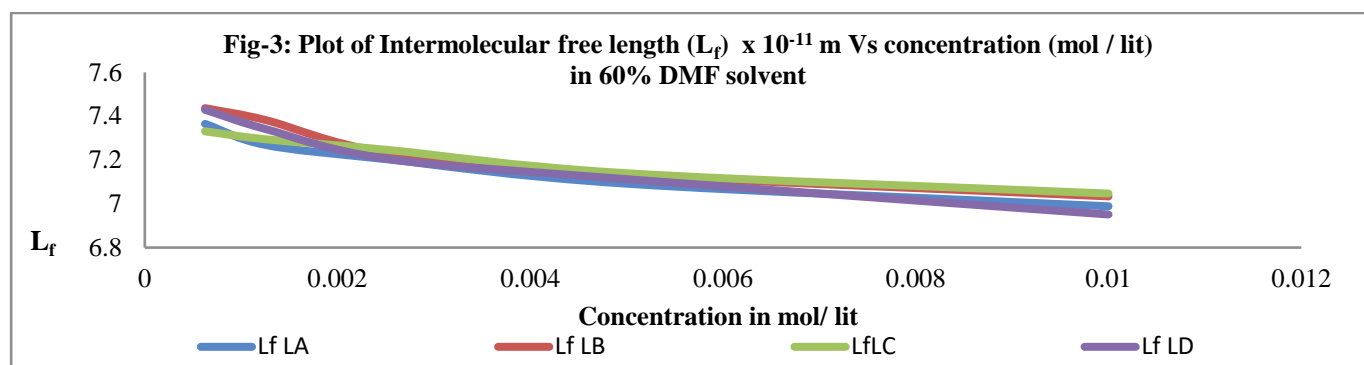
Plots of Specific acoustic impedance (Z) of different ligand at different concentration in 60% (DMF + water) solvents

Fig-4: Plot of Specific acoustic impedance (Z) kg m^{-2}s^{-1} Vs concentration (mol / lit) in 60% DMF solvent
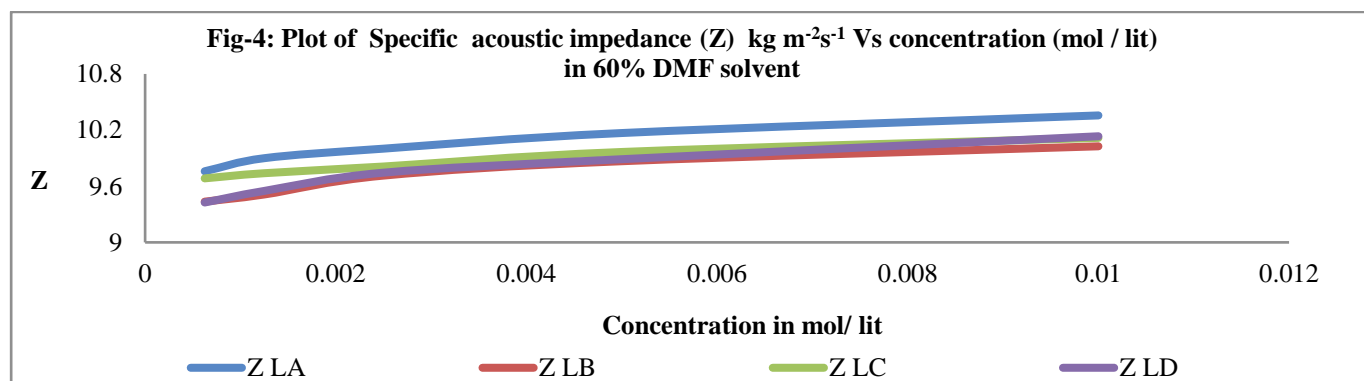
V. REFERENCES

[1]. a) Carneim T, Green D J, Bhardwaj M C, Cer. Bull., (1999); b) Kruger O, Schulze T L, Peters D, Ultrason. Sonochem., 6, (1999), 123.

[2]. Kawalkar A V, Wadekar M P, Der Pharma Chemica, 7 (8), (2015), 170.

[3]. a) Rama Rao G V, Sarma A V, Rambabu C, Indian J. Pure Appl. Phys., 42, (2004), 82; b) Valen A, Lopez M C, Urieta J S, Royo F M , Lafuente C, J. Mol. Liq., 95, (2002), 157.

[4]. Wadekar M P, Tayde R R, Raut V M, Murhekar G H, Arch. Appl. Sci. Res., 3(1), (2011), 209.

[5]. Kulhavy J, Andrade R, Barros S, Serra J, Iglesias M, J. Mol. Liq., 213, (2016), 92.

[6]. a) Kawaizumi F, Matsumoto K, Nomura H, J. Phys. Chem., 87, (1983), 3161; b) Jahagirdar D V, Arbad B R, Mirgane S R, Lande M K, Shankarvar A G., J. Mol. Liq., (75), (1998), 33.

[7]. Hedaoo D S, Kalaskar M M, Wadekar M P, Der Pharma Chemica, 7(6), (2015), 245.

[8]. Aravinthraj M, Venkatesan S, Meera D, J. Chem. Pharm. Res.,3(2), (2011), 623.

[9]. Jayamadhuri N, Glory J, Prasad K R, Res. J. Pharm. Biol. Chem. Sci., 3(2), (2012), 861.

[10]. Ramganesh C K, Yadav D, Bodke S, Venktesh K B, Indian J. Chem. Sect. B, 49, (2010), 1151.

[11]. Mehra R, Gaur A K, J. Chem. Eng. Data, 53, (2008), 863.

[12]. a) Surdo A L, Shin C, Millero F J, J. Chem. Eng. Data, 23(3), (1978), 197; b) Wadekar M P, Shrirao A S, Tayade R R, Der Chemica Sinica, 5(6), (2014), 23.

[13]. a) Santosh M S, Bhat D K, Bhat A S, J. Chem. Eng. Data, 54, (2009), 2813; b) Wadekar M P, Tayade R R, Raut V M, Murhekar G H, Arch. App. Sci. Res., 3(1), (2011), 209.

[14]. Pandey J D, Sanguri V, Yadav M K, Singh A, Indian J. Chem. Sect A, 47,   (2008), 1020.

The Role of Mathematics for Scenarios of Gastropod Diversity and Ecosystem Services

Priyanka B. Gaikwad[1], S.N. Khade[2]
[1]Department of Mathematics, P.N.College, Pusad, Maharashtra, India
[2]Department of Zoology, P.N.College, Pusad, Maharashtra, India

ABSTRACT

A present study was carried out on marine gastropod accessibility among coastline to collection, taxonomical identification and diversity by using some mathematical methods Shannon Wiener Diversity Index, One-way ANOVA, α diversity, data obtained from rocky platform, boulder field, some sheltered areas sandy beaches, and muddy habitat, SCUBA used for sampling-data collection, The molluscan fauna is rich in prevalence of various habitats, so there is urgent need to taxonomical study of species and mathematical analysis for more accuracy for current status and future planning as well as sustainable utilization in the point of view of biodiversity conservation.

Keywords : Quadrat Method, Diversity, Shannon Wiener Index.

I. INTRODUCTION

These studies focus on the congruence of α diversity (the number of species found per sampling unit) between taxa rather than on β diversity (turnover of species assemblages between sampling units). Biologists are all passionate about conserving biological diversity. We are seldom as passionate about the math we use to guide us in this task, Yet what if the mathematical tools we have always used to measure diversity, [16], the belief (or superstition) of some ecologists that a diversity index provides a basis (or talisman) for reaching a full understanding of community structure is totally unfounded-Evelyn Pielou, A good measure of biodiversity should take two things into account, how abundant the various species are; but also, how different the species are, The general mathematical and ecosystem frameworks introduced in several case studies including the coastal fisheries in both French Guiana and Solomon Islands [18], Species found at greater depth in the sea, [1]. Mangroves are one of the biologically diverse ecosystems in the world, [2]. They are confined to microhabitats below mean high water [3]. An oysters, mussels and clams are good source of minerals, protein, and glycogen and easily digestible compared to other animal food [4]. In India, till today, 5,070 species of molluscs have been recorded of which, 3,370 are from marine habitats [5]. The gastropods such as sacred chank, Trochus, Turbo are exploited from the Indian marine region [6]. The present papers investigate the diversity of gastropod from open coast of Raigad district.

II. METHODS AND MATERIAL

the sampling and data analysis obtained from five stations namely (A) Awaas (Lat. 18°46.068"North and Long. 072°51.817'East), (B) Sasvane (Lat. 18°47.159" North Long. 072°51.760"East), (C) Kolgaon (Lat. 18°48.197" North Long. 072°52.660" East), (D) Mandva (Lat. 18°48.324" North and Long. 072°52.967" East), (E) Kopropli (Lat. North 18°47.669"and Long. 072°54.305"East), The coastline of Raigad district west coast of India, The sampling was collect randomly from intertidal region-deep sea, The five quadrates of nylon rope each 1-m² was used, twice in each season post- monsoon, winter and summer October 2016 to September 2017. Soon after collection of live animals, They were stocked in filtered seawater pumped in the laboratory from the estuaries for observation, then animal preserved in 70% alcohol for taxonomical identification of morphological characters of typical animal, especially, lunal, umbo, and operculum. Internal parts teeth. The shells were identified from Zoological Survey of India, Kolkata, also using the reference [15], special guidance taken for

identification by Dr.Sherly Slack, Australia for identification.

III. RESULTS AND DISCUSSION

3.1: According to Shannon Wiener Diversity Index

Stations	No. of sample	pi=sample/sum	ln (pi)	pi*ln (pi)
A	08	0.235	-1.448	-0.340
B	06	0.176	-1.737	-0.305
C	06	0.176	-2.737	-0.305
D	05	0.147	-1.917	-0.281
E	09	0.264	-1.331	-0.351
	sum=34			Sum = -1.582

H= 1.582

Hmax= ln(N) = ln(5)=1.609

Evenness = H/Hmax = 1.582/1.609 =0.983

Result: Shannon diversity index (H) = 1.582

Evenness = 0.983

Table Analyzed	One-way ANOVA data			
Data sets analyzed	A–C			
ANOVA summary				
F	0.09934			
P value	0.9057			
P value summary	ns			
Significant diff. among means (P < 0.05)?	No			
R squared	0.006579			
Brown-Forsythe test				
F (DFn, DFd)	0.09934 (2, 30)			
P value	0.9057			
P value summary	ns			
Are SDs significantly different (P < 0.05)?	No			
Bartlett's test				

Bartlett's statistic (corrected)	0.8640			
P value	0.6492			
P value summary	ns			
Are SDs significantly different (P < 0.05)?	No			
ANOVA table	SS	DF	MS	F (DFn, DFd)
Treatment (between columns)	0.1818	2	0.09091	F (2, 30) = 0.09934
Residual (within columns)	27.45	30	0.9152	
Total	27.64	32		
Data summary				
Number of treatments (columns)	3			
Number of values (total)	33			
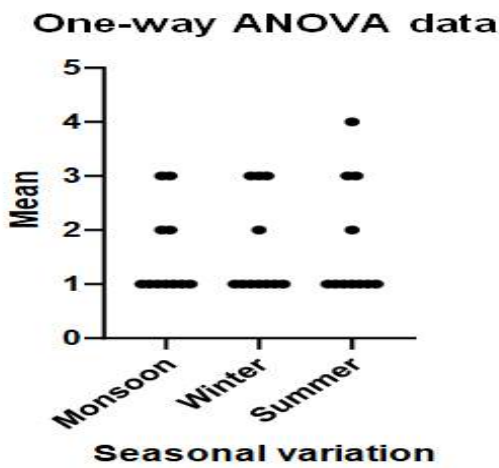
GRAPH NO.II. Obtained data families & gastropods.
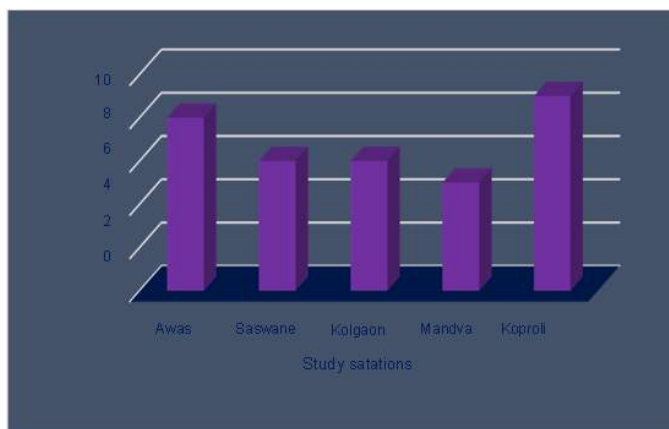
GRAPH NO.I. Obtained data according to fixed sites.
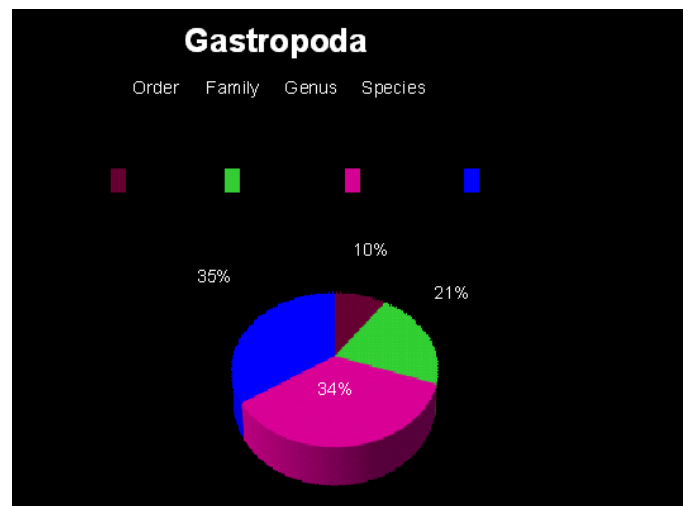
GRAPH NO.III. Total obtained of gastropods in percentage.

According Shannon diversity index (H) = **1.582** while Evenness is the **0.983** amongst the statons, according

to "graph 1" The station E more diversity according to "graph no 1" family Neritidae, Nassariidae and Turritellidae documented rich diversity. In the present study were obtained eighteen gastropods belonging to eighteen genera out of eleven families from the coast line of Raigad district, west coast of India. A study five stations respectively station A: eight species belonging eight genera out of six families, station B: six species belonging six genera out of four families, station C: six species belonging six genera out of four families, station D: five species belonging five genera out of three families, and at E: nine species belonging nine genera out of five families, obtained.

The diversity of gastropods molluscs at five stations varies significantly. The population density was at its peak in the month of November during post monsoon period. [7]. the observation of these species populations in mangrove ecosystem is important to evaluate their condition [8]. Alpha diversity at habitat level is the most widely used component in the characterization of communities. It has two components viz. species richness and equitability indices. [9]. Forty four sp., of Sematan mangrove forest of Malaysia recorded [10]. A total account of Sundarban fifty six species of molluscs thirty one gastropods & twenty five bivalves [11]. twelve bivalves & thirteen gastropods mangrove associated molluscs at Ratnagiri recorded [12] thirty-nine gastropods belongs fifteen families from Raigad district coast recorded [13]. The calcium concentration is varied in different gastropods shells, these shells can be used for preparation of calcium for the medicinal purpose [14]. Gastropods are typically one of the dominant and most conspicuous macrofauna in mangrove systems, and occupy wide range of ecological niches.

IV.CONCLUSION

According Shannon diversity index (H) = **1.582** while Evenness is the **0.983** amongst the stations, according to "graph 1" At E richness according to "graph no 1" alpha diversity obtained, Statistical analysis using Analysis of Variance One-way ANOVA F= 0.09934, P value is = 0.9057 level of significance with F-value of 0.09934 smaller than the P-value of 0.9057 This implies that there is no significant difference in the annual α- diversity of gastropods.

V. REFERENCES

[1].   Ramakrishna and A. Dey. Annotated checklist of Indian Marine Molluscs (Cephalopoda, Bivalve and Scaphopoda) Part-1. Rec.Zool.Surv.India, Occ. Paper no., 320:1-357. (Published by the Director, Zool.Surv.India, Kolkata).

[2].   Pawar R. Prabhakar, Molluscan Diversity in Mangrove Ecosystem of Uran (Raigad), Navi Mumbai, Maharashtra, West coast of India. Bull. Environ. Pharmacol. Life Sci. Vol. 1(6) May 2012: 55-59.

[3].   Macintosh, D.J. and E. C. Ashton. A review of mangrove biodiversity conservation and management. Final Report 10/06/2002. 2002. Centre for Tropical Ecosystems Research, University of Aarhus, Denmark.

[4].   G. D. Suryavanshi, A.M.Shaikh and U.H.Mane: Impact of Zink on protein content of oyster Crassostrea cattuckensis from Ratnagiri coast, Department of zoology, Yogeshwari Mahavidyalaya, Ambajogai, Dist. Beed-431517. J. Ecotoxicol. Envriron. Monit. 22. (4), 323- 328, (2012). Palani Paramount Publications- Printed in India.

[5].   Subba Rao,N. V., Mollusca in Animal Resources of India (Zoological Survey of India, Calcutta): 1991, 125-147.

[6]. Venkataraman, K. and M. Wafar, Coastal and marine biodiversity of India. Ind.J.Mar.Sci.,2005, 34 (1) : 57-75.

[7]. Thakur S., Yeragi S.G. and Yeragi S.S. Population Density and Biomass of Organisms in the Mangrove Region of Akshi Creek, Alibag Taluka,Raigad District Maharashtra. International Day for Marine Biological Diversity, Marine Biodiversity 2012.

[8]. Dewiyanti Irma, Karina Sofuatuddin. Diversity of Gastropods and Bivalves in mangrove ecosystem rehabilitation areas in Aceh Besar and Banda Aceh districts, Indonesia. 2012. Aquaculture, Aquarium, Conservation & Legislation International Journal of the Bioflux Society.

[9]. Ashwani K Thukral, A review on measurement of alpha diversity in biology, Agric Res J 54 (1) : 1-10, March 2017 DOI No. 10.5958/2395-146X.2017.00001.1

[10]. Anirudha Dey, Handbook on Mangrove Associate Molluscs of Sundarbans: 2006, 1-96. (Zool. Surv.India, Kolkata).

[11]. Khade S.N. and Mane U.H. Diversity of edible Bivalve and Gastropod Molluscs from Ratnagiri, Maharashtra. IJSPER, Vol. (8), July 2012. (1-4).

[12]. Khade S.N. and Mane U.H. Diversity of Bivalve and Gastropod Molluscs from selected localities of Raigad district, Maharashtra, West coast of India. World Journal of Science and Technology 2012, 2 (6):35-41.

[13]. Koteswara Rao and Kiran Kumar J.S. Determination of calcium content in shells of gastropod snails of Ramayanpatnam beach of Andhra Pradesh. Journal of Chemical and Pharmaceutical Research, 2016, 8(8):577-580.

[14]. Ramakrishna and Dey A.Annotated checklist of Indian Marine Molluscs (Cephalopoda, Bivalve and Scaphopoda) Part-1 Occasional Paper no. 320, ZSI -2010.

[15]. Cisse, A., Blanchard, F., Doyen, L., Pereau, J.-C. (2015). ´ Ecoviability for small- scale fisheries in the context of food security constraints. Ecological Economics, 119, 39–52.

Determination of Synthesized 1-Phenyl Naphthaoic Acid Lignan (PNAL) By Using Analytical Techniques HPLC

Rajdip Utane[1*] Ritesh Kohale[1] Sujata Deo[2]

[1]Department of Chemistry, Sant Gadge Maharaj Mahavidyalaya, Hingna. Nagpur, Maharashtra, India
[2]Department of Chemistry, Govt. Institute of Science, Nagpur, Maharashtra, India

ABSTRACT

Determination of 1-phenyl naphthalene and lignans by analytical techniques are used High Performance liquid chromatography.1-phenyl naphthalene has been synthesis via friedel craft acylation and Perkin–Oglialoro reaction followed by cyclization reaction. The key precursor use for synthesis of foresaid product by β -benzoyl propionic acid (β-BPA) through friedel craft acetylating reaction by mixture of succinic anhydride, benzene and its derivative with zeolite at streamline time to obtain blended accumulation followed by work-up with cold acid-water (1:1) treatment. The obtained accumulation distillation eliminates benzene liquor and obtained the crude mass. It was dissolved in aqueous solution of sodium carbonate (1:10) and acidification by hydrochloric acid to form crude β-benzoyl propionic acid (β-BPA) and their derivatives , perkin acid synthesize by two steps in which butenolides are prepared by β-BPA and aryl aldehyde using weak base catalyst pyridine and followed by cleavage of lactone ring methanolic base hydrolysis to form perkin acid. The perkin acid undergoes cyclization using zeolite gives 1-phenyl naphthalene. All the compounds are determined by HPLC.

I. INTRODUCTION

Among various analytical methods for standardization of Indian herbal medicines. High performance liquid chromatography (HPLC) is the most popular one, due to its versality, precision and relativity low cost. HPLC is one of the most useful analytical techniques because it is easy to learn and use. HPLC has been employed to analyze several components in a medicinal preparations composed of several crude drug. One of the main advantages of HPLC is that many detectors can be coupled with it, such as UV, MS and NMR, etc. by which detection of more constituents can be done. In recent years, coulumtric electrode array detector (HPLC-CEAD) and charge aerosol detector (CAD) have been also introduced to the analysis of herbal formulations. HPLC method with various detectors has been developed for qualitative and quantitative analysis of various phyto constituents such as isolation and identification of synthetic compounds as lignan. So, HPLC is highly versatile chromatographic method which cans separate a wide variety of chemical constituents in almost all mixture [1-2].

Liquid chromatography though troublesome than gas chromatography, has the main advantage of operating at low temperatures and can be used with advantages for separation of substances as proteins, nucleosides which are thermo labile.

In conventional liquid chromatography, a dilute solution of a sample is passed through vertical column packed with solid particle. Thus, liquid is passed

through vertical column under gravitational flow. This is passed with slow speed and especially if the packing granules were small enough to give efficient separation, then the delivery under gravity decrease even upto a few drops per minute[3-5].

The obvious way to increase the flow rate and get efficient separation is to force the liquid by a positive displacement pump or by gas pressure. This versatile can be achieved by making certain modifications in column and by using smaller, diameter and smaller surface area of column particles and by using other suitable packing structure.

Thus HPLC is high resolution and high speed liquid chromatography. It has beenseveral times more resolving power than open column liquid chromatography. Hence it is used for speedy resolution of complex mixtures.

II. METHODS AND MATERIAL

2.1 Materials:

All synthesized compound a Derivatives 1–phenyl naphthalenes and extracted component by pet. Ether from *Cleistahnthus collinus.*

2.2 Methods (HPLC)

The HPLC system used for analysis consisted of Waters, auto sampler, UV detector with Data ace software for data acquisition and processing. The chromatographic analysis was performed on thermo C18 with bonded phase octadecylsilane column (250 x 4.60 mm, 5 μ particle size) with isocratic condition at ambient room temperature. The analysis was performed at flow rate 1.0 ml per min consist of mobile phase Methanol: Water (70:30) quantification was achieved with UV detection at 230 nm. Mobile phase Retention time of aryl naphthalenes were found to be 2.215 ± 0.3 min. and . Calibrated analytical balance of mettle toledo and digital pH meter of eutech instruments pH tutor was used for analysis purpose. The chromatographic conditions are summarized in table 1.

Table 1: Optimized condition during HPLC analysis of synthetically prepared1-Phenyl naphthalene from Cleistanthus. collinus

HPLC system	Waters
Softaware	Data Ace
Detector	UV-Visible
Pump	Waters 715
Stationary phase	μ
Mobile Phase	Methanol: Water (70:30% v/v)
Injection volume	20 μl
Column	Thermo C 18
Column length	250 nm
Column temperature	RT
Particle size packing	5 μ

Table 1. Blank preparation: Diluent used as blank

2.2.1 Stationary phase (Adsorbents)

HPLC separations are based on the surface interactions and depend on the types of the adsorption sites. Modern HPLC adsorbents are small rigid porous particles with high surface area. Main adsorbent parameters are Particle size: 3 to 10 um and Particle size distribution: as narrow as possible, usually within 10% of the mean.

2.2.2 Instrumentation of HPLC system

In order to attain reasonable high flow rates and yet keep particle size of packing very low (3-10 um), pumping pressures of several hundred atmosphreres (2000-8000 psi are required.

2.2.3 Mobile phase reservoir and solvent treatment systems

A modern HPLC apparatus is equipped with one or more glass or stainless steel reservoirs, each of which contain 500ml or more of solvent. The reservoirs are often equipped with a means of removing dissolved gases O2 and N2 that interface by forming bubbles in the columns and detector systems. These bubbles cause band spreading; in addition they interface with performance of the detector. Degassers may consist of A vacuum pumping system, Distillation system, Device for heating and stirring the solvents and

Device for sparring in which the dissolved gases are swept out of solution by fine bubbles of an inert gas of low solubility.

2.2.4   Pumps:

The pumps are used to pass mobile phase through the column at high pressure and at controlled flow rate. In addition to this pumps used in HPLC should have the following features. The generation of pressures upto 60000psi. Flow rates ranging from 0.1 to 10 ml/ min. Flow control and flow reproducibility of +_ 0.5 %.

2.2.5   Sample injectors

Often the limiting factor in the precision of liquid chromatographic measurements lies in the reproducibility with which samples can be introduced into the column packing. It must be noted that overlapping of the sample causes band boarding.

2.2.6   Syringe injection

This is the earliest and simplest technique. Hence the sample is injected through a self sealing elastomeric septum and the syringes are designed to withstand pressures a self sealing elastomeric septum and the syringes are designed to withstand pressures upto 1500 psi.

2.2.7   Liquid chromatographic column

They are usually constructed smooth bore stainless steel tubing or heavy-walled glass tubing. If prepared from heavy walled glass tubing, then pressure is restricted to lower than 600psi. Size length 25 to 100cm and internal diameter 2 to 6 mm.

2.3   Synthesis of 1-phenyl naphthalene

Take a mixture of1 gm of α-arylidine, β-Benzoyl Propionic acid (1 mmol), 1 g of activated zeolite H-beta (1 mmol) and 10 ml of ethanol (10 mmol) as a reaction solvent in 250 ml round bottom flask . Stir the mixture vigorously (using magnetic stirrer) by keeping reflux at 1200 C for an appropriate time as reaction mixture was cooled at room temperature and diluted with diethyl ether (3 x 10 ml) to precipitate of zeolite H-Beta easy separation. The combined organic layers were dried over anhydrous Na2SO4. The solvent was removed and the residue was column chromatograms using petroleum

ether: ethyl acetate (2:3) as the eluent, to obtain pure compound (1 to 5) shown in scheme 1 and table 2.
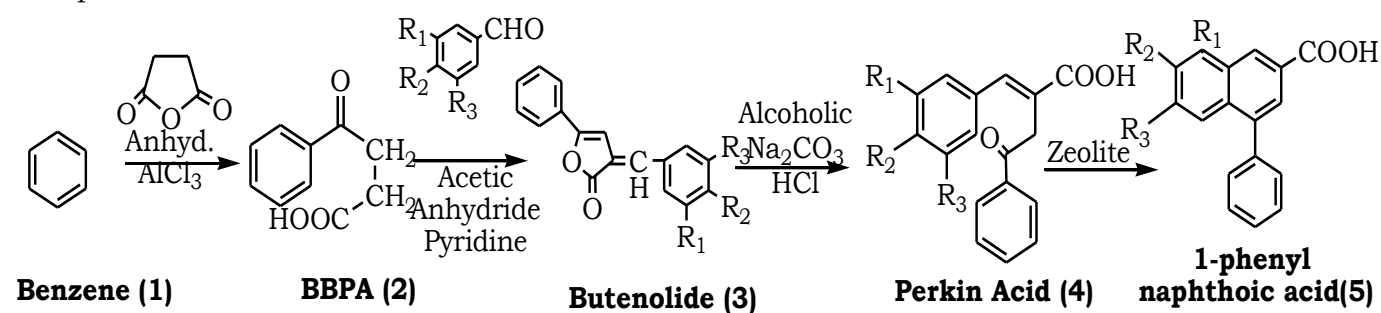
Figure 1 : Graphical Schematic Representation of Synthesis of 1-Phenyl naphthalene

2.4   Preparation of sample solution Synthetically prepared intermediates of 1-phenyl naphthalene

To prepare a stock solution for assay intermediates were weight and mixed. The average weight was determined and then they were finally powdered. An aliquot of powder equivalent to 1 mg per ml of intermediates, this add diluents to dissolve the substance by ultrasonication for 10 minutes and diluted with diluents and converted to 1 ug per ml. the resulting solution was stirred for 1 hour after that centrifuged at 1000 rpm for 10 minutes. Upper supernatant solution was used for further analysis.

These entire compounds of 1mmol β-Benzoyl Propionic acid, α-Arylidene γ -phenyl δ-β-γ-Butenolide, α-arylidine, β-Benzoyl Propionic acid and

1-phenyl naphthalene's subsidiaries are prepared by dissolving with 10 mmol of methanol. All these sample solution are examined by HPLC.

III. RESULTS AND DISCUSSION

Spectrophotometric analysis of 1-phenyl naphthoic acid

Take a mixture of 1 mmol of α-arylidine, β-benzoyl propionic acid (4a), 0.5mmol of activated zeolite H-beta (1mmol) and 10 mmol ofethanol (10 ml). 1-phenyl 7-methoxy naphthalene-3- carboxylic acid has showed molar extinction coefficient (logϵ) are 293.1

(1.82), 450.4 (0.68), HPLC chromatogram of RT values 2.679 as shown in fig. 4.22 and 4.26 . 1-phenyl 6-methoxy 7-Hydroxy naphthalene-3- carboxylic acid has showed UV max and molar extinction coefficient (logϵ) are 215.29 (1.56), 264.72 (1.23), 411.19 (2.23) , HPLC chromatogram of RT values 2.6798 as shown in fig. 2 and 5. 1-phenyl naphthalene-3- carboxylic acid has showed UV max and molar extinction coefficient (logϵ) are 238.4 (0.830), 330.8(330.8), HPLC chromatogram of RT values 2.679 respectively, as shown in fig. 4.24 and 4.28.

Table 2 : UV-visible Spectrophotometric of 1-Phenyl Naphthoic acid

S N	α-Arylidene β-benzoyl propionic acid	Derivatives of 1-Phenyl Naphthoic acid (5)	Molecular formula	HPLC (Rt values)
1	α-Anisalidene β-benzoyl propionic acid (4a)	1-phenyl 7-methoxy naphthalene-3- carboxylic acid (5a)	$C_{18}H_{14}O_3$	2.627
2	α-Varatralidene β-benzoyl propionicacid (4b)	1-phenyl 6 Hydroxy naphthalene-3- carboxylic acid (5b)	$C_{17}H_{14}O_4$	-
3	α-Salicalidene β-benzoyl propionic acid (4c)	1-phenyl 6,7-dimethoxy naphthalene-3- carboxylic acid (5c)	$C_{19}H_{18}O_5$	2.609
4	α-Vanilidene β-benzoyl propionic acid (4d)	1-phenyl 6-methoxy 7-Hydroxy naphthalene-3-carboxylic acid (5d)	$C_{18}H_{16}O_5$	2.678
5	α-Benzylidene β-benzoyl propionic acid (4e)	1-phenyl naphthalene-3-carboxylic acid (5e)	$C_{17}H_{14}O_3$	2.679

DataAce Company Pvt. Ltd.

File Name	:	DataAce - CH-I Chromatogram...c:\DataAceWorkStation\Channel-I\sample PBRI 5 4 100 PPM 2.cmg
Sample Name	:	SAMPLE PBRI 54 100 PPM 2
Method Name	:	DEFAULT1.MTH
Run date	:	3/20/2018 9:00:09 PM
Run Time	:	11 [Minutes.]
Print Date	:	3/21/2018
Print Time	:	5:25:14 PM
Created Date	:	-
Created By	:	Administrator
SubtractFile Name	:	-
Report Style	:	01
GC/HPLC Details	:	

Result-A Table

Peak No	Retn.Time	Area	Height	Area %	Height %
1	2.519	30.857	36.63	42.02	31.31
2	2.627	42.575	73.37	57.98	06.69
Total		73.432	110.00	100	100

DataAce Company Pvt. Ltd.

File Name	:	DataAce - CH-I Chromatogram...c:\DataAceWorkStation\Channel-I\sample PBRI 5 c 100 PPM 2.cmg
Sample Name	:	SAMPLE PBRI 5 c 100 PPM 2
Method Name	:	DEFAULT1.MTH
Run date	:	3/20/2018 9:23:08 PM
Run Time	:	11 [Minutes.]
Print Date	:	3/21/2018
Print Time	:	5:25:19 PM
Created Date	:	-
Created By	:	Administrator
SubtractFile Name	:	-
Report Style	:	01
GC/HPLC Details	:	

Result-A Table

Peak No	Retn.Time	Area	Height	Area %	Height %
1	2.593	30.821	36.617	41.997	33.407
2	2.609	42.569	72.980	58.003	66.593
Total		73.390	109.597	100	100

Figure 2 :HPLC chromatograms of 1-phenyl 7-methoxy naphthalene-3- carboxylic acid(5a)
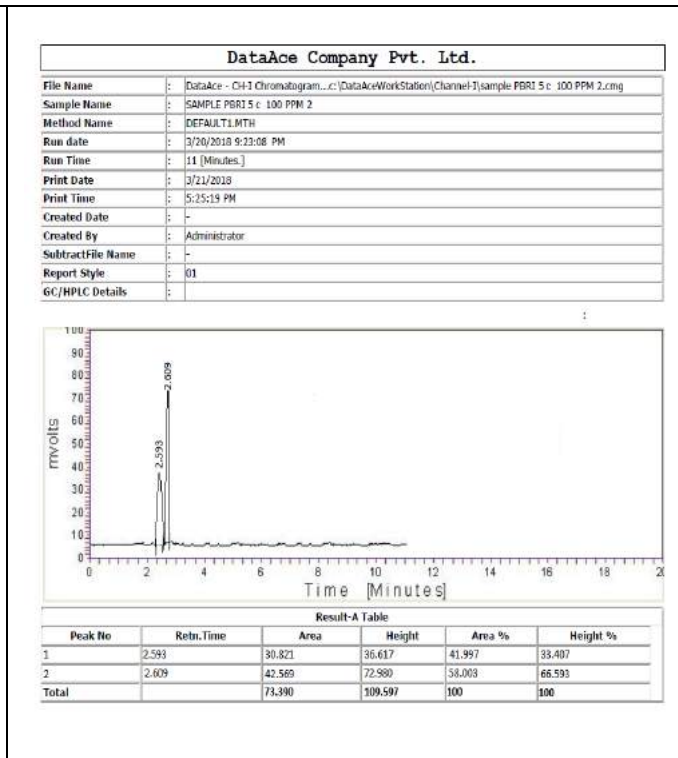
Figure 3 :HPLC chromatograms of 1-phenyl 6 , 7-dimethoxy naphthalene-3-carboxylic acid (5c)

DataAce Company Pvt. Ltd.

File Name	:	DataAce - CH-I Chromatogram...c:\DataAceWorkStation\Channel-I\sample PBRI 5d 100 PPM 2.cmg
Sample Name	:	SAMPLE PBRI 5d 100 PPM 2
Method Name	:	DEFAULT1.MTH
Run date	:	3/20/2018 9:58:25 PM
Run Time	:	11 [Minutes.]
Print Date	:	3/21/2018
Print Time	:	5:32:54 PM
Created Date	:	-
Created By	:	Administrator
SubtractFile Name	:	-
Report Style	:	01
GC/HPLC Details	:	

Result-A Table

Peak No	Retn.Time	Area	Height	Area %	Height %
1	2.325	30.592	40.736	41.301	43.313
2	2.678	43.466	53.314	58.699	56.087
Total		74.058	94.050	100	100

DataAce Company Pvt. Ltd.

File Name	:	DataAce- CH-I Chromatogram...c:\DataAceWorkStation\Channel-I\sample PBRI 5e 100 PPM 2.cmg
Sample Name	:	SAMPLE PBRI 5 e 100 PPM 2
Method Name	:	DEFAULT1.MTH
Run date	:	3/20/2018 10:22:56 PM
Run Time	:	11 [Minutes.]
Print Date	:	3/21/2018
Print Time	:	5:35:05 PM
Created Date	:	-
Created By	:	Administrator
SubtractFile Name	:	-
Report Style	:	01
GC/HPLC Details	:	

Result-A Table

Peak No	Retn.Time	Area	Height	Area %	Height %
1	2.439	30.589	40.835	41.302	43.346
2	2.675	43.474	53.374	58.698	56.654
Total		74.063	94.209	100	100

Figure 4 :HPLC chromatograms of 1-phenyl 6-methoxy 7-Hydroxy naphthalene-3- carboxylic acid (5d)
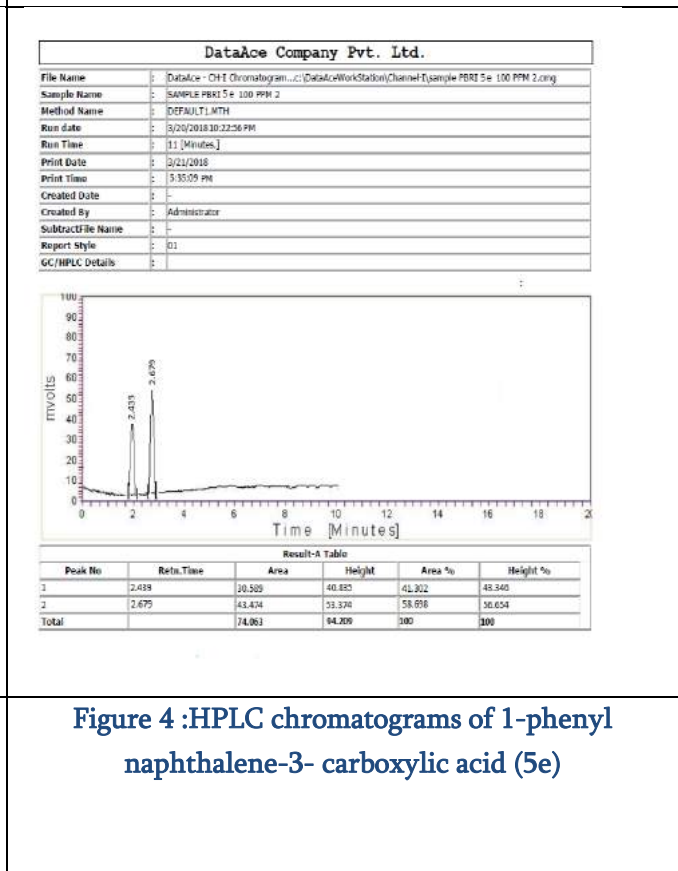
Figure 4 :HPLC chromatograms of 1-phenyl naphthalene-3- carboxylic acid (5e)

IV. CONCLUSION

In above synthesized of 1-phenyl naphthalene from benzene through stable intermediate as β-benzoyl propionic acid, α-Anisalidene γ -phenyl δ- β -γ-Butenolide, α-Arylidene β-benzoyl propionic acid and are identified and 1-Phenyl Naphthoic acid characterized by UV-visible spectrophotometric. A HPLC method has been developed for the determination of 1-phenyl naphthalene lignans. The developed method was simple rapid, linear, accurate, precise and specific. Results from the detection experiments showed that the method is reliable and accurate therefore it can be successfully applied for the routine quality control analysis of 1-phenyl naphthalene lignan.

V. REFERENCES

[1].   Sujata Deo, et. al. Microwave assisted for the perkin reaction for the synthesis of α-arylidene γ-phenyl δ- β-γ-butenolid, Vol. 53B, pp. 363-367, Indian Journal of chemistry., 2014.

[2].   Rajdip Utane, et. al. UV-Visible Determination of Synthetic Compound 1-Phenyl Naphthalene and Extracted Plant Lignans Derivatives, 11 [1]: 18-32, Scholars Research Library Der Pharmacia Lettre, 2019,

[3].   Sujata Deo, Rajdip Utane et. al. Extraction and isolation, synthesis, physiological activity of 1-phenyl naphthalene and its derivatives: AReview, ; 6(4): 21-30 The Pharma Innovation Journal 2017

[4].   J.Y. Cho, et. al. Immunomodulatory effect of arctigenin, a lignan compound, on tumour necrosis factoralpha and nitric oxide production and lymphocyte proliferation, Journal of Pharmacy and Pharmacology, vol 51,no 3,pp. 1267-1273,1999.

[5].   Y.L. Ho, et.al.- Invitro antioxidant properties and total phenolic contents of wetland medicinal plants in Taiwan Botanical Studies, vol 53, pp. 55-66, 2012.

[6].   Tanishq M Chaudhari, Comparative Study on UV Spectra of Synthetic and Natural 1-Phenylnaphthalene Lignans, International Journal of Advanced Chemical Science and Applications (IJACSA) 2347-761X, Volume -5, Issue -3, 2017.

[7].   Shabir Ahmad Parray, et al.,Traditional System of Medicine to Modern Pharmacology: an Overview.; 2(2):240-252, 2012.

[8].   Hemant Dhongadeand, et. al. A review on pharmacognostical, Phytochemical, Pharmacological properties of Phyllanthus amarus.; 4(5):281-288. 2013.

[9].   Rajdip utane et. al., Green Approach Towards The Synthesis Of 1-Phenyl Naphthalene Lignan And Their Derivatives, International Journal of Advances in Science Engineering and Technology, vol. 1, pp. 43-47, 2015.

[10].   Ramesh, C., et. al., Arylnaphthalide Lignans from Cleistanthus collinus1, Chem. Pharm. Bull,. 51(11) 1299-1300, 2003.

Green Synthesis of Silver Nanoparticles by Flowers and It's Application

Dr. Radhika Deshmukh[1], Aakanshka P. Pinjarkar[2]

Shri Shivaji College of Arts Commerce and Science, Akola, Maharashtra, India

ABSTRACT

Green synthesis of silver nanoparticle by flowers is an easy, efficient, economical, ecofriendly , biological synthesis approach. The biological synthesis of nanoparticle has provide a means for improved technique compared to the traditional method that uses the harmful reducing agents. Flowers have unique properties that are useful to synthesis nanoparticles. Chemical and physical Methods of synthesis are toxic and costly that reduce medicinal application. As compared to microbial nanoparticles are more stable and monodispersed and plant extract takes less time to reduce metal ions. Chemical and physical methods for the synthesis are toxic and very costly affects the medicinal application. Biogenic method of silver nanoparticle synthesis are eco-friendly and produced nanoparticle with the precise shape and size. To form the green synthesized silver nanoparticle by flower extract and used it in various application.

I. INTRODUCTION

Nanotechnology is a versatile field that deals with the study and application of materials at the nanoscale. Nanoparticles exhibit new and improved properties as compared to bulk counterparts due to change in their characteristics such as shape, size, size distribution and larger surface area to volume. Nowadays, metal nanoparticles have found many applications in the field of science and technology due to their unique electronic, mechanical, optical and magnetic properties In recent years, silver nanoparticles (AgNps) have greatly focused the researcher's attention because of their important application as antimicrobial, catalytic, textile fabrics and plastics to eliminate micro-organisms. Green synthesis of nanoparticles aims at minimizing generated waste and implementing sustainable processes. In recent years,

green processes using mild reaction conditions and nontoxic precursors have been emphasized in the development of nanotechnology for promoting environmental sustainability. The main aim of green synthesis is to minimize the use of toxic chemicals to prevent the environment from pollution. The biogenic routes for the fabrication of nanomaterials are therefore becoming more and more popular. The three main conditions for nanomaterials preparation are the choice of environment-friendly solvent medium, environmental friendly reducing agent and a nontoxic material for their stabilization. Nanomaterials fabricated from plants, fungi and bacteria have several potential applications in all fields of science and technology. Nanocatalysis has undergone great prosperity in the past decade. One of the main branches of nanocatalysis is nanoparticle (NP) catalysis in liquid phase. NP catalysis in traditional

solvents originated from colloidal chemistry that dated back to 19th century when Pt NPs were used to decompose hydrogen peroxide. Since 1990, it became an independent field usually called colloidal catalysis or quasi-homogenous catalysis since it was believed, at that time, to be a bridge between classical homogenous catalysis and heterogeneous catalysis. "Soluble" NPs in solution phase enabled the direct usage of in situ techniques such as in situ IR and in situ NMR, which were successfully used in homogenous complex catalysis for mechanistic studies . In some cases, NPs were the real active parts for the catalytic activity that molecular complexes generally showed . The higher efficiency of these NP catalysts under mild conditions, in comparison with that of traditional solid state catalysts, was therefore thought to be due to their higher dispersion in solvent and three-dimensional rotational freedom. Silver nanoparticles are important as they find applications in catalysis, organic transformations, synthesis of fine chemicals and organic intermediates. In this the synthesis of Ag nanoparticles, supported Ag nanoparticles and bimetallic Ag-metal nanoparticles and their characterization by various techniques. The applications of Ag nanoparticles in several organic transformations including C-C, C-N, C-S, C-O bond formation reactions as well as reduction and oxidation reactions are also discussed. The use of Ag nanoparticles in catalysis is advantageous as it avoids the use of ligands; easy separation of catalyst for recyclability makes the protocol heterogeneous and economic. Ag nanoparticles gave good catalytic activity towards desired products due to high surface area. By considering these advantages, researchers have focused their attention towards applications of Ag nanoparticles in catalysis.

II. METHODS AND MATERIAL

Catalysis of silver nanoparticles, among the metal-based nanoparticles, has been of great interest in organic synthesis and has expanded rapidly in the past ten years because of nanosilver catalysts' unique reactivity and selectivity, stability, as well as recyclability in catalytic reactions. As can be seen from the research results reported in this critical review, the application of heterogeneous silver-based nanoparticles to general organic reactions has been proven to be an effective strategy in the development of highly efficient organic transformations in terms of efficiency and selectivity. In this the strong potential of nanosilver catalysis in the total synthesis of natural products and pharmaceutical molecules.
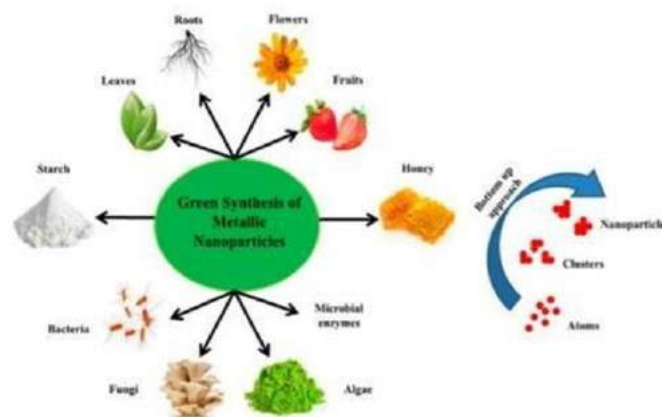
Figure 1. Different types of green synthesis used for the preparation of metal nanoparticles.

III. PREPARATION OF SILVER NANO-PARTICLES

Green-synthesized NPs can be obtained through an easy, efficient, economical and eco-friendly biological synthesis approach. Metallic nanoparticles can be obtained from cell or cell-free extracts of a variety of biological resources, as The key factor that should be considered during the nanoparticle preparation is that it should be evaluated against green chemistry principles, like the selection of a solvent medium, eco-friendly reducing agent, and non-toxic material for nanoparticle stabilization. Furthermore, compounds like peptides, polyphenolics, sugars, vitamins, and water from coffee and tea extracts were found to be

appropriate for the synthesis of nanoparticles. As compared to microbial NPs, plant-based NPs are more stable and monodispersed, and plant extract takes less time to reduce metal ions. Microbial synthesis is one of the approaches to the synthesis of nanomaterials. Beside it Flowers have unique chemical properties that can be useful for nanoparticle synthesis. The synthesis of flowermediated NPs is has various advantage, as compared with other biological NPs synthesis methods, like particularly the one mediated through microorganisms, that microorganisms need to be maintained or cultured under aseptic and pure culture conditions. It is a difficult task to separate nanoparticles during the downstream processing of microbial broth cultures. Furthermore, it takes more time to convert soluble metallic salts to elemental or element oxide NPs. A generalized mechanism for the biosynthesis of different nanoparticles using flower

Fig 2. Green synthesis of Silver nanoparticles.

Silver nanoparticles (AgNPs) show a considerably large surface area, which leads to a significant biochemical reactivity, catalytic action, and atomic behavior, when compared with large particles with an

identical chemical configuration. The synthesis of noble AgNPs is a two-step procedure that first involves the reduction of Ag+ ions to Ago, and after this agglomeration and stabilization is completed, the synthesis involves the development of oligomeric clusters of colloidal AgNPs. The reduction procedure occurs in the presence of biological catalysts. The flower-derived AgNPs have shown numerous applications. Silver Nanoparticles (AgNPs) show a considerably large surface area, which leads to a significant biochemical reactivity, catalytic action, and atomic behavior, when compared with large particles with an identical chemical configuration. Flower which is used for synthesis of silver nanoparticle was flower belonging to family Apocynaceae *Catharanthusroseus* which have the high amounts of Flavonoids, alkaloids polyphenol. The extract of flower is prepared that gets mixed with the silver metal salt as a result the reduction of Ag+ ions to Ag0 take place later on the reaction conditions are get maintained and we get the stable nanoparticle which are get analysed by various characterization technique. The flower is used in nanomaterial is Catharanthusroseus, commonly known as bright eyes, Cape periwinkle, graveyard plant, Madagascar periwinkle, old maid, pink periwinkle, rose periwinkle, is a species offlowering plantin the family Apocynaceae. It is native andendemictoMadagascar, but grown elsewhere as an ornamental and medicinal plant, a source of thedrugsvincristineandvinblastine, used to treat cancer.
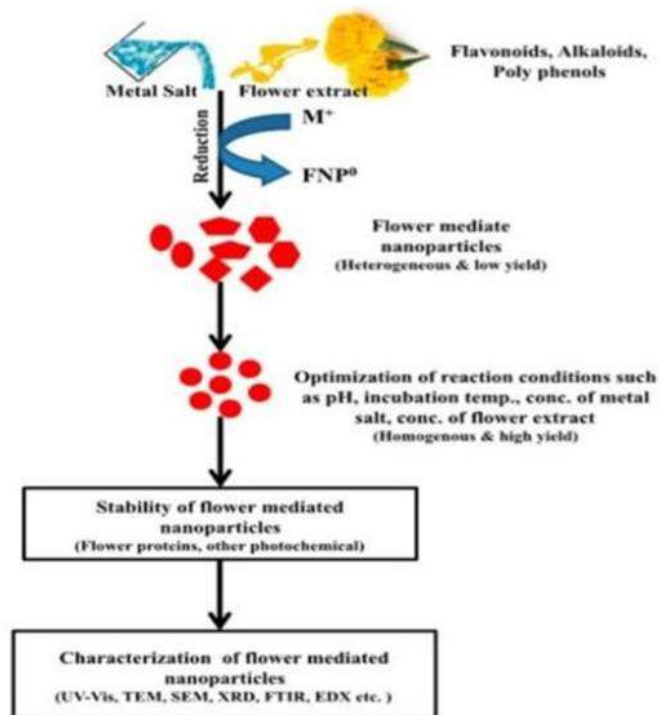
Fig3. Pictures of Catharanthus rosus

IV. RESULT AND DISCUSSION

Metallic nanoparticles synthesized from extracts of several flowers of a diverse size, shape, and surface areas are categorized using different approaches. The composition, size, structure, and crystal phase of the synthesized nanoparticles are deduced using UV–vis, XRD, FT-IR, DLS, EDS, and Raman spectroscopy. The range of the UV spectra wavelength, from 300 to 800nm, illustrates the existence of several metallic nanoparticles of a size ranging from 2nmto100nm. Usually, the detection of silver nanoparticles is conducted using UV spectroscopy in the range of 500 and580nm Estimation of the size of the synthesized nanoparticles, along with the quantification of the charges on the surface of the nanoparticles, is conducted using DLS analysis. The composition of the element is determined through EDAX analysis. XRD is performed to recognize the size of the crystallite. FT-IR spectroscopy is used to detect the residues on the surface and the functional groups- such as, phenols, and hydroxyls which bond with the surface of the nanoparticles throughout the process of the synthesis for an effective reduction and stabilization.
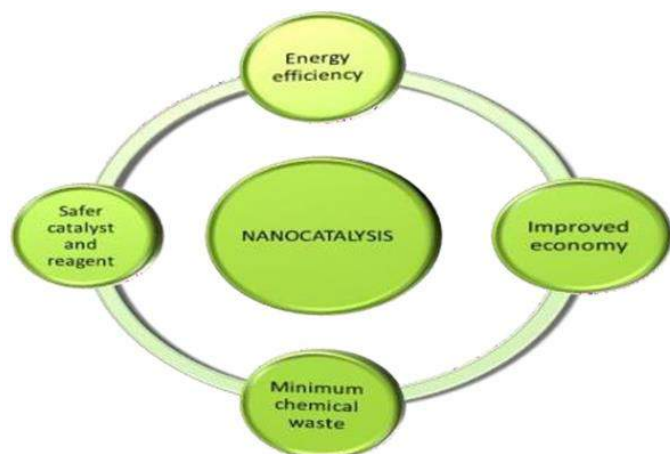
The use of biological materials for the production of nanoparticles has a great potential as a cost-effective and eco-friendly synthesis method for novel and innovative nanomaterials. Non- hazardous biological wastes also play a crucial role in green synthetic protocols for the generation of nanoparticles. The green chemistry approach is completely different from the conventional physical and chemical processes, which frequently utilize environmentally corrosive agents with the ability to cause cytotoxicity, environmental toxicity, and carcinogenicity. On the other hand, the flower-mediated green synthesis of NPs is a vigorous method that does not require any specific isolation and maintenance procedures, which are need in bacteria-,fungi-,oral ae-based nanoparticle synthesis approaches. Flower-induced nanoparticles can exhibit specialized properties, including antimicrobial, antioxidant, catalytic, and cytotoxic activities. The present study intends to highlight the potential of flower-derived metallic nanoparticles. Of all the studied nanoparticles, Au and AgNP^s were shown to be the best potential nanoparticles in terms of their effective antibacterial, antioxidant, and insecticidal activities. Bio- accumulation and toxicity are the two challenges associated with green metallic nanoparticles that prevent their use as therapeutic agents in humans and that need to be resolved through scientific intervention. With further improvement, the flower-mediated green synthesis of nanoparticles may offer important, ecofriendly end products, with wide applications, as compared to the harsh and lethal procedures used at present for the synthesis of nanoparticles. Flower-induced nanoparticles can exhibit specialized properties, including antimicrobial, antioxidant, catalytic, and cytotoxic activities. The present study intends to highlight the potential of flower- derived metallic nanoparticles. Of all the studied nanoparticles, AgNPs were shown to be the best potential nanoparticles in terms of their effective antibacterial, antioxidant, and insecticidal activities. Bio-accumulation and toxicity are the two challenges associated with green metallic nanoparticles that prevent their use as therapeutic agents in humans and that need to be resolved through scientific intervention. With further improvement, the flower-mediated green synthesis of nanoparticles may offer important, ecofriendly end products, with wide applications, as compared to the

harsh and lethal procedures used at present for the synthesis of nanoparticles.

V. CONCLUSION

Technical barriers are the obstructions that are involved during the synthesis of flower mediated nanoparticles. While green nanoscience has gained significant attention, efforts are still being made to standardized the protocols for the synthesis of uniform nanoparticles. Further advancements involving the use of tools and techniques for the scaled-up production of NPs through green synthesis need to be identified to design commercially feasible production technology at the industrial scale. Another pivotal issue regarding the large-scale use of green synthesized nanoparticles is nano-toxicity, which has to be addressed stringently.

The toxicology and analysis protocols have to be developed and updated constantly to reflect the need of the application. Furthermore, the uncertainty and ambiguity associated with the regulatory bodies and laws has to be clearly understood to allow for the use and commercialization of ecologically safe nano-based products. The end market demands need to be made clear, as there are only limited numbers of commercial grade products that can be compared to conventional materials in terms of performance. A unique idea, which still needs to be developed and established, is the use of flowers in the green synthesis of nanoparticles, as this research is still restricted to the synthesis of Au and Ag NPs. To further strengthen this field, it is important to create monodispersed nanoparticles—such as CdS, ZnO, TiO2, and Fe3O2. More studies are required to recognize the various components that may lead to the reduction of metal ions. In the literature, it has been reported that proteins are responsible for the equilibrium, but it is very difficult to recognize the proteins responsible for the functionalization of these nanoparticles.

VI. REFERENCES

[1]. Nanosilver as a new generation of silver catalysts in organic transformations for efficient synthesis of fine chemicals (RCS)-Xiao-Yun DongaZi-Wei Gao,aKe-Fang Yang,bWeiQiangZhanga and Li-Wen Xuab.

[2]. Flower-Based Green Synthesis of Metallic Nanoparticles: Applications beyond FragranceHarsh Kumar 1, Kanchan Bhardwaj 2 , KamilKucˇa 3, , AnuKalia 4, Eugenie Nepovimova 3, RachnaVerma 2 and Dinesh Kumar.

[3]. Khandel, P.; Shahi, S.K. Mycogenic nanoparticles and their bio-prospective applications: Current status and future challenges. J. Nanostruct. Chem. 2018, 8, 369–391.

[4]. Begum, R.; Najeeb, J.; Sattar, A.; Naseem, K.; Irfan, A.; Al-Sehemi, A.G.; Farooqi, Z.H. Chemical reduction of methylene blue in the presence of nanocatalysts: A critical review. Rev. Chem. Eng. 2019.

[5]. Shah, M.; Fawcett, D.; Sharma, S.; Tripathy, S.K.; Poinern, G.E.J. Green synthesis of metallic nanoparticles via biological entities. Materials 2015, 8, 7278–7308.

[6]. Li, G.; He, D.; Qian, Y.; Guan, B.; Gao, S.; Cui, Y.; Yokoyama, K.; Wang, L. Fungusmediated green synthesis of silver nanoparticles using Aspergillusterreus. Int. J. Mol Sci. 2012, 13, 466–476.

[7]. https://www.researchgate.net/figure/Photographs-of-eight-varieties-of-Catharanthus

A Parametric Study of Acoustical Properties of Salicylamide Drug at Different Temperature

Sanjay P Ramteke

Department of Physics, S. P. College, Chandrapur, Maharashtra, India

ABSTRACT

This research paper is to pin out the various molecular interactions of molecules in the alcoholic salicylamide drug at the different temperature. Evaluations of molecular interactions of alcoholic salicylamide drug at different temperature have been investigated under ultrasonic technique at 2MHz. Ultrasonic data of drug solutions has been estimated at various desired thermo-acoustical parameters. A significant existence of solute-solvent and solute-solute interactions present in the system. Hence it is evident that the ultrasonic velocity measurement in the given medium serves as a careful probe in characterizing the physico-chemical properties of the medium

This research paper has said the various types of possible molecular interaction in the drug solution. This investigation has been thoroughly analyzed and eventually interpreted at the possible molecular interactions such as structure making and structure breaking effect and also solute-solvent, ionic interaction, H-bonding effect in the alcoholic salicylamide drug solution. The results obtained from these studies can thus be helpful for pharmacological application of drugs.

Keywords : Ultrasonic velocity, Density and Acoustical parameters, Salicylamide drug, Alcohol

I. INTRODUCTION

In the pharmaceutical and chemical industries, the wide application of ultrasound to promote Chemical processes. The physical and chemical interaction of ultrasound with molecular species has been thoroughly studied (1,2) and is an important tool for promoting reactions used for synthetic and medicinal chemistry as well as for improving drug extraction processes (3-6). Ultrasound is being explored to solve pharmaceutical manufacturing and formulation issues (7) dispersion of solids, the deagglomeration of solids in liquid and the preparation of colloids. In addition, ultrasound has been used in the development of novel catalysts, nanomaterials, nanocrystals and nanoscale catalysts (8-10). Diagnostic imaging is the most widespread medical application of ultrasound.

The wide ultrasonic sense has been adequately employed in understanding the nature of molecular interactions in pure liquids and liquid mixtures. The ultrasonic characterizations are highly sensitive to molecular interactions and used to demonstrate qualitative nature and strength of molecular interaction in the drug solution [11-14]. Incorporating the pharmacokinetics and pharmacodynamics play vital role in medicine and drug chemistry to carry out the interferometry, isometric and refractometric measurements [15, 16]. This information deals with the transport properties of drugs and ion-solvent

interactions. Drug action is the ultimate consequence of physico-chemical interaction between drug and receptor. The results ultimately zero in on the dipole association, inter-molecular attraction between the solute and solvent, dielectric constant of the medium, polarizability and mutual compensation of dipoles. It also directs transmission stability, its activity and effect of drug [17-19]. Alcohols are strongly self-associating and polar behavior of attraction with any other such a group of compound. Alcohols and aromatic compounds exist as associated structures in liquid state. Thus interaction of drug with alcohols give interesting properties arising from charge-transfer, dipole-dipole, donor-acceptor and hydrogen bonding may be observed.

These research paper thermo-acoustic parameters of the mixture of salicylamide and butanol are examined at various temperature ranges i.e. 278.15K-293.15K. Explore the various interactions and their subsequent consequence on transport properties of salicylamide drug. The research of physicochemical activities of drug can be the great attention from academic as well as physiological intellect [20-23].

II. METHODS AND MATERIAL

The solvents alcohols like butanol and analgesic drug salicylamidel were used AR grade (E-Merck chemicals, Germany) without further purification. The purity of chemicals has been verified out by comparing the ultrasonic data with standard literature value [24]. The measurement of ultrasonic parameter of the solution by using ultrasonic interferometer supplied by Vi-Micro system, Chennai (Model VCT: 71) having frequency at 2 MHz with an accuracy of 0.0001 m/s. The densities are measured using 10 ml specific gravity bottle. Specific gravity bottle having accuracy of $\pm$ 2 X10^{-2} kg/m³. Automatic temperature controller water bath supplied by Lab-Hosp Company Mumbai having an accuracy $\pm$1K temperature. Viscosities were measured at particular temperature by using Oswald's viscometer; the calibration of

viscometer by using doubled distilled water with literature value. The time rate of doubled distilled water and experimental mixture are measured with digital stop clock having accuracy of 0.01 sec (Model: RACER- 10W).Weights were measured with an electronic digital balance (Contech CA-34) having accuracy 0.0001gm. Such a set up make use of to determine the ultrasonic and thermo-acoustic evaluation in butanol and salicylamide at T=278.15K-293.15K at various molar range.

Ultrasonic and thermo-acoustic parameters are formulizing as follows:

$$\text{Adiabatic Compressibility } (\beta) = 1 / U^2\rho \quad (1)$$
$$\text{Specific Acoustic Impedance } (Z) = U\,\rho \quad (2)$$
$$\text{Intermolecular Free Length } (L_f) = K_T\,\beta^{1/2} \quad (3)$$
$$\text{Relaxation Time } (\tau) = (4/3)^*\beta^*\eta \quad (4)$$
$$\text{Relative association } (Ra) = (\rho/\rho_0)\,(U_0/U)^{1/3} \quad (5)$$
$$\text{Classical Absorption } (\alpha/f^2) = (8\pi^2\eta)/(3\,U\,\rho) \quad (6)$$
$$\text{Internal Pressure } (P) = bRT\,(K\,\eta/U)^{1/2} x\,(\rho^{2/3}/M^{7/6}\text{eff}) \quad (7)$$
$$\text{Free Volume } (V_f) = (M_{eff}\,U/\eta\,K)^{3/2} \quad (8)$$
$$\text{Molar volume } (Vm) = M_{eff}/\rho \quad (9)$$
$$\text{Molar Sound Velocity or Rao Constant } (R) = M_{eff}/\rho\,(U)^{1/3} \quad (10)$$
$$\text{Molar compressibility or Wada constant } (W) = V\,\beta^{-1/7} \quad (11)$$
$$\text{Isothermal Compressibility } (\beta i) = \gamma\,\beta \quad (12)$$
$$\text{Surface Tension } (\sigma) = (6.3\ x10^{-4})\,\rho U^{3/2} \quad (13)$$

Data interpretation by graphical tactic as follows

Following figures are various ultrasonic and thermo-acoustic parameters V/S molarity

fig- 5.271

fig- 5.273

fig- 5.274

fig- 5.279

fig- 5.275

fig- 5.280

fig- 5.276

fig- 5.282

fig- 5.277

fig- 5.283

fig- 5.278

fig- 5.284

fig- 5.286

fig- 5.287
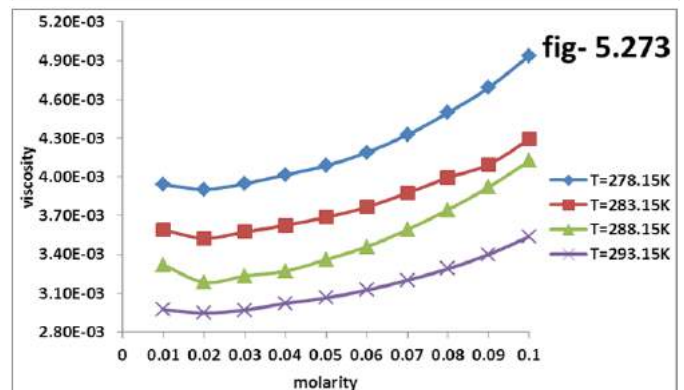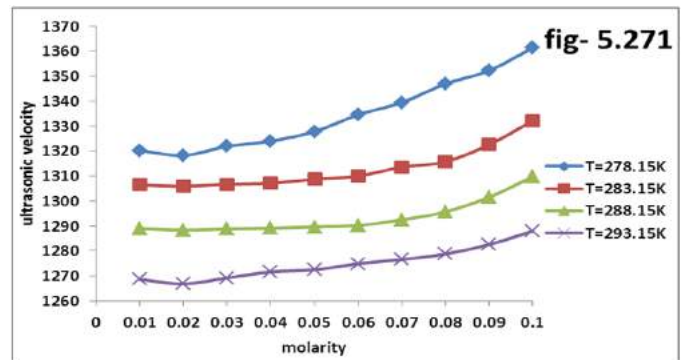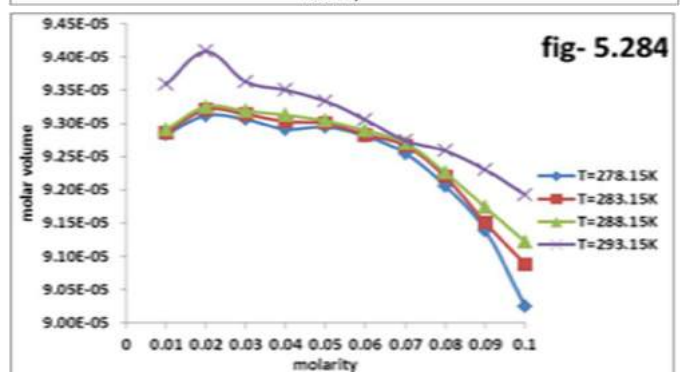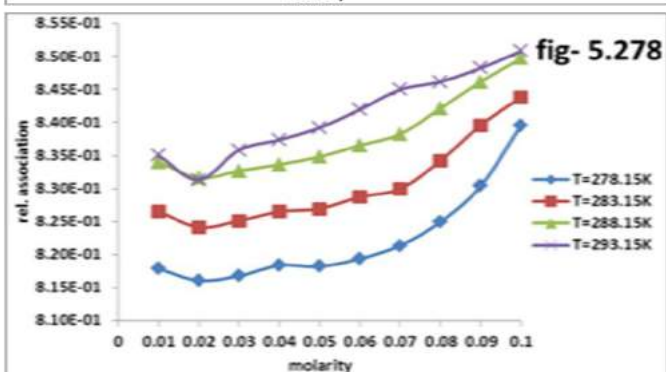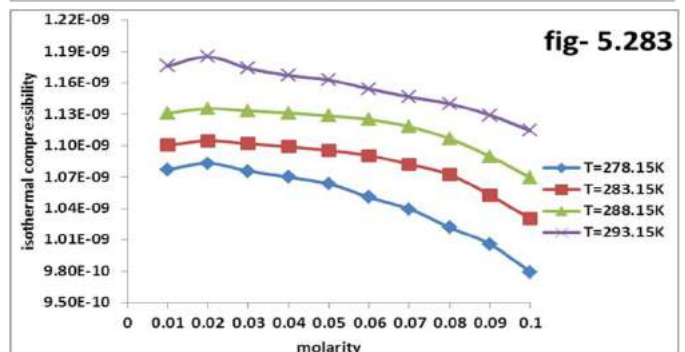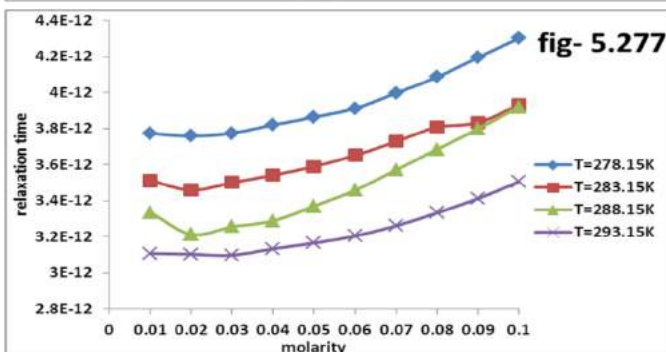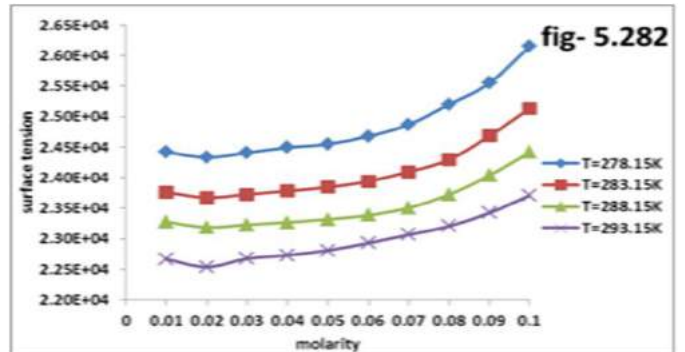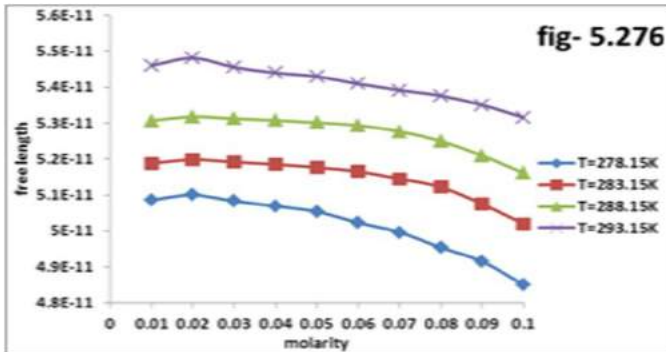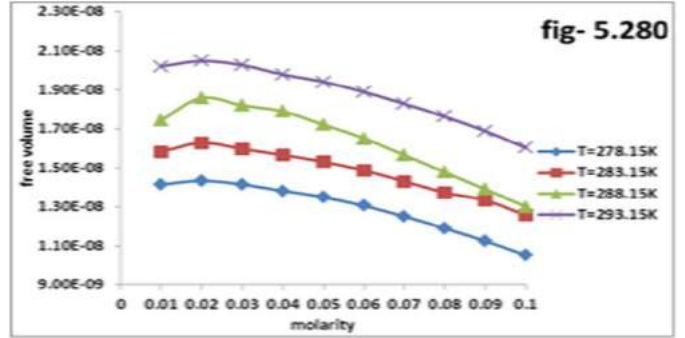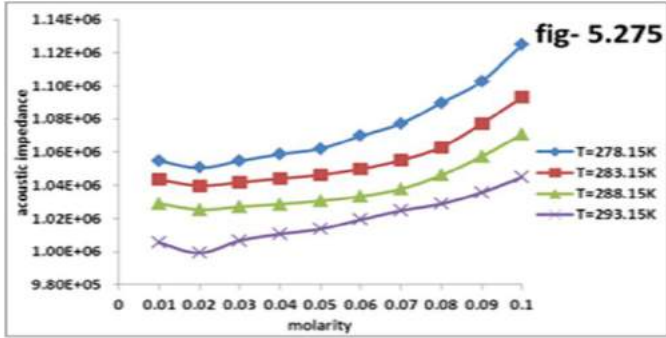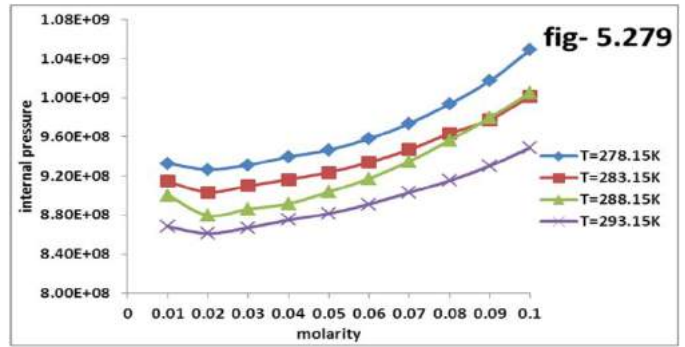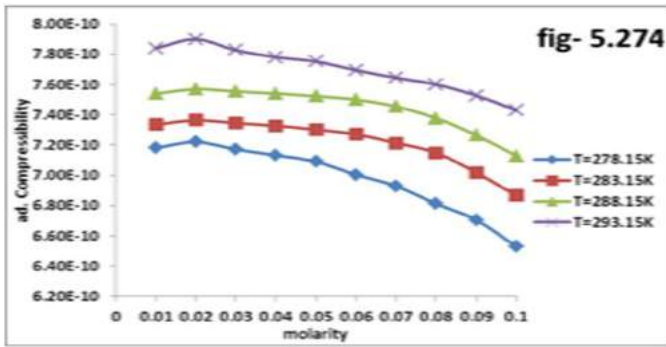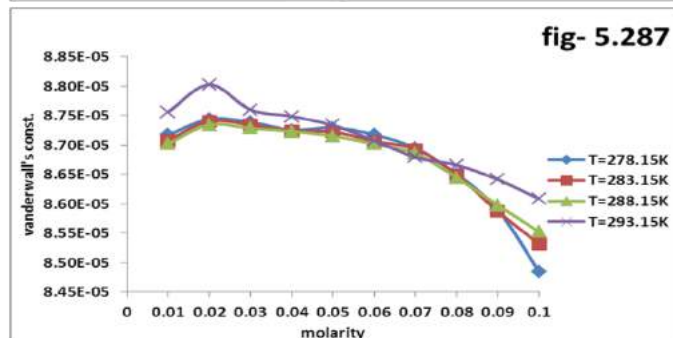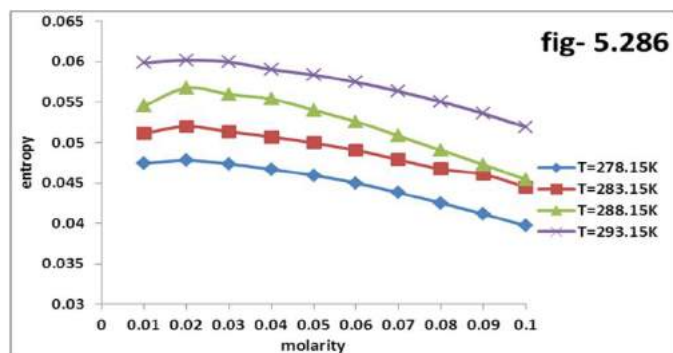
III. RESULTS AND DISCUSSION

The outcome of experiments analyzed by Ultrasonic and allied parameters with different concentration of salicylamide with butanol at temperature T=278.15K-293.15K it has been revealed graphically. Nonlinear sense of ultrasonic velocity with increase in mole fraction of salicylamide gives the dipole-dipole interaction or hydrogen bonded complex structure between unlike molecules which leads to increase in sound velocity and decrease in compressibility. At low molarities, the number of hydrogen bonds formed may less and at high molarities it may more because of solute-solute interactions and it forms a tightly bounded system. Adiabatic compressibility is a wide measure of intermolecular association or dissociation or repulsion. Free length decreases as the mole concentration increases; these considerable interactions between solute and solvent molecules.

Ultrasonic velocity rises on decrease in free length and vice-versa. A sudden decrease in molecular free length shows a tightly packing molecules or strong interaction. Increase behavior of acoustic impedance with molarities may provide the strength of inter molecular interaction so it reveal on the basis of the interaction between solute and solvent molecules. The linear changes of Relative association observe the particular interaction exists in the solution and quite it is strong in nature. Internal pressure gives an outstanding examination of the solution phenomenon and evaluating various properties of the liquid state. The changes in the internal energy of liquid mixtures, it seems to undergo a very small isothermal change. So it is a measure of cohesive or binding forces between solute and solvent molecules. The internal pressure may provide essential information regarding the nature and strength of forces exist between the molecules. The variation of surface tension also supports the significant associative nature in the solution.

Loss of di-polar associating nature and difference in size and shape of the molecules, which provide to decrease in velocity and increase in compressibility. Increase in the compressibility value indicates the weakening of molecular interactions. The positive value of entropy indicates the reaction must be spontaneous process of flipping of molecule over each other. Increase in temperature of drug solution increases the disorder of the molecules; hence there is a reduction in molecular interaction and cohesive forces between the molecules. Effect of temperature produced destruction in hydrogen bonding between the molecules and hence weakens the molecular interaction. As the effect of this drug solution behaves dissociative nature

IV. CONCLUSION

The outcome of ultrasonic measurements reveals knowledge of a number of the thermophysical properties towards the strong intermolecular interaction provides the structure making property in the liquid mixture. The various kinds of intermolecular interactions are the micro analysis of the drug in terms of solute-solute, solute-solvent, ion-ion, dipole-dipole interactions which can directly signify the utility of the drug.

V. REFERENCES

[1]. Knights K, Bryant B (2002). Pharmacology for Health Professionals. Amsterdam: Elsevier. ISBN 0-7295-3664-5.

[2]. Chilowski C, Langevin P, inventors. Production of submarine signals and the location of submarine objects 1923.

[3]. Flannigan DJ, Suslick KS. Plasma formation and temperature measurement during single-bubble cavitation Nature 2005 Mar 3;434(7029):52-55.

[4]. Skauen DM. Some pharmaceutical applications of ultrasonics J Pharm Sci 1967 Nov;56(11):1373-1385.

[5]. Shirsath SR, Sonawane SH, Gogate PR. Intensification of extraction of natural products using ultrasonic irradiations:A review of current status. Chemical Engineering and Processing: Process Intensification 2012 /3;53(0):10-23.

[6]. Higgins DM, Skauen DM. Influence of power on quality of emulsions prepared by ultrasound J Pharm Sci 1972 Oct;61(10):1567-1570.

[7]. Mason TJ. Ultrasound in synthetic organic chemistry. Chem Soc Rev 1997;26(6):443-451.

[8]. Shah RB, Zidan AS, Funck T, Tawakkul MA, Nguyenpho A, Khan MA. Quality by design: characterization of self-nano-emulsified drug delivery systems (SNEDDs) using ultrasonic resonator technology Int J Pharm 2007 Aug 16;341(1-2):189-194.

[9]. Skrabalak SE, Suslick KS. Porous MoS2 synthesized by ultrasonic spray pyrolysis J Am Chem Soc 2005 Jul 20;127(28):9990-9991.

[10]. Hill CR, Bamber JC. Methodology for clinical investigation. Physical Principles of Medical Ultrasonics, Second Edition 2004:255-302.

[11]. Essentials of Pharmacology, Surender Singh, General Pharmacology (Academa publishers), 1st edition, 2004.

[12]. K.D.Tripathi, Essentials of Medical Pharmacology, 4th Edn.,Jaypee Brothers Medical Pub.New Delhi,(1999).

[13]. A Kar, Medicinal Chemistry (Wiley Eastern Ltd.), 1993.

[14]. S. Nagar, H. Singh, J. Med Chem.;,Vol.16, pp.178-180, 2007.

[15]. Kannappan A.N. and Rajendran V., Ind.J. Pure & Appl. Phys. 29, 451.1991.

[16]. Kannappan A.N. and Rajendran V., Ind.J. Pure & Appl. Phys., 30, 240.1992.

[17]. Manoj Ku. Praharaj,Abhiram Satapathy and Prativarani Mishra, International Journal of

[18]. Chemical and Pharmaceutical Sciences Vol.3 (3),pp.6-14,2012.

[19]. S.Jain, D. Bhambi, G.L. Talesara, Ind. J. Pharm. Sci.,Vol.69(1), pp.28-32. 2007.

[20]. M. Garcia, V. Morgante, M. Perez, P. Noe, Indian J Chem; Vol.11(5), pp.589,2008.

[21]. Syal, V.K., S. chauhan and P. Sharma, J. of Electrochem Soc. India 1(53),2004.

[22]. Saneel K. Thakur and Shivani Chauhan J. Chem. Pharm. Res. 3(2):657-664,2011.

[23]. Weast, R.C CRC Hanbook of Chemistry and Physics, 51st.Edn.(CRC Press, Cleaveland),C-405,1970.

[24]. Wankhede, D.S., Lande M.K and Arbad B.R. Jof Chem Engg Data,50:260,2005.

X-Ray Diffraction Study of Polypyrrole/Fluroscein Composite Synthesized By Chemical Method

S. G. Khobragade[1], N. S. Dixit[2], M. S. Dixit[3], D. A. Pund[4]

[1]Department of Chemistry, Brijlal Biyani Science College, Amravati-444605, Maharashtra, India

[2]Department of Chemistry, G.S.Tompe Arts, Commerce & Science college, Chandur Bazar, Amravati, Maharashtra, India

[3]Department of Physics, Jagdambha Mahavidyalay, Achalpur, Maharashtra, India

[4]Department of Chemistry, Shri R. R. Lahoti Science College, Morshi, Maharasgtra, India

ABSTRACT

In-situ chemical oxidative polymerization of pyrrole (Py) was carried out by doping it with Fluoroscein in the presence of oxidizing agent ammonium peroxydisulphate to synthesize polypyrrole/Fluoroscein dye composites. The PPY/ composites were synthesized with various composition of fluorescein dye in pyrrole. Morphological characterization of synthesized composites was carried out by powder X-ray diffraction (XRD) analysis. These studies suggest that they exhibit amorphous behavior and change in surface morphology due to insertion of dopant.

Keywords : PPy, APS.

I. INTRODUCTION

Over the last few decades polymers have attracted considerable interest in research for the development of advanced materials. The organic materials that generally possess an extended conjugation of Π-electron system along a polymer backbone chain are recognized as electroactive conducting polymers.[1] These materials with interesting electron-transport behavior to a material exhibits immense potential in technological applications such as in electrochromic devices, non-linear optical system OLEDs, photoelectrochemical devices, gas sensors, biomechanical sensors.[2]

Among the number of conducting polymers, Polypyrrole (PPy) is profoundly studied material due to its superior conductivity, good thermal and environmental stability, electrochemical reversibility, high polarizability and the ease of preparation through chemical or electrochemical routes.[3] However, PPy is limited in practical use due to its very fragile structure and insolubility. It exhibits poor processability and lacks essential mechanical properties.[4] These properties and applicability of polypyrrole can be improved by some suitable modifications of existing polymers structures.[5] This can be achieved by judicious choice of making composites of PPy by doping it with suitable dopant material in order to prepare multifunctional molecular structures that open possibilities for almost any desired applications.[6-7]

The association of PPy with fluorescein in order to prepare its composite which combine the properties of

both materials is one very promising way to obtain the specific requirements of physical properties for each type of application.

II. METHODS AND MATERIAL

The 0.1 M solution of AR grade pyrrole was contained in a beaker which was placed on a magnetic stirrer. 0.1 M ammonium peroxydisulphate solution was continuously added drop-wise with the help of a burette to the above 0.1 M pyrrole solution. The reaction was allowed for 6 hours under continuous stirring by maintaining a temperature of 0°C to 5°C. The precipitated polypyrrole was filtered and dried in hot air oven and subsequently in a muffle furnace at 100 °C. For 0.1 M pyrrole solution, 0.0001 M solution of Fluorescein was added and mixed thoroughly, further 0.06 M ammonium peroxydisulphate was continuously added drop-wise with the help of a burette to the above solution to get PPy/0.0001 M Fluorescein composite. Similarly PPy/0.00001M Fluorescein is also prepared by following the above procedure. The pure PPy and PPy/ Fluorescein thin films were prepared by bath deposition technique.

The synthesized composite materials were subjected to morphological studies through X-ray diffraction analysis.

III. RESULTS AND DISCUSSION

The X-ray diffractogram of PPy/Fluorescein dye composite is shown in following fig
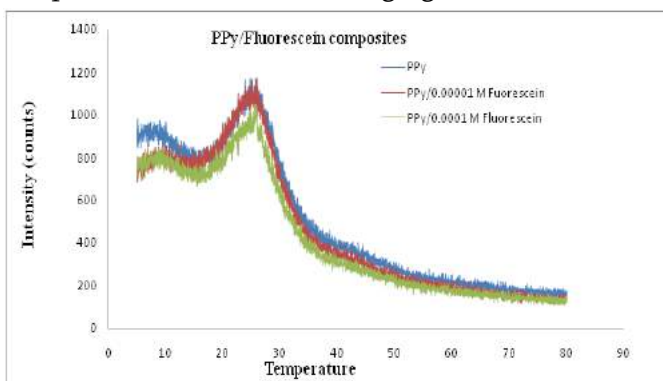
Fig 4.58: X-ray diffractogram of PPy/fluorescein dye composites

PPy (pure), exhibits a broad characteristic peak at around $2\theta = 25.73^{\circ}$, this peak is corresponding to highly disordered region, which is indicates amorphous nature of PPy. This strong diffraction peak associated with the chain–to-chain stacking distance at about $2\theta = 25.73^{\circ}$ can be attributed to scattering from all over chains due to the amorphously packed PPy polymer composites. The peak pattern obtained in PPy composites of Fluorescein is same as PPy which indicates basic polymer structure is retained after doping.

The long chains of the PPy makes it difficult for the orderly packing of chemically modified PPy and thus the crystalline nature of the chemically modified PPy is not possible. Thus chemically modified polypyrrole with fluorescein dye is in amorphous nature.

With the variation of Fluorescein concentrations i.e., from 0.01-0.2 M the PPy spectra look almost similar but with peaks shifted towards lower diffraction angle (25.68° and 24.66° in case of 0.00001 and 0.0001M dopant concentration of Fluorescein respectively) as compared to PPy (Pure). The shifting of peak towards lower diffraction angle is attributed to formation of quasi particles polarons and bipolarons which improves and enhances Polypyrrole morphology.

IV. CONCLUSION

Efforts have been made to synthesize the polypyrrole/Fluorescein dye composites to tailor the structural, morphological, and electrical properties of polypyrrole. Detailed morphological characterizations of the synthesized composites through XRD studies indicate the incorporation of dopant into the polymeric chain. The XRD study indicates the amorphous nature of the samples and the presence of hump in the diffractogram indicates the homogeneous nature of the polymer.

V. REFERENCES

[1]. T A Skotheim, Ed. Handbook of conducting Polymers, vol 1&2, Marceldekker, New York, 1986.

[2]. Wagner J B, Wagner C J, J. Chem Phys., , 1(26),1957, 597.

[3]. Baurele J.E., J Phys. Chem.Solids, , 30, 1969, 2657-2670.

[4]. Kaiser, A. B., et al., Curr. Appl. Phys., 4, 2004, 497–500.

[5]. S.N. Hoier, S.-M. Park, J. Phys. Chem., 96, 1992, 5188.

[6]. Wagner J B, Wagner C J, J. Chem Phys., 26, 1957,1597.

[7]. Baurele J.E., J Phys. Chem.Solids, 30, 1969, 2657-2670.

Synthesis and Characterization of ZnO Thin Films Using Advance SILAR Method

G. P. Save

Department of Physics, Janata Mahavidyalaya, Chandrapur, Maharashtra, India

ABSTRACT

ZnO thin films were prepared by advance SILAR method using 0.1 M Ammonium Zincate bath. The coated films were annealed 2hr at 400 ℃. The structural and optical properties were studied by X-ray diffraction and UV– vis spectroscopy respectively. The hexagonal Wurtzite structured ZnO thin films were confirmed by X-ray diffraction (XRD) and preferential orientation along the (101) plane was confirmed from structural analysis. The crystallite size is found to be in range 29-31 nm and which is increases with no. of dipping cycles. The optical properties of the ZnO thin films were estimated using the absorption spectrum in the range of 400 –700 nm.

Keywords: Ammonium Zincate bath, Structural property, Optical property, Advance SILAR.

I. INTRODUCTION

In recent research field, nanoscience and nanotechnology is become an essential subject due to its application in various field and researcher shows their interest in nano scale nanomaterials are the set of substances where at least one dimension is less than 100 nanometers. Nanomaterials occurred naturally and also engineered artificially. The property of nanomaterials is different from large scale material. In recent day many methods are available to form nano powder and nano thin films. Thin film may be two dimensional depositions of nanomaterials having thickness in range few nanometer to 100 μm typically used in different applications. The different properties of thin film are changes with thickness, temperature and composition of material. Thin film of oxide like TiO_2, PbO, CuO, CdO are studied which were prepared by different methods like evaporation and sputtering processes, LASER assisted techniques, chemical vapour deposition, spray pyrolysis, sol-gel, spin coating, SILAR etc .

Zinc oxide (ZnO) has attracted recent interest for a range of applications and has been prepared and investigated in various physical forms such as single crystals, ceramic pellets, thick films, thin films and nanostructures etc. The typical hexagonal wurtzite structure of ZnO thin films is inferred from the XRD pattern [1-4]. Pure zinc oxide thin films have certain limitations in their application. They are not stable against corrosive environments and in humid ambient and lack stability in terms of thermal edging in air [5-6]. To stabilize the ZnO system against such changes, dopant ions have to be incorporated into them to obtain certain desired properties like wider or narrower band gap, higher optical absorbance, lower or higher melting point, ferromagnetism, etc. Therefore polycrystalline ZnO films have been doped with metals of group I, group II, group III and group

V. Thus the thin films of pure and polycrystalline ZnO have been widely studied during the last few decades because of their high optical transparency (80%) in the visible region, high conductivity and technological applications particularly in the field of semiconductor electronics and optoelectronic devices includes integrated circuit chips, micro-fabricated mechanisms, micro-electromechanical systems (MEMS), micro-electronic optical systems, as well as gas sensing, light-emitting diodes (LEDs), optical coatings, photovoltaic solar cells, and thin film batteries [7-9,10].

Khadher AL-Rashedi et al. [11] was prepared the ZnO thin films by sol-gel method on glass. They were reported that crystal structure and orientation of the ZnO thin films investigated by X-ray diffractometer has peaks at $2\theta = 31.80°, 34.40°, 36.20°, 47.50°, 56.60°, 62.90°, 66.28°, 68°$, were assigned to (100), (002), (101), (102), (110), (103), (112), (201) of ZnO indicating that the samples were polycrystalline wurtzite structure. The grain size of the crystallites and band gap energy were found to be 14.7nm and 3.27 eV. ZnO thin films have been successfully deposited on silica glass substrate using chemical bath deposition technique. There was a red shift in the band gap energy as the annealing temperature was increased and band gap energy was found to be 2.66 eV [12]. ZnO thin films were deposited on a glass substrate by dip coating technique. The films were found to exhibit high transmittance, low absorbance and low reflectance in the visible regions. The thickness of the films was evaluated in the range of 173 to 323 nm [13]. O.A. Fouad et al. [14] were Prepared ZnO thin film by Thermal Evaporation Deposition method and studied the structural properties and showed the photocatalytic activity. ZnO Thin Films Deposited by RF magnetron sputtering [15].

The aim of the present work is to use a relatively simplest SILAR technique to prepare ZnO thin films from Zinc complex solutions and studied their structural, optical properties with choice of precursors, concentration and pH of the reacting precursors, temperature of deposition.

II. METHODS AND MATERIAL

2.1 Preparation of Zinc Oxide (ZnO) thin film by SILAR Method

The preparation of Zinc oxide thin film was prepared by SILAR method. This method has two beaker one is cationic and other is anionic bath. The cationic bath contain ammonium zincate solution $[(NH_4)_2ZnO_2]$ kept at room temperature and anionic bath contain hot water at near 85-90 °C. The ammonium Zincate bath was prepared by low addition of ammonium hydroxide (NH_4OH, Fischer Scientific India Pvt. Ltd. approx. 25% ammonia solution, mol. wt. 17.03 g/mol) to an aqueous solution of 0.1 M Zinc sulphate heptahydrate [$ZnSO_4.7H_2O$, Fischer Scientific India Pvt. Ltd mol wt. 281.53 g/mol]. Ammonia solution was introduced slowly under continuous stirring until the solution becomes clear and homogenous. The pH of the solution was maintained between 9.5-10 to obtain better quality films. The substrates were cleaned prior to deposition by first boiling them in hot water and subsequently cleaning them with acetone. They were further kept dipped in double ionized distilled water for some time to remove the contaminants. This pre-cleaned glass substrate was alternatively dipped in the cationic precursor ammonium zincate bath for 10s and then in the hot water bath kept at temperature between 85°-90°C. To obtain variation in thickness Zinc oxide thin films were deposited at 25, 35 and 45 dipping cycles. After the growth process thin films were washed with distilled water and dried in air at room temperature. The films were then annealed at 400°C for about 1 hour for better quality film. The thickness of Zinc oxide thin film was determined by weight difference-density consideration method or also known as the gravimetry method using an electronic high-precision balance.The structural analysis of annealed Zinc oxide thin film was was carried out with X-ray Diffraction

technique using a diffractometer Seimens D5000. This diffractograms were taken within range of diffraction angle (2θ) between 10 to 80 degree, employing a step of 2 deg/min at room temperature with CuKα radiation (λ = 1.5406 A⁰). The optical absorption was measured with a UV-Vis spectrophotometer (Perkin Elmer) within wavelength range between 400 and 700.

2.2 Film Thickness Measurement

The film thickness was determined by weight difference-density consideration method or also known as the gravimetry method using an electronic high-precision balance.

$$t = \frac{(W2-W1)}{A\rho} \times 10^{-4} \ \mu m \ \dots\dots\dots\dots\dots (1)$$

Where 't' thickness of film,'W_1' and 'W_2' be the weights of the substrate before and after film deposition in gm., and 'A' be the area of the deposited film in cm³ and 'ρ' be the theoretical density(5.6 gm/cm³) of ZnO.

Table 1 and Fig.1 shows Variation of film thickness with increase in dipping cycles.

Dipping cycles	Thickness of the film (nm)
25	573
35	700.2
45	881.8
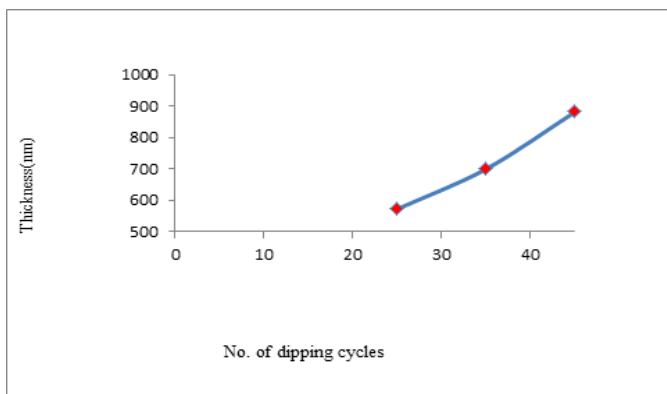
III. RESULTS AND DISCUSSION

3.1 Structural Property

The X-ray diffraction (XRD) is well known technique for characterization of bulk and thin film samples. The structural identification and determination of lattice parameters are based on the interpretation of XRD patterns. The value of interplaner spacing'd' was measured using Bragg's equation,

2 d sinθ = nλ …………………………..(2)

Where, d = interplaner spacing, θ = glancing diffraction angle, n = order of diffraction (n =1), λ = wavelength of monochromatic X-ray. The observed "d" values are compared with standard "d" values using (JCPDS) American Society for Testing Materials (ASTM) data card.

The crystallite size or particle size (D) can be determined using the Scherrer's formula,

$$D = \frac{K.\lambda}{\beta.\cos\theta} \quad \dots\dots\dots\dots\dots\dots\dots(3)$$

Where D is a average crystallite size, k is a constant determined by the geometry of the crystallites and it is approximately 0.95 for spherical particles, β is the full width at half maximum (FWHM) intensity of the observed diffraction peak and λ is a wavelength of monochromatic X-ray (1.5406 A⁰).

The dislocation density was calculated using the equation,

$$\delta = \frac{1}{D^2} \quad \dots\dots\dots\dots\dots\dots\dots(4)$$

The average strain in the film can be calculated using Williamson-Hall equation,

$$\beta \cos\theta = \frac{k\lambda}{D} + 4\varepsilon \sin\theta \quad \dots\dots\dots\dots\dots\dots(5)$$

Where β is the full-width half maxima, θ is the angle at which a particular peak is obtained in the XRD data, k is a constant, D is average particle size, and λ is the wavelength.

The lattice constants a and c are calculated using the formula,

$$a = \frac{\lambda}{\sqrt{3}\sin\theta} \quad \& \quad c = \frac{\lambda}{\sin\theta} \quad \dots\dots\dots(6)$$

The numbers of crystalline per unit are (Nc) was evaluated using the relation,

$N_c = \dfrac{t}{D^3}$ ……………………….(7)

and the lattice distortion (LD) developed in thin films can be evaluated from the relation,

$LD = \dfrac{\beta}{4\,tan\theta}$ ……………………….(8)

The structural analysis of annealed Zinc oxide thin film was carried out with X-ray Diffraction technique using a diffractometer Seimens (D5000, CuKα radiation λ = 1.5406 A⁰).
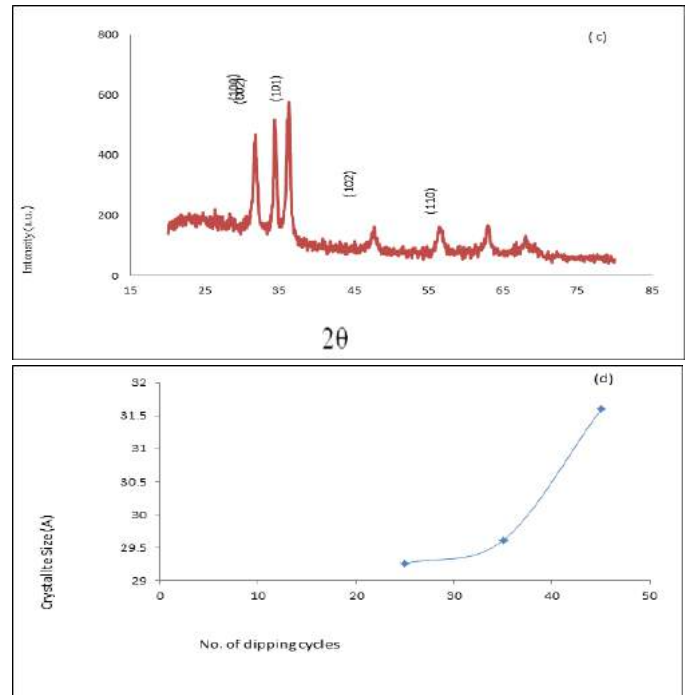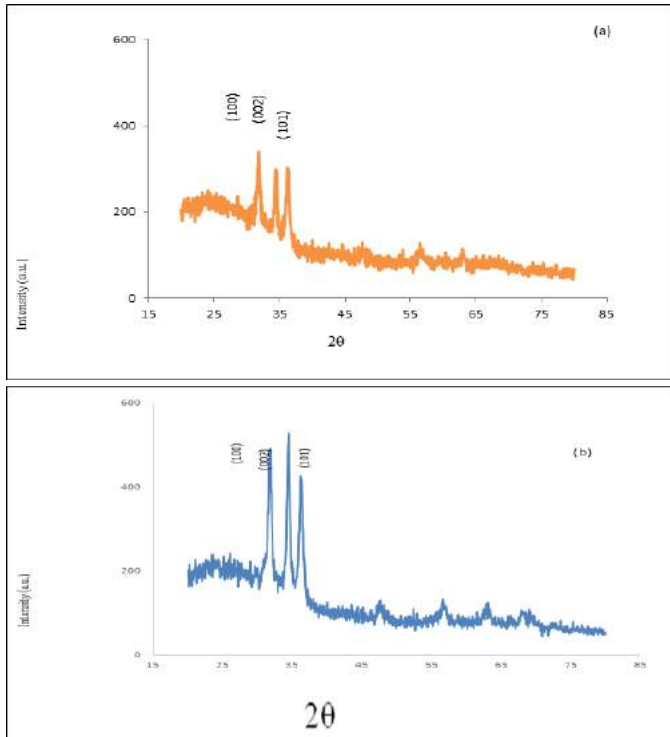
Fig.2 XRD spectra of ZnO thin films at (a) 25 cycle, (b) 35 cycle, (c) 45 cycle and (d) variation of crystallite size with dipping cycles at 101 plane.

Table 2 XRD parameters of ZnO thin films at 25, 35 and 45 dipping cycles

2θ	Plane (hkl)	No. of cycles	d (Å)	FWHM (β) (10^{-3} radian)	Crystallite Size (D) (nm)	$(\delta_{\times 10^{14}})$ (lines/m²)	Strain(ε) (lines^{-2} m^{-4})	Lattice constants (Å) a	c	Nc (10^{16})	Lattice Distortion (LD) ($\times 10^{-3}$)
36.4	101	25	2.46	5.21	29.26	11.68	0.0040	2.80	4.9	3.40	1.72
		35	2.46	5.14	29.61	11.65	0.0039	2.84	4.93	3.42	1.75
		45	2.52	4.82	31.6	10.01	0.0037	2.86	4.98	3.43	1.77

Fig.2 (a), (b), (c) are the diffraction patterns for ZnO thin film at 25, 35 and 45 cycle respectively. Peaks for pure ZnO appear at 31.79°, 34.6°, 36.35°, 47.85°, 56.85° corresponding to (100), (002), (101), (102) and (110) reflecting planes which indicate towards the hexagonal wurtzite structure of ZnO. No diffraction peaks of the impurities were detected in three cases indicating the high purity and single phase nature of the films. From the figure it is clear that ZnO film is oriented at (101) plane .Other orientation

corresponding to (100) ,(002),(102) and (110) are present with low relative intensities as compared to (101) plane. XRD pattern revealed the formation of hexagonal phase ZnO and the intensity of the film were found to increase with increasing dipping cycle. . It is found that pure ZnO films prepared from ammonium zincate baths have a polycrystalline structure with strong preferred orientation in the (101) plane. Fig.2 (d) shows the plot of relative crystallite size for (101) plane vs. increase in dipping cycle, we were found that the overall crystallite size increase with increase in dipping cycle. The crystallite size increases from 41.94nm for ZnO thin film at 25 cycle to 42.33 nm for ZnO thin film at 45 cycle corresponding to (101) plane.

3.2 Optical Property

The optical absorption spectrum of the ZnO thin films were determined at room temperature in a UV-VIS spectrophotometer ((Perkin Elmer) in the wavelength range 400-700 nm. The absorbance of ZnO thin film increases with dipping cycle due to increase in thickness. The absorbance edge not seen in graph, it was already reported that it occurred before 400 nm wavelength.
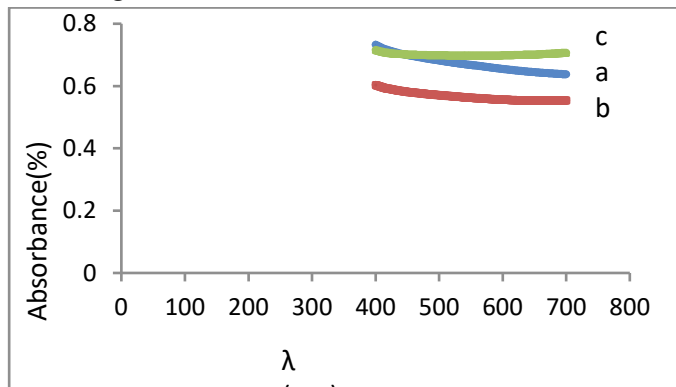
Fig.3 Spectra of absorbance vs wavelength λ (nm) of ZnO thin films at 25, 35 and 45 cycles.

The average extinction coefficient (K) calculated using the formula given by equation

$$K = \alpha\lambda/4\pi \quad \ldots\ldots\ldots\ldots\ldots\ldots\ldots\ldots(9)$$

It was\ found to be 0.393, 0.868 and 0.993 at 25, 35 and 45 cycles of ZnO thin films.

IV. CONCLUSION

ZnO thin film was prepared by advance SILAR method using Ammonium Zincate bath. The structural properties were characterised by using a diffractometer Seimens (D5000, CuKα radiation λ = 1.5406 A^0) and it is found that pure ZnO thin film has polycrystalline hexagonal wurtzite structure oriented along 101 plane.The crystallite size is increase with dipping cycle. The optical properties were characterised by using a UV-VIS spectrophotometer ((Perkin Elmer) in the wavelength range 400-700 nm. The average extinction coefficient was calculated from absorbance graph and its increased with increasing dipping cycles.

V. REFERENCES

[1]. S. Tewari and A. Bhattacharjee, Pramana - J. Phys. 76, (2011)153.

[2]. Y. Natsume , Thin Solid Films 372 (2000) 30.

[3]. T. Negami, Y. Hashimoto and S. Nishiwaki, Sol. Energy Mater. Sol. Cells 67 (2001)331.

[4]. I. A. Ezenwa, Res. J. Chem. Sc. 2 (2012) 26.

[5]. A. E. Jimenez-Gonzalez, Journal of Solid-State Chemistry 128 (1997) 176.

[6]. D. J. Qiu, H. Z. Wu, A. M. Feng, Y.F. Lao, N. B. Chen and T. N. Xu, Appl. Surf. Sci.222 (2004) 263.

[7]. K. Arshak and I. Gaiden, Mater. Sci. Engg. B118 (2005) 44.

[8]. R. Ghosh, S. Fujihara and D. Basak, J. Electron. Mater. 35 (2006)1728.

[9]. N. Shakti, Appl. Phys. Res. 2 (1010) 19.

[10]. D. Kohle, J. Phys. D: Appl. Phys. 34 (2001) 124.

[11]. Khadher AL-Rashedi, Mazahar Farooqui and 1Gulam Rabbani,IJCR,10(2018)73679.

[12]. I. Nkrumah, F.K. Ampong B. Kwakye-Awuah, R.K. Nkum, F. Boakye,IJRET,02(2013)809- 812.

[13]. Zohra nazir kayani1, Maryam iqbal1 , Saira riaz , Rehana zia1 , Shahzad naseem App.Phy.77C (2015) 171-180.

[14]. O.A. Fouad, A.A. Ismail, Z.I. Zaki, R.M. Mohamed,Applied Catalysis B Environmental, 62(1-2) (2006) 144-149.

[15]. S. Youssef P. Combette J. Podlecki R. Al Asmar,A. Foucaran, App.Phy. 43(2008) 65–71.

Molecular Interactions by Ultrasonic Measurements in Aqueous and 10% Ethanol-Water Solutions of MYO-INOSITOL At 298.15K

S. A. Shah

Department of Chemistry, Anand Niketan College, Anandwan, Warora, Maharashtra, India

ABSTRACT

Density(ρ), ultrasonic velocity(U) and viscosity(η) have been measured experimentally for aqueous solution of myo-inositol at concentration range (0.1 M- 0.9 M) and 10% ethanol-water solutions of meyo-inositol at concentration range(0.05M-0.45M) at temperature (298.15K).The acoustic parameters such as adiabatic compressibility(β),free length(L_f), free volume(V_f), relaxation time(τ) and internal pressure have been worked out. The results are correlated in terms of non-covalent molecular interaction between the constituents of solutions.

Keywords : Ultrasonic velocity, Acoustic parameters, Meyo-Inositol

I. INTRODUCTION

Ultrasonic velocity of pure liquids and liquid mixtures are basically related to the non-covalent molecular interactions (hydrogen bonding, Vander Waal's forces and dispersion forces) between molecules and atoms. The speed and efficiency of the transmission is sensitive to the nature of the bonds and the masses of the molecules present in the liquid mixtures and hence composition of system [1]. The ultrasonic technique can be used as method for providing information about physicochemical properties of the materials. The principle used in this technique is that the ultrasonic wave can be changed by the intermolecular interactions (ion-dipole, dipole-dipole, dipole-induced dipole, and hydrogen bonding and dispersion forces) of the sample while it travels through the sample. By compare the incident and resultant ultrasonic wave the structure in the sample can be concluded [2].

Chemistry and biology of meyo-inositol derivatives has been investigated widely in the recent past due to the association of phosphoinositols in cellular signal transduction mechanisms [3] and anchoring of certain proteins to cell membranes [4]. Although a bewildering array of myo-inositol phosphates and their lipid derivatives have been identified and / or isolated from plant as well as animal sources, the biological roles played by many of them is not yet clearly understood. However, receptors and effectors involved in various stages of phosphoinositol based signal transduction pathways remain potential targets for pharmacological intervention in states of disease[5].These developments in biology and medicine have necessitated the efficient synthesis of naturally occurring phosphoinositols and their synthetic analogs. Myo-Inositol is a cyclic sugar alcohol. It is also known as cyclitol. The chemistry of the cell is controlled by myo-inositol. There should be

communication between outer and inner environment of a cell. The calcium channels of cell membrane can be opened by the derivative of myo-inositol (inositol-1,4,5 triophosphate). It allows the calcium ions to enter into the extracellular fluids[6].The chemistry and biology of myo-inositol derivatives has been investigated widely in the recent past due to the association of phosphoinositols in cellular signal transduction mechanisms [7] and anchoring of certain proteins to cell membranes [8]. The ultrasonic study of this molecule in aqueous and aqueous alcoholic medium is very important for understanding the behaviour water structures, biomolecular recognition and medicinal use.

II. METHODS AND MATERIAL

The solutions of myo- Inositol was prepared by dilution method. All the chemicals are of AR grades of 99.99 % purity. Composition range of myo-inositol is from 0.1 M to 0.9M in water and for myo-inositol the concentration range from 0.05M-0.45M (solubility of myo-inositol lower in 10% ethanol-water solvent system).

The ultrasonic velocity in the liquid mixtures have been measured by means of ultrasonic interferometer (Mittal type: Model: M-83) functioning at frequency 2MHz with an overall accuracy of ±0.1 m/s, an electronically digital operate constant temperature water bath has been used to flow water through the double walled measuring cell, made up of a steel containing the experimental solution at the preferred temperature. For weighing, an electronic digital balance having an accuracy of ±0.1 mg was used. An Ostwald's viscometer was used for the measurement of viscosity of liquid mixtures with an accuracy of 0.0001Nsm2. The viscometer was calibrated before used. Time flow of water and liquid solutions were measured. Densities were determined using specific gravity bottle by relative measurement method with accuracy of ±0.1 kg.m^{-3}.

III. RESULTS AND DISCUSSION

The experimental parameters and derived parameters presented in figure myo-inositol respectively. From these parameters, the acoustic parameters such as adiabatic compressibility(β),free length(L_f), free volume(V_f), relaxation time(τ) and internal pressure have been worked out and correlation of intermolecular interactions were established by plotting graphs.

By using density, ultrasonic velocity and viscosity of aqueous and 10% ethanol-water solution of myo-inositol, various acoustic parameters such as($β_a$), intermolecular free length (L_f) , free volume (V_f),internal pressure ($π_i$), relaxation time ($τ$), were calculated. The experimental parameters as well as derived acoustic parameters have been discussed in the light of molecular association.

Figure (a): System III & VI Aqueous and 10% ethanol-water solution of myo-inositol at 298K.
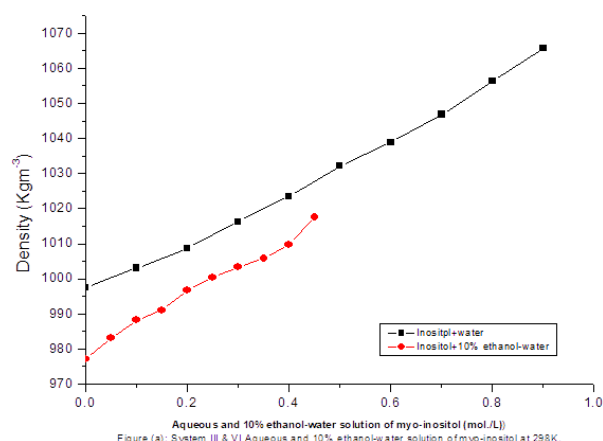
From fig.1.1 (a) the experimental values of density of aqueous and 10% ethanol-water solution of myo-insitol is found to increase with increase in concentration of solutes (myo-inositol), suggesting that the strength of interaction is enhanced. The increasing trend of density with increasing solute concentration indicates more number of components of the medium. Thus, it leads to closed packing of the medium and enhanced the intermolecular interactions. On comparing these values for aqueous and in 10% ethanol-water water solvent systems it is

found that density is minimum in 10% ethanol-water. It may be due to number of molecules per unit area is lesser as compare to aqueous medium and packing of solute molecules greater in aqueous medium than 10% ethanol-water solvent system.

Aqueous and 10% ethanol-water solution of myo-inositol (mol./L))
Figure (b): System III & VI Aqueous and 10% ethanol-water solution of myo-inositol at 298K.

From fig.1.1 (b) the experimental values of ultrasonic velocity of aqueous and 10% ethanol-water solution of myo-inositol is found to increase with increase in concentration of solutes (myo-inositol), suggesting that the strength of interaction is enhanced. The increasing trend of ultrasonic velocity with increasing solute concentration indicates more number of components of the medium. Thus, it leads to closed packing of the medium and enhanced the intermolecular interactions [9-10]. On comparing these values for aqueous and in 10% ethanol-water water solvent systems it is found that ultrasonic velocity is maximum in 10% ethanol-water. It may be due to strong hydrogen bonding between solute and solvent molecules as compare to aqueous medium and strength of interaction is greater in 10% ethanol-water solvent system than aqueous medium. It may be due to like nature of myo-inositol and alcohol molecules and strong interaction between ethanol and water molecules as compare to the interaction among the indusial molecules.

Aqueous and 10% ethanol-water solution of myo-inositol (mol./L))
Figure (c): System III & VI Aqueous and 10% ethanol-water solution of myo-inositol at 298K.

From fig.1.1 (c) the coefficient of viscosity is a fundamental property of liquids that decides the inner nature of the liquids. The coefficient of viscosity provides much more information about the medium. The variations of coefficient of viscosity depend on the surface area of the molecules, relative degrees of freedom (rotational, vibrational and translational) of the molecules and the molecular geometry [11-12]. The experimental values of viscosity of aqueous and 10% ethanol-water solution of myo-insitol is found to increase with increase in concentration of solutes (myo-inositol), suggesting that the strength of interaction is enhanced. The increasing trend of viscosity with increasing solute concentration indicates more number of components of the medium. Thus, it leads to closed packing of the medium and enhanced the intermolecular interactions. On comparing these values for aqueous and in 10% ethanol-water water solvent systems it is found that coefficient of viscosity is maximum in 10% ethanol-water. It may be due to strong hydrogen bonding between solute and solvent molecules as compare to aqueous medium and strength of interaction is greater in 10% ethanol-water solvent system than aqueous medium. It may be due to like nature of myo-inositol and alcohol molecules (like nature molecules have greater affinity) and strong interaction between ethanol and water molecules (ethanol-water) as

compare to the interaction among the indusial (water-water and ethanol-ethanol) molecules.

Figure (d): System III & VI Aqueous and 10% ethanol-water solution of myo-inositol at 298K.

Figure (e): System III & VI Aqueous and 10% ethanol-water solution of myo-inositol at 298K.

From figs.1.1 (d) and (e), the decrease in compressibility and free length implies that there is enhanced molecular association in this system upon addition of solute and less available free space between the components of the solution. The new complexes formed due to molecular association become more compact and less compressible. These also suggest that the compressibility and free length of the solution is less than that of solvent. The magnitude of compressibility depends on the electrostriction. It throws light on the hydrophobic-hydrophilic interactions in the medium. Negative values indicate hydrophobic interaction and loss of structural compressibility due to increased population of hydrogen bonded solvent molecules. This decrease trend in compressibility and free length with increase in concentration of solute (myo-inositol) indicate enhancement of solute-solvent interaction through intermolecular hydrogen bonding and dispersion forces[13-15]. If the compressibility and free length values are higher, it suggests that the medium is loosely packed and lower values indicate maximum interactions.

From fig.1.1 (d) and (e), it is found that the trend revealed by adiabatic compressibility and free length is decreased with increase in concentration for studied molecule (myo-inositol) in 10% ethanol-water system compare to the aqueous medium. It may be due to like nature of myo-inositol and alcohol molecules (like nature molecules have greater affinity) and strong interaction between ethanol and water molecules (ethanol-water) as compare to the interaction among the indusial (water-water and ethanol-ethanol) molecules.

Free volume and internal pressure:

Free volume is the average volume in which the central molecule can move inside the hypothetical cell due to repulsive interaction of neighbouring molecules. Monomer size space present in the system due to irregular packing of solvent molecules also called as free volume.
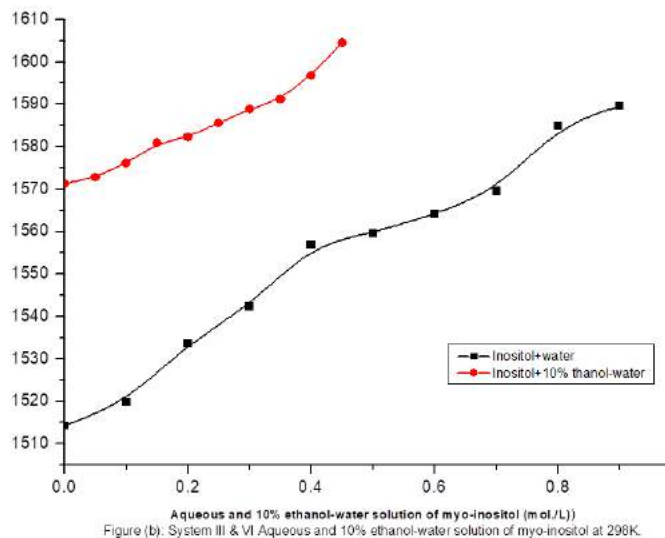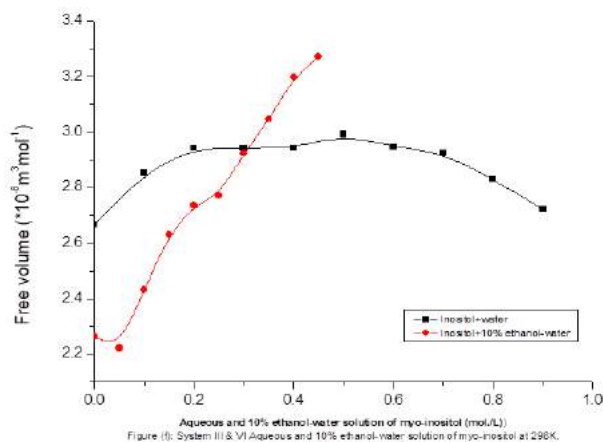

Figure (f): System III & VI Aqueous and 10% ethanol-water solution of myo-inositol at 298K.

From fig. 1.1 (f) values of free volume for 10% ethanol-water solutionof myo-inositol is found to increase with increase in concentration suggest that there is weak interaction between solute and solvent molecules. The free volume of the solution depends on the coefficient of viscosity as compare to density and ultrasonic velocity of the medium. The increase in free volume may be due to loosening of cohesive forces which result into breaking up structure of solvent system [16]. The decrease of free volume with concentration may be due to strong association between solute and solvent molecules through intermolecular hydrogen bonding and dispersion forces.

The free volume of aqueous Myo-inositol solution increases with increase in Myo-inositol concentration up to 0.6M and then decrease up to end suggest that from 0.1 to 0.6 molar concentration solution there is weak interaction between solute and solvent molecules. The enhancement of solute –solvent interaction takes place from 0.7 to 0.9 molar concentrations. The increase in free volume may be due to loosening of cohesive forces which result into breaking up structure of water. The decrease of free volume at higher concentration range may be due to strong association between solute and solvent molecules through intermolecular hydrogen bonding. Free volume and internal pressure inversely correlated with other [17].
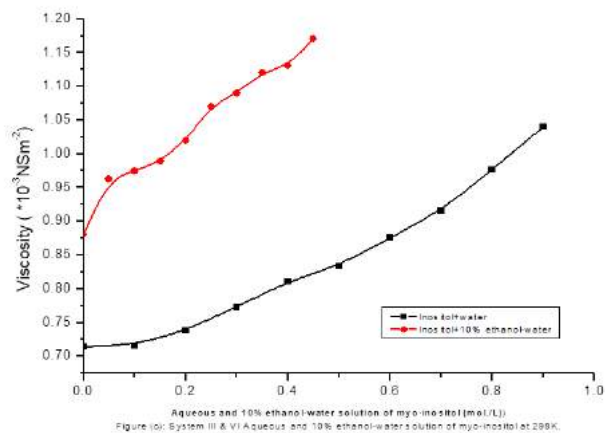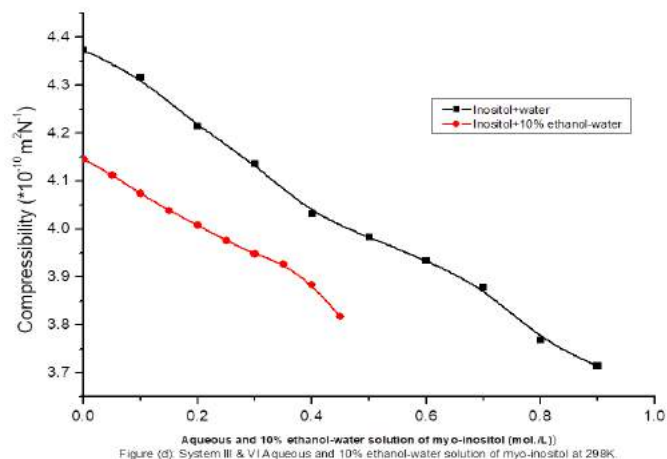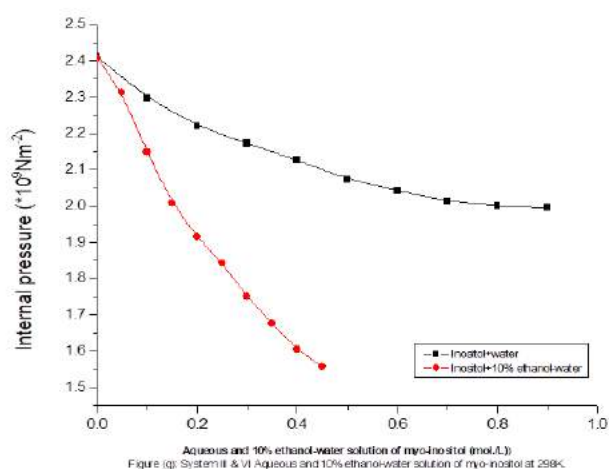

Figure (g): System III & VI Aqueous and 10% ethanol-water solution of myo-inositol at 298K.

From fig. 1.1 (g) the internal pressure of Myo-inositol solution is found to be decreases with increase in Myo-inositol concentration in both solvent systems, which indicates decrease in cohesive forces. In aqueous medium the internal pressure is found to be maximum as compare to 10% ethanol-water system, suggesting strong solute-solvent interaction in aqueous medium due strong intermolecular hydrogen bonding. In 10% ethanol-water solvent system cohesive force is found to decrease, this may be due to Repulsive forces among the solute and solvent molecules due to presence of ethyl group of ethanol molecules. Although the values of ultrasonic velocity, density, viscosity, adiabatic compressibility and free length attribute the predominance of solute-solvent interaction, the decrease in internal pressure with concentration indicates the presence of solute-solute interaction.

The relaxation time measure the closed packing of the medium. If the medium is loosely packed, it is easy to disrupt the medium and changing the equilibrium of the system. If the medium is closed packed, it is difficult to disrupt the medium and changing the equilibrium [18-19]. From fig. 1.1 (h) the increase of relaxation time with the Myo-inositol concentration strongly supports the intermolecular association through dipole-dipole (hydrogen bonding) interaction between solute and solvent molecules. When Myo-inositol is added in aqueous and 10% ethanol-water, Myo-inositol molecules may break the structure of associated solvent molecules and forms the solute-solvent complex. The Myo-inositol-water and Myo-inositol-ethanol hydrogen bonding is more favourable than water-water and water-ethanol hydrogen bonding. The Myo-inositol-water and ethanol bonding is enhanced due to extra bonding (dipole-dipole, dipole induced-dipole). Due to formation of complexes in the solution, particle size and masses increased. This leads to increase the cohesive forces, frictional forces and reduced the relative motion and rotation of freedom of the molecules of the Myo-

inositol solution. When the Myo-inositol concentration increase in both solvent system, the number of hydroxyl (-OH) groups available for hydrogen bond formation also increase and result into large number of hydrogen bonds between solute and solvent molecules. Relaxation time is found to be greater for 10% ethanol-water solvent system compare to the aqueous medium. This may be the effect of solvent system. The relaxation time is minimum for pure aqueous medium as compare to the 10% ethanol-water system.

IV.CONCLUSION

Molecular interaction depends on solvent systems. In the above present work, myo-inositol molecule strong molecular interaction in 10% ethanol-water system compare to aqueous myo-inositol. It is also concluded that ethanol-water molecules have greater molecular interaction than water-water molecules. In 10% ethanol-water system, solvent-solvent molecules have greater interaction than solute-solvent interactions.

V. REFERENCES

[1]. Coupland, J.N. & MaClements, D.J.(2001): Ultrasonics. In S. Gaunasekaran (Ed): nondestrutive food evaluation-Techniques to analyze properties and quality (pp.217-241). New York: Marcle Deckker, Inc.

[2]. MaClements, D.J.(1995) Advances in the application of ultrasound in food analysis and processing.Trends in Food Sciences and Technology 6,293-299.

[3]. K Hinchliffe; R Irvine; Nature 1997, 390, 123.

[4]. MAJ Ferguson; AF Williams; Annu. Rev. Biochem. 1988, 57, 285.

[5]. K Hinchliffe; R Irvine, Phosphoinositides: Chemistry, Biochemistry and Biomedicalapplications Bruzik, K. S. Ed.; ACS Symposium Series 718. American Chemical Society:Washington D.C. USA, 1999.

[6]. Clayden,Greeves,Warren and Wothers,Organic Chemistry, Oxford University Press(2001)pp1369.

[7]. K Hinchliffe; R Irvine; Nature 1997, 390, 123.

[8]. MAJ Ferguson; AF Williams; Annu. Rev. Biochem. 1988, 57, 285.

[9]. M. Shethu Raman, V. Ponnuswamy, P.Kolandaivel, K.Perumal, Journal of molecular Liquids,151(2010) 97-106

[10]. N.P. Rao, Ronald E. Verrall, Can. J. Chem. 65 (1987) 810

[11]. D. V. Jahagirdar, B. R. Arbad, S.R. Mirgane, M.K. Lande and A.G.Shankarwar, J. Mol. Liqids. 75 (1998) 33-43

[12]. CNR, Rao, University General Chemistry an Introduction to Chemical Science, Chennai, Macmillan pub. India Ltd. (1973) pp285-287

[13]. S. Ravichandran, K. Ramanathan, Polymer-Plastics Technology and Engineering,47: , (2008)169-173.

[14]. Gekko, K. & Noguchi, H., Journal of Physical Chemistry,83,(1979) 2706-27

[15]. M. Sethu Raman, M. Kesavan, K. Senthilkumar, V. Ponnuswamy, Journal of Molecular Liquids 202 (2015). 115-124

[16]. Samuel Glasstone, Text Book of Physical Chemistry,2nd edition, Macmillan and Co. Lit.,London(1962) pp479-480 17 N. Shanti, J.Madhumitha, Int.J.Adv.Chem., 2 (1)(2013)12-16

[17]. Mathson,A.J.,Molecular Acoustic, Wiley-Interscience, London (1971)

[18]. M. Sethu Raman, V. Ponnuswamy, P. Kolandaivel, K. Perumal, J. Mol. Liquids, 151(2010)97-106.

Thermodynamic Characterization of Dimethyl Formamide and Ethylamine by Using Ultrasonic Techniques at Different Temperatures

[1]Shweta Rode, [2]V. D. Bhandakkar, [1]O. P. Chimankar

[1] Department of Physics, RTM, Nagpur University, Nagpur, Maharashtra, India
[2]Department of Electronics, Anand Niketan College, Warora, Maharashtra, India

ABSTRACT

Ultrasonic technique provides the interaction of high frequency sound wave with matter resulting to generation of information about physico-chemical properties. Many researchers have been studies the application of ultrasonic waves in different areas like medicines, oceanography, aerospace, navy and material science. Nowadays Ultrasonic became a multidimensional area of study due to its different industrial and medical field. In present research paper, the Ultrasonic velocity (U), density (ρ) and viscosity (η) of binary liquid mixtures of Dimethylformamide (DMF) and Ethylamine (EA) have been measured using Ultrasonic Interferometer at frequency 7MHz and at different temperature (298K-308K). From the measured data of ultrasonic velocity, density and viscosity at different temperatures the acoustical parameters such as adiabatic compressibility(β_a), Free Length(L_f), Acoustical Impedance(Z), Internal Pressure(π_i), Relaxation time(τ), Free Volume(V_f), Molar Volume(V_m), Rao's Constant(R), Wada's Constant (W), Vander Waal's Constant(b), Gibb's Free Energy(ΔG), Classical Absorption(α/f^2), Isothermal Compressibility(β_i), Enthalpy(H) and Internal Latent heat of Vaporization (ΔH_i) of binary liquid mixture dimethylformamide in ethylamine at temperature range 298K-308K and frequency at 7MHz are with mole fraction and some probable reasons on the increase or decrease of acoustic and thermodynamic parameters with temperature change are also have been studied.

Keywords : Ultrasonic Velocity, Physico- Chemical, Thermodynamic, Hydrogen Bonding

I. INTRODUCTION

Recent development in science and technology for non–destructive technique are spectacular and holds significant possibilities for better new applications in molecular structure, molecular interactions, medicines and underwater acoustics. Development of sensors, electronic instrumentation and computer software added sophistication to the experimental and theoretical agreement of different ultrasonic parameters[1-3]. In many technological processes (e.g., in the chemical, petrochemical, food, and plastics industries) liquids are subjected to high pressures and temperatures. Therefore, knowledge of their thermodynamic properties is essential for understanding, design, and control of the process technology. Direct evaluation of the thermodynamic parameters of liquids under high pressure, using conventional methods, is very difficult. Therefore, the application of these methods in industrial conditions, particularly in on-line control of the technological parameters of liquids, is practically impossible[4-8].

The measurement of ultrasonic speed enables us to the accurate measurement of some useful acoustic and thermodynamic parameters and their excess values[9-14]. The study of molecular association in binary liquid mixture having DMF as one of component is of particular interest since DMF is used in the production of acrylic fibers and plastics and also used as a solvent in peptide coupling for pharmaceuticals, in the development and production of pesticides, and in the manufacture of adhesives, synthetic leathers, fibers, films, and surface coatings. The pharmaceutical industry uses DMF as a reaction and crystallization solvent because of its exceptional solvency parameters. Ethylamine is a two-carbon primary aliphatic amine. It has a role as a human metabolite. In order to have clear understanding of intermolecular interaction between component molecules of an attempt has been made to study the ultrasonic behaviors of DMF in EA at different temperature. Thermo-acoustic parameters are the essential sources of information for better understanding of non-ideal behavior of complex binary liquid system[15-18].

II. METHODS AND MATERIAL

The liquid DMF and Ethylamine were of Analar grade samples and purified before use. The binary mixture of different mole fraction of the two components in the Systems DMF with ethylamine was prepared immediately before use. The velocity of ultrasonic wave (U) of frequency 7 MHz and density (ρ) in these mixtures were measured by using a Multifrequency(1-10MHz) ultrasonic pulse interferometer (Model No. F-83, Mittal Enterprises, New Delhi). It consists of a high Multirange frequency generator (1 to 10MHz) and a measuring cell. The measurements of ultrasonic velocities were made at a fixed frequency of 7 MHz and temperature was controlled by circulating water around the liquid cell from thermostatically controlled constant temperature water bath. . The densities of pure liquids and liquid mixtures were measured by using a specific gravity bottle with an

accuracy of ± 0.5%. An Ostwald's viscometer was used for the viscosity (η) measurement of pure liquids and liquid mixtures with an accuracy of 0.0001Nm-2s. The viscometer was calibrated before used. All the precautions were taken to minimize the possible experimental error.

III. RESULTS AND DISCUSSION

Density(ρ), ultrasonic velocity(U), Viscosity(η) and thermodynamic parameters like adiabatic compressibility(βa), Free Length(Lf),Acoustical Impedance(Z), Internal Pressure(πi), Relaxation time (τ), Free Volume(Vf), Molar Volume(Vm), Rao's Constant(R), Wada's Constant (W), Vander Waal's Constant (b), Gibb's Free Energy(ΔG), Classical Absorption (α/f2), Isothermal Compressibility (βi), Enthalpy (H) and Internal Latent heat of Vaporization (ΔHi) of binary liquid mixture dimethylformamide in ethylamine at temperature range 298K-308K and frequency at 7MHz are shown in fig. 1 to 18 respectively.

In this system the molecules of dimethylformamide and ethylamine are polar with dipole moment 3.86D and 4.3D respectively. When discussing solvent effect, it is important to distinguish between the macroscopic effects of the solvents and effects that depend upon the details of the structures. Macroscopic properties refer to properties of the bulk solvent. An important example is the dielectric constant, which is a measure of the availability of the bulk material to increase the capacitance of the condenser. In terms of the structures, dielectric constant is a function of both permanent dipole moments of the molecules and its polarizibity refers to the distortion of molecules electron density. Dielectric constant increase with both dipole moment and polarizibity. An important property of solvent molecules with regard to reaction is the response of the solvent to change in charge distribution as the reaction occurs. The dielectric constant is a good indicator of the ability of the solvent to accommodate separation of charges.

Fig. 1

Fig. 2

Fig. 3

Fig. 4

Fig. 5

Fig. 6

Fig. 7

Fig. 8

Fig. 9

Fig. 13

Fig. 10

Fig. 14

Fig. 11

Fig. 15

Fig. 12

Fig. 16

Fig. 17

Fig. 18
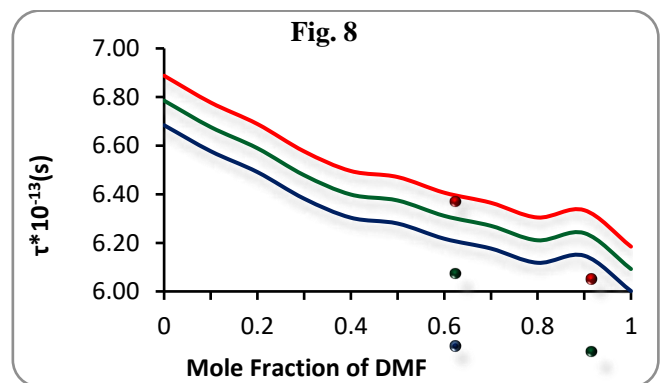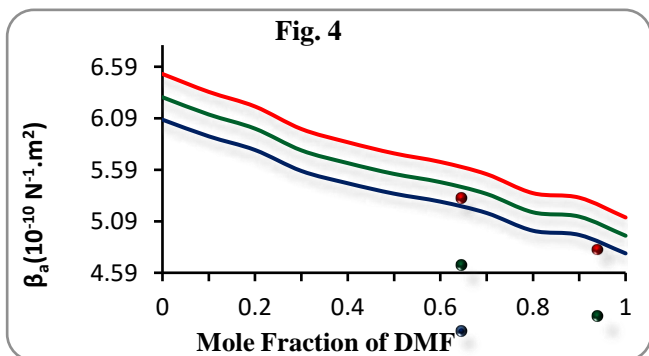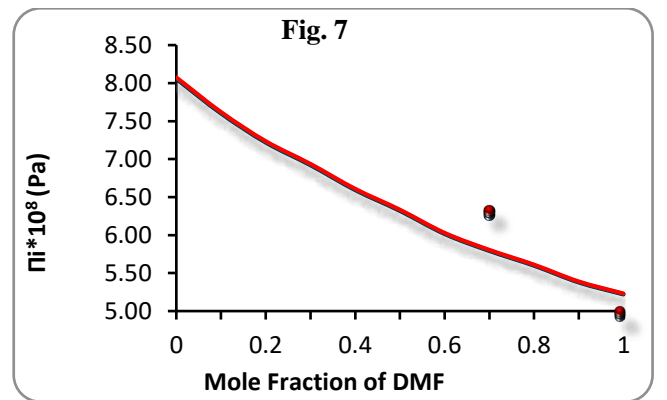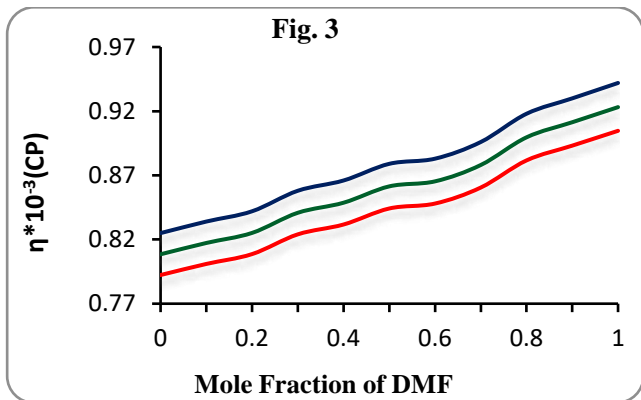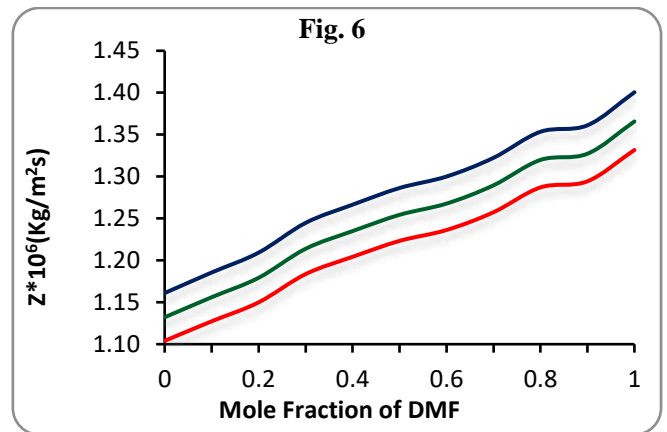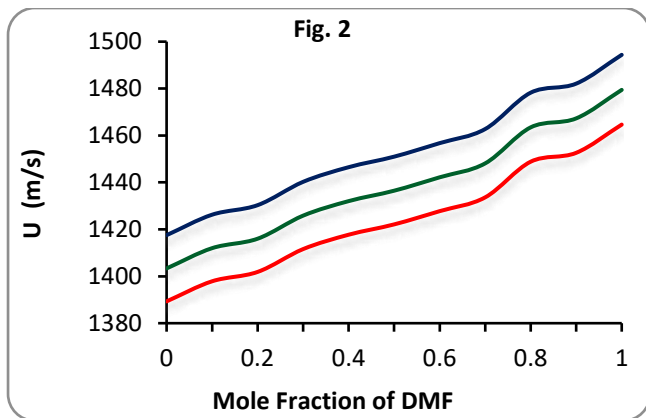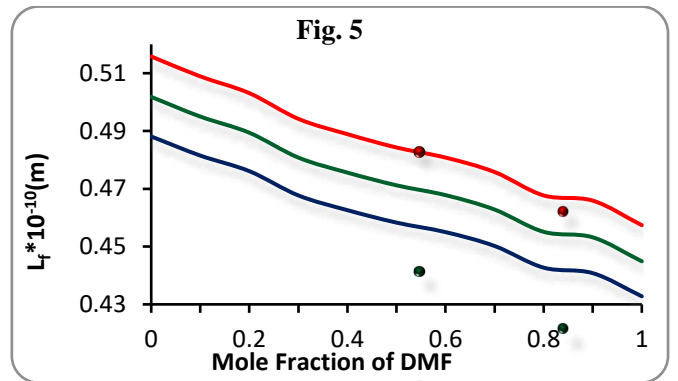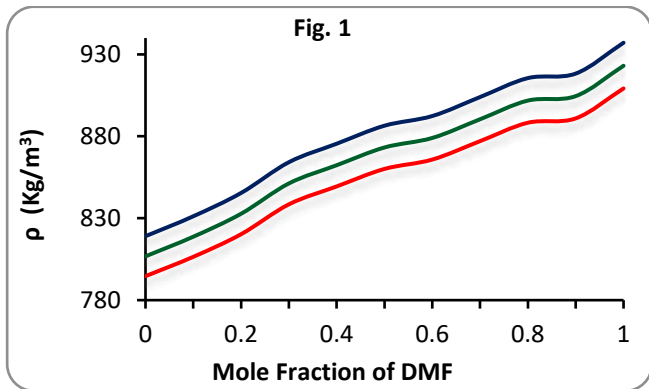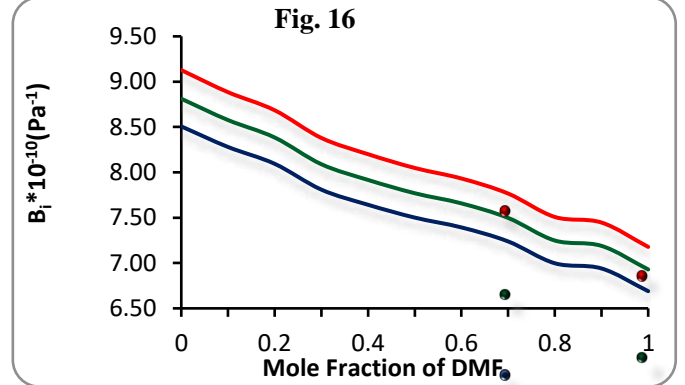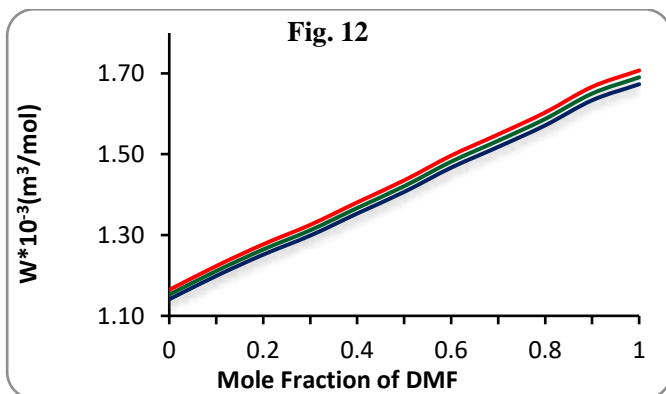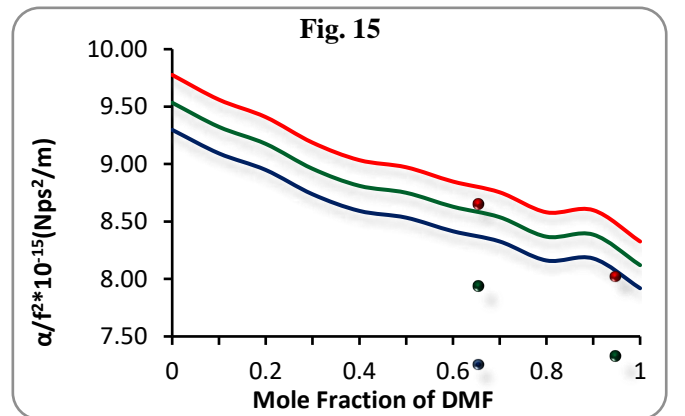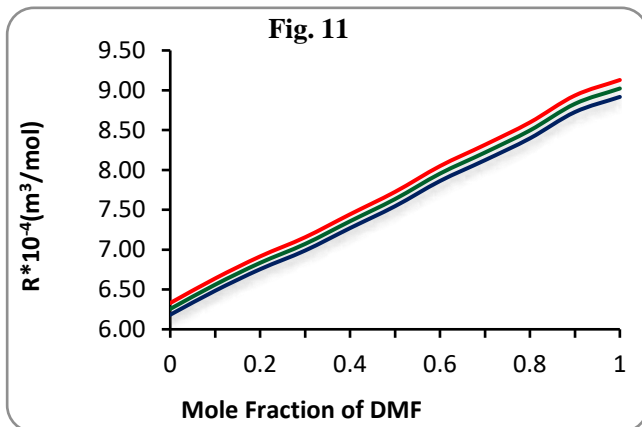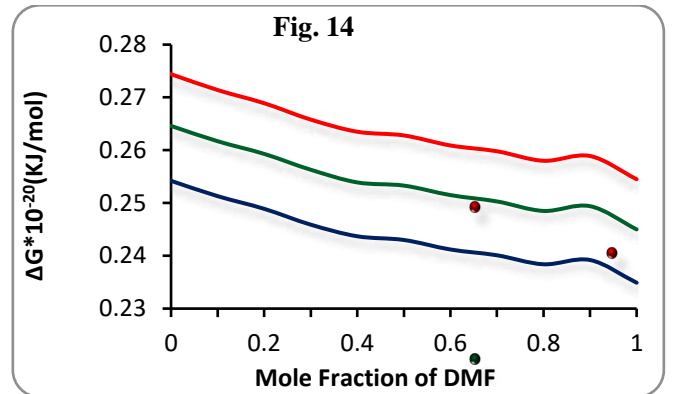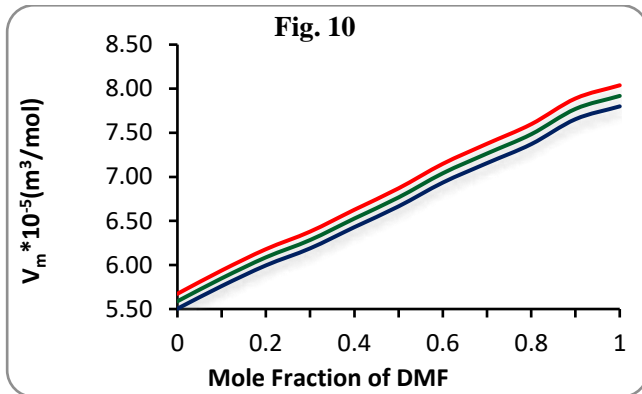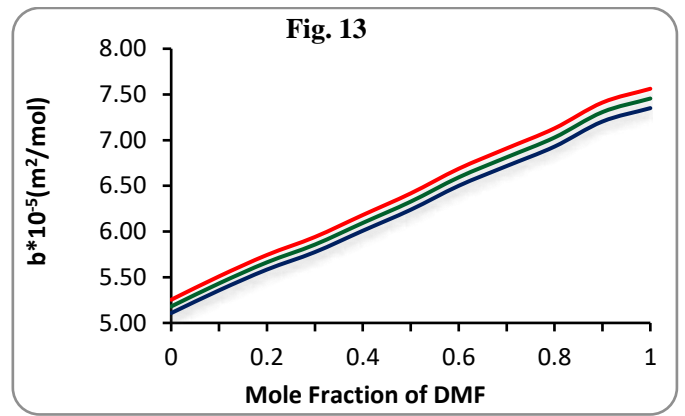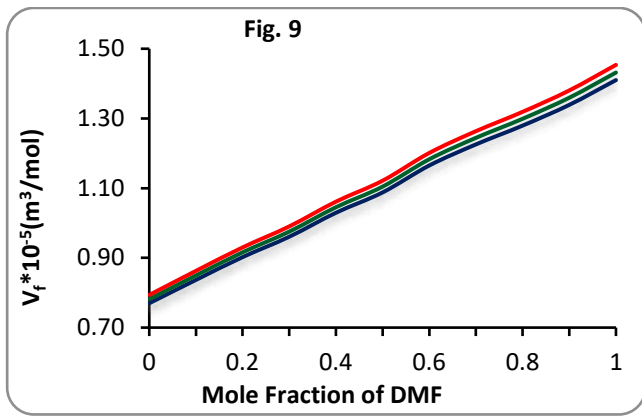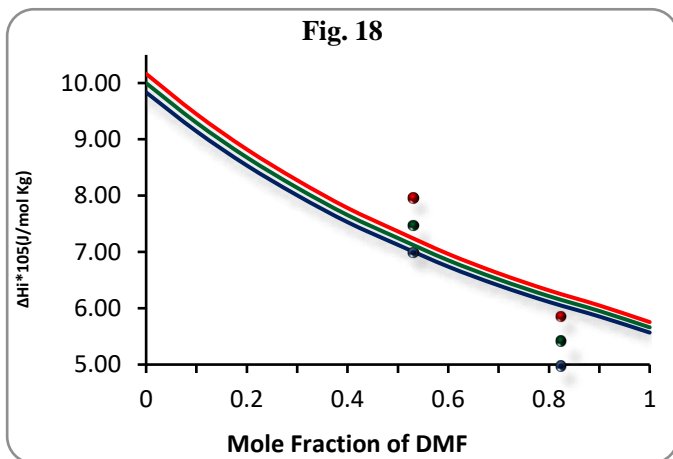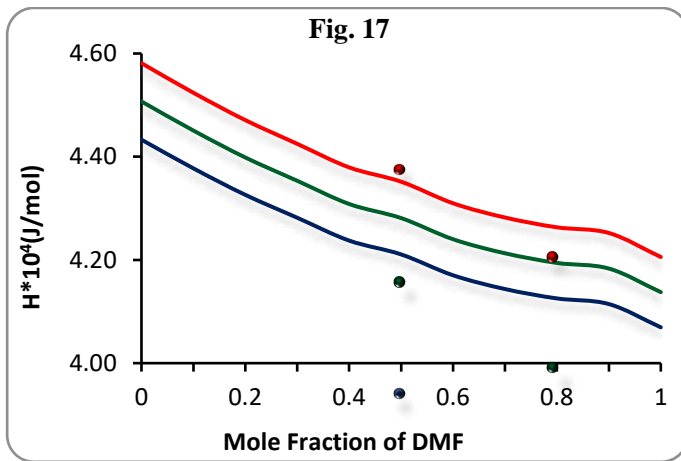
Fig. 1, represent the graph of ultrasonic density versus concentration. As the mole fraction of DMF increases the density increases. Increasing temperature of the mixture decreases its density (ρ). The decrease in density (ρ) with temperature indicates decrease in cohesive force. Thus increase of temperature favors increase of kinetic energy and volume expansion and hence decrease of density. The increasing temperature has two opposite effects namely structure formation and destruction of structure. This increase of temperature favors increase of kinetic energy and volume expansion and hence density decreases.

Fig. 2, shows the graph of ultrasonic velocity versus concentration. It is observed that ultrasonic velocity increase with increase in the concentration of DMF in EA, indicating increase in stiffness of the medium hence association in constituent's molecules[19]. The association may involve due to hydrogen bonding or dipole-dipole interaction between

dimethylformamide and ethylamine. The association is due to strong dipole-dipole interaction between the constituent molecules. This is because the size of DMF molecules is more than EA molecules. Hence higher the size more will be the polarizibility. The process may lead strong interaction forces[20,21].

Fig. 3, shows the viscosity (η) versus concentration. It is observed that viscosity increases with increase in the concentration of DMF in EA, indicating strong molecular interaction. The viscosity gives the strength of molecular interaction between interacting molecules. Increase in temperature of the mixture, increasing disorders of the medium and hence entropy increases. As entropy increases, viscosity of binary mixture decreases.

From **Fig. 4,** Adiabatic Compressibility (β_a) decreases with increasing the molar concentration of DMF in EA. This is as per general trend observed for the electrolytic solutions. In more concentrated solution, more cohesion is expected and this lead to a decrease in β_a. The decrease in β_a results in an increase in the value of ultrasonic velocity. The decrease of adiabatic compressibility with increase of concentration of solution may be due to the dispersion of solvent molecules around molecules supporting strong solute-solvent interactions.

The adiabatic compressibility (β_a) and Isothermal compressibility (β_i) exhibit similar trend as shown in the **Fig. 16**. It is observed that adiabatic compressibility (β_a) and isothermal compressibility (β_i) decreases with increase in molar concentration of DMF in EA indicating strong intermolecular interaction in the component molecules in binary mixtures shows associating tendency of the component molecules.

As the ultrasonic velocity increase due to the increases in concentration, the interacting free length has to decrease and vice-versa. Increase on intermolecular free length with rise in temperature result decrease in density and velocity in binary mixtures and this fact supported by the result of experimental observations

given in graph. From **Fig. 5,** freelength (L_f) decreases with increasing the molar concentration of DMF in EA.

In the present investigation, **Fig. 6,** represents the plot of acoustic impedance versus molar concentration. It is observed that these acoustic impedance (Z) values increase with increasing concentration of DMF in EA. Such an increasing values of acoustic impedance (Z), further supports the possibility of molecular interactions between the unlike molecules. It was reported that the linear variation of specific acoustic impedance indicates the absence of specific interaction like compound formation. In fact the specific acoustic impedance depends upon the structure and molecular packing of liquids.

From **Fig. 7,** Internal Pressure (π_i) decreases with increasing the molar concentration of DMF in EA. From graph, it is to be noticed that the variation in the internal pressure values shows exactly reverse trend as that of free volume[22]. In this system, **Fig. 7** and **Fig. 9** shows that, internal pressure decreases and free volume increases. Further the increase in free volume and decrease in internal pressure with rise in concentration clearly shows the increasing magnitude of interaction. Such behavior of internal pressure and free volume generally indicates the association through hydrogen bonding

Fig. 8, relaxation time (τ) decreases with increasing the molar concentration of DMF in EA. The dispersion of the ultrasonic velocity in the system may contain information about the characteristic time (τ) of the relaxation process that causes dispersion. The relaxation time which is in the order of 10^{-13} sec., is due to structural relaxation process[23] and in such a situation, it is suggested that, the molecules get rearranged due to co-operative process[24].

Fig. 9 represents, Free Volume (V_f) Increases with increasing the molar concentration of DMF in EA indicating association in the molecules of the component liquids. Free volume is the average volume in which the center of a molecule can move due to the repulsion of the surrounding molecules. This suggests that there is a closed packing of molecules inside the shield.

The molar volume of a liquid mixture depends on the structure arrangement in the liquid as well as on intermolecular interaction. The structural arrangement may be seceded by the molecular forces. **Fig. 10,** it is observed that the molar volume (V_m) increase with increase in concentration of DMF in EA. This is because effective mass is directly proportional to the molar volume. In present system, EA has lower effective mass in binary liquid mixture as compared to the DMF and hence it increases the molar volume of mixture with increase in concentration.

Fig. 11, Fig. 12, Fig. 13, shows the variation of Rao's Constant (R) OR Molar Sound velocity, Wada Constant (W) or Molar Compressibility and Vander Waal's Constant(b) with increasing concentration. Rao's constant is also known as molar sound velocity and it is an additive property. It has been found to be invariant with temperature and pressure for organic and inorganic liquid. It is observed that Rao constant, Wada Constant and Vander Waal's constant increase with increase in the concentration of DMF in EA. Vander Waal's constant (b) is also known as the co-volume in Vander Waal's equation and it varies in similar way to that of the available volume.

Gibb's free energy measures mobility of the medium. Higher the mobility of the medium, higher will be the entropy; lower will be the free energy. **Fig. 14,** represent the variation of Gibb's free energy (ΔG) with concentration. It is observed that Gibb's free energy decreases with increase in the concentration of DMF in EA, indicating increase in mobility of the mixture hence disorder increases due to outstanding salvation. Decrease in ΔG suggests longer time for rearrangement of molecules in the solution. The decrease of Gibb's free energy favors the formation of products after reaction[25].

Fig. 15, contains the plot classical absorption (α/f^2) versus concentration. It is observed that classical

absorption decrease with increase in the concentration of DMF in EA indicates the decrease in the stability of mixture. This process leads to dissociation and hence weak molecular interaction. This may lead solution more structured due to formation of hydrogen bond.

Fig. 17, shows that enthalpy (H) of the system decrease with increase in the concentration of DMF in EA, which indicates association. Lower the values of enthalpy; more is the interaction among the constituent molecules. It suggests less freedom of the molecules and hence strong intermolecular interaction.

Fig. 18, internal latent heat of vaporization (ΔH_i) decrease with increase in the concentration of DMF in EA. Latent heat is energy released or absorbed by a thermodynamic system, during a constant-temperature process. It is known that (ΔH_i) decreases with increase in temperature and increases with increase in pressure. Here, since the external pressure is very low, the pressure factor seems to predominate causing an increase in the values of (ΔH_i) with increase in temperature.

IV. CONCLUSION

The dependence of ultrasonic velocity and other derived parameters on composition of the mixtures is indication of the presence of molecular interactions. All the experimental determinations of thermodynamic parameters are strongly correlated with each other. In this paper, the all the derived thermodynamic parameter such as for different mole concentration of DMF with ethylamine of the binary mixtures are evaluated and shows the linear trends and hence these parameters suggests the presence of strong molecular interactions. In EA, NH_2 is active subgroup which plays important role in the association. The association in the constituent molecules may involve due to hydrogen bonding or due to dipole-dipole interactions between the constituent molecules. All these process may lead to strong interaction forces.

V. REFERENCES

[1]. B L Marvin and S N Bhatt, Acoustica, 6 (1983) 8-11.

[2]. V D Bhandakkar, V A Tabhane & Sharda Ghosh , Ind J Pure and App Phys, 41(2003).849 -854.

[3]. B L Marvin and S N Bhat,Acostica,64(1987)155.

[4]. V D Bhandakkar, G R Bedare, V D Muley, B M Suryavanshi , Adv. Appl. Sci. Res (2)4 (2011), 338-347

[5]. N R Pawar, O P Chimankar, V D Bhandakkar, N N Padole , IOP Conference Series: Materials Science and Engineering (42)1(2012) 012030 , IOP Publishing

[6]. O P Chimankar and V D Bhandakkar, Shweta Rode , Int Res J of Sci engg, special Issue A7(2020) 281-287

[7]. G Padmanabhan, R Kumar, V Kannappam& S Jaykumar, Ind J of Pure and Appli Phy, 50(2012) 99-906.

[8]. V D Bhandakkar & O P Chimankar , Shweta Rode , Imperial J of Interdisciplinary Res (IJIR) (3) 3, (2017) 952-958

[9]. Ghosh Apurba M, S A Wani, V G Meshram and J N Ramteke, Int J of Sci and Res, ISSN (Online): 2319-7064,(2015) 35-39.

[10]. N. Manohar Murthy et al, Acoustica, 48 (1981) 341.

[11]. G R Bedare, V D Bhandakkar & B M Suryavanshi , Int Jour of Mat Sci Engg. 42(2012), 012028, IOP Publishing, doi: 10.1088/1757-899X/42/1/012028.

[12]. R T Longman and W S Dunbar, J Phys chem., 49 (1945) 428.

[13]. J D Pande and R D Rai, Can J chem., 7 (1989) 437-441.

[14]. A A Mistry, V D Bhandakkar, O P Chimankar , J of Chem. and Pharm. Res, (4)1 (2012) 170-174.

[15]. O P Chimankar, Ranjeeta S Shriwas, Sangeeta Jajodia, VA Tabhane , Adv Appl Sci Res, (2)3(2011)500-508.

[16]. V D Bhandakkar, G R Bedare, V D Muley, B M Suryavanshi , Adv. Appl. Sci. Res, (2)4 (2011)338-347.

[17]. A A Mistry, V D Bhandakkar, O P Chimankar, J. of Chem. and Pharm. Res, (4)1 (2012) 170-174

[18]. L. Balu and P. Vasantharni and R. Ezhil Powel, Recent research in sci & tech, 2(4) (2010) 42-45.

[19]. R Mishr, J D Pandy,J Acoust SocInd, 7, (1979),145.

[20]. N P Rao and E V Ronald, Can J Chem, 65,(1987).

[21]. V A Tabhane, V D Muley and S B Khasare, Acoustica, 81, (1995).

[22]. Dhana Lakshmi & S Sekhar, Ind J Pure Appl Ultrasons, 21(3) (1999) 97.

[23]. L E Kinsler &A R Rray, Fundamentals of Acoustics (Wiley eastern), New Delhi, (1989).

[24]. Ali A Hyder S and A K Nair, Ind J Pure &ApplPhy, 7413(2000) 63.

[25]. M K Praharaj, Abhiram Satapathy, P R Mishra, SMishra, Archives of App Sci, Res, 4(2)(2012)837- 845.

DC Conductivity and XRD of Solid Polymer Electrolytes

[1]S. P. Bakde, [2]S. R. Jadhao

[1]Department of Physics , Shri R. R. Lahoti Science College Morshi, Dist. Amravati, Maharashtra, India.

[2]Department of Physics , Nehru Mahavidyalaya, Arts, Commerce, Science College, Nerparsopant, Dist. Yavatmal, Maharashtra, India.

ABSTRACT

A solid polymer electrolytes of polyvinyl alcohol with ammonium bromide having different composition have been prepared by solution cast technique. We have measured the DC electrical conductivity of solid polymer electrolyte at different temperature. The dc conductivity was obtained from current-voltage characteristics by using two probe technique in the different temperature range. The addition of salt in the polymer PVA increase the ionic conductivity. XRD analysis reveals the complex formation between the polymer and salt.

Keywords: Polyvinyl alcohol, Ammonium bromide, XRD, DC electrical conductivity.

I. INTRODUCTION

Polymer have been used as a insulating material and very low ionic conductivity. To increase the ionic conductivity depend on the addition of some dopant (ammonium salts) in polymer. [1]. Polyvinyl alcohol was choosen as a polymer host because it has been attractive due to dielectric strength, good charge storage capacity, good film forming ability, and dopant dependant electrical and optical properties. [2-3]Ammonium salts have been a very good proton doner to the polymer matrix system and to increase the conductivity [4-5]. So in present work, to study DC electrical conductivity of solid polymer electrolyte.

II. METHODS AND MATERIAL

Polyvinyl alcohol with molecular weight 125,000 (AR grade Sd fine), ammonium bromide (AR grade merck), and deionized distilled water as a solvent have been used to prepare solid polymer electrolyte by solution cast technique. In this method PVA and ammonium bromide have been dissolved separately in deionized distilled water by mole percent. Then different molar ratio of NH_4Br in PVA and the solution is stirred well using magnetic stirred, untiled homogneous solution was formed. These homogeneous solution was casted in petri dish and evaporated slowly at room temperature. The flim have been formed with uniformed thickness. The variation between current and voltage measured by using Kiteley 6487 picoammeter/voltage source meter instruments at various constant temperature.

III. RESULTS AND DISCUSSION

XRD analysis

Figure 1: XRD spectra of (a) Pure PVA, (b) PVA:NH₄Br(90:10), (c) PVA: NH₄Br(75:25)

The fig1 shows that the X-ray diffraction (XRD) pattern of pure PVA and PVA with 10 and 25 mole % of ammonium bromide added in PVA . The broad peak is observed for pure PVA and has been shifted in the complex. In salt added system has been found to increase in broadness and decrease in intensity [6]. The broadening of the peak due to addition of ammonium bromide is attributed to an increased amorphous of polymer complex electrolyte [7]. Thus the XRD analysis reveals the complex formation between the polymer and salt [8]. The Polyvinyl alcohol dissolves completely.

DC conductivity

I-V Characteristic of solid polymer electrolytes
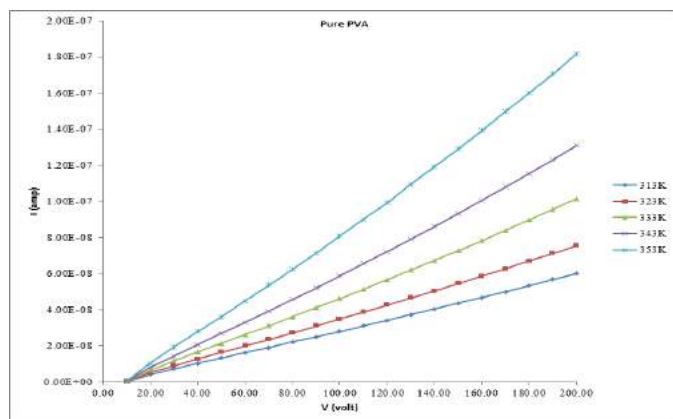
Figure 2: Variation of current (I) with Voltage (V) of Pure PVA
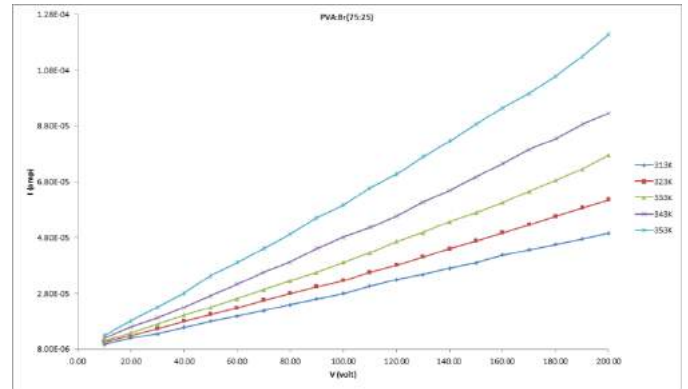
Figure 3: Variation of current (I) with Voltage (V) of PVA with 25 mole % of ammonium bromide (75:25).

Fig. 2 shows the pure PVA and fig. 3 shows PVA with 25 mole % of ammonium bromide I-V relation on five different temperatures 313 K to 353 K. The result shows ohmic behavior. In the ohmic region, the electrical conduction is governed only by the resistance of the polymeric material and controlled by thermally activated carriers. Again, it is observed that the current increases with increasing temperature in ohmic region for all samples. As the temperature increases, the probability of thermal ionization of the trapping centers increases too, hence a shift in the fermi quasi fermi level occurs and this cause the lowering of barrier across which the electrons are transported and conduction becomes ohmic [9-10].

Arrhenius plot
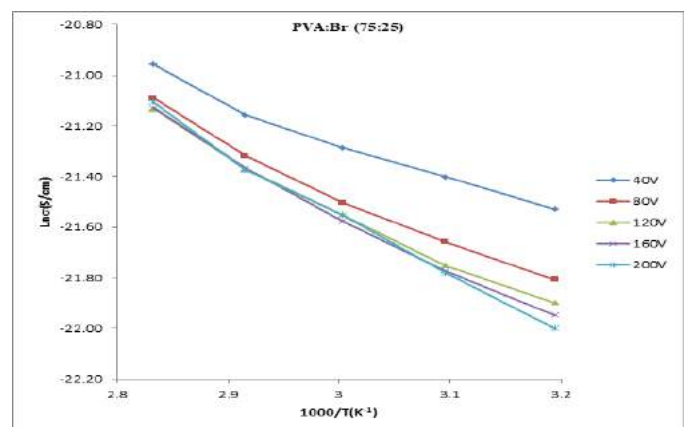
Figure 4: Variation of conductivity ln (σ) with temperature at different voltages (Arrhenius plots) for PVA with 25 mole % of ammonium bromide.

The temperature dependence of DC conductivity ln□ verses 1/T as shown in fig 4. The conductivity solid polymer electrolyte PVA-NH4BR (25mole%) is mostly depend on temperature. The temperature increases conductivity also increases in accordance with Arrhenious equation is given by -

$$\sigma_T = \sigma_0 \exp(-Ea\backslash KT)$$

Where σ_0 is the pre exponential factor, E_a is the activation energy and K is the Boltzmann constant [11-12]. The ionic conductivity is enhanced with increase of temperature and added with mole percent of ammonium bromide which suggest that the free volume around the polymer chain system increases causes the mobility of ions and polymer segments [13]. The segmental motion either allows the ions to hop from one side to another side. Hence ionic motion in polymer electrolyte is due to hopping of ions from one side to another site and the dynamic segmental motion of polymer , and accordingly the conductivity of polymer electrolyte becomes high.

IV. CONCLUSION

A solid polymer electrolyes of pure PVA and PVA with NH4Br at different mole percent shows Ohamic behavior The XRD analysis reveals the complex formation between the polymer PVA and salt ammonium. The temperature dependence ionic conductivity of these composite polymer electrolyte exihibited Arrehenius behavior. The ionic conductivity has been found to be increase depend on the concentration of the ammonium salts.

V. REFERENCES

[1]. Jr. F. Billmeyer, Text book of polymer Science , Eiley Singapore, (1984).

[2]. N. Vassal E. Salmon, J. F. Fauvarque, J. Electrochem Soc 146, 20-26, (1999).

[3]. A. Lawandowski, K. Shorupska, J. Malinska, solid state ionic 133, 265-271, (2000).

[4]. M. Kumar, S. S. Sekhon Eur polymer J 38, (2002) 1297-1304.

[5]. M. Hema, S. Svasekarapandian, A. 403, Sakunthala, D. Arunkumar, H. Nithiya, Physica, (2008), 2740-2747.

[6]. L. H. S. Perling, "Introduction to Physical Polymer Science", John Wiley, Sons, (2001).

[7]. Hasoon Salah Abdulla, Abdullah Ibrahim Abbo., Int. Electrochem. Sci. 7, 10666-10678, (2012).

[8]. J. Luo, A. H. Jensen, N. R. Brooks, J. Sniekers, M. Knipper, D. Ali, Q. Li, B. Vanroy, M. Wubbenhorst, F. Yan, L. Van Meervelt,Z. Shao, J. Fang, Z-H Luo, DE D Vos, K. Binnemans, , J. Fransaer, Energy enviormental Science 8, 1276-1291, (2015).

[9]. J. Luo, O. Conrad,IFJ. Vankelecom,J Matter chem1, 2238-2247, (2013).

[10]. T. Miyamoto, K. Shibayama, J Appl Phys 44, 5372-5376, (1973).

[11]. S. D. Druger, A. Nitzam, M. A. Ratner, J Chem Physics 79, 3133-3142, (1983).

[12]. S. D. Druger, A. Nitzam, M. A. Ratner, Phy Rev B 31, 3939-3947, (1985).

[13]. Lord Raleigh, Phil. Mag. 34, 481 (1892).

Frequency and Temperature Dependence of Ultrasonic Properties of Aqueous PVA solutions Using Pulse-Echo Technique

S. V. Khangar (Wagh)[1], O. P. Chimankar[2], R. Y. Bakale[1], Y.S Tamgadge[1], S. H. Nimkar[2]

[1]Department of Physics, S Mahatma Fule Arts, Commerce & Sitaramji Chaudhari Science Mahavidyalaya Warud, Dist. Amravati, SGBAU, Maharashtra, India

[2]PG department of Physics, RTM Nagpur University, Nagpur, Maharashtra, India

[3]Shivaji Arts, Commerce and Science College, Daryapur Road, Akot, Maharashtra, India

ABSTRACT

Molecular interaction study in polymers provides valuable information regarding internal structure, molecular association, etc. Ultrasonic investigations of polar- polar or polar- non-polar components are important in understanding the intermolecular interaction between component molecules. The ultrasonic pulse echo technique provides an effective and reliable tool to investigate properties of polymer solutions in the light of phase separation studies. The propagation of ultrasonic waves and the measurement of ultrasonic properties in solution form an important tool for the evaluation of various acoustical and thermo- dynamical parameters which give an insight into the nature of miscibility/compatibility and molecular interactions in polymer solution. The phenomenon polymer- solvent miscibility may arises due to any specific molecular interactions such as hydrogen bonding, dipole- dipole interactions and charge transfer complexes for homogeneous polymer- solvent mixture. Miscibility is an important phenomenon in polymer solution to achieve mechanical integrity, better adhesion, better processing and optimum property gain. Recently the use of ultrasonic waves has shown a great potential for characterization of polymer solutions.

In present work, aqueous PVA (Polyvinyl alcohol) are often used due to various useful properties in medical field. However, temperature changes also affect these properties. In this paper we present a method for measuring ultrasonic velocity, density, viscosity and ultrasonic absorption of polymer solutions. We also give experimental values for PVA solutions for temperatures between 288K to 308 and for 2 MHz ultrasound frequency.

Keywords : Ultrasonic, acoustic and optical parameters, PVA-polyvinyl alcohol, molecular interactions, pulse echo technique

I. INTRODUCTION

The propagation of ultrasonic waves and the measurement of their velocity in solution at different concentration (wt.%) and at different temperature form an important tool for the evaluation of various acoustical and thermo- dynamical parameters which give an insight into the nature of molecular interactions such as hydrogen bonding, dipole- dipole interactions and charge transfer complexes for homogeneous polymer- solvent mixture. Polyvinyl

Alcohol having molecular Formula $[C_2H_4O]_n$. For many applications Polyvinyl Alcohol is prepared in water solutions. On evaporation of water, transparent films are formed which have high tensile strength and tear resistance. The binder characteristics of Polyvinyl Alcohol offer excellent adhesion to porous, water-absorbent surfaces. Structural analysis of polymer is a subject of considerable interest in polymer science. It is an environmental friendly and water-soluble synthetic polymer with excellent film forming property, and emulsifying properties and outstanding resistance to oil, grease, and solvents. It has been extensively used in adhesive, in textile warp sizing and finishing, in paper size and coating, in the manufacturing of PVAc emulsion, in the suspension polymerization of PVC, and as binder for ceramics. It is sometimes supplied as beads or as solutions in water[1]. A review of literatur[2-5] reveals that ultrasonic parameters, such as adiabatic compressibility (β_a), relaxation time (τ), acoustic impedance (z), free length (L_f) and optical parameter refractive index have been used to study the molecular interactions in polymer solutions.

In present work, the authors have prepared the polyvinyl alcohol solutions at different concentrations (wt.%) with water solutions and have measured ultrasonic velocity, density and viscosity using ultrasonic pulse echo technique at temperature range 288K- 308K and at 2MHz and optical parameter refractive index (μ) in order to study the structural changes to the solutions, if any. Ultrasonic pulse-echo systems are widely used to estimate properties of liquids. A common principle is to use a buffer material (buffer-rod) fixed to the ultrasound transducer. Assuming the acoustic properties of the buffer-rod are known, it is then possible to calculate the acoustic impedance of the unknown material from reflections between the buffer-rod and the unknown material. From acoustic impedance and speed of sound it is the possible to calculate density and adiabatic compressibility of the material. The nature of polymer and polymer-solvent interactions and effect on molecular interactions have been studied.

II. METHODS AND MATERIAL

polyvinyl alcohol (AR grade) from Otto Chemi was used. Ultrasonic velocity, density, viscosity and refractive index (μ) values are estimated in the aqueous polyvinyl alcohol solutions. The solution was prepared by adding a known weight of polymer (i.e. polyvinyl alcohol) to a fixed volume of distilled water and then stirring until clear solution were obtain. The concentration range chosen in the solution are 0.05, 0.1, 0.15, 0.2, 0.25, & 0.3 wt. %. Velocity measurements are carried out using ultrasonic pulse echo technique by using MHF-400 High frequency pulser- receiver supplied by Roop Telsonic Ultrasonic Limited; Mumbai- (India) at different frequencies of 1 MHz, 2MHz & 5MHz and at temperature range 288K-308K with an accuracy of ±0.1m/sec. Density has been measured by pycnometer method. The viscosity of liquid was measured by Oswald's viscometer. And refractive index is measured by Abbes refractometer. Temperature is maintained at a constant range by Plasto Crafts (LBT-10) Thermostat and other related parameters calculated by standard formulae10.

III. RESULTS AND DISCUSSION

The variations of ultrasonic velocity (u), density (ρ), viscosity (η), refractive index (μ) and the related parameters such as adiabatic compressibility (β_a), acoustic impedance (z), relaxation time (τ), free length (L_f), volume expansivity(α) and Molwen Moelwyn-Hughes(C_1) of the various concentrations (wt.%) at temperature range 288K-308K and at 2MH frequency for aqueous PVA are given below:

Figure1. represents the variations of ultrasonic velocity with concentration (wt%). From the graph It is observed that ultrasonic velocity increases with increase in concentration (wt. %) of polyvinyl alcohol

in water indicating association in the component molecules. The increment in velocity with concentration implies a decrement in the compressibility. This behavior suggests the formation of a more rigid structure, possible due to polymer-water hydrogen bonding at sites on the polymer's hydroxyl (OH) group[3]. Ultrasonic velocity increases with increase in temperature. At higher temperature ultrasonic velocity is high and at lower temperature ultrasonic velocity is low indicates the strong association between solute and solvent. Oxygen atom (O) in polyvinyl alcohol can form hydrogen bond with hydrogen of hydroxyl molecules through hydrogen bonding.

Figure 2. shows variation of density with concentration (wt.%). From graph It is observed that density increases with increase in concentration of polyvinyl alcohol in water, increase in density decreases the volume indicating association in component molecules.
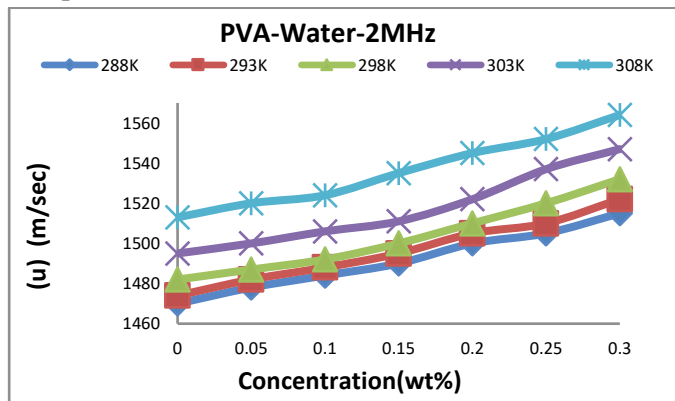
Fig.1
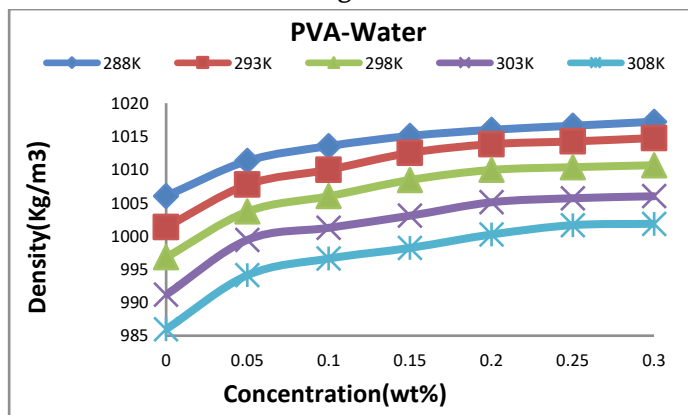
Fig.2

Increasing the temperature of the substance decreases its density (ρ) and viscosity (η). Decrease in density (ρ) and viscosity (η) with increase in temperature indicated decrease in cohesive forces. The increasing temperature has two opposite effects namely increase of molecular interactions (structure formation) and destruction of structure formed previously as a result of thermal fluctuation. Thus, increase of temperature favors increase of kinetic energy and volume expansion and hence decrease of density (ρ) and viscosity (η), while it increases intermolecular distance (free length).
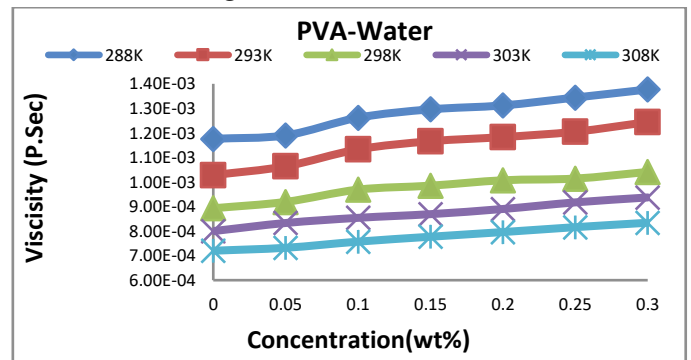
Fig.3
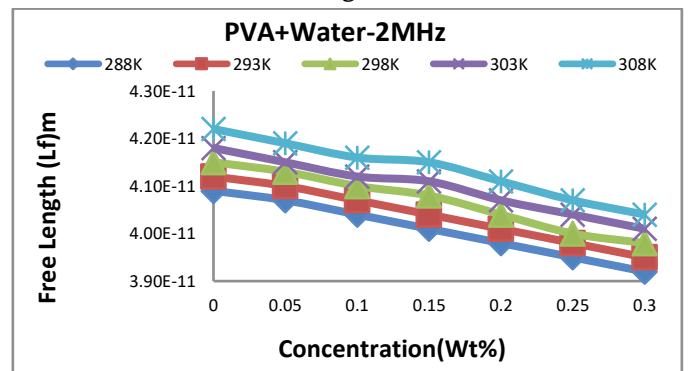
Fig. 4

Figure 3 and 4 shows the plot of viscosity (η) and free length versus concentration (wt. %) in aqueous PVA solutions. It is observed that viscosity slightly increases with increase in concentration (wt. %) of polyvinyl alcohol in water while free length decreases. Measurement of viscosity in binary mixture yields some reliable information in the study of molecular interaction. The viscosity gives the strength of molecular interaction between interacting

molecules. The dipole-dipole interactions of permanent dipoles in constituent molecules increase the viscosity in the polyvinyl alcohol + water system7.

PVA-Water-2MHz

Fig.5

PVA+Water-2MHz
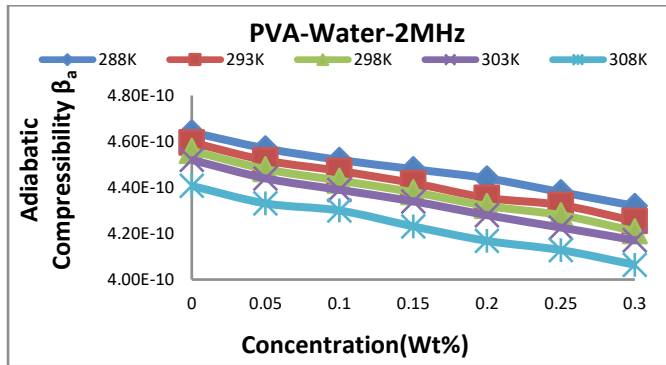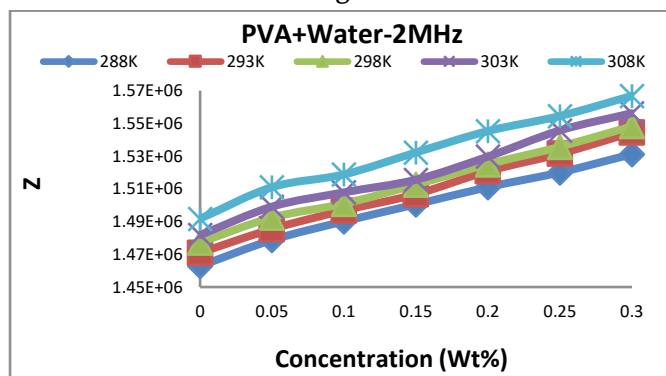
Fig.6

From figure 5, It is also observed that adiabatic compressibility decreases with increase in concentration (wt. %) of polyvinyl alcohol in water indicating strong intermolecular interaction in the component molecules in this system shows associating tendency of the component molecules. The observed decrease of adiabatic compressibility with concentration indicates the enhancement of degree of association in the component molecules. Hence the intermolecular distance decreases with increase in concentration. It is primarily the compressibility that changes with structure which leads to change in ultrasonic velocity8.

From figure 6, It is observed that, the values of acoustic impedance increase with increase in concentration. It is in good agreement with the theoretical requirements because ultrasonic velocity increases with increase in concentration. The increase in acoustic impedance (Z) with concentration can be explained on the basis of intermolecular interaction between component molecules, which decreases the intermolecular distance, making relative fewer gaps between the component molecules9.

From fig. 7, it is observed that relaxation time increases slightly with increase in concentration of polyvinyl alcohol in water indicating high stability of polyvinyl alcohol molecules. Polyvinyl alcohol is a polymer having compact structure and hence molecules are not stable which increases the relaxation time. The relaxation can be caused by the energy transfer between translational and vibrational degrees of freedom and all these degrees take part in the observed process9. Its behavior depends on viscosity and adiabatic compressibility of the liquid solution. In this system viscosity plays very important role for increasing relaxation time with increase in concentration (wt.%).

PVA+Water-2MHz

Fig.7

PVA+Water
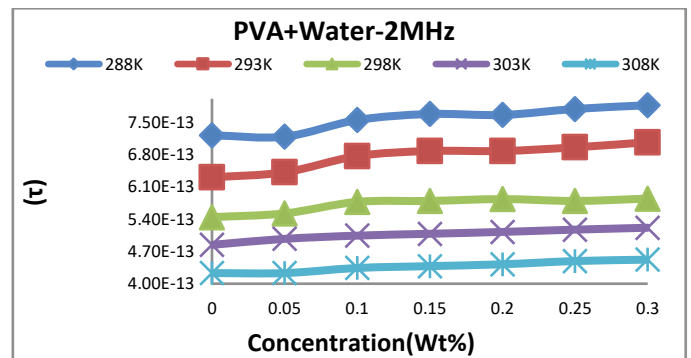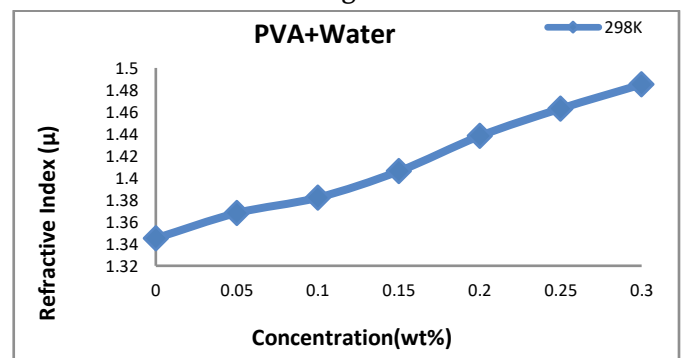
Fig.8

Figure 8 shows the variation of refractive index with concentration in aqueous PVA respectively. Refractive index (μ) increases with increase in concentration of polyacrylamide in water. It may be

due to possible specific interactions like hydrogen bonding to some extent between the hydroxyl group of water. Hence the present study indicates the existence of miscibility windows only.

IV. CONCLUSION

1. The linear nature of ultrasonic velocity suggests miscibility of polymers indicated by single phase formation and thus suggesting compatibility of the polymers.

2. Ultrasonic velocity, density, viscosity, adiabatic compressibility, acoustic impedance, relaxation time, free length, etc. indicates the strength of molecular interactions in the binary liquid mixtures of polymer.

3. Decrease in adiabatic compressibility and free length with increase in concentration (Wt. %) is due to strong association.

V. REFERENCES

[1]. Chimankar O P etal, J. Pure Appl. Ultrason.32, 18 (2010).

[2]. S.Ravichandran and K. Ramanathan,; Polymer-Plastics Technology and Engineering, 47: 169-173, 2008

[3]. Ramanathan, K.; Ravichandran, S. Ultrasonic study of mixed salt solutions of ammonium and ammonium chloride solution. Ind. J. Pure App. Ultrason. 2004, 26, 12.

[4]. Sugandha V. Khangar and Omprakash P. Chimankar; "Study of Miscibility of aqueous polyacrylamide (PAA) solution" ;International J. of Engineering and innovative technology (IJEIT); Volume 3, Issue 11, May 2014; pp. 148-150, ISSN: 2277-3754

[5]. Khangar S. V. and Chimankar O.P.; "Ultrasonic Investigation of Dipole- Induced dipole interactions in binary solution of cellulose acetate with cyclohexanone and carbon tetrachloride (CCl4) "; International J. of Advanced Information Science and Technology (IJAIST); Vol. 25, No. 25, May 2014; pp. 102-108, ISSN: 2319-2682

[6]. Schmelzer, C.E.H.; Zwirbla, W.; Rosenfeld, E.; Linde , B.B.J. Acoustic investigations of pseudo stable structures in aqueous solutions of polyethylene glycols. J. Mol Struc. 2004, 699, 47.

[7]. Sugandha V. Khangar and Omprakash P. Chimankar; "Ultrasonic Characterization of aqueous Polyvinyl Pyrrolidone (PVP)"; International journal of physical sciences; pp. 1351-1357, ISSN: 2348-0130 ; 4(10) 2014

[8]. Sugandha V. Khangar and Omprakash P. Chimankar,Ranjeeta S Shriwas and Sushma Patil; "Ultrasonic investigation of dipole- dipole interaction in binary solution of Cellulose acetate + water"; International journal of Science and Research (IJSR); pp. 331-334 ISSN (online): 2319-7064, 2015.

[9]. Falguni D. Karia; Parsania, P.H. Ultrasonic velocity studies and allied parameters of poly (4-4'- cyclohexylidene- R-R'-diphenylene diphenylmethane-4-4' disulfonate) solutions at 30'.Eur. Polym. J. 2000, 36, 519

[10]. S.U.Patil, O. P. Chimankar , S. V. Khangar and M.S. Deshpande; "Ultrasonic and spectroscopic investigation of Polychloroprene and Poly Methyl Methacrylate blends"; Acoustical society of America; vol. 38, issue 4; ISSN: 0001-4966, 2020

Copper-Silver Bimetallic Nanoparticles Synthesized by Electrochemical Reduction Method

Sunita Jadhav*, Nita Dongare

Department of Chemistry, Hutatma Rajguru Mahavidyalaya, Rajgurunagar 410505, Maharashtra, India

ABSTRACT

Copper-Silver bimetallic nanoparticles were synthesized by electrochemical reduction method which is environmental benign. The tetra butyl ammonium bromide (TBAB) used as stabilizing agent in an organic medium *viz.* tetra hydro furan (THF) and acetonitrile (ACN) in 4:1 ratio by optimizing current density. The parameters such as current density, solvent polarity, distance between electrodes, and concentration of stabilizers are used to control the size of nanoparticles. The synthesized copper-silver bimetallic nanoparticles were characterized by using UV-Visible, FT-IR, XRD, SEM-EDS and TEM analysis techniques.

Keywords : Electrochemical cell, Tetra butyl ammonium bromide, Copper-Silver bimetallic nanoparticles, SEM, TEM and XRD.

I. INTRODUCTION

Bimetallic nanoparticles exhibit interesting electronic, optical, biologicaland chemical properties due to new bifunctional or synergistic effects [1-11]. As the demand increasesfor the materials with antimicrobial properties, new methods of obtaining metal nanoparticles are constantly increasing [12]. Silver and copper nanoparticles are used as additives to enhance the biocidal activity of medical materials, textiles, paints and varnishes, plastics and other materials [13]. A combination of the antibacterial properties of silver and the antifungal properties of copper allows the generation of a material with a wide spectrum of action against microorganisms [14,15].Silver nanoparticles are the most broadly described nanomaterials [16,17], which are highly effective against bacteria and can be found in many commercial products [18]. Nanosilverdespite the many advantages such as the low concentrations that

are sufficient to limit bacterial proliferation, a wide range of activities and simple methods to produce stable suspensions, materials are also sought that would work well as a biocide whilst limiting the negative effects of nanosilver [19,20]. Examples of particles with similar effects to Ag are copper nanoparticles (Cu), which also have a high antimicrobial activity, especially antifungal [21]. In addition, Cu is more affordable and more accessible than Ag [22]. The main advantage of using Cu is the obtaining a stable suspension with a concentration of nanoparticles that ensures sufficient biocidal activity. The process of obtaining Cu is time-consuming, and the nanoparticles themselves usually have a larger size compared to Ag, which may decrease the biocidal activity of Cu [23]. In this report, we describe the synthesis and characterization of Cu-Ag bimetallic nanoparticles with tetra butyl ammonium bromide as stabilizing agent.

II. METHODS AND MATERIAL

Experimental:

Copper-silver bimetallic nanoparticles were synthesized by electrochemical reduction method. In the initial experiment we have used electrolysis cell to carry out electrolysis process. In this cell, two anodes (Cu and Ag) were positioned in such a way that they lie parallel to each other and apart from each other by a distance of 1x1 cm. The inert cathode, platinum foil was placed between the two anodes and it was perpendicular to both of them. In typical procedure, the above electrolysis vessel having anode (Cu-Ag) 1 x 1cm and a platinum cathode (1 x 1cm) were employed in the preparation of Cu-Ag bimetallic nanoclusters. A mixture of acetonitrile and tetrahydrofuran (4:1) was used as solvent. The supporting electrolyte consisted of solution of ligand, tetra butyl ammonium bromide TBAB at 0.01M. The supporting electrolyte used also act as stabilizer in the formation of bimetallic nanoclusters. Electrolysis was carried out at room temperature by passing the current of various current densities 10 mA/cm^2 for two hours. The colour changes were observed and noted during the electrolysis process. After two hours of electrolysis process the concentration of the nanoparticles increased sufficiently leading to their agglomeration process. After the electrolysis time, the solid particles of the nanoparticles settled at the bottom of the vessel. The reaction mixture was transferred into the clean and dry bottle along with solid particles and then after 15 to 20 minutes decantation process was followed for separation. The solid as well as the supernatant were collected separately. The solid sample was washed 2 to 3 times with THF to remove the excess ligand. The samples were then dried in vacuum desiccator and further stored in airtight capsules for characterization.

Characterization:

The prepared copper-silver bimetallic nanoparticles were characterized by UV-Visible spectrophotometer, FT-IR spectrophotometer, XRD, TEM, SEM-EDS

techniques. The UV-visible spectra were recorded on UV-Visible spectrophotometer [JASCO 503] using a quartz cuvette with ACN / THF (4:1) as reference solvent. The IR spectra were recorded on FT-IR spectrophotometer [JASCO, FT-IR/4100] Japan using dry KBr as standard reference in the range of 600 – 4000 cm-1. The X-ray powder diffraction patterns of the copper oxide nanoparticles were recorded on Bruker 8D advance X-ray diffractometer using CuKα radiation of wavelength = 1.54056 Å. To study the morphology and elemental composition copper (II) oxide nanoparticles were examined using SEM and energy dispersive spectrophotometer (EDS). The SEM analysis was carried out with JEOL; JSM-LA operated at 20.0 kV and 1.0000 nA. Shape, size and morphology ware calculated by TEM analysis was using Philips model CM200 operated at 200 kV.

III. RESULTS AND DISCUSSION

Figure 1 shows the UV-visible spectra of Cu-Ag bimetallic nanoparticles. The surface plasmon resonance is the most remarkable optical property of metal colloids and nanoparticles. The alloy formation is confirmed by the optical absorption spectra that shows two surface plasmon peaks and the position of the λ_{max} depends upon the composition.
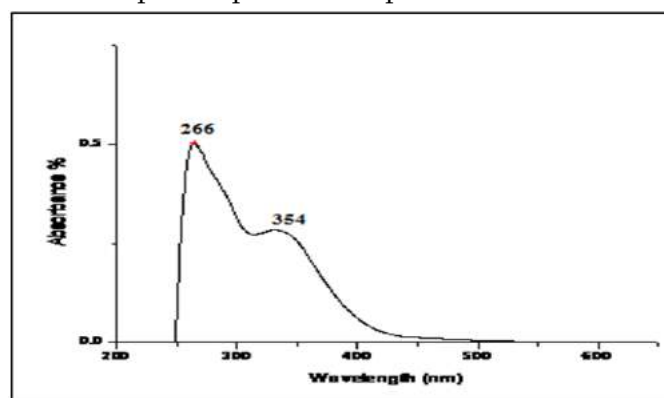
Figure 1. UV-visible spectrum of Cu-Ag nanoparticles capped with TBAB

The analysis of the prepared sample of Cu-Ag bimetallic nanoparticles reveals the chemical properties of nanoparticles. On the basis of the FTIR

spectra we have obtained the results for the surface chemistry of the nanoparticles. The frequencies for the different functional groups have been reported [24-26]. The position and the presence of these functional groups can be detected by the FTIR technique. The Fig. 2 shows the IR spectrum of the as prepared sample of Cu-Ag bimetallic nanoparticles capped with TBAB. Peak at $3736cm^{-1}$ corresponds to the O-H stretching band. This arises due to the absorption of water molecules by the sample during storage. The broad peak at $3036cm^{-1}$ and a narrow peak at $2879cm^{-1}$ correspond to the C-H stretching vibrations. The peak at $1784cm^{-1}$ corresponds to the CO_2 which is absorbed by the sample. The peak at $1684cm^{-1}$ is related to the symmetrical ammonium ion (N^+R_4). The frequency at $1491cm^{-1}$, $1442cm^{-1}$ and $1354cm^{-1}$ corresponds to the C-H bending vibrations. The C-N linkage in the N^+R_4 gives a medium band at $1236cm^{-1}$ and $1134cm^{-1}$, which are due to the stretching vibrations. The peak at $833cm^{-1}$ and $690cm^{-1}$ corresponds to the CH_2 rocking. These results indicate that the capping agent TEAB has been adsorbed on the surface of the Cu-Ag bimetallic nanoparticles. The spectrum also contains bands at $401cm^{-1}$, $453cm^{-1}$ and $540cm^{-1}$ are due to the silver nanoparticles.
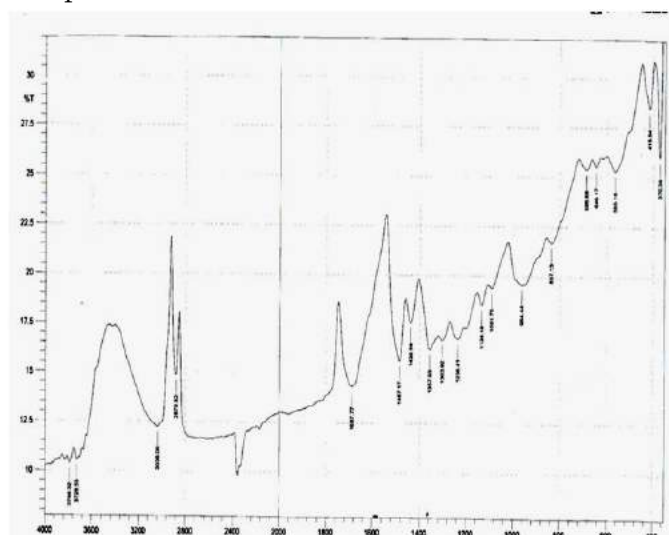
Figure 2 FTIR spectrum of Cu-Ag bimetallic nanoparticles.

The X-ray diffraction pattern of the Cu-Ag bimetallic nanoparticles synthesized with TBAB capping agent at $10mA/cm^{-2}$ is shown in Fig.3 which indicates the crystalline nature of particles. The peaks at 2θ values of corresponding plane (010), (011), (111), (201), (211), (003), (021) and (312) show the monoclinic structure of copper oxide nanoparticles (ASTM No. 7421).

The peaks at planes (110), (200), (220), (221), (310), (311) and (222) indicate the cubic structure of silver oxide nanoparticles. The data is matched with ASTM card no. 04-0783. The peak at 76.878° is the strongest peak of copper is overlapped with the peak of silver can be assigned (311) plane of the cubic structure of Ag. The mean size of Cu-Ag nanoparticles obtained from the half width of the (011) different peak using the Scherrer equation is about 8.56nm which accords with the results of TEM image for the particle sizes.
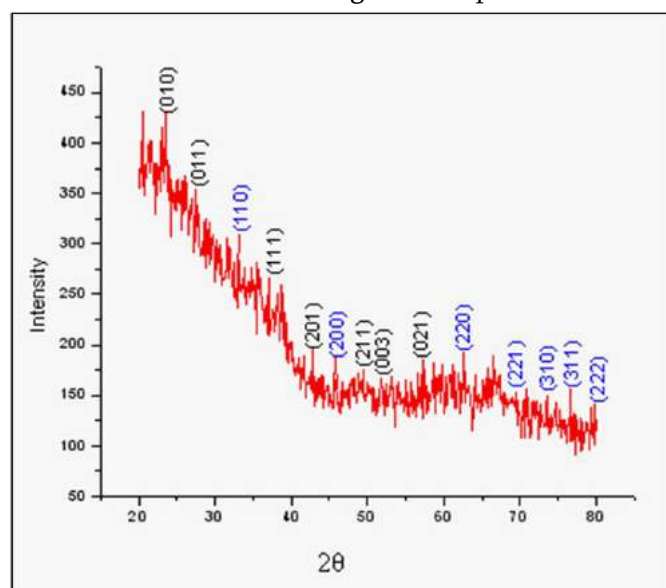
Figure 3 XRD Spctra of Cu-Ag bimetallic nanoparticles

Table 5.A.5.1. XRD analysis data for Cu-Ag bimetallic nanoparticles

h	k	l	2θ(°) (Exp)	2θ(°) (Cal)	d(A°) (Exp)	d(A°) (Cal)	Intensity (Exp)
0	1	0	26.688	26.111	3.33753	3.41000	139.39
0	1	1	31.162	31.520	2.86781	2.83609	141.69
1	1	1	37.839	37.094	2.37571	2.42170	846.83
2	0	1	43.016	42.670	2.10103	2.11724	44.30
2	1	1	51.486	50.713	1.77352	1.79873	178.60
0	0	3	54.402	53.797	1.68513	1.70267	65.82
0	2	1	57.173	56.887	1.60986	1.61728	43.27
3	1	2	76.878	77.133	1.23906	1.23560	37.40
1	1	0	30.924	30.925	2.88936	2.88924	808.36
2	0	0	44.324	44.301	2.04201	2.04300	746.46
2	2	0	64.497	64.447	1.44360	1.44462	253.03
2	2	1	69.701	68.883	1.34800	1.36200	71.00
3	1	0	73.239	73.190	1.29137	1.29211	166.33
3	1	1	77.496	77.402	1.23071	1.23197	188.02

The shape and size distribution of nanostructures were characterized by scanning electron microscopy. Fig.4 A and Fig.4. B illustrates typical morphologies of Cu-Ag bimetallic nanoparticles synthesized with TBAB capping agent with 10mA current density.The result shows they contains many tiny amorphous particles which show the polycrystalline sheet like morphology of Cu-Ag bimetallic nanoparticles. The Fig.4 A shows the microgram at a resolution of 0.5 μm wherein it is seen that the nanoparticles are in clumps and the structure is discontinuous in nature. The resolution at 1.0 μm, in Fig.4 B shows a morphology of the nanoparticles that resembles like agglomerated particles with irregular shape.
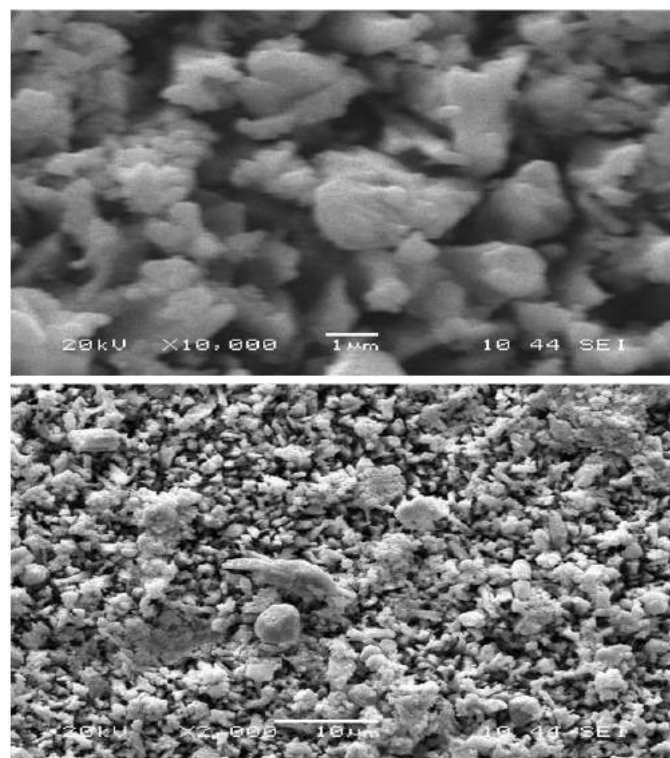
Figure 4 A and 4 B Scanning Electron Microscopic images.

The EDS spectrum of sample (Fig. 5) prepared by using TBAB as capping agent at 10mA current density shows peaks corresponding to Cu, Ag, O and Br. The analysis of spectra gives wt% and atom% of each element present in sample. The content of elements according to their wt% and atom% is shown in Table 5. In this the wt% and atom% of copper and silver clearly shows the formation of Cu-Ag bimetallic nanoparticles.
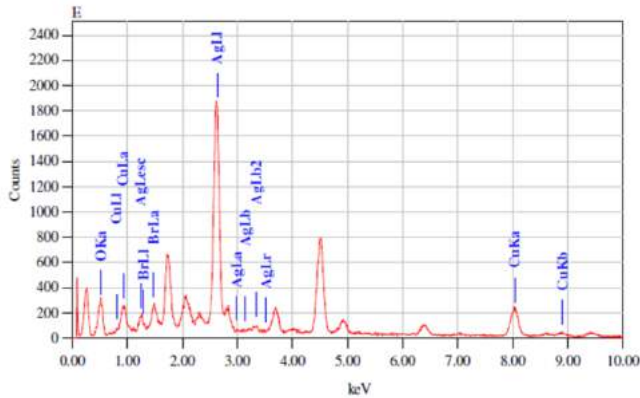
Table 5. EDS analysis of Cu-Ag nanoparticles

Constituents	Mass (%)	Atom (%)
Cu	80.52	69.15
Ag	15.78	13.19
O	7.38	24.45
Br	0.32	0.21

The physical properties of the nanosized materials depend upon the size, morphology and aggregation of the particles. These details can be better understood by a commonly used technique, Transmission Electron Microscopy (TEM). The metal nanoparticles especially those consisting of noble (precious) metal elements, give high contras [27] when the particles are placed on a thin carbon films supported by metal grids. For large crystalline metal nanoparticles, HRTEM can suggest the area composition by the fringe measurement, giving crystal information of the nanoparticles observed in the particle image [28-30].

In order to characterize the nanoparticles using TEM, a solution containing the prepared Cu-Ag nanoparticles in ethanol was sonicated for 15 minutes. A single micro drop of this solution was allowed to dry on a carbon coated copper grid for TEM imaging.

The nanoparticles exhibit nearly spherical shape and most of them aggregate together even under ultrasonic vibration for a long time. The average size of these nanoparticles is about 1-45nm, almost in accordance with that from SEM and XRD observations.

Fig.6 shows the Cu-Ag bimetallic nanoparticles, these are variable in size and spherical in shape.
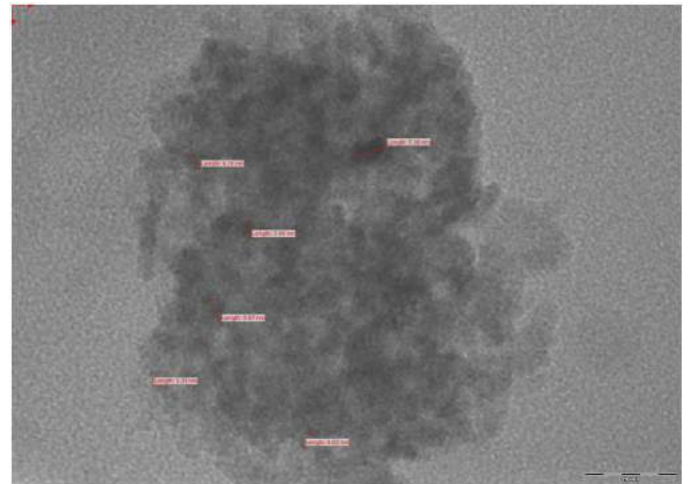
Figure 6 TEM of Cu-Ag bimetallic nanoparticles capped with 0.01M TEAB at current density 10 mA/cm²

IV. CONCLUSION

In summary, we have demonstrated the efficiency of electrochemical reduction method for the synthesis of Cu- Ag bimetallic nanoparticles. The TBAB salts used as ligands have played a significant role on controlling the particle size. The procedure offers several advantages including control the particles size, excellent yields, operational simplicity and minimum environmental effects. The copper silver bimetallic nanoparticles had average size in the range of 5 – 30 nm.Thus, the synthesis of Cu-Ag Bimetallic nanoparticles by electrochemical reduction method is easiest, cheapest, require less time and high purity of nanoparticles are obtained.

V. REFERENCES

[1]. Daniel, M. C.; Astruc, D. Chem. Rev. 2004, 104, 293.

[2]. Zhong, C. J.; et.al.In Nanotechnology in Catalysis; B. Zhou, S., Hermans, G. A., Somorjai, K., Eds.; Academic/Plenum Publishers: New York, 2004, 1, 222.

[3]. (a Hostetler, M. J.; Zhong, C. J.; Yen, B. K. H.; Anderegg, J.; Gross, S. M.; Evans, N. D.; Porter, M.; Murray, R. W. J. Am. Chem. Soc. 1998, 120, 9396. (b Mallin, M. P.; Murphy, C. J. Nano Lett. 2002, 2, 1235,

[4]. Srnova-Sloufova, I.; Vlckova, B.; Bastl, Z.; Hasslett, T. L.Langmuir 2004, 20, 3407.

[5]. Schmid, G.; West, H.; Mehles, H.; Lehnert, A. Inorg. Chem. 1997, 36, 891.

[6]. Shi, H. Z.; Zhang, L. D.; Cai, W. P. J. Appl. Phys. 2000, 87, 1572.

[7]. Shibata, T.; Bunker, B. A.; Zhang, Z.; Meisel, D.; Vardeman, C. F.; Gezelter, J. D. J. Am. Chem. Soc. 2002, 124, 11989.

[8]. Moskovits, M.; Srnova-Sloufova, I.; Vlckova, B. J. Chem. Phys. 2002, 116, 10435.

[9]. Zhong, C. J.; Maye, M. M. Adv. Mater. 2001, 13, 1507.

[10]. Bradley, J. S. In Clusters and Colloids; Schmid, G., Ed.; WileyVCH: Weinheim 1994; Chapter 6.

[11]. (a Davis, R. J.; Boudart, M. J. Phys. Chem. 1994, 98, 5471. (b Via, G. H.; Drake, K. F., Jr.; Meitzner, G.; Lytle, F. W.; Sinfelt, J. H. Catal. Lett. 1990, 5, 234.

[12]. V.K. Sharma, C.M. Sayes, B. Guo, S. Pillai, J.G. Parsons, C. Wang, B. Yan, X. Ma, Interactions between silver nanoparticles and other metal nanoparticles under environmentally relevant conditions: A review, Sci. Total Environ. 2019, 653, 1042.

[13]. W.J. Stark, P.R. Stoessel, W. Wohlleben, A. Hafner, Industrial applications of nanoparticles, Chem. Soc. Rev.2015, 44, 5793.

[14]. A. Kalińska, S. Jaworski, M. Wierzbicki, M. Gołębiewski, Int. J. Mol. Sci. 2019, 20, 1672.

[15]. T.A.J. Souza, L.P. Franchi, L.R. Rosa, M.A.M.S. da Veiga, C.S. Takahashi, Mutat. Res. - Genet. Toxicol. Environ. Mutagen. 2016, 795, 70.

[16]. M. Rai, A.P. Ingle, S. Birla, A. Yadav, C.A. Dos Santos, Crit. Rev. Microbiol. 2015, 42, 696.

[17]. J. Peszke, M. Dulski, A. Nowak, K. Balin, M. Zubko, S. Sułowicz, B. Nowak, Z. Piotrowska-Seget, E. Talik, M. Wojtyniak, A. Mrozek-Wilczkiewicz, K. Malarz, J. Szade, RSC Adv. 2017, 7, 28092.

[18]. A.K. Biswal, P.K. Misra, Mater. Chem. Phys. 2020, 250, 123014.

[19]. X.-F. Zhang, Z.-G. Liu, W. Shen, S. Gurunathan, Int. J. Mol. Sci. 2016, 17, 1534.

[20]. S. Ahmed, M. Ahmad, B.L. Swami, S. Ikram, J. Adv. Res. 2016, 7, 17.

[21]. A.K. Chatterjee, R. Chakraborty, T. Basu, Nanotechnology. 2014, 25, 135101.

[22]. M.A. Asghar, E. Zahir, S.M. Shahid, M.N. Khan, M.A. Asghar, J. Iqbal, G. Walker, LWT. 2018, 90, 98.

[23]. K.S. Tan, K.Y. Cheong,J. Nanoparticle Res. 2013, 15.

[24]. Sherman, C. P. Infrared Spectroscopy in, Handbook of Instrumental Techniques for Analytical Chemistry, F. Settle (Ed.), Prentice Hall Inc., New Jersey.

[25]. Nakamoto, K. Infrared Spectra of Inorganic and Coordination Compounds. John Wilet and Sons, 1963.

[26]. Pavia, D. L.; Lapman, G. M.; Kriz, G. S. Introduction to Spectroscopy, III Edn., Brooks / Cole Cengage Learning, Singapore, 2008.

[27]. Toshima, N.; Yonezawa, T. New J. Chem. 1998, 1179.

[28]. Schmid, G.; Morun, B.; Malm, J. O. Angew Chem. Int. Ed. Engl, 1998, 28, 778.

[29]. Duff, D. G.; Curtis, A. C.; Edwards, P. P.; Jefferson, D.A.; Logen, D. E. J. Chem. Soc. Chem. Commun. 1987, 1264.

[30]. Curtis, A. C.; Edwards, P. P.; Duff, D. G.; Jefferson, D. A.; Johnson, B. F. G.; Kirkland, A. I. J. Phys. Chem.1988, 92, 2270.

Electron Temperature as Well as Radial Profile of Spectral Emission Also Change Due to Formation of a Laser Pulse

A. P. Pachkawade[1], V. K. Jadhao[2]

[1]Rajarshee Shahu Science College, Chandur Railway, Maharashtra, India

[2]B.B. Art's, N.B. Commerence and B. P. Science College, Digras, Maharashtra, India

ABSTRACT

The radial profile go on changing the shape as a function of time. During the formation of a laser pulse the electron temperature dose not remain same consequently the radial profile of spectral emission also change. In some cases when the electron temperature is relatively low, the radial profiles are almost Gaussian at all the times, however the peak height goes on changing. We compute the temporal profiles of the spectral emission of the discharge for the initial electron temperature It is found that the diameter of the ring of the radiation is determined by the initial electron temperature at the axis. If the electron temperature is increased the diameter of the ring increases.

Keywords : dc glow discharge, radial and temporal profile, electron temperature.

I. INTRODUCTION

The CVL (Copper Vapour Laser) is well recognized source of light delivering pulsed laser beam at 5106 and5782A at the pulse repetition frequency more than 5KHz with power levels up to about 100 watts or more.The CVL has been successfully applied in the fields like medicine (Ainsworth and Piper 1989[1]), isotope separation, under water ranging, high speed photography, micromatching[2-3,4,], drilling and cutting[2,3] etc. The high power, high energy and high precision CVL are needed by the research workers in different fields of applications. The design calculations of the high power and high precision lasers need the detail information about the parameters like electron temperature, electron density, ion density, fractional abundances, electron impact excitation etc. The spatial and temporal profiles of these parameters, also must be known in

order to design efficient and sophisticated laser systems. The technique of volumetric scaling of the laser output power also needs the detailed study of the spatial profiles of the parameters in the laser discharge. Furthermore, the investigations of the spatial distribution of the density and spectral emission (Kushner and Warner 1983[6], Carman et al. 1994[7],) in the discharge gives large amount of information about various mechanisms taking place in the discharge. With the help of the knowledge of the radial profiles the total output power calculation also may be carried out and the power distribution across the laser output beam also may be obtained. The use of the efficient data acquisation system for monitoring the discharge parameters may give the desired data for the analysis of several processes taking place in the discharge. This is because of the fact that in case of temporal and radial profiles the fundamental

parameters like discharge current, the discharge voltage, the electron temperature, electron density, ion density varies from zero through their maximum values. In design of amplifier oscillator onfiguration system the detailed knowledge of the spatial distribution of the densities is very much important because different parts in the discharge tube have different densities and inversion times. Therefore, the study of the spatial and temporal profiles of the parameters is very much essential. In the present work we calculate fractional abundances of CuI (copper atoms), CuII (singly ionized copper atoms), CuIII (doubly ionized copper atoms) and CuIV (triply ionized copper atoms) as a function of electron temperature. The electron impact excitation rate coefficients are also obtained as a function of electron temperature from zero through 10ev. The radial profiles of the densities of the electronic states 2P3/2 and 2D5/2 of CuI are obtained as a function of electron temperature at the axis of the discharge tube. The radial profiles of the spectral emission of the discharge are also obtained.The temporal and spatial distribution of the laser output power are studied in details. The present results are compared with the experimental results of the research worker in the field. When the discharge pulse is fired the electron temperature is maximum as the electric field is maximum. Afterwards the time passes the electron temperature go on decreasing. The temporal profiles of electron temperature is assumed to be exponentially after firing the discharge pulse decreasing and power distribution along and across the laser beam are obtained[8,9].

II. METHODS AND MATERIAL

Radial profile of the spectral emission:

Under the steady state condition rate of decay of density of atomic level is equal to the rate of electron impact excitation of the level and therefore, if the laser plasma is considered to be in the steady state, the radiation emitted by a volume element because of a transition starting from a level is proportional to the factor Ncu Ne R where Ncu is the density of copper atoms, Ne is the density of the electrons and R is the electron impact excitation rate coefficient of the upper level of the transition. If the radial profiles of electron density, neutral copper density and the excitation rate is known, the radial profiles of the spectral emission may be obtained. While building up of the discharge current pulse, the rate of excitation and ionization would be more than the rate of decay and recombination consequently the densities of highly ionized species go on increasing. While cooling of the discharge electrons the rate of decay and recombination would be more than the rate of excitation and ionization consequently the densities of less ionized species go on increasing. The computation of the factor Ncu Ne Ru for different values of the radial distance would give the radial profiles of spectral emission.

Variation of output power along and across the laser beam:

If the pulse forming network is having low impedance the rise time of the pumping pulse may be of the order of few nsec. When the discharge pulse is fired the plasma electrons get heated suddenly to a high value within about 5-10 nsec because of the process of acceleration of electrons by the electric field generated by pump pulse. As time passes the plasma electrons undergo collisions with other particles and discharge tube wall and consequently start getting cooled. We have studied the temporal behavior of the spectral emission of the discharge pulse from the knowledge of radial profiles of spectral emission[10]. And decay time is assumed to be of the order of 120 nsec. In most of the CVL systems the temporal behaviour of the electron temperature is assumed to be given by the expression.

$$T0 = Tinio \exp(-t/\tau) \quad \text{------(1)}$$

Where Tinio is the initial electron temperature at the axis i.e. the electron temperature when the discharge

pulse is fired and the plasma gets heated to maximum temperature. T0 is the temperature at the axis of the discharge tube at the time t. The temperature T0 at the axis at any time t may be obtained using equation (1).

III. RESULTS AND DISCUSSION

We compute the temporal profiles of the spectral emission of the discharge for the initial electron temperature Tinto = 2, 4, 6, 8, and 10 eV and the results are displayed in the figures. 1, 2, 3, 4 and 5 respectively. For the low initial electron temperature (2eV) the radial profile of the spectral emission is almost Gaussian in shape and remains Gaussian during the building up of complete output pulse. Initially the peak intensity is low, then it increase reaches its maximum value and then go on decreasing. When the electron temperature at the axis is 4eV theradial and temporal profiles change their shapes. In the leading portion of the beam the profile shows dip at the axis and two side peaks. In the lagging portion of the pulse the radial profiles are flat. The dip at the axis is exhibited for about 25 nsec after the laser pulse starts building up after firing of the pumping pulse.
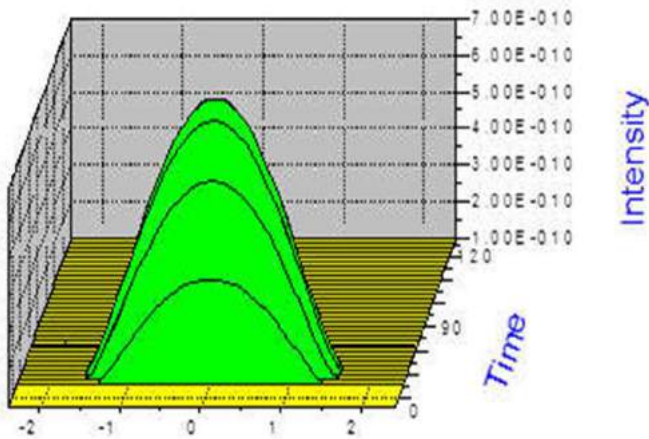
Figure 1. Temporal and Spatial distribution of laser output power for initial electron temperature Tin=2eV
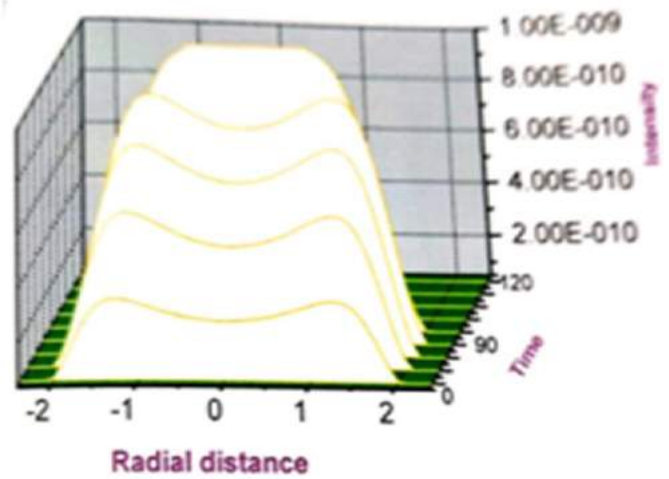
Figure 2. Temporal and Spatial distribution of laser output power for initial electron temperature Tin=4eV

The computation of radial and temporal profiles at 6eV exhibits entirely different shape. The leading part of the beam becomes completely annular. The beam coming after about 15 nsec shows the dip at the axis. At later times the radial profile go on changing the shape and the dip in the profile go on becoming shallower. It is noticeable that at all the times during the emission of output pulse the radial profiles exhibit the dip at the axis when the initial temperature at the axis is 6eV. The dip go on decreasing from leading part to the lagging part. For the initial electron temperature of 8eV the beam remains annular for considerably longer time duration and the radial profiles exhibit dip at the axis and the dip
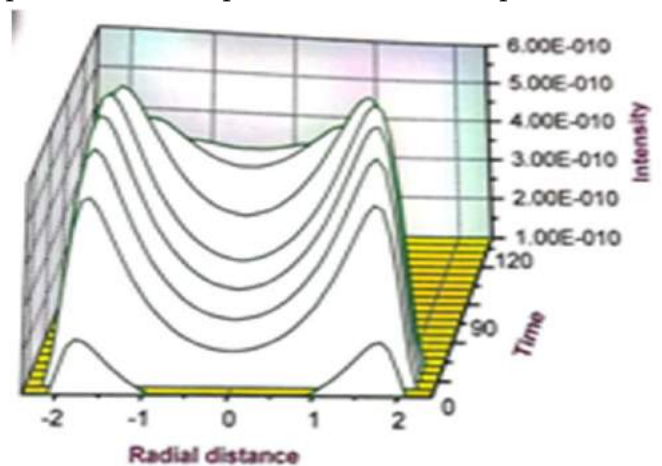
Figure 3. Temporal and Spatial distribution of laser output power for initial electron temperature Tin=6eV
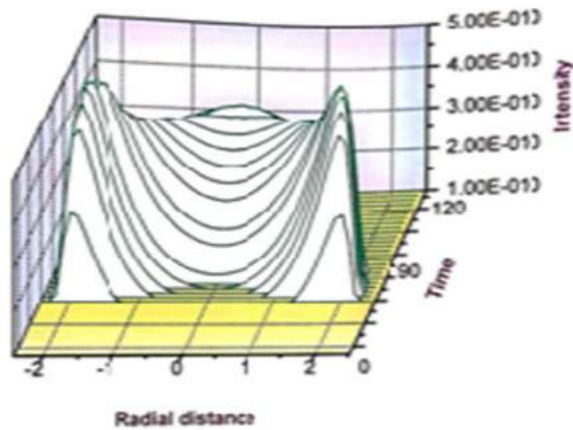
Figure 4. Temporal and Spatial distribution of laser output power for initial electron temperature Tin=10eV

IV. CONCLUSION

It is found that the diameter of the ring of the radiation is determined by the initial electron temperature at the axis. If the electron temperature is increased the diameter of the ring increases. The computed results are compared with the experimental results of Hayashi et al (Hayashi et al 1992)[11]. The profiles in the Hayashi et al experiment are measured at different charging voltages 20, 21 and 22 kV respectively. They have measured one more temporal profile by adding hydrogen gas to the dischargeby keeping the charging voltage 22kV.

V. REFERENCES

[1]. I . I. Balchev, N. I. Minkovski, I. K. Kostadinov and N. V.Sabotinov Bulg. J. Phys. 33(2006) 39-47

[2]. A. J. Kearsley and C. E. Webb, WDM solutions (October 2000)

[3]. Hong Lei, Li Lijum "A study of laser cutting engineering ceramics", Optics and laser Technology 31 531-538 (1999)

[4]. G. Andra, E. Glauche Appl. Surf.Sci. 109/110 133-136. (1997)

[5]. M. J. Kushner and B. E. Warner J. Appl. Phys.54(6),P. 2970-2982,(1983)

[6]. R. J. Carman , Daniel J. W. Brown, and J. A. Piper IEEE J. Quantum Electronics, Vol.-30, No.8, PP.1876-95,(1994)

[7]. Akira Ohzu, Massakikato and Yaichiro Maruyama, "Optics ommunications",Vol.177,PP.355-361 (2000)

[8]. R. Sadighi-Bonabi, R Mohammadpour, M.Tavalcol, M. Zand and F. Soltanmoradi, Quantum Electron, Vol.37,PP.325- 330 (2007)

[9]. N. K. Vuchkov, K. A. Temelkov, P. V.Zahariev and N. V. Sabotinov, Optics & Laser Technology, Vol.36, PP.19-25(2004)

[10]. K. Hayashi, Y. Iseki, S. Suzuki, I. Watanabe, ENoda and O. Morimiya Jpn. J. Appl. Phys . Vol.31, PP. L1689,(1992)

Dielectric Relaxation Study of Liquid Polymers of Ethylene glycol oligomers using Picosecond Time Domain Reflectometry

B. D. Watode[1], A. C. Kumbharkhane[2*]

[1]Depratment of Physics, Phulsing Naik Mahavidyalaya, Pusad, Maharashtra, India

[2]School of Physical Sciences, Swami Ramanand Teerth Marathwada University, Nanded, Maharashtra, India.

ABSTRACT

The dielectric relaxation measurement of polymers in water mixtures have been carried out over entire concentrations, at temperatures 25^0C using picoseconds time domain reflectometry technique in the frequency range of 10 MHz to 30 GHz. The complex permittivity spectra of polymer - water mixtures were fitted using Havriliak-Negami equation. The static dielectric constant (ε_0), high frequency permittivity (ε_∞) and relaxation time(τ) for all concentrations have determined using least square fit method. The variations in dielectric parameters with molecular size is studied.

Keywords: Polymers, Dielectric Relaxation, time domain reflectometry, static dielectric constant (ε_0), high frequency permittivity (ε_∞), relaxation time (τ) etc.

I. INTRODUCTION

Dielectric relaxation study on liquids provides information regarding their molecular behavior and dynamics of the molecules involved at dipolar level. Dielectric studies involve measurements of dielectric permittivity and dielectric loss. The measurement can be used to find dielectric relaxation times and distribution parameters. The relaxation time depends upon the molecular size, shape, intramolecular & intermolecular forces. Time domain reflectometry gives dielectric relaxation study over a wide frequency range [1-7].

The polymers of ethylene glycols such as Ethylene glycol(EG), Diethylene glycol(DEG),Tri ethylene glycol(TEG),Tetra ethylene glycol(TTEG),Penta-ethylene glycol(PEG)& Hexa- ethylene glycol(HEG) are organic liquids and have two -OH groups at the ends of their molecular structure. Due to present of ends -OH groups, molecules of these liquids can enter into intra & intermolecular hydrogen bonding giving rise to several conformations in water mixtures [8].Dielectric relaxation & thermodynamic properties of glycols as a function of temperature and frequency have attracted much attention from industrial and academic researchers due to strong potential in industrial and biological applications.

In this paper we have reported the values of dielectric parameters of polymers of ethylene glycols, which will be useful for the researchers.

II. METHODS AND MATERIAL

2.1 MATERIAL:

Polymers of ethylene glycol i.e. Ethylene glycol (EG) and Diethylene glycol (DEG) were obtained from S.D. Fine-Chem. Limited. Triethylene glycol (TEG), Tetra

ethylene glycol (TTEG), Pentaethylene glycol (PEG) and Hexa ethylene glycol (HEG) were obtained commercially (Aldrich) and used without further purification. The solutions were prepared at different weight fraction of water in EG, DEG, TEG, TTEG, PEG and HEG. The double distilled water is used to prepare mixtures. The dielectric spectra have been obtained by time domain reflectometry (TDR) technique. The Tektronix model no.DSA8200 Digital Serial Analyzer sampling oscilloscope along with sampling module80E08 has been used for the measurement. A repetitive fast rising voltage pulse with 18 picoseconds incident rise time was fed through coaxial line system of impedance of 50Ω. Reflected pulse without sample R_1 (t) and with sample R_x (t) were recorded in time window of 2 nanosecond and digitized in 2000 points. The Fourier transformation of pulses and data analysis were done earlier to determine the complex permittivity spectra $\varepsilon^*(\omega)$ using non linear least squares fit method [9,10].

III. RESULTS AND DISCUSSION

The frequency dependent values of dielectric permittivity (ε') and dielectric loss (ε'') of polymers of ethylene glycols at 25^0C are shown in Fig.1 (a & b).It is observed from the plot that the values of dielectric permittivity (ε') decreases with increase in the frequency and increase in number of carbon atoms and dielectric loss (ε'') peak shifts from higher to lower frequency.

In general dielectric loss spectrum of the aqueous solutions of polymers of ethylene glycol exhibits an asymmetrical shape and described by the Havriliak-Negami expression. We performed the non linear least square fitting procedure for polymers of ethylene glycol-water mixtures, in order to extract dielectric relaxation parameters with the following equation [11].

$$\varepsilon^*(\omega) = \varepsilon_\infty + \frac{\varepsilon_0 - \varepsilon_\infty}{\left[1 + (j\omega\tau)^{1-\alpha}\right]^\beta} \quad (1)$$

Where ε_0 is static dielectric constant, ε_∞ is dielectric constant at high frequency, τ is dielectric relaxation time, α and β are the distribution parameters. The value of α is kept zero and β is varied such that $0 \le \beta \le 1$. The values of ε_0 and τ for polymers studied here are reported in Table 1.

3.1 STATIC DIELECTRIC CONSTANT (ε_0):

The value of static dielectric constant depends upon number of dipoles per unit volume of given liquid system. As number of carbon atoms increases from EG to HEG, the number of dipoles per unit volume of decreases. Hence the value of static dielectric constant decreases from EG to HEG.

3.2 DIELECTRIC RELAXATION TIME (τ):

The dielectric relaxation time depends upon volume of molecule and hydrogen bonding between the molecules. As number of carbon, hydrogen and oxygen atoms increases, molecular weight increases. Hence relaxation time increases. Therefore relaxation time for DEG is more than EG. But relaxation time from TEG to HEG decreases. Because as molecular size of polymer increases, instead of whole molecule individual segments rotates fastly and relaxation time decreases.

IV. CONCLUSION

The temperature dependent complex permittivity spectra of Diethylene glycol in aqueous solution have been studied using time domain reflectometry technique in the frequency range 10 MHz to 30 GHz. The variation in dielectric constant and relaxation time with increase in molecular weight of polymers indicates the structural dynamics of polymers.

V. ACKNOWLEDGEMENTS

Figure 1 (a) Frequency dependent dielectric permittivity (ε') for pure polymers of EG at 25°C.

Figure 1(b) Frequency dependent dielectric loss (ε'') for pure polymers of EG

Table 1: Dielectric parameters obtained from Havriliak-Negami expression.

Sample	Static dielectric constant (ε_0)		Relaxation Time (τ) ps	
	Experimental Value	Literature Value	Experimental Value	Literature Value
EG	41.94	40.7[a]	104.42	121[a]
DEG	29.50	30.7[a]	216.82	237[a]
TEG	21.87	23.0[a]	221.36	205[a]
TTEG	20.02	20.90[b]	181.76	----------
PEG	18.82	17.80[*]	156.63	----------
HEG	15.12	16.60[*]	152.50	----------

[a] E.Hanke, K.V.Roden and U.Kaatze, J. Chemical Physics 125, 084507 (2006).

[b] C.M.Kinart, A.Cwiklinska, M.Maj and W.J.Kinart, Fluid Phase Equilibria 262,244 (2007).

[c] V.A. Rana, A.D.Vyas and S.C.Mehrotra, J.Mol. Liquid 102/1-3, 379 (2002).

[*] Data from Japan group.

VI. REFERENCES

[1]. Zamir S. Khan, M.P.Lokhande, Avadhut Deshmukh and A.C.Kumbharkhane, Journal of Advanced Dielectrics, Vol.10, No.03,2050004(2020).

[2]. A. A. Sonkamble , S.M. Dongarge , M. Malathi and U.V. Biradar, International Journal of Scintific Research in Physics and Applied Sciences, Vol.8, issue 4, pp 13-17 (2020).

[3]. S. X. Drakopoulos, J. Karger-Kocsis, A. Kmetty, L. Lendvai, G. C. Psarras, Carbohydrate Polymers ,Vol.157, 711-718(2017).

[4]. Abdulrahman W. Pathan & Ashok C Kumbharkhane,Physics and chemistry of liquids: An International Journal Vol.55, issue 2, 179-185(2017).

[5]. S D Chavan, B D Watode, P G Hudge, D B Suryawanshi, C G Akode, A C Kumbharkhane and S C Mehrotra, Indian J.of Physics.84(3),275(2010).

[6]. Arvind V Sarode and Ashok C Kumbharkhane, Journal of Molecular Liquids 160, 109 (2011).

[7]. Y S Joshi and A C Kumbharkhane, Journal of Molecular Liquids 161, 120 (2011).

[8]. P. Debye, Polar Molecules, Chemical Catlog Company,New York(1929).

[9]. P B Undre, P W Khirade, S B Jagdale, S N Helambe and S C Mehrotra, Lithuanian Journal of Physics, Vol 51, No.2, 147 (2011).

[10]. S.D. Chavan, A.C. Kumbharkhane, S.C. Mehrotra, J. Chin. Chem. Soc. 54, 1457(2007)

[11]. S Havriliak and S Negami, J. Polym. Sci. 14, 91 (1966).

Energy Transfer Process in MgF$_2$: Gd^{3+}, Eu^{3+} Phosphor : Application to Visible Quantum Cutting

S. R. Jaiswal*[1], P. A. Nagpure[2], S. K. Omanwar[3]

[1]* Department of Physics, Shri R.L.T. College of Science, Akola, Maharashtra, India

[2]Department of Physics, ShriShivaji Science College, Amravati, Maharashtra, India

[3]Department of Physics, SantGadge Baba Amravati University, Amravati, Maharashtra, India

ABSTRACT

Visible quantum cutting (QC) is observed in MgF$_2$ Co-doped with Gd^3, Eu^{3+} phosphor synthesis via wet chemical method. Powder X-ray diffraction analysis shows structural purity. The emission and excitation spectra of MgF$_2$:Gd^{3+}, Eu^{3+} were investigated using the VUV beam line of the Beijing Synchrotron Radiation Facility (BSRF). Energy transfer in gadolinium compounds from the Gd^{3+} ions to Eu^{3+} through cross relaxation occurs in this process. Quantum efficiency was found to be greater than 100% under the excitation of 172 nm and 203 nm corresponding $^8S_{7/2}$ ^6G_J transition of Gd^{3+} ions. The synthesized phosphor material is potential candidates for the applications of plasma display panel and mercury free fluoresce lamps.

Keywords : Quantum Cutting, Plasma Display Panels (PDPs), VUV Spectroscopy

I. INTRODUCTION

For the development of mercury free florescent lamps and plasma display panels (PDPs), we require phosphor having quantum efficiency is greater than unity under VUV excitation. The phosphors having quantum efficiency is greater than unity are called quantum cutting phosphors. Quantum cutting provides a means to obtain two or more low energy photons for each high energy absorbed photon. Therefore it serves as a down converting (DC) mechanism with quantum efficiency greater than unity and it offers the prospect of providing enhanced energy effectiveness in lighting devices [1]. In order to obtain quantum-cutting phosphors with quantum efficiencies exceeding unity, the lanthanide ions are obvious candidates for this purpose due to their energy level structures that afford metastable levels from which quantum-splitting processes are capable. [3-6]

II. METHODS AND MATERIAL

MgF$_2$: Gd^{3+}, Eu^{3+} phosphor was synthesis via reactive atmospheric process. In this method we used metal carbonate like MgCO$_3$(99.99% A.R.) as a precursor. The inorganic magnesium carbonate was taken in Teflon beaker. A little amount of double distilled water was added in beaker and stired it, then hydrofluoric acid (HF) added in it to get slurry. The slurry was dried by blowing air or heating on hot plate (80°C). A freshly prepared MgF$_2$ host was obtained. Gd$_2$O$_3$ (AR 99.9%) and Eu$_2$O$_3$ (AR 99.9%) were boiled in HNO$_3$ and evaporated to dryness, so as to convert them into relevant nitrates. The aqueous

solution of these nitrates where use as a dopants. The 1 mol% of gadolinium nitrate and 1mol% of europium nitrate where assorted in the host material and dehydrated completely.

The dried powder was transferred to a glass tube and about 1.0 wt. % RAP agent was added. In this process we used ammonium fluoride as a RAP agent. The tube was closed with a tight stopper and slowly heated to 500°C for 2 h. The stopper was removed and the powders were transferred to a graphite crucible pre-heated to a suitable temperature. After heating in the graphite crucible for 1 h the resulting phosphor was rapidly quenched to room temperature. Belsare*et al.* well discussed about RAP in their literature [7]. The complete process involved in the reaction was represented as a flow chart in Fig. 1.

III. RESULTS AND DISCUSSION

3.1 XRD Analysis

The formation of the MgF_2: Gd^{3+}, Eu^{3+} sample in the crystalline phase synthesized by RAP was confirmed by XRD pattern as shown in Fig.2. The XRD pattern for MgF_2:Gd^{3+}, Eu^{3+} agreed well with the standard data from ICDD file (01-070-8282). Also the XRD pattern show that MgF_2 lattice possesses Tetragonal structure with a space group *P42/mnm(136)* with lattice parameters *a =b=4.5964 A° and c= 3.0376 A°* and interfacial angles $\alpha = \beta = \gamma = 90°$. XRD pattern of MgF_2:Gd^{3+}, Eu^{3+} phosphor as shown in fig.1.

Fig.1   Fig.2

Fig.1. Flow chart of MgF_2: Gd^{3+}, Eu^{3+} prepared via RAP.

Fig.2.XRD patterns of MgF_2: Gd^{3+}, Eu^{3+} synthesized by RAP.
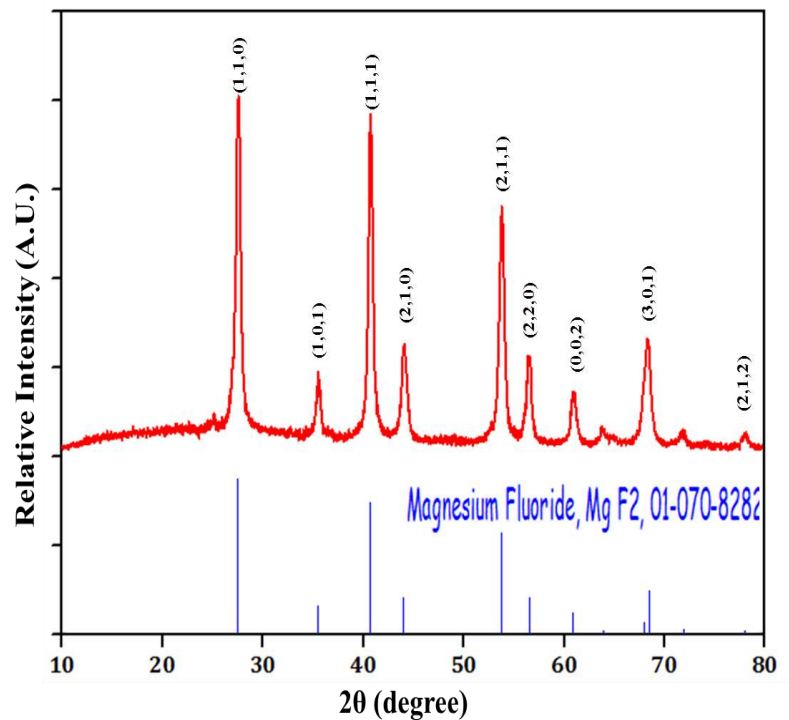
3.2 VUV-UV PL Analysis

The concentration quenching of Gd^{3+} as a sensitizer in MgF_2 host background was resolute. From the Fig.3 it can be encouraged that at 1 mol% of Gd^{3+} ions in MgF_3 host shows optimum intensity peak at 311 nm under the excitation of 273 nm. The emission spectra under excitation 273 and 203 nm are shown in Fig 5. The emission lines of Eu^{3+} peaked at about 593, 613, 650 and 700nm correspond to $^5D_0 \rightarrow ^7F_J$ (J=1, 2, 3, 4) transitions respectively and the ^5D_J (J=0, 1, 2, 3) $\rightarrow ^7F_J$ transition peaks of Eu^{3+} are much weaker than those of $^5D_0 \rightarrow ^7F_J$ transition. There are broad excitations lines spectra peaking optimum at about 203, 227 and 274 nm responsible for $^8S_{7/2} \rightarrow ^6G_J$, ^6D_J, ^6I_J respectively [8] as shown in Fig 4.

The process transfer of energy and quantum splitting can happen by the combination of Gd^{3+} and Eu^{3+} in which Gd^{3+} and absorbing a VUV photon corresponding to $^8S_{7/2} \rightarrow ^6G_J$. The incident high energy photon is cut into two visible photons emitted by Eu^{3+} ions. The energy of transitions $^6G_J \rightarrow ^6P_J$ on Gd^{3+} matches the $^7F_J \rightarrow ^5D_0$ excitation energy on Eu^{3+}. Upon excitation in the ^6G_J levels of Gd^{3+} as the first step, energy is transferred by cross-relaxation between Gd^{3+} and Eu^{3+} which make Gd^{3+} fall into the ^6P_J state and Eu^{3+} is excited into the $^5D_0$ state. The excited Eu^{3+} is responsible for the first visible photon. The first step is called as booming energy migration. In the second step the remaining excitation energy of Gd^{3+} in the ^6P_J state is transferred to another nearing Eu^{3+} ion, i.e. Eu^{3+} ion exciting into a high state. Then a fast relaxation from a high excited state to ^5D_J states will occur. After the first step, because the Eu^{3+} ion only excited into $^5D_0$ state, only the emissions of $^5D_0 \rightarrow ^7F_J$ transitions are expected. However after the second step, all levels of $^5D_{3,2,1,0}$ of Eu^{3+} are probably engaged, so the emission wavelength consists of all of the ^5D_J (J=0,1,2,3) $\rightarrow ^7F_J$ transitions [9].
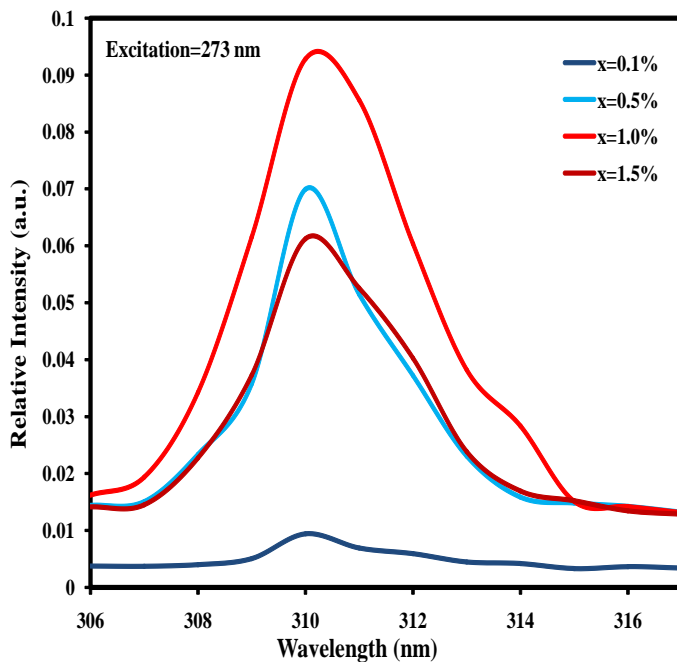
Fig.3

Fig.4

Fig.3.Emission spectra of MgF_2: X%Gd^{3+} under the excitation of 273 nm.
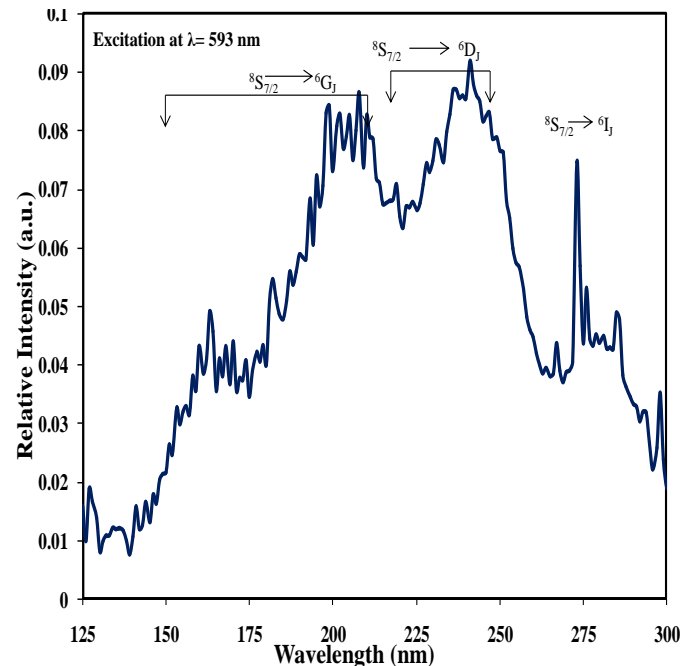
Fig.4.Excitation spectrum of MgF_2: Gd^{3+}, Eu^{3+} monitored at 593 nm.
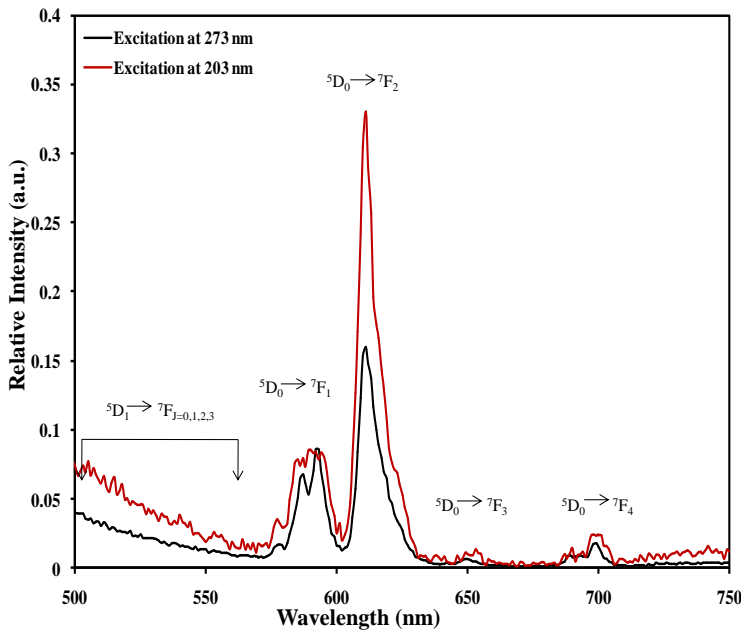
Fig.5

Fig.6

Fig.5.Emission spectra of MgF$_2$: Gd^{3+}, Eu^{3+} at excitation wavelength 203 and 274 nm.
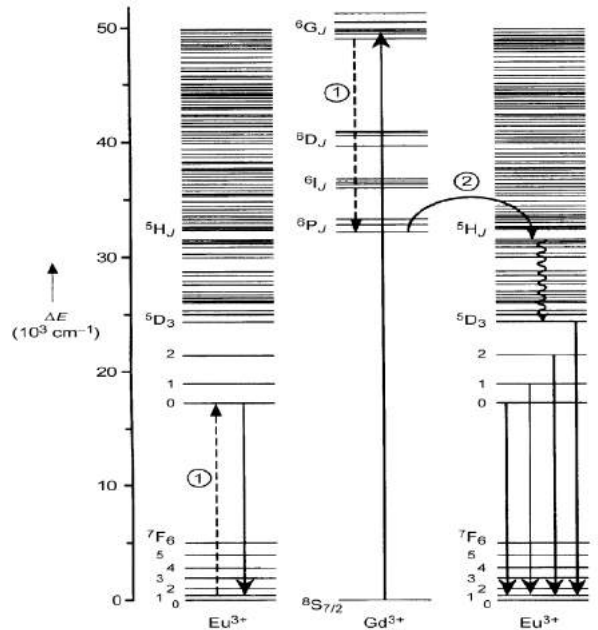
Fig.6.Energy level diagrams of Eu^{3+} and Gd^{3+} showing the cross-relaxation energy transfer process that leads to quantum splitting [9, 10]

Consecutively to calculate quantum efficiency, some assumption must be projected. The incident vacuum ultraviolet photon absorption efficiency cannot be taken into consideration. Some nonradiative losses at defects and impurities are disregarded. In the MgF$_2$:Gd^{3+}, Eu^{3+}sample, different excitations are adopted including the excitation of Gd^{3+}→^{6}G$_J$ with 203 nm and the excitation of Gd^{3+}→^{6}I$_J$ with 273 nm. Upon excitation in ^{6}I$_J$ level with 273 nm, the quantum cutting never occurs because no cross-relaxation exists, so the ^{5}D$_J$→^{7}F$_J$ transitions emission of Eu^{3+} has a normal branching ratio between ^{5}D$_0$ and ^{5}D$_{1, 2, 3}$. Upon 203 nm excitation in ^{6}G$_J$ level with, the quantum cutting can occur via two-step energy transfer. In the second step, the emission of Eu^{3+} has a normal branching ratio. The first step will pilot to the increase of ^{5}D$_0$ emission. So the ratio of ^{5}D$_0$ and ^{5}D$_{1, 2, 3}$ emissions is expected to increase. To determine the efficiency of the cross relaxation, the formula proposed by Wegh [11-20] was adopted as follows:

$$\frac{P_{CR}}{P_{CR}+P_{DT}} = \frac{R(^5D_0/^5D_{1,2,3})_{^6G_J} - R(^5D_0/^5D_{1,2,3})_{^6I_J}}{R(^5D_0/^5D_{1,2,3})_{^6I_J}+1}$$

Where P$_{CR}$ is the probability for cross-relaxation, P$_{DT}$ is the probability for the direct transfer from Gd^{3+} to Eu^{3+}. R (^{5}D$_0$/^{5}D$_{1, 2, 3}$)is the ratio of the ^{5}D$_0$ and ^{5}D$_{1, 2, 3}$ emission integral intensities. The subscript (^{6}G$_J$ or ^{6}I$_J$) represents the excitation level for which the ratio is observed. From the emission spectra, the value of R (^{5}D$_0$/^{5}D$_{1, 2, 3}$)^{6}G$_J$ and (^{5}D$_0$/^{5}D$_{1, 2, 3}$)^{6}I$_J$ can be calculated 44.12 and 29.42, respectively. Therefore, the value of P$_{CR}$/P$_{CR}$ + P$_{DT}$ is 0.32. It means that there are 32% Gd^{3+} ions in the ^{6}G$_J$ excited state settle down through a two-step energy transfer emitting two visible photons in this method. So the quantum cutting efficiency of 132% can be obtained. Quantum cutting in the Gd to Eu understanding requires energy transfer over the Gdsublattice to Eu [10].

IV. CONCLUSION

The inorganic material MgF_2: Gd^{3+}, Eu^{3+} was successfully prepared through reactive atmosphere process. The XRD pattern confirmed its cubic structure. The visible quantum cutting and energy transfer through down-conversion was observed in MgF_2:1% Gd^{3+}, 1% Eu^{3+} and the quantum efficiency was found to be around 132% under the excitation of 203 nm equivalent $^8S_{7/2} \rightarrow {}^6G_J$ transition of Gd^{3+} ions.

V. ACKNOWLEDGEMENTS

VI. REFERENCES

[1]. C.R. Ronda, J. Alloys Compd. 225 (1993) 534.

[2]. M. Y. William, Phosphor Handbook, CRC press is an imprint of the Taylor & Francis Group, ISBN: 0-8493-3564-7.

[3]. S. Pote, C. Joshi, S. Moharil, P. Muthal, S. Dhopte. ISSN 1061-3862, International Journal of Self- Propogating High-Temperature Synthesis. 22 (2013) 37-40

[4]. B. Herden, A. García-Fuente, H. Ramanantoanina, T. Jüstel, C. Daul, W. Urland, Chemical physics letter. 620 (2015) 29-34.

[5]. W. Binder, S. Dislerhoff, J. Cameron, Dosimetric Properties of CaF2: Dy, (a) Proc. II Int. Conf. on Lumin. Dosim.,Gatlinberg, 1968, pp. 45–53; (b) Health Phys., 1969, vol. 17, no. 4, pp. 613–618.

[6]. (a) A.C. Lucas, R.H. Moss, B.M. Casper, Thermoluminescent CaF2:Tm and Method for Its Use, US Patent 4 039 834, 1977; (b) Lucas, A.C. and Casper, B.M., Thermoluminescence of Thulium Doped Calcium Fluoride, Proc. Int. Conf. on Lumin. Dosim., Sao Paulo (Brazil), 1977, pp. 131-139

[7]. P. Belsare, C. Joshi, S. Moharil, V. Kondawar, P.Muthal, S. Dhopte, J. Alloys Compd. 450 (2008) 468–472.

[8]. R.T. Wegh, E.V.D. van Loef, A. Meijerink , J. Lumin., 90 (2000) 111.

[9]. B. Liua, Y. Chena, C. Shia, H. Tanga, Y. Tao, Journal of Luminescence 101 (2003) 155–159.

[10]. R.T. Wegh, H. Donker, K. Oskam, and A. Meijerink, J. Lumin., 82 (1999) 93.

[11]. R.T. Wegh, H. Donker, K. Oskam, A. Meijerink, Science 663 (1999) 283.

[12]. N. Kodama, Y. Watanabe, Appl. Phys. Lett. 4141 (2004) 84.

[13]. N. Kodama, S. Oishi, J. Appl. Phys. 103515 (2005) 98.

[14]. R. Hua1, J.H. Niu, B.J. Chen, M.T.Z. Li, T. Yu, W.L. Li, Nanotechnology 1642 (2006) 17.

[15]. Y. Zhou, S.P. Feofilov, J.Y. Jeong, D.A. Keszler,R.S. Meltzer, Phys. Rev. B 075129 (2008) 77.

[16]. M. Karbowiak, A. Mech, W. Ryba-Romanowski, J. Lumin. 65 (2005) 114.

[17]. B. Liu, Y.H. Chen, C.S. Shi, H.G. Tang, Y. Tao, J. Lumin. 101 (2003) 155.

[18]. S.K. Omanwar, S.R. Jaiswal, P.A. Nagpure, V. B. Bhatkar, J. Material Sci.: Material in Electronic(2016) 1-8

[19]. S.K. Omanwar, S.R. Jaiswal, N.S. Sawal, K.A. KoparkarP.A.Nagpure, V. B. Bhatkar, St. petrbergpolytechenicaluniversityJournal : Physics and mathematics 3 (2017) 218-224.

[20]. S.R. Jaiswal, N.S. Sawal, K.A. Koparkar, V. B. Bhatkar, S.K. Omanwar, material discovery, 7 (2017) 15-20.

Impact of Cobalt Doping on Structural and Optical Properties of ZnO Thin Films

M. B. Awale[1], S. D. Lokhande[2], L. H. Kathwate[2], V. D. Mote[2], H. C. Chaudhari[1*]

[1*]P.G. Department of Physics J. E. S. college, Jalna, Maharashtra, India.

[2]Thin Films and Materials Science Research Laboratory, Department of Physics, Dayanand Science College, Latur, Maharashtra, India

ABSTRACT

Cobalt doped zinc oxide thin films have deposited on glass substrate via spray pyrolysis techniques. The structural and optical properties of prepared thin films are characterized by Xray diffraction and UV-Vis spectrophotometer. From Xray diffraction pattern conforms single phase hexagonal wurtzite structure with c axis orientation. The average crystalline size of thin films calculated from Scherrer equation and found to be decrease with cobalt doping. The absorbances value is found to be high for cobalt doped ZnO as compared to undoped ZnO. Also, the optical characterization reveals the decrease in Energy band gap with cobalt doping.

Keywords : Semiconductor, Zinc oxide, Thin films, Xray diffraction, Absorbance.

I. INTRODUCTION

Zinc oxide is one of the efficient oxide materials among the various II-VI semiconductors. It has applications in many devices such as solar cell devices, gas sensing devices and LED [1, 2, 3]. These applications lead to the enormous increase in Zinc oxide study and its utility in different fields of science and technology. A wide band gap of 3.37eV and high exciton binding energy of 60 meV even at room temperature makes zinc oxide one of the most relevant materials in terms of research. [4 ,5] As a result of oxygen vacancies ZnO is more prominent toward n-type behavior. Standard methods of fabrication, low-cost techniques of synthesis, non-toxicity and remarkable properties make zinc oxide based thin films a topic of interest these days [6, 7, 8]. Properties of Zinc oxide may get vary with crystallite size, crystallinity, morphology, which can be varied by varying chemical composition, thermal treatment, pressure maintenance etc. [9,10,11]. All these parameters lead to improved structural, optical and morphological properties of material in most of the cases. Furthermore, properties can be enhanced by doping Zinc oxide. Dopant selection depends on ionic radii difference between and ZnO and dopant element and its electronegativity as well. As a dopant material, cobalt can enhance the optical behavior of ZnO as a result of abundant electronic state of cobalt.[12]. Such films can be obtained by means of several deposition techniques such as thermal evaporation [13] sputtering,[14], CVD [15] and spray Pyrolysis [16]. However, Spray pyrolysis is non- complicated, efficient and low-cost technique which can be implemented for large scale thin films synthesis having versatile properties.

This work deals with structural and optical study of Co doped ZnO thin films prepared by spray pyrolysis technique at constant temperature of 400ºC. Deposition of thin films are performed on glass substrates due to their easy availability and low cost. This study is mainly focusing on the impact of Co as a dopant on ZnO lattice that can be responsible for improvement in its structural and optical properties. Thin film samples were prepared for pure ZnO and 10% doping of Co at ZnO lattice. X-ray diffractometer and UV-Vis spectrophotometer is opted for the characterization of both undoped and Co doped ZnO thin films.

II. METHODS AND MATERIAL

Precursor solution were prepared for both pure and cobalt doped Zinc oxide samples using zinc acetate and cobalt acetate as the starting materials. To dissolve the acetates completely, deionized water was used. Both Zinc acetate and cobalt acetate solutions were stirred continuously to get homogenous solutions. doping percentages was taken 10% to know the variation in properties of ZnO thin films as a result of addition of cobalt. The substates where the prepared solutions were to be deposited, washed and cleaned thoroughly using distilled water and acetone. Prepared solution was transferred to spray chamber where transformation of the liquid into the stream takes place in order to get a uniform and fine droplet and allowed to spray onto the preheated glass substrates. All the parameters of spray pyrolysis set-up such as Flow rate, deposition time, Nozzle to substrate distance, substrate temperature (400ºC), Carrier gas pressure were adjusted and set to a desired value in order to get a good yield. Prepared solutions were transferred into the spray chamber and allowed to be sprayed onto the substrate for desired time. Structural characterization is performed using Rigaku XRD diffractometer consist of an X-ray beam of wavelength kα (Cu) = 1.5418 Å. The scanning range was maintained between 20 to 80 degrees. This study helped in determining the structure related parameters and purity of the phase.

III. RESULTS AND DISCUSSION

The XRD pattern for pure ZnO and 10% cobalt doped ZnO is shown in figure (1). Both the samples are observed to be single phased with hexagonal crystal structure having space group P63mc. Indicating clearly that cobalt has been successfully incorporated into the ZnO lattice as substitutional atom. No other extra peak can be observed corresponding to any other foreign impurity. The XRD pattern consist of peaks due to (100), (002), (101), (102), (110), (103), (112) planes. The position at 34.50º position the sharp and highest intense peak in obtained which corresponds to (002) plane. The peak intensity of (002) is higher than other peaks indicating that prepared films are nanocrystalline in nature and has c-axis preferred orientation perpendicular to the substrate. Peak intensity is found to be decreased with Co doping in ZnO which may be due to degradation of crystalline quality after the introduction of Co+2 in ZnO lattice [17]. Average crystallite size was evaluated for (002) plane using XRD results of samples. With the help of Full width and half maxima (FWHM) values, Grain sizes were calculated using Debye Scherrer formula. [18]

$$D = \frac{K\lambda}{\beta \cos\theta} \qquad (1)$$
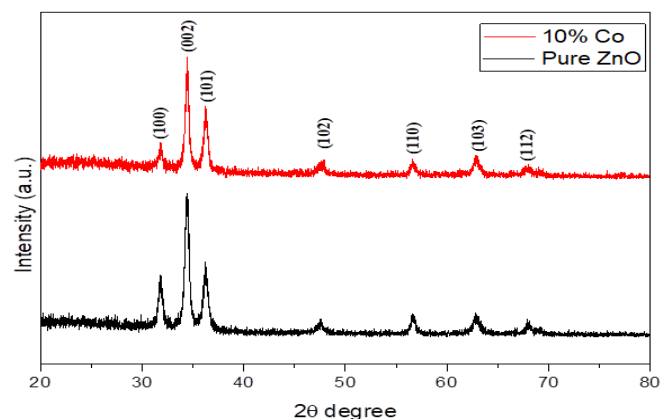
FIG (1): XRD PATTERNS OF PURE AND CO-DOPED ZNO THIN FILMS

Here, D stands for average crystallite size, β stands for full width half maxima, $\lambda = 1.54A^0$ corresponds to wavelength of X-ray, K is constant (~ 0.9), θ is Bragg's angle. The corresponding Grain sizes values are reported in Table 1. The estimated values of the crystallite size confirm that Both the samples are of nanosized in nature. With addition of Co concentration there is decrease in Grain size observed with increase in strain, which may attribute to increase in grain boundaries [19]. Lattice parameters and strain values were also estimated using XRD analysis and tabulated in the Table (1). Lattice constants have found to be decreased with addition of Co content.

The lattice parameter values 'a' & 'c' of the prepared thin films were calculated using the formula,

$$\frac{1}{d_{h,k,l}^2} = \frac{4(h^2 + hk + k^2)}{3a^2} + \frac{l^2}{c^2} \quad (2)$$

Where, $d_{h,k,l}$ - Interplaner spacing distance, h, k, l – Miller indices, a and c – Lattice parameters

Doping	a	c	c/a	D(nm)	Strain
Pure ZnO	3.248856	5.21088	1.603912	22.32566	0.004383
10% Co	3.246281	5.20740	1.604113	20.52485	0.004606

TABLE 1: STRUCTURAL PROPERTIES OF PURE AND CO-DOPED ZnO SAMPLES

Optical studies were performed using UV-Vis spectrophotometer using which optical absorption spectra of Pure and Co doped films is graphically elaborated in figure (2). Sharp and sudden change in absorption can be observed with cobalt doping as compared to pure ZnO in visible region of spectrum. This observation of increase in optical absorbance may imply the existence of direct transitions.
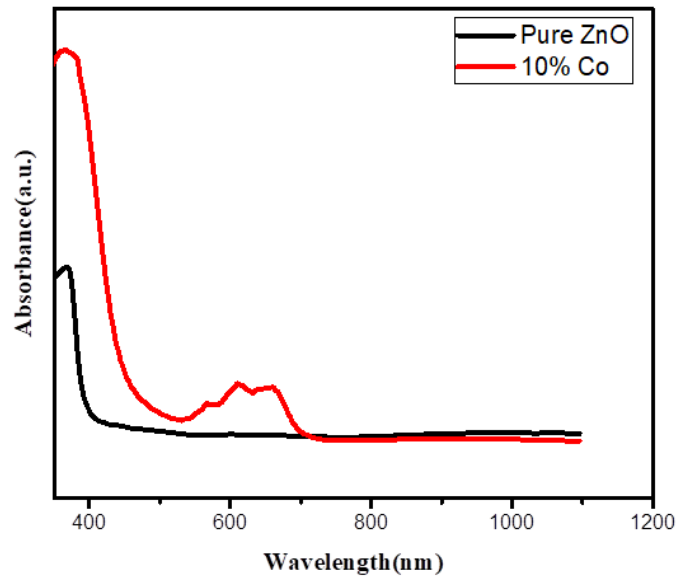
FIG (2): ABSORPTION SPECTRA OF PURE AND CO-DOPPED ZnO THIN FILMS

The optical band gap of E_g is calculated using the following Equation,

$$\alpha = \frac{A(h\nu - Eg)^n}{h\nu} \quad (2)$$

Where, 'A' and 'n' are constants, value of 'n' equal to 1/2 for the direct band gap semiconductor. The plot of $(\alpha h\nu)^2$ verses Photon energy for both the samples is shown in figure (3).
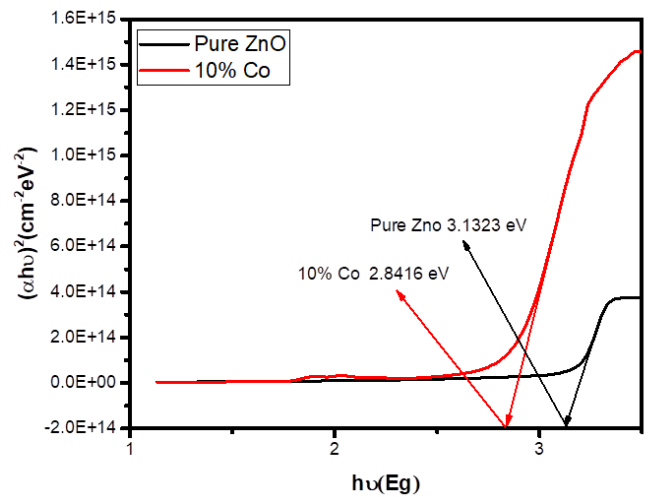
FIG (3): BANDGAP OF PURE AND 10% CO-ZnO THIN FILMS

Table (2) shows the band gap results of both pure ZnO and Co-doped ZnO samples. Evidently, the band gap

of Co-doped ZnO decreased gradually from 3.13 eV to 2.84 eV with respect to Co doping. This result may be associated sp-d hybridization that creates a shallow impurity level of dopant atom [20].

Doping	Bandgap (eV)
Pure ZnO	3.1323
10%Co	2.8416

Table 2: Band gap of Pure and Co-doped ZnO thin films

IV. CONCLUSION

In this work, we have prepared Pure and Co-doped ZnO Thin films by chemical spray pyrolysis method on glass substrate. The films observed to be polycrystalline in nature with orientation along c-axis and most intense peak along (002) plane. As a result of cobalt incorporation into ZnO lattice the hexagonal wurtzite nature remains same. As an impact of Co doping grain size decreases consequently crystalline quality decreases. Local strain values have found to be increased with doping may imposing large distortion in the lattice as a result of which reduction in crystallinity observed. Optical analysis indicates doped sample have high absorbance in range of 350nm to 450nm. This increase in absorption due to doping may imply the incorporation of Co^{+2} ions which is substituting the Zn^{+2} ions at the host lattice. This replacement is producing stress in the films thereby forming the structural deformation and resulting in higher absorbance. Optical band gap values are changing from 3.13eV to 2.84 eV for pure and Co-doped ZnO respectively due to exchange interactions.

V. REFERENCES

[1]. N.Jabena Begum K.Ravichandran Journal of Physics and Chemistry of Solids Volume 74, Issue 6, June 2013, Pages 841-848

[2]. Vithoba L.Patil Sharadrao A.Vanalakara Pramod S.Patil Jin H.Kim Sensors and Actuators B: Chemical Volume 239, February 2017, Pages 1185-1193

[3]. K.M.Sandeep Shreesha Bhat S.M.Dharmaprakash Journal of Physics and Chemistry of Solids Volume 104, May 2017, Pages 36-44

[4]. Ozgur, U.; AlivovYa, I.; Liu, C.; Teke, A.; Reshchikov, M. A.; Dogan, S.; Avrutin, V.; Cho, S. J.; Morkoc, H. Journal of Applied Physics., 2005, 98, 041301

[5]. C. Klingshirn, , Phys. Status Solidi 244 (9) (2007) 3027–3073.

[6]. Wang, X., Zhang, J., Zhu, Z., & Zhu, J. (2006). Colloids and Surfaces A: Physicochemical and Engineering Aspects, 276, 59.

[7]. Kim, D., Yun, I., & Kim, H. Current Applied Physics, 10, S459. (2010)

[8]. Shinde, V. R., Gujar, T. P., Lokhande, C. D., Mane, R. S., & Han, S.-H. Materials Science and Engineering B, 137, 119 (2007)

[9]. E.Bacaksiz M.Parlak M.Tomakin A.Özçelik M.Karakız M.Altunbaş Journal of Alloys and Compounds Volume 466, Issues 1–2, 20 October 2008, Pages 447-450

[10]. A.Zaier A.Meftah A.Y.Jaber A.A.Abdelaziz M.S.Aida Journal of King Saud University – Science Volume 27, Issue 4, October 2015, Pages 356-360

[11]. A.Saldaña-Ramírez M.R. AlfaroCruza I.Juárez-Ramírez Leticia M. Torres-Martínez Optical Materials Volume 110, December 2020, 110501

[12]. Z. Jin, T. Fukumura, M. Kawasaki, K. Ando, H. Saito, T. Sekiguchi, Y. Z. Hoo, M. Murakami, Y. Matsumuto, T. Hasegawa and H. Koinuma, Appl. Phys. Lett., 2001, 78(24), 3824.

[13]. Siti Nuuru lFatimah Hasim Muhammad Azmi Abdul Hamid Roslinda Shamsudin Azman Jalar Journal of Physics and Chemistry of Solids

Volume 70, Issue 12, December 2009, Pages 1501-1504

[14]. Wei Gao Zhengwei Li Ceramics International Volume 30, Issue 7, 2004, Pages 1155-1159

[15]. A.Dutta S.Basu Materials Chemistry and Physics Volume 34, Issue 1, April 1993, Pages 41-45

[16]. N.Lehraki M.S.Aid S.Abed N.Attaf A.Attaf M.Poulain Current Applied Physics Volume 12, Issue 5, September 2012, Pages 1283-1287

[17]. Yasemin Caglar Journal of Alloys and Compounds Volume 560, 25 May 2013, Pages 181-188.

[18]. Rao GT, Stella RJ, Babu B, Ravindrandh K, Reddy ChV, Shim J, et al Mater Sci Eng, B 2015;201:72–8.

[19]. S.Ben Ameur A.Barhoumi R.Mimouni M.Amlouk H.Guermazi Superlattices and Microstructures Volume 84, August 2015, Pages 99-112

[20]. Umadevi Godavarti, V.D. Mote, M.V. Ramana Reddy, P. Nagaraju, Y. Vijay Kumar, Kalyana Tulasi Dasari, Madhava P. Dasari Physica B: Condensed Matter Volume 553, 15 January 2019, Pages 151-160

Mechanical and Thermophysical Properties of Mg3TH7 (T= Mn, Tc, Re) Complex Hydrides

Sachin Rai, Navin Chaurasiya, Pramod K. Yadawa

Department of Physics, Prof. Rajendra Singh (Rajju Bhaiya) Institute of Physical Sciences for Study and Research, V. B. S. Purvanchal University, Jaunpur, Uttar-Pradesh, India

ABSTRACT

The Mg_3TH_7 (T= Mn, Tc, Re) compounds are hexagonal ternary complex hydrides. The characteristic features of high-temperature ternary complex hydrides are investigated by the theoretical evaluation of thermophysical and ultrasonic properties at room temperature using interaction potential model approach. From elastic constants calculations, it is noted that Mg_3MnH_7, Mg_3TcH7 and Mg_3ReH_7 brittle. With the help of second order elastic constants other elastic moduli, elastic stiffness constants and Poisson's ration are estimated at room temperature for elastic and mechanical characterization. The ultrasonic velocities and thermal relaxation time of these ternary complex hydrides are evaluated utilizing evaluated values of elastic constants and lattice parameters within the same physical conditions. The orientation dependent ultrasonic velocities and thermal relaxation time have been also evaluated for the determination of anisotropic behaviour and thermophysical properties. The obtained results are analyzed to explore the characteristic of complex hydrides compounds.

Keywords: Ternary Complex Hydrides, Elastic Properties, Ultrasonic Velocity, Thermal Relaxation Time

I. INTRODUCTION

Ternary complex transition hydrides have been considered to be very attractive candidates and have received significant attention as hydrogen storage materials. These compounds show a higher capacity for hydrogen storage in volume densities than compressed gaseous and liquid hydrogen [1]. In recent decades, research and development of new hydrogen storage materials opened up new possibilities for industrialists. On the other hand, the major challenges in solid state hydrogen storage are improved energy storage density, faster kinetics, and improved cycle life, using readily available elements at reasonable costs, with particular reference to fuel cells and rechargeable batteries [2, 3]. Matar et al. [4] have investigated the electronic structure and bonding of three different complex hydrides Mg3MnH7, Mg3ReH7 and Mg3TcH7 by the pseudo- potentials and computation of all electrons within the DFT. They have shown that both Mg3MnH7 and Mg3ReH7 have desorption energies within the range of MgH2 and are higher than those of covalent-like hydrogenated intermetallic compounds. The complex hydrides Mg3MnH7 and Mg3ReH7 compounds crystallize in hexagonal P63/mmc [5, 6].

In the present work, we have worked diligently to make the relationship between thermo physical and

microstructural properties for hexagonal Mg3TH7 (T= Mn, Tc, Re) complex hydrides. Mg3TH7 (T= Mn, Tc, Re) complex hydrides will help in understanding the mechanical behaviour of complex hydrides and it will play an important role in the diagram of industrial equipment with useful physical properties under moderate operating conditions. For that, we have considered elastic constants, stiffness constant, thermal relaxation time and ultrasonic velocity for complex hydrides. Young's modulus (Y), bulk modulus (B), shear modulus (G), Pugh's ratio (B/G), Poisson's ratio (σ) has also been evaluated and discussed for these complex hydrides.

II. METHODS AND MATERIAL

In this work, the interaction potential model approach has been used for the calculation of higher order elastic constants. The formulations of higher order elastic constants have been obtained by the second or third order strain derivatives of elastic energy density. The second (CIJ) and third (CIJK) order elastic constants of material are specify by following expressions.

$$C_{IJ} = \frac{\partial^2 U}{\partial e_I \partial e_J}; \qquad I \; or \; J = 1,......6 \qquad (1)$$

$$C_{IJK} = \frac{\partial^3 U}{\partial e_I \partial e_J \partial e_K}; I \; or \; J \; or \; K = 1,......6 \qquad (2)$$

where, U is elastic energy density, eI=eij (i or j = x, y, z, I=1, …6) is component of strain tensor. Eqs. (1) and (2) leads six second and ten third order elastic constants (SOEC and TOEC) for the hexagonal structure materials [7, 8].

$$
\left.
\begin{array}{ll}
C_{11} = 24.1\,p^4 C' & C_{12} = 5.918\,p^4 C' \\
C_{13} = 1.925\,p^6 C' & C_{33} = 3.464\,p^8 C' \\
C_{44} = 2.309\,p^4 C' & C_{66} = 9.851\,p^4 C'
\end{array}
\right\} \qquad (3a)
$$

$$
\left.
\begin{array}{ll}
C_{111} = 126.9\,p^2 B + 8.853\,p^4 C' & C_{112} = 19.168\,p^2 B - 1.61\,p^4 C' \\
C_{113} = 1.924\,p^4 B + 1.155\,p^6 C' & C_{123} = 1.617\,p^4 B - 1.155\,p^6 C' \\
C_{133} = 3.695\,p^6 B & C_{155} = 1.539\,p^4 B \\
C_{144} = 2.309\,p^4 B & C_{344} = 3.464\,p^6 B \\
C_{222} = 101.039\,p^2 B + 9.007\,p^4 C' & C_{333} = 5.196\,p^8 B
\end{array}
\right\} \qquad (3b)
$$

where p = c/a: axial ratio; $C' = \chi\, a\,/\,p^5$; $B = \psi\, a^3\,/\,p^3$; $\chi = (1/8)[\{nb_0\,(n-m)\}/\{\,a^{n+4}\}]$ $\psi = -\chi\,/\{6\,a^2(m+n+6)\}$; m, n=integer quantity; b0=Lennard- Jones parameter

Calculations of bulk modulus (B) and shear modulus (G) have been computed using Voigt and Reuss' approaches [9-12]. The Debye average velocity (VD) is well connected to longitudinal (VL) and shear wave (VS1, VS2) velocities. The expressions for ultrasonic velocities, thermal relaxation time(τ) are known in our prior papers [12, 13].

III. RESULTS AND DISCUSSION

In the current analysis we have calculate the elastic constants (six second order elastic constants and ten third order elastic constants) using the theory given by Eqn. (3) and Eqn. (4). The unit cell parameters 'a' (basal plane parameter) and 'p' (axial ratio) for Mg3MnH7, Mg3ReH7 and Mg3TcH7 are 4.46917 Å, 4.810 Å, 4.8501 Å and 2.1843, 2.792, 2.1921 respectively [14]. The value of m and n for complex hydrides are 6 and 7. The values of b0 are 8x10-63 erg cm7, 1.07x10-62 erg cm7and 1.21x10-62 erg cm7 for Mg3MnH7, Mg3ReH7 and Mg3TcH7 compounds respectively. The calculated values of SOEC and TOEC have been calculated for these complex hydrides at room temperature are offered in Table 1.

Table1. Second and third order elastic constants (SOEC and TOEC) (in GPa) at room temperature.

	C11	C12	C13	C33	C44	C66	B
Mg3MnH7	150	37	57	245	68	59	101
Mg3MnH7[14]	150.29	25.21	48.04	209.35	87.03	62.54	----
Mg3TcH7	155	38	59	255	71	61	105
Mg3TcH7 [14]	153.78	34.72	57.64	206.20	82.20	59.53	----
Mg3ReH7	162	39	62	268	74	63	110
Mg3ReH7[14]	161.68	36.85	59.22	215.85	86.93	62.41	-----

	C₁₁₁	C₁₁₂	C₁₁₃	C₁₂₃	C₁₃₃	C₃₄₄	C₁₄₄	C₁₅₅	C₂₂₂	C₃₃₃
Mg_3MnH_7	-2437	-386	-146	-186	-1652	-1549	-216	-144	-1928	-11082
Mg_3TcH_7	-2541	-403	-152	-194	-1722	-1614	-226	-150	-2011	-11547
Mg_3ReH_7	-264	-417	-159	-202	-1812	-1699	-236	-157	-2086	-12242

Complex hydrides had the highest elastic constant values, which are important for the material, as these are associated with the stiffness parameter. Second-order elastic constants are used to determine the ultrasonic attenuation and associated parameters. The highest elastic constant values found for complex hydrides are indicative of their better mechanical properties over other complex hydrides of the same group.

Clearly, for a steady hexagonal structure the five independent second order elastic constants (Cij, namely C_{11}, C_{12}, C_{13}, C_{33}, C_{44}) should satisfy the well-known Born- Huang's stability norms [15, 16] i.e. $C_{11} - |C_{12}| > 0$, $(C_{11}+C_{12}) C_{33} – 2C^2_{13} > 0$, $C_{11} > 0$ and $C_{44} > 0$. It is understandable from Table-1. It is evident that the values of elastic constant are positive and satisfies the Born-Huang's mechanical stability constraints and therefore all these compounds are mechanically stable. Using the formula $B= 2(C_{11}+ C_{12}+ 2C_{13} + C_{33}/2)/9$, the bulk modulus B, for complex hydrides can be calculated and presented in Table 1. The calculated values of C_{12}, C_{13} and C_{44} are few different than some other theoretical [14] results for these complex hydrides compound. Actually Benyelloul et al. [14] were theoretically evaluated using density functional theory (DFT), which is quite different from present approach. Although obtained order of SOEC are of the same as given in Table. 1. Relative magnitude of C_{11}, C_{33}, C_{66} are well presented by our theoretical approach. Thus, there is good agreement between the presented and the reported values which is correlated with elastic constants. Thus, our theoretical approach is well justified for the calculation of second order elastic constants of hexagonal structured compounds. We present the calculated values of TOECs in table 1. The negative values of TOECs indicate a negative strain in

the solid. The negative third order elastic constants appear in the previous paper on hexagonal structure material. Hence the theory applied for evaluation of higher order elastic constants, at room temperature, is justified [17, 18]. Hence the applied theory for the valuation of higher order elastic constants, at room temperature, is acceptable.

The values of Young's modulus (Y), shear modulus (G), bulk modulus (B), Poisson's ratio (σ) and Pugh's ratio (B/G) for Mg_3TH_7 (T= Mn, Tc, Re) complex hydrides at room temperature are calculated and presented in Table 2.

Table 2. Voigt–Reus' constants (M and C^2) Bulk modulus (in $10^{10}Nm^{-2}$), Shear Modulus (in $10^{10}Nm^{-2}$), Young's Modulus (in $10^{10}Nm^{-2}$), Poisson's ratio, Pugh's ratio for Mg_3TH_7 (T= Mn, Tc, Re) complex hydrides.

	M	C^2	B_r	B_v	G_r	G_v	Y	B/G	G/B	σ
Mg_3MnH_7	443	48517	10	93.9	66.2	65.7	16	1.53	0.65	0.231
Mg_3TcH_7	467	52460	11	97.4	69.3	68.3	11	1.52	0.66	0.230
Mg_3ReH_7	489	57464	211	102	72.0	71.0	91	1.54	0.65	0.232
			118				176			

It is found that the value of Young's modulus, Shear modulus and Bulk modulus of Mg_3MnH_7 are smaller than Mg_3ReH_7. Thus, Mg_3MnH_7 have little Stiffness and bonding with respect to Mg_3ReH_7. Pugh's ratio (B/G) and Poisson ratio (σ) are the measure of brittleness and ductility of solid. If σ=0.23≤0.26 and B/G = 1.53≤1.75, the solid is usually brittle, otherwise

it is ductile in nature [11]. Our finding of lower values of Pugh's ratio and Poisson ratio compared to their critical values indicates that Mg_3TH_7 (T= Mn, Tc, Re) complex hydrides are brittle in nature at room temperature. It is well known that for stable and elastic material the value of σ should be less than 0.5. It indicates that Mg_3TH_7 (T= Mn, Tc, Re) complex hydrides are stable against shear. A stronger degree of covalent bonding leads to higher hardness. The hardness, compressibility, ductility, brittleness, toughness, and bonding nature of the material are also well connected with the SOECs.

In the present investigation, we have correlated the mechanical and isotropic behavior of the material with the ultrasonic velocity. We have calculated the longitudinal ultrasonic velocity (V_L), shear ultrasonic velocity (V_S), the Debye average velocity (V_D) and the thermal relaxation time (τ) for Mg_3TH_7 (T= Mn, Tc, Re) complex hydrides. The data of density for these hydrides have been taken from literature [16].

The angular dependences of ultrasonic wave velocity (V_L, V_{S1}, V_{S2} and V_D) at different temperature are shown in figs. 1-4. The angles are measured form the unique axis of the crystal. Form figs. 1 and 3 the velocity V_L and V_{S2} of these complex hydrides have decreases with unique axis of the crystal and in figs. 2 and 4 it is evident that the velocity V_{S2} and V_D maxima at 55^0 and 35^0 respectively with the unique axis of the crystal. The abnormal behavior of angle dependent velocity is due to the combined effect of second order elastic constants and density. The nature of the angle dependent velocity curves in the present work is similar to the nature of angle dependent velocity curve found for other hexagonal structured material [18, 19]. Thus the angle dependence of the velocities in transition-metal disilicides is justified. As the calculation of V_D involves the velocities V_L, V_{S1} and V_{S2} [20, 21], It is understandable that the variation of V_D is affected by the constituent ultrasonic velocities. The maximum V_D at 55° is due to a significant increase in longitudinal and pure shear (V_{S2}) wave velocities

and a decrease in quasi-shear (V_{S1}) wave velocity. It may be concluded that the average sound wave velocity is maximum when a sound wave travels at 55^0 angles with the unique axis of these crystal.

Figure 1. V_L vs angle with unique axis of crystal
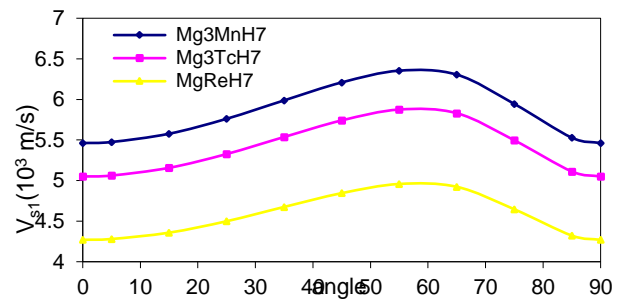
Figure 2. VS1 vs angle with unique axis of crystal
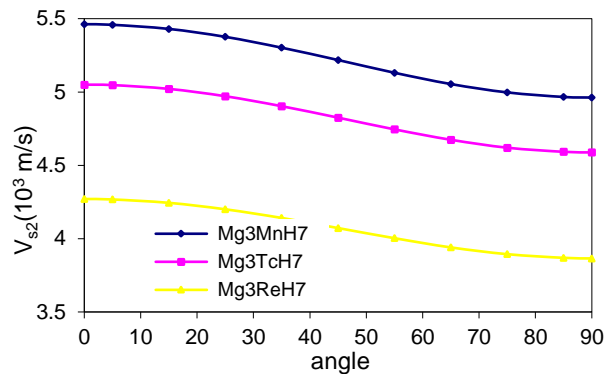
Figure 3. VS2 vs angle with unique axis of crystal
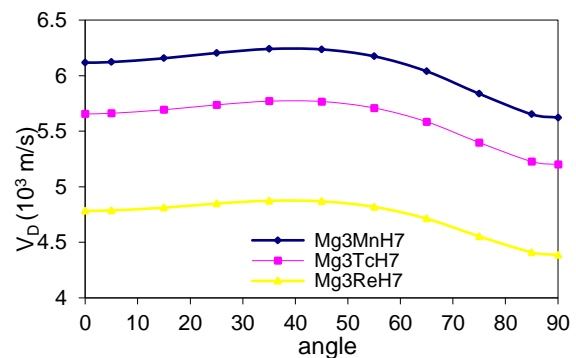
Figure 4. VD vs angle with unique axis of crystal
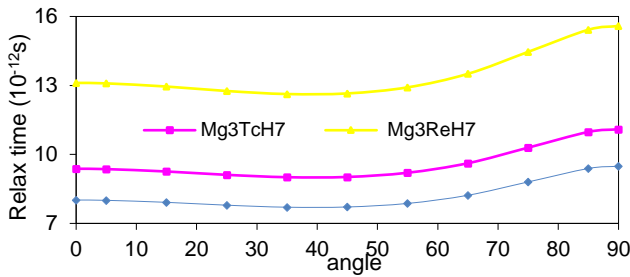
Figure 5. Relaxation time vs angle with unique axis

Fig. 5 show a that the thermal relaxation time 'τ' decreases lightly with angle up to 55^0 with unique axis of the crystal and then decreases. The angle dependent thermal relaxation time curves follow the reciprocal nature of V_D as $\tau \propto 3K/C_V V_D^2$. It is clear that thermal relaxation time for Mg_3TH_7 (T= Mn, Tc, Re) complex hydrides is mainly affected by the thermal conductivity. For hexagonal structured material τ is of the order at picosecond to femtosecond [20, 21]. Hence the calculated 'τ' justifies the hexagonal structure of transition metal disilicides. The minimum 'τ' for wave propagation along θ = 55^0 implies that the re-establishment time for the equilibrium distribution of thermal phonons will be minimum for propagation of wave along this direction.

IV. CONCLUSION

Based on the above conversation is valuable to state that:

- The principle established on simple interaction potential model remains valid for calculating higher-order elastic coefficients for hexagonally structured complex hydrides.
- At room temperature, Mg_3ReH_7 shows better mechanical properties that Mg_3MnH_7 due to larger values of stiffness and elastic constants.
- Higher order elastic constants and density for these ternary complex hydrides are mainly the affecting factor for anomalous behaviour of ultrasonic velocities.

- Mg_3TH_7 (T= Mn, Tc, Re) complex hydrides, the thermal relaxation time is found to be of the order of pico- seconds, which defends their hexagonal structure. As 'τ' has smallest value along θ = 55^0 the time for re-establishment of equilibrium distribution of phonons, will be minimum, for the wave propagation in this direction

Study can be beneficial for the processing and non-destructive characterization of ternary complex hydrides. These results will provide a ground for investigating the major thermophysical properties in the field of other ternary complex hydrides.

V. REFERENCES

[1]. C. Liu, S. Zhang, Sh. Zhang, P. Wang, H. Tian, 'Structure, Electronic Characteristic and Thermodynamic Properties of K2ZnH4 Hydride Crystal: A First-Principles Study, Journal of Alloys and Compounds, 549, 30 – 37 (2013).

[2]. M. Bououdina, D. Grant, G. Walker, Review on Hydrogen Absorbing Materials – Structure, Microstructure, and Thermodynamic Properties, International Journal of Hydrogen Energy, 31(2),177–182 (2006).

[3]. B. Sakintuna, F. Lamari-Darkrim, M. Hirscher, Metal Hybride Materials for Solid Hydrogen Storage: A Review, International Journal of Hydrogen Energy, 32(9)1121–1140 (2007).

[4]. S.F. Matar, M. Nakhl and M. Zakhour, 'Electronic Structure and Bonding of the Hybrides Mg3TH7 (T=Mn, Re) from First Principles', Solid State Sciences, Vol. 14, N°5, pp. 639–643, 2012.

[5]. M. Bortz, B. Bertheville, K. Yvon, E. R. Movlaev, N. Verbetsky, F. Fauth, Containing the First Dridomanganese (I) Complex, Journal of Alloys and Compounds, 279 (2) L8–L10 (1990).

[6]. B. Huang, K. Yvon, P. Fischer, Trimagnesium Thenium (I) Heptahybride, Mg3ReH7, Containing octahedral ReH6]5- Complex Anions,

Journal of Alloys and Compounds, 197 (1) 97–99 (1993).

[7]. P. K. Yadawa, Acoustic wave propagation in Ni3 R (R = Mo, Nb, Ta) compounds, Pramana 76 (4), 613-619 (2011).

[8]. D. K. Pandey, P. K. Yadawa, R. R. Yadav, Ultrasonic properties of hexagonal ZnS at nanoscale, Mater. Lett. 61 5194–5198 (2007).

[9]. W. Voigt, Lehrbuch der kristallphysik (mitausschluss der kristalloptik) (Leipzig Berlin, B.G. Teubner) (1928).

[10]. A. Z. Reuss, ang. Math. Und Mech. 9 49 A Reuss (1929) Berechnung der Fliessgrenze von Mischkristallen auf Grund der Plastizitätsbedingung für Einkristalle. ZAMM – Journal of Applied Mathematics and Mechanics/Zeitschrift für Angewandte Mathematik und Mechanik, 9, 49–58 (1929).

[11]. R. Hill, The elastic behaviour of a crystalline aggregate, Proc. Phys. Soc., A. 65, 349–354(1952).

[12]. N. Yadav, S. P. Singh, A. K. Maddheshiya, P. K. Yadawa, R. R. Yadav, Mechanical and thermophysical properties of high-temperature IrxRe1–x alloys. Phase Transitions, 93, 883-894 (2020).

[13]. S. P. Singh, P. K. Yadawa, P. K. Dhawan, A. K. Verma, R. R. Yadav, Effect of pressure and electrical resistivity on ultrasonic properties of MgB2 single crystal at low temperatures, Cryogenics, 100, 105-108 (2019).

[14]. K. Benyelloul, Y. Bouhadda, M. Bououdina, N. Fenineche, H. Aourag, H. Faraoun, Structural, electronic, optical and elastic properties of Mg3TH7 (T= Mn, Tc, Re) complex hydrides: First principles calculations, Revue des Energies Renouvelables, 18 (4) 611-631 (2015).

[15]. N. Turkdal, E. Deligoz, H. Ozisik, H. B. Ozisik, First-principles studies of the structural, elastic, and lattice dynamical properties of ZrMo2 and HfMo2. Ph Transit., 90, 598–609 (2017).

[16]. P. F. Weck, E. Kim, V. Tikare, J. A. Mitchell, Mechanical properties of zirconium alloys and zirconium hydrides predicted from density functional perturbation theory, Dalton Trans., 44, 8769–18779(2015).

[17]. D. Singh, D. K. Pandey, P. K. Yadawa, A. K. Yadav, Attenuation of ultrasonic waves in V, Nb and Ta at low temperatures, Cryogenics, 49, 12-16 (2009).

[18]. S. P. Singh, G. Singh, A. K. Verma, P. K. Yadawa, R. R. Yadav, Ultrasonic wave propagation in thermoelectric ZrX2 (X= S, Se) compounds, Pramana-J. Phys., 93, 83 (2019).

[19]. P. K. Yadawa, Computational Study of Ultrasonic Parameters of Hexagonal Close-Packed Transition Metals Fe, Co, and Ni. The Arabian Journal for Science and Engineering, 37, 255 (2012).

[20]. A. K. Jaiswal, P. K. Yadawa, R. R. Yadav, Ultrasonic wave propagation in ternary intermetallic CeCuGe compound, Ultrasonics, 89, 22-25 (2018).

[21]. P. K. Yadawa, Ultrasonic characterization of ceramic material titanium diboride. Ceramics-Silikaty, 55, 127-133 (2011).

Preparation and Luminescence Characteristics of Eu2+ Doped SrAL₂B₂O₇ Ceramic Phosphor

R. S. Palaspagar

Department of Physics, Shivramji Moghe College, Kelapur (Pandharkawada), Maharashtra, India

ABSTRACT

Preparation of Eu^{2+} ions activated strontium alumino-borate phosphor using the low cost and time saving combustion technique has been described. Powder X-ray diffraction (XRD) and field effect scanning electron microscope (FE-SEM) analysis were used to characterize the as prepared phosphor. The luminescence properties have been investigated by photoluminescence (PL) spectra. $Sr_xAl_2B_2O_7:xEu^{2+}$ phosphor shows a stronger excitation band near 400 nm as well as enhanced blue emissions observed under 397 nm excitation wavelength. Optimum concentration and critical transfer distance of the synthesized phosphors were determined.

Keywords: Alumino-Borate, Combustion Synthesis, Photoluminescence.

I. INTRODUCTION

Blue light emitting diodes (LEDs), phosphor-converted white LEDs (pc-WLEDs) have attracted extensive research and commercial interest due to their superior characteristics over traditional light emitting devices, such as high luminescence efficiency, long lifetime, energy-saving and environmental friendliness [1, 2]. White LEDs can be generated using two different methods, one of which is through the combination of a 450–470 nm blue InGaN chip and a yellowish phosphor coating [3]. However, the resulting white LEDs create problems, such as having a low color-rendering index (CRI), low luminous efficiency, and high color temperature [4,5]. Currently, the single-phase white light emitting phosphors pumped by UV chips present great potential with advantages of high color rendering indexes, low cost, and small color aberration [6]. Recently, alkaline earth metal (M) dialuminodiborates

$(MAl_2B_2O_7)$ have gained much attention as hosts for phosphor materials with better crystallinity, lower synthetic temperature and higher radiant efficiency, as compared to the corresponding other borates or aluminates host. In particular, Eu^{2+} ion is unique as an activator since its broad band $4f^65d^1 \rightarrow 4f^7$ transition is parity-allowed and its radiative lifetime is relatively short and most interestingly, its emission is strongly dependent on the type of host, with possible emission wavelengths (λ_{em}) ranging from ultraviolet to red spectral region [7]. However, the luminescent properties of Eu^{2+} doped strontium aluminate phosphors have been studied extensively because they show anomalous long phosphorescence and short-time decay depending on the conditions of preparation [8, 9]. Lucus et. al. was firstly reported non-linear optical behavior of $SrAl_2B_2O_7$ material; also, the rhombohedra structure of $SrAl_2B_2O_7$ is described from the $(BO_3)_\infty$ planes perpendicular to the

original axis being linked alternatively by Al–O–Al bridges and Sr atoms [10,11].

Motivated by the investigations described above, we were encouraged to synthesis by solution combustion technique and study the effect of host compositions on the luminescent properties for $SrAl_2B_2O_7:Eu^{2+}$ by systematically substituting Sr^{2+} in the host lattice.

II. METHODS AND MATERIAL

The powder samples of $Sr_{1-x}Al_2B_2O_7:xEu^{2+}$ (x = 0.01, 0.03, 0.05, 0.06, 0.07) were prepared by a solution combustion technique which is described earlier [12, 13]. The stoichiometric amounts of high purity starting materials, $Sr(NO_3)_2$ (A.R.), $Al(NO_3)_3.9H_2O$ (A.R.), Eu_2O_3, (high purity 99.9%), H_3BO_3 (A.R.), $CO(NH_2)_2$ (A.R.) have been used for phosphor preparation. The stoichiometric amounts of the ingredients were thoroughly mixed in an agate mortar, adding little amount of de-ionized water to obtain an aqueous homogeneous solution. The aqueous solution was then transferred into a china basin and slowly heated at lower temperature of 70°C in order to remove the excess water. The solution was then introduced into a preheated muffle furnace maintained at 550°C. The solution boils foams and ignites to burn with flame; a voluminous, foamy powder was obtained. The entire combustion process was over in about 5 min. Following the combustion, the resulting fine powders were annealed in a carbon reducing atmosphere at temperature 850°C for 90 min. and suddenly cooled to room temperature. The prepared materials were characterized by powder XRD and FE-SEM. Powder X-ray diffraction measurements were taken on Rigaku Miniflex II X-ray Diffractometer and compared with the ICDD files. Surface morphology of the calcined particles was observed by scanning electron microscopy (FE-SEM). PL & PLE measurements at room temperature were performed on Hitachi F-7000 spectroflurometer with spectral resolution of 2.5 nm.

III. RESULTS AND DISCUSSION

3.1 X-ray Diffraction Pattern

Fig. 1 shows the XRD pattern of $Sr_{0.95}Al_2B_2O_7:0.05Eu^{2+}$ phosphor. All the peaks of the synthesized phosphors can be indexed and there were some high intensity peaks observed because of increased in the crystallinity of the sample. The $Sr_{0.95}Al_2B_2O_7:0.05Eu^{2+}$ phosphor was consistent with the ICDD file [01-089-9063], which belongs to rhombohedral structure with space group of R32 (155). Due to the difference of the ion sizes and valence states between Eu^{2+} (0.125 nm), Sr^{2+} (0.126 nm) and Al^{3+} (0.054 nm), Eu^{2+} ions are expected to substitute for the place of Sr^{2+} in $SrAl_2B_2O_7$ lattice [14].
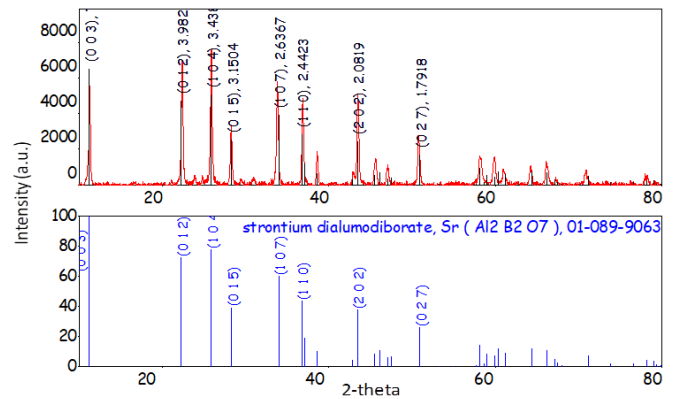
Fig. 1. X-ray diffraction patterns of the $Sr_{0.95}Al_2B_2O_7:0.05Eu^{2+}$ phosphors.

3.2 FE-SEM micrographs of phosphor powders

The FE-SEM photographs of $Sr_{0.95}Al_2B_2O_7:0.05Eu^{2+}$ powder prepared by solution combustion method are as shown in Fig. 2. The shape of the particles was observed to be rod like structure with agglomerate phenomenon for both the phosphors.

Fig. 2. FE-SEM image of $Sr_{0.95}Al_2B_2O_7:0.05Eu^{2+}$

3.3 Photoluminescence analysis of SrAl2B2O7: Eu2+

Fig. 3 shows the excitation and emission spectra of $Sr_{0.95}Al_2B_2O_7: {}_{0.05}Eu^{2+}$ phosphor. When monitoring the emission wavelength at 415 nm, the excitation spectrum of the $Sr_{0.95}Al_2B_2O_7: {}_{0.05}Eu^{2+}$ phosphor exhibited a wide band in the UV region centered at 350 nm and originating from the $4f^7 \rightarrow 4f^6 5d^1$ transition of the Eu^{2+}. Thus, it is an efficient phosphor, which can be excited by UV InGaN chips (∼400 nm). The emission spectra of $Sr_{1-x}Al_2B_2O_7:xEu^{2+}$ phosphors with different Eu^{2+} doping ratios are shown in Fig. 4. The luminescence intensities of the $Sr_{1-x}Al_2B_2O_7:xEu^{2+}$ phosphors were enhanced with increasing Eu^{2+} doping ratio and reached maximum at x = 5 mole %. When the Eu^{2+} doping ratio was above optimum concentration, the phosphors luminescence intensity reduced continually, which can be ascribed to the concentration quenching of Eu^{2+}. This quenching process often attributes to energy migration among Eu^{2+} ions, because an over-doping concentration, the non-radiative relaxation between the neighboring Eu^{2+} ions will enhance. The CIE color-coordinate parameters of $Sr_{1-x}Al_2B_2O_7:xEu^{2+}$ phosphors are shown in Table 1, which shows that (x, y) coordinates vary from (0.164, 0.030) to (0.163, 0.031). The CIE results also indicate that the hues of the $Sr_{0.99}Al_2B_2O_7:{}_{0.01}Eu^{2+}$ phosphors are closer to that of white light.
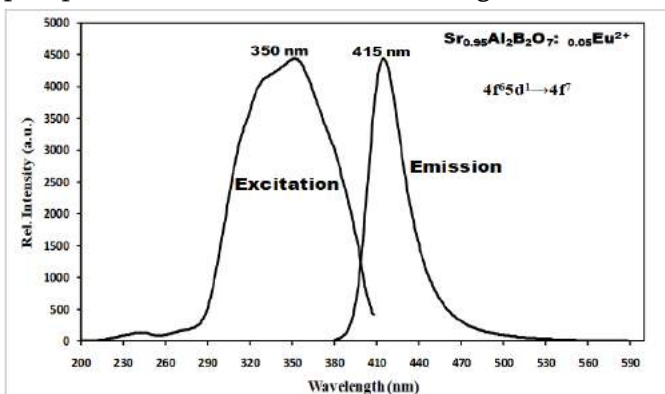
Fig. 3. Excitation (λ_{em} = 415 nm) and emission (λ_{ex} = 350 nm) spectra of $Sr_{0.95}Al_2B_2O_7:{}_{0.05}Eu^{2+}$ phosphor.
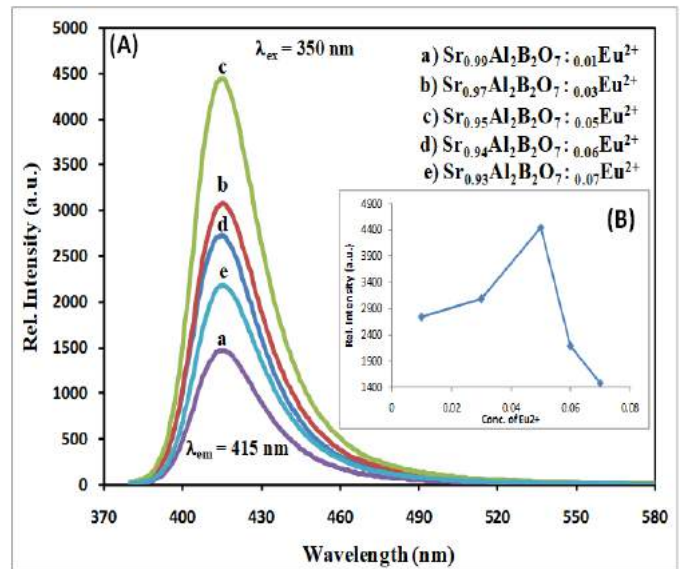
Fig. 4. (A) Emission (λ_{ex} = 350 nm) spectra of $Sr_{1-x}Al_2B_2O_7:xEu^{2+}$ phosphors. (B) Inset: The dependence of emission intensity on Eu^{2+} concentration.

The energy transfer from one activator to another generates the concentration quenching of luminescence. Blasse has pointed out that if the activator is introduced solely on Z ion sites, χ_c is the critical concentration, N is the number of Z ions in the unit cell and V is the volume of the unit cell, then there is on the average one activator ion per $V/\chi_c N$ [16]. The critical transfer distance (R_c) is approximately equal to twice the radius of a sphere with this volume:

$$R_c = 2\left[\frac{3V}{4\pi\chi_c N}\right]^{1/3} \qquad [1]$$

The critical transfer distance of the center Eu^{2+} in $SrAl_2B_2O_7:Eu^{2+}$ phosphor by taking the appropriate values of V, N, and χ_c (498.42 $Å^3$, 4, and 0.05, respectively) is 18.51Å.

A non-radiative energy transfer from one Eu^{2+} ion to another may occur by radiation re-absorption, exchange interaction, or multipole–multipole interaction [17]. The radiation re-absorption comes into effect only when there is a broad overlap of the fluorescence spectra of the sensitizer and activator in view of the emission and excitation spectra of the $SrAl_2B_2O_7:Eu^{2+}$ phosphor, this was unlikely to be occurring in this case. If the $Eu^{2+} - Eu^{2+}$ distance is larger than 3Å to 4Å, the exchange interaction

becomes ineffective, and only a multipolar interaction is important. As the R_c for $SrAl_2B_2O_7$:Eu^{2+} phosphor is shorter than 4Å, the electric multipolar–multipolar interaction is the dominant mechanism of concentration quenching. When the electric multipolar interaction is involved in the energy transfer, there are several types of interactions, such as dipole–dipole (d–d), dipole–quadrupole (d–q), quadrupole–quadrupole (q–q) interactions, and so on. Thus, there is a need to clarify which type of interaction is involved in the energy transfer. To examine the type of non-radiative energy transfer, Dexter derived a formula of emission intensity (I) per activator ion [18] as follows:

$$I/x = K[1 + \beta(x)^{Q/3}]^{-1}$$
[2]

where x is the activator concentration; Q is a constant of multipolar interaction and equals 6, 8, or 10 for dipole–dipole; dipole– quadrupole or quadrupole–quadrupole interaction, respectively; and K and β are constants under the same excitation condition for the given host crystal.

The curve of lg I/x vs. lg x in $SrAl_2B_2O_7$:Eu^{2+} phosphor is shown in Fig. 9. The figure clearly shows that the relation between lg I/x and lg x is approximately linear and the slope is about -1.08. The Q value calculated based on the linear fitting using Eq. (2) is 5.55, which is close to 6. This finding indicates that the dipole–dipole interaction is the major mechanism for the concentration quenching of the fluorescence emission of Eu^{2+} ions in $SrAl_2B_2O_7$ phosphor.
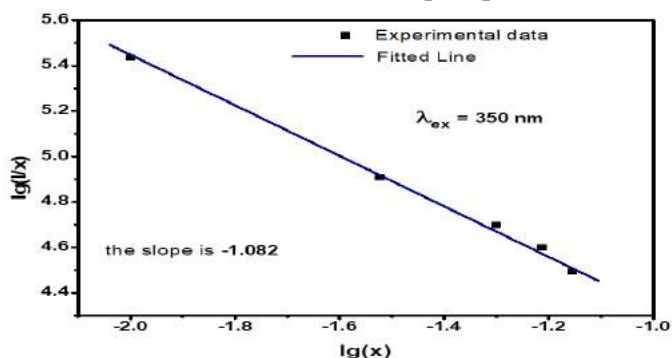
Fig. 9. Plot of lg(I/x) as function of lg(x) in $SrAl_2B_2O_7$:Eu^{2+}.

IV. CONCLUSION

In the present work, Eu^{2+} co-doped $SrAl_2B_2O_7$ phosphors have been prepared by solution combustion technique. The $SrAl_2B_2O_7$:Eu^{2+} phosphor show blue-white emissions due to Eu^{2+} d→f transitions. The PL intensity increased and an apparent red shift in emission spectrum from 415 nm (x = 0.05 mole) to 461 nm (x = 0.04 mole) was observed. The optimum doping concentration of Eu^{2+} is 5 mol%, and the concentration quenching mechanism was determined to be electric dipole-dipole interaction. The $SrAl_2B_2O_7$:Eu^{2+} phosphors may be potential blue-emitting components for UV excited w-LEDs.

V. ACKNOWLEDGEMENT

VI. REFERENCES

[1]. S Nakamura, T Mukai and M Senoh. Appl. Phys. Lett. 64 1687 (1994)

[2]. C C Lin and R S Liu. J. Phys. Chem. Lett. 2 1268 (2011)

[3]. Y X Pan, M M Wu and Q. Su. J. Phys. Chem. Solids 5 845 (2004)

[4]. J K Sheu, S J Chang, C H Kuo, Y K Su, L W Wu, Y C Lin, W C Lai, J M Tsai, G C Chi and R K Wu. IEEE Photonics Technol. Lett. 15 18 (2003)

[5]. S Neeraj, N Kijima and A K Cheetham. Chem. Phys. Lett. 387 2 (2004)

[6]. Z Lian, J Sun, L Zhang, D Shen, G Shen, X Wang and Q Yan. RSC Advances 3 16534 (2013)

[7]. K Machida, G Adachi and J Shiokawa. J. Lumin. 21 101(1979)

[8]. T Matsuzawa, Y Aoki, T Takeuchi and Y Murayama. J. Electrochem. Soc. 143 2670 (1996)

[9]. M Ashida, K Okamoto, I Ozaki, H Fukuda, K Ohmi, S Tanaka, H Kobayashi, M Hayashi and M Minamoto. Proceedings of the International Display Work-Shop' 98, Kobe 597 (1998)

[10]. F Lucas, S Jaulmes, M Quarton, T Le Mercier, F Guillen and C Fouassier. J. Solid State Chem. 150 404 (2000)

[11]. M He, X Chen, H Okudera and A Simon. Chem. Mater. 17 2193 (2005)

[12]. R S Palaspagar, A B Gawande, R P Sonekar and S K Omanwar. J. Lumin. 154 58 (2014)

[13]. R S Palaspagar, R P Sonekar and S K Omanwar. AIP Conf. Proc. 1536 895 (2013).

[14]. D Lide. CRC Press, Version 12 (2002)

[15]. C P Lin, S T Chen and T M Chen. Tamkang J. Sci. Eng. 5 81 (2002)

[16]. G Blasse, B O Bartolo (Ed.). Plenum Press, New York, USA. 463 (1978)

[17]. G. Blasse, B.C. Grabmaier, Luminescent Materials, Springer-Verlag, Berlin, 1994.

[18]. D.L. Dexter, A theory of sensitized luminescence in solids, J. Chem. Phys. 21(1953) 836–850.

Green Synthesis of Silver Nanoparticles Using Apple and Banana Peel Extract, Their Characterization and Optimization

S. S. Khandare*, M. M. Shukla, M. G. Ingale

Department of Microbiology, Bajaj College of Science, Wardha, Maharashtra, India

ABSTRACT

Since last decade, green synthesis of metal nanoparticles such as silver nanoparticles is emerging as a new path to stand against various infections. The present study aims to synthesize silver nanoparticles by a green biological route, using an extract derived from apple (AE) and banana peel waste (BPE), which acts as a reducing and capping agent for reduction of Ag^+ into Ag^0 derived from silver nitrate ($AgNO_3$) showing development of reddish-brown and yellowish-brown colour respectively. Process of synthesis was optimized using several parameters. Optimum concentration of $AgNO_3$ was found to be for AE: 1.25mM; BPE: 0.75 mM, concentration of extract for AE: 500 μl; BPE: 200 μl, pH was for AE: 9.0 and BPE: 9.0, temperature for AE: $50°C$ and BPE: $50°C$ and incubation period for AE: 96 hr; BPE: 24 hr for optimum synthesis of silver nanoparticles. Characterization of the synthesized nanoparticles with UV-Visible spectroscopy reveals a characteristic absorption of surface plasmon resonance (SPR) peak at 422 nm and 422.4 nm respectively. Fourier transform infrared spectroscopy (FT-IR) affirmed the role of AE and BPE as reducing and capping agent of silver ions.

Keywords:- Silver nanoparticles, Green synthesis, Characterization, FTIR.

I. INTRODUCTION

Nanotechnology (sometimes abbreviated to "nanotech") is the study of manipulating matter on an atomic and molecular scale. Generally, nanotechnology deals with structures sized between 1 to 100 nanometre in at least one dimension, and involves developing materials or devices within that size (Kahn et al.,2006). Nanomaterials are leading circumference of the rapidly developing field of nanotechnology. They are attracting gradually because of their unique physicochemical properties, determined by their dimensions, shape, composition and crystallinity. They were employed for the treatment of water, in catalysis, field of medicine and biotechnology etc. Among synthetic nanomaterials so far produced, the metallic nanoparticles (NPs) have distinctive properties like conduction of electricity, catalysis, high stability for chemicals and antimicrobial activities (Muzaffar and Tahir et al.,2018).Among all metal nanoparticles, Silver nanoparticles (AgNPs) are important materials that have been studied extensively, such nanoparticles possess unique electrical, optical as well as biological properties and are thus applied in catalysis, bio sensing, imaging, drug delivery, nano device fabrication and in medicine (P. K. Jain, Huang, El-Sayed, and El-Sayed et al.,2008; Nair and Laurencin et al.,2007). As Silver is a nontoxic, safe inorganic antimicrobial agent that is capable of killing about 650 types of disease causing microorganisms there is an

increasing interest in silver nanoparticles on account of the antimicrobial properties that they exhibit (Jeong, Yeo, and Yi et al.,2005). The plants or plants extract, which act as reducing and capping agents for nanoparticles synthesis, are more advantageous over supplementary biological processes since they are cost-effective, eco-friendly (Valli and Vaseeharan et al.,2012).According to the literature survey, many reports were present on biosynthesis of silver nanoparticles from plant extracts but only few reports were present on the biosynthesis of silver nanoparticles from waste plant products. The present study aims to synthesize silver nanoparticles by a green biological route, using an extract derived from banana peel waste and apple, and characterization of the synthesized nanoparticles utilizing UV-Visible spectroscopy and Fourier transform infrared spectroscopy (FT-IR) analysis.

II. METHODS AND MATERIAL

- **Preparation of Apple Extract (AE): -**
  100 g of apples measured, chopped into pieces and washed by tap water. Apple pieces were mixed up with deionized water which was heated to 75° C. Extraction was completed at a room temperature within a duration of an hour. The extract was refrigerated at 4°C for further use (Kazlagić et al., 2020).

- **Preparation of Banana Peel Extract (BPE): -**
  100 g of Banana peels were washed, boiled in deionized water for 30 minutes at 90° C. Peels were crushed in Mortar and Pestle with 100 ml deionized water and extract was filtered through cheese cloth. Filtrate was treated with chilled acetone (1:1 ratio of filtrate: acetone) and resultant precipitate was centrifuged at 1000 rpm for 5 minutes. Precipitate was resuspended in deionized water and refrigerated at 4° C for further use (Ibrahim, 2015).

- **Synthesis of silver nanoparticles using AE/BPE: -**
  The source of silver used was silver nitrate (SD Fine).Typical reaction mixtures contained 0.5 ml of AE in 4.5 ml of silver nitrate solution (1 mM in deionized water). The reaction mixture was incubated for 24 hrs. in the dark at 30°C to avoid the photo activation of silver nitrate under static conditions. AE as well as silver nitrate solution (1 mM) were used as control. Same protocol was followed for synthesis of silver nanoparticles using BPE as reducing agent and control (Ibrahim, 2015).

- **Effect of various parameters on synthesis of Silver Nanoparticle(AgNPs):-**
  The effect of the $AgNO_3$ concentration on synthesis of AgNPs was determined by varying the $AgNO_3$ concentration (0.25, 0.5, 0.75, 1.0, 1.25 mM). Similarly, the effect of AE concentration was also determined by varying its concentration (100, 200, 300, 400, 500 μl) while keeping the AgNO3 at a fixed concentration of 1.25 mM. The effect of pH was studied by adjusting the pH of the reaction mixtures to 5.0, 6.0, 7.0, 8.0 and 9.0. To study the effect of temperature on nanoparticle synthesis, the reaction mixtures containing 1.25 mM concentration of $AgNO_3$ and AE 500μl at definite pH (9.0) were incubated at 50, 60, 70, 80, 90°C for 5 min. The effect of incubation period was evaluated by incubating the reaction mixtures with optimum composition for 24, 48, 72 and 96 hr. Same protocol was followed for optimization of silver nanoparticles using BPE while keeping the AgNO3 at a fixed concentration of 0.75 mM.

- **Characterization of pre optimized and optimized Reaction mixture containing Silver Nanoparticle:-**
  The UV-Visible spectra of reaction mixtures containing AgNPs of both extracts were recorded individually. UV-Visible spectrometer (Shimadzu UV 1800) operated at resolution of 1nm with deionized water using as a blank over the range of 300-700 nm on basis of literature available. Post

optimized reaction mixtures were subjected to FTIR analysis using FTIR spectrophotometer (Bruker ATR Mode) having spectrum scanned in range of 500-4000 cm^{-1} for identification and assigning them to determine different functional groups present on the AgNPs.

III. RESULTS AND DISCUSSION

The effect of different parameters on synthesis of AE-AgNPs and BPE-AgNPs was studied. Optimum concentration of AgNO$_3$ for AE and BPE was found to be 1.25 mM and 0.75 mM respectively. Similarly, optimum concentration of extract for AE-AgNPs and BPE-AgNPs was found to be 500 μl and 200 μl respectively. Optimum pH and Temperature for both reaction mixtures were 9.0 and 50° C respectively, while optimum incubation period for synthesis of AE-AgNPs and BPE-AgNPs was found to be 96 hrs and 24 hrs respectively.

Silver nanoparticles are known to exhibit a unique optical property known as Surface Plasmon Resonance (SPR). Fig.1 (a) shows characteristic absorption peak at 444.7 nm and 471.7 nm for AE-AgNPs and BPE-AgNPs respectively.Fig.1 (b) shows characteristic absorption wavelength of 422.4 nm and 422 nm for AE-AgNPs and BPE-AgNPs respectively. FTIR measurements were also carried out to identify the major functional groups on the AE and BPE surface and their probable involvement in synthesis of silver nanoparticles. The spectra of AE-AgNPs in Fig.2 showed bands at 3319.96, 2892.06, 2118.47 and 1637.76 cm^{-1} were assigned to OH or N-H of carboxylic acid or amide, C-H stretching for CH2 and CH3 of alkane, C#C stretching of alkyne and C=O stretching of aromatic amides respectively. Similarly, BPE-AgNPs spectra in Fig.3 showed bands at 3286.90, 2118.76 and 1637.50 cm^{-1} were assigned to OH or N-H of carboxylic acid or amide, C#C stretching of alkyne, C=O stretching of aromatic amide and aliphatic amide.
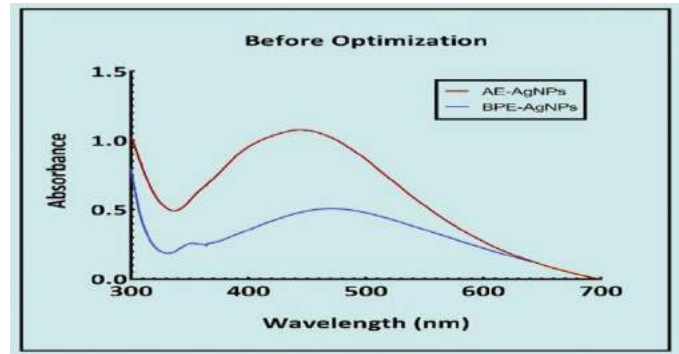
(a)
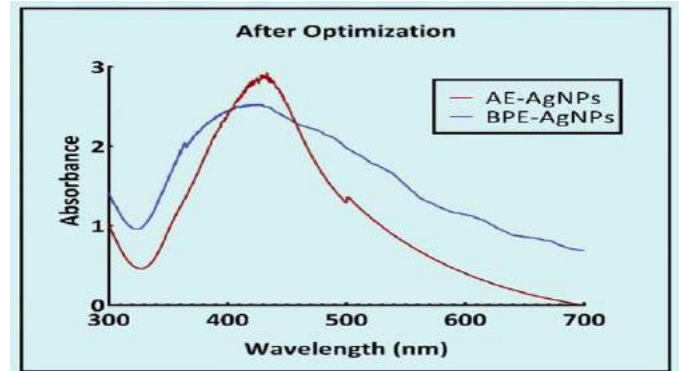
(b)

Fig.1 – UV Visible absorption spectra of apple extract-silver nanoparticles (AE-AgNPs) and banana peel extract-silver nanoparticles (BPE-AgNPs); (a) before optimization, (b) after optimization.
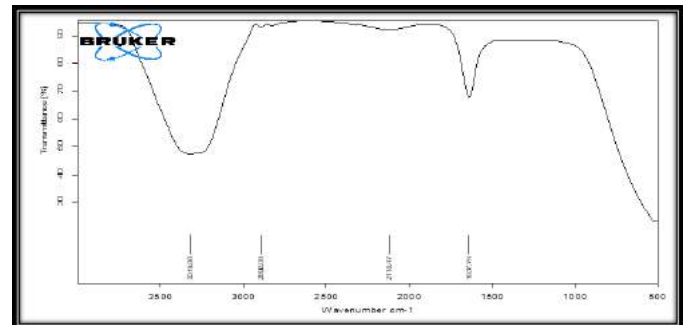
Fig.2 – FTIR spectra of AE-AgNPs after optimization
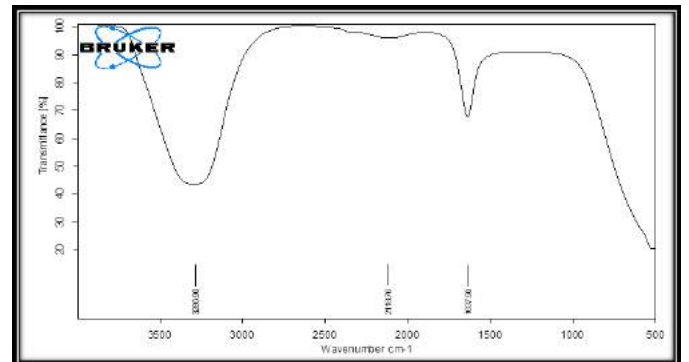
Fig.3 – FTIR spectra of BPE-AgNPs after optimization

IV. CONCLUSION

AE and BPE were successfully utilized as reducing and capping agent for the green synthesis of silver nanoparticles. Silver nanoparticles were characterized by UV-Vis spectrophotometer for confirmation of SPR which is further characterized by using FTIR spectrometer affirming role of AE and BPE as reducing and capping agent of silver ions.

V. REFERENCES

[1]. Ibrahim, H. M. (2015). Green synthesis and characterization of silver nanoparticles using banana peel extract and their antimicrobial activity against representative microorganisms.8(3), 265-275.

[2]. Jain, P. K., Huang, X., El-Sayed, I. H., & El-Sayed, M. A. J. A. o. c. r. (2008). Noble metals on the nanoscale: optical and photothermal properties and some applications in imaging, sensing, biology, and medicine. 41(12), 1578-1586.

[3]. Jeong, S. H., Yeo, S. Y., & Yi, S. C. J. J. o. M. S. (2005). The effect of filler particle size on the antibacterial properties of compounded polymer/silver fibers. 40(20), 5407-5411.

[4]. Kahn, J. J. N. G. (2006). Nano's big future. 209(6), 98-119.

[5]. Kazlagić, A., Abud, O. A., Ćibo, M., Hamidović, S., Borovac, B., & Omanović-Mikličanin, E. (2020). Green synthesis of silver nanoparticles using apple extract and its antimicrobial properties. Health and Technology, 10(1), 147-150.

[6]. Muzaffar, S., & Tahir, H. J. J. o. M. L. (2018). Enhanced synthesis of silver nanoparticles by combination of plants extract and starch for the removal of cationic dye from simulated waste water using response surface methodology. 252, 368-382.

[7]. Rai, M., Yadav, A., & Gade, A. J. B. a. (2009). Silver nanoparticles as a new generation of antimicrobials. 27(1), 76-83.

[8]. Valli, J. S., & Vaseeharan, B. J. M. L. (2012). Biosynthesis of silver nanoparticles by Cissus quadrangularis extracts. 82, 171-173.

Nanocrystalline $Mg_{0.6}Cd_{0.4}Al_2O_4$ Thick Film Gas Sensor for the Detection of LPG, CH_4, CO_2

S.V. Agnihotri [1*], V.D. Kapse [2]

[1*]Department of Physics, Amolakchand Mahavidyalaya, Yavatmal, Maharashtra, India
[2]Department of Physics, Arts, Science and Commerce College, Chikhaldara, Maharashtra, India

ABSTRACT

This paper reports that $Mg_{0.6}Cd_{0.4}Al_2O_4$ nano-powders can be used as a gas-sensing material for detecting LPG, CH_4, CO_2, gas. Powder was prepared by the co precipitation method. The powder was characterized by X-ray diffraction (XRD) and XRD pattern showed that $Mg_{0.6}Cd_{0.4}Al_2O_4$ was still cubic spinel phase with orthorhombic structure and its crystallite size is about 9.7 nm. The thick film was prepared by screen printing technology. The gas sensitivity of $Mg_{0.6}Cd_{0.4}Al_2O_4$ based sensor was investigated. The sensor exhibited high sensitivity and good selectivity towards LPG gas.

Keywords: Nanomaterial, $MgAl_2O_4$, doped $MgAl_2O_4$, X- ray diffraction, FTIR, SEM- EDS, Co precipitation, Screen printing, gas sensor.

I. INTRODUCTION

The different types of gas sensor are catalytic gas sensors, infrared gas sensors, semiconductor gas sensors, etc. The gas sensor is used for the detection of the hazardous gases in the environs. Gas sensors based on metal-oxides that are playing an important role in the detection of toxic pollutants and the control of industrial processes. Chemiresistive metal oxides are useful materials for detection of LPG, CO_2 and CH_4 due to their established advantages such as low cost, compactness and ease of implementation with integrated-circuit technology. Systematic studies have been carried out under co precipitation method. Thick and thin films are the two techniques for the fabrication of gas sensor. Thick film gas sensors based on semiconductor oxides and prepared by screen-printing technique have certain advantages over other types of gas sensors, such as low cost, simple construction, small size, and good sensing properties [1, 2, 3]. The operation of gas sensor in actual situations does the demand of analysis of the response in the presence of interfering gases. In reality the interference of mention gases is a well-known disturbance in gas detection in domestic uses. The sensing principle of semiconductor gas sensor is based on the change in the resistance of a semiconductor oxide film when specific gases interact with its surface [4]. The surface to bulk ratio is much larger than that of coarse micro-grained materials, which yields a large interface between the metal oxide and the gaseous medium. The doping concentration is increase the sensitivity of the material. The sensitivity of semiconductor oxide materials has been enhanced by reducing the particle size, and better properties have been reported for sizes in 5–50 nm range [5-7]. There are many reports available on semiconducting metal

oxide. Among these magnesium aluminate gas sensor is a potential candidates for the gas sensing device. Currently the $Mg_{0.6}Cd_{0.4}Al_2O_4$ has been prepared by coprecipitation [8], hydrothermal synthesis [9, 10], sol–gel method [11, 12]. In the present study, we report on the preparation of nanosized $Mg_{0.6}Cd_{0.4}Al_2O_4$ spinel via coprecipitation method. Characterization of the spinel was carried out by using powder X-ray diffraction, infrared spectra and scanning electron micrograph. The gas sensing properties of thick film based on the metal oxide are determined.

II. METHODS AND MATERIAL

The materials were prepared by a co precipitation method. The appropriate amounts of starting materials $Al(NO3)_2$(99.0%), $(Mg(NO_3)_2$ $6H_2O$, $Cd(NO_3)_2$ were dissolved in distilled water mixed well with each other at 80°C temperature under constant magnetic stirring, where the molar ratio of Al/Mg was 2:1. In this process, ammonia was used as precipitant. Then, the appropriate amount of aqueous ammonia solution (25 wt%) was added to the above solution and the mixture was stirred until complete precipitation occurred at a pH between 8 and 9. The precipitate was filtered, washed with distilled water and ethanol, and dried in oven at 110°C. The dry precipitate was calcinated at 800°C for 4h to obtain the $Mg_{0.6}Cd_{0.4}Al_2O_4$ nanoparticles. The $Mg_{0.6}Cd_{0.4}Al_2O_4$ sensitive layer has been prepared by screen printing technic on glass substrate. This structure underwent a subsequent annealing at 200°C for 1 hour in dry air. The sensor response was evaluated as the ratio R_{air}/R_{gas} for the n-type materials and as R_{gas}/R_{air} for the p-type. To study the sensitivity of the sensors in presence of different concentrations of LPG, CO_2, CH_4, flow of concentrated mixtures of the gases were mixed with air flow.

III. RESULTS AND DISCUSSION

3.1 Structural characterization

X-ray method are useful because they are non-destructive and do not require elaborate sample preparation. The nano-crystalline, Cd doped $MgAl_2O_4$ was characterized by XRD, at the annealed condition. Nanomaterial were amorphous became partially or fully crystalline after annealing. Peaks corresponding to the tetragonal form of $Mg_{0.6}Cd_{0.4}Al_2O_4$, the XRD patterns of the annealed catalysts with no preferred orientation or texture evident. Fig. 1 show the X-ray diffraction spectra of $Mg_{0.6}Cd_{0.4}Al_2O_4$ annealed at 800°C. It was clearly seen that the $Mg_{0.6}Cd_{0.4}Al_2O_4$ powder had cubic spinel structure. Average crystallite size was calculated using Debye Scherer formula. The average crystallite size of the prepared material is 9.7 nm. Fig.1 shows the formation of $MgAl_2O_4$ with the respective concentration of doping of Cd.
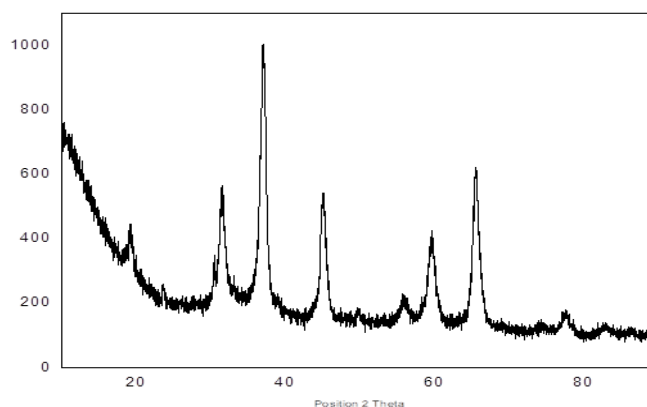
Fig.1. X-ray diffraction spectra of $Mg_{0.6}Cd_{0.4}Al_2O_4$ powder annealed at 800° c.

3.2 Fourier transforms infrared spectroscopy (FTIR)

Optical study of $Mg_{0.6}Cd_{0.4}Al_2O_4$ powder was carried out in the wavelength range 400-4000 at room temperature. Transmittance spectra recorded for the powder at 800^0c as a function of wavelength are shown in Figure (2). The large specific surface area of the powders enables the rapid adsorption of H_2O and CO_2 from the atmosphere, as evidenced by

the FT-IR spectra of the samples. The broad at $34641.87 cm^{-1}$ may be assigned to the stretching vibration of H_2O molecules, while the band from $1629.02 cm^{-1}$ band is attributed to H_2O bending. The absorption band at $2923.91 cm^{-1}$ is due to the stretching vibration of CO_2. The spiky bands, 696.26 and $510.44 cm^{-1}$ confirms the formation of normal spinel cubic structure.
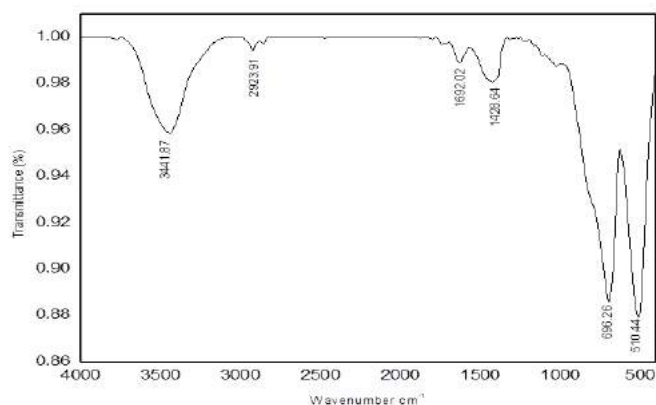
Fig. 2: FTIR Spectra of Mg0.6Cd0.4Al2O4.

3.3 Scanning Electron Microscopy with dispersive X-ray analysis (SEM-EDAX)

The SEM uses a focused beam of high-energy electrons, ranging from a few KeV to 50KeV, to generate a variety of signals at the surface of solid specimens. The SEM is also capable of performing analyses of selected point locations on the sample, this approach is especially useful in qualitatively or semi-quantitatively determining chemical compositions crystalline structure, and crystal orientations. The EDX analysis system works as an integrated feature of scanning electron microscope. An EDX spectrum normally displays peaks corresponding to the energy levels for which the most x-rays had been received. Fig.3 shows the SEM image of the thick film gas sensor. The films exhibiting a porous structure have a large fraction of atoms residing at surfaces and interfaces between the pores, which suggests that the microstructure of the films is suitable for gas-sensing purposes. The EDS spectrum of 200^0C annealed pure thick film sensor obtained is shown in fig.4. Fig. 4 shows EDS spectrum contains wt percent of MgK 8.52%, AlK 34.38% and CdK 11.62%. Spectrum reveals presence of MgO and Cd elements only. $Mg_{0.6}C_{0.4}Al_2O_4$ thick film sensor. Spectrum gives clear evidence for the presence of cadmium doped in the sample.
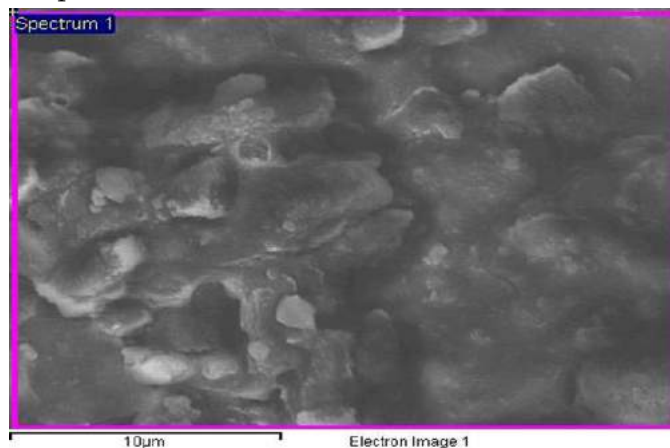
Fig. 3: SEM image of Mg0.6Cd0.4Al2O4 sensor.
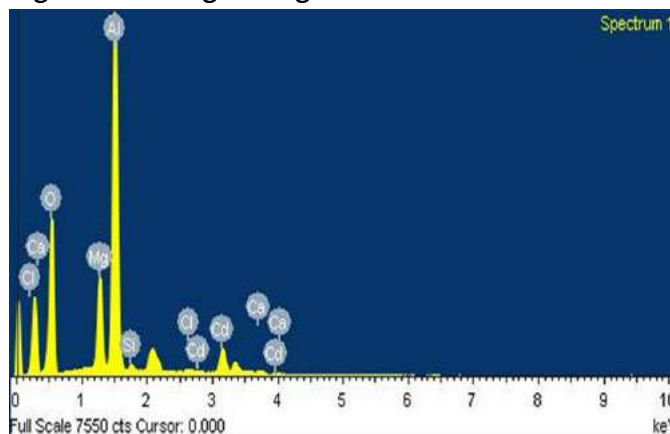
Fig. 4: EDS spectrum of $Mg_{0.6}Cd_{0.4}Al_2O_4$ thick film sensor.

3.4 Gas sensing characteristics

The morphology of the thick film catalysts were characterized by SEM. This reaction can be influenced by many factors, including internal and external causes, such as the natural properties of base materials, surface area, microstructure of sensing layers, surface additives, temperature, humidity, etc. Gas sensing characteristics of metal oxides are sensitivity, selectivity, selectivity, accuracy, speed of response, recovery time and stability.

The gas sensor performance towards LPG, CO_2, and CH_4 at operating temperature at 200ºc was examined in this study. Fig.5. shows operating temperature response to 500 ppm of LPG gas sensor based on ($Mg_{0.6}Cd_{0.4}Al_2O_4$) sample annealed at 200ºC. We can see that their sensitivity and corresponding optimal operating temperature are different. Fig.5 shows change in gas response (%) with temperature ($Mg_{0.6}Cd_{0.4}Al_2O_4$) film sensors for 500 ppm of LPG gas. The gas response initially remains very low at lower temperatures and increases with increase in temperature. With further increase in temperature, it goes on decreasing. The gas response shows a maximum which corresponds to operating temperature of the sensor film. For ($Mg_{0.6}Cd_{0.4}Al_2O_4$) thick film, the gas response is found to be 10 at an operating temperature 328K.
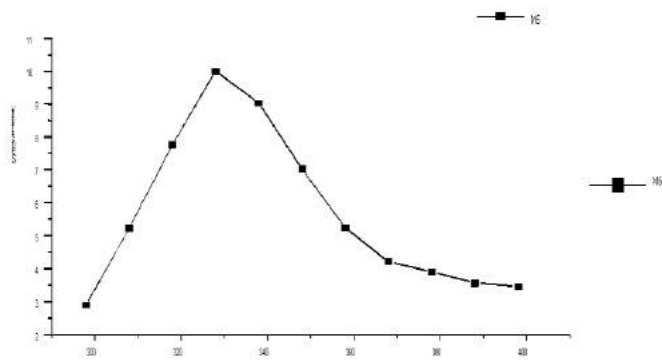
Fig.5: shows the relation between operating temperature and sensitivity.
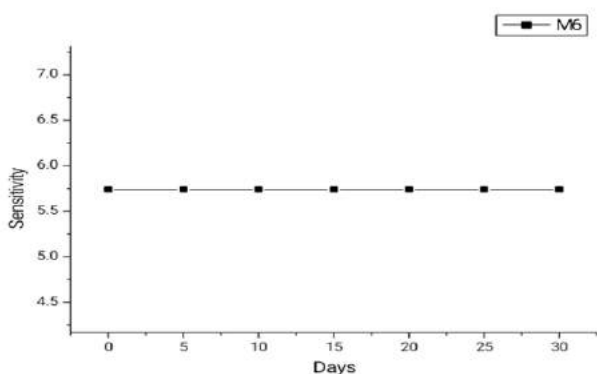
Fig.6: Long term stability curve of ($Mg_{0.6}Cd_{0.4}Al_2O_4$) based sensor.

Fig.7. shows the sensitivity of sensor at 303k temperature towards a concentration of 500 ppm. The response time is defined as the time taken by the sensor to reach 90% of maximum value and recovery time is taken as the time taken by the sensor to reach 10% of original value. The response of the sensor was measured by the R gas/ Rair. As the gas was turned-off, the response of the same film fell rapidly, indicating that the good recovery of the resistance was obtained.
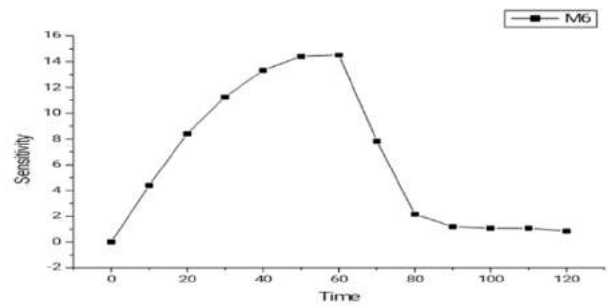
Fig.7: Response and recovery characteristics of sensor at 500 ppm LPG.

The responses of LPG, CO2, CH4 of 500 ppm at 296k is as shown in fig.8. The selectivity of the gas sensor is more than 5. The gas sensor has more response towards LPG gas.
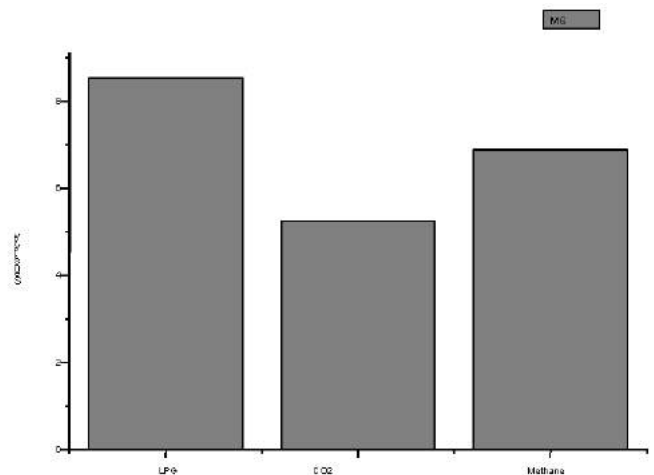
Fig.8: Gas responses to different gases at the concentration of 500 ppm.

The screen-printed sensors were tested for different gases. The choice of these sensors for LPG, CH_4 and CO_2 gas with optimum proportions. The results of the sensors when exposed to different gases at

concentrations of 0, 100, 200, 300, 400, 500, 600, 700, 800, 900 and 1000 ppm are shown in Fig.9. It can be seen that the sensors display an almost linear response over this range.
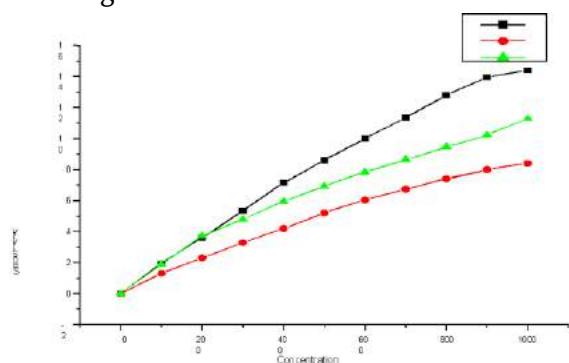
Fig.9: Curve of concentration verses sensitivity.

IV. CONCLUSION

The structural and morphological investigations have proven the nanocrystalline nature of the metal oxide powder synthesized by coprecipitation method. This method was very simple and low cost. Thick film was fabricated by screen printing technology. This can be used for the detection of the different gases in environment. LPG, CO_2, CH_4 are very important for disaster supervision purpose so that this study is quite significant. It was found that synthesized $Mg_{0.6}Cd_{0.4}Al_2O_4$ based thick film works as a sensor at room temperature. The value of sensitivity of sensor was 10 for LPG gas. The sensor was 90% reproducible. Thus the experimental results demonstrate that nanosized $Mg_{0.6}Cd_{0.4}Al_2O_4$ thick film is appropriate promising material for the LPG sensing.

V. ACKNOWLEDGEMENTS

VI. REFERENCES

[1]. W. Noh, Y. Shin, J. Kim, W. Lee, K. Hong, S.A. Akbar, J. Park, Solid State Ionics 152-153 (2002) 827–832.

[2]. M. C. Carotta, G. Martinelli, Y. Sadaoka, P. Nunziante, E. Traversa, Sens. Actuat., B Chem. 48 (1998) 270–276.

[3]. V. Guidi, M. A. Butturi, M. C. Carotta, B. Cavicchi, M. Ferroni, C. Malagu, G. Martinelli, D. Vincenzi, M. Sacerdoti, M. Zen, Sens. Actuat. B Chem. 84 (2002) 72–77.

[4]. M .J. Madou, S.R. Morrison, Academic Press, San Diego, (1999).

[5]. C. Xu, J. Tamaki, N. Miura, N. Yamazoe, Sens. Actuat. B 3(1991) 147–155.

[6]. N. Yamazoe, Sens. Actuat. B 5 (1991) 7–19.

[7]. Y. Shimizu, M. Egashira, MRS Bulletin, June (1999), pp. 18–24.

[8]. G. Aguilar-Rios, M. Valenzuela, P. Salas, H. Armendariz, P. Bosch, G. Del Toro, R. Silva, V. Bertin, S. Castillo, A. Ramirez-Solis, I. Schifter, Appl. Catal. A Gen. 127 (1995) 65–75.

[9]. J. Wrzyszcz, M. Zawadzki, J. Trawczy'nski, H. Grabowska, W. Mi'sta, Appl. Catal. A Gen. 210 (2001) 263–269.

[10]. M. Zawadzki, J. Wrzyszcz, Mater. Res. Bull. 35 (2000) 109–114.

[11]. A. R. Phani, M. Passacantando, S. Santucci, Mater. Chem. Phys. 68 (2001) 66-71.

[12]. C.O. Arean, B.S. Sintes, G.T. Palomino, C.M. Carbonell, E.E. Platero, J.B. P. Soto, Microporous Mater. 8 (1997) 187.

Simple Route Synthesis of 3-Cynocoumarin by Knoevengel Condensation of Benzaldehyde with Ethyl Cynoacetate over Si-Al-MCM-41

Manish R. Deshpande*[1], Mukund Joshi[2]

[1]Department of Physics and Material Science, N. S. B. College, Nanded, Maharashtra, India

[2]Yogeshwari Mahavidyalaya, Ambejogai, Maharashtra, India

ABSTRACT

The objective of the present study is to provide Si-Al-MCM-41 as catalyst for the Knoevengel condensation of benzaldehyde with ethyl cynoacetate. Aluminum was dopped in MCM-41 via ion exchange method and the catalytic performances of the samples were investigated for an efficient, high-yielding, one-pot synthesis of 3-cynocoumarine. The influence of aluminum loading on the basic properties of MCM-41 was also studied.

Keywords : MCM-41, Si-Al-MCM-41, Knoevengel condensation reaction, 3-cynocoumarin, solid base catalyst

I. INTRODUCTION

Porous solid can be defined in wide logic as a solid material, which includes pores, i.e. cavities, channels or interstices, which are deeper than they are wide.

According to IUPAC definition, porous materials may be divided into three types based on their pore dimensions[1]:

Type	Pore Size (nm)
Microporous	< 2
Mesoporous	2-50
Macroporous	> 50

Recognized microporous materials are zeolites and aluminophosphate molecular sieves which are inorganic composites having a crystalline three-dimensional framework woven with tetrahedral atoms (T-atoms) like aluminium, silicon, phosphorous etc. bridged by oxygen atoms.

Mesoporous materials[2-5] are like ordinary porous materials except the pore sizes are in the range of 2-50 nm and generally arranged in a uniform array.

Different types of mesoporous materials have been reported in the literature, such as silicas, pillared clays and other silicates.

The synthesis of amorphous silica-alumina in the presence of quaternary salts has also been reported, where the average pore diameter was related to the size of the tetra alkyl ammonium cations.

In 1992 researchers at Mobil Research and Development Corporation reported the synthesis of a novel family[4-7] of silicate/aluminosilicate mesoporous molecular sieves (M41S) with exceptionally large uniform pore structures[5,6].

There was an escalating demand for well-structured mesoporous molecular sieves with pores of uniform diameter. Even if, there exists large number of different mesoporous materials. Discussion is constrained to silica based mesoporous molecular sieves Si-MCM41 work presented in this paper.

The Knoevenagel condensation reaction is an important C–C bond forming reaction commonly used for the production of fine chemical intermediates and

products (e.g. coumarin derivatives) as well as pharmaceuticals (e.g. nifendipine and nitrendipine derivatives for hypertension drugs).

The reaction involves the condensation of methylene compounds (i.e., R-CH2–R' or R–CHR'–R") with ketones or aldehydes[7].

3-Cyanocoumarins have achieved gigantic importance in recent years as they are required for synthesis of methane dyes.

3-carboxycoumarins, which are used for synthesis of cephalosporins4, modified penicillin, oxygen bridged tetrahydropyridones, isourases, etc.

The amide obtained from 3-cyanocoumarines exhibit specific inhibitor of α-chymotripsin, human leukocytic elastase and polymeric compounds of biological importance.

II. METHODS AND MATERIAL

2.1 Chemicals:

Cetyltrimethyl ammonium bromide (CTAB, Spectrochem), Aqueous ammonia (25 wt. %, Fisher Scientific), Tetraethyl orthosilicate (TEOS, Aldrich), Cesium chloride (loba, chemie), Dimethyl sulpoxide (DMSO, Fisher Scientific), Salicyaldehyde (Merck), Ethylcynoacetate (ECA, S.D. fine chemicals). All chemicals were AR grade hence they were used without further purification. Syntheses were carried out at room temperature.

2.2 Catalyst Synthesis:

The mesoporous silica, MCM 41 was synthesized by hydrothermal method followed by post modification, ion exchange of cesium transition metal ion.

In the typical synthesis, CTAB is dissolved in double distilled water. In this solution a fixed amount of 9.60 g of aqueous ammonia was added. Further 10.3 g of tetraethyl orthosilicate was supplemented bit by bit under vigorous stirring to get white precipitate.

The molar composition of the resultant gel was

1TEOS: 0.152CTAB: 2.8NH₃: 141.2H₂O.

This gel was stirred for 2 hr in the autoclave at 100⁰C then after it was filtered and washed several times.

The obtained filtered lump was desiccated at 100⁰C for 10 hr. In temperature control furnace the obtained power was calcined at 550⁰C for 4.5 hr at the rate of 1⁰C/min to drive out the template.

The parent synthesized Si-MCM-41 was transformed to the H⁺ form through NH₄⁺ ion exchange and ensuing calcination. Approximately 4.5 gm of Si-MCM-41was placed in 100ml of 2.5 wt % NH₄NO₃ aqueous solution.

After being refluxed for 5 hr at 300⁰C, the solution filtered, the obtained filter cake was dried at 100⁰C for 10 hr. The NH₄ ion exchanged Si-MCM-41 was calcined in air at 500⁰C for 5 hr.

The H⁺ form of Si-MCM-41 thus obtained was ion exchanged using aqueous solution of Aluminum chloride. Al⁺⁺⁺ ion exchanged MCM-41 (Si-Al-MCM-41) catalyst were prepared by dissolving Aluminum chloride and H⁺-MCM-41 in double distilled water, which is heated at 100⁰C for 5 hr.

The solid was filtered and dried overnight at 100⁰C in air followed by calcination. The three different catalyst were prepared with three different weight percentage such as 2wt% Si-Al-MCM-41, 4wt% Si-Al-MCM-41 and 6wt% Si-Al-MCM-41.

2.3 Charactrization:

a) BET surface area: Specific BET surface area was calculated using Surface area Analyser Model SAA-2000 for all synthesized samples.

b) FI-IR: Fourier transform infra-red spectra were recorded on Bruker ALPHA FT-IR spectrometer.

c) c) Power X-ray diffraction: The powder patterns were obtained using Cu Kα radiation on a Rigakau diffractometer. The samples were scanned for 2θ from 1 to 10⁰

2.4 Catalytic reaction:

All the catalytic reactions were carried out in a RBF with a magnetic stirrer immersed in a oil bath. Before the reaction, the required quantity of catalyst i. e. Si-Al-MCM-41 was heated in the muffle furnace at 100⁰C for 2 hr so as to evaporate the moisture adsorbed by the catalyst.

In a typical experiment, 9.50 mol of Benzaldehyde, 9.50 mol of ethyl cynoacetate (ECA) and 30 ml of dimethyl sulphoxide (DMSO) were charged in the RBF.

The reaction was maintained at temperatures 100^0C under atmospheric pressure. After attaining the desired reaction temperature, 0.5 g of dried catalyst was rapidly added in the reactor and the reaction was started.

The reactions were carried out for diverse time durations. The progress of reaction was examined by the thin layer chromatography (TLC) on Merck silica plates using ethyl acetate : petroleum ether (1:1) as eluent. TLC was taken after every 10 minutes.

After reaction completion the reaction content were cooled to room temperature by natural convection. Then the catalyst was separated by filtration and washed with distilled water for several times followed by drying in air at 100^0C.

After separating the catalyst from the reaction content, reaction mixture was poured on the crushed ice, stirred with glass rod for 10 min and filtered to obtain product which was then purified by crystallization with ethanol.

III. RESULTS AND DISCUSSION

3.1 Charactrization of catalyst:

The XRD patterns of the calcined parent MCM-41, H-MCM-41 and Si-Al-MCM-41 samples with different wt.% of Al (2wt.%, 4wt.% and 6wt.%) respectively are presented in Figure1 (a, b, c, d, e) respectively.
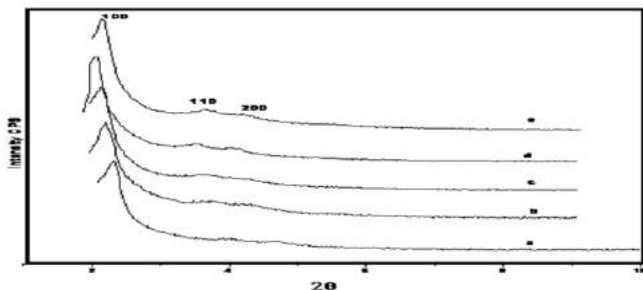
Figure1: Powder XRD Patterns of MCM-41, H-MCM-41, 2wt% Si-Al-MCM-41, 4wt% Si-Al-MCM-41 and 6wt% Si-Al-MCM-41

These XRD patterns showing three prominent reflections which can be assigned to the hexagonal lattice of the meso-porous materials. The 100, 110 and 200 are well resolved. The unit cell parameters a0 were calculated by the formula:

$$A0 = (2/\sqrt{3}) \times d100$$

The unit cell parameter and d-spacing of the MCM-41, H-MCM-41,   2wt% Si-Al-MCM-41, 4wt% Si-Al-MCM-41and 6wt% Si-Al-MCM-41 samples are given in Table 1.

The slight increase in d-spacing and unit cell parameters of Si-Al-MCM-41 compared to MCM-41 suggests the presence of Aluminum in the framework.

The increase in unit cell parameter on Al incorporation is probably due to the replacement of shorter Si-O bonds by longer Al-O bonds in the structure. It is also observed that along with an increase in the unit cell parameter, the (100) diffraction peak becomes broader and less intense with increasing cesium content, probably because of the change of the Al-O-Al bond angle due to Al incorporation, causing a distortion in the long range ordering of the hexagonal mesoporous structure.

Figure 1 illustrate that in all the modified forms MCM-41 sample, there are marginal changes in the crystallinity but almost no changes in the phase purity and structural morphology are being observed after modification with different amounts of Al+++ percentage. This indicates the structural stability of the parent sample and presence of metal ions in the intra-crystalline voids of the MCM-41.

The percent crystallinity of the samples is drawn with the amount of metal ion percent in them. However, if the 'Al' metal ion concentration in MCM-41 was 6wt%, it was 98.3% and then gradually decreased for 4wt% and 2wt% as 90.8% and 84.2% respectively.

The BET surface areas, average pore diameters calculated from N2-sorption isotherms of MCM-41 and Si-Al-MCM-41 are presented in Table 1.
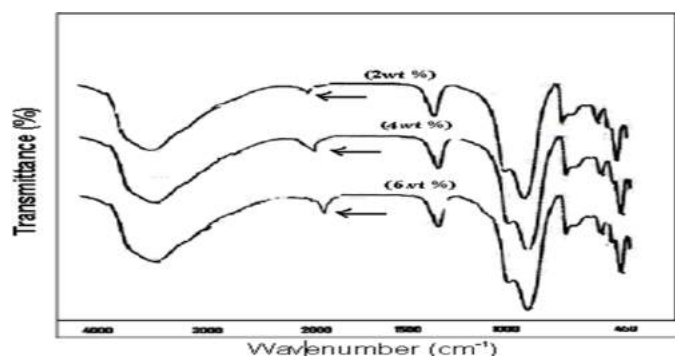
Figure 2: FT-IR of Si-Al-MCM-41

The mid-infrared region from 400-1300 cm^{-1} contains vibrations due to the framework structure of zeolites. Similarly, mesoporous molecular sieves also show series of bands that are characteristics of the SiO$_4$ tetrahedral unit and its modification by introduction of metal ions.

The FT-IR spectra of lattice vibration of calcined Si-Al-MCM-41 are presented in Figure 2. The spectra shows four main absorption bands between the regions 12oo-1250, 1050-1070, 785-830 and 425-475 cm^{-1}. FT-IR spectra exhibit a vibrational band at ~ 980 cm^{-1} which is considered as a proof for the incorporation of the heteroatom into the framework, the intensity of this band marginally increases with increase in the Al wt %.

3.2 Catalysis reaction:

The Knoevenagel condensation is of great importance to the synthetic chemists in the construction of new C–C bonds.

Here we choose the Knoevenagel reaction of Benzaldehyde with ethyl cynoacetate (Route 1) to form α,ß-unsaturated nitriles (3-cynocoumarine) as a condensation reaction to examine the catalytic performance of the obtained materials. Before the reaction the required quantity of catalyst i. e. Si-Al-MCM-41 was heated in the muffle furnace at 100⁰C for 2 hr so as to evaporate the moisture adsorbed by the catalyst.

Pure siliceous MCM-41 treated under the same condition showed no catalytic activity. Fig. 3 gives the dependency of the yields of 3-cynocoumarine on the reaction period over various Si-Al-MCM-41 materials.

No other side products except the 3-cynocoumarine were detected in the products based on TLC analysis.

All the catalysts showed rapid reaction rates in the first 150 min, after this the yields of the product only increased slightly. This might be due to the deactivation of the catalysts by adsorption of formed water.
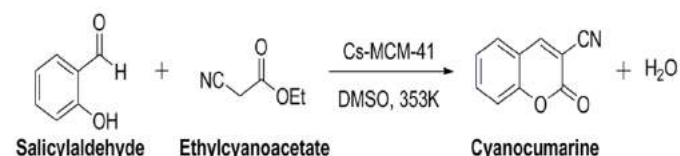
Figure 3: Knoevengel condensation of salicylaldehyde

Route 1: Synthesis of 3-Cyanocumarine

From figure 2, it is observed that percentage yield of the product increases from 78 % to 98 % with increase in cesium weight percent in parent MCM-41, it is may be due to increase in the basic site.

Reaction was completed in almost 150 min beyond that % yield increases slightly. The product, 3-cynocoumarin was confirmed by FT-IR where the peak at 2240 cm-1 corresponds to cyno-group and peak at 1790 cm-1 corresponds to carboxyl group of the product.
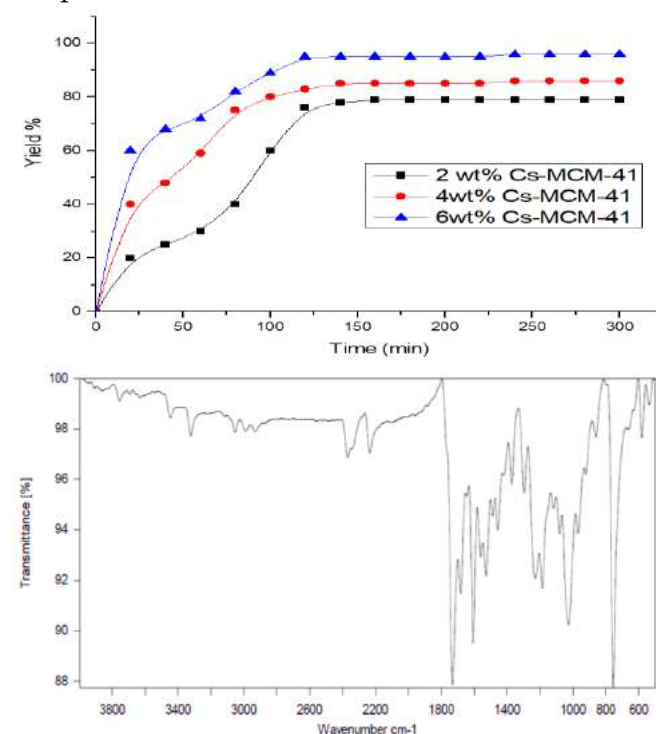
Figure 4: FT-IR of 3-cynocoumarin

IV.CONCLUSION

Highly ordered hexagonal MCM-41 and Si-Al-MCM-41 were synthesized. The synthesis of 3-cynocoumarin *via* Knoevenagel condensation over a recoverable, ordered hexagonal Si-Al-MCM-41 solid base catalyst, is reported within a short period of time *i.e.* 150 min and at lower temperature *i.e.* 100^{0}C in liquid phase.

This method produces substituted coumarins in very high yields (98%) These findings suggest that Si-Al-MCM-41 is a good candidate for the Knoevengel condensation of salicylaldehyde with ethyl cynoacetate.

Table 1: Physico-chemical properties of MCM-41

Sample Name	d_{100} spacing(nm)	Unit cell parameter a_0 (nm)	Spe. Surface area (m^2g^{-1})	Pore diameter (nm)	Particle size (nm)	% crystalinity
MCM-41	3.80	4.32	1034.0	2.7	0.21	100
H-MCM-41	3.84	4.39	1057.8	2.76	0.20	99
2wt% Si-Al-MCM-41	4.01	4.63	949.9	2.22	0.32	84
4wt% Si-Al-MCM-41	4.02	4.72	1062.4	2.27	0.21	90
6wt% Si-Al-MCM-41	4.04	4.78	1099.1	2.4	0.26	98

V. REFERENCES

[1]. A. Monnier, F. Schtlth, Q. Huo, D. Kumar, D. Margolese, R.S. Maxwell, G.D. Stucky, M. Krishnamurty, P. Petroff, A. Firouzi, M. Janicke, B.F. Chmeka, Science 261, 1993, 1299

[2]. Behrens, P. Adv. Mater. 1993, 5, 127.

[3]. J.S. Beck, J.C. Vartuli, W.J. Roth, M.E. Leonowicz, C.T. Kresge, K.D. Schmitt, C.T.W. Chu, D.H. Olson, E.W. Sheppard, S.B. McCullen, J.B. Higgins, J.L. Schlenker, J. Am. Chem. Sot. 114, 1992, 10834

[4]. J.S. Beck, J.C. Vartuli, G.J.Kennedy, C.T. Kresge, W.J. Roth, S.E.Schramn, Chem. Mat. 1994,6,1816

[5]. J.C. Vartuli, K.D. Schmitt, C.T. Kresge, W.J. Roth, M.E. Leonowicz, S.B. McCullen, S.B. McCullen, J.S. Beck, D.H. Olson, Chem. Mat. 1994,6, 2317

[6]. Y. V. Subba Rao, D. E. De Vos and P. A. Jacobs, Angew. Chem., 1997, 109, 2776

[7]. C.T. Kresge, M.E. Leonowicz, W.J. Roth, J.C. Vartuli, J.S. Beck, Nature 359, 1992, 710

Structural analysis of Lead Titanate Prepared by Wet Chemical Method

A. U. Bajpeyee, N. V. Galande*, S. H. Shamkuwar

Department of Physics, Arts, Commerce and Science College, Kiran Nagar, Amravati 444606, Maharashtra, India.

ABSTRACT

While preparing $PbTiO_3$ [usually referred as PT] nanocrystalline particles, $PbTiO_3$ was prepared from Lead Nitrate $[Pb(NO_3)_2]$ and Titanium Isopropoxide $[C_{12}H_{28}O_4Ti]$ by wet chemical technique. Thus synthesized $PbTiO_3$ nanoparticles were kept at different temperatures of 650 ° C, 700 ° C, 750° C for 4 hours. The particle size of the sample was estimated to be between 25 and 55 nm by the Scherer's formula. Also $PbTiO_3$ has been investigated using x-ray powder diffraction data to confirm the phase formations and phase purity. Also microscopic structural analysis of the sample was done using scanning electron microscopy. It showed that when the sintering temperature increases, the grain size of the particle decreases. Infrared Transmittance behavior with respect to sintering temperature of the samples sintered has been studied. The effect of sintering temperature on microstructure and other parameters have also been studied using TEM Analysis.

Keywords : Wet Chemical Route, $PbTiO_3$, XRD, FTIR, SEM, TEM.

I. INTRODUCTION

In recent years, a large number of applications based on improved lead titanate have been widely used in applications such as piezoelectric, actuators and ultrasonic transducers continuously because of its high density and optimal piezoelectric properties [1].

Materials of the perovskite family, such as $PbTiO_3$, $BaTiO_3$, and $SrTiO_3$ etc. have been of constant interest because some of these materials show ferroelectric behavior and undergo structural phase transitions [2]. $PbTiO_3$ has been considered to be one of the most important members of this family. It has a high Curie temperature, high pyroelectric coefficient, low dielectric constant, and high spontaneous polarization. Lead titanate ($PbTiO_3$), PT is a ferroelectric ceramic that has not only been proved to be a technologically important material but also it is a significant component material in electronics such as capacitors, ultrasonic transducers, thermistors, and optoelectronics [3-5].

The conventional method of synthesizing $PbTiO_3$ relies on the reaction between Lead Nitrate $[Pb(NO_3)_2]$ and Titanium Isopropoxide $[C_{12}H_{28}O_4Ti]$ at high temperature. The conventional solid-state reaction has a tendency to produce a coarse $PbTiO_3$ powder with compositional in homogeneity and a degree of particle agglomeration if the processing parameters are not carefully optimized. Therefore, many chemistry-based processing routes, including co-precipitation, sol-gel synthesis, hydrothermal and citrate routes have been devised for the preparation of an ultrafine, sintering-reactive $PbTiO_3$ powder [6-8]. However, almost all these chemistry routes require calcinations of the precursors at an elevated

temperature to develop the desired PbTiO₃ phase [9]. Furthermore, most of these chemistry-based processing routes require high purity inorganic or organ metallic chemicals as the starting materials, which are many times more expensive than the widely available oxides and carbonates. It has been observed that the synthesis of a mechanically robust, high density, monolithic ceramic pure PbTiO₃ is not simple [10]. Problems typically encountered include loss of lead (Pb) due to the volatility of PbO at elevated temperatures, porosity, and micro cracking, in extreme cases leading to spontaneous fracture. The main hurdle in the PT fabrication is the synthesis of a single phase with required perovskite structure [11-15]. The primary difficulty is due to the volatility of PbO at elevated temperatures [16]. The PbTiO₃ structure can only tolerate minor loss of lead (Pb), higher levels of which effectively promote second phase formation and the degradation of piezoelectric properties. An example is the formation of a PT phase with the pyrochlore structure observed during a coprecipitation synthesis experiment. A more common occurrence is the formation of a two-phase mixture Ti-O with Titanium Isopropoxide [C₁₂H₂₈O₄Ti] [17-20]. The volatilization of PbO is known to increase markedly at temperatures above 750°C though the critical temperature is debated. It has observed that a PbO-rich PT in liquid phase is formed above 750°C, Algueroetal found that at 650°C an excess of 20% PbO was required because of Pb-loss during thermal treatments of wet method prepared a modified PT, whereas Ananta and Thomas found that Pb volatility in PMN-PT could be minimized by careful sintering up to 750°C [21]. What is clear is that the loss of lead depends on particle size of constituent oxides, processing conditions, and chemical stability. The degree of Pb incorporation into the presintered crystal structure affects the volatility enormously. Many groups report that loss of lead (Pb) may be minimized by sintering compacted powders in a surrounding lead-based powder or a PbO vapor atmosphere although this may lead to a Pb gradient in the final sintered product. The problem of porosity has largely been addressed through particle size control of the starting powder [22]. A careful and systematic study optimization of the synthesis parameters provides an alternative means of minimizing the problem of cracking, porosity, and Pb volatility. Careful sintering at lower temperatures may restrict grain growth and on cooling internal strains are reduced. In addition, sintering at low temperatures, the problem of volatility of lead is minimized. It has been shown that homogenous powders with a fine grain size can be produced by the ceramic process on the optimization of synthesis parameters. The electrical properties result from the different contributions made from various components and processes present in the material [23].

II. METHODS AND MATERIAL

Nanocrystalline PbTiO3 powders, denoted PT, were prepared by the a solid mixture of Lead Nitrate [Pb(NO3)2], Titanium Isopropoxide [C12H28O4Ti] in liquid, and pure water stirred for 3 hr at 100o C by using the wet chemical route and first, lead nitrate was dissolved in pure water on a stirred for 1 hr at 100oC in reaction flask and then the lead nitrate was dissolved in water. When the temperature of the water reaching the oxidation and Secondly a stoichiometric amount of titanium Isopropoxide was added to the solution and the solution was refluxed at 100 °C for 3 hr. After cooling the Pb–Ti complex alkoxide solution to room temperature, a stoichiometric amount of the lead titanete. Thereby forming a PbTiO3 complex alkoxide solution.

By controlling the hydrolysis condition of the solution and adjusting the pH value of the solution about 11 during the polymerization and precipitation of metal alkoxide, the gel was then dried at a designated temperature and time. PT nanocrystalline powder

with various crystallite sizes was obtained by calcining the gel powder at different temperatures between 600 and 750 °C. Structure and phase transformation analyses were investigated by XRD using a radiation in the range of 0°–90°. The average crystallite size was calculated from the full width at half maximum of the diffraction lines using Scherrer's relation which assumes the small crystallite size causes line broadening, the diffraction peak and K the Scherrer constant.

III. RESULTS AND DISCUSSION

i) X-RAY DIFFRACTION

XRD pattern of the PbTiO$_3$ calcined at 600°C, 650°C and 700°C and 750°C is shown in Fig.1. The XRD pattern shows the integrity of the synthesized material and the formation of single phase compound. The crystallite size of the particles calcined at various temperatures could be calculated by the Scherrer's equation: t= kλ/βcosθ (where t is the average size of the particles, assuming particles are spherical, k=0.9, λ is the wavelength of X-ray radiation, β is the full width at half maximum of the diffracted peak and θ is the angle of diffraction. The average crystallite size obtained from XRD data at at 600°C, 650°C and 700°C and 750 °C were 30.875, 29.665, 25.155, 25.64 nm, respectively. The peak around 30° is getting suppressed with the elevated sintering temperature. This peak belongs to the TiO$_2$ present in the material. As sintering temperature is increased, the peak belonging to TiO$_2$ is vanished and pure phase PbTiO$_3$ is obtained. That means with increase in sintering temperature, TiO$_2$ gets attached to the PbO to form single phase crystalline PbTiO$_3$.
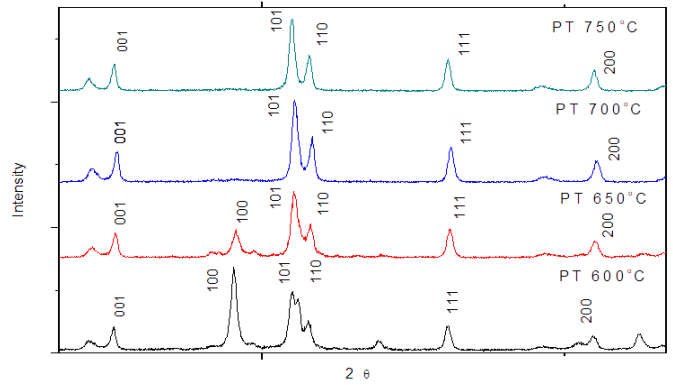
Fig 1.

Fig.2. shows the variation of c/a ratio with the sintering temperature, which clearly indicates decrease in c/a ratio along with sintering temperature. Decrease in c/a ratio indicates dispersion from tetragonality and an approach to the cubic phase with higher sintering temperature. Fig.3 shows the variation of average grain size with sintering temperature indicating decrease in average grain size with increasing sintering temperature.
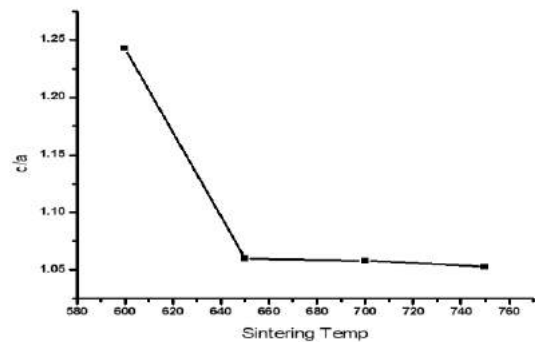
Fig. 2
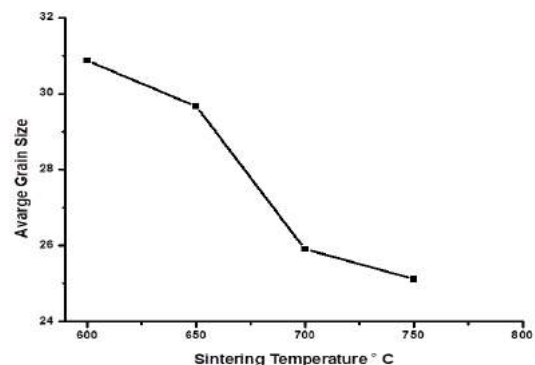
Fig. 3

ii) FTIR (Fourier transform infrared spectrum)

FTIR is a technique which is used to obtain an infrared spectrum of absorption, emission, photoconductivity or Raman scattering of a solid, liquid or gas. An FTIR spectrometer simultaneously collects high spectral resolution data over a wide spectral range. This confers a significant advantage over a dispersive spectrometer which measures intensity over a narrow range of wavelengths at a time.

Fig. (4 to 07) illustrates the FTIR spectra for $PbTiO_3$ powders derived via the wet chemical method and calcined at various temperatures ranging from 600℃, 650℃, 700℃ and 750℃ for 4 hours. The IR spectrum of the sample calcined at 650 ℃ clearly indicates the presence of Ti–O band characterized by the absorption bands at nearly 600, 700 cm. The broad band at 4000 cm was assigned to stretching vibration of weakly bound water. It was reported that absorption bands over the range of 1000–1700 cm are mainly related to the organic groups. Increasing the calcination temperature to 750℃ results in decrease in intensity of the organic absorption bands and increased intensity of the absorption Ti–O band. The organic residuals were completely eliminated when the derived powders were calcined at 650℃.

Fig.5 (Temp.650OC)

Fig.6 (Temp.700OC)

Fig.4 (Temp.600OC)
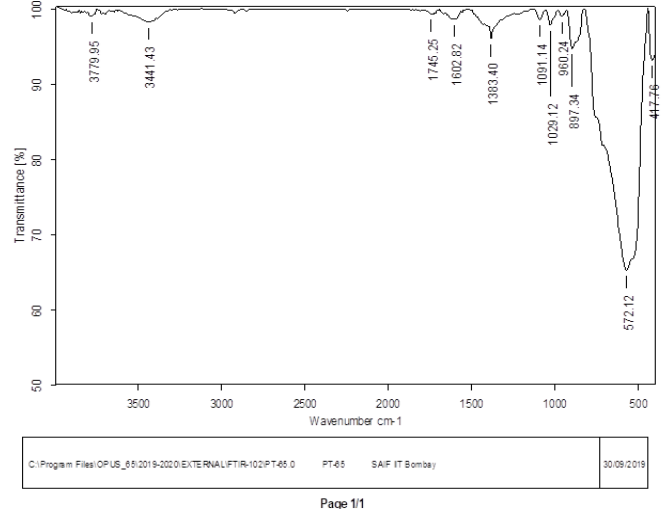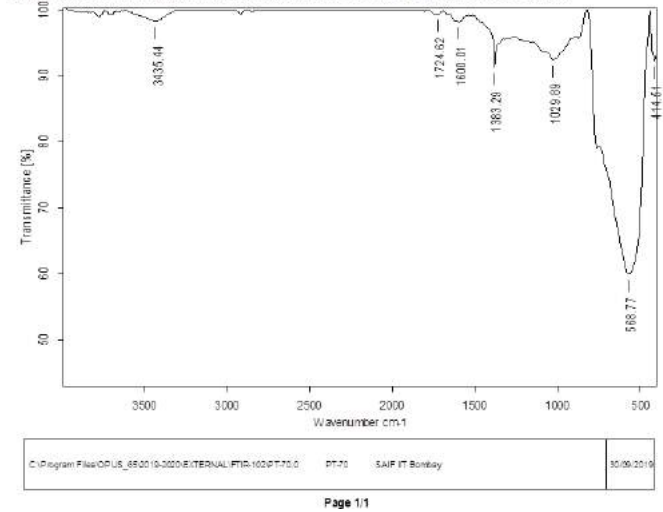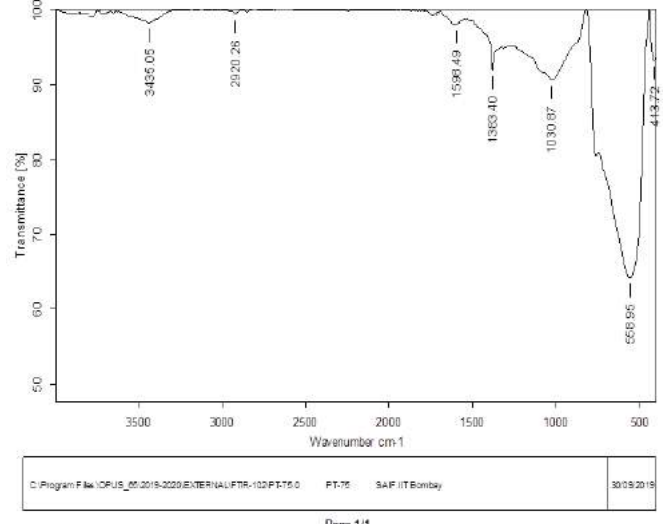
Fig.7 (Temp.750OC)

iii) SEM (scanning electron microscope)

SEM micrographs of PbTiO₃ with magnification × 100000 sintered at various temperatures have been presented in Fig.(08 to 11) It can be observed from the figure that the microstructure of the sample sintered at low temperature (600°C) is homogeneous where as the microstructure of the sample become heterogeneous at higher sintering temperatures (600°C and 750°C). It is also observed that the grain size decreases with increasing sintering temperature. Further it may be noticed that the porosity of the samples sintered at 750° C is predominately inter-granular, whereas the porosity of the samples sintered at 650°C and 750°C is located at grain boundaries and many of the very small pores disappear through diffusion kinetics as sintering temperature decreases. That's why the grain size increases and the number of grain boundary decreases and consequently the porosity decreases and results in the homogeneous grain size distribution
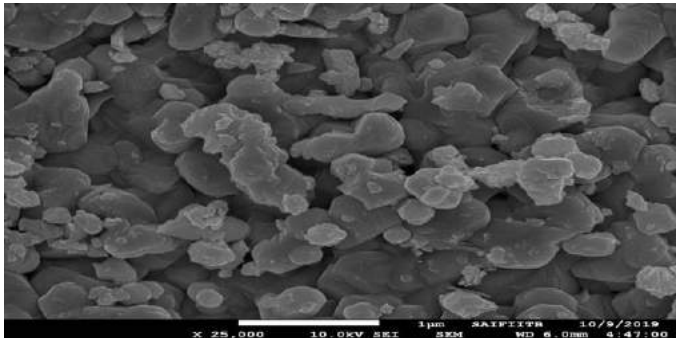
Fig.8 Temp. 600oC
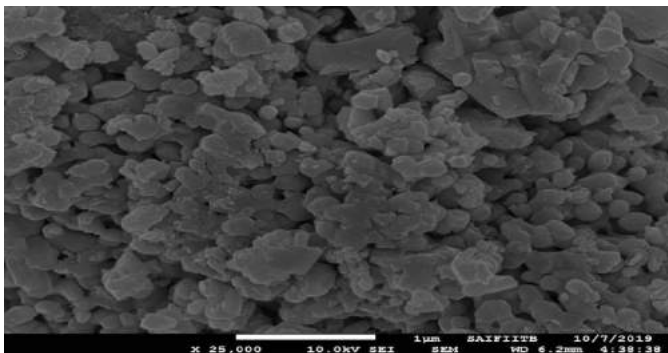
Fig.9 Temp. 650oC
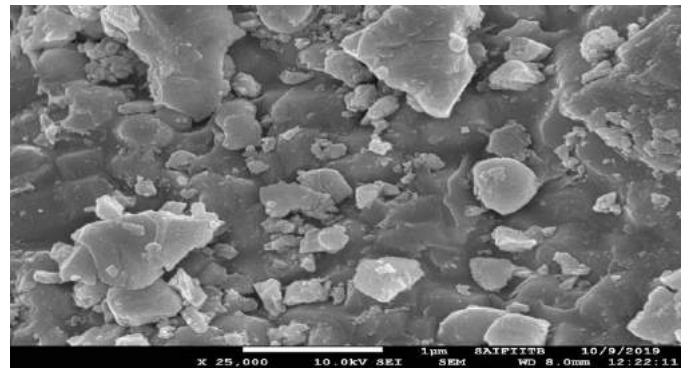
Fig.10 Temp. 700oC
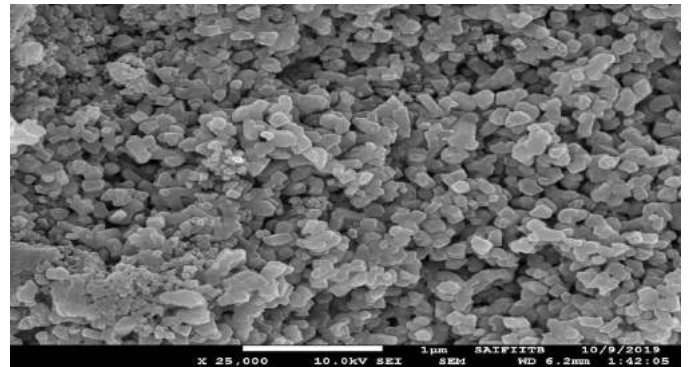
Fig.11 Temp. 750oC

iv) TEM (Transmission electron microscopy)

Fig. (12 to 15) The established multi-spot rings of selected area diffraction patterns clearly indicate the single crystalline nature of the powder. The diffraction pattern also indicates decrease in grains size with increase in sintering temperature. It also confirms that homogeneity of the material decreases with increase in sintering temperature.
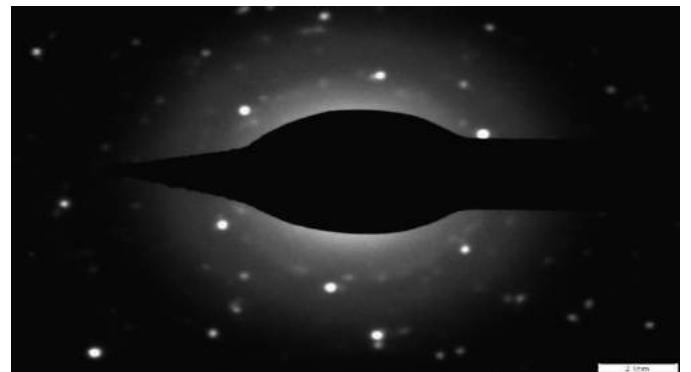
Fig.12 Temp. 600oC
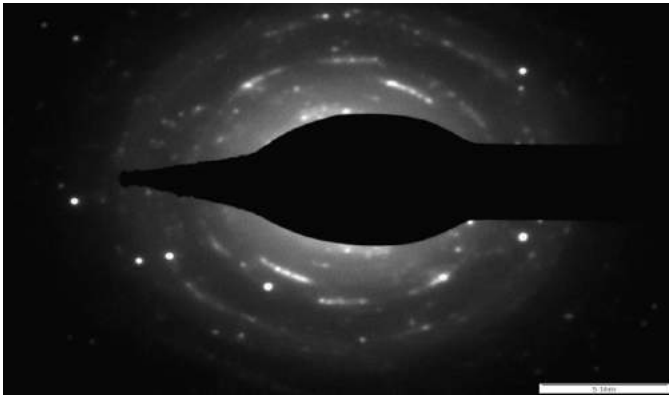
Fig.13 Temp. 650oC
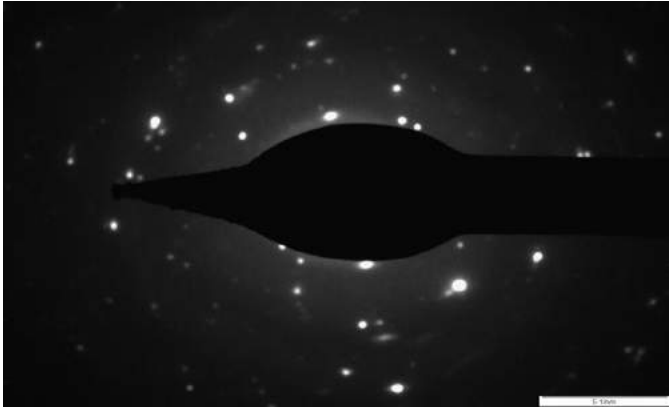
Fig.14 Temp. 700oC
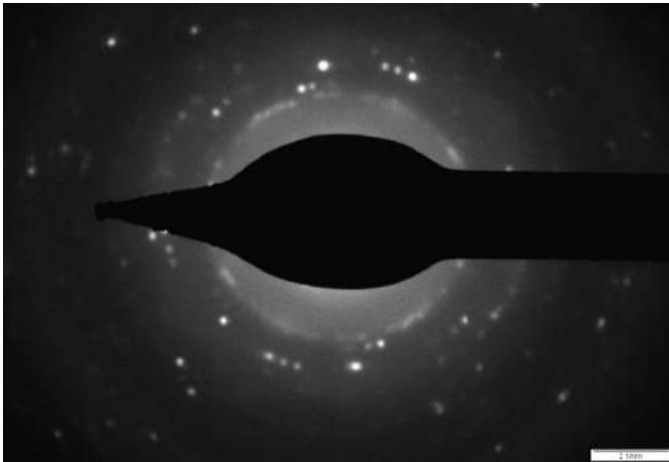
Fig.15 Temp. 750oC

IV. CONCLUSION

The PbTiO₃ (Lead Titanate) has been successfully synthesized using wet chemical method. The effect of sintering temperature on various properties have been investigated. XRD Analysis shows that with increase in sintering temperature, TiO₂ gets attached to the PbO to form single phase crystalline PbTiO₃. The variation of c/a ratio with the sintering temperature clearly indicates decrease in c/a ratio along with sintering temperature. Decrease in c/a ratio indicates dispersion from tetragonality and an approach to the cubic phase with higher sintering temperature. The variation of average grain size with sintering temperature indicates decrease in average grain size with increasing sintering temperature. A slight increase in density is observed as sintering temperature increases up to 750oC. However, a density jump occurs at 650oC, and almost dense materials are achieved. Increasing the calcinations temperature to 750°C, results in decrease in intensity of the organic absorption bands and increased intensity of the absorption Ti–O bond. The organic residuals were completely eliminated when the derived powders were calcined at 700°C. SEM Analysis reveals that increase in sintering temperature results in shift from homogeneous material to heterogeneous material which has also been confirmed by TEM. Moreover, TEM reveals the single crystalline nature of the synthesized material.

V. REFERENCES

[1].   V. D. Kapse, A. U. Bajpeyee, P. A. Murade Int Structural Properties Of Lead Titanate Nanoparticles Prepared By Wet Chemical Route international journal of chem. Tech. Research.Vol.6 No.3,PP2996-2098 May –June 2014.

[2].   Vijendra A. Chaudhari and Govind K. Bichile, Synthesis, Structural, and Electrical Properties of Pure PBTiO₃ Ferroelectric Ceramics. Research Gate Hindawi Publishing Corpoation Smart Materials Research Volume 2013, Article ID 147524,9 pages May 2013.

[3].   M\M.K. Gerges, Massaud Mostafa, Gehad M. Rashwan, Structural, optical and electrical properties of PbTi3 nanoparticles prepared by Sol-Gel method, International Journal of Latest

Research in Engineering and Technology, Volume 2,PP 42-49, Issue 4 April 2016.

[4]. Q. F. Zhou, H. L. W. chan, Q. Q. Zhang, C. L. Choy, Raman spectra and structural phase transition in nanocrystalling lead lanthanum titanate, Journal of Applied Physics, 15 JUNE 2001.

[5]. Bajpeyee A. U., Ph. D Thesis "Structural and Electrical Studies of Dielectric Layers on Semiconductor" SGB Amravati University, Amravati (Maharashtra) India, 2012

[6]. A. A. Abd El-razek, E. M. Saed, M. K. Gergs, Int J. Compu. Eng. Res. Vol, 04(9)2014,38-45

[7]. A. Abd El-razek, Y. Mendez-gonzalez, D. C. Arnold, D. J. Keeble, P. Saint- Gregoire, J. Mat. Sci.,Vol. 47(2)2012 pp 1094-1099.

[8]. O. P. Martonez, J. M. Saniger, E. T. Garcia, J. O. Flores, F. C. Pinar, J. C. Llopiz, A. P. Barranco, J. Mater. Sci. Lett. Vol. 16(13)(1997)1161-3.

[9]. Vesna paunovic, Vojislav Mitic, Vladimir Pavlovic, Miroslav Miljkvic, Ljiljana Zivkovic, Processing & App. of Cer. Vol. 4 [4] 2010 pp 253-258

[10]. V. M. Goldschmidt, Geochemische verteilungsgesetze der elemente; I Mater. Naturvid. Kl, no.2. Oslo, Skrifter Norske Videskaps-Akad (1926).

[11]. Archana Shukla, Namrata Shukla, R.N.P. Choudhary, R, Chatterjee, Physica B: Condensed Matter, Vol. 448, pp 219-222

[12]. C. Sudhama J. Kim, J, Lee, V. Chikarmane, W. Shephered and E. R. Myers, "Effect of lanthanum doping on the electrical properties of sol-gel derived ferroelectric lead-zirconate-titanate for ultra-large-scale integration dynamic random access memory applications", J Vac. Sci Technol., B 11, issue 4(1993) page 1302-9.

[13]. G. A. Rossetti Jr, L. E. Cross, J. P. Cline, "Structural aspects of the ferroelectric phase transition in lanthanum-Substituted lead titanate", Journal of Materials Science, Volume 30, Issue l (1959) pages 24-34.

[14]. P. S. Pizani, J. A. Eiras, " Short-range disorder in lanthanum-doped lead titanate ceramics probed by Raman scattering",Applied physics Letters, Volume 72, Issue 8 (1998) pages 897-899.

[15]. S. B. Majumder, S. Bhaskar, P. S. Dobal & R. S. Katiyar, "Inverstigations on sol-gel derived lanthanum doped lead titanate, (PLT) films", Intrgrated Ferroelectrics: An International Journal, Volume 23, Issue 1-4(1999) pages 127-148.

[16]. Hans Theo Langhamer, Thomas Muller, Karl-Heinz Felgner, Hans-Peter Abicht, "Crystal Structure and Related Properties of Magnase – Doped Barium Titanate Ceramics", Journal of the American Ceramic Society, Volume 83, Issue 3 (2000) Page 605-11.

[17]. Wenhua Jiang and Wenwu cao "Intrinsic and coupling-induced elastic nonlinearity of lanthanum-doped lead magnesium niobate-lead titanate electrostrictive ceramic".Applied Physics Letters, Volume 77 (2000) Pages 1387-1392.

[18]. S. Bhaskar, S. B. Majumdar, M. Jain, P. S. Dobal, R. S. Katiyar, "Studies on the structural, microstructural and optical properties of sol–gel derived lead lanthanum titanate thin films"; Materials Science and Engineering: B. Volume 87, Issue 2 (2001) Page 178-190.

[19]. S. B. Majumdar, M. Jain, R. S. Katiyar, "Investigations on the optical properties of sol–gel derived lanthanum doped lead titanate thin films"; Thin Solid Films, Volume 402, Issues 1-2 (2002) Pages 90-98.

[20]. Jong-Jin Choi, Sang-Wook Kim and Hyoun-Ee Kim, "Effect of Manganese Ion Diffusion on the Microstructural Evolution of Lead Lanthanum Zirconate Titanate Ceramic"; Journal of the American Ceramic Society, S. Bhaskar, S. B.

Majumdar, M. Jain, P. S. Dobal, R. S. Katiyar, "Studies on the structural, microstructural and optical properties of sol–gel derived lead lanthanum titanate thin films", Volume 85, Issue 3(2002) Page 733-735.

[21]. S. B. Majumdar, R. S. Katiyar, F. A. Miranda, F. W.Van Keuls "Improvement in electrical characteristics of graded manganese doped barium strontium titanate thin films";Applied Physics Latter, Volume 82, Issue 12 (2003) Pages 1911-3.

[22]. Jun Chen, Xianran Xing, Ranbo Yu and Guirong Liu, "Thermal Expansion Properties of Lanthanum-Substituted Lead Titanate Ceramics"; Journal of the American Ceramic Society,Volume 88,Issue 5 (2005) pages 1356-1358.

[23]. Arabjit Singh, O. P. Thakur, Chandra Prakash, K. K. Raina, "Structural and electrical properties of lanthanum-substituted lead titanate ceramics, Phase Transitions"; A Multinational Journal, Volume 78, Issue 7-8 (2005) Pages 655-667.

Current and Upcoming Innovations in Spintronics

Nikita Korde, Sandeep Waghuley

Department of Physics, Sant Gadge Baba Amravati University, Amravati, Maharashtra, India

ABSTRACT

In the present paper, authors briefly discussed the field of spintronics which has explored new spin related physics, including giant magnetoresistance, tunneling magnetoresistance, and spin transfer torque, which led to spin-based device applications.

Spintronics is a field of concentrate that exploits the intrinsic spin angular momentum of an electron. In conventional electronics, the charge degree of freedom of electron is considered and it focuses on improving the mobility or conductivity of the charge carriers. Whereas in spintronics, the spin degree of freedom of an electron in addition to its charge state is considered and it focuses on generation or manipulation of a spin polarized population of electrons, aiming at using the electron spins for efficient data storage and communication methods.

Keywords : Spintronics, Spin-based device, Spin angular momentum, Giant Magnetoresistance.

I. INTRODUCTION

In order to overcome the current challenges of microelectronics devices such as the power dissipation and downscaling, researchers have been exploring an additional intrinsic property of electron, called spin. The field of spin electronics or spintronics has explored new spin related physics, including giant magnetoresistance, tunneling magnetoresistance, and spin transfer torque, which led to spin based device applications.

The origin of spintronics goes back to the first understanding of the electrical conduction in transition metals by Mott in 1936, who described the conduction of electrons in ferromagnetic(F) materials as a combination of two individual current channels, one channel consisting of electrons with spins parallel to the magnetization axis of F and the other with electron spins oriented in opposite direction[1]. Spintronics materials are the material retaining the spin polarization for a long duration.

Magnetoresistance is that the tendency of a material (preferably ferromagnetic) to vary the value of its resistance in associate externally applied field of force. The first magnetoresistive effect was discovered by William Thomson, better called as Lord Kelvin, in 1856, but he was not able to lower the electrical resistance of anything by more than 5%. Nowadays, systems e.g.- semimetal or concentric ring EMR structures are better known whereever a magnetic field can change resistance by orders of magnitude[2]. There are a range of effects that can be called magneto resistance: some occur in bulk non-magnetic metals and semiconductors, such as geometrical

magnetoresistance, Shubnikov de Haas oscillations, or the common positive magnetoresistance in metals [3]. Different effects occur in magnetic metals, like negative magnetoresistance in ferromagnets or anisotropic magnetoresistance (AMR)[4]. Finally, in multicomponent or multilayer systems (e.g.- magnetic tunnel junctions), giant magnetoresistance (GMR), tunnel magnetoresistance (TMR), colossal magnetoresistance (CMR), and extraordinary magnetoresistance (EMR) can be observed. Magnetoresistance converts magnetic signal into electrical signal.

II. GIANT MAGNETORESISTANCE (GMR)

The giant magnetoresistive (GMR) effect was discovered in 1988 in multilayered structures of ferromagnetic and non-ferromagnetic thin films by Grunberg,Binaschetal [5] as well as Fert, Baibich et al[6].

Schematic of Magnetic Multilayer
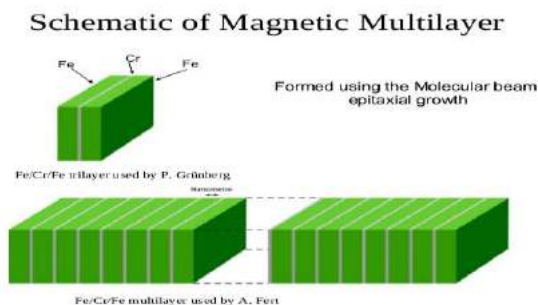
In principle, a typical GMR structure consists of a pair of ferromagnetic thin film layers separated by a non-magnetic conducting layer. The change in the resistance of this multilayer arises once the externally applied magnetic field aligns the magnetic moments of the successive magnetic layers. In absence of a magnetic field, the magnetic moments of the magnetic layers are antiparallel. Once a magnetic field is applied, the magnetic moments of the magnetic layers align with regard to each other; their magnetizations are parallel. This yields a drop in the resistance of the multilayer. Basically, the GMR is gotten from the connection of current conveying electrons and the polarization of the host attractive material. In the presence of a magnetic field the spin-dependent electron scattering among the structure reduces and the electrical resistance decreases [7, 8]. GMR structures have an advantage in size, power consumption, cost and thermal stability with respect to search coil, fluxgate, SQUID, Hall and spin resonance sensors. Furthermore, GMR sensors are ideal for low cost applications since they are simply energized by applying a constant current and the output voltage is a measure of the magnetic field[9].

The resistance of Magnetoresistance is higher if the field is parallel to the current and lower if the field is perpendicular to the current [10]. The phenomenon that the resistance of a ferromagnetic material depends on the relative angle between the current and magnetization direction of the material is known as the anisotropic Magnetoresistance effect, or AMR , that was discovered by Thomson in 1857[11].
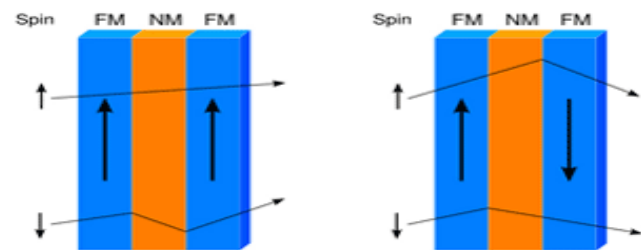
The reason for the changing electrical resistance is that the spin dependence of an electron transport, that affects the scattering rates at film interfaces for spin-up (spin parallel to layer magnetization) and spin-down (spin antiparallel to layer magnetization) electrons[12].

III. LITERATURE SURVEY

Mohamed et al [13] carried out the research on alternative method for realizing a carbon nanotube spin field-effect transistor device by the direct synthesis of single-walled carbon nanotubes (SWNTs) on substrates by alcohol catalytic chemical vapor deposition. They observed hysteretic magnetoresistance (MR) at low temperatures due to spin-dependent transport. In their devices, the

maximum ratio in resistance variation of MR was found to be 1.8%.

Shinji Yuasa et al [14] reported a giant MR ratio up to 180% at room temperature in single-crystal Fe/MgO/Fe MTJs. The origin of this enormous TMR effect is coherent spin-polarized tunneling, where the symmetry of electron wave functions plays an important role. Moreover, they observed that their tunnel magnetoresistance oscillates as a function of tunnel barrier thickness, indicating that coherency of wave functions is conserved across the tunnel barrier.

Xiong et al[15] report the injection, transport and detection of spin-polarized carriers using an organic semiconductor as the spacer layer in a spin-valve structure, yielding low-temperature giant magnetoresistance effects as large as 40 per cent.

Husmann et al [16] describe a hitherto unexplored class of magnetoresistive compounds, the silver chalcogenides. At high temperatures, the compounds Ag_2S, Ag_2Se and Ag_2Te are superionic conductors; below $\sim$400 K, ion migration is effectively frozen and the compounds are non-magnetic semiconductors, that exhibit no appreciable magnetoresistance. They show that slightly altering the stoichiometry can lead to a marked increase in the magnetic response. At room temperature and in a magnetic field of $\sim$55 kOe, $Ag_{2+\delta}Se$ and $Ag_{2+\delta}Te$ show resistance increases of up to 200%, which are comparable with the colossal-magnetoresistance materials.

Mazhar N. Ali et al [17] report the observation of an extremely large positive magnetoresistance at low temperatures in the non-magnetic layered transition-metal dichalcogenide WTe_2: 452,700 per cent at 4.5 kelvins in a magnetic field of 14.7 teslas, and 13 million per cent at 0.53 kelvins in a magnetic field of 60 teslas.

Stefan Schmaus et al [18] demonstrate giant Magnetoresistance across a single, non-magnetic hydrogen phthalocyanine molecule contacted by the ferromagnetic tip of a scanning tunnelling microscope. They measure the magnetoresistance to be 60% and the conductance to be $0.26G_0$, where G_0 is the quantum of conductance. Theoretical analysis identifies spin-dependent hybridization of molecular and electrode orbitals as the cause of the large magnetoresistance.

K. S. Novoselov et al [19] describe monocrystalline graphitic films, which are a few atoms thick but are nonetheless stable under ambient conditions, metallic, and of remarkably high quality. The films are found to be a two-dimensional semimetal with a tiny overlap between valence and conductance bands, and they exhibit a strong ambipolar electric field effect such that electrons and holes in concentrations up to 10^{13} per square centimeter and with room- temperature mobilities of $\sim$10,000 square centimeters per volt-second can be induced by applying gate voltage.

IV. Applications

1) The largest technological application of GMR is in the data storage industry. IBM was first to place on the market hard disks based on GMR technology and theseadays all disk drives make use of this technology[20].

2) Other applications of GMR are as diverse as automotive sensors, solid-state compasses and non-volatile magnetic memories.

3) Magnetoresistive materials and structures are used as sensors for magnetic recording, MRAM, motion sensors or just simply to measure the strength of a magnetic field.

4) Spin valve sensors – used in ABS and ESP systems of car.

5) Quantum computers, Spin transistor etc.

6) Biomedical diagnostic devices.

7) Integrated spintronics biochips (neuroelectronic studies and biomedical imaging).

V. CONCLUSION

Giant Magnetoresistance is the large change in electrical resistance of metallic layered systems which occurs when the magnetizations of the ferromagnetic layers are reoriented relative to one another under the application of an external magnetic field. Both the electronic structure and the scattering of the conduction electrons in these systems are altered by reorientation of the magnetic moments, which causes the change in the resistance. Various types of magnetic layered structures have been found which show sizable values of GMR. In spintronics, the spin degree of freedom of an electron in addition to its charge state is considered and it focuses on generation or manipulation of a spin polarized population of electrons, aiming at using the electron spins for efficient data storage and communication methods.

VI. REFERENCES

[1]. Tian, Y., & Yan, S. (2012). Giant magnetoresistance: history, development and beyond. Science China Physics, Mechanics and Astronomy, 56(1), 2–14.

[2]. "Unstoppable Magnetoresistance."

[3]. Pippard, A. B.: Magnetoresistance in Metals, Cambridge University Press (1989).

[4]. Coleman, R. V., Isin, A. "Magnetoresistance in Iron Single Crystals", Journal of Applied Physics, 37 :1028, 1966.

[5]. Binasch, G., Grunberg, P., Saurenbach, F., Zinn, W. Enhanced magnetoresistance in layered magnetic structures with antiferromagnetic interlayer exchange. Phys. Rev. B 1989,39,4828-4830.

[6]. Baibich, M. N., Broto, J. M., Fert, A., Van Dau, F. N., Petroff, F. Giant Magnetoresistance of (001) Fe/(001) Cr Magnetic Superlattices. Phys. Rev. Lett. 1988,61,2472-2475.

[7]. Varadan, V.K., Chen, L., Xie, J. Nanomedicine: Design and Applications of Magnetic Nanomaterials, Nanosensors and Nanosystems; John Wiley & Sons, Ltd.: West Sussex,UK,2008.

[8]. Xu, L., Yu, H., Akhras, M.S., Han, S.-J., Osterfeld, S., White, R.L., Pourmand, N., Wang, S.X. Giant magnetoresistive biochip for DNA detection and HPV genotyping. Biosens. Bioelectron. 2008,24,99-103.

[9]. Gooneratne, C., Liang, C., Giouroudi, I., Kosel, J. An integrated micro-chip for rapid detection of magnetic particles. J. Appl.Phys>2012,111,07B327.

[10]. Principles of Nanomagnetism A.P. Guimaraes Springer-Verlag, Berlin,2009.

[11]. Thomson, W., Proc. R. Soc. 8,546(1857).

[12]. Lisa Jogschies, Daniel Klaas, RahelKruppe, Johannes Rittinger, PiriyaTaptimthong, Anja Wienecke, Lutz Rissing and Marc Christopher Wurz,; Recent Developments of Magnetoresistive sensors for Industrial Applications. Sensors 2015,15,28665-28689.

[13]. Mohamed, M. A., Inami, N., Shikoh, E., Yamamoto, Y., Hori, H., & Fujiwara, A. Fabrication of spintronics device by direct synthesis of single-walled carbon nanotubes from ferromagnetic electrodes. Science and Technology of Advanced Materials. 9(2), 2008, 025019.

[14]. Shinji Yuasa, Taro Nagahama, Akio Fukushima, YoshishigeSuZuki& Koji Ando; Giant room-temperature magnetoresistance in single-crystal Fe/MgO/Fe magnetic tunnel junctions; Nature materials 3, 2004, 868-871.

[15]. Xiong, Z. H., Wu, Di, ValyVardeny Z. & Jing Shi ; Giant magnetoresistance in organic spin valves; Nature 427, 26 February 2004, 821-824 .

[16]. Xu, R., Husmann, A., Rosenbaum, T. F., Saboungi, M. L., Enderby, J. E. & Littlewood, P. B. Large magnetoresistance in non-magnetic silver chalcogenides; Nature 390,06 November 1997, 57-60 .

[17]. Mazhar N. Ali, Jun Xiong, Steven Flynn, Jing Tao, Quinn D. Gibson, Leslie M. Schoop, Tian Liang, Neel Haldolaarachchige, Max Hirschberger, OngN. P. & CavaR. J.; Large non-saturating magnetoresistance in WTe2 .

[18]. Stefan Schmaus, Alexei Bagrets, Yasmine Nahas, Toyo K. Yamada, Annika Bork, Martin Bowen, Eric Beaurepaire, Ferdinand Evers & Wulf Wulfhekel ; Giant magnetoresistance through a single molecule; Nature Nanotechnology 6,2011, 185-189 .

[19]. Novoselov, K. S., Geim, A. K., Morozov, S. V., Jiang, D., Zhang, Y., Dubonos, S. V., Grigorieva, I. V. Electric field effect in Atomically thin Carbon films.

[20]. http://simple.wikipedia.Org/wiki/Giant magnetoresistance.

Synthesis, Characterization and CO_2 Gas Sensing Response of 5% SnO_2 Doped Polyaniline Nano Composite

Hamjade PT[1], Khaire ND[1], Motke SG[2]

[1]Associate Professor, Department of Physics, Phulsing, Naik Mahavidyalaya, Pusad, , Maharashtra, India

[2]Principal, Phulsing Naik Mahavidyalaya, Pusad, Maharashtra, India

ABSTRACT

Polyaniline and its nano-composites are synthesized using in-situ chemical oxidative polymerization technique using aniline. Nano sized SnO_2 is used as received from the manufacturer. Ammonium Per Sulphate is used as oxidizing agent for polymerization. Crystalline SnO_2 is embedded in amorphous Polyaniline. The structure of the composite was confirmed by the characterization techniques FTIR, UV Visible and XRD.

Average particle size and chain separation is determined using XRD. The little shifting of the wavelengths towards higher values in FTIR confirms the formation of Polyaniline. UV Visible studies show that the composite exhibit absorption peaks at 614 nm, 328 nm and 263 nm; which corresponds to band gap energies 2.02 eV, 3.78 eV and 4.71 eV respectively. V-I characteristic is plotted using two probe method, which indicate fairly linear or ohmic behavior of the sample with high resistivity. Gas sensing response to CO_2 is observed.

Keywords – Polyaniline, nano-composites, band gap energy, gas sensing, CO_2, SnO_2.

I. INTRODUCTION

The conducting polymers made significant impact in the field of material science due to their potential applications in many electronic devices [1]. Technological uses depend crucially on the reproducible control of the molecular and supramolecular architecture of the macromolecules via a simple methodology of organic synthesis [2]. Polyaniline is one of the important conducting polymers among all other conducting polymers because of its stability in air, easy polymerization, low cost, good conductivity, and solubility in some organic solvents. It is the type of conducting polymer whose properties can be changed by protonation state, oxidation state, and also by nature of dopant [3-6]. In general the change in properties make polyaniline a versatile material. The preparation of polyaniline composites with various materials has received great attention because of their unique properties and allocations in various electrical and electronic devices. Several reports dealing with the preparation of conducting composites such as Fe_3O_4:PANI, MnO_2:PANI, TiO_2:PANI, ZrO_2:PANI [7,8], as well as preparation and characterization of ZnO:PANIcomposites have been published [9-11] . Due to the reasons it has been studied extensively for making optical and electronic devices like LEDs, solar cells, transducers, photodetectors, etc.[12-14]. In particular SnO_2 nanostructures are of intense interest

since it can be grown by a variety of methods with different morphologies.

On the other hand, functional metal oxides have received increasing attention due to their unique physical properties. Functional oxide have two structural characteristics- cations with mixed valance states and anions with deficiencies (vacancies). By varying either or both of these characteristics, the electrical, optical, magnetic, and chemical properties can be tuned, giving the possibility of fabricating smart devices that utilizes the semiconducting , superconducting, ferroelectricity and/or magnetism offered by the oxides. Among the technologically promising functional metal oxides, tin oxide (SnO_2) is used in various opto-electronic devices like flat panel display, photoconductor and solar cells. SnO_2 is n-type semiconductor with a band gap of 3.6 eV at 300 K where as PANI is a typical conductive polymer which is usually considered as a p-type material. In view of forgoing, by synthesizing nano-composite of SnO_2/PANI, electrical and optical properties can be enhanced.

Growing industrialization and increasing pollutants from vehicular exhaust have resulted into increased air pollution. The problems related to air quality monitoring are important issues of current research activity. At present, CO_2 gas is being polluting the envirnment to a large extent. This may cause severe health problems leading to reduce the efficiency of human resources. To overcome the problem, an CO_2 gas sensor is required[ ].

In the present work the composite of polyaniline with SnO_2 was synthesized at a five (5) weight percentage by chemical oxidation polymerization method using ammonium persulphate as an oxidizing agent. With this background of multifunctionality SnO_2 is used in preparation of composite [9-11]. The formation of composite was characterized by using XRD, FTIR and UV/Visible.

II. METHODS AND MATERIAL

The chemicals aniline monomer, ammonium persulphate (APS) $(NH_4)_2S_2O_8$ and hydrochloric acid (HCl) were procured from LOBA chemicals, Mumbai. The nanosized SnO_2 powder was procured from nanolabs, Jamshedpur, Zarkhand

Synthesis of PANI-SnO2 is carried out by following process.

Polyaniline hydrochloride of weight 2.59 gm and SnO2 5% by weight is dissolved in water to make 50ml solution in a volumetric flask.

Then APS of weight of 5.71gm is dissolved in water to make 50ml solutions in another volumetric flask. Both solutions were stirred and kept for 1hour at room temperature (25c). After the time, both solutions were mixed together and stirred for 4 hours in magnetic stirrer and after that left for polymerization for 24 hours.

PANI-SnO2 precipitate was formed. It is collected on filter paper and washed several times with 100ml portion of 0.1M HCl (35% conc.) and similarly with acetone (pure 99%) till clear solution is obtained.

The material collected on filter paper is dried at 60c temperature in oven overnight till it gets moisture free powder. The yield is found to be 78.66%.

The nanocomposite was characterized using XRD, FTIR and UV/Visible.

III. RESULTS AND DISCUSSION

The PANI/ SnO_2 nanocomposite powder were used for XRD measurements using Cu(Kα) radiation of wavelength 1.5418A in a range 5˚-80˚. The nanocomposites was studied using FTIR Shimandzu, Japan in the range 500-4000 cm^{-1} and UV/Visible Shimadzu, Japan in the range 200nm to 1100nm.

a) XRD

X-Ray diffraction pattern with two prominent peaks leads the amorphous nature. The XRD spectrum of

PANI/ZnO 10wt% and PANI/SnO$_2$ 10wt% are shown in fig. 1(a), 1(b).
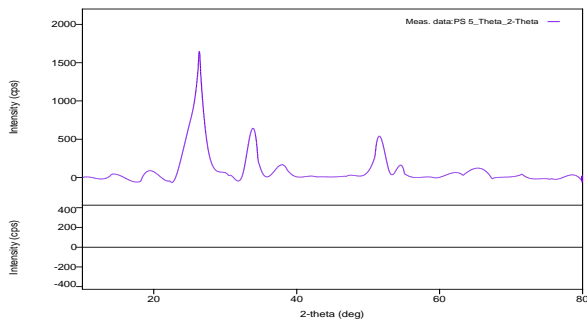
Fig. 1. XRD spectrum of PANI/SnO$_2$ 5wt%

It is notified that sharp and well defined peaks are observed. This shows that the nanocomposite is partially crystlline in nature. The peaks are observed for the composite at 20^0, 24^0 and 25.6^0 which confirms the presence of SnO$_2$. Which depicts that it has crystalline nature.

The particle size could be estimated using Debye – Scherrer's formula, $D = \frac{0.9\lambda}{\beta cos\theta}$

Where, D is the particle size, β is full width at half maximum (FWHM) for stronger peaks and λ is the wave length of X-rays. From the high intensity peaks the particle size are calculated in the range 4.1 nm.

b) FTIR-

The FTIR spectra of PANI/SnO$_2$ 5 wt% is shown in fig 2.
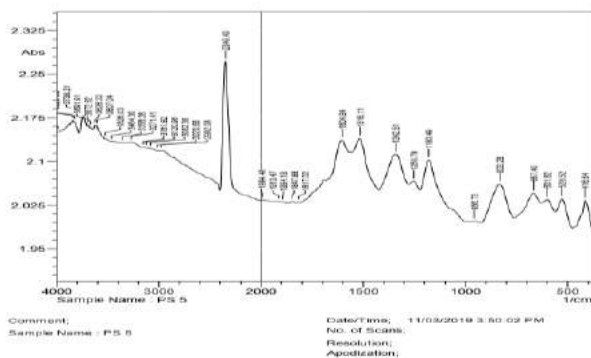
Fig 2. FTIR spectra of PANI/SnO$_2$ 5wt%

Characterization absorptions peaks are obtained from FTIR spectrum of PANI-SnO2. The characteristic absorption bands of PANI are 667.40 cm^{-1} due to C=C strong bending mode, 1342.51 cm^{-1} represents C-N strong strechting, 2982.08 cm^{-1} represents N-H strong

stretching and 3082.38 cm^{-1} indicates C-H medium streching.

c) UV-Vis

The UV-Vis spectra of nanocomposites are shown in figs. 3(a), 3(b). Using these spectra the band gap energy can be found out. The formula is, $E_g = \frac{hc}{\lambda e}$

Where h is Planck's constant (6.626 x 10^{-34} J-sec), c is the speed of light (3x 10^8 m/s), λ is the wave length and e is the charge of electron (1.602 x 10^{-19}C).
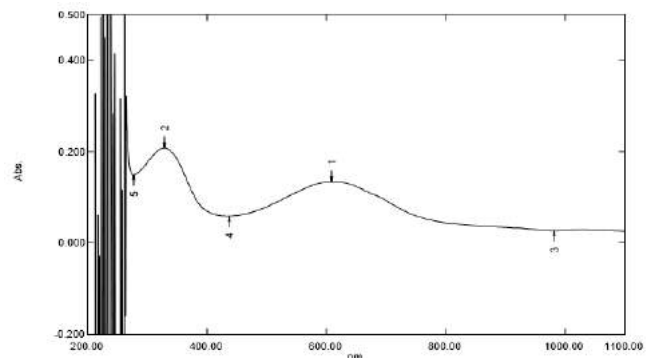
Fig. 3. UV-Vis spectra of PANI/SnO$_2$ 5wt%

The SnO$_2$ doped polyaniline nanocomposite exhibits absorption peaks at 329 nm and 608 nm which corresponds to band gap energies 3.47eV and 2.02eV respectively.

d) DC Conductivity

The film of the composite is deposited using spin coating technique on pre-cleaned glass substrate using 8% polyvinyl acetate as a binder. For measurement of conductivity, juxtaposed copper electrodes, each of length 0.6 cm and 1 mm separation between them, are gently placed on the film with the help of loose spring. Mili-ammeter (Meco-301) and a dc power supply (Agronik - 30) are used for the purpose.
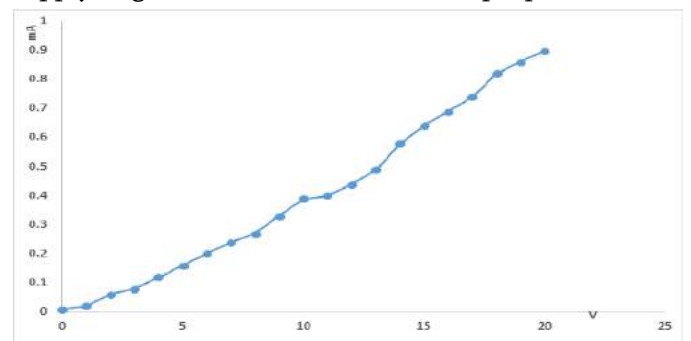
Fig. 4. V- I charectoristic of PANI/SnO₂ 5wt%

The graph represents variation of current through surface of sample with voltage. The graph is fairly linear indicating ohmic nature of the sample. This may be due to transfer of electrons as charge carriers in the direction of applied field. Surface resistivity is calculated from the formula - $\rho = \dfrac{E}{J} = \dfrac{V}{I} L$

where, V is voltage applied, I is surface current and L represents length of the electrode. The surface resistivity, ρ is evaluated as 490 Ω Mtr.

e) Gas Sensing Response

Gas sensing response of the sensor is defined as change in conductance of a sample upon exposure to target gas to the original conductance in air. The figure shows gas response of PANI/SnO₂ 5wt% thick film to CO_2 gas at room temperature.
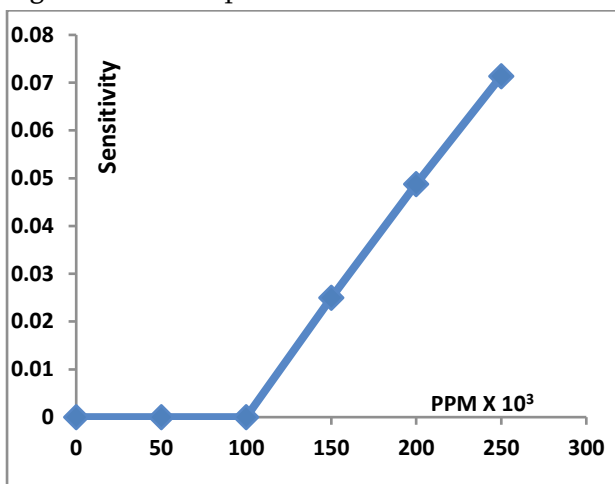
Fig. 5. Response to CO2 of PANI/SnO₂ 5wt%

From fig.5, the sensitivity increases fairly linearly with concentration of the gas. The exact fundamental mechanisms to explain gas sensing response are controversial.

IV. CONCLUSION

PANI/SnO₂ 5wt% nano composite has been successfully synthesized by in – situ polymerization using chemical oxidation method. The XRD- spectra of composite reveals partially crystalline nature. The peak positions differ from SnO₂ compared to its composites and this indicates that the modification has occurred in the composite structure. The size of the grains is in the nano-meter range as found out from XRD. The PANI/SnO₂ composite is promising materials which may be applicable in optoelectronic devices and organic solar cells.

V. ACKNOWLEDGEMENT

VI. REFERENCES

[1]. Alan G. Mac Diarmid , Synth. Met. 84, (1997), 27-34.
[2]. Debarnot D. N. and F. P. Epaillord, Anal. Chim. Acta, 475, 1-15(2003)
[3]. Mac-Diarmid A. G., Chiang J. C., Halpunm, Huang W. S. et. Al., Mol. Cryst., Liq. Cryst., 121, (1985), 173.
[4]. Mac-Diarmidet. al., Synth. Met. 18(1987)285.
[5]. Naarman H, Adv. Mater. 2, (1990)345.
[6]. Safenaz M. Reda, Sheikha M., Al Ghannam, Advances in materials Physics and Chemistry, 2 (2012), 75-81.
[7]. Gok A., Omatsova M. and Prokes J., European Polymer Journal, (2007), 43, 2471-2480.
[8]. Yavuz A., and Gok A. , Synthetic Metals , (2007)157, 235-242.
[9]. Aizyddin Abdul Rahman et. al., Journal of Physical sciences, 24 (1), (2013), 17-28.
[10]. ShahidPervwz Ansari and Faiz Mohammad, IUP Journal of chemistry 3, (2010), 4.
[11]. Zhang H., Zong R. &Zhu, The Journal of Physical Chemistry.
[12]. Yang P., YanH., Mao S., Russo R., Johnson J., Saykally R., Morris N., Pham J., He R. & Choi H., Advanced function Material, 2002, 12, 323-331.
[13]. Park W. I., Yi G., Kim M., &Pennycock S. L., Advanced Materials, 2002, 14, 1841-1843.

[14]. Yayssieres L., Keis K., Hagfeldt A. & Lindquist S.,Chemistry of Materials, 13, 4395-4398.

Synthesis and Thermo Acoustical Dynamics of PMMA/Fe2O3 Nanocomposites

P. U. Tasalwar[1], P. D. Dhone[1], A. R. Bansod[1], O. P. Chimankar[2]

[1]Dr. Ambedkar College Deekshabhoomi, Nagpur, Maharashtra, India

[2]Department of Physics, Rashatrasant Tukadoji Maharaj Nagpur University, Nagpur, Maharashtra, India

ABSTRACT

Inorganic metallic nanoparticle's incorporation into polymer matrices allows the modification of physico-chemical properties and its specific implementation. This work put forth the conventional co-precipitation method for synthesis of polymethyl methacrylate enriched in ferric oxide at nanoscale. The synthesized matrix is then structurally determined using XRD. The magnetic behavior is analyzed by VSM. The molecular interaction study is carried out using ultrasonic pulse echo technique. The specific concentration of metal ion in polymer matrix with fixed geometry has optimum magnetic property.

Keywords : polymer matrix, nanocluster, XRD, PMMA, VSM

I. INTRODUCTION

The mixing of polymer and nanoparticles is opening pathway for engineering flexible composite that exhibit advantageous magnetic, electrical, optical and mechanical properties. As part of this renewed interest in nanocomposite, researchers began seeking new strategies to engineer materials that combine the desirable properties of nanoparticles and polymers for the formation of polymer composite materials. The particle must integrate in a way leading to isolated, well-dispersed primary nanoparticles inside the matrix. There is a need for establishing processing techniques that are effective on the nanoscale yet are applicable to macroscopic processing. There have been several attempts for the synthesis of polymer composite material that can be classified under two major categories: as physical and chemical methods [1-5].

The composites are defined as materials that consist of two or more chemically and physically different phases separated by a distinct interface. The different systems are combined to achieve a system with more useful structural or functional properties not attainable by any of their constituents. The composites are wonder materials becoming an essential part of today's materials due to the advantages such as low weight, corrosion resistance, high fatigue strength, and faster assembly. They are extensively used as materials in making aircraft structures, electronic packaging, medical equipment, and space vehicle to home building [6-8]. The predominant useful materials used in our day-to-day life are wood, concrete, ceramics, and so on are surprisingly, the most important polymeric composites [1-3,6]. The composites are combinations of materials differing in composition, where the individual constituents retain their separate identities.

These separate constituents act together to give the necessary mechanical strength or stiffness to the composite part. Composite material is a material composed of two or more distinct phases [matrix phase and dispersed phase] and having bulk properties significantly different from those of any of the constituents. The matrix phase is primary phase having a continuous character. Matrix is usually more ductile and less hard phase. It holds the dispersed phase and shares a load with it. Dispersed [reinforcing] phase is embedded in the matrix in a discontinuous form. This secondary phase is called the dispersed phase. The dispersed phase is usually stronger than the matrix, therefore, it is sometimes called reinforcing phase. In structural applications composites have the following characteristics:

They have superior mechanical properties and in some cases uniquely different from the properties of their constituents

1. Among the many unique attributes of non materials especially noteworthy are their large surface to volume ratios and outstanding mechanical properties.

2. They generally consist of two or more physically distinct and mechanically separable materials.

3. They are made by mixing of the separate materials in such a way as to achieve controlled and uniform dispersion of the constituents

These properties offer venues for exciting areas of research as well as for technological innovations. Thus an important use of non materials is in reinforcing polymer matrices taking advantages of the ultra-high stiffness and hardness exhibited by them. Recent research has shown that small additions [upto ~ 5 wt%] of certain nano materials such as carbon nano tubes enhance the mechanical properties markedly, sometimes by as much as 100%. The precise mechanism responsible for this dramatic enhancement is not entirely understood. It is generally believed that molecular level interactions between the nano materials and polymer matrices

play a major role. The large interfaces are available for such interactions clearly hold the key for the dramatic enhancement of mechanical properties [9-12]. The electrical properties constitute one of the most convenient and sensitive method of studying the polymer structure. They are affected not only by the structure and nature of dopant but also by the doping procedure [13].

PMMA is an excellent host for functional particles[2,4-8]. The various types of metal oxide fillers such as $Bi_4Ti_3O_4$, SiO_2, TiO_2, Nb_2O_5, and Ta_2O_5/SiO_2 have been incorporated into polyacrylates to modify the optical properties of these polymers. For *e.g.,* the refractive indices of PMMA matrix can be increased or decreased by addition of SiO_2, Al_2O_3, or ZrO_2 filler particles[5-8,14-15]. A noteworthy property of nanoparticles is their ability to become dispersible in liquids by appropriate modification of their surface. This property makes nanophase materials very attractive since it helps their manipulation. Such as in thin film formation or homogeneous dispersion into matrices. The nano-composite polymers have been designed in a similar manner by incorporation of the nanoparticles in a polymer matrix alters, as expected the mechanical, thermal and the other characteristics of the polymer. The usual method for the preparation of such polymer composites is the dispersion of nanoparticles into a melted polymer or dissolving them in a solvent polymer [16-17]. Hence research in the field of such polymers is mainly at some suitable modifications of existing polymers. The properties of the polymer composites can be improved by involvement of organic materials and inorganic oxides or salts of different metals *viz.* SnO_2 [18-19], CeO_2 [20-21], TiO_2 [7, 22], fly ash composites [23-24], Fe_3O_4 [1-4], ZrO_2 [25] etc. Therefore PMMA and its composite with Fe_2O_3 nanoparticles were studied in this work. These were characterized for structural properties using XRD. The magnetic behavior is analyzed by VSM. The molecular interaction study is carried out using

ultrasonic pulse echo technique. The specific concentration of metal ion in polymer matrix with fixed geometry has optimum magnetic property.

II. METHODS AND MATERIAL

2.1 Synthesis
Synthesis of Fe₂O₃ NPs

The Fe_2O_3 NPs were synthesized by co-precipitation method. In a typical procedure 0.2 M aqueous solution of $FeCl_3.6H_2O$ was heated at 60 °C under mild stirring. A solution of 2 M sodium hydroxide was added drop wise into the ferric chloride solution until pH reaches 8. At this point red precipitate appeared in the solution. The slurry was heated at 100 °C for 5 h in a vacuum oven. The dried iron hydroxide nanoparticles were then finally heated at 400 °C in conventional muffle furnace for 4 h to obtain brick red Fe_2O_3 NPs.

Synthesis of PMMA/ Fe₂O₃ nanocomposites NCs

For the synthesis of binary composite of PMMA/ Fe_2O_3, particular amounts of Fe_2O_3 NPs were added, respectively, to 20 mL methyl methacrylate monomer (MMA) in weight fractions of 1 wt%, 2 wt% , 3 wt%, 4 wt% and 5 wt% and sonicated for 12 h in the presence of azobisisobutyronitrile (AIBN) as initiator. The reaction mixture was converted into a thick paste and dissolved in acetone to form uniform sheets of composites.

2.2 Characterization

The structural properties of PMMA and its composite with Fe_2O_3 nanoparticles were identified by X-ray powder diffraction (XRD) with a X'Pert PRO advanced diffractometer using Cu (K_α) radiation (λ=1.5406 Å). Ultrasonic measurements were performed at 4MHz by pulse echo method. The ultrasonic velocity (U) was determined with the experimental density and viscosity at various temperature. The magnetic measurements were made by using vibrating sample magnetometer (VSM) at room temperature.

III. RESULTS AND DISCUSSION

3.1 Structural Characterization

The XRD spectrum for polymer composite of PMMA with Fe_2O_3 is given in Fig 1. It is noticed the broader intensity peak occurred at lower angle of 2θ say 14^0, But the sharp peaks are occurred at 2θ angles of 33.14^0, 35.59^0, 40.83^0, 49.42^0, 54.04^0, 57.39^0, 62.38^0, 63.93^0, 71.93^0 and 72.25^0 correspond to the (1 0 4), (1 1 0), (1 1 3), (0 2 4), (1 1 6), (1 2 2), (2 1 4), (3 0 0), (1 0 10), (1 1 9), (0 2 10) were well matched with JCPDS No.79 -892810.
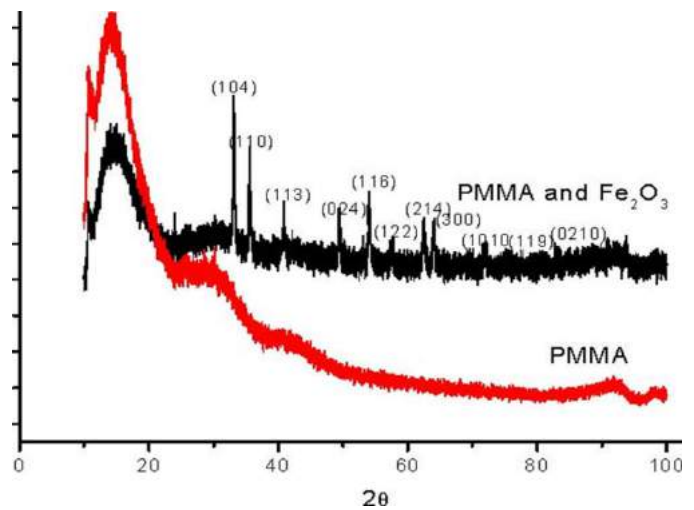
Fig. 1. The XRD Spectra of the PMMA and PMMA/Fe2O3 nanocomposites[1]

The particle size of the samples has been calculated by employing the Scherres equation:

$$D = \frac{K\lambda}{\beta \cos\theta} \qquad (1)$$

where, θ is the angle between the incident and diffracted beams (degree), β is the full with half maximum (rad.), D is the particle size of the sample (nm) and λ is the wavelength of the X-ray. The average grain size of the prepared PMMA/ Fe_2O_3 nanocomposite (3 wt%) was found to be 28 nm.

3.2 Acoustical Characterization

Ultrasonic wave produces molecular vibration in the samples [26]. The acoustic study provides intermolecular interactions present in nanocomposites. The temperature dependence

ultrasonic velocity of PMMA/ Fe_2O_3 is elaborated here. For the interpretation of PMMA matrix with the Fe_2O_3 nanoparticles, ultrasonic velocity is the most significant propriety. The variation of ultrasonic velocity with Fe_2O_3 NPs conc (wt%) and temperature are plotted as shown in fig 2a and 2b.
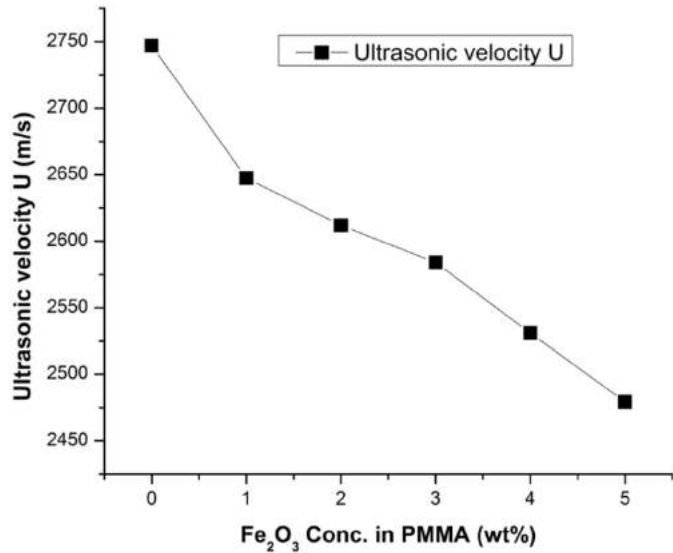
Fig.2a Variation of Ultrasonic velocity with Fe2O3 NP conc. in PMMA matrix
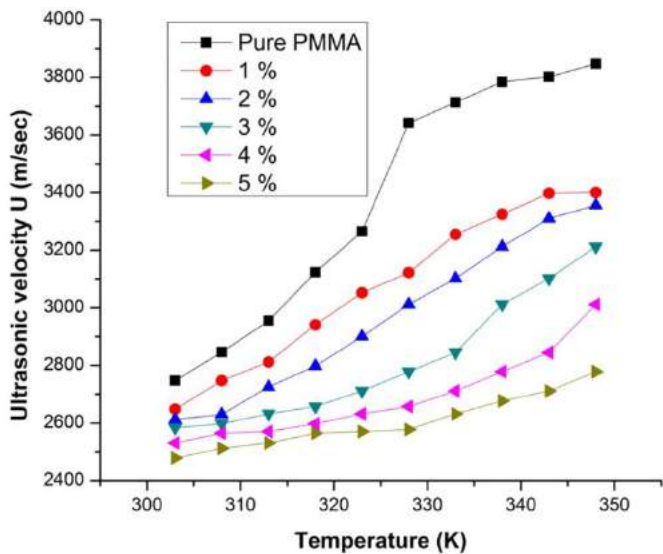
Fig.2b Temperature-dependent ultrasonic velocity of PMMA/ Fe_2O_3 matrix

From the Fig. 2a it is observed that the ultrasonic velocity was sensitive to the concentration of the nanoparticles PMMA matrix. The ultrasonic velocity of the PMMA composite decreases with the increase of nanoparticles concentration. This may be due to agglomeration of Fe_2O_3 NP in PMMA matrix. This

decrease in ultrasonic velocity with an increase of concentration is recognized by metal oxide nanoparticles – PMMA interactions, and it further confirms the dominance of intramolecular interactions over the inter-molecular interactions[27-29]. Fig. 2b also reveals the changes in ultrasonic velocity with respect to temperature. From the observed results, it is clear that the ultrasonic velocity of PMMA and its Fe_2O_3 composites also increases with increasing the temperature. it is due to nonaqueous behavior of the liquids i. e. as the temperature of fluid increases, the average speed of the molecules rises with temperature and hence ultrasonic velocity increases. it also indicates the weakening of the intermolecular forces[1].

3.3 Magnetic measurements

The magnetic properties of the synthesized nanocomposites were analyzed using a Magnetometer (VSM) at room temperature.
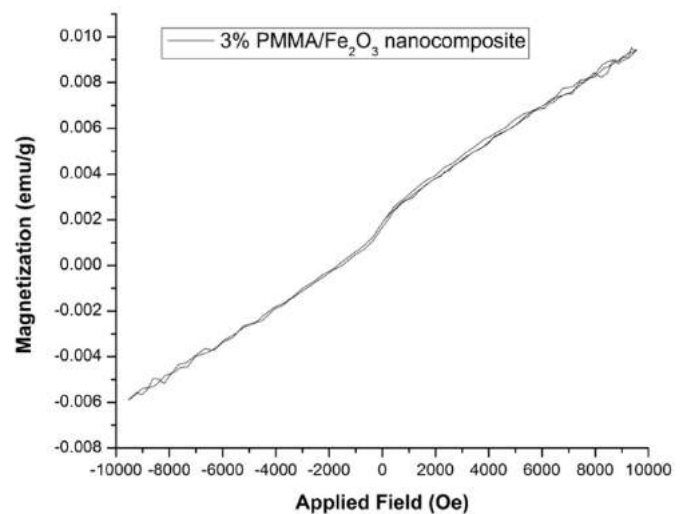
Fig.3 Hysteresis curve of PMMA/Fe_2O_3 nanocomposite (3 wt%)

Figure 3 shows the M-H curves of the prepared PMMA/ Fe_2O_3 nanocomposite (3 wt%). The saturation magnetization (Ms) values is found to be (14 emu/g) which is much greater than PMMA matrix (2 emu/g). This leads to the application of PMMA/ Fe_2O_3 nanocomposite for the synthesis of soft magnetic

materials with reasonable flexibility and moderate dielectric properties[1]

IV. CONCLUSION

The Fe_2O_3 nanoparticles of orthorhombic structure were synthesized successfully by co-precipitation method and were confirmed by XRD. PMMA and PMMA/ Fe_2O_3 nanocomposites of (1%, 2%, 3%, 4% and 5%) were characterized further for their structural, acoustical and magnetic properties. The acoustical studies were carried out at different temperatures ranging from 303 K to 348 K of the nanocomposites. . The ultrasonic velocity of the PMMA composite decreases with the increase of Fe_2O_3 nanoparticles concentration due to agglomeration whereas it increases with temperature due to intermolecular interaction. The saturation magnetization (Ms) of PMMA/ Fe_2O_3 (3 wt%) is found to be much greater than that of PMMA matrix makes it potential candidate for the fabrication of soft magnetic materials with reasonable flexibility.

V. REFERENCES

[1]. Anita, Chimankar O. P., Bansod A. R. & Sannakki B., Dielectric and Optical Study of Poly (Methyl Methacrylate) (PMMA) / Fe2O3 Films, AIP Conf. Proc. 1536(2013) 907-908, doi: 10.1063/1.4810523.

[2]. Salabat, A., Mirhoseini, F., & Valirasti, R., Engineering poly(methyl methacrylate)/Fe2O3 hollow nanospheres composite prepared in microemulsion system as a recyclable adsorbent for removal of benzothiophene., Ind. Eng. Chem. Res., 58 (2019) 7850–17858 doi:10.1021/acs.iecr.9b04322.

[3]. Ul-Haq, Y., Murtaza, I., Mazhar, S., Ullah, R., Iqbal, M., Zeeshan-ul-Huq, Amin, S. , Dielectric, thermal and mechanical properties of hybrid PMMA/RGO/Fe2O3 nanocomposites fabricated by in-situ polymerization. Ceramics International., 46 (5) (2019) 5828-5840, doi:10.1016/j.ceramint.2019.11.033

[4]. Mallikarjuna, N. N., Venkataraman, A., & Aminabhavi, T. M. A study on Fe2O3 loaded poly(methyl methacrylate) nanocomposites. Journal of Applied Polymer Science, 94(6)(2004) 2551–2554. doi:10.1002/app.21144

[5]. Liu, H., Ye, H., Lin, T., & Zhou, T. Synthesis and characterization of PMMA/Al2O3 composite particles by in situ emulsion polymerization. Particuology, 6(3)(2008) 207–213. doi:10.1016/j.partic.2008.01.003

[6]. Sun, C. C., You, A. H., Teo, L. L., & Thong, L. W. Effect of Al2O3 in poly(methyl methacrylate) composite polymer electrolytes. AIP Conference Proceedings 1958 (2018) 020028, doi:10.1063/1.5034559

[7]. Laachachi, A., Cochez, M., Leroy, E., Gaudon, P., Ferriol, M., & Lopez Cuesta, J. M. , Effect of Al2O3 and TiO2 nanoparticles and APP on thermal stability and flame retardance of PMMA. Polymers for Advanced Technologies, 17(4) (2006) 327–334. doi:10.1002/pat.690

[8]. Patel, T., Suin, S., Bhattacharya, D., & Khatua, B. B. Transparent and Thermally Conductive Polycarbonate (PC)/Alumina (Al2O3) Nanocomposites: Preparation and Characterizations. Polymer-Plastics Technology and Engineering, 52(15) (2013) 1557–1565. doi:10.1080/03602559.2013.824464

[9]. Xie H, Wang J, Xi T, Liu Y, Ai F., Dependence of the thermal conductivity of nanoparticle–fluid mixture on the base fluid., J Mater Sci Lett 21(19) (2002b) 1469–1471.

[10]. Das S.K., Putra N., Thiesen P., Roetzel W., Temperature dependence of thermal conductivity enhancement for nanofluids ASME J Heat Transf 125(4) (2003) 567–574.

[11]. Li C.H., Peterson G. P., Experimental investigation of temperature and volume fraction

variations on the effective thermal conductivity of nanoparticle suspensions (nanofluids)., J Appl Phys 99(8) (2006) 1–8.

[12]. Beck MP, Yuan Y, Warrier P, Teja AS The effect of particle size on the thermal conductivity of alumina nanofluids., J Nanopart Res 11(5) (2009) 1129–1136.

[13]. Mintsa HA, Roy G, Nguyen CT, Doucet D., New temperature dependent thermal conductivity data for water-based nanofluids., Int J Therm Sci 48(2) (2009) 363–37.

[14]. Zheng, J., Zhu, R., He, Z., Cheng, G., Wang, H., & Yao, K., Synthesis and characterization of PMMA/SiO2nanocomposites byin sitususpension polymerization. Journal of Applied Polymer Science, 115(4) (2010) 1975–1981, doi:10.1002/app.31258

[15]. Zhang, Q., Huang, W.-X., & Zhong, G.J, . Towards transparent PMMA/SiO2nanocomposites with promising scratch-resistance by manipulation of SiO2aggregation followed byin situpolymerization. Journal of Applied Polymer Science, 134(12) (2016) doi:10.1002/app.44612

[16]. Deng, Z., Jiang, Y., He, L., & Zhang, L. Aggregation–Dispersion Transition for Nanoparticles in Semiflexible Ring Polymer Nanocomposite Melts. The Journal of Physical Chemistry B, 120(44) (2016) 11574–11581, doi:10.1021/acs.jpcb.6b07292

[17]. Wang, X., Foltz, V. J., Rackaitis, M., & Böhm, G. G. A. Dispersing hairy nanoparticles in polymer melts. Polymer, 49(26) (2008), 5683-691. doi:10.1016/j.polymer.2008.10.019

[18]. Arora, R., Mandal, U., Sharma, P., & Srivastav, A. Nano composite film Based on Conducting Polymer, SnO2 and PVA. Materials Today: Proceedings, 4(2) (2017) 2733–2738. doi:10.1016/j.matpr.2017.02.150

[19]. Wei, J., Guo, F., Wang, X., Xu, K., Lei, M., Liang, Y, Xu, D. , SnO2 -in-Polymer Matrix for High-Efficiency Perovskite Solar Cells with Improved Reproducibility and Stability. Advanced Materials, Adv. Mater. (2018) 1805153. doi:10.1002/adma.201805153

[20]. Zenerino, A., Boutard, T., Bignon, C., Amigoni, S., Josse, D., Devers, T., & Guittard, F. New CeO2 nanoparticles-based topical formulations for the skin protection against organophosphates. Toxicology Reports, 2 (2015) 1007–1013. doi:10.1016/j.toxrep.2015.07.003

[21]. Calvache-Muñoz, J., Prado, F. A., Tirado, L., Daza-Gomez, L. C., Cuervo-Ochoa, G., Calambas, H. L., & Rodríguez-Páez, J. E. , Structural and Optical Properties of CeO2 Nanoparticles Synthesized by Modified Polymer Complex Method. Journal of Inorganic and Organometallic Polymers and Materials. (2019) doi:10.1007/s10904-018-01051

[22]. Xiao, J., Chen, W., Wang, F., & Du, J. Polymer/TiO2 Hybrid Nanoparticles with Highly Effective UV-Screening but Eliminated Photocatalytic Activity. Macromolecules, 46(2) (2013) 375–383. doi:10.1021/ma3022019

[23]. Nithin Kumar, N., SiddeshChincholi, Hegde, P. R., Shivagiri, S. Y., & Revanasiddappa, M. , Synthesis and characterization of Fly ash /Wooden fiber reinforced Epoxy resin polymer composite. Materials Today: Proceedings, 5(1) (2018) 501–507. doi:10.1016/j.matpr.2017.11.111

[24]. Sim, J., Kang, Y., Kim, B. J., Park, Y. H., & Lee, Y. C. Preparation of Fly Ash/Epoxy Composites and Its Effects on Mechanical Properties. Polymers, 12(1) (2020) 79. doi:10.3390/polym12010079

[25]. Fan, F., Xia, Z., Li, Q., Li, Z., & Chen, H., ZrO2/PMMA Nanocomposites: Preparation and Its Dispersion in Polymer Matrix. Chinese Journal of Chemical Engineering, 21(2) (2013) 113–120. doi:10.1016/s1004-9541(13)60448-6

[26]. Haydee A. Dalafu, Nicholas Rosa, Derak James, Dane Romar C. Asuigui,Michael McNamara., Sarah L. Stoll et al, Solid-State and Nanoparticle

Synthesis of EuSxSe1–x Solid Solutions, Chem. Mater. 30 (9) (2018), 2954-2964

[27]. Enhanced chemical stability and excellent thermochromic properties, RSC Adv., 5 (2005) 108015-108022

[28]. A. R. Bansod, O. P. Chimankar, A. Gandhe and B. Sannaki, Effect of Al2O3 Filler on Mechanical Behavior Acrylic Films, American Chemical Science 5(1) (2015) 26-31.

[29]. C. Suciu, A.C. Hoffmann, P. Kosinski, Obtaining YSZ nanoparticles by the sol-gel method with sucrose and pectin as organic recursors, Material Processing Technology 202 (2008) 316-320.

[30]. V.K. Syal, Anita Chauhan And Suvarcha Chauhan, Ultrasonic velocity, viscosity and density studies of poly (ethylene glycols)(PEG - 8,000, PEG - 20,000) in acetonitrile (AN) and water (H2O) mixtures at 250C, J. Pure Appl. Ultrason. 27 (2005) 61-69.

Structural Characterisation of conducting PPy/Rhodamine- B dye Composites Synthesized By Simple Chemical Polymerization Method

M. N. Pawar[1], N. S. Dixit[1], S. G. Khobragade[2], M.S. Dixit[3]

[1]Department of Physics, G. S. Tompe Arts, Commerce and Science College, Chandur Bazar, Maharashtra, India.
[2]Department of chemistry, BrijlalBiyani Science College, Amravati, Maharashtra, India
[3]Department of Physics, Jagadamba Mahavidyalaya, Achalpur, Maharashtra, India

ABSTRACT

This research contribution deals with thesynthesis of modified polypyrrole by doping it withxanthene dyessuch as Rhodamine-Bat different concentrations by simple chemical oxidative polymerization method by using ammonium peroxydisulphate as an oxidant. The Monomer to oxidant ratio was taken as 1:1. The synthesized composite materials was characterised by FTIR spectral analysis. The characterisation studies reveal the interaction between polymer and incorporated dopant.

Keywords : Pyrrole, Ammonium Peroxydisulphate, Polypyrrole, Triply Distilled Water

I. INTRODUCTION

Electron-conductive polymers were first reported in 1971by Nobel winners Shirakawa and his co-workers who synthesized conducting polyacetylene and found that it had a considerably high conductivity relative to other organic compounds, $10^3 Scm^{-1}$[1–3]. Since 1971, various conducting polymers and their synthesis mechanisms have been studied actively by many researchers [4]. Conducting Polymer Composites are 21st century materials used to meet the demand of improved materials and possess a combination of several desirable properties. With time the research conducted on studying more properties and improving the manufacturing process of composite material has increased[5]. Hybrid materials, are of profound interest owing to their unexpected synergistically derived properties because they can present simultaneously both the properties of a dopant molecule besides the usual properties of polymer (an organic molecule) with better chemical, mechanical, and thermal stabilities and reproducibility[6]. In this present research work conducting polymer PPy/Rhodamine-B dye composite was synthesized throughchemical oxidative polymerization route by using ammonium peroxydisulphate as an oxidant at low temperature.The monomer to oxidant ratio was 1:1M.Further its structural characterization was carried out through FTIR analysis.

II. METHODS AND MATERIAL

All the chemicals required in the present work like monomer pyrrole, oxidizing agent, ammonium peroxydisulphate and dopant Rhodamine-B are of A.R.Grade. PPy/Rhd-B dye composite was synthesized by simple chemical oxidative polymerization method.

The aqueous solution of 0.1 M Ammonium peroxydisulphatewas added to 0.0001 M aqueous solution of Rhodamine-B with constant stirring. After a vigourous stirring at 50^0 C drop by drop 0.1 M solution of monomer pyrrole was added. It was observed that as soon as monomer solution was added the color of reaction mixture changes instantaneously and the solution becomes dark green/black in color. The reaction was carried out at 50C. The reaction was stirred for few hours on magnetic stirrer which gives rise to formation of precipitate of polymer composite. This reaction mixture was allowed tostand for 24 hours in order to complete polymerization process. The resulting product was vacuum filtered. The precipitate was washed with copious amount of triply distilled water. Until the washing was clear. The polymer composite was dried in desiccator and again dried in an oven at $40-50^0$ C. similarly composite with 0.00001 M concentration of Rhd-B was also synthesized. The synthesized product was further characterized by FTIR Analysis.

III. RESULTS AND DISCUSSION

In order to find the nature of bonding in pyrrole and dopant Rhodamine-B was studied by FTIR spectrum of its composite materials.

The FTIR spectrum of PPy/ Rhodamine-Bis given in figure below-

PPy/ 0.00001M Rhodamine-B

PPy/ 0.0001M Rhodamine-B
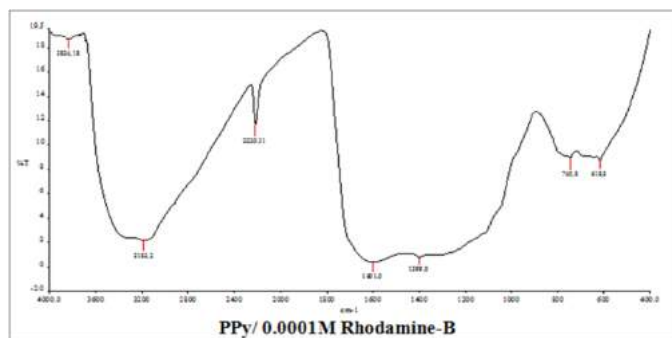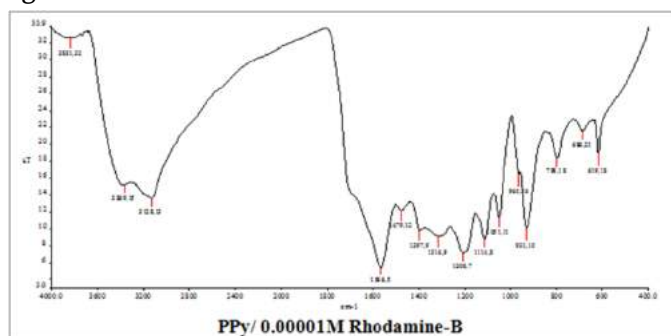
The FTIR Spectra of PPy/Rhodamine-B composites with 0.0001 and 0.00001 M concentration of $LaCl_3$ shows six principle bands which are characteristic to represent N-H, Ar-C=C-H, C=C, C-N, C-C stretching vibrations and C=C-H bending vibrations The peaks below 1000 cm^{-1} in PPy/Rhodamine-B composites may be assigned to C-C-H bending vibrations. From these peaks it is revealed that the basic nature of polymeric material is same

Compared with higher concentration spectra peaks, the peaks of lower concentration spectral peaks are sharp. The reason behind FTIR peak is broadening is vibration may be restricted in presence of high dopant concentration. On increasing dopant concentration the intensities of most of the bands affected, this can be explained on the basis of constrained growth and restricted modes of vibrations in PPy chain due to interaction of dopant ions. A very broad peak near 3834.18 cm^{-1} and 3831.32 cm^{-1} indicates –COOH group of Rhd-B dye. The peak is broadened indicating to strong H-bonding. The very short peaks near 1316 cm^{-1} in both the spectrum indicates C-O bonding present in the dye. Most of the bands are shifted to lower frequency region indicates increase in conjugation after doping.

Table : Vibrational Frequencies of FTIR spectra For PPy/ Rhodamine B composite

Polymer Composite	Position of absorption maxima (cm^{-1})					
	N-H Stretching	Ar-H Stretching	C=C Stretching	C-C Stretching	C-N Stretching	C=C-H (Bending)

Pure PPy	3400	3120.42	1563.23	1206.27	1050.32	929.31
PPy/ 0.00001M Rhd-B	3369.15	3128.13	1566.5	1208	1051.11	931.10
PPy/ 0.00001M Rhd-B	3183.2 Broad	2220.11 Broad	1601.0 Broad	˜1200.0 Broad	˜900 Broad	745.8 Broad

IV.CONCLUSION

The PPy/Rhd-B dye composite were synthesized by chemical polymerization method. It is a simple and lowcost method for synthesis. The composite formation was confirmed by FTIR analysis. The IR study that the interaction exist between PPy and Rhd-B.The principle bands obtained IR spectrum of each composite confirms aromatic and highly conjugated polymeric structure. As theconcentration of dopant increases there is shift in bands at lower frequency region indicates increase in conjugation due to doping which affect the conducting properties of the polymers.

V. REFERENCES

[1]. B.C.Roy ,M.D.Gupta, L.Bhaumik, J.K.Ray, Bull.Mater.Sci., 24 (2001) 389.

[2]. Wessling B., Handbook of conducting Polymers (New York, Marcel Dekker Inc Press) P (1998)

[3]. J.Heeger, Angrew Chem. Int. Ed. Engl. 40, 2591 (2001).

[4]. J.Kido and Y.Lizumi, Appl. Phys.Lett. 73, 2721 (2002).

[5]. A.Shakoor, T.Z. RizwiA.Nawaz, Mater Sci : Mater Electron, 22 (2011) 1076.

[6]. J. Stejskal, Pure Appl. Chem., 74 (2002) 857.

Solvent Extraction and Spectrophotometric Determination of Cobalt (II) With N,N′-BIS (Salicylaldehyde) Ethylenediamine [Salen]

S.M.Parkhi[1], V.P.Dhatrak[1], A.M.Nannaware[1]

[1]Department of Chemistry, Anand Niketan College Warora, Maharashtra, India

ABSTRACT

A method for solvent extraction and spectrophotometric determination of Cobalt (II) with N,N'-Bis(salicylaldehyde) ethylenediamine (salen) has been studied .The method is based on formation of Co - N,N'-Bis(salicylaldehyde) ethylenediamine (salen) complex. Here Co act as metal and N,N'-Bis(salicylaldehyde) ethylenediamine (salen) act as ligand .The absorption spectra of Co(II)-salen complex extracted at different pH and it was found to be maximum at pH 6 and measured against reagent blank. The light yellow Co(II)-N,N'-Bis(salicylaldehyde)ethylenediamine (salen) complex solution show maximum absorption at 410 nm .

Keywords : Solvent extraction, Spectrophotometer, Cobalt , N,N'-Bis(salicylaldehyde) ethylenediamine (salen) , pH .

I. INTRODUCTION

In its simplest form, extraction refers to the transfer of a solute from one liquid phase to another. The most common case is the extraction of an aqueous solution with an organic solvent. Diethyl ether, benzene, and other hydrocarbons are common solvent that are less dense than water and form a phase that sits on top of the aqueous phase. Chloroform, dichloromethane, and carbon tetrachloride are common solvents that are immiscible with and denser than water [4]. Solvent extraction is another name for liquid-liquid distribution that is distribution of a solute between two liquids that must not be completely mutually miscible. This method makes use of an organic compound capable of extracting the metal ion of interest, or a complex of it, from the aqueous phase into an immiscible organic solution.

Theory of Spectrophotometry and Colorimetry:-

Theory of Spectrophotometry which is helpful in the quantitative analysis of sample is very well explained [5]. When light (monochromatic or heterogeneous) is incident upon a homogeneous medium, a part of the incident light is reflected, a part is absorbed within the medium, and the remainder is transmitted. If the intensity of the incident light is expressed by Io, that of the absorbed light (Ia), the transmitted light (It), and the reflected light (Ir), then:

$$Io = Ia + It + Ir \quad \ldots\ldots\ldots\ldots\ldots (1)$$

For air-glass interface, consequent upon the use of glass cells, it may be stated that about 4 per cent of the incident light is reflected. Ir is usually eliminated by the use of a control, such as a comparison cell, hence:

$$Io = Ia + It \quad \ldots\ldots\ldots\ldots\ldots.. (2)$$

Lambert (1760) investigated the relation between Io and It. Beer (1852) extended to solutions. Spectrophotometry and colorimetry are based upon Lambert's and Beer's laws.

Basic Principles of Solvent Extraction-

The solvent extraction methods are based on the four basic principles

(a) Gibb's phase rule
(b) Distribution ratio or extraction coefficient
(c) Partition coefficient, P
(d) Percentage extraction

Classification of Solvent Extraction systems :

Extraction can be classified on the basis of

I.   Nature of extracted species
II.   Process of extraction
III.   There are two types of extraction depending on the basis of the nature of extracted species, a. Chelate extraction   b. Ion association
IV.   Classification based on the basis of process of extraction

(a) Extraction by chelation or Chelate formation
(b) Extraction by Ion pair formation
(c) Extraction by salvation
(d) Synergistic extraction

II. METHODS AND MATERIAL

All chemicals used were of A.R.grade. Separating funnels for batch extraction, glass apparatus. The instruments required for the whole solvent extraction and determination process are very simple like pH meter, spectrophotometer etc.

Preparation of stock solution :-

For 0.01 M CoSO4 Solution : Cobalt sulphate solution was prepared by dissolving 0.2811 g of CoSO4.5H2O in slightly acidic media and volume was made by distilled water till mark in 100 ml volumetric flask.

For 0.001 M CoSO4 Solution : 10 ml of 0.01 M cobalt sulphate solution was taken in 100 ml volumetric flask and volume made up to the mark by adding distilled water.

For 0.0001 M CoSO4 Solution : 10 ml of 0.001 M cobalt sulphate solution was diluted in 100 ml volumetric flask by adding distilled water.

Preparation of 0.1% reagent : 0.1g of N,N'-Bis(salicylaldehyde) ethylenediamine (salen) (purity more than 98%) was dissolved in chloroform in 100 ml volumetric flask and volume made up to mark.

III. RESULTS AND DISCUSSION

Systems were prepared, having different pH of solution with constant metal ion concentration 5.89 µg (in 1 ml). pH was adjusted with ammonium hydroxide and hydrochloric acid. Volume of aqueous phase was kept constant to 25 ml. Solution was then transferred to separating funnel, 5 ml of salen solution was added.

Each system was shaken for 5 minute allowed to equilibrate for 5 minute. Co (II) from aqueous phase was extracted into organic phase. Absorbance of organic phase was measured at 410 nm against reagent blank.

To determine λmax of a solution:

λmax = 410 nm

At this λmax , the absorbance of each system were measured

Absorbance of system at different pH :

Wavelength(nm)	Absorbance
400	0.349
<u>410</u>	<u>0.366</u>
420	0.333
430	0.305
440	0.280

From the above table it is cleared that, maximum absorbance shown at pH = 6.0, Hence the different systems were prepared at pH = 6.0 for determination of calibration graph and absorbance were measured.

Preparation of Calibration Curve at pH = 6.0

In this case different concentration of metal ion was used and reagent concentration was kept constant.

Each system was shaken for 5 minute. After equilibration organic layer was extracted and absorbance was measured for each system.

System No.	pH	0.0001 M CoSO₄ Solution (ml)	Amount of Co (II) taken in (µg)	0.1% Salen Reagent in chloroform (ml)	Distilled water (ml)	Absorbance
1	1	1	5.89	5	19	0.028
2	2	1	5.89	5	19	0.036
3	3	1	5.89	5	19	0.306
4	4	1	5.89	5	19	0.382
5	5	1	5.89	5	19	0.406
6	6	1	5.89	5	19	0.467
7	7	1	5.89	5	19	0.463
8	8	1	5.89	5	19	0.455
9	9	1	5.89	5	19	0.451
10	10	1	5.89	5	19	0.435

System No.	Volume of 0.0001 M CoSO₄ (ml)	Amount of Co(II) taken in µg	Reagent 0.1% Salen in chloroform (ml)	pH water (ml) [pH =6]	Absorbance
1	1	5.89	5	19	0.050
2	2	11.78	5	18	0.102
3	3	17.67	5	17	0.186
4	4	23.57	5	16	0.215
5	5	29.46	5	15	0.252
6	6	35.35	5	14	0.291
7	7	41.25	5	13	0.342
8	8	47.14	5	12	0.420
9	9	53.03	5	11	0.430
10	10	58.93	5	10	0.446
Blank			5	20	

System No.	Volume of Unknown sample (ml)	0.1% Reagent [Salen] in chloroform	Absorbance For Co (II) (at pH = 6.0)
1	5	5	0.237
2	4	5	0.184

Graphs:

For determination of λ_max

To determine the absorbance of unknown sample:-

Following systems of unknown sample were prepared and absorbance was measured.

Calibration graph for Co(II) at pH=6

[Plot of Absorbance Vs concentration of Co(II) in ppm]

Calculation

- Calculation for Unknown Sample No. 1 :-

Theoretical Value of Co(II) –

1000 ml of 1 M CoSO₄ Solution = 58.93 g of Co(II)

∴ 1 ml of 0.0001 M CoSO₄ Solution = X g of Co(II)

∴ $X = \frac{(1 \times 0.0001 \times 58.93)}{1000}$

∴ X = 5.893 ×10⁻⁶ g of Co(II)

∴ = 5.89 µg of Co(II)

But in Unknown Sample, 5 ml of CoSO₄ Solution was taken.

∴ 5 ml of CoSO₄ Solution = 5 × 5.89

= 29.46 µg of Co(II).

Experimental Value of Co(II) -

From calibration graph of Co(II), In unknown sample, Co(II) was extracted by solvent extraction method shows absorbance 0.237 which corresponds to 28.5 µg.

Hence experimental value = 28.5 μg

$$\% \text{ Error} = \frac{\text{Theoretical value} - \text{Experimental value}}{\text{Theoretical value}} \times 100$$

$$\% \text{ Error} = \frac{(29.465 - 28.5)}{29.465} \times 100 = 3.27\%$$

- Calculation for Unknown Sample No. 2 :-

Theoretical Value of Co(II) –

1000 ml of 1 M CoSO₄ Solution = 58.93 g of Co(II)

∴ 1 ml of 0.0001 M CoSO₄ Solution = X g of Co(II)

∴ $X = \frac{(1 \times 0.0001 \times 58.93)}{1000}$

∴ X = 5.893 ×10⁻⁶ g of Co(II)

∴ X= 5.89 μg of Co(II)

But in Unknown Sample, 4 ml of CoSO₄ Solution was taken.

∴4 ml of CoSO₄ Solution = 4 × 5.89

= 23.57 μg of Co(II).

Experimental Value of Co(II) -

From calibration graph of Co(II), In unknown sample, Co(II) was extracted by solvent extraction method shows absorbance 0.184 which corresponds to 22.3 μg.

Hence experimental value = 22.3 μg

$$\% \text{ Error} = \frac{\text{Theoretical value} - \text{Experimental value}}{\text{Theoretical value}} \times 100$$

$$\% \text{ Error} = \frac{(23.572 - 22.3)}{23.572} \times 100 = 5.39\%$$

The % Error was found to be

Absorption Spectra -

The absorption spectra of Co(II) salen complex extracted at different pH and it was found to be maximum at pH = 6.0 and measured against reagent as blank. The light yellow colour of Co(II) salen complex solution show maximum absorption at 410 nm. Hence all absorbance measured at 410 nm.

Effect of Various Solvent -

Various organic solvent such as alcohol, n-butanol, ethyl alcohol, carbon tetrachloride were tried as a solvent but chloroform was found to be most effective.

Effect of pH and Metal Concentration -

Solvent extraction behavior of Co(II) salen complex was studied in pH range 1.0 to 10.0 and varying metal concentration i.e. 0.001 M, 0.0005 M, 0.0001 M. It was observed that extraction was quantitative at the pH = 6.0 and at the concentration 0.0001 M.

Colour of the species -

Sample No	Metal	Theoretical Value	Experimental Value	% Error
1	Co(II)	29.46	28.5	3.27
2	Co(II)	23.57	22.3	5.39

Colour of the species at different pH was found to be slightly different. At pH 1.0 to 2.0, it was almost colourless but from pH = 3.0 to 10.0 it developed into pale yellow colour.

IV. CONCLUSION

The present investigation had resulted in offering a convenient liquid-liquid extraction method for separation of Cobalt (II). Cobalt (II) can be extracted by salen dissolved in chloroform.

This method has number of advantages over existing method such as easy phase separation, less equilibration time etc. Salen extracted Cobalt (II) very rapidly, equilibrium was reached within 5 minutes.

On the basis of my practical work and Literature review, it can be concluded that this technique is prominent to execute for extraction of various metal from the mixture of metals, alloys etc and above data can be used in industries.

V. REFERENCES

[1]. J. R. Dean, Extraction Method for environmental Analysis, John Wiley and Sons, Chichester 1998.

[2]. E. M. Thurman, M. S. Mills, Solid-Phase Extraction, Principle and Practice. John Wiley and Sons, New York, 1998.

[3]. P. Triangle, Method for chemical analysis of water and waste, 1983.

[4]. Y.Marcus, The Properties of Solvents, John Wiley and Sons, New York. 1998.

[5]. Sandell B.E.,"Colorimetric Determination of Traces of Metals",3rd Ed. Wiley Inter Science (1978)..

[6]. T.Sekine, Y. Hasegawa, Solvent Extraction Chemistry, Marcel Dekker, New York. 1997.

[7]. H.Stephen, T. Stephen, Solubilities of Inorganic and Oganic Compounds. Pergamon Press, London, 1963.

[8]. H.Kaur, Instrumental method of chemical analysis. Pragati Publication, 2012.

[9]. G. Raj, Advanced Physical Chemistry, 35th Ed. Goel publishing house, Meerut 2009.

[10]. D.Matheel, Al-Sabti, Eng. and Tech. 26(5), 2008.

[11]. G. H. Nikamand, B. S. Mohite, Journal of Chemical Sciences 2(1), 75-82, 2012.

[12]. Khopkar S.M.,"Analytical Chemistry of Macrocyclic and Supramolecular Compounds", 2nd Ed., Springer Verlag (2005).

Preparation and Photoluminescence Properties of Eu²⁺ Doped Lithium Alumino-Borate Phosphor, LiAlB₂O₅ : Eu²⁺

R. S. Palaspagar*, P. K. Tale

Department of Physics, Shivramji Moghe College, Kelapur (Pandharkawada), Maharashtra, India

ABSTRACT

Blue luminescence with near UV excitation has observed in $LiAlB_2O_5:Eu^{2+}$ (LABO) phosphors. Eu^{2+} doped LABO has synthesized by the solution combustion method of corresponding metal nitrates (oxidizer) and urea (fuel) at furnace temperature as low as 550 °C. The phase purity and morphology of LABO samples has characterized by powder X-ray diffraction (XRD) and scanning electron microscopy (SEM), respectively. Photoluminescence properties of the phosphor has investigated by measuring the excitation and emission spectra using spectrofluorometer at room temperature. The excitation spectrum of the blue fluorescence (λ_{em}=469 nm) shows two bands with their peaks at about 207 and 288 nm, respectively, which are due to the crystal field splitting of the Eu^{2+} d orbital. Under the excitation of 207 and 288 nm, the emission spectrum shows a strong band with a peak at about 469 nm, which corresponds to 4f–5d transition of Eu^{2+} ions, and there is a shoulder emission which are very weak in the lower energy side peaking at 594 nm and 616 nm. The Commission International de l'Eclairage (CIE) coordinates (0.126, 0.053) evidence that the phosphors emit in the blue light region.

Keywords: Borate, Blue Phosphor, Combustion synthesis, Photoluminescence.

I. INTRODUCTION

The Alumino-Borates have attracted much research interest in the past few years because of their potential applications as NLO materials [-]. Divalent europium is an important activator for luminescent materials, which have been extensively studied for years [-]. The luminescence of Eu2+ activated phosphors usually results from the ground 4f7 levels to the excited 4f65d configuration. Since the 4f–5d transition is electric-dipole allowed, the absorption and emission of Eu2+ are very efficient in many hosts. Furthermore, because of the large spatial extension of the 5d wave function, the optical spectra are usually broadened and depend on the surroundings of the Eu2+ ions. Thus, the

choice of host is a critical parameter for determining the optical properties of the Eu2+ ions [-]. Very recently, we have independently synthesized a series of alkaline earth halosilicate phosphors with excellent photoluminescence properties [-]. As the multiplex compound, alkali earth halosilicate crystal has lower synthesis temperature, higher physical and chemical stability, which makes it a suitable host lattice for luminescence materials.

In present work we discussed the solution combustion synthesis technique for fabrication of Eu2+ doped LiAlB2O5 phosphor and studied their photoluminescence properties at room temperature.

II. METHODS AND MATERIAL

Inorganic borate phosphors were prepared by a novel method described earlier [-], which is a variation of the combustion synthesis. The stoichiometric amounts of high purity starting materials, Li (NO3)2 (A.R.), Eu2O3 (high purity 99.9%), H3BO3 (A.R.), CO(NH2)2 (A.R.), Al(NO3)3.9H2O (A.R.) have been used for phosphor preparation. The starting materials with little amount of DD water were mixed thoroughly in agate mortar to obtain homogeneous solution. The excess water was removed by heating the samples at temperature 70 0C for about 10 min and the solution then transferred directly to the pre-heated furnace, maintained at temperature 550 °C, for combustion. Following the combustion, the resulting foamy samples were crushed to obtain fine particles and then annealed for 4 hr at temperature 850 °C under slightly reducing atmosphere. The prepared materials were characterized by powder XRD. Powder X-ray diffraction measurements were taken on Rigaku Miniflex II X-ray Diffractometer and compared with the ICDD files. Surface morphology of the calcined powder sample was observed by scanning electron microscopy (SEM). PL & PLE measurements at room temperature were performed on Hitachi F-7000 spectroflurometer with spectral resolution of 2.5 nm.

III. RESULTS AND DISCUSSION

3.1 X-ray Diffraction Pattern

The XRD pattern of the host lattice of LiAlB2O5 is as shown in Fig. 1 and it was found to be in good agreement with the standard ICDD file No. 01-070-5423.
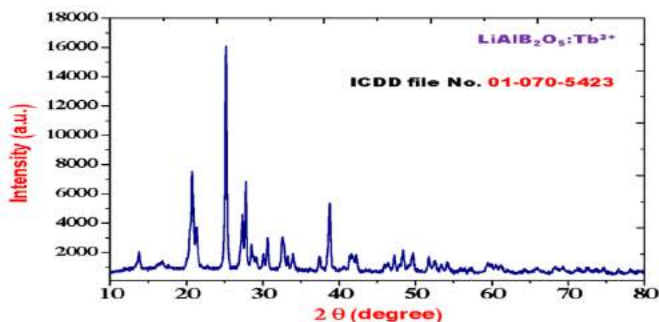
Fig. 1 XRD pattern of LiAlB2O5 phosphor.

3.2 SEM images of phosphor powders

The FE-SEM photograph of LiAl0.97B2O5:0.03Eu2+ powder prepared by solution combustion method is as shown in Fig. 2. The shape of the particles was observed to be foamy random nature with high agglomerate phenomenon.

Fig. 3 FE-SEM micrograph of LiAl0.97B2O5:0.03Eu2+ phosphor.

3.3 Photo Luminescence of LiAlB2O5:Eu3+

Fig. 4 shows the excitation and emission spectra of the Li(1-x)AlB2O5:xEu2+ (x=0.03) phosphor. The excitation spectrum of the blue fluorescence (λem=469 nm) shows two bands with their peaks at about 207 and 288 nm, respectively, which are due to the crystal field splitting of the Eu2+ d orbital. Under the excitation of 207 and 288 nm, the emission spectrum shows a strong band with a peak at about 469 nm, which corresponds to 4f–5d transition of Eu2+ ions, and there is a shoulder emission which are very weak in the lower energy side peaking at 594 nm and 616 nm. These may be due to the 5d energy level of Eu2+ and the lower level of 4f state overlap, so the electron of 4f state can be excited to 5d state. The broad luminescence of Eu2+ is due to 4f65d1→4f7 transitions. However, the 5d state is easily affected by the crystal field; that is to say, different crystal field scan split the 5d state in different way. This makes Eu2+ emit different wavelength light in different crystal fields and the emission spectrum can vary from the ultraviolet to the red region [ ]. The two possible sites for Eu2+ incorporating into LiAlB2O5 lattice are the Al3+ sites or Li+ sites. The Li+ (0.76 Å) ion has a much larger ionic radius, compared with that of Al3+

(0.54 Å) ion. However, the ionic radius of Li+ (0.76 Å) is slightly smaller than that of Eu2+ (1.12 Å). So it would be expected that Eu2+ would replace Al3+ in the crystal lattice, and could hardly incorporate into the groups [(Al2O7)8-]. The CIE chromaticity coordinates for LiAl0.97B2O5:0.03Eu2+ were calculated from the PL spectra under 288 nm excitation and marked with a star in the CIE 1931 chromaticity diagram in Fig. 5. The chromaticity coordinates (x,y) of this phosphor are calculated to be (0.126,0.053), respectively, which indicates that the emission color of the as prepared phosphors is located in the bright blue region with some greenish touch.
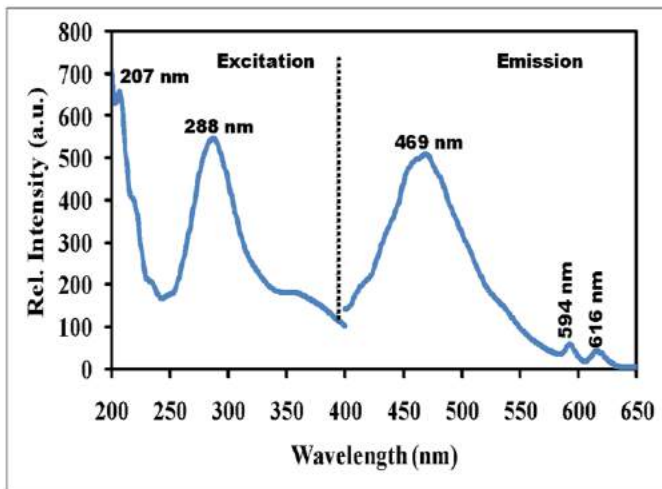
Fig. 4 Representative PL excitation and emission spectra of LiAl0.97B2O5:0.03Eu2+ phosphor.
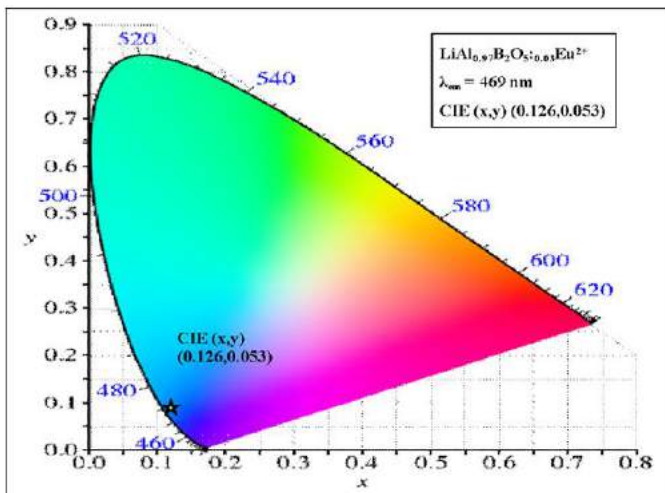
Fig. 5 Chromaticity coordinates of LiAl0.97 B2O5:0.03 Eu2+ phosphor in the CIE 1931 chromaticity diagram.

IV. CONCLUSION

The phosphor LiAl0.97B2O5:0.03Eu2+ was synthesized by a simple, time saving and cost effective solution combustion technique. Under the excitation of 207 and 288 nm, the emission spectrum shows a strong band with a peak at about 469 nm, which corresponds to 4f–5d transition of Eu2+ ions, and there is a shoulder emission which are very weak in the lower energy side peaking at 594 nm and 616 nm. The phosphor possesses excellent blue emitting property that could be attractive to a wide range of potential applications.

V. REFERENCES

[1]. H. Honingsmann, Clin Exp Dermatol 26 (2001) 343-346.

[2]. N. Ye, W.R. Zeng, J. Jiang, B.C. Wu, C.T. Chen, B.H. Feng, X.L. Zhang, J. Opt. Soc. Am. B 17 (2000) 764-768.

[3]. S.H.M. Poort, W.P. Blokoel, G. Blasse, Chem. Mater. 7 (1995)1547–1551.

[4]. Ming Yang, Siyuan Zhang, J. Phys. Chem. Solids 64 (2004) 213–221.

[5]. A. Garcia, B. Latourrette, C. Fouassier, J. Electrochem. Soc. 126 (1979)1734–1736.

[6]. A. Meijerink, G. Blasse, J. Lumin. 47 (1990) 1–5.

[7]. Zhiguo Xia, Jiayue Sun, Haiyan Du, Wei Zhou, Opt. Mater. 28 (2006)524–529.

[8]. Zhiguo Xia, Jiayue Sun, Haiyan Du, J. Rare Earths 22 (2004) 370–374.

[9]. R. S. Palaspagar, A. B. Gawande, R. P. Sonekar, S. K. Omanwar, J. Lumin. 154, 58 (2014)

[10]. R. S. Palaspagar, A. B. Gawande, R. P. Sonekar, S. K. Omanwar, Int. J. light & electron opt. 126, 5030 (2015)

[11]. R. J. Xie, N. Hirosaki, Sci. Technol. Adv. Mater., 8 (2007) 588.

Geochemical Evolution of Groundwater in the Purna Alluvial Basin, Maharashtra

Pravin S. Parimal

Department of Geology, G. S. Tompe Arts, Commerce & Science College, Chandur Bazar, District Amravati, Maharashtra, India

ABSTRACT

Groundwater qualities of Purna basin saline area have been extensively monitored in pre- and post-monsoon periods of the year 2006 to evaluate its groundwater chemistry. The interpretations on the based on a total of 94 samples each were collected in pre- and post-monsoon periods out of which, 24 belongs to dug wells and rest 70 to bore wells. Most of the samples are collected from the saline area and analyzed various physic-chemical parameters like pH, electrical conductivity (EC), total dissolved solid (TDS), alkalinity, sodium (Na), potassium (K), calcium (Ca), magnesium (Mg), hardness (TH), chloride (Cl), sulphate (SO4) and nitret (NO3). On the basis of physical and chemical parameters of groundwater of both borewells and dugwell in general, high to very high then the permissible limits of various constituents/parameters, as per the standard set by WHO (1984) and Indian Slandered (1991). In the study area the concentration pH, TDS, Na, NO_3 and total hardness show an increasing trend from pre-monsoon to post-monsoon period, in both shallow and deep aquifers. On the basis of mean value electrical conductivity and TDS are high recorded in deep aquifer.

I. INTRODUCTION

The continuation of groundwater salinity in the study area is already been reported about five decade back (Wynne, 1869) but the problem could get initial attention after a gap of five decades (Crookshank, 1926; Kailasam, 1949; Chatterjee, 1959) etc. Adyalkar (1963), for the first time, reported geology, hydrogeology, palaeogeography, pattern of sedimentation and probable cause of salinity. It is noticed that the salinity problem of the area remains the same, despite of the fact, that general groundwater problem including peripheral sweet water zone has become more acute due to lowering of groundwater table, mainly because of unwise and excessive pumping, low rain fall, poor management etc.

A close review of the salinity problem shows that systematic approach to interpret the cause, extend and present status of salinity is still lacking. As such, one-time geochemical data on the saline groundwater is not available (Adyalkar, 1996), which is probably true even today. Considering the severeness of the problem, the work has been initiated by collecting the groundwater samples from entire saline area in order to interpret the present status of the salinity.

STUDY AREA

The study region, located between longitudes 75˚56'25" to 77˚56'46"E and latitudes 20˚08'31" to

21˚40'30"N. the present study cover an area of 6,090 km2 mostly covered by the basalt of Deccan Trap while the alluvial tract occupy mostly the central part, of which, 2,726 km2 central part is marked by saline groundwater. The area experiences salinity problem, covering major parts of districts Amravati, Akola and Buldhana. It is covered by the Survey of India toposheet nos. 55G/9-12, 18; 55H/1,5; 55D/1, 9 & 13. The groundwater samples are collected from the saline track including marginal sweet water area.

II. METHODS AND MATERIAL

Ninety-four water samples each were collected in pre- and post-monsoon periods form dugwell and borewell. In case of bore wells, samples have been taken after pumping of the stagnant water, whereas, sampling from the dug wells have been carried out by the wells which were in continuous use. The analysis has been carried out as per the procedure laid down by APHA (1992). The pH and EC were measured immediately at sampling site using portable meters. Alkalinity (Al), calcium (Ca), chloride (Cl) and total hardness (TH) were determined by respective volumetric titration methods. Magnesium (Mg) is measured by subtracting calcium value from the total hardness. Bicarbonate (HCO3) was calculated by the numerical calculation of pH and phenolphthalein alkalinity values. Sodium (Na) and potassium (K) were determined by using flame photometer, whereas, SO4 and NO3 by UVVIS spectrophotometer. Total dissolved solids (TDS) concentration was calculated from EC adhering to the procedure of Hem, (1991).

III. RESULTS AND DISCUSSION

Hydrogeochemistry

The physical and chemical parameters (average value, minimum and maximum value) including pH, EC, TDS and Major cation and anion were analyzed are given in Table 1. The dugwell show values of pH, Mg, Na, NO3 and total hardness show higher concentration in the post-monsoon, where as, the

decreasing trend for TDS, Ca, Cl and SO4 in pre-monsoon period. Also the borewell of the groundwater in the study area recorded increasing trend in post-monsoon period for pH, Ca, Na, and NO3 and decreasing trend is record for TDS, Mg, Cl, SO4 and TH.

Physical parameters

The pH of shallow aquifer varies from 6.9-9.6 (mean 7.5) in pre-monsoon period to 07-9.4 (mean 7.8) in post-monsoon period, where as, in deep aquifer the pre-monsoon value range from 6.8-8.6 (mean 7.23) and 6.9-9.3 (mean 7.6) in post-monsoon period (Table 1). The exceptionally high value of pH, more then 9, is also recorded at a few places, which may be due to the localized phenomena i.e., nature and influence of alluvial constituents, decomposition of salts and anthropogenic causes etc. Electrical conductivity, which measures total dissolved solids concentration, ranges from 300 -18,300:mhos/cm and 210-15,800:mhos/cm in shallow aquifer during pre- and post-monsoon periods; and, 200-18,200:mhos/cm and 300-18,800:mhos/cm respectively in deep aquifer. Most of the values fall in high (750-2,250:mhos/cm) and very high (2,250-5,000:mhos/cm) categories of irrigation water as proposed by Richard (1954). The higest EC value indicates the presence of salinity in groundwater Jain and Vaid (2018). The total dissolved solids are comparatively high in shallow aquifer, with an average value of 2,993mg/l in pre-monsoon and 2,726mg/l in post-monsoon period, as compared to 2,028mg/l and 1,853mg/l respectively, for deeper aquifer. The higher value of TDS of shallow aquifer is quite obvious as evaporation due to high temperature in pre-monsoon, and addition of salts through meteoric water in post-monsoon periods are the common phenomena Naik et al. (2009).

Chemical parameters

The mean values of magnesium and sodium shows that both are the dominant constituents of the groundwater of both shallow and deep aquifers, however, there is a marked change in their trends

during pre- and post-monsoon periods. Magnesium in shallow aquifer ranges from 36.9-1,978mg/l (mean 253mg/l), which shoot up to the mean value of 402.8mg/l in post-monsoon period, in a ranges of 32.9 to 205mg/l, where as, in case of deep aquifer, the pre-monsoon concentration ranges from 13.1 to 4,681mg/l (mean 332.4mg/l) and show a little decreasing trend i.e., 3,043mg/l. The concentration of sodium is exceptionally high in the shallow aquifer with a mean value of 296.6mg/l in pre-monsoon to 621mg/l in post-monsoon. Similar increasing trend of sodium has also been noticed in deep aquifer with a mean of 288.7 and 363.7mg/l, respectively. The significant increase in sodium concentration of shallow aquifer during post-monsoon period is noticeable. The concentration of calcium also shows an irregular trend in shallow and deep aquifers. In shallow aquifer, the pre-monsoon mean value is 167.6mg/l, which decreases to

129.1mg/l in post-monsoon period, where as, a reverse trend is exhibited by deep aquifer i.e., 97.9mg/l in pre-monsoon, which rise up to 111.8mg/l in post-monsoon. Potassium shows a remarkable change of concentration in shallow and deep aquifers. The mean values of potassium from shallow aquifer in pre- and post-monsoon periods are 25.16mg/l and 30.28mg/l respectively, which are quite high as compared to deeper aquifer having 5.825mg/l and 2.699mg/l, respectively.

Chloride is also a significant constituent in the shallow as well as deep aquifer, and shows a decreasing trend from pre- to post-monsoon period. However, the concentration is in general high in shallow aquifer. Similar decreasing trend is also exhibited by sulphate. Nitrate, though constituting a very less quantity, experiences a higher value in post-monsoon period in both the aquifers.

Sr. No	Para-meters	monsoon / period	Dug well Concentration in Mg/l*	Mean	Bore well Concentration in Mg/l*	Mean	WHO Standard Highest Desirable	Highest Permissible	Indian Standard Highest Desirable	Highest Permissible
1.	pH	Pre- Post-	6.9-9.6 7-9.4	7.51 7.78	6.8-8.6 6.9-9.3	7.23 7.62	6.5-8.5	7.0-8.5	6.5-8.5	-
2	EC	Pre- Post-	300-18300 210-15800	-	200-18200 300-18200	-	-	-	-	-
3.	TDS	Pre- Post-	186-11346 130-9796	2993 2726	124-11284 186-11656	2028 1853	500	1000	500	2000
4.	Ca	Pre- Post-	28.8-901.8 20-665.3	167.6 129.1	14.4-681.3 12-877.7	97.9 111.8	75	200	75	200
5.	Mg	Pre- Post-	36.9-1978 32.9-2050	253 402.8	13.1-4681 26.3-2670	332.4 304.3	-	150	30	100
6.	Na	Pre- Post-	4.5-565 30.4-2545	296.6 621	5-676 10-2008	288.7 363.7	-	200	-	-
7.	Cl	Pre- Post-	25.3-3990 35.5-1491	749.7 463.4	28.4-5424 20.5-1697	497.8 332.5	200	600	250	1000
8.	SO$_4$	Pre- Post-	3.01-296 15-350	129.5 113.8	5-296 3-275	107.2 90.3	200	400	200	400**
9.	NO$_3$	Pre- Post-	0.2-22 0.1-27	14.9 16.3	0.8-26 0.1-25.2	14.8 18.4	45	-	45	100
10	TH	Pre- Post-	140-5250 100-4770	792.5 934.4	140-8550 70-5370	765.3 733.5	100	500	300	600

Table 1. Range in concentration and mean values of physical and chemical parameters of the samples and their comparison with WHO (1984) and Indian Standards (1991) for drinking water.

IV. CONCLUSION

The comparison of analytical data of both the aquifers have been made with the specifications set by WHO (1984) and Indian Standard (1991) for human consumption. The mean values of TDS of shallow aquifer in pre- and post-monsoon periods i.e., 2,993mg/l and 2,726mg/l, clearly indicates that the water is not potable even as per the specifications of Indian Standard (1991), which has the maximum permissible limit of 2,000mg/l as compared to 1,000mg/l in case of WHO (1984) Standards. Similarly, in deep aquifer, the mean values in pre- and post-monsoon periods are 2,028mg/l and 1,853mg/l respectively, which are also very close to the highest permissible limit of Indian Standard (1991). The mean sodium concentration is also high in both shallow and deep aquifers; however, in shallow aquifer the value is exceptionally high, i.e., 621mg/l during post-monsoon period.

V. REFERENCES

[1]. Adyalkar. P. G. (1963). "Palaeogeography, nature and pattern of sedimentation and groundwater potentialities of the Purna basin of Maharashtra", Proc. Nat. Instt.. Sci. Ind. Vol. 29 A.

[2]. Adyalkar, P. G. (1996). "Palaeogeography, framework of sedimentation origin of salinity and proposal for its phased amelioration in the Purna upland alluvial valley of India". Sym. Int. App. Manag. Wt. Soil Purna Riv. Bas. Spec. Ref. Salinity Characteristic. 2-4 Feb, 1996, VRCE, Nagpur, 30-38.

[3]. APHA, (1992) Standard Method for the Examination of Water and Waste Water, 16th edn. American Public Health Association. Washington, D.C.

[4]. Chaterji, G. C. (1959). "Recommendations regarding immediate groundwater development in the Purna valley, Bombay State", Geol. Surv. Ind., Unpublished report.

[5]. Crookshank, H. (1926). "Notes on Daryapur boring and watersupply investigations in Berar". Unpublished reports.

[6]. Hem J. D. (1991) Study and interpretation of the chemical characteristics of natural water. 2254. Scientific Publishers, Jodhpur

[7]. ISI (1991). "Indian Standard Institution–Indian Standard Specification for drinking water". IS: 10500, pp. 1-5.

[8]. Jain C. K. and Upma Vaid (2018) Assessment of groundwater quality for drinking and irrigation purposes using hydrochemical studies in Nalbari district of Assam, India. Environmental Earth Sciences V. 77 (254) page 1-14

[9]. Kailasam, L. M. (1949). "A geophysical gtudy of conditions of groundwater salinity in Purna valley, Berar". Geol. Sur. Ind. Report.

[10]. Pradeep Kumar Naik., A. K. Awasthi., A. V. S. S. Anand and P. N. Behera (2009) Hydrogeochemistry of the Koyna River basin, India. Environ Earth Science, V. 59, pp.613–629

[11]. Richards, L. A. (ED), (1954). "Diagnosis and improvement of saline and alkali soils". Hand Book US Dept. of Agriculture, No.60, 160p.

[12]. WHO (1984). "Guidelines for drinking water quality. Vol. 1, Recommendations, World Health Organization". Geneva, 130p.

[13]. Wynne, W. B. (1869). "Valley of Poorna river, West Berar", Rec, Geol. Surv. India. Vol. 11, Pt.1, 1-5.

Cr³⁺ Emission in Al₅GeO₉.₅ and Al₅SiO₉.₅ Phosphors

P. K. Tawalare[1], S. K. Omanwar[2], V. B. Bhatkar[3], S. V. Moharil[4]

[1]Department of Physics,JagadambaMahavidyalaya, Achalpur City, India

[2]Department of Physics, Sant Gadge Baba Amravati University, Amravati, India

[3]Department of Physics, Shri Shivaji Science College, Amravati, India

[4] Department of Physics, RashtrasantTukadoji Maharaj Nagpur University, Nagpur,India

ABSTRACT

Combustion synthesis of Cr³⁺activated Al₅GeO₉.₅ and Al₅SiO₉.₅ phosphors was attempted. XRD results indicated formation of alumina, while luminescence results showed profound changes from Al₂O₃:Cr³⁺. Al₅SiO₉.₅:Cr³⁺a did not show any photoluminescence, while Al₅GeO₉.₅:Cr³⁺ showed very intense luminescence; almost 150% of that shown by Al₂O₃:Cr³⁺.

I. INTRODUCTION

alpha Alumina α-Al₂O₃ is a remarkable host material for rare earth ions because it presents excellent mechanical hardness combined with chemical stability and solubility besides a high transparency window from the ultraviolet to the infrared [1]. It plays a major role in many technologies due to its remarkable physical properties, such as a high melting point, hydrophobicity, high elastic modulus, high optical transparency, high refractive index, thermal and chemical stability, low surface acidity, and fine optical and dielectric characteristics [2–4]. The good adhesion to Si surface makes Al₂O₃ attractive in the microelectronics and optoelectronics [5,6]. Owing to some of these properties, it is also an excellent laser host. The ruby (Al₂O₃:Cr³⁺) is the first crystal found to exhibit a laser emission as demonstrated by Maiman at the Hughes Lab in 1960 [7,8], which marked the beginning of the solid state laser technology. The wide gain and high quantum efficiency of Sapphire

(Al₂O₃:Ti) makes this material the optimum ultrafast laser crystal [9].

There are several double oxides involving Al₂O₃which might be easily prepared by combustion synthesis using exothermic reaction between aluminum nitrate and urea. From literature, we found two particular formulae quite attractive; viz. Al₅GeO₉.₅ and Al₅SiO₉.₅. Both these compounds contain high percentage of alumina. Their structures (orthorhombic) are different from beta alumina (hexagonal) and modification of luminescence properties of Cr³⁺ in these hosts is expected. With these expectations, attempts were made to synthesize Cr³⁺ activated Al₅GeO₉.₅ and Al₅SiO₉.₅ using combustion synthesis. Results of these experiments are discussed here.

II. METHODS AND MATERIAL

Phosphors were prepared by combustion method using metal nitrates as oxidizer and urea as a fuel [10,11]. Aluminium nitrate, SiO₂/GeO₂ and urea were

thoroughly mixed in molar ratio 5:1:15.83. A crucible containing the mixture was inserted at 500 C in a preheated furnace. In few minutes the mixtures swells with evolution of gases and finally a flame appears. The flame lasts for about a minute. The crucible is removed from the furnace after the flame extinguishes. The foamy product is crushed to powder and used for further characterization. For preparing Cr^{3+} doped samples Chromium nitrate in the desired quantity was added to the starting mixture.

The crystalline phases of the synthesized samples were identified by x-ray diffraction (XRD) patterns recorded on XPERT-PRO diffractometer using Cu K_α (λ=1.54059 Å) radiation. The photoluminescence (PL) and photoluminescence excitation (PLE) spectra were measured on Hitachi F-7000 spectrophotometer.

III. RESULTS AND DISCUSSION

Fig.1 shows xrd pattern of the synthesized phosphor.Surprisingly the patterns for $Al_5GeO_{9.5}$ and $Al_5SiO_{9.5}$ both matched with that of Al_2O_3. It appears that the compounds are not formed by the combustion synthesis. Further experiments proved the contrary. EDAX analysis of $Al_5GeO_{9.5}$ clearly showed presence of Ge (Fig.2). Further, luminescence properties of these compounds were entirely different. Fig.3 shows PL emission spectrum for Cr^{3+} doped $Al_5GeO_{9.5}$ and $Al_5SiO_{9.5}$ and Al_2O_3 excited by 413 nm.Intense line attributable to ($^2E \rightarrow {}^4A_{2g}$) is seen around 698 nm in the emission spectrum of Al_2O_3:$Cr^{3+}$with several components due to splitting of ^2E levels in crystal field. Similar emission peaking at 699 nm is observed for $Al_5GeO_{9.5}$:$Cr^{3+}$with much higher intensity. On the other hand, emission was totally quenched in $Al_5SiO_{9.5}$:Cr^{3+}.

Further experiments were performed on $Al_5GeO_{9.5}$:Cr^{3+}. Fig.4 shows effect of Cr^{3+}concentration on PL emission intensity. Intensity is maximum for 0.4 mol.% Cr^{3+}. Intensity decreases for higher concentrations due to concentration quenching.From

these data critical distance for Cr^{3+} - Cr^{3+} transfer can be calculated using the formula [12].

$$R_c = 2 (3V/4\pi x_c N)^{1/3} \quad (1)$$

where x_c is the critical concentration (0.004), N is the number of Al sites in the unit cell (5) and V is the volume of the unit cell (168.034 Å^3). R_c comes out to be 25.22 Å.This is considerably greater than 17 Å observed for Al_2O_3:Cr^{3+}.
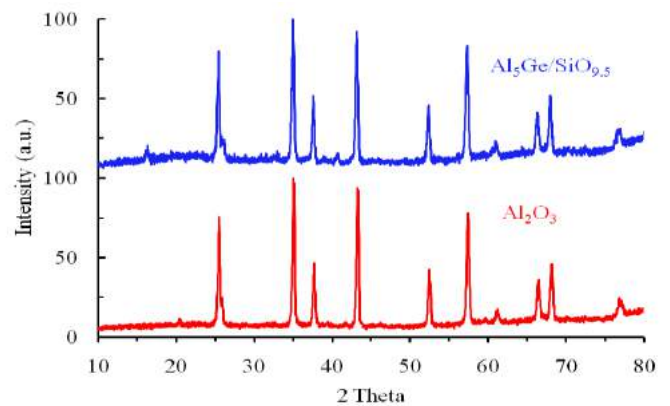
Fig.1 XRD patterns of $Al_5Ge/SiO_{9.5}$ and Al_2O_3
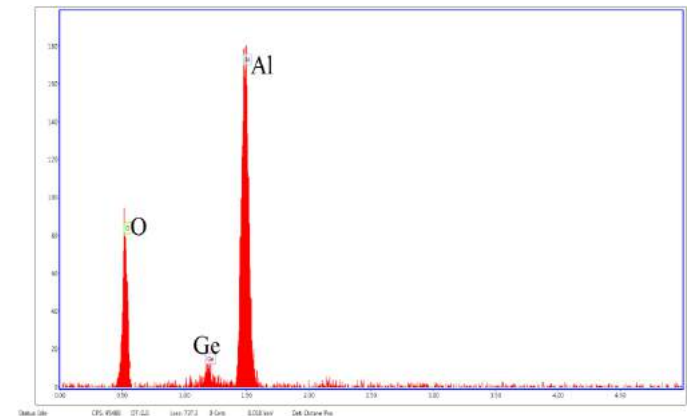
Fig.2 EDAX for Al5GeO9.5
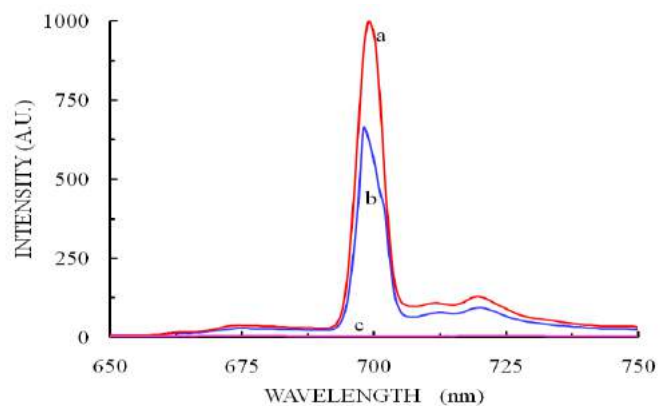
Fig.3 PL emission spectra of a) $Al_5GeO_{9.5}$, b) Al_2O_3 and c) $Al_5SiO_{9.5}$, activated with Cr^{3+}.
Excitation was by 413 nm light.
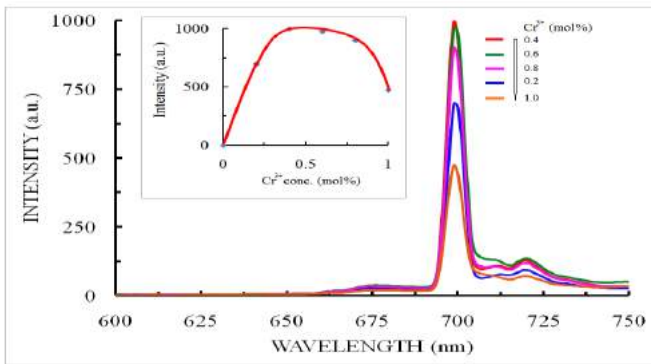
Fig.4 PL emission spectra of a) $Al_5GeO_{9.5}:Cr^{3+}$

Inset shows effect of Cr^{3+} concentration on intensity of 699 nm line.

Corresponding excitation spectrum is shown in Fig.5. $^4A_{2g} \rightarrow {}^4T_{1g}(^4F)$ and $^4T_{2g}(^4F)$ bands can be clearly seen around 413 and 556 nm. Splitting of $^4T_{1g}(^4F)$, $^4T_{2g}(^4F)$ levels is barely visible in the spectrum recorded at room temperature.

Fig.6 shows luminescence decay curve for $Al_5GeO_{9.5}:Cr^{3+}$ (0.2 mol.%). Single exponential is observed which can be fitted to decay constant $\tau = 3.5$ ms which is almost same as that for $Al_2O_3:Cr^{3+}$ (3.36 ms).
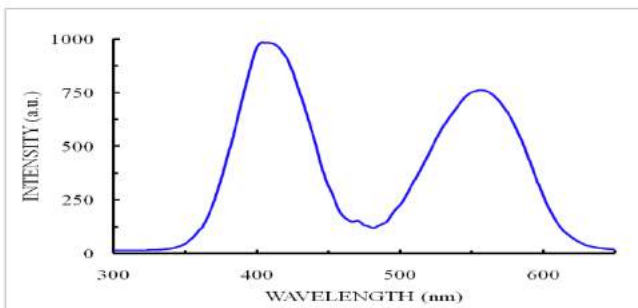
Fig.5 PL excitation spectrum for 699 nm emission of $Al_5GeO_{9.5}:Cr^{3+}$.
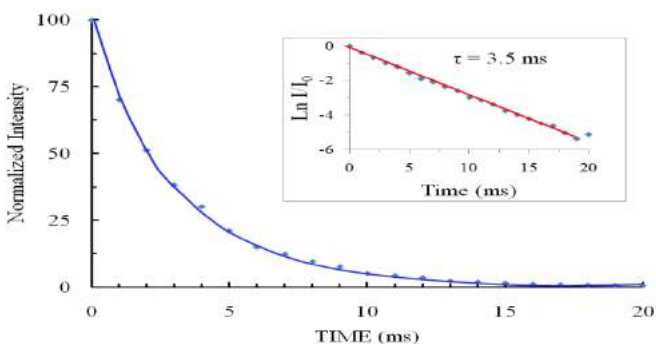
Fig.6 Luminescence decay curve for 699 nm emission of $Al_5GeO_{9.5}:Cr^{3+}$.

IV. CONCLUSION

Attempts were made to synthesize $Al_5GeO_{9.5}$ and $Al_5SiO_{9.5}$ compounds by combustion synthesis and obtain modification of luminescence properties of Cr^{3+} activated phosphors. XRD analysis of the combustion synthesized powders showed presence of alpha alumina phase. On the other hand, EDAX indicated presence of Ge. Luminescence properties were also changed a great deal. In $Al_5SiO_{9.5}$, Cr^{3+} emission was totally quenched while luminescence increased by about 50 % in $Al_5GeO_{9.5}$. These inconsistencies need to be investigated further.

V. REFERENCES

[1]. Glauco S. Maciel, NikiforRakov, Michael Fokine, Isabel C. S. Carvalho and Carlos B. Pinheiro , Appl Phys Lett, 89 (2006) 081109-1-3

[2]. Y. Kim, S.M. Lee, C.S. Park, S.L. Lee, M.Y. Lee, Appl. Phys.Lett. 71 (1997) 3604–3606.

[3]. E.P. Gusev, M. Copel, E. Cartier, I.J.R. Baumvol, C. Krug, M.A. Gribelyuk, Appl. Phys. Lett. 76 (2000) 176–178.

[4]. A. Pillonnet-Minardi, O. Marty, C. Bovier, C. Garapon, J. Mugnier, J. Opt. Mater. 16 (2001) 9–13.

[5]. L. Rebohle, M. Braun, R. Wutzler, B. Liu, J.M. Sun, M. Helm, W. Skorupa, Appl. Phys. Lett. 104 (2014) 251113.

[6]. R. Serna, C.N. Afonso, Appl. Phys. Lett. 69 (1996) 1541.

[7]. T. Maiman, Nature 187 (1960) 493.

[8]. G. Boulon, Opt. Mater. 34 (2012) 499–512.

[9]. V.B. Mikhailik, H. Kraus, D. Wahl, Appl. Phys. Lett. 86 (2005) 101909

[10]. J.J. Kingsley, K. Suresh and K.C. Patil, J.Mater. Sci. 25 (1990) 1305

[11]. J.J. Kingsley, N. Manickam and K.C. Patil, Bull. Mater. Sci. 13 (1990) 179

[12]. G. Blasse, Philips Res. Rep. 24 (1969) 131

To Study Solvation of Polyols with 5% Ethanol-Water at Room Temperature

Bhukya. P. B., Wakulkar. A. P, Nannaware. D. D

Department of Chemistry, Anand Niketan College, Warora, Maharashtra, India

ABSTRACT

Density (ρ) and viscosity(η) of Mannitol and Sorbitol have been measured in 5% Ethanol-Water solvent system in the concentration range 0.05-0.5M at room temperature 298K forthe density data, apparent molar volume (Φ_v) and partial molar volume (Φ_v^0) were worked out. The viscosity coefficient B and A constants and Staurding Constant (kn) were calculated from the viscosity data by using Jone-Dole and Staurding equation. From viscosity coefficient constant B and partial molar volume, solvation number (B/Φ_v^0) of Mannitol and Sorbitol were worked out. From these parameters, results were associated with solute-solute, solute-solvent and solvent-solvent interactions.

Keywords : Polyols, Apparent Molar Volume, Partial Molar Volume, Association Number.

I. INTRODUCTION

Solvation is one of the important intermolecular interactions. It is responsible to maintain the secondary structure of biomolecules and expressing biological and medicinal process of cellular systems [1]. Polyols (mannitol and sorbitol) are used as ingredient in products like cosmetics, health care products and pharmaceuticals [2]. Volumetric behavior of polyols gives useful information for solvation process [3, 4]. Apparent Molar Volume and Partial Molar Volume of polyols in solution are used to study solute-solvent interaction [5,6].

Polyols and carbohydrates are most important class of biomolecules and show their different biological functions such as structure and defensive metabolic recognition, receptor affinity and selectivity [7].

The molecular interactions of dilute as well as concentrated solutions of sugars in water play an important role in expressing biophysical and medicinal processes of cellular systems. The viscometric behavior of electrolytes and non-electrolytes give useful information for intermolecular interactions in the solution [8,9].Sorbitol is white crystalline powder, 6-C sugar soluble in water, it is also called Glucitol. Sorbitol is a substitute of sugar which is about 60% the sweetness of sucrose.Mannitol is a 6-Carbon sugar derived from dextrose. It has been used to treat human brain for more than 30 years. The complication of mannitol therapy is fluid and electrolyte imbalance. Hence its interaction studies with the solvent become important. [8,10].

D-Mannitol   D-Sorbitol

II. METHODS AND MATERIAL

Mannitol and Sorbitol used in this work is analytical grade with purity of > 99% was procured from SHIMADZU. Ethanol used in this work is of AR grade from CSS with 99.9% purity. Double distilled waterused for the preparation of solutions. The molar aqueous solution of solute was prepared by using digital electronic balance (Model-AJO20, aiwa) with an accuracy of ± 0.1 mg.

Densities (ρ) and viscosities (η) of aqueous solutions of Mannitol and Sorbitol in 5% Ethanol-Water were measured by using specific gravity bottle by relative measurement method with accuracy of ±0.1 kg.m⁻³ and an Ostwald's viscometer was used for the measurement of viscosity of liquid mixtures with an accuracy of 0.0001Nsm². The viscometer was calibrated before used. Time flow of water and Mannitol and Sorbitol in 5% Ethanol-Water solutions were measured respectively.

OBSERVATION TABLE:

Table 1: Apparent molar volume and partial molar volume and Sv for Mannitol and Sorbitol at 298K at different concentrations

Concentration (mol/dm³)	$\sqrt{C}$	Apparent Molar Volume (Φ_r) (m³mol⁻¹)	
		Mannitol	Sorbitol
0.05	0.2236	165.54	162.47
0.1	0.3162	164.55	161.09
0.15	0.3873	162.20	156.12
0.20	0.4472	156.04	151.24
0.25	0.5	150.91	146.43
0.3	0.5477	148.84	144.79
0.35	0.5916	143.92	140.75
0.4	0.6324	141.99	138.25
0.45	0.6708	136.92	134.32
0.5	0.7071	133.67	131.63
Partial molar volume (Φ_r^o) (m³mol⁻¹)		192.975	172.862
S_r (m³Kg¹ᐟ²mol³ᐟ²)		-82.186	-51.840

Table 2: Relative Viscosity ($\frac{\eta}{\eta_0}$) for Mannitol and Sorbitol at 298K at various concentrations.

Concentration (mol/dm³)	$\sqrt{C}$	Relative Viscosity ($\frac{\eta}{\eta_0}$)	
		Mannitol	Sorbitol
0.05	0.2236	1.05629	1.0607
0.1	0.3162	1.05968	1.06387
0.15	0.3873	1.07255	1.06967
0.20	0.4472	1.08713	1.07854
0.25	0.5	1.0981	1.09212
0.3	0.5477	1.12079	1.1288
0.35	0.5916	1.1522	1.1535
0.4	0.6324	1.1902	1.1866
0.45	0.6708	1.2255	1.2287
0.5	0.7071	1.2526	1.2841

Table 3: Values of parameters of *Staurding, Jone Dole equation* and association number for Mannitol and Sorbitol at 298K.

Compound	$\left(\frac{\eta}{\eta_0}-1\right)$ versus C	$\frac{\left(\frac{\eta}{\eta_0}-1\right)}{\sqrt{C}}$ versus $\sqrt{C}$	B x 10³/ Φ_v^o
Mannitol	$kn = 0.5649\,dm^3mol^{-1}$	B = 0.52 dm^3mol^{-1} A= -0.081 $dm^{3/2}mol^{-1/2}$	2.69
Sorbitol	$kn = 0.4958\,dm^3mol^{-1}$	B = 0.61 dm^3mol^{-1} A= -0.180 $dm^{3/2}mol^{-1/2}$	3.52

III. RESULTS AND DISCUSSION

Density and viscosity of mannitol and sorbitol were measured at room temperature at various concentrations ranging from 0.05-0.5M. Apparent Molar Volume can be calculated using density data by using the equation below [11].

$$\Phi_v = \frac{M}{\rho_0} - 1000\frac{(\rho - \rho_0)}{C\rho_0} \quad ---eqn\,(1)$$

Where, Φ_v= Apparent molar volume, C = Molarity, ρ = density of solvent, ρ₀=density of solvent and M= Molar mass of Mannitol and Sorbitol.

Volume changed due to addition of solute into solvent is called apparent molar volume. Apparent molar volume at infinite dilution, the solvent-solvent interaction is predominant known as partial molar volume [12]. The smaller values of apparent molar volumes result in strong interactions of solute-solvent molecules [13]. As the concentration increases, the interactions between solute-solute increased whereas those of solute-solvent decreases. This is because the electrostatic interaction between the solute molecules increases. The apparent molar volume data can be expressed with Messon's relation given below least square fit method [14,15].

$$\Phi_v = \Phi_v{}^0 + S_v C \qquad ----eqn\ (2)$$

Where, $\Phi_v{}^0$ is partial molar volume, it talks about the solute-solvent interactions. The values of $\Phi_v{}^0$ for mannitol and sorbitol are given in Table 1, which shows positive $\Phi_v{}^0$ values for both mannitol and sorbitol indicating positive interactions between solute and solvent molecules. Also, greater $\Phi_v{}^0$ value for mannitol indicates stronger solute-solvent interactions in mannitol as compared to sorbitol.

Negative values of S_v obtained for mannitol and sorbitol indicates breaking of water-ethanol structure due to mannitol and sorbitol. [16] This means that, mannitol and sorbitol interact strongly with water-ethanol molecules than water interacts with itself. This results in breaking of hydrogen bonds within water molecules. The value is greater for sorbitol as compared to mannitol which indicates mannitol interacts strongly with solvent system.

Relative viscosity of mannitol and sorbitol were calculated at room temperature considering solutes as monomer units of polymer system. The polymer species follows *Staurding equation* given below [17]

$$\frac{(\eta - \eta_0)}{\eta_0} = kn\ Cn \qquad ----eqn\ (3)$$

Where, η is viscosity of solution, η_0 is viscosity of pure solvent, k is constant for given solute in a given solvent, C is molar concentration of solute and n is the number of monomer units in polymer. The observed values of relative viscosity for mannitol and sorbitol at 298K are given in Table 2.

Observed data were examined to study the agreement of viscosity with *Staurding equation*. As a result, relative viscosity values were plotted as a function of different concentrations at room temperature for mannitol and sorbitol which showed linearity.

Structure breaking and making properties of solute can also be studied by considering *Jone-Dole equation* given below [18]

$$\frac{\eta}{\eta_0} = 1 + A + B\sqrt{C} \qquad ----eqn\ (4)$$

Where, $\frac{\eta}{\eta_0}$ is the relative viscosity, C is molar concentration of solute, A and B are constants for studied solute.

Coefficient A talks about the contribution for interionic electrostatic forces and coefficient B specifies chaos produced by ions in electrolyte and solutes in non-electrolytes in solvent structure [19]. Therefore, $\frac{\left(\frac{\eta}{\eta_0-1}\right)}{\sqrt{C}}$ values plotted against $\sqrt{C}$ shows linearity for mannitol and sorbitol with slope B and intercept A. The value of both the constant are reported in Table 3. The *Jone-Dole equation* is more useful for ionic solute as coefficient A gives idea about ion-ion interaction. But, in case of Mannitol and Sorbitol, being non-electrolyte covalent compounds, the values of coefficient A are found to be very small. This is because, the interionic interaction is weak in case of non-electrolytes. The very small values of intercept A may be due to non-covalent interactions like hydrogen bonding, van der waals forces, etc.

Viscosity coefficient B indicates solvation of solute and its environment [20] which depends on the solute-solvent interactions and on the relative sizes [21]. Larger and positive value of viscosity coefficient B indicates structure making property of solute with the solvent [22]. From Table 3, we can observe the positive values of B for both mannitol and sorbitol which shows their structure making ability, but the larger value is observed for sorbitol which means

structure making ability for sorbitol is greater than mannitol.

IV. CONCLUSION

The observed values for constant *kn* for mannitol and sorbitol are in close agreement with the values of coefficient B. The values of **B / Φv°** indicates the solvation of solute. Its values show important significance [23]. If the value is greater than 2.5, greater would be the association [24]. From Table 3, we can observe the values >2.5 for mannitol and sorbitol indicating their strong association with ethanol-water solvent system. The value is much greater than 2.5 in case of sorbitol showing greater association with solvent system.

V. REFERENCES

[1]. S.A. Shah and et al., Ajanta, Vol. VIII (2019) 96-102.

[2]. Wanlopchanasattru and et al., Food Hydrocolliods, 22 (2008) 1475-1484

[3]. Sudhakar S.D., et al, J.Chem. Thermodynamics,67 (2013),217-226

[4]. Muhammad A.J., et al, Food Chemistry 173(2015) 551-556

[5]. Birch,G.G, Journal of Pure and Applied Chemistry, 7(74),(2002) 1103-1108, Role of water in sweet taste chemoreception

[6]. S. Nithiyanantham, L. Palaniappan and R. Jayalaxami, J. Comp. Theo. Nano Sci., 9 (2012)1115-1119

[7]. J. F. Comesana, et al.J. Chem. Eng Data. 48 (2003) 362-366

[8]. F. J. Timmerman, Physical constant of organic compound. 1996.

[9]. Surabhi Singh and Mukhtar Singh, Indian J. Of Chem., 41A(2002) 15881-1592.

[10]. M. K. Jamal et al, Food Chemistry, 146(2014), 460-465.

[11]. F.J.Millero, et al. J. Phy. Chem, 82 (1978) 781

[12]. M.A. Jamal et al., Food Chemistry, 153 (2014) 140-444

[13]. S.A. Galema and H. Hoiland, J. Phys. Chem.,95 (1991) 5321-5326

[14]. C. Klofuftae et al, J. Acta ChimicaSlovenica, 53 (2006) 274-283

[15]. D. O. Masson, Philosophical magazine, 8(1929) 218-235

[16]. D. V Jahagirdar,Experiments in Chemistry, Himalaya Publishing House, second edition (2003)

[17]. Millard E.B (1953), Physical Chemistry for college, McGraw-Hill Book Compan: 150

[18]. G. Jone and M. Dole, J. Am. Chem. Soe, 51(1929) 2950

[19]. H. Falkenhgen and E. L. Vernon, J. Phys, 33(1932) 33.

[20]. KrishaRajgopal et al, J. Serb. Chem. Soc, 76(1) 129-142(2011)

[21]. H.d.b.Jekins et al, Chem Rev, 95 (1995) 2695

[22]. X.Ren, et al, J. Chem. Eng. Data, 43 (1998) 700

[23]. J. M. Tsagins, R.B. Martin, Arch, Biochem. Biophys. 112 (1965) 267

[24]. S. Nishikawa et al, Bull Chem Soc Japan, 67 (1994) 2870

Smart Sound Absorbing Material for Environmental Noise Reduction

Priyanka P Singh, G Nath*

Department of Physics, Veer Surendra Sai University of Technology, Burla, Sambalpur, Odisha, India

ABSTRACT

In the current scenario the insidiousness of noise issues regarded as fourth major environmental pollution in the world as per the data published by World Health Organization (WHO, 2011). In advanced countries the peripheral areas of highways, industries, airports and construction sites are well infected by the excessive sound causes significant negative impact on human's health. Thus noise reduction is essential for the present and future generation and significantly increases the importance noise control technology. Due to much unsuitability associated with synthetic sound absorber materials it needs an alternative potential candidate which has improve noise reduction coefficient without producing further pollution in environment. In that context sustainable green acoustic materials like natural fiber composites offer a great opportunity to study the acoustic attenuation technique. Natural fiber composites are carbonaceous, high dielectric value and have good sense of acoustic. The present work encompasses a smart noise absorbing material from luffa cyllindrica which is mostly found in the rural areas of Odisha. The surface modification of the raw luffa fibers are performed with optimized tartaric acid blended alcohol with non destructive ultrasonic technique. Scanning electron microscope image and energy dispersive spectroscopy analysis of the untreated treated and composite fabricated from luffa fibers indicated its potentiality as a sound absorber. The different layers of luffa cyllindrica composite controls the sound propagation in such a way that the noise reduction coefficient enhances to 0.85 making Class-B type sound absorber compared to that of single layered luffa. Further the thermal insulation and mechanical strength of the materials provides the significant support behind the enhancement of sound absorption coefficient of the luffa cyllindrica.

Keywords : Noise reduction coefficient, natural fiber, acoustic material, surface modification, ultrasonic technique

I. INTRODUCTION

It is imperious to fabricate cost effective and eco-friendly materials that can reduce noise pollution as noise is one of the vital problems of the world in these days. The utilization of different kinds of agricultural waste products like biocomposites[1] have properties like acoustic, electrical, thermal, and dielectric which is making them more interesting to be used in industries, new technology applications such as material engineering, economical development of a country, and in different fields where it is needed. The synthetic fibers are good absorbers but production of these fibers contributes to emission of carbon dioxide, methane, and nitrous oxide as a result green house gas releases into atmosphere giving rise to

global warming. The lingo cellulosic property of natural fiber composites becomes important due to its non carcinogenic and biodegradable nature. Since luffa sponges are porous material with a high degree of lignifications, they have great potential for applications in composite materials and fabric fibers [2]. In this paper the experimental data shows that the luffa fibre not only shows a good noise absorption quality but also acts as a good thermal and electrical insulator [3].

II. METHODS AND MATERIAL

Materials

Luffa cyllindrica fibers are collected locally which abundendently available. The epoxy LY 556 polymer is used as matrix material for fabrication of reinforced fiber. Hardener HY-951 is used as a curing agent. Tartaric acid with alcohol like methanol, ethanol, butanol and propanol are used for chemical treatment of luffa fibers.

Method

Alcohol treatment of luffa cylindrical fibers

Luffa cyllindrica fibers are collected from a ripe and matured luffa cyllindrica fruit. Collected fibers are now converted to small pieces by cutting it with scissor. Compatible solvent mixtures of tartaric acid blended alcohols have been prepared with the help of ultrasonic interferometer technique. The small pieces of luffa fibers are bleached with the compatible solvent system of tartaric acid blended alcohols to remove the impurities present on the surface of the luffa fiber and converting cellulose/hemicelluloses into activated carbon.
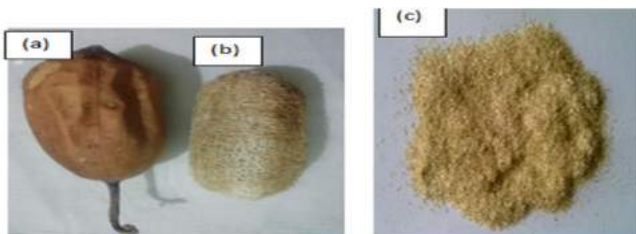
Figure 1 (a) Ripe luffa cyllindrica fruit (b) Luffa cyllindrica fiber (c) pieces of Luffa Cyllindrica fibers

Fabrication of composites

By weight proportion of 10:1 ratio the luffa fiber and epoxy are mixed together and stirrer for 15 minutes to form a uniform matrix. After stirring it well for 15 minutes, the mixture is poured into the mould. A silicon sheet is used to cover the upper and lower surface of the mould. The sample is pressed using ½ kg weight and left to dry for 24 hrs. Composites are fabricated by a general hand lay-up technique. The composites are cast with a single, double, and triple layer of a natural mat Luffa cyllindrica fiber in three different weight proportions. The weight percentage of the fiber is calculated by using the following formula:

weight % of the fiber =
$$\left(\frac{\text{Weight of fiber}}{\text{Weight of fiber}+\text{Weight of epoxy resin}}\right) \times 100$$

Each ply of the Luffa cyllindrica fiber was of dimensions $140\ mm \times 100\ mm$. The cast of each composite was cured under a load of 25 kg for 72 h. Specimens of required dimensions were cut using a diamond cutter for physical characterization and mechanical testing.

Characterization of Sample

The surface morphology of the raw luffa fiber and chemically treated luffa fibre composite has been examined with HITACHI SU 3500 Scanning Electron Microscope. Scanning electron micrographs of luffa fibers and the luffa fiber composites are shown in the Fig.2 (a-e) with EDS. SEM micrographs show porous structure in the luffa fibre and micro voids in the luffa fibre composites and randomly arrangement of carbon and silica particles.
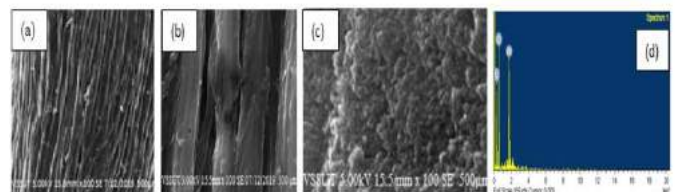
Figure 2 (a) SEM of luffa (untreated)   (b) SEM of luffa (treated) (c) SEM of luffa composite
 (d) EDS of luffa composite

Experimental measurement

A multi-frequency ultrasonic interferometer (2MHz) is used to measure the ultrasonic velocity in the blended solution of tartaric acid and different alcohols within accuracy of ± 0.01 ms^{-1} from which the compressibility has been calculated. Thermal conductivity is measured with the laboratory arrangement Lee's experimental set up.The hardness measurement of the sample has been performed with Vickers's hardness test. The sound absorption coefficient was computed by laboratory designed experimental set up with EXTECH software.

III. RESULTS AND DISCUSSION

Figure 3: Variation of with tartaric acid Blended alcohols

Figure-4 Variation of thermal conductivity with different wt. % of luffa fibre

The optimum blend for ethanol with tartaric acid has been found the suitable modifier for surface modification of the raw luffa fiber. From the variation of excess isentropic compressibility it was observed that both the values are negative over the entire mole fraction range and even with the rising of frequencies. This indicates that sound waves cover long distances due to decrease in intermolecular free length describing the dominant nature of hydrogen bond fiber and optimized blend. As shown in fig.4 thermal conductivity decreases with increase in different weight percentage of alcohol treated luffa fiber composites which indicates the thermal insulator property of luffa fiber composite.

Figure 5: Sound absorption coefficient of luffa composite

Figure-6 load v/s hardness test

Based on fig.5 it can be observed that the sound absorption of 70 wt% untreated and treated fiber have a higher sound absorption coefficient compared to other fiber contents. Which means higher fiber containt exhibits a high sound absorption coefficient as the frequency is increased. The optimum value enhances to 0.85 making Class-B type sound absorber compared to that of luffa. Fig.6 shows the load v/s hardness graph on 253mm²area of luffa composite. It is observed from the figure that the hardness of the composite increases as the load on the composite increases up to 1800gm. With the further increase of load to 6000gm, the hardness is found to remain constant. So the composite material attains its maximum breaking load at1800gm. This might be due to higher fibrillation caused at this load level, which gives rise to crack initiation.

IV. CONCLUSION

The organized paper describes the uses of bio waste material for potential sound absorber .The method of preparation involves green synthesis without producing the pollution to the environment. The synthesized material can be potentially applied as acoustic material for different purposes where it needs its application. The layered designed acoustic material shows its efficiency as a class-B material as per ASTM standard. Further the acoustic material has good thermal insulating value as well as mechanically strong which supports the material to be act as good acoustic shielding material.

V. ACKNOWLEDGEMENT

VI. REFERENCES

[1]. S P Mishraa , S Garnayaka , R K Bhuyanb & G Nath, Indian Journal of Pure & Applied Physics, 58,629-634(2020).

[2]. Niharika Mohanta and Samir K. Acharya, Sci Eng Compos Mater 25(1): 85–93, 2018;

[3]. SP Mishra, G Nath, IOP Conf. Series: Materials Science and Engineering 310, 012087 (2018)

Magnetoelectric Effects in LSMO - BCZT Multiferroic Composites

S. D. Chavan[1*], S. G. Chavan[2] , E. K. Kore[1], D. J. Salunkhe[2]

[1]Department of Physics, D.B.F. Dayanand College of Arts and Science, Solapur,413002,Maharashtra, India.

[2]Nano-composite Research Laboratory, K.B.P. Mahavidyalaya, Pandharpur, Solapur, 413304, Maharashtra, India.

ABSTRACT

$(Ba_{(1-x)}Ca_{(x)})(Zr_{(y)}Ti_{(1-y)})O_3$ (BCZT), for x= 0.05 and 0.075 & y = 0.075 and 0.10 is a ferroelectric material known to possess ferroelectric transition temperature Tc in the vicinity of room temperature is chosen to investigate their possible magnetoelectric (ME) applications. The $La_{0.67}Sr_{0.33}MnO_3$ (LSMO) is selected to be ferromagnetic phase. Hydroxide co-precipitation route is adopted so as to synthesis of LSMO phase and ceramic synthesis route is adopted for the synthesis of BCZT phase. Starting with the LSMO and BCZT powders, the composites   yLSMO + (1- y) BCZTx = yLBCZTx   with y = 0.10, 0.15 & 0.20 and x = 1, 2 & 3. are synthesized for ME properties. The parent composition of LSMO as well as the BCZT are characterized for dielectric and magnetic properties to confirm the formation of desire ferroelectric and magneto strictive phases. The composites are investigated for the structural and microstructural analysis, dielectric, magnetoelectric properties. The results show that the composite yLBCZTx exhibit excellent ME properties.

Keywords - BCZT, LSMO, Ferroelectric, Magnetoelectric.

I. INTRODUCTION

Multiferroic materials have gained momentum in recent years for their coexistence of ferroelectricity, ferromagnetism and ferroelasticity [1-3]. The coupling between ferroelectric and ferromagnetic orders can produce magnetoelectric (ME) effects. The ME composites are extensively studied over last 20 years. In recent years, ME materials prepared by combining the ferrite and ferroelectric as a constituent phases have drawn significant interest due to their multifunctionality [4].These materials provide opportunities for potential applications such as transducers, actuators and sensors [5] .The selection of ferrite and ferroelectric phases are mainly depend on the various factors viz., high magnetostriction coefficient of ferrite phase and piezoelectric coefficient of ferroelectric phase, high dielectric constant and poling strength [6]. Thus one may select a ferroelectric material with useful values of polarization P, ε and ferrite materials with sufficient CMR systems possessing Tc in the vicinity of room temperature. Therefore, considering the discussion above, it appears that after proper selection of the ferroelectric and ferromagnetic phases the composites may produce sufficiently large values of both ME effect.

BCZT is a good candidate for a variety of applications. Its properties can be controlled by varying the Ba/Ca and Zr/Ti compositions. The (Ca, Zr) co-doping plays

a critical role in maintaining the electrical properties of BaTiO$_3$ ceramics. Regarding CMR materials La$_{(1-x)}$Ba$_x$MnO$_3$ perovskite manganites have attracted considerable research interest in recent years because of the observation of a huge magneto-resistance (MR) called the colossal magneto-resistance (CMR) effect. Considering the earlier reports, (Ba$_{(1-x)}$ Ca$_{(x)}$)(Zr$_{(y)}$Ti$_{(1-y)}$)O3 (BCZT), for x= 0.05 and 0.075 & y = 0.075 and 0.10 was selected as the ferroelectric phase for the formation of composites. Similarly, La$_{0.67}$Sr$_{0.33}$MnO$_3$ (LSMO) was selected as for ferromagnetic phase. Using these compositions, the ME composites are formed using the formula yLSMO + (1- y) BCZTx = yLBCZTx with y = 0.10, 0.15 & 0.20 and x = 1, 2 & 3. The composites are investigated for their structural, microstructural and magnetoelectric properties. The present paper report details of synthesis and also presents a qualitative analysis of the observed ME properties.

II. METHODS AND MATERIAL

2.1 Synthesis of BCZT composition

The BCZT solid solutions have been synthesized using standard ceramic route of synthesis. High purity (>99.9%) BaCO$_3$, CaO, ZrO$_2$ and TiO$_2$ of AR grade are used as precursors. The stoichiometric amount of the precursors was well mixed together and grounded thoroughly for 2 h in an agate mortar with pestle. Considering the earlier reports, the pre sintering was carried out at 1150^{0}C.The pre sintered powder was mixed with a polyvinyl acetate (PVA) binder solution and compacted into disk shaped samples with a diameter of 1.0 cm and a thickness of nearly 1.0 mm. The final sintering process was carried out at 1200^{0}C for 24 h in two steps. The product of final sintering is formed as a powder. The calcinated powder of BCZT was pelletized for the investigation of physical and dielectric properties of BCZT. It is observed that the dielectric properties of BCZT are in concurrence with the earlier reports. The powder has been used for the formation of ME composites.

2.2 Synthesis of LSMO composition

To achieve near atomic level uniformity of the constituents, the hydroxide co-precipitation route has been adopted for synthesis of La$_{0.67}$Sr$_{0.33}$MnO$_3$ (LSMO). The La(NO$_3$)$_3$.6H$_2$O, Sr(No$_3$)$_2$, KMnO$_4$, and (CH$_3$COO)$_2$.Mn.4H$_2$O of AR grade are used as precursors for the hydroxide co-precipitation route of synthesis. The precursors are dissolved in distilled water to form nearly 40 mM solution of the constituents and NH$_4$OH is used as precipitant. The precipitates are thoroughly washed in distilled water keeping alkaline medium using NH$_4$OH solution with pH between 9 to 10 [7]. The dried precipitates are calcinated at 1000 ^{0}C for 12 h, and final sintering is carried out at 1100 ^{0}C for 12 h with intermediate grinding. The product of final sintering is formed as a powder and also in pellets of 1.2cm diameter. The powder has been used for the formation ME composites, while the pellets were used for determination of their physical and magnetic properties.

2.3 Formation of composites

The powder of LSMO and BCZT composition are used to form the required ME composites using the following formula

yLSMO + (1- y) BCZTx = yLBCZTx with y = 0.10, 0.15 & 0.20 and x = 1, 2 & 3.

These sintered yLBCZTx composites with y = 0.10, 0.15 & 0.20 and x = 1, 2 & 3 were studied by X-ray diffraction technique using Cu Kα (0.154nm) radiation. The microstructure of sintered composites was studied by using JEOL JSM – 6360A Analytical Scanning Electron Microscope. The linear and quadratic magnetoelectric coefficients α and β were determined using a custom designed instrument as reported earlier [8].

III. RESULTS AND DISCUSSION

Fig. 1 show the XRD pattern of 0.10LBCZT1 composite sintered at 1100°C. The peaks corresponding to BCZT and LSMO phase are separately identified in the XRD pattern of composites. This indicates that pure bi phase composites are formed in this process. The peaks of plane *(012), *(104) are corresponds to LSMO ferromagnetic phase, whereas peaks of plane (100), (110) are corresponds to BCZT ferroelectric phase.
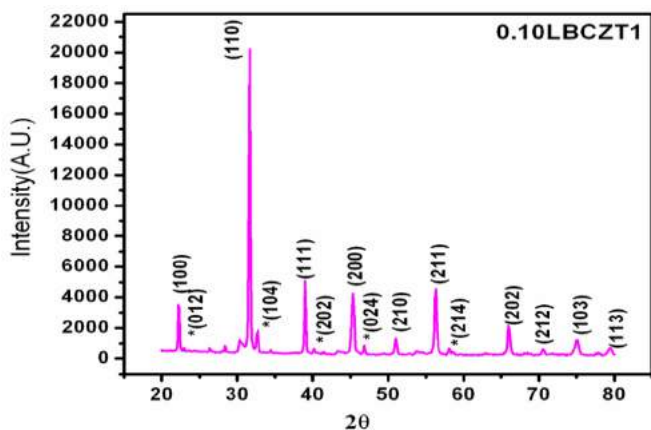
Fig.1 XRD pattern of composite 0.10LBCZT1 composite

Fig. 2 show SEM image of 0.10LBCZT1 composite. The SEM image clearly show that the sintered sample have dense structure with non-uniform grain size distribution and it is seen to be spongy. The average uneven grain size of 0.10LBCZT1composite is observed to be 0.7935 μm, 0.6135 μm for 0.15LBCZT1 composite and 0.8411 μm for 0.20BCZT1 composite. The average uneven grain size of 0.10LBCZT2 composite is observed to be 1.5628 μm, 1.1321 μm for 0.15LBCZT2 composite and 1.4653 μm for 0.20BCZT2 composite. The average uneven grain size of 0.10LBCZT3 composite is observed to be 1.5577 μm, 1.6156 μm for 0.15LBCZT3 composite and 1.1682 μm for 0.20BCZT3 composite.
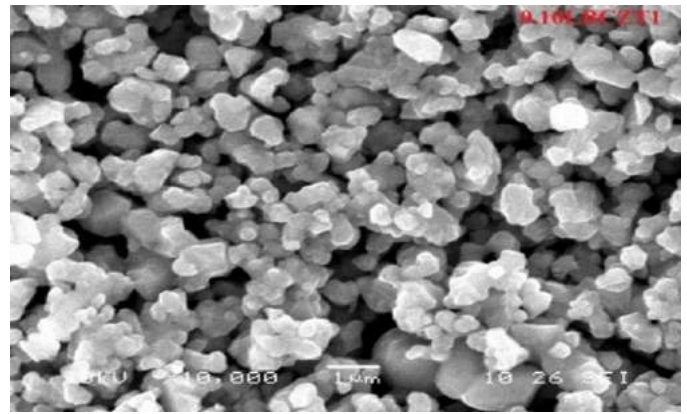
Fig.2 SEM image of 0.10LBCZT1 composite.

3.1 Magnetoelectric properties

The linear ME coefficient α and quadratic ME coefficients β of the composites has been measured at 4 KHz using a custom designed measurement unit [8]. Linear ME coefficients α is calculated using the following formula. $\alpha = \dfrac{dv}{dh \times d \times G}$

Where dv is r. m. s output voltage developed across the sample in mv, h is r. m. s value of A.C field at frequency 4KHz, G is Gain of the amplifier =19 and d are the thickness of the sample.

Quadratic ME coefficients β is calculated using the following formula. $\beta = \dfrac{dv}{dH \times 2h \times d}$

Where dv is r. m. s output voltage developed across the sample in mv , dH is imposed d. c magnetic field and h - r. m. s value of A.C field at frequency 4KHz.

Tables 1, 2 and 3 shows the variation of linear and quadratic ME coefficients α and β as a function of y for yBCZTx with y = 0.10, 0.15, 0.20 and x =1,2 and 3 composites sintered at 1100°C. Further, from these tables, it can be seen that the magnitude of linear ME coefficients α is substantially large for all studied composites and thus these composites are suitable for ME applications.

In all studied composites, linear ME coefficient α is observed to be maximum for y = 0.20 composite than y = 0.15 and 0.10 composites. This feature is attributed to the y × (1-y) type proportionality of α [9]. As expected on the basis of the magnitude of λ, linear ME coefficient α is maximum for 0.20LBCZT as compared with 0.10LBCZT & 0.15LBCZT composites, but both

of these values are large and useful. In the present case, the quadratic ME coefficient β is also determined. Here, β occurs mainly because of the variation of λ with the applied magnetic field. The greater dλ/dH, the greater β will be also. As a device requirement, quadratic ME coefficient β is required to be as low as possible. Table 1,2 and 3 presents the values of quadratic ME coefficient β for yLBCZTx composites with y = 0.10, 0.15, 0.20 and x =1,2 and 3 composites sintered at 1100 ℃. It is observed that quadratic ME coefficient β is fairly low as required for device applications.

Tables 1: Linear and Quadratic Magnetoelectric coefficients α and β for yLBCZT1composites with y = 0.10, 0.15 and 0.20.

Composition	α (mV/Oe.cm)	β × 10^{-4} (mV/Oe^2.cm)
0.10LBCZT1	2.419	3.20
0.15LBCZT1	2.762	4.502
0.20LBCZT1	3.480	4.958

Tables 2: Linear and Quadratic Magnetoelectric coefficients α and β for yLBCZT2 composites with y = 0.10, 0.15 and 0.20.

Composition	α (mV/Oe.cm)	β × 10^{-4} (mV/Oe^2.cm)
0.10LBCZT2	11.05	2.534
0.15LBCZT2	15.98	5.068
0.20LBCZT2	20.12	7.10

Tables 3: Linear and Quadratic Magnetoelectric coefficients α and β for yLBCZT3 composites with y = 0.10, 0.15 and 0.20.

Composition	α (mV/Oe.cm)	β × 10^{-4} (mV/Oe^2.cm)
0.10LBCZT3	8.718	4.520
0.15LBCZT3	9.540	6.721
0.20LBCZT3	12.54	7.820

IV.CONCLUSION

The multiferroic composites are observed to show useful magnitude of linear ME coefficient α and quadratic ME coefficient β .It is observed that the variation of ME coefficient α with y could be correctly correlated through the basic feature of ME properties of composites and observed morphological features.

V. REFERENCES

[1]. Kimura T, Goto T, Shintani H, Ishizaka K, Arima T and Tokura Y 2003 Nature 426 55.

[2]. Weber S, Lunkenheimer P, Fichtl R, Hemberger J, Tsurkan V and Loidl A 2006 Phys. Rev. Lett. 96 157202.

[3]. Mamin R F, Egami T, Marton Z and Migachev S A 2007 Phys. Rev.B75 115129.

[4]. D. R. Patil, S. A. Lokare, R. S. Devan, S. S. Chougule, Y. D. Kolekar, and B. K. Chougule, J. phys. Chem. Solids 68, 1522–1526 (2007).

[5]. C.W. Nan and D. R. Clarke, J. Am. Ceram. Soc. 80, 1333–1340 (1997).

[6]. R. S. Devan and B. K. Chougule, Physica B 393, 161–166 (2007).

[7]. X. Gang, W. Wenjian, Y. Jianxi, D. Piyi, H. Gaorong, Microele. Engg. 66, 568 (2003).

[8]. D.J. Salunkhe, S.S. Veer, S.V. Kulkarni, S.B. Kulkarni, P.B. Joshi, J. Instrum. Soc.India 38 (4) (2006) 29.

[9]. M. I. Bichurin, V. M. Petrov and G. Srinivasan, Ferroelectrics. 280, 165–175 (2002).

An Ultrasonic Study of Molecular Interactions in the Leaf Extract Solution of Thuja Occidentalis

S. S. Kamble[1], S. S. Aswale[2], S. R. Aswale[3]

[1]Department of Chemistry, Arts, commerce and Science College, Maregaon, Maharashtra, India.
[2]Department of Chemistry, Lokmanya Tilak Mahavidyalaya, Wani, Maharashtra, India.
[3]Department of Chemistry, Mahatma Gandhi College of Science, Gadchandur, Maharashtra, India.

ABSTRACT

Ultrasonic Velocity, density, viscosity have been measured experimentally for the solution of leaf extract of *Thuja Occidentalis* in 50% ethyl alcohol with various concentrations at 298.15 K, 303.15 K, 308.15 K keeping constant frequency of 2 MH_z. As the acoustical parameters like adiabatic compressibility, intermolecular free length, relative association, relaxation time , specific acoustic impedence would prove to be more useful to predict and confirm the molecular interactions, these have been determined by measuring the Ultrasonic Velocity, density, viscosity of the prepared solution. A variation in these parameters will provide a strong information regarding the molecular interactions taking place in the solution.

Keywords : Ultrasonic Velocity, Adiabatic Compressibility, Relative Association, Intermolecular Free Length.

I. INTRODUCTION

In recent years ultrasonic technique has become a powerful tool in providing information regarding the molecular behavior of the liquids, polymer solutions and mixtures etc. owing to its ability of characterizing physico-chemical behavior of the medium. Ultrasonic velocity measurements and other acoustic parameters of liquid mixtures are the powerful technique in understanding of chemical nature and the molecular interactions. Our country is very well known for Ayurveda, in the Ayurveda medicines are largely made up from plants, herbs. One of such plants is which is also known as *Thuja Occidentalis*. Thuja is known for its antifungal nature. The solution of leaf extract of *Thuja Occidentalis* in 50% ethyl alcohol is studied at 2 MHz for the concentration of 1%, 0 .5%,

0.25%, 0.125% at 298.15K, 303.15K, 308.15K. Here the effect of concentration at different temperature on molecular interaction will be predicted which may be helpful for predicting the reactivity of the extract.

II. METHODS AND MATERIAL

The leaf extract used in this study was of analytical range. 50% ethyl alcohol was used for the preparation of solution. A special thermostatic water bath arrangement was made to maintain constant temperature. 1%, 0.5%, 0.25%, 0.125% solutions of leaf extracts of *Thuja Occidentalis* was Prepared by taking accurate weights on electronic digital balance (Model CB/CA/CT-Series, Contech having

accuracy ± 0.0001 g.) The ultrasonic velocity of the 1%, 0.5%, 0.25%, 0.125% solutions of leaf extracts of *Thuja Occidentalis* was measured with the Multifrequency ultrasonic interferometer (Model M-83, Mittal Enterprizes) at 2 MHz frequency with an accuracy of $^{-+}$ 2 m/s. All the readings were taken at 298.15 K, 303.15K, 308.15K. The viscosity was measured by using Ostwald's viscometer and the density of the solution was measured by using Digital densitometer (DMA-35, Anton paar)

Computation :

By using ultrasonic velocity following ultrasonic parameters are calculated.

Adiabatic compressibility -$\beta = 1/v_s^2 d$

Where, v - velocity of solution,

d - density of liquid

Intermolecular free length -$L_f = K\sqrt{\beta_s}$

Where, K - temperature dependent known as Jacobson's constant

Specific acoustic impedance - $Z = v \times d_s$

Relative association -$R_A = d_s / d_0 [v_0 / v_s]^{1/3}$

Where, v_0 - ultrasonic velocity of solvent

v_s - ultrasonic velocity of solution

Relaxation time - $\tau = 4/3 \beta_s \times \eta$

III. RESULTS AND DISCUSSION

The experimentally determined values are listed in the following table.

Table 1 : Density, Viscosity and Velocity (at frequency 2 MHz) of Thuja occidentalis leaf extract solution.

Sr. No.	Conc. (%)	Temp. (K)	Density (d_s) (Kg m^{-3})	Velocity (v_s) (m/s)	Viscosity (η) (Kg m^{-1}s^{-2})
1	1%	298.15	931.6	1603	23.50 E^{-4}
		303.15	922.5	1342	21.80 E^{-4}
		308.15	920.4	1350	17.42 E^{-4}
2	0.5%	298.15	936.7	1384	18.30 E^{-4}
		303.15	930.4	1512	20.50 E^{-4}
		308.15	968.9	1439	12.44 E^{-4}
3	0.25%	298.15	924.5	1471	21.27 E^{-4}
		303.15	927.0	1503	21.51 E^{-4}
		308.15	927.4	1330	16.85 E^{-4}
4	0.125%	298.15	925.0	1451	18.12 E^{-4}
		303.15	921.8	1514	16.05 E^{-4}
		308.15	918.4	1385	12.85 E^{-4}

Table 2 :- Acoustic parameters of Thuja leaf extract solution in 50% Ethyl Alcohol at 2 MHz.

Sr. No.	Conc. (%)	Temp. (K)	Adiabatic Compressibility	Specific Acoustic Impedence Kg M^{-2} S^{-1}	Intermolecular free length	Relative Association	Relaxation time
1.	1%	298.15	4.177 E^{-10}	1493354	4.20 E^{-11}	3.169 E^{-1}	13.05 E^{-13}
		303.15	6.019 E^{-10}	1237995	5.09 E^{-11}	3.519 E^{-1}	17.45 E^{-13}

		308.15	5.961 E^{-10}	1242540	5.11 E^{-11}	3.410 E^{-1}	13.81 E^{-13}
2.	0.5%	298.15	5.573 E^{-10}	1296392	4.85 E^{-11}	3.689 E^{-1}	13.56 E^{-13}
		303.15	4.701 E^{-10}	1406764	4.49 E^{-11}	3.150 E^{-1}	12.80 E^{-13}
		308.15	4.984 E^{-10}	1336687	4.67 E^{-11}	3.367 E^{-1}	8.24 E^{-13}
3.	0.25 %	298.15	4.998 E^{-10}	1359939	4.59 E^{-11}	3.427 E^{-1}	14.13 E^{-13}
		303.15	4.775 E^{-10}	1393281	4.53 E^{-11}	3.156 E^{-1}	13.66 E^{-13}
		308.15	6.098 E^{-10}	1233442	5.17 E^{-11}	3.487 E^{-1}	13.67 E^{-13}
4.	0.12 5%	298.15	5.129 E^{-10}	1342804	4.65 E^{-11}	3.473 E^{-1}	12.36 E^{-13}
		303.15	4.730 E^{-10}	1395973	5.99 E^{-11}	3.117 E^{-1}	10.09 E^{-13}
		308.15	5.673 E^{-10}	1272351	4.99 E^{-11}	3.552 E^{-1}	9.69 E^{-13}
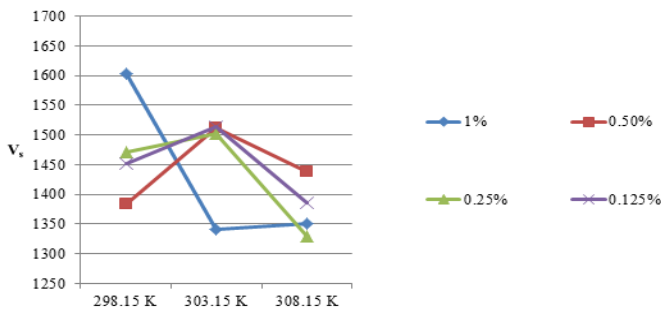
Fig.1 Variation of ultrasonic Velocity with temperature at different conc.
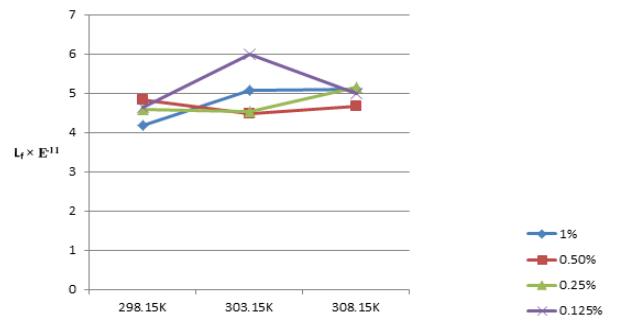
Fig. 4 Variation of Intermolecular free length with temperature at various concentrations
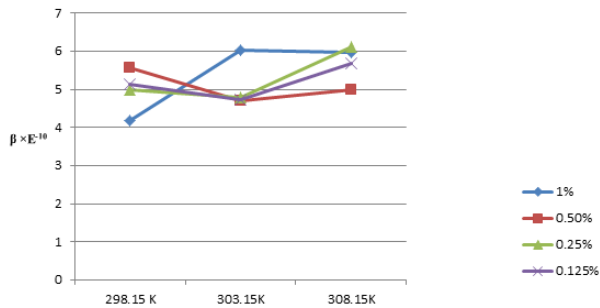
Fig.2-Variation of Adiabatic compressibility with temp. at different conc.
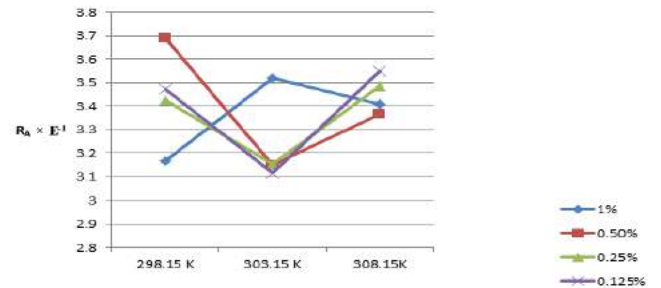
Fig. 5-Variation of Relative Association with temp. at various concentrations
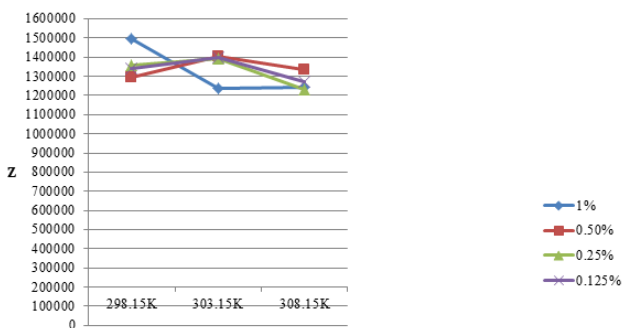
Fig.3 Variation of Specific acoustic impedence with temperaure at different concentration
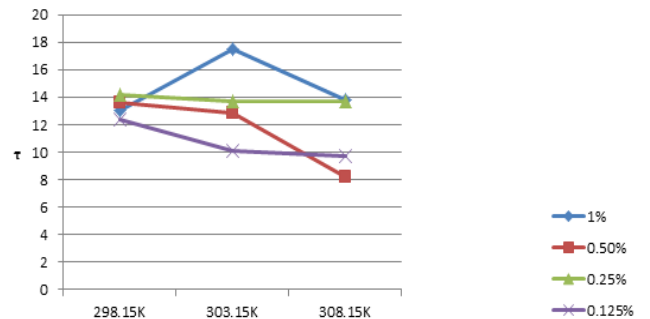
Fig.6. Variation of Relaxation time with temperature at different concentrations

The ultrasonic velocity of 1%, 0.5%, 0.25%, 0.125% Thuja occidentalis leaf extract solution in 50% ethyl alcohol was measured at 298.15 K, 303.15K, 308.15K at 2 mhz frequency. From table no.1, it is observed that the ultrasonic velocity increases with decrease in concentration particularly for 0.5% and 0.125% concentration, but this increase is not regular as we can see from the table no.1 and figure no.1. This may be due to the fact that solute molecules form a strong hydrogen bonds with solvent molecules H_2O and C_2H_5OH. It affects the propagation of ultrasonic waves through the solution. Further it is observed for selected temperatures. From table no.2 and fig.2 it is observed that Adiabatic compressibility increase with increase in concentration. The increase in adiabatic compressibility shows significant molecular interactions. A strong evidence for solute - solvent interaction is that the value of specific acoustic impedence increases with increase in concentration in figure 3.The intermolecular free length is the distance between the surfaces of the neighbouring molecules. Here the intermolecular free length decreases with increase in concentration which clearly indicates stronge solute- solvent interaction figure 4.

Relative association is a meaure of extent of association of components in the medium. It is a property of understanding the molecular interaction in liquid mixtures and solutions. As discussed relative association depends on either of breaking of solvent molecules on addition of solute to it or the salvation of ions that are present. The result shows that relaxation time and relative association increase with increase in concentration at a given temperature (fig.5 & fig.6).

IV.CONCLUSION

From the above discussion a non linear variation in adiabatic compressibility, specific acoustic impedence, free length, relative association, relaxation time is observed in the system.The ultrasonic velocity values significantly increases for lower concentrations particularly for 0.5% and 0.125% due to strong hydrogen bonding with solvent molecules. It is observed that molecular association between *Thuja occidentalis* leaf extract molecules and 50% ethanol solvent may arise from intermolecular hydrogen bonding which supports the molecular association occurring in the solution.

V. REFERENCES

[1]. P.J. Ganjare, S.S. Aswale, S.R. Aswale, Molecular interactions in the solutions of sodium salt of 4-amino-2-hydroxy benzoic acid, World Journal of pharmaceutical Research, Vol.6, Issue 1, 564-573, 2016.

[2]. Dhote A.B, Aswale S.S, Aswale S.R, Comparative study of dichlofenac sodium and (paracetamol + dichlofenac sodium) ultrasonically at 303.15k, International Research Journal of Science and Engineering, special issue A7,pp864-868, 2020.

[3]. P.J. Ganjare, S.R. Aswale, S.S. Aswale, Prediction of molecular interactions in liquids from density, viscosity, and conductance measurements, Vidyabharti International interdisciplinary Research Journal, special issue may 2020.

[4]. R.R.Tayde, A.S.Chandami and M.P.Wadekar, Ultrasonic investigation and molecular interactions studies in substituted oxoimidazoline drugs solutions at different concentrations, Journal of chemical and Pharmaceutical Research, 6(9), 114-121,2014.

[5]. K. Rathina, M. Umadevi, C.Senthamil selvi, Ramalatha Marimuthu, Research on solvent ion interactions in the inorganic liquid mixtures by ultrasonic technique, International journal of Engineering and Advanced technology, 8, 151-159,2019.

[6]. S. R. Aswale,S. S. Aswale,V. N. Gowardipe, Variation of acoustic parameters of herbal extract pomegranate solutions at frequency 4 mhz,

International journal of chemical and physical sciences, Vol.4, Special Issue, pp 308-312, 2015.

[7]. R.S. Hajare, S.S. Aswale, S.R. Aswale, Relative association , specific acoustic impedence and free volume of antibiotic cefotaxime sodium, International journal of current engineering and scientific research, Vol.6, issue -1, pp 332-337, 2019.

[8]. A. B. Dhote, S. R. Aswale, S. S. Aswale, Ultrasonic studies of molecular interactions in the solution of anti-pyrrtic drug at 6 mhz and 303.15K, Gurukul international Multidisiplinary Research Journal, pp103-105, 2016.

[9]. Z. D. Draelos - 2003A Cosmetics Dermatol - 16 (9), pp46-49, 2003 .

[10]. Z. D. Draelos - 2003B, Cosmetics Dermatol- 16 (10),pp 41-42,2003.

Study of Optical, Electrical And Structural Properties of Spray Pyrolytically Deposited CdZnSe$_{2x}$Te$_{2(1-x)}$ Thin Films for X=0.25

S.A. Gaikwad

Department of physics, Guru Nanak college of science, Ballarpur, Maharashtra, India

ABSTRACT

Spray pyrolysis is a simple, inexpensive and economical method to produce a thin film on large substrate area. Thin films of CdZnSe$_{2x}$Te$_{2(1-x)}$ for composition parameter 'x'=0.25 at a substrate temperature of 300^{0}C are prepared by spray pyrolysis technique. From the optical transmission and reflection spectra, absorption coefficient (α) was calculated and was of the order of 10^4 cm^{-1}.Band gap energy were determined from absorbance measurement in visible range as 2.27 eV using Tauc theory. It shows that the main transition at the fundamental absorption edge is a direct allowed transition. The refractive index(n) and extinction coefficient(k) both decreases as wavelength increases which shows that the optical constants are most suitable for many scientific studies and technological applications such as heat mirrors, transparent electrodes and solar cells. The activation energy increases at higher temperature may be due to attributed to the increase of band gap. Hence the grain size of the films increases. This effect reduces the grain boundary effect. The XRD pattern shows number of peaks indicating that the films are poly crystalline in nature. The analysis of spectrum indicated that the films are having throughout cubic structure. The value of lattice parameter ' a' is 6.3702 A°

Keywords: CdZnSe$_{2x}$Te$_{2(1-x)}$ thin films, spray pyrolysis ,optical, electrical properties, activation energy, lattice parameter.

I. INTRODUCTION

In the recent years much more attention has been paid in semiconducting II-VI compounds because of their optoelectronic properties and their possible applications in switching and memory devices, photodiodes and solar cells. The ternary compounds including Cadmium zinc telluride and Cadmium zinc selenide have attracted much more attention in the field of solar cells due to their interesting properties of band gap. There are several binary and ternary semiconductors, such as GaAs, GaP, CuInSe$_2$, CdZnTe, CdZnSe, etc. which have band gaps in the required range(suitable for photovoltaic conversion). The evaluation of any material for application is complete and meaningful only when its structure and composition are precisely known. The reliability factor, which is the most important one for device application, can only be assured through a systematic and detailed study of the structural, electrical and optical properties. Cadmium zinc telluride and Cadmium zinc sellenide are among II-VI series of semiconducting compounds. The growth of quarternary compound is a opens up the possibility of their application for novel optoelectronic devices such as light emitting diodes, photo electrodes, blue green lasers etc.[1] the visible region of electromagnetic

radiation [2]. The research of the optical and electrical properties of CdZnTe and CdZnSe system forms a basis of the active region of laser and LED.To the best of our knowledge, very less work has been reported on tellurium rich $CdZnSe_{2x}Te_{2(1-x)}$ polycrystalline material. Thus the present study is aimed at investing the optical and electrical properties of $CdZnSe_{0.5}Te_{1.5}$ in the form of thin films.

Several researchers studied properties in the II-VI semiconductor films using the variety of methods such as flash evaporation, chemical vapour deposition, r. f. sputtering, chemical bath deposition, electro deposition [3-5] and spray pyrolysis [6-7].

We have chosen spray pyrolysis due to simple, inexpensive and produce a thin film on large substrate area and it is suitable for scientific studies and for many technological and industrial applications. Very less work has been found on $CdZnSe_{2x}Te_{2(1-X)}$ thin films. So our aim is to study optical, electrical and structural properties of $CdZnSe_{2x}Te_{2(1-x)}$ thin films with x=0.25 prepared by spray pyrolysis technique.

II. METHODS AND MATERIAL

The aqueous solutions of Cadmium chloride($CdCl_2$), Zinc chloride ($ZnCl_2$), Selenium dioxide (SeO_2) and Tellurium tetrachloride($TeCl_4$) each of 0.02 M were prepared in double distilled water. Chemicals used were of AR grade. The solutions are mixed in one in the proportion 1:1:1:3 by volume. The film shows a tellurium and selenium deficiency [8-9] if the ratio of proportion of solution was taken as 1:1:0.5:1.5 by volume. Sprayer was mechanically moved to and fro to avoid the formation of droplets on the substrate and insure the instant evaporation from the substrate. The distance between the sprayer nozzle and substrate was kept at 30 cm. The spraying was done in the atmosphere at the spray rate 3.5 ml/min. with a maintaining pressure of 12 Kg/cm². The temperature of substrate was maintained at 300⁰C and was measured by pre-calibrated copper constantan

thermocouple. The thicknesses of the films were measured by weighing method on unipan microbalance and was of the order of 0.1695 μm at substrate temperature 300°C. At this temperature deposition occurs at optimum rate resulting in terminal thickness. 0.1695 μm. It was found that the thin films had grayish color owing to the presence of more amount of tellurium. Optical transmittance and reflectance was taken on UV-1800-Shimandzu Spectrophotometer in the wavelength range 350 nm to 1100 nm. Electrical conductivity was measured by using four probe method [10]. Analytical method of indexing the X-ray diffraction pattern was used.

III. RESULTS AND DISCUSSION

3.1 OPTICAL STUDY

3.1.1 Transmission spectra

The optical transmittance (T) of the film was recorded at room temperature using UV-1800-Shimandzu spectrophotometer. Variation of transmittance with wavelength of the incident beam was recorded for the range of wavelength 350 nm to 1100 nm. And then the graph is plotted between % transmittance and wavelengths. **Fig.1**.Shows the variation of transmission versus wavelength for as deposited $CdZnSe_{0.5}Te_{1.5}$ thin films.
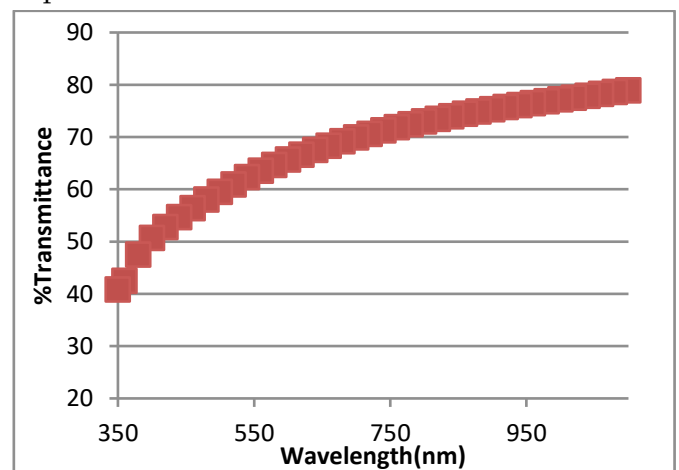
Fig.1 Transmission spectra of as deposited $CdZnSe_{0.5}Te_{1.5}$ thin films .

It was observed that the transmittance started decreasing after a particular wavelength, depending upon composition parameter (x) and remains constant for higher wavelengths.

It was also observed that onset of decrease of transmission gives the optical absorption edge. The optical coefficients were calculated for each wavelength given by relation,

$$\alpha = (1/t) * \ln(I_0/I) \quad ……………..(1)$$

Where, "t" thickness of the film," I_0" and " I" the intensities of incident and transmitted radiations respectively.

3.1.2   Reflectance spectra

Reflectance can be calculated using above values of % transmittance and graph is plotted between reflectance (R) and wavelength in nm. **Fig. 2** represents the reflectance spectra of as deposited CdZnSe$_{0.5}$Te$_{1.5}$ thin films.
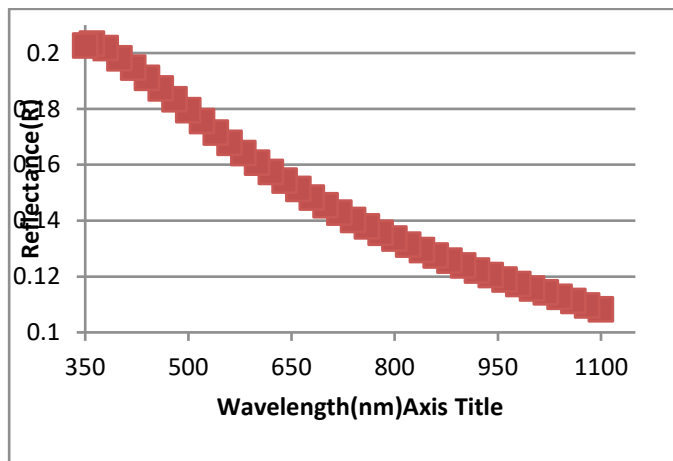
Fig. 2 Reflectance spectra of as deposited CdZnSe$_{0.5}$Te$_{1.5}$thin films.

The absorption coefficient "α" is related to the optical transmission "T" and reflectance "R" by the relation [11],

$$T = (1-R)^2 \exp(-\alpha t)/1 - R^2\exp(-2\alpha t) ………………(2)$$

Equation (2) is valid in the vicinity of fundamental absorption edge when $R^2 \exp(-2\alpha t) \ll 1$ and it is used to calculate the absorption coefficient "α".

From **fig. 2** it was observed that as the wavelength increases there is sharp decrease in the reflectance. The onset of decrease of reflectance gives the approximate value of band gap [12].

Knowing the approximate region of band gap from reflectance curve, α is calculated by using equation (2), from the knowledge of T, R and t.

An analysis of the spectrum showed that the absorption at the fundamental absorption edge can be described by the Taue relation [13],

$$\alpha = (A/hv) * (hv-Eg)^n ………………(3)$$

Where hv –photon energy, A-constant which is different for different transitions, n = 1/2 for direct band gap transition and n = 2 for indirect band gap transition. To calculate the exact value of band gap, we plotted the graph between $(\alpha hv)^2$ versus hv of as deposited CdZnSe$_{0.5}$Te$_{1.5}$ thin film of as shown in **fig.3**.
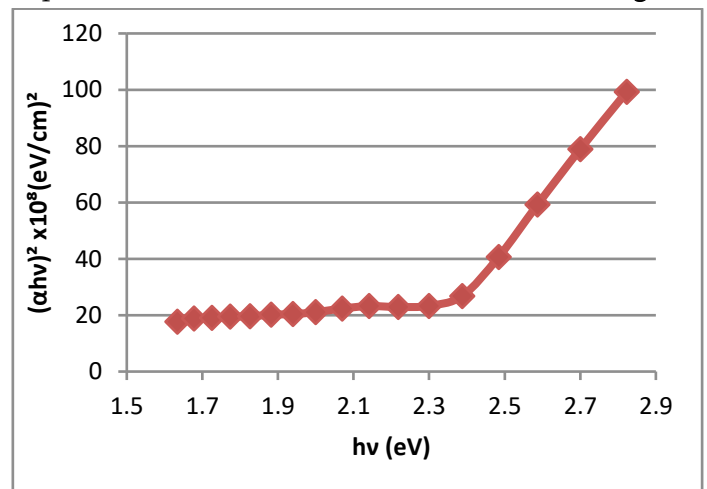
Fig.3 Graph between $(\alpha hv)^2$ versus hv of as deposited CdZnSe$_{0.5}$Te$_{1.5}$ thin film .

The linearity of the graph showed the direct allowed transition, indicating the semiconducting nature of the films. The linear portion of the plot was extrapolated to meet on hv axis yield, the value of band gap energy was found to be 2.27 eV.

These results are found to be in good agreement with that obtained by Umeshkumar *et al.* and Murali *et al.*[14-15]

The optical transmission spectrum of the films under study shows that the transmission spectra mechanism is due to the direct allowed transition. [16]

The linear plot of $(\alpha hv)^2$ versus hv over wide range of photon energies shows thin film CdZnSe$_{0.5}$Te$_{1.5}$ has a direct allowed transition.

3.1.3 Optical constants (n and k)

The refractive index was obtained from the relation [17],

$$n = [(1+R)/(1-R)] + [4R/(1-R)^2) - k^2]^{\frac{1}{2}} \quad \ldots \ldots \ldots (4)$$

Where k –is the extinction coefficient which is related to the absorption coefficient α and wavelength λ as, [18-20]

$$K = \alpha\lambda/4\pi \quad \ldots \ldots \ldots \ldots \ldots \ldots \ldots (5)$$

The value of refractive index (n) and extinction coefficient (k) were calculated using relations (4) and (5). The calculated values of refractive index (n) and extinction coefficient (k) at the wavelengths in the range 350 nm -1100nm are plotted as a function of wavelength in nm as shown in **figs.4 and 5** respectively
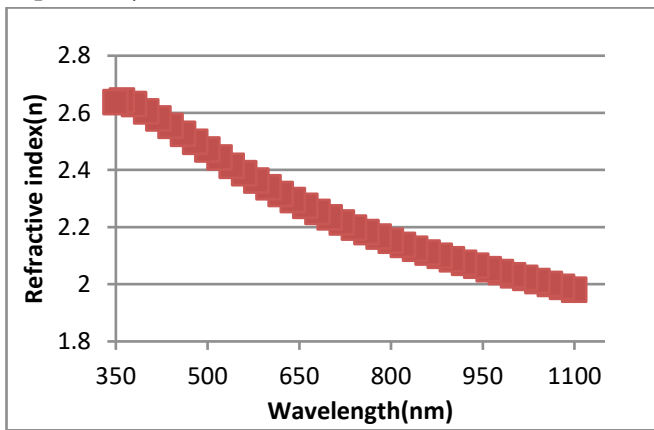
Fig. 4 Graph of refractive index (n) versus wavelength (λ) of as deposited CdZnSe$_{0.5}$Te$_{1.5}$ thin film
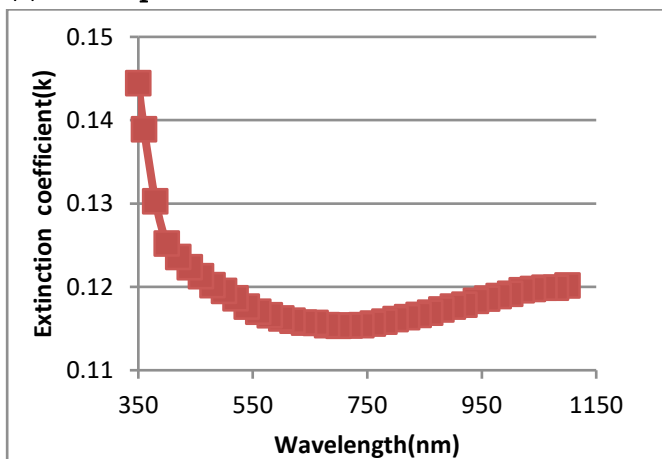
Fig. 5 Graph of extinction coefficient (k) versus wavelength (λ) of as deposited CdZnSe$_{0.5}$Te$_{1.5}$ thin film

Figs. 4 and 5 shows that both k and n decreases with increasing wavelength but at higher wavelengths remains approximately constant. Our calculated values of n and k are in well agreement with the Saliha Ilican et.al [17] for spray pyrolitically deposited some ternary semiconducting CdZn(S$_{1-x}$Se$_x$) thin films and other workers [21-22] also for ternary group of semiconducting materials. Quijada and Ross Henry[23] reported the refractive index for CdZnTe material to be 2.6.The This shows that optical constants are most suitable for many scientific studies and technological applications, such as sensors, heat mirrors, solar cells transparent electrodes and piezoelectric devices.

3.1.4 Real and imaginary parts of dielectric constant

The real (ε$_1$) and imaginary (ε$_2$) parts of dielectric constant are
given by the relations [24]

$$\varepsilon_1 = n^2 - k^2 \quad \ldots \ldots \ldots \ldots \ldots \ldots \ldots (6)$$

$$\varepsilon_2 = 2nk \quad \ldots \ldots \ldots \ldots \ldots \ldots \ldots (7)$$

We also calculated real and imaginary parts (ε$_1$ and ε$_2$) of dielectric constants at several wavelengths ranging from 350nm-1100nm as it is directly related to the density of states within the energy gaps of the films. **Figs. 6 and 7** shows the variation of real and imaginary parts of dielectric constant for CdZnSe$_{0.5}$Te$_{1.5}$ thin films at substrate temperature 300°C.
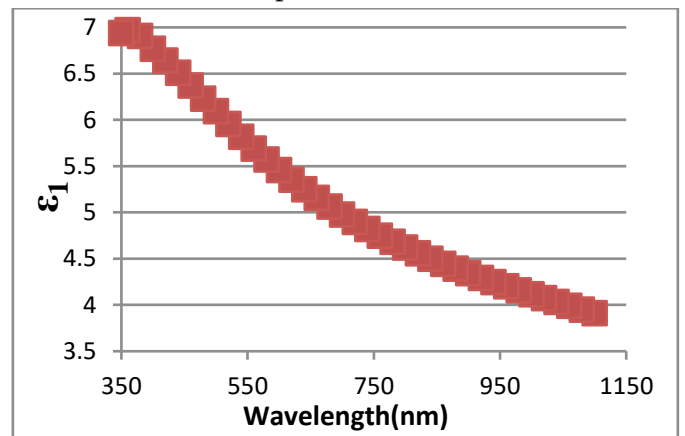
Fig 6 variation of real part of dielectric constant for CdZnSe0.5Te1.5 thin films at substrate temperatures 300°C.
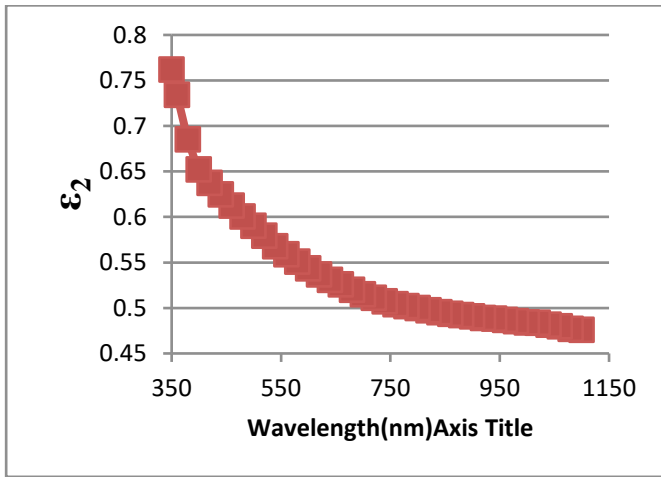
Fig 7 variation of imaginary part of dielectric constant for $CdZnSe_{0.5}Te_{1.5}$ thin film at substrate temperatures 300°C.

It is observed from the graph that both real and imaginary parts of dielectric constant decreases with increasing wavelength. The nature of curves for both ε_1 and ε_2 are found to be same, the only difference is that the values of real parts are higher than those of imaginary parts.

3.2 ELECTRICAL PROPERTIES

The temperature dependence of conductivity was studied in the temperature range 300 K to 573 K. The resistivity were measured by four- probe method [25] given by the relation,

$$\rho = [(V/I) * (2\pi S)] / [G_7(t/S)] \ldots\ldots\ldots(8) \text{ And}$$

$$G_7(t/S) = [2S/t] * \ln(2) \ldots\ldots\ldots\ldots (9)$$

Where S-the distance between the probes, t- the thickness of the film, I- the current generated from the constant current source between the inner probes, V- the voltage developed between the outer probes.

Fig.8 Shows the Arrhenius plot of conductivity versus inverse temperature of as deposited $CdZnSe_{0.5}Te_{1.5}$ thin films The activation energy was calculated from Arrhenius plot using the relation [26-27],

$$\sigma = \sigma_0 \exp\{ -E_a/kT\} \ldots\ldots(10)$$

where 'σ_0' is the pre-exponential conductivity,' E_a' is the activation energy and 'k' Boltzmann constant and 'T ' is the absolute temperature.
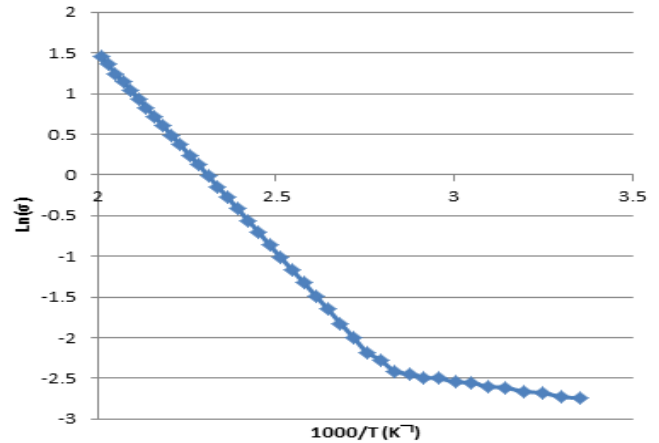
Fig. 8. Arrhenius plot of conductivity versus inverse temperature of as deposited $CdZnSe_{0.5}Te_{1.5}$ thin film

The plot shows two segments i.e. two conduction regions. Region I(lower part of graph) between the temperature 298 K to 348 K and region II(upper part of graph) between the temperatures 349K to 498 K. These two segments correspond to two values of activation energy. The temperature dependence is weak at lower temperature which confirms the low activation energy. The slope increases at high temperature which reveals the possibility of conduction due to the extended state. This indicates semiconducting nature of the films. The polycrystalline $CdZnSe_{0.5}Te_{1.5}$ thin films of do have the electrical and optical properties similar to those of single crystal. At the same time, the deposition conditions have been found to have significant effect on the electrical properties [28-29]. The activation energy increases at higher temperature may be due to attributed to the increase of band gap. Hence the grain size of the film increases.This effect reduces the grain boundary effect .Thus it is evident that $CdZnSe_{0.5}Te_{1.5}$ thin films the possibility of shallow trapping state due to the interstitials of Cd/Zn or telluride vacancies are expected to dominate the extrinsic conductivity near the room temperature. Whereas at higher temperature

deep traps states influence are probable appears. Similar results are also reported by the other workers [30-31] for same group of ternary compounds.

3.3 XRD STUDY

Phase analysis of deposited thin films is carried out by X-ray diffraction method using $CuK\alpha$ radiation(λ=1.5406A.U.) with 2θ=20° to 80°. XRD study of the sample was taken at room temperature. X-ray diffraction (XRD) spectra of as deposited $CdZnSe_{2x}Te_{2(1-x)}$ thin films deposited on glass substrate at the substrate temperature 300°C for the composition parameter x= 0.25, is shown in **Fig.8**.The XRD pattern shows number of peaks indicating that the films are polycrystalline in nature. The analysis of spectrum indicated that the ternary films are having throughout cubic structure It is observed that two main peaks corresponds to (111) and (220) planes. The experimental d-values for $CdZnSe_{0.5}Te_{1.5}$ thin films are calculated using Bragg's relation,

$$2d_{hkl}\sin\theta= n\lambda,………………..(11)$$

By taking θ values from the peaks of XRD pattern. These d-values are compared with the results of other workers [32-38}
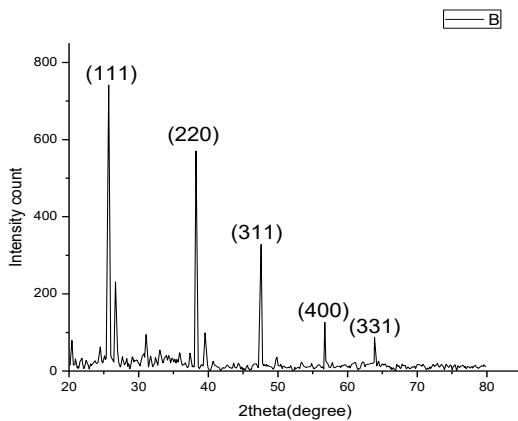
Fig.9 XRD of as deposited $CdZnSe_{2x}Te_{2(1-x)}$ thin film with x=0.25

The value of lattice parameter ˙a˙ is found to be 6.3702 A° for for $CdZnSe_{2x}Te_{2(1-x)}$ thin films deposited at substrate temperature 300°C with composition parameter ˙x=0.25˙

4 CONCLUSION

Spray pyrolysis is a simple and inexpensive method to produce a thin film. Optical band gap of $CdZnSe_{0.5}Te_{1.5}$ thin film was found to be 2.27 eV which was calculated from $(\alpha h\nu)^2$ versus $(h\nu)$ plot. The linearity of the plot shows the direct allowed transition. Arrhenius plot shows the two segments i.e. two conduction regions. Higher the conductivity value at low temperature is an evidence of the adsorption-distortion phenomenon. The XRD pattern shows number of peaks indicating that the films are polycrystalline in nature. The analysis of spectrum indicated that the films are having cubic structure(sphalerite). The value of lattice parameter ˙a˙ is 6.3702 A° for $CdZnSe_{2x}Te_{2(1-x)}$ thin films deposited at substrate temperature 300°C with composition parameter ˙x=0.25.˙

5 REFERENCES

[1]. Maissel L.I, Glang. R., Handbook of thin film Technology, Mc Graw-Hill. New York,1980.

[2]. Velumani. S,.Narayandar S.K.,.Mangalaraj. D,.Sebastian P.J and Mathew. X., Solar energy material and solar cells,81(2004)328.

[3]. Natarajan. C., Nogami G..,.Sharon M.,Thin solid films.44(1995)261.

[4]. Chandramohan R.,.Mahalingam T.,.Chu. J.P, Sebastian. P.J. Solar Energy Material and Solar Cells, 81(2004) 371.

[5]. Loglia. F,.Innacenti M.,.Pezzatini. G,.Foresti M.L .J. Electrical, chem.. 562 (2004) 117.

[6]. Tembhurkar Y.D. and.Hirde J.P.Thin solid films215(1)65-70.

[7]. Tembhurkar Y.D. and.Hirde J.P.Bull .mat.sci.15(2)143-148.

[8]. Y.Bull.mat.sci.17(5)465-468.

[9]. Tembhurkar Y.D.,.Meshram. A.S. International J. of Scientific Research 4 sept.2016 .

[10]. Valde L.B..,Proc.I.R.E..420(1954).

[11]. Hirde J.P and Tembhurkar Y.D..Indian J.Pure and Appl. Phys. 28 (1990)583.

[12]. Moss T.S. Optical properties of semiconductors.

[13]. Tauc J, Amorphous and liquid Semiconductors., Plenum Press, New York,NY,USA,1974.

[14]. Umeshkumar P, Khairnar,Sulakshana S, Behere, Panjabrao H.2011. Pawar. "The optical parameters of ZnxCd1-xTe chalcogenide thin films". Journal of surface Engineered Materials and Advanced Technology, (2011-2009). 1, 51-55.

[15]. Murali, K. R., Austine, A.2009. "Deposition of Cdx Zn1-xSe films by brush electro deposition and their characteristics" Chalcogenide Letters Vol. 6, No. 1, p. 23 – 28

[16]. MossT. S.(1961),Optical properties of semiconductors. Butterworth and Co Pub. Ltd London 2.

[17]. Saliha Ilican., Muhsin Zor.,Yasemin Caglar.,Mujdat Caglar.,Optica Applicata,vol.XXXVI,No.1(2006)29-36.

[18]. Coutts, T.J, Ward J.S., Young, D.L.,.Dessent T. A and.Noufi R (2001), "The search for and potential impact of improved transparaent conducting oxides on thin film solar cells", Technical digest of the 12th international photovoltaic science and engineering conference, Jeju Korea June 11-15.

[19]. Mahrov B., Boschloo G. Hgfeldt A., Dloczuk , L. and Th. Dittrich (2004), Photovoltage study of charge injection from dye Molecules into transparent hole and electron conductors, Appl. Phys. Lett. 84(26), 5455-5457.

[20]. Mahrov, B., Boschloo G., Hyfeldt A., Siegbahn H. and Rensmo H. (2004), Photoelectron spectroscopy studies of Ru(dcbpyH2)2(NCS)2/CuI and Ru(dcbpyH2)2/CuSCN interfaces for solar cell applications, Journal of Physical Chemistry B, 108 (31), 11604-11610.

[21]. Ammar A.H. Appl. surface sci.201(1-4)(2002) 9-19.

[22]. Yakuphanaglu F.,Sekerci.M., J.of molecular structure,751(1-3),(2005) 200-203.

[23]. Quijada A. and Ross Henry, NASA Goddard Space Flight Center,"Temperature Evolution of Excitonic Absorptions in Cd,-,Zn,Te", Materials Manuel, Code 551, Greenbelt, MD 20771, USA.

[24]. Abd El-Wahabb E. Bekheet A.E. 2001. Effect of annealing on the optical properties of Ag33Sb31Se36 thin films, Applied Surface Science, 173(1-2), pp.103-14.

[25]. Yakuphanaglu F.,.Sekerci. M.,J.of molecular structure,751(1-3),(2005) 200-203.

[26]. More P.D and.Deshmukh L.P, Indian journal of Engineering and Material Sciences,Vol.10,(2003)pp.427-432.

[27]. Datta T., Nouff R., Deb S.K.Appl.Phys.Lett.,47(1985)1102.

[28]. Sridevi D." study of semiconducting compounds CuInSe2 and CuInTe2",Ph.D. Thesis,1985,I.I.T. Madras.

[29]. Valde L.B..,IR.E.420 (1954).

[30]. Shreekanthan K.N. ,Kasturi N,.Bangera V..Ind.J.Pure and appl. Phys. 44(2006)705-708.

[31]. Rusu M.,Nicalaescu I.I and.Rusu G.G.J.Appl.Phys.A ,70,(2006) 565.

[32]. Tembhurkar Y.D..,Inter.J.Sci. and research 5 issue 12 (2016) 1293-1294.

[33]. Ringel S.A., Sudharsanan R., Rohatgi A., and Carter W.B. Journal of Electronic Materials, Vol.19 .No.3,pp.259-263,1990.

[34]. Chu T. L.,. Chu S. S,. Ferekides C, and Britt J.. Journal of Applied Physics, Vol. 71, No. 11, pp. 5635-5640,1992.

[35]. Basol B.M,.Kapur V.K,.Ferris M.L. Journal of Applied physics Vol. 66, No.4,pp.1816-1821,1989.

[36]. K.Prasada Rao,O.Md.Hussain, K.T.R.Reddy et.al. Journal of Alloys and Compounds, Vol.218,No.1,pp.86-89,1995.

[37]. Haloui A.,.Feutelais Y, Legendre B.. Journal Alloy. Compd. 260(1997)179-192.

[38]. Haitao Xu, Run Xu, Linjun Wang,Yanyan Zhu. Journal Infrared Millim. W.31(2012)411-416.

Synthesis and Characterization of Pure and Ce Modified SmFeO$_3$ Thick Films

R. B. Mankar [*1], V. D. Kapse [2]

[*1] Department of Physics, Smt. Radhabai Sarda Arts, Commerce and Science College, Anjangaon Surji, Maharashtra, India

[2] Department of Physics, Arts, Science and Commerce College, Chikhaldara, Maharashtra, India

ABSTRACT

In present work, SmFeO$_3$ perovskite oxide powder was synthesized by sol gel method. The crystalline structure and surface morphology were analyzed by X-ray diffraction and Scanning Electron Microscopy techniques. Pure SmFeO$_3$ thick films were then prepared onto a glass substrate in desired pattern by screen printing technique followed by firing at 500 ^{0}C for 30 min. As-prepared pure SmFeO$_3$ thick films were dipped into 0.1 M aqueous solution of Cerium Chloride for 1 min and fired at 550 ^{0}C for 30 min to obtained 'Ce modified SmFeO$_3$ thick films'. Both pure and surface modified SmFeO$_3$ thick films were characterized by Energy Dispersive X-Ray Analysis (EDAX) and Field Effect Scanning Electron Microscopy (FE-SEM) techniques. The effect of cerium doping on microstructure and surface morphology of pure SmFeO$_3$ thick film was discussed.

Keywords : SmFeO$_3$, Surface modification, Perovskite, Gas sensor.

I. INTRODUCTION

Detection and monitoring of hazardous gases emitting from auto and industrial exhaust is strongly required all over the world in order to provide better air quality for the survival of human being. Different techniques have been accepted for environmental monitoring. Among them solid state metal oxide gas sensor has been proved to be one of the most promising devices for the detection of variety of pollutants. After the first semiconductor metal oxide gas sensor reported by Seiyama et al in 1962, different semiconducting gas sensing materials along with complex materials have been studied for ethanol, benzene, NO$_2$ and VOCs[1-3]. But, their gas sensing characteristics such as sensitivity, selectivity, stability and operating temperature are still not meeting the ever increasing requirements of sensor in complicated systems.

Now a day, perovskites of type ABO$_3$ (A: rare earth, B: transition metal) have created a great deal of interests for chemical sensor because of their interesting novel and improved physical and chemical properties. The perovskite structure can accommodate most of the elements of periodic table in order to produce a series of potential compounds while retaining the perovskite structure. Doping of perovskite oxides with dopants of different oxidation states result in the creation of oxygen vacancies. Partial substitutions at A-site, B-site and/or both A-site and B-site can easily tailor the material properties for specific applications. Therefore

perovskites have wide range of applications including solid oxide fuel cell [4], catalysis [5] and gas sensors [6-8]. Among various perovskite oxides, SmFeO$_3$ has outstanding merit of higher sensitivity and stability in thermal and chemical atmosphere. SmFeO$_3$ is reported to be p-type semiconducting material with orthoferrite phase [9]. Its resistance decreases in presence of oxidizing gases like O$_3$,NO$_2$,ethanol and increases with the adsorption of reducing gases like CO and H$_2$ [10-12]. For the synthesis of SmFeO$_3$ perovskite different methods like sol-gel method [13] and hydrothermal method [14] have been adopted. Sol-gel method in citric system has advantage of providing SmFeO$_3$ perovskite powder with high sensitivity and selectivity [15].

ABO$_3$ type perovskite structure of SmFeO$_3$ permits the modification in microstructure and thereby sensitivity and selectivity by partial substitution at A-site and/or the B-site. Electrical conductivity of doped perovskite is affected by different factors like nature of dopants, amount of dopants and the surrounding environment. With the doping of bigger A-site cation, greater reduction stability is possible whereas doping at B-site affects electrical conductivity as well as thermal stability. Researchers have reported the advantages of introducing Ce at A-site and Co, Ni and Mg at B-site [16-19]. S.M. Bukhari et al have reported that the partial substitution of Sm by Ce within the solubility limit improves the electrical conductivity of perovskite as well as prevents it from decomposing under reducing conditions [19]. This creates the possibility of using Ce doped SmFeO$_3$ as a gas sensor for reducing gases.

Generally, doping and dipping techniques are employed for incorporating additives in pure material. Doping method was frequently reported for surface modification in SmFeO$_3$. In the present work, surface modification in SmFeO$_3$ thick films prepared by screen printing method was achieved by dipping technique.

II. METHODS AND MATERIAL

2.1 Preparation of SmFeO$_3$ powder

Sol-gel method was employed for the preparation of fine powder of SmFeO$_3$ perovskite oxide from samarium nitrate Sm(NO$_3$)$_3$.6H$_2$O, iron nitrate Fe(NO$_3$)$_3$.9H$_2$O and citric acid monohydrate. Stoichiometric amounts of samarium nitrate, iron nitrate and citric acid monohydrate were mixed in the ratio 1:1:1.provided with grounding in Agate mortar for 30 minutes. To this mixture, ethylene glycol was added under constant stirring at 75^{0}C for 2 hours to yield a sole which was then dried into a gel. The gel was dried in oven at 110^{0}C for 12 hours and allowed to cool naturally. Finally, sample was calcined at 800^{0}C for 4 hours.

2.2 Preparation of SmFeO3 thick films

Pure powder was added to the solution of ethyl cellulose and the mixture of organic solvent in ratio 75:25 to prepare the paste. This paste was then screen-printed on glass substrate in desired pattern.

2.3 Preparation of Ce surface modified thick films

In order to obtained surface modified thick films, as-prepared pure thick films were dipped into 0.1 M aqueous solution of cerium chloride for 1 min, 3min and 5 min. After drying, these films were fired at 550 ^{0}C for 30 min and then used for further characterization.

III. RESULTS AND DISCUSSION

3.1 X-ray diffraction and surface morphology analysis of pure SmFeO$_3$ powder

X-ray diffraction pattern of synthesized pure SmFeO$_3$ powder is shown in Fig. 1. This X-ray diffraction pattern matches well with the standard JCPDS card number 39-1490 conforming that the prepared powder has perovskite phase and orthorhombic symmetry. Importantly single phase perovskite structure was observed without presence of secondary

phases. The lattice parameters of the sample were calculated from XRD pattern according to the formula $d = (h^2/a^2 + k^2/b^2 + l^2/c^2)^{-1/2}$, where (h, k, l) are indices of crystallographic planes, d is the interplanar distance and (a, b, c) are lattice parameters. The values of lattice constants a, b and c are 5.604 A^0, 7.704 A^0 and 5.397 A^0 respectively for SmFeO₃ powder prepared by sol-gel method. By means of Scherer's formula, $D = 0.89\lambda/\beta\cos\theta$ where λ is wavelength of X-ray, θ is diffraction angle and β is true half-peak width, the crystalline particle size was estimated and is found to be 50.08 nm. The volume of unit cell of prepared sample is 233.05 A^{03}

Fig 2 represents the SEM images of the sample to study its surface morphology. The micrograph indicates that the morphology of the particle is irregular because sintered material being crushed until powder form is obtained. The average size of particle is 100 nm.
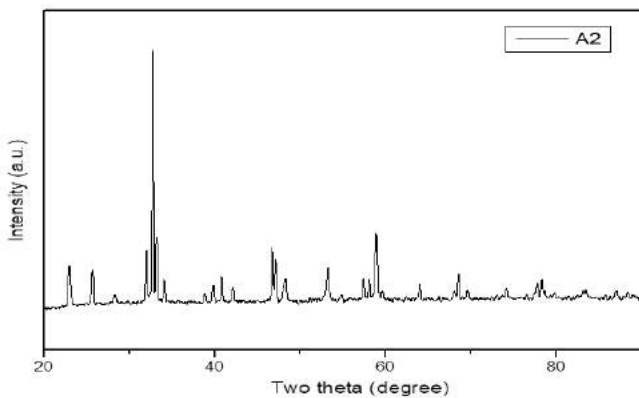
FIG. 1: XRD PATTERN OF SMFEO₃ POWDER

3.2 Surface morphology of pure and modified SmFeO3 thick films by FESEM analysis
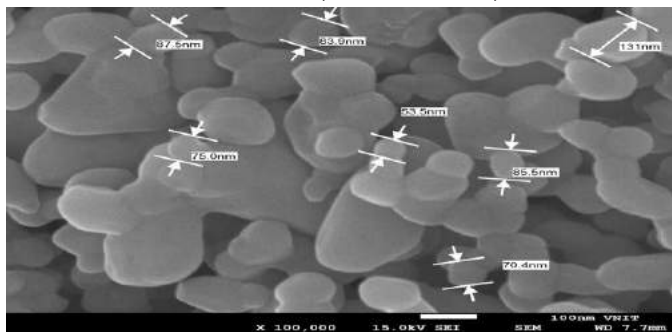
Fig. 2: FESEM of pure SmFeO₃ thick film
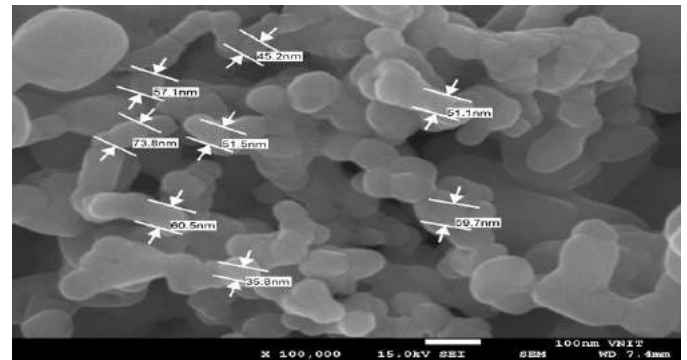
Fig. 3: FESEM of Ce doped SmFeO₃ thick film.

Fig. 2 represents the FESEM images of pure SmFeO₃ thick film fired at 500 ^{0}C for 30 min. The micrograph shows the presence of large number of grains with grain size ranging from 53 nm to 131 nm on the film. The films were highly porous with inner layer of perovskite type oxide adhere to the substrate. Due to the firing temperature, sintering proceeded and growth of the grains was observed. The composition of organic vehicle also influences the morphology of film. The presence of α-terpineol favored the sintering of grains. Fig. 3 depicts FESEM image of Ce doped SmFeO₃ thick film for dipping time interval 1 min and fired at 550 ^{0}C for 30 min. The micrograph shows the distribution of smaller particles around the larger grains. The smaller particles may be attributed as Ce species. The modified thick film appears to have comparatively high porosity and large surface area for oxygen adsorption.

3.3 Elemental composition of pure and modified SmFeO3 thick films by EDX analysis
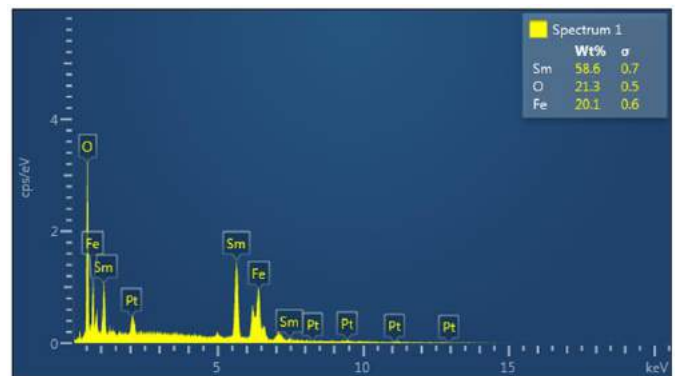
Fig 4: EDX of pure SmFeO3 thick film.
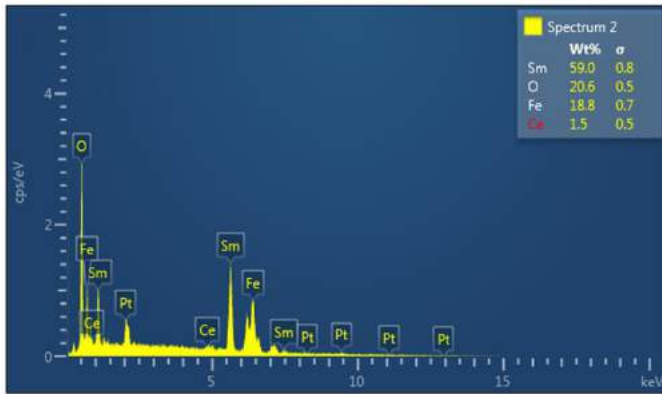
Fig 5: EDX of Ce doped SmFeO3 thick film.

Elemental analysis of pure and Ce doped thick films was carried out by EDX technique. Table 1 represents the wt % of constituent elements of both pure and modified films.

Table 1: Quantitative elemental analysis.

	Pure SmFeO$_3$ thick film	Ce modified SmFeO$_3$ thick film
Sm (wt.%)	58.6	59
O (wt.%)	21.3	20.6
Fe (wt.%)	20.1	18.8
Ce (wt.%)	---	1.5
Total	100	100

It is observed from table 1 that weight percentage of oxygen decreases due to Ce doping. Further it was observed that both the samples are oxygen deficient but oxygen deficiency is more in Ce doped thick film than pure SmFeO$_3$ thick film. Therefore, Ce doped SmFeO$_3$ thick film may facilitate increased oxygen adsorption.

IV. CONCLUSION

The results demonstrated here depict the possibility of synthesis of fine powder of SmFeO$_3$ perovskite oxide by sol-gel method in citrate system. XRD pattern confirms the presence of single phase orthorhombic perovskite structure. Surface modification of SmFeO$_3$ thick films can be achieved by dipping technique.

Moreover Surface modification promotes increased oxygen adsorption. FESEM analysis and EDX analysis respectively confirm the structural morphology and the elemental composition of both pure and modified thick films.

V. ACKNOWLEDGEMENT

VI. REFERENCES

[1]. Sachin Bangale, Sambhaji Banmane, Green synthesis of CdFe2O4 nanoparticles and their applications for ethanol vapor sensing, Carbon-Sci. Tech. 5/1 (2013) 231-235.

[2]. Masoud Salavati-Niasari, Fatemeh Davar, Masoud Farhadi, Synthesis and characterization of spinel-type CuAl2O4 nanocrystalline by modified sol–gel method, J Sol-Gel Sci. Technol. 51 (2009) 48–52.

[3]. Yüksel Köseoglu , Ismail Aldemir , Fatih Bayansal , Süleyman Kahramanb, Hacı Ali Çetinkara Synthesis, characterization and humidity sensing properties of Mn0.2Ni0.8Fe2O nanoparticles Materials Chemistry and Physics 139 (2013) 789-793.

[4]. J. Molenda, K. Swierczek, W. Zajac, J. Power Sources 173(2007) 657.

[5]. P. I.Cowin, C.T.G. Petit, R.Lan, J.T.S. Irvine, Adv. Mater 1 (2011) 314.

[6]. Peng Song, Hongwei Qin, Ling Zhang, Kang An, Zhaojun Lin, Jifan Hu, Minhua Jiang, Sensors and Actuators B: Chemical B 104 (2) (2005) 312– 316

[7]. X. Jia, H. Fan, X. Lou, J. Xu, Appl. Phys. A 94 (2009) 837.

[8]. X. Liu, J. Hu, B. Cheng, H. Qin, M. Jiang, Sensors and Actuators B, 134 (2008) 483.

[9]. Syed M. Bukhari, Javier B. Giorgi, Effect of cobalt substitution on thermal stability and electrical conductivity of Sm0.95Ce0.05FeO3–δ in

oxidizing and reducing conditions, Solid State Ionics 181 (2010) 392–401

[10]. Yuuki Hosoya, Yoshiteru Itagaki, Hiromichi Aono, Yoshihiko Sadaoka, Ozone detection in air using SmFeO3 gas sensor, Sensors and Actuators B 108 (2005) 198–201

[11]. Chang Sua, Changbai Liub, Li Liua,∗, Mucui Nia, Haiying Lia, Xiaoqing Boa,Lili Liua, Xiao Chia, Excellent acetone sensing properties of Sm-doped α-Fe2O3 Applied Surface Science 314 (2014) 931–935

[12]. Ma Zhao, Hui Peng, Jifan Hu, Zhouxiang Han, Effect of Cobalt doping on the microstructure, electrical and ethanol-sensing properties of SmFe1–xCoxO3 Sensors and Actuators B 129 (2008) 953–957

[13]. Carlos Rafael Michel, Emilio Delgado, Gloria Santillan, Alma H. Martinez, Arturo Chavez-Chavez, An alternative gas sensor material: Synthesis and electrical characterization of SmCoO3, Materials Research Bulletin 42 (2007) 84–93

[14]. Maria Cristina Carotta, Giuliano Martinelli , Yoshihiko Sadaoka, Patrizia Nunziante , Enrico Traversa , Gas-sensitive electrical properties of perovskite-type SmFeO3 thick films, Sensors and Actuators B 48 (1998) 270–276

[15]. A.M. Huízar-Félix, T. Hernández , S. de la Parra, J. Ibarra, B. Kharisov, Powder Technology 229 (2012) 290–293

[16]. S.M. Bukhari, J.B. Giorgi, Solid State Ionics 180 (2009) 198

[17]. Yoshiteru Itagaki, Masami Mori, Yuuki Hosoya, Hiromichi Aono, Yoshihiko Sadaoka, O3 and NO2 sensing properties of SmFe1–xCoxO3 perovskite oxides, Sensors and Actuators B 122 (2007) 315–320

[18]. Linfu Chena, Jifan Hua,∗, Shaoming Fanga, Zhouxiang Hana, Ma Zhaoa,ZhanleiWua, Xing Liub, Hongwei Qinb, Ethanol-sensing properties of SmFe1–xNixO3 perovskite oxides Sensors and Actuators B 139 (2009) 407–410

[19]. Xing Liu, Jifan Hu, Bin Cheng, Hongwei Qin, Minhua Jiang, Acetone gas sensing properties of SmFe1–xMgxO3 perovskite oxides Sensors and Actuators B 134 (2008) 483–487

Novel Synthesis and Characterization of PANi/ Sodium Superoxide Composites

R. V. Barde[*1], S. A. Waghuley[2]

[1]Department of Physics, Govt. Vidarbha Inatitute of Science and Humanities, Amravati, India.

[2]Department of Physics, SantGadge Baba Amravati University, Amravati, India.

ABSTRACT

The sodium superoxide was prepared by heating sodium nitrate (NaNO3) in an oxygen-rich environment in a single step process. Using the Ex-situ technique the PANi/ NaO2 composites were prepared range from 5-20 w t %. The crystallinity and structure morphology of the samples were characterized by X-ray diffraction, Scanning electron microscopy. The peak positions appear in XRD pattern of as prepared Sodium superoxide exactly index to NaO2. The peaks of NaO2 are seen in XRD of PANi/a NaO2 composite suggests that NaO2 is present in the PANi matrix. The scanning electron microscope (SEM) shows that sample exhibit an irregular granular morphology.We investigate the DC conductivity of PANi/ NaO2 composites.Activation energy (EDC) is obtain from Arrhenius plots of temperature-dependent DC conductivity, and it is found to be 0.56 eV for 20 wt. % of NaO2.

Keywords : Superoxide, DC Conductivity, Arrhenius Plots.

I. INTRODUCTION

Conducting polymer has been broadly studied because of its various applications in gas sensors [1], batteries [2], light emitting diodes [3], solar cells. Polyaniline (PANi) is the most prominent polymer amongst the various polymers due to its unique properties like electrical properties, easy for synthesis, environmental stability, intrinsic redox reaction etc.[4] and various applications like rechargeable batteries [5], photovoltaic cell [6]. Polyaniline study shows that its chemical and physical properties mainly depend on the method of the preparation and the composition of the solution [7].The preferable formation of sodium superoxide (NaO2) at the oxygen side is due to the transport limitation of gaseous oxygen through the electrolyte-filled cathode structure [8].It is known that, the sodium superoxide (NaO2) can be formed as a stable and solid compound. One of the most convenient and delicate methods for studying the polymer structure is electrical properties.

Interest has arisen in organic and polymeric semiconductors, particularly because of their electro-photographic and solar cells applications. Many synthetic polymers like polyacetylene, polypyrrole, poly-carbazolete have been studied [9].

In this work, we synthesized PANi by using chemical route. The composite of PANi/NaO2 was prepared by ex-situ approach. The as prepared samples were characterized by Fourier transform infrared spectroscopy (FTIR), X-ray diffraction (XRD), and scanning electron microscope (SEM).The DC electrical

conductivity is measured by using two probe techniques.

II. METHODS AND MATERIAL

PANi was chemically synthesized at room temperature by oxidative polymerization method. The suitable quantity of ammonium persulfate (1M) was dissolved in de-ionized water and subsequently kept for the magnetic stirring for 1 h. The aniline monomer was added in ammonium persufate solution in drop wise manner under constant magnetic stirring for 2h. The resultant product appears greenish black. The product was washed and filtered until it become colorless and dried it at 45 °C in an oven for 12 hr. The sodium superoxide was prepared by heating sodium nitrate in an oxygen-rich atmosphere using a single-step process. The PANi/ NaO_2 composites were prepared in wt. % stichometry by organic media using Ex-situ technique. The composites preparation range was fixed from 5-20 wt. %. The structural characterization of the samples performed by using Bruker D8 advance with Cu Kα radiation (λ = 1.5406A˚) is used to identify structure and phase purity of samples at room temperature. The pattern recorded with step height of 0.02º with scan rate 6.00. Scanning electron microscopy (SEM) was used for the determination of microstructure characterization by using JEOL Model JSM - 6390LV.In the present work films were fabricated by using screen printing technique. Conducting silver paste was deposited on both ends of thick film and DC electrical measurement of prepared samples was performed using two probe ceramic sample holder in temperature range 303-393 K.

III. RESULTS AND DISCUSSION

XRD Analysis

Fig. 1 shows the XRD pattern of as prepared Sodium superoxide. The peak positions appear in pattern exactly index to NaO_2 according to JCPDS reference card No. 01-077-0207 [10]. The XRD patterns for pure PANi and PANi/NaO_2 composites are shown in fig. 2(a–e), respectively, which shows changes from amorphous to semi-crystalline state. Fig. 2(a) shows the XRD pattern for pure PANi, as PANi is inherently amorphous and hence there are no sharp peaks for pure PANi. The broad diffraction peak is the characteristic peak of the PANi, which can be attributed to the periodicity parallel and perpendicular to the polymer chain respectively [11]. The peaks of NaO_2 are seen in XRD of PANi/NaO_2 composites shown in fig. 2(b-e), along with some other peaks. However, intensity of (200) and (222) peaks are suppressed in the PANi/NaO_2 composites compared to XRD of pure NaO_2. This suggests that NaO_2 is present in the PANi matrix and presence of PANi has influenced the preferred orientation of NaO_2 grains to some extent. However, these peaks are slightly shifted from their respective standard positions, which may be due presence of PANi matrix. The calculated values of d-spacing (D), inter-chain separation (R) and crystallite size (T) corresponding to the highest intense crystalline peak of PANi/NaO_2 composites are mention in Table 1.
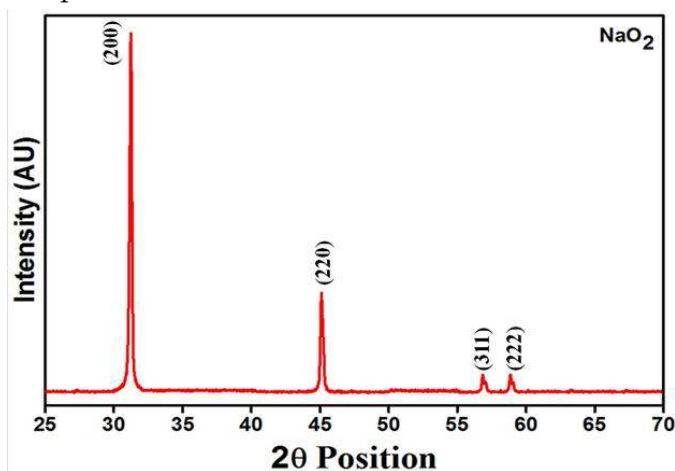
Fig. 1. XRD of Sodium Superoxide (NaO_2).
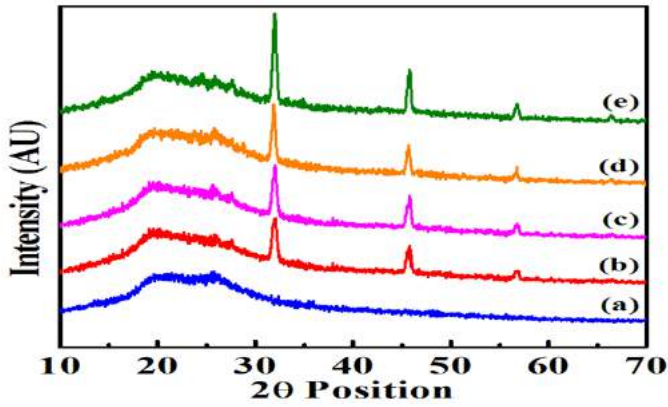
Fig. 2. XRD of (a) Pure PANi, (b) 5 wt. %, (c) 10 wt. %, (d) 15 wt. % and (e) 20 wt. % PANi/NaO₂.

PANI/NaO₂ Sample	D (A°)	R (A°)	T (A°)
5 Wt. %	5.02	3.14	91.80
10 Wt. %	5.18	3.24	107.94
15 Wt. %	6.99	4.37	137.35
20 Wt. %	5.53	3.46	160.95

Table.1. The d-spacing (D), inter-chain separation (R) and crystallite size (T) corresponding to the highest intense crystalline peak of PANi/NaO₂ composites.

SEM Analysis

Fig.3 shows the SEM image of 20wt. % of PANi/ NaO₂. From the image it is observed that, the grains are high agglomerated and good interconnectivity between the particles. Such morphology helps the transportation of charge particles through the carbon back-bone of polymer chains [12]. The entire region of micrograph shows that sample exhibit an irregular granular morphology.
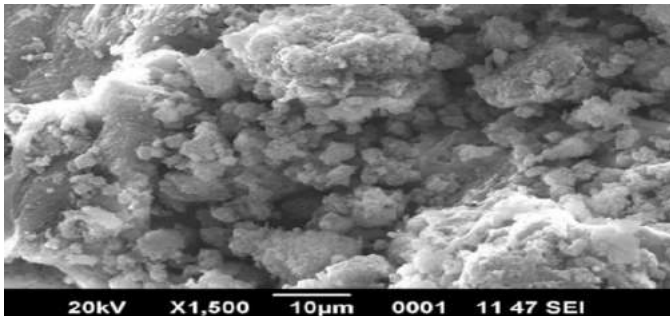
Fig. 3 SEM image of 20 wt. % of PANi/ NaO₂

DC Conductivity

Fig.4 shows a relation for the DC conductivity with temperature for different wt % of NaO₂. These values vary exponentially with temperature. The results show that the temperature-dependent conducting property of PANi, which can be caused by counter-ion mobility, has a positive effect. This is due to the alteration of the PANi/ NaO2 bulk morphology. It is noted that with temperature, the conductivity increases. The reason for the increase in the conductivity is attributed to the thermal energy at higher temperature to excite electrons to the conduction band. Such behavior can be expressed by the Arrhenius equation-[13]

$$\sigma_{DC} = \sigma_0 \exp\left(-\frac{E_{DC}}{KT}\right) \qquad (1)$$

Where E_{DC} is the activation energy which is calculated from the least square straight line fitting of plots and listed in table 1and σ_0 is the pre-exponential factor.

The dependence on temperature of the DC electrical conductivity of the composites is similar to semiconducting behavior. The electrical conductivity of these composites increases with temperature in all these composites as the wt % of NaO₂ increases (fig. 5), and this exhibits a thermal electron process and a hopping process. The highest value of conductivity is found to be 1.59×10^{-7} S/cm for 20wt. % of NaO₂.
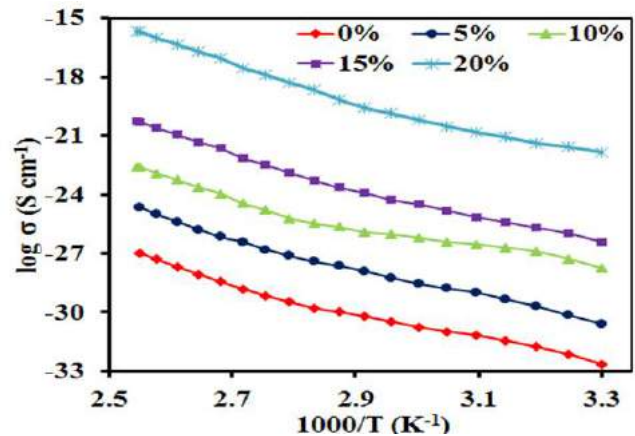
Fig. 4 Plot of DC conductivity of PANi/NaO₂ composites.
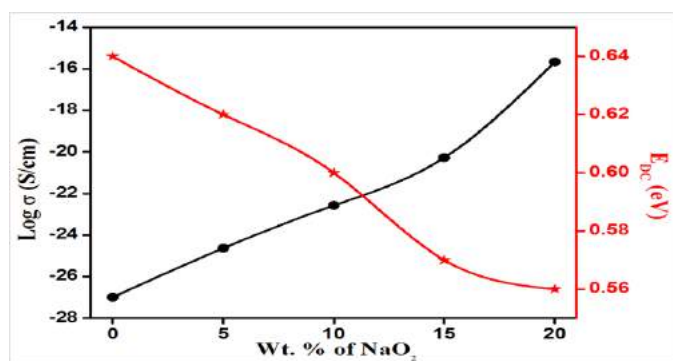
Fig. 5 Variation of Log σ and E_{DC} with wt. % of NaO2.

Table 2 Values of σ_{DC}, E_{DC} and Log σ_0 for PANi/ NaO2 composites

Samples	σ_{DC} at R.T. (S/cm)	σ_{DC} at 393 K(S/cm)	E_{DC} (eV)	Log σ_0
0 wt. %	2.98×10^{-15}	1.9×10^{-12}	0.64	9.56
5 wt. %	1.2×10^{-13}	2.01×10^{-11}	0.62	6.05
10 wt. %	9.4×10^{-13}	1.3×10^{-10}	0.60	6.54
15 wt. %	6.5×10^{-12}	2.4×10^{-9}	0.57	0.22
20 wt. %	8.9×10^{-10}	1.59×10^{-7}	0.56	5.84

IV. CONCLUSION

The sodium superoxide was prepared by heating sodium nitrate (NaNO3) in an oxygen-rich environment in a single step process. Using the Ex-situ technique PANi/ NaO2 composites were prepared range from 5-20 wt %, with the interval of 5 wt. %. The peak positions appear in XRD pattern of as prepared Sodium superoxide exactly index to NaO2. The peaks of NaO2 are seen in XRD of PANi/NaO2 composites suggests that NaO2 is present in the PANi matrix and presence of PANi has influenced the preferred orientation of NaO2 grains to some extent. The entire region of SEM shows that sample exhibit an irregular granular morphology. The DC conductivity shows Arrhenius-type temperature dependence. The electrical conductivity of these composites increases with temperature in all these composites as the wt. % of NaO2 concentration is increased, and this exhibits a thermal electron process and a hopping process. *The maximum value of conductivity and minimum value of* activation energy *are found to be in the range of* 1.59×10^{-7} S/cm and 0.56 eV for 20 wt. % of NaO2 *at 393 K respectively.*

V. REFERENCES

[1]. H. Bai, G. Shi, Sensors, 7 (2007) 267-307.

[2]. Y. Chen, S. Zeng, J. Qian, Y. Wang, Y. Cao, H. Yang, X. Ai, ACS Appl. Mater. Interfaces, 6 (5) (2014) 3508-3512.

[3]. M. Kim, Y. S. Lee, Y. C. Kim, M. S. Choi, J. Y. Lee, Synth. Met., 161 (2011) 2318-2322

[4]. K.Gupta, P.C.Jana, A.K.Meikap, Synth. Met., 160 (2010) 1566-1573.

[5]. B.C.Dalai, I.N.Basmallick, S.Gosh, Indian J. of Chem. Tech., 15 (2008) 576-580.

[6]. S. Sonmezoglu, R. Tas, S. Akin, M. Can, App. Phys. Lett., 101 (2012) 253301

[7]. A. Rahy, D.J. Yang, Mater. Lett. 62 (2008) 4311-4314.

[8]. P. Hartmann, C. L. Bender, M.Vracar, A.K.Durr, A.Garsuch, J.Janek, P. Adelhelm, , Nature Mater., (2012) DOI: 10.1038/NMAT3486.

[9]. S.H.Deshmukh, D.K.Burghate, V.P.Akhare, V.S.Deogaonkar, P.T.Deshmukh, M.S.Deshmukh, Bull. Mater. Sci., 30(1) (2007) 51-56.

[10]. R. V. Barde, Preparation, characterization and CO2 gas sensitivity of Polyaniline doped with Sodium Superoxide (NaO2), Materials Research Bulletin, 73 (2016) 70–76.

[11]. S. Sultana, M. Z. Khan, K. Umar, M. Muneer, Electrical, Thermal, Photocatalytic and Antibacterial Studies of Metallic Oxide Nanocomposite Doped Polyaniline, J. Mater. Sci. Technol., 29(9) (2013) 795-800.

[12]. V.B. Chanshetty, K. Sangshetty, G. Sharanappa, Inter. J. Eng. Res. and Appl. 2 (2012) 611-616.

[13]. R. V. Barde, S. A. Waghuley, Transport and physical properties of V2O5–P2O5–B2O3 glasses doped with Dy2O3, J. Adv. Ceram., 2(3) (2013) 246–251.

Perspectives of Substituted Ferrites in Current Scenario

R. A. Janjalkar[1*], S. P. Ramteke[1], A. R. Bansod[2], K. G. Rewatkar[2]

[1]S. P. Mahavidyalaya Chandrapur, Maharashtra, India
[2]Dr. Ambedkar College Deekshabhoomi Nagpur, Maharashtra, India

ABSTRACT

During last few decades, there has been a growing degree of interest in ferrites. The magnetic, electrical, optical and other properties of ferrites gain attention due to their use in various applications such as medical diagnostics, rechargeable lithium batteries, high frequency media, solar energy devices and magnetic fluids. The high resistivity and low eddy currents makes ferrites the better choice over metals. The aim of this review paper consists of an overview on the ferrites, classification of ferrites, synthesis methods and its potential applications in different fields of technology as well as summarize the major researches in the field of Mn-Zn ferrites on one platform.

Keywords : Ferrites, Magnetic Fluids, Spinel, Retentivity, Nanoparticles

I. INTRODUCTION

Ferrites are chemical compounds obtained as powder or ceramic bodies with ferrimagnetic ordering due to the superexchange or interaction between the magnetic moments properties formed by iron oxides as their main component. Ferrites have the molecular formula of MFe_2O_4, where M stands for the divalent metals such as Fe^{2+}, Mn^{2+}, Co^{2+}, Ni^{2+}, Cu^{2+}, Mg^{2+}, Zn^{2+} or Cd^{2+}. Like most other ceramics, ferrites are hard and brittle. They are also insulating or semiconducting metal oxides that exhibit high coercivity, high electrical resistance, low eddy current and dielectric loss with moderate permittivity. No other material has such a wide range of properties and therefore these materials are exploited for vast applications in various fields like transducers, activators, recording media, permanent magnets, phase shifters, electrode material for Lithium ion batteries, solid oxygen fuel cells and computer technology. The ferrite materials also exhibit dielectric properties and do not conduct electricity easily; therefore ferrites became an alternative for the metal magnets like iron and nickel. Ferrites are also magnetic dielectric materials that allow an electromagnetic wave to penetrate via it, thereby permitting an interaction between the wave and magnetization with in the medium. This makes them suitable for high frequencies application because an ac field does not induce undesirable eddy currents in an insulating material; even in microwave frequencies and they find very important applications in the field of microwave and optical communications. Therefore, due to the technological importance of ferrites increasing continuously as many discoveries required the processing of these materials is important to modify its properties as per the desired applications. Ferrites are structure sensitive materials and their properties critically depend on preparation method,

sintering condition, and amount of constituent metal oxides, grain size, porosity and the dopants or substituted elements. A. B. Gadkari, et al. reported that; ferrites are highly sensitive to preparation method, sintering condition, amount of constituent metal oxides, various additives include in dopants and impurities . These ferrite materials can be prepared by conventional synthesis methods such as; high-temperature solid-state reaction method, sol–gel method, co-precipitation, pulsed laser deposition, high-energy ball milling and hydrothermal synthesis methods.

II. METHODS AND MATERIAL

Types of ferrite materials

Ferrite materials can be classified depending on both crystal structure and magnetic properties. Depending on their crystal structural ferrites are classified in to three types: spinel ferrites, garnets, and hexagonal ferrites.

2.1 Spinel ferrites

Spinel ferrites are represented by the formula unit AB_2O_4. Most of the spinel ferrites form cubic spinel structure with oxygen anions in face centered cubic (fcc) positions and cations in the tetrahedral and octahedral coordinated interstitial lattice sites, forming the A and B sublattices . The spinel ferrites possess the general mineral spinel structure of $MgAl_2O_4$ which was first determined by Bragg and Nishikawa in 1915 . They are also called cubic ferrites with chemical formula of MFe_2O_4 where M is a divalent transitional metal ions such as Co^{2+}, Mn^{2+}, Zn^{2+}, Fe^{2+}, Mg^{2+}, Ni^{2+}, Cd^{2+}, Cu^{2+} and etc. Depending upon the magnetic or non-magnetic nature and distribution of cations among A and B sublattices, spinel ferrites can exhibit properties of different type magnets, like: ferrimagnet, antiferromagnet and paramagnet. Among the broad classification of magnetic oxides, the spinel ferrites, due to their high magnetic permeability and low conduction losses find wide use in high frequency devices. S. Sugimoto et al. reported that spinel ferrites are the most widely used family of ferrites because of their high values of electrical resistivity and low eddy current losses make them ideal for their use at microwave frequencies. They are used in magnetic recording media, a microwave device, and magnetic resonance imaging. The spinel ferrites have been classified in to three types due to the distribution of cations on tetrahedral (A) and octahedral (B) sites. They are normal, inverse and partial inverse spinel ferrite.

2.1.1 Normal spinel ferrites

In normal spinel ferrites, all the divalent cations occupy tetrahedral site and trivalent cations occupy the octahedral sites. The general formula is: $[M^{2+}]T$ $[M^{3+}{}_2]O$ O_4 Where letter 'O' indicates octahedral site occupancy and the 'T' indicates tetrahedral site occupancy. Here, octahedral sites are occupied by only one kind of cations. In other words, in this structure, the non-magnetic ions occupy the A sites and consequently there is no AB interaction. The negative BB interaction now becomes dominant and the trivalent cations align themselves in an anti-parallel fashion; thereby producing zero net magnetization. Examples of normal spinal ferrites are $ZnFe_2O_4$ and $CuFe_2O_4$.

2.1.2 Inverse spinel ferrites

In inverse spinel ferrites, the trivalent cations occupy both the octahedral and tetrahedral sites and divalent cations occupy only octahedral sites. The general formula is; $[M^{3+}]T$ $[M^{2+}M^{3+}]O$ O_4 In other words, in this case there are 8 M^{2+} ions that occupy 8 octahedral sites and the 16 Fe^{3+} ions are divided into 8 octahedral sites and 8 tetrahedral sites . $NiFe_2O_4$ and $CoFe_2O_4$ has an inverse spinel crystal structure.

2.1.3 Mixed spinel ferrites

In mixed spinel ferrites, the divalent and trivalent cations are randomly distributed among the tetrahedral and octahedral sites. It is intermediate

cation distribution between the normal spinel and inverse spinel. The cation distribution is given by the general formula: $(M^{3+}_{\delta}M^{2+}_{1-\delta})[M^{3+}_{2-\delta}M^{2+}_{\delta}]O_4$

where δ is the degree of inversion which depends on the synthesis techniques, calcination and sintering temperature with a value of zero for the normal and one for the inverse distribution . $MnFe_2O_4$ is an example of mixed spinel structure.

2.2 Garnets

Garnets have the general formula $M^{3+}Fe_5O_{12}$ where M = La, Y, Sm, Eu, Gd, Tb etc. and have applications in microwave systems. They have complex crystal structure with the cell shape is cubic and the edge length is about 12.5Å . The coordination of the cations is considerably more complex than spinels, with 24 M^{3+} in dodecahedral sites, 24 Fe^{3+} ions in tetrahedral sites and 16 remaining Fe^{3+} in octahedral sites. Yoder and Keith reported that substitutions of cations can be made in ideal mineral garnet of $Mn_3Al_2Si_3O_{12}$. They produced and reported the first silicon free garnet $Y_3Al_5O_{12}$ by substituting Y^{3+} Al^{3+} for Mn^{2+} Si^{4}. Bertaut and Forret prepared $Y_3Fe_5O_{12}$(YIG) in (1956) which is well-known garnet and measured their magnetic properties . In (1957) Geller and Gilleo also prepared and investigated silicon free garnet $Gd_3Fe_5O_{12}$ which is also a ferromagnetic compound. Similar to spinels and hexagonal ferrites, a wide range of transition metal cations can substitute M^{3+} or Fe^{3+}; especially rare earth ions may replace the ions on octahedral and dodecahedral sites. Each type of lattice site will accept other metal ions at dodecahedral sites, octahedral sites and at tetrahedral sites. Thus, in garnets, pentavalent ions such as V^{5+} and As^{5+} can occupy tetrahedral sites, while Ca^{2+} substitute ions on dodecahedral sites. They are important due to their applications in memory structure.

2.3 Hexagonal ferrites

Hexagonal ferrites are well established magnetic materials represented by the general Formula: $M^{2+}Fe_{12}O_{19}$ where M = Ba, Sr, Ca, Pb, etc are important in permanent applications. They can be found in cost-effective hard magnets as well as in components for high frequency applications and they are widely used as permanent magnets and characterized by possessing a high coercivity. The hexagonal ferrite lattice is similar to the spinel structure, with the oxygen ions closely packed, but some layers include metal ions, which have practically the same ionic radii as the oxygen ions. This lattice has three different sites occupied by metals: tetrahedral, octahedral, and trigonal bi pyramid surrounded by five oxygen ions. Hexagonal ferrites have a variety of magnetic structures and properties that are determined by structure and particular composition which is identified by Went et al. (1952) & Jonker et al. (1956). Out of iron oxides, hexagonal ferrites are a broad subset which is of great practical importance as well as scientific interest. These systems are ferrimagnets as dominant interaction between magnetic ions and oxygen-mediated anti-ferromagnetic superexchange. They are widely used as permanent magnets and have high coercivity. Hexagonal ferrites have larger ions than that of garnet ferrites and are formed by the replacement of oxygen ions. Most of these larger ions are barium, strontium or lead.

2.4 Classification of ferrites on the basis of magnetic property

Depending on the magnetic properties, ferrites are often classified as hard and soft ferrites. This classification is based on their ability to be magnetized or demagnetized not their ability to withstand penetration or abrasion.

2.4.1 Hard ferrites

Hard ferrites are characterized by a large value of retentivity and coercivity after magnetization that means; hard ferrites are difficult to magnetize or demagnetize as soft ferrites easily which is an essential characteristic of a permanent magnets, so they find applications as permanent magnets in radios; e.g., strontium and barium ferrite. Their maximum

magnetic field is about 0.35 T and magnetic field strength is about 30 to 160 kA/m. Hard ferrites are ferromagnetic materials that are typically oxides of mixed transition metals that containing the iron.

For example, MnFe2O4 and Mg-Zn ferrite are described as Mn1- xZnxFe2O4 . They are usually insulating in nature and like most other ceramics, they are hard and brittle. These hard ferrites are used in applications such as magnetic components in microelectronics. The most commonly used hard ferrite is Cobalt ferrite, CoFe2O4 (CoO·Fe2O3), it is used in magnetic recording applications such as audio-/video-tape and high-density digital recording disks. Most hard ferrite particles used in synthesizing magnetic fluids exhibit a spinel structure. This structure consists of a cubic closed packed case of oxygen ions with the metallic ions occupying the tetrahedral A and octahedral B sites . Magnetically hard ferrites have these advantages and particular properties: economical raw materials, very good resistance against corrosion and chemicals and easy to magnetize.

2.4.2   Soft ferrites

Ferrites which are magnetically soft are often described as soft ferrites. They are characterized by a small value of coercivity so they cause low hysteresis loss at high frequency owing to which they are widely used in electromagnetic cores of transformers, switching circuits in computers and radio field inductors. Examples of soft ferrites are manganese-zinc ferrite, nickel ferrite, and lithium ferrite. Soft ferrites are those that can be easily magnetized or demagnetized. This shows that soft magnetic materials have low coercive field and high magnetization that is required in many applications. Due to the low coercivity of soft ferrites, their magnetization can switch direction without much energy requirement or heat generation. For this reason; soft ferrites find wide applications in electronic industries or in cores of modern electronic components such as recording heads, filters, switching power supply transformers, amplifiers, etc.

2.5 Ferrites synthesis methods

There are varieties of available synthesis methods, which can be successfully used to synthesize ferrite materials. The most commonly used synthesis methods are discussed below.

2.5.1   Solid state reaction synthesis

The physical, chemical and electrochemical properties of materials depend to a great extent on the synthesis methods. Several synthesis methods have been developed for the preparation of materials. Some of them are solid state synthesis, co-precipitation, sol-gel process, hydrothermal method and etc. Solid state reaction synthesis method is one of the common methods employed for preparing powder materials from oxides, carbonates, hydroxides, nitrates, sulfates, acetates, oxalates, and other metal salts. This technique involves heating mixtures of two or more solids to form a solid phase product. In this synthesis method, solvents are not used. Since, solids do not react with each other at room temperature, solid state synthesis needs much higher temperatures and longer heating time than other techniques. Solid state reaction differs from solution reaction, since in solution all ions and molecules are available for reaction. However, this is not the case in a solid state reaction. Here, the reaction takes place only at that point where the reactions are in intimate contact with each other. Once the product layer is formed at the interface between the reactants, further progress of the reaction depends upon the diffusion of one or both reactants through this product layer. This depends on various factors such as the size of the diffusion ions, the reaction temperature, and also the presence of defects and the history of the sample.

2.5.2   Sol-gel synthesis

Sol-gel processing is a wet chemistry technique, which can be used to synthesize solid electrolyte ferrite materials and powders as well as nanoparticles by a process preparation of a sol, gelation and aging of

it and removal of the liquid . A sol is a stable colloidal suspension of solid particles or molecular precursors in a liquid solvent. The colloidal particles are agglomerates and form polymer chains creating a polymer gel, a three dimensional continuous network including a liquid phase. The most widely used precursors for the sol-gel preparation are metal alkoxides, metal chlorides, nitrates and acetates which undergo hydrolysis and poly-condensation reactions. The sol-gel process works by following mechanism. Firstly, formation of stable solutions of the alkoxide or solvated metal precursor. Then process of gelation resulting from the formation of an oxide or alcohol bridged network by a poly-condensation or polyesterification reaction resulting in a dramatic increase in the viscosity of the solution. Within the next step is the process of gel aging during which the gel transforms into a solid mass. The next stage includes drying of the gel, when water and other volatile liquids are removed from the gel network. Dehydration is the fifth phase, where the gel is stabilized against rehydration. Calcining the monolith at temperature up to 800℃ is normally required in order to achieve the final product. The sol-gel method has many advantages. The mixing of precursors taking place in a very short period of time and homogeneous gel can be obtained. During the sol-gel method, the chemical reactions occur more readily, with a much lower reaction temperature, which is advantageous in comparison to for instance solid-state reaction synthesis. Along with the advantages, the disadvantages also exist. For example, the precursors used for the synthesis could be expensive and in the case of organic precursors these could be toxic. One of the major disadvantages that the sol-gel process itself takes long processing times or several steps are involved.

2.6 Applications of ferrites

In the past decade MnZn have attracted a large amount of attention in academia due to its advantageous features that make MnZn ferrites suitable to be used in many applications of daily life. . Due to useful magnetic, electrical and optical properties of ferrite nanoparticles, researchers are taking interest in the synthesis of ferrite nanoparticles and making their use in a lot of applications that include medical field, information technology, antenna, microwave absorbing materials, biosensors and many electronic applications.

MnZn ferrites have a broad area of applications due to high saturation magnetization , high initial permeability , low power loss. The application area of MnZn ferrites include power applications, microwave devices, magnetic fluid , radar absorbing system, high frequency applications , bio-medical , water purification etc. Use of MnZn ferrites in the field of power application attracted great attention in the research areas. From last many years the MnZn ferrites are synthesized to be used in power applications for making current convertors, power inductors with magnetic cores , electronic transformer cores , high frequency applications , electronics and communication.

2.6.1 Microwave devices

Ferrite nanoparticles have low electrical conductivity and low dielectric losses , so they can be used in microwave devices. MnZn ferrites are most suitable for their use in the microwave devices because of high permittivity, high resistivity, high stability, high value of saturation magnetization, high curie temperature with low eddy current and low magnetic losses. Due to the use of ferrite nanomaterials, electronic devices can be mechanically hard, chemically stable and permit the materials to operate properly at a wide frequency range. There are a lot of advantages of the use of MnZn ferrites in the microwave devices. There is a decrease in the emission of unwanted EM waves from the device and also it absorbs the incoming EM waves that may harm the microwave device. MnZn ferrites are used in microwave systems because of their low loss and high saturation magnetization. Wang et al. synthesized MnZn ferrite nanoparticles

and the result showed that because of high reflection loss and broad absorbing band in low frequency (10 MHz to 1 GHz) these ferrites can be used in electromagnetic microwave absorbing field.

2.6.2 Radar absorbing devices

The radiations emitting from radar results in the increase in electromagnetic radiation pollution in the environment. These radiations reduce the efficiency and performance of electronic instruments and thus decrease their lifetime and safety. As MnZn ferrite belongs to the class of soft ferrites having high electrochemical stability, high permeability, high saturation magnetization and low power losses, it is used in many electronic applications. Ferrite nanoparticles can be used in the radar absorbing devices due to their high value of Curie temperature and temperature stability. Also the ferrite nanoparticles are environmentally safe that make their use easier in the radar absorbing devices. The application of MnZn ferrites in radar absorbing system is also attracting the researchers. Praveena et al. synthesized $Ni_{0.4}Zn_{0.2}Mn_{0.4}Fe_2O_4$ nano ferrites for radar absorbing. The high value of Curie temperature indicated homogeneity and temperature stability. The EPR spectra showed reduction in the peak width and increase in relaxation with increase in sintering temperature. These all results showed that the ferrite nanoparticles can be used for radar absorbing from few MHz to 2 GHz and also these materials are environmentally safe.

2.6.3 Image based diagnostics

A one-pot thermal decomposition method was used to synthesize a series of Zn^{2+} doped nanoparticles of $(Zn_xMn_{1-x})Fe_2O_4$ and $(Zn_xFe_{1-x})Fe_2O_4$ (x = 0, 0.1, 0.2, 0.3, 0.4, and 0.8). By carefully controlling Zn^{2+} doping level, nanoparticles of size 15 nm with single crystallinity and size monodispersity (s<5%) and having high magnetization value (175 emu/g) were obtained. The nanoparticles provided the large MRI contrast effects (r2 = 860 $mm^{-1}s^{-1}$) with an eight to fourteen fold increase in MRI contrast and a fourfold enhancement in hyperthermic effects compared to conventional iron oxide nanoparticles. This enhancement was significant for clinical purposes as the nanoparticle probe dosage level can be progressively lowered when using probes that have improved contrast enhancement effects. For $(Zn_xMn_{1-x})Fe_2O_4$ nanoparticles, Zn^{2+} ions mainly occupy tetrahedral sites of the spinel matrix which was confirmed by using extended X-ray absorption fine structure (EXAFS) analysis to examine the Zn and Fe K-edges. To detect small sized pathogenic targets precisely at an early stage, MRI contrast agents are often used to highlight those specific areas of interest. Due to high imaging contrast effects, magnetic nanoparticles can increase the difference between pathogenic targets and normal tissues via MRI. One of the most appropriate ways to increase the MR contrast effects is the optimization of saturation magnetization (Ms) that is directly related to the relaxivity coefficient (r2). The relaxivity coefficient (r2) is determined by a slope of R2 against nanoparticle concentration and often used as an indicator for contrast effects. The relaxivity coefficient (r2) of contrast agents can be tuned and further enhanced by engineering magnetic parameters.

2.6.4 Electronic devices

MnZn ferrite nanoparticles are used in making many electronic devices due to their enhanced electrical properties such as high value of resistivity, low ac conductivity, low power losses etc. Dobak et al. studied miniaturization of components due to low loss MnZn ferrites. Also, Sun et al. studied effect of ZrO_2 addition on the microstructure and various properties of MnZn ferrites and found that the optimal values of initial permeability (2322), saturation magnetization (522 mT) and power loss (386 kW/m^3) make it suitable for switch mode power supply applications. Due to suitable electrical and magnetic properties of the Sc^{3+} doped Mn–Zn ferrites, these were useful for modern technological application as well as for low and high frequency application. MnZn ferrites are also

used to construct power inductors , wireless power transfer applications and for making inductive components.

2.6.5 Telecommunication and others

One of the major use of MnZn ferrites is in telecommunication and high frequency applications. MnZn ferrites have applications in the field of bio–medical and hyperthermia. Hurtado et al. synthesized MnZn ferrite along with activated carbon composite for use in bio–medical applications. MnZn ferrites can be used to make ferrofluid due to high value of saturation magnetization. Arulmurugan et al. synthesized Co–Zn and Mn–Zn ferrite nanoparticles and found that because of low Curie temperature and high value of thermomagnetic coefficient, these ferrites can be used for preparing temperature sensitive ferrofluid. Praveena et al. synthesized Mn–Zn ferrite nanoparticles for high frequency applications. The ferrites had low power loss in frequency range 10Hz-1MHz. The constructed transformer with the ferrite material high efficiency and low surface temperature rise at frequency 1 MHz making it suitable for operating at high frequencies.

2.6.6 MnZn ferrites for onging COVID-19 pandemics

As nanomaterials are making a global impact on healthcare and socioeconomic development so are the viruses during pandemics. Nanoparticles of MnZn have unique physical and chemical properties that have associated benefits in development of potential therapeutic drugs, nanomaterial based environment friendly antiviral sprays, drug delivery and to develop anti-viral surface coatings in home appliances. This is attributed to the fact that the choice of synthesis method provides size and charge tunability properties to the MnZn ferrites. The size tunablity ensures that large amount of drug can be delivered into anatomically privileged sites of the virus while charge tunability would facilitate entry of drug in to charged parts of the virus . In addition, biosensors for the early detection of viral strains such the COVID 19 can also

be developed with MnZn ferrites. For instance MnZn ferrites can readily be used to develop Giant magneto-resistance based sensors which have previously been used for virus detection.

III.CONCLUSION

The synthesis of MnZn particles has increased in the last ten years and most progress can be seen in the year 2016. Due to the fascinating properties of MnZn ferrites among the class of soft ferrites like high value of saturation magnetization, low value of coercivity, high initial permeability, narrow size distribution of the ferrite particles, low remenant magnetization, the researchers are taking interest in the synthesis of these ferrites.The co-precipitation and sol-gel method are the best for getting the fine crystallite size among all synthesis techniques. The XRD pattern of the MnZn ferrites has characteristic peaks showing the cubic spinel phase having Fd3m phase group. The shape of the prepared ferrite is nearly spherical but some distortion may be observed after doping. FTIR spectra confirmed the spinel phase of the ferrite nanoparticles having tetrahedral and octahedral sites.The value of saturation magnetization is highest when we synthesize the MnZn ferrites with proper amount of nickel doping by using sol–gel auto combustion method. Also, for getting the low value of coercivity sol–gel method is preferred. Generally, MnZn ferrites have a lot of applications including biomedical field, electronic devices, for making radar absorbing materials, for making ferrofluids etc. For enhancing the applications and advantageous properties of MnZn ferrite nanoparticles, further studies are required.The electrical and magnetic properties of MnZn ferrites can be enhanced by doping other metals such as cobalt, zinc, magnesium to make them suitable for use in agricultural and electrical applications. In the context of use of nanoparticles in the pandemic outbreak, such as in the recent COVID-19, MnZn soft ferrites can play a significant role in the development

of high contrast imaging dyes for viral strains in body fluids. Perhaps MnZn can also serve as a candidate nanomaterial for developing nanomaterial based medicines and therapeutics.

IV. REFERENCES

[1]. Singh J. P., Kumar H., Singhal A., Sarin N., Srivastava R. C. & Keun Hwa C. (2016). Solubility limit, magnetic interaction and conduction mechanism in rare earth doped spinel ferrite. An interdisciplinary peerreviewed international journal. Applied Science Letter 2(1), 03-11.

[2]. Kanagesan S., Hashim M., Tamilselvan S., Alithen N.B., Ismail I., Syazwan M. & Zuikimi M. M. M. (2013). Sol-gel auto-combustion synthsis of Cobalt ferrite and its cytotoxicity properties. Journal of Nanomaterials and Biostructures. 8(4), 1601-1610.

[3]. Sharma H. B., Boinis Singh N. G., Bobby Singh S. & Dhanabati Devi Th. (2014). Synthesis and Characterization of Cobalt Ferrite (CoFe2O4). Journal of Science and Technology. 7(2), 78-84.

[4]. Cullity B. D. & Graham C. D. (2009). Introduction to magnetic materials. New Jersey, Wiley.

[5]. Mehdiye T. R., Gashimov A. M. & Habibzade A. A. (2008). Nanoferrites of Transition Metals and their Catalytic Activity. Journal of Electromagnetic Processes in frequency dependent resistor sheath. 3, 80-88.

[6]. Daliya S. M. & Juang R. S. (2007). An overview of the structure and magnetism of spinel ferrite nanoparticles and their synthesis in microemulsions. Journal of Chemical Engineering. 129 (1-3): 51–65.

[7]. Ahmed M. A., Okasha N. & El-Dek S. I. (2008). Preparation and characterization of nanometric Mn ferrite via different methods. Journal of Nanotechnology. 19, 1-6.

[8]. Wang L, Li F. S.,Wang J. B., Zhou Q. G., Zhou X. Z., Kunkel H. P. & Williams G. (2004). Site preference of Fe in nanoparticles of ZnFe2O4. Journal of Magnetic material. 268(3), 332-339.

[9]. Ladole C. A. (2012). A microwave-assisted synthesis of 3, 4-dihydropyrimidin-2 (1H)-one/thione derivatives using nanocrystalline MgFe2O4 as catalyst. International Journal of Chemical Sciences. 10 (3), 1230-1234. 32

[10]. Pullar R. C. (2012). Hexagonal ferrites: A review of the synthesis, properties and applications of hexaferrite ceramics. Prog. Mater. Sci. 57(7), 1191-1334.

[11]. Sanpo N. (2014). Solution Precursor Plasma Spray System. Journal of Springer Briefs in Materials, Chapter 2 Literature Review. The Author(s) – SpringerBriefs.

[12]. Noppakun Sanpo, Cuie Wen, Christopher C., Berndt & James Wang. (2013). Antibacterial properties of spinel ferrite nanoparticles. Journal of Microbial pathogens and strategies for combating them: science, technology and education. (A. MéndezVilas, Ed.). Formatex Research Center.

[13]. Ranjit Kumar Panda. (2015). Studies on Electric and Magnetic Properties of Cobalt Ferrite and its Modified Systems. A Thesis of Doctor of philosophy. National Institute of Technology, Rourkela Rourkela - 769008,Odisha India.

[14]. Idrees M, Nadeem M & Hassan M M. (2010). Electric transport through perovskite La(Fe,Ga)O3 nanowires formed by electrospinning. Journal of Applied Physics D: Applied Physics. 43.

[15]. Chen W., Zhu W., Tan O. K. & Chen X. F. (2010). Structural and Dielectric Properties of Bismuth Doped Cobalt Nano Ferrites Prepared by Sol-Gel Auto Combustion Method. Journal of Applied Physics. 108.

[16]. Dr. Yitzhak Mastai (Ed.). (2012). Crystalization in Spinel Ferrite Nanoparticles. Journal of

Advances in Crystallization Processes.Available from:http://www.intechope.com/books/advances-in-crystallizationprocesses/crystallization-in-spinel ferrite nanoparticles. ISBN: 978-953, 51-0581-7.

[17]. Sugimoto M. (1999). "The Past, Present and Future of Ferrites. "Journal of American Ceramic Society. 82(2), 269-280.

[18]. Gadkari A. B., Shinde T. J. & Vasambekar P. N. (2009). Structural analysis of Y3+ - doped Mg–Cd ferrites prepared by oxalate co-precipitation method. Journal of Material Chemistry and Physics. 114(2-3), 505-510. M.J.Gothe1 , A. P. Bhat2 , K.G.Rewatkar, Superparamagnetic Behaviour Of Mn Substituted Zn Ferrite Nanoparticles for RF Application. IOSR Journal of Computer Engineering (IOSR-JCE)

Synthesis, Characterization and LPG Gas Sensing Response of 5% TiO2 Doped Polypyrrole Nano Composite

Khaire ND[1], Hamjade PT[2], Motke SG[3]

[1]Ex. Associate Professor, Department of Physics, Phulsing Naik Mahavidyalaya, Pusad, Maharashtra, India
[2]Associate Professor, Department of Physics, Phulsing Naik Mahavidyalaya, Pusad, Maharashtra, India
[3]Ex. Principal, Phulsing Naik Mahavidyalaya, Pusad, Maharashtra, India

ABSTRACT

Polypyrrole and its nano-composite is synthesized using in-situ chemical oxidative polymerization technique using pyrrole monomer. Crystalline nano sized TiO2 particles are embedded in amorphous Polypyrrole. Ammonium Per Sulphate is used as oxidizing agent for polymerization. The structure of composite was confirmed by the characterization techniques XRD, FTIR and UV Visible spectra. V-I characteristics and gas sensing response to LPG at room temperature is investigated.

Average grain size and chain separation is determined from XRD. UV-Visible studies show that the composite exhibit absorption peak at 278 nm; which corresponds to band gap energy 4.4633 eV. V-I characteristic is plotted using two probe method, which indicate fairly linear or ohmic behavior of the material with very high resistivity. Gas sensing response to LPG is also observed.

Key words – Polypyrrole, nano-composites, band gap energy, LPG gas sensing, TiO2

I. INTRODUCTION

Conducting polymers have widely been studied in the last two decades due to their potential applications as chemical sensors, gas sensors, electrochemical super capacitors, electro-chromic devices, photo-voltaics, light-emitting diodes, optical computers, microwave absorbers and batteries [1- 5]. In recent years, extensive research has been performed on creating conducting polymer matrix composites with the aim of improving physical and structural properties of conducting polymers. One such class of these, attracting a special attention is to create composites which contain inorganic materials which are usually metals or metal oxides filled into the conducting polymers via various methods. Polypyrrole is one of the most extensively studied conducting polymers due to its high electrical conductivity and chemical stability and as well as its easy preparation through chemical and electrochemical oxidation of pyrrole in the organic solvents and in aqueous medium. [6-9]

Growing industrialization and increasing pollutants from vehicular exhaust have resulted into increased air pollution. The problems related to air quality monitoring are important issues of current research activity. At present, LPG gas is being used in the car, in the storage tank or service station in addition to cooking. But, due to some reasons the LPG gas might leak from the gas cylinders, this may cause severe accident leading to damage of property and live-stock.

To overcome the problem, an LPG gas sensor is required. [10 - 11]

In the present study, polypyrrole/titanium di-oxide 5 % by weight (PPy/TiO₂) nano-composite was prepared by chemical polymerization. TiO₂, which was used as a filler, also have important applications as gas sensors. Samples were characterized by using X-ray diffraction, Fourier transform infrared spectroscopy (FTIR) and ultraviolet-visible spectroscopy (UV-vis). V- I characteristic and gas sensing response to LPG are also investigated.

II. METHODS AND MATERIAL

Pyrrole was supplied by Shah Scientific Mumbai; ammonium peroxydisulphate ((NH4)2S2O8) by Fisher scientific, nitric acid (HNO3) by Loba; TiO2 nanopowder by Nanolab, Jamshedpur, Jharkhand. These materials were used without any preprocessing. In a 50 ml of de-ionized water 0.5 ml concentrated nitric acid, 3.4 ml pyrrole and titanium dioxide (5 % by wt.) were added. The mixture was kept for continuous stirring.

Aqueous solution of oxidant was made by adding 17 gm of ammonium per sulphate into 50 ml of de – ionized water. This solution was added slowly into a mixture of pyrrole-acid-TiO2 in about half an hour. Gradual change in color from light black to dark black indicated formation of PPy/TiO2 nano-composite. After addition of APS solution, the stirring was continued at room temperature for four hours. The mixture was then kept overnight to ensure complete polymerization. The precipitate obtained after polymerization was filtered and washed with de-ionized water several times. The black colored PPy/TiO2 powder so obtained was dried at 50℃ for 24 hours [12]

III. RESULTS AND DISCUSSION

Characterization:
XRD

Samples obtained were powdery with black in colour. These were characterized by XRD. The 2θ scans were recorded using Cu - Kα radiation of wavelength 1.5418 A in a range of (5-80) degree as shown in fig. 1.
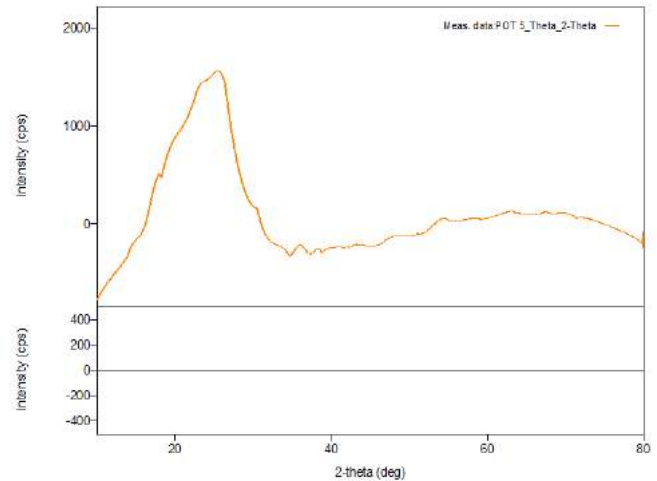
Fig. 1. X-ray diffraction of PPy/TiO₂ (5 %)

X-ray diffraction pattern shows that crystalline TiO₂ is embedded in amorphous poly-pyrrole. Broad peak is found at $2\theta = (25.46)°$. Average chain separation can be found from the maxima using the relation,

$S = 5\lambda / 8 \sin\theta$

Where S is polymer chain separation, λ is x- ray wavelength and θ is the diffraction angle at maximum intensity of amorphous halo. The average chain separation was found to be 4.37 A°.

The average crystallite size, can be estimated by using Scherrer's formula.

$D = K \lambda / \beta \cos\theta$

Where D is the crystallite size, K is the shape factor, which can be assigned a value of 0.89 if the shape is unknown, θ is the diffraction angle at maximum peak intensity and β is the full width at half maximum of diffraction angle in radians. When applied to sharp peaks, the equation leads to the average crystallite size of about 10 nm.

FTIR spectra

Infra-red spectroscopy (FTIR) was performed on Shimadzu FTIR 8201 spectrophotometer between 4000–400 cm^{-1} as shown in fig. 2.
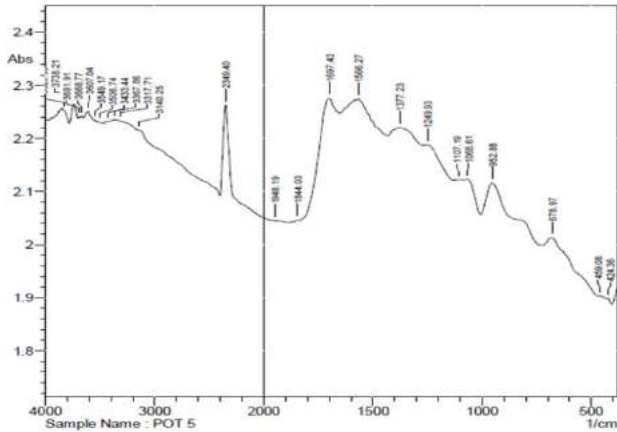
Fig. 2. FTIR spectra of PPy/TiO$_2$ (5%)

The peaks at around 3368 cm^{-1} indicates N-H stretching, 3318 cm^{-1} indicates C-H stretching, 1697 cm^{-1} indicates C= N bond, 1377 cm^{-1} is related to C-N asymmetric vibration, 1107 cm^{-1} is indicative of = C - H bond vibration, 679 cm^{-1} indicates C= C bending. The peaks at 459 cm^{-1} shows bending and stretching mode of Ti– O–Ti. [13]. The peaks observed in present work match well with literature values confirming formation of poly-pyrrole.

UV-Vis spectra

Ultra violet spectroscopy refers to absorption spectroscopy is made using Shimadzu UV-vis spectrometer between 200–1100 nm as shown in fig 3.
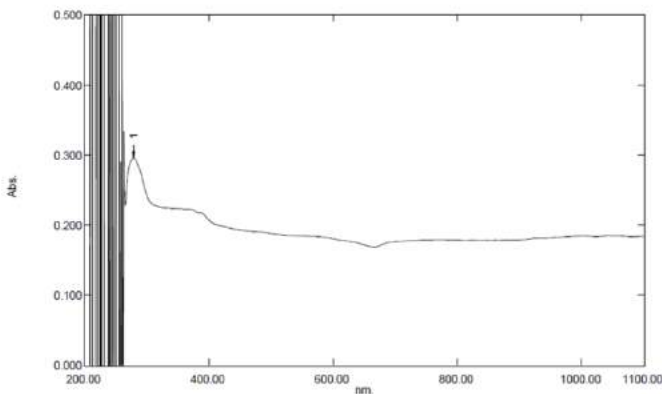
Fig.3. UV-Vis spectra of PPy/TiO$_2$(5%)

Using these spectra the band gap energy can be found out from the formula,

$E_g= hc/e\lambda$

Where h is Planck's constant, c is the speed of light, λ is the wave length and e is the charge of electron. For PPy / TiO$_2$ UV-Vis spectra exhibit absorption peak is at 278 nm, which corresponds to band gap energy 4.4633 eV.

DC Conductivity

The film of the composite is deposited using spin coating technique on pre-cleaned glass substrate using 8% polyvinyl acetate as a binder. For measurement of conductivity, juxtaposed copper electrodes, each of length 0.6 cm and 1 mm separation between them, are gently placed on the film with the help of loose spring. Pico- ammeter (DPM–111, SES, Roorky) and a dc power supply (Agronic - 93) are used for the purpose.
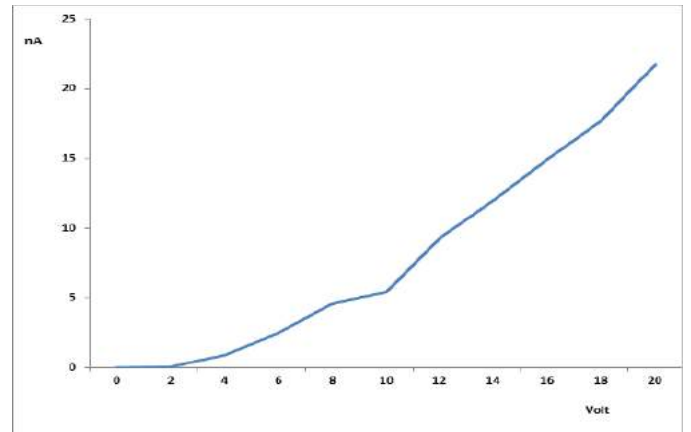
Fig.4. V-I Characteristic of PPy/TiO$_2$ (5%)

Fig. 4 represents variation of current through surface of sample with voltage. The graph is fairly linear indicating ohmic nature of the sample. As voltage increases the current increases. This may be due to transfer of electrons as charge carriers in the direction of applied field [14]. Surface resistivity is calculated from the formula -

$$\rho = \frac{E}{J} = \frac{V}{I}L$$

where, V is voltage applied, I is surface current and L represents length of the electrode. The surface resistivity, ρ is evaluated as 23.22 M Ω m.

Gas Sensing Response

Gas sensing response of the sensor is defined as change in conductance of a sample upon exposure to target gas to the original conductance in air. The figure shows gas response of PPy/TiO₂ thick film to LPG gas at room temperature.
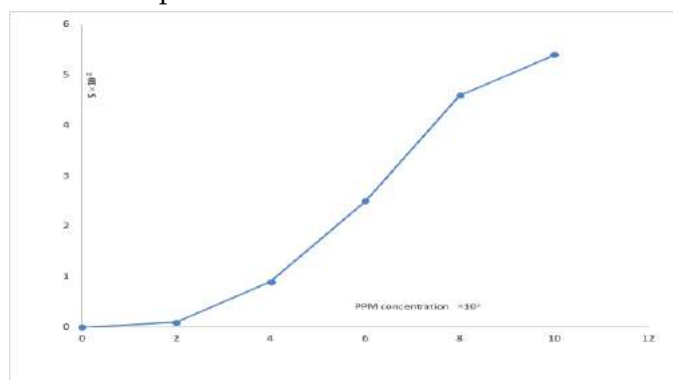
Fig.5. LPG gas response of PPy/TiO₂ (5%)

Fig. 5 shows that sensitivity increases fairly linearly with concentration of the gas. Percentage sensitivity per unit concentration is determined from the slope of linear range, is found to be 2.5866×10^{-4} % per ppm of LPG. The exact fundamental mechanisms to explain gas sensing response are controversial. But decrease in current due to increase in LPG concentration may be due to trapping of electrons in LPG molecule.

IV. CONCLUSION

PPy/TiO₂(5%) nano-composite was successfully synthesized by in situ chemical oxidative method. The characteristic peaks of PPy /TiO₂ nano-composite was observed in XRD, FTIR and UV-Vis spectra. X-ray diffraction pattern shows that crystalline TiO₂ is embedded in amorphous poly-pyrrole. Average chain separation and grain size are in the nanometer range. Band gap energy is also evaluated. DC electrical conductivity is investigated. Gas response to LPG is also determined.

V. ACKNOWLEDGEMENTS

VI. REFERENCES

[1]. S. Deivanayaki, et al, Elixir Polymer, 49B, 2012, PP 10182-10185.

[2]. Seyfullah Madakbas et al, , Chemical Papers,67(8), 2013, 1048-1053

[3]. Raza Ansari , E Jounal of Chemistry, Vol. 3, No. 4, Oct. 2006, PP - 186-201,

[4]. Ajit Chaudhari, et al, International Journal On Smart Sensing and Intelligent Systems, Vol 2, No. 4, Dec. 2009. PP – 540 - 548.

[5]. George F Fine, et al, Sensors, 10, 2010, PP – 5469 - 5502.

[6]. Manik A Chaugule et al, Soft Nanoscience Letters, Scientific Research, published online, 1, 2011, (6-10)

[7]. Tzong et al, Journal of Polymer Science, Part B, Plymer Physics, Vol. 46, 2008, PP - 727 – 733 Wiley Periodicals, Inc.

[8]. Yiqing Lu et al, Journal of Applied Polymer Science, Vol. 70, 1998, 2169-2172.

[9]. T. K. Vishnuvardhsn et al, Bull. Mat. Sci., Vol. 29, No. 1, 2006, PP 77-83.

[10]. https://www.elprocus.com/microcontroller-based-lpg-leakage-detector-circuit-and-working/

[11]. H Abederrahim, et al, J. Mater. Environ. Sci. 2(2) (2011), PP - 94-103.

[12]. Ersel Ozkazanc, et al, Polymer Engineering and Science, 2013, PP 1131-1137.

[13]. R Sharmila Devi et al, International Journal of Innovative Research In Science, Engineering And Technology, Vol. 3, Issue 8, 2014, 15206-15211.

[14]. HR Wasnik, et al, 2014, IOSR Journal of Applied Physics, Vol. 6, issue 3 ver. I, PP 106-109

Thermal Annealing Effect on Improved Structural, Morphological, Optical and Electrical Properties of Cu$_2$ZnSnS$_4$ Thin Film

Sandip V. Mahajan[1*], Sanjay R. Kamable[1] , Vishwajit R. Mhaske[2] , Anil D. Adsare[3]

[1*]Department of Physics, Shikshan Maharashri Dnyandeo Mohekar College, Kalamb,Osmanabad, Maharashtra, India

[2] Department of Botany, Shikshan Maharashri Dnyandeo Mohekar College, Kalamb,Osmanabad, Maharashtra, India

[3] Department of Botany, Arts, Commerce and Science College, Maregaon, Dist. Yavatmal, Maharashtra, India

ABSTRACT

Low-cost Cu2ZnSnS4 (CZTS) absorber layer thin films have been prepared by Successive Ionic Layer Adsorption and Reaction method (SILAR). CZTS thin film prepared at room temperature without any toxic components or precursors. After synthesis thin films have annealed at 250 ºC for 60 min to remove defects and improve the crystallinity. The crystal structure was studied by X-ray diffraction (XRD) characterization equipment. The as-grown CZTS thin films have shown amorphous structure but due to annealing effect improvement in crystallinity with a slight increase in peak intensity were observed. CZTS annealed thin film crystallite size is 15nm. A porous and granular structure of morphology of as-grown CZTS thin film has been confirmed by Scanning Electron Microscopy (SEM). Annealing effect decrease porosity and increase compact of the surface of a thin film. Optical properties show the increases the absorbance and decrease the band gap of as-grown and annealed samples respectively. Enhancement of current under the light condition has confirmed by I-V characteristics method. Higher optical absorption in visible light and enhancement of current up to mA is suitable characteristics of good absorber layer for solar cells application.

Keywords : Low Cost, CZTS, Absorber, Porous, Solar Cells.

I. INTRODUCTION

Semiconducting kesterite CZTS thin films are currently under intensive investigation for efficient solar cells. Current CuInGaS (CIGS) and CdTe materials have reached high efficiencies, but it has serious issues of cost, toxicity and rare materials [1]. CZTS is emerging candidate as replaced CIGS thin film with In and Ga replaced by Zn and Sn. Direct band gap (~1.45eV) of CZTS thin film is suitable for solar energy conversion. CZTS thin film is also a high absorption coefficient ~10^{4}cm^{-1}. Quaternary CZTS thin films have been reported as produced by pulsed laser ablation [3], DC sputtering [4], Co-Sputtering [5], chemical spray deposition[2,6], Printing technique [7], Vacuum deposition technique [8], Sol-Gel sulfurization [9,10], spin coating technique [11], electron beam evaporation [12], electroplating [13], hot injection method [14], Chemical Bath Deposition [1-3]. Successive Ionic Layer Adsorption and Reaction method [4]. However, these methods have some

drawbacks such as expensive precursors, complicated apparatus and even toxic byproducts evolved during their synthesis. SILAR method has some advantages like it is inexpensive, large area deposition, easy handling, environmentally friendly and room temperature growth. To fabricate solar cell modules at a truly competitive cost, the SILAR method is a most attractive process to cut down the expenses. Mostly ternary and quaternary materials are shows amorphous structure prepared by SILAR method at room temperature. Annealing effect has removed the defects and increase intensity peaks due to crystallinity are increased [16].

In the present research paper, we report the synthesis of CZTS thin film by SILAR method at room temperature and after preparation samples annealed at 250 ℃. The soft chemically prepared as grown and annealed CZTS thin films studied by structural, morphological, optical and electric properties have been investigated.

II. METHODS AND MATERIAL

CZTS thin films have been prepared by SILAR method on silica glass substrates. The growth of CZTS thin was carried out at room temperature. The solutions of 0.1M $CuSO_4$, 0.05M $ZnCl_2$, 0.05M $SnCl_2$ and 0.4M $SC(NH_2)_2$ were separately prepared in distilled water with analytical grade reagents. The ammonia and Triethanolamine (TEA) used as complexing agents to control precipitation in cationic reaction. Cu, Zn and Sn as used cationic precursors and S as an anionic precursor. 5 ml of TEA was added each cationic solution and stirred few min. Few drops of ammonia were also added in cationic solution to maintain reaction basic media up to ~11 pH. All cationic solutions were mixed together. The substrates were immersed in cationic solution 10 sec and dipped in distilled water to remove the loose ions then substrates were immersed in anionic solution 20 sec

and dipped in distilled water. Successive cycles repeated at 60 times to get the uniform film.

The X-ray diffraction of the thin film samples was measured on Bruker AXS, Germany (D8 Advanced) X-ray Diffractometer by using monochromatic $CuK\alpha_1$ radiation in the range of 2θ from 20-60°. Surface morphology of the samples was studied using Scanning Electron Microscope (JEOL). UV-Visible spectrum was recorded on Perkin Elmer spectrophotometer (Perkin-Elmer Lambda-25 UV-Vis Spectrophotometer). Electrical measurements of CZTS thin film was studied by the current–voltage (I–V) characteristics [LAB equipment model 24 (2004)].

III. RESULTS AND DISCUSSION

The X-ray diffraction is a widely used technique to investigate the structure and phase of the material. **Fig. 1** shows the typical XRD pattern obtained for as-grown and annealed CZTS thin films. The formation of CZTS kesterite structure was confirmed by comparing the obtained XRD pattern with standard JCPDS data (JCPDS # 26-0575). The XRD analysis of as-grown CZTS thin film shows amorphous behavior but after annealing CZTS thin film revealed small diffraction peaks at 2Θ values 28.60º, 47.32º and 58º which were assigned to (112), (220) and (224) reflection planes respectively [16]. The average crystallite size has been calculated from the X-ray diffraction pattern using the Debye-Scherer's formula given in **Eq. (1)**.

$$D(hkl) = \frac{K\lambda}{\beta cos\theta} \qquad (1)$$

Where D is the crystallite size, k is shape constant. β is the full width at half maximum (FWHM) and λ is the wavelength of the X-rays. The crystallite size of annealed CZTS thin film is to be 15 nm.
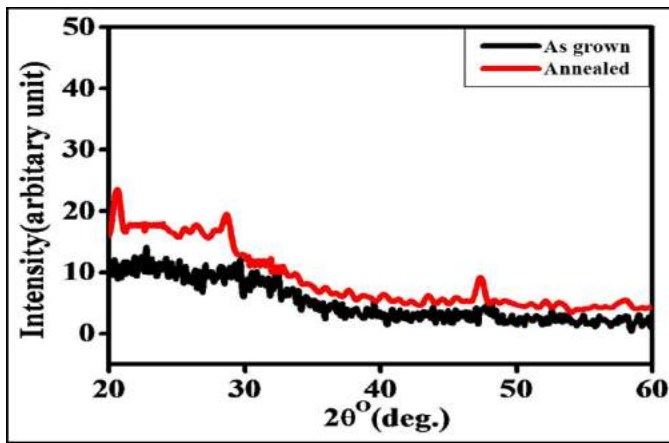
Fig.1 XRD pattern of as-grown and annealed CZTS thin film.

Fig. 2: FESEM images of as-grown (a) and annealed (b) CZTS thin films.

Surface morphology study

The surface morphology of CZTS thin films was carried out by Field Emission Scanning Electron Microscopy (FE-SEM) technique. The FE-SEM images show a smooth and homogeneous surface with the formation of granular crystallites but after annealing compactness of the surface increases and few of which came together to form agglomerates as shown in **Fig. 2**(a) and (b) respectively [1]. The **inset** images in **Fig. 2**(a) and (b) shows higher resolution images of the CZTS thin film for as-grown and annealed samples respectively. The FE-SEM images show the irregular shape particles turns into some cubic like structure due to annealing effect. Alo0ng with compactness in the surface annealing also increases the homogeneity in the surface this may be attributed to the binding of surface atoms after annealing.

Optical study

The UV-Vis spectrophotometer was used to characterize the optical absorbance and to obtain the band gap of CZTS thin films. **Fig. 3** shows the optical spectra and the band gap of (a) as-grown and (b) annealed CZTS thin films. The theory of optical absorption gives the relationship between the absorption coefficient (α) and the photon energy (hν) for direct or indirect allowed transition given in following **Eq. (2)**,

$$\alpha = \frac{\alpha_0(h\nu - E_g)^n}{h\nu} \qquad (2)$$

Both CZTS thin films show higher absorption in the visible region. Thermal annealing effect decreases the band gap of the material and it is correlated with the crystallinity of the material. Band gap values of as-grown and annealed thin film were found to be 1.58 eV and 1.56 eV respectively [16]. The decrease in band gap is assigned to the increase in crystallite size of the CZTS thin films as it increases the absorption.
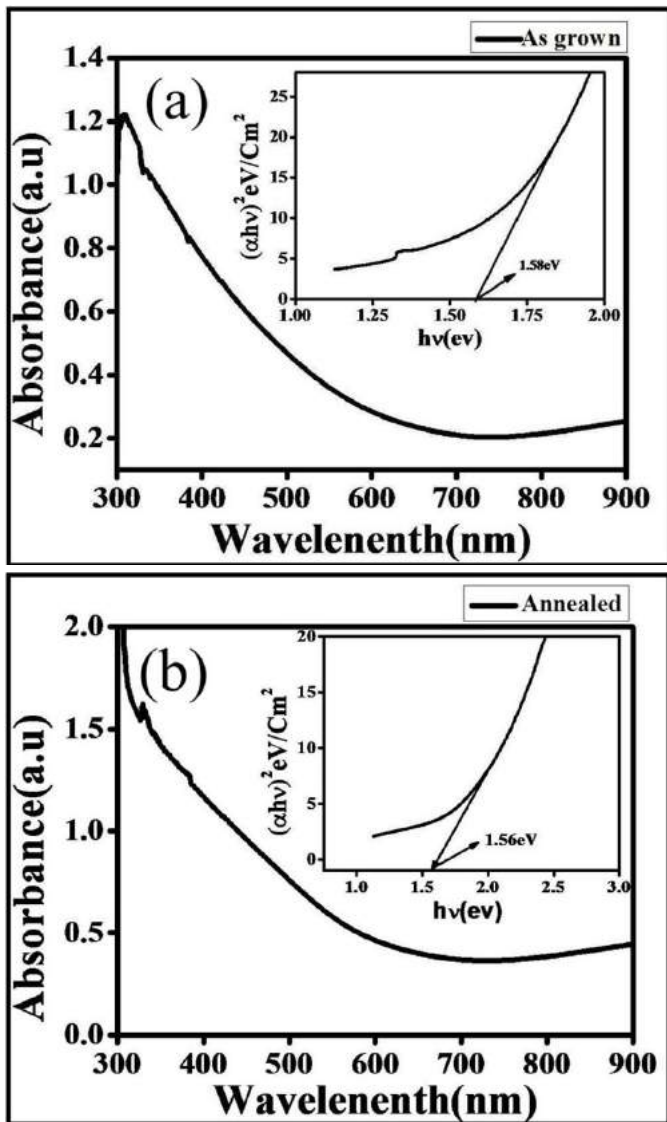
Fig. 3: Absorption of as-grown (a) and annealed (b) CZTS thin films and inserted own band gap.

Electrical Study

The electrical properties of the prepared CZTS thin film were investigated by I-V characteristic curve in dark and under illumination of light. **Fig. 4**(a) and (b) shows I-V characteristics data of as-grown and annealed CZTS thin films respectively in the applied voltage range of ±5 V. Both CZTS thin films under dark and under light illumination of 100 mW/cm² light results in higher current in the order of milliamperes. I-V curve shows straight line passing through origin indicates ohmic nature of the metal semiconductor contacts for CZTS thin films. Both the

thin films reveal photo sensing nature of the CZTS thin film as there is an increase in current after light illumination is observed [16].
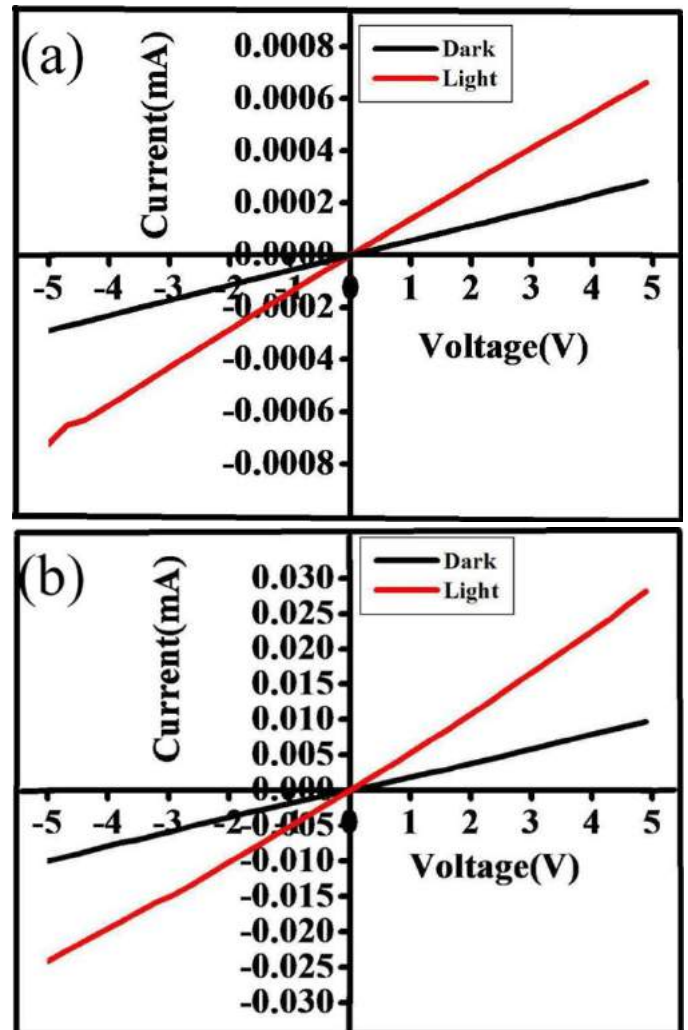
Fig.4 I-V characteristics of as-grown (a) and annealed (b) CZTS thin films.

IV. CONCLUSION

We have successfully synthesized CZTS thin films by SILAR method at room temperature on a glass substrate. Thermal Annealing effect on structural, morphological, optical and electrical properties of CZTS thin film has been reported. As-grown CZTS thin film show amorphous structure, which after annealing turns into crystalline with increased peak intensity. The estimated crystallite size of annealed CZTS thin film was found to be ~15 nm. As-grown

thin films compared to annealed film have more agglomeration of nanoparticles due to the compactness of thin film surface. The band gap value decreases and electrical current increases after annealing due to increased crystallinity in the material. From the reported results we can conclude that annealing effect induces favorable changes in the CZTS thin film.

V. REFERENCES

[1]. N.M. Shinde, C.D. Lokhande, J.H. Kim, Moon. JH. J Photochem Photobiol A 235, 14– 20 (2012).

[2]. Z. Seboui, A. Gassoumi, Turki NK. Mat Sci Semicond Process 26, 360–366 (2014).

[3]. L. Sun, J. He, H. Kong, F. Yue, P.Yang, J.Chu. Sol Energy Mater Sol Cells 95, 2907–2913 (2011).

[4]. P.A. Fernandes, P.M.P. Salomé, A.F. da Cunha, Schubert. B-A. Thin Solid Films 519, 7382–7385 (2010).

[5]. J. Ge, Y. Wu, C. Zhang, S. Zuo, J. Jiang, J. Ma, et al. Appl Surf Sci 258, 7250-7254 (2012).

[6]. N. Kamoun, H. Bouzouita, B. Rezig. Thin Solid Films 515, 5949–5952 (2007).

[7]. T. Todorov, M. Kita, J. Carda, Escribano P. Thin Solid Films 517, 2541-2544 (2009).

[8]. H.Katagiri. Thin Solid Films 480–481, 426–432 (2005).

[9]. K.Maeda, K.Tanaka, Y.Fukui, H.Uchiki. Sol Energy Mater Sol Cells 95, 2855–2860 (2011).

[10]. M. Jiang, Y. Li, R. Dhakal, P. Thapaliya, M. Mastro, J. D. Caldwell, et al. J Photonics Energy 1, 019501-019506 (2011).

[11]. A. Fischereder, T. Rath, W. Haas, H. Amenitsch, J. Albering, D. Meischler, et al. Chem Mater 22, 3399–3406 (2010).

[12]. H.Araki, A.Mikaduki, Y.Kubo, T. Sato, K.Jimbo, W.S. Maw, et al. Thin Solid Films 517, 1457–1460 (2008).

[13]. H. Araki, Y. Kubo, A. Mikaduki, K. Jimbo, W. S. Maw, H. Katagiri, et al. Sol Energy Mater Sol Cells 93, 996–999 (2009).

[14]. S. C. Riha, B. A. Parkinson, Prieto AL. J Am Chem Soc 131, 12054–12055 (2009).

[15]. A. Wangperawong, J.S. King, S.M. Herron, B.P. Tran, K. Pangan-Okimoto, Bent SF. Thin Solid Films 519, 2488-2492 (2011).

[16]. S. S. Mali, B. M. Patil, C. A. Betty, P. N. Bhosale, Y. W. Oh, S. R. Jadkar, et al. Electrochim Acta 66, 216-221 (2012).

Thermo Acoustic Study of Different Parameters for Ternary Mixture of Aqueous Potassium Hydroxide & 1, 4 Dioxane Using Ultrasonic Interferometer

S. G. Rathod*, A. A. Mistry, N. S. Ugemuge

Department of Physics, Anand Niketan College, Warora, Maharashtra, India

ABSTRACT

An analysis of different thermodynamic properties as a function of temperature provides valuable information about their characteristics. The concentration and temperature dependence of acoustic and volumetric properties of multi component liquid mixtures has proved to be a useful indicator of the existence of significant effect resulting from intermolecular interactions. The thermo-acoustic parameters such as density (ρ), ultrasonic velocity (U) and viscosity (η) are determined for the ternary mixture of aqueous potassium hydroxide and 1,4 dioxane system at 0.0% to 100% (v/v) and at different temperature. These experimental data have been used to estimate the acoustical parameters such as, adiabatic compressibility (β_a), free length (L_f), free volume (V_f), internal pressure (π_i), and Gibb's free energy (ΔG). The present paper represents the nonlinear variation of ultrasonic velocity and the thermo-acoustical parameters lead to dipole- ion interaction between 1,4 dioxane and 1N aqueous potassium hydroxide is stronger than dipole- ion interaction between water and aqueous potassium hydroxide.

Keywords: Ultrasonic velocity, acoustical parameters, molecular interactions, ternary mixtures, aqueous potassium hydroxide (aq. KOH) and 1,4 dioxane.

I. INTRODUCTION

Ultrasonic is widely useful for the investigation of various thermo-acoustic parameters such as adiabatic compressibility, free volume, intermolecular free length and relaxation time[1-3]. The molecular behavior and interactions and their mixtures can be characterized with the help of ultrasonic studies[4-6].The measurement of ultrasonic velocity in the organic liquid mixture is a useful tool to study the physiochemical properties of the liquids and also explain the mechanism of molecular interaction[7-10]. The ultrasonic velocity data for ternary liquid mixtures have been used for by many researchers[11-14]. The present work investigates thermo-acoustical properties of aqueous solution of KOH with 1,4 dioxane at different temperatures and at different composition. From these experimental values, number of thermodynamics parameters, namely adiabatic compressibility (β_a), free length (L_f), free volume (V_f), internal pressure (π_i) and Gibb's free energy (ΔG) have been calculated. The variations of these parameters with concentrations were found to be useful in understanding the nature molecular interactions in the ternary liquid mixtures.

II. METHODS AND MATERIAL

The ultrasonic velocity was measured in the ternary mixture of aqueous potassium hydroxide and 1,4 dioxane using an ultrasonic interferometer working at frequency 4 MHz with an overall accuracy range of ± 0.1 ms^{-1}.The temperature was maintained by a constant temperature water bath using circulated water through the double walled measuring cell. The density of liquid mixtures was determined using a 10ml specific gravity bottle with an accuracy of ± 0.1 Kgm^{-3}. An Ostwald's viscometer was used for the viscosity measurement of pure liquids and liquid mixtures with accuracy 0.001 NSm^{-2}. The time required for the flow of water (t_w) and time required for the flow of mixture (t_s) was measured with a digital stop watch having an accuracy ±1x10^{-6} NSm^{-2}.

III. RESULTS AND DISCUSSION

The experimental values of density, velocity and viscosity of 1N aqueous potassium hydroxide with 1,4 dioxane over entire range concentration (v/v) at different temperature range 298K-308K using ultrasonic interferometer are shown in **table-1.** It is observed that density increases with increase in concentration (vol. %) of aqueous potassium hydroxide in dioxane. Due to increase in density, the volume decreases indicating association in component molecules. The decrease in density (ρ) with rise in temperature indicates decrease in cohesive force. It is also observed that ultrasonic velocity increase with increase in concentration (vol. %) of aqueous potassium hydroxide in dioxane indicating association in the molecules of the component liquids. The association is due to ion-induced dipole interaction between K$^+$ of potassium hydroxide and dioxane is stronger than the ion-dipole interaction between K$^+$ of potassium hydroxide and water molecule. Since size of dioxane molecule is more than the size of water molecule and hence more will be polarizibility of dioxane. Thus association in the constituent molecules may involve due to dipole - induced dipole interaction between water and dioxane. It is observed that viscosity increases with increase in concentration (vol. %) of potassium hydroxide in dioxane up to 40%, indicating strong molecular interaction. The viscosity of a mixture strongly depends on molecular interaction as well as on the size and shape of the molecules. As the concentration goes higher (above 40%), viscosity gradually decreases indicating weak molecular interaction between the constituent molecules.

From table-2, it is observed that adiabatic compressibility (β$_a$) decreases with increase in concentration (vol. %) of aqueous potassium hydroxide in dioxane indicating strong intermolecular interaction in the molecules of component in the ternary liquid mixtures shows associating tendency of the component molecules. As the concentration (vol. %) of aqueous potassium hydroxide increases, the induced dipole- induced dipole and ion-dipole interaction between dioxane and aqueous potassium hydroxide becomes predominant which leads to a more compact structure and decreased adiabatic compressibility. It is also observed that free length decreases with increase in concentration of aqueous potassium hydroxide in dioxane. Free length decreases with concentration due to lack of perfect symmetry and decrease in available space between the component molecules. The decrease in free length with increase in concentration (vol. %) of aqueous potassium hydroxide in dioxane indicates increase in closed packed structure of component molecules i.e. enhancement of the closed structure. The decrease in free length may due to dipole - induced dipole interaction between dioxane and water. It is observed that free volume decreases (V_f) and internal pressure (π$_i$) increases with increase in concentration (vol. %) of aqueous potassium hydroxide in dioxane, indicating association in the molecules of the component liquids.

From table-3, Further, the decrease in free volume and increase in internal pressure with increase in concentration (vol. %) clearly show the increasing magnitude of interactions. Such behavior of free volume and internal pressure generally indicate the association through dipole - induced dipole interaction between water and dioxane. This suggests that both solute- solute and solute solvent interaction exist in the system. Thus increase in free volume and decrease in internal pressure occurs with increase in temperature. It is also observed that relaxation time increases slightly with increase in concentration (vol. %) of aqueous potassium hydroxide in dioxane up to 40%, indicating high stability. As the concentration goes higher (above 40%), the relaxation time slightly decrease indicating less stability. Gibb's free energy measure mobility of the medium. Higher the mobility of the medium, higher will be the entropy; lower will be the free energy. It is observed that initially Gibb's free energy slightly increases with increase in concentration (vol. %) of aqueous potassium hydroxide in dioxane up to 40%, indicating the mobility of the molecule is low i.e. highly ordered due to outstanding salvation. As the concentration goes higher (above 40%), the Gibb's free energy slowly decreases indicating, increase in mobility of the mixture hence disorder increases. This leads to the higher entropy and hence salvation decrease. This is due to salvation is directly proportional to size of the molecule.

TABLES

TABLE-1: - Density (ρ), Velocity (U) and Viscosity (η) of the ternary systems Aqueous KOH + 1,4 dioxane at different temperature.

Vol. % of Aq.KOH in Dioxane	ρ (Kgm⁻³)			U (ms⁻¹)			η*10⁻³ (NSm⁻²)		
	298K	303K	308K	298K	303K	308K	298K	303K	308K
00	1050.41	1049.49	1048.39	1345.64	1337.60	1324.00	1.150	1.030	0.907
10	1051.52	1050.86	1049.21	1336.00	1322.40	1306.00	1.420	1.210	1.050
20	1052.90	1051.50	1050.11	1388.80	1344.00	1329.60	1.710	1.480	1.320
30	1053.21	1052.32	1051.00	1398.40	1365.60	1345.60	1.850	1.610	1.400
40	1054.12	1053.21	1052.11	1481.60	1467.20	1444.80	2.080	1.790	1.480
50	1055.32	1054.08	1052.96	1529.60	1509.60	1481.60	1.870	1.640	1.430
60	1056.08	1055.02	1053.82	1573.60	1533.60	1516.00	1.750	1.530	1.340
70	1057.10	1055.90	1054.71	1593.60	1580.00	1568.00	1.590	1.360	1.180
80	1057.95	1055.50	1055.30	1600.00	1556.00	1549.60	1.320	1.130	0.983
90	1058.50	1057.01	1055.83	1592.00	1540.00	1547.20	1.180	1.020	0.890
100	1058.04	1055.89	1055.42	1590.00	1598.00	1612.00	1.050	0.914	0.799

TABLE-2: - Adiabatic compressibility (βa), free length (Lf) and free volume (Vf) of the ternary systems Aqueous KOH + 1,4 dioxane at different temperature.

Vol. % of Aq. KOH in Dioxane	βa *10⁻¹⁰ (m²N⁻¹)			Lf*10⁻¹⁰ (m)			Vf*10⁻⁷ (m³mol⁻¹)		
	298K	303K	308K	298K	303K	308K	298K	303K	308K
00	5.249	5.323	5.441	0.4536	0.4614	0.4688	1.1853	1.3885	1.6472
10	5.328	5.441	5.587	0.4570	0.4665	0.4751	0.7543	0.9494	1.1498
20	4.924	5.264	5.386	0.4393	0.4589	0.4665	0.5288	0.6238	0.7323
30	4.855	5.095	5.254	0.4362	0.4514	0.4607	0.4111	0.4857	0.5884
40	4.321	4.410	4.553	0.4116	0.4200	0.4289	0.3189	0.3923	0.511
50	4.050	4.162	4.326	0.3984	0.4080	0.4180	0.3248	0.3895	0.4631
60	3.823	4.030	4.128	0.3871	0.4015	0.4084	0.305	0.36	0.4287
70	3.724	3.799	3.856	0.3821	0.3895	0.3947	0.2819	0.3511	0.4281
80	3.692	3.909	3.946	0.3804	0.3954	0.3992	0.2802	0.3399	0.4158
90	3.727	3.989	3.956	0.3822	0.3994	0.3998	0.2299	0.2726	0.336
100	3.738	3.705	3.646	0.3828	0.3849	0.3838	0.1706	0.2111	0.2617

TABLE-3: - Internal pressure (πi), relaxation time (τ) and Gibb's free energy of the ternary systems Aqueous KOH + 1,4 dioxane at different temperature.

Vol. % of Aq. KOH in Dioxane	πi*10⁶ (Nm⁻²)			τ*10⁻¹² (Sec.)			ΔG *10⁻²⁰ (KJ/mol)		
	298K	303K	308K	298K	303K	308K	298K	303K	308K
00	525.43	507.62	486.00	0.8041	0.7288	0.6580	0.5468	0.5256	0.5017
10	645.89	608.95	580.11	1.0080	0.8743	0.7804	0.6297	0.5934	0.5663
20	773.58	743.74	716.04	1.1224	1.0402	0.9461	0.6690	0.6581	0.6393
30	898.4	863.59	822.74	1.1914	1.0957	0.9797	0.6920	0.6775	0.6525
40	1051.92	997.64	927.90	1.1969	1.0537	0.8980	0.6926	0.6629	0.6195
50	1135.07	1085.44	1040.78	1.0124	0.9098	0.8269	0.6312	0.6082	0.5883
60	1272.20	1223.45	1172.37	0.8922	0.8206	0.7396	0.5849	0.5697	0.5460
70	1456.06	1374.86	1307.20	0.7892	0.6883	0.6084	0.5399	0.5042	0.4720
80	1660.10	1581.35	1501.87	0.6500	0.5885	0.5172	0.4688	0.4459	0.4105
90	2081.10	1997.22	1892.20	0.5864	0.5418	0.4697	0.4311	0.4151	0.3740
100	2835.65	2683.63	2537.09	0.5227	0.4517	0.3886	0.3889	0.3473	0.3022

IV. CONCLUSION

- The non regular changes of ultrasonic velocity and the thermodynamics parameters lead to dipole-ion interaction between 1,4 dioxane and 1N aqueous potassium hydroxide is stronger than dipole-ion interaction between water and aq. potassium hydroxide.

- The ion-dipole interactions between K⁺ of potassium hydroxide and 1,4 dioxane are found to be responsible for association whereas the ion-dipole interactions between K⁺ of potassium hydroxide and water molecules are found to be responsible for dissociation in the liquid mixtures.

V. REFERENCES

[1]. Saxena Indu, Pathak R.N., Vijay Kumar and Rikkam Devi (2015), International journal of applied Research 1(9), 562-569.

[2]. Thirumaran S., Mathammal R. and Bharati M.(2012),ARPN Journal of Science and Technology 2,7.

[3]. Tabhane V. A. (1983), Indian J. Pure & Applied Physics 23, 155.

[4]. Bhandakkar V. D., Chimankar O. P. & Power N. R.(2010), J. of Chemical & Pharmaceutical Research, 4, 873-877.

[5]. Mistry A.A and Ugemuge N.S.(2020),Vol.9 Issue 3,4738-4742.

[6]. Chimankar O. P., Shriwas R. and Tabhane V. A. (2011), J. Chem. Pharm. Res., 3(3), 587-596.

[7]. Shukla B. P, Jha L. K and Dubey G. P. (1992), Indian J. Pure Appl. Phys.30, 754.

[8]. Kannapan A. N. and Rajendran V. (1992), Indian J. Pure Appl. Phys 30, 240.

[9]. Praharaj M.(2017),Int.J.Curr.Res.Aca.Rev.,5(6),1-5

[10]. Aralaguppi M. I. and Barragi J. C. (2006), K. J. Chem. Therm. 38, 434-442.

[11]. Praharaj M. K. et al., (2012), Arch. Phy. Res. 3(3), 192-200.

[12]. Bhandakkar V. D. et al. (2013), J. Pure appl. and Ind. Phys. 3(2), 80-86.

[13]. Mistry A.A and Ugemuge N.S.(2020),IRJSE,A7:201-205.

[14]. Chimankar O. P., Rewatkar K. G. & Tabhane V. A. (2001) , I. Journal of Physics, 75 B (2), 141-145.

[15]. Tadkalkar A. P. (2012), Archives of Physics Research, 3(4), 287-291.

Electrical Conductivity of Cr(III), Mn(III) And Fe(III) Metal Complexes of 2-Hydroxy-5-Methyl-3-Nitroacetophenone Thiazole Schiff Base

S. R. Kelode

Department of Chemistry, Arts, Commerce and Science College, Maregaon, Maharashtra, India

ABSTRACT

The newly coordinating metal complexes of Cr(III), Mn(III) and Fe(III) have been synthesized using 2-hydroxy-5-methyl-3-nitro acetophenone thiazole Schiff base ligand was derived from the condensation of 2-hydroxy-5-methyl-3-nitro acetophenone and thiazole. The Schiff bases behaved as charge bidentade ligand. The ligand was characterized by elemental analysis and spectral methods. Metal complexes characterized by elemental analysis, conductance measurements, molecular weight determinations and spectral studies. The synthesized products are coloured solids, soluble in DMF, DMSO and THF. The Schiff base and their metal complexes have been studies by electrical conductivity

Keywords: Schiff Base, Magnetic Susceptibility, Electrical Conductivity

I. INTRODUCTION

The chemical studies of metal complexes with heterocyclic Schiff base ligands containing nitrogen, sulfur, and oxygen has attracted increasing attention. It is well known that these heterocyclic compounds can exhibit bacterial, fungicidal, herbicidal and insecticidal activities in addition to their application as potential drugs. Such heterocyclic ligands, when complexed with metal ions, exhibit enhanced microbiological activities[1,2]. In the study of comparative reactivity of ambidendate ligand systems two or more potential donor centre of amino heterocycles plays an important role[3]. In the chemistry of organic and inorganic compound the number of Schiff base ligand and metal complexes are of substantial sake and attention because of their biological activity including anti-tumor, antibacterial, fungicidal and anti-carcinogenic properties[4,5]. Due to biological potency, pharmacological properties and synthetic flexibility of thiazole Schiff bases. The aim of present investigation is to synthesize various transition metal complexes of Schiff base derived from 2-hydroxy-5-methyl-3-nitro acetophenone and 2-amino-4-phenylthiazole.

II. METHODS AND MATERIAL

All the chemicals were of A.R. grade and used as received. 2-hydroxy-5-methyl-3-nitro acetophenone (HMNA) and 2-amino-4-phenylthiazole was prepared by known methods[6-9]. The solvents were purified by standard methods[10]. Synthesis of 2-amino-4-phenylthiazole: The Synthesis of 2-amino-4-phenylthiazole prepared by known method[7-9]. Yield: (75%); m.p.: 148-150⁰C
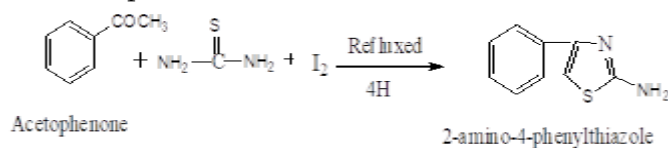
Synthesis of 2-hydroxy-5-methyl-3-nitroacetophenone 4-phenyl-2 imino thiazole [HMNAT]:

A solution of 4-phenyl-2 imino thiazole (0.02M) in 25ml of ethanol was added to an ethanolic solution(25ml) of 2-hydroxy-5-methyl-3-nitro acetophenone (0.02M) and the reaction mixture was refluxed on a water bath for 4-6h. After cooling a pale yellow coloured crystalline solid was separated out. It was filtered and washed with ethanol, crystallized from DMF and dried under reduced pressure at ambient temperature. The purity of ligand was checked by elemental analysis and m.p. It was also characterized by IR and ^{1}H NMR spectral studies. Yield:7o%; m.p. 310^{0}C
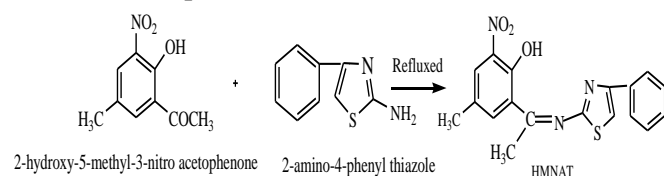

2-hydroxy-5-methyl-3-nitro acetophenone   2-amino-4-phenyl thiazole   HMNAT

Table1. Analytical data of the Ligands.

Ligand	Molecular Formula	Formula Weight	Color and nature	Elemental Analysis		
				C% found (Cal.)	H% Found (Cal.)	S% Found (Cal.)
HMNAT	$C_{18}H_{15}N_3O_3S$	353.1	Yellow Crystalline	60.42 (61.17)	04.04 (04.24)	08.84 (09.06)

Preparation of complexes: All the metal complexes were prepared in a similar way by following method. To a hot solution of ligand HMNAT (0.02M) in 25ml of ethanol a suspension of respective metal salts was added drop wise with constant stirring. The reaction mixture was refluxed on a water bath for 3-5 h. The precipitated complexes were filtered, washed with ethanol followed by ether and dried over fused calcium chloride. Yield : 55-60%

The complexes are soluble in DMSO and DMF but insoluble in water and common organic solvents. The metal chloride content of complexes were analyzed by standard methods[11,12] The ^{1}H NMR spectra of ligand was recorded and obtained from RSIC Chandigarh. IR spectra of the compounds were recorded on Perkin Elmer 842 spectrophotometer in the region 400-4000cm^{-1}, Carbon, Hydrogen and Nitrogen analysis were carried out at RSIC, Punjab University, Chandigarh. The molar conductance of the complexes at 10^{-3} M dilution in DMF were determined using equiptronic digital conductivity meter EQ-660 with a cell constant 1.00 cm^{-1} at room temperature. The magnetic moment measurement were made on a Gouy balance at room temperature using [HgCo(SCN)$_4$] as the calibrant. The molecular weights of the complexes were determined by Rast method.

Table 2. Analytical data and molar conductance of the compounds.

Ligand	Formula weight g mole^{-1}	Colour	Elemental Analysis Found (Calcd.)			μ_{eff} B.M	Λ_M (Ω^{-1} cm^2 mol^{-1})
			M%	C%	H%		
[CrL$_2$(H$_2$O)Cl] H$_2$O	827.7	Green	6.12 (6.28)	51.69 (52.19)	3.34 (3.86)	3.6	16.6
[MnL$_2$(OAc)] H$_2$O	854.1	Brown	6.28 (6.42)	53.18 (53.38)	4.15 (4.21)	4.2	17.4
[FeL$_2$(H$_2$O)Cl] H$_2$O	831.6	Black	6.40 (6.70)	51.05 (51.19)	4.03 (4.08)	5.6	20.2

III. RESULTS AND DISCUSSION

The Schiff base HMNAT and its complexes have been characterized on the basis of ^{1}H NMR, IR spectral data, elemental analysis, molar conductance, magnetic succeptibility measurements and thermogravimetric analysis data . All these values and analytical data is consistent with proposed molecular formula of ligand . All the compounds are coloured solid and stable in air. They are insoluble in water but soluble in coordinating solvents like DMF and DMSO. The molar conductance values in DMF(10^{-3} M) solution at room temperature (Table2) shows all the complexes are non electrolytes.

The ^{1}H NMR spectra of ligand HMNAT shows signals at δ 12.24,(1H, s phenolic OH), δ 7.60, 7.74, 7.63 and 7.72 (4H, m, phenyl) δ 6.87, 6.88, and 6.72(3H, s Phenyl), 6.78 (1H s thiophene), and 2.66(3H, s, methyl) [11,13-15].

IR spectra of ligand and metal complexes shows ν(C=N) peaks at 1626 cm^{-1} and absence of C=O peak at around 1700 – 1740 cm^{-1} indicates the Schiff base formation[16-19].

Table 3. IR spectra of ligand and metal complexes

Compound	ν(O−H) hydrogen bonded	ν(C=N) imine	ν(C−O) phenolic	ν(M−O)	ν(M−N)	ν(C−S)
HMNAT	3085	1626	1520	--	--	1128
[CrL₂(H₂O)Cl]H₂O	--	1596	1508	475	409	1116
[MnL₂(OAc)]2H₂O	--	1566	1466	498	420	1091
[FeL₂(H₂O)Cl]H₂O	--	1606	1502	512	440	1082

Electrical Conductivity: The electrical resistivity of the different metal chelates can be measured either with a.c. or d.c. methods. However, in the present work the d.c. method is used for resistivity measurements, over a wide range of temperature.The electrical conductivity of metal complexes varies with their nature and temperature[19-23]. The variation of electrical conductivity of the metal complexes with temperature is the basis of their classification as semiconductors or metallic conductors. The electrical conductivity of metallic conductors decreases with increasing temperature (i.e. temperature coefficient is negative) and their resistivity ranges from 10^{-6} to 10^{-3} Ω.

The electrical conductivity and activation energy of HMNAT complexes are cited in Table 4

1. Electrical conductivity of the complexes lies in the range of 1.89 x10^{-8} to 4.24x10^{-7} Ω^{-1}cm^{-1}at 373 K.
2. The electrical conductivity of these complexes at 373 K follows the order Fe > Mn > Cr.
3. The activation energy of electrical conduction of the complexes has been found to increase in the order Mn < Cr < Fe.

Table 4. Electrical Conductivity (σ) at 373 K and Activation Energy (Ea) of the complexes

Metal		Cr(III),	Mn(III)	Fe(III)
HCAT	σ (Ω^{-1} cm^{-1})	4.89×10^{-8}	1.89×10^{-8}	4.24×10^{-7}
	Ea (eV)	0.0188	0.0124	0.1636

IV. CONCLUSION

The D.C. Electrical conductivity of the synthesized complexes were measured in the temperature range 298-423 K. All the complexes indicating their semiconducting behaviour

V. REFERENCES

[1]. GuptaSP, Malik OP and Singh J, J. Indian Chem. Society., 1975, 52, 656.
[2]. Chandra S, Jain D, Sharma AK and Sharma P, Molecules, 2009, 40, 174.

[3]. Garnovskii DA, Guedes MF, Silva DA, Kopylovich MN, Granovskii AD, Frausto JJR, and Pombeiro AJ., Polyhedron. 2003, 22, 1335.

[4]. Ren S, Wang R, Komatsu K, Bonaz-Krause P, Zyrianov Y, Mckenna CE, Csipke C, Tokes ZA and Lien EJ., J. Med. Chem., 2002, 45, 410.

[5]. Raman N, Thangaraja A and Kulandaisamy C, Trans. Met. Chem., 2003, 28, 29.

[6]. Aswar A., Bahad P.,.Pardhi A. and Bhave N., J. Poym. Mater., 1988, 5, 232.

[7]. Pattan S.,.Ali M, Pattan J., Purohit S., Reddy V. and Nataraj B., Indian J. Chem., 2006, 45B, 1929.

[8]. Khrustalev D., Suleimenova A. and Fazylov S., Russian J. App. chem., 2008, 81(5), 900.

[9]. Maradiya H. and Patel V., J. Fibers and poly., 2002, 3(1), 43.

[10]. Furniss B., Hannaford A., Smith P. & Tatchell A., Vogel's practical organic chemistry 5 thEd. (Logman Scientific Technical, John Wiley and Sons), 1989.

[11]. Sadigova S., Magerramov A. and Allakhverdiev M., Russian J. Org. chem., 2008, 81(5), 900.

[12]. Vogel AI, "A Text book of quantitative inorganic chemistry"3thEd., (ELBS,London),1961.

[13]. Campbell E and Nguyen S, J. Tetrahedron, 2001, 42, 1221.

[14]. Pietikainen P and Haikarainen A, J. Mole. Catalysis., 2002, 180, 59.

[15]. Kidwai M, Poddar P and Singhal K, Indian J. Chem., 2009, 48B, 59.

[16]. Sonwane S, Srivastava S and Srivastava S, Indian J. Chem., 2008, 47B, 633.

[17]. Patel K and Mehata A, E. J. Chem., 2006, 3(13), 267.

[18]. Maurya R, Antony D, Gopinathan S, Puranic V, Tavale S and Gopinathan C, Bull. Chem. Soc. Jpn., 1995, 68, 2847.

[19]. Boghaei D and Mohebi S, J. Tetrahedron, 2002, 58, 5357.

[20]. Chetia, JR, Moulick, M. and Dutta, A, Indian J. Chem. Tech., 2004; 11: 80.

[21]. Shaktawat, V, Jain, N, Dixit, M., Saxena, NS., Sharma, K and Sharma,TP., Indian J. Pure and Appl. Physics, 2008; 46: 427.

[22]. Katon,JE. (Ed.), "Organic Semiconducting Polymers", Marcel, Dekker, Inc. New York, 89. 1968.

[23]. Ahmed, AM., Indian J. Pure and Appl. Physics, 2005; 43: 535.

Estimation of Hydration Number and Apparent Molar Volume of Ternary Liquid Mixtures by Ultrasonic Studies at Different Temperatures

Pravin J. Ganjare[1*], Sunanda S Aswale[2], Shashikant R Aswale[3]

[1*] Department of Chemistry, Shivramji Moghe Mahavidyalaya, Pandharkawada, Yavatmal, Maharashtra, India

[2] Department of Chemistry, Lokmanya Tilak Mahavidyalaya, Wani, Yavatmal, Maharashtra, India

[3] Department of Chemistry, Mahatma Gandhi Science College, Gadchandur, Maharashtra, India

ABSTRACT

In the development of molecular sciences, the studies of intermolecular interaction in binary and ternary mixtures of polar and non polar liquids play a key role. It also helps to understand the nature and behavior of solute in particular solvent. The ultrasonic velocity measurement is one of the most important and accurate technique to observe inside of the liquid mixtures. The ultrasonic velocity of liquid and liquid mixtures is fundamentally related to the attractive or repulsive forces between atoms or molecules in the system. Present study discusses about the experimental results of ultrasonic velocity (v), density (ρ) and viscosity (η) along with estimated parameters like hydration number, apparent molar volume (φ_v) for the ternary liquid mixture of sodium-2-hydroxy benzoate in 50% ethanol at 0.1M, 0.01M and 0.001M concentration range. The temperature range selected for all investigations is 298.15K, 303.15K and 308.15K. The thermo-acoustic studies are made on these liquid mixtures to access the intermolecular interactions in the liquid mixtures.

Keywords – Ultrasonic velocity, Molecular interactions, Molar cohesive energy, Apparent molar volume and molar hydration number.

I. INTRODUCTION

The ultrasonic technique is one of the simple and accurate method of analysis which is widely used in the study of liquid state[1]. Since last few decades, the ultrasonic technique is used to investigate hydration of various liquid mixtures because these properties are useful in the detection of the degree and nature of hydration[2]. In the dissolution of solute in the solvent, there are some factors studied like hydrogen bonding. One of the acoustic parameter which is important in detection of molecular interactions is the apparent molar volume. It is a simple and convenient tool for studying solute-solvent interactions in solutions[3]. The measurement of Ultrasonic velocity in liquid mixtures gives an idea about the compressibility of a fluid related to inter- and intra-molecular interactions. These parameters can be characterized with the variation of thermodynamic parameters such as temperature, pressure and volume[4]. When ultrasonic waves are passed through the solutions, these are affected by intra-molecular and inter-molecular association which is related to structural changes[5]. In the present study we passed the ultrasonic waves through the liquid mixture at different temperatures

and by using measured velocity, the values of molar hydration number (h), apparent molar volume (ϕ_v) and surface tensions are calculated. The results are interpreted at various concentrations and temperature ranging from 0.1M, 0.01M, 0.001M and 298.15K, 303.15K and 308.15K respectively. The results analyzed are presented in terms of solute-solvent, solvent – solvent interactions.

II. METHODS AND MATERIAL

Materials :

A.R. grade Sodium-2-hydroxy benzoate was used for study. Solutions were prepared by using distilled water. Weights have been taken on digital electronic balance. (Model-CB/CA/AT-Series).

Methods :

The measurements of ultrasonic velocity were carried out by using ultrasonic interferometer (Model-M-83). Mittal Enterprises, New Delhi) operating at 4MHz frequency with an accuracy of ±2m/s. The densities (ρ) were measured accurately using digital densitometer (Model - DMA-35, Anton Paar). Thermostat with continuous circulation of water was used to maintain constant temperature.

III. RESULTS AND DISCUSSION

The values of molar hydration number, apparent molar volume , surface tension are calculated from the measured values of ultrasonic velocity(v), density (ρ) by using standard formulae [6] and are given in **Table No. 1**

Apparent Molar Volume

$\phi_v = [1000(d_o-d_s)/C.d_o]+(M/d_o)$ ---------- 1

Where do – Density of solvent

Do – Density of solution, C- Molar concentration

Molar Hydration Number

$h = n_w/n_s[1-(\beta_s/\beta_o)]$ -------------- 2

n_w – Number of moles of water, n_s – Number of moles of solute.

β_s – Adiabatic compressibility of solution.

β_o - Adiabatic compressibility of solvent.

Surface Tension

$\sigma = 6.3 \times 10^{-4} \times V_s\, 3/2 \times d_s$ -----------------3

Molar Cohesive Energy

$= \pi_i \times V_m$ -----------------4

Table .1 : Molar hydration number, apparent molar volume (ϕ_v), Surface Tension (σ) and Molar Cohesive Energy of sodium-2-hydroxy benzoate in water.

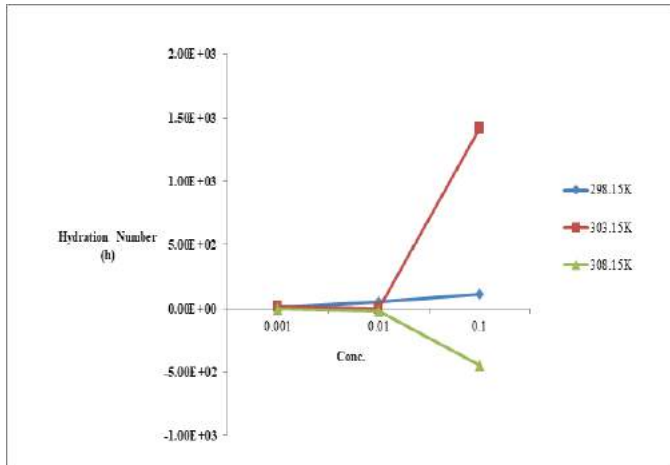| Sr.No.	Temperature (^{0}K)	Concentration (M)	Apparent molar volume (ϕ_v) (m³/mole)	Molar hydration number (h)	Surface Tension (σ) Dynes/cm	Molar Cohesive Energy ($\pi_i \times V_m$) Lit.atm/mole
01		0.1	2.03E+02	5.32E+00	2.22E+02	5.59E+07
02	298.15K	0.01	2.05E+02	5.05E+01	2.18E+02	5.64E+07
03		0.001	1.39E+04	1.17E+02	1.68E+02	5.97E+07
04		0.1	1.83E+02	-1.28E+01	9.16E+01	7.15E+07
05	303.15K	0.01	1.17E+02	1.42E+00	1.49E+02	6.14E+07
06		0.001	1.08E+04	1.42E+03	1.00E+02	6.95E+07
07		0.1	1.52E+02	-1.53E+00	1.27E+02	6.15E+07
08	308.15K	0.01	-1.14E+02	-1.72E+01	1.26E+02	6.16E+07
09		0.001	6.94E+03	-4.49E+02	1.12E+02	6.42E+07

Fig.-1: Molar hydration number (h) Vs Concentration (Sodium-2-hydroxy benzoate)

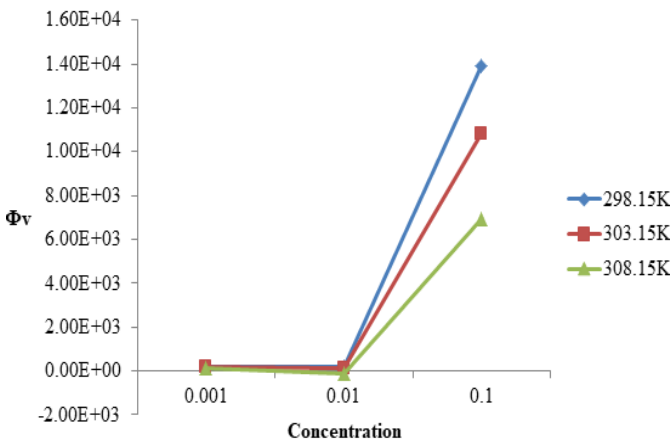

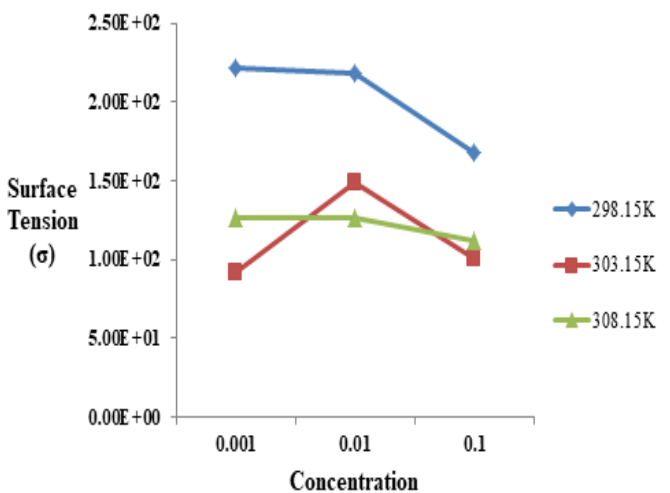Fig.-2: Apparent molar volume (φv)Vs Concentration (Sodium-2-hydroxy benzoate)

Fig.-3: Surface Tension (σ) Vs Concentration (Sodium-2-hydroxy benzoate)
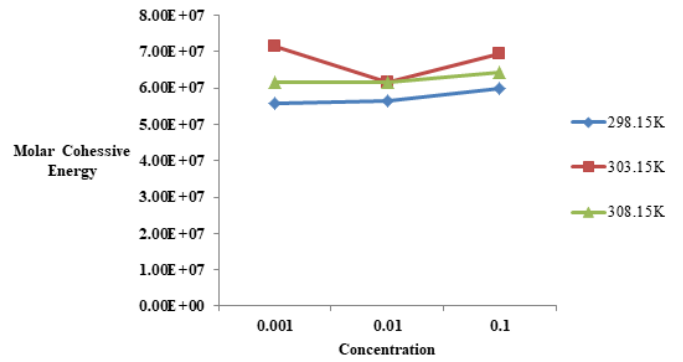
Fig.-4 : Molar Cohesive Energy Vs Concentration (Sodium-2-hydroxy benzoate)

The experimentally determined and calculated values of molar hydration number, apparent molar volumes, surface tension and molar cohesive energy are shown in **Table – 1 and fig. 1, 2, 3 and 4.** The value of molar hydration number shows nonlinear variation with concentration. Molar hydration number shows positive values at 298.15 K and 303.15K and negative values at 308.15K (Fig. 2). These value increases with concentration at 298.15 K and 303.15K. The hydration number is calculated by various researchers earlier by considering adiabatic compressibility is due to the free solvent molecules [7]. The variation in the values of hydration number may be due the hydration effect of solute over the solvent molecules also the may be effect of ethanol molecules on the solvation process. The molar hydration number decrease with rise in the temperature is due to interaction of ethanol molecules with solute effectively than the water molecules[8]. The values of surface tension and molar cohesive energy are plotted against concentration (**Fig. 3 and 4**). The linear relationship in the values of surface tension is found at 298.15L and 308.15K. Same relationship is observed in the variation of molar cohesive energy values. It may be said that molar cohesive energy of a liquid system conditions the surface tension[9]. It is noted that the solutions exhibit negative values of solvation number at 308.15K and positive values at 298.15K ,303.15K. The sign of the solvation number indicates the relative value of compressibility of solution and the solvent[10]. The negative value of solvation number shows that solutions are more

compressible than the solvent and positive solvation number suggests that compressibility of the solution is less than that of solvent supporting the fact that the ions gain high mobility.

IV. CONCLUSION

A gradual increase in solvation number from lower to higher concentration is observed at two temperatures indicates that as concentration increases solvation increases is due the effect of two different solvent molecules H_2O and C_2H_5OH. There may be interference of ethanol molecules in the solvation process between water - solute and decrease in the interaction between water molecules and Sodium-2-hydroxy benzoate molecules.

V. REFERENCES

[1]. D. S. Hedaoo, M. M. Kalaskar and M. P. Wadekar, "Adiabatic compressibility, apparent molal volume, apparent molal compressibility and solvation number of 2,3-Dihydroquinazolin-4(1H)-one derivatives in 70% DMF-Water" Pelagia Research Library Advances in Applied Science Research, , 6(6):81-88.

[2]. D. P. Kharakoz, "Volumetric properties of proteins and their analogues in diluted water solutions. 2. Partial adiabatic compressibilities of amino acids at 15-70. degree. C" J. Phys. Chem., 95, 5634 (1991).

[3]. R. Gopal, M.A. Siddiqi, "Study of ion-solvent interaction of some tetraalkylammonium and common ions in N-methylacetamide from apparent molal volume data" J. Phys. Chem., 73(10), 3390, (1969).

[4]. A. Amararene, M. Gindre, J.Y.L. Huerou, C. Nicot, W. Urbach, M. Waks, "Water Confined in Reverse Micelles: Acoustic and Densimetric Studies" J. Phys. Chem. B, 101, 10751, (1997).

[5]. Roksana Khatun, Rajia Sultanaand Ranjit K. Nath, "Volumetric and Ultrasonic Velocity Studies of Urea and Thiourea in Aqueous Solution" , Orient. J. Chem., Vol. 34(4), 1755-1764 (2018).

[6]. Rathika S, Renuka Devi K, Geetha S., "Comparative Study On Hydration Properties of Ammonium Sulphate With Potassium Nitrate And Ammonium Sulphate With Sodium Nitrate Solutions At 303k, IJEDR | Volume 6, Issue 1, (2018).

[7]. Muraliji D., Murrugodoss K. and Dhanalakshmi M.., Eighteenth National Symposium on Ultrasonics (NSU-XVIII), VIT University, Vellore. Dec. 21-23, (2009). pp. 332-335.

[8]. A. Gomathiyalini, K. Renuka Devi, S. Rathika and S. Geetha, " Solvation Studies on Sodium Dodecyl Sulphate in aqueous solutions at different temperatures", IOSR Journal of Applied Physics (IOSR-JAP) , Volume 6, Issue 5 Ver. I (Sep.-Oct. 2014), PP 63-67.

[9]. P. S. Naidu, N. Jaya Madhuri, J. Glory and D. K. Ravina Prasad, Eighteenth National Symposium on Ultrasonics (NSU-XVIII), VIT University, Vellore. Dec. 21-23, (2009). pp. 249-252.

[10]. E. Jasmine Vasantha Rani and Suhashini Ernest, Eighteenth National Symposium on Ultrasonics (NSU-XVIII), VIT University, Vellore. Dec. 21-23, (2009). pp. 260-262.

Study of Doped Blend Film and Its Application as a Sensor Material

R Y Bakale[1], Y G Bakale*[2], S V Khangar[1]

[1]Department of Physics, Mahatma fule Arts, Commerce and Sitaramji Chaudhary Science Mhavidyalaya, Warud, Maharashtra, India

[2]Department of Physics, Kavikulguru Institute of Technology and Science, Ramtek, Maharashtra, India

ABSTRACT

In this paper the results of thermally stimulated discharge current (TSDC) of thermoelectret of cinnamic acid doped polyvinyl chloride (PVC) polymethyl methacrylate (PMMA) blend film are presented. TSDC has been carried out in a temperature range 303K to 383K and at five different polarising fields. Results are discussed on the basis of space charge polarisation. these are further extended to the probable used as a sensor material.

Keywords : Polyvinylchloride (PVC), Polymethyl-methacrylate (PMMA), TSDC, Thermoelectret.

I. INTRODUCTION

TSDC of polymers has become a widely used experimental technique for the investigation of various material parameters such as charge storage properties, determination of mean depth of the internal charge, activation energies of traps and trap structure of the material. Suzuki et al [1] studied characterisation of polymers with a considerable accuracy by using TSDC technique. Kellar et al [2] studied polyblends of PS and PMMA employing TSDC. The polyblends of PMMA and polyvinyl pyrrolidone (PVP) have been studied by Khare et al [3] Negau and Negau [4] obtained new results in thermally stimulated discharge current (TSDC) peak above room temperature. Sangawar [5] measured D.C. electrical conductivity of doped electrets of PS and PMMA. Belsare et al [6] studied iodine doped polyblends of PS and PMMA using TSDC. Burghate et al [7] measured thermally stimulated discharge current (TSDC) and dielectric constant of semiconducting glasses.

The availability of new measuring techniques such as thermally stimulated discharge current [8] has freshened interest in achieving better understanding and application of the phenomena. The basic principle of this technique is to study the charge decay by heating the electret at a constant rate, and then to attempt to make use of these results in the design of a thermal sensor.

II. METHODS AND MATERIAL

2.1 Preparation of sample:

The polyvinyl chloride (PVC) of standard grade product supplied by Polychem Industries Mumbai and polymethylmethacrylate (PMMA) supplied by Dental Product of India Ltd., Mumbai were used for the study. The two polymers PVC (1.5g) and PMMA

(0.5g) were taken in the ratio of 3:1 by weight. The 1.5g of PVC in 20ml of tetrahydrofuran (THF) and 0.5g of PMMA in 10ml tetrahydrofuran were dissolved separately. After allowing them to dissolve completely the two solutions were mixed together. To prepare the cinnamic acid doped blend films, the cinnamic acid was taken in the percentage weights Viz. 0.2%, 0.4%, 0.6%, 0.8% and 1.0%. Each was dissolved in 5ml of THF to produce cinnamic acid solution. cinnamic acid The solution was later mixed with uniform solution of PVC and PMMA. The total volume of solvent was kept constant 35ml. The solution was heated at constant temperature 333K for the two hours to allow polymers to dissolved completely to yield clear solution. A glass plate (15cm x 15cm) thoroughly cleaned with hot water and then with acetone was used as a substrate.

To achieve perfect leveling and uniformity in the thickness of the film, the films were prepared on a thoroughly cleaned optically plane glass plate kept floating in a pool of mercury. The whole assembly was placed in dust free chamber maintained at constant temperature (313K). In this way the film were prepared by isothermal evaporation technique [9,10]. The film was subjected to 12hrs has heating at constant temperature 323K and another 12hrs at room temperature to remove the traces of solvent. Finally, the film was removed from the glass plate. It was cut into small pieces of suitable size, which were washed with ethyl alcohol to remove the surface impurities.

2.2 Thickness measurement:

For greater accuracy and resolution, a compound microscope in conjunction with an occulometer, which gives least count 13μm and 3.3μm at the magnification of 1:10 and 1:100 respectively was used. A small section of the sample was taken and mounted vertically to get a clear sectional view of the thickness. The films used for the present study are thickness about 80μm.

2.3 Electrode coating:

The electrode coating on the film of measured thickness was done by using the quick drying silver paste [11] supplied by Eltecks Corporation, Banglore. A mask of circular aperture of 2.5cm diameter was used while coating to ensure uniformity in size of coated silver electrode.

2.4 Electret preparation:

The sample was mounted into the sample holder. The polarising field Ep was maintained for 30min between two faces at room temperature (303K). The electric field across the sample was removed and the sample was short circuited for 15min to remove the stray charges by wrapping the sample in an aluminum foil. The electrets were prepared at different polarising fields i.e. Ep = 37.5kV/m, 75 kV/m, 112.5 kV/m, 150 kV/m, 187.5 kV/m respectively.

2.5 Measurement of thermally stimulated discharge current (TSDC):

After electret formation the sample holder assembly was placed in high temperature furnace. The sample was short circuited through a sensitive picoammeter (Model DPA III scientific equipment, Roorkee, having accuracy + 1 pA) for the measurement of discharge current. Then the sample was heated at a uniform rate (1.25oC/min) from 303K to 383K. The discharge current was measured for sample. The temperature was recorded by mercury thermometer having an accuracy + 1K.

III. RESULTS AND DISCUSSION

TSDC thermograms of PVC-PMMA polyblend films doped with cinnamic acid are presented in the form of graphs figs (1 to 5) between discharge current versus

temperature at various poling fields and constant poling temperature of 333K.

The nature of the graphs is similar with following characteristics features.

1)In almost all cases, initially a large current is observed to decay at a faster rate over a certain range of temperature. This can be explained to be due to freeing of charge carriers in shallow traps near the surface region. Subsequently these must be moving towards the injecting electrodes resulting in the initial decay.
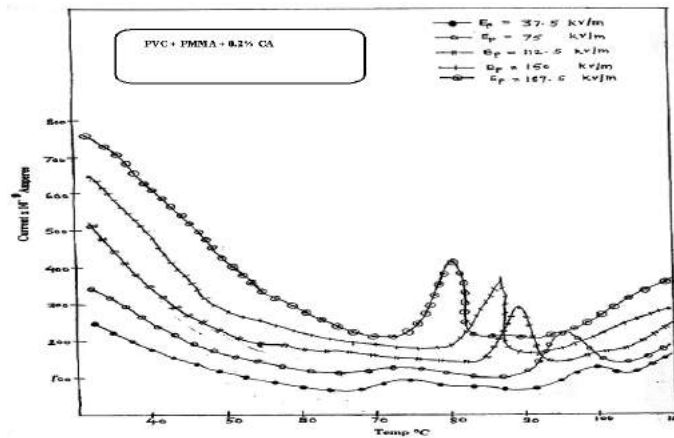

Figure 1: TSDC for sample 1 (current Vs temperature plot.)

2)In general, a single current peak is observed namely the current peak in the range of about 80oC to 95oC. The height of the peak increases with polarising field at each dopant concentration and also increases with concentration of dopant cinnamic acid.

The polarisation in polymer arises on account of orientation of dipole and trapping of charge carriers in different traps [8, 12, 13]. The

dielectric relaxation in PMMA is a high temperature – relaxation near its Tg between about 90oC to 98oC. That in PVC near its Tg = 87oC. Hence in the polyblend the current peak should occur in this vicinity. Since the present study has been done at higher temperature the low temperature peak near

about 30oC, associated with disorientation of polar side groups has not been observed.

The addition of PVC in PMMA produces a heterogeneous structure and plasticisation effect, which is further assisted by dopant cinnamic acid. Plasticization causes loosening of structure and hence charge carriers injected in the bulk may pile up at the phases boundaries, providing greater mobility to the charge carriers resulting in increase of peak current.

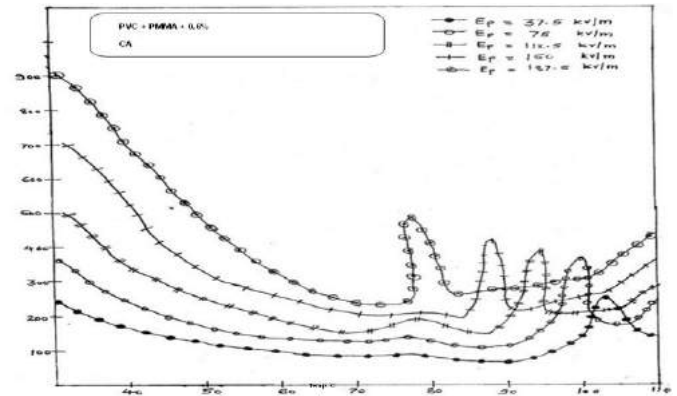Figure 2 : TSDC for sample 2 (current Vs temperature plot.)

3)A linear relation between peak current and polarisation field is observed i.e. the magnitude of peak currents increases with the magnitude of the polarising field Ep. The higher value of Ep produces ionization of large number of impurities centres there by enhancing the current.
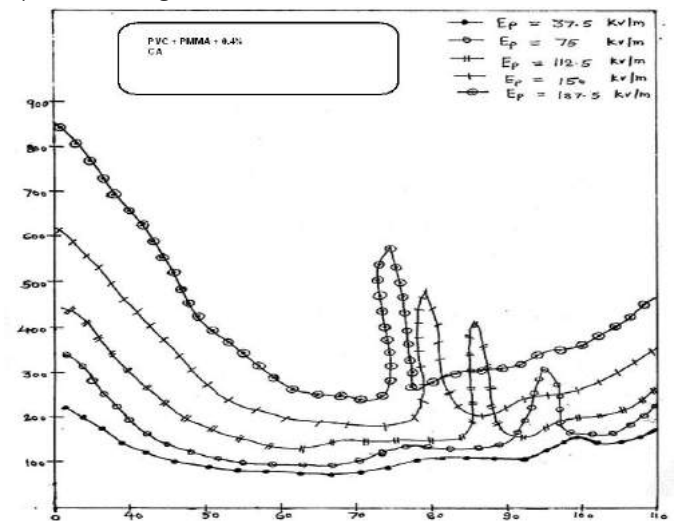

Figure 3 : TSDC for sample 3 (current Vs temperature plot.)

4)Further as the dopant concentration increases, the magnitude of peak currents also increases. This is evident because dopant introduces impurity centre, ionization of which helps to make available large number of carriers to enhance current.
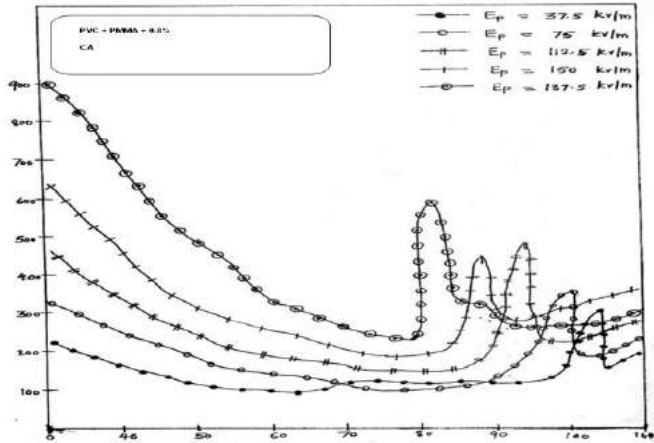

Figure 4 : TSDC for sample 4 (current Vs temperature plot.)

The TSDC of the polyblend thermoelectret, all show (Figs. 1 to 5) a current peak in the range of temperatures 80 to 95oC, in all samples. The sample with 1% cinnamic acid doping (Fig. 5) shows maximum peak current. Thus, the current response to temperature, of this electret, in this temperature range will be extremely helpful in the design of a thermoelectret as a temperature sensor. This, all the while is more important, because most of the sensors available commercially operate
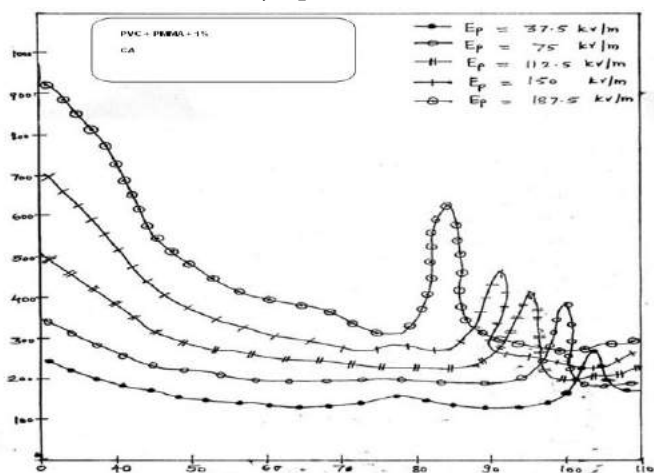
Figure 5 : TSDC for sample 5 (current Vs temperature plot.)

[14] at elevated temperature upto 300oC. Some aspects like electrical conduction in undoped films have already been reported [15]. In addition to this the present TSDC study is being presented here. Mishra et al [14] have reported semiconducting polymeric thin film sensor for detection of toxic gases the selection of the material in proper proportion and optimization in the design and fabrication are very likely to yield a thermal sensor. This can further be extended to the detection of toxic acids and also to control environmental pollution.

IV. CONCLUSION

V. REFERENCES

[1]. Y. Suzuki, T. Mizutavi and M. Ieda, Spn. J. Appl. Phys. 15, 1976.

[2]. J. M. Kellar, S. Dubey and S.C. Datta, Indian J. Pure. Appl. Phys. 29, 1991 pp150.

[3]. P.K. Khare, Indian J. Pure. Appl. Phys., 31, 1993, pp 120.

[4]. E. Negau and R. Negau, "Proc. ISE" 8, 1994, pp 528.

[5]. V.S. Sangawar, "Ph.D. Thesis" Amravati University, Amravati, 1995.

[6]. N.G. Belsare and V.S. Deogaonkar, J. Polym. Mater, 15, 1998, pp 170.

[7]. D.K. Burghate and V.S. Deogaonkar, Indian J. Pure. Appl. Phys. 26, 2003, pp 267-271.

[8]. J. V. Turnhout "TSDC of electrets" Elsevier Amsterdam, 1975, pp. 106-130.

[9]. A. Narayan and H.P. Singh, Indian J. Pure. Appl. Phys. 25, 1983, pp. 30.

[10]. R. Bahri and B.R. Sood, "Thin solid film" 100L5, 1983.

[11]. J.P. Singh and R.K. Bedi, "Thin solid film" 9, 1991, pp. 199.

[12]. J.Vanderschueren, J. Polym. Sci. Poly. Phys. Ed. (USA), 1977, pp.873.

[13]. P.K.C. Pillai "Phys status, solids (USA)", 67, 1981, pp. 649.

[14]. S.C.K. Misra, Archana Suri, Subhas Chandra and R. Bhattacharya, Indian J. Pure. Appl. Phys. 38, 2000, pp.545-551.

[15]. S.H. Deshmukh, D.K Burghate and V.S. Deogaonkar Indian J. Phys. 79(11), 2005, pp. 1263-1267.

Synthesis and Characterization of CuO Nanoparticles Prepared with Coffee Extract and To Study Its Electrical Conductivity

S. S. Gore

Department of Physics, R.A. College, Washim, Maharashtra, India

ABSTRACT

Oxides of copper have unique semiconducting and optical properties. Very few reports are available on the synthesis of copper oxide nanoparticles using plant extract. CuO Nanoparticles have tremendous applications due to their semiconducting nature. It can be prepared by different methods. In this work CuO nanoparticles were synthesis with coffee bean extract and also used to study its electrical conductivity by Four probe method. The prepared CuO nanoparticles were characterised by uv-visible spectra and XRD.

I. INTRODUCTION

The Particle of size between 1 to 100 nm are called as nanoparticles. The nanomaterials have unique properties in comparison with the same materials in the bulk form. The shape of the nanoparticle is also equally important to control its different properties. The copper oxide nanoparticle is one of the most important metal oxides which has attracted in recent years. Cupric oxide and cuprous oxide are two important oxide compounds of copper. The main features of CuO nanoparticles are due to its low cost and its easily availability. It has good electrical and optical properties. It is nontoxic and easily obtain by oxidation of copper. Nanoparticles are synthesis by different methods such as sol gel technique, thermal decomposition, sonochemical process, rapid precipitation, spin coating solid state reaction, solvothermal process and microwave irradiation. Now a day's eco-friendly methods such as biosynthesis are used to obtained nanoparticles. This method is reliable and cost effective.

The CuO nanoparticles have many applications in solar cell technology, storage media, drug delivery medicine, lithium-ion batteries, gas sensors, fuel cells, formation of FET and they also show the catalyst properties. The synthesized nanoparticles can also be used to form nanocomposite, nanowire, nanotube and Nano film. One of the important applications of CuO nanoparticles is its semiconducting properties.

II. METHODS AND MATERIAL

In 100 ml distilled water add 9 gm of coffee powder. Heat this up to one hour in a burner flame. Cool this solution and filter with the filter paper. Now take 12.05 gm of Cu (NO3)2 :6H2O and dissolve it in a 50 ml of distilled water with continuous stirring up to 3 hours at 283oC. After this add coffee extract drop by drop. The colour of solution changes from blue to black. The obtain precipitate wash with distilled water, filter and dried. The particles obtained kept in a muffle furnace for 6 hours at 450oC.

Particles disperse by using ultra sonicator having frequency of 20 kHz for 11 minute and 4 second pulse. The Titanium horn is used in sonicator.

Electrical conductivity by Four Probe Method:

This method permits measurements of resistivity in samples having a wide variety of shapes, including the resistivity of small volumes within bigger pieces of semiconductor. In this manner the resistivity of CuO nanomaterials is measured by making pallets of the CuO powder. the four-probe set-up used in this work for electrical study. In this setup, four sharp probes placed on a flat surface of the material to be measured, current is pass through the two outer electrodes, and the floating potential is measured across the inner pair. To prevent minority carrier injection and make good contacts, the surface on which the probes rest, maybe mechanically lapped.

III. RESULTS AND DISCUSSION

1) **UV-Visible Spectra:** The characteristics uv-visible spectra of biosynthesised CuO nanoparticles is as shown in fig 1. The wavelength vs Absorption graph of CuO nanoparticles shows that the maximum absorption occurs at 380 nm in uv-visible spectra. This attributed to the formation of cupric oxide CuO nanoparticles.
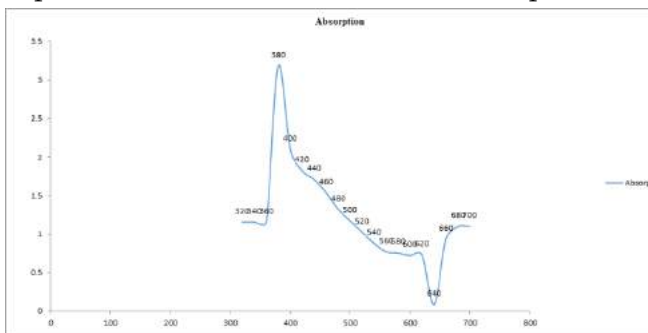
2) **XRD:** The X-ray diffraction pattern of synthesised CuO particles is carried out for 2 theta values. The XRD pattern is as shown in fig 2. The peaks for 2 theta values are obtained at 32 to 78 as shown in figure. The peaks obtained are match with the JCPDS data card

no.86-1268. This shows the presence of CuO nanoparticles.
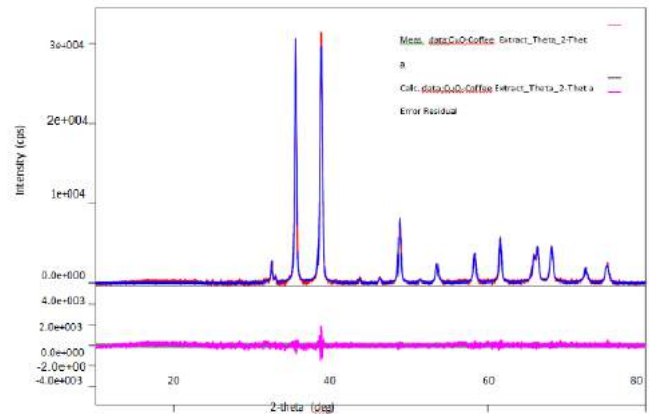
3) **Sonication:** - The process in which Ultrasonic wave are immerge in the liquid mixture of given sample for the separation of the nanoparticles. The frequencies (>20 kHz) are usually used, leading to the process also being known as ultra-sonication. The figure of sonication perform are as shown in fig.

Take a small beaker of glass in which dissolve the given sample (CuO nanoparticle) in sufficient amount of water. We apply the ultrasonic wave of frequency 50Hz for 11 minutes (pulse time is 4 second) to the given solution further start sonication. After some time, the whole particles of given sample are separate. After that by drying these mixtures we get fine powder of given sample.

4) **Electrical Conductivity of CuO nanoparticles with respect to temperature by Four Probe Method-** The electrical conductivity of material was measure by four probe method. By keeping constant current (I=3mA) and varying temperature, S=0.2cm (Distance between two probes) and W=0.92 cm (Thickness of materials). Figure depict that the conductivity rises linearly with temperature which shows the semiconducting nature of the material.

Electrical conductivity of CuO with temperature
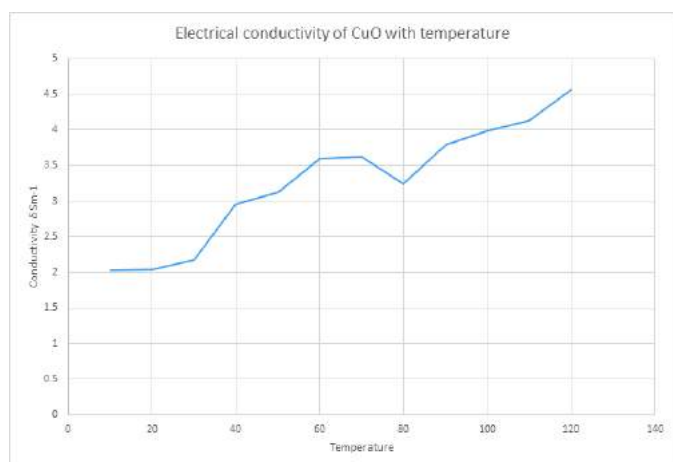
IV. ACKNOWLEDGEMENT

Authors are very much thankful to Department of Physics R. A. College, Washim. MH India for providing necessary facilities.

V. CONCLUSION

Present research has resulted in several novel and significant findings by getting knowledge of the CuO nanoparticles as well as materials literature. This report was mainly devoted on synthesis of CuO nanoparticles by green synthesis method and to study its electrical properties by Four probe method. The obtained nanoparticles were used for characterizations.

VI. REFERENCES

[1]. Amit Mathew, Green Synthesis of CuO Nanoparticles using Coffea Powder Extract, IJRASET Volume 6 Issue III, March 2018.

[2]. S. Ansilin, J. Kavya Nair, C. Aswathy, V. Rama, J. Peter, J. Jeyachynthaya Persis. in Journal of Nanoscience and Technology 2(5) (2016) 221–223.

[3]. Jagpreet Singh, Kaur G, Rawat M. Journal of Bioelectronics and Nanotechnology 2016;1(1): 9.

[4]. Thi Ha Tran and Viet Tuyen Nguyen. International Scholarly Research Notices Volume 2014, Article ID 856592, http://dx.doi.org/10.1155/2014.

[5]. S. Usha, K.T. Ramappa, Sharanagouda Hiregoudar , G.D. y and D.S. Aswathanarayana.International Journal of Current Microbiology and Applied Sciences .Volume 6 Number 11 (2017) pp. 2219-2228.

[6]. P. P. N. Vijay Kumar, U. Shameem, Pratap Kollu, R. L. Kalyani & S. V. N. Pammi DOI 10.1007/s12668-015-0171-z.BioNanoScience · May 2015.

[7]. N. Nasihat Sheno, A. Morsali. in the Int. J. Nanoscience and Nanotechnology., Vol. 8, No. 2, June 2012, pp. 99-104

[8]. Akinobu Yamaguchi, Ikuo Okada, Takao Fukuoka, Mari Ishihara,Ikuya Sakurai, and Yuichi Utsumi Journal of Nanomaterials Volume 2016, Article ID 8584304,http://dx.doi.org/10.1155/2016.

[9]. Nittaya Tamaekong, Chaikarn Liewhiran, and Sukon Phanichphant. In the Journal of Nanomaterials in Volume 2014, Article ID 507978, http://dx.doi.org/10.1155/2014

[10]. Minghan Chen, Huichao Zhu, Xiaogan Li, Jun Yu, Haitao Cai, Xiaotong Quan, Kaili Wang, and Jiaqi Zhang. In Journal of Nanomaterials Volume 2014, Article ID 461269, http://dx.doi.org/10.1155/2014.

[11]. Rula M. Allaf and Louisa J. Hope-Journal of Nanomaterials Volume 2014, Article ID 491817, http://dx.doi.org/10.1155/2014.

Conventional Method of Cancer Diagnosis : Biopsy

* S. A. Patil, N. R. Thakare

Department of Engg. Physics, P. R. Pote College of Engineering and Management, Amravati , Maharashtra, India

ABSTRACT

Biopsy is the conventional cancer diagnostic technique. In this paper, some literature survey has been done and it is observed that the conventional method of cancer diagnostic has got some drawbacks and limitations. More research work in spectroscopic techniques can lead to improvised method to detect cancer.

I. INTRODUCTION

In middle ages Abu al-Qasim Khalaf ibn al-Abbas Al – Zahrawi, an Arab Physician, surgeon and pharmacist was first to describe and perform a needle biopsy of the thyroid.[1]

In modern era, the term biopsy was introduced into medical terminology in 1879 by Ernest Besnier. The first diagnostic biopsy was performed in 1875 in Russia by M.M. Rudnev. According to Zerbino D. D., it is possible to make out three stages in more than 100 year history of the method development: an occasional use of histological procedure involving living organs and tissues accessible for observation and study (approximately until the late 19th century); restricted application of biopsy (until the mid 20th century); present stage at which the method is widely adopted and its use is general and total not only in oncology but practically in all clinical specialties.[2]

The first renal biopsy, in the modern era was performed by Eugen Hann in Berlin in 1881. This was followed by Reginall Harison in Liverpool in 1896.The first open biopsy, in which a small piece of tissue was removed for microscopy and diagnostic purposes, was done by Norman B Gwyn in Toronto in 1923.

The word biopsy is taken from Greek words that mean, "to view life". A biopsy is a medical test commonly performed by a surgeon or an interventional radiology involving sampling of cells or tissues for examination. It is the medical removal of tissue from a living subject to determine the presence or extent of a disease. The tissue is generally examined under a microscope by a pathologist and can be analyzed chemically.[3,4]

An incisional biopsy is a procedure in which a small area of tissue is taken to identify the composition of a lesion or abnormability. An excisional biopsy is more involved procedure where the entire abnormality or area of interest is removed. To further clarify this, there are four options for obtaining a tissue sample:

- In fine needle aspiration test, the smallest needle is used to simply remove cells from the abnormality.
- A core needle biopsy removes not only cells but also a small amount of the surround tissue.

- An incisional biopsy takes out even more surrounding tissue. It takes out some of the abnormality, but not all.
- An excisional biopsy generally removes the entire area in question.

If the lesion of interest is large an incisional biopsy may be performed where as if the abnormality is small an excisional biopsy may be performed. Also a core needle biopsy can be performed on most parts of the body.[5]

After the biopsy is performed the sample of tissue that is removed from the patient is sent to the pathology laboratory. A pathologist is a physician who specializes in diagnosing diseases, such as cancer by examining tissue under a microscope. When the histopathology laboratory receives the biopsy sample, the tissue is processed and an extremely thin slice of tissue is removed from the sample and attached to a glass slide. Any remaining tissue is saved for use in later studies, if required. The slide with the tissue attached is treated with dyes that stain the tissue, which allows the individual cells in the tissue to be seen more clearly. The slide is then given to the pathologist, who examines the tissue under a microscope, looking for any abnormal findings. The pathologist then prepares a report that lists any abnormal or important findings from the biopsy. This report is sent to the physician who originally performed the biopsy on the patient.

In short we can conclude that the process of biopsy is more time consuming process. The other drawbacks of biopsy are discussed below.

II. METHODS AND MATERIAL

Drawbacks of Biopsy:

According to Wang Ko-Pen, one of the major drawbacks of the transbronchial needle biopsy is its technical difficulty. It is very difficult to penetrate the bronchial wall with an 18 gauge needle even with the protruded 21 gauge inner needle functioning as a trocar. The recommended core biopsy techniques of repetitive partial withdraw of the 18 gauge needle in and out of the lesion under suction is even more cumbersome.[6]

According to Louise Tremblay, there is an unavoidable disadvantage of breast core biopsy. The disadvantage is that there can be risk of infection after the procedure. This medical procedure that breaks the skin provides an opportunity for bacteria, fungi or viruses to enter the body through the skin and colonize tissues within the breast. Another disadvantage of breast core biopsy is scaring at the biopsy site, corresponding to the needle injection sites. Insufficient tissue collection is also another disadvantage of breast biopsy. In some cases, a breast core biopsy may have the disadvantage of not allowing the doctor to collect sufficient breast lump tissue to make a diagnosis. Lumps that occur deep within the breast tissue may be difficult to access with a simple needle biopsy.[7]

According to Medical Health test team many problems also occur during prostrate biopsy also. The main problem which is identified is the risk of injury or bleeding from the gland. Many cases report infection or injury after the procedure which necessitates further treatment. The prostrate biopsy procedure collects many samples in order to reduce the chances of missing a tumor. However this does not rule out the possibility that the test will miss the cancer. Because of the small and scattered nature of prostate cancer tumors, it can be said that the test is not completely accurate at confirming or ruling out prostrate cancer.[8]

The study made by E.H. Smith says that the increasing use of fine needle biopsy of abdominal lesion is associated with an increase in serious complication. His updated questionnaire reveals five deaths after 16,381 biopsies (0.031%) . According to his study out of 33 deaths, 21 involved biopsies of liver lesions, six involved pancreatic biopsies of the 23 instances of

needle tract seeding, 10 occurred after biopsies of pancreatic malignancies.[9]

Dr. Luis A. Diaz's research reveals that in the terms of tissue acquisition, there are four major barriers that require real consideration. The first two relate to clinical topics, physician and patient opposition, and procedural toxicity. When samples are available from a cancer surgery, the availability of tissue is not an issue. However, biopsies as part of a clinical trial are complicated by physician and patient reluctance, especially since these biopsies will often not influence the outcome of the patient at hand. Biopsies are an inconvenience from a scheduling perspective, increase the cost of patient care, and are another uncomfortable, invasive procedure for patients. Furthermore, biopsies are not without complications.[10]

There are also technical barriers to tissue acquisition that require discussion: sample characteristics and tumor heterogeneity. Following a biopsy, the majority of tumor tissue is preserved in formalin-fixed paraffin-embedded blocks (FFPE), which crosslink DNA to the point that a large fraction of archived FFPE samples have been reported to be inadequate for molecular analysis, which is why freezing is the ideal choice for preserving tumor tissue. In each of these blocks of tumor tissue, the amount of tumor is dependent on the tumor cellularity (% tumor) and the size of the section of tumor. Some tumors have a high percentage of tumor cellularity (colon cancer, sarcomas, renal cell carcinomas) while other tumors have poor tumor cellularity because of necrotic tissue or stromal contamination (pancreatic cancer, glioblastoma). This is further compounded by low tissue amounts present from fine-needle aspirates and core needle biopsies, which provide a very small amount of tumor tissue for analysis in comparison to surgically respected tumors.

Tumor heterogeneity also proves to be problematic. Tumors themselves are heterogeneous, with different areas of the same tumor showing different genetic profiles (intratumoral heterogeneity); likewise, heterogeneity exists between metastases within the same patient (intermetastatic heterogeneity). A biopsy or tissue section from one part of a solitary tumor will miss the molecular intratumoral as well as intermetastatic heterogeneity. Taken together, the quality of the molecular information derived from any biopsy depends on how well the sample accounts for tumor cellularity, method of preservation, molecular and tissue heterogeneity, and quantity of tissue available for analysis.

III. RESULTS AND DISCUSSION

Drawbacks of histopathological method of cancer diagnosis:-

The optical treatment of patients with cancer depends on establishing accurate diagnosis by using a complex combination of clinical and histopathological data. According to Shridhar Ramaswamy and co-workers in some instances, this task is difficult or impossible because of atypical clinical presentation of histopathology. Also cancer classification relies on the subjective of both clinical and histopathological information with an eye toward placing tumors in currently accepted categories based on the tissue of origin of the tumor. However clinical information can be incomplete or misleading. In addition there is a wide spectrum in cancer morphology and many tumors are atypical or lack morphologic features that are useful for differential diagnosis.[11]

According to the Hiroshima Tumor Registration committee, which registers tumors that have been diagnosed by pathologists, the number of cases, registers registered has increased threefold for gastric and 20 fold for gastric adenoma over the past 20 years. This suggests that, recently many tumors have been biopsied or dissected endoscopically, while tumor tissues were collected only by surgery in earlier periods. The histopathological diagnosis is thus, extremely important for obtaining definitive and supportive diagnosis, diagnosis depends only on

histopathology has certain limitations. Many lesions have morphology which is in between that of benign and malignant lesions, and differential diagnosis is therefore difficult. Variation between pathologists may lead to changes in assessments of the lesion. Differences in diagnostic criteria such as those for early gastro intestinal cancer diagnosed by western and Japanese pathologists, lead to misunderstanding by clinicians. Furthermore information derived from morphologyis of limited use in determining the degree of malignancy and the patient's prognosis .No genetic information can be obtained in hereditary cancers.[12]

IV. CONCLUSION

Although biopsy is still carried out in medical practices for cancer diagnosis, the above literature survey suggests that this conventional technique has some disadvantages and limitations. Such as, this method may lead to complications like infection and bleeding. The lumps which are deep inside are difficult to undergo for biopsy. Spectroscopic techniques, such as Laser induced fluorescence is a powerful noninvasive method for tissue pathology recognition and monitoring. Also Raman Spectroscopic technique is a great tool to study the structure and dynamic functions of biological molecules. Extensive research is being carried out for monitoring and diagnosis of diseases such as precancerous and cancerous lesions in human soft tissues[13] .Further research in this domain can lead to more improvise cancer diagnostic technique.

V. REFERENCES

[1]. History of Renal Biopsy, Renal Med. (2014)

[2]. Zerbino D.D., (1994), "Biopsy: Its history, current and future outlook."

[3]. Anderson J. B., Webb A. J. (1987), "Fine-needle aspiration biopsy and the diagnosis of thyroid cancer", The British journal of surgery.

[4]. Saibeni S. , Rondonnotti E., Lozzelli A., Spina L., Tontini G. E., Cavallaro F., Ciscato C., De Franchis R., Sadanelli F., Vechi M., (2007), " Imaging of the small bowel in Crohn's Disease: A review of old and new techniques"

[5]. Taylor Whaley J., (29 Feb 2012), "Incisional and Excisional biopsy", The Abramson cancer center of the university of Pennsylvania.

[6]. Wang, Ko Pen M. D., (April 1994), "Transbronchial needle aspiration to obtain Histology specimen: Journal of Bronchology"

[7]. Tremlay L., (August 7,2010), "Disadvantages of Breast Core Biopsy"

[8]. Medical Health test team,(October 16,2012), " Prostrate Biopsy pros and cons"

[9]. Smith E. H. (1991), "Radiology: Complications of percutaneous abdominal fine needle biopsy", volume 178,issue 1

[10]. Dr. Luis Diaz,(April22 ,2013), "Tissue acquisition for personalized therapy: Merits and drawbacks".

[11]. Ramaswamy S.,Osteen R. T., Shulman L. N., (2001), "Clinical oncology", pp. 711-719

[12]. Wataru Yasui, Naohide Que, Hiroki Kuniyasu, Reiko Ito, Eiichi Tahare, Hiroshi Yokozaki, (2001), "The molecular diagnosis of gastric cancer present and future", Journal: Gastric cancer, Vol.4, issue 3, pp113-121

[13]. Tuan Vo-Dinh, Oak Ridge National Laboratory "Biomedical Photonics Handbook", CRC Press Washington DC, 2003

Studies of Molecular Interactions of Sugar Alcohols in Water by Volumetric and Viscometric Measurement

Saroj P. Sahare

Department of Chemistry, Anand Niketan College, Warora, Chandrapur, Maharashtra, India

ABSTRACT

In this paper, Densities (ρ) and Viscosities (η) of sorbitol and mannitol have been measured in aqueous solution in the concentration range 0.05-0.5 M at 296 K. Apparent molar volume and partial molar volume were determined from the density parameter. Using Jones-Dole equation, viscosity coefficient A and B were calculated for sorbitol and mannitol solutions from the obtained viscosities. The results obtained from the parameters were correlated with solute-solute and solute- solvent interactions.

Keywords : Apparent molar volume, Partial molar volume, Jones-Dole equation, Sugars alcohols, Staurding equation

I. INTRODUCTION

Viscosity and density are two basic physical parameters of liquid and their values must be known for the physiochemical processes(adsorption, extraction, catalysis etc.). The viscosity (η), is need to be measure at very high precision with its temperature depends behavior to used as property to determine molecular information [1]. Density is the basic physical parameter used in the field of thermodynamics for the determination of heat transfer and mass transfer [2].

Along with constantly increasing living standard of human beings, a new quality food with non-sugar and low calorific value is introduced as sugar alcohols also called as pseudo sugars. They are having good qualities such as sweet in taste, suitable for diabetes people and no tooth decay and utilized in many aspects food, pharmacy, cosmetics and chemical engineering etc. Sorbital ((2S,3R,4R,5R)-hexane-1,2,3,4,5,6-hexol) and mannitol ((2R,3R,4R,5R)-hexane-1,2,3,4,5,6-

hexol) are important sugar alcohols [3]. These pseudo sugars are found in fruits and their importance revealed in the field of medical sciences [4].

In this paper, the physical parameters are calculated from the densities and viscosities obtained experimentally. Apparent molar volume, partial molar volume, Jone-Dole constant A and B are determined for sorbitol and mannitol sugar alcohols at various concentration at 298 K.

II. METHODS AND MATERIAL

Sorbitol and Mannitol used for experimental work were AR grade (purity ≥ 99 %), purchased from Loba Chemie. Double distilled water was used for the experimental purpose. The aqueous solutions of solutes at various concentration were prepared using electronic weighing balance (Model-AJO20 aiwa) with accuracy of ± 0.1 mg.

Densities of aqueous solution of sorbitol and mannitol were performed by using specific gravity bottle with relative measurement method (accuracy ± 0.1Kg.m^{-3}). Viscosities of the solutions of these sugar alcohols were determine by using Ostwald's viscometer with accuracy of 0.0001Nsm^2.

III. RESULTS AND DISCUSSION

Data obtained from density and viscosity of sorbitol and mannitol measured at 296 K in the concentration range of 0.05-0.5M are given in Table 1. Apparent molar volume calculated from the equation (1) [5]

$$\phi_v = M/\rho_o - 1000(\rho - \rho_o)/C\rho_o \qquad (1)$$

Where ϕ_v, M, ρ_o, ρ and C are the apparent molar volume, molar mass of the solute, density of solvent (water), density of solution and molarity respectively. The apparent molar volume is defined as difference between volume of solution and volume of pure solvent per mole of solute. The change in volume is due to solute-solvent interactions. At infinite dilutions where solute-solvent interactions are completely vanished is called as partial molar volume [6].

Hydration of solute and solute-solvent structural interactions can be revealed by using apparent molar volume and partial molar volume. Hydration rate of solute-solvent interactions decreases as the concentration increases and solute-solute interactions increases it means solute-solvent interactions are replaced by solute-solute interactions [7].

Apparent molar volume was in good linear relationship with molar concentration of solute. As a result partial molar volume was calculated as a linear fit by using following equation (2)[8]

$$\phi_v = \phi^o_v + S_v C \qquad (2)$$

where, ϕ^o_v is partial molar volume, the values of ϕ^o_v were calculated by the least square regression analysis and S_v is the slope of the linear relation between ϕ_v and C. The values of ϕ^o_v and S_v for sorbitol and mannitol at 296 K in table 1.

Relative viscosity of sorbitol and mannitol aqueous solutions was calculated for concentration range 0.05-0.5 M assuming solutes as polymers monomer unit. The polymer species follow Staurding equation (3) [9] is given as follows:

$$(\eta - \eta_o)/\eta_o = kn\ Cn \qquad (3)$$

Where, η is viscosity of solution and η_o is the viscosity of water at 296K, C is concentration of solution in Molar and k is the constant. The obtained values of relative viscosity for sorbitol and mannitol are shown in table 2.

Table1: Apparent molar volume (ϕ_v), partial molar volume (ϕ^o_v) and S_v for sorbitol and mannitol at 296k at various concentration

Concentration (mol dm^{-3})	√C	ϕ_v Sorbitol	Monnitol
0.05	0.2236	136.4411	134.5082
0.1	0.3162	133.4335	132.5032
0.15	0.3872	132.4310	131.1665
0.2	0.4472	130.9273	129.4957
0.25	0.5	130.4260	128.8942
0.3	0.5477	127.7527	128.4932
0.35	0.5916	126.3587	127.0610
0.4	0.6324	124.9122807	125.7363
0.45	0.6708	124.1882484	125.3743
0.5	0.7071	123.6090226	124.4832
ϕ^o_v	(m^{3}mol^{-1})	136.85	134.6
S_v	(m^{3}Kg$^{1/2}$mol$^{-3/2}$)	-28.385	-21.21

Table 2: Relative viscosities (η/η_o) for sorbitol and mannitol at 296 K at various concentration

Concentration (C) (mol dm^{-3})	$\sqrt{C}$	(η/η_0) Sorbitol	Mannitol
0.05	0.2236	1.0537	1.0609
0.1	0.3162	1.0809	1.1072
0.15	0.3872	1.1396	1.1498
0.2	0.4472	1.1774	1.1818
0.25	0.5	1.2267	1.2433
0.3	0.5477	1.2692	1.2850
0.35	0.5916	1.3232	1.3232
0.4	0.6324	1.3602	1.3830
0.45	0.6708	1.4199	1.4482
0.5	0.7071	1.4974	1.5084

The results obtained from the data of viscosities of sorbitol and mannitol aqueous solutions are in agreement with equation (3) which is applicable for polymers. Therefore a graph is plotted of relative viscosity to the concentration of solutions of sugar alcohols shows linearity. The slope value (kn) for sorbitol and mannitol was shown in table 3.

Table 3: Parameters of Staurding and Jone-Done equation for sorbitol and mannitol at 296 K in aqueous solution

Sugar alcohols	$(\eta/\eta_0 -1)$ vs. C	$(\eta/\eta_0 -1)/ \sqrt{C}$ vs. $\sqrt{C}$	B x 10^3/ $\phi^o{}_v$
Sorbitol	kn= 0.9543 dm^{3}mol^{-1}	B= 0.9388 dm^{3}mol^{-1}	6.86
Mannitol	kn = 0.9761 dm^{3}mol^{-1}	B= 0.9436 dm^{3}mol^{-1}	7.01

By examining Jone-Dole equation (4)[10], the structure making and breaking properties of solutes are also determined from viscosity coefficient B and intercept A.

$$(\eta/\eta_0) =1+ A + B\sqrt{C} \qquad (4)$$

Where, η/η_0 is the relative viscosity, A and B are constants, C is concentration of the solution. The graph is plotted of $(\eta/\eta_0 -1)/ \sqrt{C}$ against $\sqrt{C}$ have linear relationship with slope B and intercept A. The values of B and A for sorbitol and mannitol are tabulated in table 3. In the present study, the studied sugar alcohols are non-electrolytes and hence magnitude of A is very small because very poor interionic interactions [11].

The value of partial molar volume for both sugar alcohols are positive which revealed that solutes interact by hydroxyl groups present in the solute molecules through hydrogen bonding. The solvation of solute can be determined from the magnitude of B/$\phi^o{}_v$. The values of B/$\phi^o{}_v$ from the parameters are tabulated in table 3. If the values of B/$\phi^o{}_v$, is greater than 2.5 it is solvated. Higher the magnitude higher would be association [12].

IV. REFERENCES

[1]. P. Bohuon, M. Le Maguer and A. L. Raoult-Wack, J. Chem. Eng. Data 1997, 42, 266-269

[2]. M. A. Jamal, M. K. Khosa, M. Rashad, I. H. Bukhari, S. Naz, Food Chemistry 146 (2014) 460–465

[3]. C. Zhu, Y. Ma and C. Zhou, J. Chem. Eng. Data 2010, 55, 3882–3885

[4]. X. Jiang, C. Zhu, Y. Ma, Journal of Molecular Liquids 188 (2013) 67–73

[5]. Millero, FJ., Surdo, AL., Shin, C., The Journal of Physical Chemistry, 1978. 82(9): p. 781-789.

[6]. Jamal M. A., Food Chemistry, 2014. 153(12): p. 140-444.

[7]. A. Gharsallaoui, B. Roge, J. Genotelle, M Mathlouthi, Food Chemistry 106 (2008) 1443–1453

[8]. J. Wawer, J Krakowiak, W. Grzybkowski, J. Chem. Thermodynamics 40 (2008) 1193–1199

[9]. R. Joshi and N. D. Kandpal, Der Pharmacia Lettre, 2015, 7 (10):126-133

[10]. R. S. Patil, V. R. Shaikh, P. D. Patil, A. U. Borse, K. J. Patil, Journal of Molecular Liquids (2014)

[11]. Thirumaran. S and Job Sabu, Journal of Experimental Sciences 2012, 3(1): 33-3

[12]. K. Araiab and T. Shikata, Chem.Phys., 2019, 21, 25379

Different Dielectric properties of Synthesized Mesoporous Molecular Sieves Rice Husk Ash -SBA-16

Shete S.B.

Department of Electronics S.G.B. College, Purna, Maharashtra, India

ABSTRACT

Rice Husk is the by-product produce during rice milling. Sustainable use of Rice Husk Ash (RHA) and Rice Husk (RH) in Industrial Sector and other fields depends upon its physical and chemical properties. This research contributes holistic approach to the potential use of rice husk towards synthesis of meso-porous material than the traditional uses of husks. It not only reduces the   cost of material but also results in the reduction of the environmental greenhouse effects. Attempts have been made to investigate crystallization kinetics of SBA -16. The various synthesis parameters were investigated during crystallization of SBA -16. The activation energy of crystallization kinetics of SBA -16 was calculated using Arrhenius equation and found to be 184.62 kJ / mole in the present system of synthesis.

Keywords. Rice Husk Ash, Pluronic F127, Crystallization Kinetics, Dielectric properties.

I. INTRODUCTION

Hazardous wastes are generated annually throughout the world by all industries and their disposal poses major challenges and serious environmental problems. This creates serious health risks, taking into account that the amount of discharged material is expected to increase in the future. In the recent years, there has been a growing interest to find creative ways not only to reduce natural waste and industrial hazard to overcome environmental pollution but also its effective utilization1.

As we know that, Rice is a primary source of food. Its production covers almost 1% of the Earth's surface. Globally, approximately 700 million tons of rice2 is produced every year. India is a major rice producing country and annul production of rice husk is approximately 20 million tons3. For every 100 kg of paddy milled, about 22% of husk is produced2.Even though some of this husk is converted into end product such as feedstock and adsorbent but most is either dumped as a waste or burnt openly, causing environmental and health problems. Therefore, one of the chief principles of green technology is to utilize the RHA as a raw material or renewable resource for making high value added, versatile materials rather than depleting, as it has high silica content (>90%).

Quite a lot of research groups have taken the advantage of this silica composition and made endeavors in making micro4 and mesoporous5 zeolitic materials synthesized from extracted silica through them. These materials have wide applications as adsorbents, in ion exchange, as molecular sieves, catalysts16-18 etc. Compared to conventional microporous zeolites, mesoporous materials possess many advantages such as high surface area, large pore size and an ordered structure6, 7.

Santa Barbra University discovered new family (SBA-n) of mesoporous materials, among them SBA -16 possesses hexagonal molecular sieves having fairly uniform pores with pore diameter of 20-100Å. They possesses large surface area (more than 900 m2/g), which is attractive for designing new selective heterogeneous catalyst in production of fine chemicals on large scale.

Our research endeavors the use of no-cost raw materials such as agro waste rice husk for our further investigations because it add value; reduce the cost and create effective utilization to protect the environment19-21. It has potential application in synthesis of highly useful porous materials used in water purification technology, as industrial catalyst, supporting materials, exchanger, molecular sieves etc.

II.   METHODS AND MATERIAL

Experimental: Materials and Methods for Synthesis of mesoporous SBA -16:

Hydrothermal synthesis of SBA -16 was carried out in hydrothermal reactor at autogenous pressure under stirring conditions. The chemicals used during synthesis were Pluronic F127, Butanol, Hydrochloric acid, Deionized water etc.

The rice husk silica extraction was carried out using acid hydrolysis method. Initially the collected rice husk was washed with deionized water and then dried at 800C for 24h. This husk was then treated with 3.0 M HCl acid solution along with heating at 1000C. This hydrolyzed rice husk was rinsed with distilled water until pH reaches to 7, then it was again dried at 100°C for 24 h. Finally, the rice husk was calcined at 8000C for 4h in muffle furnace. The rice husk ash was mixed with 3.75 M NaOH solution and stirred overnight to extract the silicate from the ash.

The synthesis of silica SBA-16 was made as following. Solution of 2.5 g of Pluronic F127 (Sigma Aldrich) in a mixture of 120 g of distilled water, 5 g of concentrated HCl (37%) and 7.5 g of butanol was first prepared.

After one hour stirring at 45 oC, 12 g of RHA 4.5g were added and the mixture stirred for further 24h.The ultrasonic treatment is given at 45 min. The step was followed by a hydrothermal treatment of 24 h at 100oC in Teflon coated stainless steel autoclave. Drying of the as synthesized sample was performed at room temperature overnight part of the dry sample was calcined under air flow by increasing the temperature 1.5oC per minute up to550oC and maintaining it at this temperature for 6 h sample hereafter named calc-SBA-16. by Fabio et al.,15 The samples were synthesized at 600C, 700C, 800C and 900C and are nominated as RHA-SBA-16 (60, 70, 80 and 90) respectively. After the crystallization, the solids were filtered, washed with deionized water and dried at 1000C for 2h. The products were finally calcined at 5500C for 4.5hrs in air and has been evaluated by X-ray diffraction, N2-sorption studies etc.

Characterization:

To elucidate the structural features8, morphology9, pore architecture10, thermal stability11, adsorptive12 and catalytic behavior13, surface area14 etc: the synthesized samples are characterized by techniques such as XRD, N2-sorption, FTIR, etc.

III. RESULTS AND DISCUSSION

XRD-studies:

% Crystallinity = <u>Sum of the peak heights of unknown material $\times$ 100</u> Sum of peak heights of standard material

Fig.1 shows the XRD patterns of the samples calcined at 450, 500, 550, 600 and 6500C designated as RHA-SBA-16 (450, 500, 550, 600 and 650) respectively. As shown in the Fig.1RHA-SBA-16 (450), the XRD pattern obtained for the sample calcined at calcinations temperature 4500C, the only reflection at (110) plane is more intense, it suggests that the material does not possess the well defined hexagonal arrays even after the calcination.

The diffractograms gained for the samples as increase in their calcination temperature from 500 to 650⁰C shows three weak peaks along with single most intense peak with (110) reflection at 2θ value 1.12⁰. The d_{110}value is shifted to a higher value up to 600⁰C Fig. 1 RHA-SBA-16 (500, 550, and 600).In the low 2-theta region of $1^0–10^0$, the XRD pattern at 550⁰C exhibits all prominent diffraction peaks which could be indexed as (110), (200) (210) and etc. reflections, respectively. This is characteristics of long range ordered hexagonal array of parallel silica tubes in RHA-SBA-16mesoporous phase. Therefore, the sample calcined at 550⁰C can be treated as 100 % crystalline sample. As calcinations temperature in advance increased above 600⁰C, a considerable decline in the intensity of (110) peak and d_{110} value shifted to the somewhat inferior value indicates condensation of the silanol groups in the pore walls. This can direct to the reorganization of silica walls of RHA-SBA-16 accordingly decreasing the crystallinity very immaterially.

Even though at 600⁰C, the long range order of hexagonal array and textural morphology is still preserved. This resembles that synthesized sample of RHA-SBA-16 is thermally unwavering up to 600⁰C as accounted.On the other hand, if the calcination temperature is increased up to 650⁰C and above, the hexagonal phase transforms into the lamellar form which on additional calcination crumples the structure which is reflected as the absence of XRD peaks in RHA-SBA-16 (600) at and above 650⁰C.
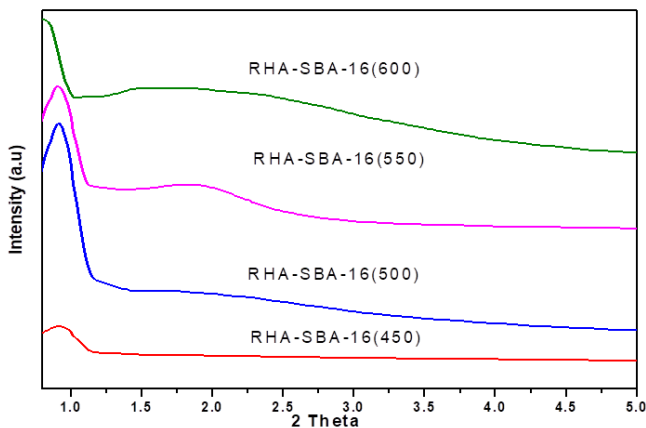

Fig. 1: (C) XRD patterns of calcined samples of RHA-SBA-16 (450, 500, 550, and 600) at various temperatures.

Therefore, the above results indicate that calcination temperature plays a noteworthy role to optimize the synthesis condition.

% Crystallinity and Activation Energy:

Table 1. Summarizes the values of inter planar spacing (d values) derived from X-ray diffraction pattern for RHA-SBA-16 (100% crystalline) sample. The percent crystallinity of the samples drawn at diverse calcination temperatures in the crystallization kinetics was calculated. The obtained values of % crystallinity were plotted as a function of calcination temperature from which the gradient of crystallization has been evaluated. The percent conversion from amorphous to100% crystalline product of RHA-SBA-16 phase is shown in the Fig. 2

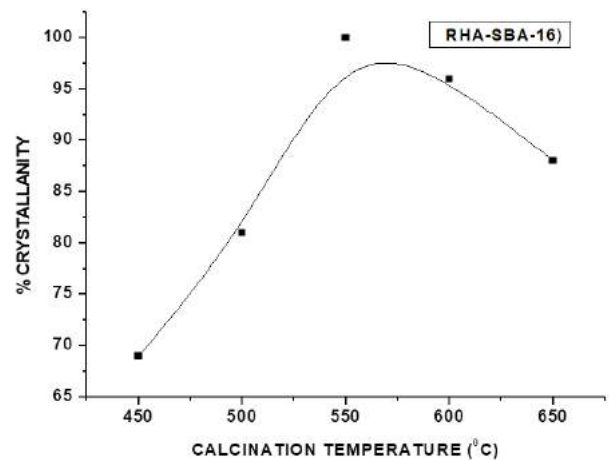Therefore, this most (100%) crystalline sample was used as a parent sample for further study.

Fig.2 Effect of calcination temperature on crystallization

The kinetic curve describing the increase in the crystallinity of the crystals with the calcination temperature depends on rate of conversion. It is seen from the Fig.2 that upto 550⁰C the rate of conversion of amorphous to crystallization of RHA-SBA-16 phase was very acute initially but followed by a subsequent slow down. Therefore, the rate of crystallization

decreases as the process approaches to the completion indicated by constancy (100 %) in percent crystallization.

Using Arrhenius equation to the kinetics of crystallization of RHA-SBA-16, activation energy was reported around 103.74kJ mole^{-1} in the present crystallization scheme.

BET surface area and pore volume of RHA-SBA-16:

The samples RHA-SBA-16 (450, 500, 550, 600 and 650) synthesized for 4.5h with different calcinations temperatures have also been characterized further by N2-sorption studies to find BET surface area and the corresponding pore size distribution. The adsorption-desorption curve obtained for RHA-SBA-16 (550, 600) is shown in the Fig3 These isotherms are of type IV as expected for SBA-16 molecular sieves.
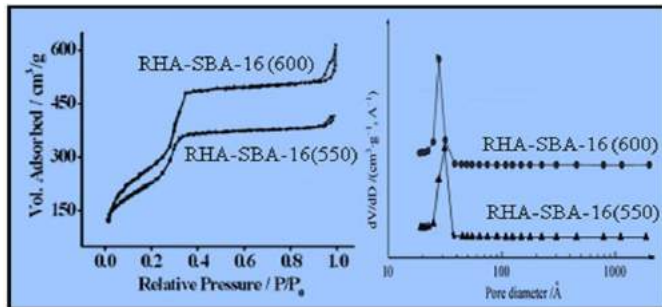

Fig .3 N2 adsorption-desorption isotherms and (B) pore size distribution of (a) RHA-SBA-16 (550°C); (b) RHA-SBA-16 (600°C)

The observations regarding N2-sorption and XRD studies are statistically depicted in Table 1. From which we can conclude that, as the calcination temperature is increased after 550°C, at the ramp of 1°C, surface area got reduced by 1.5m^2/g. It is probably because of the collapse of gel structure due to the rapid release of water from the pores. Moreover, there is an auxiliary alteration in the average pore diameter and wall thickness. Pores with narrow distribution start forming from 500 °C and increases as calcination temperature increases. The mean wall thickness of the pores and pore volume increased with calcination temperature from 500°C to 600°C.

However, there is a slight decrease in wall thickness at the calcination temperature of 600°C and above. These observations revels the hexagonal phase starts transforming to lamellar phase with lack of specific structural features, which are in well accordance with XRD patterns.

SEM and TEM-Analysis:

SEM images of RHA-SBA-16 (500, 600) are depicted in Fig.4 represents that the particles are nearly in spherical form exclusive of agglomerations. The typical diameter of the particles is moderately same although the calcination temperature is raised from 450°C to 650°C representing an excellent thermal stability. The diameter of spherical particles is found to vary in the range of 2.6A^0 to 9.98A^0, which is consistent with the XRD and N2sorption data. The SEM photo graph of RHA-SBA-16 at 550°C indicates a good structural morphology.

TEM-Analysis:

Fig.5 represents the TEM images of RHA-SBA-16synthesized at 80°C and calcined at 550°C. TEM image of the parent RHA-SBA-16samples provided sturdy verification of the retainment of mesoporous structure. The characteristic hexagonal silicate structures shown on TEM, supports the observation made by low angle XRD.
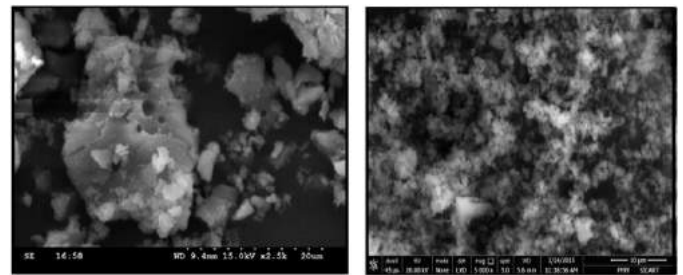

Fig. 4 SEM images of RHA-SBA-16 (500, 550) calcined at 500and 5500C
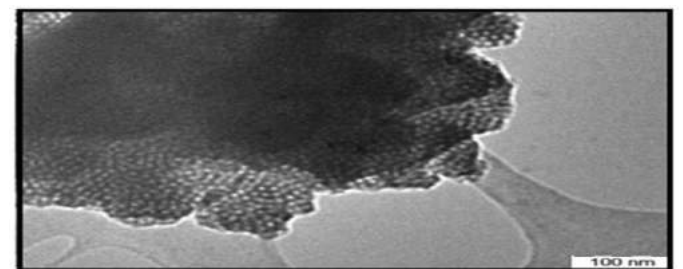

Fig. 5 TEM images of RHA-SBA-16 (550) calcined at 550°C

<div align="center">Table 1 : Effect of calcination temperature on Structural and textural properties of RHA-SBA-16</div>

Sample	d_{110}	Unit cell parameter	S.A. (m²/g)	Average pore diameter (Å)	Pore volume (ml/g)	Average Wall thickness (Å)	% Crystal-linity
RHA-SBA-16(450)	22.15	31.90	–	–	–	–	69
RHA-SBA-16(500)	23.51	33.85	618.21	26.38	0.479	7.47	81
RHA-SBA-16(550)	26.93	38.78	779.70	29.16	0.568	9.62	100
RHA-SBA-16(600)	25.89	37.28	767.13	28.25	0.547	9.03	96
RHA-SBA-16(650)	24.21	34.86	738.22	26.99	0.506	7.87	88

Dielectric properties : The sample used for dielectric properties as RHA-SBA-16 (550) .For preparing the pallets Polly vinyl alcohol (PVA) is used as binder Pallets 10mm diameter were made and mass of pallet were measured also the thickness of pallet were measured .To remove the binder from the sample the pallets were kept in furnace at 200⁰C for 2 hrs.The readings were taken on the reading impedance analyzer HIOKI model No.IM 3570

Fig.6 shows the frequency variation of dielectric constant for the samples of RHA-SBA-16. It can be observed from the figure that the dielectric constant for the samples decreases with increase in frequency.
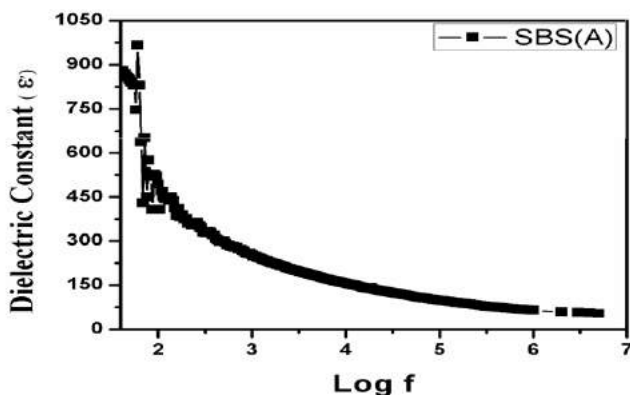

Fig.7 Dielectric loss with the frequency variation

Fig.7 shows the frequency variation of dielectric loss for the samples of RHA-SBA-16. It can be observed from the figure that the loss shows that the dissipation for the samples decreases with

Increase in frequency[22].
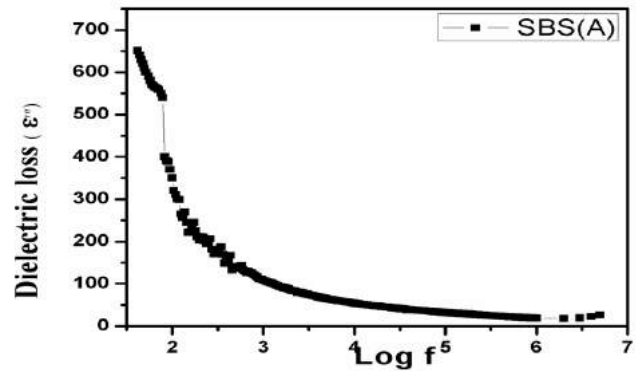

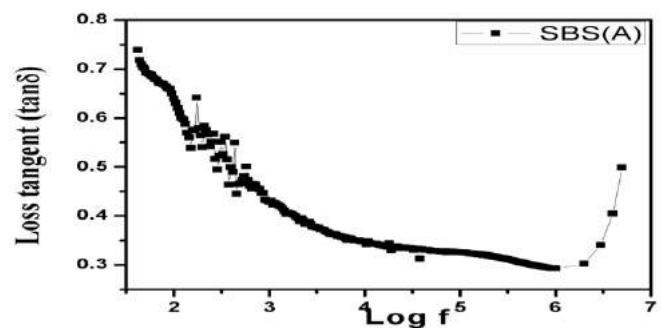Fig.6 Dielectric constant and the frequency variation

Fig.8 loss tangent with the frequency variation

Fig.8 shows the frequency variation of loss tangent for the samples of RHA-SBA-16. It can be observed from

the figure that the loss tangent for the samples decreases exponentially with Increase in frequency.
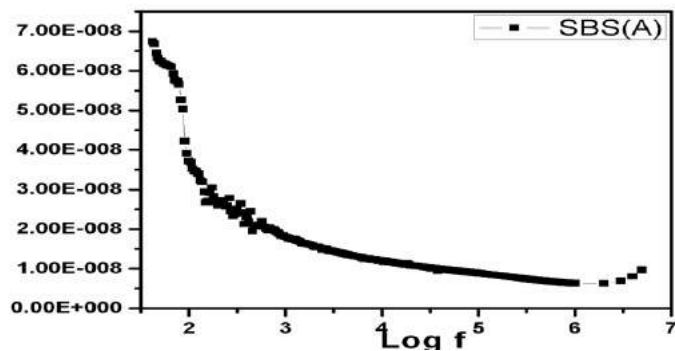

Fig.9ac conductivity with the frequency variation

Fig.9shows the frequency variation with ac conductivity for the samples of RHA-SBA-16. It can be observed from the figure that ac conductivity of the samples decreases exponentially with Increase in frequency.

IV. CONCLUSION

All the characterization techniques performed in this study reveals that well ordered mesoporous material of uniform hexagonal array can be synthesized very conveniently and in a very short span of time from an agro waste rice husk ash instead of commercial expensive silica sources. The parametric variation such as change of synthesis temperature helps to optimize the synthesis conditions. The well ordered mesoporous material RHA-SBA-16 can be synthesized at 80^0C for 4.5h keeping pH of gel 6.9 and calcined at 550^0C.The apparent activation energy of conversion of synthesis gel to 100 % crystalline RHA-SBA-16 phase was 184.62kJ/mole calculated by Arrhenius equation. The different dielectric characteristics are analyzed for the sample RHA-SBA-16.

V. REFERENCES

[1]. C.L. Carlson, D.C. Adriano, Environmental impact of coal combustion residue, J. Environ. Qual. 22, 227–247, (1993).

[2]. FAO Food Outlook, Food and Agriculture Organization of the United Nations, November, (2011).

[3]. www. maps of world.com.

[4]. Corma, A. Chem. Rev. 95, 559-614, (1995).

[5]. Kresge, C. T.; Leonowicz, M. E.; Roth, W. J.; Vartulli, J. C. U.S. Patent 5, 098, 684, (1992).

[6]. Schulz-Ekloff G, Stud. Surf. Sci. Catal., 85, p. 145, (1994).

[7]. Behrens P, Stucky G D, Angew. Chem. Intl. Ed. Engl., 32, p. 696, (1993).

[8]. J. R. Matos, M. Kruk, L. P. Mercuri, M. Jaroniec, T. Asefa, N. Coombs, G. A. Ozin, T. Kamiyama, and O. Terasaki, Chem. Mater. 14, 1903, (2002).

[9]. F. Kleitz, D. Liu, G. M. Anilkumar, I. S. Park, L. A. Solovyov, A. N. Shmakov, and R. Ryoo, J. Phys. Chem. B. 107, 14296 (2003).

[10]. J. Wloch, M. Rozwadowski, M. Lezanska, K. Erdmann, Analysis of the pore structure of the MCM-41 materials, Appl. Surf. Sci. 191, 368–374, (2002).

[11]. V. Parvulescu, S. Cman,V.I.Parvulescu,P.Grange,G.Poncelet, J. Catal. 180, 66, (1998).

[12]. Branton, P. J.; Hall, P. G.; Sing, K. S. W. J. Chem. Soc., Chem. Commun. 1257, (1993).

[13]. H. Van Bekkum, E.M. Flanigen, P.A. Jacobs, J.C. Jansen, Introduction to Zeolite Science and Practice, Elsevier, (2001).

[14]. Gregg, S. J.; Sing, K. S. W. Adsorption, Surface Area and Porosity, Second ed.; Academic Press INC. (London) LTD: London, (1982).

[15]. J.S. Beck, J.C. Vartuli, W.J. Roth, M.E. Leonowicz, C.T. Kresge, K.D. Schmitt, C.T.W Chu, D.H. Olson, E.W. Sheppard, S.B. McCullen, J.B. Higgins, J.L. Schlenker, J. Am. Chem. Soc. 114 (1992) 10834.

[16]. C.T. Kresge, M.E. Leonowicz, W.J. Roth, J.C. Vartuli, J.S. Beck, Nature 359 (1992)710.

[17]. C. Boissiere, M. Kummel, M. Persin, A. Larbot and E. Prouzet, Adv. Funct. Mater. 11 (2001) 129.

[18]. H.B.S. Chan, P.M. Budd, T.D. Naylor, J. Mater. Chem.11 (2001) 951.

[19]. Y. Sakamoto, M. Kaneda, O. Terasaki, D.Y. Zhao, J.M. Kim, G. Stucky, H.J. Shin, R. Ryoo, Nature 408 (2000) 449.

[20]. D. Zhao, Q. Huo, J. Feng, B.F. Chmelka, G.D. Stucky, J. Am. Chem. Soc. 120 (1998) 6024.

[21]. P. van der Voort, M. Benjelloun, E.F. Vansant, J. Phys. Chem. B 106 (2002) 9027.

[22]. Tatsuo Ohgushi and Kazushi Ishimaru, Phys. Chem.Chem.Phys., 3 (2001) 3229- 3234.

Temperature Dependent Conductivity of Solid Polymer Electrolyte Based On Polyvinyl Alcohol

S. R. Jadhao[1], S. P. Bakde[2]

[1] Department of Physics, Nehru Mahavidyalaya (Art, Commerce, Science) Nerpersopant, Dist. Yavatmal, Maharashtra, India

[2]Department of Physics, Shri R. R. Lahoti Science College, Morshi, Dist Amravati, Maharashtra, India

ABSTRACT

Solid polymer electrolytes have number of advantage over the conventional liquid electrolyte such as longer life, easily fabricate in desirable shape and leakage free and so on. The attempt has been made in this study with polyvinyl alcohols (PVA) doped with different percentage of Ammonium Iodide (NH_4I) were prepared by solution casting technique. It is reveal that electrical conductivity of polyvinyl alcohol doped with ammonium iodide increases with increasing salt concentration as well as temperature. The temperature dependent conductivity shows Arrhenius behavior.

Keyword – Solid polymer electrolyte, Electrical conductivity, Polyvinyl alcohol.

I. INTRODUCTION

An electrolyte is a substance that produces an electrically conducting solution when dissolved in a polar solvent, such as water. The dissolved electrolyte separates into cations and anions, which disperse uniformly through the solvent. To overcome the leakage problem in liquid electrolyte, it is replaced by solid polymer electrolyte [1]. Also solid electrolyte has a several advantages such as ease of handling, low cost, high environment stability. Polymer electrolytes (PEs) are ironically conducting material that may be used in the fabrication of solid-state electrochemical devices such as rechargeable batteries, supper capacitor, fuel cells, gas sensors [2-5]. The role of polymer electrolyte in these application are provide good electrode-electrolyte interface, provide good electrolyte insulation and allow a fast and selective transport of the ions. It is extremely important to understand the charge transport mechanism of polymer electrolyte for practical application. Electrical properties of polymer can be suitability modified by adding of salt. In present study, PVA has been chosen as polymer host due to their mechanical strength, excellent film-forming ability, dopant-depenent electrical and optical properties, low cost and high tensile strength (6-7). PVA is semicrystalline material and it contain hydroxyl group attach to methane carbon which can be source of hydrogen bounding. As per literature survey ammonium salt are very good proton donor (8-9)

II. METHODS AND MATERIAL

In the present study, polyvinyl alcohol, ammonium Iodide, and double distilled water were used to prepare solid polymer electrolyte. The film of pure

and different composition of PVA-NH4I has been prepared by solution cast technique. In this technique, appropriate amount of PVA and NH4I have been dissolved individually in double distilled water .These solution have been mixed together in different molar ratio (95:05) (90:10) (85:15) (80:20) (75:25) and stirred well by using magnetic stirred for 10-12 hr to obtained homogenous mixture. The obtained mixture is casted in petri dish. The whole assembly was placed in dust free chamber. The solvent was allowed to evaporate slowly at room temperature for 3-4 days. The thicknesses of the film were in the range of 0.032-0.024 mm.

III. RESULTS AND DISCUSSION

Electrical properties

The variation of conductivity of polymer electrolytes as a function of temperature at different voltage for 75PVA –25AI in the temperature range 310-350Kas shown in the fig1.
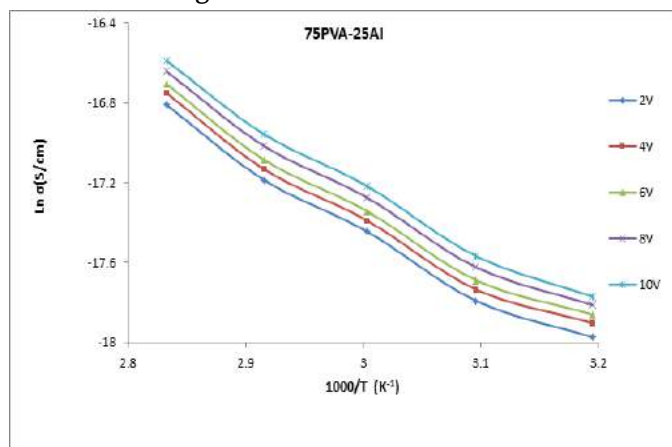

Fig 1

It was found that proton conductivity of the electrolytes increases with increasing temperature. The conductivity (σ) varies with temperature (T) according to the equation

$$\sigma T = \sigma 0 \exp(-Ea/KT)$$

Where $\sigma 0$ is the pre exponential factor,   Ea is activation energy, T is absolute temperature,
K is Boltzman constant.

The variation of conductivity of polyvinyl alcohol with ammonium iodide with different concentration as a function of temperature in the temperature range 310-350K as shown in the Fig 2. It was found that conductivity of the electrolytes increases with increasing temperature in pure PVA as well as all composition of polymer electrolyte.
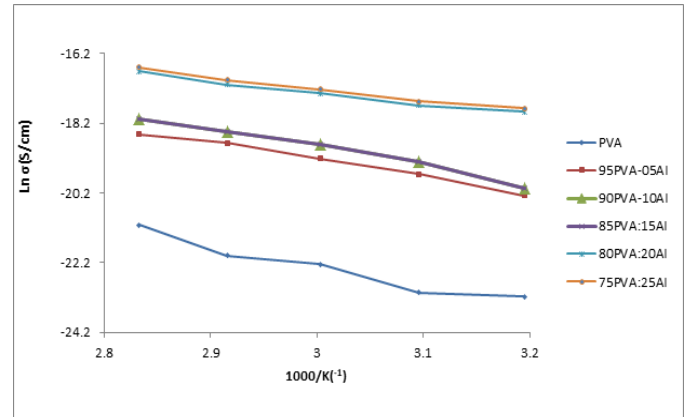

Fig 2

The increase in conductivity with temperature may be attributed to the transition from semi-crystalline phase to amorphous phase due to hoping mechanism between coordinating site and segmental motion (i.e. polymer chain) of polymer electrolyte [10]. As the amorphous region increases the polymer chain acquires faster internal modes in which bond rotations produce segmental motion to favor inter and intra-chain ion hopping, and thus the degree of conductivity becomes high. [11-12].

The activation energy, Ea is calculated for prepared polymer electrolyte by linear fit of the Arrhenius plot. It is found that the activation energy decreases with increase of salt concentration in all polymer electrolytes. Increase in the electrical conductivity and decrease in the activation energy value of polymer electrolytes can be explain on the basis that the polymer films are known to be a mixture of amorphous and crystalline region and the conductivity behavior of such films may be dominated by the properties of amorphous region[13]. The amorphous nature provides a bigger free volume in

polymer electrolytes system with increase in temperature [14].

IV. CONCLUSION

Polyvinyl alcohols (PVA) doped with different percentage of Ammonium Iodide (NH₄I) were prepared by solution casting technique. It is reveal that electrical conductivity of polyvinyl alcohol doped with ammonium iodide increases with increasing salt concentration as well as temperature. The activation energy decreases with increase of salt concentration in prepared polymer electrolytes

V. REFERENCES

[1]. A Hayashi, T. Ohtomo, F, Mizuno, K. Tadanaga Electrochem. commun. 5(8) (2003) 701.

[2]. S. Guinot, E. Salmon, J.F. Penneau ,J.F.Fauvarque, Electro-chim. Acta 43 (1998) 1163.

[3]. N. Vassal, E. Salmon, J. F. Fauvarque, J.Electrochem Soc. 146 (1999) 20.

[4]. Lawandowski, K.Skorupska, J. Malinska, Solid State Ionics 133 (2000) 265.

[5]. A. Mohamad, N. S. Mohamed, Y.Alias, A. K. Arof, J. Alloys Comp. 337 (2002) 208.

[6]. M. Krumova ,D. lopaz , R. Benavent, C.Mijangos, J. M. Parena, polymer 41(2002) 9265.

[7]. K .Masuda, H. Kaji, F. Hori, J Polym Sci Part B, 38(2002)1.

[8]. F. Billmeyer, Jr text book of polymer science Wiley Singapur (1984).

[9]. S. Chandra, S A Hashim, G. Prasad, Solid State Ionic 40-41(1990) 651.

[10]. R. M. Jaipal, T. Shreekanth, U .V. Subba Rao, Solid State Ionics, 126 (1999) 55.

[11]. S. C. Raghavendra, S. Khasim, M. Revanasiddappa, A. Prasad, A. B Kulkarni, Bull Mater Sci, 26 (2003) 733.

[12]. S. D. Druger, A. Nitzam, M. A. Ratner, J Chem Physics, 79 (1983) 3133.

[13]. K. K. Maurya, S. A. Hashmi, S. A. Chandra, J. Phys Soc. Janpan 61(1992)1709.

[14]. M.S. Michael, M.M.E. Jacob, S.R.S Prabaharan, S. Radhakrishna Solid State Ionics 98 (3-4), 167.

Acoustic and Thermal Study of Biomolecule In Aqueous Potassium Chloride

V. A. Giratkar

Department of Chemistry, Sardar Patel College, Chandrapur, 442403, Maharashtra, India

ABSTRACT

The ultrasonic velocity (u), density (ρ) and viscosity (η) of Glycine in 2% of aqueous solutions of potassium chloride have been measured. Thermoacoustic parameters like adiabatic compressibility, intermolecular free length, acoustic impedance, internal pressure were calculated. It was found that there is certain degree of variation in these parameters with change in concentration and temperature. The variations of acoustic parameters with concentration and temperature indicate the existence of intermolecular interaction in the present systems.

Keywords: Glycine, Ultrasonic Velocity, Thermodynamic Parameters, Molecular Interactions

I. INTRODUCTION

Structure and properties of proteins are greatly affected by the interaction of aqueous salt.[1] Proteins are macromolecules and needed for the most important biological processes like cell growth and their maintenance, movement and defense. Proteins are complex molecules and their behavior in solutions is governed by a combination of many specific interactions.[2] These interactions involve hydrogen bonding, electrostatic interactions, hydrophobic interaction which are non-covalent in nature. These interactions are helpful to study conformational stability and unfolding behavior of globular proteins. As proteins are complex molecules, their direct study is difficult and tedious. Hence the study of interactions of model compounds like amino acids and peptides in aqueous systems makes the work easy.[3] The standard α-amino acids have special importance among the other chemical groups they play a vital role in nearly all chemical and biological process. There has been an increased interest in physicochemical properties of amino acids in aqueous and aqueous electrolytes media.[4]

II. METHODS AND MATERIAL

The compound Glycine of purity 99% was obtained from HIMEDIA India Ltd and was used as supplied. Initially 2% aqueous KCl stock solution was prepared by using double distilled water. The digital balance having an accuracy of ±0.1mg was used for the measurement of weights. The solutions of Glycine of concentration 0.02M to 0.12M were prepared at different temperature range. Densities of these solutions were measured by specific gravity bottle by relative measurement method with accuracy of ±0.1 kgm^{-3}. Viscosity of solvent and solution under the study was measured using Ostwald's viscometer keeping temperature constant by using digital constant temperature water bath having an accuracy of ±0.1K. The ultrasonic velocity of solvent and solution of different concentration at different

temperature range (288 K to 303 K) was measured by using digital ultrasonic interferometer at frequency 2MHz (VI Microsystems Pvt. Ltd. Perungudi, Chennai) with an accuracy of ±0.1%.

THERMOACOUSTIC PARAMETERS

From density, viscosity and ultrasonic velocity various thermodynamic parameters were evaluated by using the following mathematical equations.

Adiabatic compressibility (β)

$$\beta = 1/(\rho U^2) \qquad ---------- (1)$$

Where ρ and U are the density and ultrasonic velocity of solution

Intermolecular free length (Lf)

$$L_f = K\beta^{1/2} \qquad ---------- (2)$$

Where, K is Jacobson's constant.

This constant is a temperature dependent parameter whose value at any temperature (T) is given by $(93.875+0.345T) \times \llbracket 10 \rrbracket ^{-8}$.

Acoustic impedance (Z)

$$Z = U \rho \qquad ---------- (3)$$

Internal pressure ($\pi_{(i)}$)

$$\pi_{(i)} = bRT (K\eta/U)1/2 (\rho^{2/3}/M_{eff})7/6 \qquad -------- (4)$$

Where,

b - stands for cubical packing, which is assumed to 2 for all the liquids

K- is a dimensionless constant independent of temperature

T- is the absolute temperature in Kelvin Meff - is the effective molecular weight

R- is gas constant

III. RESULTS AND DISCUSSION

The variation of experimentally measured and derived thermoacoustic parameters of glycine solution in aqueous salt of different concentrations at different temperature are as given in fig. a–g.
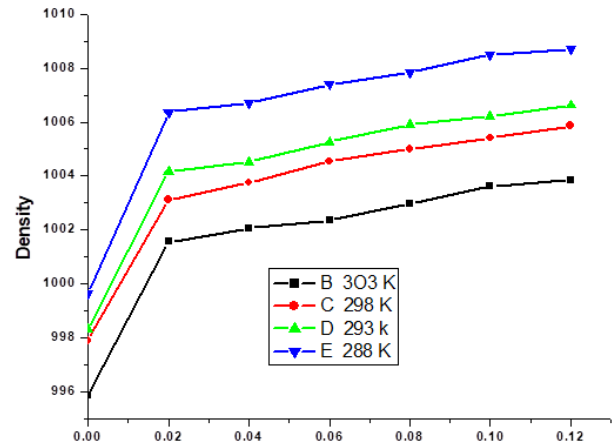

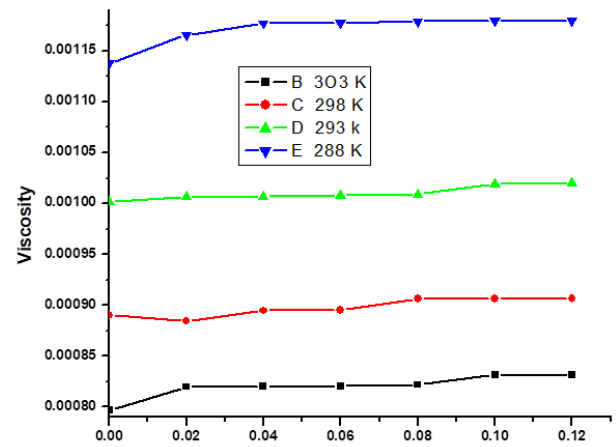Fig 1(a) Concentration in mole / dm³ of Glycine in 2% KCl

Fig 1(b) Concentration in mole / dm³ of Glycine in 2% KCl

Fig. 1(a) shows that density of glycine solution in 2 % aqueous KCl increases with increase in concentration and decreases with the increase in temperature. This result is obvious as the volume of the solution increases with the rise in temperature [5] and mass of the solution increase with the increase in concentration.

Viscosity is the parameter of the liquid, which is greatly affected by the concentration and the temperature. It is observed from fig. 1(b), that viscosity of glycine solution in 2 % aqueous electrolytes increases with increase in concentration. Increase in viscosity of solution with concentration suggests the strong interaction of solute and solvent molecule. the decrease in viscosity with rise in

temperature indicates that the molecules in the solution acquires more and more thermal energy. The motion of molecules increases at the expense of cohesive forces acting between the molecules. Since the solution faces lesser resistance to flow, the viscosity of the solution will decrease.[6]
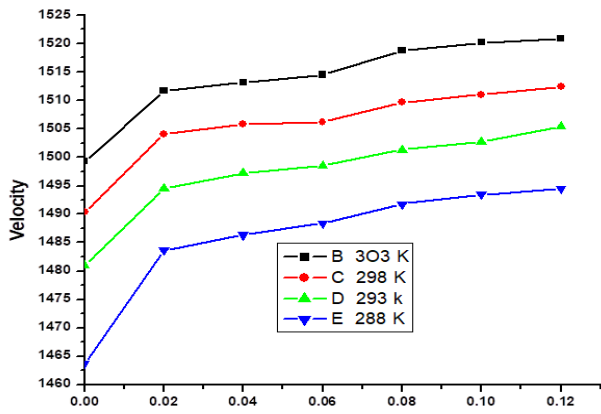

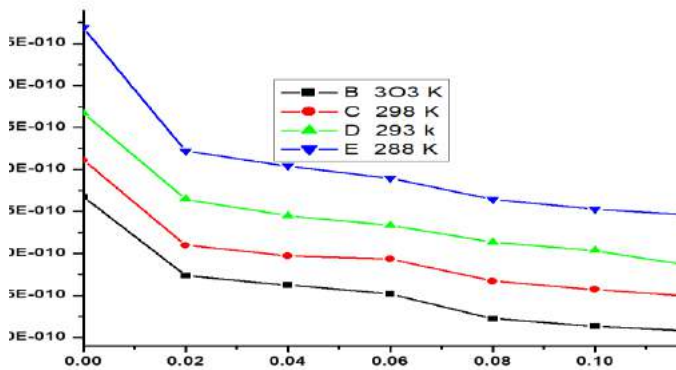Fig1(c) Concentration in mole / dm³ of Glycine in 2% KCl

Fig1(d) Concentration in mole / dm³ of Glycine in 2% KCl

The increase in ultrasonic velocity with concentration (fig. 1c) in any solution indicates the presence of solute-solvent interactions.[7] The increase in ultrasonic velocity with rise in concentration for the present system confirms the greater molecular association. As temperature increases, breaking of hydrogen bonding increases. This results in more and more number of monomeric water molecules. These molecules then enter in the cage-like water structure and get trapped to form closed packed structure. This closed-packed structure forms stiff material medium for the propagation of ultrasonic wave. Hence

ultrasonic velocity increases with the rise in temperature.

Adiabatic compressibility is inversely correlated with ultrasonic velocity which increases with increase in temperature. Hence adiabatic compressibility values decreases with increase in temperature.The dependence of adiabatic compressibility of glycine solutions in 2% aqueous solution of potassium chloride on concentration at different temperature is as shown in the fig. 1(d). The decrease in adiabatic compressibility values with concentration indicate that the hydrogen bonding between the unlike components in the solution decreases. [8]

Fig1(e) Concentration in mole / dm³ of Glycine in 2% KCl
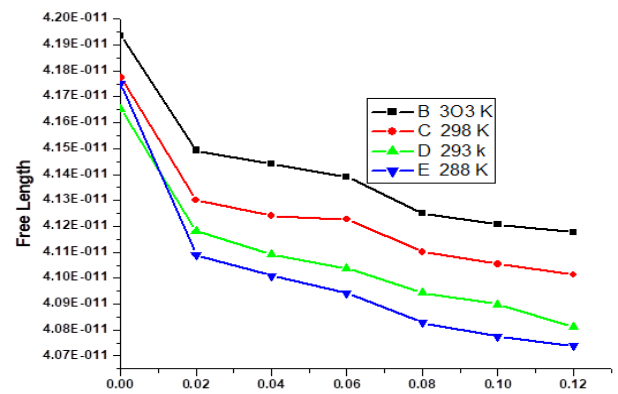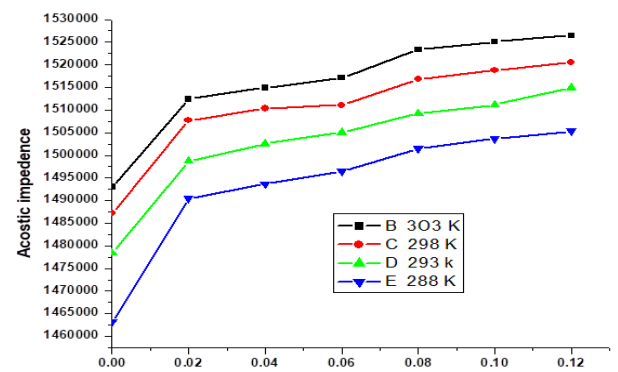

Fig1(f) Concentration in mole / dm³ of Glycine in 2% KCl

The decrease in free length (fig. 1e) with rise in concentration of glycine solution in 2% aqueous electrolytic solution suggest that there is a significant interaction between solute and solvent molecules. It also suggests the structure promoting behavior [9,10] as well as the presence of dipole-dipole and acceptor-

donor interaction between solute and solvent molecules. The higher values of free length for higher temperature are due to more spacing among the components of the medium.

The increase in acoustic impedance with the increase in concentration as well as temperature Fig.1 (f) suggests the greater association of solute and solvent through hydrogen bonding. Thus increase in acoustic impedance indicates associative nature of solute and solvent and enhancement in molecular interaction.

Fig1(g) Concentration in mole / dm^3 of Glycine in 2% KCl
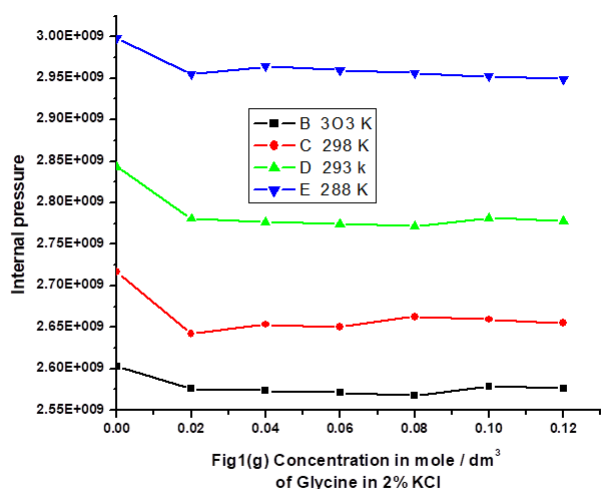
The internal pressure is the cohesive force or binding force, which is a resultant force of attraction and repulsion between the molecules. From fig. 1(g) it is observed that decrease in internal pressure with increase in temperature is due to the thermal agitation of molecules which reduces the interaction between the molecules in the system.

IV. CONCLUSION

From experimentally determined parameters of glycine solution in 2% aqueous salt of different concentration at different temperature various acoustical parameters were evaluated. The temperature and concentration effects on these parameters were studied. These parameters were interpreted in connection with the molecular interactions. The addition of solute in solvent has structure making tendency through intermolecular hydrogen bonding.

V. REFERENCES

[1]. Von Hippel P. H., Schleich T., Acc. Chem. Res., 1969, 2, 257-265.

[2]. Thirumaran S., Sathish, K., J. Chem. Sci., 2011, 8, 63-71.

[3]. Banipal T. S., Kaur J., Banipal P., J. Chem. Eng. Data.,2008, 53, 1803-1816.

[4]. Pinho S. P., J. Chem. Eng. Data., 2008, 53, 180-184.

[5]. Rajathi K., Ali S. J., Rajendran A., J. Chem. Pharm. Res., 2011, 3(5), 348-358.

[6]. Kaur K., Kumar H., J. Mol. Liq., 2013, 177, 49-53.

[7]. Godhani D. R., Dobariya P. B., Sanghani A. M., J. Mol. Liq., 2012, 168, 28-35.

[8]. Iqbal M., Verrall R. E., Can. J. Chem., 1989, 67 (4), 727-735.

[9]. Singh V.K, Singh V.K., International Journal of Scientific & Engineering Research Volume 11, Issue 1, January-2020 123 ISSN 2229-5518

[10]. Sethu Raman M., Ponnuswamy V., Kolandaivel P., Perumal K., J. Mol. Liq.,2010, 151, 97.

A Comprehensive Review on Eu Doped Zinc Aluminate Phosphor for Solid-State Lighting

Vikas[1], Vikas Lahariya[1*], Krishna Kumar Pandey[2]

[1]Department of Physics, Amity School of Applied Sciences, Amity University Haryana, India

[2]Department of Physics, School of Basic Sciences and Research, Sharda University, Greater Noida, India

ABSTRACT

Zinc based aluminate materials are the member of spinel oxide. Zinc Aluminate is a wide bandgap semiconductor. In this report, rare earth Eu doped zinc aluminate phosphor is discussed in detail. Eu3+ doped ZnAl2O4 phosphor with efficient orange-red light emission is useful for solid-state lighting and optoelectronic devices. Therefore, it is important to discuss the properties and utility of the material for phosphor applications. Different synthesis routes have been used for the preparation of Eu doped ZnAl2O4. The effect of doping concentration, calcination time, duration, and various other parameters affect the crystal structure and luminescence properties of Eu doped ZnAl2O4 spinel. The effect of doping concentration, calcination temperature, and synthetic route on luminescence properties are discussed in brief. The review explains the luminescence mechanism, their emission spectrum and potential application for Eu activated ZnAl2O4 phosphor.

Keywords - Zinc Aluminate, Luminescence, Rare Earth Ions, Eu Doped, Synthesis Method

I. INTRODUCTION

Luminescence is the most favorable phenomenon of light. It is characterized as the radiation emitted by a molecule or an atom after it had retained energy to go to the excited state. Luminescence comprises of two main types: fluorescence and phosphorescence. Phosphor emits a photon when excited by an external energy source. The optical center in the material is irradiated by an external energy source and makes a transition to an excited energy state from the ground state. The excited state ultimately returns to the ground state via the radiative or non-radiative process. Radiative transition is called luminescence. Aluminates are compounds consists of an oxyanion of aluminum such as zinc aluminate. Zinc based aluminate materials are the member of spinel oxide having general formula AB2O4 where A and B represent divalent and trivalent metal ion respectively[1]. It is a wide bandgap semiconductor with a gap of 3.8 eV [2]. It is widely used as ceramic and catalytic material due to its extremely diversified properties such as high mechanical and thermal resistance, hydrophobic nature, high quantum efficiency, high chemical, and thermal stability. Zinc aluminate is a promising host material with high luminescence efficiency and stability. Therefore, in solid-state lighting, it is being used as a host material with rare earth and transition metal dopant ions as phosphor. Rare-earth doped Zinc aluminate phosphor has been studied mostly due to stability and high

quantum yields in the visible region [3]. Rare earth (RE) doped phosphors are widely used in lighting applications, such as in fluorescent lamps, cathode-ray tubes, light-emitting diodes (LEDs) for the lighting industry, field-emission displays [4]. Among all the RE ions, the europium (Eu) activator is capable of red and green emission in trivalent Eu3+ and divalent Eu2+ states respectively. In Eu3+ ions, the line emission occurs from 5D0 excited state to 7FJ ground state transition [5].

II. METHODS AND MATERIAL

Structural Information-

Among spinel oxides, ZnAl2O4 offers high interest for solid-state lighting. It is metal aluminates having spinel face-centered cubic crystal structure with space group Fd3m where Zn2+ ions occupy tetrahedral sites and Al3+ ions occupy octahedral sites[6]. it is represented as AB2O4 since occupied divalent cations on tetrahedral site, occupied trivalent B3+ cations on octahedral voids, and oxide ions make the ratio of A2+:B3+:O2- is 1:2:4. In the ZnAl2O4 spinel structure, octahedral sites possess high coordination number six. Depending on preparation methods, ZnAl2O4 ions can crystallize in normal or inverse spinel structure [1]. In the inverse spinel structure, there is mixed occupation of divalent and trivalent cations on octahedral sites while tetrahedral sites are occupied only by trivalent B3+ cations. Furthermore, it is polycrystalline and exhibits high reflectivity in the UV region. The theoretical results on the electronic band structure of ZnAl2O4 reveal that 3d electron of the spinel oxides facilitates the electronic properties.

III. RESULTS AND DISCUSSION

Synthesis and Characterization of Eu doped ZnAl2O4 Phosphor

The binary compound ZnAl2O4 has been prepared by many synthetic routes such as solid-state reaction method [7], combustion method [8, 9], Sol-gel method, chemical [10] Co-precipitation method [5], etc. However, each method has some advantages and limitations. Among the above-mentioned chemical methods, combustion reaction synthesis is the most reliable process to obtain small grain size oxide phosphors. It is relatively fast, less energy consumption, and simple route, with no obligation of midway calcination stages [7,8]. Moreover, fine particle size and high purity are the two major advantages of this method. Barros et al. used combustion reaction synthesis for the preparation of Eu3+ doped zinc aluminate phosphor [9]. Stoichiometric compositions of metal nitrates and rare oxide as urea were taken. Single phase ZnAl2O4 spinel structure was found. However secondary ZnO phase was observed in Eu doped ZnAl2O4 nanoparticles. It was attributed to the formation of vacancies resulting from the incorporation of rare-earth ions into the host lattice [9]. Due to mismatching of valence states of substitute trivalent Al3+ ions and divalent Zn2+ ions and large ionic radius of Eu3+ (0.95 A°) ions and Al3+ (0.53 A°), trivalent Al3+ ions occupied octahedral sites in ZnAl2O4 spinel structure[10]. Moreover, the crystallinity and particle size of the ZnAl2O4 were also decreased with Eu3+ doping due to the difference between the ionic radius. Another widely used and most preferable method is Sol-gel chemical synthesis. It is a series of chemical processes that include hydrolysis, gelation, drying, and thermal treatment [10]. Lei et al. have reported a series of Eu3+ doped ZnAl2O4 phosphor prepared via the sol-gel method [11]. They studied the effect of calcination temperature on crystallization, grain size and luminescence properties. XRD patterns have revealed pure spinel phase of high crystallinity can be achieved with doping percentage of Eu3+ up to 5% and secondary calcination temperature in the range of 600-900ºC. At 500ºC calcination temperature, some characteristic peaks of zinc aluminate were observed

but the intensity was weak. When the temperature was raised from 600-900º C, no shift in the diffraction was found, it shows little effect of calcination temperature on the crystal structure. However, with increasing temperature, a secondary phase of ZnO and EuAlO3 was found. Moreover, the grain size of the Eu doped ZnAl2O4 nanoparticles increased with raising the temperature, which indicates that high temperature affects the process of crystal growth and crystallinity. The best results were observed for 5% Eu doping and 800ºC secondary calcination temperature. Over the past few years, different synthesis processes have been applied for Eu doped zinc aluminate spinel [7-10]. Most studies investigated the effect of concentration of dopant ions and annealing temperature on structure, morphology, and luminescence behavior. Strek et al. prepared Eu doped zinc aluminate spinels by hydrothermal synthesis route [4]. The calcination temperature raised up to 1273K for 1 wt.% of Eu. In agreement with the previously discussed results, they observed the complex nature of Eu3+ doping on ZnAl2O4[4]. They reported that Eu3+ creates additional sites in nanocrystals due to the high surface effect. Wiglusz et al. studied the effect of calcination temperature on Eu doped zinc aluminate nanoparticles in temperature range of 700-1400º C [10]. The reported average particle size is in the range of 10-30 nm depends on the annealing temperature. smallest crystallite size in the temperature range of 700-1200ºC was found for 5% Eu doping. Similarly, Osorio et.al. have prepared Eu doped ZnAl2-xEuxO4 (x=0,0.01,0.03,0.06,0.09,0.12) via co-precipitation method [12].It was seen that at low temperatures below 300ºC, samples showed amorphous nature, while with increasing the temperature the crystallinity improved, and after heating treatment at 900ºC for two hours spinel, ZnAl2O4 phase was found[12]. The Rietveld refinements analysis confirmed the presence of Eu3+ ions in the octahedral sites only. Doping concentration has a high impact on the crystallite size. No difference in the crystallinity was noticed with different Eu doping concentration. In 2006, Cheng et al. reported Eu3+ doped ZnAl2O4 spinel nanorods by co-precipitation method. They obtained high surface area, and narrow size distribution of porous nanorods through a transition of layered composite precursors at high temperature(900ºC)[13]. In the post-annealing treatment at 900ºC, the sample was shown FCC cubic structure with single-phase formation.ZnAl2O4 nanostructure and bulk have been prepared via a solid-state reaction of zinc and aluminum oxides above 800 ºC [7].

Luminescence Study of Eu doped ZnAl2O4 Phosphor

The photoluminescence emission spectra of Eu3+ doped zinc aluminate nanoparticles consist of a band in the orange-red visible region. Lei et al. observed five emission peaks at 580,593,618,653,700 nm for doped ZnAl2O4 with 5% Eu3+.These emissions correspond to allowed transitions from the lower excited state 5D0 to multiplets 7F0-4 of 4F ground states of Eu3+.PL was excited by 395 nm [11]. The electric dipole transition 5D0→7F2 is highly sensitive to site symmetry. Therefore, the luminescence properties of this transition influenced by the local environment and surrounding ligands. The highly intense emission peak at 618nm belongs to the 5D0-7F2 transition. However, orange-red emission corresponds to 5D0-7F1 magnetic dipole transition did not show any change in intensity. As suggested, it was due to inversion symmetry [10]. Also, they observed the concentration effect on luminescence characteristic of phosphor. Results indicated that with the increase of doping concentration up to 5 at. %, the PL intensity increased. The maximum intensity of luminescence peaks was observed for 5at% of Eu3+ doping. Thereafter, with increment in concentration, luminescence peaks were quenched. In the case of rare-earth ions doped phosphor, concentration quenching can occur due to different mechanisms. To study, Blass proposed a method by calculating crystal

critical distance Rc [14]. Lei et al. was suggested that the cause of concentration quenching was radiation reabsorption since calculated Rc > 0.5 nm[11]. Because of the larger number of Eu states multipolar interaction occur consequently, more energy transfer takes place. Hence beyond 5% Eu3+ doping, the distance between activator ions decreased and lower intensity was obtained. The CIE color coordinates of 5% doped sample confirmed the red color emission of phosphor. Thus, Zn0.95Eu0.5Al2O4 can be used as a near UV-LED based red phosphor for solid-state lighting and display. Later, PL investigations [10,11] found red emission for Eu3+ doped ZnAl2O4 phosphor. However, they found a highly intense band of transition 5D0→7F0. Moreover, they observed a noticeably increment in the intensity with higher annealing temperature. Afterglow was also noticed for samples prepared by 700 and 800ºC. It was attributed to the transfer of Eu3+ ions into asymmetrical sites due to high temperature. Osorio et.al. showed red emission band centered at 616nm corresponds to 5D0→7F2 transition excited at 260 nm[12]. In PL spectra, two broader bands were located at 616nm and 586 nm. The red band at 616 nm was relatively intense originated from electric dipole transition. However, the maximum intensity was observed at 3mol% sample and quenching was observed for a higher concentration of Eu[12]. Similarly, Verma et.al. found an enhancement in the intensity of Eu3+ ions was ascribed to cross-relaxation phenomena which are favored by overlapping between donor and acceptor transitions[15]. He et al. [7] observed an asymmetric broad green emission at 532 nm attributed to the 5d-4f transition of Eu2+ ions. At 1mol% Eu2+,the reported maximum intensity was at only 1% while calculated quantum efficiency was 54.85%. Apart from this, many other peaks associated with impurities were observed at temperature 600ºC. Further, an increase in temperature at 1000ºC, improvement of photoluminescence was found. Thus, the luminescence spectrum of Eu doped ZnAl2O4

influnced by redistribution of electrons into inner 4F shell of dopant ions. Also the local field symmetry and valence state of Eu change the emitting states and resultant emission.

IV. CONCLUSION

The structure of zinc aluminate and luminescence mechanism has been discussed. The analysis shows that zinc aluminate doped with Eu3+ ions can be used as a potential orange-red emitting phosphor while Eu2+ doped ZnAl2O4 phosphor can be used as green emitting phosphor. The strong absorption in the near UV region and intense red emission makes it suitable for near UV-LED-based red-emitting component. Different synthesis methods of phosphor preparation have been briefed. The presented results show Structural, optical, and luminescence properties can be changed with calcination temperature and doping concentration.

V. REFERENCES

[1]. Kurt E. Sikafus, John M. Wills, Journal of American Ceramic Society, Spinel Compounds, 82 (12) 3279–92 (1999)

[2]. Sampath, S.K. and Cordaro, J.F. (1998), Optical Properties of Zinc Aluminate, Zinc Gallate, and Zinc Aluminogallate Spinels. Journal of the American Ceramic Society, 81: 649-654.

[3]. S.V. Motloung,F.B. Dejene,H.C. Swart,O.M. Ntwaeaborwa, Elsevier, Journal of Luminescence,163,2015, 8-16. Doi - 10.1016/j.jlumin.2015.02.027

[4]. W Strek, P Deren, A. Bednarkiewicz, M. Zawadzki, J. Wrzyszcz Journal of Alloys and Compounds 300–301 (2000) 456–458, 10.1016/S0925-8388(99)00696-9

[5]. Sanjay J. Dhoble ,B. Deva Prasad Raju ,Vijay Singh, Phosphors Synthesis and Application ,Pan Stanford Publishing, ISBN 978-981-4774-49-9 (Hardcover) ISBN 978-042-9460-99-9 (eBook).

[6]. Mithlesh Kumar, T.K. Seshagiri, M. Mohapatra, V. Natarajan, S.V. Godbole Journal of Luminescence 132 (2012) 2810–2816

[7]. Can He, Haipaeng Ji,Zhaohui Huang,Xiaoguang Zhang,Yang'ai liu,Minghao Fang,Xiaowen Wu,Xin Min , Journal of Rare Earths,36 (9) 2018, 931-938. doi 10.1016/j.jre.2018.01.018

[8]. Sanjay Kumar Pathak, Akshkumar Verma,Ashish Verma, Journal of Materials Science: Materials in Electronics 2020. https://doi.org/10.1007/s10854-020-03715-x

[9]. B.S. Barros, P.S. Melo, R.H.G.A. Kiminami ,A.C.F.M. Costa, G.F. de Sa', S. Alves, J Mater Sci (2006) 41:4744–474810.1007/s10853-006-0035-6

[10]. Rafal J. Wiglusz, Tomasz Grzyb, Arthur Bednarkiewicz, Stefan Lis and Wieslaw Strek ,European Journal of Inorganic Chemistry, 2012,3418-3426. DOI: 10.1002/ejic.201200185.

[11]. Zhigao Lei,Dawei Meng, Yongqian Wang, Zhixi Gao,Xuelian Zhang,Qinxue Yang, Springer, (2016) 27:1840–1846, DOI 10.1007/s10854-015-3962-7.

[12]. Fernandez Osorio,C.E. rivera, J. Chavez , Proceedings of the World Congress on New Technologies (NewTech 2015) Barcelona, Spain – July 15 - 17, 2015 Paper No. 360A.

[13]. Baochang Cheng, Shengchun Qu, Huiying Zhou and Zhanguo Wang Nanotechnology 17 (2006) 2982–2987.

[14]. G. Blasse, B.C. Grabmaier,Springer A general introduction to luminescent materials, 10.1007/978-3-642-79017-1_1

[15]. Naveen Verma ,Bernabe Mari, Krishan Chander singh,Jitender Jindal ,Suprabha yadav and Anuj Mittal ,Journal of Australian ceramic Society, 2018. doi.org/10.1007/s41779-018-0223-2.

Thermoluminescence in Copper Doped Potassium Tetraborate Phosphor

R. S. Khan[1], Z. S. Khan[1*], N. B. Ingale[2], S. K. Omanwar[3]

[1]Government Vidarbha Institute of Science and Humanities, VMV Road, Amravati India

[2]Prof. Ram Meghe Institute of Technology and Research, Badnera, India

[3]Department of physics, SGB Amravati University Amravati, India

ABSTRACT

We have prepared copper doped $K_2B_4O_7$ phosphor by using simple and modified solution combustion method. This sample is confirmed with the help of X-ray diffraction (XRD). Apart from this, Scanning Electron Microscope (SEM) and FTIR studies of the prepared sample were carried out. Thermoluminescence properties of $K_2B_4O_7$: Cu phosphor is observed. Two distinct peaks at 235 ˚C and 340 ˚C with a shoulder at 420 ˚C were witnessed. The kinetic parameters and the effect of dose variation on $K_2B_4O_7$: Cu phosphor is also studied.

Keywords: Borates, Luminescence, Copper doping, Activation Energy

I. INTRODUCTION

Low synthetic temperature, high luminescent brightness and easy preparations etc are the plus points of borates in comparison with the other investigated hosts [1]. The simplistic synthesis with quite cheap raw materials like boric acid and urea results in excellent chemical and thermal stabilized alkaline earth borate [2,3]. Following Daniels et al (1953) [4] lots of researchers have applied the thermoluminescence phenomenon on dosimetry purpose. Some of the investigations on the TL characteristics of borates are un-doped and Ce-doped BaB_4O_7 [5], un-doped and Cu- and Mn-doped $K_2B_4O_7$ [6], MgB_4O_7: Dy, Na [7], SrB_4O_7: Dy [8], $Li_2B_4O_7$: Cu, In [9] and BaB_4O_7: Dy [10]. The studies for the TL phenomenon of borates were started by the work of Schulman et al (1967) [11] Thermoluminescence dosimetry (TLD) has been widely applied in areas such as clinical, personal and environmental monitoring of ionizing radiation.

Much research has been carried out to find better dosimetric materials and borates fulfilled the needs of sensitivity with near tissue equivalent absorption coefficient, to some extent [12]. The copper containing materials are among the most sensitive known thermoluminescence (TL) phosphors [13]. These phosphors are suggested to be used for dosimetry applications [14]. We studied the TL characteristics and some dosimetric properties of copper activated $K_2B_4O_7$ under the irradiation of γ-rays, which was presented in this paper

II. METHODS AND MATERIAL

The $K_2B_4O_7$: Cu Phosphor was obtained by the combustion of aqueous solution containing stoichiometric amounts (using oxidizer/fuel ratio) of potassium nitrate, copper chloride, ammonium nitrate, urea and Ammonium Pentaborate as boron source [15, 16]. All the precursors (AR grade) were

dissolved in a china dish using minimum amount of water. The dish containing the solution was introduced into a muffle furnace maintained at 823±10 K. The solution undergoes dehydration followed by decomposition with the evolution of large amount of gases (oxides of nitrogen and ammonia) and ignited to burn with a flame yielding voluminous powder of $K_2B_4O_7$: Cu This raw powder was sintered for 2 h at 1023 K and cooled to room temperature on aluminium plate and crushed into a fine powder. The same process is repeated for the different concentration of copper. The prepared powder samples were then subjected to the powder XRD analysis. Samples were exposed to gamma rays from a 60Co-source at room temperature. After the desired exposure, TL glow curves were recorded for samples at a heating

rate of 5 K/s. The photoluminescence of as prepared sample of $K_2B_4O_7$: Cu (0.007 mol) over 200–400 nm excitation range was taken on a HITACHI F-7000 fluorescence spectrophotometer

Table 1: Balanced reaction for $K_2B_4O_7$: Cu

Product	Corresponding reaction with balance molar ratios of precursors
$K_2B_4O_7$: Cu	KNO_3 + H_3BO_3 + 5 $CO(NH_2)_2$ +7.5 NH_4NO_3 + x $CuCl_2$ $\longrightarrow$ $K_2B_4O_7$: Cu + Gaseous (H_2O, NH_4 and NO_2 etc)

III. RESULTS AND DISCUSSION

Figure-1 represents the XRD pattern for polycrystalline sample of $K_2B_4O_7$: Cu. It is found to be Monoclinic with space group P21/n (14) and lattice parameter a = 12.26 A.U, b = 9.895 A.U, c = 7.796 A.U. The results are confirmed by comparing the observed XRD with standard ICDD file (00-031-0253) which is in good agreement and show peak to peak matching.
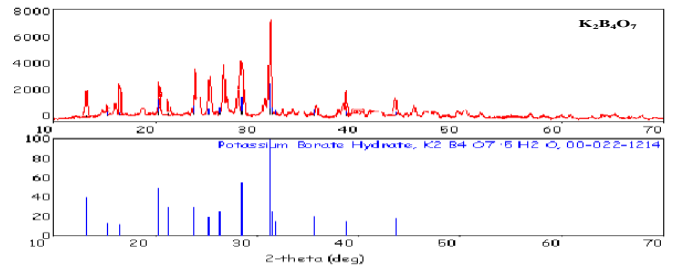

Fig. 1 XRD pattern of $K_2B_4O_7$: Cu

SEM image is represented in Fig. 2 for solution combustion synthesized $K_2B_4O_7$: Cu material. The material shows irregular shape expanded particle structure. It shows the sizes of particles from 0.5 μm to 5 μm range. The irregularity may be caused due to the irregular mass flow during combustion process.
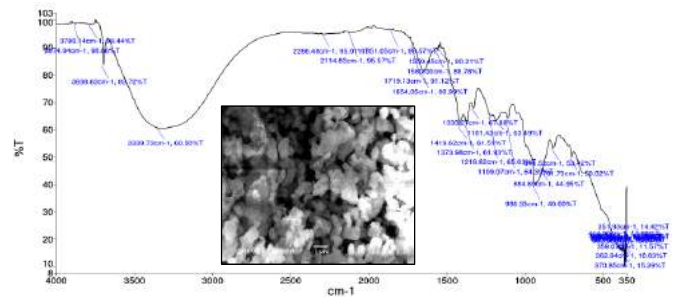

Fig. 2 FTIR and SEM image of $K_2B_4O_7$: Cu

The TL glow curve of newly developed $LiBaBO_3$ with different concentration of Eu^{3+} for a test dose of 1 Gy is shown in the Fig. 3 obtained at heating rate is 5 °C /sec. The glow curve consists of two peaks P_1 and P_2 at 170 °C and 266 °C respectively. This range (175-225 °C) is favorable for the desired dosimetry purposes [17]. Here 0.002 mole of Eu^{3+} shows optimum thermoluminescence (TL) intensity for this phosphor. The TL glow curves for $LiBaBO_3$:Eu^{3+} phosphors were deconvoluted by using the PeakFit software [18] as shown in Fig. 3. We employed the peak shape method to analyze the activation energy of $LiBaBO_3$:Eu^{3+} phosphors using formula used by Mckeever [19].

Table 2: Kinetic parameters for $K_2B_4O_7$: Cu

	Peak	T_m (°C)	$μ_g$	E (eV)	S (s^{-1})
$K_2B_4O_7$: Cu	P_1	235 °C	0.47	0.961	7.24 X 10^8

| | P$_2$ | 340 °C | 0.53 | 1.425 | 1.12×10^{11} |
| | P$_3$ | 420 °C | 0.50 | 1.341 | 8.97×10^{8} |

We have decided 5 Gy to 25 Gy dose for irradiations. After about five hours, TL reading was taken with TL readout heating rate of 5 °C/sec on TL 1009I reader designed by Nucleonix system with the temperature range of integration of the TL signal from 40 °C to 400 °C. The linearity was observed for the first peak in the range from 5 Gy to 25 Gy. The relationship between the TL response of the high intensity peak and the absorbed dose for K$_2$B$_4$O$_7$: Cu phosphor was shown in Fig. 3 which was found to be linear.

We have decided 5 Gy to 25 Gy dose for irradiations. After about five hours, TL reading was taken with TL readout heating rate of 5 °C/sec on TL 1009I reader designed by Nucleonix system with the temperature range of integration of the TL signal from 40 °C to 400 °C. The linearity was observed for the first peak in the range from 5 Gy to 25 Gy. The relationship between the TL response of the high intensity peak and the absorbed dose for K$_2$B$_4$O$_7$: Cu phosphor was shown in Fig. 3 which was found to be linear.
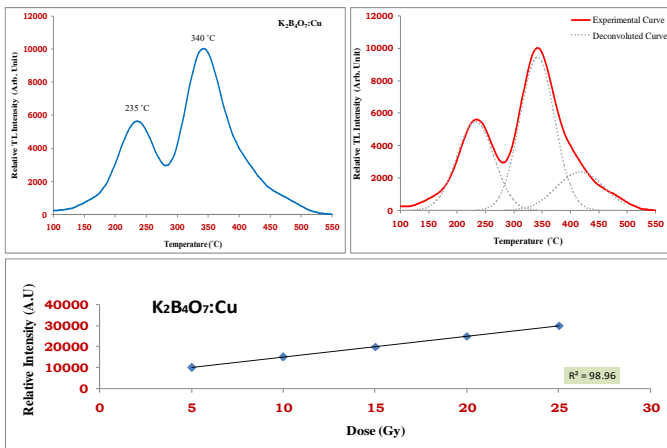

Fig. 3 TL glow peak and deconvoluted TL glow curve with dose response for K$_2$B$_4$O$_7$: Cu Phosphor

IV. CONCLUSION

Using combustion method, K$_2$B$_4$O$_7$: Cu was successfully prepared. TL and PL properties of K$_2$B$_4$O$_7$: Cu is reported with X-ray Diffraction. It witnessed maximum TL at 0.007 mole of copper irradiated with gamma dose for 15 sec. Besides a good candidate for lamp phosphor and display application, this phosphor may be applicable for environmental monitoring applications.

V. REFERENCES

[1]. Z. S. Khan, N. B. Ingale, S. K. Omanwar, Environ. Sci. Pollut. Res., 23 (2016) 9295-9302.

[2]. Z. S. Khan, N. B. Ingale, S. K. Omanwar, Optik – Int. J. Light Electron Optics, 127 (2016) 9679-9689.

[3]. Z. S. Khan, N. B. Ingale, S. K. Omanwar, AIP Conference Proceedings 2104 (1), 030035

[4]. F. Daniels, C.A. Boyd, D.F. Saunders, Science 117 (1953) 343

[5]. A.N. Yazici, M. Dogan, V. E. Kafadar, H. Toktamis, Nucl. Instrum. Methods B, 246 (2006) 402

[6]. J. Manam, S.K. Sharma, Nucl. Instrum. Methods B 217 (2004) 314

[7]. C. Furetta, G. Kitis, P.S. Weng, T.C. Chu, Nucl. Instrum. Methods A 420 (1999) 441

[8]. J. Li, J.Q. Hao, C.Y. Li, C.X. Zhang, Q. Tang, Y.L. Zhang, Q. Su, S.B. Wang, Radiat. Meas. 39 (2005) 229

[9]. C. Furetta, M. Prokic, R. Salamon, V. Prokic, G. Kitis, Nucl. Instrum. Methods A 456 (2001) 411

[10]. J. Li, J.Q. Hao, C.X. Zhang, Q. Tang, Y.L. Zhang, Q. Su, S. Wang, Nucl. Instrum. Methods B 222 (2004) 577

[11]. Schulman, J.H., Kirk, R.D., West, E.J., 1967. ProceedingsoftheInternational Conference on Luminescence Dosimetry, Stanford University, CONF-650637, 1967

[12]. Dhoble, S.J., Moharil, S.V., 2000. Preparation and characterization of Eu2+ activated Sr2B5O9Cl TLD

[13]. J.H. Schulman, R.D. Kirk E.J. West. Luminescence dosimetry (1967) CONF- 650637, US At. Energy Comm. Symp. Ser. 8, p. 113.

[14]. M. Takenaga, O. Yamamato, T. Yamashita, Health Phys. 44 (1983) 387

[15]. Z.S. Khan, N.B. Ingale, S.K. Omanwar, Mater. lett. 158 (2015) 143–146.

[16]. Z.S. Khan, N.B. Ingale, S.K. Omanwar, Combustion synthesis and luminescence properties of α-Ca2P2O7: Eu3+, Dy3+, Mater. Today: Proc., 2 (2015) 4384–4389.

[17]. Z.S. Khan, N.B. Ingale, S.K. Omanwar, Thermoluminescence studies of terbium doped calcium sulfate phosphor, Int. J. Lumin. Appl. 5 (2015) 471–474.

[18]. Z.S. Khan, N.B. Ingale, S.K. Omanwar, Synthesis and Luminescence Studies of CaSO4: Tb3+ Phosphor, Advanced Science Letters 22 (1), 164-166

[19]. Mckeever S W S, Thermoluminescence of Solids. Cambridge: Cambridge University Press, 1998. 88.

Study of Conduction Mechanism in Polypyridine - Poly(Vinyl Acetate) Films By Transference Number

A. V. Kohale*, N. D. Kolekar

Department of Physics, Shri R. R. Lahoti Science College, Morshi, Maharashtra, India

ABSTRACT

The effect of concentration of ferric chloride ($FeCl_3$) oxidant on transference number of polypyridine-polyvinyl acetate films has been described. Polypyridine (PPY) and poly vinyl acetate (PVAc) composite films were synthesized by chemical oxidative polymerization method with the solution of ferric chloride ($FeCl_3$) oxidant in methanol. The transference number for PPY-PVAc films synthesized with different concentration of $FeCl_3$ was determined by Wagner's dc polarization technique. The transference number for the films prepared with 10, 20, 25, 30 and 40 wt% of $FeCl_3$ lies between 0.51 to 0.80. It is found that, the transference number increases with the increase in concentration of $FeCl_3$. This increase is due to increase of ion concentration in PPY-PVAc composite.

Keywords : PPY-PVAc composite, Chemical oxidative polymerization, Transference number.

I. INTRODUCTION

In last few decades, there has been a great deal of increasing interest in the synthesis and characterization of conducting polymers because of their applications in organic batteries, sensors, microelectronic devices, electrocatalysis and also their electrical, electrochemical and optical properties[1].

Earlier the blends of PVC and PPy were prepared by oxidative chemical polymerization of pyrrole with an oxidizing agent $FeCl_3$. Ionic conductivity study of such material was carried out and studied the effect of oxidizing agent on conductivity of the films [2]. Polypyridine is a recent addition to the list of conducting polymers. It is of particular interest because it is soluble, thus, processable material even in its unsubstituted state, yet being chemically stable. It is considered as an important candidate material for application in light- emitting polymeric diodes.

Many research workers have studied synthesis and charge transport in composites and blends like PPy-polyvynil chloride (PPy-PVC) [3], PPy-Ferric oxide nanocomposites [4], PPy- polyvynil acid (PPY-PVA) [5], polystyrene-polyaniline (PS-PAn) [6] and PPy-poly (alkyl methacrylats) [7]. Most of them explained the charge transport behavior as a charge carrier hopping (Mott's VRH) between localized states while in case of ionically conducting solid polymer electrolytes, the conductivity is found to be temperature dependent and is more completely explained by the VTF (Vogel-Tamman-Fulcher) equatiton [8-10].

Still, polypyridine is less studied polymer as compared to others and hence an attempt is made to study conduction mechanism in PPY-PVAc composite films.

II. METHODS AND MATERIAL

PPY was synthesized at room temperature. A mixed solution of PVAc (AR grade) and FeCl₃ (E.Merck) was first prepared in methanol (AR grade). PVAc and methanol were taken in 10: 90 ratio to obtain thin films . Then pyridine monomer was added to the solution, in such a way that pyridine to PVAc ratio was constant. To study the effect of oxidizing agent, concentration of FeCl₃ was changed from 10 wt% to 80 wt% with respect to pyridine. It gives the dark brownish homogeneous solution which was then poured on chemically cleaned and plane glass substrate to prepare the films of composite. Polymerization of pyridine, which was suppressed in a mixed solution, progressed rapidly due to an increase of oxidation potential caused by evaporation of solvent. Initially this solution was homogeneous but phase separation takes place s the polymerization of pyridine proceeds. PPY aggregates were connected with each other, which resulted in PPY networks throughout the composite. After sufficient drying, films were washed with water to remove the excess FeCl₃. Thickness of these films was measured with digital micrometer (Digimatic, Japan having L.C. ± 1μm) and it is in the range of 50 to 250 μm.

The ionic/electronic transference number can be defined as:

$$t_{ion} = \sigma_{ion} / \sigma_T = I_{ion} / I_T \quad …………..(1)$$

$$t_{ele} = \sigma_{ele} / \sigma_T = I_{ele} / I_T \quad …………..(2)$$

Where, $\sigma_{ion} / \sigma_{ele}$ and I_{ion} / I_{ele} are the conductivity and current contribution due to ions / electrons respectively. Transference number gives quantitative information about the contribution of electronic and ionic conduction to the total conductivity.

Wagner's dc polarization technique [11] was used to measure the ionic/electronic transference number. In this technique, PPY-PVAc film was sandwiched between nonblocking (silver) and blocking (graphite) electrodes. A constant dc voltage 1 V was applied across the sample with help of dc regulated power supply and corresponding current (pA) was measured as a function of time at room temperature.

III. RESULTS AND DISCUSSION

The current versus time plots of the PPY-PVAc composite films are obtained which exhibit typical behavior of ionic charge transport. Current versus time plots for some of the samples prepared with 10, 20, 25, 30 and 40 wt% of FeCl₃ are shown in figure 2 (a), (b), (c), (d) and (e) respectively.
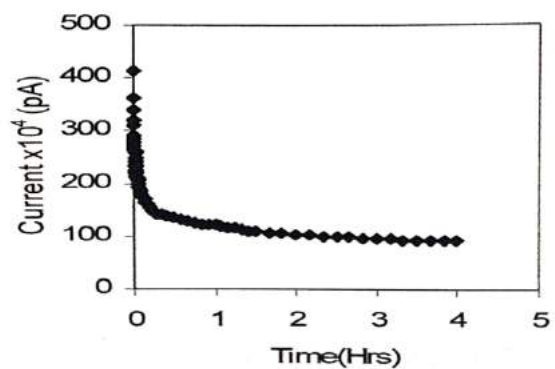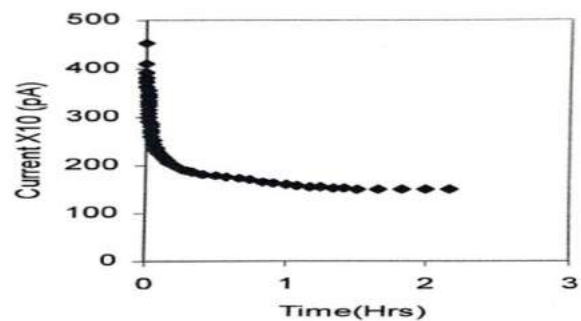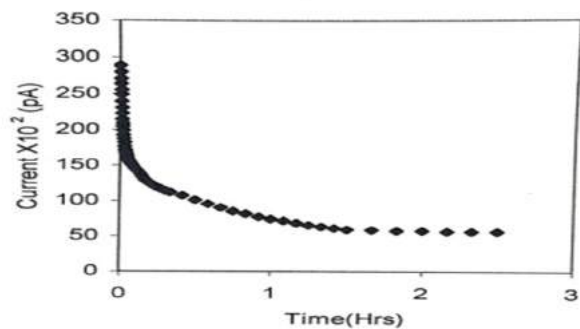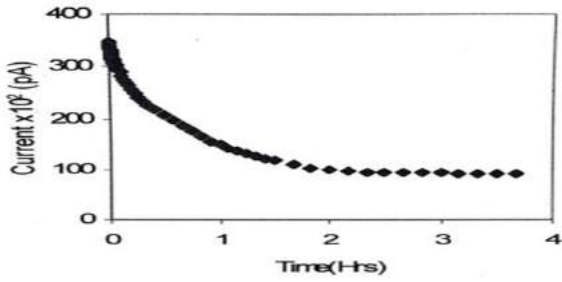

Fig. 2 (a)

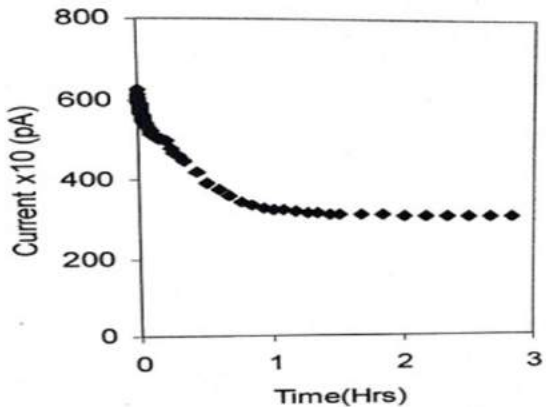Fig. 2 (b)

Fig. 2 (c)

Fig. 2 (d)

Fig. 2 (e)

Fig. 2 Polarization current as a function of time for different FeCl3 wt % films

From figure 2, it is observed that, the total current becomes nearly almost constant at some non-zero value after some time. The final residual current is mainly due to electrons/holes. The ionic and electronic transference numbers were calculated separately from the polarization current versus time plots using equations (1) and (2). Transference numbers for different FeCl$_3$ concentrations are given in the following table 1.

Table 1: Ionic transference number for different FeCl$_3$ wt %

Sr. No.	FeCl$_3$ wt %	Ionic transference number (t_{ion})
1	10	0.51
2	20	0.67
3	25	0.77
4	30	0.73
5	40	0.80

The variation of transference number with concentration of FeCl$_3$ is shown in figure 3.
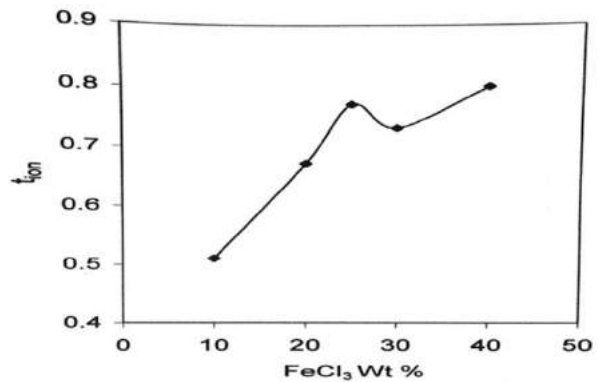

Fig. 3 Variation of transference number with FeCl3 wt %

The values of transference number increase with the increase in concentration of FeCl3. For 10 wt % FeCl3 transference number is 0.51, while for 40 wt % it becomes 0.80. This suggests that the charge transport in the PPY-PVAc composite, synthesized with higher concentration of FeCl3 is predominantly due to ions. While for the films with low concentration of FeCl3 shows both ionic and electronic charge transport. Initially ionic transference number (tion) increases with FeCl3 concentration due to increase of ion concentration in PPY-PVAc composite. For further increase in FeCl3 concentration ionic transference number decreases. This may be due to decrease in ionic mobility, which depends on segmental motion of polymer chain. Due to higher concentration of FeCl3, PVAc – FeCl3 complex become more rigid which ultimately reduces the segmental motion.

IV.CONCLUSION

PPY-PVAc composites were synthesized by chemical oxidative polymerization of pyridine by different wt % of oxidizing agent FeCl$_3$. The transference number study results that the charge transport in PPY-PVAc composite is predominantly due to ions for higher

$FeCl_3$ wt %. For further increase in $FeCl_3$ concentration ionic transference number decreases. This may be due to decrease in ionic mobility, which depends on segmental motion of polymer chain.

V. REFERENCES

[1]. T. J. Skotheim (Ed.), Handbook of conducting polymers, Marcel Dekker, NewYork, 1986.

[2]. W. S. Barde, S. V. Pakade , S. P. Yawale, J. Non-Cryst. Solids (2007).

[3]. V. Mano, M. I. Felisberti, T. Malencio, A. Macro, De Paoli, Polymer 37 (1996)5165.

[4]. R. Gangopadhyay, A. Das, J. Appl. Phys., 87 (2000) 2363.

[5]. V. Jousseaume, M. Morsli, A. Bonnet, D. Tesson, S. Lefrant, J. Polym. Sci. Polym. Chem. Ed.67 (1998) 1205.

[6]. Komilla Suri, S. Annapoorni, R. P. Tondon, Bull. Mater. Sci., 24 (2001) 563.

[7]. Eli Ruckenstein, Shiyang Yang, Polymer 34 (1993) 4655.

[8]. H. Vogel, Phys. Z. 22 (1922) 645.

[9]. G. S. Fulcher, J. Am. Chem. Soc., 8 (1925) 339.

[10]. G. Tamman, W. Hesse, Z. Anorg, Allg. Chem., 156 (1926) 245.

[11]. J. B. Wagner Jr., C. Wagner, J. Chem. Phys., 26 (1957) 1597.

Solving Transportation Problems Solve Using Various New Approch Method

Dr. Janardhan K. Mane

Department of Mathematics Sanjeevanee Mahavidyalaya, Chapoli, Tq. Chakur Dist. Latur (M.S), India

ABSTRACT

In this paper, we study the optimization processes in Mathematics, Computer Science and Economics are solving effectively by choosing the best element from set of available element. Finding an initial basic feasible solution to obtain an optimal solution for the Transportation Problems. The most importance and successful application in the optimization refers to Transportation Problem. The main objective of Transportation Problem solution method is to minimize the cost or the time of transportation. Most of the currently use methods for solving is to transportation problem are trying to reach the optimal solution, the method is also illustrated with numerical examples.

Keywords: - Transportation Problem, Transportation Cost, Optima Solution, Solving Optimization, Initial Basic Feasible Solution and Objective Function.

I. INTRODUCTION

Transportation problem was first studied by F.L. Hithcock[1]. In transportation problem, different sources supply to different destinations of demand in such a way that the transportation cost should be minimized Transportation problem is famous in operation research for its wide application in real life. This is a special kind of the network optimization problems in which goods are transported from a set of sources to a set of destinations subject to the supply and demand of the source and destination, respectively, such that the total cost of transportation is minimized. The basic transportation problem was originally developed by Hitchcock in 1941. Efficient methods for finding solution were developed, primarily by Dantzig in 1951 [2] and then by Charnes, Cooper and Henderson in 1953 [3]. Basically, the solution procedure for the transportation problem

❖ consists of the following phases:

Phase 1: Mathematical formulation of the transportation problem.
Phase 2: Finding an initial basic feasible solution.
Phase 3: Optimize the initial basic feasible solution which is obtained in Phase 2.

1. The level of supply at each source and the amount of demand at each destination.
2. The unit transportation cost of the commodity from each source to each destination.

Since there is only one commodity, a destination can receive its demand from more than one source. The objective is to determine how much should be shipped from each source to each destination so as to minimize the total transportation cost.
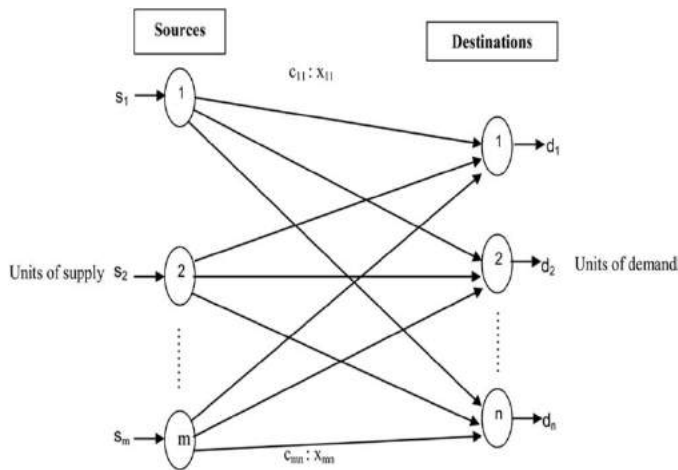
Fig. Network representation of transportation problem

This figure represents a transportation model with m sources and n destinations. Each source or destination is represented by a node. The route between a source and destination is represented by an arc joining the two nodes. The amount of supply available at source I is a_i, and the demand required at destination j is b_j. The cost of transporting one unit between source i and destination j is c_{ij}.

As shown by Figure 1, the problem is to determine an optimal transportation scheme that is to minimize the total of the shipments cost between the nodes in the network model, subject to supply and demand constraints. As well as, this structure arises in many applications such as; the sources represent warehouses and the sinks represent retail outlets.

II.   METHODS AND MATERIAL

Mathematical Formulation

Distribution Assumptions

i is the source index for all $i = 1,\ldots,m$

j is the destination index for all $j = 1,\ldots,n$

Let x_{ij} denote the quantity transported from source i to destination j. The cost associated with this movement is cost $\times$ quantity $= c_{ij}x_{ij}$. The cost of

transporting the commodity from source i to all destinations is given by

$$\sum_{j=1}^{n} c_{ij}x_{ij} = c_{i1}x_{i1} + c_{i2}x_{i2} + \cdots\ldots\ldots +c_{in}x_{in}$$

Thus, the total cost of transporting the commodity from all the sources to all the destinations is

Total Cost $= \sum_{i=1}^{m} \Sigma_{j=1}^{n} c_{ij}x_{ij}$

$= \qquad c_{11}x_{11} + c_{12}x_{12}\ldots\ldots +c_{1n}x_{1n} + c_{21}x_{21} + c_{22}x_{22}\ldots\ldots +c_{2n}x_{2n+} \vdots c_{m1}x_{m1} + c_{m2}x_{m2}\ldots\ldots +c_{mn}x_{mn}$

In order to minimize the transportation costs, the following problem must be solved:

Minimise

$$z = = \sum_{i=1}^{m} \Sigma_{j=1}^{n} c_{ij}x_{ij}$$

subject to $\Sigma_{j=1}^{n} x_{ij} \leq a_i$ for i = 1,…,m and $\Sigma_{i=1}^{m} x_{ij} \geq b_j$ for j = 1,…,n

where $x_{ij} \geq 0$ for all i and j.

The first constraint says that the sum of all shipments from a source cannot exceed the available supply. The second constraint specifies that the sum of all shipments to a destination must be at least as large as the demand. The above implies that the total supply $\Sigma_{i=1}^{m} a_i$ is greater than or equal to the total demand$\Sigma_{j=1}^{n} b_j$. When the total supply is equal to the total demand then the Transportation model is said to be balanced. In a balanced transportation model, each of the constraints is an equation:

$\Sigma_{j=1}^{n} x_{ij} = a_i$ for i = 1,……..,m

$\Sigma_{i=1}^{m} x_{ij} = b_j$ for j = 1,…,n

A transportation model in which the total supply and total demand are unequal is called Unbalanced. It is always possible to balance an unbalanced transportation problem.

Algorithms for solving: there are several algorithms for solving transportation problems which are based on different of special linear programming methods, among these are:

1.   Northwest Corner method

2. Minimum cost method
3. Genetic algorithm
4. Vogel's approximation method
5. Row Minimum Method
6. Column Minimum Method

Basically, these methods are different in term of the quality for the produced basic starting solution and the best starting solution that yields smaller objective value. In this study, we used the Vogel's approximation method, since it generally produces better starting solutions than other solving methods; as well we have used the BCM solution steps [8].

Vogel's Approximation Method (VAM):

Generally, VAM can be summarized by the following three main steps [9]:

i. The result of subtracting the smallest unit cost element in the row/column (cell) from the immediate next smallest unit cost element in the same row/column is determining a penalty measure for the target row/column.

ii. This step includes the following sub-steps:
   a. Identify the row or the column that includes the largest penalty.
   b. Break ties arbitrarily.
   c. As much as possible, the lowest cost row/column (cell) in the row or column should be allocated with the highest difference.
   d. Adjust the supply and demand, and then cross out the satisfied row or column.
   e. If a row and column are satisfied simultaneously, then only one of them is crossed out, as well the remains rows or columns are assigned to supply as zero (demand).

iii. Finally, the result should be computed as follows:
a. If a row or a column is assigned as zero supply, or demand remains uncrossed out, then stop the process.
b. If one row/column with positive supply (demand) remains uncrossed out, then

determine the basic variables in the row/column by the lowest cost method, and then stop.

c. If all the uncrossed out rows and columns have (remaining) zero supply and demand then determine the zero basic variables by the lowest cost method and stop.

d. Otherwise, go to step (i).

The Best Candidates Method (BCM):

BCM process includes three steps, these steps are shown as follows [8]:

➢ Step1: Prepare the BCM matrix, If the matrix unbalanced, then the matrix will be balanced without using the added row or column candidates in solution procedure.

➢ Step2: Select the best candidates, that is for minimizing problems to the minimum cost, and Maximizing profit to the maximum cost. Therefore, this step can be done by electing the best two candidates in each row. If the candidate repeated more than two times, then the candidate should be elected again. As well as ,the columns must be checked such that if it is not have candidates so that the candidates will be elected for them. However, if the candidate is repeated more than one time, the elect it again.

➢ Step3: Find the combinations by determining one candidate for each row and column, this shoud
be done by starting from the row that have the least candidates, and then delete that row and column. If there is situation that has no candidate for some rows or columns, then directly elect the best available candidate. Repeat Step 3 by determining the next candidate in the row that started from. Compute and compare the summation of candidates for each combination. This is to determine the best combination that give the optimal solution.

III. RESULTS AND DISCUSSION

3. PROPOSED METHOD

In this study, we proposed a new solving method for transportation problems by using BCM. The proposed method must operate the as following:

➢ Step1: We must check the matrix balance, If the total supply is equal to the total demand, then the matrix is balanced and also apply Step 2. If the total supply is not equal to the total demand, then we add a dummy row or column as needed to make supply is equal to the demand. So the transportation costs in this row or column will be assigned to zero.

➢ Step2: Appling BCM to determine the best combination that is to produce the lowest total weight of the costs, where is one candidate for each row and column.

➢ Step3: Identify the row with the smallest cost candidate from the chosen combination. Then allocate the demand and the supply as much as possible to the variable with the least unit cost in the selected row or column. Also, we should adjust the supply and demand by crossing out the row/column to be then assigned to zero. If the row or column is not assigned to zero, then we check the selected row if it has an element with lowest cost comparing to the determined element in the chosen combination, then we elect it.

➢ Step4:Elect the next least cost from the chosen combination and repeat Step 3 until all columns and rows is exhausted.

Types of Transportation Problem in Operation Research

The transportation problem is classified into two types. They are balanced transportation problem and unbalanced transportation problem. If the number of sources is equal to number of demands, then it is called balanced transportation problem. If not, it is called unbalanced transportation problem. If the source of item is greater than the demand, then we should add dummy column to make the problem as balanced one. If the demand is greater than the source, then we should add the dummy row to convert the given unbalanced problem to balanced transportation problem.

1. Balanced Transportation Problem
2. Unbalanced Transportation Problem

Algorithm:

➢ **Step 1:** Check whether the given transportation problem is balanced or not. If not, balance or by adding dummy row or column. Then go to the next step.

➢ **Step 2:** Find the harmonic mean for each row and each column. Then find the maximum value among that.

➢ **Step 3:** Allocate the minimum supply or demand at the place of minimum value of the related row or column.

➢ **Step 4:** Repeat the step 2 and 3 until all the demands are satisfied and all the supplies are exhausted.

➢ **Step 5:** Total minimum cost = sum of the product of the cost and its corresponding allocated values of supply or demand.

TRANSPORTATION PROBLEM AND ITS APPLICATIONS IN OPERATION RESEARCH

Transportation problem arises in various applications of Sample Surveys and Operation Research. For details see [10]. The cost matrices associated with these transportation problems are of special structure. Now, we raise the following question. What is the structure of the cost matrix for which North West corner solution produces an optimal solution? We consider some of the structures of the cost matrix which arise in some of the applications in the literature. Ho_man [11] studied transportation problem in the context of North West Corner Rule. Burkard et al. [12] mentioned Monge properties in connection with the transportation problem. Szwarc [13] developed direct methods for solving transportation problems with cost coefficient of the

form $c_{ij} = x_i + x_j$ having applications in shop loading and aggregate scheduling.

Example 1. Balanced Transportation Problem

Consider the following problem with 4 Company and 6 products:

	product	product	product	product	product	product	Supply
Company	c_{11}	c_{12}	c_{13}	c_{14}	c_{15}	c_{16}	8
Company	c_{21}	c_{22}	c_{23}	c_{24}	c_{25}	c_{26}	12
Company	c_{31}	c_{32}	c_{33}	c_{34}	c_{35}	c_{36}	15
Company	c_{41}	c_{42}	c_{43}	c_{44}	c_{45}	c_{46}	5
Demand	4	12	9	8	7	10	

Total supply = 08+12+15+05 = 40

Total demand = 04+12+09+08+07+10 = 40

= Total supply

Since Total supply = Total demand, the problem is balanced.
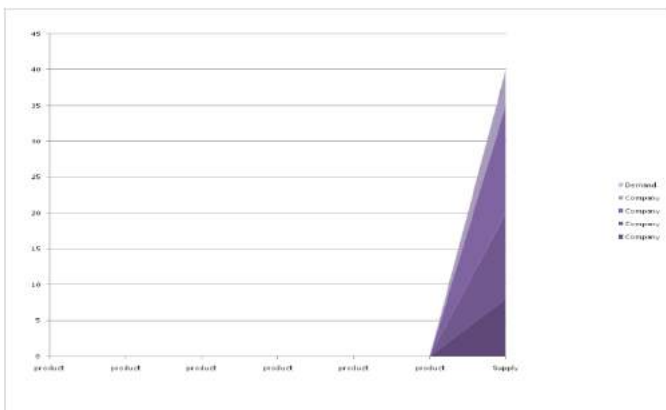
Unbalanced Transportation Problem

Total quantity available ≠ total quantity required

i.e., Total supply ≠ Total demand

The total quantity available at all the sources is equal to the total quantity required the destinations. If they do not match each other, dummy sources or dummy destination are added to make it a standard transportation problem.

There are 2 situations leading to this unbalanced condition

(i). Total Supply > Total Demand

(ii). Total supply < Total demand

(I). Total Supply > Total Demand

I.e., the total quantity available > total quantity required

Example 1. Unbalanced Transportation Problem

	product	product	product	product	product	product	Supply
Company	c_{11}	c_{12}	c_{13}	c_{14}	c_{15}	c_{16}	8
Company	c_{21}	c_{22}	c_{23}	c_{24}	c_{25}	c_{26}	12
Company	c_{31}	c_{32}	c_{33}	c_{34}	c_{35}	c_{36}	15
Company	c_{41}	c_{42}	c_{43}	c_{44}	c_{45}	c_{46}	10
Demand	4	12	9	8	7	10	

Total supply = 08+12+15+10 = 45

Total demand = 04+12+09+08+07+10 = 40

Since Total supply ≠ Total demand, the problem is Unbalanced.
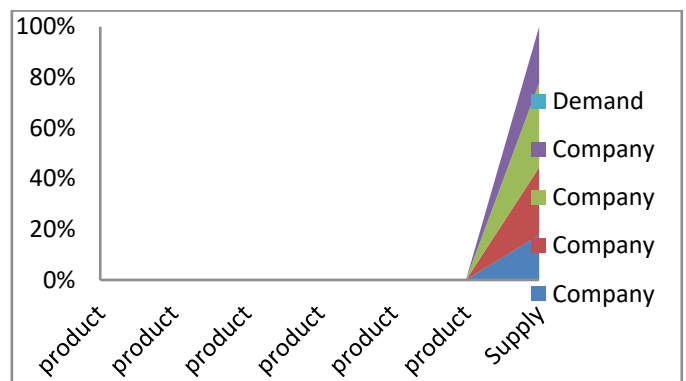
IV.CONCLUSION

At the outset this paper considers some structured transportation problems which arise in sample surveys and other areas of Operation Research. Explain the various methods in transportation problem. In today's highly competitive market, various organizations want to deliver products to the customers in a cost effective way, so that the market becomes competitive. To meet this challenge, transportation model provides a powerful framework to determine the best ways to deliver goods to the customer and also Most of the currently use methods for solving is to transportation problem are trying to reach the optimal solution, the method is also illustrated with numerical examples.

V. REFERENCES

[1]. Hitchcock, F.L. (1941) The Distribution of a Product from Several Sources to Numerous Localities. Journal of Mathematics and Physics, 20, 224-230. http://dx.doi.org/10.1002/sapm1941201224

[2]. Dantzig, G.B. (1951) Application of the Simplex Method to a Transportation Problem, Activity Analysis of Production and Allocation. In: Koopmans, T.C., Ed., John Wiley and Sons, New York, 359-373.

[3]. Charnes, A., Cooper, W.W. and Henderson, A. (1953) An Introduction to Linear Programming. John Wiley & Sons, New York.

[4]. P.K. Gupta and D.S. Hira, Operations Research, New Delhi:S. Chand and Company LTD, 2008.

[5]. H.A. Taha, Operations Research An Introduction, USA.:Macmillan Publishing, a division of Macmillan, Inc., 2007.

[6]. Prof. Reena. G. Patel, Dr. P.H. Bhathawala. (2014), The New Global Approach to a Transportation Problem, International Journal of Engineering Technology, Management and Applied Science, vol. 2 Issue3, pp. 109-113.

[7]. Appa, G., "The transportation problem and its variants", Journal of the Operational Research Society, 24(1) (1973) 79–99.

[8]. Dantzig, G.B. (1951) Application of the Simplex Method to a Transportation Problem, Activity Analysis of Production and Allocation. In: Koopmans, T.C., Ed., John Wiley and Sons, New York, 359-373.

[9]. Khan, A.R. (2011) A Re-Solution of the Transportation Problem: An Algorithmic Approach. Jahangirnagar University Journal of Science, 34, 49-62.

[10]. Arthanari, T. S., "Optimization in Statistics-Recent Trends", in Compstat, pp. 171–176, Springer, Berlin, 1990.

[11]. Ho_man, A. J., "On simple linear programming problems", Selected Papers Of Alan J Ho_man: With Commentary, pp. 317–327, World Scientific, 2003.

[12]. Burkard, R. E., Klinz, B., and Rudolf, R., "Perspectives of Monge properties in optimization", Discrete Applied Mathematics, 70(2) (1996) 95–161.

[13]. Szwarc, W., "Instant transportation solutions", Naval research logistics quarterly, 22(3) (1975) 427–440.

Photo Luminescent Properties of Dysprosium-Dy³⁺ Doped Ba₃Y(BO₃)₃ Phosphor

Sanjay P. Hargunani[1*], Rajkumar P. Sonekar[1], Ravindra Chavhan[1], Sanjay J. Dhoble[2]

[1*]Physics Department, G. S. Science, Arts and Commerce College, Khamgaon, Maharashtra, India

[2]Department of Physics R.T.M. Nagpur University Nagpur, Maharashtra, India

ABSTRACT

$Ba_3Y_{1-x}(BO_3)_3:xDy^{3+}[\ 0.005 \le x \le 0.03\ ]$ phosphor is synthesized by solution combustion method. Photo-luminescence in the range 400nm to 700nm is recorded which shows two major peaks at 485nm $[^4F_{9/2} - {}^6H_{15/2}]$, 575nm $[^4F_{9/2} - {}^6H_{13/2}]$ and minor peak at 622nm ${}^4F_{9/2} - {}^6H_{11/2}$. Under UV excitation of 349nm it shows white luminescence. Intensity ratio of Blue line of 485nm to yellow line of 575nm is calculated which also confirms the emission of near white light. The optimal doping concentration of Dy^{3+} in $Ba_3Y_{1-x}(BO_3)_3$ host matrix is found to be 2 mole percentage. The 1931-CIE color coordinates and the CCT value of phosphor is also calculated using McCamy empirical formula. All the results indicate that Dy^{3+} doped $Ba_3Y_{1-x}(BO_3)_3$ powder phosphor could be used as an efficient luminescent material for solid state lighting as well as NUV based w-LEDs.

Keywords:- Photoluminescence, White Light Emitting Diodes, Solution Combustion Synthesis

I. INTRODUCTION

Dy^{3+} ion has been extensively studied to generate white light in various hosts like oxides, silicates, aluminates, alumininoborates, aluminisilicates, nitrides, borates, etc. due to its two main emission bands the blue band (455–500 nm) due to the magnetic dipole transition and the yellow band (570–600 nm) due to the electric dipole transition. In most cases trivalent dysprosium ion (Dy^{3+})-doped phosphors shows intense blue (455-490nm) and yellow (570-590nm) emissions and generate white-light emission. As a result white light can be obtained by balancing the ratio of blue to yellow emissions. The yellow emission of Dy^{3+} is dependent to the local environment in crystal, and the blue emission of Dy^{3+} is not very sensitive to the local environment. Owing the high sensitivity property to the local environment, Dy^{3+} can be used to probe the crystal structure of the host lattice. A white light emission with proper correlated color temperature (CCT) and chromaticity coordinates can be achieved by suitable adjustment of the yellow/blue (Y/B) intensity ratio of Dy^{3+}-doped phosphors. Because of this, Dy^{3+}-doped host lattices can be develop as a single host phosphor as source of white light in light emitting diodes[1].Poor color rendering index and high CCT are the drawbacks of blueInGaN LED chip and YAG:Ce3+ yellow phosphors used for white light emitting diodes. So research on new blue and yellow phosphors which balances the red component in white light emission is going on[2,3]. In recent years, many phosphors doped with Dy^{3+} have been reported, such as SrGa12O19: Dy3+ [4], LaB3O6:Dy3+[5], KBaY(BO3) 2: Ce3+, Dy3+ [6], Ba2CaZn2Si6O17:Dy3+ [7], Li4CaB2O6: Dy3+ [8]. Li4CaB2O6: Dy3+ [9] etc.

II. METHODS AND MATERIAL

Powder samples of $Ba_3Y_{1-x}(BO_3)_3:xDy^{3+}$[$0.005 \leq x \leq 0.03$] were synthesized by a modified exothermic solution combustion method. In the SCS, nitrate solution of A.R. grade [99.9% purity] precursors [$Ba(NO_3)_2,Y(NO_3)_3,H_3BO_3,Dy(NO3)3·xH2O$] in the stoichiometric amount was used as an oxidizer while $NH_2CONH_2$is a fuel for combustion [10,11]. In deionized water paste of all precursors is made and then kept in preheated furnace at 680°C. The paste boiled - ignited within a few minutes and develops a self-propagating yellow-orange flame for4 to 5 minutes.To ensure the complete decomposition of chemicals and for proper phase of phosphor the crucible is kept in furnace for 20 minutes.After removing crucible from the furnace it cooled to room temperature and grinded into fine powder.The synthesized powder phosphor were post annealed at 950⁰C for 3 hours in a muffle furnace in air.

III. RESULTS AND DISCUSSION

3.1 XRD:-The formation of the phosphor in desired crystallographic phase was determined by powder XRDrecorded by X-ray diffraction using the Cu-Kα wavelength (λ= 1.54060 Å) and scanning in the 2θ range from 20°–80°. Figure (1) shows the powder XRD pattern of the phosphor $Ba_3Y_{1-0.02}(BO_3)_3:0.02Dy^{3+}$. It is in agreement with standard pattern given in ICSD File NO. 39744 and standard JCPDS file no 51-1849.This host crystal compound has two phases i.e. low temperature phase α-$Ba_3Y(BO_3)_3$andhigh temperature β-$Ba_3Y(BO_3)_3$[12   ]. XRD pattern of synthesized phosphor matches with the standard low temperature phase.Few extra peaks at 68.92° and75.94° are present in the XRD.Low temperatureα-$Ba_3Y(BO_3)_3$ phosphor possess hexagonal crystal structure with the space group $P6_3$ cm (No.185)[13]. All B^{3+} are co-ordinated with three O^{2-} forming the BO_3^{3-} triangles. Y and Ba sites are separated by parallel planes constructed by BO_3^{3-} anion group. All Ba sites has the 9 co-ordination number. All Y^{3+} ions has the 6 co-ordination number. As shown in figure (2) crystal structure comprised of isolated BO_3 triangles; YO_6 octahedral and BaO_4polyhedral. $Ba_3Y(BO_3)_3$ possess layer structure of BO_3 triangles[14]. Cell parameters are a=b=9.419A°; c= 17.590A°;V=1352.67A°³.
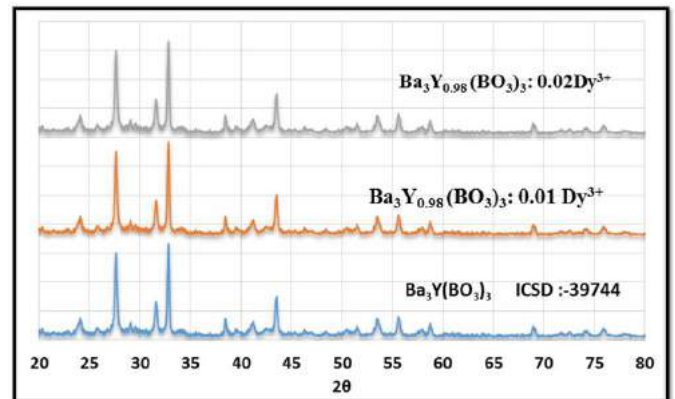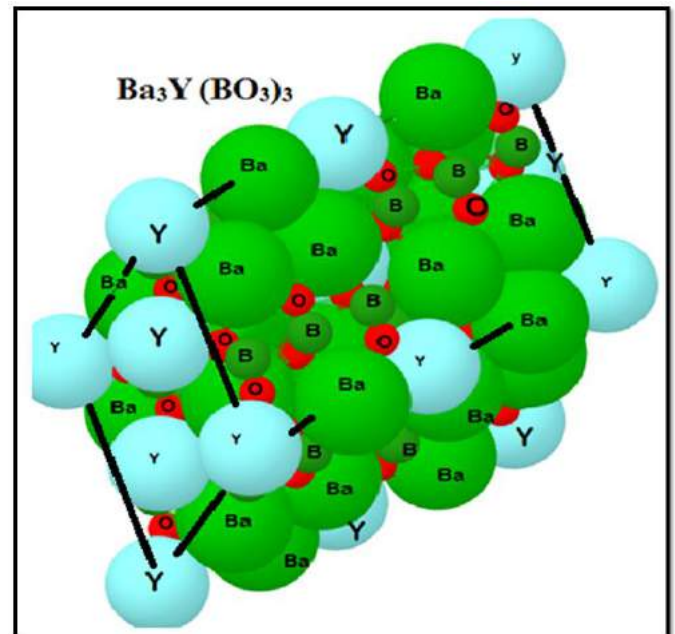

Figure [1] X-ray diffraction $Ba_3Y_{1-0.02}(BO_3)_3:0.02Dy^{3+}$

3.2 SEM-EDS:-

SEM micrographs of $Ba_3Y(BO_3)_3:0.02Dy^{3+}$ given in figure(3)shows that powder phosphor is made of a network of agglomerated irregular particles. The surface consists of voids due to large gaseous matter that escaped due to high exothermicity during combustion process. SEM micrographs of $Ba_3Y(BO_3)_3:0.02Dy^{3+}$powder phosphors were

recordedat 20KV X 10000; 20KV X 20000; 20KV X 30000; 20KV X 55000 magnifications. Elemental composition of powder phosphor is studied using EDS along with SEM. EDS Spectrum given in figure(4) confirms the presence of Barium (Ba), Yettrium(Y),Boron(B),Oxygen(O), and Dysperium (Dy) elements.
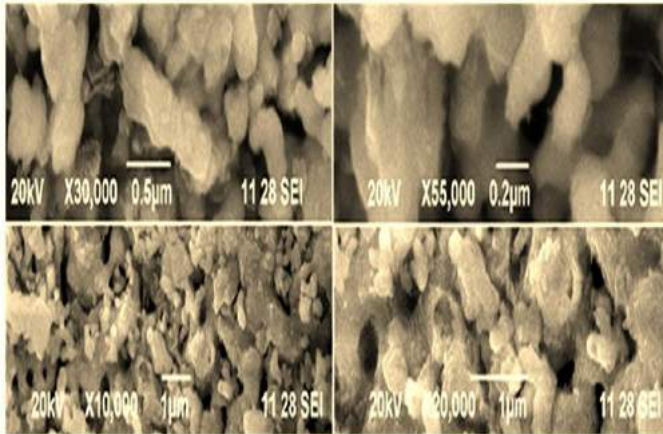

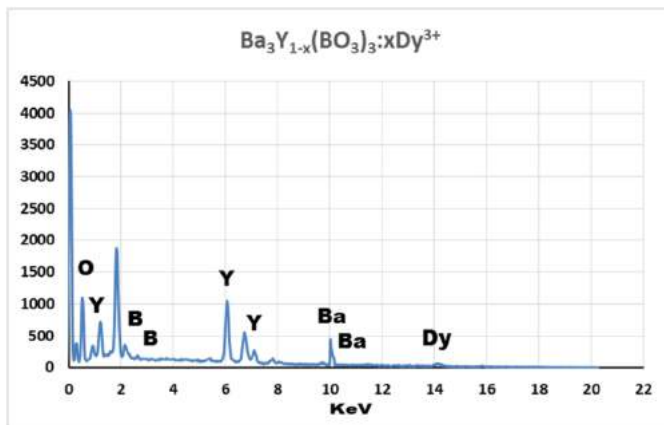Figure 2 SEM images of Ba3Y(BO3)3:0.02Dy3+ at different resolution

Figure 3 EDS of Ba3Y(BO3)3:0.02Dy3+

3.3 FTIR:-To confirm the coordination environment of B-O in $Ba_3Y(BO_3)_3$structure, the IR spectra of $Ba_3Y(BO_3)_3$were recordedat room temperature & shown in Figure(5). The FTIR spectrum exhibit broad absorptions in the 650 - 1600 cm^{-1} range. All the bands in the 1200 - 1600 cm^{-1} range correspond to the stretching of the B–O bonds of BO_3 units. The bands in the region of 800 - 1200 cm^{-1} correspond to the B–O bond stretching of tetrahedral BO_4 units. All the bands below 800 cm^{-1} correspond to the B–O–B bending vibrations of borate networks. The peak at

3300-3500 cm^{-1} corresponds the stretching mode of O–H are also absent. The absence of peaks in 1500- 2000 cm^{-1} indicates the complete residual of nitrate and organic matter. Comparing the FTIR spectra of $Ba_3Y(BO_3)_3$ and that of $Ba_3Y(BO_3)_3$:0.02Dy^{3+} , $Ba_3Y(BO_3)_3$:0.03Dy^{3+}, $Ba_3Y(BO_3)_3$:0.04Dy^{3+} , it was observed that there is no change in the FTIR spectrum structure, and only difference in intensity was observed. It can be concluded that incorporating different dopant ions in the $Ba_3Y(BO_3)_3$ host matrix did not influence the main structure or form any type of bonds in the development of the powder phosphors, which is in agreement with the XRD spectra.
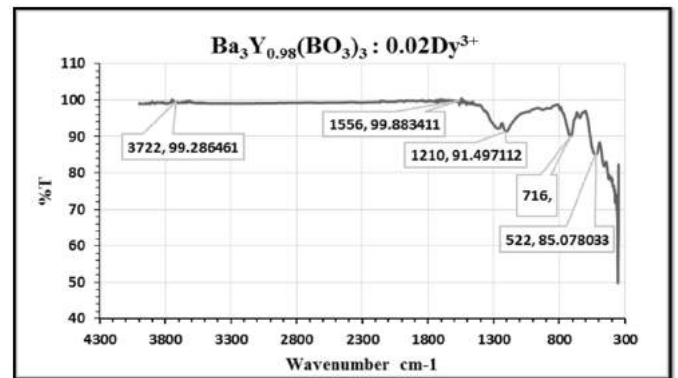

Figure 4 FTIR of Ba3Y(BO3)3:0.02Dy3+

3.4 Photo-Luminescence study:-

PL-PLE spectra of $Ba_3Y_{0.98}(BO_3)_3$:0.02Dy^{3+} phosphor was measured at room temperature and shown in figure(6). PLE spectra monitored at 485nm luminescence exhibit intense absorption peak for 349nm because of $^6H_{15/2} \to {}^6F_{9/2}$ transition of Dy^{3+} in host crystal.PLE spectra also shows less intensity multiple peaks at 324nm, 364nm and 387nm. PL spectra was measured in the range 450nm -680nm for 349nm near UV excitation. In PL three major peaks was present at 485nm, 575nm and 622nm. $^4F_{9/2} \to {}^6H_{15/2}$magnetic dipole transition of Dy^{3+}independent of surrounding crystal fieldproduce blue emission line at 485nm.Crystal field hypersensitive $^4F_{9/2} \to {}^6H_{13/2}$electric dipole transition of Dy^{3+}produce yellow line at 575nm.Disordered crystal field transition $^4F_{9/2} \to {}^6H_{11/2}$of Dy^{3+}produce near red

spectral line at 622nm.Ratio of intensities of 485nm to 575nm spectral line is 1.28, which results in near white light emission from the material. So $Ba_3Y_{0.98}(BO_3)_3$:$0.02Dy^{3+}$phosphor is NUV excited white light emitting phosphor.

According to Judd-Ofelt theory when Dy^{3+} take low symmetry local site without inversion symmetry in host crystal the $^4F_{9/2} \rightarrow {}^6H_{13/2}$electric dipole transitionresulting in yellow emission will be dominant in PL spectra[15]. In this phosphor blue emissionat485nm which is independent of Dy^{3+} surrounding crystal field is prominent. Yellow emission line decide the color correlated temperature of phosphor and generate white light. The effect of Dy^{3+} concentration on photo luminescent property of $Ba_3Y_{1-x}(BO_3)_3$:xDy^{3+} is shown in figure(7). At all concentrations of Dy^{3+} position of PL peaks is at the same wavelength and only intensity changes. At 2mole% weight of Dy^{3+} intensity of PL-PLE line is maximum and above it intensity decreasesi.e. concentration quenching occurs.Figure (8) shows concentration quenching curve. As concentration of Dy^{3+} increases the probability of non radiative energy transfer among them increases leading to decrease in PL intensity.Critical distance Rcamong Dy^{3+} ions will decide the type of interaction i.e. an exchange, radiation reabsorption or multipole-multipole leading to concentration quenching.
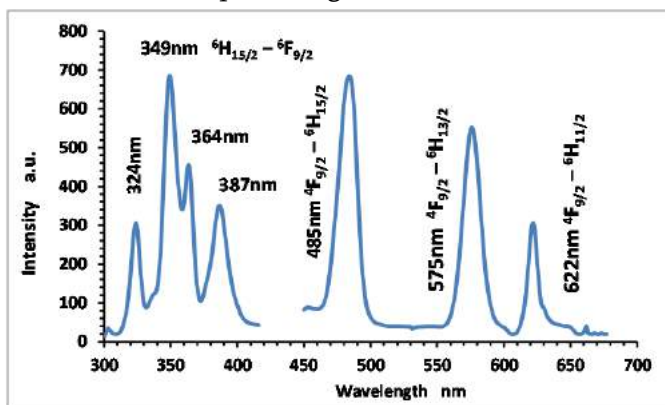

Figure 5PL-PLE of Ba3Y0.98(BO3)3:0.02Dy3+

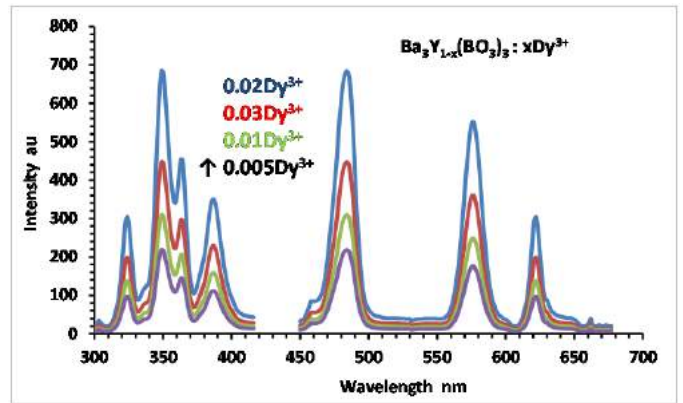

Figure 6 PL-PLE OF Ba3Y1-x(BO3)3:xDy3+
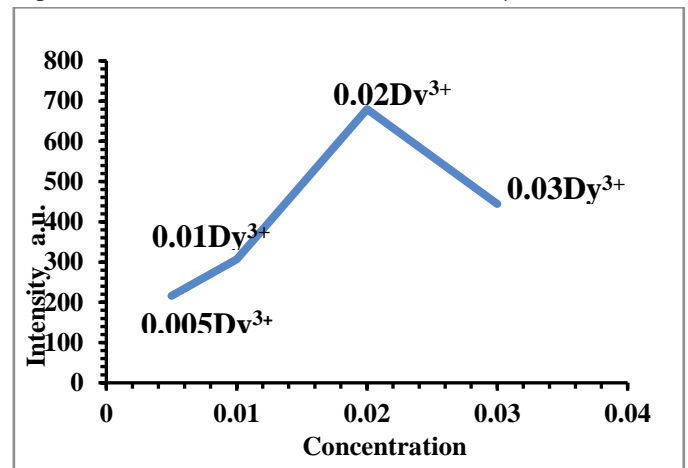
Figure 7 Concentration quenching curve of Ba3Y1-x(BO3)3:xDy3+

3.5 CIE-Chromaticity Diagram:-The Commission International de l'Eclariage (CIE-1931) chromaticity is an important system for checkingcolors of phosphors[16]. Figure(9) shows 1931-CIE chromaticity co-ordinates diagram of phosphor $Ba_3Y_{1-x}(BO_3)_3$:xDy^{3+}.The 1931-CIEco-ordinates of $Ba_3Y_{0.98}(BO_3)_3$:$0.02Dy^{3+}$phosphor are X=0.410,Y=0.380and lie in the white region but away from ideal same intensity white light illumination (X=0.333, Y=0.333). CIE- co-ordinates of $0.005Dy^{3+}$.and $0.03Dy^{3+}$ dopedphosphor are the yellowish-white region. 0.04Dy3+ and 0.01Dy3+ phosphor are in radish-white region of 1931-CIE diagram.The color quality of white light in terms of color correlated temperature (CCT) is given by the McCamy empirical formula [17].

$$CCT = -437\,n^3 + 3601\,n^2 - 6861\,n + 5514.31$$

Where n is the inverse slope line having value, n = (X-Xe) / (Y-Ye). Here (X,Y) are CIE-co-ordinates and (Xe=0.332,Ye=0.186) co-ordinates of epicenter.

Lamps with CCT value below 3200K are considered as Warmth sources and having value more than 4000K are considered Cool sources of light in appearance. For each phosphor CCT value and CIE- co-ordinates are given in table (1).

Table 1 CCT value and CIE- co-ordinates of synthesized phosphor

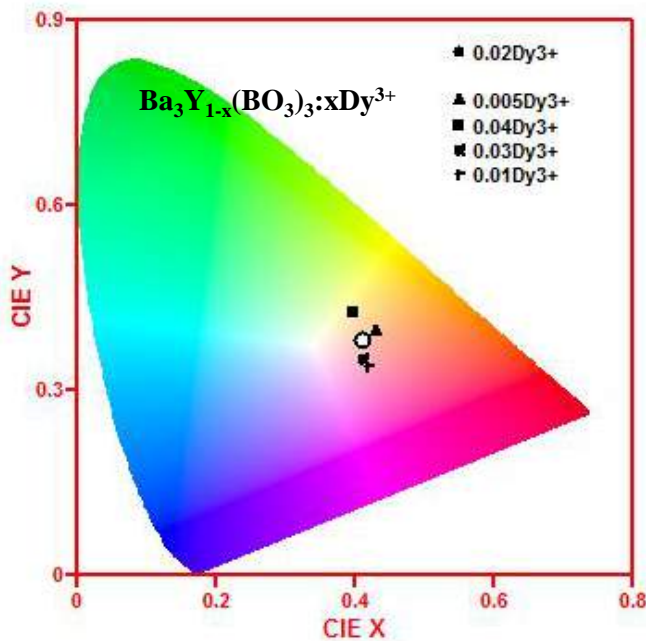| $Ba_3Y_{1-x}(BO_3)_3:xDy^{3+}$	CIE-Co-ordinates (X,Y)	CCT
0.005 Dy^{3+}	(0.430,0.395)	3043.877892
0.01 Dy^{3+}	(0.420,0.340)	2688.035948
0.02 Dy^{3+}	(0.410,0.380)	3309.475983
0.03 Dy^{3+}	(0.410,0.350)	3018.699669
0.04 Dy^{3+}	(0.398,0.425)	3885.047021

Figure 8 CIE-Chromaticity diagram of Ba3Y1-x(BO3)3:xDy3+

IV. CONCLUSION

$Ba_3Y_{1-x}(BO_3)_3:xDy^{3+}$ phosphors doped with different concentrations of Dy^{3+} ions were prepared by the solution combustion method in air. The crystalline structure, excitation, emission properties of the phosphors were characterized by XRD and photoluminescence spectrophotometry, respectively. The PLE spectrum shows that $Ba_3Y_{1-x}(BO_3)_3:xDy^{3+}$ powder phosphor exhibit a strong peak at 349 nm which is acceptable wavelength for w-LEDs. Upon 349 nm excitation, this phosphor shows peaks at 485 nm (blue), 575 nm (yellow) and 622 nm (red). The optimal doping concentration of Dy^{3+} in $Ba_3Y_{1-x}(BO_3)_3$ host matrix was found to be x = 0.02.The 1931-CIE color coordinates for $Ba_3Y_{1-x}(BO_3)_3:xDy^{3+}$ (x = 0.02) phosphor is calculated by LED tuning software to be (0.410,0.380) which falls near the white region with the CCT value of 3309.475983 K. All the results indicate that Dy^{3+} doped $Ba_3Y_{1-x}(BO_3)_3$ powder phosphor could be used as an efficient luminescent material for solid state lighting as well as NUV based w-LEDs.

V. REFERENCES

[1]. Shrivastava, Ravi, Jagjeet Kaur, and VikasDubey. "White light emission by Dy 3+ doped phosphor matrices: A short review." Journal of fluorescence 26, no. 1 (2016): 105-111.

[2]. Y. Narukawa, J. Narita, T. Sakamoto, T. Yamada, H. Narimatsu, M. Sano, T. Mukai, Recent progress of high efficiency white LEDs, Phys. Status Solidi A. 204 (6) (2007) 2087-2093.

[3]. Z.G. Xia, Q.L. Liu, Progress in discovery and structural design of color conversion phosphors for LEDs, Prog. Mater Sci. 84 (2016) 59-117.

[4]. Lai, Junan, Zhangwen Long, JianbeiQiu, Dacheng Zhou, Junhe Zhou, Congcong Zhu, Songhan Hu, Ke Zhang, and Qi Wang. "Warm white light emitting from single composition SrGa12O19: Dy3+ phosphors for AC-LED." Journal of the American Ceramic Society 103, no. 1 (2020): 335-345.

[5]. Wu, Xiao, Chuanxing Jiang, Zijian Liang, Qiang Wang, Junqin Feng, Daoyun Zhu, Shengbiao Pan, Zekai Lin, Defu Tan, and Zhongfei Mu.

"Photoluminescence properties of LaB3O6: Dy3+ phosphors for white light-emitting diodes." Optik (2020): 164877.

[6]. Han, Bing, Yazhou Dai, Jie Zhang, Beibei Liu, and Hengzhen Shi. "Development of near-ultraviolet-excitable single-phase white-light-emitting phosphor KBaY (BO3) 2: Ce3+, Dy3+ for phosphor-converted white light-emitting-diodes." Ceramics International 44, no. 12 (2018): 14803-14810.

[7]. Annadurai, G., S. Masilla Moses Kennedy, and V. Sivakumar. "Synthesis of novel Dy3+ activated Ba2CaZn2Si6O17 phosphors for white light-emitting diodes." Luminescence 33, no. 3 (2018): 521-527.

[8]. Kumar, Vinay, Vivek K. Singh, J. Sharma, O. M. Ntwaeaborwa, and H. C. Swart. "Synthesis and photoluminescence study of a single dopant near white light emitting Li4CaB2O6: Dy3+ nanophosphor." Journal of Alloys and Compounds 688 (2016): 939-945.

[9]. Li, Panlai, Zhiping Yang, Zhijun Wang, and QinglinGuo. "White-light-emitting diodes of UV-based Sr3Y2(BO3)4: Dy3+ and luminescent properties." Materials Letters 62, no. 10-11 (2008): 1455-1457.

[10]. Mimani, T., and K.C.Patil. 2001"Solution combustion synthesis of nanoscale oxides and their composites." Materials Physics and Mechanics (Russia) 4, no. 2 134-137.

[11]. Bajaj, N. S., and S. K. Omanwar.2012 "Combustion synthesis and luminescence characteristic of rare earth activated LiCaBO3." Journal of Rare Earths 30, no. 10: 1005-1008.

[12]. Hargunani, Sanjay P., Rajkumar P. Sonekar, Ritesh S. Palaspagar, PranitaPatil, and Shriniwas K. Omanwar. "Blue Luminescent Phosphor Sr3Y1– X (BO3) 3: XBi3+ for WLED Applications." In Macromolecular Symposia, vol. 387, no. 1, p. 1800184. 2019.

[13]. Hargunani, S. P., R. S. Palaspagar, R. P. Sonekar, and S. K. Omanwar. "Photo-luminescence study of red borate phosphor Sr3 Y1– x (BO3) 3: xEu3+." In AIP Conference Proceedings, vol. 2104, no. 1, p. 030027. AIP Publishing LLC, 2019.

[14]. Kuang, Jinyong, and Yingliang Liu. "White-emitting long-lasting phosphor Sr2SiO4: Dy3+." Chemistry letters 34, no. 4 (2005): 598-599.

[15]. Nagpure, I. M., V. B. Pawade, and S. J. Dhoble. "Combustion synthesis of Na2Sr (PO4) F: Dy3+ white light emitting phosphor." Luminescence 25, no. 1 (2010): 9-13.

[16]. Maggay, Irish Valerie B., and Wei-Ren Liu. "Novel red-emitting Ba3Y (BO3) 3: Bi3+, Eu3+ phosphors for N-UV white light-emitting diodes." Journal of nanoscience and nanotechnology 18, no. 1 (2018): 3-10.

[17]. Kumar, Vinay, Vivek K. Singh, J. Sharma, O. M. Ntwaeaborwa, and H. C. Swart. "Synthesis and photoluminescence study of a single dopant near white light emitting Li4CaB2O6: Dy3+ nanophosphor." Journal of Alloys and Compounds 688 (2016): 939-945.

Wet Chemical Synthesis, Characterization and Biocompatibility Study of Hydroxyapatite Used As Biomaterials

V. G. Thakare[1], V. B. Bhatkar[2], P.A.Wadegaonkar[3], S. K. Omanwar[4]

[1]Department of Physics, SPM College Nandura, Dist: Buldana (MS), India
[2]Department of Physics, Shri Shivaji College, Amravati (MS), India
[3]Department of Biotechnology, SGB Amravati University, Amravati (MS), India
[4]Department of Physics, SGB Amravati University, Amravati (MS), India

ABSTRACT

Calcium phosphate based bioceramics are promising candidates as biomaterials for tissue engineering. The wet chemical method is used for synthesis of hydroxyapatite which is calcium based bioceramic used for orthopaedic and dental applications. This paper discusses the synthesis and characterization of hydroxyapatite which has shown good *in vitro* bioactivities. Hydroxyapatite was synthesized from aqueous solutions that contain calcium nitrate and di-ammonium hydrogen orthophosphate. X-ray diffraction identified HAp as crystalline phase with hexagonal structure. X-Ray diffraction of HAp is in good agreement with the standard of lattice constant a = b = 9.418 Å, c = 6.884 Å with space group P63/m. The Fourier transform infrared spectra of the sintered HAp shows the absorption bands characteristic to hydroxyapatite. Scanning electron microscopy revealed that the surface morphology was spherical with particle sizes in range of micrometer. The hydroxyapatite was evaluated for the biocompatibility characteristics such as antimicrobial activity, cytotoxicity and biodegradation.

Keywords: Hydroxyapatite, Bioceramic, Wet Chemical, Antimicrobial Activity, Cytotoxicity, Orthopaedic.

I. INTRODUCTION

Tissue engineering offers a new approach to regenerate diseased or damage tissues such as bone (Rezaei et al. 2014). The use of bone-substituted materials in the science of biomaterials is an important objective due to their bioactive and biocompatible properties. Calcium phosphates, major components of natural bone, have bioactive and biocompatible properties. Therefore calcium phosphates have been used in an interdisciplinary field of science involving chemistry, biology, medicine, dentistry and geology for over 20 years. Among calcium phosphate ceramics

tri-calcium phosphate ($Ca_3(PO_4)_2$, TCP), tetracalcium phosphate ($Ca_4P_2O_9$, TetCP), and hydroxyapatite ($Ca_{10}(PO_4)_6(OH)_2$, HAp) have been studied for application in medical fields. The only TCP, a resorbable material and HAp, a bioactive ceramic, that induces bone formation on its surface, are mainly used as bone-substituted materials (Cengiz et al. 2008; Dorozhkin et al. 2007; Zhou et al. 2013).

Hydroxyapatite (HAp) ceramics have been recognized as substitute materials for bone and teeth in orthopedic and dentistry field due to their chemical and biological similarity to human hard tissue (Yarosh et al. 2001). More over HAp has been recognized as a

bioactive material having the direct bonding capability to the surrounding tissues therefore it has an excellent biocompatibility with human teeth and bone, making it very attractive for biomedical applications (Quan et al. 2008; Bouyer et al. 2000; Jillavenkatesa et al. 1998 Silva et al. 1997). The greatest potential for bone substitution is shown by materials based on hydroxyapatite (HAp), which can develop tight bonding with bone tissue, exhibits osteoconductive behavior, is stable toward bioresorption, and has no adverse effects on the human organism (Orlovskii et al. 2002).

In literature, so many methods have been reported for synthesizing HAp, including Sol-gel (Dou et al. 2012), co-precipitation reaction (Shen et al. 2010), mechanochemical synthesis (Mostafa et al. 2005), The Chemical precipitation process is the most reported method for preparing HAp particles. This process is simple, low cost and suitable for industrial production. In this research, we have used a simple aqueous precipitation process that could produce HAp crystalline powder at a relatively low temperature, with a fairly short synthesis time. We have also assessed cytotoxicity, antimicrobial and biodegradation behavior of this ceramic. This paper presents the synthesis and characterization of pure crystalline HAp ceramic and their biocompatibility in detail.

II. METHODS AND MATERIAL

2.1. Materials and methods

The hydroxyapatite powders were prepared by a simple aqueous wet chemical method. Calcium nitrate $Ca(NO_3)_2 \cdot 4H_2O$ and di-ammonium phosphate $(NH_4)_2HPO_4$ were dissolved in deionized water at concentrations. Then pH value of the solution was adjusted to 10–11 with an ammonia (NH_4) solution. The $(NH_4)_2HPO_4$ solution was mixed with the $Ca(NO_3)_2$ solution drop by drop under continuous stirring heating at 40^0c. HAp precipitation by the following reaction:

$$10Ca(NO_3)_2 \cdot 4H_2O + 6(NH_4)_2HPO_4 + 8NH_4OH = Ca_{10}(PO_4)_6(OH)_2 + 20NH_4NO_3 + 20H_2O$$
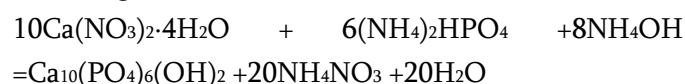
After stirring for 4 h, the precipitates were centrifuged, rinsed with deionized water 3 times, dried at 80^0C for 24 hrs, After drying a dried sample was obtained this was crushed to obtained powders. The powders were then compacted into pellets with the help of die and punch in a hydraulic press at a load of 4 Ton for 90 seconds with a diameter of 10 mm and thickness of 2 mm. After the pellets were sintered at 900^0C for 2hrs to improve their resistance, they were degreased, ultrasonically cleaned, and sterilized in a steam autoclave at 120^0C for 30 min.

2.2 Biocompatibility screening

Cell culture studies

The cell culture study was done in direct contact method (ISO 10993–5, 1999) using normal human fibroblast cells 3T3. The test samples were prepared by setting the powder in the form of discs of 10 mm diameter and 2 mm thickness by using KBr pellet machine. They were cleaned ultrasonically and sterilized by autoclaving.

The culture medium consisted of Eagle's MEM (containing glutamine) and fetal bovine serum (10%) along with antibiotics. First the pellet seeded into 24 well dishes then Human fibroblast cells (3T3, supplied by NCCS, Pune) were sub-cultured and seeded on pellet into the 24 multiwell dishes to form a monolayer and incubated at 37°C under 5% CO_2 for 24 hrs. The morphology of the cells of the material was examined under a phase contrast microscope. Test was done in duplicate, along with control samples.

Antimicrobial Activity

Antibacterial property of HAp sample was investigated using the quantitative viable count method. The stock solution was prepared by mixing 1mL *E. coli* with 9 Ml of LB (Luria- Bertani) broth and incubated at 37^0 C for 24 h with shaking at 250 rpm. The broth was then serially diluted upto 10^6. The

dilutions of 10^5 and 10^6 were used as working concentrations. 0.01g HAp powder was autoclaved and mixed with the stock solution of dilution 10^5 and 10^6. 0.1mL of the prepared mixture was then inoculated on LB agar plates followed by incubation at 37^0 C for 24 h. Finally, the number of colony-forming units was counted for each dilution.

Test of Biodegradation

Biodegradation test of HAp pellet was done by taking Tris-HCl buffer solution. 0.05M Tris- HCl Solution was prepared using distilled water. The pH of solution was maintained 7.4 at 37^0c by adding 1M HCl. HAP pellet was soaked in Tris-HCl buffer solution, the samples was dried at 120°c after every one week and final weight of sample was taken. This process was repeated for five weeks.

$$\%Weight\ loss = \frac{W_0-W_t}{W_0} * 100$$

Where, W_0 = initial weight of sample

W_t = final weight of sample after soaking in Tris-HCl solution

2.3 Powder Characterization Techniques

X-ray powder diffraction (XRD) technique was used to study the effect of calcination temperature on the phase evolution and phase identification. The dried powder obtained after heat treatment at 85 °C and the calcined powder at 900 °C were ground into fine powder using a mortar and pestle to breakdown the powder agglomerates before analyzing in an X-ray diffractometer. Powder samples were placed in the specimen holder of a Rigaku diffractometer (XRD, miniflex Rigaku), and then analyzed, using Ni-filtered CuKα radiation (λ = 0.1542 nm) in the step scanning mode, with tube voltage of 40 kV and tube current of 40 mA. The XRD patterns were recorded in the 2θ range of 20 to 70°, with a step size of 0.02° and step duration of 1 s.

The FTIR spectra of the samples were recorded in a wave number range of 450 –4000cm^{-1} using a Fourier

Transform Infrared spectrophotometer (SHIMDZU IR Affinity 1 FTIR Spectrometer).

Scanning electron microscopy (SEM) technique was also used to observe the particle-size and agglomeration of the as-synthesized HAp powder calcined at 900 °C. For this, a very small amount of powder was placed on an adhesive carbon tape, coated with gold/palladium and then observed in a FE-SEM (HITACHI S-4800).

III. RESULTS AND DISCUSSION

FTIR analysis

The presence of OH and PO_4 functional groups was confirmed by the FTIR spectrum. FTIR spectra of the prepared and calcinated samples are given in Fig. 1a and b. Peak at 1629 cm^{-1} belongs to the bending mode of OH group while the sharp peak at 3570 cm^{-1} denotes the OH stretching vibrations. The broad peak around 3432 cm^{-1} is due to water molecules. All the phosphate modes (962 cm^{-1} -υ_1, 495 cm^{-1}- υ_2, 1082 cm^{-1} and 1091 cm^{-1} - υ_3, 561 cm^{-1} and 603 cm^{-1} -υ_4) are present. The peaks at 1456 cm^{-1} and 1415 cm^{-1} are due to the carbonate, which might be incorporated from the atmosphere to these samples during the preparation (Jaworski et al. 2009).
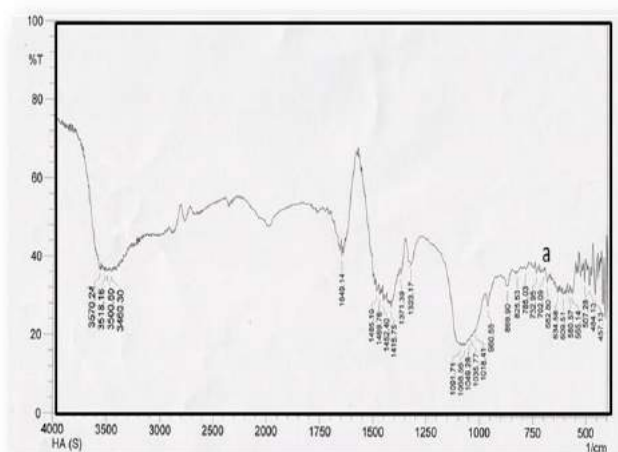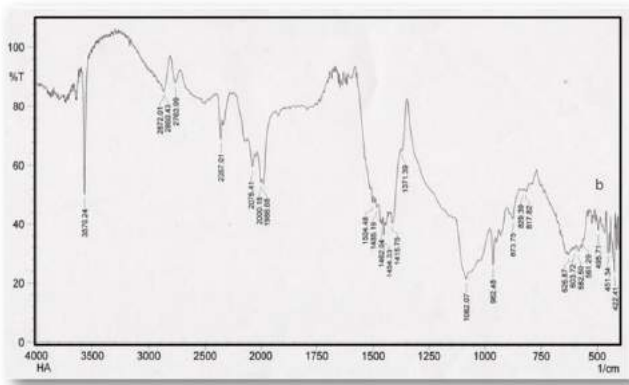
Fig 1: FTIR spectra of HAp (a) as prepared (b) calcinated.

XRD analysis

The structural analysis of sample was done by the powder X-ray diffraction. The XRD patterns of the synthesized and calcinated samples are shown in Fig. 2a and b. The XRD pattern of calcinated sample shows sharper peaks which indicate better crystallinity. The peak positions are in good agreement with the ICDD file number (01-072-1243) having lattice parameters a≈b≈0.9418 nm, c≈0.6884 nm and space group P63/m (176). Thus, standard HAp with hexagonal structure is formed during synthesis, which remains stable after the calcinations. The investigated powders show no secondary phases such as tricalcium phosphate and calcium oxide.
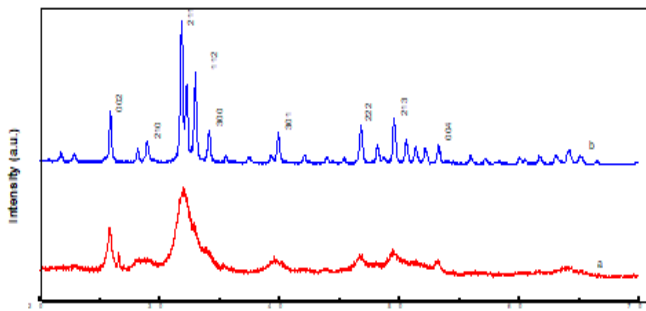

Fig. 2 XRD patterns of HAp (a) as prepared (b) calcinated

Morphology

The surface morphologies of as prepared and calcinated sample were investigated by FESEM, as given in Fig. 3. Fig. 3a shows FESEM image of as prepared powder of HAp consists of agglomerated which are composed of fine crystallites and fig. 4b and 4c shows FESEM images of calcinated powder of HAp

shows that spherical-like shape with mean particle sizes 41.20 nm. This shows the agglomeration it is due to heating.
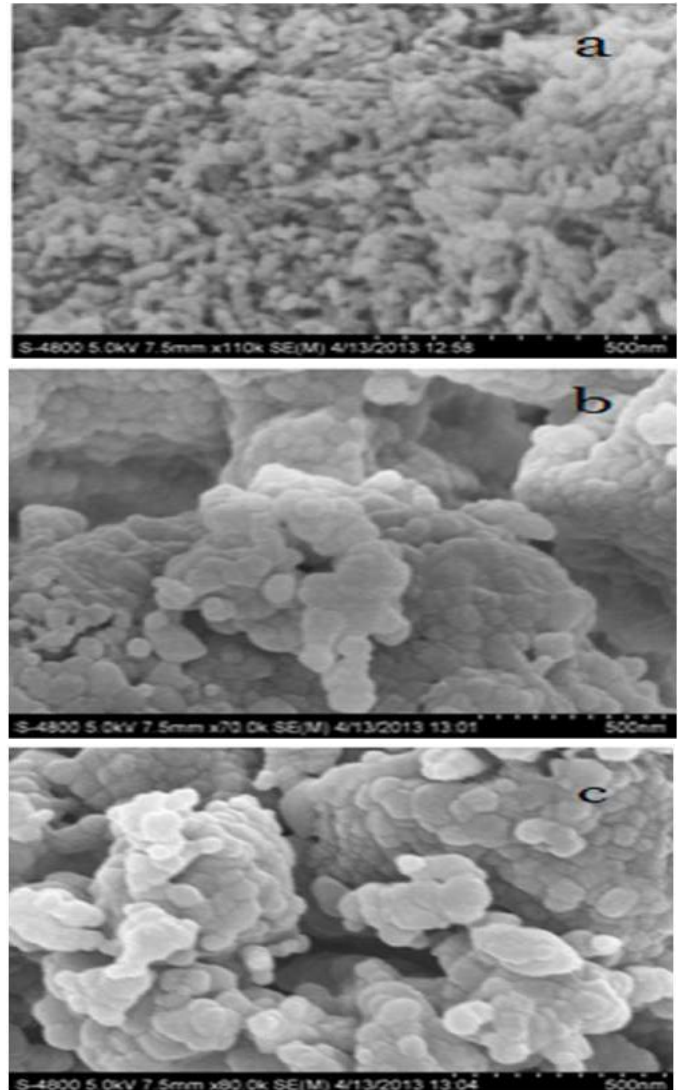
Fig.3 FESEM image of HAp a) as prepared b) calcinated

Cytotoxicity

The cytotoxicity of the HAp pellets was evaluated with mouse fibroblast 3T3 cell line. The cells were grown in presence of HAp pellets for 24, 48 and 72 hrs in 24 well plates. cell proliferation was observed under phase contrast microscope as shown in fig.4 The phase contrast microscope images in Fig.4 (a,b) shows the live cells near HAp pellets after 24, 48 hrs of growth. The cells in both the images show a typical

elongated shape characteristic of live fibroblast, suggesting the presence of normal cell growth behavior and absence of cytotoxicity. After 72 hrs of culture cells became more confluent as shown in Fig.4.d. After 74 hrs of growth, the cell population increased significantly near HAp pellets surface and (M) area of HAp pellet as shown in fig4.d. Increasing numbers of fibroblast cells with time suggests an increase in cell proliferation and/or survival near HAp pellets surface. Thus, the presence of HAp pellets does not negatively affect the fibroblast cells.
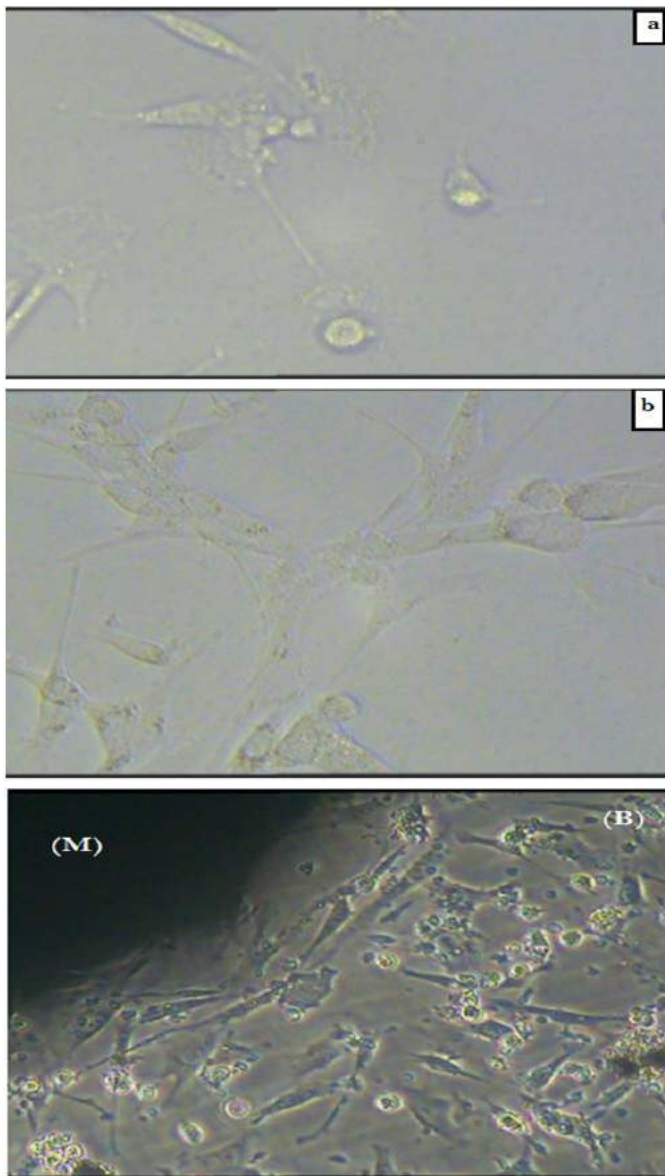

Fig. 4. 3T3 mouse fibroblasts (a, b, B) were cultured in DMEM for 24, 48, 72 hrs on pellets of

HAp observed by microscope. (M) Area of pellets of HAp

Antimicrobial Activity

Antibacterial property of HAp samples calcinated at 900^0c was investigated using quantitative viable count method. 0.01gm powder of HAp was autoclaved at 120^0c for 30 min. Then this powder was incubated with *E. Coil* suspension for 24 hrs as shown in fig. 5. In this study agar plates a and b were control plates (in the absence HAp powder) with 10^5 and 10^6 times dilution of *E. Coil* culture and plates c and d shows the decrease in the number of colonies of *E. Coil* in the presence of 0.01gm powder of HAp. HAp powder shows significant antibacterial effect.
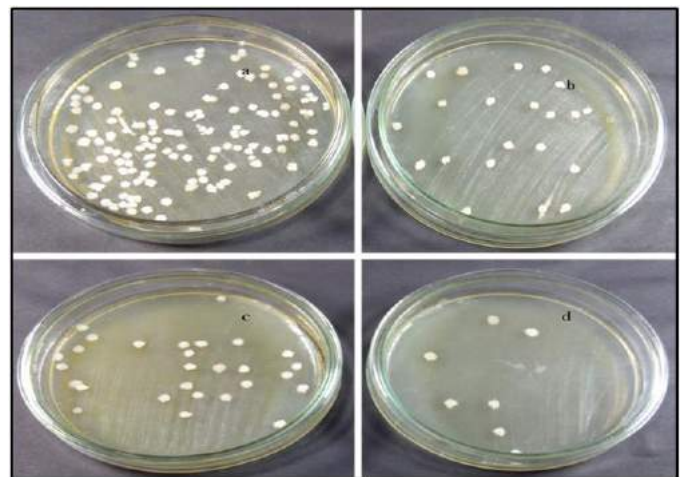
Fig. 5 a and b control 10^5 1nd 10^6 times dilution of *E. coli* culture

Fig. 5 c and d 0.01g HAp powder with 10^5 1nd 10^6 times dilution of *E. coli* culture

In-Vitro degradation:

Degradation of HAp pellet sample was carried out in Tris-HCL solution. HAp samples were soaked in Tris buffer solution at pH 7.4 and temperature 37℃ for four week. When the HAp pellet was soaked in Tris buffer solution, the pH of buffer increases from 7.4 to 7.8 which confirms the biodegradation of HAp. The weight loss of the HAp pellet was approximate 1.06% in five week as shown in fig 6.
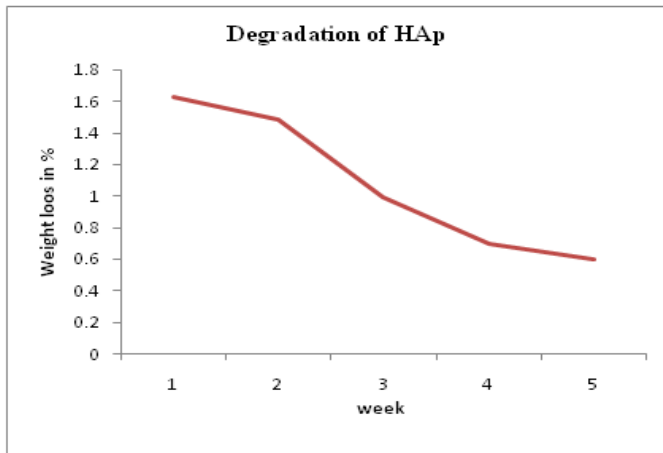
Fig: 6 Degradation of HAp

IV. CONCLUSION

The present study reveals that HAp powder can be synthesized by aqueous wet chemical method by using calcium nitrate and di-ammonium hydrogen orthophosphate. Crystalline HAp has been achieved by simple calcination at 900°C (for 2 hrs). FTIR, X- ray diffraction indicated the phase purity and crystallinity of the HAp powder. FTIR, XRD studies confirm the formation hexagonal structure of HAp. Moreover, the HAp particles showed antibacterial activity against *E. coli.* The weight loss of the HAp pellet was approximate 1.06%.

Cell culture, cytotoxiciy assays and staining show that HAp has no cytotoxic effect on cells and

Possess good biocompatibility. Cell viability and cell attachment studies proved the non-toxic nature of these scaffolds with enhanced cell attachment. All these results essentially suggest that hydroxyaptite can be superior candidates for bone tissue engineering.

V. REFERENCES

[1]. Rezaei A, and Mohammadi MR, (2012) Development of Hydroxyapatite Nanorods–Polycaprolactone Composites and Scaffolds Derived from a Novel In-Situ Sol-Gel Process. Tissue Engineering and Regenerative Medicine 9:295-303.

[2]. Cengiz B, Gokce Y, Yildiz N, Aktas Z, (2008) Synthesis and characterization of Hydroxyaptite nanoparticles. A Colloids and Surfaces A: Physicochem. Eng. Aspects 322:29–33

[3]. Dorozhkin SV (2007) calcium orthophosphates. Journal Mater Science 42:1061–1095.

[4]. Zhou S, Ma J, Shen Y, Haapasalo M, Ruse N, Yang Q, Troczynski T, In vitro studies of calcium phosphate silicate bone cements. (2013) Journal Mater Science: Mater Med 24:355–364.

[5]. Yarosh EB. Dmitrevskii BA, Naryzhnyi VP, Tsvetkov SK (2001) Some Characteristics of Synthetic Hydroxyapatite. Russian Journal of Applied Chemistry 74:1058-1060.

[6]. Quan R. Yang D. Wu X. Wang H. Miao X. Li W, (2008) In vitro and in vivo biocompatibility of graded hydroxyapatite–zirconia composite bioceramic. Journal Mater Science: Mater Med 19:183–187.

[7]. Bouyer E, Gitzhofer F, Boulos MI, (2000) Morphological study of hydroxyapatite nanocrystal suspension. Journal of materials science: materials in medicine 11: 523-531.

[8]. Jillavenkatesa AR, (1998) sol-gel processing of hydroxyapatite. Journal of materials science 33: 4111 – 4119.

[9]. Silva VV, Domingues RZ, (1997) Hydroxyapatite–zirconia composites prepared by precipitation method. Journal of materials science: materials in medicine 8:907- 910.

[10]. Orlovskii VP, Komlev VS, Barinov SM, (2002) Hydroxyapatite and Hydroxyapatite-Based. Ceramics Inorganic Materials 38:973–984.

[11]. Dou Y, Cai S, Xu G, Hu H, Ye X, (2012) Preparation of mesoporous hydroxyapatite films used as biomaterials via sol–gel technology. Journal Sol-Gel Science Technology 61:126–132.

[12]. Shen SC, Chia L, Ng WK, Dong YC, Tan BH, (2010) Solid-phase steam-assisted synthesis of hydroxyapatite nanorods and nanoparticles. Journal Mater Science 45:6059–6067.

[13]. Mostafa NY, (2005) Characterization, thermal stability and sintering of hydroxyapatite powders prepared by different routes Materials. Chemistry and Physics 94 333–341.

[14]. Andiappan M, Sundaramoorthy S, Panda N, Meiyazhaban G, Winfred SB, Venkataraman G, Krishna P, (2013) Electrospun eri silk fibroin scaffold coated with hydroxyapatite for bone tissue engineering applications. Progress in Biomaterials 2(6):1-11.

[15]. Jaworski R, Pierlot C, Pawlowski L, Bigan M, Martel M, (2009) Design of the synthesis of fine HA powder for suspention plasma sparaying. Surface & Coatings Technology 203:2092–2097.

Enlisting Some Ethnic Plants Species in Ner Region Dist. Yavatmal (M.S.) India

Chavhan V. N.

Dept. of Botany, Arts, Commerce and Science College, Maregaon (Road) Dist. Yavatmal, Maharashtra, India

ABSTRACT

Present paper deals with some ethno medicinal uses of 20 plant species, by the tribal of Ner region, in Yavatmal district of Maharashtra. A number of villages were visited in this region. The information was documented involving field study by contacting and interviewing traditional healers for plants used in cure of various diseases. This region is inhibited by tribal communities like Banjara, Gond, Mang, Paradhi etc. The ethno botanical information on plants viz., botanical name, family, local name, plant part used and mode of administration is enumerated.

Keywords: Tribal People, Medicinal Plant, Ner region, Yavatmal district.

I. INTRODUCTION

In India, it is reported that traditional healers use 2500 plant species and 100 species of plants serve as regular sources of medicine, Pei (2001). Plants are the basis of life on earth and are central to people's livelihoods. Tribal people are the ecosystem people who live in harmony with the nature and maintain a close link between man and environment. Indian subcontinent is being inhabited by over 53.8 million tribal people in 5000 forest dominated villages of tribal community and comprising 15% of the total geographical area of Indian landmasses, representing one of the greatest emporia of ethno-botanical wealth (Chowdhari S. K., 2000). Therefore, effort should be initiated for the documentation and computerization of useful medicinal plants and their traditional knowledge (Mehrotra & Mehrotra, 2005).

The value of medicinal plants to the mankind is very well proven. It is estimated that 70 to 80% of the world population rely chiefly on traditional health care system and largely on herbal medicines (Shanley and Luz, 2003). Only 15% of pharmaceutical drugs are consumed in developing countries (Toledo, 1995). The affluent people have little alternative to herbal medicine, and they depend on traditional health care system (Marshall, 1998).

The 30 plant species from Jalgaon district, are useful for different human ailments (Pawar S. and D. A. Patil, 2004). The documented 39 plant species used in treatment of reproductive disorders while 20 monocotyledonous plant species are used in various diseases by the tribal of Umarkhed tehsil in Yavatmal district. They have further documented 36 ethnic formulations that are prepared using 50 plant species by locals of Umarkhed tehsil (Bhogaonkar and Kadam, 2005 and 2006). The 177 medicinal plants are used by Banjaras of Vidarbha on various ailments (Bhogaonkar and Chavhan, 2013).

In the present paper, folk medicinal preparations of 20 plant species used for different ailments has been enumerated.

Study Area

The district Yavatmal is situated in the eastern part of the Maharashtra between north latitudes 19^0 23` and

20^0 48` and longitudes $77^0$ 19` and 79^0 07. `It occupies an area of 13,582 Sq. Km.

The Ner region is situated in eastern part of the Maharashtra between north latitudes 20.06423 and longitudes 77.866386 respectively. It occupies an area of 699 meters^2. According to the census of 2011, the total population of the region was 1, 20,232.

II. METHODS AND MATERIAL

Tribal medicine practitioner men, village heads and local people were interviewed to record different plant part used for folk remedies. Plants were collected, documented and identified with the help of standard floras (Hooker 1997, Cooke 1967, Naik 1998, Karthikeyan and Kumar 1993,Yadav and Sardesai, 2002) and herbarium specimens were prepared.

Enumeration:

The interviewed of local people and tribal medicine men's information are recorded, is as follows-

Sr. No.	Plant Name	Family	Local Name	Part Used	Mode of Uses
1.	Abrus precatorius L.	Leguminosae	Lal gunj	Root, Leaves	Mouth Ulcer
2.	Acacia nilotica (Benth.) Brenan	Mimosaceae	Babhul	Inner bark	Thoothache, Diabetes

3.	Achyranthus aspera L.	Amranthaceae	Aaghada	Root	Typhoid
4.	Aegle marmelos (L.) Corr.	Rutaceae	Bel	Leaves, Roots	Diabetes, Piles
5.	Barleria prionitis L.	Acanthaceae	Korati	Leaves	Healing wound, Mouth ulcer
6.	Blepharis repens (Vahl) Roth	Acanthaceae	Hadsan	Leaves	Bone fracture, Rheumatism
7.	Bombax ceiba L.	Bombacaceae	Katsawar	Inner bark, Flower	Dysentery,
8.	Buchanania cochinchinensis (Lour.) Almeida	Anacardiaceae	Charoli, Char	Leaves	Dysentry, Diarrhoea
9.	Cadaba fruticosa (L.) Druce	Capparidaceae	Kalitakal	Fruit	Rheumatism, Joint pain
10.	Cassia fistula L.	Caesalpiniaceae	Bahava, Amaltas	Seed	Fever
11.	Chloroxylon swietenia DC.	Meliaceae	Behera	Outer & Inner Bark	Jaundice
12.	Cyperus rotundus L.	Cyperaceae	Nagarmotha	Root	Dandruff, Hair fall, Hairwash
13.	Diospyros melanoxylon Roxb.	Ebenaceae	Tembhurna	Bark	Wound
14.	Enicostemma axillare (Lam.) Raynal	Gentianaceae	Nai, Naichapala	Whole Plant	Fever, Diabetes
15.	Ficus racemosa L.	Moraceae	Umbar	Leaves, Fruit	Fever, Nutrition
16.	Gloriosa superba L.	Liliaceae	Kalalawi	Tuber	Labour Pain
17.	Grewia abutilifolia Vent.ex Juss.	Tiliaceae	Dhaman	Fruit	Digestive
18.	Helicteres isora L.	Sterculiaceae	Murud shenga	Fruit	Stomach ache
19.	Hemidesmus indicus (L.) R. Br.	Periplocaceae	Kawalvel	Root	Leucorrhoea
20.	Vitex negundo L.	Verbenaceae	Nirgudi	Leaves	Joint Pain, Rheumatism

III. RESULTS AND DISCUSSION

The present communication deals with the local people of Ner region, Yavatmal District (M. S.) India, were used medicinally important plants of 20 genera and twenty species of angiosperms for different ailments. These are herb, shrub, climber, small and large trees. These plants are common and medicinally important to treat various diseases like Diabetes, jaundice, typhoid, fever, dysentery, diarrhea, rheumatism, leucorrhoea etc. Some therapeutic uses of such plants in Ner region were documented. The present information is used in drug standardization and estimation of compound content for further studies.

IV. CONCLUSION

Traditional knowledge systems cure different diseases by the tribal of Ner region. They use plant as a source of drug through trial and error basis and the process is experienced over hundreds of years. It has been observed that the use of the medicinal plants is also a routine practice in the local people.

Acknowledgment

V. REFERENCES

[1]. Bhogaonkar, P.Y. and Chavhan, V.N. 2013. Traditional Banjara Herbal Medicine of Vidarbha, M.S., India. Lap Lambert Academic Publishing, Germany.

[2]. Bhogaonkar P. Y. and V. N. Kadam, 2005. Ethnobotanical survey of Umarkhed area (Dist. Yavatmal, M. S.) I. Monocotyledonous Drug Plants. J. Bot. Univ. Sagar; 40: 36-42.

[3]. Bhogaonkar P. Y. and V. N. Kadam, 2006. Ethnopharmacology of Banjara tribe of Umarkhed taluka, district Yavatmal, Maharashtra for reproductive disorders. Indian J. of Trad. Knowl.; 5(3): 336-341.

[4]. Chowdhuri S. K., 2000. From Ethnobotany. In Studies in Botany Volume 2. 7th edition. Edited by: Mitra D, Guha Chowdhuri SK, Kolkata: Manasi Press; 855-867.

[5]. Cook, T., 1965. The Flora of Presidency of Bombay, (Bishan Singh Mahendra Pal Singh, Dehra Dun).

[6]. Hooker JD, 1997 (Rpr.) The Flora of British India. Vol. IV, Periodical Expert Book Agency, New Delhi

[7]. Karthikeyan S. and Anand Kumar 1993. Flora of Yavatmal District, Maharashtra, Botanical Survey of India. Pune.

[8]. Marshall, N.T. 1998. Searching for a cure: Conservation of medicinal wildlife resources in East and Southern Africa. TRAFFIC-International, Cambridge.

[9]. Mehrotra, S. & Mehrotra, B. N. 2005. Role of traditional and folk lore herbals in the development of new drugs. Ethnobot.17: 104-111.

[10]. Naik VN, 1998. Flora of Marathwada. Amrut Prakas, Aurangabad.

[11]. Pawar Shubhangi and D. A. Patil, 2004. Observations on Folkloric Medicinal Plants of Jalgaon District, Maharashtra. Indian Journal of Traditional Knowledge, vol. 3(4) pp. 437-441.

[12]. Pei, S.J., 2001. "Ethnobotanical approaches of traditional medicine studies: Some experiences from Asia." Pharmaceutical Biology, 39:74-79.

[13]. Shanley, P. & Luz, L. 2003. The impacts of forest degradation on medicinal plant use and implication for health care in Eastern Amazonia. Bioscience, 53 (6): 573-584.

[14]. Toledo, V. M. (1995). New paradigms for a new ethnobotany; reflections on the case of Mexico. In: Schultes, R.E. and Von Reis, S.

(eds.) Ethnobotany: evolution of a discipline. Chapman and Hall, London. pp. 75-88.

[15]. Yadav SR and Sardesai MM, 2002. Flora of Kolhapur District. Shivaji University, Kolhapur (India). Pp XIV + 680.

Novel Molten Salts Synthesis and Photoluminescence Properties of Eu (III) Doped Y_2O_3 Phosphor

R. G. Korpe[*1], K. A. Koparkar[2], N.S. Bajaj[3], S. K. Omanwar[4]

[1]Department of Physics, Shri. Shivaji College of Arts, Commerce and Science Akola, India

[2] Department of Physics, M.S.P. Arts, Science and K.P.T. Commerce College Manora, Washim,(MS), India

[3] Department of Physics, Toshniwal Arts, Commerce & Science College, Sengaon, Dist. Hingoli (MS) India

[4] Department of Physics, Sant Gadge Baba Amravati University, Amravati, (MS), India

ABSTRACT

A novel molten salt method used for the synthesis of Eu^{3+} doped yttriumbased phosphor. It is well known that Y_2O_3:Eu^{3+} is highly efficient red phosphors used for Lamp phosphor. The Y_2O_3:Eu^{3+} phosphor was synthesized by reactions in molten salts method.The red emitting phosphor characterized through powder X-ray diffraction (XRD), and PL spectra. A novel molten salt is one step methodand decrease calcining temperature.

Keywords : Y_2O_3:Eu^{3+},Molten salts method, PL spectra.

I. INTRODUCTION

The production of reliable and reproducible ceramic materials for high technology applications require strict control over their powder characteristics, which includes chemical homogeneity, low impurity levels, small particle size, narrow size distribution and freedom from agglomeration. A variety of methods e.g. sol-gel, chemical precipitation of precursors in aqueous or organic solutions, thermal decomposition of solutions by spraying technique, high alkaline and hydrothermal precipitation have been proposed for obtaining small, uniform un-agglomerated powders. These methods so-called wet chemical method, have been found to be successful for number of systems. Also self-sustaining combustion synthesis is a simple, inexpensive and quick way of synthesizing various oxide materials in comparison to the wet chemical techniques [1].

Compounds containing rare earths have long been used as phosphors and laser materials because of their sharp, intensely luminescent f-f electronic transitions.In particular, Eu^{3+} has five narrow emission bands corresponding to the $^5D_0 \rightarrow {}^7F_j$ transitions where, j = 0,1,2,3,4. The strongest transition, $^5D_0 \rightarrow {}^7F_2$ occurs at 613 nm, which is a characteristic of red fluorescence of Eu^{3+}. This transition has also been shown to exhibit laser emission under appropriate conditions in Eu^{3+} doped crystals [2, 3]. It is well known that the Y_2O_3:Eu^{3+} is highly efficient red phosphor and has its own importance in scintillation, lamp and color TV picture tubes [4].

The preparation of these red emitting phosphors is critical and requires special methods such as wet chemical methods. Recently preparation of Eu^{3+} doped yttria was carried out by the alkoxide route and combustion process [5, 6]. Though these processes are efficient, requires expensive chemicals and special

equipment. Here we report the preparation of Y_2O_3: Eu^{3+} by the novel method of reactions in molten salts. The term molten salt refersto the liquid state of compound, which melts to give liquids displaying a degree of ionic properties [7, 8]. Alkali metal nitrates have relatively low melting points (Table:1) whereas even lower melting points are obtained in their eutectic mixtures. A molten salt can behave as a solvent or as a reactant. Thus in a nitrate melt acid-base reactions can occur according to the Lux -flood formalism, whereby an acid is an oxide ion acceptor and a base is an oxide ion donor; nitrate ions are bases in this formalism [9]. Nitrite melts are more basic than nitrate melts whereas addition of Lux-flood bases such as Na_2O_2, Na_2O and NaOH to a nitrate melt, which its basicity.

The precursors are the inorganic compounds, in particular sulphates and chlorides that are blended with the alkali metal nitrates or nitrites as a powder mixture before heating to the reaction temperature. Table:1 shows the various eutectic mixtures and corresponding melting points.

Table-1   Melting points for alkali metal nitrates and eutectic mixtures.

Metal Nitrate	Melting point (^{0}C)
$NaNO_3$	307
KNO_3	334
50 mol% $NaNO_3$-50 mol% KNO_3	220
43 mol% $LiNO_3$- 57 mol% KNO_3	132

II.   METHODS AND MATERIAL

2.1 Synthesis of Y_2O_3:Eu^{3+}

The precursors used were Y_2O_3 (AR) and Eu_2O_3 (AR). Both were mixed together in a china basin. A small quantity of double distilled (DD) water was added and paste was formed. Then HCl was added drop by drop and mixture was heated slowly under observation at 50^0C till the paste dissolved completely. The solution was further heated till the excess of acid was boiled off. Little quantity of double distilled (DD)water was again added and slowly evaporated to dryness. The resulting powder was YCl_3: Eu. The chemical reaction is $0.97\ Y_2O_3 + 0.03\ Eu_2O_3 + HCl \rightarrow 2\ Y_{0.97}Cl_3 : Eu_{0.03} + 3H_2O$ ---------- (1)

The eutectic mixture of nitrates $LiNO_3.3H_2O$ (43 mole %) and KNO_3 (57 mole %) were taken in a china basin and mixture was dried at 50^0C.The dry chloride YCl_3:Eu was added to this mixture of dried nitrates and thoroughly ground in a china basin. This mixture was then heated in a resistive furnace first at 100^0C for 1h and then with the gradual rise of temperature it was further heated at 425^0C for12 hours. The chemical reaction is $2Y_{0.97}Cl_3 :Eu_{0.03} + 0.43\ LiNO_3.3H_2O + 0.57\ KNO_3 \rightarrow\ Y_{1.94}O_3 : Eu_{0.06}$ --------- (2)

The mixture was then cooled slowly. A semi convex white solid was formed. With the help of sufficient lukewarm DD water, the solid was transferred to a glass beaker. Keeping the beaker in an oven at 60^0C for 10 minutes, the white solid was partly dissolved in water and the fine particles of Y_2O_3:Eu started settling down at the bottom. The precipitate was washed repeatedly by DD water and then dried. The dried precipitate was then calcinated at 800°C for 2h and quenched suddenly at room temperature.The calcinated and quenched powder was Y_2O_3:Eu^{3+} phosphor.

2.2 Material characterization

The phase purities of Y_2O_3:Eu^{3+} phosphor was studied using Rigaku miniflex II X-ray Diffractometer with scan speed of 2.000°/min and Cu Kα (λ = 1.5406 Å) radiation in the range 10° to 90°. PL and PL excitation (PLE) spectra were measured on (Hitachi F-7000) fluorescence spectrophotometer at room temperature. The parameters such as spectral resolution, width of the monochromatic slits (1.0 nm), photomultiplier

tube (PMT) detector voltage and scan speed were kept constant throughout the analysis of samples

III. RESULTS AND DISCUSSION

3.1 Powder XRD pattern of Y_2O_3:Eu^{3+}

The formation of the phase purity and crystal structure of Y_2O_3 synthesized by using molten salts at 800°C was confirmed by XRD pattern as shown in Figure. 1. All the peaks in XRD pattern very well agree with the standard data from ICDD file no. 01-071-0049. Also the XRD shows that the formed material was completely crystalline and was in single phase with cubic structure where a=b=c=10.5957 Å. The space group for Y_2O_3 is Ia-3 (206).The average crystallite size of Y_2O_3:Eu^{3+}determined from XRD pattern using Scherrer formula and it was found to be 965.52 nm [10]
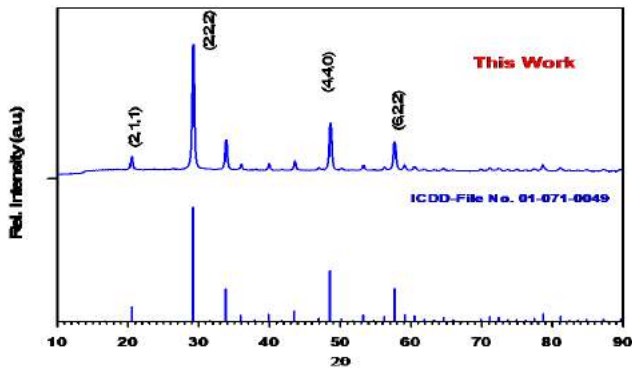

Figure:2 XRD pattern of Y_2O_3:Eu^{3+}.

Figure 2 shows PL spectra of Y_2O_3:Eu^{3+} phosphor. It consists of a broadband excitation spectrum peaking at 246 nm, monitored at emission wavelength 613 nm. The emission spectrum is sharp peaking at 613 nm at excitation wavelength 254 nm, corresponding to the transition $^5D_0 \rightarrow ^7F_2$ of Eu^{3+}. The intensity of emission is found to be comparable and excitation, emission wavelengths matches well with those of reported in literature.

The rare earth compounds such as Y_2O_3:Eu^{3+} mainly belong to luminescent materials with individual luminescent center. Luminescence of these materials is due to the transition between 4f energy levels.

Because of spin-orbit interaction, the degenerate 4f configuration is split into several energy levels such as ^5Dj and ^7Fj. The crystal field of host lattice affects the electronic transitions in Eu^{3+} [11]. For $^5D_0$ term, j = 0, so it cannot split (only one energy level). For the term $^7F_2$, j = 2 and 2_{j+1}=5, so it can split into five energy levels (Γ_1, Γ_2,Γ_3, Γ_4, Γ_5). The strongest peak at 613 nm in Y_2O_3:Eu^{3+} phosphor corresponds to the transition $^5D_0 \rightarrow ^7F_2$ of Eu^{3+}. This method of reactions in molten salts is a low temperature and single step synthesis. This method is easy to synthesis and precursors used are readily available. The sample synthesized is a snow-white powder and particle size varies from sub-micron to nano. Frequent washing and calcinations enhances the PL intensity.

Figure:1 Photoluminescence emission and excitation Spectrum of Y_2O_3:Eu^{3+}

This method of reactions in molten salts is a low temperature and single step synthesis. This method is easy to synthesis and precursors used are readily available. The sample synthesized is a snow-white powder and particle size varies from sub-micron to nano. Frequent washing and calcinations enhances the PL intensity.
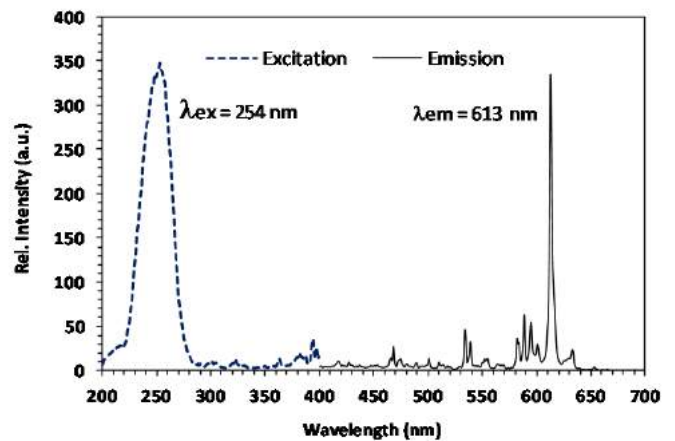
IV. CONCLUSION

The excitation and emission wavelengths in PL spectra of Y_2O_3:Eu^{3+} synthesized by molten salts method confirms the formation of desired phase and crystal structure in the compounds. As phosphors

with particles of required size and colour are needed for their use in the display devices and other applications. This method has new horizons in the lighting industries.

V. ACKNOWLEDGEMENT

VI. REFERENCES

[1]. P. Fauchais, G. Montavon, G. Bertrand, Journal of Thermal Spray Technology, 19 (2010) 56–80.

[2]. P. K. Sharma, R. Nass, H. Schmidt, Optical Materials 10 (1998) 161-169.

[3]. Q. Li, L. Gao, D. Yan, Nano Struct. Mat. 8 (1997) 825-831.

[4]. N.B. Ingale, D. S. Thakare, S.K. Omanwar, S.V. MoharilProc. NSLA-2002.

[5]. Y. H. Zhou, J. Lin, S. B. Wang, S. J. Zhang, 20 (2002) 13-20.

[6]. N. Dasgupta, R. Krishnamoorthy, J. K. Thomas, Int. J. of Inorg. Mat. 3 (2001) 143-149.

[7]. Wilkes, John. (2002). A short history of ionic liquids - From molten salts to neoteric solvents. Green Chemistry 4. pp 73-80.

[8]. Segal D.L., Chemical Synthesis of Adv. Ceramic Materials, Cambridge Univ. Press, Cambridge, 1989 pp 182.

[9]. H. Lux, Z. Elektrochem, 45 (1939) 303.

[10]. K.A. Koparkar, N.S. Bajaj, S.K. Omanwar, Indian J Phys. DOI 10.1007/s12648-014-0554-y.

[11]. K.A. Koparkar, S.K. Omanwar, Bull Mater Sci 39 (2016) 1127–1132.

Aldo-Keto Gel Synthesis and Photoluminescence Properties of YVO$_4$: Eu^{3+} Microsphere

K. A. Koparkar[1]*, R. G. Korpe[2], G. V. Korpe[2], S. K. Omanwar[3]

[1]Dept of Physics, M.S.P. Arts, Science and K.P.T. Commerce College Manora, Washim, Maharashtra, India
[2]Dept of Physics, Shri. Shivaji College of Arts, Commerce And Science Akola, Maharashtra, India
[3]Dept of Physics, Sant Gadge Baba Amravati University, Amravati, Maharashtra, India

ABSTRACT

The Eu^{3+} doped YVO$_4$ phosphor synthesized via simple aldo-keto gel method by using Benzaldehyde and Acetone which then compared with conventional solid state diffusion. Powder X-ray diffraction (XRD) and field emission scanning electron microscopy (FE-SEM) studies indicate that the prepared samples were well crystalline and free from organic impurities. However, the nature of as-prepared phosphor by using aldo-keto gel method does not having any agglomeration. Further photoluminescence (PL), photoluminescence excitation (PLE) spectra and decay curves were superior as compared to solid state diffusion method.

Keywords: Aldo-keto gel method; aldehydes and ketones; spherical particle, PL properties; CIE diagram.

I. INTRODUCTION

Yttrium based materials doped with europium (III) have attracted more attentions among the many researcher group because these are important excellent commercial red-emitting phosphors used in various applications such as color television, the cathode ray tube and plasma display panel [1-3] due to its high quantum efficiency, dip red color purity, and high thermal stability [4]. Among all these yttrium based phosphors, the Eu^{3+} doped YVO$_4$ is still more demanding in the field of luminescence for the upcoming research because, its wide band gap. Also, absorption spectrum of YVO$_4$ shows strong and broad bands in the ultraviolet (UV) region [5].

The effect of synthesis method is important in the rare earth doped host lattice because luminescence efficiency is depending on nature of particles (agglomerated or un-agglomerated) [6]. A lot of efforts have been focused on the enhancement in luminescent properties of YVO$_4$:Eu^{3+} phosphor with non agglomerated and narrow particle size. For the synthesis of phosphors, a variety of conventional and non conventional techniques have been adopted. The conventional method such as solid-state reaction is required lot of time with high temperature for preparation of phosphor [7]. Therefore, there is need to synthesis of such a phosphors at low temperature. The particle size of material prepared by solid state method is in the range of few micrometers and non homogeneous nature of as-prepared phosphor particle size.

All conventional and non conventional synthesis approach is sophisticated synthesis techniques for preparation of YVO$_4$:Eu^{3+}, but suffers with drawback. Because precursor require for synthesis is very costly and other additive chemical required for these methods are very expensive which leads to increase cost of application devices. Therefore in progressive

research we developed a novel synthesis technique for preparation of phosphors.

Inspiring from the above discussions, the present work planned to study the luminescent properties of $YVO_4:Eu^{3+}$ phosphor synthesized by using aldo-keto gel method and compared with very famous method is known as solid state diffusion.

II. METHODS AND MATERIAL

2.1 Solid state diffusion

The phosphor $YVO_4: Eu^{3+}$ was synthesized by solid state methods with Eu concentration 0.01 mole. The precursor Y_2O_3 (99.99%, AR), NH_4VO_3 (AR) and Eu_2O_3 (99.90%, AR) were mixed thoroughly in a mortar with small amount of acetone. The resultant mixture was transferred to an alumina crucible and oven dried at 50°C. The mixture was heated in a resistive furnace at 1100ºC for 10h with intermittent grindings. The white powder of $YVO_4:Eu^{3+}$ so obtained was used for characterization.

2.2 Aldo-keto gel method

Aldo-keto gel method is uses to synthesis of $YVO_4:Eu^{3+}$ phosphor as per the previous work [8]. The precursors used $Y(NO_3)_3$ (99.99%, AR) and $Eu(NO_3)_3$ (99.99%, AR) were mixed together in a china clay basin. In basin $VOSO_4$ (AR) were mixed with some amount of water. On slowly heating to dryness, precipitated changed its color to reddish black. The acidic traces were removed by adding small quantity of deionized water to precipitated and drying 2-3 times; it finally changes to red color.

The red dried compound was finally milled. The benzaldehyde (1M) and acetone (1M) were added to this compound after that NaOH added drop by drop with increasing temperature.

On further slow heating, pyrolysis of foam was started at 450°C and shining black foam was formed at 500°C, which started burning from 700°C. After that one time washing and drying is required for better luminescence properties.

2.3 Material characterization

The phase purities of $YVO_4:Eu^{3+}$ samples were studied using Rigaku miniflex II X-ray diffractometer with scan speed of 2.000°/min and CuK_α (λ = 1.5406 Å) radiation in the range 10° to 90°. The PL and PLE spectra were measured on (Hitachi F-7000) fluorescence spectrophotometer at room temperature. The parameters such as spectral resolution, width of the monochromatic slits (1.0 nm), photomultiplier tube (PMT) detector voltage and scan speed were kept constant throughout the analysis of samples.

III. RESULTS AND DISCUSSION

3.1 XRD analysis

The formation of the crystalline phase of as-prepared products of solid state diffusion and aldo-keto gel method was confirmed by X-ray diffraction patterns as shown in Fig.1, to verify the phase purity and crystal structure. The X-ray pattern of both method samples indicated a pure phase of the standard YVO_4 and all the peaks are in good agreement with the (ICDD, 01-082-1968). Also the XRD shows that the formed material is completely crystalline and is in single phase, where a = b = 7.11 and c = 6.28 Å. The space group for YVO_4 is a I41/amd(141).

3.2 Morphology of $YVO_4:Eu^{3+}$ phosphors

FE-SEM analysis was done and resulting image displayed in Fig. 2 (A and D). The representative micrograph (A) for solid state diffusion and (D) for aldo-keto gel method shows that synthesized sample comprises regular shape with agglomerated and non agglomeration particles. The $YVO_4:Eu^{3+}$ phosphor prepared by aldo-keto gel method gives the non agglomerated and fine spherical particles. Also the grain boundaries of as-prepared materials were fine and well separated with no organic additives. On the other hand, sample prepared by solid state diffusion method reflects the agglomerated irregular nature of particles.
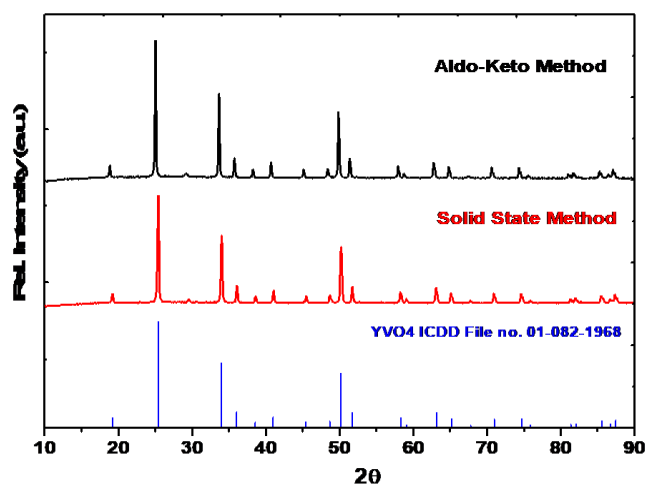
Fig. 1 XRD patterns of the YVO$_4$:Eu^{3+} nanophosphor synthesized through solid state diffusion and aldo-keto gel method.

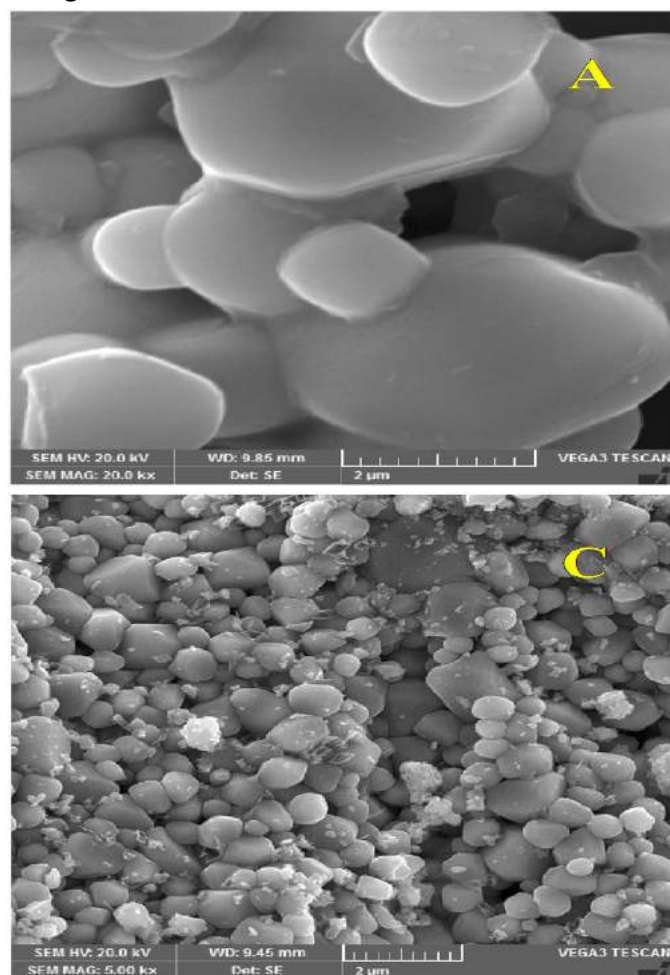Fig. 2 FE-SEM images of the YVO$_4$:0.01Eu^{3+} phosphor synthesized through solid state diffusion (A) and aldo-keto gel method D).

3.3 Photoluminescence properties

Fig. 3 demonstrates excitation and emission spectra of YVO$_4$:Eu^{3+} phosphor synthesized by using solid state method and aldo-keto method with same concentration of Eu^{3+} ions (0.01 mole). The excitation and emission spectrum reflects that the phosphor prepared by aldo-keto gel method gives highest PL emission intensity as compared to solid state diffusion. The excitation attributed at 615 nm and emission monitored at 621 nm wavelength. The excitation spectrum shows similar nature except for a difference in intensity. It consists of a broad band with high intensity from 200 to 350 nm centered at 315 nm due to a charge-transfer transition from the oxygen ligands to the central vanadium atom inside the VO$^{3-}_4$ ion. Also, several narrow bands with low intensity in the range of 350–500 nm are due to the f–f transitions within Eu^{3+} 4f6 electron configuration [9].
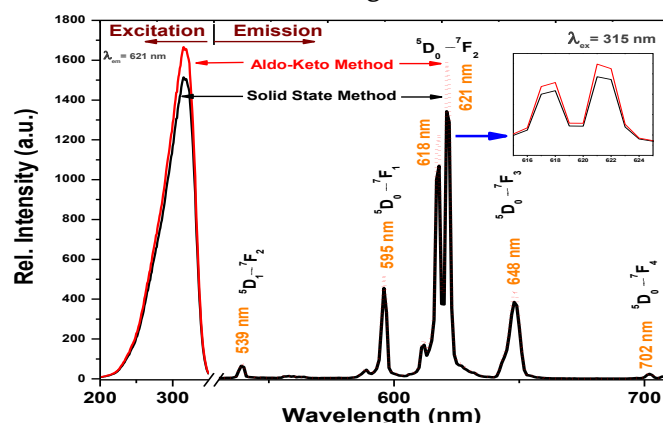

Fig. 3 PL excitation and emission spectra of YVO$_4$:0.01Eu^{3+} phosphor synthesized via solid state diffusion (Black lines) and aldo-keto gel method (Red lines) (Inset of emission at 618 nm and 621 nm.

The emission spectra of YVO$_4$:Eu^{3+} is as shown in Fig. 3. It consist of number of emission peaks in the ranging 550 to 710 nm corresponding to of $^5D_0 \rightarrow {}^7F_J$ (J = 1, 2, 3, 4) transitions of Eu^{3+} ions. The peak at 595 nm is corresponding to $^5D_0 \rightarrow {}^7F_1$ transition in the orange region due to magnetic dipole interaction and peaks at 618 and 621 nm are corresponding to $^5D_0 \rightarrow {}^7F_2$ transition in the red region due to electric dipole transition. The electric dipole transition is sensitive to

chemical bonds in the vicinity of the Eu^{3+} ion. On the other hand, the magnetic dipole transition is changes with the crystal field strength around the Eu^{3+} ion. Therefore, the PL intensity ratio of $^5D_0 \rightarrow {}^7F_2$ (Red) to $^5D_0 \rightarrow {}^7F_1$ (Orange) transitions is depend on the Eu^{3+} ions local surrounding environment. Generally, Eu^{3+} ions occupies an inversion symmetry site in the host matrix, then the orange emission ($^5D_0 \rightarrow {}^7F_1$) could be a dominant emission. Moreover, The peaks at 648 and 702 are corresponding to $^5D_0 \rightarrow {}^7F_3$ and $^5D_0 \rightarrow {}^7F_4$ transition respectively. In $YVO_4{:}Eu^{3+}$ phosphor the electric dipole transition ($^5D_0 \rightarrow {}^7F_1$) shows superior PL intensity than magnetic dipole transition ($^5D_0 \rightarrow {}^7F_2$). The small peak at 539 nm is attributed to $^5D_1 \rightarrow {}^7F_2$ transition. [10].

IV. CONCLUSION

The inorganic intense red emitting $YVO_4{:}Eu^{3+}$ phosphor was first time successfully prepared by aldo-keto gel method and compared with solid state diffusion method. The experimental results indicate that aldo-keto gel method requires low temperature than that of solid state reaction and also reaction complete in less time.

The aldo-keto gel method does not need expensive equipment and result in good PL intensity. The aldo-keto gel method is based on molecular synthesis of particles so that agglomeration of phosphor particle can be avoided.

V. ACKNOWLEDGEMENT

VI. REFERENCES

[1]. Q. Lin, Y. Xu, E. Fu, S. Baber, Z. Bao, L. Yu, S. Deng, J. Kundu, J. Hollingsworth, E. Bauer, T. M. Mccleskey, A. K. Burrell, Q. Jia, H. Luo, Polymer-assisted chemical solution approach to YVO4:Eu panoparticle networks, J. Mater. Chem. 22 (2012) 5835-5839.

[2]. A. K. Levine, F. C. Papilla, A new, highly efficient red-emitting chatodoluminescent phosphor (YVO4 Eu) for color television, Appl. Phys. Lett. 5 (1966) 118-120.

[3]. J. T. Ingle, R. P. Sonekar, S. K. Omanwar, Y. Wang, L. Zhao, Combustion synthesis and VUV photoluminescence studies of borate host phosphors YBO3:RE3+ (RE = Eu3+, Tb3+) for PDPs Applications, Combust. Sci. Technol. 186 (2014) 83-89.

[4]. V. Pankratov, A. I. Popov, L. Shirmane, A. Kotlov, C. Feldmann, LaPO4:Ce,Tb and YVO4:Eu nanophosphors: Luminescence studies in the vacuum ultraviolet spectral range J]. Jpn. J. Appl. Phys., 2011,110:053522.

[5]. J. K. Komal, P. Karimi, K. S. Hui, Hydrothermal synthesis of yttrium orthovanadate (YVO4) and its application in photo catalytic degradation of sewage water, Iran. J. Mater. Sci. Eng. 7 (2010) 25-30.

[6]. B. K. Grandhe, V. R. Bandi, K. Jang, S. Ramaprabhu, S-S Yi, J-H Jeong, Enhanced red emission from YVO4:Eu3+ nano phosphors prepared by simple Co-precipitation method, Electron. Mater. Lett. 7 (2011) 161-165.

[7]. L. Tian, S. Mho, Enhanced photoluminescence of YVO4:Eu3+ by codoping the Sr2+, Ba2+ or Pb2+ ion, J. Lumin., 122 (2007) 99–103.

[8]. K. A. Koparkar, N. S. Bajaj, S. K. Omanwar, Photoluminescence in a novel Aldo-Keto synthesized YPO4:Eu3+ nanophosphor, Solid State Phenom. 222 (2015) 179-185.

[9]. J. Livage, Hydrothermal Synthesis of Nanostructured Vanadium Oxides, Mater. 2010, 3:4175-4195.

[10]. R. Han, R. Hu, K. Chen, CTAB-assisted precipitation synthesis and photoluminescence properties of olive-like YVO4:Eu nanocrystallites, Opt. Mater. 32 (2009) 329–333.

Solid Waste Management in India: Current Situation and Opportunities

N. D. Kolekar, A. V. Kohale

Department of Physics, Shri R. R. Lahoti Science College, Morshi, Maharashtra, India

ABSTRACT

India's solid waste management system is the big hurdle in the way of India's development. This inadequate managements system is because of high rate of population growth and quantum population specially in metro cities. Also the unawareness of people is responsible for this. There is a need to upgrade solid waste management systems. The informal sector can be used as resource. This paper covers such challenges and some future opportunities for the sustainable development of India's solid waste management systems.

Keywords: Waste Management, Sustainable Development, India, Population Growth

I. INTRODUCTION

India is a developing country. But there are many issues those are being hurdles in the way of development. Solid waste management is one of such issues. In spite of the remarkable development in social, economical and environmental areas, solid waste management systems in India are not developed relatively. The population explosion is the main reason for the increased solid waste. But the urbanization made solid waste management more difficult. There is an urgent need of more sustainable solid waste management systems. The current situation of solid waste management is not so good, and also it has negative impact on public health.

Purpose of this paper is to discuss the challenges in solid waste management systems and the scope of future improvement.

II. METHODS AND MATERIAL

Waste generation and urbanization in India

India is at the 2nd highest populated country. The rate of increase in the population is also significant. This results increase in solid waste generationin urban as well as rural areas of the country. But the rate of urbanization is very high in India which makes solid waste generation more intense in the urban areas, especially in metro cities. In rural area, mostly household waste is generated and it is more biodegradable. There are many sources of waste generation in the urban area other than household waste. The waste from urban area is more non-biodegradable and also hazardous.

Table 1 shows Trends of Solid waste generation in some major metro cities. Which clearly shows the fast increase in waste generation. The waste produced in urban areas of India is approximately 170 000 tons per day and it is expected that this waste generation will increase by 5% per year.

Table 1: Trends of Solid waste generation in some major metro cities.

Source: Central pollution control board, MoEFC, GOI

Rank	City	Population	Waste Generation (Tons per day)			
			1999-2000	2004-2005	2010-2011	2015-2016
1	Mumbai	12,442,37	5355	5320	6500	11,00

|						
		3				0
2	Delhi	11,034,555	400	5922	6800	8700
3	Bangalore	8,443,675	200	1669	3700	3700
4	Chennai	7,088,000	3124	3036	4500	5000
5	Hyderabad	6,731,790	1566	2187	4200	4000
6	Ahmedabad	5,577,940	1683	1302	2300	2500
7	Kolkata	4,496,694	3692	2653	3670	4000
8	Surat	4,467,797	900	1000	1200	1680
9	Pune	3,124,458	700	1175	1300	1600
10	Jaipur	3,046,163	580	904	310	1000
11	Lucknow	2,817,105	1010	475	1200	1200
12	Kanpur	2,765,348	1200	1100	1600	1500
13	Nagpur	2,405,665	443	504	650	1000
14	Visakhapatnam	2,035,922	300	584	334	350
15	Indore	1,960,631	350	557	720	850

III. RESULTS AND DISCUSSION

Waste Management in India

In India, many old methods are used for the waste management. Burning is one of them. But it actually causes pollution, so it has negative impact. In this time, almost all the metro cities use dumping method to take away solid waste from cities. All waste from city is dumped outside or far from the city. But there are some disadvantages of this method. Most prominent issue is land acquisition. As there will be an increase in waste generation, the more land will be required for dumping the generated waste. Figure 1 shows the prediction of land required for dumping of Solid waste. This clears that the requirement of land will increase day by day. But the spreading of metro cities and migration of more people to urban areas makes this land problem more intense.

Figure 1:Land required for dumping of Solid Waste.
Source: Singhal & Pandey, Solid waste managementin India: status and future directions
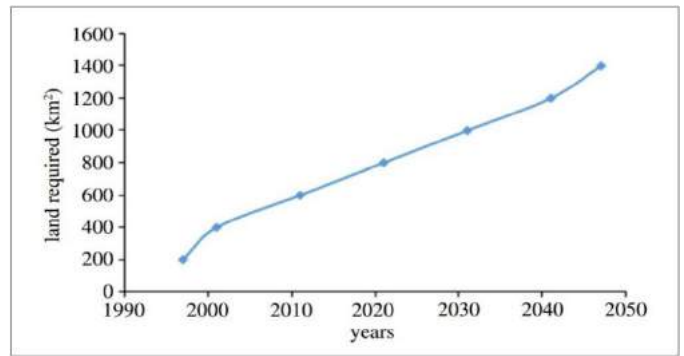
The other problem of dumping is the hazardous effects on the health of the people working or living near the dumping site. Not only human beings, it also effects birds and animals in the areas. Open dumps release methane from decomposition of biodegradable waste under anaerobic conditions. Methane causes fires and explosions and is a major contributor to global warming.There are also problems associated with odour and migration of leachates to receiving waters.

The informal sector has a very important role in India's solid waste management. The informal sector means small-scale, labor-intensive, largely unregulated and unregistered low-technology manufacturing or provision of materials and services. Waste pickers collect household or commercial/industrial waste and many hundreds of thousands of waste pickers in India depend on waste for an income, despite the associated health and social issues. Pickers extract potential value from waste bins, trucks, streets, waterways and dumpsites. Some work in recycling plants owned by cooperatives or waste picker associations. Waste picking is often the onlysource of income for families, providing a livelihood for significant numbers of urban poor and usable materials to other enterprises. Waste pickers also make a significant contribution by keeping cities clean.

In recent years, the government and local authorities in India have given considerable attention to the solid waste management. A number of partnerships/alliances are found to exist in the field of solid waste management in Indian cities.

Suggestions for Future Improvement

- The major issues of the solid waste management systems in India are lack of awareness, lack of collection and classification of waste at the primary source, land problem, etc. So, there is a room for improvement simply with the change of method of collection or the classification of waste while collection at primary source, to separate materials that can be recycled and to reduce the amount of wastes requiring collection and disposal.

- Efforts to improve waste storage and collection are required.

- Instead of simple dumping, the advanced technology can be used. It will be bit expensive but it can make big difference.

- The informal sector can be regulated to use it as a good resource. Waste pickers can be hired for their work and provide some facilities to them. This will affect positively in the solid waste management of India.

- The number of recycling plants, should be increased, so that the waste can be minimized.

- Composting units can be used for the degradable waste.

- The general public level waste management units can be run by self-help groups, youth groups or small entrepreneurs. This will help in making the solid waste management self-supportive and sustainable.

- All Indian school children should understand the importance of waste management, the effects of poor waste management on the environment and public health, and the role and responsibilities of each individual in the waste management system. This will develop responsible citizens who regard waste as a resource opportunity.

IV. CONCLUSION

India's population and particularly gathering of the more population at metro cities make the solid waste management of India worse. The current situation of the solid waste management system is not reliable or not adequate for such big problem. There is a need that the solid waste management system of India should be improved. Also, there is lack of awareness among people, that should be changed. The major issues can be solved with the participation of public and private organizations. Until the fundamental requirements are met, India will continue to suffer from poor waste management and the associated impacts on public health and the environment.

V. REFERENCES

[1]. Central Pollution Control Board of India (CPCB) (2016), "Status of solid waste management in metro cities", CPCB.

[2]. Singhal S, Pandey S. (2001), "Solid waste management in India: status and future directions". TERI Inf. Monitor Environ Sci. 6

[3]. Sunil Kumar, Stephen R. Smith, Geoff Fowler, "Challenges and opportunities associated with waste management in India" Royal Society Open Science 4:160764

[4]. R. Agarwal, Mona Chaudhary, Jayveer Singh (2015) "Waste Management Initiatives In India For Human Well Being", European Scientific Journal

Synthesis and Characteristics of MgO Doped Polyaniline Nano Composites

D.R. Bijwe[1], A. V. Rajgure*[1], S. S. Yawale[2], S.P. Yawale[2], P. S. Deole[1], P. A. Thakare[1], B. D. Dhole,
S. D. Gularande[1], S. R. Warathi[1], D. R. Chorpagar[1]

[1]Department of Physics, G. S. Tompe Arts, Commerce & Science College, Chandur Bazar, Dist.- Amravati
(M.S.), India

[2]Govt. Vidarbha Institute of Science and Humanities, Amravati 444604, Maharashtra, India

ABSTRACT

In this paper, Magnesium oxide nano particles were prepared by sol-gel technique. In this synthesized using magnesium nitrate as a precursor. The PAni- MgO samples are prepared with 30 and 40 wt%. The structural changes of prepared composite materials were carried out by X-ray diffraction (XRD) tool.

Keyword:- PAni, MgO, XRD

I. INTRODUCTION

Conducting polymers have emerged as a very important class of materials because of their unique electrical, optical, and chemical properties leading to the wide range of technological applications. This class of materials provides tremendous scope for tuning of their electrical conductivity from semiconducting to metallic regime by way of doping [1, 2]. The unique properties of conducting polymers not only provide great scope for their applications but also have led to the development of new models to explain their observed properties, particularly various mechanisms of charge transport [3, 4].The importance of polymers is mainly because polymers are still regarded as a cheap alternative material that is manufactured easily. The intensive use of polymer in broad has led to the development of materials for specific applications namely composites [5]. Recently polymer matrix-ceramic filler composites receive increased attention due to their interesting electrical and electronic properties, integrated decoupling capacitors, angular acceleration accelerometers, acoustic emission sensors and electronic packaging. Ceramic materials are typically brittle, possess low dielectric strength and in many cases are different to be processed requiring high temperature. On the other hand, polymers are flexible, can be easily processed at low temperatures and exhibit high dielectric break down fields. Practical application of conducting polymers such as polypyrrole, polythiophene and polyaniline is limited particularly because of their poor mechanical properties.

Magnesium oxide can be used as a wood chips, sound-proof, light weight, heat- insulating and refractory fiber board and metallic ceramics. Also magnesium oxide applied in electronics, catalysis, ceramics, coatings and many other fields. Many researchers have discussed the synthesis and applications of magnesium oxide nano particles [6-11]. Magnesium oxide is also used as an additive in heavy fuel oils [12], reflecting and anti-reflecting coating [13] in optical applications and is used as the substrate in superconducting and ferroelectric thin films [14-16].

When size of MgO is reduced to Nano scale then properties of novel MgO are further magnified.

II. METHODS AND MATERIAL

1.1. Synthesis of Polyaniline (PAni):

Project participants followed the same instruction to oxidize 0.2M aniline hydrochloride with 0.25 M ammonium peroxydisulfate in aqueous medium. Aniline hydrochloride (purum, 2.59g, 20 mmol) was dissolved in distilled water in a volumetric flask to 50 ml solution. Ammonium peroxydisulfate (purum, 5.71 g, 25 mmol) was dissolved in water to make 50ml solution. Both solutions were kept for 1 h. at room temperature ($\sim$ 291 -297° K), then mixed in a beaker, briefly stirred, and left at rest to polymerize. Next day, the PAni precipitate was collected on a filter, washed with 100 ml portions of 0.2 M HCl and similarly with acetone. Polyaniline (emeraldine) hydrochloride powder was dried in air and then in vacuum at 60°C.

1.2. Synthesis of Magnesium Oxide:

Magnesium oxide was prepared by sol-gel technique. These were synthesized using magnesium nitrate ($MgNO_36H_2O$) as a precursor. Firstly 0.2 M magnesium nitrate was mixed in 100 ml of de-ionized water. Thereafter 0.5 M sodium hydroxide solution was added to the magnesium nitrate solution drop wise with continuous stirring (30min). Appearance of white precipitate in the beaker shows the formation of magnesium hydroxide. The pH of the solution was 12.5, as measured by digital pH meter. Filtered precipitate washed with methanol is dried at room temperature. Washing with methanol removes ionic impurities. The dried white powder was annealed in air for one to two hours to obtain MgO powder.
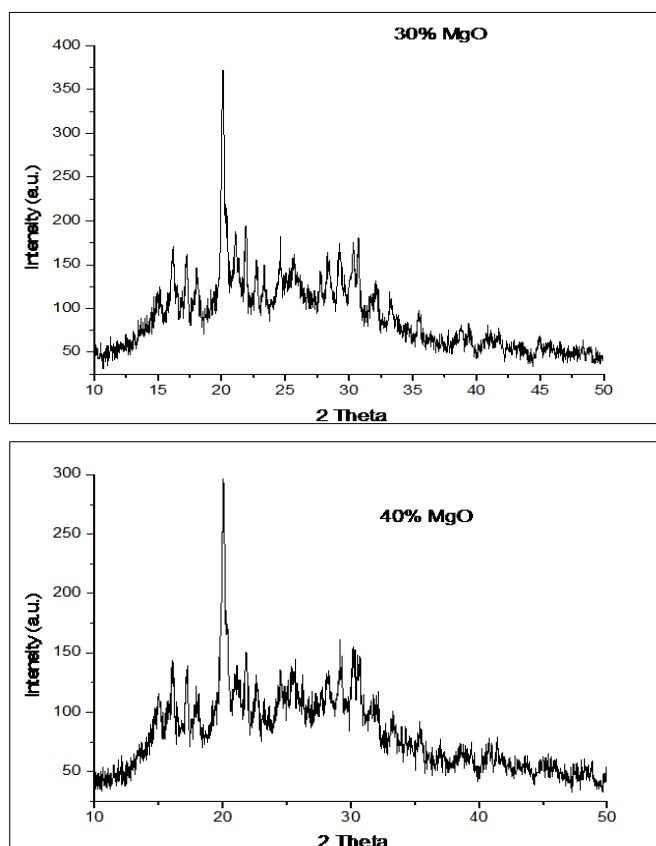
III. RESULTS AND DISCUSSION

Fig.1(a)X-rd of 30 wt% MgO-PAni Nanocomposite
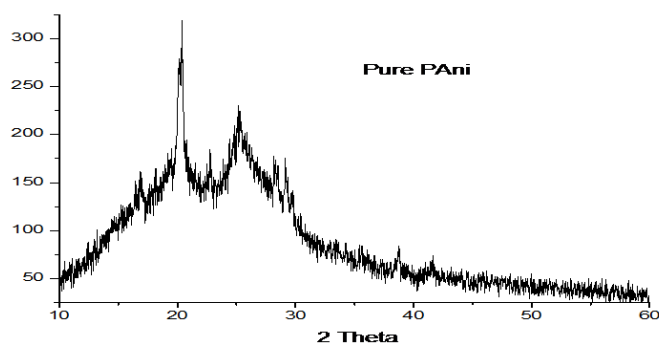Fig.1(b)X-rd of 40wt% MgO-PAni Nanocomposite

Fig. 1(c) X-rd of Pure Polyaniline

The X-ray diffraction patterns of the sample in the present study are obtained on Rigaku Miniflex-600 X-ray diffracto meter using Cukα radiation (λ = 1.5406 A^{o}). The diffract grams were recorded in the terms of 2θ in the range of 10- 80° with a scanning rate of 15 per minute.

Fig. 1(a) and (b) shows XRD patterns of 30wt% MgO-PAni and 40wt% MgO- PAni nanocomposites were scrutinized to compute their crystallite size. The

technique was used to examine the lattice constant, cell volume of the synthesized polyaniline and MgO-PAni nano composites. The X-ray diffraction pattern presents the peaks with the reference pattern of polyaniline and MgO which confirms the successful synthesis of the Nano composites with cubic structure. Fig. 1(c) shows the X-ray diffraction pattern of polyaniline . analysis of X-ray diffraction of polyaniline suggest that it has amorphous nature with broad peaks.

IV. CONCLUSION

The sol-gel method was used for preparation of PAni-MgO nano composites. This method may be used for the preparation of PAni nano composites with various metal oxide materials. Structure changes of pure PAni and PAni-MgO is observed by XRD pattern

V. REFERENCES

[1]. Mac Diarmid A G and Epstein A J (1994), Frontiers of polymers andadvanced materials(New York :Plenum press), 251

[2]. Wessling B (1999), Synth.Met 102, 1396

[3]. Kaiser A B , Subramanium C K, Gilberd P W,andWessling B,(1995), Synth Met., 69, 197

[4]. Kaiser A B, Liu C J, Gilberd P W, Kemp N T, Wessling B, Partridge A C, Smith W T and Shapiro J C,(1997),Synth Met., 84, 699

[5]. Comelio P, Lazzeri V and Waggle P,(1996), Polymer, 37(2) , 17-21

[6]. Jun-Kai Gao, Li-An Hou, Gung-Hui Zhang, Ping Gu, (2015), Journal of Hazardous Materials, 286, 325

[7]. Wancheng Zhu,Linlin Zhang,Gui-Li Tian,Ruguo Wang,Heng Zhang,Xianglan Piao,QiangZhang, (2014), CrystEngComm, 16, 3, 308

[8]. Amit Bhatnagar, Mika Sillanpää, (2014), Nanomaterials for Environmental Protection, 237

[9]. K R Nemade,S A Waghuley,(2014),InternationalJournal of Metals, 2014,1

[10]. S.Balamurugan,L Ashna,P Parthiban, (2014) Journal of Nanotechnology, 2014,1

[11]. S Devi Meenakshi, M Rajarajan, Susai Rajendran, Z Robert Kennedy and G Brindha, (2012), Nanotechnology,ElixirNanotechnology, 50, 10618-10620

[12]. Davini P and Tartarelli R, (1985), 64, 380-3

[13]. Duyar O and Durusoy H Z, (2004), J Phys, 28, 139-44

[14]. Phillips J M, (1996), Journal of Applied Physics, 79, 1829-48

[15]. Hamet J, Mercey B, Hervieu M and Raveau B, (1992), Physica C: Superconductivity, 193, 465-70

[16]. Liu S, Weaver J, Yuan Z, Donner W, Chen C, Jiang J, Meletis E, Chang W, Kirchoefer S and Horwitz J, (2005), Applied Physics Letters, 87, 142905--3

Arm Rehabilitation Assistive Device

Sudhanshu Tripathi*, Ashutosh Thakur, Tarun

Dept. of Instrumentation and Control Engineering, Amity School of Engineering and Technology, Delhi, India

ABSTRACT

This work proposed an Arduino based arm rehabilitation assistive device. The proposed approach helped us in identifying the problems that a stroke patient might suffer during their rehabilitation and how they can be helped by developing such a device. Certain perimeters that we took into consideration were the angular movement of the arm, the angular movement of fingers and the muscle strength of the forearm. These are some of the basic parameters that can be used to determine the movement of the arm. Presently the devices that are being used by doctors are very expensive and complex, this idea can revolutionize the process of the treatment of the stroke patients. The device designed is cheap and less complex which can easily be used by the patient at their home.

Keywords : Arm Rehabilitation, diagnostic tools, Arduino, Sensors, Treatment

I. INTRODUCTION

The stroke patients mainly include elderly people who undergo the rehabilitation process to cure their disability. Post stroke rehabilitation is necessary for them to regain their mobility of their arms and do their work. After a stroke the patients undergo a rehabilitation process which include certain types of exercises and certain motivation to cure themselves. The exercises can be exhausting for the patients as the patients are old and hand not working properly[2][3]. Due to this they need self-motivation to complete this rehabilitation process successfully. The series of exercises might become exhausting and sometimes they lose interest in doing the exercises because of which certain motivational speech is needed by the patient from family or the doctors[1].

Researchers from various universities and companies are continuously trying to figure various methods, exercises or devices that will or might help the stroke patients in curing their disability. These systems may include attaching thedevices to their limbs in order to monitor the patient's movement in any environment during rehabilitation.

These robots are called the ARM which has six degrees of freedom and are equipped with position and force measurement sensors. There are other robot-assisted devices which show some promising results. However, due to its heavy and complex structure it is only suitable for the usage in clinics.

There are researchers who have developed devices which are complex and heavy in structure and can be attached to the patient's limb. However, these devices do not include data logging capabilities. Due to this incapability after every reading it has to be worn off and as they are heavy and complex it becomes a very hectic job for the patient as well as some time for the doctors.

Further the motion sensors are only calibrated to measure certain range of motion and do not tell us

about the muscle activity. Strong muscle activity is important to provide information regarding fatigue due to certain movements or physical workouts. Therefore the work described in this paper describes the designing the arm rehabilitation assistive device which includes various sensors and data logging capabilities. We aim to produce a device which will help the post stroke patients and improve their condition[5].

We used three types of sensors : the gyroscope sensor, electromyogram sensor and a flex sensor.

All the three sensors have three different work to do and the combined data of all the three sensors will tell us about the condition of the hand of the stroke patients.

II. METHODS AND MATERIAL

The stroke patients suffer during their rehabilitation process. This is due to the reduction of interest in the process or the lack of motivation. This can occur due to the difficult exercises, heavy and complex machines etc. This isone of the major reasons why most of the people do not complete the rehabilitation process. As most of the people suffering stroke are elderly people, their self-motivation is already low due to certain factors, increasing their self-motivation is the main and most important factor. Which can only be done by removing the fear from them of the heavy and complex devices. These complex devices make some people impatient due to which they refuse the full treatment process [1].
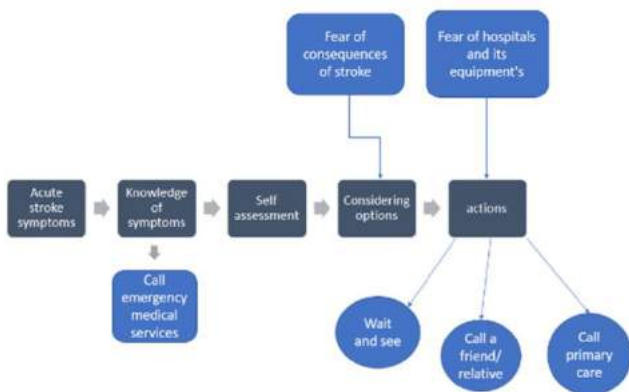

Fig 1. Block diagram of various phases during the treatment process

Furthermore, some devices do not even have data loggingcapability which can help the patient in many ways. The block diagram in Fig 1 shows some of the phases that a stroke patient goes through while being diagnosed with stroke.Two of the major problems showcased in this diagram are the,

- Fear of consequences stroke
- Fear of hospital professionals

Fear of the consequences of stroke is the psychological problem which can be treated by doing enough exercises and for doing enough exercises the patient needs self motivation. For this self motivation the patient needs to see and feel the improvement in his/her condition. Through this the fear of consequences of stroke in the patient might be reduced and the patient can recover as quickly as possible.

Fear of hospital professionals is the fear which is caused by seeing the heavy machines and devices which are used for the treatment of the stroke patients. The patients get feared of the process that the patient has to go through in their whole rehabilitation process. Some of the fear caused is also due to the high cost due to the using of complex devices for the rehabilitation process.

The device discussed in this paper is designed to tackle all the problems that a stroke patient might face.

The device discussed is light, less complex and has data logging capability which tackles almost every type of problems faced by a stroke patient.

First to make it light and less complex only three types of sensors are used which will be fitted on the gloves and the elbow guard which can be worn and taken off easily. So for the first problem that is related to the lack of motivation, when a patient can monitor their improvement on their own then they become self motivated on their own as it affects directly on

their psychology and mind that leads them in doing more of the physiotherapy which leads to the more improvement in their condition.

For the second problem that is the fear of the hospital professionals, according to us is due to the heavy and complex devices which are used in the treatment of the patient. The device discussed in this paper has data logging capability which in most of the current devices used in the industry does not exist. With the help of this data logging capability the patient with the comfort of their home can record the readings in a micro SD card or a personal computer and then send the reports to the doctor who then can analyze the report and give suggestions based on the data. As the device is less complex and easy to wear andtake out it can be bought and used in their own houses at their own comfort.

HARDWARE/ SOFTWARE REQUIREMENTS

The software portion of the module is developed using Arduino integrated development environment (IDE) and MATLAB. The Arduino module programming is created to take the data from the sensors used and to store it into the memory card. In the MATLAB all the data which is collected by the arduino is sent to it and the MATLAB creates graphs showing the betterment or the worsening of the patient's condition[8].

There are certain modules that are included in the MATLABwhich connects it with Arduino and provide a synchronized output.

There are mainly five hardware components used in this device, namely Arduino microcontroller, Arduino shield, flex sensors, accelerometer, electromyogram (EMG) sensor.

The Arduino UNO[4] is an open-source microcontroller which is developed by arduino.cc.The Arduino board has a number of ways to communicate with the computer. It can communicate through the USB cable and the other way is that it has Rx and Tx pins where we can connect the wifi or the bluetooth module which can communicate with the computer.

Arduino shield is a board that can be mounted on the top of the Arduino board[10]. The bending angle of the arm from elbow is measured using flex sensor, directly connected to the Arduino board[9]. To measures the force of acceleration due to gravity accelerometer is utilized. The sensor measures the acceleration in the X,Y and Z axis and gives analog voltage output proportional to the three axis[6].measure the small electrical pulses generated by the muscles during slightest of the muscle activity is measured by EMG sensor.Electrical activity detected is either stored in the SD card or displayed on the computer screen in the form of waves[9].

III. RESULTS AND DISCUSSION

The device discussed in this paper has three sensors attached to it which should give expected outputs. As per the expectations the flex sensor should show that when it will bend inwards the output resistance reading will increase significantly and vice versa. The readings will be taken when the sensor will be attached to the subject's elbow. An expected result as an example is shown in the figure 2 with 10 readings,
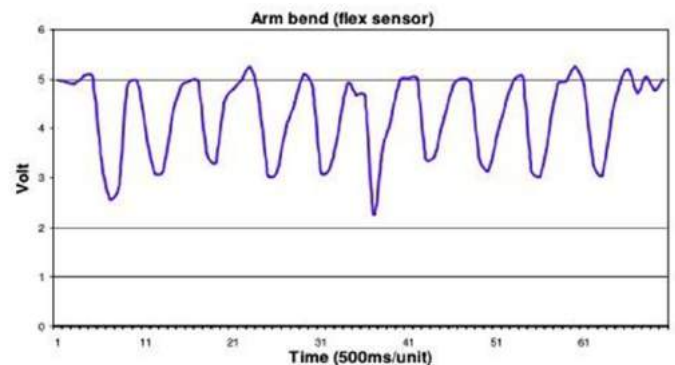

Fig 2. OUTPUT OF THE FLEX SENSOR

These assumptions suggest that the flex sensor is the best suitable sensor for the recording of the angular movementof the arm. The output of EMG can be shown on the LCD The accelerometer measures the force generated due to the movement of the arm in the presence of gravity in g units. There are certain activities designed which the subject will do with the

device on the hand and due to these activities the accelerometer can record as per the expectation readings as the hand will move in each and every direction.
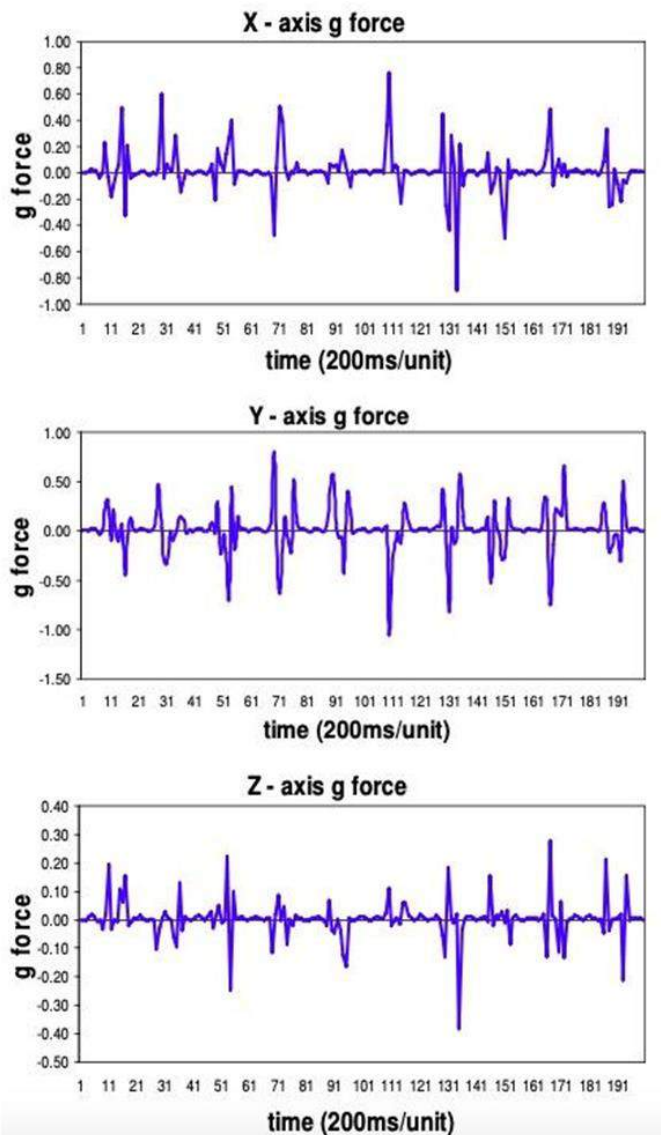

Fig 3. OUTPUT OF THE ACCELEROMETER

An expected result is shown in the figure 3 which is shown in the graphical form different for every X,Y and Z-axis by combining various readings.The quantified results such as force generated during certain workouts could be useful in estimating the fatigue conditions of the subject due to certain continuous workouts.

IV. CONCLUSION

A wearable rehabilitation device with a monitoring system is designed for stroke patients. The describedmicrocontroller based system has mainly three sensors that are flex sensor, accelerometer and the EMG sensor. The device discussed will have two types of monitoring systems: first the data logging capability which is present in very few machines in the market and second the real time monitoring by connecting devices with the computer. This rehabilitation system has certain advantages,

System is compact and lightweight.
Easy to attach to arms without assistance.
Two types of data logging capability
Can be used in the patients comfort at home.

Our future work will focus on the treatment of the subject by the addition of pulse generators which produce electric pulses in synchronous with the movement. As when hand moves muscle activates and this activation releases some very sensitive and small electrical pulses which is sensed by the EMG sensor this then activates the pulse generator.

V. REFERENCES

[1]. R.Ambar,M.SAhmad,A.MMohd.   Ali,M.M Abdul Jamil Arm rehabilitation assistive device (2011) Journal of Engineering Technology

[2]. Muscular Dystrophy Association (MDA) ALS Division (2010). Everyday Life with ALS: A Practical Guide. MDA Publications Department.

[3]. Peggy A. Houglum. (2010). Therapeutic Exercise for Musculoskeletal Injuries. Human Kinetics Publisher,229.

[4]. John Sarik, IoannisKymissis (2010). Lab Kits Using the Arduino Prototyping Platform. 40th ASEE/IEEE Frontiers in Education Conference,2010.

[5]. H.Zheng, N.D.Black, N.D. Harris (2005). Position-sensing technologies for movement analysis in stroke rehabilitation. Med. Biol. Eng. Comput.;2005;43;413-420.

[6]. Takashi Sakaguchi et al. (1996). Human Motion Capture by Integrating Gyroscopes and Accelerometers. International Conference on Multisensor Fusion and Integration for Intelligent Systems",1996.

[7]. S. Masiero, A. Celia, G. Rosati, and M. Armani (2007). Robotic-assisted rehabilitation of the upper limb after acutestroke.Arch Phys Med Rehabil, 88, 142-149, 2007

[8]. J. L. Patton, G. Dawe, C. Scharver, F. A. Muss-Ivaldi, and R. Kenyon (2006). Robotics and virtual reality: A perfect marriage for motor control research and rehabilitation. Assistive Technology, 18, 181-195,2006.

[9]. Oliver Amft et al, "Sensing Muscle Activities with BodyWorn Sensors", International Workshop on Wearable andImplantableBody Sensor Networks, IEEE Computer Society. 2006.

[10]. John Sarik, IoannisKymissis (2010). Lab Kits Using the Arduino Prototyping Platform. 40th ASEE/IEEE Frontiers in Education Conference,2010.

Thermoluminescence Properties of KAl(SO$_4$)$_2$:Eu^{3+} Phosphors

S. R. Bargat[1,2*], Yatish R. Parauha[1], G.C. Mishra[2], S. J. Dhoble[1]

[1]Department of Physics, R.T.M. Nagpur University, Nagpur, Maharashtra, India

[2] Department of Physics, O.P. Jindal University, Punjipathra, Raigarh, Maharashtra, India

ABSTRACT

In the present work, a series of Eu^{3+} activated KAlSO$_4$ phosphors were synthesized by solid state reaction method. The present paper reports thermoluminescence (TL) glow curves of the synthesized Eu^{3+} activated KAlSO$_4$ phosphors. TL glow curves were recorded for different concentration of Eu^{3+} ions by gamma exposure at a heating rate of 5 °C s^{-1}. The TL glow curve shows broad emission band at 6200 Gy irradiation of gamma rays in the temperature range of 50° to 400°C. It was found that the TL emission intensity increases linearly up to 0.7 mol% and then decreases with increasing concentration of Eu^{3+}. The TL glow curves show linearity with increasing exposure. The response curve of the synthesized phosphor showed linearity in the range 800–9300 Gy. All these results represent synthesized phosphor may be useful for future work in field of dosimetric application.

Keywords : Solid state reaction method; Thermoluminescence (TL); Gamma rays; TL response curve

I. INTRODUCTION

Rare earth doped phosphors material have many useful applications such as phosphor converted LEDs, thermoluminescence dosimeter, phototherapy lamp, solar cell, fingerprint detection, etc [1]. Thermoluminescence emission is also known as thermally stimulated luminescence. When the sample, which may be a semiconductor or an insulator containing defects, is irradiated by energetic ionizing radiations, energy gets stored at this sample. When this sample is heated, the stored energy is emitted in the form of light. Heating plays an important role of a stimulant or a trigger for initiating the emission of light. It is usually considered that TL is caused by electron-hole recombination, one of which is released thermally from a trap[2]. Thermoluminescence is a significant tool for evaluating the depth of the trap of solids and heating a crystal lattice that can result in the release of trapped electrons with associated emission of light. In the past few years, high-performance thermoluminescence (TL) materials gained more popularity in the field of radiation dosimetry due to the increasing demand for thermoluminescence dosimeters (TLDs), which have widespread application in the field of industrial, environmental, personal and clinical and radiation safety [1,3,4]. Generally, thermoluminescent dosimeters (TLD) badges are used in several radiations monitoring purpose. At present several oxide, fluoride, and sulfate-based phosphors have been prepared and they are used as cost-effective TL identification; however all prepared dosimeters are not perfect for radiation dose measurement [3]. Some of them are used for the low radiation dose field and some of them are used for high radiation dose field.

In the recent few years, many researchers and scientists are developed various rare earth doped phosphors to improve the dosimetric properties of existing materials for use as effective TLD materials over a wide range of radiation doses. Developments of new materials are being made very often to improve the properties of the materials and to find alternative precursors that can give attractive properties. Rare earth activated sulfate materials are widely investigated by the researchers because of their marked benefits as sulfate is an important host. In the category of sulfate materials $CaSO_4$:Dy is one of the most investigated materials to date and is frequently used as commercial TLD phosphor[5]. As per literature, upto till date various sulfate-based luminescence materials have been synthesized and reported by researchers for various applications. Sulfate based phosphors have amazing properties such as excellent chemical energy, large bandgap, low sintering temperature, flexible structure, fast ionic conductivity, moderate phonon energy, high stability [6–8].

In the luminescence process rare earth ions play vital role. Rare earth elements have partially filled 4f and 5f energy levels. Usually divalent or trivalent lanthanide ions used for luminance based applications. Eu^{3+} is one of them, it is well known and widely used rare earth ions in red emitting phosphors. In this paper we are dealing with Eu^{3+} ion doped $KAl(SO_4)_2$ phosphors. Trivalent europium possesses line emission and band emission gives line emission, it is also known as characteristic emission. This is due to 4f-4f transition. In this proposed work, we synthesis $KAl(SO_4)_2$ phosphors doped with trivalent europium with the help of Combustion synthesis route and perform thermoluminescence characterization.

II. METHODS AND MATERIAL

Synthesis of materials:

A series of Eu^{3+} activated $KAlSO_4$ phosphors were synthesized by solid state reaction method. In this work, K_2CO_3, Al_2O_3, $(NH_4)_2SO_4$ and Eu_2O_3 precursors are used as starting materials. All these starting materials weighed according to stoichiometric ratios. These weighed samples were crushed properly by a mortar pestle and converted into powder. The obtained powder was transferred to the crucible and placed in a furnace for heating at a temperature of 700°C for 24 hours. After 24 hours, turn off the furnace and leave it to cool. The obtained samples were again crushed after cooling to room temperature.

III. RESULTS AND DISCUSSION

3.1 XRD Measurement:

Figure 1 shows the XRD pattern of synthesized Eu^{3+} activated $KAl(SO_4)_2$ phosphor. The crystal structure and phase purity of as-synthesized Eu^{3+} doped $KAl(SO_4)_2$ phosphor was analysed by XRD diffraction pattern shows all diffraction peaks are well match with the standard ICSD data file no. 98-017-3667. Some impurity peaks can also be observed which may be possible due to the presence of Eu^{3+} ions and instrumental noise. In addition, figure 1 depicts sharp XRD peaks which are indicated that the homogeneous and crystalline nature of the synthesized phosphor.
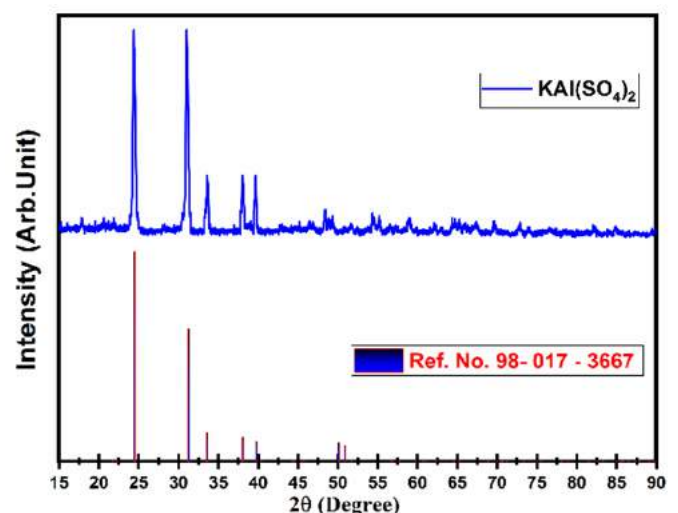

Figure 1: XRD pattern of synthesized Eu^{3+} activated $KAl(SO_4)_2$phosphor

3.2 Thermoluminescence Properties

The TL glow curves of the synthesized phosphors were irradiated with γ-rays from a ^{60}Co γ-ray irradiation source. The TL glow curve of this phosphor was obtained using a Nucleonix 1009I TL reader. The TL glow curves of the irradiated phosphors were recorded in the temperature range 50–400 °C and heating rate was 5 °C/s; 5 mg irradiated phosphors were used for each TL glow curve examination. Figure 2 (a) shows TL glow curve of the Eu^{3+} activated $KAl(SO_4)_2$ phosphor for different concentration of Eu^{3+} ions. TL glow curve shows broad emission band for each concentration of Eu^{3+} ions. The emission band depicts maximum emission intensity at 0.7mol% concentration of Eu^{3+} ion at around 300°C. It is clear from the figure, emission intensity varies with variation of Eu^{3+} concentration. The emission intensity increased up to 0.7mol% as shown in Figure 2 (b) after that TL emission intensity decreased due to concentration quenching effect. The emission intensity depends on the formation of defects in the conduction and valence bands. These defects occur up to a certain level, after which the defects overlap, and prohibit any increase in the emission intensity; this may be directly responsible for the concentration quenching effect [9].
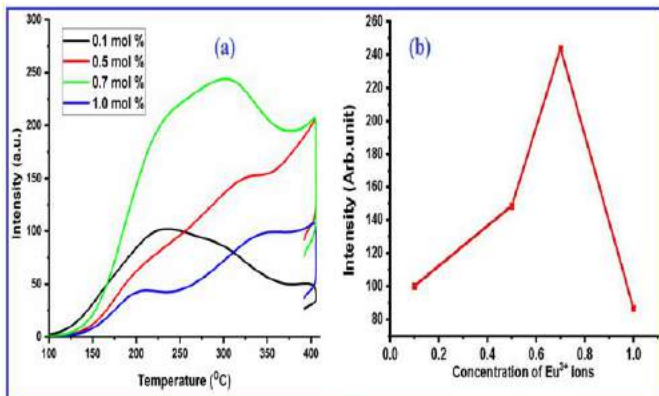

Figure 2 (a) Thermoluminescence (TL) glow curves of Eu^{3+} activated $KAl(SO_4)_2$ phosphor monitored under 6200 Gy γ-rays irradiation (b) Variation of emission intensity with concentration of Eu^{3+} ions

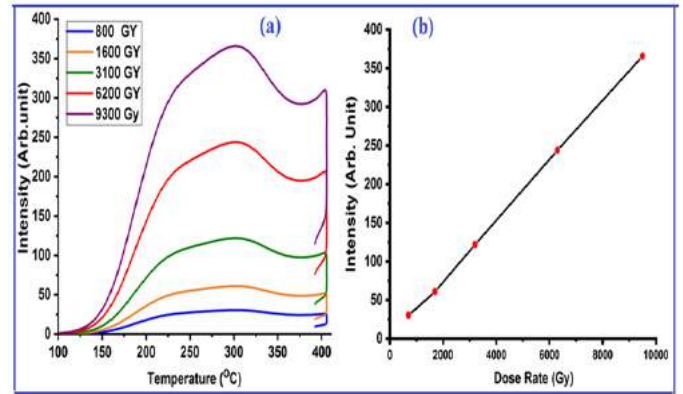**Figure 3 (a) TL glow curve of $KAl(SO_4)_2$:0.7mol%Eu^{3+} phosphor for different exposure of γ-rays irradiation. Figure 3(b) Linear Response curve of the $KAl(SO_4)_2$:0.7mol%Eu^{3+} phosphor**

As per our study, we have maximum TL emission intensity at 0.7mol% concentration of Eu^{3+} ions. Therefore $KAl(SO_4)_2$:0.7mol%Eu^{3+} phosphor is irradiated with different doses of γ-rays irradiation. Figure 3 (a) shows glow curve of the synthesized $KAl(SO_4)_2$:0.7mol%Eu^{3+} phosphor for different exposure of γ-rays irradiation. The emission intensity of the glow curve increased with increase in irradiation dose in the range of 800 Gy to 9300 Gy. With the variation of gamma exposure only TL emission intensity increased but structure of the dosimetric peak remained the same. Figure 3 (b) shows the TL response curve of the synthesized $KAl(SO_4)_2$:0.7mol%Eu^{3+} phosphor at different irradiation doses. The response curve of the synthesized phosphor showed linearity in the range 800 Gy to 9300 Gy. In this study, saturation in intensity has not been observed; it is possible that, along with the increasing the exposure of γ-rays, intensity may increase.

IV.CONCLUSION

In this study, Eu^{3+} activated $KAlSO_4$ phosphors were synthesized by Solid state reaction method. The phase confirmation of synthesized phosphors is done with the XRD pattern. Further, their luminescence properties are characterized by thermoluminescence

technique with irradiation of γ-rays using from a ^{60}Co γ-ray irradiation source. The glow curves shows broad emission band in the temperature range 50 °C – 400 °C. The TL glow curve spectra depict maximum emission intensity at 0.7mol% concentration of Eu^{3+} ions. The TL glow curves show linearity with increasing exposure. The response curve of the synthesized phosphor showed linearity in the range 800–9300 Gy. All these results represent synthesized phosphor may be useful for future work in field of dosimetric application.

Acknowledgement

V. REFERENCES

[1]. Y.R. Parauha, S.J. Dhoble, Thermoluminescence study and evaluation of trapping parameter of rare earth activated Ca3Al2O6: RE (RE = Eu2+,Ce3+) phosphors, J. Mol. Struct. 1211 (2020) 127993. https://doi.org/10.1016/j.molstruc.2020.127993.

[2]. A. Duragkar, A. Muley, N.R. Pawar, V. Chopra, N.S. Dhoble, O.P. Chimankar, S.J. Dhoble, Versatility of thermoluminescence materials and radiation dosimetry – A review, Luminescence. 34 (2019) 656–665. https://doi.org/10.1002/bio.3644.

[3]. S.R. Bargat, Y.R. Parauha, G.C. Mishra, S.J. Dhoble, Thermoluminescence study of CaNa2 (SO4)2 phosphor doped with Eu3+ and synthesized by combustion method , Luminescence. 2 (2020) 0–2. https://doi.org/10.1002/bio.3940.

[4]. J. Singh, J. Manam, F. Singh, Synthesis and thermoluminescence studies of -irradiated Dy3+ doped, Mater. Res. Bull. 94 (2017) 113–121. https://doi.org/10.1016/j.materresbull.2017.05.052.

[5]. M.S. Bhadane, S.S. Dahiwale, K.R. Sature, B.J. Patil, V.N. Bhoraskar, S.D. Dhole, TL studies of a sensitive CaNa2(SO4)2:Dy nanophoshor for gamma dosimetry, Radiat. Meas. 96 (2017) 1–7. https://doi.org/10.1016/j.radmeas.2016.11.009.

[6]. A. Deshpande, N.S. Dhoble, S.C. Gedam, S.J. Dhoble, Photoluminescence and thermoluminescence of K2Mg(SO4)2:Eu and evaluation of its kinetic parameters, J. Lumin. (2016). https://doi.org/10.1016/j.jlumin.2016.08.003.

[7]. C. Ghanty, N.S. Dhoble, S.J. Dhoble, Thermoluminescence dosimetry properties and kinetic analysis of, 2 (2020). https://doi.org/10.1002/bio.3957.

[8]. A. Deshpande, N.S. Dhoble, S.C. Gedam, S.J. Dhoble, Photoluminescence and thermoluminescence of K2Mg(SO4)2:Eu and evaluation of its kinetic parameters, Luminescence. 32 (2017) 757–764. https://doi.org/10.1002/bio.3247.

[9]. G.B. Nair, S. Tamboli, S.J. Dhoble, H.C. Swart, Comparison of the thermoluminescence properties of NaCaPO4:Dy3+ phosphors irradiated by 75 MeV C6+ ion and γ -rays, 224 (2020) 1–11. https://doi.org/10.1016/j.jlumin.2020.117274.

White Light Emission from La₂(MoO4)₃ : Dy³⁺ Phosphor

Yatish R. Parauha, S.J. Dhoble˙

Department of Physics, R.T.M.Nagpur University, Nagpur, Maharashtra, India

ABSTRACT

White light-emitting Dy3+ activated La2(MoO4)3 phosphor was successfully synthesized by a solid-state reaction method. Their structural, morphological, and luminescence properties were characterized by Photoluminescence techniques. Under ultraviolet (UV) and blue excitation, synthesized phosphor exhibits two emission bandsat blue (484nm) and yellow (575 nm),which correspond to $4F9/2 \rightarrow 6H15/2$ and $4F9/2 \rightarrow 6H13/2$ transitions of Dy3+, respectively.The optimized concentration of Dy3+ ions is 0.7mol% after the concentration quenching takes place. The CIE chromaticity coordinates for the optimized phosphor are (0.329, 0.377), and they lie in the white light region. The above-mentioned results demonstrate thatDy3+ activated La2(MoO4)3 is a potential phosphor for solid-state lighting applications.

Keywords : Solid-state reaction method; Photoluminescence; Concentration quenching; Solid-State lighting application

I. INTRODUCTION

In the recent few years, pc-WLEDs have gained more popularity due to their marvellous advantages. Now, it is commercially used, as like, traffic signals, large outdoor displays, interior and exterior lighting in aircraft, cars, and buses, as bulbs in flashlights and as backlighting for cell phones and liquid-crystal displays[1–3].At present three methods are known for production of WLEDs: first is mixing of Red, Green, Blue (RGB) LEDs, second is the commercial WLEDs, which consists of an InGaN-based blue LED chip and yellow-emitting phosphors (YAG: Ce³⁺), and another one is near UV chip excited tricolour (RGB) phosphors [4]. Currently, commercial WLEDs have realized some drawbacks such as low color rendering effects, high color temperatures, and the absence of red-emitting components. Because of these shortcomings and weaknesses, researchers, scientists, and industrialists have made several attempts to develop inorganic phosphors for white light generation. So far, various rare-earth activated phosphors have been investigated, but these phosphorus have some drawbacks, such as shorter lifetime and lower quantum efficiency [5].Near UV-LEDs in combination with blue, green, and red-emitting phosphors show superior luminescence properties over the commercialized blue-emitting LED with yellow-emitting phosphors. However, phosphor development for near UV LEDs is a challenging problem and a vibrant area of research. The rare earth (RE) ions, activated phosphors found to be excellent luminescent materials.Trivalent dysprosium (Dy³⁺) rare earth ions most suitable rare earth for potential single white light center because its emission is very close to white owing to the blue (⁴F9/2→⁶H15/2) and yellow (⁴F9/2→⁶H13/2) emission. Moreover its red spectral part comparing to the ⁴F9/2→⁶H11/2transition can improvethe color temperature[6,7]. For solid-state lighting applications, the Molybdanate materials have gained significant

attention as self-activated and rare-earth ions doped Molybdanate host materials. Molybdanate based hosts have broadband absorption and emission band in the UV and visible regions due to the electronic charge transfer band. The Molybdanate-based host materials doped with Dy^{3+} phosphors are mostly used in WLEDs because Molybdanate have higher chemical stabilities and absorption in the UV region to the visible region. In the past, Molybdanate host matrices have been widely used in optoelectronic applications due to their many advantages, such as low cost, high stability, easy fabrication, and excellent physical-chemical properties[8,9].

According to the literature, photoluminescence properties never reported for the $La_2(MoO_4)_3$:xDy^{3+} phosphor. In this study, $La_2(MoO_4)_3$:xDy^{3+} phosphor was synthesized using Solid State Reaction method and their luminescence properties were analyzed by Photoluminescence Technique.

II. METHODS AND MATERIAL

Synthesis

All sample powder was synthesized by solid-state diffusion method. The $La_2(MoO_4)_3$:xDy^{3+} phosphors (x = 0, 0.1, 0.2, 0.5, 1 and 2mol%) were preparedby using La_2O_3, $(NH_4)_2MoO_4$ and Dy_2O_3 as starting materials.These materials were weighed according to the designed compositions. The stoichiometric amounts of starting reagents were thoroughly mixed for 1 h using a mortar and pestle. The obtained powder was annealed in a furnace at 400 °C for 2 h using ceramic crucible. The obtained powder was again ground for 1 h using a mortar and pestle and, then, it was heated at 800 °C for 24 h for proper interaction of all reagents via diffusion. After the treatment, the samples were cooled to room temperature and grounded in the final powder products.

La_2O_3 + $3(NH_4)_2MoO_4 \rightarrow$ $La_2(MoO_4)_3$ + $6.NH_3\uparrow$ + $3.H_2O\uparrow$
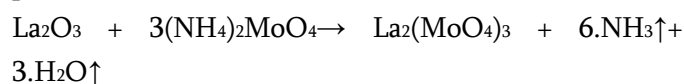
III. RESULTS AND DISCUSSION

3.1 XRD and SEM measurement

The phase confirmation and the crystallinity of synthesized phosphors were analyzed by XRD measurement and particle size, morphological behavior was observed by scanning electron microscope. XRD pattern and SEM images of $La_2(MoO_4)_3$:1mol%Eu^{3+} phosphor phosphors are already recently published [10] . The XRD pattern of synthesized phosphor shows a good crystalline nature and XRD patterns well matched with that of ICSD Ref. Code 98-2634. The phase of the phosphors is identified as monoclinic structure in space group C2/c. The SEM images show that the phosphor consists of spherical shape. The particle size of the synthesized phosphor is around 1μm.

3.2 Photoluminescence study

The excitation spectrum of synthesized Dy^{3+} activated $La_2(MoO_4)_3$ phosphor monitored under 482nm emission wavelength in the range of 300nm to 460nm. The excitation spectrum depicts fivehighly intense excitation peaks in the UV and visible region as shown in Figure 1. The Excitation peaks are situated around at 324nm, 350nm, 365nm, 386nm and 454nm, which are ascribed due to $^6H_{15/2} \rightarrow {}^6P_{3/2}$, $^6H_{15/2} \rightarrow {}^6P_{7/2}$, $^6H_{15/2} \rightarrow {}^6P_{5/2}$, $^6H_{15/2} \rightarrow {}^4I_{13/2}$, and $^6H_{15/2} \rightarrow {}^4I_{15/2}$ respectively [11].All the excitation peaks situated in 320nm to 460nm, which is indicating that Dy^{3+} ions may be used as efficient activators for white LEDs[11].
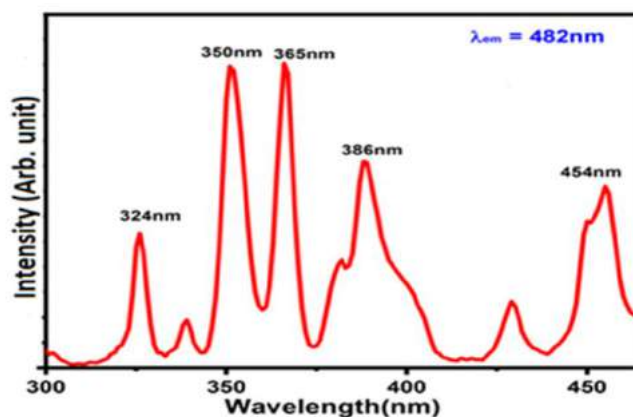
Figure 1: PL excitation spectrum of Dy³⁺ activated La₂(MoO₄)₃phosphor under 482nm emission wavelength

Figure 2 (A) represents PL emission spectra of La₂(MoO₄)₃:xDy³⁺(x = 0.1, 0.2, 0.5, 0.7, 1.0mol%)phosphors under 350nm excitation wavelength. The emission spectra depicts two emission peak around at 481nm, 491 (blue region) and 573nm (Yellow region), corresponding to the ⁴F₉/₂ →⁶H₁₅/₂ and ⁴F₉/₂ → ⁶H₁₃/₂ transitions, respectively.The ⁴F₉/₂→⁶H₁₅/₂ transition can be stated as a magnetic dipole transition, whereas the ⁴F₉/₂ →⁶H₁₃/₂ transition can be attributed to a forced electric dipole transition[12].However, the peak intensity is found to increase when the dopant concentration varies from x=0.05 to 0.7mol%. After 0.7mol% concentration of Dysprosium ions PL emission intensity suddenly decrease because of concentration quenching effect.Figure 2(b)shows concentration quenching spectra of La₂(MoO₄)₃:Dy³⁺ phosphor.
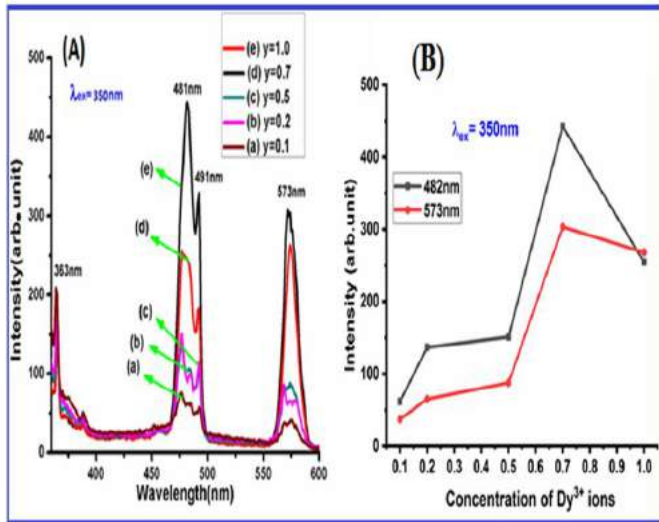

Figure 2 (A) PL emission spectrum of La₂(MoO₄)₃:xDy³⁺ (x 0.1, 0.2, 0.5, 0.7, 1.0mol%)phosphor under 350nm excitation wavelength and **Figure 2 (B)**Variation in PL emission intensity with concentration of Eu³⁺ ions

3.3 Photometric Characterization

In 1931, the Commission International de l'Eclairage (CIE) co-ordinates were used to study color emission of the synthesized phosphor in the visible spectrum. Figure 5 shows CIE chromaticity coordinate of synthesized 0.7mol% Dy³⁺ activated La₂(MoO₄)₃ phosphor, CIE coordinate were calculated by using OSRAM SILVANIYA Color calculator and PL emission intensity under 350nm, 365nm, 386nm and 454nm excitation wavelength. The calculated coordinate is represented in table 1.
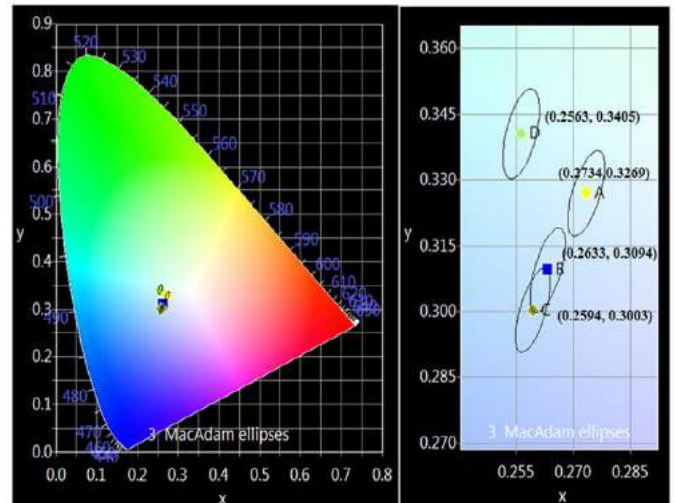
Figure 5:CIE chromaticity Diagram of La₂(MoO₄)₃:0.7mol%Dy³⁺ phosphors at different excitation wavelength

Table: 1: CIE Chromaticity diagram and Color Purity ofLa₂(MoO₄)₃:0.7mol%Dy³⁺phosphors

Sr. No	Compound Name	Excitation wavelength	CIE Chromaticity Coordinates	Color Purity
1.	La₂(MoO₄)₃ 0.7mol%Dy³⁺	350nm	(0.2734, 0.3269)	79%
2.	La₂(MoO₄)₃ 0.7mol%Dy³⁺	365nm	(0.2633, 0.3094)	76%
3.	La₂(MoO₄)₃ 0.7mol%Dy³⁺	386nm	(0.2594, 0.33003)	75%
4.	La₂(MoO₄)₃ 0.7mol%Dy³⁺	454nm	(0.2563, 0.3405)	77%

IV. CONCLUSION

In the present work, the Dy^{3+} activated $La_2(MoO_4)_3$ phosphor were synthesized by solid state reaction method. Under 350nm excitation wavelength, PL emission spectra observed. It shows blue and yellow color emission around 482nm and 573nm transition, which ascribed $^4F_{9/2} \to ^6H_{15/2}$ and $^4F_{9/2} \to ^6H_{13/2}$ transitions of Dy^{3+} ions. PL investigation shows PL Emission spectra shows highest intensity under 350nm excitation wavelength. The concentration quenching (CQ) spectra shows highest PL emission intensity observed at 0.7mol% Dy^{3+} concentration. The CIE coordinates for synthesized phosphor were also calculated by using OSRAM SILVANIA color calculator and PL emission intensity. All these results shows that Dy^{3+} activated $La_2(MoO_4)_3$ phosphor may be a potential phosphor for solid-state lighting applications.

ACKNOWLEDGEMENT

V. REFERENCES

[1]. G.R. Dillip, S.J. Dhoble, L. Manoj, C.M. Reddy, B.D. Prasad, A potential red emitting K 4 Ca(PO4)2:Eu3+ phosphor for white light emitting diodes, J. Lumin. 132 (2012) 3072–3076. https://doi.org/10.1016/j.jlumin.2012.06.029.

[2]. J. Sun, F.T. Rabouw, X. Yang, X. Huang, X. Jing, S. Ye, Facile Two-Step Synthesis of All-Inorganic Perovskite CsPbX3 (X = Cl , Br , and I) Zeolite-Y Composite Phosphors for Potential Backlight Display Application, 3 (2017) 43–47. https://doi.org/10.1002/adfm.201704371.

[3]. G. Li, Y. Tian, Y. Zhao, J. Lin, Chem Soc Rev, Chem. Soc. Rev. (2015). https://doi.org/10.1039/C4CS00446A.

[4]. G. Zhang, L. Zhao, F. Fan, Y. Bai, B. Ouyang, W. Chen, Y. Li, L. Huang, Spectrochimica Acta Part A : Molecular and Biomolecular Spectroscopy Near UV-pumped yellow-emitting Ca3TeO6:Dy3+ phosphor for white light-emitting diodes, Spectrochim. Acta Part A Mol. Biomol. Spectrosc. 223 (2019) 117343. https://doi.org/10.1016/j.saa.2019.117343.

[5]. B. Si, O.O. Ge, D. Xiang, Y. Chu, X. Xiao, J. Xu, Z. Zhang, Z. Liu, Y. Zhang, Tunable luminescence and energy transfer of Dy3+ - activated, J. Solid State Chem. 268 (2018) 130–135. https://doi.org/10.1016/j.jssc.2018.08.038.

[6]. K. Dev, A. Selot, G.B. Nair, C.M. Mehare, F.Z. Haque, M. Aynyas, S.J. Dhoble, Optik Synthesis and photoluminescence study of Dy3+ activated SrAl12O19 phosphor, Opt. - Int. J. Light Electron Opt. 194 (2019) 163051. https://doi.org/10.1016/j.ijleo.2019.163051.

[7]. M.K. Sahu, White light emitting thermally stable bismuth phosphate phosphor Ca3Bi(PO4)3 :Dy3+ for solid-state lighting applications, (2019) 6087–6099. https://doi.org/10.1111/jace.16479.

[8]. A. Xie, X. Yuan, F. Wang, Y. Shi, J. Li, L. Liu, Z. Mu, Synthesis and luminescent properties of Eu3+ -activated molybdate-based novel red-emitting phosphors for white LEDs, J. Alloys Compd. 501 (2010) 124–129. https://doi.org/10.1016/j.jallcom.2010.04.057.

[9]. M. Haque, H. Lee, D. Kim, Luminescent properties of Eu3+ -activated molybdate-based novel red-emitting phosphors for LEDs, 481

(2009) 792–796. https://doi.org/10.1016/j.jallcom.2009.03.083.

[10]. Y.R. Parauha, R.S. Yadav, S.J. Dhoble, Enhanced photoluminescence via doping of phosphate, sulphate and vanadate ions in Eu3+ doped La2(MoO4)3 downconversion phosphors for white LEDs, Opt. Laser Technol. (2019) 105974.
https://doi.org/10.1016/J.OPTLASTEC.2019.105974.

[11]. T.R. Raman, Y.C. Ratnakaram, Concentration dependent Dy3+ activated LiPbB5O9 phosphor : Structure and luminescence studies for white LED applications, Opt. Mater. (Amst). (2019) 109515.
https://doi.org/10.1016/j.optmat.2019.109515.

[12]. R. Mahajan, S. Kumar, R. Prakash, V. Kumar, R.J. Choudhary, D.M. Phase, AC SC, J. Alloys Compd. (2018).
https://doi.org/10.1016/j.jallcom.2018.10.355.

Using Some Transform Techniques to Find Thermal Stresses and Temperature of An Annular Disc.

Gaikwad Priyanka B.

Department of Mathematics, Phulsing Naik Mahavidyalaya, Pusad, District-Yavatmal, Maharashtra, India

ABSTRACT

In this paper, an attempt has been made to solve problems of thermoelasticity and determine the unknown temperature, displacement and stress components. In this problem the zero temprerature is maintained on the curved surface and third kind boundary condition is maintained on lower and upper surface. The governing heat conduction has been solved by using finite Hankel transform technique. The results are obtained in series form in terms of Bessel's functions and have been computed numerically and illustrated graphically.

Keywords : Hankel transform, Thermoelastic problem, Annular Disc, Third kind boundary value Problem, Steady- state.

I. INTRODUCTION

During the second half of the twentieth century, non – isothermal problems of the theory of elasticity became increasingly important. This is due mainly to their many applications in diverse fields. First, the high velocity of modern aircrafts give rise to an aerodynamic heating, which produce intense thermal stresses reducing the strength of aircrafts structure.

Three-Dimensional Thermoelastic Problem Under Two-Temperature Theory studied by (Abhik et al., 2016). A Study on the Generalized Thermoelastic Problem for an Anisotropic Medium studied by (Ghosh et al. 2018)Two dimensional transient problems for a thick annular disc in thermoelasticity studied by (Dange et al., 2009). An inverse temperature field of theory of thermal stresses investigated by (Grysa et al; 1981) while A note of quasi –static thermal stresses in steady state thick annular disc and an inverse quasti-

static thermal stresses in thick annular disc are studied by (Gaikwad et al; 2010).

In this paper, the problem of third kind boundary condition is maintained on lower and upper surface of an annular disc. The governing heat conduction equation has been solved by using Hankel transform technique. The results are obtained in series form in terms of Bessel's functions and illustrated graphically.

This paper contains new and novel contribution of thermal stresses in an annular disc under steady state. The above results were obtained under steady state field. The result presented here are useful in engineering problem particularly in the determination of the state of strain in an annular disc constituting foundations of containers for hard gases or liquids, in the foundations for furnaces etc.

II. STATEMENT OF PROBLEM

Consider an annular disc of thickness 2h occupying the space D: $a \leq r \leq b$, $-h \leq z \leq h$. The thermoelastic displacement function as in [(Nowacki; 1962) is governed by Poisson's equation

$$\nabla^2 U = (1+v)a_t\, T \tag{2.1}$$

$$\text{with } U_r = 0 \text{ at } r = a \text{ and } r = b \tag{2.2}$$

$$\nabla^2 = \frac{\partial^2}{\partial r^2} + \frac{1}{r}\frac{\partial}{\partial r}$$

where

v and a_t are the poisson's ratio and the linear coefficient of thermal expansion of the material of the disc and T is the temperature of the disc satisfying the differential equation

$$\frac{\partial^2 T}{\partial r^2} + \frac{1}{r}\frac{\partial T}{\partial r} + \frac{\partial^2 T}{\partial z^2} = 0 \tag{2.3}$$

Subject to the boundary conditions

$$T(r,z) = 0 \text{ at } r = a, -h \leq z \leq h \tag{2.4}$$

$$T(r,z) = 0 \text{ at } r = b, -h \leq z \leq h \tag{2.5}$$

$$\frac{\partial T}{\partial z} + k_1\, T = f(r), \text{at } z = h, a \leq r \leq b \tag{2.6}$$

$$\frac{\partial T}{\partial z} - k_2\, T = g(r), \text{at } z = -h, a \leq r \leq b \tag{2.7}$$

where k_1 and k_2 are the radiation constants on the two plane surfaces.

The stress functions σ_{rr} and $\sigma_{\theta\theta}$ are given by,

$$\sigma_{rr} = -2\mu\frac{1}{r}\frac{\partial U}{\partial r} \tag{2.8}$$

$$\sigma_{\theta\theta} = -2\mu\frac{\partial^2 U}{\partial r^2} \tag{2.9}$$

Where μ is the Lame's constant, while each of the stress functions σ_{rz}, σ_{zz} and $\sigma_{\theta z}$ are zero within the disc in the plane state of stress.

The equations (2.1) to (2.9) constitute the mathematical formulation of the problem under consideration.

III. SOLUTION OF PROBLEM

On applying the finite Hankel transform defined in (Sneddon;1972) to Eq. (2.3), one obtain

$$\frac{d^2\bar{T}}{dz^2} - \xi_n^2\,\bar{T} = 0 \tag{3.1}$$

---

where T is the Hankel transform of T.

On applying Eq. (3.1) under the conditions given in Eq.(2.6) and Eq.(2.7), one obtains

$$\bar{T} = \sum_{n=1}^{\infty} \bar{f}(\xi_n) \times \left[\frac{\xi_n \cosh[\xi_n(z+h)] + k_2 \sinh[\xi_n(z+h)]}{(\xi_n^2 + k_1 k_2)\sinh(2\xi_n h) + \xi_n(k_1 + k_2)\cosh(2\xi_n h)} \right]$$

$$- \sum_{n=1}^{\infty} \bar{g}(\xi_n) \times \left[\frac{\xi_n \cosh[\xi_n(z-h)] - k_1 \sinh[\xi_n(z-h)]}{(\xi_n^2 + k_1 k_2)\sinh(2\xi_n h) + \xi_n(k_1 + k_2)\cosh(2\xi_n h)} \right] \qquad (3.2)$$

Applying the inverse Hankel transform to the equation (3.2), one obtain the expression for the temperature as

$$T = \sum_{n=1}^{\infty} \bar{f}(\xi_n) \left[J_0(r\xi_n) G_0(b\xi_n) - J_0(b\xi_n) G_0(r\xi_n) \right]$$

$$\times \left[\frac{\xi_n \cosh[\xi_n(z+h)] + k_2 \sinh[\xi_n(z+h)]}{(\xi_n^2 + k_1 k_2)\sinh(2\xi_n h) + \xi_n(k_1 + k_2)\cosh(2\xi_n h)} \right]$$

$$- \sum_{n=1}^{\infty} \bar{g}(\xi_n) \left[J_0(r\xi_n) G_0(b\xi_n) - J_0(b\xi_n) G_0(r\xi_n) \right]$$

$$\times \left[\frac{\xi_n \cosh[\xi_n(z-h)] - k_1 \sinh[\xi_n(z-h)]}{(\xi_n^2 + k_1 k_2)\sinh(2\xi_n h) + \xi_n(k_1 + k_2)\cosh(2\xi_n h)} \right] \qquad (3.3)$$

where

$$\bar{f}(\xi_n) = \int_a^b f(r) r \left[J_0(r\xi_n) G_0(b\xi_n) - J_0(b\xi_n) G_0(r\xi_n) \right] \qquad (3.4)$$

$$\bar{g}(\xi_n) = \int_a^b g(r) r \left[J_0(r\xi_n) G_0(b\xi_n) - J_0(b\xi_n) G_0(r\xi_n) \right] \qquad (3.5)$$

Equation (3.3) is the desired solution of the given problem.

DETERMINATION OF THERMELASTIC DISPLACEMENT

Substituting the value T(r, z) from Eq. (3.3) in Eq. (2.1) one obtains the thermoelastic displacement function U(r, z) as,

$$U(r,z) = -(1+v)a_t \sum_{n=1}^{\infty} \left(\frac{\bar{f}(\xi_n)}{\xi_n^2} \right) [J_0(b\xi_n) G_0(b\xi_n) - J_0(\xi_n) G_0(r\xi_n)]$$

$$\times \left[\frac{\xi_n \cosh[\xi_n(z+h)] + k_2 \sinh[\xi_n(z+h)]}{(\xi_n^2 + k_1 k_2)\sinh(2\xi_n h) + \xi_n(k_1 + k_2)\cosh(2\xi_n h)} \right]$$

$$+(1+v)a_t \sum_{n=1}^{\infty} \frac{\bar{g}(\xi_n)}{(\xi_n^2) J_0} [(r\xi_n) (G_0 b\xi_n) - J_0(\xi_n) G_0(r\xi_n)]$$

DETERMINATION OF STRESSES

Using Eq. (3.6) in Eq. (2.8) and Eq. (2.9), one obtains the stress function σ_{rr} and $\sigma_{\theta\theta}$ as,

$$\sigma_{rr} = -\frac{2\mu}{r}(1+v)a_t \sum_{n=1}^{\infty} \left(\frac{\bar{f}(\xi_n)}{\xi_n} \right) [J_1(b\xi_n) G_0(b\xi_n) - J_0(\xi_n) G_1(r\xi_n)]$$

$$\times \left[\frac{\xi_n \cosh[\xi_n(z+h)] + k_2 \sinh[\xi_n(z+h)]}{(\xi_n^2 + k_1 k_2)\sinh(2\xi_n h) + \xi_n(k_1 + k_2)\cosh(2\xi_n h)} \right] \qquad (3.7)$$

$$\sigma_{\theta\theta} = -2\mu(1+v)a_t \sum_{n=1}^{\infty} \bar{f}(\xi_n) [J'_1(r\xi_n) G_0(b\xi_n) - J_0(b\xi_n) G'_1(r\xi_n)]$$

$$\times \left[\frac{\xi_n \cosh[\xi_n(z+h)] + k_2 \sinh[\xi_n(z+h)]}{(\xi_n^2 + k_1 k_2)\sinh(2\xi_n h) + \xi_n(k_1 + k_2)\cosh(2\xi_n h)} \right] \qquad (3.8)$$

SPECIAL CASE AND NUMERICAL RESULTS

Set

$f(r)=(r-a)(r-b)e^h, g(r)=(r-a)(r-b)e^{-h}, \alpha=(1-a-b)$ in (3.3) one obtains

$$\frac{T(r,z)}{\alpha} = \sum_{n=1}^{\infty} e^h (G_0(b\xi_n) - J_0(b\xi_n)) \left\{ \frac{b^2}{\xi_n^2} [2J_0(b\xi_n) + (b\xi_n - \frac{4}{b\xi_n})J_1(b\xi_n)] \right.$$

$$-\frac{a^2}{\xi_n^2}[2J_0(a\xi_n)+(a\xi_n-\frac{4}{a\xi_n})J_1(a\xi_n)]$$

$$+\frac{ab}{(1-a-b)}[bJ_1(b\xi_n)-aJ_1(a\xi_n)]\}[J_0(r\xi_n)G_0(b\xi_n)-J_0(b\xi_n)G_0(r\xi_n)]$$

$$\times\left[\frac{\xi_n\cosh[\xi_n(z+h)]+k_2\sinh[\xi_n(z+h)]}{(\xi_n^2+k_1k_2)\sinh(2\xi_n h)+\xi_n(k_1+k_2)\cosh(2\xi_n h)}\right]$$

$$-\sum_{n=1}^{\infty}e^h(G_0(b\xi_n)-J_0(b\xi_n))\{\frac{b^2}{\xi_n^2}[2J_0(b\xi_n)+(b\xi_n-\frac{4}{b\xi_n})J_1(b\xi_n)]$$

$$-\frac{a^2}{\xi_n^2}[2J_0(a\xi_n)+(a\xi_n-\frac{4}{a\xi_n})J_1(a\xi_n)]$$

$$+\frac{ab}{(1-a-b)}[bJ_1(b\xi_n)-aJ_1(a\xi_n)]\}[J_0(r\xi_n)G_0(b\xi_n)-J_0(b\xi_n)G_0(r\xi_n)]$$

$$\times\left[\frac{\xi_n\cosh[\xi_n(z-h)]-k_1\sinh[\xi_n(z-h)]}{(\xi_n^2+k_1k_2)\sinh(2\xi_n h)+\xi_n(k_1+k_2)\cosh(2\xi_n h)}\right]\tag{3.9}$$

The numerical calculation have been carried out for steel (SN 50 C) plate with parameters $a = 1m$, $b = 2m$, $h = 0.5m$. thermal diffusivity $k = 15.9 \times 10{-}6(m2s{-}1)$ and poisons ratio $\nu = 0.281$, while $\xi_1 = 3.1965$, $\xi_2 = 6.3123$, $\xi_3 = 9.4445$, $\xi_4 = 12.5812$, $\xi_5 = 15.7199$ being the positive roots of transcendental equation $[J_0(r\xi_n)G_0(b\xi_n) - J_0(b\xi_n)G_0(r\xi_n)] = 0$ as in (Ozisik;1968).

IV. DISCUSSION

In this paper, equations (3.8) and (3.9) have been calculated and shown graphically by using Matlab, and the conclusion is as under:

Initially the temperature of the annular disc has been determined by using the conditions given in the problem and applying finite Hankel transform technique and its inverse. In this problem the temperature of the disc has been kept at zero on the curved surfaces and third kind boundary condition has been kept on lower and upper surface of the disc. Here, we have considered steel plate (SN 50C) as the metal and hence the graph shows a particular pattern resembling the properties of steel plate.

In an annular disc the change of temperature does not lead to any change in shear angles, except the stress and strain of the disc. These properties are clearly reflected in the plotted graph given below. The following conclusion can be drawn:

From fig.1 we see that temperature decreases from lower surface to outer curved surface in axial direction. Form fig.2 we observe that temperature decreases from upper surfaces to lower surface in axial direction.
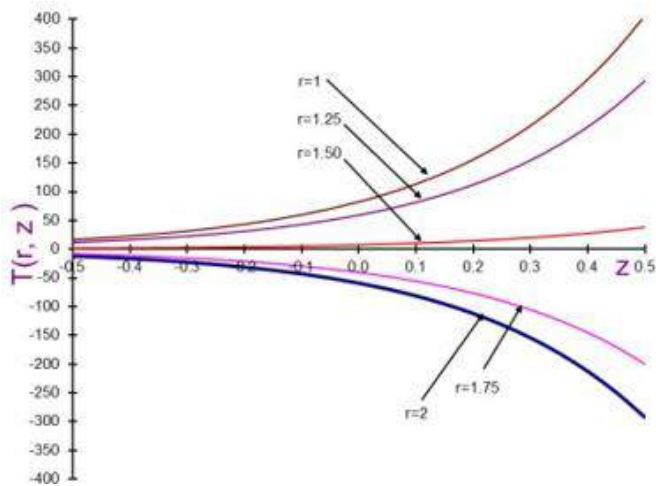

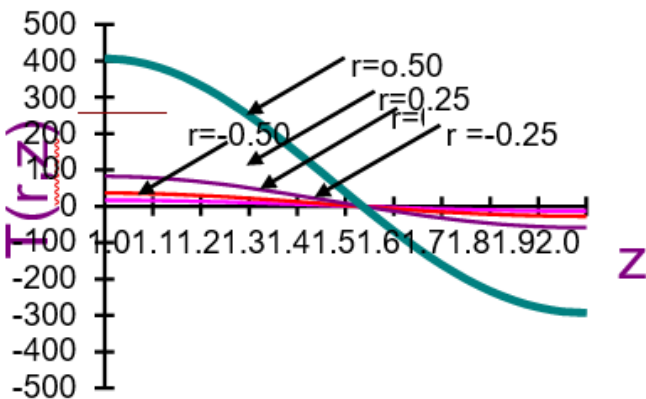Fig1. The temperature distribution T(r, z) in axial direction

Fig2. The temperature distribution T(r, z)in axial direction

V. REFERENCES

[1]. Abhik Sur and Mridula Kanoria., (2016). Three-Dimensional Thermoelastic Problem Under Two-Temperature Theory. International Journal of Computational Methods 14(03).

[2]. Dange, W.K., Khobraade, N.W., and Varghese, V., (2009). Two dimensional transient problems for a thick annular disc in thermoelasticity. Far East Journal of Applied Mathematics, Vol.43, 205-219.

[3]. Ghosh Debkumar and Lahiri Abhijit.,(2018) A Study on the Generalized Thermoelastic Problem for an Anisotropic Medium., J. Heat Transfer. 140(9): 094501 (8 pages) Paper No: HT-17- 1497 https://doi.org/10.1115/1.4039554

[4]. Grysa, K., Cialkowski, M. J and Kaminski H., (1981). An inverse temperature field of theory of thermal stresses. NUCL. Eng. Des. Vol.64. 161-184.

[5]. Gaikwad K.R., Ghadle K.P., (2010) A note of Quasi-Static Thermal Stresses in Steady State Thick Annular Disc.Acta Ciencia Indica,Vol.XXXVI M,No.3,385.

[6]. Gaikwad K.R.,Ghadle K.P. (2010). An Inverse Quasi-Static Thermal Stresses in Thick Annular Disc., International Journal of Applied Mathematics & Statistics. Vol.19. D10.

[7]. Nowacki, W. 1962. Thermoelasticity Mass. Addition-Wesley Publication Co. Chapter-1. Ozisik N.M. 1968. Boundary value problem of Heat Conduction, International text book Comp. Scranten, Pennsylvania, pp.481-492.

[8]. Sneddon, I.N. 1972.The use of integral transform, McGraw Hill, New York, 235-238.

Synthesis and Transport Properties of Polythiophene Polymer Composite

P. D. Shirbhate [1*], S. R. Vadrabade[1], S. P. Yawale [2], S.V. Pakade [3]

[1]Department of Physics, Gopikabai Sitaram Gawande College Umarkhed, India

[2]Department of Physics, Government Vidarbha Institute of Science and Humanities, Amravati, Maharashtra, India

[3]Director, Government Pre-IAS Training Centre, Amravati-, Maharashtra, India

ABSTRACT

Polythiophene-Polyethylene oxide (PTh-PEO) polymer composite was synthesized using Ferric Chloride (FeCl3) as oxidant by in situ chemical oxidative polymerization method. The polymerization was carried out at room temperature. Attempts were made to increase the electrical conductivity by using various concentration of Li2SO4. PTh-PEO polymer composite was characterized using FTIR for confirmation of successful polymerization of polymer composite. The transference numbers of PTh-PEO composite films, synthesized with different wt. % of Li2SO4 were investigated by dc polarization techniques. The value of transference number of all polymer composite samples was found to be in the range of 0.80 to 0.89. This suggests that the charge transport in the PTh-PEO composite doped with different wt. % of Li2SO4 is predominantly due to ions only.

Keywords : Ferric Chloride (FeCl3), Lithium sulphate (Li2SO4), and transference number

I. INTRODUCTION

In recent three decades intrinsically conducting polymers were discovered and this discovery withdraw attention of researchers because of numerous applications of these polymers in scientific field. These are also called as synthetic metals as their electrical conductivity is very high analogous to those of metals. The examples of various conducting polymers (CPs) are: polyacetylene, poly furan, polypyrrole, polythiophene, which are in sulaters in their neutral state. The insulating behavior of polymers can be converted into conducting by carrying out doping of different salts by chemical and electrochemical redox reactions Among the conjugated polymers, Polythiophene (PTh) and its derivatives have been studied for various applications. Polymer composite doped with lithium salts have attracted considerable attention due to the possibility of application in ambient and moderate temperature lithium or lithium ion batteries. Polythiophene (PTh) is one of the most studied polymers due to its flexibility, ease of doping , good thermal and electrical stability that exhibit some unique advantages of PTh for the development of various applications [1].

In the present work, Polythiophene-Polyethylene oxide (PTh-PEO) composite doped with Li2SO4 were prepared by *in situ* chemical oxidative polymerization method. Polymerization was confirmed by FTIR spectroscopy. The effect of various concentrations of Li2SO4 on the transport properties of the PTh-PEO composite films was investigated.

II. EXPERIMENTAL

PTh-PEO composite doped with Li_2SO_4 was synthesized at room temperature (303 K) by chemical oxidative method. Anhydrous $FeCl_3$ was used as an oxidizing agent. A solution of PEO was first prepared in methanol by stirring for 6 h and kept over a night. Appropriate amount of Anhydrous $FeCl_3$ and Li_2SO_4 were added and stirred for 15 min. When monomer thiophene was added drop by drop to the solution a dark brown homogeneous solution was obtained. The solution was then poured on a polypropylene dishes (Petri dishes), to prepare the composite films. The wt. % of Li_2SO_4 in this solution was changed from 1 to 6. For each wt. % of Li_2SO_4, quantity of thiophene was kept constant at 0.5 ml. The thiophene polymerization progresses because the evaporation of the solvent increases the oxidation potential of cast solution. After evaporation of the solvent, the composite films were formed.

III. RESULTS AND DISCUSSION

Polythiophene-Polyethylene oxide (PTh-PEO) composite doped with different wt. % i.e. 10, 20, 30, 40 50 and 60 of Li2SO4 were prepared by *in situ* chemical oxidative polymerization method. Figure (1) Shows the FTIR spectroscopy of polymer composite.
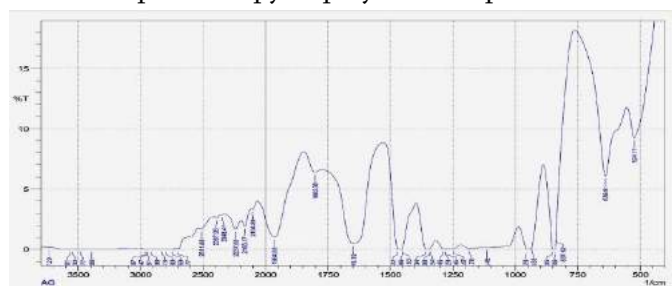

Figure 1. FTIR Spectroscopy of PTh- PEO Polymer Composite doped with of Li_2SO_4.

The major peaks at 1084.42 cm^{-1} and 1645.82 cm^{-1} are due to the presence of C-S and C=C bonds in polythiophene respectively. The strong intensity of the 846.30 cm^{-1} band which is characteristic of 2,5-disubstituted thiophene rings indicates that the coupling of thiophene ring occurs preferentially at 2,5 positions. The absorption band at the region of 650-600cm^{-1} shows the ion–ion interactions in PEO –Li^+ ions. Two medium peaks at 1474 and 1451 cm^{-1} are assigned to stretching vibrational modes of the thiophene ring [2]. The spectrum of PTh-PEO shows characteristic peaks in the range of 900 and 1200 cm^{-1} due to the C–O–C symmetric and asymmetric stretching and C- O- C deformation modes that confirmed the crystalline phase of PEO by the presence of triplet peak of C-O-C stretching [3, 4].

 The electric conductivity of PTh- PEO polymer composite was measured by tow probe method at different temperature It can be observed that ionic conductivity for all the compositions of PTh-PEO composite doped with the different wt. % Li_2SO_4 increases with increasing temperature for the entire range. The ionic conductivity increases with increasing lithium salt concentration due to the increase in the carrier density [5]. However, the formation of ion-pairs becomes more in the case of high salt concentration than in the case of low concentration, leading to a drop in the ionic conductivity.

The variation of conductivity with Li_2SO_4 wt. % is shown in figure 2. As compared to PTh-PEO composite the conductivity increases with Li_2SO_4 wt. % except 2 and 5 wt. % Li_2SO_4 samples. PTh-PEO composite doped with the 4 wt. % Li_2SO_4 shows the maximum value of ionic conductivity. Addition of Li_2SO_4 results in increase in the conductivity value due to the aggregation of excess Li_2SO_4 salt.
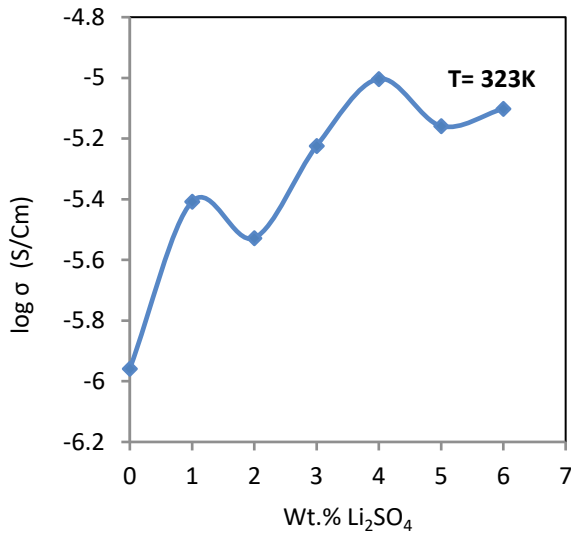
Figure 2. Variation of ionic conductivity as a function of wt. % of Li_2SO_4

The transference number gives quantitative information of the extent of ionic and electrical contribution to the total conductivity. The ionic/ electronic transference number can be given as:

$$t_{ion} = \sigma_{ion}/\sigma_T = I_{ion}/I_T \qquad (2)$$

$$t_e = \sigma_e/\sigma_T = I_e/I_T \qquad (3)$$

Where σ_{ion} / σ_e and I_{ion} / I_e are the conductivity and current contribution due to ions/electrons, respectively. The ionic / electronic transference number (t_{ion}/t_e) was measured using polarization technique [6].

Figure (3) shows the variation of polarization current as a function of time for PTh-PEO Composite doped with different wt. % of Li_2SO_4. As seen from figure (3) the total current becomes nearly constant at some non zero value after some time. The final residual current is mainly due to electrons/holes. The ionic and electronic transference numbers were calculated separately from the polarization current versus time plot using the Equations (2) and (3). The values of transference number, for sample synthesis with different wt. % of Li_2SO_4 are found to be in the range of 0.80 to 0.89. This suggests that the charge transport in the PTh-PEO

composite doped with different wt. % of Li_2SO_4 is predominantly due to ions only.
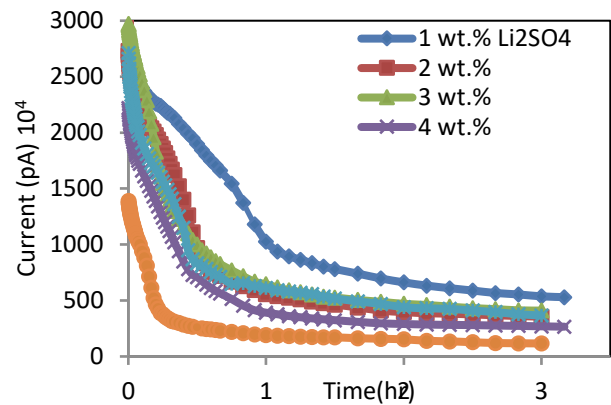
Figure 3. Variation of polarization current as a function of time for PTh-PEO Composite

IV. CONCLUSION

PTh-PEO polymer composites were prepared successfully by in situ chemical oxidative polymerization of thiophene doped with Li2SO4. FTIR study confirms the successful polymerization of polymer composite. The value of transference number of all polymer composite samples was investigated by dc polarization techniques and found to be in the range of 0.80 to 0.89. This suggests that the charge transport in the PTh-PEO composite doped is predominantly due to ions only.

V. REFERENCES

[1]. M. Nicolas, F. Guittard, S. Géribaldi, Angew. Chem. Int. Ed. 45 (2006) 2251.

[2]. O. Tnganas, B. Liedberg, W. Chang-Ru, H. Wynberg, Synth. Methods, 239.11, (1985).

[3]. M. Jaipal Reddy, P.P. Chu, J. Power Sources, 340 109, (2002).

[4]. P.P. Chu, M. Jaipal Reddy, Tsai Joyce, Polym. Sci. Part B: Polym. Phys.,pp.3866 42, (2004).

[5]. P. D. Shirbhate, S.V. Pakade, S. P. Yawale, trans. Indian Inst Met 69(3) (2016) 669.

[6]. J. B. Wagner, Jr, C. Wagner, J. Chem. Phys. 26 (1957) 1597.

Synthesis and Characteristics of In$_2$O$_3$ Doped Polyaniline Nano Composites

D. R. Bijwe[1], A. V. Rajgure*[1], S. S. Yawale[2], S. P. Yawale[2], P. S. Deole[1], A. A. Nimbhorkar[1], S. S. Sonar[1],
A. R. Bhojane[1], R. B. Rajas[1], P. L. Dabhade[1], D. R. Chorpagar[1]

[1]Department of Physics, G. S. Tompe Arts, Commerce & Science College, Chandur Bazar, Amravati,
Maharashtra, India

[2]Department of Physics, Govt. Vidarbha Institute of Science and Humanities, Amravati, Maharashtra, India

ABSTRACT

In this paper, Indium oxide nano particles were prepared by chemical oxidation method. In this synthesized using ammonium persulphate [(NH$_4$)$_2$S$_2$O$_8$] as an oxidant. The PAni- In$_2$O$_3$ samples are prepared with 5 and 10 wt%. The structural changes of prepared composite materials were carried out by X-ray diffraction (XRD) tool.

Keywords : PAni, In$_2$O$_3$, XRD

I. INTRODUCTION

It is the new approach on conducting polymer composite materials compose the technology of conducting polymeric materials. Polymer composite is the inserted the metal oxide, which are studies for its properties [1-3]. The first generation of conducting polymer have a applications in various fields, like Industry, scientific and medical fields. Second generation of electric polymers have applications such as transistors, LEDs, solar cell batteries. These materials attractive in the engineering and scientific world due to controlled conductivity, high temperature resistance, low cost and ease of bulk preparation make. Polyaniline is most extensively studied polymer obtained by simple chemical or electrochemical route among the conducting polymer. The polyaniline have its high electrical conductivity and ease of preparation at low cost. Many researchers have interest to metal oxides dispersed polymer composite because they frequently exhibit unexpected hybrid properties

synergistically derived from both components. One of the oxide material are Indium oxide which have progressive properties and applications [4]. Composite of indium oxide with PAni lead to desirable properties and new applications. These materials are important owing to their important role between the worlds of conducting polymers [5]. Indium oxide which shows good electrical and optical properties [6-7]. The very high surface to volume ratio of indium oxide can be facilitate new and novel applications. Indium oxide (In$_2$O$_3$) material has recently attracted much attention due to its controversial basic material properties [8]. It has a wide band gap (3.4-3.7) eV [9,10], and is a suitable for the fabrication of various devices such as field effect transistors, light emitting diodes, barrier layer in tunnel junctions[11-13], transparent conducting material in liquid crystal displays[14], photovoltaic and solar cells[9] as well as a sensing material in a gas sensors[15,16]. In this paper, we follow the polymerization method for synthesis of PAni and indium oxide (In$_2$O$_3$).

II. EXPERIMENTAL METHOD

2.1. *Synthesis of Polyaniline (PAni)-Indium Oxide(In$_2$O$_3$):*

1.1 M aniline hydrochloride dissolved in distilled water. Indium oxide was added in the weight percent of 5 and 10 to the above solution with vigorous stirring in order to keep the indium oxide suspended in the solution. 0.1M of ammonium persulphate [(NH$_4$)$_2$S$_2$O$_8$] as an oxidant was added slowly to the reaction mixture with continuous stirring for 4-6 hours at 0-5°C. The precipitated powder recover was vacuum-filtered and washed with deionizer water. Finally, the resultant precipitate was dried in an oven for 24 hours to achieve a constant weight. Similarly five different PAni- In$_2$O$_3$ composites with different weight of In$_2$O$_3$ (5 and 10) in PAni have been synthesized.

III. RESULTS AND DISCUSSION
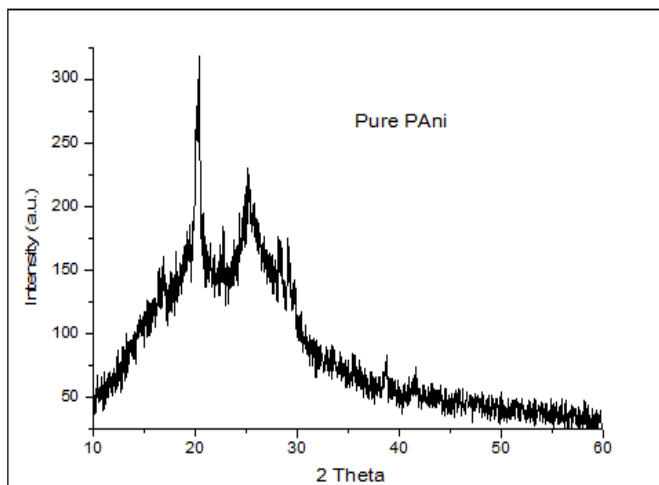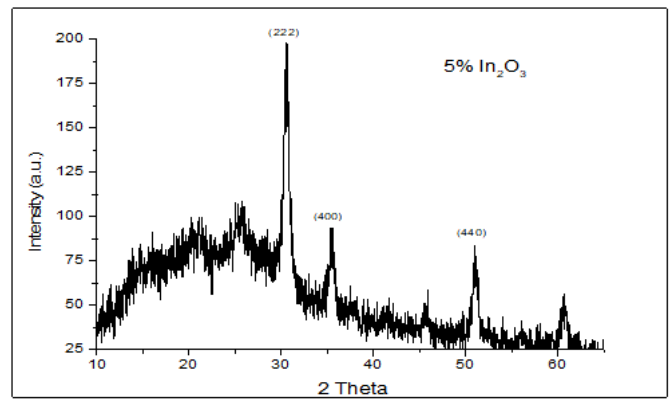
Fig. 1(b) X-rd of 5wt% of PAni-In2O3 Nano Composites
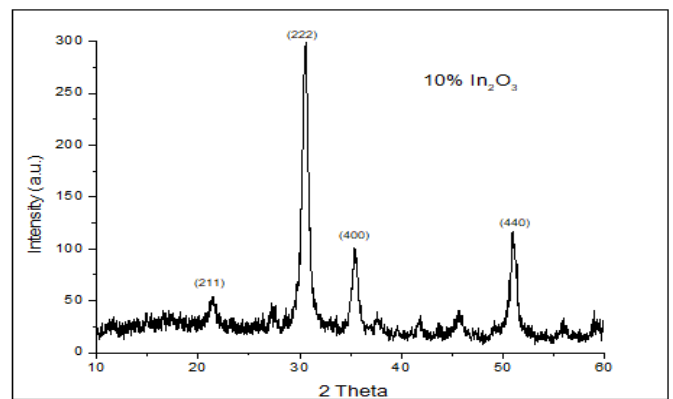
Fig. 1(c) X-rd of 10 wt% of PAni-In2O3 Nano Composites

Fig. 1(a) X-rd of Pure Polyaniline

The X-Ray powder diffraction were recorded using Rigaku Miniflex-600 diffracto meter using Cukα having wave length λ = 1.5406 A$^\circ$. X-Ray diffraction is a high-tech, nondestructive technique for analyzing a wide range of materials.

Fig. 1(a) shows the X-ray diffraction pattern of polyaniline . analysis of X-ray diffraction of polyaniline suggest that it has amorphous nature with broad peaks. Fig. 1(b & c) shows the X-ray diffraction pattern of 5 and 10 wt% of PAni-In$_2$O$_3$ nano composites. The sharper and stronger diffraction peaks in PAni-In$_2$O$_3$ nano particles curves show that the In$_2$O$_3$ nano particles have a high degree of crystallization. The diffraction peaks agree with those given in JCPD data card of bulk cubic In$_2$O$_3$ reflections from (211), (222), (400) and

(440) planes. This oxide peaks in the composite pattern confirms the formation of Indium oxide dispersed polyaniline composite.

IV. CONCLUSION

The chemical oxidation method was used for preparation of PAni-In$_2$O$_3$ nano composites. This method may be used for the preparation of PAni nano composites with various metal oxide materials. Structure changes of pure PAni and PAni-In$_2$O$_3$ is observed by XRD pattern.

V. REFERENCES

[1]. X. Peng, Synthesis and photoluminescence of single-crystalline In2O3 nanowires, 2002, J. Mater. Chem.,12, 1602-1605

[2]. Devindrappa, U. S. Rao, M.V.N.Ambika Prasad, Study of dc conductivity and Battery application of PEO/PANI Composites., 2006, J. Power sources,155, 3689-3695

[3]. R. Sinha, Outlines of polymer technology,(New Delhi: Prentice Hall of India private Limited,2002)

[4]. M.V. Murgendraappa, M.V.N. Ambika Prasad, Dielectric spectroscopy of Polypyrrole-Fe2O3 composites Mater. 2006, Res. Bull.,41, 1363-1371

[5]. A. Lagashetty, A.M. Bhavikatti, B. Mahadevi and S. Kulkarni, Synthesis and characterization of BaTiO3 by thermal decomposition of metal oxalate precursors, 2010, Int. J. Ele. Engg. Res., 2(4), 581-588

[6]. M.D. Benoy, E.M. Mohammed, Suresh Babu M. and Binu P.J, B. Pradeep, Thickness dependence of the properties of indium tin oxide (ITO) FILMS prepared by activated reactive evaporation, 2009, Brazilian J. of Phy., 39(4), 629-632

[7]. J. Parrondo, R. Santhanam, F. Mijangos, B. Rambhau, Magnetic field effects in ferrocenealkane thiol self assembeled monolayer modified electrodes, 2010, Int. J. Electrochem Sci., 5, 1310-1317

[8]. King P.D.C. et al., Band gap, electronic structure and surface electron accumulation of cubic and rhombohedral In2O3, 2009, Phys.Rev.;79 Suppl.20:205211-205212.

[9]. Tanaka I, Mizuno M and Adachi H., Electronic structure of indium oxide using cluster calculations., 1997, Phys.Rev., 56,Suppl.15:3536-33539.

[10].Fuchs F and Bechstedt F:Indium-oxide polymorphs from first principles,Quasiparticle electronic states, 2008, Phys.Rev., 77, Suppl.4:55107-55109.

[11].Zhang D. et al., Diameter-controlled Growth of Single-crystalline In2O3Nanowires and Their Electronic Properties, 2003, Adv. Mater., 15, 143-145.

[12].Kim H. et al., Indium Tin Oxide Thin Films for Organic Light-Emitting Devices., 1999, Appl. Phys. Sci. Lett., 74, Suppl.23:3444-3446.

[13].Kasiviswanathan S and Rangarajan G:Direct current magnetron sputtered In2O3films as tunnel barriers., 1994, J. Appl. Phys., 75, 2572–2577.

[14].Falcony C. et al., Electroluminescence from indium oxide and indium-tin oxide., 1985, J. Appl. Phys., 58:,3556-3558.

[15].Mane R S, Pathan HM, Lokhande CD, and Han SH: An Effective Use of Nanocrystalline CdO Thin Films in Dye-Sensitized Solar Cells., 2006, Solar Energy, 80, Suppl.2:185-190.

[16].Zhang D.H. et al., Detection of NO2down to ppb levels using individual and multiple In2O3nanowire devices., 2004, Nano. Lett., 4, 1919–1924.

Ultrasonic Wave Propagation in Hexagonal SrMnO₃ Compound

Navin Chaurasiya[1,2], Sachin Rai[1], Pramod Kumar Yadawa[1]

[1]Department of Physics, Prof. Rajendra Singh (Rajju Bhaiya) Institute of Physical Sciences for Study and Research, V. B. S. Purvanchal University, Jaunpur, India

[2]Department of Mechanical Engineering, UNSIET, V. B. S. Purvanchal University, Jaunpur, India

ABSTRACT

In the present study, the ultrasonic attenuation due to phonon-phonon interaction has been investigated in hexagonal SrMnO₃ compound. Higher order elastic constants have been computed at temperature dependent following the Lenard-Jones Potentials. Second order elastic constants are used for the determination of other ultrasonic parameters. The temperature variation of the ultrasonic velocities is evaluated along different angles with unique axis of the crystal using the second order elastic constants. Temperature variation of the thermal relaxation time and Debye average velocities is also calculated along the same orientation. The temperature dependency of the ultrasonic properties is discussed in correlation with elastic, thermal and electrical properties. It has been found that the thermal conductivity and thermal relaxation times is the main contributor to the behaviour of ultrasonic attenuation as a function of temperature and the responsible cause of attenuation is phonon-phonon interaction. The mechanical properties of SrMnO₃ material at low temperature (50K) are better than room temperatures because at this temperature it has low ultrasonic attenuation

Keywords: Elastic constants, Ultrasonic velocity, Ultrasonic attenuation, Thermal properties

I. INTRODUCTION

Perovskite manganese oxides, commonly represented as AMnO₃ (A: rare-earth alkaline earth metals), have been instrumental in condensed matter physics as well as in technical applications. Perovskite SrMnO₃ (SMO) is a polymorphism that has complex magnetic ordering and dielectric polarization and thus attracted a lot of attention as a multiferroic material [1, 2]. An inorganic chameleon has been inorganic chameleon because of the great flexibility of the hexagonal perovskite structure. Many different compounds take it or the corresponding structure, as the mother structure is easily deformed or diffused to the relative sizes of the ions of the compounds [3]. The hexagonal

SrMnO₃ is antiferromagnetic below at Néel temperature. Néel temperatures is reported to be 260 K by Takeda and Ohara [4]. Hexagonal polymorphisms are semiconductors. The hexagonal SrMnO₃ when heated in air is stoichiometric at room temperature but loses oxygen at high temperature [5].

In the present work, we have worked diligently to make the relationship between thermo physical and microstructural properties for hexagonal SrMnO₃ compound. SrMnO₃ compound will help in understanding the mechanical behaviour of this compound and it will play an important role in the illustration of industrial applications with useful physical properties under moderate operating

conditions. For that, we have considered ultrasonic attenuation, thermal relaxation time and ultrasonic velocity for SrMnO₃ compound have also been evaluated and discussed for this perovskite manganese oxides.

II. METHODS AND MATERIAL

In the present consideration, the theory is divided into two parts:

2.1 Second-and third order Elastic constants

The second (C_{IJ}) and third (C_{IJK}) order elastic constants of material are specified by following expressions.

$$C_{IJ} = \frac{\partial^2 U}{\partial e_I \partial e_J}; \qquad I \ or \ J = 1,......6 \qquad (1)$$

$$C_{IJK} = \frac{\partial^3 U}{\partial e_I \partial e_J \partial e_K}; I \ or \ J \ or \ K = 1,......6 \qquad (2)$$

where, U is elastic energy density, $e_I = e_{ij}$ (i or j = x, y, z, I=1, …6) is component of strain tensor. Eqs. (1) and (2) leads six second and ten third order elastic constants (SOEC and TOEC) for the hexagonal structure materials [6, 7].

$$
\begin{aligned}
C_{11} &= 24.1\,p^4 C' & C_{12} &= 5.918\,p^4 C' \\
C_{13} &= 1.925\,p^6 C' & C_{33} &= 3.464\,p^8 C' \\
C_{44} &= 2.309\,p^4 C' & C_{66} &= 9.851\,p^4 C'
\end{aligned} \qquad (3a)
$$

$$
\begin{aligned}
C_{111} &= 126.9\,p^2 B + 8.853\,p^4 C' & C_{112} &= 19.168\,p^2 B - 1.61\,p^4 C' \\
C_{113} &= 1.924\,p^4 B + 1.155\,p^6 C' & C_{123} &= 1.617\,p^4 B - 1.155\,p^6 C' \\
C_{133} &= 3.695\,p^6 B & C_{155} &= 1.539\,p^4 B \\
C_{144} &= 2.309\,p^4 B & C_{344} &= 3.464\,p^6 B \\
C_{222} &= 101.039\,p^2 B + 9.007\,p^4 C' & C_{333} &= 5.196\,p^8 B
\end{aligned} \qquad (3b)
$$

where p = c/a: axial ratio; $C' = \chi a / p^5$; $B = \psi a^3 / p^3$; $\chi = (1/8)[\{nb_0 (n-m)\}/\{a^{n+4}\}]$ $\psi = -\chi/\{6a^2(m+n+6)\}$; m, n=integer quantity; b_0=Lennard- Jones parameter

2.2 Ultrasonic attenuation and allied Parameters

Phonon-phonon (Akhieser loss) interaction and thermo elastic relaxation mechanism are basic reasons for the ultrasonic attenuation in solid at room temperature. The following equation expressed attenuation coefficient's $(A)_{Akh}$ due to phonon –

phonon interaction mechanism and thermo elastic relaxation mechanism respectively [8, 9].

$$(A/f^2)_{Akh} = 4\pi^2 \left(3E_0 < (\gamma_i^j)^2 > - <\gamma_i^j>^2 C_V T\right) \tau / 2\rho V^3 \qquad (4)$$

$$(A/f^2)_{Th} = 4\pi^2 <\gamma_i^j>^2 kT / 2\rho V_L^5 \qquad (5)$$

where, f: frequency of the ultrasonic wave; V: ultrasonic velocity for longitudinal and shear wave; V_L: longitudinal ultrasonic velocity; E_0: thermal energy density; γ_i^j: Grüneisen number (i, j are the mode and direction of propagation).

The Grüneisen number for hexagonal structured crystal along <001> orientation or θ=0⁰ is direct significance of second and third order elastic constants. $D = 3\left(3E_0 < (\gamma_i^j)^2 > - <\gamma_i^j>^2 C_V T\right)/E_0$ is identified as acoustic coupling constant, which is the measure of acoustic energy improved to thermal energy. When the ultrasonic wave propagates through crystalline material, the equilibrium of phonon distribution is concerned. The time for renew of equilibrium of the thermal phonon distribution is called thermal relaxation time (τ) and is given by following expression:

$$\tau = \tau_S = \tau_L / 2 = 3k / C_V V_D^2 \qquad (6)$$

Here 'τ_L' and 'τ_S' are the thermal relaxation time for longitudinal and shear wave. 'k' and 'C_V' are the thermal conductivity and specific heat per unit volume of the compound respectively. The Debye average velocity (V_D) is well connected to longitudinal (V_L) and shear wave (V_{S1}, V_{S2}) velocities. The expressions for ultrasonic velocities are known in our prior papers [8, 9].

III. RESULTS AND DISCUSSION

3.1 Higher order elastic constants

In the current analysis we have calculate the elastic constants (six second order elastic constants and ten third order elastic constants) using the theory given by Eqn. (3) and Eqn. (4). The unit cell parameters 'a' (basal plane parameter) and 'p' (axial ratio) for

SrMnO$_3$ compound is 5.489Å, and 1.66 respectively [10]. The value of m and n for chosen materials are 6 and 7. The value of b$_0$ is 5.5x10^{-62} erg cm^7 for SrMnO$_3$ compound. The calculated values of SOEC and TOEC have been calculated for this compound at room temperature are offered in Table 1.

Table1. Second and third order elastic constants (SOEC and TOEC) in the unit of 10^{10}Nm^{-2} of SrMnO$_3$ compound at room temperature.

	C_{11}	C_{12}	C_{13}	C_{33}	C_{44}	C_{66}			
This work	28.14	6.91	6.194	30.71	7.43	11.03			
[10]	28.52	9.25	9.36	30.5		9.64			
	C_{111}	C_{112}	C_{113}	C_{123}	C_{133}	C_{344}	C_{144}	C_{155}	C_{222}	C_{333}
	-459	-73	-16	-20	-103	-97	-24	-157	-363	-402

SrMnO$_3$ compound had the highest elastic constant values, which are important for the material, as these are associated with the stiffness parameter. Second-order elastic constants are used to determine the ultrasonic attenuation and associated parameters. The highest elastic constant values found for superhard materials are indicative of their better mechanical properties over other hexagonal materials. Clearly, for a steady hexagonal structure the five independent second order elastic constants (Cij, namely C$_{11}$, C$_{12}$, C$_{13}$, C$_{33}$, C$_{44}$) should satisfy the well-known Born-Huang's stability norms [11, 12] i.e. $C_{11} - |C_{12}| > 0$, $(C_{11}+C_{12}) C_{33} - 2C^2_{13} > 0$, $C_{11} > 0$ and $C_{44} > 0$. It is understandable from Table-1. It is evident that the values of elastic constant are positive and satisfies the Born-Huang's mechanical stability constraints and therefore all these compounds are mechanically stable. The calculated values of C$_{12}$ and C$_{66}$ are few different than some other theoretical [10] results for SrMnO$_3$ compound. Actually R. Sondena et al. [10] were theoretically evaluated using DFT investigations, which is quite different from present approach. Although obtained

order of SOEC are of the same as given in Table. 1 [10]. Relative magnitude of C$_{11}$ and C$_{33}$ are well presented by our theoretical approach. Thus, there is good agreement between the presented and the reported values which is correlated with elastic constants. Thus, our theoretical approach is well justified for the calculation of second order elastic constants. We present the calculated values of TOECs in table 1. The negative values of TOECs indicate a negative strain in the solid. The negative TOECs appear in the previous paper on hexagonal structure material. Hence the theory applied for evaluation of higher order elastic constants is justified [13, 14]. Hence the applied theory for the valuation of higher order elastic constants, at room temperature, is acceptable.

3.2 Ultrasonic Velocity and allied parameters

In the present investigation, we have correlated the mechanical and isotropic behavior of the material with the ultrasonic velocity. We have calculated the longitudinal ultrasonic velocity (V$_L$), shear ultrasonic velocity (V$_S$), the Debye average velocity (V$_D$) and the thermal relaxation time (τ) for SrMnO$_3$ compound. The data for the temperature dependent density (ρ) SrMnO$_3$ compound presented in Table 3 and have been taken from literature [15]. Thermal conductivity (k) of SrMnO$_3$ compound presented in Table 3 has been taken form the literature [15]. The values of temperature dependent specific heat per unit volume (C$_V$) and the thermal energy density (E$_0$) have been calculated using the tables of physical constant and Debye temperatures and calculated values of temperature dependent acoustic coupling constant D$_L$ and D$_S$ are presented in Table.3.

Table 3. Density (ρ: in 10^3 kg m^{-3}), specific heat per unit volume (C$_V$: in 10^{5}Jm^{-3}K^{-1}), thermal energy density (E$_0$: in 10^{7}Jm^{-3}), thermal conductivity (k: in Wm^{-1}K^{-1}) and acoustic coupling constant (D$_L$, D$_S$) of SrMnO$_3$ compound.

Temp	ρ	E_0	C_V	k	D_L	D_S
50	5.345	1.27	0.96	4.367	48.32	1.758
100	5.340	1.25	3.52	5.633	49.66	1.758
150	5.3335	3.35	4.99	5.483	50.49	1.758
200	5.330	6.16	5.77	4.950	51.01	1.758
250	5.325	9.16	6.17	4.517	51.28	1.758
300	5.320	12.31	6.39	4.467	51.46	1.758

It is clear form Table 3 that for all temperature, the values of D_L are larger than those of D_S for all temperatures. It indicates that for the shear ultrasonic wave the conversion of ultrasonic energy into thermal energy is less than that for the longitudinal ultrasonic wave.

The orientation dependences of ultrasonic wave velocity (V_L, V_{S1}, V_{S2} and V_D) at different temperature are shown in Figs 1-4. The angles are measured form the unique axis of the crystal. Form Fig. 1-2 the velocity V_L and V_{S1} of SrMnO$_3$ compound have minima and maxima at 45° with the unique axis of the crystal and Fig. 3, we find that V_{S2} increases with angle form the unique axis. The abnormal behavior of angle dependent velocity is due to the combined effect of second order elastic constants and density. The nature of the angle dependent velocity curves in the present work is similar to the nature of angle dependent velocity curve found for other hexagonal structured material [16, 17]. Thus the angle dependence of the velocities in SrMnO$_3$ compound is justified.
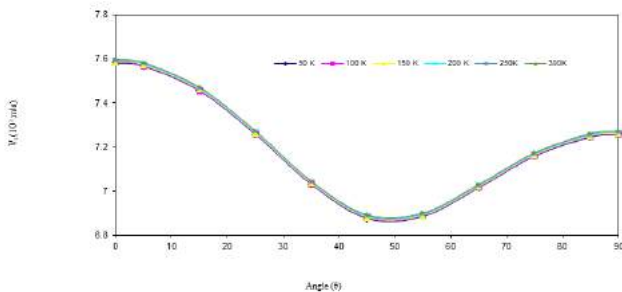

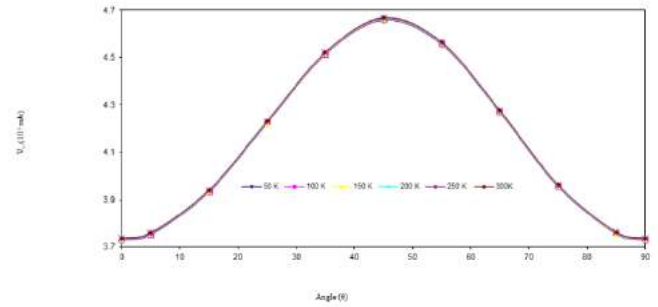**Figure 1.** V_L vs angle with unique axis of crystal
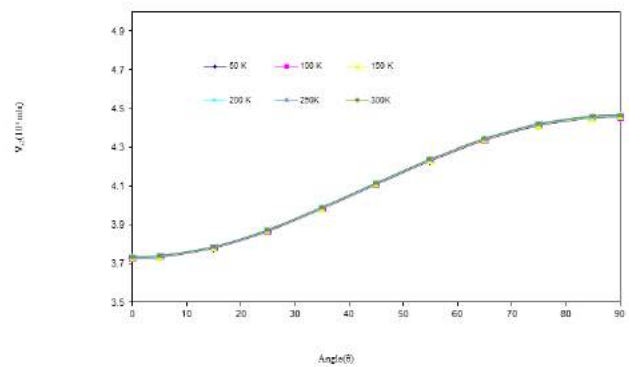

Figure 2. VS1 vs angle with unique axis of crystal

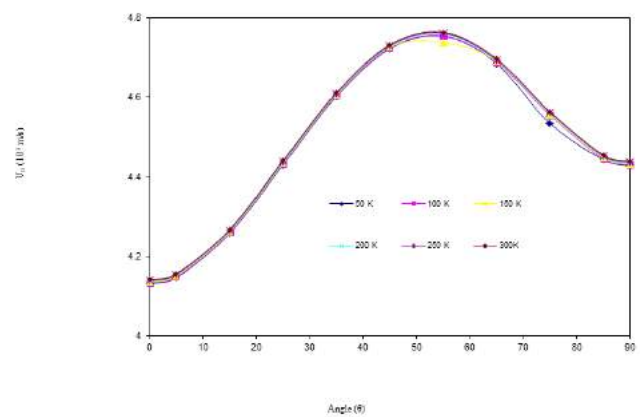Figure 3. VS2 vs angle with unique axis of crystal

Figure 4. VD vs angle with unique axis of crystal

Fig. 4 shows the variation of the Debye average velocity (V_D) with the angle made with the unique

axis of the crystal. It is clear that V_D increases with the angle and reaches maximum at 55^0 for SrMnO$_3$ compound. As the calculation of V_D involves the velocities V_L, V_{S1} and V_{S2} [18,19], It is understandable that the variation of V_D is affected by the constituent ultrasonic velocities. The maximum V_D at $55°$ is due to a significant increase in longitudinal and pure shear (V_{S2}) wave velocities and a decrease in quasi-shear (V_{S1}) wave velocity. It may be concluded that the average sound wave velocity is maximum when a sound wave travels at 55^0 angles with the unique axis of these crystal.
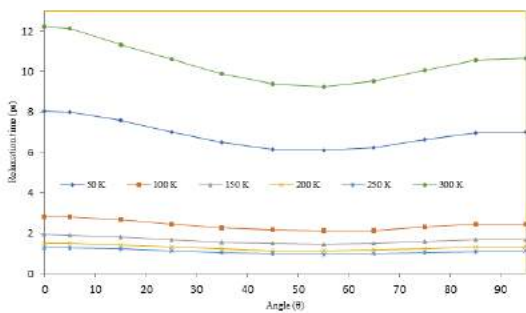

Figure 5. Relaxation time vs angle with unique axis of crystal

Fig. 5 shows a plot of the calculated thermal relaxation time 'τ' with the angle. The angle dependent thermal relaxation time curves follow the reciprocal nature of V_D as $\tau \propto 3K / C_V V_D^2$. It is clear that thermal relaxation time for SrMnO$_3$ compound is mainly affected by the thermal conductivity. For hexagonal structured material 'τ' is of the order at picoseconds [16, 20]. Hence the calculated 'τ' justifies the hexagonal structure of SrMnO$_3$ compound. The minimum 'τ' for wave propagation along θ = 55^0 implies that the re-establishment time for the equilibrium distribution of thermal phonons will be minimum for propagation of wave along this direction.

3.3 Ultrasonic attenuation due to phonon-phonon interaction and thermal relaxation phenomena

While evaluating the ultrasonic attenuation, it is assumed that the wave is propagating along the unique axis [<001> direction] of SrMnO$_3$ compound. The attenuation coefficient divided by frequency squared $(A/f^2)_{Akh}$ is calculated for longitudinal wave $(A/f^2)_L$ and for shear wave $(A/f^2)_S$ using Eqn. 4 under the condition $\omega\tau<<1$ at different temperature. Eqn. 5 has been used to calculate the thermo-elastic loss divided by frequency squared $(A/f^2)_{Th}$. Figs. 6-7 present the values of the temperature dependent $(A/f^2)_L$, $(A/f^2)_S$, $(A/f^2)_{Th}$ and total attenuation $(A/f^2)_{total}$ of SrMnO$_3$ compound.
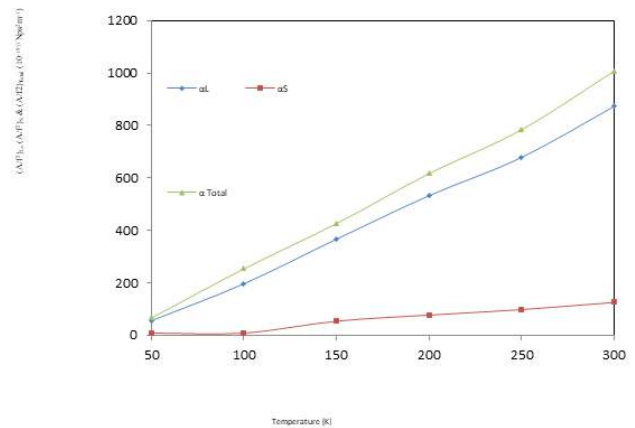
Fig. 6. Long. & Shear attenuation vs temp. of SrMnO3
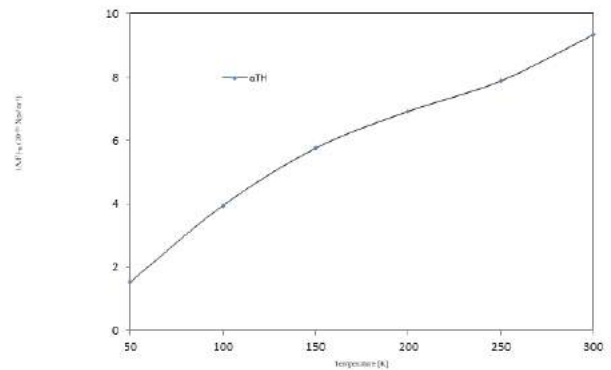
Fig. 7 Th. attenuation vs temp of SrMnO3

In the present work, the ultrasonic wave is propagating along the unique axis of the crystal from figs. 6-7. It is evident that the Akhieser type of energy losses for longitudinal and shear waves have minimum at temperature at 50K and the thermo-electric loss increase with the temperature of material. $(A/f^2)_{Akh}$ is proportional to D, E_0 , τ and V^{-3} (Eqns. 4 and 6). Table 3 shows that' E_0' and 'V' are increasing with

temperature, while thermal relaxation time is decreasing with temperatures. Hence Akhieser losses in $SrMnO_3$ compound is overwhelmingly affected by thermal energy density E_0 and the thermal conductivity 'k' and relaxation time. Therefore, the ultrasonic attenuation is combined effect of thermal conductivity and relaxation time. Thus, ultrasonic attenuation is mainly governed by the phonon–phonon interaction mechanism. A comparison of the ultrasonic attenuation could not be made due to lack of experimental data in the literature.

From figs. 6-7, it is clear that the thermo-elastic loss is very small in comparison to Akhieser loss for $SrMnO_3$ compound, and also the ultrasonic attenuation for the longitudinal wave $(A/f^2)_L$ is greater than that for the shear wave $(A/f^2)_S$ of the total attenuation $(A/f^2)_{Total} = (A/f^2)_{Th} + (A/f^2)_L + (A/f^2)_S$. The ultrasonic attenuation due to phonon –phonon interaction for longitudinal wave is governing factor. The thermal relaxation time, thermal energy density and the thermal conductivity are the main factor that affects the total attenuation. Thus, it may be predicted that $SrMnO_3$ compound behave as its purest form at 50K and are more ductile demonstrated by the minimum attenuation while at other temperatures of $SrMnO_3$ compound are least ductile. Therefore, at low temperature (50K) there will be least impurity in $SrMnO_3$ compound.

IV. CONCLUSION

Based on the above discussion is worthwhile to state that:

- The theory formed on a simple interaction potential model for the calculation of higher-order elastic constants is supported for the hexagonal s $SrMnO_3$ compound.
- For $SrMnO_3$ compound, the thermal relaxation time is found to be of the order of pico seconds, which defends their hexagonal structure. As 'τ' has smallest value along $\theta = 55^{0,}$ at all temperatures, the time for re-establishment of equilibrium distribution of phonons, will be minimum, for the wave propagation in this direction.
- The acoustic coupling constant of $SrMnO_3$ compound for the longitudinal waves is found larger than other hexagonal materials. Hence the change of acoustic energy into thermal energy will be large for $SrMnO_3$ compound.
- The ultrasonic attenuation due to phonon-phonon interaction mechanism is intense over total attenuation as a governing factor thermal conductivity and thermal relaxation time.
- The mechanical properties of $SrMnO_3$ compound at low temperature 50K are better than at room temperature because at this temperature it has low ultrasonic attenuation.

The study may be fruitful for the processing and non-destructing characterization of $SrMnO_3$ compound. These findings will provide a base for further investigation of crucial thermophysical properties in the field of other perovskite polymorph compounds.

V. REFERENCES

[1]. T. Negas, R. S. Roth, The system SrMnO3-X, J. Solid State Chem. 1, 409–418 (1970).

[2]. T. Takeda, S. Ohara, Magnetic structure of the cubic perovskite type SrMnO3, J. Phys Soc.Jap. 37, 275–275 (1974).

[3]. A R. H. Mitchell, Perovskites: Modern and Ancient, Almaz Press,Ontario, Canada (2002).

[4]. R. Sondena P. Ravindran, S. Stolen, Electronic structure and magnetic properties of cubic and hexagonal SrMnO3, Physical Review B 74, 144102 (2006).

[5]. S. Hashimoto, H. Iwahara, Structural thermal and electrical properties of Ce-doped SrMnO3, J. Electroceram. 4, 225 (2000).

[6]. D. K. Pandey, P. K. Yadawa, R. R. Yadav, Ultrasonic properties of hexagonal ZnS at nanoscale, Mater, Lett. 61, 5194–5198 (2007).

[7]. W. Voigt, Lehrbuch der kristallphysik (mitausschluss der kristalloptik) (Leipzig Berlin, B.G. Teubner) (1928).

[8]. S. P. Singh, P. K. Yadawa, P.K. Dhawan, A.K. Verma, R.R. Yadav, Effect of pressure and electrical resistivity on ultrasonic properties of MgB2 single crystal at low temperatures, Cryogenics 100, 105-108 (2019).

[9]. D. Singh, P. K. Yadawa, S.K. Sahu, Effect of electrical resistivity on ultrasonic attenuation in NpTe, Cryogen. 50, 476-479 (2010).

[10]. R. Sondena, S. Stolen, P. Rvindran, T. Grande, Ab initio calculation of elastic constants and derived mechanical properties of cubic and hexagonal SrMnO3, Physical Review B,75, 214307, (2007).

[11]. P. F. Weck, E. Kim, V. Tikare, J. A. Mitchell, Mechanical properties of zirconium alloys and zirconium hydrides predicted from density functional perturbation theory, Dalton Trans. 44,18769–18779 (2015).

[12]. D. Singh, D. K. Pandey, P.K. Yadawa, A.K. Yadav, Attenuation of ultrasonic waves in V, Nb and Ta at low temperatures, Cryogen. 49, 12-16 (2009).

[13]. P. K. Yadawa, Computational Study of Ultrasonic Parameters of Hexagonal Close-Packed Transition Metals Fe, Co, and Ni, The Arabian Journal for Science and Engineering 37, 255 (2012).

[14]. P. K. Yadawa, Behaviour of ultrasonic velocities and elastic constants in Ag-Zn alloys, Adv. Mat. Lett. 2, 157 (2011).

[15]. S. Kamba, V. Goian, V. Skoromets, J. Hejtmanek, V. Bovtun, M. Kempa, F. Borodavka, P. Vanek, A.A. Belik, J.H. Lee, O. Pacherova, and K.M. Rabe, Strong spin-phonon coupling in infrared and Raman spectra of SrMnO3 Physical Review B 89(6) (2014)

[16]. P. K. Yadawa, Ultrasonic characterization of superhard material: Osmium Diboride, IOP Conf. Series, Materials Science and Engineering 42, 012034 (2012).

[17]. P. K. Yadawa, Ultrasonic characterization of ceramic material titanium diboride., Ceramics-Silikaty 55, 127-133 (2011).

[18]. A. K. Jaiswal, P. K. Yadawa, R. R. Yadav, Ultrasonic wave propagation in ternary intermetallic CeCuGe compound, Ultrasonics 89, 22-25(2018).

[19]. S. P. Singh, G. Singh, A. K. Verma, P. K. Yadawa, R. R. Yadav, Ultrasonic wave propagation in thermoelectric ZrX2 (X= S, Se) compounds, Pramana-J. Phys., 93, 83 (2019).

[20]. D. K. Pandey, P. K. Yadawa, R. R. Yadav, Acoustic wave propagation in Laves-phase compounds, Materials Letters 61, 4747-4751 (2007).

Molecular Interaction In Aqueous Solution of Ceftriaxone Sodium and Cefotaxime Sodium : An Ultrasonic Study

Rajesh S. Hajare[*], Shashikant R. Aswale[1], Sunanda S. Aswale[2]

[*]Nilkanthrao Shinde College, Bhadrawati, Dist. Chandrapur, Maharashtra, India
[1]Mahatma Gandhi College of Science, Gadchandur, Dist. Chandrapur, Maharashtra, India
[2]Lokmanya Tilak Mahavidyalaya, Wani, Dist. Yavatmal, Maharashtra, India
Corresponding author: Rajesh S. Hajare[*]
**Email :** rajeshhajare34@yahoo.com

ABSTRACT

Ultrasonic velocity, viscosity and density have been measured for antibiotic Cefotaxime sodium and Ceftriaxone sodium in water at different concentrations, temperatures and frequency at 2MHz. As the acoustical parameters like relative association, specific acoustic relaxation time and free volume would be more useful to predict the molecular interaction. By using ultrasonic velocity, viscosity and density of the prepared solution of Cefotaxime sodium and Ceftriaxone sodium in water these acoustical parameter have been determined. It has been identified that the molecular interactions in aqueous solution of Cefotaxime sodium were stronger than that of in aqueous solution of Ceftriaxone sodium. And also there is a strong solute - solvent interaction occurring in aqueous solution of Cefotaxime sodium than that of aqueous solution of Ceftriaxone sodium.

Keywords : Viscosity, density, Ultrasonic velocity, Cefotaxime sodium, Ceftriaxone sodium

I. INTRODUCTION

Ultrasound creates number of applications in medicine and research. After first antibiotic penicillin invention number of natural, semi synthetic and synthetic antimicrobials were discovered and applied in clinics, achieving great progress in bacterial infection therapy[1]. However, many decades later, Due to lack of new drug development and rapid emergence of resistant bacteria, bacterial infections have again become a serious threat [2]. To understand the physical and chemical properties of drug action, it is necessary to consider the bonds formed by drug molecules which are influenced by thermal agitation and chemical invironment[3]. A number of researchers[4-15]have investigated molecular interaction in aqueous solution of different antibiotics. In pharmaceuticals Cefotaxime sodium and Ceftriaxone sodium is used as an antibiotic.

Cefotaxime sodium –
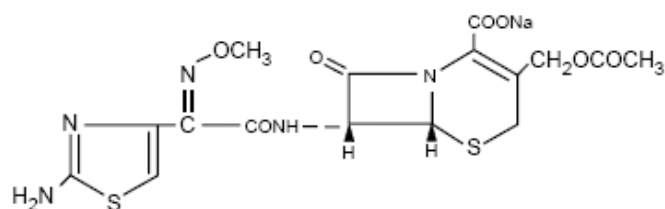
Ceftriaxone sodium –
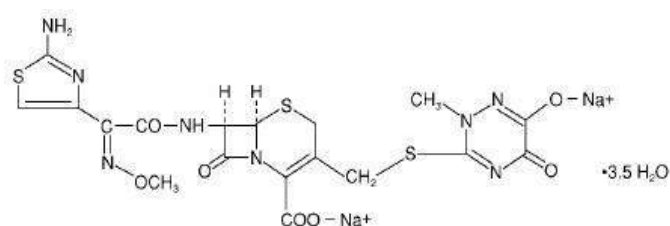
Comparative study of Cefotaxime sodium and Ceftriaxone sodium was studied at different temperature, concentration and at 2MHz frequency in the investigation. Intermolecular interactions in aqueous solution of Cefotaxime sodium and Ceftriaxone sodium have been investigated on the basis of acoustical and thermodynamic parameters like relative association, specific acoustic relaxation time and free volume.

II. EXPERIMENTAL

From Alkem laboratories Limited cefotaxime sodium obtained and ceftriaxone sodium obtained from Prosperity 6 pharmaceutics Limited was used as a antibiotic. All the chemicals used were of analytical grade. For preparation of solutions double distilled water was used. Using specific gravity bottle densities of various solutions were measured. These values were accurate up to $\pm$ 0.1 kg/m^3. For measurement of Viscosities of the various solutions Oswald's viscometer was used. A special thermostatic water bath was used for measurement of density and ultrasonic velocity during which temperature variation was maintained within $\pm 0.01^0$C. For measurement of ultrasonic velocity of various solutions Multi frequency interferometer (Mittal Enterprises, Model F-83) with accuracy of $\pm 0.03\%$ was used. CA-124 (CB/CA/CT series, Contech) digital electronic balance having an accuracy of $\pm$ 0.0001g was used for weighing.

III. RESULT AND DISCUSSION

Measurements of densities, viscosities and ultrasonic velocities of water and aqueous solution of cefotaxime sodium and ceftriaxone sodium have been made in the present investigation.

Specific acoustic relaxation time is calculated by equation as

$$\Tau = 4/3\beta.\eta \qquad \dots \dots (1)$$

Relative association is calculated by the equation as

$$R_A = \frac{d_s}{d_0} \left(\frac{v_0}{v_s} \right)^{1/3}$$

Where, v_0 and v_s are ultrasonic velocities in solvent and solution respectively.

Free volume is calculated by following equation as

$$V_f = [M_{eff}v/K \, \eta]^{3/2} \qquad \dots\dots.(3)$$

Where, M_{eff} is effective molecular weight, K is a temperature independent constant which is equal to 4.28×10^9 for all liquids.

Viscosity of Solution is calculated by equation as

$$\eta_2 = \eta_1.t_2.d_s/t_1.d_0 \qquad \dots \dots (4)$$

Where, η_1=viscosity of water, η_2= viscosity of experimental liquid, t_1=time flow of water, t_2=time flow of experimental liquid, d_0=density of water and d_s=density of experimental liquid.

For aqueous solution of cefotaxime sodium and ceftriaxone sodium the values of ultrasonic velocities, densities, viscosities, specific acoustic relaxation time, relative association and free volume at different concentrations, temperatures and frequency at 2MHz are tabulated in table 1 and 2 respectivel

Table 1 : Acoustic parameters of aqueous solution of Cefotaxime sodium at 2MHz.

Temperature (K)	Concentration (M)	Ultrasonic Velocity (m/s)	Density (Kg/m³)	Viscosity $\eta x10^3$ (NSm^{-2})	Specific relaxation time $T x10^{-10}$ (sec)	Relative association (R_A)	Free Volume $V_f x10^{-8}$ (m3/mole)
303.15	0.001	1489.33	1016.16	0.8699	5.13	1.0225	1.27
	0.01	1491.21	1025.55	0.9301	4.19	1.0315	1.41
	0.1	1524.10	1043.55	1.1765	6.46	1.0420	2.20
308.15	0.001	1526.54	1006.14	0.9168	4.32	1.0143	1.43
	0.01	1527.13	1016.52	0.9262	5.50	1.0246	1.46
	0.1	1564.90	1039.00	0.9467	5.26	1.0388	1.66
313.15	0.001	1563.38	999.53	0.7559	3.85	1.0004	1.11
	0.01	1528.29	1010.52	0.7642	4.12	1.0191	1.10
	0.1	1637.99	1038.66	0.7855	4.05	1.0235	1.34

Table 2 : Acoustic parameters of aqueous solution of Ceftriaxone sodium at 2MHz.

Temperature (K)	Concentration (M)	Ultrasonic Velocity (m/s)	Density (Kg/m³)	Viscosity $\eta x10^3$ (NSm^{-2})	Specific relaxation time $T x10^{-10}$ (sec)	Relative association (R_A)	Free Volume $V_f x10^{-8}$ (m3/mole)
303.15	0.001	1488.09	1025.40	0.8431	4.9508	1.0321	1.2128
	0.01	1488.34	1030.70	0.8736	5.1022	1.0374	1.2873
	0.1	1489.44	1054.37	1.1529	6.5722	1.0609	2.0700
308.15	0.001	1524.32	1020.93	0.7507	4.2197	1.0297	1.0600
	0.01	1525.20	1026.42	0.7794	4.3523	1.0350	1.1300
	0.1	1525.49	1044.61	1.0019	5.4956	1.0533	1.7400
313.15	0.001	1554.55	1015.52	0.6720	3.6511	1.0183	0.9220
	0.01	1563.54	1016.94	0.7208	3.8670	1.0178	1.0400
	0.1	1598.64	1038.52	0.8508	4.2745	1.0317	1.4600

From Table1 it is observed that for aqueous solution of cefotaxime sodium at 2MHz frequency, values of ultrasonic velocity increases with increases in concentration and temperature. Increase in ultrasonic velocity is due to addition of solute is indicative of greater association of molecules which in turn due to effective solute-solvent interaction. Molecular forces weaken due to increase in concentration and hence change in velocity is observed. On increasing the concentration, ultrasonic velocity increases indicate

greater solute -solvent interaction due to formation of hydrogen bond between molecule of cefotaxime sodium and water. The value of density and viscosity deceases with increase of temperature and same increases with increase in concentration. Increase in temperature, values of density and viscosity decrease shows decrease in intermolecular forces due to increasing the thermal energy of the system. Moderate attraction between solute and solvent molecules reflect due to increasing values of density, viscosity and ultrasonic velocity. Relaxation time and relative association decreases with rise in temperature and same increases with increase in concentration. This suggests between molecules of solute cefotaxime sodium and solvent water strong intermolecular interaction. Free volume increase with increasing concentration and temperature suggests molecular packing in medium increase this supports strong of molecular interaction in aqueous solution of cefotaxime sodium.

Table 2 suggests at 2MHZ frequency, with increases in concentration and temperature values of ultrasonic velocity of aqueous solution of ceftriaxone sodium increases. The increased values of ultrasonic velocity indicate of greater molecular association due to cohesion brought by the ionic hydration and also due to effective solute-solvent interaction. With increase in concentration relaxation time, relative association and free volume increases and same decreases with increase in temperature. This confirms in aqueous solution cefriaxone sodium presence of specific molecular interaction.

Aqueous solution of cefotaxime sodium has high value of ultrasonic velocity than aqueous solution of ceftriaxone sodium. It reflects that in aqueous solution of cefotaxime sodium strong solute-solvent interaction exists than ceftriaxone sodium. Cefotaxime sodium has low relaxation time, relative association and free volume than ceftriaxone sodium which shows that cefotaxime sodium forms the closely pack structure,

high breaking of solvent structure and higher close packing of molecules in aqueous solution of cefotaxime sodium than ceftriaxone sodium. Thus on comparing acoustic and thermodynamic parameters, in aqueous solution of cefotaxime sodium strong intermolecular interaction exists than ceftriaxone sodium.

IV. CONCLUSION

On the basis of acoustic and thermodynamic parameters, it is confirm that in aqueous solution of cefotaxime sodium strong intermolecular interaction exist than ceftriaxone sodium solution. Thus cefotaxime sodium may be thought as potent and more powerful antibiotic than ceftriaxone sodium.

PTh-PEO polymer composites were prepared successfully by in situ chemical oxidative polymerization of thiophene doped with Li2SO4. FTIR study confirms the successful polymerization of polymer composite. The value of transference number of all polymer composite samples was investigated by dc polarization techniques and found to be in the range of 0.80 to 0.89. This suggests that the charge transport in the PTh-PEO composite doped is predominantly due to ions only.

V. REFERENCES

[1]. Golkar Z., Bagasra O., Pace D. G., 2014, Bacteriophage therapy: A potential solution for the antibiotic resistance crisis. Journal of Infection in Developing Countries, 8, 129-136.

[2]. Ventola C. L., 2015,The antibiotic resistance crisis—part 1: causes and threats. Pharmacy and Therapeutics, 40(4), 277-283.

[3]. Foye, W. O., 1976, Principles of medicinal chemistry, 210, 9-51.

[4]. Hedges, M.., Lewis M., Lunec J. and Cramp W. A., 1980, the effect of ultrasound at 1.5 MHz on Escherichia coli. Int. J. Radiat. Biol., 37, 103-108.

[5]. Kadurugamuwa J. L., Clarke A. J., and Beveridge T. J. 1993a, Surface action of gentamicin on Pseudomonas aeruginosa. J. Bacteriol., 175, 5798-5805.

[6]. Kadurugamuwa J. L., Lam J. S., and Beveridge T. J., 1993b, Interaction of gentamicin with the A Band and B Band lipopolysaccharides of Pseudomonas aeruginosa and its possible lethal effect, Antimicrob. Agents Chemother. 37, 715–721.

[7]. Kondo T., Kukushima Y., Kon H., and Riesz P., 1989, Effect of shear stress and free radicals induced by ultrasound on erythrocytes. Arch. Biochem. Biophys., 269, 381-389.

[8]. Williams R. G. and Pitt, W. G., 1997, In vitro response of Escherichia coli to antibiotics and ultrasound at various insonation intensities, J. Biomater. Appl., 12, 20-30.

[9]. Pitt W. G., McBride M. O., Lunceford J. K., Roper R. J., and Sagers R. D., 1994, Ultrasonic enhancement of antibiotic action on Gram-negative bacteria. Antimicrob. Agents Chemother, 38, 2577-2582.

[10]. Baluja, S. H., Solanki, A. and Kaachadia, N., 2007, Russian J. of Physical Chemistry, 81 (5), 742-746.

[11]. Kumar R., Mohammed Kamil M. G., Shri prsad S., Gayatri, G. S. and Shabeer, T. K., 2013, Indian J. of pure and applied physics, 51, 701-707.

[12]. Paliwal S. K. and Tabhane V. A., 2004, J. Pure Appl. Ultrason., 26, 105-110.

[13]. Swamy, K. M. Ranganathan, S. Murayama, K. L. and Bapuji, 2009, Proceedings of Eighteenth National Symposium on Ultrasonics, NSU-XVIII, Vellore, 110-112.

[14]. Harish Kumar and Deepika, 2012, International Journal of Chemical Science and Technology, 2(1), 1.

[15]. Roumana C., Velraj, G., Akilandeswari P. E. and Mohammed Kamil, M. G., 2009, Proceedings of Eighteenth National Symposium on Ultrasonics, NSU-XVIII, Vellore, 144-148.

A Nano Analytical attempt on Hibiscus Rosa-Sinensis Pollens Using Scanning Electron Microscopy (SEM) and the UV-Vis Spectroscopy

*Rajesh Katru, I. Johnson, and S. Anbarasu

PG and Research Department of Physics, St. Joseph's college, Tiruchirappalli, Tamil Nadu, India

ABSTRACT

Mother Nature has the best of the solutions for today's rising pathological problems that often make the world hazardous, putting the life forms at stake. This study includes the characterisation of the pollen grains of Hibiscus Rosa-Sinensis using **Scanning Electron Microscope (SEM)** and the **UV- Visible Diffuse Reflectance Spectroscopy**. The attempt made is to characterise and study the Nano-Particle analysis of the Pollen grains. HRS (Hibiscus Rosa Sinensis) has a lot of medical applications and it has received a great attention all over the world in its taxonomical studies. Especially, the pollen studies are important for assessing the biodiversity of life, and the sexual reproduction of plants and plant-pollinator interactions. Pollen morphology on the other hand is one of the significant tools in solving some taxonomic problems on the family, and has become a part of the multidisciplinary and a collaborative approach in plant systems and their evolution. The pollen study would have a great scope in the field of medicine. The result suggests that the pollens have a strong symmetry regarding the distribution of its spines over the spherical grain. The work on the pollen morphology of Hibiscus Rosa-Sinensis is an inter-departmental venture combining both life and physical sciences.

Keywords : Hibiscus Rosa-Sinensis (HRS), pollen grains, SEM analysis, UV analysis

*Corresponding Author- katrurajeshsj@gmail.com

I. INTRODUCTION

Nature always provides everything what man needs not what he wants. For the sustenance of the bio-diversity of life, plant families play an important role. Moreover, flowers for man have always been a matter of great interest due to their fragrance, colour, beauty and feel. In fact, the biological function of a flower in plants is to initiate the reproduction process, usually by providing a mechanism for the union of sperm with eggs. They are the organs of sexual reproduction. They form as a bud, grow into flower and then convert into fruit after pollination. They are the most beautiful structures on the surface of plants. The flowers regulate breeding and support the food cycle. They provide food in the form of nectar [1]. Interestingly, the pollen grains carry the responsibility of taking forward the flower and its plants progeny. This process of reproduction through pollens occurs by the transfer of male gametes.

Therefore, the morphological study and the absorptive behaviour of the biochemical composition of the pollens give us a deeper understanding of their taxonomical nature. The main object of the present

study is to investigate and describe the behaviour of the pollen grains of Hibiscus Rosa Sinensis of the family Malvaceae, through the instrumentation methods of SEM and UV Vis Spectroscopy, by studying which we realize that there is a lot more to explore and discover in attaining some efficacious results in medicinal and the advanced sciences.

II. HIBISCUS ROSA SINENSIS

China rose is a popular name for the beautiful flowering plant Hibiscus Rosa Sinensis. It is mainly found in south-east China and some islands in the Pacific and Indian Ocean. The name to this species was believed to have been given the name "rosa sinensis" which means "Rose of China" in Latin, by the famous Swedish biologist, Carolus Linnaeus in the early 1750s [2].

Fig 1. Flower of Hibiscus Rosa Sinensis (Clive's house)

The reports say that Hibiscus flowers possess antitumor properties, as well as their uses have been as analgesic, antipyretic, anti-asthmatic, and anti-inflammatory agents. The studies also have proved the presence of anti-oxidant, anti-fungal, and antimicrobial properties in flowers of Hibiscus rosa-sinensis. More importantly, the investigations on extracts of stems, roots, leaves, and flowers from Hibiscus reveal that its photochemical components contributed to very

striking findings that are useful to human's health such as antioxidant activity, which is the removal of free radicals that can lead to DNA damage [3].

III. METHODOLOGY

HRS Flower Collection: The flower for the experiment is collected from Clive's house of St. Joseph's College, Tiruchirapalli, Tamil Nadu, and India. It was collected in the month of January. The approximate temperature at the time of the collection was found to be around 25^0 to 27^0C.

Dissection method is one of the easiest methods in the taxonomy of the flowers used to segregate them by parts. It is also one of the easiest methods in extracting the pollen grains from any flower. **There are various steps that are involved in the dissection:** careful removal of the flower from the plant, extraction of the sepals and petals from the flower: sepals are the small, green leaf-like structures in between the petals and the stem. Careful removal of the anthers and their stems: where anthers create pollen inside the stamen of the flower, finally, slicing the stamens and anther in half with a scalpel where the pollen is produced. Caution should be taken in slicing the anther as it is very small and fragile.

Sample Preparation:

The pollen grains are directly mounted on the specimen holder of the SEM. The dimension of the holder is 1 cubic centimetre. For the UV Vis analysis the pollen grains are dissolved in ethanol (CH_3CH_2OH) as it is a good solvent and it is also unabsorptive in the UV region.

IV. RESULTS AND DISCUSSION

SCANNING ELECTRON MICROSCOPE (SEM)

Scanning electron microscope (SEM) is one of the most popular instrumentation techniques in the characterization of the nanomaterials and

nanostructures. Besides the surface morphology (texture), the signals that derive from electron-sample interactions also reveal information about the chemical composition present in the sample. As for my study, the prima-facie attempt was to characterise material in the Nano-particulate form. However, the material magnification is stable and intact at the micro level itself.

However, when we analyse them under the Particle Size Analyser, the size of the pollen particle is 252 nm taking the study towards the Nano analysis. Here, the SEM analysis is precisely to study the morphology of the pollen grains. The Fig.2a depicts microphotography of a pollen grain. The spines are sharp and long, and also symmetrically distributed over the pollen grain surface. The positions of pollen spines are similar to those of carbons in the buckminster C_{60} fullerene molecule.

The carbons on the buckminster C_{60} fullerene surface form polygons such as hexagon and pentagon. Similarly the spines form hexagons on the pollen grain surface. But polygon pattern in pollen grain is different from that of the fullerene. Spherical hexagons are regularly patterned and each polygon is centred in a pollen grain. In a fullerene molecule 20 hexagons and 12 pentagons are patterned by connecting 60 carbon point centres. Similarly in pollen grain also. 32 additional spine point centres are observed in each polygon centre. It is estimated that 92 spines could be distributed over a pollen grain sphere and also the measured mathematical parameters associated with the symmetrical distribution of spines on the surface of the pollen grain are analogized with buckminster C_{60} fullerene [4].

In C_{60} fullerene molecule, carbons are separated in a symmetrical manner and their chemical bonds are same length due to the electrical polarity. Here spines also play a vital role in structuring the pollen [5]. Mechanical and electrical properties of pollen of *H.*

Rosa were also studied. The super stability of this spherical pollen structure was analysed on the basis of mechanical and chemical properties [6, 7]. It is found that the electrical charges are existing in the spines and those charges are separated in equidistance by electrostatic repulsion. In pollination process, the negative charged surface of pollen grains are attracted by positively charged surface in the legs of Honey bee.
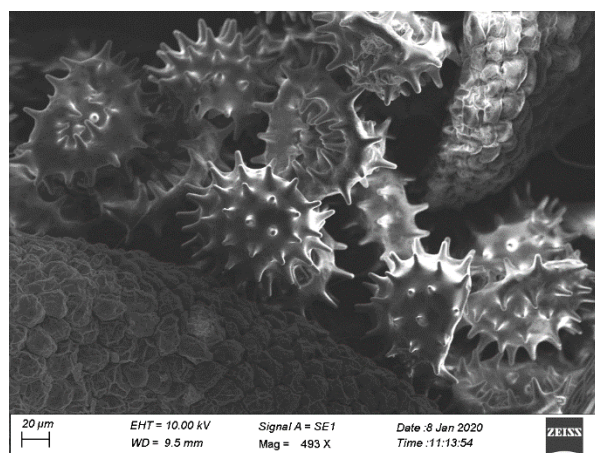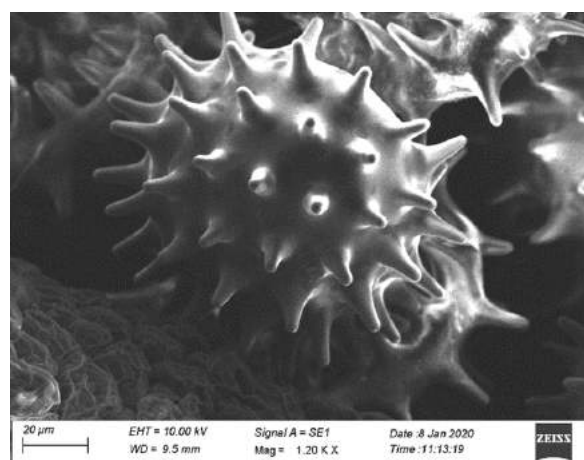

Fig. 2. SEM image of the pollen grain

Fig. 2a. SEM Micro-image of the pollen grain

UV-vis-NIR

Varian Carry 5E model UV-vis-NIR spectrometer recorded the optical transmittance against the wavelengths of UV-vis-NIR region from 200 nm to 1400 nm. Fig. 3.depicts the optical absorption spectrum of latex of CG. The UV-Vis spectra profile of HRS Pollen grains reveals the absorptive behaviour of the

biochemical composition in the pollen. This is applied to identify the number and the characteristics (position, intensity, shape) of absorption peaks, in order to determine the specific bioactive classes of compounds. Mostly, the Carboxylic acids absorb the UV light of wavelength region from 200 to 240 nm [8]. In HRS pollen, the Carboxylic acids make absorptive peaks at 204 nm and 219 nm. The peaks in the UV region ranging from 250-400 nm reveal the presence of phenolicacids and their derivatives, e.g., flavones, flavonols, flavanones, flavonoids. The peak at 271 nm is pertained to flavonoids present in the HRS pollens.
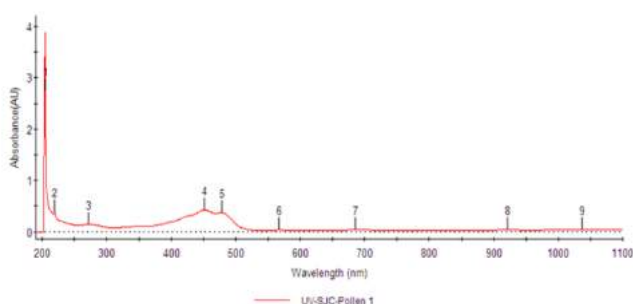

Fig. 3. UV-vis-NIR spectrum of HRS pollens

SUMMARY and CONCLUSION:

It is becoming clear that Hibiscus Rosa Sinensis plays a very important role, physiologically, ecologically, and evolutionarily, in anti-herbivore plant defences and in plant–insect interactions in a very unique way. **The Future studies will unveil:** The enhancement of carrier multiplication in pollen grains attracts a great deal of attention owing to their potential application in the field of research and the medicine. The advantages of HRS are at the medicinal level and the pollen morphology in specific makes us understand the inner nature of the plant. This surely paves way for a deeper research on pollen grains. Access to HRS pollens is based on review and scientific merits and it provides a cutting edge scientific idea to carry out research on characterizing HRS pollens for further applications. Optical absorption and transmission behaviour of HRS pollens witnessed the biochemicals present in the HRS

pollen grains. Eco-friendly and pollutant free material selection is always a matter of the greatest priority as it enhances the knowledge about the secrets that remain hidden in the nature and as a matter of fact the Nature never stops revealing itself to us.

V. CONCLUSION

PTh-PEO polymer composites were prepared successfully by in situ chemical oxidative polymerization of thiophene doped with Li2SO4. FTIR study confirms the successful polymerization of polymer composite. The value of transference number of all polymer composite samples was investigated by dc polarization techniques and found to be in the range of 0.80 to 0.89. This suggests that the charge transport in the PTh-PEO composite doped is predominantly due to ions only.

VI. REFERENCES

[1]. https://www.flowersworld.com/uses-of-flowers/

[2]. Komal Arora, POLLEN IDENTIFICATION OF HIBISCUS ROSA-SINENSIS AND SIDA ACUTA THROUGH FTIR SPECTROSCOPY, October 2014, Department of Botany, DAV College, Jalandhar, Punjab, India 144008

[3]. Kawase, hl. And Takahashi. M. 1995. Chemical composition of sporopollenin in Magnolia grandij7ora (hlagnoliaceae) and Hibiscus syriacirs (hialvaceae). - Gana 31: 242-245. ISSN 0017-3134.

[4]. Andrade K, Guerra S, Debut A (2014), Fullerene-Based Symmetry in Hibiscus rosa-sinensis Pollen. PLoS ONE 9(7): e102123. doi:10.1371/journal.pone.0102123

[5]. Bowker GE, Crenshaw HC (2007) Electrostatic forces in wind-pollination–Part 1: Measurement of the electrostatic charge on pollen. Atmospheric Environment Vol. 41 (8), 1587–1595.

[6]. Karton A, Chan B, Raghavachari K, Radom L (2013) Evaluation of the heats of formation of corannulene and C60 by means of high-level theoretical procedures. The Journal of Physical Chemistry Vol. 117, 1834–1842.

[7]. Zhang JY, Ohsaki (2012) Self-equilibrium and stability of regular truncated tetrahedral tensegrity structures. Journal of the Mechanics and Physics of Solids Vol.60, 1757–1770

[8]. Andrade K, Guerra S, Debut A (2014), Fullerene-Based Symmetry in Hibiscus rosa-sinensis Pollen. PLoS ONE 9(7): e102123. doi:10.1371/ journal.pone.0102123

High Gas Sensor Performance of Spinel-Type $Zn_{0.7}Mg_{0.3}Co_2O_4$ Nanoparticles Prepared by sol-gel method

T. R. Tatte[a], V.D. Kapse[b]

[a]Department of Physics, Shri. Dr. R. G. Rathod Arts and Science College, Murtizapur, Maharashtra, India

[b]Department of Physics, Arts, Science and Commerce College, Chikhaldara, Maharashtra, India

ABSTRACT

This work devotes to investigate synthesis of spinel $Zn_{0.7}Mg_{0.3}Co_2O_4$ structure was successfully synthesized by sol–gel method. Surface morphology was examined by means of Scanning electron microscopy (SEM). The gas sensing investigations revealed that $Zn_{0.7}Mg_{0.3}Co_2O_4$ nanostructures based gas sensor exhibited high response (50 ppm) and selectivity towards hydrogen sulfide. Besides, enhanced gas sensing properties of $Zn_{0.7}Mg_{0.3}Co_2O_4$ nanostructures are observed. The excellent gas sensing characteristics of $Zn_{0.7}Mg_{0.3}Co_2O_4$ nanostructures might be attributed to their high porosity and large specific surface area. Moreover, hydrogen sulfide gas sensing mechanism was proposed to explain the high sensor response.

Keywords : Sol–gel; Oxalic acid; Spinel; $Zn_{0.7}Mg_{0.3}Co_2O_4$; XRD.

I. INTRODUCTION

Rapid technological and industrial developments continuously result in the emission of hazardous gases, toxins, harmful, flammable and explosive gases and biomolecules. Therefore, sensing of such undesirable chemical or biochemical forms has become a significant research endeavor in recent years [1–3]. The effective detection and removal of toxic gases in the atmosphere is important for human as well as any living organisms. The uncontrolled release of toxic gases such as CO, H_2S, NH_3, CH_3CH_2OH, etc. from automobiles, industries, laboratories, etc. cause severe health problems and they may even cause death [4-6]. Advanced sensing materials have been adopted in this context to achieve high responsivity combined with less response/recovery time and continuous detection of gas molecules for gas sensors, which are key quality factors that define the sensor performance. In particular, oxides are extensively researched for gas sensing, in view of their robust material properties and their ability to change valence through charge transfer [7-9].

Nanocrystalline $ZnCo_2O_4$ has also been applied as electro catalyst for many anodic processes such as oxygen evolution [10], photocatalyst [11] and semiconductor gas sensor [12]. In cobalt based $ZnCo_2O_4$ cubic spinel structure, where Zn divalent ions occupy the tetrahedral and Co trivalent ions occupy octahedral site [13]. Nanostructured $ZnCo_2O_4$ is stable and cheaper than nobel metals [14]. Moreover, it is also active in alkaline solutions.

In this work, we present the synthesis and study of the gas sensing properties of $Zn_{0.7}Mg_{0.3}Co_2O_4$ nanomaterial for the detection of H_2S. The operating temperature of the material and its interaction mechanism with the H_2S has a crucial effect on the response and selectivity of the sensing device. The results obtained show that the $Zn_{0.7}Mg_{0.3}Co_2O_4$ nanostructure exhibits an excellent sensing performance for potential applications in H_2S gas sensors.

II. EXPERIMENTAL

2.1 Preparation of $Zn_{0.7}Mg_{0.3}Co_2O_4$ powder

The appropriate amounts of start materials $Co(NO_3)_2 \cdot 6H_2O$ (99.0%) and $Zn(NO_3)_2 \cdot 6H_2O$ (99.0%) were dissolved in ethanol (95.0%), mixed well with each other, and then slowly adding ethanol solution of oxalic acid (99.8%) at room temperature under constant magnetic stirring. The mixture was then stirred for 3 h and then evaporated at 80 ^{0}C for 1 h under constant stirring, which led to the formation of a sol. The sol was heated at 100^{0}C for 1 h until a gel was formed. Subsequently dried for 1 h in an electric oven and ground the gel, thus the oxalate precursor powder was attained. The resulting material was calcined at 500^{0}C for 2 h and well-crystallized spinel $Zn_{0.7}Mg_{0.3}Co_2O_4$ powder was obtained.

2.2. Fabrication of sensor

Appropriate quantity of mixture of organic solvents such as butyl cellulose, butyl carbitol acetate and turpineol was added to the mixture of $Zn_{0.7}Mg_{0.3}Co_2O_4$ and a solution of ethyl cellulose (a temporary binder). The mixture was then ground to form paste. The paste obtained was screen printed onto a glass substrate in desired patterns. The thick films so prepared were fired at 500℃ for 1h.

III. RESULT AND DISCUSSION

3.1. X-ray powder diffraction (XRD) analysis

Fig. 1 shows the XRD pattern of the synthesized $Zn_{0.7}Mg_{0.3}Co_2O_4$ nanomaterial at 500^{0}C for 2 h. It exhibits the diffraction peaks appeared at 2θ values 19.6^0, 31.15^0, 36.711^0, 63.06^0, 65.047^0 and 68.0^0 correspond to the crystal planes of (111), (220), (311), (222), (422), (511), (440), (620), (533) and (622) respectively which confirms the formation of pure $Zn_{0.7}Mg_{0.3}Co_2O_4$ spinel structure. The crystallite size was calculated by using the Debye–Scherrer equation.

$$D = \frac{k\lambda}{B cos\theta} \tag{1}$$

Where, D is the average size of the crystallite, assuming that the grains are spherical, k is 0.9, λ is the wavelength of X-ray radiation, B is the peak full width at half maximum (FWHM) and θ is the angle of diffraction. The crystalline size of the calcined mixed precursor is found to be 18 nm.
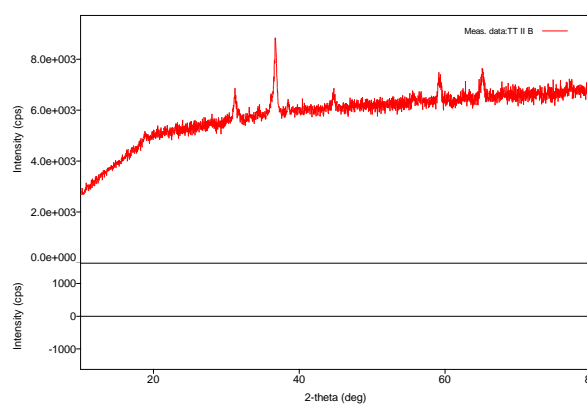

Fig. 1. XRD patterns of $Zn_{0.7}Mg_{0.3}Co_2O_4$ annealed at 500^{0}C.

3.2. Fourier transform-Infrared spectra (FT-IR) analysis

$Zn_{0.7}Mg_{0.3}Co_2O_4$ powder spectrum presented in Fig. 2. From Fig. 2, it can be obtained that the peak at 667 cm−1 is attributed to the stretching vibration mode of M–O for the tetrahedrally coordinated metal ions. The

band at 573 cm–1 can be assigned to the octahedrally coordinated metal ions.
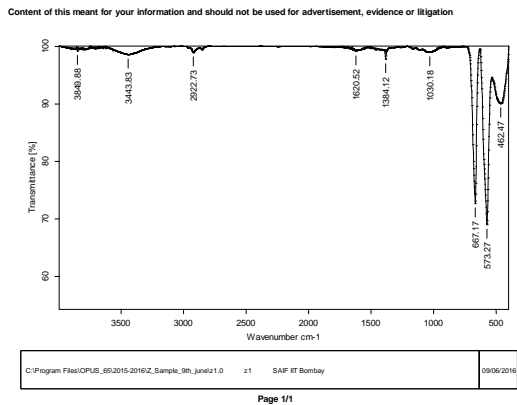

Fig. 2. FTIR spectrum of $Zn_{0.7}Mg_{0.3}Co_2O_4$ powder.

3.3. Scanning electron microscopy (SEM) analysis

Fig. 3 depicts SEM image of $Zn_{0.7}Mg_{0.3}Co_2O_4$ thick film. It can be observed that $Zn_{0.7}Mg_{0.3}Co_2O_4$ thick film show structure having large grains size with soft agglomerations has a regular morphology (polygons).
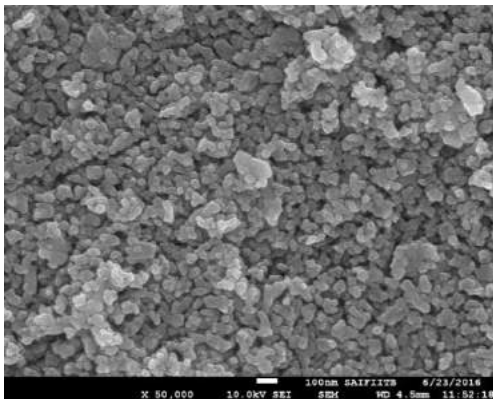

Fig. 3. SEM image of nanosized $Zn_{0.7}Mg_{0.3}Co_2O_4$.

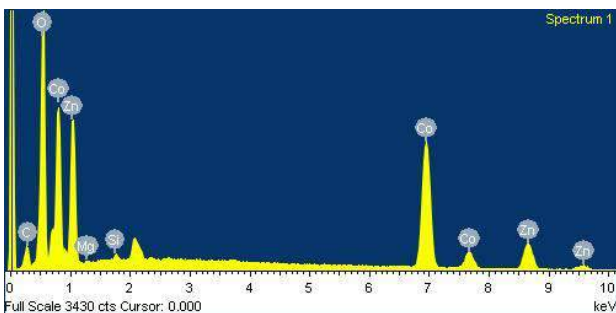### 3.4. Energy dispersion X-ray (EDX) analysis

Fig. 4. EDX spectrum for nanosized $Zn_{0.7}Mg_{0.3}Co_2O_4$.

Fig. 4 shows EDX patterns of the nanosized spinel $Zn_{0.7}Mg_{0.3}Co_2O_4$. From the EDX spectrum, the presence of Zn, Co and O elements alone in the sample, has been confirmed the absence of any other impurities.

3.5 Transmission electron microscopy (TEM) analysis

The TEM image of the $Zn_{0.7}Mg_{0.3}Co_2O_4$ calcined at 500 ^{0}C for 2 h are shown in Fig. 5(a). It indicates the presence of $Zn_{0.7}Mg_{0.3}Co_2O_4$ nanoparticles with size 30–40 nm which form beed type of oriental aggregation throughout the region.
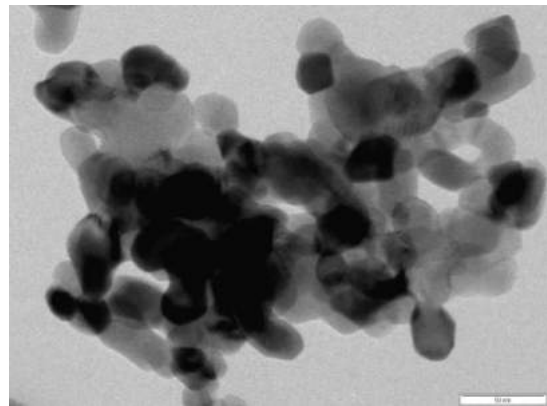

Fig. 5(a). TEM image of nanosized $Zn_{0.7}Mg_{0.3}Co_2O_4$.

Fig. 5(b) shows the selected area electron diffraction (SAED) pattern the spot type pattern which is indicative of the presence of single crystallite particles.
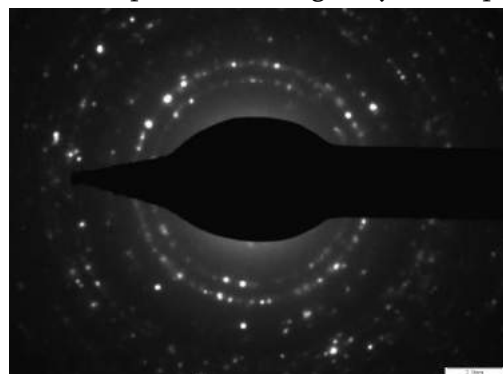

Fig. 5(b). Image of $Zn_{0.7}Mg_{0.3}Co_2O_4$ nanoparticles with SAED pattern.

4. Gas sensing properties

To study the selective behavior of nanocrystalline $Zn_{0.7}Mg_{0.3}Co_2O_4$ gas response (S) towards 50 ppm for

various test gases such as LPG, NH_3, CO_2, H_2S, Cl_2, H_2 and C_2H_5OH at optimal operating temperature 100^oC and is depicted in Fig. 6.
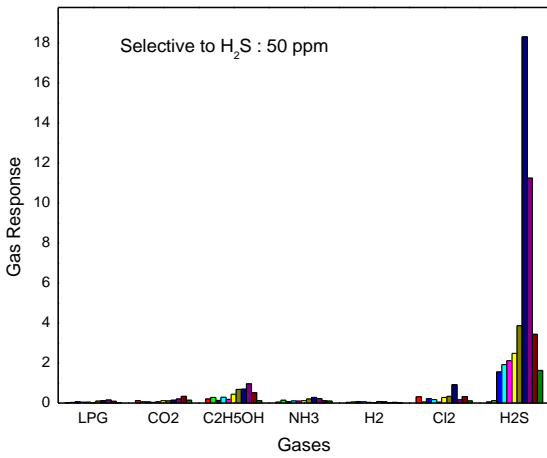

Fig. 6. Selectivity of nanocrystalline $Zn_{0.7}Mg_{0.3}Co_2O_4$ thick films.

The $Zn_{0.7}Mg_{0.3}Co_2O_4$ sample exhibited the higher gas response 18.31 towards H_2S. Hence, the $Zn_{0.7}Mg_{0.3}Co_2O_4$ sensors show maximum selectivity for H_2S gas towards 50 ppm among all the tested gases.
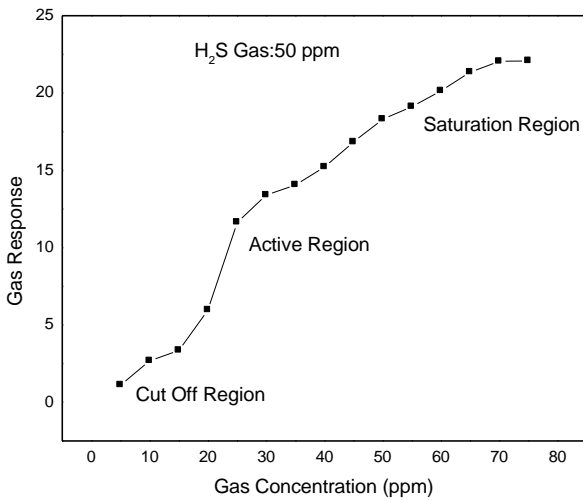

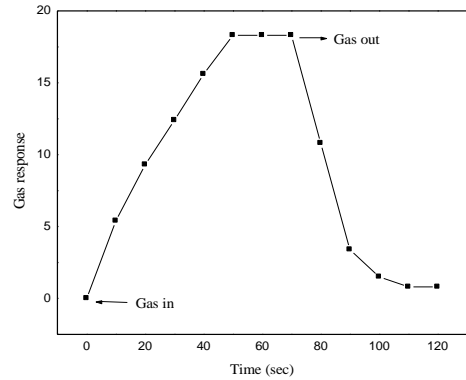**Fig. 7.** Gas response of $Zn_{0.7}Mg_{0.3}Co_2O_4$ as a function H_2S concentration.

Fig. 8. Response characteristics of $Zn_{0.7}Mg_{0.3}Co_2O_4$ thick film to 50 ppm H_2S

The response of $Zn_{0.7}Mg_{0.3}Co_2O_4$ as a function of H_2S gas concentration at 100^oC is shown in Fig. 7. The gas response was observed to increase with increase in the gas concentration and thereafter it remains almost constant. The response and recovery time characteristics of nanocrystalline $Zn_{0.7}Mg_{0.3}Co_2O_4$ based sensor to 50 ppm H_2S at 100^0C are depicted in Fig. 8. The nanocrystalline $Zn_{0.7}Mg_{0.3}Co_2O_4$ have quick response time 16 s and fast recovery time 52 s. Therefore, nanocrystalline $Zn_{0.7}Mg_{0.3}Co_2O_4$ based sensor exhibits the good response and recovery time to H_2S.
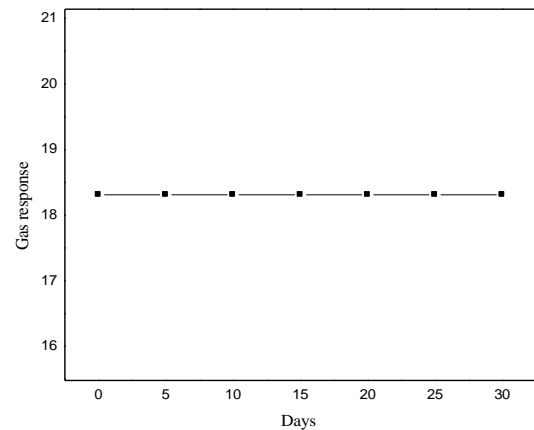

Fig. 9. Stability nanocrystalline $Zn_{0.7}Mg_{0.3}Co_2O_4$ thick film.

The reproducible nature of nanocrystalline $Zn_{0.7}Mg_{0.3}Co_2O_4$ based thick film sensor to 50 ppm H_2S

was measured for a month in the interval of 10 days and result are shown in Fig. 9. From figure, it was found that nanocrystalline $Zn_{0.7}Mg_{0.3}Co_2O_4$ based sensor possesses a very good stability and durability.

IV. CONCLUSION

In summary, we have reported the synthesis and investigations of gas sensing properties of $Zn_{0.7}Mg_{0.3}Co_2O_4$ nanomaterial for the detection of H_2S. The material was fabricated by the sol-gel method. TEM investigation reveals the average crystallite size is in accordance with XRD results. The excellent gas sensing performance of the prepared $Zn_{0.7}Mg_{0.3}Co_2O_4$ nanomaterial was attributed to its morphology, the operating temperature and the disparity in the sensing mechanism between H_2S and other reducing gases. The obtained results demonstrate the potential suitability of the application of $Zn_{0.7}Mg_{0.3}Co_2O_4$ in gas sensing devices for the detection of H_2S.

V. REFERENCES

[1]. K. Wetchakun, T. Samerjai, N. Tamaekong, C. Liewhiran, C. Siriwong, V. Kruefu, A. Wisitsoraat, A. Tuantranont, S. Phanichphant, Sens. Actuators, B, 160 (2011) 580.

[2]. J. Zhang, Z. Qin, D. Zeng, C. Xie, Phys. Chem. Chem. Phys., 19 (2017) 6313.

[3]. G. Korotcenkov, Mater. Sci. Eng., B, 139 (2007) 1.

[4]. A. M. Azad, S. A. Akbar, S. G. Mhaisalkar, et al., J Electrochem Soc., 139 (1992) 3690.

[5]. R. W. Bogue, Meas Sci Technol., 1(1996) 1.

[6]. Y. R. Wu, J. Singh, Appl. Phys. Lett., 85 (2004) 1223.

[7]. N. Barsan, D. Koziej, U. Weimar, Sens. Actuators, B, 121 (2007) 18.

[8]. Q. Wang, X. Li, F. Liu, C. Liu, T. Su, J. Lin, P. Sun, Y. Sun, F. Liu, G. Lu, RSC Adv., 6 (2016) 80455.

[9]. C. Wang, L. Yin, L. Zhang, D. Xiang, R. Gao, Sensors, 10 (2010) 2088.

[10]. B. Chi, J. Li, X. Yang, H. Lin, N. Wang, Electrochim. Acta, 50 (2005) 2059.

[11]. S. V. Bangale, R. D. Prashale, S. R. Bamane, J. Chem. Pharm. Res., 3 (2011) 527.

[12]. X. Niu, W. Du, W. Du, Sens. Actuators, B, 99 (2004) 405.

[13]. K. Karthikeyan, D. Kalpana, N. G. Renganathan, Ionics, 15 (2009) 107.

[14]. S. Trasatti, J. Lipkowski, P. N. Ross, The Electrochemistry of Novel Materials, VCH Publishers, Weinheim, (1994) 207.

Synthesis and Characteristics of Cuo Doped Polyaniline Nano Composites

A. V. Rajgure[1], D.R. Bijwe*[1], P. S. Deole, S .S. Kawar[2], S. P. Ganorkar[1], A. R. Bhojane[1], N. B. Nimkar[1],
R. K. Kitukale[1], P. A. Pethe[1], P. S. Pathare[1]

[1]Department of Physics, G. S. Tompe Arts, Commerce & Science College, Chandur Bazar,
Dist.- Amravati, Maharashtra, India

[2]Department of Physics, Dr. R.G. Rathod Arts and Science College, Murtizapur, Dist.- Akola, Maharashtra,
India

ABSTRACT

In this present paper, Nano crystalline and bulk CuO are prepared by thermal decomposition of freshly prepared $Cu(OH)_2$. The PAni-CuO samples are prepared with 10 and 35 wt%. The structural changes of prepared composite materials were carried out by X-ray diffraction (XRD) tool.

Keywords : PANI, CuO, XRD

I. INTRODUCTION

Rapid development of industrialization need to stable, low cost ecofriendly effective battery. Day to Day Advance in technology leads to the need of energy storage systems of eco-friendly nature with fast charging and discharging time[1-3]. Nanotechnology is wide progressing to produce growing media with public interest since from the past decade which has broad application in many research areas, development and industrial application.The electrical conductivity of the PAni can be modified by the process of doping with suitable metal oxide. The CuO nanoparticles are the primary dopants which vary the structural, magnetic, optical and/or electronic properties of the PAni and it is accompanied by large increase in conductivity[4-5].Nano particles of copper oxide exhibit the nature of a semiconductor with a band gap of 1.5 to 1.8 eV with their application in photo detectors, solar cells, gas sensors, biosensors, super

capacitors, removal of organic, magnetic storage media etc8.

In this research work, Copper oxide nanoparticles were prepared by eco friendly low temperature solution Co-pracipated synthesis and the polyaniline- CuO Nano Composites of doping concentrations (10, 35wt%) were synthesized . The samples were characterized by XRD, studies and specific surface area.

II. EXPERIMENTAL

2.1. Synthesis of Polyaniline (PAni):

The analytical grade 0.2M aniline hydrochlorideand 0.25 M ammonium peroxydisulfate were used as precursors. Aniline hydrochloridewas dissolved in distilled water to form a transparentsolution; ammonium peroxydisulfate was added drop-wise to the solution under continuous stirring until pH becomes around 8. The precipitate obtained was washed with distilled water for several times to remove chlorine

ions. It was further it was dried at 60°C for 2 h in air to obtain fine Nano crystalline powder.

2.2. Synthesis of CuO Nano Composite

Nano crystalline and bulk CuO are prepared by thermal decomposition of freshly prepared $Cu(OH)_2$ at different temperatures. The $Cu(OH)_2$ is prepared by reacting aqueous solution of 0.1M copper nitrate,$Cu(NO_3)_2$. $3H_2O$ and 0.5M sodium hydroxide. The NaOH solution is added drop wise with constant stirring until the PH of the system reaches to 12. The chemical reaction between copper nitrate and sodium hydroxide solution is as follows

$$Cu(NO_3)_2 + 2NaOH \longrightarrow Cu(OH)_2 + 2NaNO_3$$
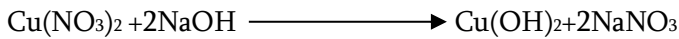
The resulting blue-green gel is washed several times with distilled water until free nitrate ions. Finally the gel is dried by heating at 100°C for 10 h. Copper hydroxide decomposes into nano crystalline copper oxide on heating as follows

$$Cu(OH)_2 \longrightarrow CuO + H_2O$$
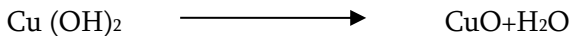
III. RESULTS AND DISCUSSION

3.1. XRD analysis

The X-ray Diffraction Study was carried out using X-ray diffractro meter in the 2Θ range from 10° to 80°. X-ray diffraction (XRD) method is used for materials characterization as it provides important information about the internal structure of matter such as crystallite size and crystal structure. All patterns exhibit peaks corresponding to the rutile structure of polycrystalline CuO with the maximum intensity peak corresponding to (110) plane [6]. It was observed that the relative intensities of all the peaks reduce with an increase in PAni Content. It was also observed that the peak broadening takes place with the increasing PAni content which is in good agreement with the earlier studies [7-9]. The increase in FWHM along with the reduction in peak intensity suggests that PAni incorporation into CuO lattice results in lowering of

crystallite size of CuO. The Pure PAni shows larger voids Fig. 3(a) as compared to doped samples which have smaller uniformly distributed voids in Fig. 3(b and c).
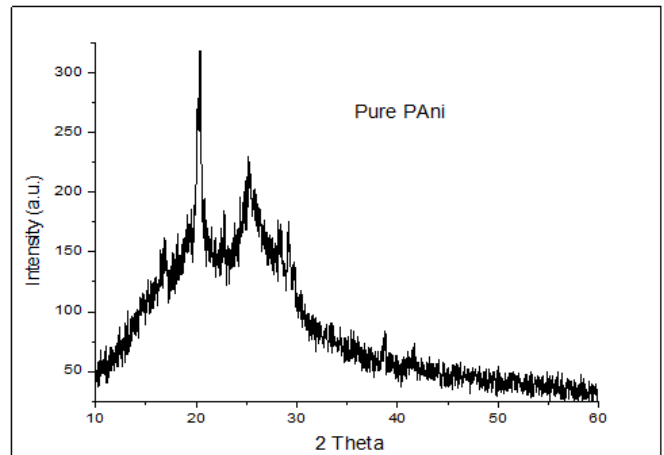

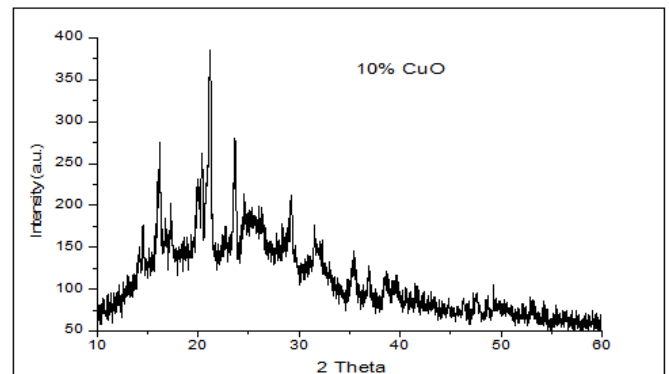Fig. 1(a) XRD of Pure Polyaniline (PAni)
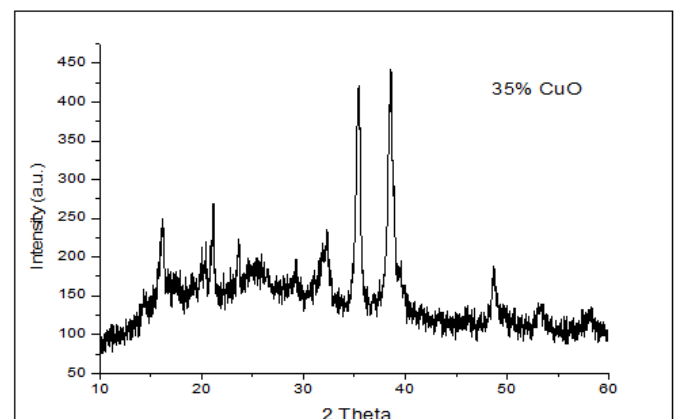

Fig.1(b)XRD of 10wt%CuO-PAni Nano Composite

Fig.1(c) XRD of 35wt%CuO-PAni Nano Composite

IV. CONCLUSION

The study of the pure PAni and (10 &35wt%) PAni doped CuO polyaniline increases due to addition of PAni wt %. The 35wt% PAni nano omposite plays the important role in the contribution Surface modification.

V. REFERENCES

[1]. Sexena, V, Malhotra, B D, Curr. Appl. Phys., 3, 293-305 (2003)

[2]. M. Chang, H. Liu and C.Y. Tai (2011) Powder Technology 207, 378–386.

[3]. Chaudhari, S, Mandate, AB, Patil, KR, Sainkar, SR, Patil, PP, J. Appl. Polym. Sci., 106,220-229 (2007)

[4]. Gupta K, Jana P C, Meikap A K., Synthetic Metals 160 (2010) 1566-1573.

[5]. Mathai C J, Saravanan S, Anantharaman M R,Venkitachalam S, Jayalekshmi S., J. Phys. D: Appl. Phys., 35 (2002) 240

[6]. Amnerkar R H, Adgaonkar C S, Yawale S S, Yawale S P., Bull. Mater. Sci. 25 (2002) 431-434

[7]. Lanje, A.S., Sharma, S.J., Pode, R.B., Ningthoujam, R.S., Advances in Applied Science Research, 1 (2) 36-40, (2010)

[8]. A. B. Kaiser, C. K. Subramanium, P. W. Gilberd and B. Wessling, Synth. Met., 69, 197 (1995).

[9]. Mittal, H., Kaith B., Jindal R, Advances in Applied Science Research, 1 (3) 56-66, (2010)

The Development of PVA Based Proton Conducting Solid Polymer Composite Electrolyte System

R. Risodkar

Assistant Professor Department of Physics, R.A. College, Washim, Maharashtra, India

ABSTRACT

In this Study the attempt was to improve the proton conductivity by dispersing the Nano sized GDC to obtain (100-x) (80PVA:20AN) (x)(GDC) Nano-composite system. X-ray diffraction (XRD) study shows that the addition of filer GDC in polymer not only reduces the intensity of the characteristic (110) peak but also broadens which is an indication of the increase in amorphousness. The Arrhenius plots for different concentrations of GDC in (80PVA:20AN) polymer blend shows the initial increase in ionic conductivity of the composite polymer electrolyte upto 20 wt% filler GDC. The proton conductivity increases with increased relative humidity within entire studied range of H_2 partial pressures.

Keywords : Nano Composite System, XRD, polymer blend, proton conductivity.

I. INTRODUCTION

Solid proton conductors are compounds containing loosely bound molecules where conductivity generally strongly depends on their state of hydration. Composite solid electrolytes are heterogeneous, multiphase, typically two-phase solid systems. The significant enhancement in ionic conductivity in LiI and other ion conducting materials on addition of submicron size particles of inert insulating second phase such as Al_2O_3, or SiO_2 is reported [1-5]. Two main aspects for understanding the conductance of composite materials are (i) the microscopic mechanism, which determines the magnitude of interfacial conductivity and (ii) the percolation theory [6,7]. These complexes are relatively inexpensive and can be easily processed as thin films for applications such as hydrogen sensors [8], electrochromic displays, and PEFC systems. During the present work, efforts were directed to prepare new proton conducting polymer electrolyte materials and characterized for PEMFC/sensors device applications. A good number of attempts are made in the past and continuing to develop the fast solid proton conducting polymer electrolytes [9]. There is a growing interest in the use of fuel cells (FC) with hydrogen as the main fuel for stationary, mobile and transportation applications. In this context, different types of membranes based on PVA investigation are due to Nikolic et al. [10]. Water-soluble polymer, i.e. PVA used in practical applications because of its ease of preparation, excellent chemical and thermal stability along with good mechanical properties. The PVA/SiO2 nanocomposites exhibit a significantly improvement in thermal resistance in comparison with the pure PVA [11].

During this work an attempt was made to improve further the proton conductivity of highest conductivity giving 80PVA:20AN complex polymer, the nano sized GDC was dispersed to obtain (100-x)(80PVA:20AN):(x)(GDC) nano-composite systems.

II. MATERIALS AND METHOD

Poly(vinyl alcohol) (PVA), with a degree of hydrolysis more than 99% and average molecular weight of 146000, was procured from Aldrich, USA. Ammonium nitrate (AN-(NH_4NO_3), gadolinium doped ceria ($Ce_{0.8}GD_{0.2}O_2$/GDC) having particle size 100 nm, were obtained from Aldrich, USA. The double-distilled-deionized water was obtained using TKA, Germany, water purifier. The materials were Synthesized in the form of homogeneous and uniform film by solution cast technique.

The aqueous solutions with desired mole ratios of PVA:AN as (80:20), was prepared by dissolving PVA and AN separately in deionized water and then mixing them together. Later, this aqueous solution was thoroughly stirred for 8–10 h at 60–70 °C using magnetic stirrer so as to obtain the homogeneous single-phase solution. PVA is doped with ammonium nitrate and dispersed with GDC powder with compositions = (100-x) (80PVA:20AN):x(GDC), where x = 5, 10, 15, 20 and 25 wt%. The viscous gel mixture was then casted on the glass plate and dried for one week. The smooth and uniform films were obtained. All the prepared composite polymer electrolytes during present study were then thoroughly characterized using various analytical tools.

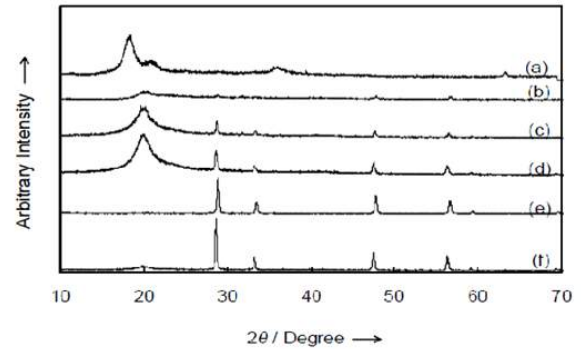## III. RESULTS AND DISCUSSION

X-ray Diffraction

Fig. I : XRD patterns of (a) Pure PVA, (b) 95(80PVA:20AN):5GDC, (c) 90(80PVA:20AN): 10GDC, (d) 85(80PVA:20AN):15GDC, (e) 80(80PVA:20AN):20GDC and (f) 75(80PVA:20AN): 25GDC.

The XRD patterns of pure PVA and (100-x) (80PVA:20AN):(x) GDC (x = 5, 10, 15, 20 and 25 wt%) composite solid polymer electrolytes are shown in Fig.I.-(a) to (e) and (f), respectively.

Addition of filler GDC in polymer not only reduces the intensity of the characteristic (110) peak but also broadens, which is an indication of the increase in the degree of amorphousness. Chand et al. [12], also, reported the similar results. The interaction of the polymer chain with the filler (GDC) during the preparation of film usually increases the interlayer spacing of polymer chain and that tends to shift the diffraction peak towards lower angle [13]. But in the present case the peak shifts to higher diffraction angle suggesting decrease in inter planer distance. The characteristic peaks corresponding to GDC are clearly identified in 5wt% GDC (Fig.I(b)). The intensities of all characteristic peaks of filler GDC increases with an increase in its content in complex polymer. Evidently, the amorphousness of composite solid polymer electrolyte, in general, increases due to the addition of GDC filler as in the previous case of GDC addition. At higher concentration of filler (GDC), the GDC peak

appeared prominently due to formation of GDC clusters.The degree of amorphousness is compared in Table I.

Samples	X_C (%)
Pure PVA	40
95(80PVA:20AN):5GDC	35
90(80PVA:20AN):10GDC	30
85(80PVA:20AN):15GDC	25
80(80PVA:20AN):20GDC	17
75(80PVA:20AN):25 GDC	10

Table 1 : The degree of crystallinity obtained from XRD pattern for (100-x)(80PVA:20AN):(x)(GDC)composites.

Ionic Conductivity

Arrhenius plots for (100-x) (80PVA:20AN) : (x)(GDC) complexes when x = 5, 10, 15, 20 and 25 (in wt%) are shown in Fig.IV.37. All the samples obey the Arrhenius law. In this case also, the ionic conductivity of the nano composite polymer electrolyte increases with increasing the GDC filler concentration up to 20 wt%, beyond which conductivity decreases.

Furthermore, the magnitude of conductivity enhancement due to GDC addition is higher at low temperature vis-à-vis high temperature. Further, The activation energy is found to be minimum for the maximum conductivity giving composition.
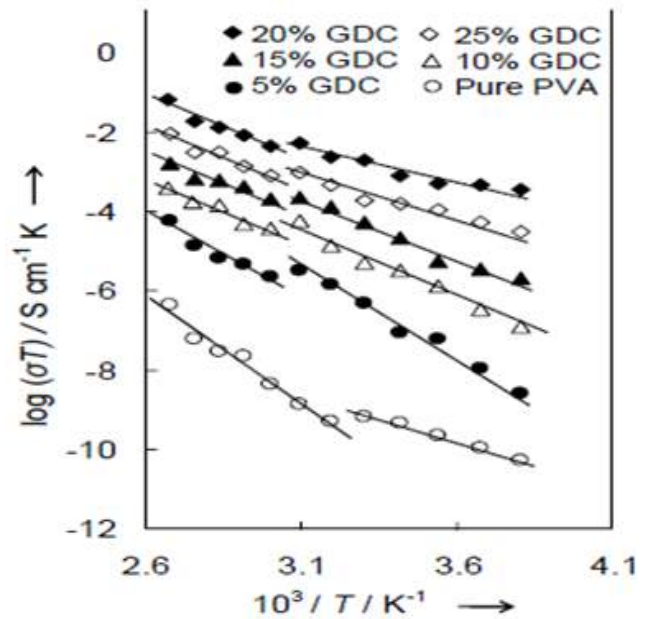

Fig.II: Arrhenius plots for different concentrations of GDC in (80PVA:20AN) polymer complex

The XRD results discussed already, revealed the dispersion of nano particles of GDC in 80PVA:20ANpolymer complex. In other words, the GDC nano particle do not chemically react with polymer but are disperse uniformly in the polymer matrix. Since GDC is insoluble in PVA polymer it forms heterogeneous composite system and at about 20 wt% gave maximum conductivity (order of magnitude), the possibility of increased conductivity due to dissociation of salt is ruled out. The system under consideration is a heterogeneous i.e., there exists more or less sudden structural changes. The space charge region across the polymer/GDC interface is higher conducting compared to bulk polymer complex. The increase in conductivity up to 20 wt% of filler GDC in (PVA:AN) polymer complex is due to the increase in space charge layers in composites. The maximum conductivity at 20 wt% GDC added polymer is attributed to the percolation threshold where ion conducing paths throughout the polymer composites are optimum. Addition of filler in polymer complex beyond 20 wt% leads to aggregation of GDC particles which disrupts the proton percolating

paths across the film leading decrease in conductivity. Additionally, such aggregation of filler grains could make the long polymer chains more immobilized, leading to the decrease in the conductivity. Dissanayake et al. [14] have also reported the similar results for 80(80PVA:20AN):20GDC. The highest conducting 80(80PVA:20AN):20GDC Nano composite polymer electrolyte film was further studied in detail.

interface due to electrochemical reaction. Concurrently, more mobile charge carriers (H⁺) are available for charge transport through the polymer electrolyte under external electric potential difference leading to an enhancement in conductivity.
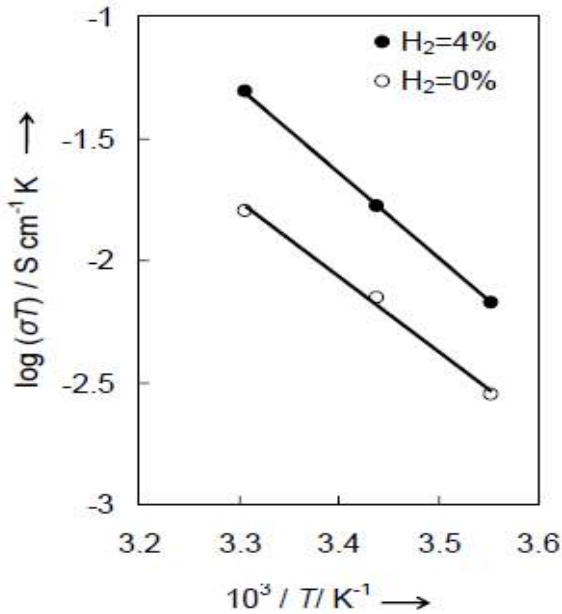

Fig. III (a) : Arrhenius plots of 80(80PVA:20AN):20(GDC) at fixed hydrogen concentration.

Fig. III (b): Variation of proton Conductivity with relative humidity at Constant hydrogen concentration
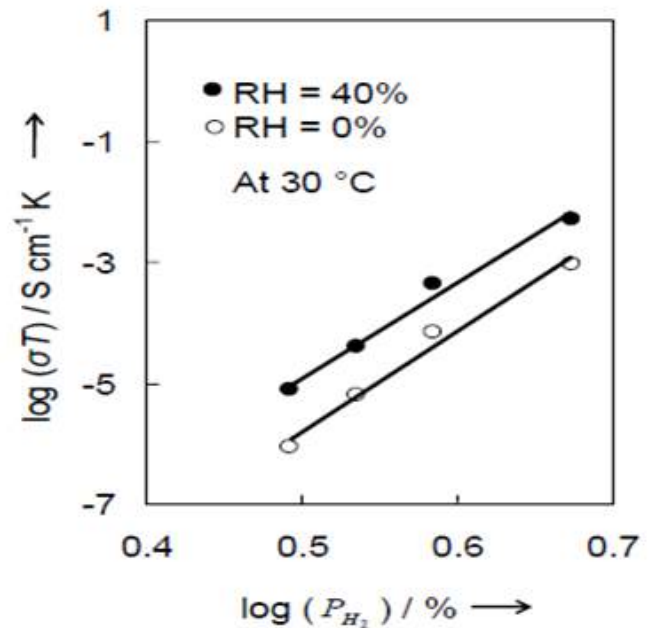
Fig.III(c): Variation of conductivity of 80(80PVA:20AN):20(GDC) with H2 partial pressure at fixed (0.0 and 40%) relative humidity

The Arrhenius plot for 80(80PVA:20AN):20GDC in presence of different hydrogen concentrations are shown in Fig.IIIa. In this system also the conductivity increases with an increase hydrogen concentration. Also, the proton conductivity increases, at fixed H_2 partial pressure, with an increase in relative humidity (Fig.III). The proton conductivity increases with increased relative humidity within entire studied range of H_2 partial pressures as shown in Fig.IIIb. The linear dependence of log(σ) on RH (%) and log(σ) on log(H_2P) are clear from Fig.III(a-c). As already discussed that the increased H_2 partial pressure at porous Pt-electrode increases H⁺ concentration across Pt-electrolyte
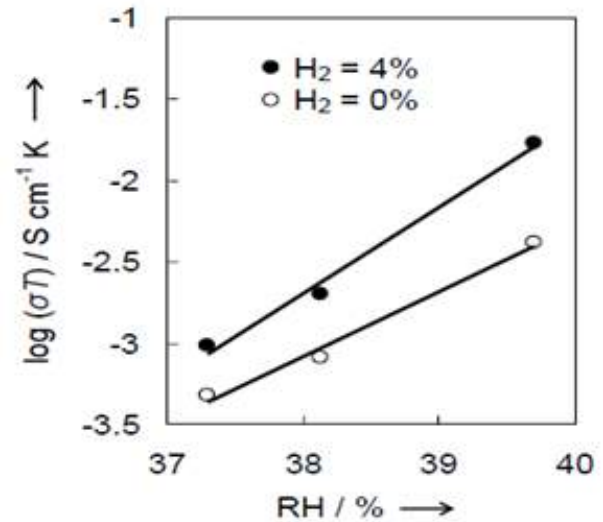
IV. CONCLUSION

During this work a new type of proton conducting AN doped PVA and filler GDC were studied. PVA is doped with ammonium nitrate and dispersed with Gadolinium doped ceria powder with compositions = (100-x) (80PVA:20AN):x(GDC), where x = 5, 10, 15, 20 and 25 wt%. The XRD results revealed the dispersion of Nano particles of GDC in 80PVA:20AN polymer complex and at about 20 wt% gave maximum conductivity under normal atmospheric conditions. The ionic conductivity of the Nano composite solid polymer electrolyte initially increases with an increase in the filler GDC concentration up to 20 wt%; beyond this concentration conductivity decreases. The proton conductivity increases with increased relative humidity within entire studied range of H$_2$partial pressures. Above all, PEFCs based on proton donor and filler hold the largest potential for developing low temperature PEFCs to be operated at room temperature.

V. REFERENCES

[1]. C. C. Liang, J. Electrochem. Soc., 120 (1973) 1289.

[2]. J. B. Wagner, Mater. Res. Bull., 15 (1980) 1691.

[3]. K. Shahi and J. B. Wagner, Jr., J. Electrochem. Soc., 128 (1981) 6.

[4]. O. Nakamura and J. B. Goodenough, Solid State Ionics, 7 (1982) 119.

[5]. F. W. Poulsen, N. H. Andersen, B. Kindle and J. Scoonman, Solid State Ionics, 9/10 (1983) 131.

[6]. T. Jow and J. B. Wagner, Jr., J. Electrochem. Soc., 135 (1988) 529.

[7]. D. Stauffer, in Introduction to Percolation, Eds. Taylor and Francis, (London), (1985).

[8]. R. Bouchet, E. Siebert, G. Vitter, J ElectrochemSoc 144(1997)L95-7.

[9]. H. Pu, M. Luo and Z. Yang, Euro. Polym.J., 43 (2007) 5076.

[10]. Z. Peng and L. X. Kong, Polym. Degrad. Stab., 92 (2007) 1061

[11]. N. Chand, N. Rai, T. S. Natarajan and S. L. Agrawal, Fibers and Polym., 12 (2011) 438.

[12]. Lord Raleigh, Phil. Mag. 34(1892) 481.

[13]. M. A. K. L. Dissaanayake, P. A. R. D. Jayathilaka, R. S. P. Bokalawala, I. Albinsson and B. E. Mellander, J. Power Sources, 119-121 (2003) 409

[14]. J. Fleig and J. Maier, Solid State Ionics, 85 (1996) 9.

Solvent Extraction and Spectrophotometric Determination of Cobalt (Ii) with N, N'-Bis (Salicylaldehyde) Ethylenediamine [Salen]

S. M. Parkhi , V. P. Dhatrak , A. M. Nannaware

Department of Chemistry, Anand Niketan College Warora, Maharashtra, India

ABSTRACT

A method for solvent extraction and spectrophotometric determination of Cobalt (II) with N,N'-Bis(salicylaldehyde) ethylenediamine (salen) has been studied .The method is based on formation of Co - N,N'-Bis(salicylaldehyde) ethylenediamine (salen) complex. Here Co act as metal and N,N'-Bis(salicylaldehyde) ethylenediamine (salen) act as ligand .The absorption spectra of Co(II)-salen complex extracted at different pH and it was found to be maximum at pH 6 and measured against reagent blank .The light yellow Co(II)- N,N'-Bis(salicylaldehyde) ethylenediamine (salen) complex solution show maximum absorption at 410 nm .

Keywords : Solvent extraction, Spectrophotometer, Cobalt, N,N'-Bis(salicylaldehyde) ethylenediamine (salen), pH .

I. INTRODUCTION

In its simplest form, extraction refers to the transfer of a solute from one liquid phase to another. The most common case is the extraction of an aqueous solution with an organic solvent. Diethyl ether, benzene, and other hydrocarbons are common solvent that are less dense than water and form a phase that sits on top of the aqueous phase. Chloroform, dichloromethane, and carbon tetrachloride are common solvents that are immiscible with and denser than water [4]. Solvent extraction is another name for liquid-liquid distribution that is distribution of a solute between two liquids that must not be completely mutually miscible. This method makes use of an organic compound capable of extracting the metal ion of interest, or a complex of it, from the aqueous phase into an immiscible organic solution.

Theory of Spectrophotometry and Colorimetry:-

Theory of Spectrophotometry which is helpful in the quantitative analysis of sample is very well explained [5]. When light (monochromatic or heterogeneous) is incident upon a homogeneous medium, a part of the incident light is reflected, a part is absorbed within the medium, and the remainder is transmitted. If the intensity of the incident light is expressed by Io, that of the absorbed light (Ia), the transmitted light (It), and the reflected light (Ir), then:

$$Io = Ia + It + Ir \ldots\ldots\ldots\ldots\ldots (1)$$

For air-glass interface, consequent upon the use of glass cells, it may be stated that about 4 per cent of the incident light is reflected. Ir is usually eliminated by the use of a control, such as a comparison cell, hence:

Io = Ia + It ………………….. (2)

Lambert (1760) investigated the relation between Io and It. Beer (1852) extended to solutions. Spectrophotometry and colorimetry are based upon Lambert's and Beer's laws.

Basic Principles of Solvent Extraction-

The solvent extraction methods are based on the four basic principles

(a) Gibb's phase rule
(b) Distribution ratio or extraction coefficient
(c) Partition coefficient, P
(d) Percentage extraction

Classification of Solvent Extraction systems : Extraction can be classified on the basis of

I] Nature of extracted species

II] Process of extraction

II] There are two types of extraction depending on the basis of the nature of extracted species,

a. Chelate extraction b. Ion association

IV] Classification based on the basis of process of extraction

(a) Extraction by chelation or Chelate formation
(b) Extraction by Ion pair formation
(c) Extraction by salvation
(d) Synergistic extraction

II. MATERIALS AND METHODS

All chemicals used were of A.R.grade. Separating funnels for batch extraction, glass apparatus. The instruments required for the whole solvent extraction and determination process are very simple like pH meter, spectrophotometer etc.

Preparation of stock solution :-

For 0.01 M $CoSO_4$ Solution : Cobalt sulphate solution was prepared by dissolving 0.2811 g of $CoSO_4.5H_2O$ in slightly acidic media and volume was made by distilled water till mark in 100 ml volumetric flask.

For 0.001 M $CoSO_4$ Solution : 10 ml of 0.01 M cobalt sulphate solution was taken in 100 ml volumetric flask and volume made up to the mark by adding distilled water.

For 0.0001 M $CoSO_4$ Solution : 10 ml of 0.001 M cobalt sulphate solution was diluted in 100 ml volumetric flask by adding distilled water.

Preparation of 0.1% reagent : 0.1g of N,N'-Bis(salicylaldehyde) ethylenediamine (salen) (purity more than 98%) was dissolved in chloroform in 100 ml volumetric flask and volume made up to mark.

III. RESULT AND DISCUSSION

Systems were prepared, having different pH of solution with constant metal ion concentration 5.89 µg (in 1 ml). pH was adjusted with ammonium hydroxide and hydrochloric acid. Volume of aqueous phase was kept constant to 25 ml. Solution was then transferred to separating funnel, 5 ml of salen solution was added.

Each system was shaken for 5 minute allowed to equilibrate for 5 minute. Co (II) from aqueous phase was extracted into organic phase. Absorbance of organic phase was measured at 410 nm against reagent blank.

To determine λmax of a solution:

Wavelength(nm)	Absorbance
400	0.349
410	0.366
420	0.333
430	0.305
440	0.280

System No.	pH	0.0001M CoSO$_4$ Solution (ml)	Amount of Co(II) taken in (µg)	0.1% Salen Reagent in chloroform (ml)	Distilled water (ml)	Absorbance
1	1	1	5.89	5	19	0.028
2	2	1	5.89	5	19	0.036
3	3	1	5.89	5	19	0.306
4	4	1	5.89	5	19	0.382
5	5	1	5.89	5	19	0.406
6	**6**	**1**	**5.89**	**5**	**19**	**0.467**
7	7	1	5.89	5	19	0.463
8	8	1	5.89	5	19	0.455
9	9	1	5.89	5	19	0.451
10	10	1	5.89	5	19	0.435

System No.	Volume of 0.0001M CoSO$_4$ (ml)	Amount of Co(II) taken in µg	Reagent 0.1% Salen in chloroform (ml)	pH water (ml) [pH=6]	Absorbance
1	1	5.89	5	19	0.050
2	2	11.78	5	18	0.102
3	3	17.67	5	17	0.186
4	4	23.57	5	16	0.215
5	5	29.46	5	15	0.252
6	6	35.35	5	14	0.291
7	7	41.25	5	13	0.342
8	8	47.14	5	12	0.420
9	9	53.03	5	11	0.430
10	10	58.93	5	10	0.446
Blank			5	20	

$\lambda_{max} = 410$ nm

At this λ_{max} , the absorbance of each system were measured

Absorbance of system at different pH :

From the above table it is cleared that, maximum absorbance shown at pH = 6.0, Hence the different systems were prepared at pH = 6.0 for determination of calibration graph and absorbance were measured.

Preparation of Calibration Curve at pH = 6.0

In this case different concentration of metal ion was used and reagent concentration was kept constant.

Each system was shaken for 5 minute. After equilibration organic layer was extracted and absorbance was measured for each system.
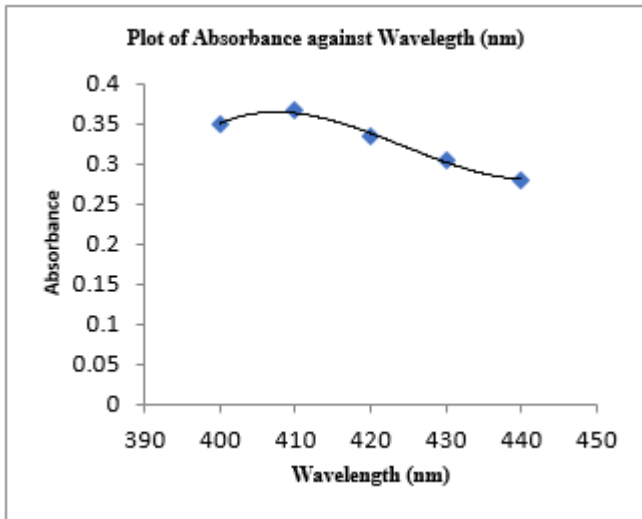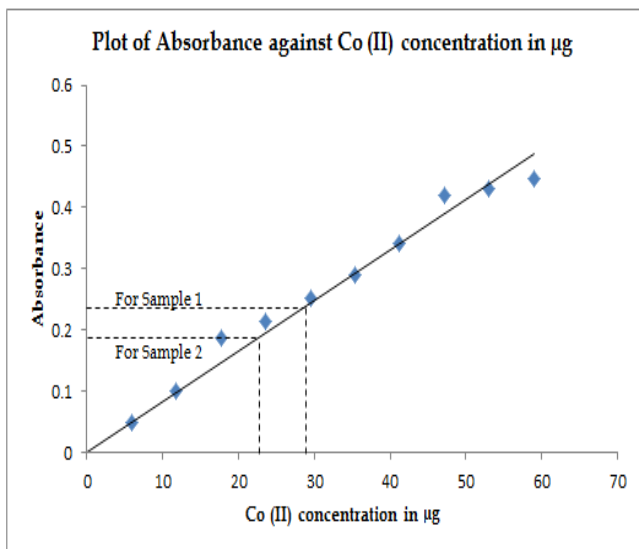
Graphs:

For determination of λ_{max}

To determine the absorbance of unknown sample:-
Following systems of unknown sample were prepared and absorbance was measured.

System No.	Volume of Unknown sample (ml)	0.1% Reagent [Salen] in chloroform	Absorbance For Co (II) (at pH = 6.0)
1	5	5	0.237
2	4	5	0.184

Calibration graph for Co(II) at pH=6

[Plot of Absorbance Vs concentration of Co(II) in ppm]

Calculation

- Calculation for Unknown Sample No. 1 :-

Theoretical Value of Co(II) – 1000 ml of 1 M CoSO$_4$ Solution = 58.93 g of Co(II)

$\therefore$ 1 ml of 0.0001 M CoSO$_4$ Solution = X g of Co(II)

$\therefore$ X = $\frac{(1 \times 0.0001 \times 58.93)}{1000}$

X = 5.893 $\times$10^{-6} g of Co(II)

= 5.89 µg of Co(II)

But in Unknown Sample, 5 ml of CoSO$_4$ Solution was taken.

$\therefore$ 5 ml of CoSO$_4$ Solution = 5 $\times$ 5.89

= 29.46 µg of Co(II).

Experimental Value of Co(II) -

From calibration graph of Co(II), In unknown sample, Co(II) was extracted by solvent extraction method shows absorbance 0.237 which corresponds to 28.5 µg.

Hence experimental value = 28.5 µg

% Error = $\frac{\text{Theoretical value} - \text{Experimental value}}{\text{Theoretical value}}$ $\times 100$

% Error = $\frac{(29.465 - 28.5)}{29.465} \times 100 = 3.27\%$

- Calculation for Unknown Sample No. 2 :-
Theoretical Value of Co(II) –

1000 ml of 1 M CoSO$_4$ Solution = 58.93 g of Co(II)

$\therefore$ 1 ml of 0.0001 M CoSO$_4$ Solution = X g of Co(II)

$\therefore$ X = $\frac{(1 \times 0.0001 \times 58.93)}{1000}$

$\therefore$ X = 5.893 $\times$10^{-6} g of Co(II)

$\therefore$ X= 5.89 µg of Co(II)

But in Unknown Sample, 4 ml of CoSO$_4$ Solution was taken.

$\therefore$ 4 ml of CoSO$_4$ Solution = 4 $\times$ 5.89

= 23.57 µg of Co(II).

Experimental Value of Co(II) -

From calibration graph of Co(II), In unknown sample, Co(II) was extracted by solvent extraction method shows absorbance 0.184 which corresponds to 22.3 µg.

Hence experimental value = 22.3 µg

% Error = $\frac{\text{Theoretical value} - \text{Experimental value}}{\text{Theoretical value}}$ $\times 100$

% Error = $\frac{(23.572 - 22.3)}{23.572} \times 100 = 5.39\%$

Sample No	Metal	Theoretical Value	Experimental Value	% Error
1	Co(II)	29.46	28.5	3.27
2	Co(II)	23.57	22.3	5.39

The % Error was found to be

Absorption Spectra -

The absorption spectra of Co(II) salen complex extracted at different pH and it was found to be maximum at pH = 6.0 and measured against reagent as blank. The light yellow colour of Co(II) salen complex solution show maximum absorption at 410 nm. Hence all absorbance measured at 410 nm.

Effect of Various Solvent -

Various organic solvent such as alcohol, n-butanol, ethyl alcohol, carbon tetrachloride were tried as a solvent but chloroform was found to be most effective.

Effect of pH and Metal Concentration -

Solvent extraction behavior of Co(II) salen complex was studied in pH range 1.0 to 10.0 and varying metal concentration i.e. 0.001 M, 0.0005 M, 0.0001 M. It was observed that extraction was quantitative at the pH = 6.0 and at the concentration 0.0001 M.

Colour of the species -

Colour of the species at different pH was found to be slightly different. At pH 1.0 to 2.0, it was almost colourless but from pH = 3.0 to 10.0 it developed into pale yellow colour.

IV. CONCLUSION

The present investigation had resulted in offering a convenient liquid-liquid extraction method for separation of Cobalt (II). Cobalt (II) can be extracted by salen dissolved in chloroform.

This method has number of advantages over existing method such as easy phase separation, less equilibration time etc. Salen extracted Cobalt (II) very rapidly, equilibrium was reached within 5 minutes.

On the basis of my practical work and Literature review, it can be concluded that this technique is prominent to execute for extraction of various metal from the mixture of metals, alloys etc and above data can be used in industries.

V. REFERENCES

[1]. J. R. Dean, Extraction Method for environmental Analysis, John Wiley and Sons, Chichester 1998.
[2]. E. M. Thurman, M. S. Mills, Solid-Phase Extraction, Principle and Practice. John Wiley and Sons, New York, 1998.
[3]. P. Triangle, Method for chemical analysis of water and waste, 1983.
[4]. Y.Marcus, The Properties of Solvents, John Wiley and Sons, New York. 1998.
[5]. Sandell B.E.,"Colorimetric Determination of Traces of Metals",3rd Ed. Wiley Inter Science (1978)..
[6]. T.Sekine, Y. Hasegawa, Solvent Extraction Chemistry, Marcel Dekker, New York. 1997.
[7]. H.Stephen, T. Stephen, Solubilities of Inorganic and Oganic Compounds. Pergamon Press, London, 1963.
[8]. H.Kaur, Instrumental method of chemical analysis. Pragati Publication, 2012.
[9]. G. Raj, Advanced Physical Chemistry, 35th Ed. Goel publishing house, Meerut 2009.
[10]. D.Matheel, Al-Sabti, Eng. and Tech. 26(5), 2008.
[11]. G. H. Nikamand, B. S. Mohite, Journal of Chemical Sciences 2(1), 75-82, 2012.
[12]. Khopkar S.M.,"Analytical Chemistry of Macrocyclic and Supramolecular Compounds", 2nd Ed., Springer Verlag (2005).

Diversity of Butterflies in Wani, District-Yavatmal (M.S.)

Paresh Patel*, Priya Uttarwar, Dnyaneshwar Khamankar

Lokmanya Tilak Mahavidyalaya, Wani. Dist- Yavatmal, Maharashtra, India

ABSTRACT

The present paper deals with a study of the diversity and abundance of butterflies in and around Wani city, district Yavatmal (M.S.), India. A Total 34 species of butterflies belonging to 26 genera and 05 families, namely, Hesperiidae, Lycaenidae Nymphalidae, Papilionidae and Pieridae were recorded from different habitats, urbanized habitat i.e. Wani locality (Site I) and less urbanized habitat (Agricultural area) (Site II). The family Nymphalidae (44.11%) was found abundant and family Hespiridae (2.94%) was found least abundant among all the families. The study area is rich in butterfly diversity and further research could be conducted to obtain more details and documentation on butterfly diversity for the conservation

Keywords: Wani, Butterfly, Diversity, Habitat, Shannon Index

I. INTRODUCTION

Biodiversity is the total variety of life on the earth. The abundance and diversity of butterflies mainly depend upon various factors such as availability of host and larval food plants, foliage, humid climate and various other features etc. As butterflies are mainly dependent on these factors, interruption in any of the above will directly affect their standing in ecosystem. India is one of the 17 "mega diverse" countries of the world. It is host to an impressive number of butterflies, many of which are widely spread to the Indian Region, which makes this an important region particularly for butterfly diversity and conservation. But deforestation and increased human approach in forest and other ecosystems have resulted into loss of habitat for most of the local species diversity (Gupta, 2018).

Heppner (1998) reported 19238 species of butterflies in the world. Gaonkar (1996) listed 1504 species in Indian subcontinent. Study by Abreau (1931) reported about 177 species of butterflies in Central Provinces. Tiple (2011) recorded a total of 167 species of 90 genera from Vidarbha region. A total of 92species of butterflies were reported in Gorewada International Biopark situated in Central India (Patil and Shende,2014).

The aim of current study is to find out the current status of butterflies in Wani area of Yavatmal district and to prepare a checklist of butterflies of this region for the purpose of conservation of native species present in this area.

II. MATERIALS AND METHODS

Study Area: Wani is a city in Yavatmal district in Indian state of Maharashtra. It is situated at eastern side of Yavatmal district about 107 kms from Yavatmal on Yavatmal-Chandrapur road. Wani is located on river side of Nirguda, flowing from western side of Wani. The city has large belt of agriculture which produce mostly cotton, soya-bean and red gram (Toor). Wani is located at co-ordinates 20°07'N, 78°95'E at 228m AMSL (Above Mean Sea Level).

Methods

Active Searching and Photography: The field surveys on butterflies were carried out in the study area three times a week for the period of six months from December 2018 to May, 2019. Butterflies were accessed in the study area from 7am to 11am in the morning and 4pm to 6pm in the evening by random observations during walking through the selected sites based on habitats present in the study area. In the field, photographs of the butterflies were taken with the aid of camera for the identification purpose based on (Dey et al., 2017). Butterflies were actively searched near water bodies, rocks, shrubs, grounds debris, and on barks of trees on the ground surface for Photography. Photography was done by using Cannon p900 Cameras.

Identification: Identification was done by available keys and with the help of experts.

Statistical Analysis:-
Identified species of butterfly observed in the study area were analyzed by using Simpson index of diversity formula adopted by (Sunil et al., 2016) and (Ashok, 2017).

The Simpson index of diversity mathematical formula is giving as follows:

$$(D) = 1 - \frac{\sum n(n-1)}{N(N-1)}$$

Where:

D = Simpson Index of Diversity

Σ = sum of (Total)

n = the number of individuals of each different species

N = the total number of individuals of all the species

III. RESULTS AND DISCUSSION

In present study 34 Species belonging to 26 genera of 5 families were recorded. Where Nymphalidae represents higest numbers of species (15) which are followed by Pieridae (07), Lycaenidae (06), Papilinidae (05) and Hespiridae (01) (Table No-02). Thus Nymphalidae is most dominant family exploring (44.11 %) and Pieridae is exploring (20.60%) of species while family Lycaenidae is 17.64 % , family Papilionidae is 14.71%. and family Hespiridae is with 2.94%.(Table no-1, Fig-1). The results calculated so far clearly specify that the overall diversity of Butterflies in this region is quite good. This study reveals that the butterflies at different regions of the desired area show high diversity.

Table 01 : Number of Families, Genera, and Species of butterfly recorded In Site I (Urbanized) and Site II (least Urbanized).

Sr.No.	Family	Genera	Species	Species %
1	Hespiridae	1	1	2.94%
2	Lycaenidae	5	6	17.64%
3	Nymphalidae	11	15	44.11%
4	Papilionidae	3	5	14.71%
5	Pieridae	6	7	20.60%
Total		26	34	100%

Table 02: List of Butterflies recorded in the study area (SI-Wani locality, SII-Agriculture land)

Common Name	Scientific Name	Local Status	IUCN Status
Family: Papilionidae			
Tailed Jay	*Graphium agamemnon* (Linnaeus, 1758)	Common	Ne
Common rose	*Pachliopta aristolochiae* (Fabricius, 1775)	Common	Lc
Crimson rose	*Pachliopta hector* (Linnaeus, 1758)	Common	Ne
Lime butterfly	*Papilio demoleus* (Linnaeus, 1758)	Abundant	Ne
Common Mormon	*Papilio polytes* (Linnaeus, 1758)	Abundant	Ne
Family: Pieridae			
Common emigrant	*Catopsilia pomona* (Fabricius, 1775)	Abundant	Ne
Mottled emigrant	*Catopsilia pyranthe* (Linnaeus, 1758)	Common	Ne
Common Gull	*Cepora nerissa* (Fabricius, 1775)	Abundant	Ne
Common Grass yellow	*Eurema hecabe* (Linnaeus, 1758)	Abundant	Ne
Great Orange Tip	*Hebomola glaucippe* (Linnaeus, 1758)	Occasional	Ne
White Orange Tip	*Ixias Marianne* (Cramer, 1775)	Common	Ne
Common Wanderer	*Pareronia valeria* (Cramer, 1776)	Common	Ne
Family: Nymphalidae			
Tawny castor	*Acraea violae* (Fabricius, 1775)	Common	Ne
Angled castor	*Ariadne ariadne* (Linnaeus, 1763)	Common	Ne
Plain Tiger	*Danaus chrysippus* (Linnaeus,1758)	Abundant	Ne
Striped Tiger	*Danaus genutia* (Cramer, 1779)	Abundant	Ne
Common crow	*Euploea core* (Cramer, 1780)	Abundant	Lc
Great eggfly	*Hypolimnas bolina* (Linnaeus, 1758)	Common	Ne
Danaid eggfly	*Hypolimnas misippus* (Linnaeus, 1764)	Common	Ne
Lemon Pansy	*Junonia lemonias* (Linnaeus, 1758)	Abundant	Ne
Blue Pansy	*Junonia orithya* (Linnaeus, 1764)	Abundant	Ne
Common evening brown	*Melanitis leda* (Linnaeus, 1758)	Abundant	Ne
Common Sailer	*Neptis hylas* (Linnaeus, 1764)	Common	Ne
Blue Tiger	*Tirumala limniace* (Cramer, 1775)	Abundant	Ne
Dark Blue Tiger	*Tirumala septentrionis* (Cramer, 1775)	Abundant	Ne
Painted Lady	*Synthia cardui* (Linnaeus, 1764)	Common	Ne
Common Three ring	*Ypthima asterope* (klug, 1832)	Common	Ne
Family: Lycaenidae			
Lime blue	*Chilades lajus* (Stoll, 1780)	Abundant	Ne
Gram blue	*Euchrysops cnejus* (Fabricius, 1798)	Abundant	Ne
Pea blue	*Lampides boeticus* (Linnaeus, 1767)	Abundant	Ne

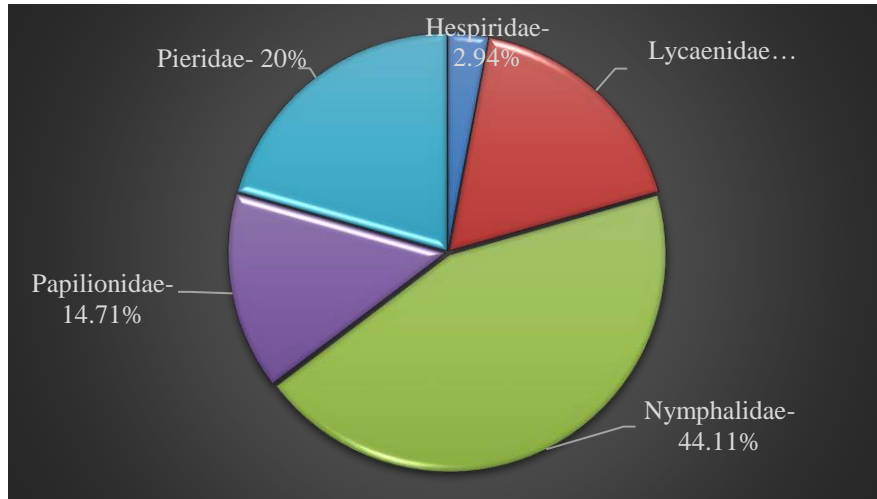| Lesser Grass blue	*Zizina otis* (Fabricius, 1787)	Abundant	Ne
Common Pierrot	*Castalius rosimon* (Fabricius, 1775)	Frequent	Ne
Plains cupid	*Luthrodes pandava* (Horsfield, 1829)	Frequent	Ne
Family: Hespiridae			
Rice swift	*Borbo cinnara* (Wallace, 1866)	Abundant	Ne

Fig-1: Families of Butterflies with % of species

Fig. 2 : Photographs of Butterflies from Wani Area

IV. ACKNOWLEDGMENT

V. REFERENCES

[1]. Ashok, K. (2017): Species diversity and distribution of butterfly fauna with heterogeneous habitats in Jhansi, India. International Journal of Advanced Research in Biological Sciences, 4(7): 104-110.

[2]. D'Abreu EA (1931): The Central Provinces Butterfly List. Records of the Nagpur Museum Number VII. Government Printing Press, Nagpur, India.

[3]. Dey, P., Payra, A. and Mondal, K. (2017): A study on butterfly diversity in Singur, West Bengal, India. Journal of e – planet, 15(1): 73-77.

[4]. Gaonkar H (1996): Butterflies of Western Ghats with notes on those of Sri Lanka. A Report to the Centre of Ecological Sciences. Indian Institute of Science, Bangalore, Zoological Museum, Copenhagen and Natural History Museum, London, UK

[5]. Gupta SS (2018): Study of Butterfly Diversity from Campus area of Amolokchand Mahavidyalaya Yavatmal, Maharashtra, India, Int. J. of. Life Sciences, Volume 6(1): 279-281.

[6]. Heppner J (1998): Classification of Lepidoptera Part I: Introduction. Holarctic Lepidoptera. 5(Suppl.): 148

[7]. Nimbalkar R.K. (2018): Diversity of Butterflies from Ajanta Caves area of Aurangabad District (MS). Int. Res. J. of Science & Engineering. Special issue A6:20-25

[8]. Patil KG, Shende VA (2014): Butterfly diversity of Gorewada International Bio Park, Nagpur, Central India. Arthropods, 3(2): 111-119

[9]. Sunil, K., Deepti, M., Priyanka, V.L. and Lily, S.N. (2016): Butterfly diversity of the Gangetic plain (Doaba) at Allahabad, U.P, India. Journal of Entomology Studies, 4(6): 268-271.

[10]. Tiple AD (2011): Butterflies of Vidarbha region, Maharashtra State, central India. Journal of Threatened Taxa, 3(1): 1469-1477.

Synthesis and Spectroscopic Characterization of Modified Schiff Bases Derived from 2,4-Dinitro Phenyl Hydrazine

*M. S. Ansari[1], R. D. Utane[2], F. Inam[1], S. S. Deo[2]

[1]Department of Chemistry, Govt. Institute of Science, Nagpur, Maharashtra, India

(Affiliated to RTM Nagpur University)

[2]Department of Chemistry, Sant Gadge Maharaj Mahavidyalaya, Hingna, Nagpur, Maharashtra, India

(Affiliated to RTM Nagpur University)

ABSTRACT

Ambient synthesis of modified Schiff bases derived by condensation of 2,4-dinitro phenyl hydrazine has refluxing with aryl aldehydes such as veratraldehyde (3,4-dimethoxybenzaldehyde), 3-nitrobenzladehyde, Anisaldehyde (4-Methoxy Benzaldehyde) and Furfuraldehyde (Furan-2-carbaldehyde) followed by magnetic stirring gives derivatives of Schiff bases. All the modified Schiff bases has analysing by Spectroscopic technique including FTIR, H1NMR and LCMS were used to identify the desired products.

Keywords : Schiff base, 2,4-dinitrophenylhydrazine, FTIR, H[1]NMR, Schiff bases and LCMS.
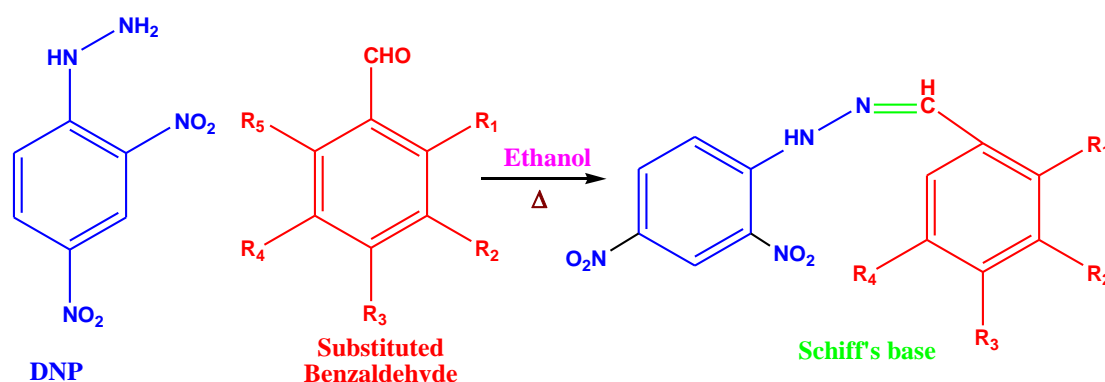
Scheme : Ambient Synthesis of Modified Schiff Bases
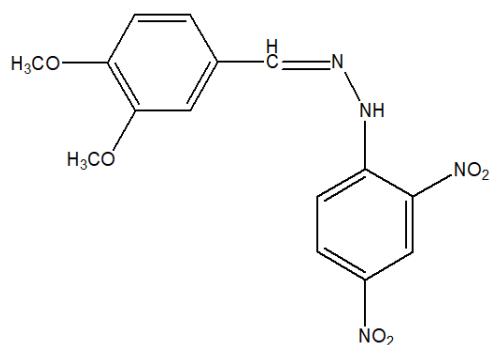
I. INTRODUCTION

The condensation of primary amines with aldehydes and ketones has a numerous applications [1] for preparative, detection, determination, purification and biological uses. These applications [2-3] encourage the workers to prepare these imines for the last 10 decades.

The classical method [1] for synthesis of imines is by mixing equimolar quantities of aldehyde or ketone with the primary amines. Schiff bases or imines have the general formula RN=CR` where there the R and R` are alkyle, aryl ,cyclo alkyl or hetro cyclic groups. Imines play an important role in many biochemical reactions because some of the enzymes use an amine group of an amino acid to react with an aldehyde or

ketone to form an imine linkage. In the present work nitro Schiff bases[7] aresyntheiszedfrom reactions of verateraldehyde, 3-nitrobenzaldehyde, anisaldehyde and furfuraldehyde with 2,4-di nitro phenyl hydrazine. In this study we report the synthesis and characterization of four potential Schiff base ligands. Structural formulas for the following ligands, depicted in their Schiff base forms, are given in Fig. 1.

a) 1-(3,4-dimethoxybenzylidene)-2-(2,4-dinitrophenyl)hydrazine,

b) (Z)-1-(3-nitrobenzylidene)-2-(2,4-dinitrophenyl)hydrazine,

c) 1-(4methoxy phenyl amino)-2-(2,4-dinitrophenyl)hydrazine,

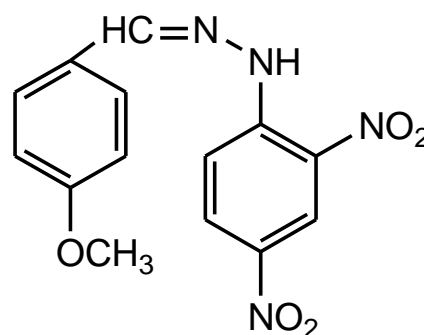d) (E)-1-((furan-2-yl)methylene)-2-(2,4-dinitrophenyl)hydrazine,

A special care is given to the structural elucidation of these new Schiff's base or imines by using analytical techniques namely, UV, FT-IR, H[1]NMR and Mass spectra.
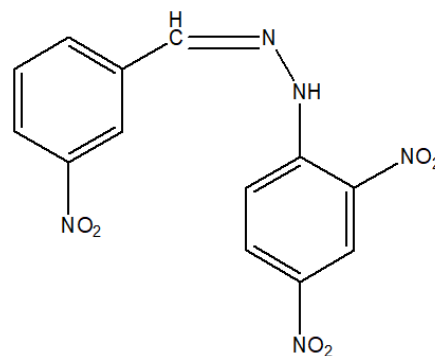
(Z)-1-(3-nitrobenzylidene)-
2-(2,4-dinitrophenyl)hydrazine

(b)

1(phynoxymethaneamino)-
2-(2,4-dinitrophenyl)hydrazine

(c)

1-(3,4-dimethoxybenzylidene)-
2-(2,4-dinitrophenyl)hydrazine

(a)
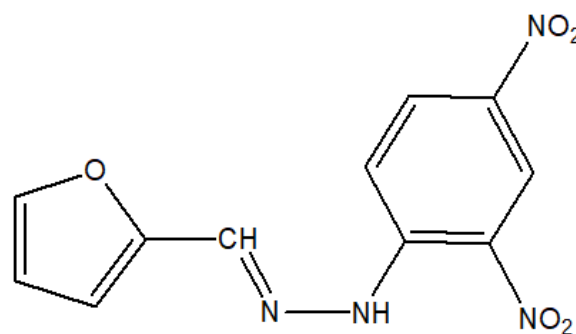
(E)-1-((furan-2-yl)methylene)-
2-(2,4-dinitrophenyl)hydrazine

(d)

Figure 1 : Structure of Synthesized Schiff's Bases

II. MATERIALS AND METHODS

Materials and Physical Measurements

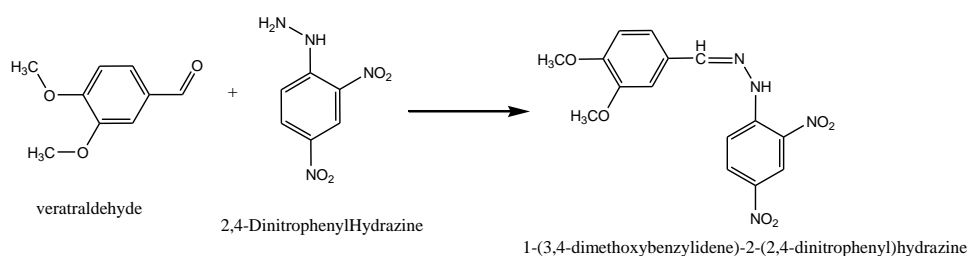All the chemicals which has been used during the synthesis of schiff's base were supplied by Sigma Aldrich, Loba used as received. FTIR spectra were recorded using Bruckner spectrometer, H1NMR characterization were carried by using Bruker Avance Neo 500 MHz NMR spectrometer and LCMS were carried out using Tetra methyl Silane (TMS) as standard.
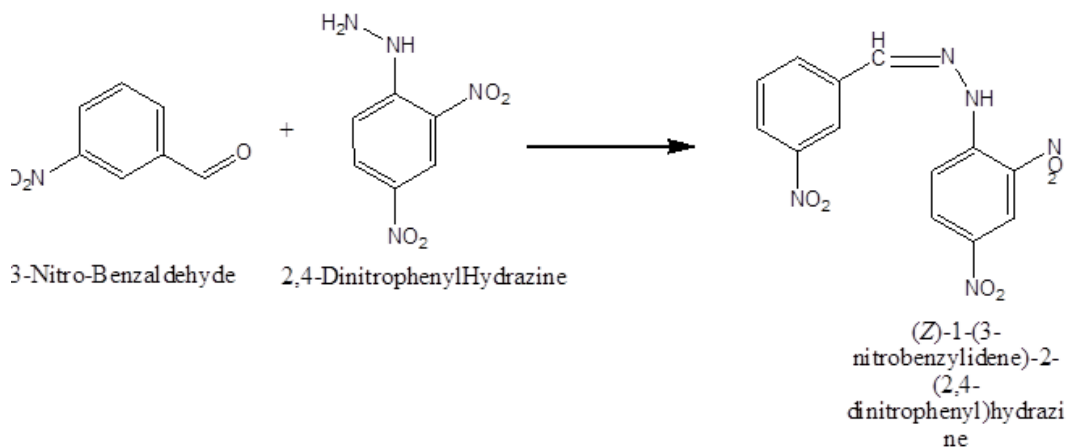
III. EXPERIMENTAL

Synthesis of Schiff's base (S-1, S-2, S-3 & S-4)

Schiff's bases were synthesized by addition of 2,4-dinitrobenzaldehyde (mmole) and ethanol (ml) in 100 ml beaker equipped with stirrer bar placed on magnetic stirrer and stirred the solution at room temperature about 10min or until all the solid has dissolved. Add a solution of aldehyde (mmole) in ethanol (ml) and continuous stirred the solution and transferred into 100 ml round bottom flask equipped with water condenser placed on heating mental the solution turns semisolid mass before the product precipitate over 30 min as remarkable colour ppt. the product recovered quantitatively yield by filtration and washed with small quantities of ethanol to remove any unreacted starting materials. The product was recrystallized from a minimum volume of ethanol. The preparation scheme of Schiff's bases are given in figure 2.
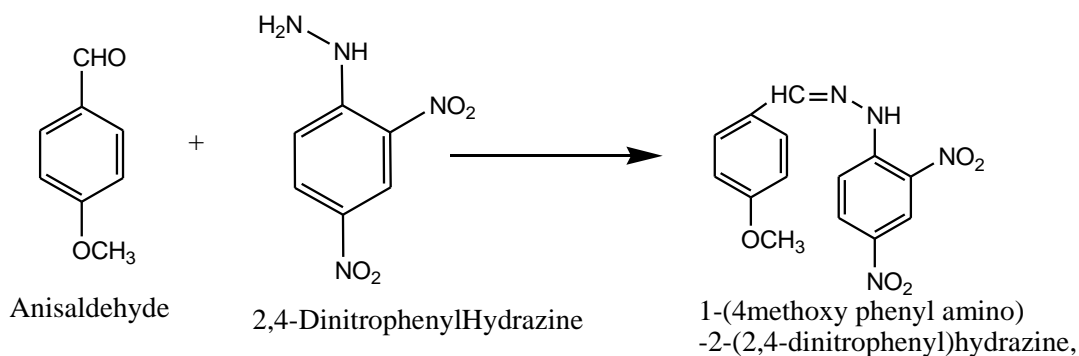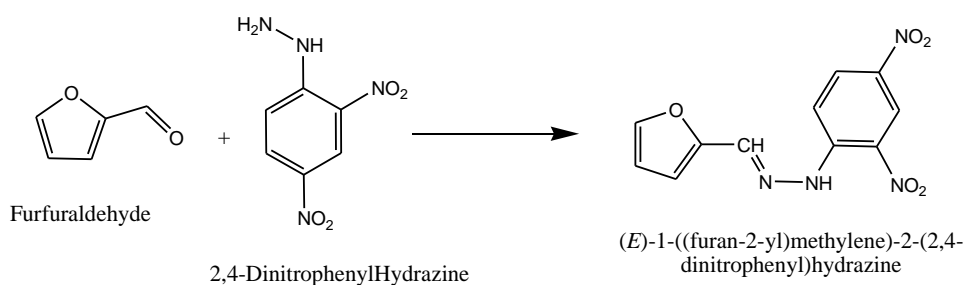
S-1

veratraldehyde   2,4-DinitrophenylHydrazine

1-(3,4-dimethoxybenzylidene)-2-(2,4-dinitrophenyl)hydrazine

S-2

3-Nitro-Benzaldehyde   2,4-DinitrophenylHydrazine

(Z)-1-(3-nitrobenzylidene)-2-(2,4-dinitrophenyl)hydrazine

S-3

Anisaldehyde   2,4-DinitrophenylHydrazine   1-(4methoxy phenyl amino)
                                                          -2-(2,4-dinitrophenyl)hydrazine,

S-4

Furfuraldehyde

2,4-DinitrophenylHydrazine

(*E*)-1-((furan-2-yl)methylene)-2-(2,4-
dinitrophenyl)hydrazine

IV. RESULTS AND DISCUSSIONS

H¹NMR Spectra:

H¹NMR spectra of the investigated compounds which were dissolved in denatured di methyl sulphoxide (DMSO) are shown in table 1.The H1NMR spectra of Schiff's base ligand shows the multipe signals in the region of δ7.12-7.95 ppm which can attributed the aromatic proton. The singlate band at δ 8.14-8.80 ppm due to single proton of HC=N moiety and singlate band at δ7.05-7.17 ppm for proton –NH.

Table 1 : H¹NMR spectral data's of synthesized compounds

Scheme	Aldehyde	Compound	Remarkable Colour Property	HC=N	–NH	Aromatic Proton
S-1/DNP-1	Varatraldehyde	1-(3,4-dimethoxybenzylidene)-2-(2,4-dinitrophenyl)hydrazine	Tomato Red	8.602 (s)	7.07 (s)	7.12-7.95 (m)
S-1/DNP-2	3-Nitro Benzaldehyde	(Z)-1-(3-nitrobenzylidene)-2-(2,4-dinitrophenyl)hydrazine	Dark Yellow	8.807 (s)	7.17 (s)	7.39-7.95 (m)
S-1/DNP-3	Anisaldehyde	1-(4methoxy phenyl amino)-2-(2,4-dinitrophenyl)hydrazine,	Faint Orange	8.64 (s)	7.06 (s)	7.75-7.77 (m)

S-1/DNP-4	Furfuraldehyde	(E)-1-((furan-2-yl)methylene)-2-(2,4-dinitrophenyl)hydrazine	Blackish Gray	8.14 (s)	7.05 (s)	7.12-7.88 (m)

IR Spectra

The FTIR spectra indicated the ν(C=N) bands appear as a strong bands at 1608.6 – 1647.7 cm^{-1}. The appearance of bands in the region 2846.0 – 2946.0 cm^{-1} which could be attributed to asymmetric and symmetric stretching vibration of ν (-CH). The peaks appeared at 1506.4 – 1525.7 cm^{-1} due to ν(C=C) starching vibrations.

Mass Spectra

Mass spectra provide a vital clue for elucidating the structure of compounds[18]. The observed molecular ion peak(s) at m/e 349.12, 327.15, 327.17 and 252.96 for Schiff's base S-1, S-2, S-3 and S-4 respectively. The results were complement with the proposed molecular formulae of the Schiff's base.

Table 2 : Mass and IR spectral data's of synthesized compounds

Scheme	Aldehyde	Compound	IR Spectra cm^{-1}	Mass Spectra
S-1/DNP-1	Varatraldehyde	1-(3,4-dimethoxybenzylidene)-2-(2,4-dinitrophenyl)hydrazine	1608.5, 1647.7, 2876.0, 1500.9	349.12
S-1/DNP-2	3-Nitro Benzaldehyde	(Z)-1-(3-nitrobenzylidene)-2-(2,4-dinitrophenyl)hydrazine	1677.9, 1671.8, 2851.6 1512.3	327.15
S-1/DNP-3	Anisaldehyde	1-(4methoxy phenyl amino)-2-(2,4-dinitrophenyl)hydrazine,	1554.6 1671.2, 1643.5, 1531.2	327.17
S-1/DNP-4	Furfuraldehyde	(E)-1-((furan-2-yl)methylene)-2-(2,4-dinitrophenyl)hydrazine	1528.1, 1639.8, 1525.7, 1238.6	252.96

V. CONCLUSION

Schiff bases are imine derivative prepared by the condensation of primary amines with carbonyl compounds such as aldehyde or ketone. Schiff bases gaining importance day by day in present scenario due to pharmacological activities as anticancer, AIDS diseases. In this research work 2,4dinitrophenyl hydrazine is used as a source of primary amine to prepare modifies Schiff's bases with product yield more than 90%. Schiff bases are the compounds carrying imine or azomethine (–C=N–) functional group and are found to be a versatile pharmacophore in antigenotoxicity.

VI. ACKNOWLEDGMENT

thankful to SAIF Chandigarh for Spectrometric characterization of all synthesized Schiff bases compounds.

VII. REFERENCES

[1]. Mostafa M. H. Khalil, Eman H. Ismail, Gehad G. Mohamed, Ehab M. Zayed, Ahmed Badr, Open Journal of Inorganic Chemistry, 2, 2012, 13-21.

[2]. C A M A Huq, S Fouzia, Indian Journal of Chemistry, Vol. 54B, April 2015, pp 551-555.

[3]. Muhammad Aqeel Ashraf, KaramatMahmood, Abdul Wajid, International Conference on Chemistry and Chemical Process, Vol. 10, 2011.

[4]. Ed.S.Patai, "The chemistry of carbon-nitrogen double bond", John Wiley and Sons, New York, 1970, pp.61-146.

[5]. E. Brand and M. Sandberg, Org. Synth. Coll., 1943, 2, 49.

[6]. J.C. Sheehan and V.J.Grenda, J.Amer.Chem.Soc., 1962, 84, 2417.

[7]. R.B.Moffet and W.M.Hoehn, J.Amer.Chem.Soc., 1947, 69, 1792.

[8]. M. Freifelder, J.Org. Chem., 1966, 31, 3875.

[9]. J. H. Billman and K. M. Tai, J.Org. Chem., 1958, 23, 535.

[10]. M. E. Taylor and T. J. Fletcher, J.Org. Chem., 1961, 26, 940.

[11]. A.A.H.saeed, A.W.A. Sultan, S.A.Selman and N.A.Abood, Canad. J.Spectroscopy, 1983, 28, 104.

[12]. A.S.P.Azzouz, Z. phys. Chem., 2002, 216, 1053.

[13]. A.S.P.Azzouz and A.B.N.AL-Dabagh, National J. Chem., 2007, 26, 295.

[14]. A.S.P.Azzouz, M.S.Saeed and K.I. AL-Niemi, J. Edu. Sci., 2005, 17, 29. ibid, 2005, 17, 16.

[15]. A.S.P.Azzouz, National J. Chem., 2006, 22, 214.

[16]. D.Y.Curtin and J.W.Hausser, J.Amer.Chem.Soc., 1961, 83, 3474.

[17]. Hamming, N & Foster, N 1972, Interpretation of mass spectra of Organic compounds, Academic Press, New York, USA

Dielectric and Characterization Study of BaNb$_2$O$_6$ Nanoparticles Synthesized by Sol-Gel Method

Sanjay. B. Nagdeote

Department of Physics, Amolakchand Mahavidyalaya, Yavatmal, India

ABSTRACT

The BaNb2O6 (BN) is synthesis by sol-gel method in Nanoscale. The Particle sized was rod like structure with diameter ~ 100nm. The X-ray diffraction patterns of BaN$_b2$O$_6$ powder is used for the identification of tetragonal Phase by indexing of the peak in predominant tetragonal phase using list square fit method and Bragg's relation. The dielectric property of material has studied with various temperature and frequencies.

In the present work the BaNb$_2$O$_6$ (BN) in nano scale was synthesis by sol-gel method. The XRD characterisation was used for the identification of the polymorphic tetragonal phase. The particle sized was observed by Transmission electron microscopy (TEM), dielectrics behaviour with temperature and frequency has been also studied.

Keywords : Tetragonal Phase, Nanoparticles, Dielectrics

I. INTRODUCTION

BaNb2O6 (BN) is an important member of alkaline earth niobates group. Its orthorhombic phase is studied for dielectric properties [1]. However, Tetragonal tungsten bronze (TTB) structure of this material is highly interesting and applicable due its ferroelectric and dielectric properties. Tetragonal tungsten bronze (TTB) family with a general formula (A1)2(A2)4C4 (B1)2(B2)8O30. The point group of this family is 4 mm and space group is P4bm. The ferroelectric behavior in these materials is mainly due to noncentrosymmetry of the structure. This structure is characterized by a network of BO6 octahedra [2,3]. The literature survey shows single Tetragonal Phase of BaNb2O6 (BN) is the not yet to be investigated, only two alkaline earth niobates compounds belonging to this class are studied. The first one is Sr$_x$Ba1- $_x$Nb2O6 (SBN) with 0.25<x<0.75 and the second is newly reported Ca$_x$Ba1-

xNb2O6 with 0.20< x<0.40 (CBN). SBN, other than ferroelectric behavior, is widely studied for the optical, pyroelectric, piezoelectric and dielectric properties [4-6]. Various properties of CBN are being investigated [7-9]. Now there is an increasing interest of the researchers on synthesis and investigation of dielectric and ferroelectrics properties of BaNb2O6 (BN) in single Tetragonal Phase. This material is very useful for microwave dielectric properties, Photocatalytic activity and Sr$_x$Ba1-$_x$Nb2O6 (SBN), Ca$_x$Ba1-xNb2O6(CBN) synthesis [10-12].

II. EXPERIMENTAL

BaNb2O6 nanoparticles in tetragonal phase were prepared by the sol-gel method. The Detail sol-gel method has been described in our previous paper[13] in brief First, the Nb2O5 was dissolved in minimum amount of HF after heating in a water bath to get transparent NbF5 solution. Another solution was

obtained by dissolving $BaCl_2.2H_2O$ in distilled water. Two solutions were mixed together by using a magnetic stirrer for 4-5 hours. While stirring, an excess quantity of concentrated HCl was added to dissolve the barium fluoride formed by the mixing of NbF_5 and $BaCl_2.2H_2O$. An appropriate amount of citric acid was added to the above mixture. This mixture solution was then kept in a water bath, which was maintained at 100^0C to evaporate water slowly from the mixture. After evaporation of water, a yellowish gel was formed which was dried in air and decomposed at 600^0C for ~15 h.

III. RESULTS AND DISCUSSION

X-Ray Diffraction:

The X-ray diffraction patterns of $BaNb_2O_6$ powder is shown in Fig. 1. The indexing of the peak in predominant tetragonal phase was done by list square fit method and Bragg's relation,

$$2d_{hkl} \sin\theta = n\lambda$$

where λ is the wavelength of $CuK\alpha$ (1.5406) x-ray radiation, d_{hkl} is interplaner spacing and θ is the Bragg's angle. Since, it was seen that the reflecting angles of XRD pattern of BN resemble to the JCPDS file no. 73-0126 of SBN, we prefer tetragonal structure of which d_{hkl} is given by,

$$\frac{1}{d^2_{hkl}} = \frac{h^2 + k^2}{a^2} + \frac{1^2}{c^2}$$

Indexing of all planes and the difference between observed and calculated d are listed in Table-1. A maximum intensity peak is obtained as (410) corresponding to $d_{obs} = 3.019$Å. Two other major peaks are observed corresponding to d_{obs} values 2.80 Å and 3.976 Å as (311) and (001) respectively. The lattice parameters in tetragonal phase are found to be $a = b = 12.445$Å, and $c = 3.975$ Å.
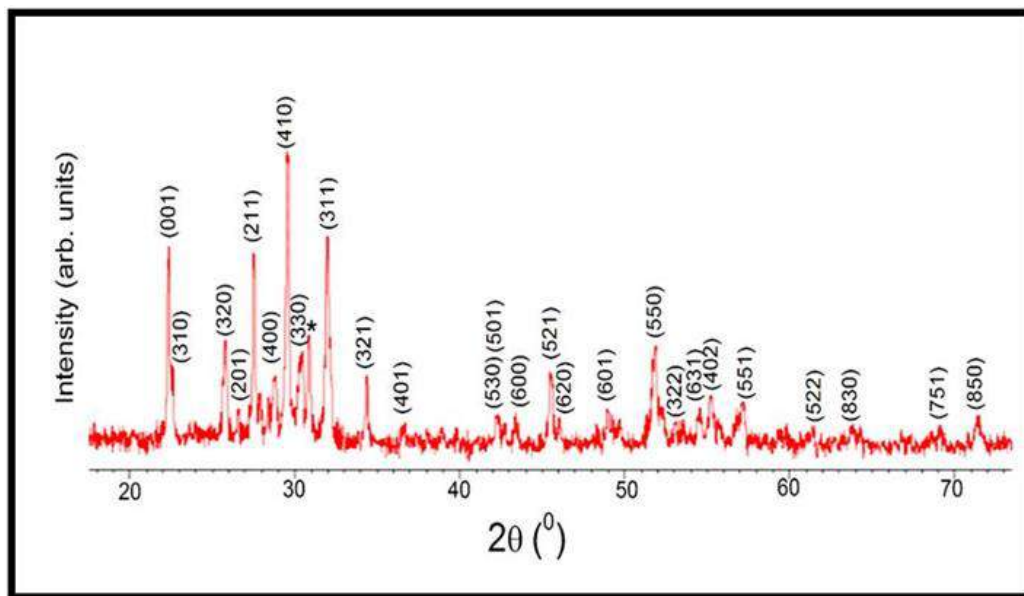

Fig. 1 : XRD pattern of as synthesized $BaNb_2O_6$.

It is observed from the Table1 that reflection angles $2\theta = 28.35^0$ and 30.9^0 do not fit in this pattern. The reflection at 28.35^0 is recognized as a characteristic peak of orthorhombic BN. However, its relative intensity is small; therefore, we can expect that the TTB cell structure get disturbed negligibly due to this trace.

Table 1 : Indexing of XRD diffraction pattern of BaNb$_2$O$_6$ nanoparticles in (TTB) structure

S.N.	2θ	% Intensity	d$_{obs}$	d$_{cal}$	(hkl)	Δd(d$_{cal}$~d$_{obs}$)
1	22.34	69	3.9763	3.9756	(001)	0.0007
2	22.6	22	3.9311	3.9355	(310)	0.0044
3	25.78	40	3.4530	3.4516	(320)	0.0014
4	26.57	12	3.3521	3.3502	(201)	0.0019
5	27.54	65	3.2362	3.2350	(211)	0.0012
6	28.35 #	16	3.1455	-	-	-
7	28.82	28	3.0953	3.1113	(400)	0.0160
8	29.56	100	3.0195	3.0184	(410)	0.0011
9	30.46	34	2.9323	2.9333	(330)	0.0010
10	30.9 *	37	2.8915	-	-	-
11	31.93	73	2.8005	2.7969	(311)	0.0036
12	34.35	23	2.6086	2.6064	(321)	0.0022
13	36.6	6	2.4532	2.4502	(401)	0.0030
14	42.24	11	2.1378	2.1343	(530)	0.0035
15	42.74	5	2.1139	2.1096	(501)	0.0043
16	43.37	8	2.0846	2.0742	(600)	0.0104
17	45.52	30	1.9910	1.9979	(521)	0.0069
18	46.07	7	1.9686	1.9677	(620)	0.0009
19	49	14	1.8575	1.8389	(601)	0.0186
20	51.87	32	1.7698	1.7600	(550)	0.0098
21	53.06	8	1.7245	1.7226	(322)	0.0019
22	54.53	11	1.6814	1.6811	(631)	0.0003
23	55.2	21	1.6626	1.6751	(402)	0.0125
24	57.17	17	1.6099	1.6093	(551)	0.0006
25	61.23	3	1.5116	1.5070	(522)	0.0046
26	63.78	6	1.4581	1.4566	(830)	0.0015
27	69.14	4	1.3575	1.3595	(751)	0.0020
28	71.41	9	1.3198	1.3191	(850)	0.0007

Orthorhombic BN,* no reflection without twinning

IV. MORPHOLOGY

The morphology of BaNb2O6 particles is shown in Fig. 2(a). The particles are rod-like shaped with diameter ~ 100nm and slightly agglomerated. The representative HRTEM image of the crystallite and SAED pattern are shown in Fig. 2(b) and 2(c), respectively. Fig. 2(b) shows, the inter-planer distance is about 0.275nm which corresponds to (311) plane of the tetragonal BaNb2O6. The SAED pattern shows many white dots on the rings, which confirms the well crystallization of the material. The diffraction rings corresponding to planes in SAED are also identified (Fig.2c). Interestingly, the plane (311) appeared in all the three investigations namely XRD, HRTEM and SAED, indicating that it is one of the characteristic peak of TTB structured BN.
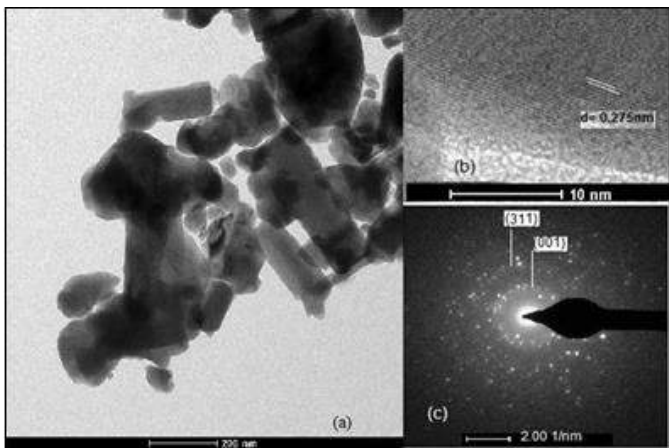

Fig. 2: (a) TEM image, (b) HRTEM images and (c) SEAD pattern of BaNb2O6

Dielectric study

Dielectric permittivity variation against temperature measured at 100Hz of the synthesized BN powder is shown in Fig 3(a). With the rise in temperature, the permittivity increases suddenly to 4000 at 40^{0}C then remain constant up to 110^{0}C. It is then falls sharply to 180^{0}C and remains constant thereafter. The nature of peak indicates a 'relaxor' type behaviour of the material. Since the material shows ferroelectric behaviour, the ferroelectric- paraelectric phase transition is diffused type. This may be a special feature of TTB type ferroelectrics.
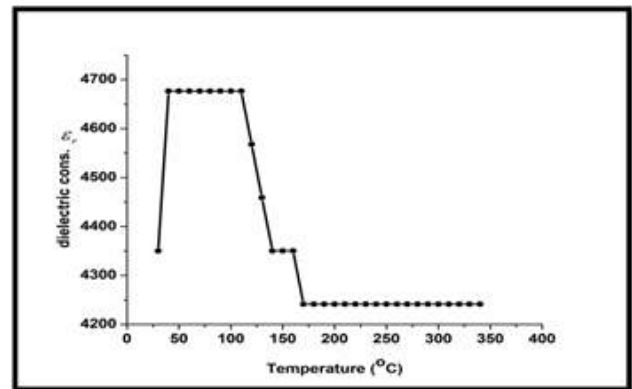

Fig. 3(a): Dielectric constant variation against temperature

The variation of dielectric constant with frequency as shown in the fig3(b). The polarization factor affects on the dielectric behaviour with frequency. AT low frequencies side the surface charge polarization and dipole polarization are predominant and hence the dielectric constant has higher values. From the frequency response plot it is clearly shows that dielectric constant has higher values at lower frequencies side and it sharply decreases as the frequencies increases to higher value. It nearly remains constant above 10KHz frequency as electronic and ionic polarization are predominant at the higher frequencies sides.
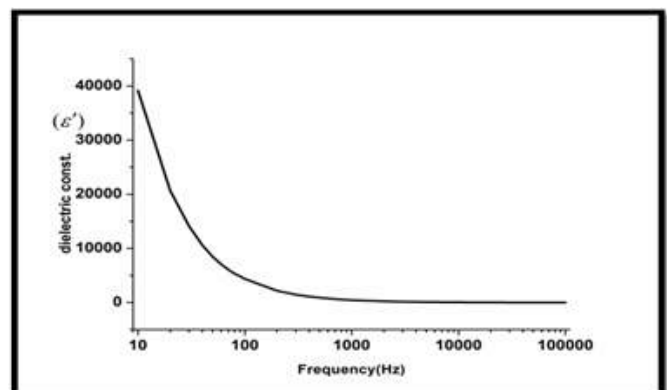

Fig. 3(b) : The variation of dielectric const. with frequency

V. CONCLUSION

The nanoparticles of BaNb2O6 were successfully obtained by the sole-gel technique by increasing the reaction period. Indexing and structural analysis of the XRD pattern used to conform the tetragonal Phase of material successfully. The dielectric study shows that it is a 'relaxor' type of ferroelectrics. Material has very high value of dielectric constant at low frequency. Dielectric constant is temperature and frequency dependent.

VI. REFERENCES

[1]. K. N. Singh, R. Mishra, P. K. Bajpai, and A. K. Srivastava, Int. J. Advance Res. Applied physics, 1 (2013) 1.

[2]. M. E. Lines and A. M. Glass, 'Principles and Applications of Ferroelectrics and Related Materials', Clarendon press, Oxford, (1977).

[3]. Y. Xu, 'Ferroelectric Material and their Applications' North Holland, Amsterdam, Netherlands, 1991.

[4]. G.L. Wood, W.W. Clark, M.J. Miller, E.J. Sharp, G. J. Salamo, R. R. Neurgaonkar, IEEE J. Quantum Electron.23 (1987) 2126.

[5]. S. Wanmei, L. Shijun, S. Ranran, W. Chulong, J. Cream. Process. Research. 12 (2011) 716.

[6]. S. I. Lee, W.K. Choo, Ferroelectrics 87 (1988) 209.

[7]. M. Muehlberg, M. Burianek, B. Joschko, D. Klimm, A. Danilewsky, M. Gelissen, L. Bayarjargal, G. P. Görler, B.O. Hildmann. J. Cryst. Growth 310 (2008) 2288.

[8]. W. L. Gao, H. J. Zhang, S. Q. Xia, B. B. Huang, D. Liu, J. Y. Wang, M. H. Jiang, L. M. Zheng, J. F. Wang, C. J. Lu, Mater. Res. Bull. 45 (2010) 1209.

[9]. H.A. Graetsch, J. Schreuer, M. Burianek, M.M. Uhlberg, J. Solid State Chem.196 (2012) 255.

[10]. S. C. Abrahams, P. B. Jamieson, J. L. Bernstein J. Chem. Phys. 54 (1971) 2355.

[11]. S. P. Gaikwad, V. Samual, R. Pasricha, and V. Ravi, Bull. Mater. Sci. 28 (2005) 121.

[12]. S M. Kaczmarek, M. Berkowski, K. Repow, M. Orowski, A. Worsztynowicz, M. Wlodarski, Rev. Adv. Mater. Sci. 14 (2007) 49.

[13]. C.M.Dudhe,S.B.Nagdeote,R.G. Atram, Materials Letters 176 (2016) 202.

Microwave Absorption Efficiency of CNBs synthesized from Brassica Nigra Oil

Dattatraya E. Kshirsagar

Nanotech Lab., B. K. Birla College, Kalayn, Maharashtra, India

Corresponding author's e-mail address: kesagar2008@gmail.com

ABSTRACT

Spherical carbon nano beads (CNBs) were synthesized by pyrolysis of brassica nigra oil at 850℃ in hydrogen atmosphere in presence of transition metal powder as a catalyst. Micro-Raman spectrum exposes the graphitic nature of material. Scanning electron microscopy (SEM) and Transmission electron microscopy (TEM) illustrate that CNBs are interconnected with outer shell of thickness around 100 nm. A microwave reflection measurement explores an ability of CNBs as an absorber with absorption up to 89% corresponds to reflection coefficient about ˜ -22dB for maximum band width of 0.8GHz in Ku-band.

Keywords : Carbon nano-beads, Pyrolysis, Natural oïl vapour deposition, Microwave absorption

I. INTRODUCTION

Carbon materials have attracted increasing attentions due to their significant electrical and mechanical properties. With rapid developments of information technology and extensive applications of electrical and electronic devices cause increasing electromagnetic wave radiation which is drawing considerable attention as a potential kind of environmental pollution. As one of the ways to overcome these problems is a carbon-based material which play an important role due to their light weight, large surface area, good conductivity and thermal and chemical stability. Usually precursors for getting carbon nano materials are various types of hydrocarbons derived from fossil fuels like methane etc. [1-3], which can be catalytically decomposed into carbon atoms in a chemical vapour deposition unit. But these sources are about to deplete in near future. Therefore there is a need to look for precursors which can be cultivated as and when required like plants material, oil seeds etc. [4-7]. Dubey and Kshirsagar et al [8] tried to synthesize carbon nanomaterial from coconut shell, a natural precursor. Where Sharon et al [9] studied the microwave properties of nanomaterial obtained from camphor. Later on, the attempts were made to utilize carbon nanomaterials for giga hertz frequency applications [10-15]. In this paper we have reported the synthesis of CNBs from natural brassica nigra oil and its properties in Ku-band of microwave frequency region.

II. EXPERIMENTAL

2.1. Materials

Natural brassica nigra oil is pale yellow to brownish yellow liquid, also known as mustard oil. It was used as a precursor, which is derived by hydro-distillation of small round dark brown seeds of mustard plant.

2.2 Sample Preparation

Vapour deposition of linseeds oil was used to synthesize CNBs using a CVD system. This method is discussed in details elsewhere [10]. Ceramic material sheet of 1×3 cm² was used as a substrate for film deposition. A quartz tube of length one meter and 45 mm in diameter was inserted in the vaporizing furnaces. Substrate was kept in the quartz tube at the central hot zone of furnace, temperature of which was maintained at 850°C. Precursor was kept near hot zone whose temperature was maintained around 300°C. The flow rate of hydrogen was maintained in such a way that 5ml of linseeds oil could be transferred to the reaction zone in about 1hr. In the beginning, the entire assembly was flushed with hydrogen for 15 minutes to ensure removal of oxygen from the system. After completion of the reaction, thick films of CNBs deposited on ceramic sheet was taken out at room temperature. Film was characterized before use to study its properties in the range of Ku-band of microwave frequency region.

2.3 Characterizations

Scanning electron microscopy (SEM) with Hitachi S-4300 was used to study the surface morphology of film. Transmission electron microscopy (TEM) image of the film was taken with Field effect TEM, JEOL- 2100F. Micro-Raman spectra using green laser with 532nm excitation was also used to characterize the film. Vander Pauw method was used to measure the sheet resistance of the film. Microwave conductivity, absorption and shielding effectiveness was studied using microwave test bench in 13-18 GHz range.

III. RESULTS AND DISCUSSION

Figure 1 shows the CNBs with diameter of around 550 nm along with some micro size beads of dimension ~2.5μm. These beads are merging with each other and formed a string along with free beads.
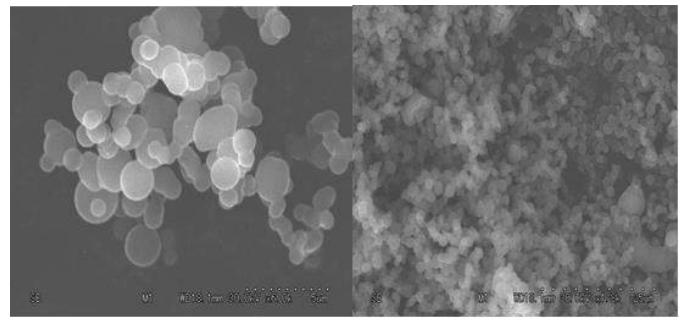

Figure 1. SEM images of CNBs synthesized using brassica nigra oil

TEM shows (figure 2) , the carbon beads are interconnected with each other through outer wall. Here, the inner diameter of beads was observed in the range of 0.45 nm with the thickness of wall about ~ 100nm.
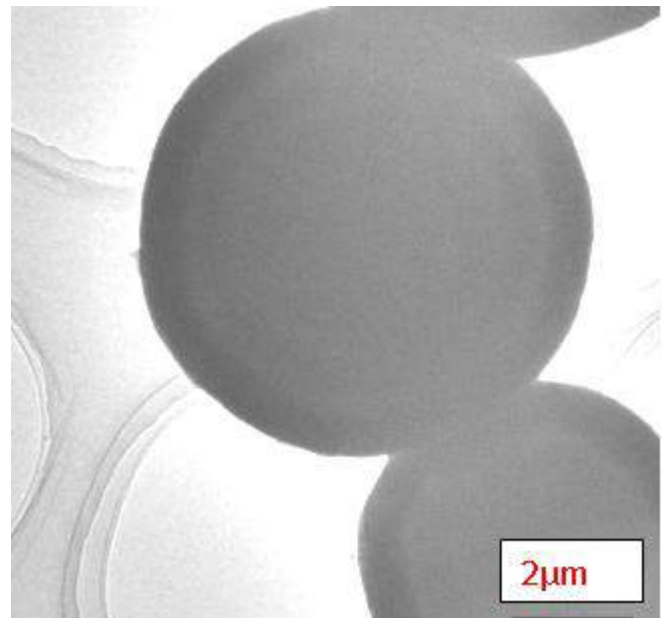

Figure 2. TEM image of CNBs synthesized using brassica nigra oil.

In micro-Raman analysis of samples two broad peaks were observed for the carbon beads, the peak centred at 1588 cm^{-1} was corresponds to standard graphitic G-peak commonly occurring at 1580cm^{-1} .The other peak centred at 1345cm^{-1}, was observed comparatively broad and could be corresponding to disordered carbon D-peak normally observed at 1300-1350cm^{-1}. The ratio of

G to D band intensities indicates the relative amount of highly ordered graphite carbon as compared to amorphous carbon. IG to ID band ratio much greater than unity indicates as abundance of highly ordered graphite and a low amount of undesired carbon content. From the micro-Raman spectra, intensity ratio of graphitic (IG) and disordered graphitic peak (ID) i.e. I_D/I_G for brassica nigra oil based carbon nano beads was found to be 0.89.
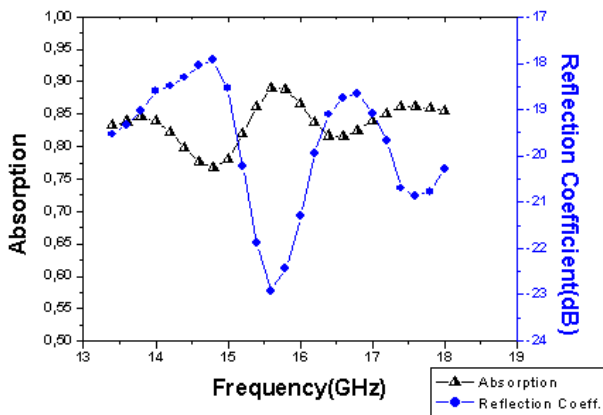

Figure 3. Set of curves showing the relation between reflection coefficient and absorption Vs. Frequency for CNBs films

Figure3, Shows the relation between of reflection coefficient and absorption with respect to frequency. From the curve (figure3),it is seen that, the film of CNBs gives a low reflection of microwave energy on overall frequency range. The reflection coefficient for the film was observed from -20dB to - 22dB in the frequency range 15.2 -16GHz and17.4-18 GHz. For the remaining frequencies RC varies in the range of -17dB to -19dB.As a result the absorption curve explores the efficiency of CNBs as potential microwave absorber in Ku-band with absorption band width of 0.8GHz and 0.6GHz.Overall absorption for the CNBs films was observed in the range of 0.76-0.89 .

An ability to block the passage of microwaves by CNBs was confirmed from EMI shielding effectiveness (SE) study of films in Ku-band. Here, effectiveness of shielding microwave was calculated using equation (1)

$$SE = -20\log T \qquad (1)$$

Where, T is an electromagnetic radiation transmittance.

From the study of shielding effectiveness against frequency , it is observed that CNBs has potential to block the passage of microwaves through the system with EMI SE between -29dB to -40dB on overall Ku-band of microwaves frequency region.

IV. CONCLUSION

Natural Brassica nigra oil was used as a source of carbon nano-beads using simple natural oil vapour deposition method. Microwave absorption study of the as prepared CNBs films material exposed its capability as an absorber in Ku-band of electromagnetic waves with absorption band width of 0.8GHz and 0.6GHz in the frequency range 15.2 -16 GHz and 17.4-18 GHz .Ku-band absorption between 76-89% was observed on overall frequency range indicates its efficiency as an absorber material for various applications.

V. ACKNOWLEDGMENTS

VI. REFERENCES

[1]. Tkachev A. G.; Blinov S. V.; Memetov N. R.; Carbon nanomaterials on the base of catalytic hudrocarbon pyrolysis: Development and Perspective Use Hydrogen materials science and chemistry of carbon nanomaterials 2007,l3,515-519.

[2]. Rud A. D.; Perekos A. E.; Ogenko V. M.; Shpak A. P.; Uvarov V. N.; Chuistov K. V.; Lakhnik A. M.; Voynash V. Z.; Ivaschuk L. I.; Different states

of carbon produced by high-energy plasmochemistry synthesis J. Non-Cryst. Solids 2007, 353, 3650-3654.

[3]. Makeiff D. A.; Huber T.; Microwave absorption by polyaniline-carbon nanotube composites Synth. Met.2006,156, 497-505

[4]. Maheshwar Sharon and Madhuri Sharon, Carbon Nanomaterials and their Synthesis from Plant-Derived Precursors, Int.J. Synthesis and Reactivity in Inorganic, Metal-Organic, and Nano-Metal Chemistry 2006,36,1–15

[5]. Maheshwar Sharon, Cabon Nanomaterials Encyliopedia NanoScience and Nanotechnology, 2004,1, 517-546.

[6]. Mukul Kumar, Xinluo Zhao, Yoshinori Ando, Sumio Iijima, Maheshwar Sharon, and Kaori Hirahara, Carbon nanotubes from camphor by catalytic CVD Mol. Cryst. Liq. Cryst., 2002, 387, 341-345.

[7]. Maheshwar Sharon and Madhuri Sharon, Carbon Nanomaterials: Applications in Physico-chemical and Bio-Systems, Defense Science Journal, Vol. 58, No. 4, July 2008, pp.460-485

[8]. Harish K. Dubey, D. E. Kshirsagar, L. P. Deshmukh, Madhuri Sharon, and Maheshwar Sharon, A New Carbon Material Synthesized from Coconut Shell Advanced Science, Engineering and Medicine 2011, 3, 1–4.

[9]. Maheshwar Sharon, Debabrata Pradhan, Renju Zacharia and Vijaya Puri, Application of carbon nanomaterials as a microwave absorber J. Nanoscience and Nanotechnology, 2005, 5(12), 2117-2120.

[10]. Dattatray E. Kshirsagar, Vijaya Puri, Maheshwar Sharon1, and Madhuri Sharon, Carbon Science, Microwave Absorption Study of Carbon Nano Materials Synthesized from Natural Oils, 2006, 7(4), 245-248.

[11]. Dattatray E. Kshirsagar, Vijaya Puri, Maheshwar Sharon and Madhuri Sharon, Electromagnetic Wave-Absorbing Properties of Pongamia Glabra

Based-CNMs in the 8–12 GHz Range, Synthesis and Reactivity in Inorganic, Metal-Organic, and Nano- Metal Chemistry, 2007, 37:477–479.

[12]. Maheshwar Sharon, Ritesh R Vishwakarma, Datta E Kshirsagar, Madhiri Sharon, Nanotechnology, Carbon for Microwave Absorption, Defence Application, volume 5, chapter-12, page 231-256, Studium Press, LLC, Houston USA),(2013).

[13]. Du J. H.; Sun C.; Bai S.; Su G.; Ying Z.; Cheng H. M.; Microwave electromagnetic characteristics of a microcoiled carbon fibers/paraffin wax composite in Ku band J. Mater. Res. 2002, 17,1232-1236.

[14]. Kwon S. K.; Ahn J. M.; Kim G. H.; Chun C. H.; Hwang J. S.; Lee J. H.; Microwave absorbing properties of carbon black/silicone rubber blend Polym. Eng. Sci. 2002, 42, 2165-2171.

[15]. D.E. Kshirsagar, V. Puri, H. Dubey, M. Sharon, Giga hertz frequency absorber carbon nano fibers synthesized using linseed oil, Materials Today Communications , 2017,13, 23-25.

Comparison of Free Length Thermodynamically and Acoustically of alpha-Alumina (α-Al₂O₃) Nano Suspension in Ethanol Base Fluid

P. D. Bageshwar[1], V. K. Jadhao[2] and N. R. Pawar[3]

[1]Department of Physics, Mungsaji Maharaj Mahavidyalaya, Darwha, Maharashtra, India

[2]Department of Physics, B. B. Arts, N. B. Commerce and B. P. Science College, Digras, Maharashtra, India

[3]Department of Physics, Arts, Commerce and Science College, Maregaon, Maharashtra, India

*Corresponding Author : pdbageshwar@gmail.com

ABSTRACT

The present paper reports the comparison of free length thermodynamically and acoustically of alpha alumina (α-Al₂O₃) nano suspension in ethanol base fluid. α-Al₂O₃ nanoparticles were synthesized through alkoxide route using sol-gel method. Intermolecular free length has been calculated by thermo acoustical method at different temperatures over the entire range of concentrations and compared with the valued obtained from well established thermodynamic method. The ultrasonic velocity measurement at 4 MHz with an interferometric technique has been made on alpha alumina (α-Al₂O₃) nano suspension in ethanol base fluid. Measurement was taken for the density. The intermolecular free length was calculated from the velocity and density measurements. Free length is related with the surface of nanoparticles and nanoparticle surfactant interactions and help for the study of thermo acoustic and thermodynamic properties of nanosuspension.

Keywords : α-Al₂O₃, Ethanol, Free Length, Nanosuspension

I. INTRODUCTION

Extensive use of free length has been made to study the attraction and repulsion forces between the nanoparticles in nanosuspension. Thermo acoustically free length of nanoparticles in nanosuspension is given by, $L_f = K (\beta a)^{1/2} = K/U\rho^{1/2}$

Where βa, U and ρ respectively the adiabatic compressibility, ultrasonic velocity and density of nanoparticles in suspended medium. The constant K is called Jacobson's constant, which depends on temperature. Jacobson determined the value of K empirically between 0 and 50⁰C.

Thermodynamically, free length of nanoparticles in nanosuspension is given by,

$$L_f = 2V_a / A$$

Where V_a and A represents the available volume and the surface area of nanoparticles in nanosuspension. Also,

$$V_a = V - V_O$$

$$A = (36\pi N V_O^2)^{1/3}$$

Where N is the Avogadro number V_O, and V is the molar volume at zero temperature and at temperature T, respectively.

Thermodynamically, the value of V_a can be calculated using critical temperature from the following relation,

$$V_a = V [1- (1- T/Tc)^{0.3}]$$

Where Tc is the critical temperature.

The free length has been widely used to interpret the interactions between nano suspensions in the base fluid. There has been an increasing interest in the study of interactions between the nanoparticles in the suspended medium [1-2]. Ultrasonic study of nanosuspension has been extensively carried out in different branches of science to measure the thermodynamic properties to predict the nature of interactions of nanosuspension in base fluid [3-4]. Ultrasonic velocity and thermo acoustic parameters as a function of the concentration in nanoparticle suspension are useful in gaining insight into the structure and bonding of associated nano complexes and other processes in nanosuspension. The materials of interest in this study are α-Al_2O_3 and ethyl alcohol (C_2H_5OH). Thus ethyl alcohol has an OH group that might be expected to lead to the formation of a hydrogen-bonded nano complex with α-Al_2O_3 at the oxygen site and perhaps electrostatic bonding at the other sites. These types of nanosuspension are of interest to organic chemists who want to know about the type of bond and the number of each kind of nanoparticles in the α-Al_2O_3 nano complex.

In this work, measurements of free length acoustically and thermodynamically are functions of concentration and temperatures are reported. The data presented may stimulate other researchers to consider the interactions of nanoparticles in nanosuspension. Such data are valuable in building a core of basic information about nanosuspension. The method used in the measurement of ultrasonic velocity at 4 MHz was the interferometric method over the temperature range 25-40°C.

The main objective of present work is to contribute the free length of α-Al_2O_3 nanosuspension properties database in current literature in order to better understand the effects of various parameters such as particle size and temperatures. Free length is highly dependent on specific surface area of nanoparticle in nanosuspension.

II. EXPERIMENTAL AND METHODS

The test liquid samples used were spectroquality. All these samples are of BDH analar grade and were assume to be sufficiently pure so that no further purification was necessary. In this study the ultrasonic measurements have been made by interferometric method at fixed frequency 4 MHz over the entire range of concentrations and in the temperature range 25 – 40°C. The velocity of ultrasound thus measured was accurate to within 0.01%. The densities were measured with an Anton Paar DMA 35 N vibrating tube densimeter with a $\pm0.5 \times 10^{-3}$g/cm³ resolution. The temperature of nanosuspension medium was controlled to within 0.2°C. Nanoparticles of alpha alumina (α-Al_2O_3) was prepared by sol-gel method [6-11] from Aluminum isopropoxide [Al $(OC_3H_7)_3$] and aluminum nitrate. The average particle size α-Al_2O_3 has been estimated by using Debye-Scherrer formula. The average estimate size of α-Al_2O_3 nano particles is found to be 20-30 nm Pawar et.al. The prepared α-Al_2O_3 nano particles were suspended in ethanol.

III. RESULTS AND DISCUSSION

The intermolecular forces, which in one way or another determine the said properties of nanosuspension, consist of attractive forces and repulsive forces. These forces have opposite directions but are numerically equal under given external conditions. The attractive forces are dependent on the distance between what are called the centres of attraction of the nanoparticles, whereas the repulsive forces are dependent on the distance between the surfaces of the nanoparticles. Centres of attraction do not coincide with the geometrical centre of the nanoparticles. The distances between the surfaces have a clear physical significance, and thus lend themselves

more easily. Surface tension, viscosity, thermal expansion and molecular association will be related to the intermolecular free length. The acoustic wave which was excited in the nano suspended medium is momentarily to the intermolecular length. Free length is long, ultrasonic velocity has a low value. Its value corresponded to the molecular shape Fig.11 contains the plot of free length computed acoustically versus molar concentration. It shows similar trend as that of adiabatic compressibility and reverse trend as that of ultrasonic velocity which is in good agreement with the theoretical requirement.
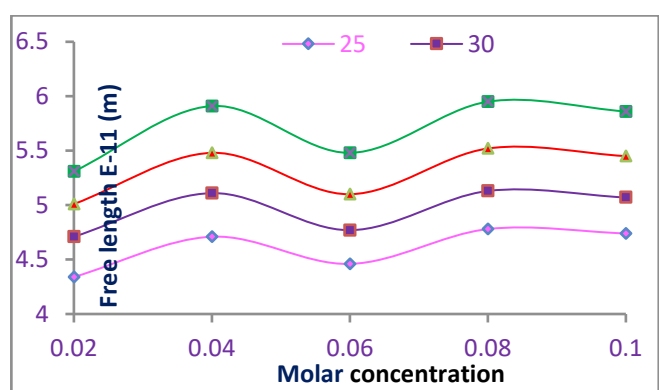

Figure.1 Free length versus molar concentration of α-Al$_2$O$_3$ nanosuspension in ethanol

IV. CONCLUSION

1. The free length computed acoustically and thermodynamically shows considerable deviation from any linear variation with respect to molar concentrations.

2. Non linear variation of free length versus molar concentration is due to Brownian motion of nanoparticles in nanosuspension.

3. Behavior of nanoparticles in ethanol base fluid nano suspension dependent on its specific surface area.

4. Free length study of nanoparticles in nanosuspension highly useful in understanding nature of interactions, internal structure and the aggregation behavior.

V. REFERENCES

[1]. D.H. Kumar, H.E. Patel, V.R.R. Kumar, T. Sundararajan, T. Pradeep, S.K. Das, Model for heat conduction of nanofluids, Physical Review Letters, 2004, 94, 14, 1-3.

[2]. S. Rajagopalan, S. J. Sharma and V. Y. Nanotkar, Ultrasonic Characterization of Silver Nanoparticles, Journal of Metastable and Nanocrystalline Materials 2005, 23 271-274.

[3]. Gan Z, Ning G, Lin Y, Cong Y, Morphological control of mesoporous alumina nanostructures via template-free solvothermal synthesis. Mater Lett 2007, 61, 31, 3758–3761.

[4]. Zhan X, Honkanen M, Leva E Transition alumina nanoparticles and nanorods from boehmite nanoflakes. J Crystal Growth, 2008, 310, 30, 3674–3679.

[5]. Y. K. Park, E. H. Tadd, M. Zubris, and R. Tannenbaum, Size controlled synthesis of alumina nanoparticles from aluminum alkoxides, Materials Reasearch Bulletin, 2005, 40, 9, 1512.

[6]. D. G. Wang, F. Guo, J. F. Chen, H. Liu, and Z. Zhag, Preparation of nano aluminium trihydroxide by high gravity reactive precipitation, Chemical Engineering Journal, 2006, 121, 2-3, 109-114.

[7]. R. Aghababazadeh, A. R. Mirhabibi, J. Pourasad, A. Brown, A. Brydson, and N. Ameri Mahabad, Economical synthesis of Nanocrystalline alumina using an environmentally low-cost binder, Journal of Surface Science, 2007, 601,13,2864-2867

[8]. P. Christian and M. Bromfield, Preparation of small silver, gold and copper nanoparticles which disperse in both polar and non-polar solvents, J. Mater. Chem, 2010, 20, 1135 – 1139.

[9]. Rogojan R, Andronescu E, Ghitulica C, Stefan B, Synthesis and characterization of alumina nano-powder by sol-gel method. UPB Sci Bull Ser B , 2011, 73, 2, 27, 67–76.

[10]. Bhalla V., Kumar R., Tripathi S. and Sing D., Mechanical and thermal properties of praseodymium nanoparticles: an ultrasonic study, Int. J. Mod. Phys. B, 2013, 27, 1350116.

[11]. Pawar N. R., Ph.D thesis Summary on Investigation of Ultrasonic wave absorption in some Bio-liquids, J Pure and Appl Ultrasonic, 2014, 36, 69.

[12]. Pawar N. R. and Chimankar O. P., Comparative Study ultrasonic absorption and relaxation behavior of polar solute and non-polar solvent, Pure and Appl Ultrasonic, 2015, 37, 11.

[13]. Johari G K & Mishra R L, Acustica, 1984, 56, 66.

International E-Conference on Recent Advances in Material Science and Nanotechnology

Organised by

Department of Physics, Arts, Commerce and Science College,
Maregaon, Maharashtra, India
In Association with
Department of Physics, P. N. College, Pusad, Maharashtra, India

Publisher

Technoscience Academy

Website : www.technoscienceacademy.com
Email: info@technoscienceacademy.com